



# **Materials and Acoustics Handbook**

edited by

**Michel Bruneau  
Catherine Potel**

**ISTE**

 **WILEY**

This page intentionally left blank

## Materials and Acoustics Handbook

This page intentionally left blank



# **Materials and Acoustics Handbook**

Edited by  
Michel Bruneau  
Catherine Potel

**ISTE**

 **WILEY**

First published in France in 2006 by Hermes Science/Lavoisier entitled: *Matériaux et acoustique* in 3 volumes © LAVOISIER, 2006

First published in Great Britain and the United States in 2009 by ISTE Ltd and John Wiley & Sons, Inc.  
Translated from French to English by Laure Bossy, Luc Jonveaux, Nicolas Etaix and Aniss Bendjoudi, ESPCI, ParisTech, coordinated by Didier Cassereau, ESPCI, ParisTech

Apart from any fair dealing for the purposes of research or private study, or criticism or review, as permitted under the Copyright, Designs and Patents Act 1988, this publication may only be reproduced, stored or transmitted, in any form or by any means, with the prior permission in writing of the publishers, or in the case of reprographic reproduction in accordance with the terms and licenses issued by the CLA. Enquiries concerning reproduction outside these terms should be sent to the publishers at the undermentioned address:

ISTE Ltd  
27-37 St George's Road  
London SW19 4EU  
UK

[www.iste.co.uk](http://www.iste.co.uk)

John Wiley & Sons, Inc.  
111 River Street  
Hoboken, NJ 07030  
USA

[www.wiley.com](http://www.wiley.com)

© ISTE Ltd, 2009

The rights of Michel Bruneau and Catherine Potel to be identified as the authors of this work have been asserted by them in accordance with the Copyright, Designs and Patents Act 1988.

---

Library of Congress Cataloging-in-Publication Data

Matériaux et acoustique. English

Materials and acoustics handbook / edited by Michel Bruneau, Catherine Potel.

p. cm.

Includes bibliographical references and index.

ISBN 978-1-84821-074-5

1. Acoustical engineering--Handbooks, manuals, etc. 2. Materials--Testing--Handbooks, manuals, etc.  
3. Acoustical materials--Handbooks, manuals, etc. I. Bruneau, Michel, 1937- II. Potel, Catherine. III. Title.

TA365.M3813 2009

620.2--dc22

2009016649

---

British Library Cataloguing-in-Publication Data

A CIP record for this book is available from the British Library

ISBN: 978-1-84821-074-5

---

Printed and bound in Great Britain by CPI/Antony Rowe, Chippenham and Eastbourne.



# Table of Contents

<b>Foreword.</b> . . . . .	xvii
<b>Preface</b> . . . . .	xxi
<b>PART 1. HOMOGENOUS AND HOMOGENOUS STRATIFIED MEDIA:</b>	
<b>LINEAR MODEL OF PROPAGATION</b> . . . . .	1
<b>Chapter 1. Equations of Propagation</b> . . . . .	3
Jean-François DE BELLEVAL, Catherine POTEL and Philippe GATIGNOL	
1.1. Introduction. . . . .	3
1.1.1. Fluid medium . . . . .	3
1.1.2. Elastic solid . . . . .	8
1.2. Solutions of the propagative equation: monochromatic waves, plane waves . . . . .	17
1.2.1. Fluid medium or isotropic solid . . . . .	18
1.2.2. Anisotropic solid . . . . .	20
1.3. Bibliography . . . . .	28
<b>Chapter 2. Interaction of a Plane Wave and a Plane Interface.</b> . . . . .	29
Philippe GATIGNOL, Catherine POTEL and Jean François DE BELLEVAL	
2.1. Introduction. . . . .	29
2.1.1. Boundary conditions in acoustics . . . . .	30
2.1.2. Plane interface separating two fluid or isotropic solid media. . . .	42
2.1.3. Interface separating two anisotropic solid media . . . . .	55
2.2. Bibliography . . . . .	59

<b>Chapter 3. Propagation of Plane Waves in Multilayered Media . . . . .</b>	<b>61</b>
Catherine POTEL, Jean François DE BELLEVAL, Michel CASTAINGS and Philippe GATIGNOL	
3.1. Introduction. . . . .	61
3.1.1. Propagation on a single material layer . . . . .	62
3.1.2. Propagation in a multilayered medium . . . . .	71
3.1.3. Propagation in a periodic multilayered medium . . . . .	82
3.2. Bibliography . . . . .	93
<b>Chapter 4. Propagation in Continuously Stratified Media. . . . .</b>	<b>97</b>
Cécile BARON, Olivier PONCELET, Alexander SHUVALOV and Marc DESCHAMPS	
4.1. Introduction. . . . .	97
4.2. Wave equation for 1D inhomogenous media . . . . .	98
4.2.1. Second-order differential system. . . . .	98
4.2.2. First-order ordinary differential system for the case of 1D inhomogeneity. . . . .	98
4.3. Solution to the wave equation in 1D inhomogenous media. . . . .	101
4.3.1. The matricant . . . . .	101
4.3.2. Evaluation of the matricant by the Peano series . . . . .	102
4.4. Remarks on the numerical implementation . . . . .	104
4.4.1. The Peano series as a power series in dispersion parameters . . . . .	104
4.4.2. Examples. . . . .	105
4.5. Bibliography . . . . .	109
<b>Chapter 5. Modal Waves in Plane Structures. . . . .</b>	<b>113</b>
Philippe GATIGNOL, Catherine POTEL and Jean François DE BELLEVAL	
5.1. Introduction. . . . .	113
5.1.1. General properties of modal waves in plane structures. . . . .	115
5.1.2. Usual modal waves. . . . .	116
5.1.3. Dispersion effects for modal waves . . . . .	128
5.1.4. Generalized modal waves – pseudo modal waves. . . . .	133
5.1.5. A generic example . . . . .	135
5.2. Appendix: non-null elements of determinant $D$ . . . . .	141
5.3. Bibliography . . . . .	143
<b>PART 2. POROUS AND STRATIFIED POROUS MEDIA LINEAR MODELS OF PROPAGATION. . . . .</b>	<b>147</b>
<b>Introduction to Part 2. . . . .</b>	<b>149</b>
Denis LAFARGE	

<b>Chapter 6. The Equivalent Fluid Model</b> . . . . .	153
Denis LAFARGE	
6.1. Introduction. . . . .	153
6.2. Geometry definitions . . . . .	153
6.2.1. Ideal fluid . . . . .	155
6.2.2. Thermoviscous fluids . . . . .	167
6.3. Bibliography . . . . .	202
<b>Chapter 7. Biot's Model</b> . . . . .	205
Denis LAFARGE	
7.1. Introduction. . . . .	205
7.1.1. Perfect fluid and elastic solid . . . . .	207
7.1.2. Thermoviscous fluid and visco-elastic structure. . . . .	225
7.2. Bibliography . . . . .	228
<b>Chapter 8. Propagation Equations in the Time Domain</b> . . . . .	229
Zine EL ABIDINE FELLAH, Mohamed FELLAH and Claude DEPOLLIER	
8.1. Introduction . . . . .	229
8.1.1. Materials: frequency and temporal approach . . . . .	229
8.1.2. Fractional derivative and behavior of materials . . . . .	230
8.1.3. Fractional derivative and viscoelasticity . . . . .	231
8.1.4. Fractional derivative and model of the equivalent fluid . . . . .	231
8.2. Inertial regime (high frequency approximation) . . . . .	232
8.2.1. A semi-infinite medium . . . . .	234
8.2.2. Cases of a finite medium . . . . .	237
8.2.3. Reflection and transmission operators . . . . .	240
8.3. Viscous regime (low frequency approximation) . . . . .	243
8.3.1. Resolution for the semi-infinite medium . . . . .	244
8.3.2. Solution in a finite medium . . . . .	245
8.3.3. Reflection and transmission operators . . . . .	248
8.4. Application to Biot's theory . . . . .	252
8.4.1. Wave propagation in porous materials with a flexible structure . . . . .	252
8.4.2. Displacement equations . . . . .	253
8.4.3. Stress-strain relationships . . . . .	253
8.4.4. Dissipation . . . . .	254
8.4.5. Mass coefficients $\rho_{ij}$ . . . . .	256
8.4.6. Equations in the time domain . . . . .	256
8.4.7. Materials saturated by a liquid . . . . .	258
8.5. Bibliography . . . . .	273

<b>Chapter 9. Scattering in Porous Media</b> . . . . .	277
Denis LAFARGE	
9.1. Introduction. . . . .	277
9.1.1. Analysis of multiple scattering in the context of the Independent Scattering Approximation (ISA) . . . . .	278
9.1.2. Array of cylinders in air . . . . .	279
9.2. Bibliography . . . . .	284
<b>Chapter 10. Stratified Porous Media</b> . . . . .	285
Bruno BROUARD	
10.1. Introduction . . . . .	285
10.2. Matrix representation of the propagation in fluid or solid layers. . . .	286
10.2.1. Propagation in fluids . . . . .	286
10.2.2. Propagation in viscoelastic solids – reciprocity and antireciprocity . . . . .	289
10.2.3. Acoustic behavior of a viscoelastic plate . . . . .	292
10.3. Matrix representation of the propagation in porous layers . . . . .	294
10.3.1. Propagation in porous media with a rigid structure – equivalent fluid model . . . . .	294
10.3.2. Matrix representation of the propagation in porous media with an elastic structure – Biot’s model. . . . .	295
10.4. Modelization and properties of multilayered media . . . . .	296
10.4.1. Generalities . . . . .	296
10.4.2. The matrix representation . . . . .	298
10.4.3. Evaluation of the properties of multilayered structures . . . . .	304
10.5. Appendices . . . . .	308
10.5.1. Appendix A: elements of the transfer matrix $[T_s]$ of a viscoelastic solid . . . . .	308
10.5.2. Appendix B: elements of the impedance matrix $[Z_s]$ of a viscoelastic solid . . . . .	309
10.5.3. Appendix C: elements of the transfer matrix $[T_B]$ of a porous material with elastic frame – Biot’s model . . . . .	310
10.5.4. Appendix D: calculation of the surface impedances on both sides of a multi-layered medium surrounded by two semi-infinite layers of air	313
10.5.5. Appendix E: calculation of the transmission coefficient $T_n$ through a multi-layered medium surrounded by two semi-infinite air layers . . . . .	315
10.6. Bibliography . . . . .	315

<b>Chapter 11. Surface Wave Propagation</b> . . . . .	317
Jean-François ALLARD and Michel HENRY	
11.1. Introduction . . . . .	317
11.1.1. Summary . . . . .	317
11.1.2. Porous material–heavy-fluid interfaces . . . . .	317
11.1.3. Porous material–light-fluid interfaces . . . . .	319
11.2. Bibliography . . . . .	326
<b>Chapter 12. The Finite Element Method for Porous Materials</b> . . . . .	327
Olivier DAZEL and Nicolas DAUCHEZ	
12.1. Introduction . . . . .	327
12.1.1. Position of the problem . . . . .	327
12.1.2. Outline of the finite element method . . . . .	327
12.1.3. History of the finite element method for porous materials . . . . .	328
12.1.4. Continuous problems considered . . . . .	329
12.2. Boundary problem equations . . . . .	329
12.2.1. The $\{u, U\}$ formulation . . . . .	329
12.2.2. The $\{u, P\}$ formulation . . . . .	330
12.2.3. The boundary conditions . . . . .	331
12.3. Poroelastic variational formulations . . . . .	332
12.3.1. The displacement formulations . . . . .	332
12.3.2. Mixed formulations . . . . .	333
12.4. Discretized systems . . . . .	334
12.4.1. Discussion about discretization . . . . .	335
12.5. Conclusion . . . . .	336
12.6. Bibliography . . . . .	336
<b>PART 3. EXPERIMENTAL AND NUMERICAL METHODS.</b> . . . .	339
<b>Chapter 13. Transducer for Bulk Waves.</b> . . . .	341
Daniel ROYER	
13.1. Introduction . . . . .	341
13.1.1. Piezoelectric materials – structures. . . . .	342
13.1.2. One-dimensional model – equivalent circuits . . . . .	348
13.1.3. Frequency and time responses – emitted power . . . . .	353
13.2. Bibliography . . . . .	358
<b>Chapter 14. Modeling of Ultrasonic Beams</b> . . . . .	359
Jean-François DE BELLEVAL, Nicolas GENGEMBRE, Alain LHÉMERY and Pierre CALMON	
14.1. Introduction . . . . .	359
14.2. Plane wave decomposition . . . . .	359

14.2.1. Monochromatic regime . . . . .	360
14.2.2. Impulse regime . . . . .	366
14.2.3. Decomposition into impulse plane waves . . . . .	367
14.3. The pencil method . . . . .	373
14.3.1. General principle of modeling an ultrasonic beam using the pencil method . . . . .	374
14.3.2. The Fermat path . . . . .	376
14.3.3. Definition of a pencil . . . . .	380
14.3.4. Propagation of a pencil . . . . .	384
14.3.5. Reconstruction of the ultrasonic field . . . . .	391
14.3.6. Example . . . . .	393
14.3.7. Conclusions . . . . .	395
14.4. Bibliography . . . . .	396
<b>Chapter 15. Time-Reversal of Waves . . . . .</b>	<b>399</b>
Mickaël TANTER and Mathias FINK	
15.1. Overview . . . . .	399
15.1.1. Introduction . . . . .	399
15.1.2. Time-reversal of acoustic waves: principle . . . . .	400
15.1.3. Time-reversal cavities and mirrors . . . . .	402
15.1.4. Time-reversal or temporal and spatial adapted filtering . . . . .	406
15.1.5. The iterative time-reversal . . . . .	410
15.2. Bibliography . . . . .	412
<b>Chapter 16. Introduction to Inverse Scattering in Acoustics and Elasticity . . . . .</b>	<b>413</b>
Marc LAMBERT, Marc BONNET and Dominique LESSELIER	
16.1. General framework . . . . .	413
16.2. Inverse problem of wave scattering . . . . .	414
16.3. Direct problem . . . . .	417
16.4. Optimizations . . . . .	418
16.5. Other approaches . . . . .	421
16.6. General configuration . . . . .	422
16.7. Illustrations . . . . .	423
16.7.1. Controlled evolution of level sets . . . . .	423
16.7.2. Topological derivative . . . . .	426
16.8. Bibliography . . . . .	428



<b>PART 4. NONLINEAR ACOUSTICS</b>	431
<b>Chapter 17. Nonlinear Acoustic Phenomena in Micro-inhomogenous Media</b>	433
Vitalyi GUSEV, Vincent TOURNAT and Bernard CASTAGNÈDE	
17.1. Introduction	433
17.2. Models of acoustic nonlinearity in micro-inhomogenous media	434
17.2.1. Elastic nonlinearity of an ideal solid	435
17.2.2. Hysteretic nonlinearity of micro-inhomogenous media.	438
17.2.3. Nonlinear acoustic waves in micro-inhomogenous materials with hysteresis independent of the strain rate	448
17.2.4. Nonlinear and non-hysteretic absorption in micro-inhomogenous materials	457
17.2.5. Hysteretic nonlinearity of relaxation processes or relaxation of the hysteretic nonlinearity	461
17.2.6. Hertzian nonlinearity in unconsolidated granular materials	463
17.3. Conclusions	465
17.4. Bibliography	466
<b>Chapter 18. Non-destructive Evaluation of Micro-inhomogenous Solids by Nonlinear Acoustic Methods</b>	473
Vincent TOURNAT, Vitalyi GUSEV and Bernard CASTAGNÈDE	
18.1. Introduction	473
18.2. Classic methods	474
18.2.1. Acousto-elasticity	474
18.2.2. Frequency-mixing	477
18.2.3. Nonlinear resonance	484
18.3. Modern experiments	486
18.3.1. The Luxembourg-Gorky effect (modulation transfer).	486
18.3.2. Self-modulation instability and bistability	491
18.3.3. Nonlinear acoustic effects with a threshold	493
18.3.4. Conclusions	498
18.4. Bibliography	499
<b>PART 5. THE GREEN FUNCTION IN ANISOTROPIC MEDIA</b>	505
<b>Chapter 19. The Cagniard–de Hoop Method</b>	507
Olivier PONCELET and Marc DESCHAMPS	
19.1. Introduction	507
19.2. Preliminaries	508
19.2.1. Principle of the Cagniard–de Hoop method.	508
19.2.2. Inhomogenous plane waves	509
19.3. Propagation in anisotropic media	511

19.3.1. Equations of elastodynamics . . . . .	512
19.3.2. Solutions of the homogenous and non-homogenous wave-equation. . . . .	515
19.4. Two-dimensional Green function in an infinite isotropic medium. . .	517
19.4.1. Analysis of the result . . . . .	523
19.4.2. Why “generalized-rays”? . . . .	523
19.4.3. Graphical interpretation of the Cagniard–de Hoop method . . . .	524
19.4.4. Some examples of waveforms . . . . .	527
19.5. Two-dimensional Green function in an infinite anisotropic medium .	528
19.5.1. Equations of the contours (Cagniard–de Hoop polynomial) . . . .	530
19.5.2. Practical aspects when using the Cagniard–de Hoop contours. . .	533
19.5.3. Examples of waveforms . . . . .	536
19.6. Two-dimensional Lamb problem . . . . .	540
19.6.1. Isotropic medium . . . . .	541
19.6.2. Anisotropic medium . . . . .	546
19.7. Three-dimensional Green function on the surface of an anisotropic medium. . . . .	549
19.8. Bibliography . . . . .	557
 <b>PART 6. LINEAR METHODS OF ULTRASONIC NON-DESTRUCTIVE TESTING AND EVALUATION.</b> . . . . .	 559
 <b>Chapter 20. Measurement of Viscoelastic Modules</b> . . . . .	 561
Michel CASTAINGS	
20.1. Introduction . . . . .	561
20.1.1. General principle . . . . .	561
20.1.2. General scheme of an inverse problem . . . . .	564
20.1.3. Material characterization by measurement of the transmitted ultrasonic field . . . . .	565
20.1.4. Conclusion . . . . .	573
20.2. Bibliography . . . . .	575
 <b>Chapter 21. Interaction of an Ultrasonic Field with a Composite Plate.</b> . .	 577
Philippe GATIGNOL, Catherine POTEL and Jean-François DE BELLEVAL	
21.1. Introduction . . . . .	577
21.1.1. Geometry of the problem and writing of the fields by spatial Fourier representations . . . . .	578
21.1.2. Implementation of a field-calculation method by FFT algorithm. . . . .	586
21.2. Bibliography . . . . .	594

<b>Chapter 22. Flaw Detection by Lamb Waves . . . . .</b>	<b>595</b>
Catherine POTEL, Philippe GATIGNOL and Jean-François DE BELLEVAL	
22.1. Introduction . . . . .	595
22.1.1. Transmission control . . . . .	596
22.1.2. Scan control . . . . .	599
22.1.3. Control using the stress distribution . . . . .	601
22.1.4. Deviation of the Lamb wave beam . . . . .	603
22.2. Bibliography . . . . .	606
<b>Chapter 23. Non-Destructive Testing of Concrete by Ultrasonic Methods. . . . .</b>	<b>609</b>
Vincent GARNIER, Jean-François CHAIX and Gilles CORNELOUP	
23.1. Non-destructive testing of concrete by ultrasonic methods . . . . .	609
23.1.1. The material . . . . .	610
23.1.2. Implementation of ultrasonic measurements . . . . .	612
23.1.3. Examples of applications and developments . . . . .	616
23.1.4. Homogenization applied to concrete . . . . .	636
23.1.5. Conclusions . . . . .	648
23.2. Bibliography . . . . .	648
<b>Chapter 24. Non-Destructive Evaluation and Testing and Structural Health Monitoring of Composite Materials by Ultrasound and Acoustic Emission . . . . .</b>	<b>651</b>
Rachid EL GUERJOUMA, Anne MAREC, Hanane NECHAD and Jean-Hugh THOMAS	
24.1. Introduction . . . . .	651
24.1.1. Health monitoring of polymer matrix based composites in hygrothermal ageing . . . . .	653
24.1.2. On-site health monitoring of polymer based composites stressed in creep: global ultrasonic and acoustic emission approach. . . .	661
24.1.3. Conclusions . . . . .	672
24.2. Bibliography . . . . .	672
<b>PART 7. CHARACTERIZATION OF POROELASTIC MATERIALS . . . . .</b>	<b>675</b>
<b>Chapter 25. Metrology of Physical Parameters of Absorbing Materials. . . . .</b>	<b>677</b>
Michel HENRY, Christophe AYRAULT, Bernard CASTAGNÈDE, Zine EL ABIDINE FELLAH, Claude DEPOLLIÉ, Mohamed FELLAH, Walter LAURIKS and Sohbi SAHRAOUI	
25.1. Introduction . . . . .	677
25.1.1. Acoustical parameters . . . . .	677
25.1.2. Mechanical parameters . . . . .	704
25.2. Bibliography . . . . .	715

<b>Chapter 26. Metrology of Acoustical Properties of Absorbing Materials: Surface Impedance</b> . . . . .	719
Michel HENRY	
26.1. Introduction . . . . .	719
26.1.1. Method of the Kundt tube . . . . .	719
26.1.2. T.M.T.C. method of the Kundt tube . . . . .	723
26.1.3. Other methods: Chung and Blaser . . . . .	729
26.2. Bibliography . . . . .	730
<b>Chapter 27. The Nearfield Acoustical Holography Method</b> . . . . .	733
Bruno BROUARD	
27.1. Principles of the acoustical holography . . . . .	733
27.2. Application to plane geometries . . . . .	734
27.3. Backpropagation . . . . .	736
27.4. Physical interpretation . . . . .	737
27.5. Principle of the experience developed by Tamura . . . . .	737
27.6. Hypothesis . . . . .	738
27.7. Theory . . . . .	739
27.8. Some remarks . . . . .	741
27.9. Appendix A: 2D Fourier transform in cylindrical coordinates . . . . .	742
27.10. Bibliography . . . . .	742
<b>Chapter 28. Prediction of Acoustic Properties of Multilayer Structures – Some Examples of Applications</b> . . . . .	745
Nicolas DAUCHEZ	
28.1. Introduction . . . . .	745
28.1.1. Absorption . . . . .	745
28.1.2. Insulation . . . . .	753
28.2. Bibliography . . . . .	755
<b>PART 8. BIOMEDICAL FIELD</b> . . . . .	757
<b>Chapter 29. Ultrasonic Characterization of the Bone</b> . . . . .	759
Marie-Christine HO BA THO and Pascal LAUGIER	
29.1. Introduction . . . . .	759
29.1.1. <i>In-vitro</i> determination of acoustical and elastic properties . . . . .	759
29.1.2. <i>In vivo</i> determination of acoustic properties (ultrasonic bone mineral density test) . . . . .	779
29.1.3. Simulation and inverse problems . . . . .	787
29.2. Bibliography . . . . .	791

<b>Chapter 30. Medical Ultrasonography</b> . . . . .	793
François TRANQUART, Aurore BLEUZEN, Bruno RICHARD and Léandre POURCELOT	
30.1. Introduction . . . . .	793
30.1.1. Principles, technology, acquisitions and parameters of influence . . . . .	793
30.1.2. Ultrasound modes . . . . .	798
30.1.3. Vascular study by ultrasonic Doppler . . . . .	800
30.1.4. Nonlinear ultrasound imaging. . . . .	804
30.1.5. Medical applications of ultrasound. . . . .	812
30.2. Bibliography . . . . .	824
<b>Chapter 31. Use of Time-reversal</b> . . . . .	827
Mickaël TANTER and Mathias FINK	
31.1. Use of time-reversal . . . . .	827
31.1.1. Monitoring and destruction of kidney stones by time-reversal . .	827
31.1.2. Ultrasound focalization in the brain by time-reversal . . . . .	833
31.1.3. Time-reversal mirror for brain therapy by ultrasound. . . . .	836
31.2. Bibliography . . . . .	839
<b>Chapter 32. Elastography</b> . . . . .	841
Stefan CATHELIN and Rémi SOUCHON	
32.1. Introduction . . . . .	841
32.1.1. Quasi-static elastography . . . . .	842
32.1.2. Dynamic and transient elastography . . . . .	847
32.2. Bibliography . . . . .	859
<b>Chapter 33. Ultrasound and Therapy</b> . . . . .	863
Cyril LAFON, Dominique CATHIGNOL and Jean-Yves CHAPELON	
33.1. Introduction . . . . .	863
33.1.1. Shock waves and extracorporeal lithotripsy . . . . .	864
33.1.2. High intensity focused ultrasounds for ultrasound surgery. . . .	871
33.1.3. Conclusion . . . . .	877
33.2. Bibliography . . . . .	877
<b>Chapter 34. Ultrasound Characterization of Bone Tissues by Poroelastic Theories</b> . . . . .	879
Naima SEBAA, Zine EL ABIDINE FELLAH, Claude DEPOLLIÉ and Walter LAURIKS	
34.1. Introduction . . . . .	879
34.2. Model . . . . .	880
34.3. Longitudinal wave . . . . .	881
34.4. Transmission and reflection operators . . . . .	881

34.5. Inverse problem . . . . .	883
34.6. Experimental set-up and results . . . . .	883
34.7. Conclusion . . . . .	886
34.8. Bibliography . . . . .	886
<b>Chapter 35. Acoustic Tomography, Ultrasonic Tomography . . . . .</b>	<b>887</b>
Jean-Pierre LEFEBVRE, Philippe LASAYGUES, and Serge MENSAH	
35.1. Introduction . . . . .	887
35.1.1. Tomography and inverse propagation/scattering. . . . .	887
35.1.2. Ultrasonic transmission tomography. . . . .	889
35.1.3. Ultrasonic diffraction tomography . . . . .	894
35.1.4. Conclusion . . . . .	905
35.2. Bibliography . . . . .	906
<b>List of Authors . . . . .</b>	<b>907</b>
<b>Index . . . . .</b>	<b>913</b>

## Foreword

It is with great pleasure that we are writing a few lines of introduction for the book *Materials and Acoustics Handbook*: after being persuaded that this book responds to an obvious need and that it contributes to the affirmation of a research field, which is currently experiencing much development, situated as it is at the crossroads of several disciplines.

It is interesting first of all to spend several moments reflecting on the title of this book. Those who have followed the recent developments of the fields to which this book makes reference will have noticed the structuring efforts carried out on the one hand by the Acoustics community and on the other hand the Material Mechanics community over the last 20 years. These respective structurings corresponded to the desire by researchers involved in these fields to be better identified and thus better recognized. However, they were also made necessary by the need for training specific to these fields, expressed by the world of work. A better identification of each of these fields is thus accompanied by the birth of new educational pathways in universities or engineering schools, of benefit, along with this book, as an extremely useful teaching tool. The two communities concerned, although certainly very different, have naturally interacted, and the creation of actions in the fields of “Materials for Acoustics” or “Acoustics for Materials” have been assisted, in which the role of each has been clearly identified, either as regards the final objective or as regards the means to achieve it. This book goes further, Materials and Acoustics are closely linked, and we are convinced this will play a driving role in bringing together these two communities, which is already underway.

The content of this book thus principally covers the propagation of acoustic waves in solid or porous, i.e. multi-phase (fluid-solid), materials. All of these terms can be discussed endlessly as they are evolving as research and applications advance. Thus, acoustics basically means what we assume on the one hand to be a propagation medium (fluid) and on the other hand a so-called audible range of

frequencies. Inevitable extensions are made to high or low frequencies (ultrasound or infrasound) and other media. In order to illustrate this, let us discuss the terms medium and frequency.

As far as the medium is concerned, propagation in a solid is more complicated than in a fluid (in any case, a fluid at rest and without dissipation), due to the presence of transverse waves. The (vectorial) “elastic waves” are more general than (scalar) “acoustic waves”. However, for the porous materials often used to reduce the “audible” noise and in this case called “acoustic materials”, we tend to talk about acoustic waves instead, even if all waves existing in solids are found there! Often, if the excitation is made via a fluid, the material in fact behaves in a similar way to a fluid, but this is not the case when the excitation is solid in nature. Many media other than acoustic materials are porous, and wave propagation within them is the object of countless works of research with essential applications such as geophysics or oil exploration.

As far as frequency is concerned, even if this work devotes a large part to ultrasound, particularly for applications such as non-destructive testing (NDT) and medical imaging, the methods developed are as general as possible. In certain problems, low frequency waves propagating in solids are in fact essential; for example, when it is a question of “seismic waves” in the earth. It is thus necessary not to immediately limit ourselves to a range of frequencies. Furthermore, it is becoming increasingly common to use temporal methods (rather than frequential methods) for both the generation of testing frequencies as well as for the analysis of the response of propagation media.

This book does not discuss vibroacoustics, another field where the mechanics of solids and acoustics are closely linked. Vibroacoustics are concerned with the response of structures (rather than propagation in a 3D element) and modeling tools corresponding to this are of a different type.

Having finished with these preliminaries, we will now move on to the essential matters. We will not analyze the book chapter by chapter. For the benefit of the reader however, it is useful to point out several notable characteristics in order to guide the reader through the various parts. Parts 1 to 5 contain the mathematical or physical foundations, useful theories for comprehension of the subject. Parts 6 to 8 are mainly dedicated to putting into practice the concepts and methods from Parts 1 to 5.

– Any reader concerned with becoming more familiar with the basics on linear waves will find a complete discussion on their propagation in different types of media, whether fluid or solid, isotropic or anisotropic, homogenous or stratified, in Part 1. This discussion can be used directly at a Master’s level, but can also be used



for a direct algorithmic implementation (we are thinking for example of transfer matrix formalism, which is well adapted to the systematic study of stratified media).

- This general discussion is completed by more technical results on research into Green functions in anisotropic media or into propagation in continuously stratified media, detailed in Chapters 4 and 19, which benefit from a second reading to deepen knowledge.

- Porous media, very important on the fundamental plane on that of its applications (acoustic comfort, imaging of biological tissues) and their modeling, are the subject of Part 2. The derivation of Biot's model (around which the international community is forming itself into regular annual world conferences) is discussed in several types of literature, ranging from everything macroscopic to the micro-macro passage through asymptotic developments. The presentation here favors average methods as well as the Lagrangian formalism approach. The first step clearly affects the essential role played by the microstructure of materials especially through the concepts of tortuosity or permeability as well as the frequency limit of different developed models. Part 2 furthers and completes the founding work by Johnson and the pioneering book by Jean-François Allard using recent developments. It also contains an opening on numerical methods (implementation of Biot's model in a finite element code).

- Still in Part 2 we will find, in addition to the highly expanded frequential analysis, a formulation in the temporal domain of the behavior laws of porous materials, particularly with the viscoelasticity models with fractional derivatives which are still relatively little-known concepts, at least sparingly covered by reference works.

- Nonlinear acoustics, which reveal for example wave propagation in granular media and more generally in heterogeneous nonlinear media or media with nonlinear interactions, are discussed in Chapter 17.

- In Part 3, under the rubric of experimental or numerical methods, we will find the foundations of the experimental approaches (impulse response of a sensor, problems of temporal reversal, an approach using inverse problems for the identification of characteristics of a propagation media).

Parts 6 to 8 echo the concepts and methods presented in the previous parts but on the level of applications and implementation:

- Any reader interested in non-destructive testing applications of linear propagation methods of the different types of waves described in Part 1 should look at Part 6. You will find there in particular a discussion on the application of Lamb waves for checking thin composite structures that are found throughout aeronautics (plates or shells).

– If we want to understand how to exploit the subtleties of nonlinear acoustics discussed in Chapter 17 within the framework of NDT we should move to Chapter 18, the defects often being accompanied by the apparition of nonlinearities (like frictional contact on the edges of a crack).

– If we would like to put the models of porous media from Part 2 into practice and measure, either in the frequential domain or the temporal domain, the different parameters existing in Biot's models, should go directly to Part 7.

– Finally, if we would like to have a complete view of the different imaging methods being developed in the biomedical domain, including ultrasonic tomography, we will be happy to discover it in Part 8.

The 50 or so authors contributing to this book offer us a panorama of the state of the art of the field of Materials and Acoustics in 2006 that is as complete as possible. The fact that this book was originally created in French shows in our eyes the driving force and creativity of the French School in this field. This is a reference work which will be of interest to both Master's and PhD students, as well as research engineers in the fields of materials, acoustic comfort, non-destructive testing and medical imaging – to mention only a few of the possible fields of application.

We must finally applaud the work of the coordinators of this book, Michel Bruneau and Catherine Potel. To obtain manuscripts from 50 authors, avoiding redundancies and interferences between the different contributions as far as possible, was not an easy task. They have managed it and for this they must be congratulated and thanked.

*Jean Kergomard*  
CNRS Research Director  
President of the Société Française  
d'Acoustique

*Pierre Suquet*  
CNRS Research Director  
Professor at the Ecole Polytechnique, Paris  
Membre de l'Institut

## Preface

This collective work tries to fill a gap in scientific publishing in the fields grouped under the expression “Materials and Acoustics”. At least, that was the starting objective of the editorial committee who gave us the mission of coordinating everything that needed to be done.

From the preliminary outlines of the book, to the creation of the index, this project has enjoyed varying fortunes. However, the result is such that the basics of the fields covering the themes of “acoustics for materials” and “materials for acoustics”, from current results of basic research (Parts 1 to 5 for the essentials) to applications (especially Parts 6 to 8), are presented in this work.

The construction of this book has been governed by a certain logic, following which the essential, imperative elements generally precede presentations of applications. However, the contribution of each author remains understandable on its own.

Ignoring the fact that no-one can ever be completely happy, we would sincerely like to thank every author for the confidence they have put in us and for their support in this collective work.

*Michel BRUNEAU*  
*Catherine POTEL*

This page intentionally left blank

Part 1

# Homogenous and Homogenous Stratified Media: Linear Model of Propagation

This page intentionally left blank

## Chapter 1

# Equations of Propagation

### 1.1. Introduction

Acoustic (or elastic) waves are disturbances of a deformable medium (fluid or solid) propagating step by step into it by the actions of elementary particles on their neighbors. They do not exist in a vacuum.

We will consider the medium as continuous (continuum mechanics), that is to say we will take an interest in elementary volumes which are much larger than atoms or molecules; it will be assumed that this volume contains a great number of these elements. We will sometimes name this volume “fluid or solid particles”. The acoustic equations will therefore result from those of continuum mechanics.

We will first consider the medium as homogenous. In the absence of acoustic waves, it is in equilibrium. The acoustic waves will disturb this equilibrium but this disturbance will be small and will allow the equations to be linearized. The movement of the particles related to the wave will be described by a specific number of variables which will depend on the nature of the medium studied.

#### 1.1.1. *Fluid medium*

In the case of fluid media, the classic variables we are interested in are the vector of the particle speed  $\vec{v}$ , the pressure  $p$  and the density  $\rho$ ; consequently, there are three variables among which one is vectorial, and we need the same number of

equations in order to solve the problem. We will assume a certain number of simplifying hypotheses; we will specifically neglect the viscosity and will suppose that, in the absence of acoustic waves, the fluid is at rest (no flow) and that there is no external force. Then the variables considered satisfy three equations. One is vectorial, the mass conservation law, one is the fundamental equation of dynamics, general equations for all fluids, and the other is the medium state equation which characterizes its properties.

#### 1.1.1.1. *Mass conservation law*

This relationship shows that the mass rise in a particular volume is opposed to the mass outflow through the surface surrounding the volume. Locally it is given by the following equation:

$$\frac{\partial \rho}{\partial t} + \text{div}(\rho \vec{v}) = 0 . \quad [1.1]$$

#### 1.1.1.2. *Fundamental equation of dynamics*

In the absence of external forces, the only force applied on the elementary volume is the pressure gradient. This equation is therefore:

$$\rho \left\{ \frac{\partial \vec{v}}{\partial t} + (\vec{v} \cdot \text{grad}) \vec{v} \right\} + \text{grad}(p) = 0 . \quad [1.2]$$

#### 1.1.1.3. *State equation*

The mechanical properties of the fluid medium are characterized by its state equation. We are generally interested in sufficiently fast pressure variation (and consequently in density variation), which allows the thermal exchanges between the elementary volumes to be neglected, the transformation of each element being adiabatic. Then the state equation can be expressed as a relationship between pressure and density:

$$p = g(\rho) . \quad [1.3]$$

We will be interested only in fluids that have the following properties (barotropic ideal fluids): the function  $g(\rho)$  is positive as well as its first and second derivatives. We now introduce the following notation:



$$V_0^2 = \frac{dg}{d\rho}. \quad [1.4]$$

The quantity  $V_0$  has the dimension of a speed; that is the definition of the velocity of sound in a fluid. The compressibility factor of the fluid is defined by:

$$\chi = \frac{1}{\rho} \frac{d\rho}{dp}. \quad [1.5]$$

The velocity is then:

$$V_0 = \sqrt{\frac{1}{\chi\rho}}. \quad [1.6]$$

#### 1.1.1.4. Linearization of equations

Linear acoustics studies motions with small amplitudes of the particles around a balance state characterized by a constant pressure  $p_0$  and density  $\rho_0$ , and a null flow speed. That is why these quantities are written as unchanging values to which are added small variations, that is to say:

$$p = p_0 + p_1, \quad \rho = \rho_0 + \rho_1, \quad \text{and} \quad \vec{v} = \vec{v}_1, \quad [1.7]$$

with

$$p_1 \ll p_0, \quad \rho_1 \ll \rho_0, \quad \text{and} \quad |\vec{v}_1| \ll V_0. \quad [1.8]$$

Considering these equations and conserving only first-order terms, equations [1.1] to [1.3] become:

$$\frac{\partial \rho_1}{\partial t} + \text{div}(\rho_0 \vec{v}_1) = 0, \quad [1.9]$$

$$\rho_0 \frac{\partial \vec{v}_1}{\partial t} + \overrightarrow{\text{grad}} p_1 = 0, \quad [1.10]$$

$$p_0 + p_1 = g(\rho_0 + \rho_1) = g(\rho_0) + \rho_1 \frac{dg}{d\rho}. \quad [1.11]$$

Considering  $\overline{p_0} = g(\rho_0)$  and  $V_0^2 = dg/d\rho$ , these equations become:

$$\frac{\partial \rho_1}{\partial t} + \rho_0 \operatorname{div}(\vec{v}_1) = 0, \quad [1.12]$$

$$\rho_0 \frac{\partial \vec{v}_1}{\partial t} + \overrightarrow{\operatorname{grad}} p_1 = 0, \quad [1.13]$$

$$p_1 = V_0^2 \rho_1. \quad [1.14]$$

There are five scalar equations for five unknown quantities  $p_1$ ,  $\rho_1$  and  $v_1$ .

#### 1.1.1.5. Velocity potential and Wave equation

It can be shown, from equation [1.13], that the particle speed vector is irrotational, that is to say it derives from a scalar potential  $\varphi$  ( $\vec{v}_1 = \overrightarrow{\operatorname{grad}} \varphi$ ). Equations [1.12] and [1.14] also allow us to calculate the variables  $p_1$  and  $\rho_1$  from this potential:

$$\vec{v}_1 = \overrightarrow{\operatorname{grad}} \varphi, \quad [1.15]$$

$$p_1 = -\rho_0 \frac{\partial \varphi}{\partial t}, \quad [1.16]$$

$$\rho_1 = -\frac{\rho_0}{V_0^2} \frac{\partial \varphi}{\partial t}. \quad [1.17]$$

Transferring equations [1.15] and [1.17] in the linearized mass conservation law [1.12], and considering the relationship  $\operatorname{div} \overrightarrow{\operatorname{grad}} \varphi = \Delta \varphi$  where  $\Delta \varphi$  refers to the Laplacian of  $\varphi$ , we obtain successively:

$$-\frac{\rho_0}{V_0^2} \frac{\partial^2 \varphi}{\partial t^2} + \rho_0 \operatorname{div} \overrightarrow{\operatorname{grad}} \varphi = 0,$$

then:

$$\Delta \varphi - \frac{1}{V_0^2} \frac{\partial^2 \varphi}{\partial t^2} = 0. \quad [1.18]$$

Equation [1.18] is called the wave equation; it is applied here to the scalar variable  $\varphi$ . The three variables  $p_1$ ,  $\rho_1$  and  $v_1^2$  are deduced from  $\varphi$  by equations [1.15] to [1.17]. Furthermore, each of these variables satisfies the wave equation.

#### 1.1.1.6. *Energy conservation law*

Combining the previously obtained equations, it is easy to deduce the energy conservation law. It is written:

$$\frac{\partial}{\partial t} \left( \frac{1}{2} \rho_0 \vec{v}_1^2 + \frac{1}{2} \frac{p_1^2}{\rho_0 V_0^2} \right) + \text{div} (p_1 \vec{v}_1) = 0. \quad [1.19]$$

This is a first order partial differential equation that contains only small terms of the second order. In this equation:

$\frac{1}{2} \rho_0 \vec{v}_1^2$  is the bulk density of kinetic energy,

$\frac{1}{2} \frac{p_1^2}{\rho_0 V_0^2}$  is the bulk density of potential energy.

This energy conservation law expresses that the energy variation in a closed volume is equal to the energy outflow of the volume considered.

#### 1.1.1.7. *Remarks*

It is essential that the evolution of acoustic perturbations is described by a wave equation which can be applied to any of the variables  $\phi$ ,  $p_1$ ,  $\rho_1$  and  $\vec{v}_1$  or to the particular displacement vector  $\vec{u}_1$ . A direct consequence of linear acoustics is the irrotational property of the speed (or displacement) field of the acoustic perturbation; that explains the equivalence between the vectorial fields ( $\vec{v}_1$  or  $\vec{u}_1$ ) and the scalar fields  $p_1$  and  $\rho_1$ . This will not be true in the case of solids, for which the problem will be a little more complicated.

Later, we will focus on small variations of physical quantities (until now denoted with subscript 1); they will be written without subscript, in order to simplify the forward expressions, keeping the subscript 0 for average values of these quantities.

### 1.1.2. Elastic solid

The mechanical properties of solids are basically different from those of fluids; they are expressed by relationships between internal stresses (more complex than a simple pressure) and local deformation of the solid around a point. Thus, it is necessary to introduce the strain tensor in order to characterize these deformations and the stress tensor to characterize the internal efforts. The acoustic field can no longer be expressed by a simple scalar variable; the base variable generally used is the particular displacement  $\vec{u}$ .

#### 1.1.2.1. Strain tensor

The local deformations of a solid around a given point will naturally be expressed from the total differential of the displacement vector, which can be written in a Cartesian coordinate system:

$$d\vec{u} = \frac{\partial \vec{u}}{\partial x_1} dx_1 + \frac{\partial \vec{u}}{\partial x_2} dx_2 + \frac{\partial \vec{u}}{\partial x_3} dx_3 = (\overrightarrow{\text{grad}} \vec{u}) \cdot d\vec{x}, \quad [1.20]$$

$\overrightarrow{\text{grad}} \vec{u}$  is a second order tensor, which can be broken up as a sum of a symmetric tensor and a antisymmetric tensor:

$$\overrightarrow{\text{grad}} \vec{u} = (\overrightarrow{\text{grad}} \vec{u})_s + (\overrightarrow{\text{grad}} \vec{u})_a. \quad [1.21]$$

The antisymmetric part corresponds to a rotation of the considered element, while the symmetric part corresponds to its deformation, that is to say it represents its length variation. This tensor is called the strain tensor and will be noted  $\underline{S}$ . Considering its symmetry, it has six independent components which are written in the considered Cartesian system:

$$S_{ij} = \frac{1}{2} \left( \frac{\partial u_i}{\partial x_j} + \frac{\partial u_j}{\partial x_i} \right). \quad [1.22]$$

#### 1.1.2.2. Stress tensor

In the case of solids, the internal strains are due to molecular interaction forces with very short range. They can be modeled by forces acting through the surface separating two small adjacent elements of the solid. That is why they will be characterized by a surface density of forces at each point, that depends on the orientation of the normal  $\vec{n}$  to the considered elementary surface  $dS$ .

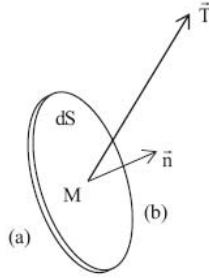


**Figure 1.1.**

Within the solid, the elementary surface  $dS$  divides, in the neighborhood of the considered point  $M$ , the material into two domains (a) and (b). On each side of  $dS$ , particles of both domains are found; particles of (a) apply an elementary force  $d\vec{F} = \vec{T} dS$  on the particles of (b). The vector  $\vec{T}(M, \vec{n})$ , which has the dimension of a surface force, is the stress vector at the point  $M$  relative to the direction  $\vec{n}$ . According to the action–reaction principle, particles of (b) apply on particles of (a) an equal and opposite force. Let us note that in the solid case, the vector  $\vec{T}(M, \vec{n})$  is generally not collinear to  $\vec{n}$ ; its normal component (projection on  $\vec{n}$ ) corresponds to a traction–compression strain and its tangential component (projection on the plane normal to  $\vec{n}$ ) to a shear strain.

We can show that the fundamental equation of dynamics implies that the relationship between  $\vec{n}$  and  $\vec{T}$  is linear. Consequently, this relationship defines a tensor  $\overline{\overline{T}}$ , of second order, named stress tensor. It can be shown that this tensor is symmetric.

It follows from the definition of this tensor that, in a Cartesian system, the components of the  $i$ th column vector of the matrix of the components of  $\overline{\overline{T}}$  represent the components of the stress vector corresponding to a surface element perpendicular to the axis  $i$ . In the fluid case, this tensor is reduced to a spherical tensor whose components are equal to  $-p\delta_{ij}$ . The minus sign comes from the difference of sign convention adopted between stress in the case of solids and pressure in the case of fluids.

The mechanical properties of solids will be characterized by relationships between stress and strain (behavior law). We will first take an interest only in linear elasticity (as for the fluids, the stresses and strains will be considered small enough),

that is to say that the stress and strain tensors will be deduced from each other by a linear transform (Hooke's law).

### 1.1.2.3. *Isotropic solids*

#### 1.1.2.3.1. Stress-strain relationship

If the solid is isotropic, that is to say if its properties are the same in every direction, it can be shown that these relationships are expressed by two constants only, for example the Lamé constants, which enables us to write them in the following way:

$$T_{ij} = \lambda S_{ll} \delta_{ij} + 2\mu S_{ij}. \quad [1.23]$$

In all the following, indicial expressions will use the Einstein convention (also known as the Einstein summation): when an index variable appears twice in a single term, it implies that we are summing over all of its possible values. Using this convention, we obtain:  $S_{ll} = S_{11} + S_{22} + S_{33}$ .

These relationships can also be expressed as a function of the Young's modulus  $E$  and Poisson's ratio  $\nu$  in the following ways (direct and inverse):

$$S_{ij} = \frac{1}{E} [(1 + \nu) T_{ij} - \nu T_{ll} \delta_{ij}], \quad [1.24]$$

$$T_{ij} = \frac{E}{1 + \nu} \left[ S_{ij} + \frac{\nu S_{ll}}{1 - 2\nu} \delta_{ij} \right]. \quad [1.25]$$

The comparison of equations [1.23] and [1.25] allows us to deduce the relationships between these constants:

$$\lambda = \frac{E \nu}{(1 + \nu)(1 - 2\nu)} \quad \text{and} \quad \mu = \frac{E}{2(1 + \nu)}. \quad [1.26]$$

#### 1.1.2.3.2. Equation of motion

In the solid case, the fundamental equation of dynamics is written:

$$\rho \frac{\partial^2 \vec{u}}{\partial t^2} = \vec{F} + \text{div} \vec{T}, \quad [1.27]$$

where  $\vec{F}$  is the resultant of the exterior bulk forces which will be supposed static. Taking account only in small variations around the equilibrium position, let us

separate stresses into two parts, one corresponding to static stresses at equilibrium (subscript 0) and another (subscript 1) corresponding to elastic waves:

$$\bar{\bar{T}} = \bar{\bar{T}}_0 + \bar{\bar{T}}_1 . \quad [1.28]$$

The equation at equilibrium is written in the following way:

$$\bar{F} + \text{div } \bar{\bar{T}}_0 = 0 , \quad [1.29]$$

which allows us to write equation of motion [1.27] as a function of the only part corresponding to the perturbation of equilibrium in the following way:

$$\rho \frac{\partial^2 \bar{u}}{\partial t^2} = \text{div } \bar{\bar{T}}_1 . \quad [1.30]$$

As we are only interested in waves, thus to the part of the stress tensor with subscript 1, we now omit this subscript in order to simplify the forward expressions, as has been done for fluids.

Considering the stress-strain relationships given by equation [1.25] and the expression of the strain tensor as a function of the displacement vector [1.22], the right-hand side of [1.30] can be expressed as a function of the single variable  $\bar{u}$ . The equation then becomes:

$$\rho \frac{\partial^2 \bar{u}}{\partial t^2} = \frac{E}{2(1+\nu)} \left[ \Delta \bar{u} + \frac{1}{(1-2\nu)} \overrightarrow{\text{grad}}(\text{div} \bar{u}) \right] . \quad [1.31]$$

#### 1.1.2.3.3. Elastic wave equation

Let us introduce the following quantities which have the dimensions of a speed:

$$V_L = \sqrt{\frac{E(1-\nu)}{\rho(1+\nu)(1-2\nu)}} , \quad V_T = \sqrt{\frac{E}{2\rho(1+\nu)}} , \quad [1.32]$$

That leads us to write equation [1.31] in the following way:

$$\frac{\partial^2 \bar{u}}{\partial t^2} = V_T^2 \Delta \bar{u} + (V_L^2 - V_T^2) \overrightarrow{\text{grad}}(\text{div} \bar{u}) . \quad [1.33]$$

A vectorial field can be broken into two fields, one with null rotational and the other with null divergence. We can then write:

$$\vec{u} = \vec{u}_L + \vec{u}_T, \quad [1.34]$$

with:

$$\overrightarrow{\text{rot}} \vec{u}_L = 0 \quad \text{and} \quad \text{div} \vec{u}_T = 0. \quad [1.35]$$

From these relationships, it is possible to show that each of the two strain fields  $\vec{u}_L$  and  $\vec{u}_T$  satisfies a wave equation. These equations are written:

$$\frac{\partial^2 \vec{u}_L}{\partial t^2} - V_L^2 \Delta \vec{u}_L = 0 \quad \text{or} \quad \Delta \vec{u}_L - \frac{1}{V_L^2} \frac{\partial^2 \vec{u}_L}{\partial t^2} = 0 \quad [1.36]$$

$$\frac{\partial^2 \vec{u}_T}{\partial t^2} - V_T^2 \Delta \vec{u}_T = 0 \quad \text{or} \quad \Delta \vec{u}_T - \frac{1}{V_T^2} \frac{\partial^2 \vec{u}_T}{\partial t^2} = 0 \quad [1.37]$$

The perturbation field is broken into two wave fields, the one whose curl is zero corresponds to waves propagating with speed  $V_L$ ; these waves will be named compression waves (associated strains are of traction–compression type). The other one, whose divergence is zero, corresponds to waves propagating with speed  $V_T$  and these waves will be named shear waves (associated strains are of shear type).

Let us observe that the propagation speeds can be expressed from Lamé's constants; they become:

$$V_L = \sqrt{\frac{\lambda + 2\mu}{\rho}}, \quad \text{and} \quad V_T = \sqrt{\frac{\mu}{\rho}}. \quad [1.38]$$

The displacement field corresponding to compression waves being irrotational, derives from a scalar potential and can therefore be written:

$$\vec{u}_L = \overrightarrow{\text{grad}} \phi. \quad [1.39]$$

The field corresponding to shear waves, having a null divergence, can be written as the curl of a vector  $\vec{\psi}$ , called potential vector of these waves:

$$\vec{u}_T = \overrightarrow{\text{rot}} \vec{\psi}. \quad [1.40]$$

These two potentials satisfy the wave equation, with a speed  $V_L$  for  $\phi$  and a speed  $V_T$  for  $\vec{\psi}$ .



*Remarks*

The variables  $\phi$  and  $\vec{\psi}$  correspond to four scalar variables, whereas the displacement field depends only on three. An additional relationship can therefore be set between these variables, for example the relationship:

$$\text{div } \vec{\psi} = 0 . \quad [1.41]$$

$\phi$  and  $\vec{\psi}$  are displacement potentials whereas, in the case of fluids, the potential  $\phi$  was a velocity potential.

The compression waves can be expressed as a function of a scalar variable (for example the potential  $\phi$ ); these waves are of the same kind as those which propagate in a fluid. Shear waves are expressed as a function of a vectorial variable (displacement or vector potential  $\vec{\psi}$ ) whose components are not independent (they are related by a relationship, for example equation [1.41]) and then are expressed as a function of two scalar variables.

1.1.2.4. *Anisotropic solid*

## 1.1.2.4.1. Stress-strain relationship

An anisotropic solid has, by definition, properties which depend on the direction in which we are interested. For example if traction is applied on such a solid, its reaction to this force will depend on the direction in which the force is applied. The parameters characterizing the local mechanical state are the same as those defined for isotropic solids (strain tensor and stress tensor), however the stress-strain relationships will be expressed by a larger number of parameters [ROY 96]. If we always consider only linear elasticity (Hooke's law), as it has already been specified, the strain and stress tensors are deduced from one another by a linear transform; considering that the two tensors are of second order, this transform corresponds to a fourth-order tensor (called the elastic stiffness tensor), which is expressed theoretically with the help of  $3^4 = 81$  components.

Then the relationships can be written:

$$\vec{T} = \underset{\text{c}}{\overset{\equiv}{\equiv}} : \vec{S} , \quad [1.42]$$

or in Cartesian coordinates:

$$T_{ij} = c_{ijkl} S_{kl} . \quad [1.43]$$

Actually, the stress and strain tensors being both symmetric, each depends only on six independent components, which reduces the number of independent components for the stiffness tensor to 36. The components obtained by commuting the first two or last two indices are equal:

$$c_{ijkl} = c_{jikl} \text{ and } c_{ijkl} = c_{ijlk} . \quad [1.44]$$

Hooke's law is written as a function of the displacements:

$$T_{ij} = \frac{1}{2} c_{ijkl} \frac{\partial u_k}{\partial x_l} + \frac{1}{2} c_{ijkl} \frac{\partial u_l}{\partial x_k} . \quad [1.45]$$

As  $c_{ijkl} = c_{ijlk}$  , the two sums are equal:

$$T_{ij} = c_{ijkl} \frac{\partial u_k}{\partial x_l} = c_{ijlk} \frac{\partial u_l}{\partial x_k} . \quad [1.46]$$

As it is difficult to write all these components of the stiffness tensor in this form, equation [1.46] is often written in a matrix form using a 6 x 6 matrix, where each set of indices  $ij$  and  $kl$  is replaced by a single one, noted  $\alpha$  and  $\beta$ , and numbered from 1 to 6 with the help of the following relationships:

$$\begin{aligned} (11) &\leftrightarrow 1 & (22) &\leftrightarrow 2 & (33) &\leftrightarrow 3 \\ (23) = (32) &\leftrightarrow 4 & (13) = (31) &\leftrightarrow 5 & (12) = (21) &\leftrightarrow 6 \end{aligned} \quad [1.47]$$

By using this notation for the components of the stress and strain tensor, the relationships are written:

$$T_\alpha = c_{\alpha\beta} S_\beta \quad \text{with} \quad \alpha, \beta = 1, 2, 3, \dots, 6. \quad [1.48]$$

where

$$T_\alpha = T_{ijkl} ,$$

and

$$S_1 = S_{11} \quad S_2 = S_{22} \quad S_3 = S_{33} \quad S_4 = 2S_{23} \quad S_5 = 2S_{13} \quad S_6 = 2S_{12} , \quad [1.49]$$

It is possible to express the strains as function of the stresses by inverting the formula [1.43]. Then the flexibility tensor is obtained:

$$S_{ij} = s_{ijkl} T_{kl} . \quad [1.50]$$

This inversion can also be done using equation [1.48]. The matrix  $s_{\alpha\beta}$  being the inverse of the matrix  $c_{\alpha\beta}$ , we obtain:

$$S_{\alpha} = s_{\alpha\beta} T_{\beta}, \quad [1.51]$$

with

$$s_{\alpha\beta} = 2^p s_{ijkl}, \quad [1.52]$$

where  $p$  is the number of indices greater than 3 in the pair  $\alpha\beta$ .

Some thermodynamic considerations [ROY 96], demonstrating the symmetry of the matrix  $c_{\alpha\beta}$  (and  $s_{\alpha\beta}$ ), reduce again, in general, the number of elastic independent constants to a maximum of 21. This is equivalent to saying that the constants  $c_{ijkl}$  (and  $s_{ijkl}$ ) are unchanged when the pairs of indices  $ij$  and  $kl$  are exchanged.

The maximum number, 21, of elastic independent constants is reached when the structure of the material has no symmetry (the material is then called triclinic). Such symmetries reduce this number, and, in practice, it is frequently smaller. We will not consider all the cases of possible symmetries, which are listed in reference [ROY 96], but we will simply give some common examples for some materials.

#### *Orthotropic material*

The structure of such a material possesses three binary axes of symmetry orthogonal with each other. The number of elastic independent constants is then reduced to 9. If the axes of the coordinates system are chosen parallel to these axes of symmetry, the table of elastic constants is:

$$c_{\alpha\beta} = \begin{pmatrix} c_{11} & c_{12} & c_{13} & 0 & 0 & 0 \\ c_{12} & c_{22} & c_{23} & 0 & 0 & 0 \\ c_{13} & c_{23} & c_{33} & 0 & 0 & 0 \\ 0 & 0 & 0 & c_{44} & 0 & 0 \\ 0 & 0 & 0 & 0 & c_{55} & 0 \\ 0 & 0 & 0 & 0 & 0 & c_{66} \end{pmatrix}. \quad [1.53]$$

#### *Isotropic transverse material*

The structure of this type of material possesses a rotation symmetry axis of any angle (the properties of this type of material are the same in each direction perpendicular to this axis). Then the number of elastic constants is reduced to 5. If the axis  $Ox_3$  is chosen parallel to this symmetry axis, the table is:

$$c_{\alpha\beta} = \begin{pmatrix} c_{11} & c_{12} & c_{13} & 0 & 0 & 0 \\ c_{12} & c_{11} & c_{13} & 0 & 0 & 0 \\ c_{13} & c_{13} & c_{33} & 0 & 0 & 0 \\ 0 & 0 & 0 & c_{44} & 0 & 0 \\ 0 & 0 & 0 & 0 & c_{44} & 0 \\ 0 & 0 & 0 & 0 & 0 & \frac{c_{11} - c_{12}}{2} \end{pmatrix}. \quad [1.54]$$

### *Isotropic material*

As we have already seen, an isotropic material has the same properties in all directions. The number of elastic constants is then reduced to 2. The table can be written:

$$c_{\alpha\beta} = \begin{pmatrix} c_{11} & c_{12} & c_{12} & 0 & 0 & 0 \\ c_{12} & c_{11} & c_{13} & 0 & 0 & 0 \\ c_{12} & c_{12} & c_{11} & 0 & 0 & 0 \\ 0 & 0 & 0 & \frac{c_{11} - c_{12}}{2} & 0 & 0 \\ 0 & 0 & 0 & 0 & \frac{c_{11} - c_{12}}{2} & 0 \\ 0 & 0 & 0 & 0 & 0 & \frac{c_{11} - c_{12}}{2} \end{pmatrix}, \quad [1.55]$$

which yields the same result as equation [1.23] with

$$c_{11} = \lambda + 2\mu \quad \text{and} \quad c_{12} = \lambda. \quad [1.56]$$

#### 1.1.2.4.2. Elastic wave equation in an anisotropic solid

The movement equation is written in the same way as for the isotropic solid, if we focus only on small variations around equilibrium, it is written according to formula [1.30]:

$$\rho \frac{\partial^2 \vec{u}}{\partial t^2} = \text{div} \bar{\bar{T}} \quad [1.57]$$

The tensor  $\bar{\bar{T}}$  representing the variation of the stress tensor with respect to the position of equilibrium, the subscript 1 has been omitted in order to simplify the equation.

Considering the expression of the stress tensor as a function of the displacements in expression [1.46], it becomes, with indicial writing:

$$\rho \frac{\partial^2 u_i}{\partial t^2} = c_{ijkl} \frac{\partial^2 u_l}{\partial x_j \partial x_k}. \quad [1.58]$$

This equation can be considered as a generalization of the wave equation which is applied for anisotropic solid media.

## 1.2. Solutions of the propagative equation: monochromatic waves, plane waves

Among the solutions of the propagative waves equations (from a general point of view, that is to say also in anisotropic media), there are two types which are of particular interest and use. The first concerns the temporal dependence of the solution: monochromatic waves, and the other its spatial dependence: the case of plane waves.

A monochromatic wave is a wave whose temporal dependence is sinusoidal (harmonic); it will be expressed with real notation as a sine or cosine, multiplied by any function of the spatial coordinates, or with complex notation as a complex exponential, multiplied by the same spatial function. The latter notation will be used, knowing that the real physical variable corresponds to the real part of this complex function. This notation is usable thanks to the linearity of the equations, and only for physical quantities associated with variables of degree one. For example, if the used variable is the displacement vector, this type of solution will be written:

$$\vec{u}(x_1, x_2, x_3; t) = \underline{\vec{u}}(x_1, x_2, x_3) \exp\{i\omega t\}, \quad [1.59]$$

or in indicial form:

$$u_i(x_1, x_2, x_3; t) = \underline{u}_i(x_1, x_2, x_3) \exp\{i\omega t\}, \quad [1.60]$$

where  $\omega$  is the wave pulsation, its frequency  $\nu$  is equal to  $\omega/2\pi$ .

We chose to use the + sign before  $i\omega t$  in the exponential formula [1.59], another convention uses the – sign. These two conventions are strictly equivalent but cause sign changes in the resulting formulas and should therefore not be mixed.

A plane wave is a wave whose physical quantities are identical in planes parallel with each other. We call these planes, “wave planes”, and direction of propagation, their perpendicular direction. If  $\vec{n}$  is the unit vector of the propagation direction, the

equation of the wave planes can be written in the form:

$$\vec{n} \cdot \vec{x} = \text{cste} \quad \text{or} \quad n_1 x_1 + n_2 x_2 + n_3 x_3 = \text{cste} . \quad [1.61]$$

This type of solution can therefore be written:

$$\vec{u}(x_1, x_2, x_3; t) = \vec{a} F\left(t \pm \frac{\vec{n} \cdot \vec{x}}{V}\right). \quad [1.62]$$

The  $-$  sign corresponds to waves propagating in the direction of  $\vec{n}$  and the  $+$  sign to waves propagating in the opposite direction.  $V$  is the phase velocity. If the environment is isotropic (liquid or solid), it is the speed appearing in the wave equation [1.18], [1.36] and [1.37].

A monochromatic plane wave is, in complex notation, of the form:

$$\vec{u}(x_1, x_2, x_3; t) = \vec{a} \exp\left\{i\omega\left(t - \frac{\vec{n} \cdot \vec{x}}{V}\right)\right\} = \vec{a} \exp i(\omega t - \vec{k} \cdot \vec{x}). \quad [1.63]$$

The vector  $\vec{k}$ , the wave number vector, is parallel to the direction of propagation, and its module is the wave number  $k = \omega/V$ . The wavelength is then defined by the formula  $\lambda = 2\pi/k$  and represents the spatial periodicity of the wave. The vector  $\vec{a}$  is a constant vector characterizing the direction of motion of the particles; it can be written in the form of its module “a” multiplied by a unit vector  $\vec{P}$ , called the polarization vector. It can also be complex in which case the movement of particles is elliptical rather than linear.

Note that these types of solutions have no physical reality: monochromatic waves because they cover all the times from minus infinity to plus infinity, and planes waves for a similar reason but in the geometric space. Their interest, however, is double: on one hand, they approximately approach a number of practical cases (the waves will be “almost monochromatic” and/or “almost plane”) and on the other hand, because Fourier transformations can decompose any field into these types of waves.

### 1.2.1. *Fluid medium or isotropic solid*

If the environment is a fluid or an isotropic solid, the propagation equations are wave equations (one for fluids, two independent for isotropic solids). Searching for solutions in the form of monochromatic waves [1.59] leads to the equation for the displacement vector:

$$\Delta \underline{\vec{u}} + \frac{\omega^2}{V_0^2} \underline{\vec{u}} = 0 \quad \text{or} \quad \Delta \underline{\vec{u}} + k^2 \underline{\vec{u}} = 0, \quad [1.64]$$

where  $k = \omega/V$  is the wave number. Equation [1.64] is called the Helmholtz equation.

#### 1.2.1.1. *Fluid medium*

What has just been described for the displacement vector also applies to the velocity vector (these two vectors, in the case of monochromatic waves, are formed from one another simply by multiplying by  $i\omega$ ) but also applies to the velocity potential defined in 1.1.1.5.

We have then, according to equations [1.15] and [1.16]:

$$\varphi(x_1, x_2, x_3; t) = \varphi_0 \exp i(\omega t - \vec{k} \cdot \vec{x}), \quad [1.65]$$

$$\vec{v}(x_1, x_2, x_3; t) = \overrightarrow{\text{grad}} \varphi = -i\vec{k} \varphi_0 \exp i(\omega t - \vec{k} \cdot \vec{x}), \quad [1.66]$$

$$p(x_1, x_2, x_3; t) = -\rho_0 \frac{\partial \varphi}{\partial t} = -i\omega \varphi_0 \exp i(\omega t - \vec{k} \cdot \vec{x}). \quad [1.67]$$

The particle velocity and particle displacement vectors are parallel to the wave number vector, and hence to the direction of propagation. These waves (compression waves) will be called “longitudinal waves”. The term “longitudinal wave” is often used synonymously with compression wave whereas, strictly speaking, it applies only to waves whose displacement vector is at every point parallel to the direction of propagation, such as plane waves.

#### 1.2.1.2. *Isotropic solid*

We have seen in paragraph 1.1.2.3.3. that, in the case of isotropic solid media, there are two types of waves, one which is derived from a scalar potential  $\phi$  and the other derived from a vectorial potential  $\vec{\psi}$ . The first wave is the same kind as waves in fluids; the displacement vector is written for monochromatic plane waves:

$$\vec{u}_L(x_1, x_2, x_3; t) = \overrightarrow{\text{grad}} \phi = -i\vec{k} \phi_0 \exp i(\omega t - \vec{k} \cdot \vec{x}). \quad [1.68]$$

These are the “longitudinal waves”.

The second type is written:

$$\vec{u}_T(x_1, x_2, x_3; t) = \vec{\text{rot}} \vec{\psi} = -i\vec{k} \wedge \vec{\psi}_0 \exp i(\omega t - \vec{k} \cdot \vec{x}). \quad [1.69]$$

The divergence of  $\vec{u}_T$  is zero, which leads to:

$$\vec{k} \cdot \vec{u}_T = 0. \quad [1.70]$$

The displacement vector is then perpendicular to the direction of propagation. Such waves (shear waves) are called “transverse waves”. In the plane perpendicular to the direction of propagation, the displacement vector has two components corresponding to two polarizations. As for longitudinal waves, strictly speaking, the term “transvers waves” applies only for waves whose displacement vectors are at any point perpendicular to the direction of propagation, such as plane waves.

### 1.2.2. Anisotropic solid

The equation of propagation is no longer in this case the wave equation, it is equation [1.58]. Let us again seek solutions in the form of plane waves that we write in the general form (limited to waves propagating in the  $\vec{n}$  direction and using the indicial form):

$$u_i(x_1, x_2, x_3; t) = a_i F\left(t - \frac{n_j x_j}{V}\right). \quad [1.71]$$

#### 1.2.2.1. Christoffel tensor

Inserting the solution given by [1.71] in the equation of propagation [1.58], gives:

$$\rho V^2 a_i = c_{ijkl} n_j n_k a_l. \quad [1.72]$$

Let us introduce the second order tensor defined by:

$$\Gamma_{il} = c_{ijkl} n_j n_k. \quad [1.73]$$

Then the former equation, called Christoffel equation, is written:



$$\Gamma_{il} a_l = \rho V^2 a_i \quad \text{or} \quad \overline{\overline{\Gamma}} \cdot \vec{a} = \rho V^2 \vec{a} . \quad [1.74]$$

This equation shows that the direction of displacement given by the vector of components  $a_i$  (polarization) is an eigenvector of the tensor of components  $\Gamma_{il}$  with the eigenvalue  $\rho V^2$ .

Consequently, speed and polarizations of plane waves propagating in a direction  $\vec{n}$  in an anisotropic solid (whose stiffness tensor components are  $c_{ijkl}$ ) can be obtained by searching the eigenvalues and eigenvectors of the tensor of components  $\Gamma_{il}$ . There are, in general, for a given direction, three propagation velocities, which are the roots of the secular equation:

$$\left\| \Gamma_{il} - \rho V^2 \delta_{il} \right\| = 0 , \quad [1.75]$$

formulating the compatibility condition of the three homogenous equations [1.74], where the notation  $\| A \|$  corresponds to the determinant of the square matrix A.

$\delta_{il}$  represents the components of the Kronecker tensor, equal to one if  $i$  is equal to  $l$  and zero if  $i$  is not equal to  $l$ .

An eigenvector defining the direction of the particle displacement vector of the wave corresponds to each velocity.

In addition, the Christoffel tensor is symmetric: in fact, by swapping the first two indices, the last two or the pairs  $ij$  and  $kl$ , the coefficients  $c_{ijkl}$  are unchanged, then successively:

$$\Gamma_{il} = c_{ijkl} n_j n_k = c_{klij} n_j n_k = c_{lkji} n_j n_k = c_{ljki} n_k n_j = \Gamma_{li} . \quad [1.76]$$

Its eigenvalues are therefore real and there is always an orthonormed basis of eigenvectors. Moreover, we can show [ROY 96] that its eigenvalues are always positive, which defines a real phase velocity  $V$  if the elastic stiffness tensor is real (in the case of non-absorbent materials seen so far).

In general, for each direction  $\vec{n}$ , there are three waves propagating at three different speeds, whose displacement vectors are orthogonal with each other: they are eigenvectors of the Christoffel tensor. Thereafter the polarization of the waves will be represented by a normed vector  $^{(n)}\vec{P}$  and the displacement vector will be

equal to:  $(n)_a (n)\vec{P}$  where  $(n)_a$  is the amplitude of the wave  $\eta$ . Figure 1.2 represents these polarizations for a given direction of propagation of the wave.

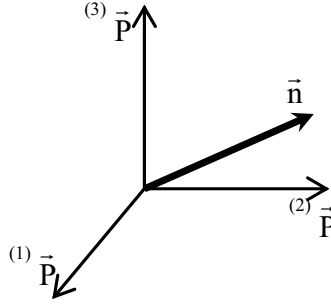


**Figure 1.2.** Polarization of the waves propagating in a given direction

The wave whose direction of polarization is the closest to the direction of propagation will be called quasi-longitudinal and the other two quasi-transverse (slow and fast). These terms are commonly used but are not very appropriate.

If an eigenvalue is twofold, a plane of eigenvectors will then be associated with this value and any vector belonging to this plane will be a possible polarization of a wave whose speed corresponds to this value.

The isotropic solid is obviously a special case of an anisotropic solid; the components of the stiffness tensor are then given by the following formula:

$$c_{ijkl} = \lambda \delta_{ij} \delta_{kl} + \mu (\delta_{ik} \delta_{jl} + \delta_{il} \delta_{jk}), \quad [1.77]$$

and the Christoffel tensor is written:

$$\Gamma_{il} = (\lambda + \mu) n_i n_l + \mu \delta_{il}. \quad [1.78]$$

Then there is a twofold eigenvalue associated with a plane of polarization of the waves perpendicular to the direction of propagation (it corresponds to the transverse waves), and one single value associated with a polarization parallel to the direction of propagation corresponding to longitudinal waves.

### 1.2.2.2. Poynting vector – energy velocity

Bulk densities of kinetic energy and potential energy respectively are classically defined by:

$$\mathcal{E}_c = \frac{1}{2} \rho \left( \frac{\partial u_i}{\partial t} \frac{\partial u_i}{\partial t} \right) \text{ and } \mathcal{E}_p = \frac{1}{2} c_{ijkl} S_{ij} S_{kl}. \quad [1.79]$$

Then, starting from the propagation equation, it is possible to establish the following relationship [ROY 96]:

$$\frac{\partial}{\partial t} \{ \mathcal{E}_c + \mathcal{E}_p \} = \text{div} \left( \bar{\bar{T}} \cdot \frac{\partial \vec{u}}{\partial t} \right). \quad [1.80]$$

This relationship may also be expressed locally using an integral form. By integrating on a volume  $V$  bounded by a closed surface  $\Sigma$ , and applying the theorem of the divergence, it becomes successively:

$$\int_V \frac{\partial}{\partial t} ( \mathcal{E}_c + \mathcal{E}_p ) dV = \int_V \text{div} \left( \bar{\bar{T}} \cdot \frac{\partial \vec{u}}{\partial t} \right) dV = \int_\Sigma \left( \bar{\bar{T}} \cdot \frac{\partial \vec{u}}{\partial t} \right) \cdot \vec{n} d\Sigma. \quad [1.81]$$

with

$$\vec{\mathcal{P}} = -\bar{\bar{T}} \cdot \frac{\partial \vec{u}}{\partial t}, \quad [1.82]$$

and by inverting the order of the integral and derivation, this equation can be written as:

$$\frac{\partial}{\partial t} \left\{ \int_V ( \mathcal{E}_c + \mathcal{E}_p ) dV \right\} = - \int_\Sigma \vec{\mathcal{P}} \cdot \vec{n} d\Sigma \quad [1.83]$$

This equation describes an energy conservation where  $\vec{\mathcal{P}}$ , the Poynting vector, is a surface density of energy flows. It expresses the variation, during the time interval  $dt$ , of the total energy (sum of kinetic energy and potential energy) as equal to the outflow of energy through the surface  $\Sigma$ .

The speed of energy transportation (or speed energy) is then defined as the ratio of this vector  $\vec{\mathcal{P}}$  to the total energy density:

$$\vec{V}^e = \frac{\vec{\mathcal{P}}}{\mathcal{E}} \text{ with } \mathcal{E} = \mathcal{E}_c + \mathcal{E}_p \quad [1.84]$$

In the case of a plane wave, all variables depending on the displacement vector can be rewritten, using the expression given in equation [1.62]; then we can demonstrate that, for this type of wave, the bulk densities of kinetic and potential energy are equal, and equation [1.84] becomes:

$$V_i^e = \frac{c_{ijkl} P_j P_k n_l}{\rho V}. \quad [1.85]$$

Remember that  $P_j$  and  $P_k$  are the components of the polarization vector (unitary vector of the direction of particular displacement).

The energy velocity  $\vec{V}^e$  indicates the direction of travel of the energy that is, in general, different from the propagation direction of the wave defined by the vector  $\vec{n}$ .

Similarly, it is easy to show that the projection of the energy velocity on the direction of propagation is equal to the phase velocity of the plane wave (Figure 1.3):

$$\vec{V}^e \cdot \vec{n} = V. \quad [1.86]$$

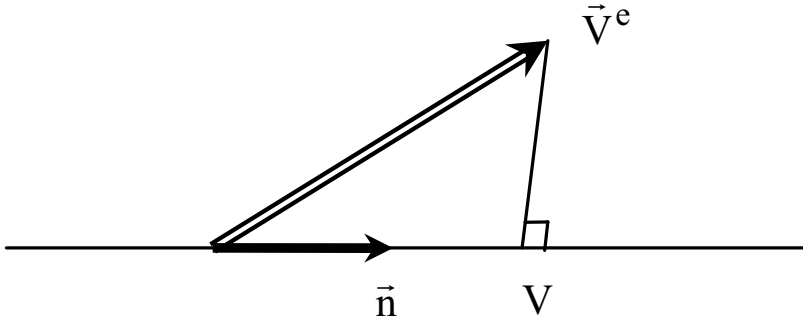


**Figure 1.3.** *Projection of the energy velocity on the direction of propagation*

This implies that the energy velocity is always greater than or equal to the phase velocity.

*In conclusion*, in an anisotropic medium, unlike in isotropic media, a plane wave propagating in a given direction generally has a speed of energy transportation (energy velocity) whose direction is different from the propagation direction.

### 1.2.2.3. Slowness surface

The *slowness surface* corresponds to the points M obtained by drawing, from a given origin O, a vector  $\overrightarrow{OM}$  (slowness vector) whose direction is the direction of propagation, and of module the inverse of the phase velocity, for all directions of propagation  $\vec{n}$ , i.e.:

$$\overrightarrow{OM} = \vec{m} = \frac{\vec{n}}{V}, \quad [1.87]$$

For each direction of propagation, generally, three waves propagate at three different phase velocities; consequently, this surface is composed of three distinct layers: one corresponds to quasi-longitudinal waves and the other two to quasi-transverse waves. If, as it is often the case, the phase velocity of longitudinal waves is lower than these of transverse waves, the corresponding layer is then located inside the two others.

The calculation of the differential of the slowness vector yields the relationship:

$$\overrightarrow{V^e} \cdot d\vec{m} = 0 \quad \forall \quad d\vec{m}. \quad [1.88]$$

This relationship applies to all vectors  $d\vec{m}$  of the plane tangential to the slowness surface. It follows that the energy velocity is normal to the slowness surface.

The phase velocity remaining unchanged if we invert the direction of propagation, the slowness surfaces are symmetric with respect to the origin O. This comes from the fact that the stiffness tensor affecting the propagation properties is a tensor of even order (order 4). When the material considered has, in addition, a particular symmetry axis, slowness surfaces have the same symmetry.

In the case of fluids, a single wave propagates in a given direction. The slowness surface has only one layer, which is a sphere because the medium is isotropic. The normal to the slowness surface is parallel to the corresponding radius, so the energy velocity is parallel to the direction of propagation. For isotropic solids for which two types of waves propagate, the slowness surface is composed of two spheres: one corresponds to longitudinal waves and the other to transverse waves. The former is external because the transverse waves are slower than longitudinal waves. For the same reasons as above, in this case also, the energy velocity is parallel to the direction of propagation.

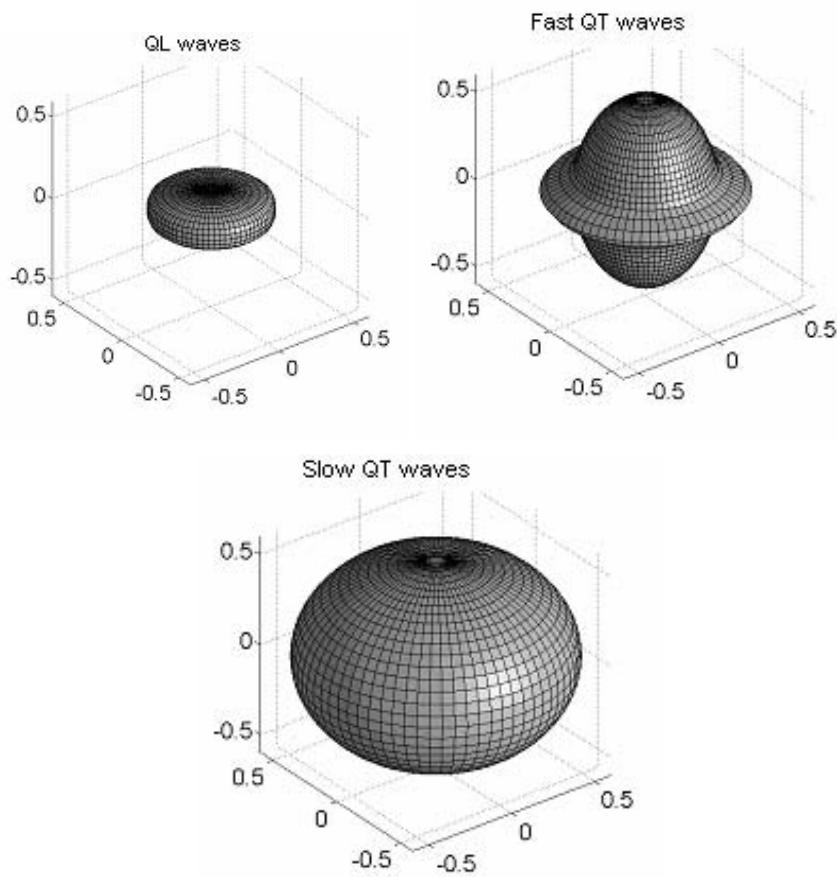


**Figure 1.4.** *Slowness surface of an unidirectional carbon/epoxy composite: top right corresponds to the quasi-longitudinal waves, top left to the quasi-transverse fast waves and down to the quasi-transverse slow waves. These three layers have the same scale in s/km*

Figure 1.4 represents the slowness surface of a unidirectional carbon/epoxy composite (carbon fibers embedded in an epoxy resin), whose fibers are oriented vertically. We observe the three layers (plotted separately for readability) corresponding to quasi-longitudinal waves (the smallest since it is the fastest wave), as well as quasi-transverse fast and slow waves. In this case, these layers are axisymmetric since the material is transverse isotropic.

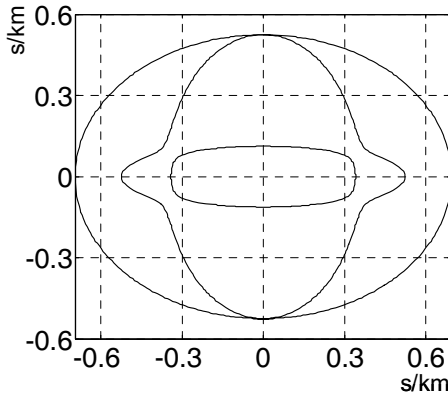


**Figure 1.5.** *Slowness surface of an unidirectional carbon/epoxy composite, cut following a plane containing the axis parallel to the fibers*

Figure 1.5 shows a cut of this surface on which the three layers are superimposed.

The strong anisotropy of this material may be noted on these figures. The layer corresponding to the quasi-longitudinal waves (furthest inside in Figure 1.5) shows a phase velocity that is much higher in the direction of the fibers than in the perpendicular direction. The anisotropy of quasi-transverse waves is less marked.

The *wave surface* corresponds to the points M obtained by drawing a vector  $\vec{OM}$ , equal to the energy velocity, from a given origin O. The vector joining O to any point on the wave surface represents the distance traveled by the energy of the wave during the unitary time.

Figure 1.6 presents, on the left hand-side, a partial cut of the wave surface of the same material as above (layer of quasi-transverse fast waves of unidirectional carbon/epoxy composite) and on the right hand-side the cut corresponding to the slowness surface (slow curve). We observe some singular points on the cut of the wave surface; they correspond to the inflection points of the slowness curve. We also find that for some directions, there are three values of the energy velocity (for example:  $Oa$ ,  $Ob$  and  $Oc$ ) for a single layer of the wave surface. These three values of the energy velocity correspond to three directions of propagation identified by the vectors  $\vec{OA}$ ,  $\vec{OB}$  and  $\vec{OC}$  on the corresponding slowness curve. We observe, in fact, that the normals to tangents of this curve at the three points A, B and C are parallel to the energy velocities we considered. So there are more than three waves that propagate with an energy velocity parallel to this direction.

To simplify the presentation, these remarks were made in a case where the energy velocity vector is in the same plane as the slowness curve considered (section of a slowness surface). In general, the vector is outside this plane and the representation should be three-dimensional.

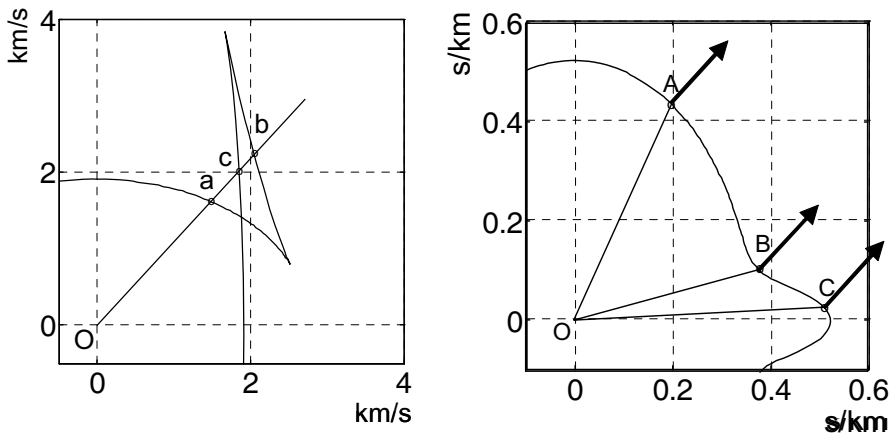


**Figure 1.6.** On the left, a partial cut of the layer of the surface wave corresponding to the quasi-transverse fast waves, on the right, a cut of the slowness surface corresponding to the unidirectional carbon/epoxy

### 1.3. Bibliography

[ROY 96] Royer D., Dieulesaint E., *Ondes élastiques dans les solides, Tome 1: Propagation libre et guidée*, Masson, 1996.



## Chapter 2

# Interaction of a Plane Wave and a Plane Interface

### 2.1. Introduction

Mechanical structures and the materials themselves (composites for example), are often composed of different media linked with each other through interfaces of various kinds (welds, bondings, etc.). In addition, these structures are limited by surface boundaries that separate them from the environment. It is essential to understand how acoustic waves behave when meeting such surfaces.

After having established the equations of propagation in an infinite medium and studied the particular case of plane waves and monochromatic waves, we are now studying the interaction of these waves with interfaces separating two media. We consider the special case where the surfaces are plane and where the incident wave is itself a plane wave. In addition, although this is not always necessary, the problem will be restricted to the case of monochromatic waves.

When two semi-infinite distinct media (liquid, isotropic or anisotropic solid) are separated by an interface, the interaction of a plane oblique and monochromatic wave with the interface generates reflected waves in medium ① and transmitted waves in medium ② (Figure 2.1). Knowing the characteristics of the incident wave (propagation direction, polarization, amplitude) and the properties of both materials constituting the semi-infinite media (density, elastic constants), the writing of the boundary conditions on the interface allows the determination of the characteristics

of the transmitted and reflected waves. In terms of non-destructive testing, the understanding of these phenomena is fundamental for the interpretation of various echoes, reflected or transmitted from the control sample.

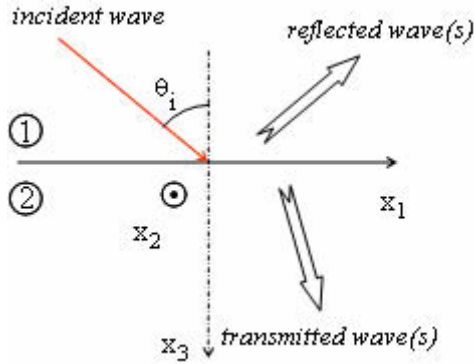


**Figure 2.1.** Interaction of a plane monochromatic oblique wave with a plane interface separating two distinct media. The plane  $(Ox_1x_2)$  is the plane of the interface

As a starting point, we review the various boundary conditions that may appear in the problems of acoustic in fluids or solids.

### 2.1.1. Boundary conditions in acoustics

#### 2.1.1.1. General background of boundary conditions in linear physics

The boundary conditions in acoustics concern surfaces limiting the propagation medium, such as walls or free surfaces, or surfaces between two media with different physical characteristics. The latter are called interfaces.

The boundary conditions, which have to be written, deal with the physical quantities related to the acoustic field: displacements or particle velocity, fluctuations of pressure or stress. They can be kinematic, when expressing conservation of mass, non-penetration of bodies, or dynamic when they translate, in a simplified form, the fundamental principle of dynamics. More complex circumstances will also be explored when the boundary conditions represent the impact caused by the presence of a medium or structure whose details are to be ignored, while we wish to take into account its only influence on the neighboring propagation media. This will be the case of impeding walls or interfaces between two solids showing an effect of elastic bonding.

**Linearization rule at the boundaries.** Before going into the details of the equations representing various types of circumstances, it is necessary to formulate a general rule, which is valid within the scope of linear physics and which simplifies the mathematical representation of boundary conditions.

The surfaces involved participate most often in vibratory movement of the acoustic field around them. Naturally, it is the case for free surfaces and interfaces, whose particles oscillate with the acoustic phenomenon affecting them. On the other hand, walls can be fixed. But they can also vibrate, either actively if they are part of a vibrating source of the acoustic field, or passively if sufficiently light (a vibration is then transmitted to the walls by the acoustic medium they surround). The latter is known as vibro-acoustic coupling. If the surface occupies the position  $\Sigma_o$  in its resting state (without acoustic phenomenon), it occupies a position  $\Sigma(t)$ , which varies with time, in the presence of the acoustic wave.

The general rule (valid in the frame of the linearized theory under the assumption of low amplitudes of the vibratory phenomenon) comes from the fact that the boundary conditions affecting the surface can be simply written, at any time  $t$ , on  $\Sigma_o$  corresponding to its resting position, instead of the instantaneous distorted surface  $\Sigma(t)$ .

To convince ourselves, let us look at the condition of equal pressure which should be written on both sides of an interface between two fluids (1) and (2) in vibratory motion (Figure 2.2), as a consequence of the action–reaction reciprocity principle.

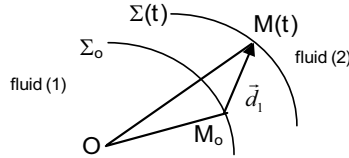


**Figure 2.2.** The interface  $\Sigma_o$  and the corresponding distorted surface  $\Sigma(t)$  at time  $t$

If  $M_o$  is any point of this interface in its resting position  $\Sigma_o$ , this point occupies a position  $M(t)$  on  $\Sigma(t)$  during the vibration. The equality of (total) pressure at point  $M$ , on both sides of the interface  $\Sigma(t)$  :

$$p^{(1)}(M) = p^{(2)}(M), \quad [2.1]$$

breaks up, according to equation [1.7], showing the reference pressure and acoustic pressure (here we temporarily reintroduce the subscript 1 when referring to acoustic disturbances):

$$p_0^{(1)}(M) + p_1^{(1)}(M) = p_0^{(2)}(M) + p_1^{(2)}(M) . \quad [2.2]$$

According to the assumptions made on the reference state (see 1.1.1.4), the pressures  $p_0^{(1)}(M)$  and  $p_0^{(2)}(M)$  are constant (in space and time). This reference state being a state of equilibrium, the equality of pressure on both sides of the interface  $\Sigma_0$  should be ensured,

$$p_0^{(1)} = p_0^{(2)} , \quad [2.3]$$

such that condition [2.1] on the total pressures reduces to the equality of acoustic pressures:

$$p_1^{(1)}(M) = p_1^{(2)}(M) \quad [2.4]$$

For the moment, this condition is also written on the distorted interface  $\Sigma(t)$ . However, the point  $M(t)$  is deduced from its reference position  $M_0$  by a displacement  $\vec{d}_1(t)$  which is supposed to be a small perturbation, as well as the fluctuating quantities introduced in section 1.1.1.4.

Symbolically, we can write:

$$\vec{M}(t) = \vec{M}_0 + \vec{d}_1(t) , \quad [2.5]$$

and specify boundary condition [2.5] in the form:

$$p_1^{(1)}(\vec{M}_0 + \vec{d}_1) = p_1^{(2)}(\vec{M}_0 + \vec{d}_1) . \quad [2.6]$$

Then a first-order development of this equation yields

$$p_1^{(1)}(\vec{M}_0) + \overrightarrow{\text{grad}}(p_1^{(1)}) \cdot \vec{d}_1 = p_1^{(2)}(\vec{M}_0) + \overrightarrow{\text{grad}}(p_1^{(2)}) \cdot \vec{d}_1 . \quad [2.7]$$

However, the second terms of each member above are infinitely small and of second order, as were those that have been neglected in the linearization process of the propagation equations in section 1.1.1.4. It would therefore be unrealistic to keep them at the interface condition.

Thus, in the frame of linear acoustics, the pressure condition at the interface between two media is expressed by the equality of acoustic pressures on the interface in its position at rest:

$$p_1^{(1)}(\vec{M}_0) = p_1^{(2)}(\vec{M}_0). \quad [2.8]$$

It is clear that the scope of the argument developed here is actually general, and that the conclusion extends to all possible boundary conditions we have to write, under the assumptions of linear acoustics.

We shall now write the boundary conditions for a few typical cases. The subscript 1 for acoustic perturbations will again be implied.

#### 2.1.1.2. Various border surface conditions

In this context, *borders* are surfaces that limit the domain of acoustic propagation in space. Thus, fixed or vibrating free surfaces or walls are considered as borders.

##### 2.1.1.2.1. Free surfaces

Free surfaces are borders on which the propagation medium applies no mechanical stress, during its vibratory motion, other than those resulting from equilibrium conditions in the reference state. By contrast, the vibratory motion of such a border is completely free: it depends only on the acoustic movement of the medium. Strictly speaking, a free surface is found only in the case of a medium in contact with a vacuum; in practice such conditions are written on an interface separating the considered medium from a much less dense medium.

The free surface conditions on the mechanical stress are expressed as follows:

*for a fluid medium:* cancelation of the acoustic pressure

$$p(M_0) = 0, \quad [2.9]$$

*for a solid medium:* cancelation of the (acoustic) normal stress vector

$$\overline{\overline{T}}(M_0) \cdot \vec{n}_0 = \vec{0}, \quad [2.10]$$

where  $\overline{\overline{T}}(M_0)$  is the fluctuation of the stress tensor introduced in [1.28]. The linearization rule at the borders applies here: the current point  $M_0$  is located on the free surface at rest  $\Sigma_0$  and  $\vec{n}_0$  is the unitary vector normal to  $\Sigma_0$  at  $M_0$ .

## 2.1.1.2.2. Border walls of a fluid medium

Various types of boundary conditions can be considered on a wall limiting fluid propagation media.

The *perfectly reflective wall* represents an ideal situation in which the fluid particles cannot penetrate into the wall. From an acoustical point of view, it may also be said that such a wall has a rigid property, although it remains deformable from a mechanical point of view. The term *perfectly rigid wall* is then also often used. The fluid being assumed as not viscous (see section 1.1.1), it is appropriate to write the classic sliding condition of the fluid. If the wall is fixed, this condition is expressed by:

$$\vec{v}(M_0) \cdot \vec{n}_0 = 0. \quad [2.11]$$

In practice, such a circumstance occurs when the fluid is in contact with an extremely dense and non-porous material, which does not participate in the vibratory motion. It is the extreme opposite to the free surface condition.

When the perfectly reflective wall has a vibratory motion, the sliding condition of the fluid must be expressed in relative velocity. If  $\vec{w}(M_0)$  is the speed of the point  $M_0$  considered as belonging to the wall, then, with the linearization rule at the borders, the sliding condition is written:

$$\left\{ \vec{v}(M_0) - \vec{w}(M_0) \right\} \cdot \vec{n}_0 = 0. \quad [2.12]$$

It should be noted that, as a consequence of the linearization rule at the borders, these sliding conditions may be indifferently expressed in terms of velocity, as above, or in terms of displacement. In fact, if  $\vec{u}(M_0)$  represents the fluid displacement at  $M_0$  on the wall, we can write, showing the temporal dependence explicitly:

$$\vec{v}(M_0, t) = \frac{\partial}{\partial t} \left\{ \vec{u}(M_0, t) \right\}. \quad [2.13]$$

A simple integration over  $t$  allows us to deduce from [2.11] or [2.12] similar conditions expressed in terms of the displacement at  $M_0$ .

Another point about the conditions of free surfaces or perfectly reflective walls is worth raising. As they have been written, the boundary conditions for these

somewhat ideal situations do not involve any characteristic lengths. If the border, due to its geometry, does not introduce any length scale (which will be the case for an infinite plane boundary), the problem of the interaction of an acoustic wave with this border will be independent of the wavelength, and consequently of the frequency.

However, this observation is no more valid in the more realistic situation of *impeding walls* that we now consider. Such boundaries are representative of walls with a partial penetration of fluid particles (for example due to some porosity, possibly including a dissipation mechanism of acoustic energy, by viscosity or thermal effect). The penetrable nature of the wall imposes a proportionality relationship between the variations of the pressure in its neighborhood and the penetration velocity of particles. It is clear that the penetration or extraction direction of particles plays an essential role in this mechanism and that, in those circumstances, the choice of the unitary normal vector  $\vec{n}_0$ , of no consequence in equations [2.10], [2.11] and [2.12], must here be precisely defined. Usually, the unitary vector  $\vec{n}_0$  is shown penetrating into the wall (thus away from the fluid medium). The condition of impeding wall, written under the assumption of a vibrating wall, is then expressed in the following form:

$$p(M_0) = Z_w \left\{ \vec{v}(M_0) - \vec{w}(M_0) \right\} \cdot \vec{n}_0 = 0. \quad [2.14]$$

The coefficient of proportionality  $Z_w$ , which reflects the physical nature of the wall, is called *wall impedance*. This impedance has the physical dimension of an acoustic impedance, such as the characteristic impedance of the fluid medium  $Z_0 = \rho_0 V_0$ . It is measured in Rayleigh units ( $1 \text{ Rayl} = 1 \text{ kg} / \text{m}^2 \text{ s}$ ).

Generally, because the physical properties of an impeding wall reveal length scales (thickness, porosity), boundary condition [2.14] depends on frequency, and it can be expressed in the simple multiplicative form above only in the frequency domain, using the complex representation of physical quantities.

It must therefore be assumed that, in practice, wall impedance is a complex-valued function of the frequency, which can be written:

$$Z_w(\omega) = X_w(\omega) + i Y_w(\omega). \quad [2.15]$$

The real part  $X_w(\omega)$ , called *wall resistance*, is due to the effects of acoustic energy dissipation. This quantity is always positive (or zero), with the choice that was made for the unitary normal vector  $\vec{n}_0$ , penetrating into the wall.

The imaginary part  $Y_w(\omega)$ , called *wall reactance*, does not have an imposed sign. It represents advancing or delaying mechanisms that can be observed between pressure effects and input–output movements of fluid particles.

#### 2.1.1.2.3. Border walls of a solid medium

The case of a wall surrounding a solid medium is less usual, and we will refer to two specific situations, corresponding to fixed walls.

The *fixed wall with embedding*, or perfect adhesion, requires the solid medium having zero displacement at the contact with the border:

$$\vec{u}(M_0) = \vec{0}. \quad [2.16]$$

However, no conditions are imposed on the normal stress vector. That is, again, the extreme opposite to the free surface, which led to condition [2.10].

Another ideal situation, but intermediate between these two extreme cases, is the *fixed wall with sliding*. Displacements of solid particles are allowed along the wall. However, the solid can only exert a normal action on the wall. Such a situation is reflected in the next two conditions:

$$\vec{u}(M_0) \cdot \vec{n}_0 = 0, \quad [2.17-a]$$

$$\left\{ \vec{T}(M_0) \cdot \vec{n}_0 \right\} \wedge \vec{n}_0 = \vec{0}. \quad [2.17-b]$$

The first equation expresses the geometric condition of sliding, written in terms of displacement. The second requires the two components of the normal stress vector in the plane that is tangent to the wall at the current point  $M_0$  to be zero.

#### 2.1.1.3. Usual interface conditions

Regarding solids involved in the formation and implementation of materials, the problems related to the interfaces between two solids or between a solid and a fluid are of a more practical interest. We will begin by quickly mentioning the simple case of the interface between two fluids.

Two types of conditions usually occur along an interface. The first one is a kinematic condition that expresses the non-penetration of media. It may be written in terms of velocity or in terms of displacement, due to the linearization rule at the borders, and referring to the comment that was made earlier (relationship [2.12]). The second condition stems from the dynamic laws applied to the interface itself,



considered as a mechanical system of mass zero. It follows from the fundamental principle that, at any moment and any point of the interface, stress forces carried by each of the media should counterbalance each other.

#### 2.1.1.3.1. Interface separating two fluid media

The fluids being supposed to be not viscous, the kinematic condition of non-penetration of the media leads us to write that the fluids slip one over the other. This condition is usually expressed in terms of particle velocities. The dynamic balance condition of stress forces amounts to the equality of acoustic pressure, as it has been shown earlier to illustrate the linearization rule at the borders.

In summary, using the same notations as introduced earlier, the conditions at an interface between two fluids (1) and (2) will be written:

$$\vec{v}^{(1)}(M_0) \cdot \vec{n}_0 = \vec{v}^{(2)}(M_0) \cdot \vec{n}_0, \quad [2.18-a]$$

$$p^{(1)}(M_0) = p^{(2)}(M_0). \quad [2.18-b]$$

#### 2.1.1.3.2. Interface separating a fluid and a solid

Solid structures which are studied are normally immersed in a fluid (liquid or gas) and such interfaces play the role of entry or exit areas for the acoustic phenomena involving the structure.

Although one of the media is a fluid, it is preferable to write the kinematic condition in terms of displacement. This condition, which expresses the sliding of the fluid along the solid, its motion being relative to the solid, results in the equality of normal displacements of the two fluid and solid particles located at  $M_0$  on both sides of the interface.

Moreover, as the pressure force exerted by the fluid is purely normal, the dynamic condition requires that the two components of the normal stress vector located in the plane tangent to the interface are zero. The normal component of this stress vector must balance the pressure exerted by the fluid. It should be noted, in this balanced relationship of forces, that the difference of sign convention between the definition of the pressure in a fluid and the stress vector for a solid yields a minus sign here.

The conditions for an interface between a fluid (1) and a solid (2) will then be written:

$$\vec{u}^{(1)}(M_0) \cdot \vec{n}_0 = \vec{u}^{(2)}(M_0) \cdot \vec{n}_0, \quad [2.19-a]$$

$$p^{(1)}(M_0) = - \left\{ \vec{T}^{(2)}(M_0) \cdot \vec{n}_0 \right\} \cdot \vec{n}_0, \quad [2.19-b]$$

$$\vec{0} = \left\{ \vec{T}^{(2)}(M_0) \cdot \vec{n}_0 \right\} \wedge \vec{n}_0. \quad [2.19-c]$$

#### 2.1.1.3.3. Interfaces separating two elastic solids

Such interfaces, which are fundamental for the mechanical behavior of materials composed of several solid components (sandwiches, multilayered media, composites), can be of quite different physical natures. We consider for the moment the simple cases of i) an interface with perfect adhesion and ii) a sliding interface. A special section (2.1.1.4) will be dedicated to the more complex case of bonding interfaces.

The two specific cases considered here are the generalization, in the case of the junction between two solids, of the two types of wall conditions introduced in section 2.1.1.2.3.

The *interface of perfect adherence*, which reflects the existence of an embedding or a weld between the two solids, is expressed first by the equality of displacements of particles in contact  $M_0^{(1)}$  and  $M_0^{(2)}$ , belonging respectively to solids (1) and (2), at any point  $M_0$  on the interface  $\Sigma_0$  and at any time during the vibratory motion. This kinematic requirement is supplemented by the dynamic equation expressing the equality of stress vectors normal to  $\Sigma_0$  at  $M_0$ :

$$\vec{u}^{(1)}(M_0) = \vec{u}^{(2)}(M_0), \quad [2.20-a]$$

$$\vec{T}^{(1)}(M_0) \cdot \vec{n}_0 = \vec{T}^{(2)}(M_0) \cdot \vec{n}_0. \quad [2.20-b]$$

The *sliding interface* allows relative motions of the particles of each solid relative to the other one in the plane tangent at  $M_0$  to the interface  $\Sigma_0$ . Only the normal component of the displacements has to satisfy the continuity condition. However, the solids do not exert any shear action on one another: the components of the normal stress vectors must be zero in the tangent plane. Equality of mutually

applied efforts is expressed only by the continuity of the normal components of these vectors:

$$\vec{u}^{(1)}(M_0) \cdot \vec{n}_0 = \vec{u}^{(2)}(M_0) \cdot \vec{n}_0, \quad [2.21-a]$$

$$\left\{ \vec{T}^{(1)}(M_0) \cdot \vec{n}_0 \right\} \cdot \vec{n}_0 = \left\{ \vec{T}^{(2)}(M_0) \cdot \vec{n}_0 \right\} \cdot \vec{n}_0, \quad [2.21-b]$$

$$\left\{ \vec{T}^{(1)}(M_0) \cdot \vec{n}_0 \right\} \wedge \vec{n}_0 = \left\{ \vec{T}^{(2)}(M_0) \cdot \vec{n}_0 \right\} \wedge \vec{n}_0 = \vec{0}. \quad [2.21-c]$$

It should be noted, in a similar way to what was observed on the usual border conditions, that the various interface situations analyzed in section 2.1.1.3 lead to relationships in which no reference length is involved. Therefore, the interface equations so-written do not, in themselves, induce a dependence on the wavelength, nor consequently on the frequency.

It is different for bonding interfaces studied in the next section.

#### 2.1.1.4. Conditions on solid/solid interface of bonding type

Hypotheses of perfect adhesion or sliding contact, between two solids, describe ideal situations which appear to be specific, extreme cases of reality, in which a slight normal relative shift between the two solids is possible. We shall now study the more general circumstance under the term: contacts of bonding type.

In practice, the two solids are linked together with a thin layer which is the result of the process of contact, either by surface modification of these materials, or by the addition of a third material, the “glue”. The latter has a certain thickness  $d$  and has an elastic or more generally visco-elastic behavior (we shall return to this later, taking into account the viscous effects inside the collage). In the context of the vibro-acoustic assumptions, the behavior of the glue will be considered as linear.

The thickness of the glue is generally sufficiently small, compared to the wavelengths involved in the vibro-acoustic signal, as to be negligible, and we can consequently neglect the inertial effects of the glue. This will be explained below in a formal statement, see equations [2.26] and [2.27].

Under these simplifying hypotheses, the behavior of the thin layer of glue, treated like a single interface, can be described by a rheological model without mass. Using a linear law of behavior, this model connects the displacement discontinuity

on both sides of the interface to the normal stress vector, which is continuous at the crossing of the glue layer (whose mass has been neglected):

$$\overline{\overline{T}}^{(1)}(M_0) \cdot \vec{n}_0 = \overline{\overline{T}}^{(2)}(M_0) \cdot \vec{n}_0 = \mathcal{K} \left[ \vec{u}^{(2)}(M_0) - \vec{u}^{(1)}(M_0) \right], \quad [2.22]$$

where  $\mathcal{K}$  is a three-dimensional second order tensor with real components (see later in this section), which represents the (by surface unit) stiffness of the glue, and where the normal unitary vector  $\vec{n}_0$  is oriented from (1) to (2) so that the components of the tensor  $\mathcal{K}$  (or rather their real parts) are positive.

It is usual to assume that the effects of compression and shear on the glue layer are uncoupled, and that the effects of shear are isotropic in the plane tangent to  $M_0$  at the interface (see for example [ROK 81] or [PIL 82]). In a local orthonormal coordinate system with  $\vec{n}_0$  as third vector, the stiffness tensor takes the following diagonal form:

$$\mathcal{K} = \begin{bmatrix} K_T & 0 & 0 \\ 0 & K_T & 0 \\ 0 & 0 & K_N \end{bmatrix}, \quad [2.23]$$

reducing the characterization of the collage to the knowledge of two parameters: the normal stiffness  $K_N$  and the tangential stiffness  $K_T$ . The conditions through the interface described by [2.22] are then uncoupled and may be written:

$$\left[ \overline{\overline{T}}^{(1)}(M_0) \cdot \vec{n}_0 \right] \cdot \vec{n}_0 = \left[ \overline{\overline{T}}^{(2)}(M_0) \cdot \vec{n}_0 \right] \cdot \vec{n}_0 = K_N \left[ \vec{u}^{(2)}(M_0) - \vec{u}^{(1)}(M_0) \right] \cdot \vec{n}_0, \quad [2.24-a]$$

$$\left[ \overline{\overline{T}}^{(1)}(M_0) \cdot \vec{n}_0 \right] \wedge \vec{n}_0 = \left[ \overline{\overline{T}}^{(2)}(M_0) \cdot \vec{n}_0 \right] \wedge \vec{n}_0 = K_T \left[ \vec{u}^{(2)}(M_0) - \vec{u}^{(1)}(M_0) \right] \wedge \vec{n}_0 \quad [2.24-b]$$

Three limit cases can be underlined in the general context of these relationships:

– When  $K_N$  and  $K_T$  tend towards infinity, relationships [2.24] imply the continuity of the displacement vector. We find again the perfect adherence condition [2.20-a].

– If  $K_N$  tends towards infinity and  $K_T$  towards zero, relationship [2.24-a] reduces to the continuity of the normal component of displacement [2.21-a], whereas relationship [2.24-b] leads to the nullity of the tangential components of the normal stress vector, thus to relationships [2.21-c]. We again find the situation of the sliding interface.

– Finally, when  $K_N$  and  $K_T$  both tend towards zero, the normal stress vectors cancel both. This is the case of total decohesion between the two solids.

*Note 1.* The thickness  $d$  of the adhesive layer is not involved in writing the boundary conditions [2.24]. However, if we want to determine the stiffness parameters  $K_N$  and  $K_T$  of the rheological model from the Lamé coefficients  $\lambda_c$ ,  $\mu_c$  of the bonding material, we will write:

$$K_N = \frac{\lambda_c + 2\mu_c}{d} = \frac{\rho_c V_{Lc}^2}{d}, \quad K_T = \frac{\mu_c}{d} = \frac{\rho_c V_{Tc}^2}{d}, \quad [2.25]$$

where  $\rho_c$  is the density of the glue, and  $V_{Lc}$  and  $V_{Tc}$  are the velocities of longitudinal and transverse waves in the bonding material. Following [BAL 03], we can introduce dimensionless stiffness, depending on the angular frequency  $\omega$ , in the form:

$$\bar{K}_N = \frac{K_N}{\rho_c V_{Lc} \omega}, \quad \bar{K}_T = \frac{K_T}{\rho_c V_{Tc} \omega}. \quad [2.26]$$

The hypothesis of a glue thickness which is small compared to the wavelengths involved can be expressed by the conditions:

$$k_{Lc}d = \frac{1}{\bar{K}_N} \ll 1, \quad k_{Tc}d = \frac{1}{\bar{K}_T} \ll 1, \quad [2.27]$$

where we introduced the longitudinal and transverse wave numbers associated with the frequency  $\omega$  in the bonding material.

*Note 2.* We might think that, on the hypothesis that has just been made, the problem of the interaction of an acoustic wave with a plane interface with a bonding

of very small thickness does not involve any characteristic length, and consequently does not depend on the wave frequency. This is not correct. The thickness  $d$  of the glue will not affect the result (due to conditions [2.27]), but another characteristic length appears by comparing the elastic constants of the two bonded solids and the stiffnesses of the rheological model characterizing the bonding.

Indeed, the elasticity constants of the materials that constitute the bonded solids (such as Lamé coefficients or Young modulus) have the dimension of a stress, whereas the parameters of stiffness  $K_N$  and  $K_T$  have the dimension of a stress divided by a length. The modeling of bonding with small thickness by a rheological model therefore introduces a characteristic length depending on both the bonding and the elastic nature of the materials that are bonded.

Thus, a problem of interaction between an acoustic wave and a bonding plane interface will be discussed under the assumption of a monochromatic wave.

*Note 3.* As a consequence of the previous notes, there will be some interest in expressing gluing relationships [2.24], in terms of the complex representations of monochromatic stresses and displacements fields. Under this complex formulation, the stiffness parameters  $K_N$  and  $K_T$  may themselves be considered as complex valued (imaginary parts then representing the effects of viscoelasticity of the bonding material as mentioned at the beginning of this section).

### **2.1.2. Plane interface separating two fluid or isotropic solid media**

We return now to the particular case of a plane interface between two fluid or solid propagation media. The incident field will be composed of a monochromatic plane wave whose interaction with the interface yields the generation of a reflected and a transmitted field. Each of these two fields is made up of one, two or three plane waves, according to the nature of the propagation medium: a single wave (longitudinal) if the medium is fluid, one or two waves (longitudinal or transverse) for an isotropic solid, three-waves (general case) for an anisotropic solid.

In the following section, we describe the nature of these waves, limiting ourselves to the case of fluid or isotropic solid media.

#### **2.1.2.1. Nature of the reflected and transmitted waves**

With the exception of the special case of normal incidence, the wave vector of the incident plane wave defines a plane that is normal to the plane interface. This plane is commonly called “incidence plane” or “sagittal plane” (from *sagitta*, the arrow).

Without losing the general character of the problem, since the coordinate system  $(O, x_1, x_2, x_3)$  just has to be chosen correctly, the wave vector  $\vec{k}^{inc}$  of the incident wave is supposed to be contained in the incidence plane  $(O x_1 x_3)$ :

$$\vec{k}^{inc} = k_1^{inc} \vec{e}_{x_1} + k_3^{inc} \vec{e}_{x_3}, \quad [2.28]$$

where  $k_1^{inc}$  and  $k_3^{inc}$  are the projections of  $\vec{k}^{inc}$  on the unitary vectors  $\vec{e}_{x_1}$  and  $\vec{e}_{x_3}$ , respectively.

The modulus of wave vector  $\vec{k}^{inc}$  is given by

$$k^{inc} = \omega^{inc} / V^{inc}, \quad [2.29]$$

where  $\omega^{inc}$  and  $V^{inc}$  are respectively the angular frequency and the propagation velocity of the incident wave.

The nature of the transmitted and reflected waves at the interface depends on the nature of the incident wave (longitudinal denoted  $L$  or transverse denoted  $T$ ) and on the nature of the medium (isotropic solid or fluid media). In an isotropic solid medium, for a given propagation direction that is not perpendicular to the interface, it is necessary to distinguish, among the transverse waves, those whose displacement vector is located in the sagittal plane (called Transverse Vertical or Shear Vertical and noted TV or SV respectively) and those whose displacement vector is perpendicular to the sagittal plane (called Transverse Horizontal or Shear Horizontal and noted TH or SH respectively). In this terminology of transverse waves, the plane  $(O x_1 x_2)$  of the interface is considered to be the “horizontal” reference. It should be noticed that, because of the boundary conditions at the interface (Section 2.1.2.4.), the wave number vectors are all located in the incidence plane (Figure 2.3). In soil mechanics and seismics, TV waves are easily borne by humans (the vibrations felt when a train passes through, for example), while TH waves are not easy to bear and are more dangerous (earthquakes).

As it creates a particle displacement in the incidence plane, the incident wave ( $L$  or TV) yields the generation of transmitted or reflected waves which are also polarized in the incidence plane ( $L$  or TV). On the other hand, an incident wave with polarization perpendicular to the incidence plane (TH) can generate only TH waves. It should be noted that this reasoning is no longer true in anisotropic media where, in any case, the waves are no longer purely longitudinal or transverse.

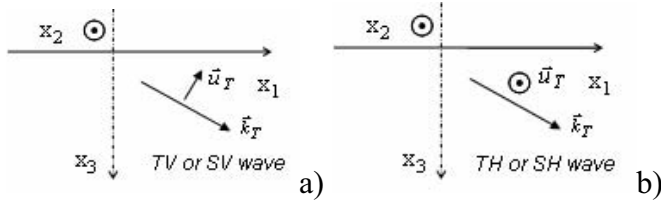


**Figure 2.3.** Transverse waves of wave vector  $\vec{k}_T$  and displacement vector  $\vec{u}_T$ . a) transverse vertical wave ( $\vec{u}_T$  in the incidence plane) b) transverse horizontal wave ( $\vec{u}_T$  perpendicular to the incidence plane)

The examples in Figures 2.4-a and 2.4-b show symbolically which waves can be reflected or transmitted, according to the nature of the incident wave and the media involved. Thus, an incident L wave, polarized in the sagittal plane (the corresponding particle displacement is located in this plane), can generate only waves for which the resulting particle displacement is also located in the same plane, i.e. L and/or TV waves (Figure 2.4-b). A similar argument can be used for an incident TV wave. There is a *mode conversion*, since a L wave can generate a TV wave of a different nature. Similarly, an incident TH wave, polarized perpendicularly to the sagittal plane, can generate only waves with a particle displacement perpendicularly to the sagittal plane, i.e. TH waves (Figure 2.4-c).

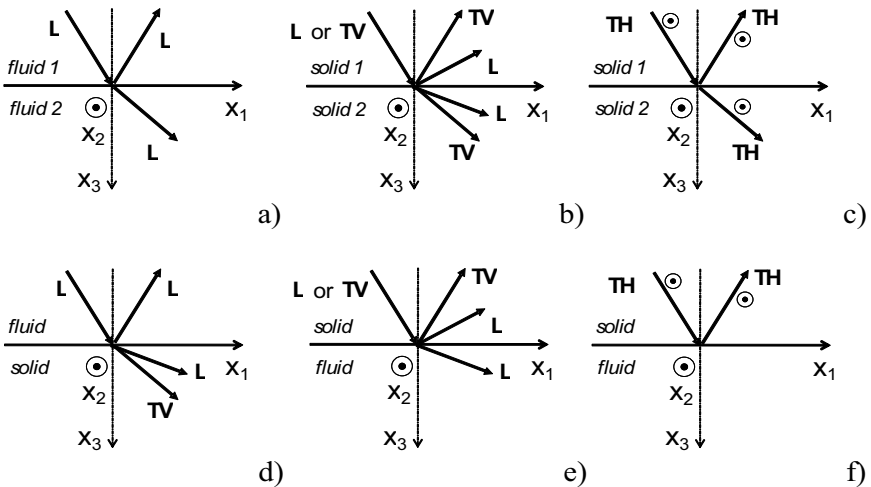


**Figure 2.4.** Nature of reflected and transmitted waves depending on the media and the nature of the incident wave



### 2.1.2.2. Writing of the boundary conditions

As we have just seen in section 2.1.2.1. concerning Figures 2.4, according to the incidence and transmission media involved (liquid or isotropic solid), the incident plane wave generates 1, 2, 3 or 4 reflected and transmitted waves. We will see in section 2.1.3. that, for anisotropic solid media, the number of transmitted and reflected waves can be up to 6. The amplitudes of the transmitted and reflected waves are the unknown quantities of the reflection–transmission problem so considered. The continuity equations at the interfaces, deduced from the general presentation given in section 2.1.1., lead here to a number of scalar equations equal to the number of those unknown amplitudes. Thus, the former reflection–transmission problem is fully determined.

It should be noted that this problem is perfectly determined solely because a radiation to infinity criterion (no wave returning from infinity) has been applied. Thus, the propagative reflected waves are such that their energy velocity (see section 1.2.2.3.) is directed towards the  $x_3 < 0$  direction, while propagative transmitted waves are such that their energy velocity is directed towards the  $x_3 > 0$  direction (the case of non-propagative or evanescent waves is dealt with in section 2.1.2.6). With our choice of coordinate system (see Figure 2.1), a transmitted propagative wave in an isotropic solid or fluid medium is such that  $k_3$  is positive, while a propagative reflected wave is such that  $k_3$  is negative.

We now briefly write these conditions of continuity for the plane waves involved in this reflection–transmission problem. We will note by the superscripts *inc*, *ref* and *tr* the fields related to the incident, reflected and transmitted waves, respectively.

Using the indicial notation, equations [2.18] in the case of a fluid–fluid interface, [1.107] in the case of a fluid–solid interface or [2.20] in the case of a solid–solid interface (perfect adherence) can be written in general, at the interface  $x_3 = 0$ :

– for the continuity of the  $i^{\text{th}}$  component of displacement vectors

$$u_i^{inc} + \sum_{ref} u_i^{ref} = \sum_{tr} u_i^{tr} \quad (x_3 = 0, \forall x_1, x_2, t); \quad [2.30-a]$$

– for the continuity of the  $j^{\text{th}}$  component of stress vectors applied on a surfacic element at the interface, of normal  $\vec{e}_{x_3}$ , i.e.  $\vec{T} \cdot \vec{e}_{x_3}$

$$T_{j3}^{inc} + \sum_{ref} T_{j3}^{ref} = \sum_{tr} T_{j3}^{tr} \quad (x_3 = 0, \forall x_1, x_2, t). \quad [2.30-b]$$

It should be noted that, in the case of a fluid medium, the stress tensor is diagonal, with components  $-p$ .

*Fluid/fluid interface (Figure 2.4-a)*

- incident wave is necessarily longitudinal;
- only one reflected wave ( $ref = 1$ );
- only one transmitted wave ( $tr = 1$ );
- displacements: continuity of the components normal to the interface ( $i = 3$ );
- stresses: continuity of the components normal to the interface ( $j = 3$ ).

*Solid/solid interface, incident L or TV wave (Figure 2.4-b)*

- two reflected waves ( $ref = 1.2$ );
- two transmitted waves ( $tr = 1.2$ );
- displacements: continuity of the components in the sagittal plane ( $i = 1.3$ );
- stresses: continuity of the components in the sagittal plane ( $j = 1.3$ ).

*Solid/solid interface, incident TH wave (Figure 2.4-c)*

- only one reflected wave ( $ref = 1$ );
- only one transmitted wave ( $tr = 1$ );
- displacements: continuity of the components normal to the sagittal plane ( $i = 2$ );
- stresses: continuity of the components normal to the sagittal plane ( $j = 2$ ).

*Fluid/solid interface (Figure 2.4-d)*

- only one reflected wave ( $ref = 1$ );
- two transmitted waves ( $tr = 1.2$ );
- displacements: continuity of the components normal to the interface ( $i = 3$ );
- stresses: continuity of the components in the sagittal plane ( $j = 1.3$ ).

*Solid/fluid interface, incident L or TV wave (Figure 2.4-e)*

- two reflected waves ( $ref = 1.2$ );
- only one transmitted wave ( $tr = 1$ );
- displacements: continuity of the components normal to the interface ( $i = 3$ );
- stresses: continuity of the components in the sagittal plane ( $j = 1.3$ ).

*Solid/fluid interface, incident TH wave (Figure 2.4-f)*

- only one reflected wave ( $ref = 1$ );
- no transmitted wave ( $tr = 0$ );
- displacements: continuity of the components normal to the interface (not involved here:  $0 = 0$ );
- stresses: continuity of the components normal to the sagittal plane ( $j = 2$ ).

#### 2.1.2.3. Conservation of the frequency through an interface

Let  $\omega^{inc}$ ,  $\omega^{ref}$  and  $\omega^{tr}$  be the angular frequencies of the incident, reflected and transmitted waves, respectively. The monochromatic plane waves are described by expressions involving the exponential factor  $\exp\{i(\omega t - \vec{k} \cdot \vec{x})\}$  that describes the propagation, the particle displacement vector given by equation [1.63] being one example.

The condition of displacement continuity [2.30-a] at the interface in  $x_3 = 0$  is written

$$a_i^{inc} \exp(i\omega^{inc} t - \vec{k}^{inc} \cdot \vec{x}) + \sum_{ref} a_i^{ref} \exp(i\omega^{ref} t - \vec{k}^{ref} \cdot \vec{x}) = \sum_{tr} a_i^{tr} \exp(i\omega^{tr} t - \vec{k}^{tr} \cdot \vec{x}),$$

$$(x_3 = 0, \forall x_1, x_2, t), \quad [2.31]$$

where  $a_i^{inc}$ ,  $a_i^{ref}$  and  $a_i^{tr}$  are the projections on axis  $\vec{e}_{x_i}$  of the amplitude vectors of the incident, reflected and transmitted waves. Since equation [2.31] must be satisfied for any given time  $t$ , the angular frequencies are necessarily equal, such that the time dependence can be factorized, and eliminated:

$$\omega^{inc} = \omega^{ref} = \omega^{tr} = \omega. \quad [2.32]$$

#### 2.1.2.4. Conservation of the projection of wave vectors on the interface

Omitting the factor  $\exp(i\omega t)$  and substituting  $x_3$  by 0 (as initial assumption, the projection  $k_2^{inc}$  is zero), enables equation [2.31] to be written as:

$$a_i^{inc} \exp(-i k_1^{inc} x_1) + \sum_{ref} a_i^{ref} \exp(-i k_1^{ref} x_1 - i k_2^{ref} x_2) = \sum_{tr} a_i^{tr} \exp(-i k_1^{tr} x_1 - i k_2^{tr} x_2), \forall x_1, x_2. \quad [2.33]$$

Satisfying equation [2.33] for any given values of  $x_1$  and  $x_2$ , results in factorizing the exponential terms that depend on these variables in order to eliminate them; therefore, the projections of the different wave number vectors on the plane of the interface must all be equal

$$k_1^{ref} = k_1^{tr} = k_1^{inc} = k_1, \quad [2.34-a]$$

and  $k_2^{ref} = k_2^{tr} = k_2^{inc} = 0.$  [2.34-b]

As indicated in section 2.1.2.1, equations [2.34-b] show that all wave vectors are located in the sagittal plane. On the other hand, equations [2.34-a] lead to the Snell–Descartes reflection and refraction laws [2.35]. In fact, the introduction of the reflected and transmitted angles  $\theta^{ref}$  and  $\theta^{tr}$  (Figure 2.5) allows equation [2.34-a] to be expressed as

$$\sin \theta^{inc} / V^{inc} = \sin \theta^{ref} / V^{ref} = \sin \theta^{tr} / V^{tr}, \quad [2.35]$$

where  $V^{ref}$  and  $V^{tr}$  are the propagation velocities of the reflected and transmitted waves. In particular, when  $V^{ref} = V^{inc}$ , angles  $\theta^{ref}$  and  $\theta^{inc}$  are equal, which leads to the classical law of reflection symmetry.

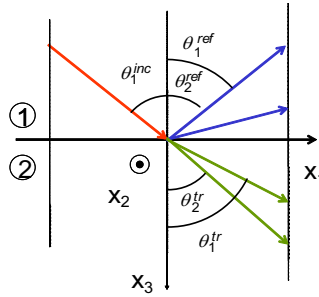


**Figure 2.5.** Graphical illustration of Snell–Descartes laws

#### 2.1.2.5. Graphical construction: the slowness surfaces

As each term of equation [2.35] corresponds to the projection on axis  $x_1$  of the slowness vector of the incident, reflected and transmitted waves, the use of the

intersection of the slowness surfaces of both semi-infinite media 1 and 2 with the incident plane (circles in the present case, see section 1.2.2.3.), enables us to visualize, graphically, which waves propagate in each medium. It is sufficient to plot a vertical straight line corresponding to the incident angle  $\theta^{inc}$  to obtain, on the horizontal axis, the quantity  $\sin \theta^{inc} / V^{inc}$  (see on Figure 2.6 the case of the interaction of an oblique monochromatic TV plane wave with the plane interface separating two isotropic solid media). The transfer of this quantity on the right enables us to obtain an intersection with each slowness curve of media 1 and 2, and thereafter, the reflected and transmitted angles.

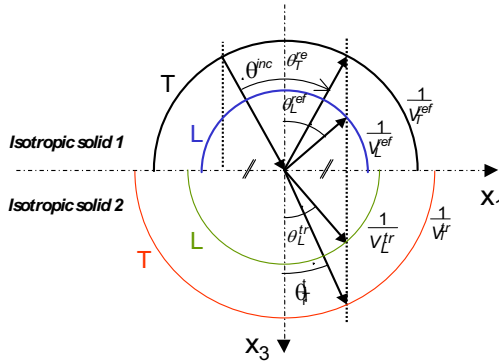


**Figure 2.6.** Representation of reflection and transmission laws using the intersection of the slowness surfaces of each semi-infinite media with the incident plane; case of an interface between two isotropic solids, with an incident transverse vertical wave

#### 2.1.2.6. Critical angles – evanescent waves

Using the construction of Figure 2.6, it appears that, beyond a certain incident angle, the intersection of the above mentioned vertical line with one of the slowness curves does not occur anymore. Thus the corresponding waves are not propagative anymore and are characterized as *inhomogenous*: their energy propagates parallel to the interface whereas the displacement amplitude decreases exponentially with the distance to the interface (this is demonstrated below). In an isotropic medium, an inhomogenous wave is more commonly called an *evanescent wave*. For a fluid/isotropic solid interface, Figures 2.7 show that L and T waves become inhomogenous when the incident angle is larger than  $\theta_{c_1}$  and  $\theta_{c_2}$ , named first and second *critical angles* for the fluid–isotropic solid interface, respectively. It should be noted that the notion of critical angle always involves an interface between two materials, and that speaking of the first critical angle in steel for example is a language misuse (unfortunately usual) and can lead to confusion. For example, the

first critical angle for a water–steel interface is not equal to the first critical angle for a Plexiglas–steel interface.

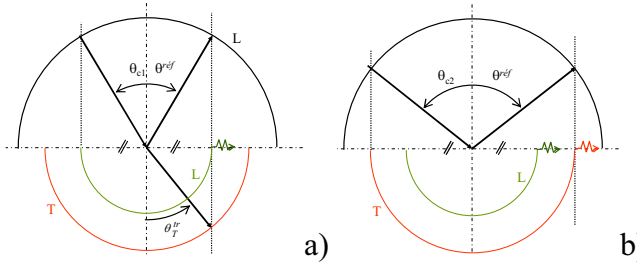


**Figure 2.7.** Critical angles for a water–isotropic solid interface. a) 1st critical angle: the  $L$  wave becomes inhomogeneous, b) 2nd critical angle: all the transmitted waves are inhomogeneous

The values of the first and second critical angles are respectively given by

$$\sin \theta_{c_1} = V_{fluid} / V_L \quad [2.36-a]$$

and  $\sin \theta_{c_2} = V_{fluid} / V_T$ , [2.36-b]

where  $V_{fluid}$  is the wave propagation velocity in the fluid medium, and  $V_L$  and  $V_T$  are the longitudinal and transverse propagation velocities in the isotropic solid medium, respectively.

In a fluid or isotropic solid medium, when a wave is no longer propagative, it is called evanescent. To simplify the calculation, the following explanations are given in the case of an interface separating two fluid media (1) and (2) (we suppose here  $V^{(1)} < V^{(2)}$ ) (Figure 2.8), but the reasoning is the same in an isotropic solid medium. In the transmission medium 2, the dispersion equation is written

$$k_1^2 + (k_3^{tr})^2 = k_L^2, \quad [2.37]$$

where  $k_1$  and  $k_3^{tr}$  are the projections on axes  $x_1$  and  $x_3$  of the wave number vector of the transmitted wave, and  $k_L$  is the wave number in medium 2. The incident angle  $\theta^{inc}$  being larger than the critical angle, the projection  $m_1 = k_1 / \omega$  on  $x_1$ -axis of the slowness vector of the incident wave is larger than  $1/V^{(2)} = k_L / \omega$ , hence

$$k_1 > k_L. \quad [2.38]$$

Inserting inequality [2.38] in dispersion equation [2.37] enables us to write

$$(k_3^{tr})^2 = k_L^2 - k_1^2 < 0. \quad [2.39]$$

The projection on  $x_3$ -axis of the wave vector of the transmission medium is thus purely imaginary and can therefore be written in the following form

$$k_3^{tr} = i k_3''. \quad [2.40]$$

The wave vector is then complex, with a real part  $\vec{k}'_L = k_1 \vec{e}_{x_1}$  and an imaginary part  $\vec{k}''_L = k_3'' \vec{e}_{x_3}$ , these two components being orthogonal (Figure 2.9-a).

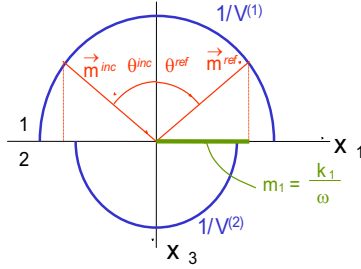


**Figure 2.8.** Interface fluid 1/fluid 2; the incident angle  $\theta^{inc}$  is larger than the critical angle, the projection on axis  $x_f$  of all the slowness vectors being noted  $m_1$ ; the reflected wave is propagative whereas the transmitted wave is evanescent

The particle displacement vector in the transmission medium is written

$$\vec{u}^{tr}(x_1, x_2, x_3; t) = \vec{a}^{tr} \exp(-i k_1 x_1 - i k_3^{tr} x_3 + i \omega t), \quad [2.41]$$

then, using equation [2.40]

$$\vec{u}^{tr}(x_1, x_2, x_3; t) = \vec{a}^{tr} \exp(k_3'' x_3) \exp(-i k_1 x_1 + i \omega t). \quad [2.42]$$

When  $x_3$  tends towards  $+\infty$ , the radiation to infinity criterion imposes that the complex amplitude  $\bar{a}^{tr} \exp(k_3'' x_3)$  decreases with  $x_3$ , which means that

$$k_3'' < 0. \quad [2.43]$$

It should be noted that the choice of the alternate temporal convention  $\exp(-i\omega t)$  would have led to  $k_3'' > 0$  representing the same physical phenomenon.

The complex amplitude  $\bar{a}^{tr}$  can be written as a function of the polarization vector  $\bar{P}^{tr}$ , unitary vector collinear to the wave vector  $\bar{k}^{tr}$ ,

$$\bar{a}^{tr} = \underline{a}^{tr} \bar{P}^{tr} = \underline{a}^{tr} \left( k_1/k_L \bar{e}_{x_1} + k_3^{tr}/k_L \bar{e}_{x_3} \right), \quad [2.44]$$

$$\text{i.e.} \quad \bar{a}^{tr} = \underline{a}^{tr} \left( k_1/k_L \bar{e}_{x_1} + i k_3''/k_L \bar{e}_{x_3} \right), \quad [2.45]$$

$$\text{with } \underline{a}^{tr} = \left| \underline{a}^{tr} \right| \exp(i\alpha), \quad [2.46]$$

The real particle displacement vector then has the following components

$$u_1 = \text{Re}(u_1^{tr}) = \left| \underline{a}^{tr} \right| k_1/k_L \exp(k_3'' x_3) \cos(-k_1 x_1 + \omega t + \alpha), \quad [2.47-a]$$

$$\text{and } u_3 = \text{Re}(u_3^{tr}) = -\left| \underline{a}^{tr} \right| k_3''/k_L \exp(k_3'' x_3) \sin(-k_1 x_1 + \omega t + \alpha). \quad [2.47-b]$$

The particles' trajectory at the distance  $x_3$  of the interface is thus elliptical, with a large axis parallel to the propagation direction (Figure 2.9-b) and its equation is:

$$\left( \frac{u_1}{\left| \underline{a}^{tr} \right| k_1/k_L \exp(k_3'' x_3)} \right)^2 + \left( \frac{u_3}{\left| \underline{a}^{tr} \right| k_3''/k_L \exp(k_3'' x_3)} \right)^2 = 1. \quad [2.48]$$



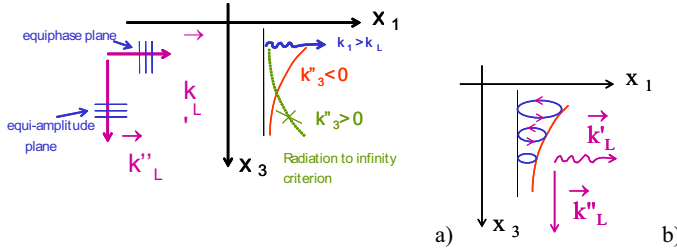


**Figure 2.9.** Decrease of the evanescent wave perpendicular to the interface, and energy propagation parallel to the interface

By anticipating the subject of section 2.1.2.7., we see that, although the reflection is total in medium 1 (the amplitude of the reflected wave is equal to that of the incident wave), a wave does exist in medium 2, and consequently some energy is transmitted to the second medium. The evanescent wave should be understood as a companion wave in medium 2, related to the total reflection phenomenon in medium 1, but having its own energy. This phenomenon can be understood only if we refer to the transient regime and to the phenomenon of oblique plane waves. In fact, every monochromatic problem is a steady-state issue: during the transient regime, energy having entered medium 2 is permanently present for infinite values of time. Thus, the monochromatic hypothesis corresponds to the asymptotic behavior of transient problems valid for a very large time  $t$ . The addition of the evanescent wave is thus needed to overcome this difficulty.

#### 2.1.2.7. Reflection and transmission coefficients

Particle displacement, associated with transverse and longitudinal waves and to incident, reflected and transmitted waves ( $X=inc, ref$  or  $tr$ ), can be written in the following form

$$u_i^X(x_1, x_2, x_3; t) = \underline{a}^X P_i^X \exp i(\omega t - \vec{k}^X \cdot \vec{x}), \quad [2.49]$$

where  $\underline{a}^X$  is the complex amplitude of wave  $X$  and  $P_i^X$  the projection on the  $x_i$ -axis of the polarization vector of this wave. The reflection and transmission coefficients  $R^{ref}$  and  $T^{tr}$  (in terms of the displacement amplitude) are

$$R^{ref} = \underline{a}^{ref} / \underline{a}^{inc} \quad \text{and} \quad T^{tr} = \underline{a}^{tr} / \underline{a}^{inc}. \quad [2.50]$$

These coefficients result from the boundary conditions written in [2.30]. As an example, Figure 2.10 shows the module of these reflection and transmission coefficients, versus the incident angle, for a water–isotropic aluminum interface (water being the incident medium). The zones where we observe a rapid variation of the reflection coefficient of the wave in the fluid medium, versus the incident angle, indicate the two critical angles for the interface considered (see section 2.1.2.6.). Another characteristic angle can also be seen on this figure: showing the propagation of a Rayleigh wave (see section 5.1.2.1.), appearing after the two critical angles.

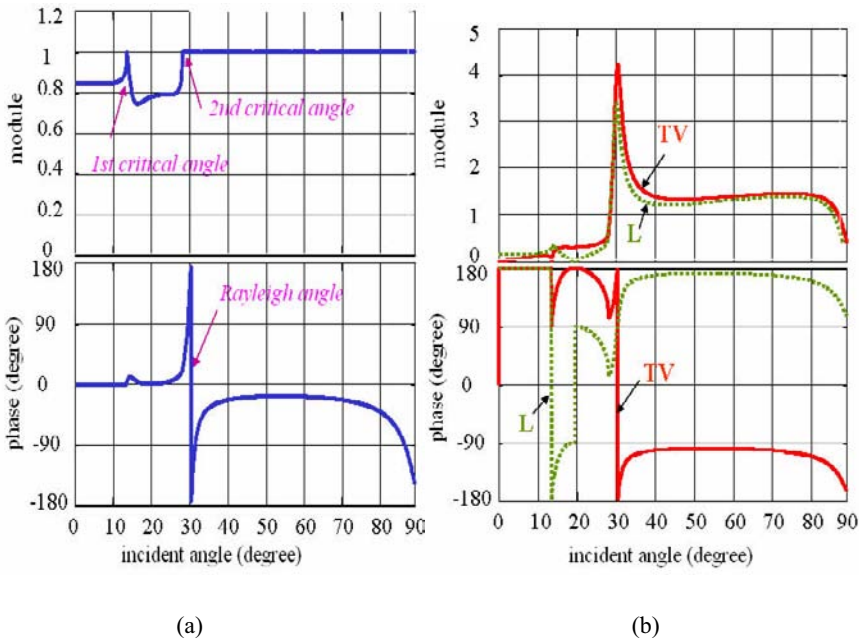


**Figure 2.10.** For a water–isotropic aluminum interface, -a) reflection coefficient (module and phase), -b) transmission coefficient (module and phase; dashed curve: longitudinal transmitted wave; continuous curve: transverse vertical transmitted wave). Water properties are:  $\rho_{\text{water}} = 1000 \text{ kg.m}^{-3}$  and  $V_{\text{water}} = 1480 \text{ m.s}^{-1}$ ; isotropic aluminum's are:  $\rho = 2786 \text{ kg.m}^{-3}$ ,  $V_L = 6650 \text{ m.s}^{-1}$ , and  $V_T = 3447 \text{ m.s}^{-1}$ . The reflection and transmission coefficients are calculated in terms of the displacement amplitude

### 2.1.3. Interface separating two anisotropic solid media

For a given propagation direction, in an anisotropic medium, three waves can propagate. They are no longer purely longitudinal or transverse, as in an isotropic solid medium, but are quasi-longitudinal or quasi-transverse (see section 1.2.2.1). The interaction of an incident wave with an interface separating two anisotropic media (perfect adherence) consequently produces three waves in each medium (Figure 2.11a). In the practical case of a control in immersion, the incident wave is always longitudinal and produces three waves in the anisotropic medium to be tested: a quasi-longitudinal wave (QL) and two quasi-transverse waves (QT1 and QT2) (Figure 2.11b). For a hexagonal symmetric medium, that is to say transversely isotropic as an unidirectional composite ply, one of the three waves may have a null transmission coefficient.

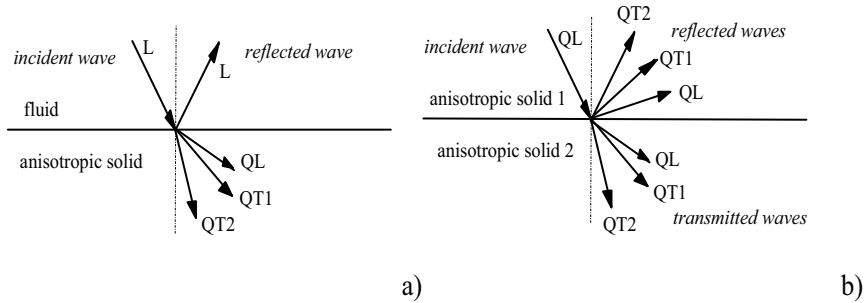


**Figure 2.11.** Interaction of an incident wave with an interface separating two media, of which one at least is anisotropic. a) fluid incident medium, b) anisotropic incident medium

Some principles formulated in section 2.1.2 remain valid (as frequency conservation through the interface, Snell–Descartes laws), but the determination of the reflected and transmitted waves is not as simple.

#### 2.1.3.1. Choice of reflected and transmitted waves

In an anisotropic medium, since the propagation velocity of waves depends on the propagation direction, intersections of slowness surfaces with the incident plane are no longer circular (see section 1.2.2.3) and the propagation direction of the energy of a wave  $\eta$  is no longer parallel to the one of the wave vector. Therefore, the determination of reflected and transmitted waves no longer results from the sign of the projection of the wave vector on  $x_3$ -axis, as before (see section 2.1.2.2). Introducing slownesses, and with our choice of coordinate system (Figure 2.1), the choice criterion of section 2.1.2.2. is now expressed as follows: a transmitted propagative wave in a fluid or isotropic solid medium such as  $m_3$  is positive,

whereas a reflected propagative wave such as  $m_3$  is negative. In an anisotropic medium, the only criterion allowing the attribution to a wave of the reflected or transmitted property is the sign of the projection of the Poynting vector (or of the energy speed) on the axis perpendicular to the interface, thus the  $x_3$  axis. Thus, the display of the reflected and transmitted waves, with the help of a graphical construction and using the slowness curves, requires using the complete curves, and not only the half part corresponding to  $x_3 > 0$  or  $x_3 < 0$ .

Figure 2.12 shows the intersection of the slowness surface of a transversely isotropic material (carbon/epoxy) with the incident plane. In the case of a water-carbon/epoxy interface, the incident angle chosen for Figure 2.12a) could make it seem as if only the slowness curve corresponding to  $x_3 > 0$  is enough to determine the transmitted waves. On the other hand, Figure 2.12b) clearly shows that the sign of the projection on the  $x_3$ -axis of the slowness vector  $^{(3)}m_3 < 0$  of wave  $\eta = 3$  (which would have led, in an isotropic solid medium, to the consideration of this wave propagating towards  $x_3 < 0$ ) is not sufficient. In fact, the projection on the  $x_3$ -axis of its Poynting vector is positive, which leads, on the contrary, for us to consider the wave as propagating towards  $x_3 > 0$ . We will note in Figure 2.12-b) that, on the contrary, one of the three waves whose  $m_3$  is positive propagates towards  $x_3 < 0$ , such that the number of waves propagating towards  $x_3 < 0$  remains equal to three. This result is general.

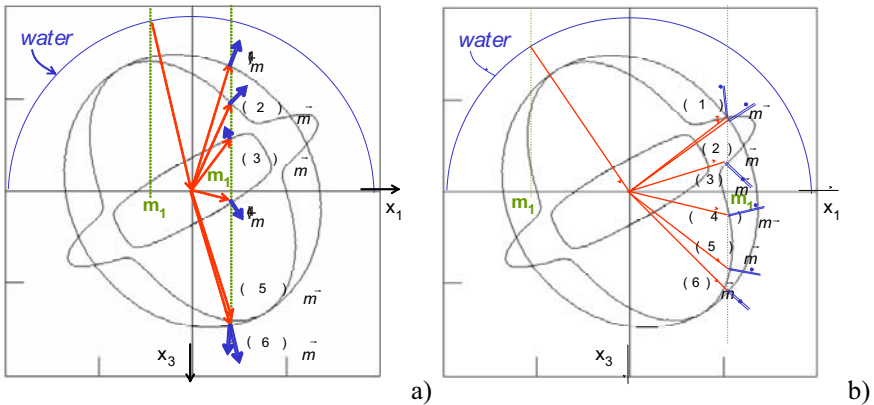


**Figure 2.12.** Case of a water-carbon/epoxy interface; intersection of slowness surfaces of carbon/epoxy and water with the incident plane. The double arrows represent the direction of the Poynting vector of each wave

### 2.1.3.2. Writing of the boundary conditions

When two solids are rigidly linked, the embedding conditions express the continuity of the particle displacement and stress vectors applied on a surface element of the interface (of normal direction  $\vec{e}_{x_3}$ ). Thus, these three continuity conditions are written in the plane  $x_3 = 0$  that corresponds to the interface. They are identical to those written in equations [2.20] and [2.30], except that for anisotropic solids, these vectors can have three non-zero components. These equations are then written

$$u_i^{inc} + \sum_{ref} u_i^{ref} = \sum_{tr} u_i^{tr}, \quad i = 1, 2, 3 \quad (x_3 = 0, \forall x_1, x_2, t), \quad [2.51-a]$$

$$\text{and} \quad T_{j3}^{inc} + \sum_{ref} T_{j3}^{ref} = \sum_{tr} T_{j3}^{tr}, \quad j = 1, 2, 3 \quad (x_3 = 0, \forall x_1, x_2, t), \quad [2.51-b]$$

where  $T_{j3} = (\vec{T} \cdot \vec{e}_{x_3}) \cdot \vec{e}_{x_j}$ .

Each continuity equation [2.51] thus gives three relationships, i.e. a total of six equations, for six unknown amplitudes.

For a fluid–solid interface, the displacement continuity concerns only the components normal to the interface ( $i = 3$ ) in equation [2.51a], which leads to four continuity equations, with four unknown quantities (amplitudes of the three waves in the anisotropic solid medium and amplitude of the longitudinal reflected wave in the fluid medium).

As in section 2.1.2.6., when the incident angle increases, beyond a certain value, there is no longer an intersection between the vertical line (corresponding to the projection  $m_1$  of the slowness vector of the incident wave on axis  $x_1$ ) and the different slowness curves; this corresponds to waves becoming inhomogenous. Again, the corresponding limit incident angles are also named critical angles; we can usually find three such critical angles, as shown on Figure 2.13 in the case of a water–carbon/epoxy interface (due to the material symmetry, only half of the slowness curves are represented).

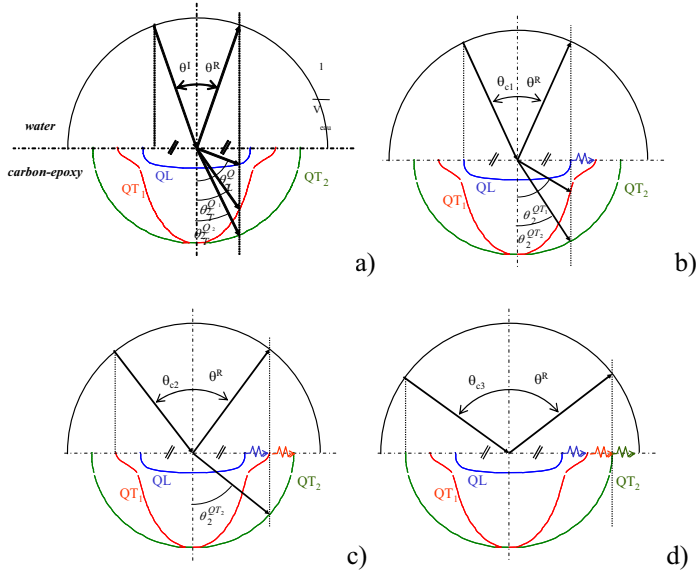


**Figure 2.13.** Critical angles for a water–carbon/epoxy interface. a) sub critical incident angle (all the waves are propagative) b) 1st critical angle: QL wave becomes inhomogeneous, c) 2nd critical angle: QT1 wave also becomes inhomogeneous, d) 3rd critical angle: all transmitted waves are inhomogeneous

The decrease direction of an inhomogeneous wave is given, as in section 2.1.2.6., by a reasoning on the decrease of the amplitude of the wave, that depends on an exponential propagation factor  $\exp(-ik_3 x_3)$ . In the anisotropic case, the projection  $k_3$  of the wave number vector on axis  $x_3$  is complex in the general case (and not purely imaginary as in the fluid or isotropic solid case), and is written

$$k_3 = k'_3 + ik''_3 \quad [2.52]$$

The exponential propagation factor is thus given by  $\exp(-ik'_3 x_3) \exp(k''_3 x_3)$ , which leads to the expression  $k''_3 < 0$  for waves decreasing towards  $x_3 > 0$ , and  $k''_3 > 0$  for waves decreasing towards  $x_3 < 0$ . This results from the radiation to infinity criterion that imposes a decrease of the complex amplitude.

## 2.2. Bibliography

- [BAL 03] BALTAZAR A., WANG L., XIE B., ROKHLIN S.I., “Inverse ultrasonic determination of imperfect interfaces and bulk properties of a layer between two solids”, *J. Acoust. Soc. Am.* 114(3), Sept 2003.
- [PIL 82] PILARSKI A., “Ultrasonic wave propagation in a layered medium under different boundary conditions”, *Arch. Acoust.*, 7, 1982.
- [ROK 81] ROKHLIN S.I., HEFETS M., ROSEN M., “An ultrasonic interface-wave method for predicting the strength of adhesive bonds”, *J. Appl. Phys.*, 52, 1981.

This page intentionally left blank



## Chapter 3

# Propagation of Plane Waves in Multilayered Media

### 3.1. Introduction

Multilayered anisotropic materials, such as composites, are being used increasingly, particularly in the aviation industry, because they have good mechanical properties, associated with a low mass. The literature dedicated to their non-destructive testing and evaluation has become more and more profuse over the last few years. In addition to the application to composite materials, a part of the literature concerns the study of the sea bed and soils which are also multilayered. That is why several works have focused on geophysics and earthquakes since the 1950s [THO 50], [HAS 53], [KNO 64], [SCH 74]: the the studied layers were mostly isotropic, glued on a substrate, however those studied later were triclinic [SCH 74]. This section aims to present the general principle of propagation in a multilayered anisotropic medium. Then we will deal with the case of periodical media (such as composites) which give rise to particular phenomena as angular or frequential stopping bands. The understanding of wave propagation in a single layer of an anisotropic solid is a necessary preamble, and will be the subject of section 3.1.1.

### 3.1.1. Propagation on a single material layer

#### 3.1.1.1. Number of waves propagating in a layer

A layer 1 of thickness  $h$ , made of an anisotropic material, is surrounded by two semi-infinite media 0 and 2, *a priori* distinct, which can be fluid or solid (Figure 3.1). When media 1 and 2 are solid, embedding conditions with the layer are considered. As it has been seen before in Chapter 2, the interaction of an oblique monochromatic plane wave, with an incident angle  $\theta$  and an angular frequency  $\omega$ , propagating in medium 0 and meeting the first interface medium 0/layer 1, yields three waves propagating or decreasing towards  $x_3 > 0$  in the layer, and one or several reflected waves (depending on the nature of medium 0) propagating towards  $x_3 < 0$ . Each of these waves behaves like an incident wave for the interface layer 1/medium 2, and then yields three waves in layer 1, and three waves in medium 2 if this is anisotropic (Figure 3.1-a). There is thus an infinity of waves in the layer, if all the reflections are taken into account. However, there are only six types of generated waves at each interface: two quasi-longitudinal waves (QL), two quasi-transverse 1 waves (QT1) and two quasi-transverse 2 waves (QT2). Thus it is not necessary to consider the infinity of waves propagating into the layer, and the linear combination of each type of generated waves is sufficient; that leads to the presence of six waves in the layer (Figure 3.1-b).

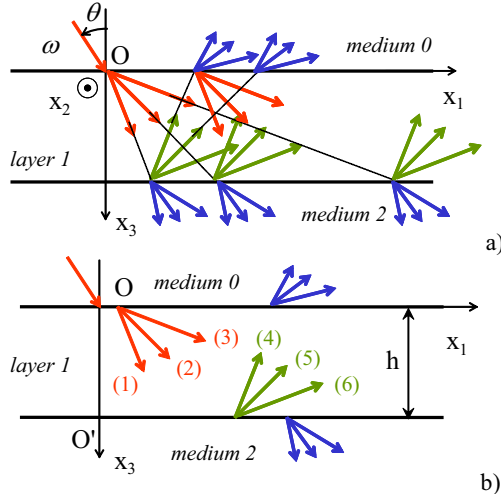


**Figure 3.1.** Interaction of an oblique monochromatic plane wave with an anisotropic solid layer. The plane  $(O x_1 x_2)$  is the plane of interface. a) each wave propagating in the layer yields three waves when it meets an interface; b) the linear combination of each type of waves allows the consideration of only six waves propagating in the layer

Another way of considering this matter is to focus on the intersection of the incident plane with the slowness surfaces of the material composing the layer 1. Figure 2.9-a) of section 2.1.3.1 shows that there can be at the most only six intersections with the vertical line corresponding to the projection on the interface of the slowness vector of the incident wave. The waves propagate or decrease in the  $x_3 > 0$  direction and in the  $x_3 < 0$  direction at the same time, thus there is no need to select waves in order to study the propagation in a layer, as in the case of an interface between two semi-infinite media.

### 3.1.1.2. Obtaining slowness and polarization vectors

This section aims to obtain the slowness and polarization vectors of the six waves propagating or decreasing in layer 1, knowing the properties of the incident wave (incident angle  $\theta$ , amplitude  $a^{inc}$ , polarization vector  $\vec{P}^{inc}$ , velocity  $V^{inc}$ , angular frequency  $\omega$ ), density  $\rho^q$  and elastic constants  $\left(c_{ijkl}^q = c_{\alpha\beta}^q\right)$  of each medium: medium 0 ( $q = 0$ ), layer 1 ( $q = 1$ ) and medium 2 ( $q = 2$ )).

It should be noted here that the problem is very different from that consisting in searching velocities and polarization vectors in an infinite medium, for a given propagation direction (see section 1.2.2.1). In fact, in an infinite medium, for a single propagation direction  $\vec{n}$ , three waves propagate; the three polarization vectors are perpendicular to each other, and there are three propagation velocities, obtained by the search of eigenvalues and eigenvectors of the Christoffel's tensor. In the present case, for a given incident wave (that is to say for the incident wavevector projection  $k_1$  on axis  $x_1$  of the interface (or a projection  $m_1$  of the slowness vector)), six waves (marked by the quantum number  $\eta$ ) can propagate, each one having its own propagation direction  $^{(\eta)}\vec{n}^1$ . For example, Figure 3.2 shows the intersection of the three layers of the slowness surface of carbon-epoxy with the incident plane, and their six intersections with the vertical line corresponding to a given projection  $m_1$ . The reflected QL wave has thus a propagation direction and a slowness  $1/V_1$ . However, for this propagation direction, there are three intersections with the slowness curves, corresponding to the propagation of three waves in an infinite medium. Among these three waves, only one corresponds to the projection  $m_1$  of the slowness vector of the incident wave. It should also be noted that if the three polarization vectors are perpendicular to each other, this is not the case of the six polarization vectors corresponding to the intersection of the vertical line with the slowness curves.

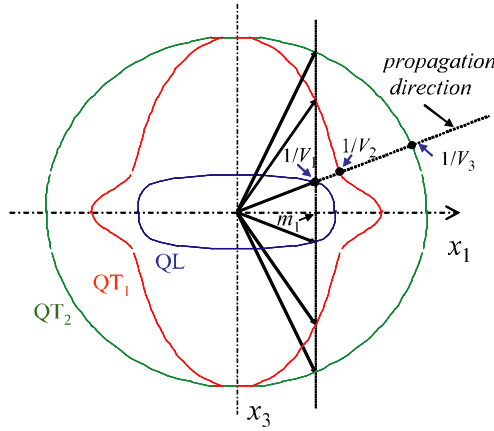


**Figure 3.2.** Intersection of the slowness surfaces of carbon-epoxy with the incident plane  $(Ox_1x_2)$ . To a projection  $m_1$  of the slowness vector of all the waves, correspond six intersections with the slowness curves. To each propagation direction correspond three velocities, thus three slownesses  $1/V_i$ ,  $(i = 1, 2, 3)$  and three polarization vectors perpendicular to each other

Christoffel's equation [1.74], enabling the search of plane wave solutions (marked by  $\eta$ ) of the propagation equation, is written

$$^{(\eta)}\Gamma_{ik}^{(\eta)}P_k = \rho^{(\eta)}V^2^{(\eta)}P_i, \quad [3.1-a]$$

$$\text{with } ^{(\eta)}\Gamma_{ik} = c_{ijkl}^{(\eta)}n_j^{(\eta)}n_l^{(\eta)}, \quad [3.1-b]$$

where  $^{(\eta)}\Gamma_{ik}$  is the Christoffel tensor,  $^{(\eta)}P_k$  and  $^{(\eta)}n_k$  are the projections on  $x_k$ -axis of the polarization and propagation direction vectors of wave  $\eta$  (normalized vectors), respectively, and  $c_{ijkl}$  is a coefficient of the elastic stiffness tensor of the considered medium. This equation can also be written as a function of the slowness vector  $^{(\eta)}\vec{m}$ , of projection  $^{(\eta)}m_k = ^{(\eta)}n_k / ^{(\eta)}V$  on  $x_k$ -axis:

$$\left( c_{ijk\ell}^{(\eta)}m_j^{(\eta)}m_\ell^{(\eta)} - \rho\delta_{ik} \right) ^{(\eta)}P_k = 0, \quad [3.2-a]$$

$$\text{or } ^{(\eta)}G_{ik}^{(\eta)}P_k = 0, \quad [3.2-b]$$

$$\text{with } {}^{(\eta)}G_{ik} = c_{ijk\ell} {}^{(\eta)}m_j {}^{(\eta)}m_\ell - \rho \delta_{ik} \quad [3.2-c]$$

where  $\delta_{ik}$  is the unitary tensor.

In equation [3.2], besides the medium properties, only the projections  $m_1$  and  $m_2$  of the slowness vector of the incident wave on the interface are known, and thus, according to the Snell–Descartes law, of all the waves  $\eta$  ( $\eta = 1, \dots, 6$ ), the incident plane is chosen so that  $m_2 = 0$ . Thus the only unknown component of the slowness vector of wave  $\eta$  is its projection  ${}^{(\eta)}m_3$  on the  $x_3$ -axis. Moreover, the three components  ${}^{(\eta)}P_k$  of the polarization vector on axis  $x_k$  are also unknown. Equation [3.2-a] has non-zero solutions in  ${}^{(\eta)}P_k$  if the determinant of  ${}^{(\eta)}G_{ik}$  is zero, that is to say

$$\left\| c_{ijk\ell} {}^{(\eta)}m_j {}^{(\eta)}m_\ell - \rho \delta_{ik} \right\| = 0. \quad [3.3]$$

The cancelation of the 6-order determinant gives a 6-degree equation in  ${}^{(\eta)}m_3$ , with real coefficients if the medium absorption is neglected, that is to say if the elastic stiffness constants are real. This equation solving, explained in [ROK 86], gives six real or complex roots conjugated with each other, which enables us to obtain the six slowness vectors for each wave  $\eta$ . For each wave  $\eta$  whose slowness vector is determined, equation [3.2-a] enables us to calculate  ${}^{(\eta)}P_k$  up to a multiplicative factor. This vector is normalized with a hermitian norm defined by  ${}^{(\eta)}P_k {}^{(\eta)}P_k^*$  where  ${}^{(\eta)}P_k^*$  is the complex conjugate of  ${}^{(\eta)}P_k$ . The slowness and polarization vectors are complex, the real part corresponding to the propagative part and the imaginary one to the decreasing part of the wave.

This method of solution also allows us to find the slowness and polarization vectors of the reflected and transmitted waves in the external media 0 and 1; in this case, we must add an energetic criterion for selecting waves propagating or decreasing in the  $x_3 > 0$  or  $x_3 < 0$  direction for transmitted or reflected waves, respectively (see section 2.1.3.1. and 2.1.3.2).

3.1.1.3. *Displacement and stress vectors*

The particle displacement vector of a plane monochromatic wave  $\eta$  with angular frequency  $\omega$ , amplitude  $^{(\eta)}a$  and polarization vector  $^{(\eta)}\vec{P}$  is written

$$^{(\eta)}\vec{u}(\vec{x};t) = ^{(\eta)}a^{(\eta)}\vec{P} \exp i(\omega t - ^{(\eta)}\vec{k} \cdot \vec{x}), \quad [3.4]$$

that is to say, as a function of the slowness vector  $^{(\eta)}\vec{m}$

$$^{(\eta)}\vec{u}(x_1, x_2, x_3; t) = ^{(\eta)}a^{(\eta)}\vec{P} \exp i\omega \left( t - m_1 x_1 - ^{(\eta)}m_3 x_3 \right). \quad [3.5]$$

The total particle displacement in layer 1 is thus the sum of particle displacements of each wave  $\eta$ , i.e.

$$\vec{u}(x_1, x_2, x_3; t) = \exp i\omega \left( t - m_1 x_1 \right) \sum_{\eta=1}^6 ^{(\eta)}a^{(\eta)}\vec{P} \exp \left( -i ^{(\eta)}m_3 x_3 \right). \quad [3.6]$$

The stress vector is given by Hooke's law (equation [1.46] or [1.48])

$$^{(\eta)}T_{ij} = c_{ijk\ell} \frac{\partial ^{(\eta)}u_k}{\partial x_\ell}, \quad [3.7-a]$$

$$\text{or } ^{(\eta)}T_\alpha = c_{\alpha\beta} ^{(\eta)}S_\beta, \quad [3.7-b]$$

with conventions explained in section 1.1.2.4.1.

The total stress vector in layer 1 is thus the sum of stress vectors of each wave  $\eta$  involved in the writing of boundary conditions, i.e., for a stress vector applied on a surfacic element at the interface (with normal  $\vec{e}_{x_3}$ ), i.e.  $T_{i3}$  ( $i=1,2,3$ ) or  $T_\alpha$  ( $\alpha=3,4,5$ ), [1.117]. Replacing  $^{(\eta)}u_k$  in equation [3.7] by its expression [3.6] projected on  $x_k$ -axis, the stress vector is finally written

$$\begin{aligned} T_\alpha = & -i\omega \exp i\omega \left( t - m_1 x_1 \right) \\ & \sum_{\eta=1}^6 ^{(\eta)}a \exp \left( -i ^{(\eta)}m_3 x_3 \right) \left[ c_{\alpha 1 m_1} ^{(\eta)}P_1 + c_{\alpha 3} ^{(\eta)}m_3 ^{(\eta)}P_3 \right. \\ & + c_{\alpha 4} ^{(\eta)}m_3 ^{(\eta)}P_2 + c_{\alpha 6 m_1} ^{(\eta)}P_2 + \\ & \left. + c_{\alpha 5} \left( ^{(\eta)}m_3 ^{(\eta)}P_1 + m_1 ^{(\eta)}P_3 \right) \right], \alpha = 3, 4, 5. \end{aligned} \quad [3.8]$$

It should be noted that the projection  $^{(\eta)}P_2$  of the polarization vector  $^{(\eta)}\vec{P}$  on the  $x_2$ -axis (perpendicular to the incident plane) is involved in equation [3.8]. In fact, the incident plane has been chosen so that it contains the wave vector of the incident wave, and thus,  $^{(\eta)}m_2 = 0$ . On the other hand, particles can have a displacement outside the incident plane, and thus,  $^{(\eta)}P_2 \neq 0$  in general.

It is convenient to introduce two vectors: the state vector  $\mathcal{W}(x_3)$ , named *displacement-stress vector*, comprising the three components of the total particle displacement vector  $\vec{u}$  and the three components  $(T_{33}, T_{23}, T_{13})$  of the stresses applied on an area parallel to the interfaces, and the displacement amplitude vector  $\mathcal{H}$  comprising the six displacement amplitudes  $^{(\eta)}a$ :

$$\mathcal{W}(x_3) = \langle u_1, u_2, u_3, T_{33}, T_{23}, T_{13} \rangle^T, \quad 0 \leq x_3 \leq h, \quad [3.9]$$

$$\text{and } \mathcal{H} = \langle {}^{(1)}a, {}^{(2)}a, {}^{(3)}a, {}^{(4)}a, {}^{(5)}a, {}^{(6)}a \rangle^T, \quad [3.10]$$

where  $^T$  refers to the transposition operation.

From equations [3.6] and [3.8], it is possible to express the state vector  $\mathcal{W}(x_3)$  as a function of the amplitude vector  $\mathcal{H}$  by the equation

$$\mathcal{W}(x_3) = \Omega A \mathcal{H}(x_3) \exp(i\omega(t - m_1 x_1)), \quad [3.11]$$

where  $\Omega$  and  $\mathcal{H}(x_3)$  are 6th-order diagonal matrices defined by

$$\Omega_{jj} = 1 \quad \text{if } j = 1, 2, 3 \quad \text{and} \quad \Omega_{jj} = -i\omega \quad \text{if } j = 4, 5, 6, \quad [3.12]$$

$$\text{and } \mathcal{H}_{\eta\eta}(x_3) = \exp(-i {}^{(\eta)}m_3 x_3), \quad [3.13]$$

respectively.

Matrix  $A$  is a squared 6th-order matrix such that its  $\eta^{th}$  column is

$$(A)_\eta = \left\{ \begin{array}{c} {}^{(\eta)}P_1 \\ {}^{(\eta)}P_2 \\ {}^{(\eta)}P_3 \\ c_{31}m_1{}^{(\eta)}P_1 + c_{33}{}^{(\eta)}m_3{}^{(\eta)}P_3 + c_{34}{}^{(\eta)}m_3{}^{(\eta)}P_2 + c_{36}m_1{}^{(\eta)}P_2 \\ \quad + c_{35}\left({}^{(\eta)}m_3{}^{(\eta)}P_1 + m_1{}^{(\eta)}P_3\right) \\ c_{41}m_1{}^{(\eta)}P_1 + c_{43}{}^{(\eta)}m_3{}^{(\eta)}P_3 + c_{44}{}^{(\eta)}m_3{}^{(\eta)}P_2 + c_{46}m_1{}^{(\eta)}P_2 \\ \quad + c_{45}\left({}^{(\eta)}m_3{}^{(\eta)}P_1 + m_1{}^{(\eta)}P_3\right) \\ c_{51}m_1{}^{(\eta)}P_1 + c_{53}{}^{(\eta)}m_3{}^{(\eta)}P_3 + c_{54}{}^{(\eta)}m_3{}^{(\eta)}P_2 + c_{56}m_1{}^{(\eta)}P_2 \\ \quad + c_{55}\left({}^{(\eta)}m_3{}^{(\eta)}P_1 + m_1{}^{(\eta)}P_3\right) \end{array} \right\}. \quad [3.14]$$

#### 3.1.1.4. Numerical problems

The writing of displacement–stress vector  $\mathcal{W}(x_3)$  shows exponential propagation terms such as  $\exp\left(-i{}^{(\eta)}m_3x_3\right)$  which are contained in matrix  $\mathcal{H}(x_3)$ . Thus it clearly appears that if the product  $\left(-i{}^{(\eta)}m_3x_3 = -i\omega^{(\eta)}k_3x_3\right)$  is real, which leads us to consider inhomogenous waves with  ${}^{(\eta)}m_3 = {}^{(\eta)}m'_3 + i{}^{(\eta)}m''_3$  being complex, the calculation of the exponential can outreach the calculation limits of the computer system. This situation occurs when the product of the layer thickness with the incident wave frequency is huge. The exponential propagation factor, combined with first-order values, yields important precision losses.

Figure 3.3 shows the case where waves numbered from 1 to 3 propagate or decrease in the  $x_3 > 0$  direction (wave 1 being inhomogenous) and where waves numbered from 4 to 6 propagate or decrease in the  $x_3 < 0$  direction (wave 4 being inhomogenous).



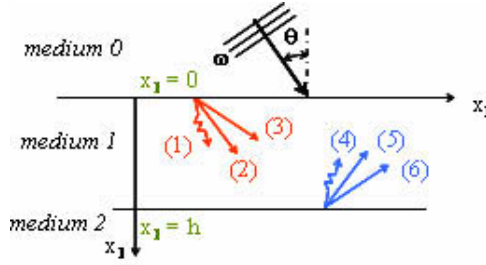


**Figure 3.3.** Propagation in a layer of material, waves 1 and 4 being inhomogenous, decreasing in directions  $x_3 > 0$  and  $x_3 < 0$  respectively

The amplitude of wave 1 is finite at  $x_3 = 0$ , and that of wave 4 is also finite at  $x_3 = h$  because of the mode conversion. The displacement amplitude of wave 4 is thus very small at  $x_3 = h$ , and, if its reference is set up at  $x_3 = 0$ , it is multiplied by a huge exponential propagation factor in order to have a finite value at  $x_3 = h$ , which yields precision losses and thus numerical problems.

To avoid this, a solution consists of referencing the displacement amplitudes of waves propagating (or decreasing) in the  $x_3 > 0$  direction at  $x_3 = 0$ , the reference of displacement amplitudes of waves propagating (or decreasing) in the opposite direction being made at  $x_3 = h$ . Displacements and stresses in the layer are thus of the form:

$$\sum_{\eta=1}^3 \alpha_{\eta} e^{-i \omega^{(\eta)} m_3 (x_3 - 0)} + \sum_{\eta=4}^6 \alpha_{\eta} e^{-i \omega^{(\eta)} m_3 (x_3 - h)}, \quad [3.15-a]$$

$$\text{i.e. } \sum_{\eta=1}^3 \alpha_{\eta} + \underbrace{\sum_{\eta=4}^6 \alpha_{\eta} e^{+i \omega^{(\eta)} m'_3 h} e^{-\omega^{(\eta)} m''_3 h}}_{\rightarrow 0 \text{ if } \eta = 4} \text{ at } x_3 = 0, \quad [3.15-b]$$

$$\text{and } \underbrace{\sum_{\eta=1}^3 \alpha_{\eta} e^{-i \omega^{(\eta)} m'_3 h} e^{+ \omega^{(\eta)} m''_3 h}}_{\rightarrow 0 \text{ if } \eta = 1} + \sum_{\eta=4}^6 \alpha_{\eta} \text{ at } x_3 = h. \quad [3.15-c]$$

It clearly appears in equations [3.15] that, as  $^{(\eta)}m''_3 > 0$  when wave  $\eta$  decreases in the  $x_3 > 0$  direction whereas  $^{(\eta)}m''_3 < 0$  in the opposite case, the exponential propagation factors, initially sources of numerical problems, tend towards zero.

This method completely eliminates the numerical problems during propagation in a single layer of the material, and reduces to a simple *basis change* for the displacement amplitudes. In the case of multilayered media, the use of this method layer by layer (global matrix method) is also very competitive if the number of layers is not too big (see section 3.1.2.1). On the other hand, the more synthetic use of the transfer matrix method, which limits the size of the linear system which can be solved, requires the use of adapted methods (see section 3.1.3.3).

#### 3.1.1.5. *Writing of boundary conditions in the case of a layer immersed in a fluid*

This section aims to explain equations that must be written in order to determine the reflection and transmission coefficients in the fluid, as well as displacement amplitudes of the six waves propagating in the anisotropic solid layer. The problem is thus that of Figure 3.1-b with identical fluid media 0 and 2; there is thus only one reflected longitudinal wave, and only one transmitted longitudinal wave.

There are eight unknowns in this problem: the six displacement amplitudes  $^{(\eta)}a$ , grouped in the column vector  $\mathcal{A}$ , the reflection coefficient  $\mathcal{R}$  and the transmission coefficient  $\mathcal{T}$ .

There are also eight continuity equations (see section 2.1.3.2): at each interface, at  $x_3 = 0$  and at  $x_3 = h$ , equality of the normal displacements  $u_3$  (one equation) and equality of stresses  $T_{33}$ ,  $T_{23}$  and  $T_{13}$  (three equations) have to be written.

Denoting  $P_3^{inc}$ ,  $P_3^{ref}$  and  $P_3^{tr}$ , the projections on the  $x_3$ -axis of polarization vectors of the incident, reflected and transmitted waves,  $a^{inc}$ ,  $a^{ref}$ , and  $a^{tr}$  the displacement amplitudes of the incident, reflected and transmitted waves,  $V_f$  the propagation velocity of waves in the fluid and  $\rho_f$  the density of the fluid, the boundary conditions are written, at  $x_3 = 0$ :

$$u_3 : a^{inc} P_3^{inc} + a^{ref} P_3^{ref} = \sum_{\eta=1}^6 {}^{(\eta)}a \underbrace{{}^{(\eta)}P_3}_{A_{3\eta}}, \quad [3.16-a]$$

$$T_{33} : a^{inc} \rho_f V_f + a^{ref} \rho_f V_f = \sum_{\eta=1}^6 {}^{(\eta)}a A_{4\eta}, \quad [3.16-b]$$

$$T_{32} : 0 = \sum_{\eta=1}^6 {}^{(\eta)}a A_{5\eta}, \quad [3.16-c]$$

$$T_{31} : 0 = \sum_{\eta=1}^6 {}^{(\eta)}a A_{6\eta}. \quad [3.16-d]$$

At  $x_3 = h$ , noticing that  ${}^{(\eta)}P_3 = A_{3\eta}$  and  $\exp(-i {}^{(\eta)}m_3 h) = \mathcal{H}_{\eta\eta}(h)$ , these conditions are written:

$$u_3 : \sum_{\eta=1}^6 {}^{(\eta)}a A_{3\eta} \mathcal{H}_{\eta\eta}(h) = a^{tr} P_3^{tr}, \quad [3.17-a]$$

$$T_{33} : \sum_{\eta=1}^6 {}^{(\eta)}a A_{4\eta} \mathcal{H}_{\eta\eta}(h) = a^{tr} \rho_f V_f, \quad [3.17-b]$$

$$T_{32} : \sum_{\eta=1}^6 {}^{(\eta)}a A_{5\eta} \mathcal{H}_{\eta\eta}(h) = 0, \quad [3.17-c]$$

$$T_{31} : \sum_{\eta=1}^6 {}^{(\eta)}a A_{6\eta} \mathcal{H}_{\eta\eta}(h) = 0. \quad [3.17-d]$$

Matrices  $A$  and  $\mathcal{H}$  are defined by equations [3.13] and 3.14], respectively. It should be noted that the amplitude of the transmitted wave is referenced here at  $x_3 = h$  (point O' on Figure 3.1-b), and that, in order to simplify calculations, displacement amplitudes of waves in the layer are all referenced here at  $x_3 = 0$  using the reference change method described earlier (section 3.1.1.4.) The system of equations to solve [3.16] and [3.17] is thus a linear six-order system.

### 3.1.2. Propagation in a multilayered medium

#### 3.1.2.1. Problem setting – global matrix method

The multilayered medium shown in Figure 3.4 is made by stacking  $Q$  anisotropic solid layers supposed rigidly linked, infinite in the plane ( $Ox_1x_2$ ), with any thickness and orientation. The axis perpendicular to the interfaces is denoted  $x_3$ . This assembly is surrounded by two semi-infinite media 0 and  $Q+1$ , *a priori* distinct and they can be fluid or solid. Each layer is marked by the quantum number

$q$  ( $1 \leq q \leq Q$ ), has a thickness  $h^q$  and consists of material with elastic stiffness constants  $c_{ijkl}^q$  and density  $\rho^q$ . Its upper and lower interfaces are at  $x_3 = \zeta_{q-1}$  and  $x_3 = \zeta_q$ , respectively. The multilayered medium thus has a total thickness  $H = \sum_{q=1}^Q h^q$ . The plane  $(Ox_1x_3)$  is the incident plane: an oblique monochromatic plane wave of angular frequency  $\omega$  and incident angle  $\theta$  propagates in medium 0.

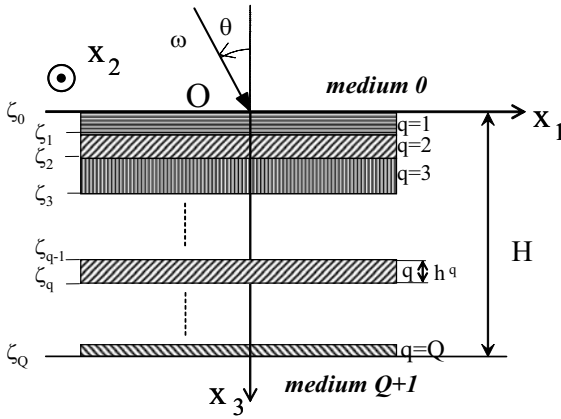


**Figure 3.4.** Geometry of the multilayered medium

All equations in section 3.1.1, written for a single layer, are valid for the layer  $q$ ,  $\zeta_{q-1} \leq x_3 \leq \zeta_q$ , adding a superscript  $q$  to all quantities (displacement  $\vec{u}^q$ , stress  $T_{ij}^q$ , amplitude  $^{(\eta)}a^q$ , polarization  $^{(\eta)}\vec{p}^q$ , slowness  $^{(\eta)}\vec{m}^q$ , etc.). Also, matrices  $A$  and  $\mathcal{H}(x_3)$  and column vectors  $\mathcal{W}(x_3)$  and  $\mathcal{A}$ , defined in this same section, are now written  $A^q$ ,  $\mathcal{H}^q(x_3)$ ,  $\mathcal{W}^q(x_3)$  and  $\mathcal{A}^q$ . In this way, the displacement–stress vector is written

$$\mathcal{W}^q(x_3) = B^q \mathcal{H}^q(x_3) \mathcal{A}^q \exp i\omega \left( t - m_1 x_1 \right), \quad \zeta_{q-1} \leq x_3 \leq \zeta_q, \quad [3.18a]$$

$$\text{where } B^q = \Omega A^q. \quad [3.18b]$$

Knowing the properties of the incident wave and the physical characteristics of materials constituting each medium, the amplitudes of waves propagating in each

layer of the multilayered medium and the reflection and transmission coefficients in extreme media are obtained by writing the boundary conditions at the interface separating two successive layers (i.e.  $6*(Q-1)$  equations), and at the extreme interfaces (i.e., depending on the nature of the media, at most  $2*6=12$  equations). The number of equations is thus at most equal to  $6*(Q+1)$ .

The number of unknowns in the problem is also  $6*(Q+1)$ : the  $6*Q$  amplitudes of waves propagating in each layer, the three reflection coefficients in medium 0 (if it is an anisotropic solid) and the three transmission coefficients in medium  $(Q+1)$  (if it is an anisotropic solid).

The linear system to be solved is thus at most  $6*(Q+1)$ -order. If we apply the method of reference change for the displacement amplitude in each layer  $q$  (described in section 3.1.1.4.), and if the memory capacity of the computer system used is not overwhelmed, this method of solution, sometimes called *global matrix method* [LOW 95], has the advantage of always being numerically stable. On the other hand, the size of the system being solved depends on the number of layers.

### 3.1.2.2. Transfer matrix method

Frequently used in other parts of physics, the transfer matrix method, often called Thomson–Haskell method in the frame of wave propagation in multilayered media [THO 50], [HAS 53], has the advantage of giving reflection and transmission coefficients by solving an equation system of order at most equal to 12, by simple 6th-order matrices multiplications, whatever the number of layers. Unfortunately, this method leads to numerical problems, due to the physical problem explained in section 3.1.1.4, and therefore needs the use of an adapted method to avoid this difficulty.

The transfer matrix of layer  $q$  enables us to express the state displacement–stress vector  $\mathcal{W}^q(x_3)$  at the lower interface of the layer at  $x_3 = \zeta_q$ , as a function of that at the former interface at  $x_3 = \zeta_{q-1}$ . Replacing  $x_3$  by  $\zeta_q$  and by  $\zeta_{q-1}$ , with  $\mathcal{H}^q = \mathcal{H}^q(h^q)$  and denoting  $X^{-1}$  the inverse matrix of  $X$ , equation [3.18] is written

$$\mathcal{W}^q(\zeta_{q-1}) = B^q \mathcal{A}^q \exp i\omega(t - m_1 x_1) \text{ for } x_3 = \zeta_{q-1}, \quad [3.19\text{-a}]$$

$$\text{and } \mathcal{W}^q(\zeta_q) = B^q \mathcal{H}^q \mathcal{A}^q \exp i\omega(t - m_1 x_1) \text{ for } x_3 = \zeta_q, \quad [3.19\text{-b}]$$

$$\text{i.e. } \mathcal{W}^q(\zeta_q) = \tau^q \mathcal{W}^q(\zeta_{q-1}), \quad [3.19\text{-c}]$$

$$\text{where } \tau^q = B^q \mathcal{H}^q \left( B^q \right)^{-1}. \quad [3.20]$$

The 6th-order matrix  $\tau^q$  is called transfer matrix of layer  $q$ , in displacement–stress.

Step by step, using relationship [5.7-c] and writing the boundary conditions at the interface separating two successive layers (that is to say writing the equality of displacement–stress vectors  $\mathcal{W}^q(\zeta_q)$  and  $\mathcal{W}^{q+1}(\zeta_q)$  at  $x_3 = \zeta_q$ ), it is then possible to express the displacement–stress vector at the last interface of the multilayered medium,  $x_3 = \zeta_Q$ , as a function of that at the first interface at  $x_3 = 0$ :

$$\mathcal{W}^Q(\zeta_Q) = \tau \mathcal{W}^1(\zeta_0), \quad [3.21]$$

$$\text{where } \tau = \tau^Q \tau^{Q-1} \dots \tau^1. \quad [3.22]$$

The 6th-order matrix  $\tau$  is called the *transfer matrix* of the entire multilayered medium, for displacement–stress.

Instead of expressing state vectors at an interface as a function of those of the former interface, it is possible, in an equivalent way, to express displacement amplitudes in the layer  $(q + 1)$  as a function of those in the former layer  $q$ . In order to do this, the boundary conditions should be written at the interface separating the two layers at  $x_3 = \zeta_q$ , i.e., using relationship [3.18]

$$B^q \mathcal{H}^q \mathcal{A}^q = B^{q+1} \mathcal{A}^{q+1}, \quad [3.23-a]$$

$$\text{thus } \mathcal{A}^{q+1} = \left( B^{q+1} \right)^{-1} B^q \mathcal{H}^q \mathcal{A}^q, \quad [3.23-b]$$

$$\text{or else } \mathcal{A}^{q+1} = \left( A^{q+1} \right)^{-1} A^q \mathcal{H}^q \mathcal{A}^q, \quad [3.23-c]$$

using relationship [3.19] between matrices  $A^q$  and  $B^q$ . In addition, step by step, the use of equation [3.23-b] enables us to express displacement amplitudes of waves in the last layer  $Q$  as a function of those in the first layer:

$$\mathcal{A}^Q = \left( B^Q \right)^{-1} \left( \prod_{q=Q-1}^2 B^q \mathcal{H}^q \left( B^q \right)^{-1} \right) B^1 \mathcal{H}^1 \mathcal{A}^1. \quad [3.24]$$

The two methods are completely equivalent, and enable us to go from the first to the last interface through only six equations, whatever the number of layers, whereas the global method needs  $6*(Q-1)$  equations.

### 3.1.2.3. *Writing of boundary conditions at the extreme interfaces*

When the multilayered medium is surrounded by two fluid media, writing the boundary conditions at the extreme interfaces is equivalent to writing the equality of displacements normal to the interfaces, and the equality of stress vectors, i.e. four equations at  $x_3 = 0$  and  $x_3 = \zeta_Q$ , which, added to the six equations [3.24], gives 14 equations. The number of unknowns is also 14: the reflection coefficient in medium 0, the transmission coefficient in medium  $Q+1$ , the six displacement amplitudes in layer 1 and the six displacement amplitudes in layer  $Q$ .

When the multilayered medium is surrounded by two solid media, writing the boundary conditions at the extreme interfaces is equivalent to writing the equality of displacements and stress vectors, i.e. six equations at  $x_3 = 0$  and  $x_3 = \zeta_Q$ , which, added to the six equations [3.24], gives 18 equations. The number of unknowns is also 18: the three reflection coefficients in medium 0, the three transmission coefficients in medium  $Q+1$ , the six displacement amplitudes in layer 1 and the six displacement amplitudes in layer  $Q$ .

When the multilayered medium is surrounded by a solid medium and a fluid medium (for example, medium 0 is fluid and medium  $Q+1$  is solid), the boundary conditions at the extreme interfaces consist of writing the equality of normal displacements and stress vectors at  $x_3 = 0$ , i.e. four equations, and the equality of displacement and stress vectors at  $x_3 = \zeta_Q$ , i.e. six equations, which, added to the six equations [3.24], gives 16 equations. The number of unknowns is also 16: one reflection coefficient in medium 0, the three transmission coefficients in medium  $Q+1$ , the six displacement amplitudes in layer 1 and the six displacement amplitudes in layer  $Q$ .

### 3.1.2.4. *Numerical problems*

Although the transfer matrix method is very synthetic and never needs more than 18 equations to solve the problem, it leads to huge numerical problems, particularly when the product  $\omega m_3 H$  is large (see section 3.1.1.4.). Several methods have been developed which bring more and more precision: for example, the separation of propagation matrices in sub-matrices in the isotropic case [LEV 92], delta operator method [CAS 95], or the use of Floquet waves with a judicious choice of amplitude references [POT 93]. Anticipating section 3.1.3.3, let us remark that this last

method, developed more practically in the cases of periodic media, can also be used in the case of any multilayered media: we just have to take one for the number of periods  $P$ . More recently, the method of stiffness matrices of layers [ROK 02], and that coming from matrices of surfacic impedances [HOS 04], enable the complete elimination of numerical instability problems. The first method appreciably increases computation times, in comparison with the transfer matrix method, whereas the second one reduces them significantly. These two methods are presented in section 3.1.2.5 and 3.1.2.6, respectively.

### 3.1.2.5. Layer stiffness matrix (or impedance matrix)

Besides the transfer matrix method, another approach consists of using the stiffness matrices of layers which connect the stresses applied to the two interfaces in  $x_3 = \zeta_{q-1}$  and  $x_3 = \zeta_q$  of layer  $q$  to the displacements existing in these interfaces [ROK 02]. Similarly, it is possible to link these stresses to the particle velocities (temporal derivative of displacements), thus transforming the stiffness matrices in matrices of layer impedance, which will ease, in the following, the introduction of the surfacic impedance method [HOS 04]. The impedance matrix of layer  $q$ , called  $\mathbf{Z}^q$ , then enables us to write the following relationship:

$$\begin{bmatrix} \mathbf{T}^{\zeta_{q-1}} \\ \mathbf{T}^{\zeta_q} \end{bmatrix} = \mathbf{Z}^q \begin{bmatrix} \mathbf{V}^{\zeta_{q-1}} \\ \mathbf{V}^{\zeta_q} \end{bmatrix} = \begin{bmatrix} \mathbf{Z}_{11}^q & \mathbf{Z}_{12}^q \\ \mathbf{Z}_{21}^q & \mathbf{Z}_{22}^q \end{bmatrix} \begin{bmatrix} \mathbf{V}^{\zeta_{q-1}} \\ \mathbf{V}^{\zeta_q} \end{bmatrix}, \quad [3.25]$$

where  $\mathbf{V}^{\zeta_q} = \langle u_1, u_2, u_3 \rangle^T$  and  $\mathbf{T}^{\zeta_q} = \langle T_{33}, T_{23}, T_{13} \rangle^T$ , in  $x_3 = \zeta_q$ . Depending on the nature of the element constituting layer  $q$  – perfect fluid, isotropic (or anisotropic but with a principal plane coinciding with the propagation plane) solid or anisotropic solid (general case) – the square matrix  $\mathbf{Z}^q$  will be of order 2, 4 or 6, respectively. In the case of a layer  $q$  constituted of an anisotropic material, equations [3.6] and [3.8] constitute the starting point to establish the expressions of sub-matrices  $\mathbf{Z}_{ij}^q$ . After some manipulation, it is possible to express particle velocities at the interfaces  $x_3 = \zeta_{q-1}$  and  $x_3 = \zeta_q$ , as functions of the amplitudes  $\mathbf{A}_q$  of waves in the layer, as follows:

$$\begin{bmatrix} \mathbf{V}^{\zeta_{q-1}} \\ \mathbf{V}^{\zeta_q} \end{bmatrix} = \mathbf{E}_q^v \mathbf{A}_q, \quad [3.26]$$

To ensure the numerical stability of the method, this writing of particle velocities has to reference the amplitudes of waves propagating (or decreasing) in the  $x_3 > 0$



direction in  $x_3 = \zeta_{q-1}$ , and to reference the amplitudes of waves propagating (or decreasing) in the opposite direction in  $x_3 = \zeta_q$ . Then, applying Hooke's law, the stresses applied in the interfaces  $x_3 = \zeta_{q-1}$  and  $x_3 = \zeta_q$  are expressed as a function of the wave amplitudes  $\mathbf{A}_q$ :

$$\begin{bmatrix} \mathbf{T}^{\zeta_{q-1}} \\ \mathbf{T}^{\zeta_q} \end{bmatrix} = \mathbf{E}_q^\sigma \mathbf{A}_q, \quad [3.27]$$

In this last equation, replacing the wave amplitudes extracted from the velocity equation, we can establish the link between stresses applied at the interfaces  $x_3 = \zeta_{q-1}$  and  $x_3 = \zeta_q$  and the particle velocities at these same interfaces:

$$\begin{bmatrix} \mathbf{T}^{\zeta_{q-1}} \\ \mathbf{T}^{\zeta_q} \end{bmatrix} = \mathbf{E}_q^\sigma \mathbf{E}_q^{v-1} \begin{bmatrix} \mathbf{V}^{\zeta_{q-1}} \\ \mathbf{V}^{\zeta_q} \end{bmatrix}, \quad [3.28]$$

The matrix  $\mathbf{Z}^q = \mathbf{E}_q^\sigma \mathbf{E}_q^{v-1}$  is then the impedance matrix of layer  $q$ . It is made of four sub-matrices:  $\mathbf{Z}_{11}^q$  and  $\mathbf{Z}_{22}^q$  which represent the impedances of layer  $q$ , for  $x_3 = \zeta_{q-1}$  and  $x_3 = \zeta_q$ , respectively. The two other sub-matrices,  $\mathbf{Z}_{12}^q$  and  $\mathbf{Z}_{21}^q$ , ensure the connection between interfaces  $x_3 = \zeta_{q-1}$  and  $x_3 = \zeta_q$ . All these sub-matrices have the same dimension: an impedance which expresses the ratio between a stress and a particle velocity. The stress continuity at the interfaces of a stratified medium enables the establishment, by a step-by-step method, of the impedance matrix for a group of layers. For example, for the first  $q + 1$  layers of a pile, the impedance matrix  $\mathbf{Z}^{1..q+1}$  comes from the impedance matrix  $\mathbf{Z}^{1..q}$  of the first  $q$  layers, and from the impedance matrix  $\mathbf{Z}^{q+1}$  of layer  $q+1$ , by the relationship:

$$\mathbf{Z}^{1..q+1} = \begin{bmatrix} \mathbf{Z}_{11}^{1..q} + \mathbf{Z}_{12}^{1..q} \mathbf{z} \mathbf{Z}_{21}^{1..q} & -\mathbf{Z}_{12}^{1..q} \mathbf{z} \mathbf{Z}_{12}^{q+1} \\ \mathbf{Z}_{21}^{q+1} \mathbf{z} \mathbf{Z}_{21}^{1..q} & \mathbf{Z}_{22}^{q+1} - \mathbf{Z}_{21}^{q+1} \mathbf{z} \mathbf{Z}_{12}^{q+1} \end{bmatrix}, \quad [3.29]$$

where  $\mathbf{z} = (\mathbf{Z}_{11}^{q+1} - \mathbf{Z}_{22}^{1..q})^{-1}$  and  $\mathbf{Z}_{ij}^{1..q}$  ( $i, j = 1, 2$ ) are the sub-matrices of the first  $q$  layers.

Then, the impedance matrix  $\mathbf{Z}^{1..Q}$  of a multilayered medium made of  $Q$  layers enables us to link the stresses applied at the interfaces  $x_3 = \zeta_0$  and  $x_3 = \zeta_Q$  to the particle velocities existing at these same interfaces:

$$\begin{bmatrix} \mathbf{T}^{\zeta_0} \\ \mathbf{T}^{\zeta_Q} \end{bmatrix} = \mathbf{Z}^{1..Q} \begin{bmatrix} \mathbf{V}^{\zeta_0} \\ \mathbf{V}^{\zeta_Q} \end{bmatrix} = \begin{bmatrix} \mathbf{Z}_{11}^{1..Q} & \mathbf{Z}_{12}^{1..Q} \\ \mathbf{Z}_{21}^{1..Q} & \mathbf{Z}_{22}^{1..Q} \end{bmatrix} \begin{bmatrix} \mathbf{V}^{\zeta_0} \\ \mathbf{V}^{\zeta_Q} \end{bmatrix}, \quad [3.30]$$

Contrary to the global matrix method, the origin change (within each layer  $q$ ) between progressive and retrograde waves does not lead to an increase of dimension of the multilayered medium matrix with the number of layers. It is an advantage of the layer (stiffness) impedance matrices method, which is perfectly stable thanks to a mathematical trick. In spite of the necessity of a recursive algorithm that is a little more complex than simple matrix multiplications, the principle of the layer impedance matrices method is similar to that of the transfer matrix method. Indeed, in both cases, we need to establish a matrix for each layer, to deduce the matrix of the stratified medium in order to, finally, write the boundary equations at the surfaces of the stratified medium, whose solution gives the required answer. However, the number of operations (multiplications and additions) due to the recursive algorithm of the layer impedance matrices method is approximately 1.6 times bigger than that necessary for transfer matrix products, in the general case for layers comprising anisotropic materials, with the same number of layers. However, this additional cost of calculation is lower than that caused by the use, for example, of the Delta operator method, which eliminates the numerical instabilities of the transfer matrix method [CAS 95].

When the multilayered medium is surrounded by fluids and solids, the writing of boundary conditions at extreme interfaces enables us to establish the expressions of the reflection coefficient in medium 0, as well as the transmission coefficient in medium  $Q+1$ . The method is similar to that described in section 3.1.2.3, but the solutions are different as these coefficients are functions of the elements of the impedance matrix of the stratified medium, instead of being functions of the elements of its transfer matrix. In the case where the multilayered medium is immersed in a fluid, the reflection and transmission coefficients are given by the relationships:

$$\mathbf{R} = \frac{(\mathbf{S}_{11}^{33} - \Lambda)(\mathbf{S}_{22}^{33} - \Lambda) - \mathbf{S}_{21}^{33}\mathbf{S}_{12}^{33}}{(\mathbf{S}_{11}^{33} + \Lambda)(\mathbf{S}_{22}^{33} - \Lambda) - \mathbf{S}_{21}^{33}\mathbf{S}_{12}^{33}}, \quad [3.31-a]$$

$$\mathbf{T} = \frac{2\Lambda\mathbf{S}_{21}^{33}}{(\mathbf{S}_{11}^{33} + \Lambda)(\mathbf{S}_{22}^{33} - \Lambda) - \mathbf{S}_{21}^{33}\mathbf{S}_{12}^{33}}, \quad [3.31-b]$$

where  $\mathbf{S}_{ij}^{33}$  are the elements of rank (3,3) of the sub-matrices  $\mathbf{S}_{ij}$  obtained by inversion of the impedance matrix  $\mathbf{Z}^{1..Q}$  of the multilayered medium (equation [3.30]):

$$\mathbf{S} = [\mathbf{Z}^{1..Q}]^{-1} = \begin{bmatrix} \mathbf{S}_{11} & \mathbf{S}_{12} \\ \mathbf{S}_{21} & \mathbf{S}_{22} \end{bmatrix}, \quad [3.32]$$

with  $\Lambda = \frac{\cos \theta}{i\omega \rho_f V_f}$ , where  $\rho_f$  is the density of the fluid,  $V_f$  the velocity in the fluid,  $\theta$  the incident angle and  $\omega$  the angular frequency.

### 3.1.2.6. Matrix of surfacic impedance

By definition, a matrix of surfacic impedance connects the stress vector and the particle velocity vector, in a given surface [LI 72, HON 91]. For example, at the interface  $x_3 = \zeta_q$  of the stratified medium presented in Figure 3.4, this relationship is written:

$$\mathbf{T}^{\zeta_q} = \mathbf{Z}\mathbf{I}^{\zeta_q} \mathbf{V}^{\zeta_q}, \quad [3.33]$$

where  $\mathbf{Z}\mathbf{I}^{\zeta_q}$  is the impedance matrix at the interface  $x_3 = \zeta_q$ . The above equation is equivalent, apart from the sign, to the classical expression of the acoustic impedance of a medium [AUL 90]. In fact, at the interface  $x_3 = \zeta_q$ , the impedance matrix represents the impedance of the semi-infinite medium located on one side or the other of this interface. At each interface of the stratified medium, there are then two matrices of surfacic impedance: one, noted  $\mathbf{Z}\mathbf{I}^{\zeta_q}$ , for the semi-infinite medium located on the side of negative  $x_3$ , and one, noted  $\mathbf{Z}\mathbf{I}_+^{\zeta_q}$ , for the semi-infinite medium located on the side of positive  $x_3$ . The principle of the surfacic impedance matrices method is quite different from that of the transfer matrix method or that of the layer impedance matrices method. In fact, it consists first of writing, in  $x_3 = \zeta_0$  (upper surface of the stratified medium) a matrix  $\mathbf{Z}\mathbf{I}_-^{\zeta_0}$  representative of the impedance of the semi-infinite medium 0 located above. Then, step-by-step, the impedance matrices of semi-infinite media located above the interfaces  $x_3 = \zeta_1, \zeta_2, \dots$  and  $\zeta_q$  are calculated. The result is then an impedance matrix  $\mathbf{Z}\mathbf{I}_-^{\zeta_q}$ , representative of the impedance of the whole medium located above the interface  $x_3 = \zeta_q$ . In the same way, the matrix  $\mathbf{Z}\mathbf{I}_+^{\zeta_Q}$ , representative of the impedance of the semi-infinite medium  $Q+1$  located under the interface  $x_3 = \zeta_Q$ , is written. Then, by iteration, the impedance matrix  $\mathbf{Z}\mathbf{I}_+^{\zeta_q}$  of the whole medium located under the interface  $x_3 = \zeta_q$  is obtained. The boundary conditions at the two

surfaces of the stratified medium are thus systematically taken into account in the recursive algorithm, which enables the propagation of the impedances from one interface to the other of the medium. The writing of stress and particle velocity continuity, at the interface  $x_3 = \zeta_q$ , gives the undetermined system

$$\left( \mathbf{Z}\mathbf{I}_+^{\zeta_q} - \mathbf{Z}\mathbf{I}_-^{\zeta_q} \right) \mathbf{V}^{\zeta_q} = 0, \quad [3.34]$$

whose non-zero solutions are obtained by canceling the determinant. Depending on the problem, these solutions are the reflection or transmission coefficients of a monochromatic plane wave incident on the plate, or the modal solutions representative of the waves guided along the stratified medium. The position of the interface  $x_3 = \zeta_q$  can be chosen arbitrarily or selected in order to highlight some solutions more than others, as for example the existence of waves localized in a layer of a stratified medium [HOS 04].

To calculate all the surfacic impedance matrices, a link between two adjacent interfaces limiting a same layer has to be used. This link can be ensured by elements of the transfer matrix (section 3.1.2.2) or of the impedance matrix (section 3.1.2.5) of the considered layer. Choosing the elements of the layer impedance matrix is better, as their calculation is numerically more stable [HOS 04]. Moreover, thanks to the definitions of the diagonal sub-matrices  $\mathbf{Z}_{11}^q$  and  $\mathbf{Z}_{22}^q$  of the impedance matrix  $\mathbf{Z}^q$  of layer  $q$  (section 3.1.2.5), the surfacic impedance matrices, at  $x_3 = \zeta_0$  and then at  $x_3 = \zeta_Q$ , are obtained from the diagonal sub-matrices  $\mathbf{Z}_{22}^0$  and  $\mathbf{Z}_{11}^{Q+1}$ , respectively. They represent the impedances of the two semi-infinite media 0 and  $Q+1$ , respectively, that is:

$$\mathbf{Z}\mathbf{I}_-^{\zeta_0} = \mathbf{Z}_{22}^0 \text{ and } \mathbf{Z}\mathbf{I}_+^{\zeta_Q} = \mathbf{Z}_{11}^{Q+1}. \quad [3.35]$$

These matrices connect the stress and particle velocity vectors, at  $x_3 = \zeta_0$  or at  $x_3 = \zeta_Q$ :

$$\mathbf{T}^{\zeta_0} = \mathbf{Z}\mathbf{I}_-^{\zeta_0} \mathbf{V}^{\zeta_0} \text{ and } \mathbf{T}^{\zeta_Q} = \mathbf{Z}\mathbf{I}_+^{\zeta_Q} \mathbf{V}^{\zeta_Q}. \quad [3.36]$$

If one of these media is a vacuum or a perfect fluid, the corresponding surfacic impedance matrix ( $\mathbf{Z}\mathbf{I}_-^{\zeta_0}$  or  $\mathbf{Z}\mathbf{I}_+^{\zeta_Q}$ ) will be a zero or non-zero scalar, respectively. When these media are solids, the surfacic impedance matrices are square matrices of two or three dimensions, depending on whether the plane of propagation coincides or not with a plane of symmetry of these solids.

After the impedance matrices have been calculated at the surfaces, the stratified

medium must be “penetrated”. First, the surfacic impedance matrix at the interface  $x_3 = \zeta_1$  will be deduced from the one, known, at the interface  $x_3 = \zeta_0$ , and so on until an interface  $x_3 = \zeta_q$ . The following developments will show, in a general way, how to calculate, recursively, the surfacic impedance matrix at an interface  $x_3 = \zeta_q$  from that at the interface  $x_3 = \zeta_{q-1}$ . We begin with the known relationship at  $x_3 = \zeta_{q-1}$ :

$$\mathbf{T}^{\zeta_{q-1}} = \mathbf{Z}\mathbf{I}^{\zeta_{q-1}} \mathbf{V}^{\zeta_{q-1}}, \quad [3.37]$$

This we will combine with the first equation of relationship [3.25], proper to the layer impedance matrix method, in order to obtain:

$$\mathbf{V}^{\zeta_{q-1}} = -\tilde{\mathbf{Z}}_{11}^{q-1} \mathbf{Z}_{12}^q \mathbf{V}^q, \quad [3.38]$$

where  $\tilde{\mathbf{Z}}_{11}^q = \mathbf{Z}_{11}^q - \mathbf{Z}\mathbf{I}^{\zeta_{q-1}}$ . This result is a first link between interfaces  $x_3 = \zeta_{q-1}$  and  $x_3 = \zeta_q$ , involving the known surfacic impedance matrix  $\mathbf{Z}\mathbf{I}^{\zeta_{q-1}}$ . But the developments have to be pushed further to obtain the required surfacic impedance matrix  $\mathbf{Z}\mathbf{I}^{\zeta_q}$ . From the second equation of relationship [3.25], the stress vector  $\mathbf{T}^{\zeta_q}$  is expressed as a function of the particle velocity vectors  $\mathbf{V}^{\zeta_q}$  and  $\mathbf{V}^{\zeta_{q-1}}$ , then  $\mathbf{V}^{\zeta_{q-1}}$  is replaced by its formerly established expression. It becomes:

$$\mathbf{T}^q = \mathbf{Z}_{21}^q \mathbf{V}^{q-1} + \mathbf{Z}_{22}^q \mathbf{V}^q = \left( -\mathbf{Z}_{21}^q \tilde{\mathbf{Z}}_{11}^{q-1} \mathbf{Z}_{12}^q + \mathbf{Z}_{22}^q \right) \mathbf{V}^q. \quad [3.39]$$

From this result, the surfacic impedance matrix appears at  $x_3 = \zeta_q$ , and is representative of the impedance of the semi-infinite medium located above (on the side of the negative  $x_3$ ), as a function of the known surfacic impedance matrix  $\mathbf{Z}\mathbf{I}^{\zeta_{q-1}}$ :

$$\mathbf{Z}\mathbf{I}^{\zeta_q} = \mathbf{Z}_{22}^q - \mathbf{Z}_{21}^q \left( \mathbf{Z}_{11}^q - \mathbf{Z}\mathbf{I}^{\zeta_{q-1}} \right)^{-1} \mathbf{Z}_{12}^q. \quad [3.40]$$

This approach has been made by progressing along the positive  $x_3$  and always considering the semi-infinite medium located on the side of negative  $x_3$ . Conversely, the same approach can be made by progressing along the negative  $x_3$  and considering the semi-infinite medium located on the side of positive  $x_3$ . The surfacic impedance matrix in  $x_3 = \zeta_q$ , representative of the semi-infinite medium located under this interface, is then obtained from the known surfacic impedance

matrix  $\mathbf{Z}\mathbf{I}_+^{\zeta_{q+1}}$ , by the relationship:

$$\mathbf{Z}\mathbf{I}_+^{\zeta_q} = \mathbf{Z}_{11}^{q+1} - \mathbf{Z}_{12}^{q+1} \left( \mathbf{Z}_{22}^{q+1} - \mathbf{Z}\mathbf{I}_+^{\zeta_{q+1}} \right)^{-1} \mathbf{Z}_{21}^{q+1}. \quad [3.41]$$

Both results [3.40] and [3.41] represent recursive algorithms quite similar to the one proposed in section 3.1.2.5. However, the number of operations (additions and multiplications) of the surfacic impedance matrix method is approximately 2.6 times smaller than that required by the layer impedance matrix method, and 1.6 times smaller than that needed for transfer matrix products, in the general case of layers comprising anisotropic materials, and with the same number of layers. Moreover, this surfacic impedance matrix method is numerically perfectly stable, whatever the frequencies, thickness and number of layers of the stratified medium, with homogenous waves or not. Let us also highlight that, because the boundary conditions at the surface of the plate are systematically taken into account, the use of this method is the same for a problem of reflected–transmitted waves by an immersed plate and for a problem of modal solutions. Only the unknowns of the problem will change: coefficients  $\mathcal{R}$  and  $\mathcal{T}$  in the case of a reflection–transmission problem, or the wave number in the case of a problem of eigenmodes. Finally, the possibility of choosing the interface at which the matrices  $\mathbf{Z}\mathbf{I}_-^{\zeta_q}$  and  $\mathbf{Z}\mathbf{I}_+^{\zeta_q}$  are “connected” by the stress continuity, allows us to find particular solutions that the usual methods do not give, except if complicated tricks are used, like for instance the existence of guided waves producing very localized displacements around an interface or a given layer. For example, a “fluid” mode guided by a water thickness between two aluminum plates [HOS 04] or well-insulated skin modes on one side or the other of a sandwich structure composite–foam–composite [CAS 02]. Consequently, the surfacic impedance matrix method presents undeniable advantages in comparison with the classical methods (global matrix, transfer matrix) or recent methods (layer impedance matrix).

### 3.1.3. Propagation in a periodic multilayered medium

The multilayered medium of Figure 3.5 consists of the reproduction  $P$  times of a pattern, called periodic or “superlayer”, and labeled by the quantum number  $p$  ( $1 \leq p \leq P$ ). This periodic pattern results from the stacking of  $Q$  layers (each being marked by the quantum number  $q$  ( $1 \leq q \leq Q$ ) and with any given thickness  $h^q$ ), comprised of distinct anisotropic materials, with elastic stiffness constants  $c_{ijkl}^q$  and

density  $\rho^q$ . Each period thus has a thickness  $h = \sum_{q=1}^Q h^q$ , the total thickness of the medium being  $H = Ph$ . This multilayered medium, periodic or not (when  $P = 1$ ), is surrounded by two semi-infinite media (0) and  $(N + 1)$  *a priori* distinct and with any anisotropy.

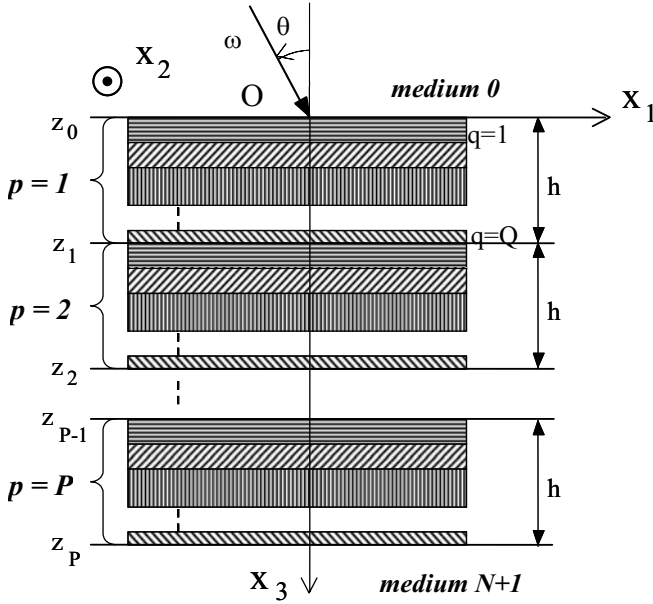


Figure 3.5. Geometry of the periodic multilayered medium

The interaction of an oblique monochromatic plane wave (with incident angle  $\theta$  and angular frequency  $\omega$ ) propagating in medium (0) with the multilayered medium yields, in each layer, six plane waves which are now called “classical waves” (marked by the superscript  $\eta$ ,  $1 \leq \eta \leq 6$ ), in order to distinguish them from Floquet waves specific to periodical structures (marked by the superscript  $\beta$ ,  $1 \leq \beta \leq 6$ , see section 3.1.3.2.). The incident wave propagates in the plane  $(Ox_1x_3)$ , which does not reduce the general problem, and the perpendicular axis is denoted by  $x_3$ . The extreme interfaces of the multilayered medium are noted  $z_0$  and  $z_P$ , the coordinate along the  $x_3$ -axis of the interface separating period  $p$  from the next period  $p + 1$

being called  $z_p$ , with  $z_{p+1} = z_p + h$  and  $z_0 = 0$ . The corresponding interface is called *period interface*.

### 3.1.3.1. Transfer matrices

In order to simplify the writing of equations, the displacement–stress state vector at the period interface at  $x_3 = z_p$  is denoted  $\mathcal{W}^P$ . In the case of perfect adherence at the interfaces, whatever the state vector  $\mathcal{W}^P$  is at  $z_p$ , the state vector  $\mathcal{W}^{P+1}$  at the next period interface at  $x_3 = z_{p+1}$  is deduced from matrix relationship [3.41] which is written, using the new notations:

$$\mathcal{W}^{P+1} = \tau \mathcal{W}^P, \quad [3.42]$$

where  $\tau$  is the transfer matrix of displacement–stress period, defined by equation [3.22].

Step by step, equation [3.42] enables us to write without any difficulty that the transfer matrix of the entire multilayered periodic medium is  $\tau^P$ :

$$\mathcal{W}^P = \tau^P \mathcal{W}^1. \quad [3.43]$$

It is also possible to obtain a transfer matrix of amplitude period  $\Phi$  such as:

$$\mathcal{A}^{P+1} = \Phi \mathcal{A}^P, \quad [3.44]$$

where  $\mathcal{A}^P$  is the column vector containing the six displacement amplitudes of classical plane waves propagating in the first layer of the period  $p$ , their reference being taken at the upper interface of layer 1 in  $(z^B)^{-1}_1$ . Using equation [3.24] in which matrix  $(B^Q)^{-1}_1$  has to be replaced by matrix  $(B^q)^{-1}_1$ , and the multiplication has to begin with  $q = Q$  instead of  $q = Q - 1$ , relationship [3.44] is written

$$\mathcal{A}^{P+1} = (B^1)^{-1} \left( \prod_{q=Q}^2 B^q \mathcal{H}^q (B^q)^{-1} \right) B^1 \mathcal{H}^1 \mathcal{A}^P, \quad [3.45-a]$$

$$\text{i.e. } \mathcal{A}^{P+1} = (B^1)^{-1} \left( \prod_{q=Q}^1 B^q \mathcal{H}^q (B^q)^{-1} \right) B^1 \mathcal{A}^P, \quad [3.45-b]$$



$$\text{thus } \Phi = (B^1)^{-1} \tau B^1, \quad [3.46]$$

$$\text{and } \mathcal{A}^{p+1} = \Phi^P \mathcal{A}^1. \quad [3.47]$$

Matrices  $\tau$  and  $\Phi$  are similar, both being period transfer matrices, which depend, for an angular frequency  $\omega$  and a given incidence, only on the material properties constituting each layer.

As in section 3.1.2, the writing of boundary conditions at the extreme interfaces would lead to a linear system of order at most 18. However, the numerical problems already mentioned in section 3.1.2.4, which are already huge, lead us to adopt an adapted method, with the intervention of particular solutions enabling us to pass from one interface to another by the means of a diagonal matrix. These solutions are called *Floquet waves*.

### 3.1.3.2. Floquet waves

#### 3.1.3.2.1. Introduction

In the case of perfect adherence at the interfaces, relationship [3.42] shows that, knowing the state vector  $\mathcal{W}^P$  at the period interface  $x_3 = z_p$ , the transfer matrix of period  $\tau$  allows us to know this same state vector at the next period interface, at  $x_3 = z_{p+1}$ , and so on, step by step. The transfer matrix eigenvectors lead to Floquet waves, which are particular solutions for which the passing from one interface to the next is made by the intermediary of a scalar matrix [ROU 87], [ROU 89], [BRA 92], [POT 93], and [POT 01]. For some frequency bands (with a constant incident angle) or for some angular bands (with a constant frequency), called stop-bands, the periodical medium behaves like a mechanical filter and does not accept the propagation of Floquet waves [BRI 53], [BRA 90], [HAS 53]. These bands correspond to inhomogenous Floquet waves. On the contrary, in the pass-bands, Floquet waves are propagative, and correspond to a complex eigenvalue whose modulus is equal to 1.

Among all the possible state vectors  $\mathcal{W}^P$ , there are some particular ones, namely state vectors  $\mathcal{V}$  of matrix  $\tau$ . These are such as:

$$\tau \mathcal{V} = \lambda \mathcal{V}. \quad [3.48]$$

Here, matrix  $\tau$  is a 6th-order matrix and consequently has six eigenvalues  $^{(\beta)}\lambda$  associated with six eigenvectors  $^{(\beta)}\mathcal{V}$  ( $1 \leq \beta \leq 6$ ) such that:

$$\tau^{(\beta)\mathcal{V}} = {}^{(\beta)}\lambda^{(\beta)\mathcal{V}}. \quad [3.49]$$

Therefore, if, on interface  $p$ , state vector  ${}^{(\beta)}\mathcal{V}$  is an eigenvector associated with  ${}^{(\beta)}\lambda$ , it is the same as at interface  $p+1$ , with the relationship between state vectors coming from equation [3.42] replacing  $\mathcal{W}$  with  $\mathcal{V}$ :

$${}^{(\beta)}\mathcal{V}^{p+1} = \tau^{(\beta)\mathcal{V}^p}, \quad [3.50]$$

which is equivalent to a simple multiplication, by the use of equation [3.49]:

$${}^{(\beta)}\mathcal{V}^{p+1} = \tau \lambda^{(\beta)\mathcal{V}^p}. \quad [3.51]$$

These results are summarized in Figure 3.6.

As Matrix  $\tau$  has an inverse, its eigenvectors are linearly independent. Consequently, Floquet waves are independent solutions such that, whatever the solution, the state vector  $\mathcal{W}^p$  at  $z_p$  can be expressed as a linear combination of the eigenvectors  ${}^{(\beta)}\mathcal{V}$ :

$$\mathcal{W}^p = \sum_{\beta=1}^6 {}^{(\beta)}\mathcal{F}^p {}^{(\beta)}\mathcal{V}, \quad {}^{(\beta)}\mathcal{F}^p \in \mathbb{C}, \quad [3.52]$$

up to a factor  $\exp(i\omega t)$ , complex numbers  ${}^{(\beta)}\mathcal{F}^p$  being the participation factors of each Floquet wave.

From equation [3.42], [3.48] and [3.52], we have:

$$\mathcal{W}^{p+1} = \tau \mathcal{W}^p = \sum_{\beta=1}^6 {}^{(\beta)}\mathcal{F}^p {}^{(\beta)}\lambda^{(\beta)\mathcal{V}}. \quad [3.53]$$

The comparison of equation [3.53] with the direct decomposition of state vector  $\mathcal{W}^{p+1}$  by replacing  $p$  by  $p+1$  in equation [3.52], shows by identification that the passing of Floquet amplitudes at interface  $p$  to those at interface  $p+1$  is done by the following relationship:

$${}^{(\beta)}\mathcal{F}^{p+1} = {}^{(\beta)}\lambda {}^{(\beta)}\mathcal{F}^p, \quad 1 \leq \beta \leq 6. \quad [3.54]$$

Step by step, it is then possible to obtain:

$$^{(\beta)}\mathcal{F}^p = \left(^{(\beta)}\lambda\right)^p {}^{(\beta)}\mathcal{F}^0, \quad 1 \leq \beta \leq 6, \quad [3.55]$$

hence, using equation [3.52] and [3.55]:

$$\mathcal{W}^p = \sum_{\beta=1}^6 {}^{(\beta)}\mathcal{F}^0 \left(^{(\beta)}\lambda\right)^p {}^{(\beta)}\mathcal{V}. \quad [3.56]$$

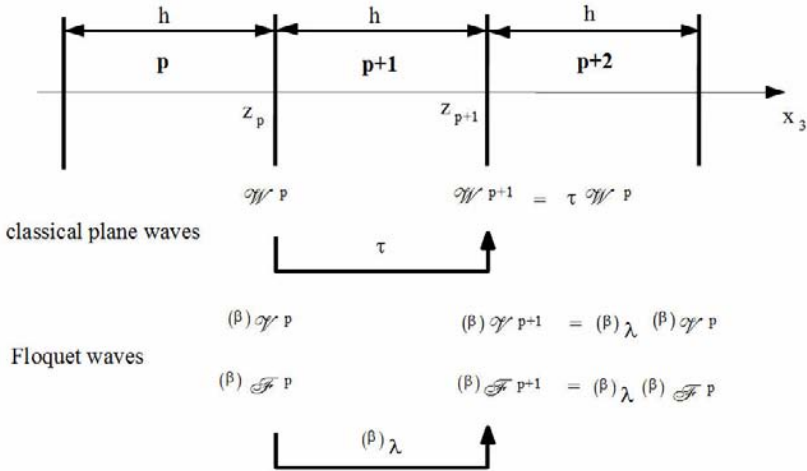


**Figure 3.6.** Passing from a period on to the next one for general wave solutions and for Floquet wave solutions

### 3.1.3.2.2. Strobe character of Floquet waves

The distance between the interfaces separating two successive periods is denoted  $h$ , a “pseudo-Floquet wavenumber”  $^{(\beta)}\kappa$  can be defined, by analogy with propagation in homogenous media:

$$^{(\beta)}\lambda = \exp\left(-i^{(\beta)}\kappa h\right), \quad 1 \leq \beta \leq 6. \quad [3.57]$$

In the case of a Floquet propagative wave  $^{(\beta)}$ , the pseudo-Floquet wavenumber  $^{(\beta)}\kappa$  is not uniquely defined by equation [3.57] because:

$$^{(\beta)}\kappa = -\arg\left(^{(\beta)}\lambda\right) \text{ modulo } 2\pi/h, \quad [3.58]$$

with here,  $\ln|^{(\beta)}\lambda| = 0$ .

Due to the indetermination on the modulus value, trying to define a phase velocity is illusory. In fact, if  $^{(\beta)}\kappa > 0$ , nothing ensures that the corresponding Floquet wave could propagate in the  $x_3 > 0$  direction, as the only available references are the two points A and B at the interfaces separating successive periods (see Figure 3.6). In fact, it should be noted that the multiplicative factor between the state vector at a distance  $x$  from point A, and that at A is not equal to  $\exp(-i^{(\beta)}\kappa x)$ . That is to say, if an eigenvalue of the transfer matrix  $\tau$  of a period is  $\exp(-i^{(\beta)}\kappa h)$ , the eigenvalue of the transfer  $\tau_x$  is not  $\exp(-i^{(\beta)}\kappa x)$ . The propagation of Floquet waves thus contains an aspect similar to *strobe phenomena*. The phase information is discrete and not continuous. The situation is similar to a wheel, whose rotation direction would be determined by lighting it up periodically. The sign of  $^{(\beta)}\kappa$  gives thus only an *apparent propagation direction*.

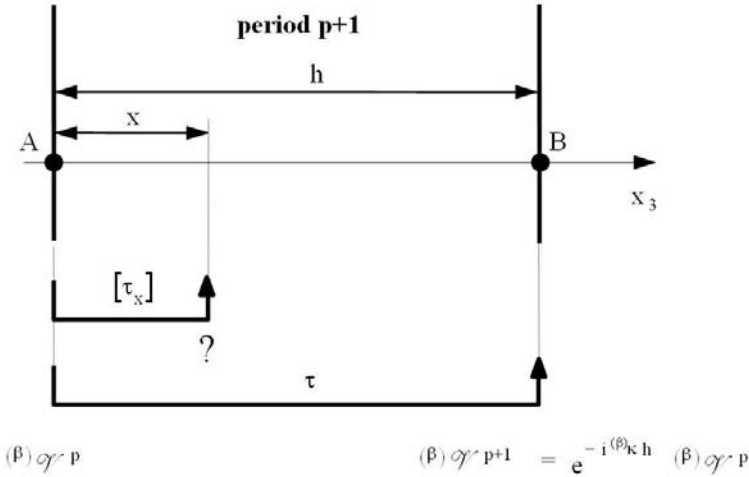


**Figure 3.7.** Spatial strobe effect of Floquet waves

The effective propagation direction is then given by the sign of the normal power flux of the considered Floquet wave [ROU 87], [ROU 89] and [POT 01]. This power flux can be calculated by the following relationship [SYN 56], where  $X^*$  refers to the complex conjugate of  $X$ :

$$F_3 = -i\omega \left( -T_{i3} u_i^* + T_{i3}^* u_i \right) / 4. \quad [3.59]$$

Each eigenvector  $^{(\beta)}\mathcal{V}$  being a particular state vector  $\mathcal{W}^P$ ,  $u_i$  corresponds to the first three components of  $^{(\beta)}\mathcal{V}$  and  $T_{i3}$  to its last three. Consequently, for each Floquet wave  $(\beta)$  and depending on the organization of the state vector (see equation [3.9]), equation [3.59] can be written:

$$\begin{aligned} ^{(\beta)}F_3 = -i\omega \bigg( & -^{(\beta)}\gamma_6^{*} ^{(\beta)}\gamma_1 + ^{(\beta)}\gamma_6^{*} ^{(\beta)}\gamma_1 - ^{(\beta)}\gamma_5 ^{(\beta)}\gamma_2^{*} \\ & + ^{(\beta)}\gamma_5^{*} ^{(\beta)}\gamma_2 - ^{(\beta)}\gamma_4 ^{(\beta)}\gamma_3^{*} + ^{(\beta)}\gamma_4^{*} ^{(\beta)}\gamma_3 \bigg) / 4 . \end{aligned} \quad [3.60]$$

In summary, the study of periodical media involves the *Floquet waves*, which are propagation modes of the infinite periodic medium. The propagation of these *non-plane and dispersive waves* can be seen as the propagation in a medium “equivalent” to the stratified medium, by analogy with the classical plane waves in homogenous media. The notion of “equivalent” medium has to be taken literally only in the limit case of low frequencies. Except in this case, it is only an image, related to the interpretation of Floquet eigenvalues from period to period. Although this interpretation is very elegant, we should not forget that, even if the Floquet waves are defined in the whole space, they are characterized only from interface to interface, that is to say in a *discrete* way. Consequently, a phenomenon of spatial stroboscopy appears. The writing of the radiation conditions in a semi-infinite periodical medium gives an illustration of this problem: the definition of a Floquet wave number, known only from interface to interface, does not single-handedly enable us to foresee the propagation direction of such a wave. Only the sign of the normal component of the power flux enables us to write the radiation conditions correctly.

### 3.1.3.2.3. Basis change for displacement amplitudes

From what has been said before, the passing from one period interface to another can be done by a diagonal matrix  $\mathcal{H}^f$ , obtained by diagonalization of the period matrix. If  $\Xi$  refers to the eigenvectors matrix of the transfer matrix of amplitude period  $\Phi$ , then

$$\Phi = \Xi \mathcal{H}^f \Xi^{-1}, \quad [3.61]$$

where  $\mathcal{H}^f$  is the diagonal matrix of  $\Phi$ , with coefficients  $^{(\beta)}\lambda$  (which can be written as in [3.57]). Equation [3.54] can then be written

$$^{(\beta)}\mathcal{F}^{P+1} = \mathcal{H}^f ^{(\beta)}\mathcal{F}^P, \quad [3.62]$$

hence, using equation [3.61]

$$\Xi^{(\beta)} \mathcal{F}^{p+1} = \Phi \Xi^{(\beta)} \mathcal{F}^p. \quad [3.63]$$

By identification, the comparison of equations [3.63] and [3.44] leads to a relationship between displacement amplitudes  $\mathcal{A}^p$  of “classical” plane waves in the first layer of period  $p$ , and the participation factors  $^{(\beta)}\mathcal{F}^p$  of the six Floquet waves at the interface separating period  $p-1$  from period  $p$ :

$$\mathcal{A}^p = \Xi \mathcal{F}^p, \quad [3.64]$$

equation [3.58] can also be written

$$^{(\beta)}\mathcal{F}^p = \left( \mathcal{H}^f \right)^p {}^{(\beta)}\mathcal{F}^0. \quad [3.65]$$

Relationship [3.64] represents a simple basis change for the displacement amplitudes.

#### 3.1.3.2.4. Displacement–stress vector at extreme interfaces

The use of equation [3.56] for  $p=0$  and  $p=P$  yields the displacement–stress vector at extreme interfaces at  $x_3 = z_0$  and at  $x_3 = z_P$ :

$$\mathcal{W}^0 = \sum_{\beta=1}^6 {}^{(\beta)}\mathcal{F}^0 {}^{(\beta)}\mathcal{V} = \mathcal{G} \mathcal{F}^0 \quad [3.66]$$

$$\text{and } \mathcal{W}^P = \sum_{\beta=1}^6 {}^{(\beta)}\mathcal{F}^0 \left( {}^{(\beta)}\lambda \right)^P {}^{(\beta)}\mathcal{V} = \mathcal{G} \left( \mathcal{H}^f \right)^P \mathcal{F}^0, \quad [3.67]$$

where  $\mathcal{F}^0$  is the column vector containing the six participation factors  $^{(\beta)}\mathcal{F}^0$  of the six Floquet waves at the first interface  $z_0$ .  $\mathcal{G}$  is the eigenvectors matrix of the transfer matrix of displacement–stress period  $\tau$ , related to the eigenvectors matrix  $\Xi$  of the transfer matrix for amplitudes period  $\Phi$  through the relationship

$$\mathcal{G} = B^1 \Xi, \quad [3.68]$$

since  $\Phi$  and  $\tau$  are similar matrices.

### 3.1.3.3. Return to numerical problems

The use of transfer matrices enables us to write the propagation equation in a synthetic way and to obtain a linear system whose order does not exceed 18 (and even 14 when using Floquet waves), depending on the extreme media surrounding the multilayered medium. However, when  $\omega h$  and the total period number  $P$  are large, and when Floquet waves become inhomogenous, some coefficients of the transfer matrix become very large and some other very small, which produces huge precision losses. This problem already exists when we consider only one material layer (see section 3.1.1.4). In this very simple case, the problem is entirely solved by referencing the displacement amplitudes of classical plane waves propagating or decreasing in the  $x_3 > 0$  direction at the upper interface of the layer, and those propagating or decreasing in the opposite direction at the lower interface. Consequently, it is possible to proceed by analogy using Floquet waves [POT 93]. This reference change of participation factors  $\mathcal{F}^0$  of the six Floquet waves at the first interface  $z_0$  is equivalent to a simple basis change in the solution space:

$$\mathcal{F}^0 = \mathbf{E} \mathcal{G}^0, \quad [3.69]$$

where  $\mathcal{G}^0$  is the column vector of the six participation factors of Floquet waves, whose reference has been changed, and  $\mathbf{E}$  is the basis change matrix of participation factors of Floquet waves, such as  $E_{\eta\eta} = 1$  if Floquet waves propagate or decrease in the  $x_3 > 0$  direction and  $E_{\eta\eta} = 1 / \left( {}^{(\beta)}\lambda \right)^P$  if Floquet waves propagate or decrease in the opposite direction. The Floquet wave selection is made on a radiation criterion, using relationship [3.60] for a propagative Floquet wave  $(\beta)$ , ( $|{}^{(\beta)}\lambda| = 1$  and this wave propagates in the  $x_3 > 0$  direction if  ${}^{(\beta)}F_3 > 0$ ). If the Floquet wave  $(\beta)$  is inhomogenous,  $|{}^{(\beta)}\lambda| \neq 1$  and the decreasing condition in the  $x_3 > 0$  direction is simply given by the choice  $|{}^{(\beta)}\lambda| < 1$  (decreasing condition in the opposite direction being given by  $|{}^{(\beta)}\lambda| > 1$ ).

The displacement–stress vectors at the extreme interfaces at  $x_3 = z_0$  and at  $x_3 = z_P$  are then written, substituting relationship [3.69] in relationships [3.66] and [3.67]:

$$\mathcal{W}^0 = \mathcal{G} \mathbf{E} \mathcal{G}^0 \quad [3.70]$$

$$\text{and } \mathcal{W}^P = g(\mathcal{H}^f)^P \mathbf{E} \mathcal{G}^0 . \quad [3.71]$$

### 3.1.3.4. Examples of reflection and transmission coefficients – stop-bands

The writing of boundary conditions at the extreme interfaces of the multilayered medium at  $z_0$  and at  $z_P$ , according to the fluid or solid nature of media 0 and  $N+1$ , enables us to obtain all the unknowns of the problem, including the reflection and transmission coefficients. If the method used involves Floquet waves, the writing of boundary conditions enables us to obtain the six participation factors of Floquet waves  $\mathcal{G}^0$  (whose reference has been changed) at the first interface  $z_0$  and the reflection and transmission coefficients in these media. It is then possible to entirely determine the properties of classical plane waves propagating in each layer of the multilayered medium.

Consequently, for a multilayered medium immersed in a fluid, four boundary conditions have to be written on extreme interfaces, i.e. eight equations in all: normal displacement equality and stress vector equality. There are also eight unknowns: the six participation factors of Floquet waves  $\mathcal{G}^0$ , the reflection coefficient and the transmission coefficient. Figure 3.8 shows the example of a composite carbon–epoxy plate, with periodic stacking, a period being constituted by the stacking of four layers, with an angle of  $45^\circ$  between each layer. Figure 3.8-e) shows the number of Floquet waves which are inhomogenous (for  $\left|^{(\beta)}\lambda\right| > 1$ ) as a function of the incident angle, with fixed frequency. This figure is valid whatever the total period number  $P$  is. Figures 3.8-a) and c) show the moduli of the reflection coefficient in water for a plate with  $P=5$  and  $P=20$  periods, respectively. The two curves present the same angular stop-bands (for which the modulus of the reflection coefficient is equal to one and the modulus of the transmission coefficient is equal to zero): the system behaves as a mechanical filter, reflection is total, and all Floquet waves are inhomogenous. Between these stop-bands, some Floquet waves again become propagative and this leads to a reflection coefficient module not equal to one. Conversely, the period number being higher than in the case of Figure 3.8-c), the oscillation number between two stop-bands is higher in the case of Figure 3.8-a), this number being a function of the period number  $P$ .

*Notes:* i) in the multilayered media, the notion of critical angle is no longer appropriate, since Floquet waves can be propagative, then become inhomogenous, then become propagative again; ii) the knowledge of (angular or frequential) stop-band positions is crucial for non destructive testing: if a flaw is sought, it is futile to use a frequency range and/or an angular area corresponding to a stop-band since the reflection is total; iii) the use of Floquet waves is not necessary for obtaining the



reflection and transmission coefficients (see section 3.1.2.1, 3.1.2.5 or 3.1.2.6 for example), but it is indispensable for understanding and interpreting the physical propagation phenomena in periodical multilayered media.

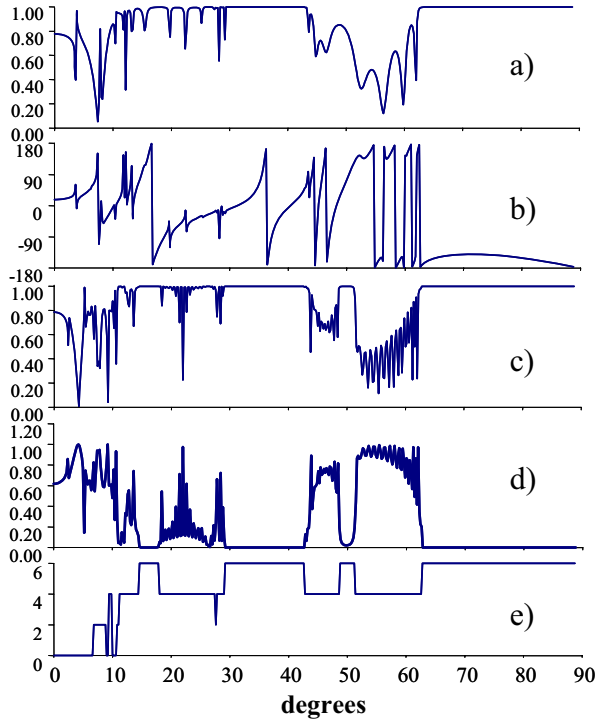


**Figure 3.8.** Composite carbon–epoxy plate immersed in water; the orientation between two successive layers being rotated by  $45^\circ$ . Incident wave of frequency 3 MHz. Curves plotted as a function of the incident angle. a) Modulus of the reflection coefficient  $P = 5$ ; b) Phase of the reflection coefficient  $P = 5$ ; c) Modulus of the reflection coefficient  $P = 20$ ; d) Modulus of the transmission coefficient  $P = 20$ ; e) number of inhomogeneous Floquet waves

### 3.2 Bibliography

- [AUL 73] Auld B.A., *Acoustic Fields and Waves in Solids*, vol. I, Wiley, 1973.
- [AUL 90] Auld B.A., *Acoustic Fields and Waves in Solids*, Robert E Krieger Publishing Company, Malabar, Florida, 1990.
- [BRA 90] Braga A.M.B., Hermann G., “Plane waves in anisotropic layered composites”, 81–98, *Wave Propagation In Structural Composites* (Am. Soc. of Mech. Eng., New York, (1988), AMD-Vol 90, A.K. Mal and T.C.T. Ting Eds)

- [BRA 92] Braga A.M.B., Hermann G., “Floquet waves in anisotropic periodically layered composites”, *J. Acoust. Soc. Am.*, 91, 3, 1211–27, 1992.
- [BRI 53] Brillouin, *Wave Propagation in Periodic Structures*, 2nd ed., Dover, New York, 1953.
- [CAS 95] Castaings M., Hosten B., “Delta operator technique to improve the Thomson–Haskell method stability for propagation in multilayered anisotropic absorbing plates”, *J. Acoust. Soc. Am.*, 95, 4, 1931–41, 1994.
- [CAS 02] Castaings M., “Contrôle et évaluation non destructifs de matériaux par ondes ultrasonores guides”, Habilitation à Diriger des Recherches de l’Université Bordeaux 1, n° d’ordre 230, 2002 (Available at: [www.lmp.u-bordeaux.fr/~um/Castaings/](http://www.lmp.u-bordeaux.fr/~um/Castaings/))
- [HAS 53] Haskell N.A., “The dispersion of surface waves in multilayered media”, *Bull. Seismol. Soc. Am.* 43, 17–34, 1953.
- [HON 91] Honein B., Braga A.M., Barbone P., Herrmann G., “Wave propagation in piezoelectric layered media with some applications”, *J. of Intell. Mater. Syst. and Struct.*, 2, 542–557, 1991.
- [HOS 04] Hosten B., Castaings M., “Surface impedance matrices to model the propagation in multilayered media”, *Ultrasonics*, 41, 501–7, 2004.
- [KNO 64] Knopoff L., “A matrix method for elastic wave problems”, *Bull. Seismol. Soc. Am.* 54, 1, 431–8, 1964.
- [LEV 92] Levesque D., Piché L., “A robust transfer matrix formulation for the ultrasonic response of multilayered absorbing media”, *J. Acoust. Soc. Am.*, 92, 1, 452–67, 1992.
- [LI 72] Li R., Yen K-H., “Elastic waves guided by a solid layer between adjacent substrates”, *IEEE Trans. MTT-20*, 7, 477–86, 1972.
- [LOW 95] Lowe M.J.S., “Matrix techniques for modelling ultrasonic waves in multilayered media”, *IEEE Trans. Ultrason. Ferroelec. Freq. Control*, vol. 42, 525–42, 1995.
- [POT 93] Potel C., de Belleval J.F., “Acoustic propagation in anisotropic periodically multilayered media; a method to solve numerical instabilities”, *J. Appl. Phys.*, 74, 4, 2208–15, 1993.
- [POT 01] Potel C., Gagniol Ph., de Belleval J.F., “Energetic criterion for the radiation of Floquet waves in infinite anisotropic periodically multilayered media”, *Acustica-Acta Acustica*, 87, 3, 340–51, 2001.
- [ROK 86] Rokhlin S.I., Bolland T.K., Adler A., “Splitting of domain of angles for incident wave vectors in elastic anisotropic media”, *J. Appl. Phys.*, 59, 11, 1986.
- [ROK 02] rokhlín S.I., wang l. “Stable recursive algorithm for elastic wave propagation in layered anisotropic media: Stiffness matrix method”, *J. Acoust. Soc. Am.*, 112, 3, 822–34, 2002.
- [ROU 87] Rousseau M., Gagniol Ph., “Propagation acoustique dans un milieu périodiquement stratifié”, *Acoustica*, 64, 188–94, 1987.

- [ROU 89] Rousseau M., "Floquet wave properties in a periodically layered medium", *J. Acoust. Soc. Am.* 86, 6, 2369–76, 1989.
- [SCH 47] Scholte J.G., "The range of existence of Rayleigh and Stoneley waves", *Mon. Not. R. Astr. Soc. Geophys.*, Suppl. 5, 1947.
- [SCH 74] Schoenberg M., "Plane wave propagation in stratified anisotropic media", *J. Acoust. Soc. Am.*, 55, 5, 922–925, 1974.
- [SYN 56] Synge J.L., Flux of energy for elastic waves in anisotropic media, *Proc. Royal Irish Academy*, 58, sect A, Elastic waves in anisotropic media, p. 13-21, 1956.
- [THO 50] Thompson W.T., "Transmission of elastic waves through a stratified solid medium", *J. Appl. Phys.*, 21, 89-93, 1950.

This page intentionally left blank

## Chapter 4

# Propagation in Continuously Stratified Media

### 4.1. Introduction

The propagation of elastic waves in inhomogeneous media has already been the subject of several sections in Part 1 of this book. In this part, a one-dimensional (1D) inhomogeneity is assumed to be continuous (or piecewise continuous), so that the material properties are arbitrary smooth functions of one of the Cartesian coordinates (say,  $y$ ), possibly with jumps at welded-contact interfaces  $y = \text{const.}$  This is often the case because of the intentional manufacturing process of functionally graded materials, or it may be due to natural damage or to intrinsic physical properties. It is thus encountered in the broad area of acoustic-wave applications ranging from non-destructive testing to seismology. In contrast to the case of infinite homogeneous layers stacked normally to the  $Y$ -axis (a piecewise homogeneous structure), elastic waves in continuously inhomogeneous media are described by the differential system with varying coefficients, which rules out plane modes with an exponential dependence on  $y$ . Thus the classical Thomson–Haskell’s transfer matrix [THO 50, HAS 53], which is “sewn” from exponential plane modes of each layer, is no longer a solution to the problem. However, the Thomson–Haskell method is often used in the context of approximate calculations, by way of “artificial” discretization of a given profile of continuous inhomogeneity. There are also other numerical or semi-analytical approaches to computing waves in inhomogeneous materials (finite-elements method, Runge–Kutta algorithms, polynomial expansion of inhomogeneity profile etc; see [PRE 97, LEF 01, LIU 02]).

At the same time, the wave equation for a 1D inhomogenous medium admits an analytically exact and numerically viable general solution. It is outlined in this chapter. More details may be found in [SHU 03, SHU 04, ALS 05, SHU 08].

## 4.2. Wave equation for 1D inhomogenous media

### 4.2.1. Second-order differential system

Assuming the Cartesian coordinates and absence of sources, recall the governing equations of linear elastodynamics which are the equation of motion and Hooke's law:

$$\begin{cases} \rho(\mathbf{r}) \frac{\partial^2 u_i(\mathbf{r}, t)}{\partial t^2} = \frac{\partial \sigma_{ij}(\mathbf{r}, t)}{\partial x_j}, \\ \sigma_{ij}(\mathbf{r}, t) = c_{ijkl}(\mathbf{r}) \frac{\partial u_k(\mathbf{r}, t)}{\partial x_l}, \end{cases} \quad [4.1]$$

where  $\rho$  is the mass density and  $c_{ijkl}$  the elasticity tensor, both generally dependent on the position vector  $\mathbf{r}$ ;  $\sigma_{ij}$  is the stress tensor and  $u_i$  the particle displacement vector. Eliminating the stress in [4.1] yields the equation

$$\rho \frac{\partial^2 u_i}{\partial t^2} = c_{ijkl} \frac{\partial^2 u_k}{\partial x_j \partial x_l} + \frac{\partial c_{ijkl}}{\partial x_j} \frac{\partial u_k}{\partial x_l}. \quad [4.2]$$

For a 3D inhomogenous medium, equation [4.2] is a system of second-order partial differential equations in unknown  $u_i$ . It usually admits only an approximate analytical treatment, see [CHE 01]. For 1D inhomogeneity, applying an appropriate integral transform reduces [4.2] to the system of ordinary differential equations with coefficients  $\rho(y)$ ,  $c_{ijkl}(y)$  varying along the inhomogeneity direction  $Y$ . Provided the material symmetry uncouples a scalar equation, certain inhomogeneity profiles may lead to its closed-form solution in terms of special functions (e.g. [MAU 83, BRE 92]). These model cases apart, the form of [4.2] as a second-order differential system is not actually handy for the analysis. A more suitable formulation is in the form of a first-order differential system of twice the number of equations.

### 4.2.2. First-order ordinary differential system for the case of 1D inhomogeneity

In the following, the Fourier transform in time and in the plane orthogonal to the inhomogeneity direction  $Y$  is supposed to have been applied. Let us choose the axes

$X, Z$  so that  $\mathbf{r} = (x, y, 0)^T$ , where  $^T$  means transposition,  $x = \mathbf{r} \cdot \mathbf{m}$ ,  $y = \mathbf{r} \cdot \mathbf{n}$  and  $\mathbf{m}, \mathbf{n}$  are unit vectors along  $X, Y$ , respectively. The plane  $XY$  is called the sagittal plane. The displacement  $\mathbf{u}$  and the surface traction  $\mathbf{f}$  ( $f_i = \sigma_{ij}n_j$ ) acting on a unit area orthogonal to  $Y$  may be written in the form:

$$\begin{aligned}\mathbf{u}(\mathbf{r}, t) &= \mathbf{A}(y) \exp[i(kx - \omega t)], \\ \mathbf{f}(\mathbf{r}, t) &= \mathbf{F}(y) \exp[i(kx - \omega t)],\end{aligned}\tag{4.3}$$

where  $k$  is the wave number,  $\omega$  angular frequency, and  $i = \sqrt{-1}$ . Inserting  $\mathbf{u}$  [4.3] into [4.1] and eliminating the stresses would lead to [4.2] specified as a system of three second-order ordinary differential equations in the displacement amplitude  $\mathbf{A}(y)$ . Once  $\mathbf{A}(y)$  is found, the amplitudes of six stress components  $\sigma_{ij}$  ( $= \sigma_{ji}$ ) follow from Hooke's law. Alternatively equation [4.1] may be manipulated into the form of a system of six first-order differential equations

$$\mathbf{Q}(y)\boldsymbol{\eta}(y) = \frac{d\boldsymbol{\eta}(y)}{dy},\tag{4.4}$$

where the  $6 \times 6$  matrix  $\mathbf{Q}(y)$  of system coefficients incorporates the material properties  $\rho(y)$ ,  $c_{ijkl}(y)$  (which are not differentiated, see [4.2]), and the so-called state vector  $\boldsymbol{\eta}(y)$  is composed of the displacement and traction amplitudes  $\mathbf{A}(y)$ ,  $\mathbf{F}(y)$ . The amplitudes of the three remaining stress components may be expressed in  $\mathbf{A}$  and  $\mathbf{F}$ .

The first-order differential system [4.4] is broadly used in anisotropic elasticity, regardless of whether the matrix of coefficients  $\mathbf{Q}$  is constant, piecewise constant or continuously varying. Its derivation is available in the extensive literature, e.g. [AKI 80, KEN 83, VDH 87, TIN 96]. One of the common approaches is related to the Stroh formalism (see [TIN 96] and the bibliography therein). Following this approach,  $\mathbf{Q}(y)$  is constructed from the  $3 \times 3$  blocks of the Stroh matrix  $\mathbf{N}(y)$  (also called the fundamental elasticity matrix), which is defined as follows

$$\mathbf{N}(y) = \begin{pmatrix} \mathbf{N}_1(y) & \mathbf{N}_2(y) \\ \mathbf{N}_3(y) & \mathbf{N}_1^T(y) \end{pmatrix}, \quad \begin{aligned} \mathbf{N}_1 &= -(nn)^{-1}(nm), \mathbf{N}_2 = -(nn)^{-1}, \\ \mathbf{N}_3 &= (mm) - (mn)(nn)^{-1}(nm). \end{aligned}\tag{4.5}$$

Here  $(ab)_{jk} = a_i c_{ijkl}(y) b_l$  with  $\mathbf{a}, \mathbf{b} = \mathbf{m}$  or  $\mathbf{n}$  is the conventional Lothe–Barnett [LOT 76] notation for  $3 \times 3$  matrices obtained by contracting the elasticity tensor of the medium with the unit vectors  $\mathbf{n}$ ,  $\mathbf{m}$  defining the geometry of the problem. The components  $c_{ijkl}$  and  $n_i$ ,  $m_i$  may be referred to any basis  $X_1 X_2 X_3$  arbitrary oriented with respect to  $XYZ$ . The system matrix  $\mathbf{Q}(y)$  also involves any two of three dispersion parameters, which are the wave number  $k$ , the frequency  $\omega$  and the velocity  $v = \frac{\omega}{k}$  or slowness  $s = v^{-1}$ . An optional choice of a pair of dispersion parameters specifies an explicit form of  $\boldsymbol{\eta}(y)$  and  $\mathbf{Q}(y)$ , which may be written as follows

$$\begin{aligned} \boldsymbol{\eta}(y) &= \begin{pmatrix} \mathbf{A}(y) \\ ik^{-1}\mathbf{F}(y) \end{pmatrix}, & \mathbf{Q}(y) &= ik \begin{pmatrix} \mathbf{N}_1 & \mathbf{N}_2 \\ \mathbf{N}_3 - \rho v^2 \mathbf{I} & \mathbf{N}_1^T \end{pmatrix}; \\ \boldsymbol{\eta}(y) &= \begin{pmatrix} i\omega \mathbf{A}(y) \\ \mathbf{F}(y) \end{pmatrix}, & \mathbf{Q}(y) &= i\omega \begin{pmatrix} s\mathbf{N}_1 & -\mathbf{N}_2 \\ -s^2 \mathbf{N}_3 + \rho \mathbf{I} & s\mathbf{N}_1^T \end{pmatrix}; \\ \boldsymbol{\eta}(y) &= \begin{pmatrix} \mathbf{A}(y) \\ i\mathbf{F}(y) \end{pmatrix}, & \mathbf{Q}(y) &= i \begin{pmatrix} k\mathbf{N}_1 & \mathbf{N}_2 \\ k^2 \mathbf{N}_3 - \rho \omega^2 \mathbf{I} & k\mathbf{N}_1^T \end{pmatrix}; \end{aligned} \quad [4.6]$$

where the dependence of  $c_{ijkl}$  (residing in  $\mathbf{N}_i$ ) and  $\rho$  on  $y$  is understood. For a common case of non-dispersive  $c_{ijkl}$  and  $\rho$ , the first two representations of  $\mathbf{Q}(y)$  in [4.6] may be preferable, for they admit factoring out one of the dispersion parameters. The Hamiltonian form of  $\mathbf{N}$  and hence of  $\mathbf{Q}$  is discussed in [FU 07].

As an elementary example, consider the waves [4.3] in the sagittal plane  $XY$  parallel to a symmetry plane of an orthotropic medium. The governing equations decouple into two separate systems, describing the SH waves polarized along the  $Z$ -direction and the P/SV waves polarized in the  $XY$  plane. Hereafter we use the matrix indices of elastic coefficients and, for brevity, take their reference basis  $X_1 X_2 X_3$  aligned with  $XYZ$ . For the SH waves, system [4.1] of motion equation and Hooke's law obviously reduces to

$$\begin{cases} -\rho(y)\omega^2 A_z(y) = \frac{dF_z(y)}{dy}, \\ F_z(y) = c_{44}(y) \frac{dA_z(y)}{dy}. \end{cases} \quad [4.7]$$



Inserting  $[4.7]_2$  into  $[4.7]_1$  furnishes the second-order differential equation in  $A_z(y)$ . Otherwise,  $[4.7]$  may be treated directly as two first-order equations uncoupled from others within the system  $[4.4]$ . The corresponding vector  $\mathbf{\eta}_{\text{SH}}(y)$  and  $2 \times 2$  system matrix  $\mathbf{Q}_{\text{SH}}(y)$  adjusted, say, to the format  $[4.6]_2$  are

$$\mathbf{\eta}_{\text{SH}}(y) = \begin{pmatrix} i\omega A_z \\ F_z \end{pmatrix}, \quad \mathbf{Q}_{\text{SH}}(y) = i\omega \begin{pmatrix} 0 & c_{44}^{-1} \\ \rho - s^2 c_{55} & 0 \end{pmatrix}. \quad [4.8]$$

The system of four remaining equations of  $[4.4]$  describing the P/SV waves involves

$$\mathbf{\eta}_{\text{PSV}}(y) = \begin{pmatrix} i\omega A_x \\ i\omega A_y \\ F_x \\ F_y \end{pmatrix}, \quad \mathbf{Q}_{\text{PSV}}(y) = i\omega \begin{pmatrix} 0 & -s & c_{44}^{-1} & 0 \\ -sc_{12}c_{22}^{-1} & 0 & 0 & c_{22}^{-1} \\ \rho - s^2(c_{11} - c_{12}^2 c_{22}^{-1}) & 0 & 0 & -sc_{12}c_{22}^{-1} \\ 0 & \rho & -s & 0 \end{pmatrix}. \quad [4.9]$$

Note that  $\mathbf{Q}_{\text{SH}}(y)$  and  $\mathbf{Q}_{\text{P/SV}}(y)$  are traceless, hence the matricants  $\mathbf{M}_{\text{SH}}(y, y_0)$  and  $\mathbf{M}_{\text{P/SV}}(y, y_0)$  introduced in section 4.3 both have unit determinant for any  $y, y_0$ .

### 4.3. Solution to the wave equation in 1D inhomogenous media

#### 4.3.1. The matricant

A homogenous linear differential system  $[4.4]$  with a bounded integrable matrix of coefficients  $\mathbf{Q}(y)$  considered in a finite interval of  $y$  admits six linearly independent partial solutions  $\mathbf{\eta}_\alpha(y)$ ,  $\alpha = 1, \dots, 6$ . The  $6 \times 6$  matrix  $\mathcal{N}(y)$  whose columns are  $\mathbf{\eta}_\alpha(y)$  is thus the fundamental matrix solution (the integral matrix) to  $[4.4]$ . Obviously any linear superposition of  $\mathbf{\eta}_\alpha(y)$  is also a solution to  $[4.4]$ . In other words, if  $\mathcal{N}(y)$  is an integral matrix, then so is its product  $\mathcal{N}(y)\mathbf{C}$  with an arbitrary non-singular constant matrix. In the theory of differential systems, a particular fundamental solution uniquely defined by the relation

$$\mathbf{M}(y, y_0) = \mathcal{N}(y)\mathcal{N}^{-1}(y_0) \quad [4.10]$$

is called the matricant [GAN 59, PEA 65]. By its definition,  $\mathbf{M}(y, y_0)$  is a matrix solution of [4.4]

$$\mathbf{Q}(y)\mathbf{M}(y, y_0) = \frac{d}{dy}\mathbf{M}(y, y_0), \quad [4.11]$$

which enables the expression of the sought state vector  $\boldsymbol{\eta}(y)$  through a vector  $\boldsymbol{\eta}(y_0)$  of “initial” conditions at  $y_0$ ,

$$\boldsymbol{\eta}(y) = \mathbf{M}(y, y_0)\boldsymbol{\eta}(y_0). \quad [4.12]$$

In view of [4.12],  $\mathbf{M}(y, y_0)$  may be said to “propagate” or “transfer” the wave field from some reference coordinate  $y_0$  to any running  $y$ , that is why the matricant in the context of waves is often called a propagator or a transfer matrix. Definition [4.10] renders evident identities  $\mathbf{M}(y_0, y_0) = \mathbf{I}$ ,  $\mathbf{M}(y, y_0) = \mathbf{M}^{-1}(y_0, y)$  and the so-called product rule

$$\mathbf{M}(y, y_0) = \mathbf{M}(y, y_{n-1})\mathbf{M}(y_{n-1}, y_{n-2})\dots\mathbf{M}(y_1, y_0). \quad [4.13]$$

Appealing to the Hamiltonian form of  $\mathbf{Q}(y)$ , to the energy considerations and to the other mathematical and physical particularities of the problem in hand provides a number of helpful properties and symmetries of the matricant  $\mathbf{M}(y, y_0)$  detailed in [SHU 04, SHU 08].

#### 4.3.2. Evaluation of the matricant by the Peano series

Having introduced the matricant solution as a mathematical object, we have not yet defined an explicit form of its evaluation. Let us first remind ourselves of the simple cases of homogenous and piecewise homogenous media. For brevity of writing, we hereafter set  $y_0 = 0$ . The matricant through the range  $[0, y]$ , within which the material properties and hence the matrix of coefficients  $\mathbf{Q}$  are independent from  $y$ , is simply an exponential:  $\mathbf{M}(y, 0) = \exp(\mathbf{Q}y)$ . If the range  $[0, y]$  is occupied by  $n$  welded homogenous layers with a constant  $\mathbf{Q}_j$  and thickness  $\Delta_j$  ( $j = 1, \dots, n$ ) each, then  $\mathbf{M}(y, 0)$  is given by the Thomson–Haskell formula

$$\mathbf{M}(y,0) = \prod_{j=n}^1 \exp(\mathbf{Q}_j \Delta_j). \quad [4.14]$$

In view of [4.13], the homogenous layers  $[y_{j-1}, y_j]$  may be “fictitious”, i.e. obtained by way of discretizing the actual continuous profile via introducing spurious interfaces.

Loosely speaking, a continuously inhomogenous medium with varying  $\mathbf{Q}(y)$  may be seen from this perspective as a stack of infinitely thin layers, and the matricant solution to [4.4] may be defined as a *continuous* product [4.14] with  $n \rightarrow \infty$  and  $\Delta_j \rightarrow 0$ . Each exponential in this product admits truncation by the linear term in  $\Delta_j$  and  $\mathbf{M}(y,0)$  can thus be written as

$$\mathbf{M}(y,0) = \lim_{\substack{n \rightarrow \infty \\ \Delta_j \rightarrow 0}} \prod_{j=n}^1 (\mathbf{I} + \mathbf{Q}_j \Delta_j) \equiv \widehat{\int_0^y} [\mathbf{I} + \mathbf{Q}(\zeta) d\zeta], \quad [4.15]$$

which is a definition of the so-called Volterra multiplicative integral [GAN 59, PEA 65]. Developing the product

$$\begin{aligned} \prod_{j=n}^1 (\mathbf{I} + \mathbf{Q}_j \Delta_j) &= \mathbf{I} + \sum_{j=n}^1 \mathbf{Q}_j \Delta_j + \sum_{j=n}^1 \sum_{k=j}^1 \mathbf{Q}_j \mathbf{Q}_k \Delta_j \Delta_k + \\ &+ \sum_{j=n}^1 \sum_{k=j}^1 \sum_{l=k}^1 \mathbf{Q}_j \mathbf{Q}_k \mathbf{Q}_l \Delta_j \Delta_k \Delta_l + \dots \end{aligned} \quad [4.16]$$

and taking the limit indicated in [4.15] specifies  $\mathbf{M}(y,0)$  as an infinite series of multiple integrals

$$\begin{aligned} \mathbf{M}(y,0) &= \mathbf{I} + \int_0^y \mathbf{Q}(\zeta) d\zeta + \int_0^y \int_0^\zeta \mathbf{Q}(\zeta) \mathbf{Q}(\zeta_1) d\zeta d\zeta_1 + \\ &+ \int_0^y \int_0^{\zeta_1} \int_0^{\zeta_2} \mathbf{Q}(\zeta) \mathbf{Q}(\zeta_1) \mathbf{Q}(\zeta_2) d\zeta d\zeta_1 d\zeta_2 + \dots \end{aligned} \quad [4.17]$$

Alternatively this series may be introduced through the recursive procedure of solving [4.11] (also called Picard’s method of successive iterations [PIC 99, ARC 96]), namely,

$$\begin{aligned}
\mathbf{M}(y, 0) &= \sum_{m=0}^{\infty} \mathbf{M}_m \quad \text{where} \quad \mathbf{M}_0 = \mathbf{I}, \quad \mathbf{Q}(y) \mathbf{M}_{m-1} = \frac{d}{dy} \mathbf{M}_m, \\
\Rightarrow \mathbf{M}_1 &= \int_0^y \mathbf{Q}(\zeta) d\zeta, \quad \mathbf{M}_2 = \int_0^y \int_0^{\zeta} \mathbf{Q}(\zeta) \mathbf{Q}(\zeta_1) d\zeta d\zeta_1, \dots,
\end{aligned} \tag{4.18}$$

which is the same as [4.17]. It is seen that the particularity of this solution rests on the non-commutativity of matrices  $\mathbf{Q}(y)$  taken at different  $y$ . Obviously, if  $\mathbf{Q}(y)$  is constant or if it has eigenvectors independent of  $y$ , then series [4.17] reduces to  $\exp(\mathbf{Q}y)$  or to  $\exp \int_0^y \mathbf{Q}(\zeta) d\zeta$ , respectively. Note also that equation [4.17] remains valid for a piecewise continuous matrix  $\mathbf{Q}(y)$ , when the given interval  $[0, y]$  goes through different inhomogenous and/or homogenous layers with welded-contact interfaces maintaining continuity of displacement and traction along the axis  $Y$ .

Series [4.17] evaluating the matricant  $\mathbf{M}(y, 0)$  in a 1D inhomogenous medium is well known in different areas of physics under the names of the Peano series [PEA 88] (referred to as such hereafter), or else the Neumann or the Dyson series, see [DYS 49, MIC 64, ROM 65, REE 75, AKI 80, KEN 83, ISE 04]. A rigorous analysis of its convergence may be found in the above-cited references [GAN 59, PEA 65] and many other mathematical textbooks. Interestingly, although the series expansion of the matricant in inhomogenous elastic media has been used in various analytical derivations for acoustic waves (e.g. [NOR 93, WAN 05, ALS 05]), it had not until recently been employed as a direct input for practical calculations. Nowadays it has proved to be perfectly amenable for this purpose as well.

#### 4.4. Remarks on the numerical implementation

##### 4.4.1. The Peano series as a power series in dispersion parameters

Numerical evaluation of an infinite Peano series certainly requires its truncation. Roughly speaking, the broader the frequency–thickness range under study, the more terms of the series must be retained. However, truncating the Peano series [4.17] keeps the inhomogeneity profile intact. Such a truncation is therefore irrelevant to replacing the actual continuous profile by the piecewise constant one and using Thomson–Haskell formula [4.14] with a large enough number  $n$  of discretization steps.

A useful attribute of the Peano-series solution is that it can be re-cast into the form of a polynomial series in dispersion parameters. Inserting the matrix of coefficients  $\mathbf{Q}(y)$  given by [4.6]<sub>1</sub> or [4.6]<sub>2</sub> into [4.17] defines the matricant  $\mathbf{M}(y, 0)$  as a power series in  $k$  or  $\omega$ :

$$\begin{aligned}\mathbf{M}(y, 0) &= \mathbf{I} + \sum_{m=1}^{\infty} (ik)^m \mathbf{P}^{(m)}(y, v^2), \\ \mathbf{M}(y, 0) &= \mathbf{I} + \sum_{m=1}^{\infty} (i\omega)^m \mathbf{S}^{(m)}(y, s),\end{aligned}\tag{4.19}$$

where each  $m$ th term is the  $m$ -tuple integral of the Peano series. Correspondingly, the matrix coefficients  $\mathbf{P}^{(m)}$  or  $\mathbf{S}^{(m)}$  can be rearranged as polynomials in  $v^2$  or  $s$  with integral coefficients. For a given dependence of material properties, a single integral computed as a function of its upper limit  $y$  is then used as an integrand for computing a double integral, which is used for computing a triple integral, etc. These integrals are calculated only once and then stored, while the pairs  $(v, k)$  or  $(\omega, s)$  remain as free parameters. This is especially advantageous for computing the dispersion spectrum of an inhomogenous layer. It is in contrast to the Thomson–Haskell method, for which refining the discretization of a given inhomogenous profile redefines the number and properties of the constituent layers and hence requires calculating anew each propagator  $\mathbf{M}(y_j, y_{j-1})$  in [4.14].

#### 4.4.2. Examples

In this very basic overview, we restrict ourselves to a few simple examples related to the SH waves. Taking [4.17] with the matrix of coefficients  $\mathbf{Q}_{\text{SH}}(y)$  in the form [4.8] enables writing the Peano series for  $2 \times 2$  matricant  $\mathbf{M}_{\text{SH}}$  as a power series in  $\omega$ ,

$$\mathbf{M}_{\text{SH}}(y, 0) \equiv \begin{pmatrix} M_1 & M_2 \\ M_3 & M_4 \end{pmatrix} = \begin{pmatrix} 1 + \sum_{k=1}^{\infty} S_1^{(2k)} \omega^{2k} & i \sum_{k=0}^{\infty} S_2^{(2k+1)} \omega^{2k+1} \\ i \sum_{k=0}^{\infty} S_3^{(2k+1)} \omega^{2k+1} & 1 + \sum_{k=1}^{\infty} S_4^{(2k)} \omega^{2k} \end{pmatrix}, \tag{4.20}$$

where the coefficients  $S_i^{(m)}(y; s^2)$  contain  $m$ -tuple integrals of the products of  $\rho(y) - s^2 c_{55}(y)$  with  $c_{44}^{-1}(y)$ . If these are real, then, for any  $y$ , the diagonal components  $M_1$ ,  $M_4$  are real, and the off-diagonal components  $M_2$ ,  $M_3$  are purely imaginary.

First, as an elementary illustration of numerical implementation of the Peano series, it is instructive to compare it with a primary benchmark which is a well-known exact expression for the SH matricant (say, with  $s = 0$ ) through a homogenous isotropic medium,

$$\mathbf{M}_{\text{SH}}(y, 0) = \begin{pmatrix} \cos(\omega c^{-1} y) & \frac{i}{\rho c} \sin(\omega c^{-1} y) \\ i \rho c \sin(\omega c^{-1} y) & \cos(\omega c^{-1} y) \end{pmatrix}, \quad [4.21]$$

where  $c = \sqrt{c_{55}/\rho}$ . It is obvious that, due to constant integrands in the Peano series [4.17], equation [4.20] reduces indeed to the Taylor series of the sine and cosine functions. However, the purpose of our test is to disregard this analytical shortcut and to compute  $\mathbf{M}_{\text{SH}}(y, 0)$  directly from its Peano-series definition, taking the  $m$ -tuple integrals appearing in there numerically. Thereby we intend to demonstrate two aspects. The first is that our numerical integration provides an accurate evaluation of the series coefficients (in this case, those of the Taylor series). The second is the effect of this series truncation. Assume the material constants  $\rho = 1 \text{ g/cm}^{-3}$  and  $c_{55} (= c_{44}) = 1 \text{ GPa}$ , the frequency  $f = \omega/2\pi = 3 \text{ MHz}$ , and consider the interval  $y \in [0, d]$  with  $d = 1 \text{ mm}$ . This interval is sampled into 201 equidistant steps and the  $m$ -tuple integrals are computed recursively as mentioned in section 4.4.1. The result of this calculation for one of the components ( $M_3$ ) of  $\mathbf{M}_{\text{SH}}(y, 0)$ , truncated at different orders  $k$  of the Peano series, is compared to the exact sinusoidal curve in Figure 4.1. It is noted that instead of increasing the number  $k$  of the series terms, we can split the interval  $[0, d]$  into several segments and use the product rule [4.13] with notably fewer terms for each co-factor matricant. This is a generally helpful recipe for computing the Peano series.

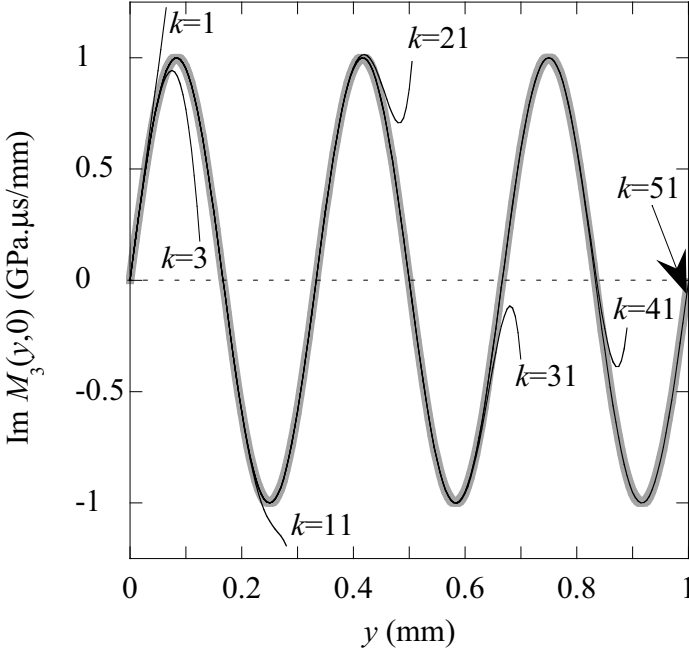


**Figure 4.1.** Imaginary part of the SH matricant component  $M_3(y, 0)$  computed for a homogenous isotropic medium: the Peano-series computation (thin line) versus the exact curve  $\sin(6\pi y/d)$  (thick gray line). See the details in the text

The next example, presented in Figure 4.2, shows the components of the SH matricant [4.20] computed via the Peano series for an orthotropic medium with constant  $\rho = 1 \text{ g/cm}^{-3}$ ,  $c_{44} = 4 \text{ GPa}$  and varying  $c_{55} = C_0(1 + 5y - 5y^2)$ , where  $C_0 = 1 \text{ GPa}$ . The frequency and slowness are taken to be  $f = 9 \text{ MHz}$  and  $s = 0.68 \mu\text{s/mm}$ . The interval  $y \in [0, d]$  under study ( $d = 1 \text{ mm}$ ) is sampled into 100 points, and the integrals in the Peano-series coefficients are calculated by means of the Simpson method. The series is truncated after 40 terms. Note that the assumed velocity value  $v = s^{-1}$  exceeds the “local” velocity  $c(y) = \sqrt{c_{55}(y)/\rho(y)}$  near the layer edges and is less than that in the center of the layer. These two cases correspond to locally supersonic and subsonic (undamped and damped along  $y$ ) propagation. That is why the variation of the propagator components in Figure 4.2 is more pronounced near the layer edges than in its center.

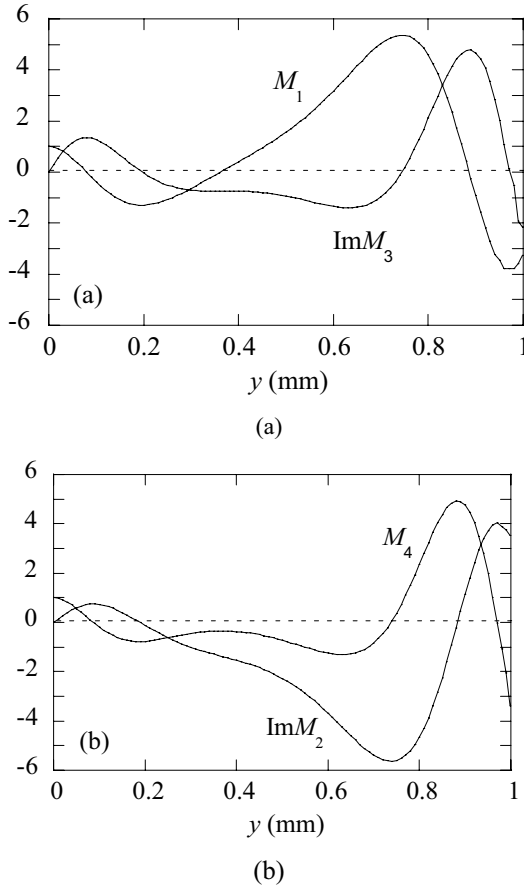


**Figure 4.2.** The components (a)  $M_1$ ,  $\text{Im}M_3$  and (b)  $\text{Im}M_2$ ,  $M_4$  of the SH matricant  $\mathbf{M}_{SH}(y, 0)$  for an inhomogeneous orthotropic medium described in the text ( $M_1$  and  $M_4$  are dimensionless,  $M_2$  and  $M_3$  are in  $\text{GPa} \cdot \mu\text{s}/\text{mm}$  and  $\text{mm}/\text{GPa} \cdot \mu\text{s}$ )

Given a transversely inhomogeneous plate of thickness  $d$ , computing the matricant  $\mathbf{M}(d, 0)$  as a polynomial in  $\omega$  and  $s$  is suitable for calculating the dispersion spectrum  $s(\omega)$ . Provided the plate faces  $y = 0$  and  $y = d$  are subjected to the traction-free boundary condition, the dispersion equation implies asking a zero determinant of the  $3 \times 3$  left off-diagonal block of  $\mathbf{M}(d, 0)$ . For the SH waves, it simplifies to the equation  $M_3(d, 0) = 0$  on a scalar component of the  $2 \times 2$  matricant  $\mathbf{M}_{SH}$ , see [4.20]. Figure 4.3 presents the dispersion spectrum of SH waves



calculated in this way for a transversely inhomogeneous isotropic plate ( $d = 1\text{ mm}$ ). The dispersion curves are monotonically decreasing and have two plateaux associated with the minima of the velocity profile  $c(y)$ . Pairwisely close near the intermediate minimum, they in fact never cross each other (their repulsion is not resolved to the scale of the figure). These spectral properties, as well as the closed-form approximation of the shape of the SH dispersion curves at low and high frequency and near the cutoffs are discussed in detail in [SHU 08].

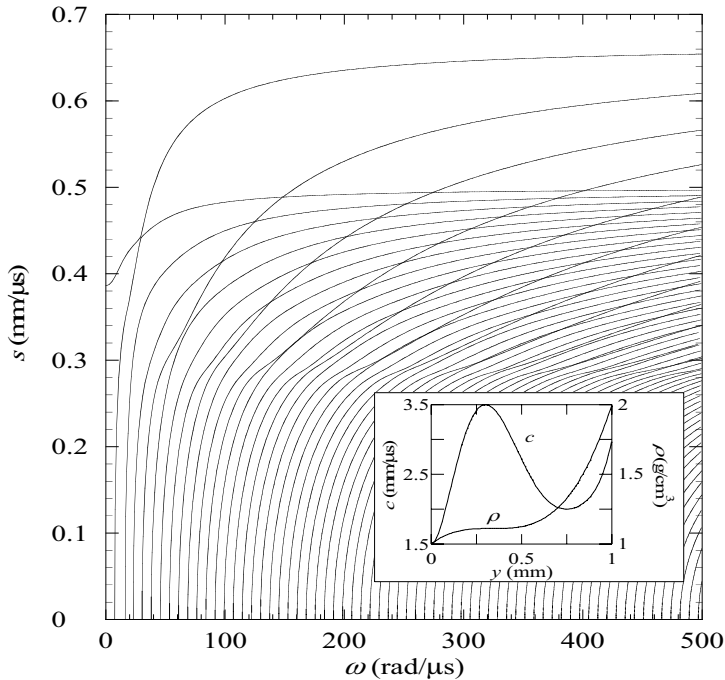


**Figure 4.3.** Dispersion spectrum of the SH guided waves in an inhomogeneous isotropic plate. The through-thickness profiles of the density  $\rho(y)$  and shear velocity  $c(y)$  are displayed in the inset

#### 4.5. Bibliography

- [AKI 80] Aki K., Richard P. G., *Quantitative Seismology, Theory and Methods*, Freeman and Co., New York, 1980
- [ALS 05] Alshits V.I., Maugin G.A., “Dynamics of multilayers: elastic waves in an anisotropic graded or stratified plate”, *Wave Motion*, 41, 357–94, 2005

- [ARC 96] Archibald T., “From Attraction Theory to Existence Proofs: The Evolution of Potential-Theoretic Methods in the Study of Boundary-value Problems, 1860–1890”, in *Revue d'histoire des mathématiques*, 2, 67–93, 1996
- [BRE 92] Brekhovskikh L.M., Godin O.A., *Acoustics of Layered Media II*, Springer, Berlin, 1992
- [CHE 01] Červený V., *Seismic Ray Theory*, Cambridge University Press, 2001
- [DYS 49] Dyson F. J., “The S matrix in quantum electrodynamics”, *Phys. Rev.*, 75, 1736–55, 1949
- [FU 07] Fu Y. B., “Hamiltonian interpretation of the Stroh formalism in anisotropic elasticity”, *Proc. Roy. Soc., A* 463, 3073–87, 2007
- [GAN 59] Gantmacher F. R., *The Theory of Matrices*, Wiley Interscience, New York, 1959
- [HAS 53] Haskell N. A., “The dispersion of surface waves on multilayered media”, *Bull. Seism. Soc. Am.*, 43, 377–93, 1953
- [ISE 04] Iserles, A. *On the Method of Neumann Series for Highly Oscillatory Equations*, Technical Report NA2004/02, DAMTP University of Cambridge, 2004
- [KEN 83] Kennett B. L. N., *Seismic Wave Propagation in Stratified Media*, Cambridge University Press, Cambridge, 1983
- [LIU 02] Liu G. R., Xi Z. C., *Elastic Waves in Anisotropic Laminates*, CRC Press, Boca Raton FL, 2002
- [LEF 01] Lefebvre J. E., Zhang V., Gazalet J., Gryba T., Sadaune V. “Acoustic wave propagation in continuous functionally graded plates: An extension of the Legendre polynomial approach”, *IEEE Trans. Ultrason., Ferroelect., Freq. Contr.*, 48, 1332–40, 2001
- [LOT 76] Lothe J., Barnett D. M., “On the existence of surface-wave solutions for anisotropic half-spaces with free surface”, *J. Appl. Phys.*, 47, 428–33, 1976
- [MAU 83] Maugin G. A., “Elastic surface waves with transverse horizontal polarization”, *Adv. Appl. Mech.*, 23, 373–434, 1983
- [MIC 64] Mickhlin S. G., *Integral Equations and their Applications to Certain Problems in Mechanics, Mathematical Physics and Technology*, Pergamon Press, Oxford, 1964
- [NOR 93] Norris A. N., “Waves in periodically layered media: A comparison of two theories”, *SIAM. J. Appl. Math.*, 33, 1195–209, 1993

- [PEA 88] Peano G., “Intégration par séries des équations différentielles linéaires”, *Mathematische Annalen*, 32, 450–6, 1888
- [PEA 65] Pease III, M. C., *Methods of Matrix Algebra*, Academic Press, New York, 1965
- [PIC 99] Picard E., “Mémoire sur la théorie des équations aux dérivées partielles et la méthode des approximation successives”, *Journal de Mathématiques Pures et Appliquées*, 6, 145–210, 1899
- [PRE 97] Press W. H., Flannery B. P., Teukolsky S. A., *Numerical Recipes in C: the Art of Scientific Computing*, Cambridge University Press, 1997
- [REE 75] Reed M., Simon B., *Methods of Modern Mathematical Physics*, Academic Press, New York, 1975
- [ROM 65] Roman P., *Advanced Quantum Theory*, Addison-Wesley, Palo Alto, 1965
- [SHU 03] Shuvalov A. L., “A sextic formalism for three-dimensional elastodynamics of cylindrically anisotropic radially inhomogenous materials”, *Proc. R. Soc. Lond., A* 459, 1611–39, 2003
- [SHU 04] Shuvalov A. L., Poncelet O., Deschamps M., “General formalism for plane guided waves in transversely inhomogenous anisotropic plates”, *Wave Motion*, 40, 413–26, 2004
- [SHU 08] Shuvalov A. L., Le Clezio E., Feuillard G., “The state-vector formalism and the Peano-series solution for modelling guided waves in functionally graded anisotropic piezoelectric plates”, *Int. J. Eng. Sci.*, 46, 929–47, 2008
- [SHP 08] Shuvalov A. L., Poncelet O., Kiselev A. P., “Shear horizontal waves in transversely inhomogenous plates”, *Wave Motion*, 45, 605–15, 2008
- [THO 50] Thomson W. T., “Transmission of elastic waves through a stratified solid medium”, *J. Appl. Phys.*, 21, 89–93, 1950
- [TIN 96] Ting T. C. T., *Anisotropic Elasticity*, Oxford University Press, 1996
- [VDH 87] Van Der Hijden J. H. M. T., *Propagation of Transient Elastic Waves in Stratified Anisotropic Media*, Elsevier, Amsterdam, 1987
- [WAN 05] Wang L., Rokhlin S. I., “Recursive geometric integrators for wave propagation in a functionally graded multilayered elastic medium”, *J. Mech. Phys. Solids*, 52, 2473–506, 2005

This page intentionally left blank

## Chapter 5

# Modal Waves in Plane Structures

### 5.1. Introduction

Without any dissipation mechanism, vibratory systems with a finite number of degrees of freedom support free modes, or *eigenmodes*, in finite number, with well determined frequencies. Each eigenmode is characterized by its frequency and by a *modal pattern* which comes from proportionality relations between displacements of the different parts of the system.

In the same way, without any dissipation mechanism, an acoustical structure, made of one or several fluid or solid propagation media bounded by surfaces and interfaces, can support free, generally monochromatic, modes which are self-sustained, without any exterior energy source.

If the acoustical structure fills a totally bounded portion of the physical space, there are only free modes with well determined frequencies, in finite number (discrete set of eigenfrequencies). They are called *vibrational modes* or *eigenvibrations* of the acoustical structure. The simplest example is the fluid-filled waveguide closed at both extremities and vibrating in plane modes. Each vibrational mode is characterized, in addition to its eigenfrequency, by its modal pattern which comes from a particular spatial distribution of the vibratory amplitude: antinodes and nodal surfaces of pressure, for example, for a fluid medium.

If the acoustical structure is only partially bounded in the physical space, the free modes can evolve up to infinity along a family of curves or surfaces. The frequency can take any value, and, according to this value, the mode evolution *ad infinitum* will have a propagative or an evanescent character. Usually a radiation condition *ad infinitum* will specify the mode by choosing the direction of propagation or decreasing amplitude.

In this context, free modes are often called *free waves* in the literature. In a totally infinite, homogenous medium, free waves are the plane waves studied in section 1.2, Chapter 1. If there are surfaces or interfaces in the acoustical structure, the free waves are supported on these surfaces. They evolve up to infinity along some directions carried by these surfaces, but boundary conditions give them a modal character along the orthogonal directions. At least locally, the physical space appears to be the sum of a sub-space of evolution up to infinity and of a supplementary modal sub-space (see Figure 5.1). That is why, according to W.D. Hayes [HAY 70], we call these free waves *modal waves*.

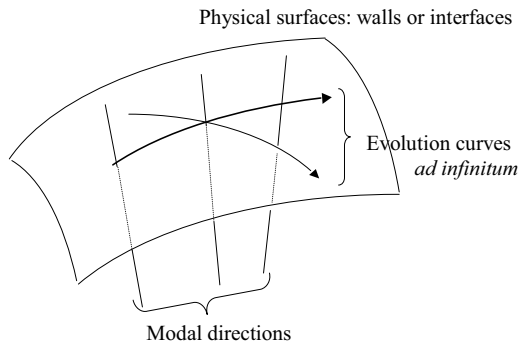


**Figure 5.1.** *Evolution and modal directions*

An example of modal waves is given by acoustic waves in a cylinder-shaped waveguide of bounded section. Each mode is characterized by a modal pattern in the plane of the cross-section. Its evolution *ad infinitum* occurs along the straight lines parallel to the generating lines. This evolution is propagative or evanescent according to the frequency value. In this example, the modal sub-space is two-dimensional and the sub-space of evolution *ad infinitum* is one-dimensional.

A detailed study of modal waves in elastic waveguides will be found in [AUL 73] (Vol II, Ch. 10). Here, the study will be restrained to an introduction of modal waves in plane structures: media bounded by parallel plane surfaces or interfaces or plane multilayered structures, as they have been introduced in Chapter 3.

### 5.1.1. General properties of modal waves in plane structures

We will limit the study to the case of structures made of various propagation media (fluids or elastic solids) separated or limited by parallel plane surfaces. In this configuration, the evolution sub-space is of dimension 2: the plane direction common to the bounding surfaces; the modal sub-space is of dimension 1: the direction normal to these planes.

The essential property of the modal direction is that it does not convey any acoustic energy carried by the wave. If the wave transfers some energy, this transfer can only occur in a direction of the evolution sub-space. We can say that the acoustic energy is “trapped” by the bounding surfaces.

This energy trapping property is seen well if the propagation structure is bounded, in the modal direction, by two extreme, perfectly reflecting (or with purely reactive impedance), planes. This is the case of fluid-filled waveguides bounded by two rigid walls or of an elastic layer in a vacuum (Figure 5.2).

However, by extension to what has been described in the introduction to this chapter, modal waves can also be observed if the structure is not bounded in the modal direction. The only condition is the exclusion of the energy transfer in this direction. It is fulfilled when, in the semi-infinite extreme medium or media, there are some evanescent waves attenuated *at infinitum* in the modal direction (see Figure 5.3). This will be the case for surface or interface waves along a plane interface (Rayleigh or Stoneley waves). In the case described in Figure 5.3, a fluid layer separates two semi-infinite elastic media. The case of an elastic layer separating two fluids has been studied by Osborne and Hart [OSB 45]. We will come back to it in section 5.1.2.2.2.

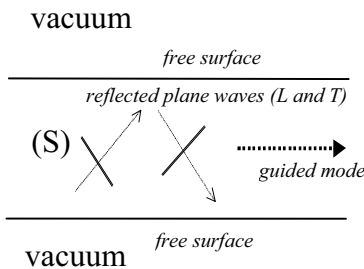


Figure 5.2. Lamb type wave

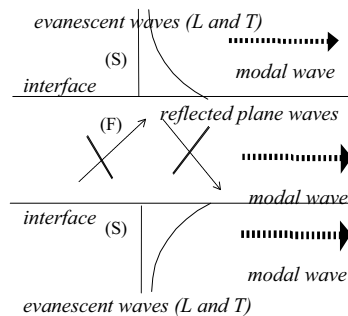


Figure 5.3. Guided wave in a fluid layer imbedded in an infinite solid

The property of a modal wave to carry acoustic energy in preferential directions in the physical space is of great interest for the implementation of ultrasonic non-destructive testing techniques. The generation of a modal wave will enable us to reach a flawed area at a greater distance than with a bulk wave. If the modal wave has a unidirectional propagation, its amplitude remains constant in theory, that is to say, when energy dissipation mechanisms are neglected. If the propagation occurs in all the directions of the evolution sub-space, the modal wave is bi-dimensional and its amplitude decreases with  $1/\sqrt{r}$ . In comparison, a bulk wave amplitude decreases with  $1/r$ , thus much faster.

Generally, modal waves are monochromatic. They are independent of the frequency only if the propagation structure does not involve any reference length. This case will happen only if there is only one plane surface and if the boundary condition along this plane has no internal length scale. This will be the case for the Rayleigh wave for a solid–vacuum interface or for the Stoneley wave along a solid–solid plane interface of embedding type. On the contrary, for a plane interface of bonding type, for which an internal length exists (see section 2.1.1.4), the possible modal waves are necessarily monochromatic.

We will now review the most common modal waves.

### 5.1.2. Usual modal waves

In a plane multilayered structure, a modal wave can be localized on the neighborhood of a separation plane (surface or interface wave) or in one or several layers of the structure, or else in the whole structure.

#### 5.1.2.1. Surface and interface waves

##### 5.1.2.1.1. Rayleigh wave

The simplest and most well-known surface wave is certainly the Rayleigh wave which propagates along the free (plane) surface separating an elastic medium from a very light medium that can be assimilated to a *vacuum*. Referring to section 2.1.1.2.1, equation [2.10], we can see that the physical condition to write on such a surface is the cancelation of the normal stress vector.

The elastic medium fills the half-space  $x_3 \geq 0$  (see Figure 5.4). As we have seen in the former section, for a modal wave, the acoustic energy transfer must occur parallel to the plane  $x_3 = 0$ . This condition will be fulfilled only if the waves existing in the medium are evanescent, decreasing towards the direction  $x_3 > 0$ .



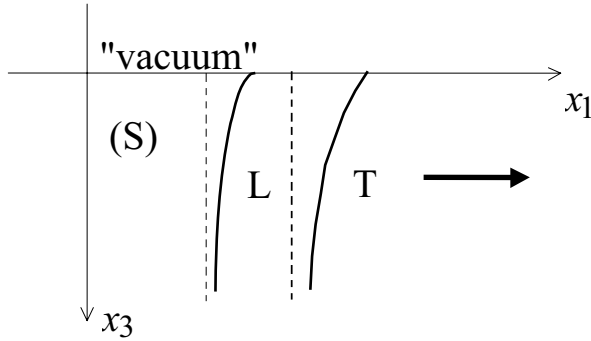


**Figure 5.4.** *Rayleigh wave*

The elastic medium will be assumed isotropic. Under these conditions, the surface wave propagates in any given direction of the evolution sub-space,  $Ox_1$  for example, and can be described in the plane  $Ox_1x_3$ . In this plane, the Rayleigh wave consists of a longitudinal L wave and a transverse T wave (polarized in the propagation plane), both evanescent towards the direction  $x_3 > 0$ .

The boundary condition is thus written:

$$\vec{T}_3 = \vec{T}_{3L} + \vec{T}_{3T} = \vec{0}, \quad [5.1]$$

where each wave contribution has been separated. If we first suppose that both waves are monochromatic with the same angular frequency  $\omega$ , the stress vector components in the plane  $Ox_1x_3$  can be expressed, with the notations already introduced, as:

– *longitudinal wave*

$$T_{31L} = 2i\rho_S V_T^2 k_1 k_{3L}'' A_L e^{-k_{3L}'' x_3} e^{i(\omega t - k_1 x_1)}, \quad [5.2-a]$$

$$T_{33L} = -\rho_S V_T^2 (k_T^2 - 2k_1^2) A_L e^{-k_{3L}'' x_3} e^{i(\omega t - k_1 x_1)}, \quad [5.2-b]$$

– *transverse wave*

$$T_{31T} = \rho_S V_T^2 (k_T^2 - 2k_1^2) A_T e^{-k_{3T}^* x_3} e^{i(\omega t - k_1 x_1)}, \quad [5.3-a]$$

$$T_{33T} = 2i\rho_S V_T^2 k_1 k_{3T}^* A_T e^{-k_{3T}^* x_3} e^{i(\omega t - k_1 x_1)}. \quad [5.3-b]$$

The condition of null normal stress in the plane  $x_3 = 0$  can thus be put in the form of a linear 2-order system whose determinant must be zero. In an equivalent way, the following geometrical argument can be used: in every point of the plane  $Ox_1x_3$ , the extremity of each vector  $\vec{T}_{3L}$  and  $\vec{T}_{3T}$  describes an ellipse with its larger axis parallel to the free surface  $x_3 = 0$ . This ellipse is followed in the clockwise direction for vector  $\vec{T}_{3T}$  and, for vector  $\vec{T}_{3L}$ , in the clockwise or counter-clockwise direction depending whether the phase velocity

$$V_{x1} = \frac{\omega}{k_1}, \quad [5.4]$$

is lower or greater than  $V_T\sqrt{2}$  respectively (see Figure 5.5). However, the evanescence condition of waves implies that this phase velocity is lower than each bulk wave velocity:

$$V_{x1} < V_T < V_T\sqrt{2} < V_L. \quad [5.5]$$

We will note that this last inequality comes from expressions [1.38] (Chapter 1) for longitudinal and transverse waves velocities in an isotropic medium.

With these conditions, both ellipses are described in the same (negative) direction. As the two vectors must remain opposite, in order to fulfill condition [5.1], it is necessary and sufficient that both ellipses are similar. This condition is necessary as in reality the two ellipses must be equal. It is sufficient because if the two ellipses, with parallel axes, have the same axis ratio, we only need to adjust the complex amplitudes  $A_L$  and  $A_T$  in module in order to equalize the two ellipses, and in phase so that the two stress vectors are opposite (and remain opposite at all times) (Figure 5.5).

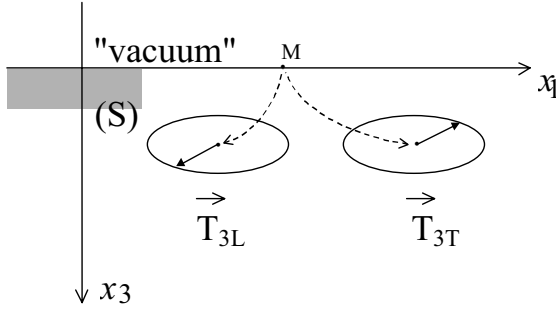


**Figure 5.5.** Rayleigh wave: geometric construction of free surface condition

An algebraic shape ratio may be associated with each ellipse. Its arithmetical value is equal to the axes' ratio and its sign determines clockwise (negative) or counter-clockwise (positive) travel direction:

$$E_L = \frac{V_L(V_{x1}^2 - 2V_T^2)}{2V_T^2\sqrt{V_L^2 - V_{x1}^2}}, \quad E_T = \frac{2V_T\sqrt{V_T^2 - V_{x1}^2}}{V_{x1}^2 - 2V_T^2}. \quad [5.6]$$

The Rayleigh wave velocity is given by the intersection point of the graphs of these two shape ratios, Figure 5.6.

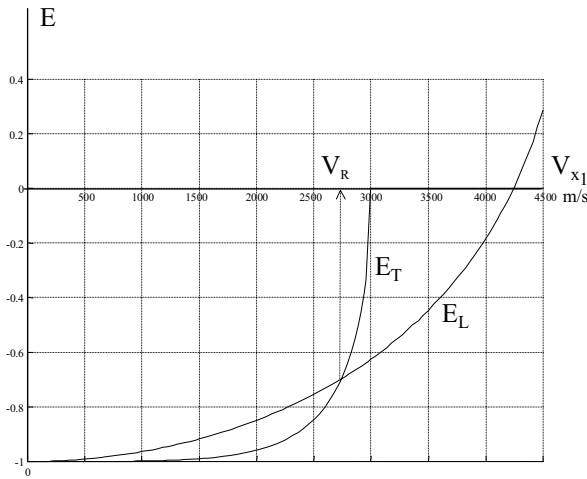


**Figure 5.6.** Graphical determination of the Rayleigh velocity ( $V_L = 5000$  m/s,  $V_T = 3000$  m/s)

This construction clearly shows the existence of the Rayleigh wave. Moreover, as the shape ratios [5.6] are independent of frequency, the Rayleigh wave velocity does not depend on frequency too. This result was expected as there is no reference length in this problem.

The same geometrical argument would lead to the absence of a surface wave along a plane embedded wall. In fact, the surface condition will then be the displacement vector nullity. For evanescent longitudinal and transverse waves, the larger axes of ellipses described by the displacement vectors have different directions: parallel to the bounding plane for the longitudinal wave and perpendicular for the transverse wave.

The proportionality relationship between complex amplitudes  $A_L$  and  $A_T$ , which then yields two opposite vectors  $\vec{T}_{3L}$  and  $\vec{T}_{3T}$ , is nothing more than the reduced equation of the linear system whose determinant has been canceled by the condition  $E_L = E_T$ . It defines the modal pattern of the Rayleigh wave and enables, among other things, the description of the stress and displacement fields distribution as a function of the depth  $x_3$ . As an example, Figure 5.7 shows the stress profile  $|\vec{T}_3|$  with arbitrary units. The depth  $x_3$  is expressed in terms of the longitudinal wavelength.

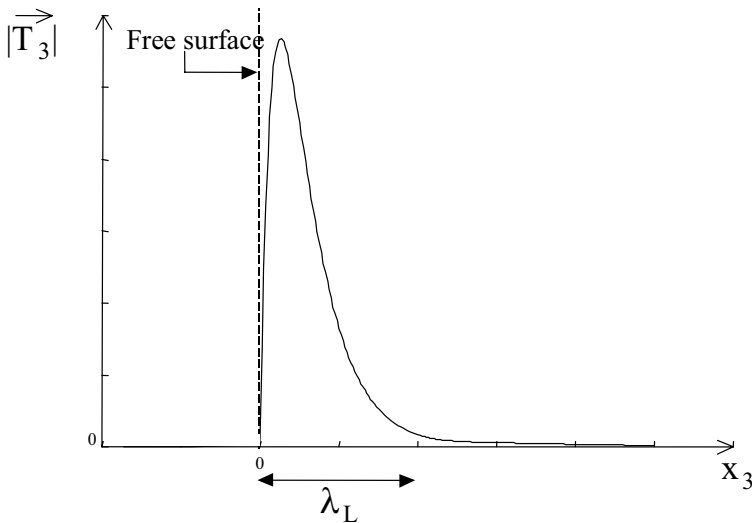


**Figure 5.7.** *Stress profile of a Rayleigh wave*

#### 5.1.2.1.2. Scholte–Stoneley wave

When the upper medium ( $x_3 < 0$ ) is made of a fluid which can no longer be considered as a vacuum, the pure Rayleigh wave does not exist anymore. However, we will see in section 5.1.4 how the Rayleigh wave can be generalized.

However, an interface wave coupling the fluid and the solid appears. It is made of two evanescent longitudinal L and transverse T waves in the solid (as for the Rayleigh wave) and an evanescent (longitudinal) wave, decreasing towards  $x_3 < 0$ , in the fluid, so that the acoustic energy of the interface wave propagates in the  $x_1$  direction (Figure 5.8).

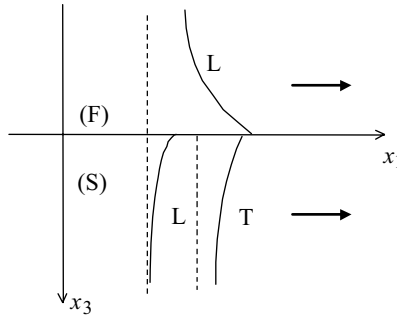


**Figure 5.8.** Scholte–Stoneley wave at the fluid–solid interface

This interface wave is often pointed out as the (Scholte–) Stoneley wave in the literature. To show its existence, a geometrical study may be performed, similar to the one which has just been made for the Rayleigh wave, if we substitute the normal stress vector with the vector of stresses *compensated* by the dynamic fluid load:

$$\vec{T}_3' = \vec{T}_3 + \frac{\rho_F \omega^2}{k_{3F}''} u_3 \vec{e}_3, \quad [5.7]$$

where  $k_{3F}''$  is the absorption factor of the evanescent wave in the fluid F,  $u_3$  the normal (continuous) component of the displacement and  $\vec{e}_3$  the unitary vector in the  $x_3$  direction.

Consequently, the interface boundary conditions for normal displacements and normal stress vectors (see section 2.1.1.3.2, equations [2.18]) amount to prescribing

the nullity of vector  $\vec{T}_3$  on the interface, that is to say searching the phase velocity  $V_{x1}$  for which the algebraic shape ratios of the compensated stress ellipses are equal, for the longitudinal and transverse waves in the solid:

$$E'_L = \frac{V_L(V_{x1}^2 - 2V_T^2)}{2V_T^2\sqrt{V_L^2 - V_{x1}^2}} + \tilde{\rho} \frac{V_F}{2V_T^2} \frac{V_{x1}^2}{\sqrt{V_F^2 - V_{x1}^2}}, \quad [5.8-a]$$

$$E'_T = \frac{2V_T\sqrt{V_T^2 - V_{x1}^2}}{V_{x1}^2 - 2V_T^2} - \tilde{\rho} \frac{V_F}{V_{x1}^2 - 2V_T^2} \frac{V_{x1}^2}{\sqrt{V_F^2 - V_{x1}^2}}, \quad [5.8-b]$$

where  $\tilde{\rho} = \rho_F / \rho_S$  refers to the ratio of densities of both media. Figure 5.9 shows the intersection point of  $E'_L(V_{x1})$  and  $E'_T(V_{x1})$  graphs, which leads to the existence of a surface wave and to its phase velocity value. This last one is very close to the wave velocity in the fluid. For this reason, the absorption factor  $k_{3F}''$  in the fluid is much smaller than the ones in the solid:

$$k_{3F}'' \ll k_{3T}'' < k_{3L}'', \quad [5.9]$$

so that the amplitude of the Scholte–Stoneley interface wave has its main part localized in the fluid, as shown in Figure 5.8.

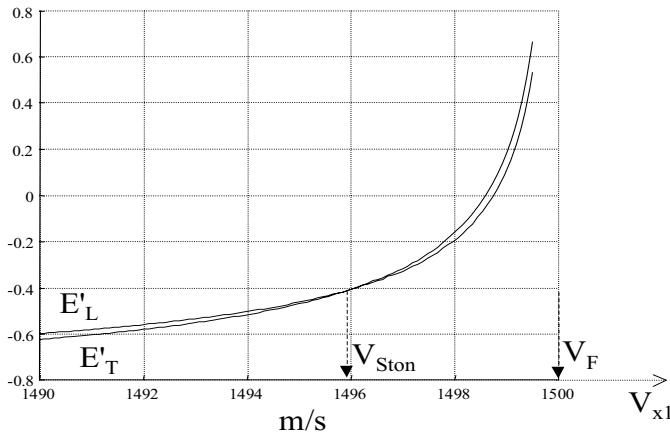


**Figure 5.9.** *Determination of the Scholte–Stoneley velocity*

We will finally remark that, as for the Rayleigh wave, the phase velocity of the Scholte–Stoneley wave is independent of the frequency.

#### 5.1.2.1.3. Stoneley wave

The study of modal waves along a (plane) interface separating two elastic solids  $S_1$  and  $S_2$ , with an embedding condition, is more complex. The interface wave, generally called the Stoneley wave, exists only if the physical parameters describing the two media are in some specific ranges. A detailed analysis of these existence ranges can be found in [SCH 47].

When it exists, the Stoneley wave is made of four evanescent waves as indicated in Figure 5.10. Most of its amplitude is located in the medium whose transverse wave velocity is the smallest. The modal wave phase velocity is lower than this last one. Furthermore, it is independent of frequency.

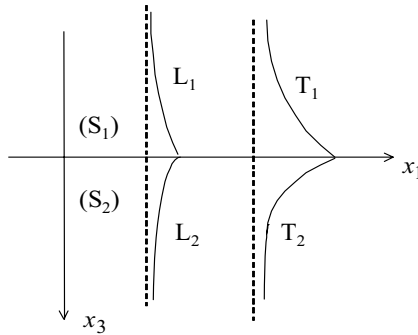


**Figure 5.10.** *Stoneley wave at the solid–solid interface*

The Stoneley wave existence for an interface  $S_1$ – $S_2$  with a sliding contact has been studied by J.D. Achenbach [ACH 67]. A generalization to the case of an interface with bonding (see section 2.1.1.4, Chapter 2) is given by H. Franklin *et al.* [FRA 94]. In this case, the phase velocity of the modal wave generally depends on frequency.

The dispersion equation enabling the determination of the Stoneley wave phase velocity for any of these interface conditions could be obtained in section 5.1.5 as a particular case of a generic example.

#### 5.1.2.2. Guided waves in an elastic isotropic layer

The study of a plane elastic layer is of great interest, as such a structure is part of many multilayered assemblies. The particular case of the layer located *in vacuo* has

been greatly studied. It can yield guided waves which are the famous Lamb waves that we describe in the next section. We will also deal with the case of an immersed layer in a fluid.

#### 5.1.2.2.1. Lamb wave

Lamb waves have been the object of an abundant literature. See for example [AUL 73] or [ROY 96]. The isotropic elastic layer of thickness  $h$  is considered as being located in a vacuum, which corresponds in reality to the exterior presence of a sufficiently light fluid, such that the acoustic couplings through the plane interfaces are very small. As in the classical case of a fluid waveguide, guided waves, which are called Lamb waves, are the result of multiple reflections of plane bulk waves on the two free surfaces  $x_3 = 0$  and  $x_3 = h$ , see Figure 5.11. As seen in section 2.1.2, these reflections involve coupling between longitudinal and transverse waves. Consequently, these two wave types take part at the same time in the Lamb wave construction.

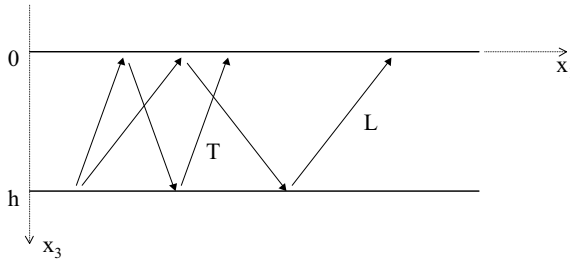


**Figure 5.11.** *Lamb wave construction in an elastic layer*

Lamb waves, as vibratory eigensolutions of an isotropic symmetric structure, are necessarily symmetric or antisymmetric, apart from the particular case of multiple eigenvalues. Symmetric Lamb waves are associated with the propagation of a succession of strictions and expansions of the elastic plate. Antisymmetric Lamb waves correspond to the propagation of bending effects along the sheet; see Figures 5.12 a and b.

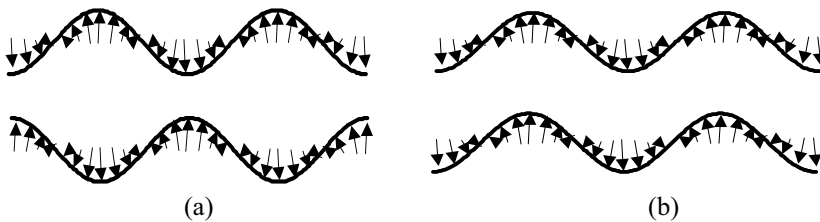


**Figure 5.12.** (a) *Symmetric Lamb wave*, (b) *Antisymmetric Lamb wave*



Lamb wave phase velocities depend on frequency. The general shape of the dispersion equation that enables the determination of these velocities, or the corresponding slownesses  $m_1$ , could be obtained from the results of section 5.1.5.

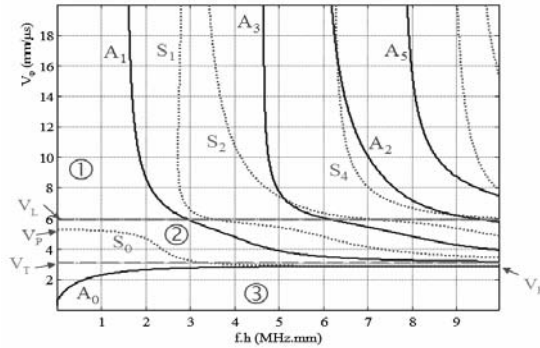
This equation can be factorized to give the symmetric mode equation separately:

$$\begin{aligned} \left(2m_1^2 - m_T^2\right)^2 \cos\left(\frac{\omega h}{2} m_{3L}\right) \sin\left(\frac{\omega h}{2} m_{3T}\right) \\ + 4m_1^2 m_{3L} m_{3T} \sin\left(\frac{\omega h}{2} m_{3L}\right) \cos\left(\frac{\omega h}{2} m_{3T}\right) = 0, \end{aligned} \quad [5.10-a]$$

and the antisymmetric mode equation:

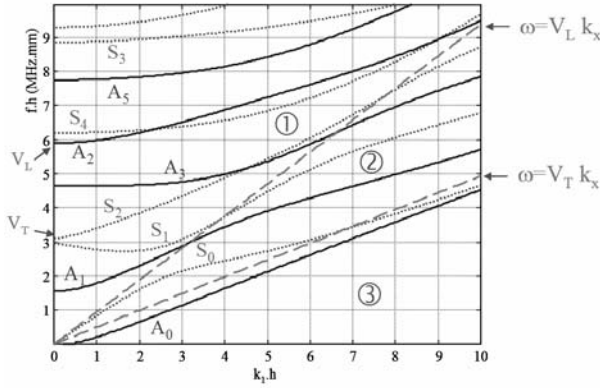
$$\begin{aligned} \left(2m_1^2 - m_T^2\right)^2 \sin\left(\frac{\omega h}{2} m_{3L}\right) \cos\left(\frac{\omega h}{2} m_{3T}\right) \\ + 4m_1^2 m_{3L} m_{3T} \cos\left(\frac{\omega h}{2} m_{3L}\right) \sin\left(\frac{\omega h}{2} m_{3T}\right) = 0. \end{aligned} \quad [5.10-b]$$

Figure 5.13 shows the variation of modal phase velocities as functions of frequency or plate thickness. Figure 5.13 represents the dispersion curves that link the modal wavenumber  $k_1$  to frequency  $f$ . The continuous lines refer to antisymmetric modes (A), and the dotted ones to symmetric modes (S).



**Figure 5.13.** Dispersion curves of Lamb waves in the plane ( $f.h, V\phi$ ) for a steel plate (longitudinal and transverse wave velocities given by  $V_L = 5900 \text{ m/s}$  and

$V_T = 3100 \text{ m/s}$ , respectively)



**Figure 5.14.** Dispersion curves of Lamb waves in the plane  $(k_1.h, f.h)$  for a steel plate (longitudinal and transverse wave velocities given by  $V_L = 5900 \text{ m/s}$  and  $V_T = 3100 \text{ m/s}$ , respectively), figure from [POT 06]

Depending on the value of the frequency  $f$ , a solution  $m_1$  of former equations could be real (the associate Lamb wave is propagative in the guide direction), purely imaginary (evanescent wave), or complex-valued. In this last situation (which is the that of an infinite number of modes at a given frequency), the corresponding mode shows a propagation effect in the guide direction and an exponential decay effect at the same time (we will remark that this is a specific case of solid media; we do not find it for modal waves in a fluid guide). The plane of Figures 5.13 and 5.14 is thus separated in three areas: area 1 ( $m_{3L}$  and  $m_{3T}$  are real, L and TV waves are propagative), area 2 ( $m_{3L}$  is purely imaginary and  $m_{3T}$  is real, L wave is evanescent and TV wave is propagative), area 3 ( $m_{3L}$  and  $m_{3T}$  are purely imaginary, L and T waves are evanescent). When the product  $f.h$  or  $k_1.h$  tends towards infinity, phase velocities of modes  $A_0$  and  $S_0$  tend towards the propagation velocity  $V_R$  of the Rayleigh wave.

#### 5.1.2.2.2. Modal waves of the immersed elastic layer

As in section 5.1.2.1.2 when introducing the Scholte–Stoneley wave, we now consider the surrounding medium as a *fluid* sufficiently *heavy* that it can no longer be assimilated to a *vacuum*. The acoustic couplings which appear at both interfaces disturb the groupings of Lamb waves which have just been described. This situation will be clarified in section 5.1.4.

However, two new modal waves appear: a symmetric wave and an antisymmetric wave. Each is made of six evanescent waves: four in the elastic layer (two longitudinal and two transverse) and one (longitudinal) in each fluid, see Figure 5.15. This configuration has been studied by M.F.M. Osborne and S.D. Hart [OSB 45]. It has also been mentioned by H. Überall in [UBE 73].

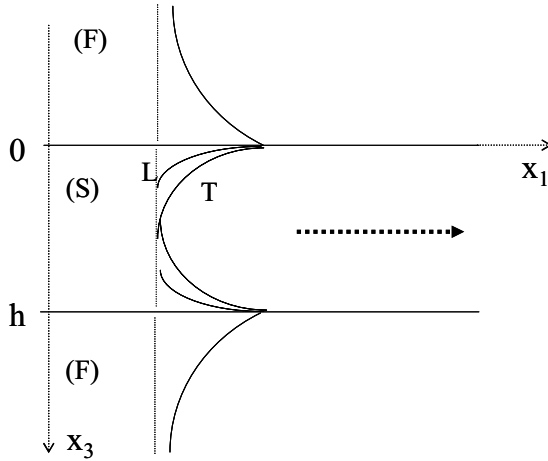


**Figure 5.15.** *Modal waves, from Osborne and Hart*

The modal (symmetric or antisymmetric) wave above is, in the solid, the sum of L and T waves evanescent along the  $x_3$  coordinate, whereas the Lamb propagative waves, apart from the first two symmetric and antisymmetric waves, for small frequencies, are made of plane L or T waves.

If the layer thickness becomes sufficiently large in comparison with wavelengths in the solid, the modal wave splits up into two interface waves which are both a Scholte–Stoneley wave described in section 5.1.2.1.2.

#### 5.1.2.3. Modal waves in multilayered structures

In the case of a structure made of  $N+2$  anisotropic media, whose extreme media  $S_0$  and  $S_{N+1}$  are semi-infinite (see Figure 5.16), the searched modal wave comes from the writing of  $6(N+1)$  scalar equations expressing the boundary conditions in the  $N+1$  interfaces (as they have been written in 2.1.1.4 equations [2.22] for example) for the  $6N + 3 + 3 = 6(N+1)$  amplitudes of plane waves constituting the searched modal waves. In fact, in the case of anisotropic media, we have to consider the six waves present in each layer. The evolution conditions at infinity on the modal direction in extreme media require the rejection of three waves among six in each

medium. Moreover, to obtain an effective modal wave (energy propagation in the layer direction), we must search the six extreme waves as inhomogeneous.

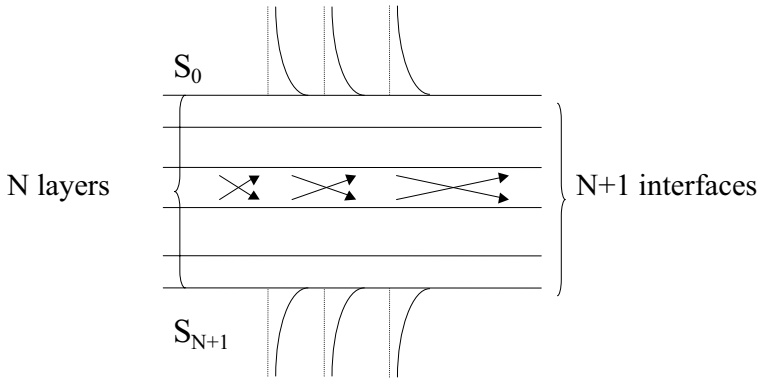


**Figure 5.16.** Modal wave in an immersed multilayered medium

The dispersion equation enabling the search of modal phase velocities is obtained by canceling the determinant of the linear  $6(N+1)$ -order system. The example of an elastic bilayered structure separating two fluids is seen in section 5.1.5.

### 5.1.3. Dispersion effects for modal waves

The dispersion effects of modal waves come from the variation of their phase velocities as a function of the frequency, or as a function of their propagation directions in the evolution sub-space.

#### 5.1.3.1. Frequency dispersion

If a modal wave family has a phase velocity independent of frequency, we can consider modal waves with any temporal profile propagating with this common phase velocity. It is the case of the Rayleigh, Scholte–Stoneley and Stoneley waves when, for these last, the interface is of embedding or sliding type.

However, many modal waves have a phase velocity which depends on frequency. We have seen it for Lamb waves; it is also the case for Stoneley waves along an interface with bonding. In these conditions, a non-monochromatic modal wave of such a type, localized at a given time in a small space, will spread with time because its frequency components propagate with different velocities. If we can

identify a nominal phase velocity, that is to say a principal Fourier component, the modal wave will be concentrated in a frequency band centered on this frequency. However, the corresponding modal wave packet will not propagate with the phase velocity of the principal wave but with an other velocity, called *group velocity*, which also represents the acoustic energy propagation velocity of the (principal) modal wave.

The concept of group velocity can be seen as follows. Let us consider a monochromatic (modal) wave whose propagation in an evolution direction is governed by the exponential factor

$$\exp i(\omega t - k_1 x_1). \quad [5.11]$$

According to the dispersion equation, the angular frequency  $\omega$  is a function

$$\omega = f(k_1), \quad [5.12]$$

of the axial modal wavenumber  $k_1$ , as shown for example in Figure 5.14. If this function is linear homogenous, the phase velocity

$$V_{x1} = \frac{\omega}{k_1}, \quad [5.13]$$

is constant and the waves are not dispersive. Let us suppose that it is not the case here and that there is a small frequency perturbation  $d\omega$  of the modal wave. It is associated with a perturbation  $dk_1$  of the wavenumber  $k_1$  and these two perturbations are linked as dispersion relationship [5.12] has to be satisfied. In other words, it becomes

$$d\omega = f'(k_1)dk_1. \quad [5.14]$$

The propagation factor of the disturbed wave is then written

$$\exp i[(\omega + d\omega)t - (k_1 + dk_1)x_1]. \quad [5.15]$$

If we bear in mind the initial modal wave, we can write this propagation exponential in the following factorized form

$$\exp i[d\omega t - dk_1 x_1] \exp i(\omega t - k_1 x_1), \quad [5.16]$$

which makes the modified wave appear as the initial wave with an additional modulation amplitude factor. This modulation effect does not propagate with the wave phase velocity, but with the speed

$$V_{g1} = \frac{d\omega}{dk_1} = f'(k_1), \quad [5.17]$$

called group velocity of the modal wave (in the propagation direction  $x_1$ ).

Figure 5.17 shows the geometrical representation of the phase velocity and the group velocity on the dispersion curve of a modal wave family.

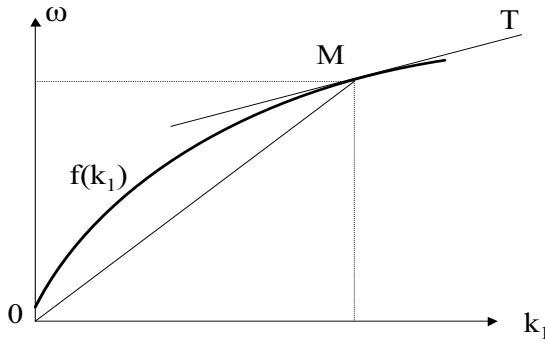


**Figure 5.17.** Graphical representation of phase and group velocities

The phase velocity is given by the slope of the line OM, whereas the group velocity is equal to the slope of the tangent MT to the dispersion curve.

#### 5.1.3.2. Angular dispersion

The phase velocity of modal waves can depend on their propagation direction in the evolution plane. Such a circumstance will be found in the case of anisotropic media when the multilayered structure has some mechanical properties that depend on the azimuthal angle around the modal direction (perpendicular to the interface planes).

In the same way as in section 1.2.2.3, Chapter 1, in the evolution space  $(x_1, x_2)$ , we can associate a modal family with its slowness curve represented by the implicit dispersion equation, expressed here in terms of the wavenumbers:

$$F(k_1, k_2, \omega) = 0. \quad [5.18]$$

In the angular dispersion case, this slowness curve is not circular. We give, for example, in Figure 5.18, the slowness curve of the Rayleigh wave at the free surface of an anisotropic medium. This curve has quite a strong elliptical nature.

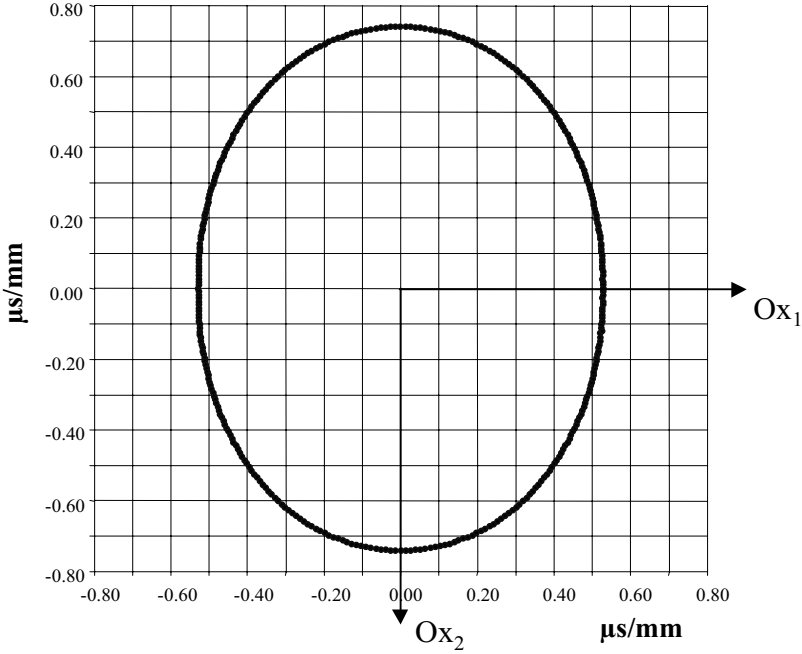


**Figure 5.18.** *Slowness curve of the Rayleigh wave in an anisotropic medium (hexagonal symmetry, axis  $A_6$  parallel to axis  $Ox_1$ )*

In these conditions, a packet of modal waves of the family, with propagation directions close to each other, will not propagate in the direction of the principal wave vector but in another direction, called *group direction*, parallel to the normal to the slowness curve at point M corresponding to the principal wave.

To demonstrate this phenomenon, we can again consider the propagation exponential of modal wave

$$\exp i(\omega t - k_1 x_1 - k_2 x_2), \quad [5.19]$$

where  $\omega, k_1, k_2$  are linked by dispersion equation [5.18]. The wave packet is monochromatic; the angular frequency  $\omega$  is the same for all waves. On the contrary, wavenumbers  $k_1, k_2$  vary so that the wave vector follows the slowness

curve (see Figure 5.19), that is to say the elementary variations of these wavenumbers satisfy the differential relationship

$$F_{,1}dk_1 + F_{,2}dk_2 = 0 . \quad [5.20]$$

where  $F_{,1}$  and  $F_{,2}$  refer to the partial derivatives of the dispersion function  $F$ .

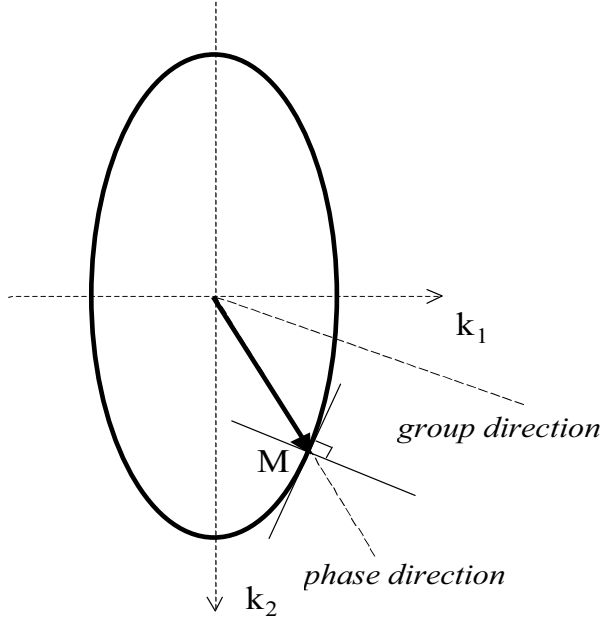


**Figure 5.19.** *Geometrical construction of group and phase directions*

Moreover, let us consider a point  $(x_1, x_2)$  of the evolution plane. With the classical stationary phase argument, we can estimate that the acoustic field in this point is essentially made of the modal wave for which the phase function in the propagation exponential is stationary with the wavenumber variation, that is to say

$$x_1dk_1 + x_2dk_2 = 0 . \quad [5.21]$$

The comparison of relationships [5.20] and [5.21] shows that the position vector  $(x_1, x_2)$  and the gradient vector  $(F_{,1}, F_{,2})$  are parallel. In other words, the points of space where we mainly find the modal wave with wavenumbers  $(k_1, k_2)$  are located on a parallel to the normal to the slowness curve at point  $(k_1, k_2)$ . This group



direction also corresponds to the energy propagation direction of the modal wave in the plane  $(x_1, x_2)$ .

This results in an angular deviation of the modal wave packet propagation. We will come back, in Parts 6–8 of this work, to Lamb wave propagation in an anisotropic medium (see Figures 22.3 and 22.4 of section 22.1.1 of Chapter 22 for the dispersion curve layout) and we will describe in section 22.1.4 the angular deviation of a wave beam due to anisotropy.

#### 5.1.4. Generalized modal waves – pseudo modal waves

As we have seen, the energy of a modal wave propagates in the evolution sub-space, where it is constant. However, in practice, this energy conservation will not be strictly fulfilled. Two reasons can lead to energy loss in the evolution directions. The first is the possible presence of dissipation mechanisms in media. If these mechanisms are not very active, the loss will be small and the modal wave will not be much affected; it will still be detectable.

The energy can also decrease in the evolution directions if a small propagation becomes possible in the modal direction, perpendicular to the evolution sub-space, leading to energy loss at infinity. This circumstance has been dismissed in the exact description of modal waves. However, in reality, such propagation can happen. Here again, if the phenomenon is sufficiently small, we can still talk about a modal wave, but in an approximate meaning.

##### 5.1.4.1. Generalized modal waves

In section 5.1.2, modal waves which take place in structures in contact with a *vacuum* have been presented. It was the case of the Rayleigh wave for the half-space limited by a free surface, and of Lamb waves in an elastic sheet in a vacuum. In practice, a *vacuum* consists of a sufficiently light fluid (gas) so that acoustic exchanges with the solid structure do not happen.

We have also seen that when the structure is immersed, that is to say put in a heavier fluid (liquid), other modal waves can appear. What then happens to the modal waves of the “dry” structure (Rayleigh or Lamb for example)? In general, the acoustic propagation velocity in the exterior fluid is smaller than the modal wave phase velocity. This leads to a propagation effect in the direction perpendicular to the interfaces (modal direction) and if the fluid medium extends up to infinity, some energy radiates to infinity in this direction. This energy is thus lost for the modal wave whose amplitude decreases. However, if the acoustic impedance ratios are small, this radiation effect will be sufficiently weak and the modal wave can propagate for a sufficiently large distance before being totally attenuated. It will thus

be detectable and useable. In this case, we usually use the term *generalized modal wave*. This scenario is represented in Figure 5.20.

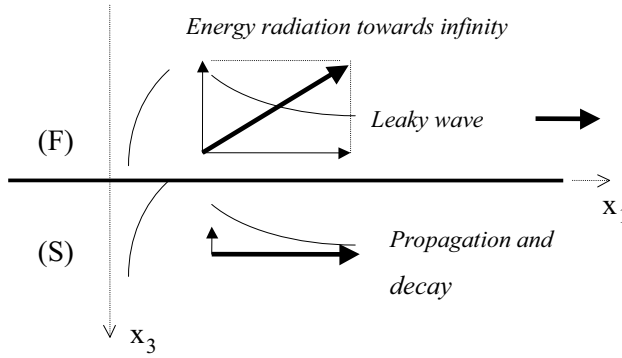


**Figure 5.20.** Schematic description of the generalized Rayleigh wave

Mathematically, at a given frequency, the exact modal wave corresponds to a real zero in  $k_1$  of the dispersion equation for the structure in a vacuum. For the immersed structure, this dispersion relationship presents some additional imaginary terms, proportional to the acoustical impedance ratios. Consequently, if the impedance ratios are weak, the zero of the exact modal wave is moved in the complex plane while remaining in the neighborhood of the real zero. Then the exponential propagation factor of the generalized modal wave takes the form

$$\exp\left\{i\left[\omega t - (k_1' + ik_1'')x_1\right]\right\} \quad [5.22]$$

where  $k_1'$  is very close to  $k_1$  and where  $k_1''$  is weak, negative and proportional to the impedance ratios (practically, proportional to the ratio of densities of the exterior fluid and of the solid of the structure). This phase factor  $k_1''$  represents the generalized modal wave decrease in the evolution direction  $x_1$ . In the exterior fluid, the acoustic field has the same propagation factor along  $x_1$  [5.22]. It comes along with the generalized modal wave during the re-radiation of the latter in the fluid, and thus it is attenuated too. It is a *leaky wave*.

The complex zero which has just been mentioned for the generalized modal wave also plays a part in the reflection–transmission problem of an incident plane wave, coming from the upper fluid (see Chapter 2). In fact, this modal zero cancels the (common) denominator of the reflection and transmission coefficients. In

particular, it is thus a pole of the reflection coefficient. However, we can show that this reflection coefficient has at the same time a zero in the neighborhood of this pole. Consequently, during a frequency scanning with a given incidence, or an incidence scanning with a given frequency, the passing through the real value  $k_1$  of the exact modal wave will cause a serious decrease of the reflection coefficient module, which could even cancel in some cases (total transmission incidences).

The study of the behavior of the reflection coefficient during such scanings is thus a way to detect modal waves in the dry structure, exact Lamb waves for example, and enables us in particular to draw the dispersion curves such as those given on Figures 5.13 and 5.14. This method is particularly useful in the case of anisotropic media for which the determination of the reflection and transmission coefficients can only be done numerically. The weaker the ratio of the fluid density to the solid one, the more precise this method is.

#### 5.1.4.2. *Pseudo-modal waves*

It can happen that this energy transfer phenomenon at infinity in the modal direction occurs in the medium where the wave propagates. The literature refers to this type of generalized modal wave using the name *pseudo-modal wave*. In practice, these waves are surface waves along the free surface of a semi-infinite medium.

This circumstance is found in the case of an anisotropic medium when a Rayleigh-type wave can be built by interaction between the quasi-longitudinal QL and the fast quasi-transverse QT1 waves. These two waves are evanescent in the modal direction. If the phase velocity of this modal wave is greater than that of the slow quasi-transverse QT2 wave, the latter propagates partially in the modal direction and transfers at infinity some acoustic energy collected at the free surface by coupling between the three waves. Here again, the modal number  $k_1$  becomes complex and a leaky wave of low transverse type accompanies the pseudo surface wave which decreases as it propagates. If the effect remains weak, it will be possible to detect a surface wave and eventually to use it. A description of these types of waves can be found in references [ACH 84] and [NAY 95]. It should be noted that there are not normalized definitions for naming the different waves and that some authors call some generalized waves “pseudo-modal”.

#### 5.1.5. *A generic example*

We will end this presentation of modal waves by the example of the determination of a dispersion equation from which we will be able to deduce, as particular cases, the dispersion equations of most of the modal waves which have been presented in the former sections. The structure considered is made of two solid

elastic isotropic layers  $(S_1)$ ,  $(S_2)$ , of thicknesses  $h^{(1)}$  and  $h^{(2)}$ , bonded by interface II, see Figure 5.21. This bi-layer separates two fluids  $(F_0)$  and  $(F_3)$ . The corresponding interfaces will be designated I and III, respectively. The bonding condition between the two layers includes the particular cases of perfect adherence, sliding and total decohesion.

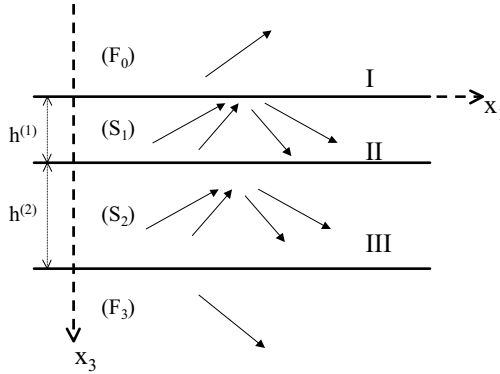


**Figure 5.21.** *Modal waves of an immersed elastic bi-layer*

A modal wave, eventually generalized, will be made on the basis of ten plane, or plane evanescent waves: a wave in each extreme fluid medium (which must fulfill appropriate propagation or decrease conditions in the modal direction  $x_3$ ) and four waves in each layer (two longitudinal waves and two transverse ones, symmetric with one another with respect to the evolution direction  $x_1$ ).

The acoustic fields in each layer will be represented by their (complex) displacement potentials. These potentials must have in common the same exponential propagation factor in the evolution direction  $x_1$ :

$$\exp[i(\omega t - k_1 x_1)] = \exp[i(\omega t - m_1 x_1)] \quad [5.23]$$

The searched dispersion equation will establish the relationship between the wavenumber  $k_1$  and the angular frequency  $\omega$ .

Exponential factor [5.23] being omitted in the following, the complex displacement potentials can be written as below. The superscript refers to the medium. In each elastic layer, we have to introduce the scalar potential for

longitudinal displacements and the vectorial potential (with only one component along the  $x_2$  axis) for the transverse displacements.

$$\psi^{(0)} = b^{(0)} e^{i\omega m_3^{(0)} x_3}, \quad [5.24]$$

$$\psi_L^{(1)} = a_L^{(1)} e^{-i\omega m_{3L}^{(1)} x_3} + b_L^{(1)} e^{i\omega m_{3L}^{(1)} (x_3 - h^{(1)})}, \quad [5.25-a]$$

$$\psi_T^{(1)} = a_T^{(1)} e^{-i\omega m_{3T}^{(1)} x_3} + b_T^{(1)} e^{i\omega m_{3T}^{(1)} (x_3 - h^{(1)})}, \quad [5.25-b]$$

$$\psi_L^{(2)} = a_L^{(2)} e^{-i\omega m_{3L}^{(2)} (x_3 - h^{(1)})} + b_L^{(2)} e^{i\omega m_{3L}^{(2)} (x_3 - h)}, \quad [5.26-a]$$

$$\psi_T^{(2)} = a_T^{(2)} e^{-i\omega m_{3T}^{(2)} (x_3 - h^{(1)})} + b_T^{(2)} e^{i\omega m_{3T}^{(2)} (x_3 - h)}, \quad [5.26-b]$$

$$\psi^{(3)} = a^{(3)} e^{-i\omega m_3^{(3)} (x_3 - h)}, \quad [5.27]$$

where, for the total thickness of the bi-layer,

$$h = h^{(1)} + h^{(2)}, \quad [5.28]$$

and where the slowness components on the  $x_3$ -axis are functions of  $m_1$  through the dispersion relationships in each layer. We will note that for each plane wave, the spatial origin of the phase of the wave is chosen at the interface where it is generated.

The ten introduced amplitudes are noted  $a$  for the five waves progressing towards  $x_3 > 0$  and  $b$  for the five others, which progress towards  $x_3 < 0$ . These amplitudes will be determined, up to a common factor, by the ten linear homogenous equations which correspond to the boundary conditions at each interface (see section 2.1.1, Chapter 2): three equations for each interface I and III, and four equations for interface II. The searched dispersion equation will correspond to the cancelation of the ten-order determinant of this linear homogenous system.

In the writing of this determinant, each column will correspond to one of the amplitudes. The chosen order for these amplitudes is the following:

$$b^{(0)}, a_L^{(1)}, a_T^{(1)}, b_L^{(1)}, b_T^{(1)}, a_L^{(2)}, a_T^{(2)}, b_L^{(2)}, b_T^{(2)}, a^{(3)}. \quad [5.29]$$

Each line will correspond to a boundary equation. We also write these equations in a well-defined order.

### *Interface I*

- line 1: continuity of the normal displacements

$$u_3^{(0)} = u_3^{(1)} ; \quad [5.30-a]$$

- line 2: continuity of the normal components of stress vectors

$$-p^{(0)} = T_{33}^{(1)} ; \quad [5.30-b]$$

- line 3: continuity of the tangential components of the stress vectors

$$0 = T_{31}^{(1)} . \quad [5.30-c]$$

### *Interface II*

- line 4: bonding condition in projection on axis  $x_3$

$$\alpha_N T_{33}^{(1)} = K_N (u_3^{(2)} - u_3^{(1)}) ; \quad [5.31-a]$$

- line 5: bonding condition in projection on axis  $x_1$

$$\alpha_T T_{31}^{(1)} = K_T (u_1^{(2)} - u_1^{(1)}) ; \quad [5.31-b]$$

where we have introduced, in addition to the bonding coefficients  $K_N$  and  $K_T$  (see section 2.1.1.4), some coefficients  $\alpha_N$  and  $\alpha_T$  which are 1 or 0 depending on the type of interface (this allows us to take into account the case of perfect adherence and sliding contact);

- line 6: continuity of the normal components of stress vectors

$$T_{33}^{(1)} = T_{33}^{(2)} ; \quad [5.31-c]$$

- line 7: continuity of the tangential components of stress vectors

$$T_{31}^{(1)} = T_{31}^{(2)} . \quad [5.31-d]$$

*Interface III*

– line 8: continuity of the tangential components of stress vectors

$$T_{31}^{(2)} = 0 ; \quad [5.32-a]$$

– line 9: continuity of the normal components of stress vectors

$$T_{33}^{(2)} = -p^{(3)} ; \quad [5.32-b]$$

– line 10: continuity of normal displacements

$$u_3^{(2)} = u_3^{(3)} . \quad [5.32-c]$$

We will let the reader express each equation as a function of the displacement potentials, using Chapter 1. We then obtain a determinant of the following form

$$D = \begin{vmatrix} X & X & X & X & X & 0 & 0 & 0 & 0 & 0 \\ X & X & X & X & X & 0 & 0 & 0 & 0 & 0 \\ 0 & X & X & X & X & 0 & 0 & 0 & 0 & 0 \\ 0 & X & X & X & X & X & X & X & X & 0 \\ 0 & X & X & X & X & X & X & X & X & 0 \\ 0 & X & X & X & X & X & X & X & X & 0 \\ 0 & X & X & X & X & X & X & X & X & 0 \\ 0 & 0 & 0 & 0 & 0 & X & X & X & X & 0 \\ 0 & 0 & 0 & 0 & 0 & X & X & X & X & X \\ 0 & 0 & 0 & 0 & 0 & X & X & X & X & X \end{vmatrix} . \quad [5.33]$$

The non-null elements  $D(i, j)$  of this determinant, denoted here by an  $X$ , are given in the appendix of this section.

From this matrix, we can obtain the following dispersion equations (where we use the notation  $D(i_1 : i_2, j_1 : j_2)$ , quite classical in programming languages, to refer to all the lines numbered from  $i_1$  to  $i_2$  and columns numbered from  $j_1$  to  $j_2$ ):

– *Rayleigh equation* for the free solid/vacuum surface

$$D(2 : 3, 2 : 3) = 0 ; \quad [5.34]$$

– *Scholte–Stoneley equation* for the fluid–solid interface (and generalized Rayleigh wave)

$$D(1:3, 1:3) = 0 \quad [5.35]$$

– *Lamb equation* for an elastic layer in a vacuum

$$D(2:5, 2:5) = 0 \quad [5.36]$$

with  $K_N = K_T = 0$  and  $\alpha_N = \alpha_T = 1$  ;

– *Stoneley equation* for the solid–solid interface (various interface types)

$$D(4:7, 4:7) = 0 \quad [5.37]$$

The particular case of perfect bonding will be obtained with:

$$\alpha_N = \alpha_T = 0, \text{ with } K_N \neq 0, K_T \neq 0 \quad [5.38\text{-a}]$$

and the sliding one with:

$$\alpha_N = 0, K_N \neq 0, \text{ and } \alpha_T = 1, K_T = 0 \quad [5.38\text{-b}]$$

– Dispersion equation for modal wave of a bi-layer in a vacuum (with any bonding condition and particular cases of type [5.38])

$$D(2:7, 2:7) = 0 \quad [5.39]$$

– Dispersion equation for an immersed layer (generalized Lamb waves and Osborne waves).

We could take the whole determinant identifying the two solids and imposing perfect adherence to interface II. In addition, we will choose the two extreme fluids to be identical. However, the dispersion equation of generalized Lamb waves results from the cancelation of a six-order determinant. It is possible to check that such a determinant can be extracted from determinant  $D$  in the following way:

$$\begin{vmatrix} D(1:3, 1:5) & D(1:3, 10) \\ D(8:10, 1) & D(8:10, 6:10) \end{vmatrix} = 0. \quad [5.40]$$



## 5.2. Appendix: non-null elements of determinant $D$

### Notations

$\rho^{(i)}$  density of medium  $(i)$ .

$m_T^{(i)}$  slowness of transverse waves in solid  $(i)$ .

$\mu^{(i)} = \rho^{(i)} / m_T^{(i)2}$  Lamé coefficient of solid  $(i)$ .

### Expressions of elements $D(i, j)$

$$D(1, 1) = m_3^{(0)}; D(1, 2) = m_{3L}^{(1)}; D(1, 3) = m_1; D(1, 4) = -m_{3L}^{(1)} e^{-i\omega h^{(1)} m_{3L}^{(1)}};$$

$$D(1, 5) = m_1 e^{-i\omega h^{(1)} m_{3T}^{(1)}};$$

$$D(2, 1) = \rho^{(0)} m_T^{(1)2}; D(2, 2) = \rho^{(1)} (2 m_1^2 - m_T^{(1)2}); D(2, 3) = -2 \rho^{(1)} m_1 m_{3T}^{(1)}$$

$$D(2, 4) = \rho^{(1)} (2 m_1^2 - m_T^{(1)2}) e^{-i\omega h^{(1)} m_{3L}^{(1)}}; D(2, 5) = 2 \rho^{(1)} m_1 m_{3T}^{(1)} e^{-i\omega h^{(1)} m_{3T}^{(1)}}$$

$$D(3, 2) = 2 m_1 m_{3L}^{(1)}; D(3, 3) = 2 m_1^2 - m_T^{(1)2}; D(3, 4) = -2 m_1 m_{3L}^{(1)} e^{-i\omega h^{(1)} m_{3L}^{(1)}}$$

$$D(3, 5) = (2 m_1^2 - m_T^{(1)2}) e^{-i\omega h^{(1)} m_{3T}^{(1)}}$$

$$D(4, 2) = [K_N m_{3L}^{(1)} + i\omega \alpha_N \mu^{(1)} (2 m_1^2 - m_T^{(1)2})] e^{-i\omega h^{(1)} m_{3L}^{(1)}}$$

$$D(4, 3) = [K_N - 2i\omega \alpha_N \mu^{(1)} m_{3T}^{(1)}] m_1 e^{-i\omega h^{(1)} m_{3T}^{(1)}}$$

$$D(4, 4) = -K_N m_{3L}^{(1)} + i\omega \alpha_N \mu^{(1)} (2 m_1^2 - m_T^{(1)2})$$

$$D(4, 5) = [K_N + 2i\omega \alpha_N \mu^{(1)} m_{3T}^{(1)}] m_1$$

$$D(4, 6) = -K_N m_{3L}^{(2)}; D(4, 7) = -K_N m_1; D(4, 8) = K_N m_{3L}^{(2)} e^{-i\omega h^{(2)} m_{3L}^{(2)}}$$

$$D(4, 9) = -K_N m_1 e^{-i\omega h^{(2)} m_{3T}^{(2)}}$$

$$D(5, 2) = [K_T - 2i\omega \alpha_T \mu^{(1)} m_{3L}^{(1)}] m_1 e^{-i\omega h^{(1)} m_{3L}^{(1)}}$$

$$\begin{aligned}
D(5,3) &= -\left[K_T m_{3T}^{(1)} + i\omega \alpha_T \mu^{(1)} \left(2 m_1^2 - m_T^{(1)2}\right)\right] e^{-i\omega h^{(1)} m_{3T}^{(1)}} \\
D(5,4) &= \left[K_T + 2i\omega \alpha_T \mu^{(1)} m_{3L}^{(1)}\right] m_1; \quad D(5,5) = K_T m_{3T}^{(2)} - i\omega \alpha_T \mu^{(1)} \left(2 m_1^2 - m_T^{(1)2}\right) \\
D(5,6) &= -K_T m_1; \quad D(5,7) = K_T m_{3T}^{(2)}; \quad D(5,8) = -K_T m_1 e^{-i\omega h^{(2)} m_{3T}^{(2)}} \\
D(5,9) &= -K_T m_{3T}^{(2)} e^{-i\omega h^{(2)} m_{3T}^{(2)}} \\
D(6,2) &= \mu^{(1)} \left(2 m_1^2 - m_T^{(1)2}\right) e^{-i\omega h^{(1)} m_{3L}^{(1)}}; \quad D(6,3) = -2\mu^{(1)} m_1 m_{3T}^{(1)} e^{-i\omega h^{(1)} m_{3T}^{(1)}} \\
D(6,4) &= \mu^{(1)} \left(2 m_1^2 - m_T^{(1)2}\right); \quad D(6,5) = 2\mu^{(1)} m_1 m_{3T}^{(1)} \\
D(6,6) &= -\mu^{(2)} \left(2 m_1^2 - m_T^{(2)2}\right); \quad D(6,7) = 2\mu^{(2)} m_1 m_{3T}^{(2)} \\
D(6,8) &= -\mu^{(2)} \left(2 m_1^2 - m_T^{(2)2}\right) e^{-i\omega h^{(2)} m_{3L}^{(2)}}; \quad D(6,9) = -2\mu^{(2)} m_1 m_{3T}^{(2)} e^{-i\omega h^{(2)} m_{3T}^{(2)}} \\
D(7,2) &= 2\mu^{(1)} m_1 m_{3L}^{(1)} e^{-i\omega h^{(1)} m_{3L}^{(1)}}; \quad D(7,3) = \mu^{(1)} \left(2 m_1^2 - m_T^{(1)2}\right) e^{-i\omega h^{(1)} m_{3T}^{(1)}} \\
D(7,4) &= -2\mu^{(1)} m_1 m_{3L}^{(1)}; \quad D(7,5) = \mu^{(1)} \left(2 m_1^2 - m_T^{(1)2}\right) \\
D(7,6) &= -2\mu^{(2)} m_1 m_{3L}^{(2)}; \quad D(7,7) = -\mu^{(2)} \left(2 m_1^2 - m_T^{(2)2}\right) \\
D(7,8) &= 2\mu^{(2)} m_1 m_{3L}^{(2)} e^{-i\omega h^{(2)} m_{3L}^{(2)}}; \quad D(7,9) = -\mu^{(2)} \left(2 m_1^2 - m_T^{(2)2}\right) e^{-i\omega h^{(2)} m_{3T}^{(2)}} \\
D(8,6) &= 2m_1 m_{3L}^{(2)} e^{-i\omega h^{(2)} m_{3L}^{(2)}}; \quad D(8,7) = \left(2 m_1^2 - m_T^{(2)2}\right) e^{-i\omega h^{(2)} m_{3T}^{(2)}} \\
D(8,8) &= -2m_1 m_{3L}^{(2)}; \quad D(8,9) = 2 m_1^2 - m_T^{(2)2} \\
D(9,6) &= \rho^{(2)} \left(2 m_1^2 - m_T^{(2)2}\right) e^{-i\omega h^{(2)} m_{3L}^{(2)}}; \quad D(9,7) = -2\rho^{(2)} m_1 m_{3T}^{(2)} e^{-i\omega h^{(2)} m_{3T}^{(2)}} \\
D(9,8) &= \rho^{(2)} \left(2 m_1^2 - m_T^{(2)2}\right); \quad D(9,9) = 2\rho^{(2)} m_1 m_{3T}^{(2)}; \quad D(9,10) = \rho^{(2)} m_T^{(2)2} \\
D(10,6) &= m_{3L}^{(2)} e^{-i\omega h^{(2)} m_{3L}^{(2)}}; \quad D(10,7) = m_1 e^{-i\omega h^{(2)} m_{3T}^{(2)}}; \quad D(10,8) = -m_{3L}^{(2)} \\
D(10,9) &= m_1; \quad D(10,10) = -m_3^{(3)}
\end{aligned}$$

### 5.3. Bibliography

- [ACH 67] Achenbach J. D., “Dynamic interaction of a layer and a half space”, *J. Eng. Mec. Divis.*, EM 5, 1967
- [ACH 84] Achenbach J.D., *Wave Propagation in Elastic Solids*, Elsevier, 1984
- [AUL 73] Auld B.A., *Acoustic Fields and Waves in Solids*, Vol. I, Wiley, 1973
- [AUL 90] Auld B.A., *Acoustic Fields and Waves in Solids*, Dover, New York, Robert E Krieger Publishing Compagny, Malabar, Florida, 1990
- [BAL 03] Baltazar A., Wang L., Xie B., Rokhlin S.I., “Inverse ultrasonic determination of imperfect interfaces and bulk properties of a layer between two solids”, *J. Acoust. Soc. Am.*, 114(3), Sept., 2003
- [BRA 90] Braga A.M.B., Hermann G., “Plane waves in anisotropic layered composites”, 81–98, “Wave Propagation In Structural Composites”, *Am. Soc. of Mech. Eng.*, New York, (1988), AMD-Vol 90, A.K. Mal and T.C.T. Ting (Eds.)
- [BRA 92] Braga A.M.B., Hermann G., “Floquet waves in anisotropic periodically layered composites”, *J. Acoust. Soc. Am.*, 91, 3, 1211–27, 1992
- [BRI 53] Brillouin, *Wave Propagation in Periodic Structures*, 2nd ed., Dover, New York, 1953
- [BRU 98] Bruneau M., *Manuel d'acoustique fondamentale*, Hermès, 1998
- [CAS 95] Castaings M., Hosten B., “Delta operator technique to improve the Thomson–Haskell method stability for propagation in multilayered anisotropic absorbing plates”, *J. Acoust. Soc. Am.*, 95, 4, 1931–41, 1994
- [CAS 02] Castaings M., “Contrôle et évaluation non destructifs de matériaux par ondes ultrasonores guides”, *Habilitation à Diriger des Recherches de l'Université Bordeaux I*, n° d'ordre 230, 2002, Available at: [www.lmp.u-bordeaux.fr/~um/Castaings/](http://www.lmp.u-bordeaux.fr/~um/Castaings/)
- [FED 68] Fedorov F.I. *Theory of Elastic Waves in Crystals*, Plenum Press, 1968
- [FRA 94] Franklin H., Rousseau M., Gatignol Ph., “Influence des conditions de collage sur l'existence de l'onde d'interface entre deux solides élastiques”, *Acustica*, 80, 2, 147–155, 1994
- [HAS 53] Haskell N.A., “The dispersion of surface waves in multilayered media”, *Bull. Seismol. Soc. Am.*, 43, 17–34, 1953
- [HAY 70] Hayes W.D., “Conservation of action and modal wave action”, *Proc. Roy. Soc.*, London A, 320, 1970
- [HON 91] Honein B., Braga A.M., Barbone P., Herrmann G., “Wave propagation in piezoelectric layered media with some applications”, *J. of Intell. Mater. Syst. and Struct.*, 2, 542–57, 1991

- [HOS 93] Hosten B., Castaings M., “Transfer matrix of multilayered absorbing and anisotropic media. Measurements and simulations of ultrasonic wave propagation through composite materials”, *J. Acoust. Soc. Am.*, 94, 3, 1488–95, 1993
- [HOS 04] Hosten B., Castaings M., “Surface impedance matrices to model the propagation in multilayered media”, *Ultrasonics*, 41, 501–7, 2004
- [KNO 64] Knopoff L., “A matrix method for elastic wave problems”, *Bull. Seismol. Soc. Am.*, 54, 1, 431–8, 1964
- [LEV 92] Levesque D., Piché L., “A robust transfer matrix formulation for the ultrasonic response of multilayered absorbing media”, *J. Acoust. Soc. Am.*, 92, 1, 452–67, 1992
- [LI 72] Li R., Yen K-H., “Elastic waves guided by a solid layer between adjacent substrates,” *IEEE Trans. MTT-20*, 7, 477–86, 1972
- [LOW 95] Lowe M.J.S., “Matrix techniques for modelling ultrasonic waves in multilayered media”, *IEEE Trans. Ultrason. Ferroelec. Freq. Control*, vol. 42, 525–42, 1995
- [MIK 78] Miklovitz J., *The Theory of Elastic Waves and Waveguides*, North Holland, 1978
- [NAY 95] Nayfeh A.H., *Wave Propagation in Layered Anisotropic Media*, North Holland, 1995
- [OSB 45] Osborne M.F.M., Hart S.D., “Transmission, reflection and guiding of an exponential pulse by a steel plate in water, I Theory”, *J. Acoust. Soc. Am.*, 17, 1, 1–18, 1945
- [PIL 82] Pilarski A., “Ultrasonic Wave Propagation in a Layered Medium Under Different Boundary Conditions”, *Arch. Acoust*, 7, 1, 61–70, 1982
- [POT 93] Potel C., de Belleval J.F., “Acoustic propagation in anisotropic periodically multilayered media; a method to solve numerical instabilities” *J. Appl. Phys.*, 74, 4, 2208–15, 1993
- [POT 01] Potel C., Gagniol Ph., de Belleval J.F., “Energetic criterion for the radiation of Floquet waves in infinite anisotropic periodically multilayered media”, *Acustica-Acta Acustica*, 87, 3, 340–51, 2001
- [POT 06] Potel C., Bruneau M., *Acoustique Générale – équations différentielles et intégrales, solutions en milieux fluide et solide, applications*, Technosup collection, Ellipse, 2006
- [ROK 81] Rokhlin S.I., Hefets M., Rosen M., “An ultrasonic interface-wave method for predicting the strength of adhesive bonds”, *J. Appl. Phys.*, 52, 2847–2851, 1981
- [ROK 86] Rokhlin S.I., Bolland T.K., Adler A., “Splitting of domain of angles for incident wave vectors in elastic anisotropic media”, *J. Appl. Phys.*, 59, 11, 1986
- [ROK 02] Rokhlin S.I., Wang I. “Stable recursive algorithm for elastic wave propagation in layered anisotropic media: Stiffness matrix method”, *J. Acoust. Soc. Am.*, 112, 3, 822–34, 2002
- [ROS 99] Rose J.L., *Ultrasonic Waves in Solid Media*, Cambridge Univ. Press, 1999
- [ROU 87] Rousseau M., Gagniol Ph., “Propagation acoustique dans un milieu périodiquement stratifié”, *Acustica*, 64, 188–94, 1987

- [ROU 89] Rousseau M., “Floquet wave properties in a periodically layered medium”, *J. Acoust. Soc. Am.*, 86,6, 2369–76, 1989
- [ROY 96] Royer D., Dieulesaint E., *Ondes élastiques dans les solides, Tome 1: Propagation libre et guidée*, Masson, 1996
- [SCH 47] Scholte J.G., “The range of existence of Rayleigh and Stoneley waves”, *Mon. Not. R. Astr. Soc. Geophys.*, Suppl. 5, 1947
- [UBE 73] Überall H., “Surface waves in acoustics”, *Physical Acoustics*, Vol X, W.P. Mason and R.N. Thurston (eds.), 1973

This page intentionally left blank

Part 2

# Porous and Stratified Porous Media Linear Models of Propagation

This page intentionally left blank



## Introduction to Part 2

In this chapter, we shall consider the propagation of acoustic waves in fluid-saturated porous media. They are no longer homogenous solids or homogenous fluids, but, in general, finely divided media consisting in of a solid matrix saturated by a fluid, a liquid or a gas. As a result of the finely divided structure, the contact surface between solid and fluid per unit volume (an inverse length), often takes significant values, and we are, in general, to consider media with relatively small characteristic pore sizes. Many examples of such environments, natural as well as artificial, can be given (e.g. saturated rocks, sediments, bones, sponges, glass wool, plastic and metal foams, woven media, fibers, ceramics, asphalts, etc.).

Concerning the sound propagation, a particular interest focuses on porous materials said to have an “open porosity”, saturated by ambient air, and characterized by pore dimensions on of the order of the viscous and thermal boundary layer thicknesses. A very symbolic image of their structure [BER 42] is given below, in Figure 2.1. The rods that connect the solid cubes define a solid, connected skeleton, conferring on it some rigidity. The inertial and elastic aspects involved in sound propagation are both incorporated in this symbolic representation of the structure of the material.

When a monochromatic wave in the ambient fluid encounters such a structure, the presence of the solid obstacles modifies the characteristics of its propagation. A macroscopic theory is generally possible, because wavelengths are long enough compared to characteristic length. When the wavelengths become comparable to microscopic dimensions, scattering by the solid skeleton must be taken into consideration. Finally, with even shorter wavelengths, any macroscopic description of the propagation becomes impossible. We will limit this study to long wavelength

situations, allowing the construction of a macroscopic description of the propagation.

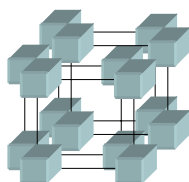


**Figure P2.1.** *Symbolic representation of the structure of the material*

In the simplest, “equivalent fluid”, case, the saturating fluid is a gas, and the solid parts are not significantly moved: they are either too heavy or sufficiently attached to their neighbors, or both. The macroscopic acoustic behavior of the material is that of an equivalent dissipative fluid, having mostly high dispersion characteristics (due to the important contact surface inducing viscous friction, and thermal exchanges between the fluid and the solid).

In the more complicated cases where fluid and solid are both set in motion, the macroscopic acoustic behavior of the material is no longer that of a fluid nor a solid, and the “Biot theory” is to be used. This theory predicts that three different kinds of waves can propagate in the material. They consist of two longitudinal waves of different kinds and a transverse shear wave.

The “Biot theory” is essentially a generalization of the theory of elasticity in the case of a macroscopically homogenous two component solid–fluid medium, where each phase forms its own connected network and where it is assumed that:

- i*) there are purely local (in space) macroscopic action–response laws;
- ii*) the macroscopic shear of the fluid does not contribute to any macroscopic shear stresses.

The restriction (*i*) (usually made in a tacit manner) is an implicit restriction on the possible microgeometry of the fluid–solid medium. In the particular case where the solid is not significantly moved, this model yields the same results as the usual equivalent fluid description (indeed, the latter also assumes (*i*) and – even if in tacit manner – (*ii*) [LAF 08]).

This generalization was developed in the 1950s by Maurice Anthony Biot [BIO 56] in the context of geophysical applications (oil saturated rocks). Its very general physical and predictive character has been well established, particularly after the seminal work of T.J. Plona, and David Linton Johnson [JOH 86]. It was

continued in the 1980s by Jean-François Allard [ALL 93], who successfully applied it to the porous materials saturated by air and used for their absorption of sound. Even for these materials – saturated by a very light fluid compared to the liquids initially considered by Biot – there are situations where the solid skeleton is set in vibrations (e.g. in the vicinity of “resonances”). As shown by Allard, these can be described by using the full “Biot theory”, generalized to include the thermal losses. Thermal losses, which are not significant when the saturating fluid, a liquid, has a very small thermal expansion coefficient, become non-negligible when this fluid is a gas.

From a physical point of view, the problem of the conception of a long-wavelength sound propagation theory in these environments is similar to the problem of the conception of macroscopic electrodynamics theory. Generally speaking, Figure P2.1 could describe the structure of a crystal, with molecules replacing the solid and void space replacing the ambient fluid.

Macroscopic electrodynamics [LAN 69] raises the questions of how the waves with large wavelengths propagate, and how macroscopic equations can be written, based on microscopic equations and specificities specific details of the environment. Macroscopic equations are often preserved when these specificities specifications vary. The constitutive coefficients of the medium are the only parameters that change. It highlights the importance to know of knowing or being able to determine them.

The same is true here. The general form of equations such as “equivalent fluid” or “Biot” will be achieved quite independently of the environmental features (e.g. liquid-saturated or gas-saturated material). These features will be included in the values and frequency dependencies of constitutive coefficients that are to be determined.

The dispersion of electromagnetic waves involves, in general, both temporal and spatial dispersion, respectively induced by the temporal and spatial variations of the external fields [LAN 69]. The most general dispersion of acoustic waves in porous media should also involve the phenomena of temporal and spatial dispersion. In the presence of spatial dispersion, non-local constitutive coefficients need to be considered.

But “equivalent fluid” and “Biot theory”, as they have so far been understood, are two models obtained by taking into account the temporal dispersion only. Indeed, these two models are only those obtained when assuming the existence of purely local constitutive laws. For some materials involving which involve microgeometries more complicated than usually found or assumed, there must be

more general descriptions that have not been discussed so far, involving spatial dispersion.

Considering a few orders of magnitude associated with the geometrical dimensions of structures encountered in the materials explains why it has not so far been necessary to introduce spatial dispersion in the equivalent fluid theory. The reason is the “incompressibility–uniformity” of the velocity–pressure field, that is verified at the microscopic level. We may call, in short, this simplification (which will be discussed at length, see for example section 26.1.1.4-5-12 and section 26.1.2.4-6-18), the condition of “divergenceless motion” of the fluid at the microscopic level. We will explicitly base our construction of the equivalent fluid theory on this simplification. The necessity of a more general non-local equivalent fluid theory, if it happened not to be verified, will be briefly outlined (see section 26.1.1.13 and section 26.1.2.19).

For a similar justification of the usual local Biot theory we note that, in likewise similar manner, the existence of local constitutive laws will express (in addition to the former condition of divergenceless fluid motion verified at the microscopic level) the condition that the solid motion at the microscopic level will be that of a “solid divergenceless motion”, that is, a “uniform motion”. We will explicitly base our construction of the Biot theory on this simplification (see Figure 26.5). A justification of this simplification, and the derivation of a more general non-local Biot theory when it is not verified, would need a more thorough study.

## Bibliography

- [ALL 93] Allard J. F., *Propagation of Sound in Porous Media. Modelling Sound Absorbing Materials*. Elsevier, 1993.
- [BER BER 42] Beranek L. L., *J. Acoust. Soc. Am.*, 13, 248, 1942.
- [BIO BIO 56] Biot M., “The theory of propagation of elastic waves in a fluid-saturated porous fluid. I. Low frequency range. II. Higher frequency range”, *J. Acoust. Soc. Am.*, 28, 168–191, 1956.
- [JOH JOH 86] Johnson D. L., “Recent developements in the acoustic properties of porous media”, in *Proc. Int. School of Physics Enrico Fermi, Cours XCIII*, D. Sette (Ed.), North Holland Publishing Co. Amsterdam, p. 255, 1986.
- [LAF LAF 08] Lafarge D., Duclos A., “Acoustic non-local permittivities in rigid-framed porous metamaterials”, *Proceedings of the Conference ‘Days on Diffraction’ 2008*, 3–6 June 3-6, St. Petersburg, Russia, 2008.
- [LAN LAN 69] Landau L., Lifshitz E., *Electrodynamique des milieux continus*, Editions Mir, Moscow, 1969.

## Chapter 6

# The Equivalent Fluid Model

### 6.1. Introduction

In this chapter, we assume that the solid structure is not set in motion by the acoustic wave. The wave is only conveyed by the fluid.

We first consider the lossless ideal case where the saturating fluid is a perfect fluid (section 6.2.1). We will then consider the general case (section 6.2.2) where the saturating fluid is a viscous fluid (with viscous losses occurring), and, when necessary, a thermal fluid with a non-negligible thermal expansion coefficient (with thermal losses occurring). Before proceeding, we state our geometry definitions.

### 6.2. Geometry definitions

The material consists of two phases, a static solid phase  $\Omega_s$  (connected or not, it is not important), and a connected fluid phase  $\Omega_f$ . We can introduce the characteristic function  $I(\vec{x})$  of the fluid domain, defined as follows:

$$I(\vec{x}) = 1, \text{ if } \vec{x} \in \text{ the fluid region } \Omega_f,$$

$$I(\vec{x}) = 0, \text{ if } \vec{x} \in \text{ the solid region } \Omega_s. \quad [6.1]$$

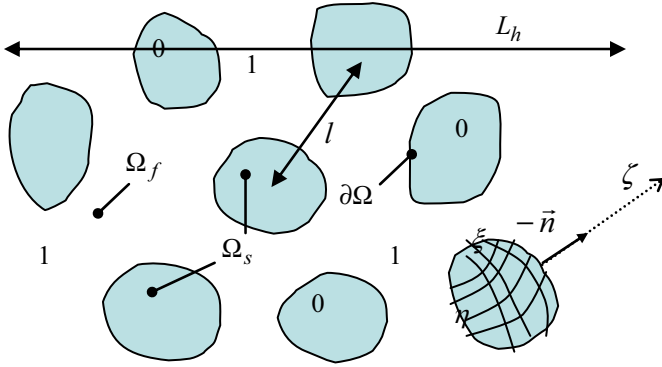


**Figure 6.1.** Schematic representation of the geometry

The solid–fluid interface is labeled  $\partial\Omega$ . A point  $\vec{x}'$  belonging to  $\partial\Omega$  can be identified by means of two Gaussian curvilinear coordinates  $\xi, \eta$ . A point  $\vec{x}$  located in a neighborhood close enough to  $\partial\Omega$  can be identified by the two Gauss coordinates  $\xi, \eta$ , of its normal projection  $\vec{x}'$  on  $\partial\Omega$ , and by a third coordinate  $\zeta$  along the normal to the interface.

With these definitions, we can give, in the sense of distributions, the following expression for the gradient of the characteristic function  $I(\vec{x})$ , in the vicinity of the interface,

$$\vec{n}(\vec{x}')\delta(\zeta) = -\vec{\nabla} I(\vec{x}), \quad [6.2]$$

where  $\vec{n}(\vec{x}')$  is the outgoing normal to the fluid domain at position  $\vec{x}'$ ,  $\delta(\zeta)$  is a Dirac delta function, and  $\vec{\nabla} = \partial/\partial\vec{x}$  is the gradient operator, used on the bulk fluid microscopic position variable  $\vec{x}$ .

The  $I(\vec{x})$  function will be considered as a fluctuating stationary random field [RUB 89] (in the case of stationary random geometry) or a periodic field (in the case of periodic geometry). We assume that its fluctuations disappear by spatial averaging above a certain scale  $L_h$ , that we call the homogenization scale. This scale is assumed to be well separated from the characteristic scale of macroscopic wavelengths  $\lambda$  ( $\lambda \gg L_h$ ), and long enough compared with the characteristic size of microstructures  $l$  ( $L_h > l$ ). The material is therefore supposed to appear as homogenous on a macroscopic scale ( $> L_h$ ); it may be anisotropic.

### 6.2.1. Ideal fluid

An acoustic wave coming from outside is propagating in the permeating ideal fluid; we wish to describe its propagation in the material in a long wavelength limit (allowing the construction of a macroscopic theory).

#### 6.2.1.1. Microscopic equations

For  $\vec{x} \in \Omega_f$ , the linearized equations of perfect fluid motion are given by the continuity equation,

$$\frac{\partial \rho_1}{\partial t} + \rho_0 \vec{\nabla} \cdot \vec{v}_1 = 0, \quad [6.3]$$

the fundamental equation of dynamics,

$$\rho_0 \frac{\partial \vec{v}_1}{\partial t} = -\vec{\nabla} p_1, \quad [6.4]$$

with the condition of zero normal velocity at the (motionless) pore walls  $\partial\Omega$ ,

$$\vec{v}_1 \cdot \vec{n} = 0, \quad [6.5]$$

and the adiabatic equation of state,

$$p_1 = \rho_1 c_0^2. \quad [6.6]$$

These can be summarized in terms of the pressure and velocity fields  $p_1$  and  $\vec{v}_1$ , and using the two fluid constants, the density  $\rho_0$  and adiabatic compressibility  $\chi_0 = 1/\rho_0 c_0^2$ ,

$$\rho_0 \frac{\partial \vec{v}_1}{\partial t} = -\vec{\nabla} p_1, \quad (\vec{x} \in \Omega_f), \quad \vec{v}_1 \cdot \vec{n} = 0, \quad (\vec{x} \in \partial\Omega), \quad [6.7 \text{ and } 6.8]$$

$$\chi_0 \frac{\partial p_1}{\partial t} = -\vec{\nabla} \cdot \vec{v}_1, \quad (\vec{x} \in \Omega_f). \quad [6.9]$$

#### 6.2.1.2. Macroscopic averaging and the spatial averaging theorem

Microscopic fields contain many unnecessary details. They must be averaged to stop showing irrelevant microscopic variations.

Macroscopic electrodynamics already highlight this question. Because of the great separation of scales and the huge number of atoms or molecules in any part of a macroscopic volume, it is useless to work with microscopic fields. Macroscopic fields, resulting from a spatial averaging of microscopic fields over “physically infinitesimal” ( $\sim L^3$ ) elements of volume, must be introduced. Averaging has the effect of eliminating the microscopic fluctuations of these values, related to the atomic heterogeneous structure of the substance. Such “smoothed” fields vary on a much larger scale (considered wavelength  $\lambda \gg L$ ) than the microscopic scale of the substance of interest.

Given a microscopic field  $a(\vec{x}, t)$ , a convenient definition of its macroscopic value at point  $\vec{r}$  is [JAC 99]:

$$\langle a \rangle(\vec{r}, t) = \int d^3\vec{x} f(\vec{x}) a(\vec{r} + \vec{x}, t), \quad [6.10]$$

where  $f(\vec{x})$  is a real, isotropic and positive “hat” test function, different from zero mainly in a neighborhood  $L^3$  of  $\vec{x} = \vec{0}$  and normalized to 1:  $\int d^3\vec{x} f(\vec{x}) = 1$ . The extent  $L$  of the plateau and decreasing region in the function  $f$ , is chosen large enough compared to the typical microscopic scale  $l$  of the material medium (e.g. the typical intermolecular dimensions).

In macroscopic electrodynamics, the physical structures to be introduced into the vacuum are ultimately made of “point-like” particles. Integration [6.10] is therefore to be performed in the whole space, and the averaging operation  $\langle \rangle$  commutes with both temporal and spatial derivatives:  $\frac{\partial}{\partial t} \langle . \rangle = \langle \frac{\partial}{\partial t} . \rangle$ ,  $\vec{\nabla} \langle . \rangle = \langle \vec{\nabla} . \rangle$  (where  $\vec{\nabla}$  stands for the macroscopic  $\frac{\partial}{\partial \vec{r}}$  and microscopic  $\frac{\partial}{\partial \vec{x}}$  respectively, before and inside the averaging symbol  $\langle \rangle$ ).

In our case, the structures to be introduced into the fluid are not point-like particles and the averaging operation only concerns fields distributed in the fluid phase. More generally, remembering the huge value of the Avogadro number, it is clear that the scale separation will be much less easily ensured, and that there will be comparatively very few microstructures in a representative volume. Nevertheless, the material is supposed to be built on a sufficiently reduced scale, or the wavelength to be sufficiently large, so that we can continue using a similar scheme. We can therefore generalize [6.10] by introducing the characteristic function  $I$  under the integral,



$$\langle a \rangle(\vec{r}, t) = \int d^3\vec{x} f(\vec{x}) I(\vec{r} + \vec{x}) a(\vec{r} + \vec{x}, t), \quad [6.11]$$

where the characteristic spatial extent of the test function  $f$  will be determined by the homogenization length  $L_h$ , which depends on the structure of the material, and is chosen large compared to the typical dimensions  $l$  of spatial inhomogeneities (Figure 6.2).

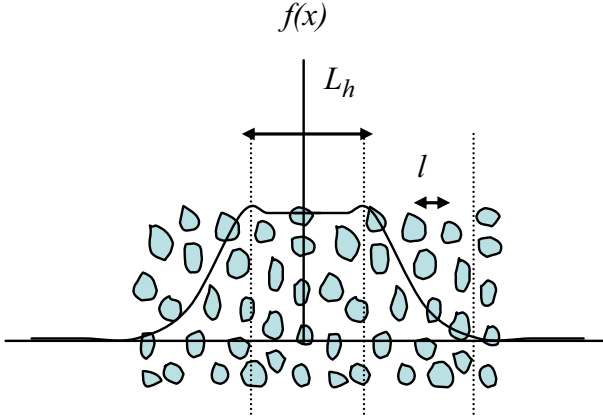


**Figure 6.2.** Schematic representation of a test function  $f(\vec{x})$  used to calculate spatial averaging. The extent  $L_h$  of the plateau and of the decreasing region of  $f$  are both large compared to the typical microscopic scale  $l$  (e.g. the typical pore radius)

Arbitrariness in the choice of the normalization of the test function now appears as a consequence of the introduction of the function  $I(\vec{r} + \vec{x})$  under the integral; also, the averaging operation  $\langle \rangle$  no longer commutes with the spatial derivative  $\vec{\nabla}$ .

Using the normalization rule  $\int f(\vec{x}) d^3\vec{x} = 1$ , we define a “total volume” averaging. Since the fluctuations of the field  $I(\vec{x})$  are supposed to disappear by spatial averaging over a spatial scale  $L_h$  (smoothing the effects of microscopic disorder), it should be observed that the integral  $\int I(\vec{r} + \vec{x}) f(\vec{x}) d^3\vec{x}$  mainly takes only one single value at the different macroscopic positions  $\vec{r}$ . With the above choice of normalization, this value is precisely the porosity factor  $\phi = \int I(\vec{x}) d^3\vec{x}$  of the material (fluid volume to total volume ratio,  $\Omega_f / \Omega$ ).

Using the alternate normalization rule  $\int I(\vec{r} + \vec{x})f(\vec{x})d^3\vec{x} = 1$ , we define a “fluid phase” averaging. As the fluctuations of the field  $I$  are supposed to disappear, it is not necessary to introduce an index  $\vec{r}$  for the function  $f$ , that reduces to  $\frac{1}{\phi} \times$  the one used in the first choice of “total volume” averaging. Thus, both averages are simply linked together by the factor of porosity  $\phi$ :  $\langle \rangle_{total\ volume} = \phi \langle \rangle_{fluid\ phase}$ . In all the following, we will use “fluid phase” averaging, unless indicated.

The new commutation law for the symbols  $\vec{\nabla}$  and  $\langle \rangle$  is easily inferred from definition [6.11] and formula [6.2] for the gradient of the characteristic function  $I$ . This law is expressed in the following *spatial averaging theorem*,

$$\langle \vec{\nabla} a \rangle(\vec{r}, t) = \vec{\nabla} \langle a \rangle(\vec{r}, t) + \int_{\vec{x} \in \partial\Omega} dS f(\vec{x} - \vec{r}) \vec{n}(\vec{x}) a(\vec{x}, t). \quad [6.12]$$

By using this theorem, the formal transition from microscopic to macroscopic equations is made very easy, though it remains a non-trivial task: evaluating in terms of macroscopic variables the pore-surface terms which may appear and will contain the relevant physics. This is illustrated below in our present ideal fluid case.

### 6.2.1.3. Averaging microscopic equations

Averaging microscopic equations [6.7] and [6.9] and using the spatial averaging theorem, we have:

$$\rho_0 \frac{\partial \langle \vec{v}_1 \rangle}{\partial t}(\vec{r}, t) = -\vec{\nabla} \langle p_1 \rangle(\vec{r}, t) - \int_{\partial\Omega} f(\vec{x} - \vec{r}) \vec{n}(\vec{x}) p_1(\vec{x}, t) dS, \quad [6.13]$$

$$\chi_0 \frac{\partial \langle p_1 \rangle}{\partial t}(\vec{r}, t) = -\vec{\nabla} \cdot \langle \vec{v}_1 \rangle(\vec{r}, t). \quad [6.14]$$

In [6.14] there is no pore-surface term: it automatically vanishes because of the condition of zero normal velocity at the pore walls [6.8]. In [6.13] a pore-surface term appears, and we wish to express it in terms of macroscopic variables such as  $\langle \vec{v}_1 \rangle$  or  $\langle p_1 \rangle$  (wavelengths are assumed to be sufficiently long to allow for a complete description of the propagation at the macroscopic level). This pore-surface term is nothing but the reaction force exerted on the accelerating fluid by the pore walls at rest,

$$\vec{R}_1(\vec{r}, t) = - \int_{\partial\Omega} f(\vec{x} - \vec{r}) \vec{n}(\vec{x}) p_1(\vec{x}, t) dS. \quad [6.15]$$

Physically, [6.13] may be interpreted as follows: the rate of change of the fluid momentum  $\rho_0 \frac{\partial \langle \vec{v}_1 \rangle}{\partial t}(\vec{r}, t)$  is the sum of the external action  $-\vec{\nabla} \langle p_1 \rangle(\vec{r}, t)$ , and the internal reaction force  $\vec{R}_1(\vec{r}, t)$ . To relate this reaction force to the velocity or pressure macroscopic variables in simple manner, we now introduce one important simplifying assumption (i) mentioned in the introduction (assumption (ii) is here automatically fulfilled as the fluid is assumed inviscid).

#### 6.2.1.4. Local action–response law

We assume that, at long wavelengths, the internal reaction force above is given by a macroscopic, purely local (in space), action–response law. It is also necessarily an instant (local in time) action–response law in the absence of losses. Thus, the assumed action–response law reads,

$$R_{1i}(\vec{r}, t) = \lambda_{\infty ij} \nabla_j \langle p_1 \rangle(\vec{r}, t), \quad [6.16]$$

where  $\lambda_{\infty ij}$  is an adimensional *constitutive coefficient* of the medium – a symmetric tensor of rank 2 called the “hydrodynamic drag tensor” [JOH 81]. An index “ $\infty$ ” is introduced in the notation of this purely geometrical factor. Indeed, the perfect fluid will be seen later as the high frequency limit (“ $\omega = \infty$ ”) of the more common case of viscous and viscothermal fluid.

To specify the action, we have chosen the macroscopic gradient of pressure. We could equally choose the rate of change of momentum, resulting in the definition of another equivalent adimensional constitutive tensor  $\chi_{\infty ij}$ ,

$$R_{1i}(\vec{r}, t) = -\rho_0 \chi_{\infty ij} \frac{\partial \langle v_{1j} \rangle(\vec{r}, t)}{\partial t}. \quad [6.17]$$

Signs in [6.16] and [6.17] are chosen such that the reaction force is opposed to the macroscopic fluid acceleration. According to their definitions [6.16–17], tensors  $\lambda_{\infty ij}$  and  $\chi_{\infty ij}$  are not independent:

$$\chi_{\infty ij} = \lambda_{\infty ik} \alpha_{\infty kj}, \quad [6.18]$$

where  $\alpha_{\infty ij}$  is the new adimensional tensor,

$$\alpha_{\infty ij} = (I - \lambda_{\infty})_{ij}^{-1} = \delta_{ij} + \chi_{\infty ij}, \quad [6.19]$$

with  $I$  the identity matrix,  $(I)_{ij} = \delta_{ij}$ , and  $\delta_{ij}$  the Kronecker delta. The tensor  $\alpha_{\infty ij}$  is called the “tortuosity” tensor and satisfies the action–response relationship,

$$\rho_0 \alpha_{\infty ij} \frac{\partial \langle v_{1j} \rangle}{\partial t}(\vec{r}, t) = -\nabla_i \langle p_1 \rangle(\vec{r}, t). \quad [6.20]$$

We can see that the constitutive tensor  $\alpha_{\infty ij}$  determines the effective inertia of the fluid, taking into account an added mass effect described by the tensor  $\chi_{\infty ij}$ .

#### 6.2.1.5. Interpretation: incompressibility at a local scale

The theoretical content in the *local* action–response relations written above entirely resides in the following fact.

In the limit of large wavelengths, the velocity field becomes *divergenceless* ( $\vec{\nabla} \cdot \vec{v}_1 \approx 0$ ) at the local scale of microstructures, for most geometries encountered in practice. However, there is a single solution to the problem of an incompressible perfect fluid flowing through the porous structure [LAN 87]. The solution to this problem determines in a unique way the tensors  $\lambda_{\infty ij}$ ,  $\chi_{\infty ij}$ , or  $\alpha_{\infty ij}$ .

Conversely, the existence of these tensors reflects the incompressibility of the fluid motion at the local scale, which is satisfied in the limit of large wavelengths. This incompressibility ensures that we have local action–response relations. We will see that the incompressibility of the fluid motion is not guaranteed at large wavelengths in all geometries (see section 6.2.1.12). Assuming that the local relationships written in section 6.2.1.4 are valid is therefore an implicit assumption about the type of geometries and range of frequencies considered.

#### 6.2.1.6. Electrical problem

The problem of incompressible perfect fluid flow we want to solve coincides formally with the following electrical problem [BRO 80].

Let the fluid phase be conducting, having an uniform conductivity  $\sigma$ , and the solid phase be insulating. Let us also suppose a normalized ( $|\vec{e}| = 1$ ) constant external macroscopic electric field  $\vec{e} = -\vec{\nabla} \psi$ , applied to the media. The problem is to determine the microscopic electric field  $\vec{E} = -\vec{\nabla} \Psi$  that appears in the fluid phase in response to it. The conservation ( $\vec{\nabla} \cdot \vec{j} = 0$ ) of the current ( $\vec{j} = \sigma \vec{E}$ ), implies that this electric response field  $\vec{E}$  is divergence-free.

Let  $\Phi = \Psi - \psi$  be the potential deviation between the microscopic potential  $\Psi$  and the imposed macroscopic potential  $\psi = Cste - \vec{e} \cdot \vec{x}$ . This deviation is due to the fact that the microscopic field lines are not straight lines; instead they are the least tortuous lines that bypass the insulating solid obstacles. By construction, the potential  $\Phi$  results from the complex geometry of the environment, and must be a fluctuating stationary (or periodic) field. This means that, unlike the potentials  $\psi$  and  $\Psi$ , the potential  $\Phi$  does not see any decrease in the direction of  $\vec{e}$  globally. On the contrary, it is statistically invariant by translation in this direction. This condition of stationarity (in stationary random geometries), replaces the usual condition of periodicity (in periodic structures).

Equations and boundary conditions of the problem are consequently written as follows:

$$\vec{E} = -\vec{\nabla}\Phi + \vec{e}, \text{ in } \Omega_f, \quad [6.21]$$

$$\vec{\nabla} \cdot \vec{E} = 0, \text{ in } \Omega_f, \quad [6.22]$$

$$\vec{E} \cdot \vec{n} = 0, \text{ on } \partial\Omega, \quad [6.23]$$

$$\Phi: \text{stationary random.} \quad [6.24]$$

Problem [6.21–24] is well conditioned. There is a single solution for the canonical fields  $\vec{E}$ ,  $\vec{\nabla}\Phi$ , which appear in response to the unit external field  $\vec{e}$ .

#### 6.2.1.7. Identification of the tensor $\chi_{\infty ij}$

The relationship between the fields  $\vec{E}$ ,  $\Phi$ , and  $\vec{v}_1$ ,  $p_1$ , may be developed as follows. In the limit of large wavelengths, the velocity field  $\vec{v}_1$  becomes divergence-free [see section 6.2.1.5] in a neighborhood  $L_h^3$  of the point  $\vec{r}$ . Consequently it should, in this neighborhood, satisfy the relationship,

$$\rho_0 \frac{\partial \vec{v}_1}{\partial t}(\vec{x}, t) \approx \left| \vec{\nabla} \cdot p_1 >(\vec{r}, t) \right| \vec{E}(\vec{x}). \quad [6.25]$$

In this expression, the macroscopic pressure gradient  $-\vec{\nabla} \cdot p_1 >$  is oriented in the same direction as  $\vec{e}$ . Replacing  $\vec{E}$  by its expression [6.21], the previous equation may be written in an equivalent way,

$$-\vec{\nabla} p_1(\vec{x}, t) \approx -\vec{\nabla} \langle p_1 \rangle(\vec{r}, t) - |\vec{\nabla} \langle p_1 \rangle(\vec{r}, t)| \vec{\nabla} \Phi(\vec{x}). \quad [6.26]$$

We now take the macroscopic average  $\langle \rangle$  at the point  $\vec{r}$  of the equation above. It results from the definition of the reaction force  $\vec{R}_1$  that the average of the left-hand side term yields  $\langle -\vec{\nabla} p_1 \rangle = -\vec{\nabla} \langle p_1 \rangle + \vec{R}_1$ . Concerning the right-hand side, the quantities  $-\vec{\nabla} \langle p_1 \rangle(\vec{r}, t)$  or  $|\vec{\nabla} \langle p_1 \rangle(\vec{r}, t)|$  are constant and can be extracted from the averaging; this leads to,

$$\vec{R}_1 \approx -|\vec{\nabla} \langle p_1 \rangle(\vec{r}, t)| \langle \vec{\nabla} \Phi \rangle(\vec{r}). \quad [6.27]$$

Finally, by combining equations [6.17], [6.25] and [6.27], the identification of the tensor  $\chi_{\infty ij}$  is completed:

$$\langle \nabla_i \Phi \rangle = \chi_{\infty ij} \langle E_j \rangle. \quad [6.28]$$

This equation uniquely determines the constants  $\chi_{\infty ij}$ , knowing the fields  $\vec{E}$ ,  $\vec{\nabla} \Phi$ , solutions of electrical problem [6.21–24] for different orientations of the vector  $\vec{e}$ .

#### 6.2.1.8. Identification of the hydrodynamic drag tensor $\lambda_{\infty ij}$

Once the incompressibility of the fluid motion at the pore scale is recognized, the physical meaning of the hydrodynamic drag tensor clearly appears from the following “gedanken experiment”. Suppose that both the incompressible perfect fluid and the solid structure (unlimited in space) are initially at rest, the structure is then forced through the fluid in a given direction, partially draining the latter. In this case, the macroscopic velocity of the fluid  $\langle \vec{v}^f \rangle$  will be proportional at each instant to the instantaneous velocity of the solid,  $\vec{v}^s = v^s \vec{e}$ , with  $\lambda_{\infty ij}$  giving the proportionality constants:

$$\langle v_i^f \rangle = \lambda_{\infty ij} v_j^s. \quad [6.29]$$

The proof will not be given but is straightforward to obtain, by reasoning in the non-inertial rest frame of the structure. The uniform external pseudo-force acting on the fluid plays the role of the constant stirring field  $\vec{e}$ , and the stationary random fluctuating pressure field appearing in the fluid plays the role of the potential  $\Phi$ .

### 6.2.1.9. Symmetry

The tensors previously introduced are symmetric. Like every symmetric tensor of rank 2, they reduce to the diagonal form in some system of three orthogonal axes, the principal axes of the material.

To prove the symmetry of these tensors, we arbitrarily choose directions for the axes such that the cross components are non-zero. According to equations [6.19], [6.21], [6.28], the tortuosity tensor  $\alpha_{\infty ij}$  and its inverse  $\alpha_{\infty ij}^{-1}$  satisfy the following equations,

$$\alpha_{\infty ij} \langle E_j \rangle = e_i, \quad [6.30]$$

$$\langle E_j \rangle = \alpha_{\infty jk}^{-1} e_k. \quad [6.31]$$

Let us now consider the fields  $\vec{E}^{(i)}$  and  $\Phi^{(i)}$ , which appear when the three unit stirring fields  $\vec{e}^{(i)}$  ( $i = 1, 2, 3$ ) are applied in the three directions  $x$ ,  $y$ , and  $z$ . According to [6.31], we obtain  $\langle \vec{E}_j^{(i)} \rangle = \alpha_{\infty jk}^{-1} \vec{e}_k^{(i)}$  or  $\langle \vec{E}_j^{(i)} \rangle = \alpha_{\infty ji}^{-1}$ , since  $\vec{e}_k^{(i)} \equiv \delta_{ik}$ . This can be written,

$$\alpha_{\infty ji}^{-1} = \langle \vec{E}_l^{(i)} \delta_{jl} \rangle = \langle \vec{E}_l^{(i)} \vec{e}_l^{(j)} \rangle = \langle \vec{E}^{(i)} \cdot \vec{e}^{(j)} \rangle.$$

We now show that the quantities,

$$\alpha_{\infty ji}^{-1} = \langle \vec{E}^{(i)} \cdot \vec{e}^{(j)} \rangle, \quad [6.32]$$

define a symmetric tensor. Imposing the field  $\vec{e}^{(j)}$  in [6.21], and substituting it in [6.32], we obtain,

$$\langle \vec{E}^{(i)} \cdot \vec{e}^{(j)} \rangle = \langle \vec{E}^{(i)} \cdot \vec{E}^{(j)} \rangle + \langle \vec{E}^{(i)} \cdot \vec{\nabla} \Phi^{(j)} \rangle.$$

The last term is removed by integration by parts, because of the stationary nature of the fields and the boundary condition [6.23]. We finally obtain:

$$\alpha_{\infty ji}^{-1} = \langle \vec{E}^{(i)} \cdot \vec{E}^{(j)} \rangle, \quad [6.33]$$

which explicitly shows the symmetry of the tensors.

#### 6.2.1.10. *Principal axes*

In the principal axes system, cross components disappear. The tensor  $\alpha_{\infty ij}$  reduces to the diagonal form  $\alpha_{\infty ij} = \alpha_{\infty i} \delta_{ij}$ . The mean field  $\langle \vec{E}^{(i)} \rangle$  is colinear to the field  $\vec{e}^{(i)}$  and given by  $\alpha_{\infty i}^{-1} \vec{e}^{(i)}$ . A clear expression of the tortuosity along the principal axis  $i$  is,

$$\alpha_{\infty i} = \frac{\langle \vec{E}^{(i)} \cdot \vec{E}^{(i)} \rangle}{\langle \vec{E}^{(i)} \rangle \cdot \langle \vec{E}^{(i)} \rangle}. \quad [6.34]$$

The factor  $\alpha_{\infty i}$  (obviously  $\geq 1$ ) is a measure of “disorder” in the distribution of velocities  $\vec{E}^{(i)}$  of the perfect fluid circulating through the porous structure in the macroscopic direction  $\vec{e}^{(i)}$ . Due to the principle of least action, the microscopic pattern  $\vec{E}^{(i)}$  is just that, which minimizes the expression [6.34]. This means that the perfect fluid is flowing in such a way that the added mass effects are minimized. Notice that in the electrical conduction problem, the tensor  $\alpha_{\infty ij}$  determines the effective conductivity

$$\sigma_{ij} = \phi \alpha_{\infty ij}^{-1} \sigma, \quad [6.35]$$

which by definition allows us to write one macroscopic level Ohm’s law in the form

$$J_i = \phi \langle j_i \rangle = \sigma_{ij} e_j. \quad [6.36]$$

This result follows from [6.31] by averaging the microscopic level Ohm’s law,  $\vec{j} = \sigma \vec{E}$ . In this context, the fact that the electric field  $\vec{E}$  or current distribution  $\vec{j}$  minimizes expression [6.34] just expresses a principle of minimum dissipation.



In the isotropic case, the tortuosity tensor  $\alpha_{\infty ij} = \alpha_{\infty} \delta_{ij}$  is characterized by the unique scalar constant,  $\alpha_{\infty} = \langle \vec{E}^2 \rangle / \langle \vec{E} \rangle^2 = 1 / \langle \vec{E} \cdot \vec{e} \rangle = 1 / \langle \vec{E}^2 \rangle$ .

#### 6.2.1.11. Equivalent fluid

To summarize, the assumption that there are (spatially) *local* action–response laws at large wavelengths is nothing but the assumption that the fluid motion becomes *incompressible* at a microscopic scale. In the absence of losses, the response is necessarily local in time, i.e. instantaneous. These simplifications are expressed in the following macroscopic equations, called the “*equivalent fluid*” equations,

$$\rho_0 \alpha_{\infty ij} \frac{\partial \langle \vec{v}_1 \rangle_j}{\partial t} = -\vec{\nabla}_i \langle p_1 \rangle, \quad [6.37]$$

$$\chi_0 \frac{\partial \langle p_1 \rangle}{\partial t} = -\vec{\nabla} \cdot \langle \vec{v}_1 \rangle, \quad [6.38]$$

where the symmetric tortuosity tensor  $\alpha_{\infty ij}$  is determined by the solution of the electrical conduction problem [6.21–24], as given by equations [6.32] or [6.33].

This is called “equivalent fluid” because:

i) the equations we obtain are the same as those of a free flowing fluid, with the condition that the density  $\rho_0$  is renormalized and replaced by the effective density  $\rho_0 \alpha_{\infty ij}$  which takes into account the added mass effect;

ii) the boundary conditions at the interface with the external free fluid will be those appropriate for ordinary fluids: the continuity of normal flow and continuity of pressure (see sections 6.2.2.15 and 6.2.1.7 for more details).

A similar situation is encountered in electrodynamics, with dielectric media, when we may neglect losses and when the environment only reacts locally. The vacuum electric permittivity  $\epsilon_0$  is replaced by the quantity  $\epsilon_0 \epsilon_{rij}$ . No dispersion is involved and the eigenvalues of the symmetric quantities  $\alpha_{\infty ij}$  and  $\epsilon_{rij}$  are real positive constants necessarily greater than or equal to 1.

#### 6.2.1.12. Limitations of the incompressibility condition

A warning must nevertheless be expressed about the central hypothesis that the fluid motion is divergenceless at the microscopic scale.

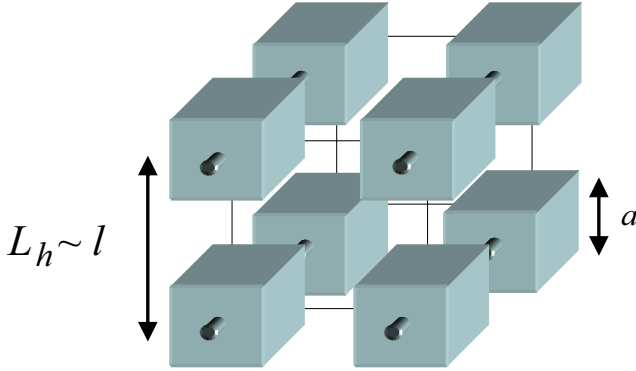


**Figure 6.3.** *Example of a geometry that can illustrate the limitations of the condition of incompressibility*

Often, the macroscopic equations are fully calculated from the microscopic equations via a homogenization method, using the multi-scale expansion technique. Initially introduced for periodic structures [BEN 78], [SAN 80], this homogenization method automatically ensures that the fluid motion is, at a first approximation, incompressible at a microscopic scale [LEV 77, 79], [BUR 81], [AUR 80, 85] [NOR 86], [SHE 88], [SME 92].

But this conclusion is not necessarily valid if more than two well-separated scales (one microscopic and one macroscopic) are to be introduced into the problem. To understand the limitations of the condition of incompressibility, we introduce the example in Figure 6.3. It apparently represents solid cubes that are actually hollow cubes with a small neck, or in other words, Helmholtz resonators.

By taking relatively small and long openings for the resonators it is possible to ensure that the wavelength is still large compared to the grid of the network,  $\lambda \gg l$ , at the resonant frequency of the resonators. The grid may roughly be considered as the length of homogenization  $L_h$ , hence also,  $\lambda \gg L_h$ .

To make this more definite, let us denote  $V = a^3$  the volume of the resonator,  $S = \varepsilon^2 a^2$  the surface of the neck opening,  $L = ma$  the length of the neck;  $\varepsilon$  is small and  $m$  can be assumed to be approximately 1. For the sake of simplicity,  $m$  will be considered as equal to 1. The smallness of parameter  $\varepsilon$  manifests the presence of two widely different relevant pore sizes (the cube size  $a$  and opening radius  $\varepsilon a$ ). Around the resonance frequency  $f \approx \frac{c_0}{2\pi} \sqrt{\frac{S}{VL}}$  of the Helmholtz

resonators, a simple estimate  $c_0 / f$  of the wavelength  $\lambda$  yields  $\lambda \sim 2\pi a / \varepsilon$ . Now, observe that the homogenization length  $L_h$  may be similar to  $a$ , when the resonators are close to each other. Thus, a “large wavelengths” condition  $\lambda \gg L_h \sim a$  can be satisfied at the resonance, provided that we take  $\varepsilon \ll 2\pi$ .

This rough reasoning shows that, in the neighborhood of the resonance frequency of the resonator, we could encounter a situation where a macroscopic long-wavelength theory should be applicable, while the incompressibility of the fluid motion at the microscopic level would not be ensured.

#### 6.2.1.13. *Most general form of the macroscopic theory*

The incompressibility condition will not always be satisfied; in this situation, the pore-surface term in [6.13] will not take its value [6.16] or [6.17] with constitutive tensors  $\lambda_{\infty ij}$  or  $\chi_{\infty ij}$  determined as explained by solving the electrical conduction problem. The generalization of the theory poses specific mathematical problems to be properly formulated, in the absence of losses, and we do not consider this problem here further (see the indications given in section 6.2.2.19 for the more general form of the macroscopic theory in presence of losses).

### 6.2.2. *Thermoviscous fluids*

The permeating fluid is no longer a perfect fluid. It is supposed to be viscous and to have a non-negligible thermal expansion coefficient.

#### 6.2.2.1. *Microscopic equations*

The linearized equations of the fluid motion are given by [LAN 87]:

– the equation of continuity,

$$\frac{\partial \rho_1}{\partial t} + \rho_0 \vec{\nabla} \cdot \vec{v}_1 = 0 ; \quad [6.39]$$

– Newton’s second law,

$$\rho_0 \frac{\partial v_{li}}{\partial t} = \frac{\partial \sigma_{lik}}{\partial x_k}, \quad [6.40]$$

where the different stresses are written,

$$\sigma_{lik} = -p_1 \delta_{ik} + \sigma'_{lik}, \quad [6.41]$$

$$\sigma'_{lik} = \eta \left( \frac{\partial v_{li}}{\partial x_k} + \frac{\partial v_{lk}}{\partial x_i} - \frac{2}{3} \delta_{ik} \frac{\partial v_{ll}}{\partial x_l} \right) + \zeta \delta_{ik} \frac{\partial v_{ll}}{\partial x_l}, \quad [6.42]$$

with the no-slip condition on the (motionless) pore walls,

$$\vec{v}_1 = \vec{0}; \quad [6.43]$$

– the fluid constitutive equation,

$$\rho_1 = \frac{\rho_0}{K_0} p_1 - \rho_0 \beta_0 \tau_1; \quad [6.44]$$

– and the heat equation,

$$\rho_0 C_p \frac{\partial \tau_1}{\partial t} = \beta_0 T_0 \frac{\partial p_1}{\partial t} + \kappa \Delta \tau_1, \quad [6.45]$$

with the continuity condition on the (ambient temperature) pore walls,

$$\tau_1 = 0. \quad [6.46]$$

In these equations,  $\eta$  and  $\zeta$  are the first and second viscosity coefficients,  $K_0$  is the isothermal bulk modulus,  $\beta_0$  is the thermal expansion coefficient,  $C_p$  is the specific heat coefficient at constant pressure,  $T_0$  is the ambient temperature, and  $\kappa$  is the thermal conduction coefficient. The isothermal bulk modulus  $K_0$  (equal to the ambient pressure  $P_0$ , in a gas), differs from the adiabatic bulk modulus  $K_a = \gamma K_0$ , when the ratio  $\gamma = C_p / C_v$  of the specific heat coefficients at constant pressure and constant volume differs from 1.

The following general thermodynamic identity [LAN 87], [PIE 91],

$$\gamma - 1 = \frac{\beta_0^2 T_0}{\rho_0 C_p \chi_0}, \quad [6.47]$$

where  $\chi_0$  is the adiabatic compressibility, i.e.,

$$\chi_0 = \frac{1}{K_a} = \frac{1}{\gamma K_0}, \quad [6.48]$$

shows that the deviation of factor  $\gamma$  from unity is a second order effect on the thermal expansion coefficient  $\beta_0$ .

For a liquid, the coefficient of thermal expansion  $\beta_0$  is very small because the molecules are “in contact” with each other, i.e. trapped at a minimum distance allowed by the van der Waals intermolecular forces. A small heat input is not reflected by an expansion but by a greater agitation of the molecules, which remain at a minimum distance. The smallness of the coefficient  $\beta_0$  implies that the factor  $\gamma$  becomes virtually indistinguishable from unity. In this case, the equations above are significantly simplified. Isothermal compression and adiabatic compression modules,  $K_0$  and  $K_a$ , nearly coincide. We can ignore the term with the coefficient of thermal expansion in [6.44] which becomes,

$$\frac{\rho_1}{\rho_0} = \gamma \chi_0 p = \chi_0 p. \quad [6.49]$$

Pressure and density variations are not coupled to the temperature variations. At the macroscopic level, equation [6.38] is still correct, with  $\chi_0 = 1/K_a = 1/K_0$ . Only [6.37] will have to be modified to account for the viscous effects.

On the other hand, if a gas is considered, the coefficient of thermal expansion is not very small ( $\beta_0 T_0 = 1$  for an ideal gas), leading to a deviation, generally non-negligible, of the factor  $\gamma$  compared to unity. Indeed, simple considerations of the kinetic theory of gases give  $\gamma = (d + 2)/d$ , where  $d$  is the number of excited degrees of freedom of a typical molecule of gas. For air, mainly composed of diatomic molecules, having five degrees of freedom (three for translation and two for rotation), we obtain  $\gamma \approx 7/5 \approx 1.4$ . Thus, the variations of pressure and density are not decoupled from the variations of temperature and, therefore, we have to consider equations [6.44–45]. The isothermal bulk modulus of the gas,  $K_0 = P_0$ , is significantly less than the adiabatic bulk modulus  $K_a = \gamma P_0$ . At the macroscopic level, both equations [6.35] and [6.36] will have to be modified.

#### 6.2.2.2. Averaging the microscopic equations

If we average  $\diamond$  microscopic equations [6.39–40] [6.44–45], we obtain the following,

$$\frac{\partial \langle \rho_1 \rangle}{\partial t}(\vec{r}, t) + \rho_0 \vec{\nabla} \cdot \langle \vec{v}_1 \rangle(\vec{r}, t) = 0, \quad [6.50]$$

$$\rho_0 \frac{\partial \langle v_{li} \rangle}{\partial t}(\vec{r}, t) = -\nabla_i \langle p_1 \rangle(\vec{r}, t) + \frac{\partial}{\partial x_k} \langle \sigma'_{lik} \rangle(\vec{r}, t) + \int_{\partial\Omega} f(\vec{x} - \vec{r}) \vec{n}_k(\vec{x}) \{ -\delta_{ik} p_1(\vec{x}, t) + \sigma'_{lik}(\vec{x}, t) \} dS, \quad [6.51]$$

$$\langle \rho_1 \rangle(\vec{r}, t) = \frac{\rho_0}{K_0} \langle p_1 \rangle(\vec{r}, t) - \rho_0 \beta_0 \langle \tau_1 \rangle(\vec{r}, t), \quad [6.52]$$

$$\rho_0 C_p \frac{\partial \langle \tau_1 \rangle}{\partial t}(\vec{r}, t) = \beta_0 T_0 \frac{\partial \langle p_1 \rangle}{\partial t}(\vec{r}, t) + \kappa \int_{\partial\Omega} f(\vec{x} - \vec{r}) \vec{n}(\vec{x}) \cdot \vec{\nabla} \tau_1(\vec{x}) dS. \quad [6.53]$$

In this latter equation, the spatial averaging theorem has been used twice, and the condition for the excess temperature to be zero on the pore walls [6.46] has been considered. We neglected the term  $\kappa \Delta \langle \tau_1 \rangle$  because it is expected to be of the

order  $\kappa \frac{\omega^2}{c_0^2} \langle \tau_1 \rangle$ , which can be comparable to the term

$\rho_0 C_p \frac{\partial \langle \tau_1 \rangle}{\partial t} = \rho_0 C_p i \omega \langle \tau_1 \rangle$ , only for frequencies on the order  $\omega \approx c_0^2 / \nu$ , where,

$$\nu \equiv \frac{\kappa}{\rho_0 C_p} = \frac{\nu}{\text{Pr}}, \quad \nu \equiv \frac{\eta}{\rho_0}. \quad [6.54]$$

In this expression,  $\nu$  is the kinematic viscosity,  $\nu$  is the thermal diffusivity and Pr is the Prandtl number. Such frequencies, corresponding to wavelengths comparable to the mean free path  $\nu / c_0$  in a gas (not even allowing the use of mechanics of continuous media), are well beyond the permitted frequencies. For similar reasons, (one more use of the spatial averaging theorem combined with the no-slip condition for velocity), there is no need to keep the term  $\frac{\partial}{\partial x_k} \langle \sigma'_{lik} \rangle$  in

the second part of [6.51] when the fluid is a gas (or even a liquid which is not characterized by a very large viscosity). This omission, indeed, is made here because of the assumption (ii) mentioned in the introduction.

There remains the non-trivial task of evaluating the pore-surface terms in [6.51] and [6.53],

$$R_{1i}(\vec{r}, t) \equiv \int_{\Omega} f(\vec{x} - \vec{r}) n_k(\vec{x}) \{-p_1(\vec{x}, t) \delta_{ik} + \sigma'_{1ik}(\vec{x}, t)\} dS, \quad [6.55]$$

and,

$$Q_1(\vec{r}, t) \equiv \kappa \int_{\Omega} f(\vec{x} - \vec{r}) \vec{n}(\vec{x}) \cdot \vec{\nabla} \tau_1(\vec{x}) dS, \quad [6.56]$$

which contain the relevant physics. As before, this evaluation can be done easily by introducing one important simplifying assumption (assumption (i) mentioned in the introduction).

### 6.2.2.3. Local action–response laws

We assume that the quantities mentioned above,  $\bar{R}_1$  and  $Q_1$ , are given (in terms of the velocity or pressure macroscopic variables) by macroscopic, purely local, action–response laws. This assumption is similar to the one made in section 6.2.1.4. However, because of losses, these action–response laws are no longer instant (local in time) relations. Indeed, the viscous and thermal processes are always delayed in time.

Thus, relation [6.16] becomes, for example,

$$\begin{aligned} R_{1i}(\vec{r}, t) = & \lambda_{\infty ij} \nabla_j < p_1 >(\vec{r}, t) \\ & + \int_0^{\infty} \lambda_{vij}(t') \nabla_j < p_1 >(\vec{r}, t - t') dt'. \end{aligned} \quad [6.57]$$

Loss processes, which occur with a delay, do not affect the instant response which must therefore be described by the same factor  $\lambda_{\infty ij}$  as before. They only affect the delayed response, described by the constitutive kernel  $\lambda_{vij}(t)$ . The index “v” is written down because it will be shown that only the viscous losses effects (and not the thermal losses) are involved in this case. It may be noticed that a similar generalization of relation [6.17] would lead in same manner to the definition of a related constitutive kernel  $\chi_{vij}(t)$ ,

$$\begin{aligned} R_{1i}(\vec{r}, t) = & -\rho_0 \chi_{\infty ij} \frac{\partial < v_{1j} >(\vec{r}, t)}{\partial t} \\ & - \rho_0 \int_0^{\infty} \chi_{vij}(t') \frac{\partial < v_{1j} >(\vec{r}, t - t')}{\partial t} dt', \end{aligned}$$

(see equation [6.61b] below – which generalizes [6.19] – for the relation between both kernels).

Similar considerations apply to the thermal response  $Q_1(\vec{r}, t)$ . Comparing [6.53] with [6.51] we cannot note that the term  $\beta_0 T_0 \frac{\partial \langle p_1 \rangle}{\partial t}(\vec{r}, t)$  has the same role as the term  $-\nabla_i \langle p_1 \rangle(\vec{r}, t)$ . We can then deduce the thermal counterpart of equation [6.57],

$$Q_1(\vec{r}, t) = - \int_0^\infty \lambda_{th}(t') \beta_0 T_0 \frac{\partial \langle p_1 \rangle}{\partial t}(\vec{r}, t - t') dt', \quad [6.58]$$

which describes the delayed thermal response through the constitutive scalar kernel  $\lambda_{th}(t)$ . To define a counterpart  $\chi_{th}(t)$  of  $\chi_{vij}(t)$ , we would write the above action–response law in the form,  $Q_1(\vec{r}, t) = - \int_0^\infty \chi_{th}(t') \rho_0 C_P \frac{\partial \langle \tau_1 \rangle}{\partial t}(\vec{r}, t - t') dt'$ .

Proportionality relationships between action and response will be found in the harmonic regime  $e^{-i\omega t}$ . Therefore, considering the complex amplitudes of the fields (for the sake of simplicity, we will use the same notations, and will not indicate that the amplitudes are taken at the same point  $\vec{r}$ ), equations [6.57–58] then read,

$$R_{li} = \lambda_{ij}(\omega) \nabla_j \langle p_1 \rangle, \quad \lambda_{ij}(\omega) \equiv \lambda_{\infty ij} + \int_0^\infty dt \lambda_{vij}(t) e^{i\omega t}, \quad [6.59a, b]$$

$$Q_1 = -\lambda(\omega) \beta_0 T_0 (-i\omega) \langle p_1 \rangle, \quad \lambda(\omega) \equiv \int_0^\infty dt \lambda_{th}(t) e^{i\omega t}. \quad [6.60a, b]$$

For the inertial and viscous action–response laws [6.57], the most used harmonic forms are, first, the form defining the “dynamic tortuosity”  $\alpha_{ij}(\omega)$ , an adimensional factor:

$$\rho_0 \alpha_{ij}(\omega) \frac{\partial \langle \vec{v}_1 \rangle_j}{\partial t}(\vec{r}) = -\vec{\nabla}_i \langle p_1 \rangle, \quad [6.61a]$$

$$\alpha_{ij}^{-1}(\omega) = \delta_{ij} - \lambda_{ij}(\omega) = \alpha_{\infty ij}^{-1} - \lambda_{vij}(\omega) = \left( \alpha_{\infty ij} + \chi_{vij}(\omega) \right)^{-1}, \quad [6.61b]$$

(where [6.61a] is written in analogy with [6.35] and  $\partial / \partial t = -i\omega$ ), and, second, the form defining a “dynamic permeability”  $k_{ij}(\omega)$ , a factor having the dimension of a surface:



$$\phi < \vec{v}_1 >_i (\vec{z}) = -\frac{1}{\eta} \ell_j(\omega) \vec{\nabla}_j < p_1 >, \quad [6.62a]$$

with,

$$k_{ij}(\omega) = \frac{\nu\phi}{-i\omega} \alpha_{ij}^{-1}. \quad [6.62b]$$

Expression [6.62a] is written in analogy with “Darcy’s Law”,

$$\phi < \vec{v}_1 >_i = -\frac{1}{\eta} k_{0ij} \vec{\nabla}_j < p_1 >, \quad [6.63]$$

which applies in the d.c., (time-independent) regime. This law states that in a permanent regime, the filtration rate is proportional to the pressure gradient. A purely geometric parameter appears, called the permeability, which has the dimension of a surface and can be interpreted as an effective section of the pores. Relation [6.63] is called “Darcy’s law” in reference to his statement in a note “Détermination des lois de l’écoulement de l’eau à travers le sable” in the appendix of the book *Les fontaines publiques de la ville de Dijon*, written by the engineer Henry Darcy, and published in 1856 [DAR 56]. Darcy’s permeability  $k_{0ij}$  is the value of the dynamic permeability  $k_{ij}(\omega)$  at  $\omega = 0$ .

Similarly, it is useful for the thermal action–response law [6.58] to consider the following harmonic form, written in analogy with [6.61a, b],

$$\rho_0 C_p \chi(\omega) \frac{\partial < \tau_1 >}{\partial t} = \beta_0 T_0 \frac{\partial < p_1 >}{\partial t}, \quad [6.64a]$$

with,

$$\chi^{-1}(\omega) = 1 - \lambda(\omega) = (1 + \chi(\omega))^{-1}, \quad [6.64b]$$

as well as the following expression, written in analogy with [6.62a, b],

$$\phi < \tau_1 > = \frac{1}{\kappa} k(\omega) \beta_0 T_0 \frac{\partial < p_1 >}{\partial t}, \quad [6.65a]$$

with

$$k(\omega) = \frac{\nu\phi}{-i\omega} \chi^{-1}(\omega). \quad [6.65b]$$

We will call the scalar response factors  $\lambda(\omega)$  (with no dimension) and  $k(\omega)$  (with the dimension of a surface) the “thermal dynamic tortuosity” and “thermal dynamic permeability” although these names are not really precise. The scalar parameter having the role of the Darcy’s permeability, which is  $k_0 = k(\omega = 0)$ , is further identified as nothing more than the inverse of a geometrical constant, the “trapping constant”, often introduced in the context of “diffusion-controlled” reactions [TOR 89]. Yet, the concept of viscous permeability introduced by Darcy is old; the notion of thermal permeability has been introduced more recently [LAF 97]. The thermal analog of “Darcy’s Law” would then read,

$$\phi < \tau_1 > = \frac{1}{\kappa} k_0 \beta_0 T_0 \frac{\partial < p_1 >}{\partial t}, \quad [6.66]$$

where we consider a “d.c. regime” with a constant input of heat in the fluid:  $\beta_0 T_0 \partial p_1 / \partial t = Cste = \beta_0 T_0 \partial < p_1 > / \partial t$ . In response to this constant, uniform input of heat in the fluid, an average excess temperature “ $\tau_1$ ” appears in the pores of the material. The solid parts of the material are supposed sufficiently inert thermally, so that they behave as a thermostat, staying at the ambient temperature.

#### 6.2.2.4. Interpretation: Incompressibility at the pore scale

The theoretical content in the local action–response relations written above entirely resides in the following fact.

In the limit of large wavelengths, the velocity field becomes divergenceless ( $\vec{\nabla} \cdot \vec{v}_1 \approx 0$ ) at the local level of microstructures, for most geometries encountered in practice. But there is a unique solution to the oscillating flow of an incompressible viscous fluid through the porous structure. The harmonic solution to this purely inertial and viscous problem determines the tensors  $\lambda_{ij}(\omega)$ ,  $\alpha_{ij}(\omega)$  or  $k_{ij}(\omega)$  in a unique way.

Meanwhile, the variations of the pressure field become uniform ( $\vec{\nabla} \partial p_1 / \partial t \approx 0$ ) at the local level of microstructures, for most geometries encountered in practice (see section 6.2.2.6 for this consideration). However, there is a single solution to the problem of the diffusion of heat created evenly in the saturating fluid, and absorbed by the porous structure. The harmonic solution to this purely thermal problem determines the scalars  $\lambda(\omega)$ ,  $\alpha(\omega)$  or  $k(\omega)$  in a unique way.

Conversely, the existence of the above tensors and scalars reflects the incompressibility of the fluid motion at the local level on one hand, and the related condition of the uniformity of pressure variations at the local level, on the other

hand. This incompressibility, in short, ensures that we have local action–response relations. We will see in section 6.2.2.18 that the incompressibility of the fluid motion is not guaranteed at large wavelengths in all geometries. Assuming that the relationships written in section 6.2.2.3 are valid is therefore an implicit assumption about the type of geometries and range of frequencies considered.

#### 6.2.2.5. Canonical problems

With the interpretation made in section 6.2.2.4 of the local relations stated in section 6.2.2.3, the following equations are to be solved: first for the vectorial problem of an incompressible viscous and non-stationary flow; second for the problem of heat exchanges,

$$\frac{-i\omega}{\nu} \vec{w} = -\vec{\nabla} \pi + \Delta \vec{w} + \vec{e}, \text{ in } \Omega_f, \quad \frac{-i\omega}{\nu} w = \Delta w + 1, \text{ in } \Omega_f, \quad [6.67a, b]$$

$$\vec{\nabla} \cdot \vec{w} = 0, \text{ in } \Omega_f, \quad [6.68]$$

$$\vec{w} = \vec{0}, \text{ on } \partial\Omega, \quad w = 0, \text{ on } \partial\Omega. \quad [6.69a, b]$$

$$\pi \text{ stationary.} \quad [6.70]$$

There is one single solution,  $\vec{w}$ ,  $\pi$ , and  $w$ , to these canonical inertial–viscous and thermal microscopic problems.

#### 6.2.2.6. Identification of the permeabilities $k_{ij}(\omega)$ and $k(\omega)$

The relationship between the canonical scaled fields  $\vec{w}$ ,  $\pi$ ,  $w$ , and the physical fields  $\vec{v}_1$ ,  $p_1$ , and  $\tau_1$ , will be developed. At large wavelengths, the velocity field  $\vec{v}_1$  becomes divergence-free in a neighborhood  $L_h^3$  of the point  $\vec{r}$ . In this neighborhood, the pressure  $p_1(\vec{x})$  can be seen as the sum of two terms  $\langle p_1 \rangle(\vec{x}) + \Pi_1(\vec{x})$ . The first one,  $\langle p_1 \rangle(\vec{x})$ , represents macroscopic behavior, with  $\langle p_1 \rangle(\vec{x}) \approx \langle p_1 \rangle(\vec{r}) + \vec{\nabla} \langle p_1 \rangle(\vec{r}) \cdot (\vec{x} - \vec{r})$  because the wavelengths are sufficiently long compared to  $L_h$ . The second one,  $\Pi_1(\vec{x})$ , represents a small fluctuating deviation,  $\langle \Pi_1(\vec{x}) \rangle(\vec{r}) = 0$ . This field appears as a consequence of the non-trivial geometry of the problem. It allows the fluid to follow, at a microscopic level, the different paths that bypass the solid obstacles. These obstacles are characterized by a microscopic dimension  $a$  well below the wavelength  $\lambda$ . Therefore, when the variations of the macroscopic component of the pressure

$\langle p_1 \rangle(\vec{x})$  happen at a given scale  $\lambda$ , the variations of the fluctuating component happen at a different scale  $a$ . Since the gradients of  $\Pi_1(\vec{x})$  are a reaction, their order of magnitude is at most comparable to the external force, meaning that they can reach the value,  $\Pi_1/a \approx \langle p_1 \rangle/\lambda$ . Thus, even though the fluctuating pressures  $\Pi_1$  are a key element in determining the microscopic gradients of the pressure field  $p_1$ , the corresponding amplitudes are completely negligible ( $a/\lambda < L_h/\lambda \ll 1$ ) compared to the mean pressure  $\langle p_1 \rangle$ . To summarize, while one can write  $\vec{\nabla} \cdot \vec{v}_1 \approx 0$  to determine the velocity pattern  $\vec{v}_1(\vec{x})$  at a microscopic scale, we can also write  $\vec{\nabla} \partial p_1 / \partial t \approx 0$  to determine the excess temperature pattern  $\tau_1(\vec{x})$  at a microscopic scale, e.g. replace in [6.45] the field  $\partial p_1 / \partial t(\vec{x})$  with the constant  $\partial \langle p_1 \rangle / \partial t(\vec{r})$ , in a neighborhood  $L_h^3$  of the point  $\vec{r}$ .

We can deduce from these considerations that for very large wavelengths, and in the frame of the hypothesis considered above, we have the following expressions in a neighborhood  $L_h^3$  of the point  $\vec{r}$ , (we set  $-\vec{\nabla} \langle p_1 \rangle = |\vec{\nabla} \langle p_1 \rangle| \vec{e}$ ),

$$v_{1i}(\vec{x}) \approx |\vec{\nabla} \langle p_1 \rangle(\vec{r}) / \eta| w_i(\vec{x}), \quad \Pi_1(\vec{x}) \approx |\vec{\nabla} \langle p_1 \rangle(\vec{r})| \pi(\vec{x}), \quad [6.71a, b]$$

$$\tau_1(\vec{x}) \approx \{\beta_0 T_0 (-i\omega) \langle p_1 \rangle(\vec{r}) / \kappa\} w(\vec{x}). \quad [6.72]$$

In order to obtain [6.71a, b], we note that, given the incompressibility condition, it is not necessary to write down the viscous terms containing  $\vec{\nabla} \cdot \vec{v}_1$  in [6.40–42]. Putting  $p_1 = \langle p_1 \rangle + \Pi_1$ , the latter then reads,

$$\frac{-i\omega}{\nu} \vec{v}_1 \approx -\frac{1}{\eta} \vec{\nabla} (\langle p_1 \rangle + \Pi_1) + \Delta \vec{v}_1 = -\frac{1}{\eta} \vec{\nabla} \Pi_1 + \Delta \vec{v}_1 + \frac{1}{\eta} |\vec{\nabla} \langle p_1 \rangle| \vec{e}.$$

Expressions [6.71a, b] are obtained by comparing the latter equation to [6.67a].

To obtain [6.72], we note that, given the condition  $\vec{\nabla} \partial p_1 / \partial t \approx 0$  which expresses that  $\Pi_1 \approx \langle p_1 \rangle a / \lambda \ll \langle p_1 \rangle$ , [6.45] can be rewritten,

$$\frac{-i\omega}{\nu} \tau_1 \approx \Delta \tau_1 - \frac{1}{\kappa} \beta_0 T_0 i\omega \langle p_1 \rangle.$$

Expression [6.72] is obtained by comparing this equation to [6.67b].

Finally, averaging equations [6.71a] and [6.72], and comparing the results obtained with relations [6.62a] and [6.65a], we obtain the following expressions:

$$\phi < \bar{w}_i > = k_{ij}(\omega) \bar{e}_j, \quad \phi < w > = k(\omega). \quad [6.73a, b]$$

These relations determine in one way the dynamic permeabilities  $k_{ij}(\omega)$  and  $k(\omega)$ , knowing the scaled fields  $\bar{w}$  and  $w$ , respectively solutions to the inertial–viscous canonical problem [6.67a, 6.68, 6.69a, 6.70] (for the different orientations of the vector  $\bar{e}$ ) and the thermal canonical problem [6.67b, 6.69b].

#### 6.2.2.7. Identification of the hydrodynamic drag tensor $\lambda_{ij}(\omega)$

Once the incompressibility of the fluid motion at the pore scale is recognized, the physical meaning of the hydrodynamic drag tensor is clearly expressed in the following “gedanken experiment”.

We start with a situation where the fluid and the solid (unlimited) are at rest. We then abruptly set the solid into uniform oscillating motion  $\bar{v}^s = v^s \bar{e} e^{-i\omega t}$ . The fluid is partially drained and acquires, after the fading of transient terms, a (macroscopically) uniform oscillating motion given by the equation,

$$< \bar{v}_i^f > = \lambda_{ij}(\omega) v^s e_j e^{-i\omega t} \quad [6.74]$$

This identification of the drag tensor  $\lambda_{ij}(\omega)$  may be obtained as follows. In a non-inertial reference system attached to the solid, moving at a speed  $\bar{v}^s = v^s \bar{e} e^{-i\omega t}$ , an external and uniform volumic pseudo-force  $-\rho_0 \partial \bar{v}^s / \partial t$  is exerted on the fluid. In this reference system, the fluid is moving with velocities  $\bar{v}^f - \bar{v}^s$ . The equation of motion of the incompressible fluid is,

$$\rho_0 \frac{\partial (\bar{v}^f - \bar{v}^s)}{\partial t} = -\nabla p^f + \eta \Delta \bar{v}^f + (-\rho_0 \frac{\partial \bar{v}^s}{\partial t}),$$

with a stationary pressure field  $p^f$ . Therefore, the term  $-\rho_0 \partial \bar{v}^s / \partial t$  replaces the macroscopic gradient of the pressure and a comparison with [6.61a] leads to,

$$\rho_0 \alpha_{ij}(\omega) \frac{\partial < \bar{v}^f - \bar{v}^s >_j}{\partial t} = -\rho_0 \frac{\partial \bar{v}_i^s}{\partial t},$$

or, after a simplification by  $\rho_0 \partial / \partial t = -i\omega \rho_0$ ,

$$(\langle \vec{v}^f \rangle - \vec{v}^s)_i = -\alpha_{ij}^{-1}(\omega) \vec{v}_j^s,$$

$$\langle \vec{v}_i^f \rangle = (\delta_{ij} - \alpha_{ij}^{-1}(\omega)) \vec{v}_j^s = \lambda_{ij}(\omega) \vec{v}_j^s,$$

as stated above.

#### 6.2.2.8. Symmetry

The tensor  $k_{ij}(\omega)$  is symmetric. The symmetry of the tensor can be easily seen considering the fields  $\vec{w}^{(i)}$  and  $\pi^{(i)}$  appearing as a response to the three unit fields  $\vec{e}^{(i)}$  ( $i=1, 2, 3$ ) chosen along the three directions  $x, y$ , and  $z$ . According to [6.73a], it becomes  $\phi < \vec{w}_j^{(i)} \rangle = k_{jk}(\omega) \vec{e}_k^{(i)}$ , or  $\phi < \vec{w}_j^{(i)} \rangle = k_{ji}(\omega)$  since  $\vec{e}_k^{(i)} \equiv \delta_{ik}$ . This can be written as,

$$k_{ji}(\omega) / \phi = \langle \vec{w}_l^{(i)} \delta_{jl} \rangle = \langle \vec{w}_l^{(i)} \vec{e}_l^{(j)} \rangle = \langle \vec{w}^{(i)} \cdot \vec{e}^{(j)} \rangle. \quad [6.75]$$

Imposing the unit field  $\vec{e}^{(j)}$  in [6.67a], then calculating the scalar product with  $\vec{w}^{(i)}$ , and averaging the result, we can obtain from [6.75] the following equation, from which the symmetry of the tensor results,

$$k_{ji}(\omega) / \phi = \frac{-i\omega}{\nu} \langle \vec{w}^{(i)} \cdot \vec{w}^{(j)} \rangle + \langle \nabla_l \vec{w}_m^{(i)} \nabla_l \vec{w}_m^{(j)} \rangle, \quad [6.76]$$

where we have taken into account the two relationships  $\langle \vec{w}^{(i)} \cdot \vec{\nabla} \pi^{(j)} \rangle = 0$  and  $-\langle \vec{w}^{(i)} \cdot \Delta \vec{w}^{(j)} \rangle = \langle \nabla_l \vec{w}_m^{(i)} \nabla_l \vec{w}_m^{(j)} \rangle$ ; they have been obtained by integration by parts, taking into account the stationary property of the fields  $\vec{w}^{(i)}$  and  $\pi^{(i)}$ , the incompressibility condition, and the no-slip boundary condition at the pore walls for  $\vec{w}^{(i)}$ .

The symmetry of the tensor  $k_{ij}(\omega) = k_{ji}(\omega)$  was expected, according to the general principle of the symmetry of the kinetic coefficients [LAN 80] (see section 6.2.2.15).

For the same reasons (stationary nature of the fields  $\vec{w}^{(i)}$  and  $\Phi^{(i)}$ , incompressibility condition and no-slip boundary condition),  $\langle \vec{w}^{(i)} \cdot \vec{\nabla} \Phi^{(j)} \rangle = 0$ , and we can also write [6.75] under the following form, that will be useful later on,

$$k_{ji}(\omega) / \phi = \langle \vec{w}^{(i)} \cdot \vec{E}^{(j)} \rangle. \quad [6.77]$$

#### 6.2.2.9. Equivalent fluid

To summarize, in the presence of losses the theory, as before (section 2.1.1.11), assumes (spatially) *local* action–response laws at large wavelengths, which is nothing but the assumption that:

– the fluid motion becomes *incompressible* at a microscopic scale for the purpose of determining the velocity pattern:

and in corresponding manner,

– the pressure becomes *uniform* for the purpose of determining the temperature pattern.

These simplifications are expressed in the following macroscopic equations, known as the “*equivalent fluid*” equations (where we write  $-i\omega = \partial / \partial t$  as in equations [6.35–36]),

$$\rho_0 \alpha_{ij}(\omega) \frac{\partial \langle \vec{v}_1 \rangle_j}{\partial t} = -\vec{\nabla}_i \langle p_1 \rangle, \quad [6.78]$$

$$\chi_0 \beta(\omega) \frac{\partial \langle p_1 \rangle}{\partial t} = -\vec{\nabla} \cdot \langle \vec{v}_1 \rangle. \quad [6.79]$$

The dynamic tortuosity factor is given by (see [6.62b])

$$\alpha_{ij}(\omega) = \frac{\nu \phi}{-i\omega} k_{ij}^{-1}(\omega), \quad [6.80]$$

where  $k_{ij}(\omega)$  can be evaluated using, for example, relation [6.75] or [6.77].

The dynamic compressibility factor  $\beta(\omega)$  is linked to the dynamic thermal tortuosity/permeability, as described below.

Substituting equation [6.52] into [6.50], we obtain,

$$\frac{\partial \langle \tau_1 \rangle}{\partial t} = \frac{1}{K_0 \beta_0} \frac{\partial \langle p_1 \rangle}{\partial t} + \frac{1}{\beta_0} \vec{\nabla} \cdot \vec{v}_1.$$

Returning to [6.64a], the latter gives,

$$\left\{ \frac{1}{K_0} - \frac{\beta_0^2 T_0}{\rho_0 C_p \alpha(\omega)} \right\} \frac{\partial \langle p_1 \rangle}{\partial t} = -\vec{\nabla} \cdot \langle \vec{v}_1 \rangle.$$

From general identity [6.47] and definition [6.48], this expression has the same form as [6.79] with,

$$\beta(\omega) = \gamma - \frac{\gamma - 1}{\alpha(\omega)}, \quad [6.81]$$

or, using relation [6.65b] that exists between  $\alpha(\omega)$  and  $k(\omega)$ ,

$$\beta(\omega) = \gamma + (\gamma - 1) \frac{i\omega}{\nu \phi} k(\omega). \quad [6.82]$$

Therefore, the effective compressibility  $\beta(\omega)$  is determined by the solution  $w$  of the canonical thermal problem through the relation,

$$\beta(\omega) = \gamma + (\gamma - 1) \frac{i\omega}{\nu} \langle w \rangle. \quad [6.83]$$

This is called “equivalent fluid” because:

i) the equations we obtain are the same as those of a free flowing fluid, with the condition that the density  $\rho_0$  is renormalized and replaced by the effective density  $\rho_0 \alpha_{ij}(\omega)$  which takes into account the inertial and viscous effects, and the compressibility  $\chi_0$  is renormalized and replaced by the effective compressibility  $\chi_0 \beta(\omega)$  which takes into account thermal effects;

ii) the boundary conditions at the interface with the external free fluid will be those appropriate for ordinary fluids: the continuity of normal flow and continuity of pressure (see sections 6.2.2.15 and 6.2.1.7 for more details).



A similar situation takes place in the domain of electrodynamics of continuous media when losses cannot be ignored and the medium reacts locally. The magnetic and electric permittivities of the vacuum  $\varepsilon_0$  and  $\mu_0$  are replaced with the quantities  $\varepsilon_0 \varepsilon_{rij}(\omega)$  and  $\mu_0 \mu_{rij}(\omega)$ .

Due to the condition of incompressibility, which is another way of expressing the local character of the responses, we have been able to separate the viscous effects and the thermal effects, and introduce them separately in the factors  $\alpha_{ij}(\omega)$  and  $\beta(\omega)$ . Similarly in electrodynamics, the existence of factors  $\varepsilon_{rij}(\omega)$  and  $\mu_{rij}(\omega)$  supposes that the responses are local, the first one taking into account the effects of electric polarization, and the second the effects of magnetic polarization.

It is interesting to note that for large classes of materials,  $\beta(\omega) \approx 1$  or  $\mu_{rij}(\omega) \approx \delta_{ij}$ . This occurs respectively when the saturating fluid is a liquid (as has been observed in section 6.2.2.1) or when the material is a non-ferromagnetic material ([LAN 84]). Actually, the thermal effects appear as second order effects on the coefficient of thermal expansion  $\beta_0$ , which is very small for a liquid. Similarly, for non-ferromagnetic materials, the effects of magnetic polarization are relativistic second order effects on the coefficient  $\beta = v/c$ , where  $v$  is the velocity of electrons in the atoms, which is very small compared to the speed of light.

#### 6.2.2.10. *Nature of the frequency dependence of the susceptibilities $\alpha_{ij}(\omega)$ and $\beta(\omega)$*

The determination of the factors  $\alpha_{ij}(\omega)$  and  $\beta(\omega)$  requires the solution of the canonical problems written in section 6.2.2.5, which is not readily feasible given the complexity due to the geometries encountered. In the absence of such a solution, it is nevertheless possible to draw very general conclusions about the nature of the frequency dependencies of the factors  $\alpha_{ij}(\omega)$  and  $\beta(\omega)$ .

The quantities  $\varepsilon_{rij}(\omega)$  and  $\mu_{rij}(\omega)$ , or  $\alpha_{ij}(\omega)$  and  $\beta(\omega)$ , belong to the class of functions called “generalized susceptibilities”. They verify their properties, well-detailed in [LAN 80], among which the Kramers–Krönig relations, which reflect the causality of the responses.

The principle of causality requires that the various response functions introduced above are analytic functions of the frequency – having singularities (like poles, branch points or zeros) in the half lower part of the complex plane of the variable  $\omega$  only. In electrodynamics, the position of singularities can be found everywhere in

the lower half plane, including positions adjacent to the real axis: it reflects a wide variety of possible dispersive behaviors.

In the present (rigid frame) acoustic case, the singularities of the response factors can only be found on the negative imaginary axis (see, for a proof, [JOH 87] Appendix A, [LAF 97] Appendix C, and, for a discrete formulation making the same property in periodic geometries apparent [AVE 91, LAF 93]). This can be seen using, respectively, the conditions of incompressibility and of uniform pressure discussed above. The possible dispersive behaviors are thus drastically reduced. The frequency dependence of the functions  $\alpha_{ij}(\omega)$  and  $\beta(\omega)$  results from a pure “distribution of relaxation times”, i.e., it can be seen as resulting from a continuous (or discrete, in periodic geometries) sum of poles under the form  $1/(1 - i\omega\theta)$ . This is a major simplification.

Thus for example, it means that the Fourier transforms  $\lambda_{vij}(\omega)$  and  $\lambda_{th}(\omega)$  of functions  $\lambda_{vij}(t)$  and  $\lambda_{th}(t)$  in [6.59–60] may be written (in periodic geometries)

$$\lambda_{vij}(\omega) = \sum_{n=1}^{\infty} b_{ni}b_{nj} / (1 - i\omega\theta_n) \quad \text{and} \quad \lambda_{th}(\omega) = \sum_{n=1}^{\infty} b_n^2 / (1 - i\omega\theta_n). \quad \text{These}$$

expressions make the different viscous and thermal characteristic relaxation times  $\theta_n$  and  $\vartheta_n$  (which accumulate at the origin for  $n \rightarrow \infty$ ) and the different weighting coefficients  $b_{ni}b_{nj}$  and  $b_n^2$  (“oscillatory strengths”) associated with them apparent. By defining the cumulative distributions of eigensurfaces  $\sigma_n = \nu\theta_n$  and  $\vartheta_n = \nu\vartheta_n$ ,

namely, the functions  $G_{ij}(\sigma) = \sum_{\sigma_n \leq \sigma} b_{ni}b_{nj}$  and  $\vartheta G(\sigma) = \sum_{\vartheta_n \leq \sigma} b_n^2$ , it becomes

possible to write  $\lambda_{vij}(\omega)$  and  $\lambda_{th}(\omega)$  in the form of Stieltjes integrals,

$$\lambda_{vij}(\omega) = \int_0^{\infty} \frac{dG_{ij}(\sigma)}{1 + \frac{-i\omega}{\nu}\sigma}, \quad \lambda_{th}(\omega) = \int_0^{\infty} \frac{d\vartheta G(\sigma)}{1 + \frac{-i\omega}{\nu}\sigma}.$$

Finally, in the case of arbitrary stationary random geometry, functions  $G_{ij}$  and  $\vartheta G$  become continuous functions, having well-defined derivatives  $g_{ij} = dG_{ij}/d\sigma$ ,  $\vartheta g = d\vartheta G/d\sigma$ , so that we may

write, in general terms,  $\lambda_{vij}(\omega) = \int_0^{\infty} \frac{g_{ij}(\sigma)d\sigma}{1 + \frac{-i\omega}{\nu}\sigma}$ ,  $\lambda_{th}(\omega) = \int_0^{\infty} \frac{\vartheta g(\sigma)d\sigma}{1 + \frac{-i\omega}{\nu}\sigma}$ .

From the results that will be obtained in the next sections, it can be shown that, in general, the purely geometrical viscous and thermal distributions  $g_{ij}(\sigma)$  and

$$\begin{aligned} \dot{g}(\sigma) \text{ will have to respect definite "sum rules", e.g., } \alpha_{\infty ij}^{-1} &= \int_0^\infty g_{ij}(\sigma) d\sigma, \\ k_{0ij} &= \phi \int_0^\infty \sigma g_{ij}(\sigma) d\sigma, \quad k_{0ik} \frac{\alpha_{0kl}}{\phi} k_{0lj} = \phi \int_0^\infty \sigma^2 g_{ij}(\sigma) d\sigma, \text{ etc., and likewise,} \\ 1 &= \int_0^\infty \dot{g}(\sigma) d\sigma, \quad \dot{k}_0 = \phi \int_0^\infty \sigma \dot{g}(\sigma) d\sigma, \quad \dot{k}_0 \frac{\alpha_0}{\phi} \dot{k}_0 = \phi \int_0^\infty \sigma^2 \dot{g}_{ij}(\sigma) d\sigma, \text{ etc.} \end{aligned}$$

They also have to respect definite and relatively universal behaviors at  $\sigma \rightarrow 0$ . These behaviors determine the viscous and thermal responses at very short times immediately after the removal of external actions (or equivalently, at high frequencies). They lead to relaxation laws of exactly the same nature as the corresponding “Curie von Schweidler” laws [CUR 89a, b] [SCH 07] observed in many materials for the relaxation of the electric polarization  $\vec{P}(t)$ . (A quantity which will play a similar role will be, for example, the vector  $\vec{P}(t)$  such that  $-\frac{\partial \vec{P}}{\partial t} = \vec{R}_1(t)$ , with  $\vec{R}_1(t)$  defined by [6.57]).

Indeed, we later show that the correct high-frequency limits of the dynamic tortuosities are characterized by equations [6.85a, b] (in geometries having a smooth, non fractal fluid–solid boundary). From them, it can be shown, by generalizing a reasoning given in [AVE 91] Appendix C, that the distributions  $g_{ij}(\sigma)$  and  $\dot{g}(\sigma)$  have to verify definite universal divergent behaviors at  $\sigma \rightarrow 0$ :

$g_{ij}(\sigma) = \frac{1}{\pi} L_{\infty ij}^{-1} \sigma^{-1/2}$ ,  $\dot{g}(\sigma) = \frac{1}{\pi} \dot{L}_{\infty}^{-1} \sigma^{-1/2}$ , where the viscous and thermal parameters  $L_{\infty ij}^{-1}$  and  $\dot{L}_{\infty}^{-1}$ , having dimension of inverse lengths, are by definition the quantities  $L_{\infty ij}^{-1} = \langle |\vec{\nabla} I| \vec{E}^{(i)} \cdot \vec{E}^{(j)} \rangle$  and  $\dot{L}_{\infty}^{-1} = \langle |\vec{\nabla} I| \rangle$ . This leads to a “Curie von Schweidler”  $t^{-1/2}$  decrease at short time for the above  $\vec{P}(t)$ . A modified exponent for the divergence would be involved if we were to replace our locally plane smooth interface with a fractal one.

In the next sections, we will study in detail the low and high frequency regimes from which the above results follow, and we will express the simplest models of the functions  $\alpha_{ij}(\omega)$  and  $\beta(\omega)$ , that are consistent with these behaviors.

#### 6.2.2.11. “Relaxed” and “frozen” limits

The comparison of the characteristic relaxation time scale and the period of the motion defines the regime.

In the “relaxed” limit, the thermal and viscous processes have enough time to develop during a period of the motion. In the “frozen” limit, they do not have enough time for that. The “relaxed” limit corresponds to the low frequencies where

the viscous and thermal boundary layer thicknesses,  $\delta = \left(\frac{2\nu}{\omega}\right)^{1/2}$  and

$\delta' = \left(\frac{2\nu'}{\omega}\right)^{1/2}$ , are “large” compared to the characteristic dimensions of the “pores”

of the material. The “frozen” limit corresponds to the high frequencies where the boundary layer thicknesses are “small” compared to the same dimensions. A transition between the “relaxed” and “frozen” states occurs at intermediate frequencies.

The permeability in Darcy’s law  $k_{0ij} = k_{ij}(\omega = 0)$  and its analog the thermal permeability  $\gamma_0 = \gamma(\omega = 0)$ , are examples of “relaxed” parameters; on the other hand, the tortuosity  $\alpha_{\infty ij} = \lim_{\omega \rightarrow \infty} \alpha_{ij}(\omega)$  is an example of a “frozen” parameter (its thermal analogue  $\lim_{\omega \rightarrow \infty} \gamma(\omega)$  is just equal to 1 and need not be mentioned).

These parameters, being purely real, cannot completely describe the behaviors in the “relaxed” and “frozen” limits, which are complex in nature. We have to introduce some other “relaxed” and “frozen” parameters to describe them completely. The form of the behaviors for the “relaxed” and “frozen” limits can be written *a priori*. They are as follows,

At low frequencies:

$$\alpha_{ij}(\omega) \approx \frac{\nu\phi}{-i\omega} k_{0ij}^{-1} + \alpha_{0ij}, \quad \gamma(\omega) \approx \frac{\nu'\phi}{-i\omega} \gamma_0^{-1} + \gamma_0, \quad [6.84a, b]$$

At high frequencies:

$$\alpha_{ij}^{-1}(\omega) \approx \alpha_{\infty ij}^{-1} - 2\left(\frac{\nu}{-i\omega}\right)^{1/2} L_{\infty ij}^{-1}, \quad \gamma^{-1}(\omega) \approx 1 - 2\left(\frac{\nu'}{-i\omega}\right)^{1/2} L_{\infty}^{-1}. \quad [6.85a, b]$$

Indeed, at low frequencies, we can expect an expansion in power series of  $-i\omega$ . The constants  $\alpha_{0ij}$  and  $\gamma_0$  consequently appear as the first corrections to the leading imaginary terms in  $(-i\omega)^{-1}$ . They will be called the viscous and thermal “relaxed” tortuosities.

At high frequencies, the term correcting the purely inertial–adiabatic behavior comes from the presence of the boundary layers. With a locally plane interface, having no fractal character, an expansion in power series of the thickness of the boundary layer is expected. But the frequency can only be involved with the combinations  $\frac{-i\omega}{\nu}$  and  $\frac{-i\omega}{\nu}$ , respectively. The additional terms in [6.85a, b] result

from these remarks, with “frozen” parameters  $L_{\infty ij}$  and  $\gamma L_{\infty}$  having the dimensions of lengths. For convenience, the expansion is written here for the inverse tortuosity, and a factor of 2 is introduced in the correction term; the characteristic lengths so defined  $L_{\infty ij}$  and  $\gamma L_{\infty}$  will be shown to be those mentioned before ( $L_{\infty ij}^{-1} = \langle |\vec{\nabla} I| \vec{E}^{(i)} \cdot \vec{E}^{(j)} \rangle$  and  $\gamma L_{\infty}^{-1} = \langle |\vec{\nabla} I| \rangle$ ).

#### 6.2.2.12. General model of the relaxation

Function  $g_{ij}(\sigma)$  (which is symmetric and positive) necessarily diagonalizes (with positive eigenvalues) in a system of orthogonal principal axes. In the following, it is very reasonable to assume that there is no “axes dispersion”. This means, the axes of the distribution function  $g_{ij}(\sigma)$  will not depend on  $\sigma$ . The possibility of axes dispersion is known in electrodynamics: the principal axes of a tensor  $\varepsilon_{rij}(\omega)$  may differ for the real and imaginary parts, and depend on the frequency [BOR 02]. It could also be the case here. However, this case generally does not occur due the chaotic nature of the media.

In the absence of axes dispersion, the different tensor mentioned above  $\alpha_{\infty ij}$ ,  $L_{\infty ij}$ ,  $k_{0 ij}$ ,  $\alpha_{0 ij}$ , and the tensor  $\alpha_{ij}(\omega)$  itself, obviously become diagonal in the same principal axes basis (that of  $g_{ij}(\sigma)$ ). In this case, without limiting the generality of the following formulation, we can replace the tensors above by scalars that are, in the case of anisotropy, their eigenvalues along the considered axis.

The simplest analytic functions of  $\omega$ ,  $\alpha(\omega)$  and  $\gamma(\omega)$ , having their singularities on the negative imaginary axis and reproducing the limits mentioned above, will give a very good representation of the relaxation. Indeed, we may expect functions  $g(\sigma)$  and  $\gamma(\sigma)$  to be shaped in the following characteristic generic manner (in “single porosity” materials), and these functions will be almost fixed by the above-mentioned sum rules, and divergences at the origin.

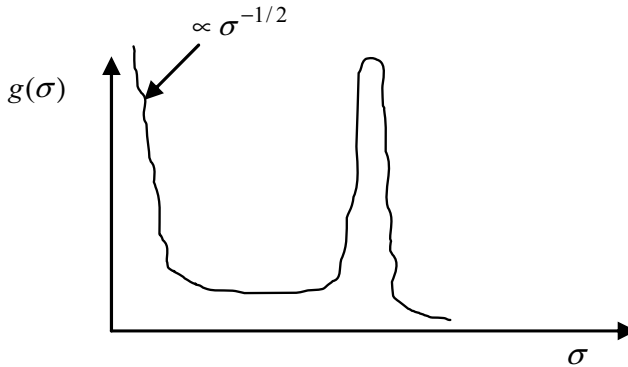


**Figure 6.4.** Typical (approxiamtely symmetric) distributions  $g(\sigma)$  of eigensurfaces  $\sigma$  in "single porosity" materials

An interpretation for the above general shape of the distribution functions is as follows: the first bump (at the origin) is determined by the high-frequency "Curie von Schweidler" behavior, the second bump manifests the presence, in general, of a well defined pore size which is seen at low frequencies. The area under the two bumps will be comparable, so that typical pore size lengths, either constructed from the permeabilities  $k_0$ ,  $\gamma_0$ , or lengths  $L_\infty$ ,  $\gamma_\infty$ , will be comparable.

In the particular special case where the distribution functions take a purely symmetric form represented in Figure 6.5,

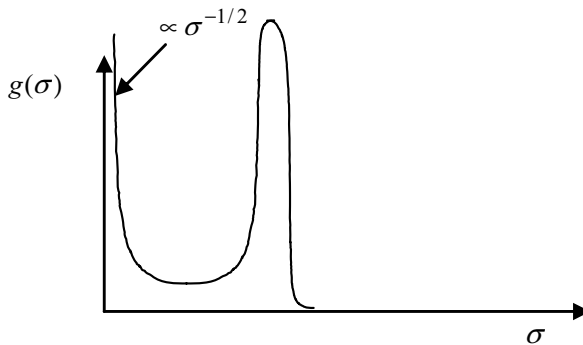


**Figure 6.4.** Typical (approximately symmetric) distributions  $g(\sigma)$  of eigensurfaces  $\sigma$  in "single porosity" materials

i.e.  $g(\sigma) = \frac{1}{\pi\alpha_\infty} \sigma^{-1/2} \left\{ (L_\infty/\alpha_\infty)^2 - \sigma \right\}^{-1/2}$ , for  $0 < \sigma < (L_\infty/\alpha_\infty)^2$ , ( $g(\sigma) = 0$

for  $\sigma \geq (L_\infty/\alpha_\infty)^2$ ), and similarly for  ${}'g(\sigma)$ , we find that the relaxation is

described by a simple “Davidson–Cole” form:  $\lambda_v(\omega) = \frac{\alpha_\infty^{-1}}{\left(1 - \frac{i\omega}{\nu} \sigma_\infty\right)^{1/2}}$ ,

( $\sigma_\infty = (L_\infty/\alpha_\infty)^2$ ), and similarly for  $\lambda_{th}(\omega)$ . Indeed, this “Davidson–Cole” form of relaxation describes in a reasonable manner what is found from a direct calculation of the functions  $\lambda_v(\omega)$  and  $\lambda_{th}(\omega)$  in cylindrical circular pores, based on Zwicker and Kosten’s well-known analytic solutions [ZWI 49]. Actually, the eigensurface distributions will not be exactly symmetric, leading to slightly more complicated relaxational forms. These more complicated relaxational forms may be searched as follows, directly on the functions  $\alpha(\omega)$  and  ${}'\alpha(\omega)$ .

Searching  $\alpha(\omega)$  and  ${}'\alpha(\omega)$  as,

$$\alpha(\omega) = \frac{\nu\phi}{-i\omega k_0} F(\omega) + \alpha_\infty, \quad {}'\alpha(\omega) = \frac{{}'\nu\phi}{-i\omega k_0} {}'F(\omega) + 1, \quad [6.86a, b]$$

limits [6.84] and [6.85] impose that the functions  $F(\omega)$  and  ${}'F(\omega)$  verify the following properties,

for  $\omega \rightarrow 0$ :

$$F \rightarrow 1 + \frac{-i\omega k_0}{\nu \phi} (\alpha_0 - \alpha_\infty), \quad {}'F \rightarrow 1 + \frac{-i\omega k_0}{\nu \phi} ({}'\alpha_0 - 1), \quad [6.87a, b]$$

for  $\omega \rightarrow \infty$ :

$$F \rightarrow 2 \frac{k_0}{\phi} \alpha_\infty \Lambda^{-1} \left( \frac{-i\omega}{\nu} \right)^{1/2}, \quad {}'F \rightarrow \frac{{}'k_0}{\phi} \frac{2}{{}'\Lambda} \left( \frac{-i\omega}{{}'\nu} \right)^{1/2}, \quad [6.88a, b]$$

where we have introduced the new notations  $\Lambda = L_\infty / \alpha_\infty$ ,  ${}'\Lambda = {}'L_\infty$  (the so-called viscous and thermal characteristic lengths). The following functions are the simplest admissible ones leading to these behaviors,

$$F(\omega) = 1 - p + p \left\{ 1 + \frac{2k_0}{p\phi} (\alpha_0 - \alpha_\infty) \frac{-i\omega}{\nu} \right\}^{1/2}, \quad [6.89a]$$

$$\text{'}F(\omega) = 1 - \text{'}p + \text{'}p \left\{ 1 + \frac{2\text{'}k_0}{\text{'}p\phi} (\text{'}\alpha_0 - 1) \frac{-i\omega}{\text{'}\nu} \right\}^{1/2}, \quad [6.89b]$$

with

$$p = \frac{\frac{2k_0\alpha_\infty^2}{\phi\Lambda^2}}{\alpha_0 - \alpha_\infty}, \quad \text{'}p = \frac{\frac{2\text{'}k_0}{\phi\text{'}\Lambda^2}}{\text{'}\alpha_0 - 1}. \quad [6.90a, b]$$

Therefore, the simplest complete general model for the two functions  $\alpha(\omega)$  and  $\text{'}\alpha(\omega)$  is,

$$\alpha(\omega) = \frac{\nu}{-i\omega} \frac{\phi}{k_0} \left[ 1 - p + p \left\{ 1 + \frac{2k_0}{p\phi} (\alpha_0 - \alpha_\infty) \frac{-i\omega}{\nu} \right\}^{1/2} \right] + \alpha_\infty, \quad [6.91a]$$

$$\text{'}\alpha(\omega) = \frac{\text{'}\nu}{-i\omega} \frac{\phi}{\text{'}k_0} \left[ 1 - \text{'}p + \text{'}p \left\{ 1 + \frac{2\text{'}k_0}{\text{'}p\phi} (\text{'}\alpha_0 - 1) \frac{-i\omega}{\text{'}\nu} \right\}^{1/2} \right] + 1, \quad [6.91b]$$

with the dimensionless form factors  $p$  and  $\text{'}p$  defined by [6.90a, b].

In the presence of axes dispersion, the above construction generalizes in a straightforward manner. The simplest general model for the tensor  $\alpha(\omega)$  will be obtained with parameters  $k_0$ ,  $\alpha_0$ ,  $\alpha_\infty$ ,  $L_\infty$ , becoming second order symmetric tensors, having in general different axes, and [6.91a] is now to be written as ( $I$  is the unit tensor  $I_{ij} = \delta_{ij}$ ),

$$\alpha(\omega) = \frac{\nu\phi}{-i\omega} k_0^{-1} \left[ I - p + p \left\{ I + p^{-1} \frac{2k_0}{\phi} (\alpha_0 - \alpha_\infty) \frac{-i\omega}{\nu} \right\}^{1/2} \right] + \alpha_\infty,$$



with, *a priori*, non-symmetric adimensional ( $3 \times 3$ ) matrix of coefficients  $p$  to be determined by solving the following ( $3 \times 3$ ) condition, imposed by the HF limit:

$$\left\{ p^{-1} \frac{2k_0}{\phi} (\alpha_0 - \alpha_\infty) \right\}^{1/2} = p^{-1} \frac{2k_0}{\phi} \alpha_\infty L_\infty^{-1} \alpha_\infty .$$

#### 6.2.2.13. “Relaxed” parameters

Additional details are given here on the meaning of the “relaxed” parameters  $k_0$ ,  $\alpha_0$ , (for simplicity, isotropy is assumed here), and  $\bar{k}_0$ ,  $\bar{\alpha}_0$ .

Let us denote  $\vec{w}_0$  and  $\bar{w}_0$  the canonical relaxed fields, defining the relaxed velocity and excess temperature patterns established in the pores:

$$-\Delta \vec{w}_0 = -\vec{\nabla} \pi_0 + \vec{e}, \text{ in } \Omega_f, \quad -\Delta \bar{w}_0 = 1, \text{ in } \Omega_f, \quad [6.92a, b]$$

$$\vec{\nabla} \cdot \vec{w}_0 = 0, \text{ in } \Omega_f, \quad [6.93]$$

$$\vec{w}_0 = \vec{0}, \text{ on } \partial\Omega, \quad \bar{w}_0 = 0, \text{ on } \partial\Omega. \quad [6.94a, b]$$

$$\pi_0 \text{ stationary.} \quad [6.95]$$

We can have the following identifications of the “relaxed” parameters:

$$k_0 / \phi = \langle \vec{w}_0 \rangle \cdot \vec{e}, \quad \bar{k}_0 / \phi = \langle \bar{w}_0 \rangle, \quad [6.96a, b]$$

$$\alpha_0 = \frac{\langle \vec{w}_0^2 \rangle}{\langle \vec{w}_0 \rangle^2}, \quad \bar{\alpha}_0 = \frac{\langle \bar{w}_0^2 \rangle}{\langle \bar{w}_0 \rangle^2}. \quad [6.97a, b]$$

Equations [6.96] are equations [6.73] written for  $\omega = 0$ . The Darcy permeability  $k_0$  is a well known parameter. Notice that we can also write the expressions of the permeabilities in this way:

$$k_0 = \phi \frac{\langle \vec{w}_0 \rangle^2}{-\langle \vec{w}_0 \cdot \Delta \vec{w}_0 \rangle}, \quad \bar{k}_0 = \phi \frac{\langle \bar{w}_0 \rangle^2}{-\langle \bar{w}_0 \cdot \Delta \bar{w}_0 \rangle}. \quad [6.98a, b]$$

Relaxed fields patterns are precisely those that minimize the expressions above, expressing a principle of minimum dissipation.

In general, the definition of thermal permeability  $\gamma k_0$  shows that it is directly related to the “trapping constant”  $\Gamma$  of the porous network. This constant is defined in the following manner. Inside the fluid which saturates the structure, species are created equally in terms of volume, with a spatial density  $s$ . Species diffuse with a diffusion coefficient  $D$ , and are instantly absorbed on contact with the solid walls. Absorption being instantaneous on the walls, the concentration pattern of the species that appears is entirely controlled by the diffusion. The equations governing this “diffusion-controlled” process are,

$$\frac{\partial u}{\partial t} - D\Delta u = s, \text{ in } \Omega_f, \quad [6.99]$$

$$u = 0, \text{ on } \partial\Omega, \quad [6.100]$$

with  $u$  the concentration of species per unit of volume of the saturating fluid. At equilibrium,  $\partial u / \partial t = 0$ , and the trapping constant is defined as,

$$\Gamma = s / (< u > \phi D). \quad [6.101]$$

This purely geometric constant has the dimension of the inverse of a surface. It is related to the *mean survival time*  $\theta = < u > / s$  of the considered species, by the relationship,

$$\theta = 1 / \Gamma \phi D. \quad [6.102]$$

Comparing equations [6.99–100] and [6.92b–2.94b] shows that the relation  $\gamma w_0 = Du / s$  is satisfied (at equilibrium), and, therefore, that the thermal permeability  $k'_0$  coincides with the inverse of the trapping constant  $\Gamma$ :

$$\gamma k_0 = 1 / \Gamma \quad [6.103]$$

We can show that the thermal permeability is strictly related to the viscous permeability, with the relation [TOR 90],

$$\gamma k_0 \geq k_0. \quad [6.104]$$

The equality is reached for a material composed of pores that are exactly aligned. In this case there is no difference between the viscous and thermal problems. In the case of a material with a porosity  $\phi$ , made of exactly aligned pores of radius  $R$ , and taking into account the parabolic profile of Poiseuille, we obtain,

$$k_0 = \gamma_0 = \phi \frac{R^2}{8} \quad [6.105]$$

A ratio 2-3 for  $\gamma_0 / k_0$  can often be observed, in the case of polyurethane foams or fibrous materials.

Equations [6.97a, b] show that the factors  $\alpha_0$  and  $\gamma_0$  are calculated like the tortuosity factor  $\alpha_\infty$  (see [6.44]), considering that the relaxed fields  $\vec{w}_0$  and  $\gamma_0$  replace the frozen field  $\vec{E}$ . They are indicators of the “disorder” that exists in the distribution of the relaxed fields, and verify

$$\alpha_0 > \alpha_\infty, \gamma_0 > 1. \quad [6.106]$$

The first is because only the perfect fluid can minimize the inertial effects of added mass. Also, we should expect that  $\alpha_0 / \alpha_\infty \geq \gamma_0$ , given the vectorial nature of the inertial-viscous problem which brings additional complications in the fields, not present in the scalar thermal case. The equality  $\alpha_0 = \gamma_0$  is obtained for a material composed of exactly aligned pores, as there is, in this case, no difference between the viscous and thermal problems. For organized circular pores, the substitution of the parabolic profile of Poiseuille yields  $\alpha_0 = \gamma_0 = 4/3$ .

Identifications [6.97a, b] can be obtained, for example, with the following method. At low frequencies, the solutions of the canonical problems (section 6.2.2.5) can be written as expansions,

$$\vec{w} = \vec{w}_0 + \frac{-i\omega}{\nu} \vec{w}_1 + \left(\frac{-i\omega}{\nu}\right)^2 \vec{w}_2 + \dots, \quad [6.107a]$$

$$\pi = \pi_0 + \frac{-i\omega}{\nu} \pi_1 + \left(\frac{-i\omega}{\nu}\right)^2 \pi_2 + \dots,$$

$$\gamma_w = \gamma_0 + \frac{-i\omega}{\nu} \gamma_1 + \left(\frac{-i\omega}{\nu}\right)^2 \gamma_2 + \dots. \quad [6.107b]$$

Reporting these expansions and identifying the different terms having the same power in frequency leads to equations [6.92–95] for  $\vec{w}_0$  and  $\gamma_0$  for order 0. For the next orders ( $i = 1, 2, \dots$ ), successive identifications give the following equations for  $\vec{w}_i$  and  $\gamma_i$ :

$$\Delta \vec{w}_i = \vec{\nabla} \pi_i + \vec{w}_{i-1}, \text{ in } \Omega_f, \quad \Delta w_i = w_{i-1}, \text{ in } \Omega_f, \quad [6.108a, b]$$

$$\vec{\nabla} \cdot \vec{w}_i = 0, \text{ in } \Omega_f, \quad [6.109]$$

$$\vec{w}_i = \vec{0}, \text{ on } \partial\Omega, \quad w_i = 0, \text{ on } \partial\Omega. \quad [6.110a, b]$$

$$\pi_i \text{ stationary.} \quad [6.111]$$

Limiting the expansions to the first order,  $\vec{w} = \vec{w}_0 + \frac{-i\omega}{\nu} \vec{w}_1$ , and

$w = w_0 + \frac{-i\omega}{\nu} w_1$ , in [6.73a, b], the following limits are obtained:

$$\frac{k(\omega)}{\phi} = \bar{w}_0 > \bar{e} + \frac{-i\omega}{\nu} < \bar{w}_1 > \bar{e}, \quad \frac{k'(\omega)}{\phi} = w_0 > + \frac{-i\omega}{\nu} < w_1 >. \quad [6.112a, b]$$

However, we also have,

$$< \bar{w}_1 > \bar{e} = \bar{w}_0^2, \quad < w_1 > = w_0^2. \quad [6.113a, b]$$

The proof of [6.113a], also easily transposable to [6.113b], may be found in [NOR 86] Appendix B. Finally, comparing [6.112–113] with the following expansions, which can be derived from [6.62b], [6.84a] and [6.65b], [6.84b],

$$\frac{k(\omega)}{\phi} = \frac{k_0}{\phi} + \frac{-i\omega}{\nu} \left(\frac{k_0}{\phi}\right)^2 \alpha_0, \quad \frac{k(\omega)}{\phi} = \frac{k_0}{\phi} + \frac{-i\omega}{\nu} \left(\frac{k_0}{\phi}\right)^2 \alpha_0, \quad [6.114a, b]$$

we can express the quantities  $\alpha_0$  and  $\alpha_0$  as given in [6.97].

#### 6.2.2.14. “Frozen” parameters

We explain here the meaning of the frozen parameters  $\Lambda = L_\infty / \alpha_\infty$  (with isotropy assumed for simplicity) and  $\Lambda = L_\infty$ . At high frequencies, the inertial and adiabatic terms  $\frac{-i\omega}{\nu} \vec{w}$  and  $\frac{-i\omega}{\nu} w$  are much more important than the viscous and thermal exchange terms  $\Delta \vec{w}$  and  $\Delta w$  in equations [6.67a, b].

The “frozen” fields  $\vec{w}$ ,  $\pi$ , and  $\nabla w$ , which result from the suppression of the viscous and thermal effects, are  $\vec{w} \approx \frac{\nu}{-i\omega} \vec{E}$ ,  $\pi \approx \Phi$ , and  $\nabla w \approx \frac{\nu}{-i\omega} I$ .

These fields, substituted in the averages  $\phi < \vec{w} \cdot \vec{E} >$  and  $\phi < \nabla w >$ , lead to the following dominant behaviors – purely inertial and adiabatic – of the permeabilities, at high frequencies:

$$k(\omega) \approx \frac{\nu\phi}{-i\omega} < \vec{E} \cdot \vec{E} > = \frac{\nu\phi}{-i\omega} \alpha_{\infty}^{-1}, \quad \gamma k(\omega) \approx \frac{\nu\phi}{-i\omega} < I > = \frac{\nu\phi}{-i\omega} \quad [6.115a, b]$$

However, the fields  $\vec{w}$ ,  $\pi$ , and  $\nabla w$ , expressed above do not verify the no-slip boundary condition and zero excess temperature boundary condition at the pore walls. These conditions can be fulfilled only because of the presence of thin viscous and thermal boundary layers. At high frequencies, we can assume that the corresponding boundary layers correspond to those above a plane interface. With  $\zeta$  being the normal coordinate to the walls, we have to add to the inertial–adiabatic fields the additional terms,

$$\delta \vec{w} = -\frac{\nu}{-i\omega} e^{-\zeta \sqrt{\frac{\nu}{-i\omega}}} \vec{E}, \quad \delta \nabla w = -\frac{\nu}{-i\omega} e^{-\zeta \sqrt{\frac{\nu}{-i\omega}}} I \quad [6.116a, b]$$

which are constructed and supposed to vanish in the volume in same manner as above a plane interface.

These additional viscous–thermal parts introduced in the means  $\phi < \vec{w} \cdot \vec{E} >$  and  $\phi < \nabla w >$  can easily be integrated with the formal replacement  $\langle \rangle = \int f(\vec{x} - \vec{r}) dS \int_0^{\infty} d\zeta$ . The sum of the adiabatic–inertial and viscous–thermal contributions gives the following asymptotic behavior for the permeabilities at high frequencies:

$$k_{ij}(\omega) \approx \frac{\nu\phi}{-i\omega} \alpha_{\infty}^{-1} \left\{ 1 - 2 \left( \frac{\nu}{-i\omega} \right)^{1/2} \Lambda^{-1} \right\}, \quad \gamma k(\omega) \approx \frac{\nu\phi}{-i\omega} \left\{ 1 - \left( \frac{\nu}{-i\omega} \right)^{1/2} \frac{2}{\Lambda} \right\}$$

[6.117a, b]

with

$$\begin{aligned} 2\alpha_\infty^{-1}\Lambda^{-1} &= \int f(\vec{x} - \vec{r}) \vec{E}(\vec{x}) \cdot \vec{E}(\vec{x}) dS, \quad \frac{2}{\Lambda'} = \int f(\vec{x} - \vec{r}) dS \\ &= \langle |\vec{\nabla} I| \vec{E} \cdot \vec{E} \rangle, \quad = \langle |\vec{\nabla} I| \rangle, \end{aligned} \quad [6.118a, b]$$

having the dimension of inverse lengths.

The meaning of the characteristic viscous and thermal lengths  $\Lambda$  and  $\Lambda'$  shall be more transparent discarding the presence of the test function:

$$\frac{2}{\Lambda} = \frac{\int_{\partial\Omega} \vec{E}^2 dS}{\int_{\Omega_f} \vec{E}^2 dV}, \quad \frac{2}{\Lambda'} = \frac{\int_{\partial\Omega} dS}{\int_{\Omega_f} dV}. \quad [6.119a, b]$$

These lengths appear respectively as the electrically-weighted, or direct (not weighted), pore-volume-to-surface ratios. The factor 2 is introduced to ensure that they are equal to the hydraulic radius of the pores in the case of a material formed by a set of straight cylindrical pores, aligned or not (but not intersecting). In a non-trivial geometry, the square of the electric field will always tend to be greater at the surface of the pores than in the volume:  $\int_{\partial\Omega} \vec{E}^2 dS / \int_{\partial\Omega} dS \geq \int_{\Omega_f} \vec{E}^2 dV / \int_{\Omega_f} dV$ . A consequence is that we will always have  $\Lambda \leq \Lambda'$ . A ratio of 2 or 3 can often be supposed between the two characteristic lengths.

The limit [6.117a] and the expression of the characteristic length [6.119a] have been given by Johnson *et al.* [JOH 87]. Notice that there is a subtlety in the derivation, given above, of this expression. Indeed, we carefully substituted the viscous profile [6.116a] in the averaging operation  $\phi < \vec{w} \cdot \vec{E} >$ , and not in the (in principle equivalent) averaging operation  $\phi < \vec{w} \cdot \vec{e} >$ : this last substitution would lead to an incorrect result. This is because the presence of the viscous boundary layer at the pore walls changes the boundary conditions applicable to the potential flow appearing in the bulk. Due to this, the bulk potential flow is not totally described by the dominant term  $\frac{V}{-i\omega} \vec{E}$ , but also includes a small orthogonal

perturbation  $\vec{\nabla} \Pi$ . Like every “perturbation”, it is orthogonal to the “ground state”  $\vec{E}$ , ( $\langle \vec{E} \cdot \vec{\nabla} \Pi \rangle = 0$  is obviously verified here, since  $\Pi$  is stationary). It means we do not need to bother with this perturbation when evaluating the permeability from the average  $\phi < \vec{w} \cdot \vec{E} >$ . However, we should take it into account when using the

average  $\phi < \vec{w} \cdot \vec{e} >$  instead. (This point is a source of recurrent errors in the literature. It is definitively clarified in [COR 03]).

Limit [6.117b] (written for  $\beta(\omega)$ ) and expression of the thermal characteristic length [6.119b]) have been given by Allard and Champoux [CHA 91].

#### 6.2.2.15. *Conditions of continuity*

As in macroscopic electrodynamics, to determine the behavior of a medium immersed in an external field, we have to know the equations that govern the fields in the medium on one hand, and the equations of continuity through the interface of the material on the other.

Once again, it is interesting to emphasize the similarity of the physical position of both problems. Consider first the macroscopic electrodynamics. The equations are written in a comparable form in the vacuum and in the material. In the vacuum, the electric field  $\vec{e}$  and the magnetic induction field  $\vec{h} = \vec{b} / \mu_0$  are involved, whereas, in the material, we see the electric field  $\vec{E} = < \vec{e} >$  and the magnetic induction field  $\vec{H} = < \vec{b} > / \mu_0 \mu_r(\omega)$ . Therefore,

In a vacuum:

$$\epsilon_0 \frac{\partial \vec{e}}{\partial t} = \vec{\nabla} \times \vec{h}, \quad \mu_0 \frac{\partial \vec{h}}{\partial t} = -\vec{\nabla} \times \vec{e}, \quad [6.120]$$

In the material:

$$\epsilon_0 \epsilon_r(\omega) \frac{\partial \vec{E}}{\partial t} = \vec{\nabla} \times \vec{H}, \quad \mu_0 \mu_r(\omega) \frac{\partial \vec{H}}{\partial t} = -\vec{\nabla} \times \vec{E}. \quad [6.121]$$

Through the interface vacuum–material, the tangential components of the electric and magnetic induction fields are continuous. The vector giving the flow of energy in a vacuum is the Poynting vector  $\vec{s} = \vec{e} \times \vec{h}$ . In the material, the flow of energy is given by the same expression,  $\vec{S} = \vec{E} \times \vec{H}$ : because of the continuity of the tangential components of  $\vec{E}$  and  $\vec{H}$ , this expression derives uniquely from the continuity condition of the normal component of  $\vec{S}$  on the surface of the material, and from the fact that this expression is also true in the vacuum, outside the medium. The character of generalized susceptibilities of the tensors  $\epsilon(\omega)$  and  $\mu(\omega)$  derives directly from this [LAN 80], [LAN 84].

In the acoustic problem, we can introduce the “*condensation*” field  $b_1 = \rho_1 / \rho_0$ . The pressure  $p_1 = b_1 / \chi_0$ ,  $\langle p_1 \rangle = \langle b_1 \rangle / \chi_0 \beta(\omega)$ , has the same roles as the fields  $\vec{h}$  and  $\vec{H}$ . Therefore,

free fluid:

$$\rho_0 \frac{\partial \vec{v}_1}{\partial t} = -\vec{\nabla} p_1, \quad \chi_0 \frac{\partial p_1}{\partial t} = -\vec{\nabla} \cdot \vec{v}_1 \quad [6.122]$$

material:

$$\rho_0 \alpha(\omega) \frac{\partial \langle \vec{v}_1 \rangle}{\partial t} = -\vec{\nabla} \langle p_1 \rangle, \quad \chi_0 \beta(\omega) \frac{\partial \langle p_1 \rangle}{\partial t} = -\vec{\nabla} \cdot \langle \vec{v}_1 \rangle \quad [6.123]$$

Until now, we have only used the concept of a “fluid phase” normalization for the averaging symbol  $\langle \rangle$ . Here, it is interesting to use both the “fluid phase” and “total volume” normalization conceptions and to define the macroscopic pressure and velocity fields as,

$$P_1 = \langle p_1 \rangle_{\text{fluid phase}}, \quad [6.124]$$

$$\vec{V}_1 = \langle \vec{v}_1 \rangle_{\text{total vol}} = \phi \langle \vec{v}_1 \rangle_{\text{fluid phase}}. \quad [6.125]$$

In doing this, the classical continuity conditions (continuity of the normal actions and continuity of the normal flow) are simply expressed by the *continuity of the pressure field*, and the *continuity of the normal component of the velocity* on the interface between the free fluid and the material.

The continuity of the pressure field is a direct consequence of the simplification, made in section 6.2.2.3, that there are local action–response laws. As we have seen, this simplification is to assume the “incompressibility” of the fluid motion, and this in turn is expressed by the splitting  $p = \langle p \rangle + \Pi$ , with  $\Pi \ll \langle p \rangle$ , leading to the mentioned continuity.

If the material is “leaning” on an immobile solid surface, there is on this surface no condition on the pressure, and there is only one remaining boundary condition: the vanishing of the normal component of the velocity  $\vec{V}_1$ .

With definitions [6.124–5], equations [6.123] become,



$$\rho_0 \frac{\alpha(\omega)}{\phi} \frac{\partial \vec{V}_1}{\partial t} = -\vec{\nabla} P_1, \quad \chi_0 \beta(\omega) \phi \frac{\partial P_1}{\partial t} = -\vec{\nabla} \cdot \vec{V}_1. \quad [6.126]$$

The vector describing the flow of energy in the free fluid is the vector  $\vec{s}_1 = p_1 \vec{v}_1$ . In the material, the flow of energy associated with the wave propagation is given by the same expression,  $\vec{S} = P_1 \vec{V}_1$ : because of the continuity of  $P_1$  and the normal component of  $\vec{V}_1$ , this expression derives uniquely from the continuity condition of the normal component of  $\vec{S}$  on the surface of the medium, and from the fact that this expression is also true in the fluid, outside the medium. The character of generalized susceptibilities of the factors  $\alpha(\omega)/\phi$  and  $\beta(\omega)\phi$ , having exactly the same role as  $\epsilon_r(\omega)$  and  $\mu_r(\omega)$ , is derived directly. In particular, the tensor  $\alpha(\omega)$  is symmetric. This was checked before.

#### 6.2.2.16. Propagation constant and characteristic impedance

Knowing the two “susceptibilities” of the medium  $\alpha(\omega)/\phi$  and  $\beta(\omega)\phi$ , we can determine the characteristics of the propagation in this medium fully. Assuming a plane wave solution  $\exp(i\omega t - i\vec{k}(\omega) \cdot \vec{x})$  of equations [6.126], we find the following relationships between the velocity and pressure complex amplitudes:

$$\omega \rho_0 \frac{\alpha(\omega)}{\phi} \vec{V}_1 = \vec{k}(\omega) P_1, \quad [6.127]$$

$$\omega \chi_0 \phi \beta(\omega) P_1 = \vec{k}(\omega) \cdot \vec{V}_1. \quad [6.128]$$

Substituting in [6.128] the expression of  $\vec{V}_1$  obtained from [6.127], the propagation constant  $q(\omega)$ , such that  $q^2(\omega) = \vec{k}^2(\omega)$ , can be determined as:

$$q(\omega) = \frac{\omega}{c_0} \sqrt{\alpha(\omega) \beta(\omega)}. \quad [6.129]$$

Using [6.127] and [6.129] we can obtain  $P_1^2 = \frac{\rho_0^2 c_0^2}{\phi^2} \frac{\alpha(\omega)}{\beta(\omega)} \vec{V}_1^2$ . In the case of a one-dimensional motion along the  $x$ -axis ( $\vec{k} = q\hat{x}$ ), the relation above gives  $P_1 = Z_c(\omega) V_{1x}$ , where  $Z_c(\omega)$  is the characteristic impedance defined as follows:

$$Z_c(\omega) = \frac{\rho_0 c_0}{\phi} \sqrt{\frac{\alpha(\omega)}{\beta(\omega)}}. \quad [6.130]$$

The characteristics of the propagation  $q(\omega)$  and  $Z_c(\omega)$  are determined by the product and the ratio of the functions  $\alpha(\omega)$  and  $\beta(\omega)$ .

#### 6.2.2.17. Simplified models

In practice, it is difficult to know or to evaluate all the parameters involved in the general models for the functions  $\alpha(\omega)$  and  $\alpha'(\omega)$  introduced above. Simplified descriptions are useful because of the inhomogeneities of the materials, making the use of over elaborated models illusory. Moreover, the function  $\alpha'(\omega)$  is not directly involved in the characteristics  $q(\omega)$  and  $Z_c(\omega)$  of the propagation, we should use the function  $\beta(\omega)$  instead.

At low frequencies the most important parameters are  $\phi$ ,  $k_0$ , followed by the parameters  $\alpha_0$ ,  $\gamma k_0$ . Actually, if only the two first terms of the expansions in powers of  $-i\omega$  are kept, we can see that,

$$\frac{\alpha(\omega)}{\phi} \approx \frac{\nu}{-i\omega} k_0^{-1} + \frac{\alpha_0}{\phi}, \quad \phi\beta(\omega) \approx \phi\gamma - (\gamma-1) \frac{-i\omega}{\nu} k_0. \quad [6.131]$$

Parameters  $\alpha_\infty$  and  $\gamma k_0$  do not appear here.

At high frequencies,  $\phi$ ,  $\alpha_\infty$ , are the most important parameters, followed by  $\Lambda$  and  $\gamma\Lambda$ :

$$\frac{\alpha(\omega)}{\phi} \approx \frac{\alpha_\infty}{\phi} \left\{ 1 + \left( \frac{\nu}{-i\omega} \right)^{1/2} \frac{2}{\Lambda} \right\}, \quad \phi\beta(\omega) \approx \phi + \phi(\gamma-1) \left( \frac{\nu}{-i\omega} \right)^{1/2} \frac{2}{\gamma\Lambda}. \quad [6.132]$$

In the intermediate domain, it may also be useful to use more basic forms of the relaxation than expressed by the complete expressions in [6.91a, b], e.g. those given in [WIL 97] which are nothing but Davidson–Cole forms, and may provide a sufficiently accurate modeling. Another simplification, which is often made, consists of writing  $p = \gamma p = 1$  in [6.91a, b] and setting, because of [6.90a, b],

$$\alpha_0 - \alpha_\infty = \frac{2k_0\alpha_\infty^2}{\phi\Lambda^2}, \quad \gamma k_0 - 1 = \frac{2\gamma k_0}{\phi\gamma\Lambda^2}. \quad \text{This leads to the model developed by Johnson}$$

*et al.* [JOH 87], which is generally sufficiently accurate in the whole frequency range, because the factors  $p$  and  $\bar{p}$  often tend to have values comparable to unity.

In fact, there must be some correlation between the values of the various parameters for some particular kinds of micro-geometries. Delany and Bazley [DEL 70] have found the following empirical expressions (derived by averaging many measurements on fibrous materials, with a porosity close to 1):

$$q(\omega) = \frac{\omega}{c_0} \left[ 1 + 0.0978X^{-0.700} - i0.189X^{-0.595} \right], \quad [6.133]$$

$$\phi Z_c(\omega) = \rho_0 c_0 \left[ 1 + 0.0571X^{-0.754} - i0.087X^{-0.732} \right], \quad [6.134]$$

with  $X = \rho_0 f / \sigma$ ,  $\omega = 2\pi f$ ,  $\sigma = \eta / k_0$ . These very useful expressions only depend on the permeability, and are found applicable for  $0.01 < X < 1.0$ . We cannot hope that these expressions describe the behavior of all materials that we can meet in practice precisely, but they often give an order of magnitude that is enough, and is useful in applications. Other modified versions of these laws have also been proposed [MEC 76]. They are consistent with the idea of a correlation of the values of the parameters  $\phi, \alpha_\infty, \Lambda, \bar{\Lambda}, k_0, \bar{k}_0, \alpha_0, \bar{\alpha}_0$ , producing the above form factors  $p$  and  $\bar{p}$  around the value 0.5, and the form factors  $M = 8\alpha_\infty k_0 / \Lambda^2 \phi$  and  $\bar{M} = 8\bar{k}_0 / \bar{\Lambda}^2 \bar{\phi}$  considered in [JOH 87] and [LAF 97], around the value 0.8, in many geometries.

#### 6.2.2.18. Limitations of the incompressibility condition

We now examine the central hypothesis, expressing that the fluid motion is incompressible at the microscopic scale.

We have seen in section 6.2.1.12 that the presence of structures like “Helmholtz resonators” could permit the fluid to not to obey the condition of incompressibility. But in the presence of viscous losses, the small neck openings of the resonators oppose the passage of the fluid. To ensure that the effects of viscous resistance do not hide the resonances of the resonators, the dimension of the neck openings has to be large enough, compared to the thickness of the boundary layers at the resonance,

which is  $\delta = \left( \frac{2\nu a}{c_0 \mathcal{E}} \right)^{1/2}$ , with  $\omega \approx \frac{c_0 \mathcal{E}}{a}$  an estimate of the Helmholtz resonance frequency. Therefore, let us write, to fix some ideas, that we have  $\varepsilon a \geq 10\delta$ . This

yields the condition  $a \geq 200 \frac{V}{c_0 \varepsilon^3}$ . If  $\varepsilon$  is chosen equal to 0.1, we obtain (for air-saturated material) a dimension  $a$  of at least a centimeter.

Thus, it is expected that the incompressibility condition can be inadequate in a multi-scale porous material including Helmholtz resonating cavities with centimetric dimensions. Such large mesostructures are generally not present in the porous media studied for the absorption of sound – and that is why it has not been necessary so far to incorporate the effects of spatial dispersion in the models.

However, the considerations above suggest that it should be possible to observe these effects in adequately constructed media. Moreover, viscous friction will not always be an adverse effect on divergent flow motions of pores and large volume of cavities in series. We assume that the cavities are so large that they have negligible resistance to fluid flow. During passage of a long-wavelength acoustic wave, the flow will be almost incompressible in the former small resistive volume (almost linear pressure variation and constant mean velocity along one pore) and almost entirely compressible in the latter large compliant volume (almost linear velocity variation and constant pressure along one cavity).

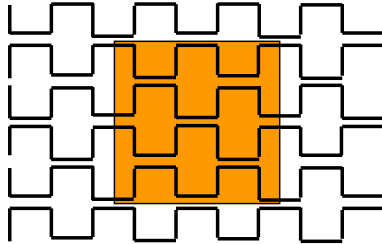


**Figure 6.6.** 2D example of a geometry that can illustrate the limitations of the condition of incompressibility

In such case, if (as is represented on Figure 6.6) the connecting pores are of two different natures, the transported flow currents are also different, and mass is either added or subtracted at one given instant in one cavity. In one period there is of course no global exchange, but at every intermediate instant there is a non-zero exchange. Obviously, to describe this exchange, we have to relax the usual simplification that the fluid flow appears divergenceless at the pore scale. Once again, a wide distribution of pore sizes is required to manifest this limitation of the condition of incompressibility and this is why it was not necessary so far to incorporate the effects of spatial dispersion in the models when dealing with

ordinary porous materials used in noise control (such as polyurethane foams with open cells). But when dealing with porous rocks for example, in which networks of pores and cracks can be found playing the role of the above cavities, the above limitations of the incompressibility condition principle should be borne in mind.

#### 6.2.2.19. Most general form of the macroscopic theory.

In the materials that do not verify the condition of incompressibility, the action-response laws seen in section 6.2.2.3 should be generalized to non-local, non-instantaneous relations, e.g.

$$\begin{aligned} R_{1i}(\vec{r}, t) &\equiv \int_{\partial\Omega} f(\vec{x} - \vec{r}) n_k(\vec{x}) \{-p_1(\vec{x}, t) \delta_{ik} + \sigma'_{1ik}(\vec{x}, t)\} dS \\ &= -\rho_0 \int_0^\infty \int \chi_{ij}(\vec{r}, \vec{r}'; t') \frac{\partial < v_{1j} >(\vec{r}', t - t')}{\partial t} dV' dt', \end{aligned} \quad [6.135]$$

and

$$\begin{aligned} Q_1(\vec{r}, t) &\equiv \kappa \int_{\partial\Omega} f(\vec{x} - \vec{r}) \vec{n}(\vec{x}) \cdot \vec{\nabla} \tau_1(\vec{x}) dS \\ &= -\rho_0 C_p \int_0^\infty \int \chi(\vec{r}, \vec{r}'; t') \frac{\partial < \tau_1 >(\vec{r}', t - t')}{\partial t} dV' dt'. \end{aligned} \quad [6.136]$$

The difficulty of constructing the macroscopic theory is reported to the construction of the kernels  $\chi_{ij}(\vec{r}, \vec{r}'; t')$  and  $\chi(\vec{r}, \vec{r}'; t')$ . It supposes a resolution for large wavelengths of the system of coupled equations [6.3–6], where all the characteristics of the fluid are effectively present.

In fact, without demonstration here, it turns out that the most natural new expression for the reaction  $R_{1i}$ , consistent with assumption (ii) given in the introduction, will be the sum of two non-local terms constructed using both forms [6.16] and [6.17], with the resulting indeterminacy appearing in  $\chi_{ij}(\vec{r}, \vec{r}'; t')$  and  $\lambda_{ij}(\vec{r}, \vec{r}'; t')$  being exploited to diagonalize this latter:

$$\begin{aligned} R_{1i}(\vec{r}, t) &= -\rho_0 \int_0^\infty \int \chi_{ij}(\vec{r}, \vec{r}'; t') \frac{\partial < v_{1j} >(\vec{r}', t - t')}{\partial t} dV' dt' \\ &\quad + \frac{1}{\chi_0} \int_0^\infty \int \lambda(\vec{r}, \vec{r}'; t') \nabla_i < b_1 >(\vec{r}', t) dV' dt', \end{aligned}$$

with  $b_1$  the condensation ( $\partial b_1 / \partial t \equiv -\nabla \cdot v_1$ ).

We will not consider this problem further here, it has not been addressed as such in literature until now, as far as we know. Its solution is the subject of recent and ongoing work [LAF 08], making the affinity of the new description with the general Maxwellian non-local macroscopic electrodynamics apparent. Let us just mention here that the general solution will lead (in unbounded homogenous medium) to equivalent fluid equations of the same type as above (equations [6.78–79]):

$$\rho_0 \alpha_{ij}(\omega, \mathbf{k}) \frac{\partial \langle \vec{v}_1 \rangle_j}{\partial t} = -\vec{\nabla}_i H_1,$$

$$\chi_0 \beta(\omega, \mathbf{k}) \frac{\partial H_1}{\partial t} = -\vec{\nabla} \cdot \langle \vec{v}_1 \rangle,$$

except that, in addition to making the formal replacement,  $\partial / \partial t \rightarrow -i\omega$ , we now also have to make,  $\vec{\nabla} \rightarrow i\mathbf{k}$ , consider susceptibility functions of both  $\omega$  and wavenumber  $\mathbf{k}$ , and replace the mean pressure by an abstract new “Maxwell” field  $H_1$ . This may be taken as an illustration of one comment made in the introduction, namely, that the general form of equations is often preserved, while introducing the particulars of the medium in the constitutive functions.

### 6.3. Bibliography

- [AUR 80] Auriault J.L., “Dynamic behavior of a porous medium saturated by a Newtonian fluid”, *Int. J. Eng. Sci.*, 18, 775, 1980
- [AUR 85] Auriault J.L., Borne L., Chambon R., “Dynamics of porous saturated media, checking of the generalized law of Darcy”, *J. Acoust. Soc. Am.*, 77, 1641, 1985
- [AVE 91] Avellaneda M., Torquato S., “Rigorous link between fluid permeability, electrical conductivity, and relaxation times for transport in porous media”, *Phys. Fluids*, A 3 (11), 2529, 1991
- [BEN 78] Bensoussan A., Lions J.L., Papanicolaou G., *Asymptotic Analysis for Periodic Structures*, North-Holland Publishing Company, Amsterdam, 1998
- [BOR 02] Born M., Wolf E., *Principles of Optics*, Cambridge University Press, 2002
- [BRO 80] Brown R.J.S., “Connection between formation factor for electrical-resistivity and fluid–solid coupling factor in Biot equations for acoustic-waves in fluid-filled porous media”, *Geophys.*, 45, 1269, 1980
- [BUR 81] Burrige R., Keller J.B., “Poroelasticity equations derived from micro-structure”, *J. Acoust. Soc. Am.*, 70, 1140, 1981
- [CHA 91] Champoux Y., Allard J.F., “Dynamic tortuosity and bulk modulus in air saturated. porous media”, *J. Appl. Phys.*, 70, 1975, 1991

- [COR 03] Cortis A., Smeulders D.M.J., Guermont J.L., Lafarge D., “Influence of pore roughness on high-frequency permeability”, *Phys. Fluids*, 15, 1766, 2003
- [CUR 89a] Curie J., “Recherches sur le pouvoir inducteur spécifique et la conductibilité des corps cristallisés”, *Ann. Chim. Phys.* 17, 385, 1889
- [CUR 89b] Curie J., “Recherches sur la conductibilité des corps cristallisés (deuxième mémoire)”, *Ann. Chim. Phys.* 18, 203, 1889
- [DAR 56] Darcy H., *Les fontaines publiques de la ville de Dijon*, Victor Dalmont, Paris, 1856
- [DEL 70] Delany M.E., Bazley E.N., “Acoustical Properties of Fibrous Absorbent Materials”, *Applied Acoustics*, 3, 105, 1970
- [JAC 99] Jackson J.D., *Classical Electrodynamics*, 3<sup>rd</sup> edition, John Wiley & Sons, Inc., 1999
- [JOH 81] Johnson D.L., Sen P.N., “Multiple scattering of acoustic waves with application to the index of refraction of fourth sound”, *Phys. Rev. B* 24, 2486, 1981
- [JOH 87] Johnson D.L., Koplik J., Dashen R., “Theory of dynamic permeability and tortuosity in fluid-saturated porous media”, *J. Fluid. Mech.*, 176, 379, 1987
- [LAF 93] Lafarge D., “Rigorous link between fluid permeability, electrical conductivity, and relaxation times for transport in porous media”, *Phys. Fluids*, A 5 (2), 500, 1993
- [LAF 97] Lafarge D., Lemarinié, Allard J.F., Tarnow V., “Dynamic compressibility of air in porous structures at audible frequencies”, *J. Acoust. Soc. Am.*, 102, 1995, 1997
- [LAF 08] Lafarge D., Duclos A., “Acoustic non-local permittivities in rigid-framed porous metamaterials”, *Conference ‘Days on Diffraction’ 2008*, 3–6 June, St. Petersburg, Russia, 2008
- [LAN 80] Landau L.D., Lifshitz E.M., *Statistical Physics*, Part 1 – 3<sup>rd</sup> edition, Course of Theoretical Physics vol. 5, Pergamon Press, Oxford, 1980
- [LAN 84] Landau L.D., Lifshitz E.M., *Electrodynamics of Continuous Media*, 2<sup>nd</sup> edition, Course of Theoretical Physics vol. 8, Pergamon Press, Oxford, 1984
- [LAN 87] Landau L., Lifshitz E., *Fluid Mechanics*, 2<sup>nd</sup> edition, Course of Theoretical Physics vol. 6, Pergamon Press, Oxford, 1987
- [LEV 77] Levy T., Sanchez-Palencia E., “Equations and interface conditions for acoustic phenomena in porous media”, *J. of Math. Analysis and Appl.*, 61, 813, 1977
- [MEC 76] Mechel F.P., “Ausweitung der Absorberformel von Delany und Bazley zu tiefen Frequenzen”, *Acustica*, 35, 210, 1976
- [NOR 86] Norris A.N., “On the viscodynamic operator in Biot’s equations of poroelasticity”, *J. Wave Mat. Interact.*, 1, 365, 1986
- [PIE 91] Pierce A.D., *Acoustics, an Introduction to its Physical Principles and Applications*, McGraw-Hill, New York, 1991
- [RUB 89] Rubinstein J., Torquato S., “Flow in random porous media: mathematical formulation, variational principles, and rigorous bounds”, *J. Fluid Mech.*, 206, 25, 1989

- [SAN 80] Sanchez-Palencia E., *Non-Homogenous Media and Vibration Theory, Lecture Notes in Physics, 127*, Springer-Verlag, Berlin, 1980
- [SCH 07] von Schweidler, E., "Studien ber anomalien im verhalten der Dielektrika", *Ann. Phys.*, 24, 711, 1907
- [SHE 88] Sheng P., Zhou M.Y., "Dynamic Permeability in Porous Media", *Phys. Rev. Lett.*, 61, 1591, 1988.
- [SME 92] Smeulders D.M.J., Eggels R.L.G., van Dongen M.E.H., "Dynamic permeability: reformulation of theory and new experimental. data", *J. Fluid Mech.*, 245, 211, 1992
- [TOR 89] Torquato S., Rubinstein J., "Diffusion-controlled reactions. II. Further bounds on the rate constant", *J. Chem. Phys.*, 90, 1644, 1989
- [TOR 90] Torquato S., "Relationship between permeability and diffusion- controlled trapping constant of porous media", *Phys. Rev. Lett.*, 64, 2644, 1990
- [WIL 97] Wilson D. K., "Simple, relaxational models for the acoustical properties of porous media", *Applied Acoustics*, 50, 171, 1997.
- [ZWI 49] Zwikker C., Kosten C.W., *Sound Absorbing Materials*, Elsevier, New York, 1949.



## Chapter 7

# Biot's Model

### 7.1. Introduction

In this chapter, we relax the condition of immobility of the solid phase, now conceived as a deformable and connected phase. Waves of various kinds in the medium propagate in both fluid and solid connected phases, which are in mutual interaction.

Obviously, stresses of both compression–dilatation and shear types can propagate through the connected solid phase. Conversely, it will be explicitly assumed that only the compression–dilatation stresses can propagate via the fluid. The fluid network does not transmit the (macroscopic) shear actions efficiently. Hence the simplification will be made that the (macroscopic) shear deformations of the fluid will not be associated with any (macroscopic) restoring shear forces exerted on solid or fluid: this is the hypothesis (ii) mentioned in the introduction to Part 2.

For this reason, there will be only one type of shear wave. However, there will be two types of compression–dilatation waves.

For the shear wave, although there are no macroscopic shear stresses in the fluid phase, there may be a macroscopic fluid shear that is non-zero. This is because the fluid is partially drained by the solid phase.

Considering longitudinal waves, macroscopic stresses and strain compression–dilatation appear in the two phases, explaining why two modes generally exist.

For the sake of simplicity, it will be easy to restrict ourselves to the case of an isotropic structure, and we will consider in the first place (section 7.1.1.) the ideal lossless case where the saturating fluid is a perfect fluid, and where the solid constituting the structure is an elastic solid. The two compression–dilatation waves are then called “fast” and “slow”, and respectively correspond to solid–fluid motions in phase and out of phase.

Then, we will study (section 7.1.2.) the general case, where the saturating fluid is a viscous fluid (a fluid with viscous losses occurring), and, when necessary, a thermal fluid (a fluid with thermal losses occurring, as a result of this fluid having a significant thermal expansion coefficient). The viscoelastic nature of the solid will also be very important to consider, when the losses related to the internal friction will be significant. In this case the two compression waves are no longer associated with fluid–solid motions purely in phase or out of phase, and a high dispersion may occur mainly because of viscous losses.

It is commonly admitted that these different situations may be described within the domain of the Biot theory [BIO 56]. The introduction of new factors (compared to those already seen in section 6.1) is not required to model the dispersion due to the viscous and thermal losses. Indeed, in the context of the Biot theory the solid and fluid motions may be sketched in the following manner, and in this simplification is expressed the hypothesis (i) mentioned in the introduction to Part 2.

Whereas the velocity field  $\vec{v}^f$  of the fluid is non-uniformly distributed over the local, microscopic scale, and depends on the considered point  $\vec{x}$ ,  $\vec{v}^f = \vec{v}^f(\vec{x}, t)$ , the velocity field of the solid  $\vec{v}^s$  can be supposed to be (quasi) uniformly distributed at a local scale,  $\vec{v}^s = \vec{v}^s(t)$ .

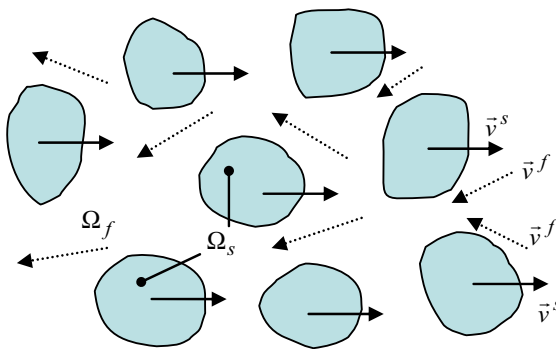


**Figure 7.1.** Principle scheme of the motions considered in the Biot theory, in a representative volume of characteristic extent  $L_h^3$

Thus, during the motion of the medium, the solid is seen, at the local level, as moving uniformly without deformation. Hence also, the fluid is seen (as previously discussed in section 6.1) as moving in a divergence-free manner. That is the reason why the response factors considered in section 6.1.2 will still be useful to describe the dispersion induced by the thermal and viscous losses. Note that the two-scale homogenization technique, mentioned in section 6.1.1.12, predicts, in the presence of a solid, deformable and connected phase, the uniformity of the solid motion at a local scale [BUR 81], as a first approximation. The non-uniform terms are small, of order  $a/\lambda$  compared to the mean solid velocity  $\bar{v}^s$ , where  $a$  is some relevant microscopic scale length.

### 7.1.1. *Perfect fluid and elastic solid*

We will not try to analyze how to pass from the microscopic equations to the macroscopic equations after an averaging operation in general. The restriction shown in Figure 7.1, and the remarks we made, suggest that there are, once again, different results or possible models depending on the more or less complex microgeometry assumed for the medium. With the limitation to the case described in Figure 7.1, however, a completely general analysis is not necessary. The same elements as already introduced in the rigid skeleton equivalent-fluid theory (namely the previously discussed notions of tortuosity  $\alpha_\infty$  or hydrodynamic drag tensor  $\lambda_\infty$ ) will be part of the more general theory. And later on, in same manner, when introducing losses, we will find that the viscous and thermal factors we have already studied  $\alpha(\omega)$ ,  $\beta(\omega)$ , will be part of the more general theory.

This more general form of the equations, given by Biot, can be deduced in a simple way from the assumption that a macroscopic local description of the motion is possible, using the symmetries present in the problem [JOH 86]. Identification of the local constitutive parameters – elastic parameters and densities – will be made through the “gedanken experiments” of Biot–Willis [BIO 57] and with the help of the observation made above, that the motion of the solid can be seen as uniform at the microscopic level.

Basically, the assumption that there is a macroscopic theory means that we can build a Lagrangian of the system using only the mean displacement vectors of the fluid and the solid,

$$\bar{U}^f = \langle \bar{u}^f \rangle_{\text{"fluid phase"}}, \quad \bar{U}^s = \langle \bar{u}^s \rangle_{\text{"solid phase"}}, \quad [7.1]$$

and their successive spatial and temporal derivatives,  $\dot{\bar{U}}^f$ ,  $\partial_i \bar{U}^f$ , etc. Limiting ourselves to the first derivatives we then yield Biot's equations.

7.1.1.1. *Field theory and Euler equations*

The reduction of the laws of physics to variational principles is very general. In the field theory, a continuous system is often described by a continuous set of “coordinates”  $q_i(x, t)$  ( $i = 1, 2, \dots$  counts the different independent fields). These coordinates are in the core of the Lagrangian density  $L(t, q_i, \dot{q}_i, q_{i,k}, \dots)$ . To facilitate the reading of the equations, we use the notations  $\frac{\partial}{\partial t} q_i \equiv \dot{q}_i$ ,  $\frac{\partial}{\partial x_k} q_i \equiv q_{i,k}$ . Further below, due to temporal and spatial invariance, we will not have to consider a dependence of  $L$  with time nor with  $q_i$ . The Lagrangian density  $L(\dot{q}_i, q_{i,k}, \dots)$  determines after integration an action  $S = \int_1^2 dt \int dV L(\dot{q}_i, q_{i,k}, \dots)$ , which must be stationary, i.e., verifies the relationship  $\delta S = 0$ , when performing variations of the path around the one effectively followed by the system. (In this variation process, the initial and final positions do not change, since they are given). The extremum condition  $\delta S = 0$  therefore produces the motion equations given by Euler [GOL 64],

$$\frac{\partial}{\partial t} \frac{\partial L}{\partial \dot{q}_i} = - \frac{\partial}{\partial x_k} \frac{\partial L}{\partial (q_{i,k})}, \quad [7.2]$$

where the sum occurs on the repeated index  $k$ .

The application of such a principle can easily be used to find the equations of motion of a fluid or an isotropic elastic solid. Replacing  $q_i$  by the three components  $u_i$  of the particular displacement, we require that the Lagrangian density can be written  $L = T - V$ , where  $T(\dot{u}_i, \delta_{ij})$  is the density of kinetic energy which has to be a quadratic scalar formed from  $\dot{u}_i$  and the unit tensor  $\delta_{ij}$ , and  $V(u_{ij}, \delta_{ij})$  is the density of potential energy of deformation, which has to be a quadratic scalar formed from the deformation tensor  $u_{ij} = \frac{1}{2}(u_{i,j} + u_{j,i})$  and the unit tensor  $\delta_{ij}$  (the tensor is linearized, because we consider a linear theory). For the kinetic energy there is only one independent scalar:  $\dot{u}_i \dot{u}_j \delta_{ij} = \dot{u}_i^2$ . For the potential energy, we have two possibilities  $u_{ik} u_{ik}$  and  $u_{ii} u_{jj}$ . In a (perfect) fluid, however, the first must be discarded because no deformational energy is associated with the shear deformations, which may occur without giving any restoring force.

Therefore, the Lagrangian density is written as follows:

$$\text{Fluid: } L = \frac{1}{2} \rho \dot{u}_i^2 - \frac{1}{2} \lambda u_{ii}^2, \text{ Solid: } L = \frac{1}{2} \rho \dot{u}_i^2 - \frac{1}{2} \lambda u_{ii}^2 - \mu u_{ik}^2, \quad [7.3]$$

where  $\rho$ ,  $\lambda$  and  $\mu$  are scalar coefficients depending on the medium.  $\rho$  is the density. In the fluid case,  $\lambda$  is the bulk modulus, which is often called  $K$  or  $1/\chi$ . In the solid case,  $\lambda$  is the first Lamé coefficient, which determines the bulk modulus  $K = \lambda + \frac{2}{3}\mu$ , and  $\mu$  is the shear modulus [LAN 81].

Euler equations [7.2] give,

$$\frac{\partial}{\partial t} \frac{\partial L}{\partial \dot{u}_i} = - \frac{\partial}{\partial x_k} \frac{\partial L}{\partial (u_{i,k})}, \quad [7.4]$$

which can be expressed as,

$$\frac{\partial \pi_i}{\partial t} = \frac{\partial \sigma_{ik}}{\partial x_k}, \quad [7.5]$$

where the different components  $\pi_i$  are the conjugated moments,

$$\pi_i \equiv \frac{\partial L}{\partial \dot{u}_i} = \frac{\partial T}{\partial \dot{u}_i}, \quad [7.6]$$

and the  $\sigma_{ik}$  are expressed as,

$$\sigma_{ik} \equiv - \frac{\partial L}{\partial u_{i,k}} = \frac{\partial V}{\partial u_{i,k}}. \quad [7.7]$$

The interpretation of equations [7.4–7.5] follows. The right-hand side component represents the volumic force which is exerted on the material, per unit volume. This force comes from the actions exerted by the contiguous parts of the unit volume. Due to the small range of intermolecular forces, these actions are exerted at the volume boundary only. Therefore, they take the form of the divergence of a tensor [LAN 81], the stress tensor  $\sigma_{ik}$ . The left-hand side component, on the other hand, represents the variation rate of the momentum  $\pi_i = \rho \dot{u}_i$  of the material per unit of volume.

We now verify (according to the evident identities  $\frac{\partial u_{k,l}}{\partial u_{i,j}} = \delta_{ik} \delta_{jl}$ ,  $\frac{\partial u_{kl}}{\partial u_{ij}} = \frac{1}{2}(\delta_{ik} \delta_{jl} + \delta_{il} \delta_{jk})$ , from which we conclude that  $\frac{\partial u_{kl}}{\partial u_{i,j}} = \frac{\partial u_{kl}}{\partial u_{ij}}$ ), that the  $\sigma_{ik}$  coefficients, forces by unit surface area of the medium, can be written as:

$$\sigma_{ik} = \frac{\partial V}{\partial u_{i,k}} = \frac{\partial V}{\partial u_{k,i}} = \frac{\partial V}{\partial u_{ik}}. \quad [7.8]$$

In the case of a fluid and a solid, the stress-strain relations [7.8] yield respectively,

$$\text{fluid: } \sigma_{ik} = -p \delta_{ik} = Ku_{ll} \delta_{ik},$$

$$\text{solid: } \sigma_{ik} = \lambda u_{ll} \delta_{ik} + 2\mu u_{ik} = Ku_{ll} \delta_{ik} + 2\mu(u_{ik} - \frac{1}{3} \delta_{ik} u_{ll}). \quad [7.9]$$

We can use exactly the same procedure to find the form of the macroscopic “Biot” equations describing the (long-wavelength) propagation of waves in the perfect solid-fluid porous medium.

#### 7.1.1.2. Biot equations

To describe the perfect, porous, fluid-saturated material, based on the approaches above, we have to introduce six fields  $q_i$  (the six displacement fields  $\vec{U}^s$  and  $\vec{U}^f$ ).

In an isotropic structure, the Lagrange density is searched in the form  $L = T - V$ , with  $T(\dot{U}_i^s, \dot{U}_i^f, \delta_{ij})$  and  $V(U_{ij}^s, U_{ij}^f, \delta_{ij})$ .

For the kinetic energy, there are three possible quadratic scalars:  $\dot{U}_i^s \dot{U}_i^s$ ,  $\dot{U}_i^f \dot{U}_i^f$ ,  $\dot{U}_i^s \dot{U}_i^f$ . Therefore, introducing three constitutive scalar constants of the medium, we can write,

$$T = \frac{1}{2} \rho_{11} \dot{\vec{U}}^s{}^2 + \frac{1}{2} \rho_{22} \dot{\vec{U}}^f{}^2 + \rho_{12} \dot{\vec{U}}^s \cdot \dot{\vec{U}}^f. \quad [7.10]$$

The  $\rho_{ij}$  constants will be defined such that [7.10] expresses the kinetic energy per unit of total volume of the material. They will be interpreted in the next section

in terms of the intrinsic densities of the solid and fluid phases, and of the geometric parameters associated with the morphology of the porous network (tortuosity  $\alpha_\infty$  and porosity  $\phi$ ),

For the potential energy, we can form the six following quadratic scalars:  $U_{ij}^s U_{ij}^s$ ,  $U_{ii}^s U_{jj}^s$ ,  $U_{ij}^f U_{ij}^f$ ,  $U_{ii}^f U_{jj}^f$ ,  $U_{ij}^s U_{ij}^f$ ,  $U_{ii}^s U_{jj}^f$  with the tensors  $U_{ij}^s, U_{ij}^f, \delta_{ij}$ .

But the fluid is not able to transmit the macroscopic shear stresses. It means that the fluid shear strain cannot contribute to the potential energy. This simplification eliminates the scalars  $U_{ij}^f U_{ij}^f$  and  $U_{ij}^s U_{ij}^f$ . It does not mean that these terms are zero (the macroscopic shear of the fluid is generally non-zero). It means that the two constitutive scalar constants of the medium associated with these two terms must be equal to zero. Therefore, by introducing only four constitutive scalar constants of the medium, and writing  $e$  and  $\varepsilon$  the dilatations of the solid and the fluid ( $e = \vec{\nabla} \cdot \vec{U}^s = U_{ii}^s$ ,  $\varepsilon = \vec{\nabla} \cdot \vec{U}^f = U_{ii}^f$ ), we obtain,

$$V = \frac{1}{2} A e^2 + \frac{1}{2} B \varepsilon^2 + C U_{ij}^s U_{ij}^s + D e \varepsilon. \quad [7.11]$$

The constants  $A$ ,  $B$ ,  $C$  and  $D$  will be defined such that [7.11] represents the potential energy per unit of the total volume of the material. They will be interpreted later on in terms of the intrinsic bulk moduli of the solid and fluid phases, and of the porosity  $\phi$  and elastic constants of the porous structure.

In the following, we return to more usual notations [JOH 86] in the Biot theory, and the constants  $A$ ,  $B$ ,  $C$  and  $D$  are replaced by the following alternate constants:

$$A \leftrightarrow P - 2N, \quad B \leftrightarrow R, \quad C \leftrightarrow N, \quad D \leftrightarrow Q. \quad [7.12]$$

Euler equations [7.2] are,

$$\frac{\partial}{\partial t} \frac{\partial L}{\partial \dot{U}_i^s} = - \frac{\partial}{\partial x_k} \frac{\partial L}{\partial (\partial U_{i,k}^s)}, \quad \frac{\partial}{\partial t} \frac{\partial L}{\partial \dot{U}_i^f} = - \frac{\partial}{\partial x_k} \frac{\partial L}{\partial (\partial U_{i,k}^f)}, \quad [7.13]$$

which can be expressed as,

$$\frac{\partial \pi_i^s}{\partial t} = \frac{\partial \sigma_{ik}^s}{\partial x_k}, \quad \frac{\partial \pi_i^f}{\partial t} = \frac{\partial \sigma_{ik}^f}{\partial x_k}, \quad [7.14]$$

where the  $\pi_i^{s,f}$  are the conjugated moments,

$$\pi_i^{s,f} \equiv \frac{\partial L}{\partial \dot{U}_i^{s,f}} = \frac{\partial T}{\partial \dot{U}_i^{s,f}}, \quad [7.15]$$

and  $\sigma_{ik}^{s,f}$  are given by,

$$\sigma_{ik}^{s,f} \equiv -\frac{\partial L}{\partial U_{i,k}^{s,f}} = \frac{\partial V}{\partial U_{i,k}^{s,f}}. \quad [7.16]$$

The interpretation of equations [7.13–7.14] is discussed below.

The left-hand side components represent the volumic forces respectively acting on the fluid and solid phases, per unit of the total volume of the material. These forces, on a given volume, coming from the actions exerted at its boundary by the contiguous parts of the body, necessarily take the form of the divergence of tensors – the stress tensors  $\sigma_{ik}^s$  for the solid phase, and  $\sigma_{ik}^f$  for the fluid phase. It is important to note that it means that  $\sigma_{ik}^s$  and  $\sigma_{ik}^f$  are, respectively, the stresses exerted on the solid and fluid parts, *per unit of total surface* of the material.

The right-hand side components represent the rate of change in the momentum of the body per unit of total volume, induced by the application of forces in either one or other of the two phases. As for the presence of indices  $s$  and  $f$  on the moments  $\pi$ , it should not be considered that  $\pi^{s,f}$  represents the momentum of the solid and of the fluid per unit of total volume. On the contrary, while the forces in the right-hand side are applied respectively to the solid and to the fluid, they generate a momentum variation in both the solid and fluid phases, since these two phases are coupled.

According to [7.15], the different momentums are  $\pi_i^s = \rho_{11}\dot{U}_i^s + \rho_{12}\dot{U}_i^f$ ,  $\pi_i^f = \rho_{22}\dot{U}_i^f + \rho_{12}\dot{U}_i^s$ , which gives, for equations [7.14],



$$\rho_{11}\ddot{U}_i^s + \rho_{12}\ddot{U}_i^f = \frac{\partial \sigma_{ik}^s}{\partial x_k}, \quad [7.17]$$

$$\rho_{22}\ddot{U}_i^f + \rho_{12}\ddot{U}_i^s = \frac{\partial \sigma_{ik}^f}{\partial x_k}. \quad [7.18]$$

The stresses  $\sigma_{ik}^{s,f}$ , forces applied to a unit surface of the medium, can be written as,

$$\sigma_{ik}^s \equiv \frac{\partial V}{\partial U_{i,k}^s} = \frac{\partial V}{\partial U_{k,i}^s} = \frac{\partial V}{\partial U_{ik}^s}, \quad [7.19]$$

$$\sigma_{ik}^f \equiv \frac{\partial V}{\partial U_{i,k}^f} = \frac{\partial V}{\partial U_{k,i}^f} = \frac{\partial V}{\partial U_{ik}^f}. \quad [7.20]$$

As in the previous section, we easily verify the equivalence of the different forms given above, from the obvious identities:

$$\frac{\partial U_{k,l}^a}{\partial U_{i,j}^a} = \delta_{ik}\delta_{jl}, \quad \frac{\partial U_{kl}^a}{\partial U_{ij}^a} = \frac{1}{2}(\delta_{ik}\delta_{jl} + \delta_{il}\delta_{jk}) = \frac{\partial U_{kl}^a}{\partial U_{i,j}^a},$$

with  $a = s, f$ .

Equations [7.19–7.20] give the stress–strain relationships:

$$\sigma_{ik}^s = [(P - 2N)e + Q\varepsilon]\delta_{ik} + 2NU_{ik}^s, \quad [7.21]$$

$$\sigma_{ik}^f = [Qe + R\varepsilon]\delta_{ik}, \quad [7.22]$$

and, by substitution in [7.17–7.18], we obtain the following “Biot’s Equations”,

$$\rho_{11}\ddot{\vec{U}}^s + \rho_{12}\ddot{\vec{U}}^f = P\vec{\nabla}e + Q\vec{\nabla}\varepsilon - N\vec{\nabla} \times \vec{\nabla} \times \vec{U}^s, \quad [7.23]$$

$$\rho_{22}\ddot{\vec{U}}^f + \rho_{12}\ddot{\vec{U}}^s = Q\vec{\nabla}e + R\vec{\nabla}\varepsilon. \quad [7.24]$$

The constitutive constants  $\rho_{11}$ ,  $\rho_{12}$ ,  $\rho_{22}$ ,  $P$ ,  $Q$ ,  $R$ ,  $N$ , introduced in the model, will now be expressed.

#### 7.1.1.3. Identification of the effective densities

As  $\sigma_{ik}^s$  and  $\sigma_{ik}^f$  are respectively the stresses on the solid parts and on the fluid parts, *per unit of surface area* of the material, the fundamental equation of dynamics is obviously written, per unit of total volume of the material, for the fluid and solid phases respectively,

$$\rho_f \phi \ddot{U}_i^f = \frac{\partial \sigma_{ik}^f}{\partial x_k} + R_i, \quad [7.25]$$

$$\rho_s (1 - \phi) \ddot{U}_i^s = \frac{\partial \sigma_{ik}^s}{\partial x_k} - R_i, \quad [7.26]$$

where we have introduced in the first equation, concerning the fluid phase, the internal reaction force  $R_i$  due to the solid walls. Because of the action–reaction principle, an equal and opposite force is introduced in the second equation. The densities  $\rho_f$  and  $\rho_s$  are those of the fluid and the solid.

The equations above should give equations [7.17–7.18] if we substitute the expression of the reaction force  $R_i$ . This expression has been given in section 6.1.1.4 for a structure at rest. In Biot's theory, the structure is not immobile anymore, but it is considered that, according to the model of Figure 7.1, it was locally undergoing a uniform motion. We can therefore start from the expression of  $R_i$  given by [6.17], where we have to replace the acceleration of the fluid  $\frac{\partial < \vec{v}_{1j} >}{\partial t}$  by the relative acceleration of the fluid  $\ddot{U}_j^f - \ddot{U}_j^s$ , which gives (adding the factor  $\phi$  to take into account the fact that the force is expressed per unit of total volume and no longer per unit of fluid volume, as in [6.17], and putting  $\chi_{\infty ij} = (\alpha_\infty - 1)\delta_{ij}$  for an isotropic structure):

$$R_i = -\phi \rho_f (\alpha_\infty - 1) (\ddot{U}_i^f - \ddot{U}_i^s). \quad [7.27]$$

Writing this expression in [7.25–7.26], and comparing with [7.17–7.18], we finally obtain the following expressions of the densities  $\rho_{ij}$ :

$$\rho_{11} = \rho_s(1 - \phi) + \rho_f \phi(\alpha_\infty - 1), \quad [7.28]$$

$$\rho_{22} = \phi \rho_f \alpha_\infty, \quad [7.29]$$

$$\rho_{12} = -\phi \rho_f (\alpha_\infty - 1). \quad [7.30]$$

Thus, Biot's densities  $\rho_{ij}$  contain the information of the fluid and solid densities  $\rho_f$  and  $\rho_s$ , the information of the tortuosity, and the information of the fluid and solid volume fractions.

#### 7.1.1.4. Identification of the elastic coefficients

The three “gedanken experiments” of Biot and Willis [BIO 57] are usually mentioned to identify the elastic parameters  $P$ ,  $Q$ ,  $R$ , and  $N$ . One of these, which is to subject a volume of material to a pure uniform shear strain, is trivial and directly yields the interpretation of the coefficient  $N$ : this coefficient represents the shear modulus of the porous structure, with no consideration of the saturating fluid. This only expresses the condition that has been set up in the first place: the fluid does not contribute to a restoring macroscopic shear force.

The interpretation of the remaining coefficients  $P$ ,  $Q$ ,  $R$ , is more delicate, and needs the two following “gedanken experiments”. It is customary to present them in a static limit. However, our presentation below shows that the argument applies in the harmonic regime as well, in the framework of the simplifications we have made.

##### 1. First “gedanken experiment” (“jacketed” material)

Let us consider a volume of the material, of scale  $L_h^3$ . Let it be jacketed with a flexible membrane, subjected to an external uniform pressure  $p_0 + p_1 e^{-i\omega t}$  which is the ambient constant pressure  $p_0$  in the external fluid, plus a small time harmonic normal action  $p_1 e^{-i\omega t}$  directly applied to the membrane. A small hole in this membrane, connected to a capillary, allows the equalization of the pressure of the fluid with the internal “tank” pressure  $p_0$ . According to the condition that the wavelengths are long enough  $\lambda \gg L_h^3$ , the variables of interest have a uniform spatial distribution in the volume. In the remaining, we simply write  $p_1$  the term  $p_1 e^{-i\omega t}$ , and will proceed the same way for the other deviations “1”.

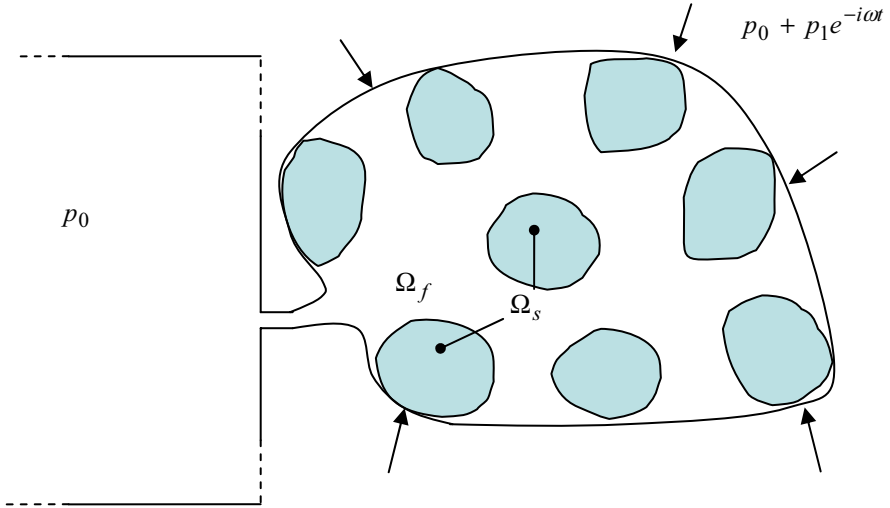


**Figure 7.2.** First “gedanken experiment”: “jacketed”

The excitation by an uniform excess pressure  $p_1$  does not generate macroscopic shear but uniform compressions:  $U_{lij}^s = e_1 \delta_{ij}$ ,  $U_{lij}^f = \varepsilon_1 \delta_{ij}$ . Because the fluid stays at the ambient pressure, we have  $\sigma_{lij}^f = 0$  and the additional pressure  $p_1$  is totally transmitted to the solid:  $\sigma_{ij}^s = -p_1 \delta_{ij}$ . Stress–strain relationships [7.21–7.22] therefore give

$$-p_1 = \left(P - \frac{4N}{3}\right)e_1 + Q\varepsilon_1, \quad 0 = Qe_1 + R\varepsilon_1 \quad [7.31]$$

Let  $K_b$  be the bulk modulus of the solid structure, at constant pressure in the fluid (or the bulk modulus of the solid structure in a vacuum). It is given by the equation  $K_b = -p_1 / e_1$  and the relationships above [7.31] show that,

$$K_b = P - \frac{4}{3}N - \frac{Q^2}{R}. \quad [7.32]$$

## 2. Second “gedanken experiment” (“unjacketed” material)

Let us consider the same volume of material directly submitted to a uniform excess pressure  $p_1 e^{-i\omega t}$  in the fluid. For the same reasons as above, this excess pressure remains uniform in the volume considered at the relevant frequencies. (It has to be the case when there are no resonators like the ones seen in section 7.1.2.13).

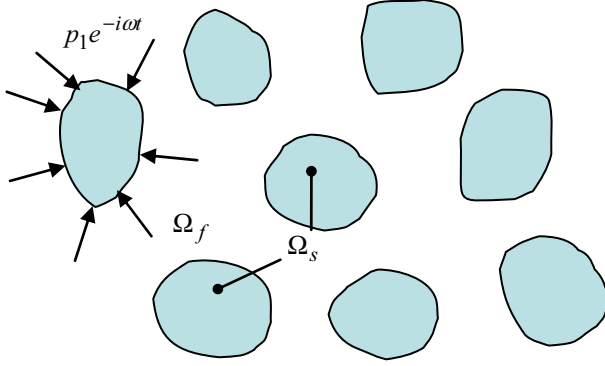


**Figure 7.3.** Second “gedanken experiment”: “unjacketed”

This hydrostatic excess pressure is transmitted to the solid, and the stress–strain relations give,

$$-(1 - \phi)p_1 = (P - \frac{4N}{3})e_1 + Q\varepsilon_1, \quad -\phi p_1 = Qe_1 + R\varepsilon_1. \quad [7.33]$$

The structure compresses and expands with no deformation, and the quantity  $K_s = -p_1 / e_1$  is now interpreted as the bulk modulus of the solid itself, that is part of the structure. Therefore, we obtain the relationship:

$$(1 - \phi)K_s = P - \frac{4}{3}N + \left( \phi \frac{K_s}{R} - \frac{Q}{R} \right) Q. \quad [7.34]$$

Similarly, the quantity  $K_f = -p_1 / \varepsilon_1$  can be interpreted as the compressibility modulus of the fluid, because the porosity does not vary and  $\varepsilon_1$  consequently represents the microscopic uniform dilatation of the fluid. Hence, by removing  $e_1$  from the two relationships [7.33] we obtain,

$$(1-\phi)K_f = (P - \frac{4}{3}N)(\phi\frac{K_f}{Q} - \frac{R}{Q}) + Q. \quad [7.35]$$

Finally, combining the three relations [7.32], [7.34] and [7.35], we can determine the following complete expressions of the different elastic coefficients  $P$ ,  $Q$ , and  $R$ :

$$P = \frac{(1-\phi)\left(1-\phi-\frac{K_b}{K_s}\right)K_s + \phi\frac{K_s}{K_f}K_b}{1-\phi-\frac{K_b}{K_s} + \phi\frac{K_s}{K_f}} + \frac{4}{3}N, \quad [7.36]$$

$$Q = \frac{\left(1-\phi-\frac{K_b}{K_s}\right)\phi K_s}{1-\phi-\frac{K_b}{K_s} + \phi\frac{K_s}{K_f}}, \quad [7.37]$$

$$R = \frac{\phi^2 K_s}{1-\phi-\frac{K_b}{K_s} + \phi\frac{K_s}{K_f}}. \quad [7.38]$$

Thus, Biot's elasticity constants  $P$ ,  $Q$ ,  $R$ ,  $N$  contain information of the two bulk moduli of the fluid and the solid  $K_f$  and  $K_s$ , the information of the shear and bulk moduli of the structure in a vacuum  $N$  and  $K_b$ , and information of the solid and fluid volume fractions.

#### 7.1.1.5. The three kinds of Biot's waves

Biot's equations [7.23–7.24] imply that three different modes of propagation can spread through the material, two longitudinal and one transverse mode. To prove this result, the divergence and rotational operators are alternately applied to these equations, thus giving the two systems:

$$\begin{pmatrix} \rho_{11} & \rho_{12} \\ \rho_{12} & \rho_{22} \end{pmatrix} \begin{pmatrix} \ddot{e} \\ \ddot{e} \end{pmatrix} = \begin{pmatrix} P & Q \\ Q & R \end{pmatrix} \begin{pmatrix} \Delta e \\ \Delta e \end{pmatrix}, \quad [7.39]$$

$$\begin{pmatrix} \rho_{11} & \rho_{12} \\ \rho_{12} & \rho_{22} \end{pmatrix} \begin{pmatrix} \ddot{\vec{\omega}} \\ \ddot{\vec{\Omega}} \end{pmatrix} = \begin{pmatrix} N\Delta\vec{\omega} \\ \vec{0} \end{pmatrix}, \quad [7.40]$$

where  $\vec{\omega} = \nabla \times \vec{U}^s$  and  $\vec{\Omega} = \vec{\nabla} \times \vec{U}^f$  are the solid and fluid rotation vectors, and  $\Delta$  is the Laplacian operator.

The first system above describes the compression waves. The second system describes the rotation wave (shear).

Searching the solutions as plane waves  $\exp(-i[\omega t - \vec{q} \cdot \vec{r}])$ , we have, for the compression waves:

$$-\omega^2 \begin{pmatrix} P & Q \\ Q & R \end{pmatrix}^{-1} \begin{pmatrix} \rho_{11} & \rho_{12} \\ \rho_{12} & \rho_{22} \end{pmatrix} \begin{pmatrix} e \\ \varepsilon \end{pmatrix} = \vec{q}^2 \begin{pmatrix} e \\ \varepsilon \end{pmatrix}. \quad [7.41]$$

The square of the wave vector  $\vec{q}^2$  admits two possible values  $\delta_1^2$  and  $\delta_2^2$ , that are the eigenvalues of the matrix on the left-hand side; they are given by the following expressions:

$$\delta_1^2 = \frac{\omega^2}{2(PR - Q^2)} (P\rho_{22} + R\rho_{11} - 2Q\rho_{12} - \sqrt{\Delta}), \quad [7.42]$$

$$\delta_2^2 = \frac{\omega^2}{2(PR - Q^2)} (P\rho_{22} + R\rho_{11} - 2Q\rho_{12} + \sqrt{\Delta}), \quad [7.43]$$

where

$$\Delta = (P\rho_{22} + R\rho_{11} - 2Q\rho_{12})^2 - 4(PR - Q^2)(\rho_{11}\rho_{22} - \rho_{12}^2) \quad [7.44]$$

Quantities  $\delta_1$  and  $\delta_2$  are the propagation constants of the two compression waves.

For the rotation wave, we have  $\vec{\Omega} = -\frac{\rho_{12}}{\rho_{22}} \vec{\omega}$ , and  $\vec{q}^2$  is necessarily equal to the

only possible value  $\delta_3^2$  given by,

$$\delta_3^2 = \frac{\omega^2}{N} \frac{\rho_{11}\rho_{22} - \rho_{12}^2}{\rho_{22}}. \quad [7.45]$$

The quantity  $\delta_3$  is the propagation constant of the shear wave. The positive character of the quadratic forms associated with the potential and kinetic energies require that quantities  $PR - Q^2$  and  $\rho_{11}\rho_{22} - \rho_{12}^2$  are positive. A direct conclusion is that expressions [7.42–7.45] are, as it should be in the absence of losses, positive. Propagation speeds of each of the waves  $c_i = \omega/\delta_i$  are constant, independent of the frequency.

For each of the three waves  $i = 1, 2, 3$  the fluid and solid motions are collinear:  $\vec{U}^f = \mu_i \vec{U}^s$ . This is due to the supposed isotropy. Amplitude ratios  $\mu_i$  are fixed, and given by,

$$(i = 1, 2), \mu_i = -\frac{\omega^2 \rho_{11} - P\delta_i^2}{\omega^2 \rho_{12} - Q\delta_i^2} = -\frac{\omega^2 \rho_{12} - Q\delta_i^2}{\omega^2 \rho_{22} - R\delta_i^2}, \quad [7.46]$$

$$\mu_3 = -\frac{\rho_{12}}{\rho_{22}} = \lambda_\infty. \quad [7.47]$$

The result expressed by [7.47] could be *a priori* predicted from the physical interpretation given in section 6.1.1.8 for the hydrodynamic drag parameter  $\lambda_\infty$ . Indeed, in the “gedanken experiment” discussed in section 6.1.1.8, the motion of the fluid is non-divergent, like the motion due to the rotation wave. That is the reason why  $\vec{\Omega} = \lambda_\infty \vec{\omega}$  and  $\vec{U}^f = \lambda_\infty \vec{U}^s$  for the shear wave. Likewise, equation [7.45] for the propagation constant of this wave can easily be interpreted: it makes the shear coefficient  $N$  of the structure (the fluid does not contribute to the macroscopic restoring force) and the density  $\frac{\rho_{11}\rho_{22} - \rho_{12}^2}{\rho_{22}} = (1 - \phi)\rho_s + \lambda_\infty\phi\rho_f$ , representing

the mass of the structure plus the mass of the fluid drained by the rotational motion of the latter, apparent.

For compression waves, expressions [7.46] and [7.42–7.43] of the ratios between the amplitudes and the propagation constants have a more complicated structure, due to the fact that we have here, when transmitting the compression–expansion actions, two phases to be treated on an equal footing.



Unlike the situation above, the propagation constants cannot be written as a ratio  $\frac{\omega}{c}$ , with  $c = \sqrt{\frac{K}{\rho}}$ , where  $K$  would be an elastic constant depending only on  $P$ ,  $Q$ ,  $R$ , and  $\rho$  a density constant depending only on  $\rho_{11}$ ,  $\rho_{12}$ ,  $\rho_{22}$ . Such a dynamic separation of the inertial and elastic effects is no longer possible (if we exclude the relation of dynamic compatibility given further below). This can also be observed from the amplitude ratios, in which the elastic properties  $P$ ,  $Q$ ,  $R$  are involved, as well as the inertial properties  $\rho_{11}$ ,  $\rho_{12}$ ,  $\rho_{22}$ . Nevertheless, the two ratios  $\mu_i$  ( $i = 1, 2$ ) may be connected together either by the densities only, or by the elastic parameters only. Indeed, the amplitudes  $\mu_1$  and  $\mu_2$  verify the orthogonality relations:

$$\begin{aligned} & \rho_{11} + \rho_{12}(\mu_1 + \mu_2) + \rho_{22}\mu_1\mu_2 \\ & = P + Q(\mu_1 + \mu_2) + R\mu_1\mu_2 = 0, \end{aligned} \quad [7.48]$$

that we can extract from system [7.41], replacing  $\begin{pmatrix} e \\ \varepsilon \end{pmatrix}$  by the eigenvectors corresponding to waves 1 and 2, and multiplying the left-hand side term respectively by the transposed  $(e, \varepsilon)$  eigenvectors 2 and 1. We can see, from [7.48], that the amplitudes  $\mu_1$ ,  $\mu_2$ , always have opposite signs. In other words, the solid–fluid motions are in phase for one of the two waves, and in antiphase for the other. Motions are in phase for the wave with the greatest speed of propagation. This wave is called the “fast wave” or wave of the first kind. The opposite-phase wave is called the “slow wave” or wave of the second kind. (These are respectively the solutions identified by the indices 1 and 2 above).

The solid–fluid relative motions are generally more important in the case of the slow wave. For the fast wave, it is possible to have a special situation for which these relative motions vanish ( $\mu_1 = 1$ ). According to [7.48], we then have

$$\mu_2 = -\frac{(1 - \phi)\rho_s}{\phi\rho_f} = -\frac{P + Q}{R + Q}. \text{ Such a situation requires that the parameters of the}$$

porous medium verify the following “dynamic compatibility condition”:

$$\frac{P + Q}{(1 - \phi)\rho_s} = \frac{R + Q}{\phi\rho_f}. \quad [7.49]$$

For this very special situation, the behavior of compression–dilatation waves is once more described by a propagation speed with the usual form  $\sqrt{K/\rho}$ .

#### 7.1.1.6. Displacement potentials

Generally, the field will be a superposition of the three types of waves. It will be convenient to represent it using the scalar and vector potentials associated with the three types of waves. Compression waves 1 and 2 are described by the scalar potentials  $\varphi_1$  and  $\varphi_2$ , and wave 3 is described by a vector potential  $\vec{\psi}$  that can always have, by corresponding choice of gauge [MOR 53], a divergence equal to zero,

$$\vec{U}^s = \vec{\nabla}\varphi_1 + \vec{\nabla}\varphi_2 + \vec{\nabla} \times \vec{\psi}, \quad [7.50]$$

$$\vec{U}^f = \mu_1 \vec{\nabla}\varphi_1 + \mu_2 \vec{\nabla}\varphi_2 + \mu_3 \vec{\nabla} \times \vec{\psi}. \quad [7.51]$$

For the harmonic regime, the potentials verify the following wave propagation equations:

$$\Delta\varphi_1 + \delta_1^2\varphi_1 = 0, \quad [7.52]$$

$$\Delta\varphi_2 + \delta_2^2\varphi_2 = 0, \quad [7.53]$$

$$\Delta\vec{\psi} + \delta_3^2\vec{\psi} = \vec{0}. \quad [7.54]$$

#### 7.1.1.7. Continuity conditions

Some continuity conditions have to be set at the interface between the free fluid and the material.

##### 1. Continuity of the normal fluid flow

Let  $\dot{\vec{u}}^f$  be the velocity field in the free fluid and in the porous material, and  $\dot{\vec{U}}^f$  the “fluid phase” averaging of  $\dot{\vec{u}}^f$  in the material. Let us consider these fields on both sides of the interface  $I$  separating the porous material and the fluid, at small distances, respectively  $\sim a$  and  $a + L_h$ , so that we can neglect the interface edge effects (see Figure 7.4.). With no motion of the solid, and neglecting the effect of these distances because of the condition  $\lambda \gg L_h > a$ , flow conservation imposes the surfacic integrals  $\int_G \dot{\vec{u}}^f \cdot \vec{n} dS$  and  $\int_D \dot{\vec{U}}^f \cdot \vec{n} dS$  to be equal. The first integral is

equal to  $S\dot{\vec{u}}^f \cdot \vec{n}$ , and the second one is  $S\phi\dot{\vec{U}}^f \cdot \vec{n}$ . We therefore have the continuity condition,  $\dot{\vec{u}}^f \cdot \vec{n} = \phi\dot{\vec{U}}^f \cdot \vec{n}$ , that we can impose on  $I$ .

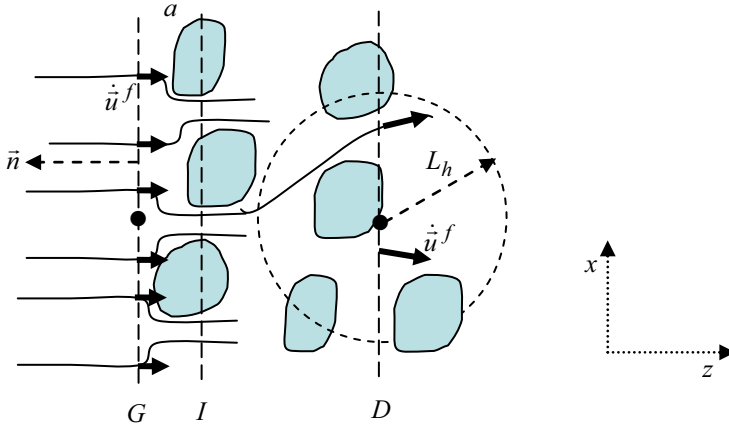


**Figure 7.4.** Conservation of the flow in the neighborhood of the free fluid–material interface

In the presence of a motion of the solid  $\dot{\vec{u}}^s = \dot{\vec{U}}^s$ , we have to consider the fluid flow relative to the porous solid, i.e. we replace the speeds  $\dot{\vec{u}}^f$ ,  $\dot{\vec{U}}^f$ , by the relative speeds  $\dot{\vec{u}}^f - \dot{\vec{U}}^s$ ,  $\dot{\vec{U}}^f - \dot{\vec{U}}^s$ . The continuity condition expressing the conservation of the flow generally reads,

$$\dot{\vec{u}}^f \cdot \vec{n} = (1 - \phi)\dot{\vec{U}}^s \cdot \vec{n} + \phi\dot{\vec{U}}^f \cdot \vec{n}. \quad [7.55]$$

The quantity  $(1 - \phi)\vec{U}^s + \phi\vec{U}^f$  is nothing but the “total volume average” of the microscopic displacements:  $\langle \vec{u} \rangle_{tot vol} = \langle \vec{u}^s + \vec{u}^f \rangle_{tot vol} = (1 - \phi)\vec{U}^s + \phi\vec{U}^f$ . Thus, equation [7.55] is nothing but a continuity condition for the total volume, normal velocity field component.

## 2. Continuity of the pressure

Let us choose, as above, two points located on both sides of the interface. The stress tensor applied to the fluid is diagonal:  $\sigma_{ik}^f = -\phi P^f \delta_{ik}$ . The factor of porosity

$\phi$  is also present because  $\sigma_{ik}^f$  is a force per unit of total surface area of the material. Only a part  $\phi$  is occupied by the fluid. Here,  $P^f$  is the macroscopic pressure, but we can consider it equal to the microscopic pressure. Indeed, as discussed in section 6.1.2.6, the pressure field  $p^f$  breaks into the form  $p^f = P^f + \Pi^f$  with  $\Pi^f$  having an order of magnitude small compared to  $P^f$  ( $\Pi^f \sim P^f a / \lambda$ ). That is why, neglecting as above the effect of the spatial separations  $a$  and  $a + L_h$ , the field  $P^f$  on the surface  $D$  must have the same value as the pressure in the free fluid  $p^f$  on the surface  $G$ . We therefore have the following continuity condition, that we can impose on  $I$ :

$$p^f = P^f. \quad [7.56]$$

It should be noted that in the presence of resonators such as those seen in section 6.1.1.12, continuity condition [7.56] is no longer satisfied: the deviation  $\Pi^f$  is not necessarily small anymore.

### 3. Continuity of normal actions

The normal actions acting at the level of the surfaces  $G$  and  $D$  must be equal. In the free fluid, the normal stress at the level of  $G$  is  $\sigma_{zz}^f = -p^f$ , in the material the total normal stress at the level of  $D$  is  $\sigma_{zz}^f + \sigma_{zz}^s = -\phi P^f + \sigma_{zz}^s$ , where  $z$  is the coordinate along the normal axis. The equality of normal stresses reads

$$-p^f = -\phi P^f + \sigma_{zz}^s. \quad [7.57]$$

We observe that [7.56] and [7.57] express the two conditions,

$$-\phi p^f = \sigma_{zz}^f, \quad -(1 - \phi)p^f = \sigma_{zz}^s. \quad [7.58-59]$$

The normal pressure stresses in the free fluid are equally distributed on the two phases, proportionally to the surface they occupy.

### 4. Continuity of tangential stresses

There is no tangential stress in the free (perfect) fluid, as well as no macroscopic (or even microscopic) tangential stresses in the saturating (perfect) fluid. Therefore, the continuity of tangential actions is generally expressed by the condition,

$$0 = \sigma_{zx}^s, \quad [7.60]$$

where  $x$  is an axis, normal to the  $z$ -axis.

Biot's equations and the four continuity equations above provide everything necessary to predict the behavior of the porous material subject to an external incident field.

### 7.1.2. Thermoviscous fluid and visco-elastic structure

#### 7.1.2.1. Considering losses

The fluid is no longer a perfect fluid. It will be considered as viscous and with a non-negligible thermal expansion coefficient. Furthermore, the solid will no longer be considered as a perfectly elastic solid.

In the presence of losses, linear stress–strain relations of the type [7.21–7.22] are still valid in the harmonic regime, with complex elastic coefficients that possibly depend on frequency. The reason is that the two scalar terms discarded in section 7.1.1.2 are still to be discarded here, as a result of our simplification that no restoring shear forces are exerted by the fluid on the solid, on a macroscopic scale. Indeed, let us suppose that the viscous and inertial effects are of the same order of magnitude at the local level. In other words, let us consider that the thickness of the boundary layer is of the same order of magnitude as the radius of the pores. The dimensionless viscosity appropriate at the microscopic scale is comparable to 1:  $\eta / \rho_0 \omega a \sim O(1)$ . Thus, the dimensionless viscosity appropriate for a macroscopic scale  $\lambda$  is comparable to  $\eta / \rho_0 \omega \lambda \sim O(a / \lambda) \ll 1$ . We make a negligible error considering the latter equal to zero, and we can conclude as before that there is no restoring shear force applied by the fluid on a macroscopic scale, even though there are non-vanishing shear stresses in the fluid, at the microscopic level. That is why we must still obtain relation [7.21–7.22] for the stress–strain relationships.

The “gedanken experiments” described in section 7.1.1.4 are therefore used with no change, with the only difference that the elastic coefficients appearing can now be frequency-dependent, complex values because of the viscoelastic nature of the solid. The modulus  $N$  still represents the shear modulus of a single structure or of a saturated sample, the fluid does not contribute to its value. It may be complex and frequency-dependent to reflect losses due to the solid. In the first and second “gedanken experiments” where the material is excited in compression–dilatation in the “jacketed” and “unjacketed” configurations, the modulus,  $K_b$ ,  $K_f$  and  $K_s$  become complex and frequency-dependent quantities, due to losses in the solid for

$K_b$  and  $K_s$ , and due to thermal losses in the fluid for  $K_f$ . The latter is written now  $K_f = K_a / \beta(\omega)$  where  $K_a$  is the fluid adiabatic bulk modulus, and  $\beta(\omega)$  the dynamic compressibility already studied in section 6.1.2. With these changes, we obtain relations [7.36–7.38] in the harmonic regime for the complex coefficients  $P$ ,  $Q$  and  $R$ .

Moreover, the reaction force  $R_i$  of the solid on the fluid is still given by equation [7.27] in the harmonic regime, where we have to replace the tortuosity in a perfect fluid  $\alpha_\infty$  by the dynamic tortuosity  $\alpha(\omega)$ , already studied in section 6.1.2. It follows that the densities  $\rho_{ij}$  become complex functions of  $\omega$ , which are still given by expressions [7.28–7.30], where  $\alpha(\omega)$  replaces  $\alpha_\infty$ .

Complete relations [7.36–7.38] are very general, and make it possible to describe a wide variety of situations: rigid structure  $K_b$ ,  $N \gg K_f$ , soft structure  $K_b$ ,  $N \ll K_f$ ,  $K_s$ , “sol–gel” transition in which the shear modulus goes from zero in the “sol” phase, to a small value in the “gel” phase [JOH 86]. For materials used in practice, saturated with air, such as glass wool, plastic polyurethane foams, fibrous materials, and so on, the modulus  $K_s$  satisfies  $K_s \gg K_b$ ,  $K_s \gg K_f$ , and complete expressions [7.36–7.38] can be simplified as,

$$P = \frac{4}{3}N + K_b + \frac{(1-\phi)^2}{\phi} K_f, \quad [7.61]$$

$$Q = (1 - \phi)K_f, \quad [7.62]$$

$$R = \phi K_f. \quad [7.63]$$

Note that we sometimes prefer to write the elastic properties of the skeleton in a vacuum  $K_b$  and  $N$ , in terms of a Young’s modulus  $E$  and a Poisson’s coefficient  $\nu$  :

$$E = \frac{9K_b N}{3K_b + N}, \quad \nu = \frac{1}{2} \frac{3K_b - 2N}{3K_b + N}. \quad [7.64]$$

We often represent the losses in the solid by an additional small angle  $\delta$  on the Young’s modulus,

$$E = E_0(1 + i \tan \delta), \quad [7.65]$$

while the Poisson’s coefficient remains real.

The continuity conditions examined in section 7.1.1.7 without losses remain unchanged when we introduce the viscous friction, thermal exchanges, and viscoelastic losses in the medium.

Let us, in particular, detail why the vanishing of tangential stresses at the material boundaries [7.60] is still justified. We consider that there are no tangential stresses in the free fluid, because we do not intend to describe the bulk attenuation mechanisms in this free fluid. This fluid is viewed as a perfect fluid as long as there are no viscous friction and thermal exchanges with the solid, to manifest its real viscothermal nature. There are no *macroscopic* tangential stresses in the saturating fluid, because, in a consistent manner with this neglect of bulk attenuation in the free fluid, we do not (in the framework of Biot's theory) take into account the fluid contribution to the *macroscopic* shear stresses. Hence the persistent validity of the boundary condition [7.60].

Materials are sometimes covered with a resistive screen. A screen can be seen as a porous layer whose thickness— but not the corresponding resistance — can be neglected. We can observe a discontinuity of the pressure, because of the Darcy-like law of resistance, due to the viscous losses.

#### 7.1.2.2. *Some consequences on the propagation properties*

Even if the algebra of the relationships obtained for the harmonic regime is formally the same with and without losses, the properties of the propagation can be deeply modified, as a result of the quantities becoming complex.

Generally, the motions are neither in phase nor in antiphase, like they are in the lossless case. The hydrodynamic drag parameter  $\lambda(\omega) = 1 - 1/\alpha(\omega)$  becomes a complex function, with the consequence that the motions of the solid and the fluid are no longer in phase. In particular, for the shear wave,

$$\mu_3 = \lambda(\omega), \quad \delta_3^2 = \omega^2 \frac{\rho_s(1 - \phi) + \lambda(\omega)\rho_f\phi}{N}. \quad [7.66]$$

In general, nearly in phase motions and antiphase motions may be found in the low frequency and high frequency limits, where the hydrodynamic drag parameter becomes equal to the real values 1 and  $\lambda_\infty = 1 - 1/\alpha_\infty$ , respectively.

Thus for example, at low frequencies, a motion in phase, with an amplitude ratio of 1, appears for the fast wave, and for the shear wave, corresponding to a total drainage of the fluid by the solid, due to the viscous forces. These two waves can propagate with nearly no attenuation, the propagation constants ( $\omega \rightarrow 0$ ) being,

$$\delta_1^2 = \omega^2 \frac{\rho_s(1 - \phi) + \rho_f \phi}{P + R + 2Q}, \quad [7.67]$$

$$\delta_3^2 = \omega^2 \frac{\rho_s(1 - \phi) + \rho_f \phi}{N}. \quad [7.68]$$

In this limit the slow wave is now diffusive with,

$$\delta_2^2 = \omega^2 \frac{(P + R + 2Q)}{(PR - Q^2)} \frac{\eta \phi^2}{-i\omega k_0}. \quad [7.69]$$

For higher frequencies, there is no general simplifications of the quantities  $\mu_1$ ,  $\mu_2$ ,  $\delta_1$ ,  $\delta_2$ . At the limit of high frequencies, the expressions of the various quantities yield the expressions seen in the study of the perfect fluid.

## 7.2 Bibliography

- [BIO 56] Biot M. "The theory of propagation of elastic waves in a fluid-saturated porous fluid. I. Low frequency range. II. Higher frequency range", *J. Acoust. Soc. Am.*, 28, 168–91, 1956.
- [BIO 57] Biot M.A., Willis D.G., "The elastic coefficients of the theory of consolidation", *J. Appl. Mech.*, 24, 594, 1957
- [BUR 81] Burridge R., and Keller J.B., "Poroelasticity equations derived from micro-structure", *J. Acoust. Soc. Am.*, 70, 1140, 1981
- [GOL 64] Goldstein H., *Mécanique classique*, P.U.F., Paris, 1964
- [JOH 86] Johnson D. L., "Recent developements in the acoustic properties of porous media", in Sette D (ed.), *Proc. Int. School of Physics Enrico Fermi, Cours XCIII*, North Holland Publishing Co., Amsterdam, 255, 1986
- [LAN 81] Landau L., Lifshitz E., *Theory of Elasticity*, 2<sup>nd</sup> edition, Course of Theoretical Physics vol.7, Pergamon Press, Oxford, 1981
- [MOR 53] Morse P.M., Feshbach H., *Methods of Theoretical Physics*, McGraw-Hill, New York, 1953



## Chapter 8

# Propagation Equations in the Time Domain

### 8.1. Introduction

#### 8.1.1. *Materials: frequency and temporal approach*

During the last 20 years, a major effort was made to understand the physics of the propagation of acoustic waves in saturated porous media. The result today is a set of models [ALL 92b, JOH 87, LAF 93], whose predictions agree quite well with the experimental results; and more generally, a good understanding of the propagation of monochromatic waves in these environments. It is due to the Fourier analysis and the advancement of computers and instrumentation that most of these models have been developed in the frequency domain. One consequence of this is that few articles addressing this subject refer to the time domain [BOU 87, CAR 96, NOR 86].

Although they are often effective, the frequency methods used for the characterization of acoustic materials also present some limitations in their implementation that encourage the development of other analysis techniques for these materials. For example, we can mention the problem of the phase unfolding for a signal carrying information. There are currently no satisfactory solutions.

It is within this context that we propose our temporal approach to propagation in porous media. There are several reasons justifying this approach:

- Time-modeling is often easier to develop because it is closer to the reality of experiments.

- In many situations, the introduction of the “time” parameter facilitates the analysis of experimental results.
- For certain applications, it is fast because it avoids back and forth operations between time and frequency domains by FFT.
- It provides an elegant solution of the direct problem necessary for the resolution of the inverse problem.
- It is well suited for comparison between theory and experiment.

A drawback is the necessity of introducing a new mathematical formalism. In the frequency domain, relevant values for the characterization of a porous medium are functions of the frequency that can be interpreted as susceptibilities. Some of these quantities, such as impedance, have no equivalent in the time domain. What happens to these concepts while we are working with the dual variable of the frequency?

While frequency techniques lead to the frequency response of the medium, in the temporal approach, we are more interested in impulse responses. The relationship between the strain  $\epsilon(t)$ , seen as a function of time  $t$ , and the stress  $\sigma(t)$ , is essential for the conventional description of elasticity. In traditional theory, stresses and strains are linked by a constant: thus the evolution of each of these functions is similar, i.e. simply proportional, and the deformation process is reversible. However, due to the dissipation of energy, most materials do not obey this type of behavior during deformation caused by stresses. These deviations from the theory of elasticity can be taken into account by replacing the constants by integral or differential operators. Thus, in the time domain, susceptibilities become operators. They act as a convolution on temporal functions like excitations, the memory effect reflecting the dispersion of waves being simply the result of this convolution.

### **8.1.2. Fractional derivative and behavior of materials**

The idea of the fractional derivative is almost as old as the concept of the derivative [LEI 45]: yet, its use outside mathematics is recent. In recent years, many articles describe different applications where the fractional derivative appears to be a very efficient tool [BAG 83, CAP 66, CAP 71, RIE 96, RIE 97], and recently, several books have also been devoted to it [MIL 93, OLD 74, SAM 93, POD 99]. The work of Samko, Kilbas and Marichev [SAM 93] is certainly the most comprehensive statement on mathematic research on fractional derivatives and integrals. For the users of fractional calculation, the book written by Podlubny [POD 99] is easier to read and offers many methods and solutions.

In mechanics, at the end of the 1960s, Caputo [CAP 66] and a little later, Caputo and Mainardi [CAP 71] were the first authors to use the fractional derivative to model dissipation in solids. In the 1980s, Bagley and Torvik [BAG 83] developed a model for viscoelastic solids using the fractional derivative. In acoustics, the most important contribution was made by Matignon [MAT 94].

### 8.1.3. Fractional derivative and viscoelasticity

Fractional calculation models the viscoelastic behavior by introducing fractional derivatives into the constitutive stress/strain relationships. Bagley and Torvik [BAG 83] have explored models with the form

$$\sigma(t) + bD^\lambda[\sigma(t)] = G_0\epsilon(t) + G_1D^\nu[\epsilon(t)], \quad [8.1]$$

where  $b$ ,  $G_0$ ,  $G_1$ ,  $\lambda$  and  $\nu$  are five parameters to be determined by a least squares method applied to experimental data.  $D^\nu[x(t)]$  is the fractional derivative of order  $\nu$  defined by:

$$D^\nu[x(t)] = \frac{1}{\Gamma(-\nu)} \int_0^t (t-u)^{-\nu-1} x(u) du, \quad [8.2]$$

where  $\nu$  is a real number and  $\Gamma(\cdot)$  is the Gamma function. Obviously, the fractional derivative does not represent the local variations of the function. On the contrary, it acts as an integral operator. Some of the properties of the fractional derivative are given in [POD 99].

### 8.1.4. Fractional derivative and model of the equivalent fluid [FEL 00]

The success of this model encourages its general use for the case of propagation in a porous material; however, this model is used in a slightly different form. This leads to the basic equations of acoustics of these materials in the time domain.

As noted above, the model of the equivalent fluid developed in the frequency domain gives results which are in close agreement with experimental measurements. The time domain approach relies on the expressions of the susceptibilities  $\alpha(\omega)$  and  $\beta(\omega)$ , consisting simply of taking their expression in the time domain  $t$ . The functions are therefore written as a power series of  $\omega$ :

$$\alpha(\omega) = \sum_{\nu} a_{\nu}(j\omega)^{\nu}, \quad \beta(\omega) = \sum_{\lambda} b_{\lambda}(j\omega)^{\lambda}, \quad [8.3]$$

where  $\lambda$  and  $\nu$  can be fractional numbers. We can then use the properties of fractional calculation and the Fourier transform:

$$F[g(t)] = \int_{-\infty}^{+\infty} e^{j\omega t} g(t) dt, \quad [8.4]$$

to write the relationship:

$$F[D^\nu g(t)] = (j\omega)^\nu F[g(t)]. \quad [8.5]$$

Finally, we replace the powers of  $\omega$  with the fractional derivatives:

$$(j\omega)^\nu \xrightarrow{t} D^\nu[\cdot].$$

Unfortunately, this method leads to very complicated equations if we want their expressions to be valid for all values of  $\omega$ ; their solutions for general conditions are difficult to obtain. For example, the equations of the equivalent model can be written as:

$$\rho_f \sum_{\nu} a_{\nu} D^{\nu} \left[ \frac{\partial v_i}{\partial t} \right] = -\nabla_i p, \quad \frac{1}{K_a} \sum_{\lambda} b_{\lambda} D^{\lambda} \left[ \frac{\partial p}{\partial t} \right] = -\nabla \cdot \mathbf{v}. \quad [8.6]$$

An alternative approach to this problem is to consider the asymptotic expressions of  $\alpha(\omega)$  and  $\beta(\omega)$  when  $\omega$  tends towards zero and infinity. In this case, we obtain equations that are simple.

The fact that we should consider several equations (one for each frequency domain) may appear to be a major disadvantage of the method. Of course a situation with a single equation would be more interesting. However, we know that the relative importance of the effects governing the behavior of the fluid in the porous medium is significantly changed when the frequency range varies from low to high frequencies. In this case, it seems reasonable for the laws of physics that govern the propagation to be different from one domain to the another. We will therefore study the time-domain equations of propagation at low and high frequencies.

## 8.2. Inertial regime (high frequency approximation) [FEL 00]

In this frequency range, the asymptotic development of the results obtained by Johnson [JOH 86] and Allard [ALL 92b] for the dynamic tortuosity and compressibility can be expressed in the following form:

$$\alpha(\omega) = \alpha_{\infty} \left( 1 + \frac{2}{\Lambda} \left( \frac{\eta}{j\omega\rho_0} \right)^{1/2} \right), \quad [8.7]$$

$$\beta(\omega) = 1 + \frac{2(\gamma - 1)}{\Lambda'} \left( \frac{\eta}{P_r\rho_0} \right)^{1/2} \left( \frac{1}{j\omega} \right)^{1/2}. \quad [8.8]$$

To return to the time domain, we can use the temporal equivalent of  $j\omega$ , which is the operator  $\partial/\partial t$ . The high frequency expression of  $\alpha(\omega)$  and  $\beta(\omega)$  includes the term  $\sqrt{1/j\omega}$ , whose equivalent expression in the time domain is a fractional derivative of the order  $1/2$ . The definition of a fractional derivative  $D^{\nu}[x(t)]$  of order  $\nu$  is given by:

$$D^{\nu}[x(t)] = \frac{1}{\Gamma(-\nu)} \int_0^t (t-u)^{-\nu-1} x(u) du, \quad [8.9]$$

where  $\Gamma$  is the Gamma function.

According to definition [8.9], the expressions of the response factors  $\alpha$  and  $\beta$  are given in the time domain by:

$$\alpha(\omega) \xrightarrow{t} \alpha_\infty \left( \delta(t) + \frac{2}{\Lambda} \left( \frac{\eta}{\rho_f \pi} \right)^{1/2} t^{-1/2} \right) *, \quad [8.10]$$

$$\beta(\omega) \xrightarrow{t} \left( \delta(t) + \frac{2(\gamma - 1)}{\Lambda'} \left( \frac{\eta}{Pr \rho_f \pi} \right)^{1/2} t^{-1/2} \right) *, \quad [8.11]$$

where  $*$  is the time domain convolution, and  $\delta(t)$  represents the Dirac function. The constitutive equations thus yield:

$$\rho_f \alpha_\infty \frac{\partial v}{\partial t} + 2 \frac{\rho_f \alpha_\infty}{\Lambda} \left( \frac{\eta}{\pi \rho_f} \right)^{1/2} \int_0^t \frac{\partial v / \partial t'}{\sqrt{t - t'}} dt' = - \frac{\partial p}{\partial x}, \quad [8.12]$$

$$\frac{1}{K_a} \frac{\partial p}{\partial t} + 2 \frac{\gamma - 1}{K_a \Lambda'} \left( \frac{\eta}{\pi Pr \rho_f} \right)^{1/2} \int_0^t \frac{\partial p / \partial t'}{\sqrt{t - t'}} dt' = - \frac{\partial v}{\partial x}. \quad [8.13]$$

Note that for the first equation, for example, the first term represents a force related to inertial effects, and the second term (with the fractional derivative) represents a force due to the viscous process. Thus, the dispersion is expressed by a memory effect that manifests itself through the convolution operation with the fractional derivative.

The wave equation can be deduced from relationships [8.12] and [8.13] by a basic calculation:

$$\frac{\partial^2 v(x, t)}{\partial x^2} - A \frac{\partial^2 v(x, t)}{\partial t^2} - B \int_{-\infty}^t \frac{\partial^2 v(x, t) / \partial t'^2}{\sqrt{t - t'}} dt' - C \frac{\partial v(x, t)}{\partial t} = 0, \quad [8.14]$$

where the coefficients are given by:

$$A = \frac{\rho_f \alpha_\infty}{K_a}, \quad B = \frac{2\alpha_\infty}{K_a} \sqrt{\frac{\rho_f \eta}{\pi}} \left( \frac{1}{\Lambda} + \frac{\gamma - 1}{\sqrt{Pr} \Lambda'} \right), \quad C = \frac{4\alpha_\infty(\gamma - 1)\eta}{K_a \Lambda \Lambda' \sqrt{Pr}}.$$

The first term is related to the speed of the wave  $c = A^{-1/2}$  in the fluid saturating the porous medium, where the density of the fluid is changed by a factor  $\alpha_\infty$ . The other factors depend mainly on the viscous and thermal characteristic lengths  $\Lambda$  and  $\Lambda'$ , and express the interactions between the fluid and the structure. The knowledge of these coefficients can be traced back to the tortuosity and the characteristic lengths. We first focus on Green's function of the propagation equation, which solves the opposite problem for the characterization of the environment.

### 8.2.1. A semi-infinite medium [FEL 03a, FEL 01]

It is still possible to write equation [8.14] in terms of distributions as:

$$\begin{aligned} \frac{\partial^2 v(x, t)}{\partial x^2} - \int_0^t \frac{\partial^2 v(x, t')}{\partial t'^2} \left( \frac{1}{c^2} \delta(t - t') + CH(t - t') + \frac{B}{\sqrt{t - t'}} \right) dt' \\ = C \cdot \frac{\partial v(x, 0)}{\partial t} \end{aligned} \quad [8.15]$$

where  $\delta$  and  $H(t)$  are the Dirac and the Heaviside distributions, respectively. We propose solving this equation using the Laplace method. Writing  $V(x, z) = \mathcal{L}[v(x, t)]$  the Laplace transform of  $v(x, t)$ , with respect to the variable  $t$ :

$$V(x, z) = \mathcal{L}[v(x, t)] = \int_0^\infty e^{-zt} v(x, t) dt.$$

The Laplace transform of equation [8.15] reads:

$$\begin{aligned} \frac{\partial^2 V(x, z)}{\partial x^2} - z^2 \left( \frac{1}{c^2} + \frac{C}{z} + B\sqrt{\frac{\pi}{z}} \right) V(x, z) \\ = - \left( \frac{1}{c^2} + B\sqrt{\frac{\pi}{z}} \right) \cdot \left( zv(x, 0) + \frac{\partial v(x, 0)}{\partial t} \right) - C \cdot v(x, 0). \end{aligned} \quad [8.16]$$

Taking into account the initial conditions that reflect that the field is zero in the material for  $t < 0$ ,

$$v(x, 0) = \frac{\partial v(x, 0)}{\partial t} = 0, \quad [8.17]$$

equation [8.16] simplifies to:

$$\frac{\partial^2 V(x, z)}{\partial x^2} - z^2 \left( \frac{1}{c^2} + \frac{C}{z} + \beta\sqrt{\frac{\pi}{z}} \right) V(x, z) = 0 \quad [8.18]$$

which is a differential equation of the second order with constant coefficients, whose characteristic equation is:

$$r^2 - z^2 \left( \frac{1}{c^2} + \frac{C}{z} + \beta\sqrt{\frac{\pi}{z}} \right) = 0. \quad [8.19]$$

The general solution can be written as:

$$V(x, z) = e^{-\frac{x}{c}\sqrt{f(z)}} \Phi(z) + e^{\frac{x}{c}\sqrt{f(z)}} \Psi(z) \quad [8.20]$$

where:

$$\begin{aligned} f(z) &= z^2 \left( 1 + \frac{Cc^2}{z} + \beta c^2 \sqrt{\frac{\pi}{z}} \right) = z^2 + \beta c^2 \sqrt{\pi} z \sqrt{z} + Czc^2 \\ &= z(z + b' \sqrt{z} + c'), \end{aligned}$$

with:

$$b' = \beta c^2 \sqrt{\pi}, \quad c' = C \cdot c^2. \quad [8.21]$$

The functions  $\Phi(z)$  and  $\Psi(z)$ , which are the constants of integration, are  $x$ -independent.

As  $V(x, z)$  keeps finite values at infinity, the second term must be set to zero, thus we have:

$$V(x, z) = e^{-\frac{x}{c} \sqrt{f(z)}} \Phi(z). \quad [8.22]$$

The solution  $v(x, t)$  is therefore the inverse Laplace transform of  $V(x, z)$ . It is the convolution of the inverse Laplace transforms of  $\exp(-\frac{x}{c} \sqrt{f(z)})$  and  $\Phi(z)$ . To calculate:

$$\mathcal{L}^{-1} \left( e^{-\frac{x}{c} \sqrt{f(z)}} \right), \quad [8.23]$$

we write  $\Delta^2 = b'^2 - 4c'$ . If  $b'^2 - 4c' \geq 0$  (i.e.  $\Delta^2 \geq 0$ ) then  $f(z)$  is simply written:

$$f(z) = z \left( \left( \sqrt{z} + \frac{b'}{2} \right)^2 - \frac{\Delta^2}{4} \right), \quad [8.24]$$

which is always positive since  $c' > 0$  and  $z > 0$ . We therefore have:

$$V(x, z) = \phi(z) \exp \left( -\frac{x}{c} \sqrt{\left( z + \frac{b'}{2} \sqrt{z} \right)^2 - \left( \frac{\Delta \sqrt{z}}{2} \right)^2} \right). \quad [8.25]$$

The form of the solution primarily depends on the value of  $\Delta$ .

Cases where  $\Delta^2 = 0 \implies b'^2 = 4 \cdot c'$

In this case:

$$V(x, z) = \phi(z) \exp \left( -\frac{x}{c} \left( z + \frac{b'}{2} \sqrt{z} \right) \right). \quad [8.26]$$

Knowing that:

$$\mathcal{L}^{-1} \exp \left( -\frac{x}{c} z \right) = \delta(t - x/c), \quad [8.27]$$

and that:

$$\mathcal{L}^{-1}\left(\exp\left(-\frac{b'x}{2c}\sqrt{z}\right)\right) = \frac{1}{4\sqrt{\pi}} \frac{b'x}{c} \frac{1}{t^{3/2}} \exp\left(-\frac{b'^2x^2}{16c^2t}\right), \quad [8.28]$$

we obtain:

$$\begin{aligned} & \mathcal{L}^{-1}\left(\exp\left(-\frac{x}{c}\left(z + \frac{b'}{2}\sqrt{z}\right)\right)\right) \\ &= \mathcal{L}^{-1}\left(\exp\left(-\frac{x}{c}z\right)\right) * \mathcal{L}^{-1}\left(\exp\left(-\frac{b'x}{2c}\sqrt{z}\right)\right), \end{aligned}$$

as:

$$\begin{aligned} & \mathcal{L}^{-1}\left(\exp\left(-\frac{x}{c}\left(z + \frac{b'}{2}\sqrt{z}\right)\right)\right) \\ &= \frac{1}{4\sqrt{\pi}} \frac{b'x}{c} \frac{1}{(t - x/c)^{3/2}} \exp\left(-\frac{b'^2x^2}{16c^2(t - x/c)}\right). \end{aligned}$$

The solution  $v(x, t)$  is given, in this case, by:

$$v(x, t) = \begin{cases} 0 & \text{if } 0 \leq t \leq x/c, \\ \frac{1}{4\sqrt{\pi}} \frac{b'x}{c} \int_{x/c}^t \frac{1}{(\tau - x/c)^{3/2}} \times \exp\left(-\frac{b'^2x^2}{16c^2(\tau - x/c)}\right) \phi(t - \tau) d\tau & \text{if } t > x/c \end{cases} \quad [8.29]$$

where  $\phi(t)$  is the inverse Laplace transform of  $\Phi(z)$ :  $\phi(t) = \mathcal{L}^{-1}(\Phi(z))$ .

Cases where  $\Delta^2 > 0 \implies b'^2 > 4 \cdot c'$

Calculation of the solution is developed in article [FEL 01]. In this case, the solution of the equation reads

$$\begin{cases} 0 & \text{if } 0 \leq t \leq x/c, \\ \frac{x}{c} \int_{x/c}^t \left( \frac{b'}{4\sqrt{\pi}} \frac{1}{(\tau - x/c)^{3/2}} \exp\left(-\frac{b'^2x^2}{16c^2(\tau - x/c)}\right) + \Delta \int_0^{\tau - x/c} h(\xi) d\xi \right) \phi(t - \tau) d\tau. \end{cases}$$

In this expression, we note that if  $\Delta = 0$ , we reobtain the solution given by equation [8.29]. We can also verify that  $v(0, t) = \phi(t)$ .



### 8.2.2. Cases of a finite medium

In the case of porous materials with a medium or high porosity, it is not always possible to ignore the effect of the waves reflected by the interfaces. To take into account this effect, we must solve the problem of the propagation for a slice of material of finite thickness. In this part, we discuss the resolution of the problem of fields, reflected and transmitted by a slice of porous material, at high frequencies.

It is assumed that the porous material occupies the spatial domain  $0 \leq x \leq L$ . An acoustic pulse arrives at  $x = 0$  under a normal incidence on the material at time  $t = 0$ . For  $0 \leq x \leq L$ , the acoustic pulse verifies the propagation equation at  $t = 0$ .

$$\frac{\partial^2 p(x, t)}{\partial x^2} - \left( \frac{1}{c^2} \delta(t) + CH(t) + \frac{B}{\sqrt{t}} \right) * \frac{\partial^2 p(x, t)}{\partial t^2} = 0. \quad [8.30]$$

where  $H(t)$  is the Heaviside function. The pressure field is assumed to be continuous on the boundaries of the material.

$$p(0^+, t) = p(0^-, t), \quad p(L^-, t) = p(L^+, t) \quad [8.31]$$

where  $\pm$  indicates the limit to the left and to the right respectively. [8.31] verifies the initial conditions:

$$p(x, t)|_{t=0} = \frac{\partial p}{\partial t}|_{t=0} = 0. \quad [8.32]$$

The total field in the domain  $x \leq 0$  is the sum of the incident and reflected fields:

$$p_1(x, t) = p^i(t, x) + p^r(t, x) \quad x < 0. \quad [8.33]$$

Here,  $p_1(x, t)$  is the pressure field in the domain  $x < 0$ ,  $p^i$  and  $p^r$  represent the incident and reflected fields, respectively. The transmitted field in the domain on the right of the porous medium has the following form:

$$p_3(x, t) = p^t \left( t - \frac{L}{c} - \frac{(x - L)}{c_0} \right), \quad x > L. \quad [8.34]$$

The incident, reflected and transmitted fields are connected by the reflection/transmission operators in accordance with the following relationships:

$$\begin{aligned} p^r(t) &= \int_0^t \tilde{R}(\tau) p^i \left( t - \tau + \frac{x}{c_0} \right) d\tau = \tilde{R}(t) * p^i(t) * \delta \left( t + \frac{x}{c_0} \right), \\ p^t(t) &= \int_0^t \tilde{T}(\tau) p^i \left( t - \tau - \frac{L}{c} - \frac{(x - L)}{c_0} \right) d\tau \\ &= \tilde{T}(t) * p^i(t) * \delta \left( t - \frac{L}{c} - \frac{(x - L)}{c_0} \right). \end{aligned}$$

In these equations, the functions  $\tilde{R}$  and  $\tilde{T}$  represent the reflection and transmission kernels respectively, for an incidence coming from the left. We can also note that the limits of integration are taken between 0 and  $t$ , which corresponds with the arrival of the incident wave front on the material at time  $t = 0$ .

These reflection/transmission operators are independent of the incident field and only depend on the properties of the material.

The resolution of equation [8.30], taking into account conditions [8.31] and [8.32], uses the Laplace's method. Note:

$$P(x, z) = \mathcal{L}[p(x, t)], \quad [8.35]$$

the Laplace transform of  $p(x, t)$ . We also have:

$$\mathcal{L}[\delta(t)] = 1, \quad \mathcal{L}[H(t)] = \frac{1}{z} \quad \text{and} \quad \mathcal{L}\left[\frac{1}{\sqrt{t}}\right] = \sqrt{\frac{\pi}{z}}. \quad [8.36]$$

The Laplace transform of equation [8.30] satisfying the initial conditions [8.32] is given by:

$$\frac{\partial^2 P_2(x, z)}{\partial x^2} - \frac{f(z)}{c^2} P_2(x, z) = 0 \quad [8.37]$$

where  $f(z) = z^2 + b'z\sqrt{z} + c'z$ ,  $b' = B \cdot c^2\sqrt{\pi}$  and  $c' = Cc^2$ .

The Laplace transform of the field outside the material is:

$$P_1(x, z) = \left[ \exp\left(-z\frac{x}{c_0}\right) + R(z) \exp\left(z\frac{x}{c_0}\right) \right] P(z), \quad x \leq 0 \quad [8.38]$$

$$P_3(x, z) = T(z) \left[ \exp\left(-\left(\frac{L}{c} + \frac{(x-L)}{c_0}\right)z\right) \right] P(z), \quad x \geq 0 \quad [8.39]$$

where  $P_1(x, z)$  and  $P_3(x, z)$  are the Laplace transforms of the field to the left and to the right of the material respectively;  $P(z)$  is the Laplace transform of the incident field  $p^i(t)$  and  $R(z)$  and  $T(z)$  are the Laplace transforms of the reflection and transmission kernels, respectively. Using conditions [8.31], we have:

$$P_2(0^+, z) = P_1(0^-, z) \quad \text{and} \quad P_2(L^-, z) = P_3(L^+, z), \quad [8.40]$$

hence the following equalities:

$$P_1(0^-, z) = (1 + R(z))P(z), \quad [8.41]$$

$$P_3(L^-, z) = T(z) \exp\left(-\frac{L}{c}z\right)P(z). \quad [8.42]$$

From equations [8.37] and [8.40] we can infer the expression of the field  $P_2(x, z)$  inside the material:

$$P_2(x, z) = P_1(0^-, z) \frac{\sinh\left(\frac{L-x}{c} \sqrt{f(z)}\right)}{\sinh\frac{L}{c} \sqrt{f(z)}} + P_3(L^+, z) \frac{\sinh\left(\frac{x}{c} \sqrt{f(z)}\right)}{\sinh\frac{L}{c} \sqrt{f(z)}}. \quad [8.43]$$

The inverse Laplace transform of  $\exp(-k\sqrt{f(z)})$ , where  $k$  is a positive constant, is given by:

$$F(t, k) = \begin{cases} 0 & \text{if } 0 \leq t \leq k \\ \Xi(t) + \Delta \int_0^{t-k} h(t, \xi) d\xi & \text{if } t \geq k \end{cases} \quad [8.44]$$

with:

$$\Xi(t) = \frac{b'}{4\sqrt{\pi}} \frac{k}{(t-k)^{3/2}} \exp\left(-\frac{b'^2 k^2}{16(t-k)}\right). \quad [8.45]$$

The function  $h(\tau, \xi)$  has the following form:

$$h(\xi, \tau) = -\frac{1}{4(\pi\xi)^{3/2}} \frac{1}{\sqrt{(\tau-\xi)^2 - k^2}} \int_{-1}^1 \frac{\exp\left(-\frac{\chi(\mu, \tau, \xi)}{2}\right) (\chi(\mu, \tau, \xi) - 1) \mu d\mu}{\sqrt{1-\mu^2}}$$

where  $\chi(\mu, \tau, \xi) = (\Delta\mu\sqrt{(\tau-\xi)^2 - k^2} + b'(\tau-\xi))^2/8\xi$ , with  $b' = Bc_0^2\sqrt{\pi}$ ,  $c' = C \cdot c_0^2$  and  $\Delta = b'^2 - 4c'$ . The inverse Laplace transform of  $P_2(x, z)$  gives us the complete and general solution of the propagation equation in the time domain for porous materials, considering the multiple reflections at the interfaces located at  $x = 0$  and  $x = L$  (see [FEL 03b]):

$$\begin{aligned} p_2(x, t) = & \sum_{n \geq 0} \left[ F\left(t, 2n\frac{L}{c} + \frac{x}{c}\right) - F\left(t, (2n+2)\frac{L}{c} - \frac{x}{c}\right) \right] * p_1(0, t) \\ & + \sum_{n \geq 0} \left[ F\left(t, (2n+1)\frac{L}{c} - \frac{x}{c}\right) - F\left(t, (2n+1)\frac{L}{c} + \frac{x}{c}\right) \right] * p_3(L, t), \end{aligned}$$

which can also be written as:

$$\begin{aligned} p_2(x, t) = & \sum_{n \geq 0} \int_{2n\frac{L}{c} + \frac{x}{c}}^t F\left(\tau, 2n\frac{L}{c} + \frac{x}{c}\right) p_1(0, t-\tau) d\tau \\ & - \sum_{n \geq 0} \int_{(2n+2)\frac{L}{c} - \frac{x}{c}}^t F\left(\tau, (2n+2)\frac{L}{c} - \frac{x}{c}\right) p_1(0, t-\tau) d\tau \end{aligned}$$

$$\begin{aligned}
& + \sum_{n \geq 0} \int_{(2n+1)\frac{L}{c} - \frac{x}{c}}^t F\left(\tau, (2n+1)\frac{L}{c} - \frac{x}{c}\right) p_3(L, t - \tau) d\tau \\
& - \sum_{n \geq 0} \int_{(2n+1)\frac{L}{c} + \frac{x}{c}}^t F\left(\tau, (2n+1)\frac{L}{c} + \frac{x}{c}\right) p_3(L, t - \tau) d\tau.
\end{aligned}$$

### 8.2.3. Reflection and transmission operators

To express the reflection and transmission coefficients, it is necessary to write the conditions of conservation of the flow on the interfaces  $x = 0$  and  $x = L$ . The Euler equations in medium (1) ( $x \leq 0$ ) and medium (2) ( $0 \leq x \leq L$ ) are:

$$\rho_f \frac{\partial v_1(x, t)}{\partial t} \Big|_{x=0-} = - \frac{\partial p_1(x, t)}{\partial x} \Big|_{x=0-} \quad x \leq 0, \quad [8.46]$$

$$\rho_f \tilde{\alpha}(t) * \frac{\partial v_2(x, t)}{\partial t} \Big|_{x=0+} = - \frac{\partial p_2(x, t)}{\partial x} \Big|_{x=0+} \quad 0 \leq x \leq L, \quad [8.47]$$

where  $v_1(x, t)$  and  $v_2(x, t)$  are the particle velocity fields in portions (1) and (2) of the material, respectively. The conservation of the flow is written in accordance with:

$$v_1(x, t) = \phi v_2(x, t). \quad [8.48]$$

Using equations [8.47] and [8.48], we can easily write:

$$\tilde{\alpha}(t) * \frac{\partial p_1(x, t)}{\partial x} \Big|_{x=0} = \phi \frac{\partial p_2(x, t)}{\partial x} \Big|_{x=0}, \quad [8.49]$$

with:

$$\frac{\partial p_1(x, t)}{\partial x} \Big|_{x=0} = \frac{1}{c_0} (-\delta(t) + \tilde{R}(t)) * \frac{\partial p^i(t)}{\partial t}. \quad [8.50]$$

The Laplace transform of equation [8.49] gives the relationship between the reflection and transmission kernels:

$$\begin{aligned}
& (R(z) - 1) \sinh\left(\frac{L}{c} \sqrt{f(z)}\right) \\
& = \frac{\phi c_0}{c} \frac{\sqrt{f(z)}}{z\alpha(z)} \left[ T(z) \exp\left(\frac{-L}{c}\right) - (1 + R(z)) \cosh\left(\frac{L}{c} \sqrt{f(z)}\right) \right],
\end{aligned} \quad [8.51]$$

where  $\alpha(z)$  is the Laplace transform of  $\tilde{\alpha}(t)$ .

On the interface  $x = L$ , the Euler equation written for media (2) and (3),

$$\begin{aligned}\rho_f \tilde{\alpha}(t) * \frac{\partial v_2(x, t)}{\partial t} \Big|_{x=L} &= - \frac{\partial p_2(x, t)}{\partial x} \Big|_{x=L}, \\ \rho_f \frac{\partial v_3(x, t)}{\partial t} \Big|_{x=L} &= - \frac{\partial p_3(x, t)}{\partial x} \Big|_{x=L},\end{aligned}\tag{8.52}$$

and the continuity condition of the flow,

$$v_3(x, t) = \phi v_2(x, t),\tag{8.53}$$

lead to the system:

$$\tilde{\alpha}(t) * \frac{\partial p_3(x, t)}{\partial x} \Big|_{x=L} = \phi \frac{\partial p_2(x, t)}{\partial x} \Big|_{x=L},\tag{8.54}$$

$$\frac{\partial p_3(x, t)}{\partial x} \Big|_{x=L} = - \frac{1}{c_0} \tilde{T}(t) * \frac{\partial p^i}{\partial t} \left( t - \frac{L}{c} \right).\tag{8.55}$$

Given these equations, we find:

$$\begin{aligned}T(z) \exp \left( - \frac{L}{c} z \right) \sinh \left( \frac{L}{c} \sqrt{f(z)} \right) \\ = \frac{\phi c_0}{c} \frac{\sqrt{f(z)}}{z \alpha(z)} \left[ - T(z) \exp \left( - \frac{L}{c} z \right) \cosh \left( \frac{L}{c} \sqrt{f(z)} \right) + 1 + R(z) \right].\end{aligned}\tag{8.56}$$

When the following approximation

$$\frac{\phi c_0}{c} \frac{\sqrt{f(z)}}{z \alpha(z)} \simeq \frac{\phi}{\sqrt{\alpha_\infty}},\tag{8.57}$$

is valid, the system given by equations [8.51] and [8.56] has the following solution for the reflection and transmission coefficients  $R(z)$  and  $T(z)$ :

$$R(z) = \frac{\left( - \frac{\phi^2}{\alpha_\infty} + 1 \right) \sinh \left( \frac{L}{c} \sqrt{f(z)} \right)}{2 \frac{\phi}{\sqrt{\alpha_\infty}} \cosh \left( \frac{L}{c} \sqrt{f(z)} \right) + \left( \frac{\phi^2}{\alpha_\infty} + 1 \right) \sinh \left( \frac{L}{c} \sqrt{f(z)} \right)}\tag{8.58}$$

$$T(z) = \frac{2 \frac{\phi}{\sqrt{\alpha_\infty}} \exp \left( \frac{L}{c} z \right)}{2 \frac{\phi}{\sqrt{\alpha_\infty}} \cosh \left( \frac{L}{c} \sqrt{f(z)} \right) + \left( \frac{\phi^2}{\alpha_\infty} + 1 \right) \sinh \left( \frac{L}{c} \sqrt{f(z)} \right)}.\tag{8.59}$$

After expanding the expressions of equations [8.58] and [8.59] in a series of exponentials ([FEL 03b]), their inverse Laplace transforms give us the expressions for the reflection and transmission kernels:

$$\begin{aligned} \frac{\tilde{R}(t)}{\left(\frac{-\phi + \sqrt{\alpha_\infty}}{\phi + \sqrt{\alpha_\infty}}\right)} &= \sum_{n \geq 0} \left(\frac{\phi - \sqrt{\alpha_\infty}}{\phi + \sqrt{\alpha_\infty}}\right)^{2n} \left[ F\left(t, 2n \frac{L}{c}\right) - F\left(t, (2n + 2) \frac{L}{c}\right) \right], \\ \frac{\tilde{T}(t)}{\left(\frac{4\phi\sqrt{\alpha_\infty}}{(\sqrt{\alpha_\infty} + \phi)^2}\right)} &= \sum_{n \geq 0} \left(\frac{\phi - \sqrt{\alpha_\infty}}{\phi + \sqrt{\alpha_\infty}}\right)^{2n} F\left(t + \frac{L}{c_0}, (2n + 1) \frac{L}{c}\right). \end{aligned} \quad [8.60]$$

These expressions take into account the multiple reflections in the material. As the attenuation in the porous media is sufficiently high, the waves reflected more than twice can be neglected.

Considering only one reflection on the first and second interfaces,  $x = 0$  and  $x = L$ , the pressure field  $p_2(x, t)$  inside the material reads:

$$\begin{aligned} p_2(x, t) &= \left[ F\left(t, \frac{x}{c}\right) - F\left(t, \frac{2L}{c} - \frac{x}{c}\right) \right] * p_1(0, t) \\ &\quad + \left[ F\left(t, \frac{L}{c} - \frac{x}{c}\right) - F\left(t, \frac{L}{c} + \frac{x}{c}\right) \right] * p_3(L, t). \end{aligned} \quad [8.61]$$

This expression can also be written as:

$$\begin{aligned} p_2(x, t) &= \int_{\frac{x}{c}}^t F\left(\tau, \frac{x}{c}\right) p_1(0, t - \tau) d\tau \\ &\quad - \int_{\frac{2L}{c} - \frac{x}{c}}^t F\left(\tau, \frac{2L}{c} - \frac{x}{c}\right) p_1(0, t - \tau) d\tau \\ &\quad + \int_{\frac{L}{c} - \frac{x}{c}}^t F\left(\tau, \frac{L}{c} - \frac{x}{c}\right) p_3(L, t - \tau) d\tau \\ &\quad - \int_{\frac{L}{c} + \frac{x}{c}}^t 6tF\left(\tau, \frac{L}{c} + \frac{x}{c}\right) p_3(L, t - \tau) d\tau. \end{aligned}$$

The reflection operator is then given by:

$$\tilde{R}(t) = \frac{\sqrt{\alpha_\infty} - \phi}{\sqrt{\alpha_\infty} + \phi} \delta(t) - \frac{4\phi\sqrt{\alpha_\infty}(\sqrt{\alpha_\infty} - \phi)}{(\sqrt{\alpha_\infty} + \phi)^3} F\left(t, \frac{2L}{c}\right), \quad [8.62]$$

while the transmission operator is given by:

$$\tilde{T}(t) = \frac{4\phi\sqrt{\alpha_\infty}}{(\phi + \sqrt{\alpha_\infty})^2} F\left(t + \frac{L}{c}, \frac{L}{c}\right). \quad [8.63]$$

### 8.3. Viscous regime (low frequency approximation)

In the low frequency range, the asymptotic developments of the functions  $\alpha(\omega)$  and  $\beta(\omega)$  are:

$$\alpha(\omega) = \alpha_0 \left( 1 + \frac{\eta\phi}{j\omega\alpha_0\rho_f k_0} \right), \quad [8.64]$$

$$\beta(\omega) = \gamma - \frac{(\gamma - 1)\rho_f k'_0 P_r}{\eta\phi} j\omega. \quad [8.65]$$

In the time domain, they correspond to the operators:

$$\alpha(\omega) \xrightarrow{t} \alpha_0 \left( I + \frac{\eta\phi}{\alpha_0\rho_f k_0} \partial_t^{-1} \right), \quad [8.66]$$

$$\beta(\omega) \longrightarrow t \gamma - \frac{(\gamma - 1)\rho_f k'_0 P_r}{\eta\phi} \partial_t \quad [8.67]$$

where  $I$  is the identity operator and  $\partial_t^{-1}g(t) = \int_0^t g(t')dt'$ ;  $\partial_t$  is the partial derivative with respect to time  $t$ . For a wave propagating along the direction  $Ox$ , the generalized form of the equations,

$$\rho_0\alpha(\omega)\frac{\partial v}{\partial t} = -\frac{\partial p}{\partial x}, \quad K^{-1}(\omega)\frac{\partial p}{\partial t} = -\frac{\partial v}{\partial x}$$

is therefore given by:

$$\rho_f\alpha_0\frac{\partial v(x,t)}{\partial t} + \frac{\eta\phi}{k_0}v(x,t) = -\frac{\partial p(x,t)}{\partial x}, \quad [8.68]$$

$$\frac{\gamma}{K_a}\frac{\partial p(x,t)}{\partial t} - (\gamma - 1) \cdot \left( \frac{\rho_f k'_0 P_r}{K_a\eta\phi} \right) \frac{\partial^2 p(x,t)}{\partial t^2} = -\frac{\partial v(x,t)}{\partial x}. \quad [8.69]$$

In this approximation, the first term of Euler's equation [8.68] corresponds to the low frequency inertial force. The second term expresses the proportionality between the gradient of the pressure ( $\frac{\partial p}{\partial x}$ ) and the velocity given by Darcy [JOH 86]. In the very low frequency range, the inertial effects are negligible, and the only force that opposes the gradient of pressure is the force due to the viscous effects, resulting in diffusive properties (no propagation) of the acoustic wave.

Using these two relationships the propagation equation is:

$$\frac{\partial^2 v(x, t)}{\partial x^2} - \frac{1}{c^2} \frac{\partial^2 v(x, t)}{\partial t^2} - \varrho \frac{\partial v(x, t)}{\partial t} + \varpi \frac{\partial^3 v(x, t)}{\partial t^3} = 0. \quad [8.70]$$

The coefficients of this equation are:

$$\frac{1}{c^2} = \frac{\rho_f}{K_a} \left( \alpha_0 \gamma - \frac{(\gamma - 1) P_r k'_0}{k_0} \right), \quad \varrho = \frac{\eta \phi}{\rho_0 k_0} = \frac{\phi \sigma \gamma}{K_a} \quad [8.71]$$

and:

$$\varpi = - \frac{\rho_0^2 (\gamma - 1) k'_0 P_r \alpha_0}{K_a \eta \phi}. \quad [8.72]$$

Resolution of this equation is achieved using the Laplace transform. The expression of the solution in the time domain enables us to determine the reflection and transmission operators, which depend on the parameters characterizing the propagation ( $\alpha_0$ ,  $k'_0$ ,  $k_0$  or  $\sigma$ ) in this frequency range.

### 8.3.1. Resolution for the semi-infinite medium

We consider the equation obtained in the section above:

$$\frac{\partial^2 v(x, t)}{\partial x^2} - \frac{1}{c^2} \frac{\partial^2 v(x, t)}{\partial t^2} - \varrho \frac{\partial v(x, t)}{\partial t} + \varpi \frac{\partial^3 v(x, t)}{\partial t^3} = 0. \quad [8.73]$$

where  $\varrho$ ,  $\varpi$  and  $c$  are three positive real numbers. Writing  $V(x, z)$  the Laplace transform of  $v(x, t)$ , with respect to the time variable  $t$ , and imposing the initial conditions:

$$v(x, 0) = \frac{\partial v}{\partial t}(x, 0) = 0, \quad [8.74]$$

the Laplace transform of equation [8.73] leads to the following equation:

$$\frac{\partial^2 V(x, z)}{\partial x^2} - \frac{1}{c^2} (-b' z^3 + z^2 + c' z) V(x, z) = 0 \quad [8.75]$$

with  $b' = \varpi c^2$  and  $c' = \varrho c^2$ . It is a second order differential equation with constant coefficients. The roots of the characteristic equation,

$$r^2 - \frac{1}{c^2} (-b' z^3 + z^2 + c' z) = 0 \quad [8.76]$$

are:

$$r_{1,2} = \pm \frac{x}{c} \sqrt{-b' z^3 + z^2 + c' z}. \quad [8.77]$$



The general solution of [8.75] reads:

$$\begin{aligned}
 V(x, z) &= \exp\left(-\frac{x}{c}\sqrt{-b'z^3 + z^2 + c'z}\right)\Phi(z) \\
 &\quad + \exp\left(\frac{x}{c}\sqrt{-b'z^3 + z^2 + c'z}\right)\Psi(z) \\
 &= V_1(x, z) + V_2(x, z).
 \end{aligned} \tag{8.78}$$

To express the solution in the time domain, we have to calculate the inverse Laplace transforms:  $\mathcal{L}^{-1}[V_1(x, z)]$  and  $\mathcal{L}^{-1}[V_2(x, z)]$ . Since the transform  $\mathcal{L}^{-1}[V_2(x, z)]$  is inferred from  $\mathcal{L}^{-1}[V_1(x, z)]$  replacing  $x$  with  $-x$  and  $\Phi(z)$  with  $\Psi(z)$ , we just have to calculate  $\mathcal{L}^{-1}[V_1(x, z)]$ .

The inverse Laplace transform of the function  $\exp(-\frac{x}{c}\sqrt{-b'z^3 + z^2 + c'z})$  is

$$\begin{aligned}
 \mathcal{L}^{-1}\left[\exp\left(-\frac{x}{c}\sqrt{-b'z^3 + z^2 + c'z}\right)\right] \\
 = \frac{1}{\sqrt{\pi}}\frac{x}{c}\sqrt{b'}\left[\frac{\sqrt{\Delta}}{4b'}\frac{1}{t^{3/2}}\exp\left(-\frac{x^2\Delta}{16c^2b't}\right) - \frac{1}{\pi\sqrt{\pi}}\int_{\frac{x}{c}\sqrt{b'}}^{\infty}\frac{F(\eta, t)}{\sqrt{\eta^2 - \frac{x^2}{c^2}b'}}d\eta\right]
 \end{aligned}$$

where  $\Delta = 1 + 4b'c'$  and:

$$\begin{aligned}
 F(\eta, t) &= \int_0^{\infty} \exp(-st)\sqrt{s}(s + 1/2b')G(\eta, s)ds \\
 G(\eta, s) &= \int_{-1}^1 \cos\left[\frac{\sqrt{\Delta}}{2b'}\eta\sqrt{s} - y\sqrt{s}(s + 1/2b')\sqrt{\eta^2 - \frac{x^2}{c^2}b'}\right]\frac{ydy}{\sqrt{1-y^2}}.
 \end{aligned}$$

### 8.3.2. Solution in a finite medium

It is assumed that the porous medium is limited in space by the domain  $0 \leq x \leq L$ . To determine the reflection and transmission coefficients, we can calculate their expressions in the Laplace domain, then in the time domain to obtain the reflection and transmission operators.

An acoustic pulse (at low frequency) is sent on a porous material located at  $x = 0$  under a normal incidence, therefore resulting in a pressure field  $p(x, t)$  inside the material which verifies the propagation equation:

$$\frac{\partial^2 p(x, t)}{\partial x^2} - \frac{1}{c^2}\frac{\partial^2 p(x, t)}{\partial t^2} - \varrho\frac{\partial p(x, t)}{\partial t} + \varpi\frac{\partial^3 p(x, t)}{\partial t^3} = 0. \tag{8.79}$$

We suppose that the pressure field is continuous on the boundaries of the material:

$$p(0^+, t) = p(0^-, t), \quad p(L^-, t) = p(L^+, t) \quad [8.80]$$

and satisfies the following initial conditions:

$$p(x, t)|_{t=0} = \frac{\partial p}{\partial t} \Big|_{t=0} = 0. \quad [8.81]$$

The general solution of equation [8.79] in the domain  $x < 0$  is the sum of the incident and reflected waves:

$$p_1(x, t) = p^i(t, x) + p^r(t, x), \quad x < 0. \quad [8.82]$$

Here,  $p_1(x, t)$  represents the field in the region  $x < 0$ ,  $p^i$  and  $p^r$  respectively represent the incident and reflected fields. The field transmitted in the domain  $x > L$  can be written as:

$$p_3(x, t) = p^t \left( t - \frac{L}{c} - \frac{(x-L)}{c_0} \right), \quad x > L. \quad [8.83]$$

The incident, reflected and transmitted fields are related together through the reflection/transmission operators:

$$\begin{aligned} p^r(t) &= \int_0^t \tilde{R}(\tau) p^i \left( t - \tau + \frac{x}{c_0} \right) d\tau \\ &= \tilde{R}(t) * p^i(t) * \delta \left( t + \frac{x}{c_0} \right). \end{aligned} \quad [8.84]$$

$$\begin{aligned} p^t(t) &= \int_0^t \tilde{T}(\tau) p^i \left( t - \tau - \frac{L}{c} - \frac{(x-L)}{c_0} \right) d\tau \\ &= \tilde{T}(t) * p^i(t) * \delta \left( t - \frac{L}{c} - \frac{(x-L)}{c_0} \right). \end{aligned} \quad [8.85]$$

In equations [8.84] and [8.85], the functions  $\tilde{R}$  and  $\tilde{T}$  respectively represent the reflection and transmission kernels for an incident wave arriving from the left side of the medium. Again, the operators are given by equations [8.84] and [8.85] are totally independent of the incident field and only depend on the properties of the material. In the domain  $x \leq 0$ , the field  $p_1(x, t)$  is given by:

$$p_1(x, t) = \left[ \delta \left( t - \frac{x}{c_0} \right) + \tilde{R}(t) * \delta \left( t + \frac{x}{c_0} \right) \right] * p^i(t). \quad [8.86]$$

We now wish to solve the propagation equation [8.79] taking into account the initial and boundary conditions. The Laplace transform of the propagation equation [8.79] satisfying the conditions [8.81] can be written as follows:

$$\frac{\partial^2 P_2(x, z)}{\partial x^2} - \frac{f(z)}{c^2} P_2(x, z) = 0, \quad [8.87]$$

where  $f(z) = -b'z^3 + z^2 + c'z$ ,  $b' = \varpi c^2$  and  $c' = \varrho \cdot c^2$ .

The Laplace transform of the field outside the material is given by:

$$P_1(x, z) = \left[ \exp\left(-z \frac{x}{c_0}\right) + R(z) \exp\left(z \frac{x}{c_0}\right) \right] P(z) \quad x \leq 0, \quad [8.88]$$

$$P_3(x, z) = T(z) \left[ \exp\left(-\left(\frac{L}{c} + \frac{(x-L)}{c_0}\right)z\right) \right] P(z) \quad x \geq 0. \quad [8.89]$$

The Laplace transform of the field is  $P_1(x, z)$  to the left of the material, and  $P_3(x, z)$  to the right of the material.  $P(z)$  is the Laplace transform of the incident field  $p^i(t)$  and  $R(z)$  and  $T(z)$  are the Laplace transforms of the reflection and transmission kernels, respectively.

The Laplace transforms of boundary conditions [8.80] are given by:

$$P_2(0^+, z) = P_1(0^-, z) \quad \text{and} \quad P_2(L^-, z) = P_3(L^+, z). \quad [8.90]$$

Thus, equations [8.88] and [8.89] become, for  $x = 0$  and  $x = L$

$$P_1(0^-, z) = (1 + R(z))P(z), \quad [8.91]$$

$$P_3(L^-, z) = T(z) \exp\left(-\frac{L}{c}z\right)P(z). \quad [8.92]$$

Using equations [8.87] and [8.90], we can deduce the expression of the field inside the material  $P_2(x, z)$

$$P_2(x, z) = P_1(0^-, z) \frac{\sinh\left(\left(\frac{L-x}{c}\sqrt{f(z)}\right)\right)}{\sinh\left(\frac{L}{c}\sqrt{f(z)}\right)} + P_3(L^+, z) \frac{\sinh\left(\left(\frac{x}{c}\sqrt{f(z)}\right)\right)}{\sinh\left(\frac{L}{c}\sqrt{f(z)}\right)}. \quad [8.93]$$

The inverse Laplace transform of  $\exp(-K\sqrt{f(z)})$ , where  $K$  is a real constant, is:

$$F(t, K) = \frac{K\sqrt{b'}}{\sqrt{\pi}} \left[ \Xi(t) - \frac{1}{\pi\sqrt{\pi}} \int_{K\sqrt{b'}}^{\infty} \frac{H(\eta, t)}{\sqrt{\eta^2 - K^2b'}} d\eta \right], \quad [8.94]$$

with:

$$\Xi(t) = \frac{\sqrt{\Delta}}{4b'} \frac{1}{t^{3/2}} \exp\left(-\frac{\Delta t^2}{16b't}\right), \quad [8.95]$$

$$H(\eta, t) = \int_0^\infty \exp(-st) \sqrt{s} \left(s + \frac{1}{2b'}\right) D(\eta, s) ds, \quad [8.96]$$

$$D(\eta, s) = \int_{-1}^1 \cos\left[\frac{\sqrt{\Delta}}{2b'} \eta \sqrt{s} - y \sqrt{s} \left(s + \frac{1}{2b'}\right) \sqrt{\eta^2 - b'K^2}\right] \frac{y dy}{\sqrt{1-y^2}},$$

and  $\Delta' = 1 + 4b'c'$ .

The inverse Laplace transform of  $P_2(x, z)$  gives us a complete solution for the propagation equation in the time domain for a porous material, taking into account the multiple reflections at the interfaces  $x = 0$  and  $x = L$ :

$$\begin{aligned} p_2(x, t) = & \sum_{n \geq 0} \left[ F\left(t, 2n \frac{L}{c} + \frac{x}{c}\right) - F\left(t, (2n+2) \frac{L}{c} - \frac{x}{c}\right) \right] * p_1(0, t) \\ & + \sum_{n \geq 0} \left[ F\left(t, (2n+1) \frac{L}{c} - \frac{x}{c}\right) - F\left(t, (2n+1) \frac{L}{c} + \frac{x}{c}\right) \right] * p_3(L, t). \end{aligned} \quad [8.97]$$

This solution can be also written as:

$$\begin{aligned} p_2(x, t) = & \sum_{n \geq 0} \int_0^t F\left(\tau, 2n \frac{L}{c} + \frac{x}{c}\right) p_1(0, t - \tau) d\tau \\ & - \sum_{n \geq 0} \int_0^t F\left(\tau, (2n+2) \frac{L}{c} - \frac{x}{c}\right) p_1(0, t - \tau) d\tau \\ & + \sum_{n \geq 0} \int_0^t F\left(\tau, (2n+1) \frac{L}{c} - \frac{x}{c}\right) p_3(L, t - \tau) d\tau \\ & - \sum_{n \geq 0} \int_0^t F\left(\tau, (2n+1) \frac{L}{c} + \frac{x}{c}\right) p_3(L, t - \tau) d\tau. \end{aligned} \quad [8.98]$$

### 8.3.3. Reflection and transmission operators

To obtain the expressions of the reflection and transmission coefficients, it is necessary to write the continuity conditions of the flow at the interfaces  $x = 0$  and  $x = L$ . Euler's equations are written in domains (1)  $x \leq 0$  and (2)  $0 \leq x \leq L$  as:

$$\rho_f \frac{\partial v_1(x, t)}{\partial t} \Big|_{x=0^-} = - \frac{\partial p_1(x, t)}{\partial x} \Big|_{x=0^-} \quad x \leq 0, \quad [8.99]$$

$$\rho_f \tilde{\alpha}(t) * \frac{\partial v_2(x, t)}{\partial t} \Big|_{x=0^+} = - \frac{\partial p_2(x, t)}{\partial x} \Big|_{x=0^+} \quad 0 \leq x \leq L, \quad [8.100]$$

where  $v_1(x, t)$  and  $v_2(x, t)$  represent the particle velocity fields in (1) and (2), respectively. The continuity equation of the flow is given by:

$$v_1(x, t) = \phi v_2(x, t). \quad [8.101]$$

From [8.99], [8.100] and [8.101], it is easy to write

$$\tilde{\alpha}(t) * \frac{\partial p_1(x, t)}{\partial x} \Big|_{x=0} = \phi \frac{\partial p_2(x, t)}{\partial x} \Big|_{x=0}, \quad [8.102]$$

with:

$$\frac{\partial p_1(x, t)}{\partial x} \Big|_{x=0} = \frac{1}{c_0} (-\delta(t) + \tilde{R}(t)) * \frac{\partial p^i(t)}{\partial t}. \quad [8.103]$$

The Laplace transform of equation [8.102] gives us a relationship between the reflection and transmission coefficients:

$$\begin{aligned} & (R(z) - 1) \sinh \left( \frac{L}{c} \sqrt{f(z)} \right) \\ &= \frac{\phi c_0}{c} \frac{\sqrt{f(z)}}{z \alpha(z)} \left[ T(z) \exp \left( \frac{-L}{c} \right) - (1 + R(z)) \cosh \left( \frac{L}{c} \sqrt{f(z)} \right) \right], \end{aligned} \quad [8.104]$$

where  $\alpha(z)$  is the Laplace transform of  $\tilde{\alpha}(t)$ .

At the interface  $x = L$ , Euler's equation is written in domains (2) and (3)  $x \geq L$  as:

$$\begin{aligned} \rho_f \tilde{\alpha}(t) * \frac{\partial v_2(x, t)}{\partial t} \Big|_{x=L} &= - \frac{\partial p_2(x, t)}{\partial x} \Big|_{x=L}, \\ \rho_f \frac{\partial v_3(x, t)}{\partial t} \Big|_{x=L} &= - \frac{\partial p_3(x, t)}{\partial x} \Big|_{x=L}. \end{aligned} \quad [8.105]$$

The continuity equation of the flow is  $v_3(x, t) = \phi v_2(x, t)$ . From [8.105] and [8.101], we obtain:

$$\tilde{\alpha}(t) * \frac{\partial p_3(x, t)}{\partial x} \Big|_{x=L} = \phi \frac{\partial p_2(x, t)}{\partial x} \Big|_{x=L}, \quad [8.106]$$

with

$$\frac{\partial p_3(x, t)}{\partial x} \Big|_{x=L} = - \frac{1}{c_0} \tilde{T}(t) * \frac{\partial p^i}{\partial t} \left( t - \frac{L}{c} \right). \quad [8.107]$$

The Laplace transform of equation [8.106] leads to:

$$\begin{aligned} T(z) \exp\left(-\frac{L}{c}z\right) \sinh\left(\frac{L}{c}\sqrt{f(z)}\right) \\ = \frac{\phi c_0}{c} \frac{\sqrt{f(z)}}{z\alpha(z)} \left[ -T(z) \exp\left(-\frac{L}{c}z\right) \cosh\left(\frac{L}{c}\sqrt{f(z)}\right) + 1 + R(z) \right]. \end{aligned} \quad [8.108]$$

The system made by equations [8.104] and [8.108] allows us to determine the reflection and transmission coefficients  $R(z)$  and  $T(z)$  as:

$$R(z) = \frac{(1 - \zeta^2 z) \sinh\left(\frac{L}{c}\sqrt{f(z)}\right)}{2\zeta\sqrt{z} \cosh\left(\frac{L}{c}\sqrt{f(z)}\right) + (1 + \zeta^2 z) \sinh\left(\frac{L}{c}\sqrt{f(z)}\right)}, \quad [8.109]$$

$$T(z) = \frac{2\zeta\sqrt{z} \exp\left(\frac{L}{c}z\right)}{2\zeta\sqrt{z} \cosh\left(\frac{L}{c}\sqrt{f(z)}\right) + (1 + \zeta^2 z) \sinh\left(\frac{L}{c}\sqrt{f(z)}\right)}. \quad [8.110]$$

Replacing the hyperbolic functions with their analytical expressions, we obtain the expressions of the reflection and transmission coefficients for  $n$  reflections inside the material:

$$\begin{aligned} \frac{R(z)}{\frac{1-\zeta\sqrt{z}}{1+\zeta\sqrt{z}}} &= \sum_{n \geq 0} \left( \frac{1 - \zeta\sqrt{z}}{1 + \zeta\sqrt{z}} \right)^{2n} \left[ \exp\left(-2n\frac{L}{c}\sqrt{f(z)}\right) - \exp\left(-(2n+2)\frac{L}{c}\sqrt{f(z)}\right) \right] \\ \frac{T(z)}{\frac{4\zeta\sqrt{z}}{(1+\zeta\sqrt{z})^2}} &= \exp\left(\frac{L}{c}z\right) \sum_{n \geq 0} \left( \frac{1 - \zeta\sqrt{z}}{1 + \zeta\sqrt{z}} \right)^{2n} \cdot \exp\left(-(2n+1)\frac{L}{c}\sqrt{f(z)}\right). \end{aligned}$$

The general calculation of the inverse Laplace transforms of the expressions above for  $n$  internal reflections is very difficult. Therefore, taking into account only the reflections on the first and second interfaces, at  $x = 0$  and  $x = L$ , we find:

$$R(z) = \frac{1 - \zeta\sqrt{z}}{1 + \zeta\sqrt{z}} \left[ 1 - \frac{4\zeta\sqrt{z}}{(1 + \zeta\sqrt{z})^2} \exp\left(-2\frac{L}{c}\sqrt{f(z)}\right) \right], \quad [8.111]$$

$$T(z) = \frac{4\zeta\sqrt{z}}{(1 + \zeta\sqrt{z})^2} \exp\left(\frac{L}{c}(z - \sqrt{f(z)})\right). \quad [8.112]$$

### *The reflection operator*

The expression of the reflection operator is given by:

$$\tilde{R}(t) = \mathcal{L}^{-1}(R(z))$$

$$\begin{aligned}\mathcal{L}^{-1}\left[\frac{1-\zeta\sqrt{z}}{1+\zeta\sqrt{z}}\right] &= \mathcal{L}^{-1}\left[-1 + \frac{2}{\zeta}\frac{1}{\left(\sqrt{z} + \frac{1}{\zeta}\right)}\right] \\ &= -\delta(t) + \frac{2}{\zeta\sqrt{\pi}}\frac{1}{\sqrt{t}} - \frac{2}{\zeta^2}\exp(t/b^2)\operatorname{erfc}(\sqrt{t}/\zeta),\end{aligned}$$

where  $\operatorname{erfc}(x) = 1 - \operatorname{erf}(x)$ ,  $\operatorname{erf}(x)$  is the error function given by:

$$\operatorname{erf}(x) = \frac{2}{\sqrt{\pi}} \int_0^\infty \exp(-t^2) dt. \quad [8.113]$$

Let us write:

$$g(z) = \frac{\zeta z - 1}{(1 + \zeta z)^3} = \frac{1}{\zeta^2} \frac{z - 1/\zeta}{(1/\zeta + z)^3}.$$

We have:

$$\mathcal{L}^{-1}[g(z)] = \frac{1}{\zeta^2} \mathcal{L}^{-1}\left[\frac{z - 1/\zeta}{(1/\zeta + z)^3}\right] = \frac{1}{\zeta^2} (t - t^2/\zeta) \exp(-t/\zeta) = R_1(t),$$

however,

$$\begin{aligned}\mathcal{L}^{-1}[\sqrt{z}g(\sqrt{z})] &= \frac{1}{2\sqrt{\pi}} \frac{1}{t^{3/2}} \int_0^\infty \left(\frac{u^2}{2t} - 1\right) \exp\left(-\frac{u^2}{4t}\right) f(u) du \\ &= \frac{1}{2\zeta^2\sqrt{\pi}} \frac{1}{t^{3/2}} \int_0^\infty \left(\frac{u^2}{2t} - 1\right) \left(u - \frac{u^2}{\zeta}\right) \exp\left(-\frac{u^2}{4t} - \frac{u}{\zeta}\right) du\end{aligned}$$

hence,

$$\begin{aligned}\mathcal{L}^{-1}\left[\frac{4\zeta\sqrt{z}(\zeta\sqrt{z} - 1)}{(1 + \zeta\sqrt{z})^3}\right] &= \frac{2}{\zeta\sqrt{\pi}} \frac{1}{t^{3/2}} \int_0^\infty \left(\frac{u^2}{2t} - 1\right) \left(u - \frac{u^2}{\zeta}\right) \exp\left(-\frac{u^2}{4t} - \frac{u}{\zeta}\right) du \\ &= \frac{2\zeta}{\sqrt{\pi}} \frac{1}{t^{3/2}} \int_0^\infty \left(\frac{\zeta^2 y^2}{2t} - 1\right) (y - y^2) \exp\left(-\frac{\zeta^2 y^2}{4t} - y\right) dy = R_2(t)\end{aligned}$$

after making the change of variable defined by  $\frac{u}{\zeta} = y$ .

The reflection operator  $\tilde{R}(t)$  therefore reads:

$$\tilde{R}(t) = (R_1(t) + R_2(t))$$

*The transmission operator*

The transmission coefficient in the Laplace domain is given by:

$$T(z) = \frac{4\zeta\sqrt{z}}{(1 + \zeta\sqrt{z})^2} \exp\left(\frac{L}{c}\left(z - \sqrt{f(z)}\right)\right). \quad [8.114]$$

Since:

$$\mathcal{L}^{-1}\left[\frac{4\zeta}{(1 + \zeta z)^2}\right] = 4\frac{t}{\zeta} \exp(-t/\zeta),$$

we obtain:

$$\begin{aligned} \mathcal{L}^{-1}\left[\frac{4\zeta\sqrt{z}}{(1 + \zeta\sqrt{z})^2}\right] \\ = \frac{2}{\zeta\sqrt{\pi}} \frac{1}{t^{3/2}} \int_0^\infty \left(\frac{u^2}{2t} - 1\right) u \exp\left(-\frac{u}{\zeta} - \frac{u^2}{4t}\right) du = D(t). \end{aligned} \quad [8.115]$$

The inverse Laplace transform of equation 8.114 is thus given by:

$$\begin{aligned} \tilde{T}(t) &= D(t) \star \delta(t + L/c) \star F(t, L/c) = D(t) \star F(t + L/c, L/c) \\ &= \int_0^t D(\tau) F(t - \tau + L/c, L/c) d\tau. \end{aligned} \quad [8.116]$$

## 8.4. Application to Biot's theory

### 8.4.1. Wave propagation in porous materials with a flexible structure

When the structure of a porous material is not rigid, the equivalent fluid model, on which the previous chapters are based, no longer applies because the waves propagate in both the skeleton and the saturating fluid. The fluid-structure interactions then play an essential role in the propagation. The study of these effects has been largely developed by Biot [BIO 56a, BIO 56b] for applications in the domain of oil exploration since 1950. The main success of this model is the prediction of three propagation modes: two longitudinal modes called fast and slow waves (or first and second waves), and a transverse mode.

More recently, Johnson [JOH 86] and Allard [ALL 92b] and Lafarge have introduced some parameters that extend the validity of the Biot model to a large class of porous materials on a large frequency range, taking into account the thermal effects that happen when the saturating fluid is a gas.



First we briefly revise the Biot model; the propagation equations in the time domain are then established for low and high frequencies. This results in the dynamic response of these materials, which is well suited for an estimation of their physical characteristics.

#### *Biot's model [BIO 56a]*

In the Biot's model, the porous material is treated as a continuum consisting of a solid phase and a saturating fluid. The solid phase is the skeleton whose pore space is filled with the fluid. In addition, we consider the occluded porosity to be a part of the solid. As a result, the two phases are connected, meaning that we can move from one point of the material to another, by a path contained in the solid and another path contained in the fluid. To apply the methods of continuous media mechanics, we must consider this material homogenous, i.e. the wavelength is large compared to the size of the homogenization volume. Finally, we consider the theory to be linear, i.e. the displacements of the solid and the fluid are small.

#### **8.4.2. Displacement equations**

There are several methods for establishing the equations of motion of the solid and of the fluid in the Biot's theory. The homogenization method [BUR 81, AUR 95, NOR 86] is certainly the most rigorous, and is often cited as a *a posteriori* justification of other methods such as the Lagrangian method. However, this latter method, as described by Johnson [JOH 86], has the advantage of demonstrating that Biot's theory model of propagation is the most general theory for a linear description of the fluid-structure interactions in biphasic materials. The major drawback of this approach is that the viscothermal losses due to the propagation of the waves in these environments are not taken into account. In this context, the equations of motion are given by the Euler equations:

$$\rho_{11} \frac{\partial^2 \vec{u}}{\partial t^2} + \rho_{12} \frac{\partial^2 \vec{U}}{\partial t^2} = P \vec{\nabla} (\vec{\nabla} \cdot \vec{u}) + Q \vec{\nabla} (\vec{\nabla} \cdot \vec{U}) - N \vec{\nabla} \wedge (\vec{\nabla} \wedge \vec{u}), \quad [8.117]$$

$$\rho_{21} \frac{\partial^2 \vec{u}}{\partial t^2} + \rho_{22} \frac{\partial^2 \vec{U}}{\partial t^2} = Q \vec{\nabla} (\vec{\nabla} \cdot \vec{u}) + R \vec{\nabla} (\vec{\nabla} \cdot \vec{U}). \quad [8.118]$$

In these equations  $\vec{u}$  is the displacement of the solid, and  $\vec{U}$  of the fluid.  $P$ ,  $Q$ ,  $R$ ,  $N$  and the quantities  $\rho_{ij}$  are the phenomenological coefficients of Biot and the densities to be determined.

#### **8.4.3. Stress-strain relationships**

When a material is subject to a mechanical disturbance, it reacts to the constraints by distorting. In the case of small deformations, the constraints and deformations are linked by linear relations that define the moduli of elasticity. In the case of a porous

material, the stress-strain relationships can be used to interpret and express the Biot coefficients  $P$ ,  $Q$ ,  $R$  and  $N$  that appear in the equations of motion.

The components of the tensor of stresses  $\tau_{ij}^a$  applied to the solid phase ( $a = s$ ) or to the fluid phase ( $a = f$ ) can be obtained from the Lagrangian:

$$\tau_{ij}^s = \left( (P - 2N) \vec{\nabla} \cdot \vec{u} + Q \vec{\nabla} \cdot \vec{U} \right) \delta_{ij} + N(u_{i,j} + u_{j,i}) \quad [8.119]$$

$$\tau_{ij}^f = \left( R \vec{\nabla} \cdot \vec{U} + Q \vec{\nabla} \cdot \vec{u} \right) = -p_f \delta_{ij}. \quad [8.120]$$

Biot and Willis [BIO 56a] showed that  $N$  is the shear modulus of the material, only due to the rigid skeleton; and that the elasticity coefficients  $P$ ,  $Q$  and  $R$  are expressed in terms of (i) the elasticity moduli of the phases and (ii) the porosity  $\phi$  of the material, as shown below:

$$P = \frac{(1 - \phi) \left( 1 - \phi - \frac{K_b}{K_s} \right) K_s + \phi \frac{K_s}{K_f} K_b}{1 - \phi - \frac{K_b}{K_s} + \phi \frac{K_s}{K_f}} + \frac{4}{3} N \quad [8.121]$$

$$Q = \frac{\left( 1 - \phi - \frac{K_b}{K_s} \right) \phi K_s}{1 - \phi - \frac{K_b}{K_s} + \phi \frac{K_s}{K_f}} \quad [8.122]$$

$$R = \frac{\phi^2 K_s}{1 - \phi - \frac{K_b}{K_s} + \phi \frac{K_s}{K_f}} \quad [8.123]$$

where  $K_f$ ,  $K_s$  and  $K_b$  are the incompressibility moduli of the fluid, the solid structure and the coated material, respectively. When the fluid is a gas, the modulus  $K_f$  is always very small compared to  $K_s$  and  $K_b$ . The Biot coefficients therefore become:

$$P = K_b + \frac{4}{3} N + \frac{(1 - \phi)^2}{\phi} K_f, \quad [8.124]$$

$$Q = (1 - \phi) K_f, \quad [8.125]$$

$$R = \phi K_f. \quad [8.126]$$

The  $Q$  coefficient that appears in equations [8.117] and [8.118] corresponds to coupling (called potential coupling) between the two phases. We see in particular that for a material with a high porosity ( $\phi \approx 1$ ), saturated by a gas, this coupling between the solid and fluid parts is low. This partially explains the difficulty we encounter when observing the wave of Biot in acoustic materials.

#### 8.4.4. Dissipation

In the mechanism of propagation, the dissipation of energy is due to different processes depending on whether the fluid is a gas or a liquid.

For a propagation in a gas, the dissipation is mainly due to (i) the viscosity of the gas and (ii) the thermal effects developed by the expansion and compression processes during the passage of the wave.

In a porous material with a flexible structure saturated by a fluid, viscothermal phenomena mainly appear in the fluid. To describe them, we use the model of propagation in cylindrical pipes, described by Zwikker and Kosten [ZWI 49]. Starting from the Kirchhoff theory [KHI 68], Zwikker and Kosten showed that as a first approximation, the viscous and thermal effects are decoupled: thermal effects apply a correction  $\beta(\omega)$  to the compressibility coefficient of the gas, while viscous effects change its density by a factor  $\alpha(\omega)$ . This study is still the basis of the developments on the propagation of sound in pipes and porous materials, although several improvements have been made, in particular to generalize the result to the case of non-cylindrical pores, and to broaden the frequency range of the model.

The correction factors of the density and of the incompressibility modulus of the gas used in our model are those given by Johnson *et al.* [JOH 87], Allard *et al.* [ALL 92b] and Lafarge [LAF 93, LAF 96]

$$\alpha(\omega) = \alpha_\infty \left( 1 + \frac{\eta\phi}{j\omega\alpha_\infty\rho_f k_0} \sqrt{1 + j \frac{4\alpha_\infty^2 k_0^2 \rho_f \omega}{\eta\Lambda^2 \phi^2}} \right), \quad [8.127]$$

$$\beta(\omega) = \gamma - (\gamma - 1) \left( 1 + \frac{\eta\phi}{j\omega\rho_f k'_0 Pr} \sqrt{1 + j \frac{4k_0'^2 \rho_f \omega Pr}{\eta\phi^2 \Lambda'^2}} \right)^{-1}, \quad [8.128]$$

where  $\Lambda$  and  $\Lambda'$  are the characteristic viscous and thermal lengths introduced by Johnson [JOH 87] and Allard [ALL 92b];  $\alpha_\infty$  is the tortuosity of the material;  $Pr$  the Prandtl number;  $\eta$  the viscosity of the fluid;  $\omega = 2\pi f$  the angular frequency of the wave and  $\gamma = c_p/c_v$  the adiabatic constant. The function  $\alpha(\omega)$  is called the dynamic tortuosity of the material, and  $\beta(\omega)$  is the dynamic compressibility factor of the gas in the porous material.

In the frame of Biot's theory, the viscous effects lead to a change in densities  $\rho_{ij}$ ; while the thermal effects are involved in the definition of the compressibility modulus  $K_f$ , changing  $1/K_f$  into  $\beta(\omega)/K_f$ . These corrections must be understood within the meaning of renormalization: it is the sum of all the interactions of the gas with its environment (fluid-structure interactions), which modifies the value of its characteristics (density and compressibility modulus).

Considering the propagation of waves in a liquid, the dissipation is mainly due to the viscosity of the fluid. In this case, we only consider the viscous correction  $\alpha(\omega)$ .

#### 8.4.5. Mass coefficients $\rho_{ij}$

The coefficients  $\rho_{ij}$  involved in the equations of motion have the dimension of a density and are related to the densities of the solid (the rigid structure)  $\rho_s$  and of the fluid  $\rho_f$ :

$$\rho_{11} = \rho_1 - \rho_{12}, \quad [8.129]$$

$$\rho_{22} = \rho_0 - \rho_{12} \quad [8.130]$$

where  $\rho_1 = (1 - \phi)\rho_s$ ,  $\rho_0 = \phi\rho_f$  and  $\rho_{12}$  is the density induced by the fluid-structure interactions through the term of tortuosity  $\alpha(\omega)$

$$\rho_{12} = -\rho_0(\alpha(\omega) - 1). \quad [8.131]$$

#### *Coupling Biot's theory*

Biot's theory thus shows three types of coupling between the fluid and the structure:

- the inertial coupling which is a consequence of the tortuosity of the material and is responsible for the density term  $\rho_{12}$ ;
- the viscous coupling generated by the relative movement of the two phases, which also contributes to the density by the term  $\alpha(\omega)$ ;
- the potential coupling due to the elasticity modulus  $Q$  that takes into account the effect of the stresses exerted by one phase on another.

The competition between these coupling effects induces a large diversity of phenomena that may appear during the propagation of an acoustic wave in a saturated porous medium.

#### 8.4.6. Equations in the time domain [FEL 03e]

During the last 15 years, several authors have proposed numeric solutions to the Biot equations for geophysical applications [NOR 86, BOU 87, CAR 96]. We propose here to generalize the temporal approach developed in the frame of materials with a rigid structure to the case of flexible-structure materials.

Since the phenomena involved in the propagation are different depending on the frequency of the wave, it is clear that the equations describing them are also different. Thus, one can distinguish between two types of temporal equations that describe the propagation of waves: an equation for low frequencies, where the effects of viscosity are present everywhere in the fluid, and another equation for high frequencies, where these effects are concentrated near the surface of the pores.

The equations for each frequency range are obtained from the low- or high-frequency development of the susceptibilities  $\alpha(\omega)$  and  $\beta(\omega)$ , followed by the transformation in the time domain. We first consider the case of a material saturated with a liquid, before analyzing the situation of an acoustic material saturated by a gas. In all the following, we introduce the notations  $u = \vec{\nabla} \varphi_1$  and  $U = \vec{\nabla} \varphi_2$  for longitudinal waves, and  $u = \vec{\nabla} \wedge \vec{\psi}_1$  and  $U = \vec{\nabla} \wedge \vec{\psi}_2$  for transverse waves. The Laplace transforms with respect to time  $t$  of the functions  $\phi_k(\vec{r}, t)$  and  $\vec{\psi}_k(\vec{r}, t)$  are noted  $\Phi_k(\vec{r}, s)$  and  $\vec{\Psi}_k(\vec{r}, s)$ , respectively. The Laplace transform of the function  $f(\vec{r}, t)$  is defined by

$$\mathcal{L}\{f(\vec{r}, t)\} = \int_0^\infty e^{-st} f(\vec{r}, t) dt.$$

Finally, when there is no ambiguity, we will omit those function's parameter arguments. The general method of obtaining the equations in the time domain can be summarized as follows:

- We start with the development of the susceptibilities  $\alpha(\omega)$  and  $\beta(\omega)$  as power series of  $\omega$  for each frequency range.
- We report these expressions in the equations of motion for the compression waves and shear waves.
- We obtain the matrix equation of propagation replacing the powers  $(j\omega)^\nu$  with the corresponding pseudo-differential operators (according to the properties of Fourier transforms),

$$(j\omega)^\nu \xrightarrow{t} \frac{\partial^\nu}{\partial t^\nu}.$$

- We eliminate the temporal derivative by taking the Laplace transform of the propagation equation, obtaining the relationship

$$\Delta \begin{pmatrix} \Xi \\ \Pi \end{pmatrix} = M \begin{pmatrix} \Xi \\ \Pi \end{pmatrix}, \quad [8.132]$$

where  $M$  is a matrix whose elements are functions of the densities  $\rho_{ij}$ , of the elasticity moduli  $P, Q, R, N$  and the Laplace variable  $s$ .  $\Xi$  and  $\Pi$  are the Laplace transforms of the solid and fluid displacements

$$\Xi(\vec{r}, s) = \mathcal{L}\{\xi(\vec{r}, s)\} \quad \text{and} \quad \Pi(\vec{r}, s) = \mathcal{L}\{\varpi(\vec{r}, s)\},$$

where  $\xi$  (resp.  $\varpi$ ) is indifferently  $\varphi_1$  or  $\vec{\psi}_1$  (resp.  $\varphi_2$  or  $\vec{\psi}_2$ ).

- We decouple the modes with the diagonalization of matrix  $M$  (the eigenvalues  $\lambda_\pm$  of matrix  $M$  determine the velocities and attenuations of the two displacement modes, and the eigenvectors give the respective contributions of these modes to the solid and fluid displacements).

– We establish the propagation equations of each mode, by returning to the time domain.

– We finally obtain the solution to the problem by calculating the Green function of each of these equations.

#### 8.4.7. Materials saturated by a liquid

When the saturating fluid is a liquid, only the viscous effects are taken into account.

##### Very low frequencies

At very low frequencies, the dynamic tortuosity  $\alpha(\omega)$  becomes:

$$\alpha(\omega) \simeq \frac{\eta\phi}{j\omega\rho_f k_0}. \quad [8.133]$$

Densities are therefore:

$$\begin{aligned} \rho_{11} &= \rho_1 - \phi\rho_f + \frac{\eta\phi^2}{j\omega k_0} = \widetilde{\rho}_{11} + \frac{\eta\phi^2}{j\omega k_0}, \\ \rho_{12} &= +\phi\rho_f - \frac{\eta\phi^2}{j\omega k_0} = \widetilde{\rho}_{12} - \frac{\eta\phi^2}{j\omega k_0}, \\ \rho_{22} &= \frac{\eta\phi^2}{j\omega k_0}, \end{aligned} \quad [8.134]$$

where  $\widetilde{\rho}_{11} = \rho_1 - \phi\rho_f$  and  $\widetilde{\rho}_{12} = +\phi\rho_f$ . To write the equations of motion, we replace the factor  $1/j\omega$  with a fractional derivative of the order  $-1$ . Then, Biot's equations become:

$$\widetilde{\rho}_{11} \frac{\partial^2 \vec{u}}{\partial t^2} + \widetilde{\rho}_{12} \frac{\partial^2 \vec{U}}{\partial t^2} + \frac{\eta\phi^2}{k_0} \left( \frac{\partial \vec{u}}{\partial t} - \frac{\partial \vec{U}}{\partial t} \right) \quad [8.135]$$

$$= P \vec{\nabla} \cdot (\vec{\nabla} \cdot \vec{u}) + Q \vec{\nabla} \cdot (\vec{\nabla} \cdot \vec{U}) - N \vec{\nabla} \wedge (\vec{\nabla} \wedge \vec{u}),$$

$$\widetilde{\rho}_{12} \frac{\partial^2 \vec{u}}{\partial t^2} + \frac{\eta\phi^2}{k_0} \left( \frac{\partial \vec{U}}{\partial t} - \frac{\partial \vec{u}}{\partial t} \right) = Q \vec{\nabla} \cdot (\vec{\nabla} \cdot \vec{u}) + R \vec{\nabla} \cdot (\vec{\nabla} \cdot \vec{U}). \quad [8.136]$$

##### Longitudinal waves

Equations [8.136] for longitudinal waves are then written using the following matrix notation:

$$\begin{pmatrix} \widetilde{\rho}_{11} & \widetilde{\rho}_{12} \\ \widetilde{\rho}_{12} & 0 \end{pmatrix} \frac{\partial^2}{\partial t^2} \begin{pmatrix} \varphi_1 \\ \varphi_2 \end{pmatrix} + \frac{\eta\phi^2}{k_0} \begin{pmatrix} 1 & -1 \\ -1 & 1 \end{pmatrix} \frac{\partial}{\partial t} \begin{pmatrix} \varphi_1 \\ \varphi_2 \end{pmatrix} = \begin{pmatrix} P & Q \\ Q & R \end{pmatrix} \Delta \begin{pmatrix} \varphi_1 \\ \varphi_2 \end{pmatrix}. \quad [8.137]$$

Considering the Laplace transform of this equation with respect to time, we obtain:

$$\Delta \begin{pmatrix} \Phi_1 \\ \Phi_2 \end{pmatrix} = \begin{pmatrix} P & Q \\ Q & R \end{pmatrix}^{-1} \left[ \begin{pmatrix} \widetilde{\rho}_{11}s^2 & \widetilde{\rho}_{12}s^2 \\ \widetilde{\rho}_{12}s^2 & 0 \end{pmatrix} + \frac{\eta\phi^2}{k_0} \begin{pmatrix} s & -s \\ -s & s \end{pmatrix} \right] \begin{pmatrix} \Phi_1 \\ \Phi_2 \end{pmatrix}.$$

The equation,

$$\begin{pmatrix} P & Q \\ Q & R \end{pmatrix}^{-1} = \begin{pmatrix} R' & -Q' \\ -Q' & P' \end{pmatrix}, \quad [8.138]$$

is associated with the matrix:

$$\begin{bmatrix} (R'\widetilde{\rho}_{11} - Q'\widetilde{\rho}_{12})s^2 + \frac{\eta\phi^2}{k_0}(R' + Q')s & R'\widetilde{\rho}_{12}s^2 - \frac{\eta\phi^2}{k_0}(R' + Q')s \\ (-Q'\widetilde{\rho}_{11} + P'\widetilde{\rho}_{12})s^2 - \frac{\eta\phi^2}{k_0}(P' + Q')s & -Q'\widetilde{\rho}_{12}s^2 + \frac{\eta\phi^2}{k_0}(P' + Q')s \end{bmatrix}.$$

The eigenmodes  $\Phi^\pm$  of the displacements can be obtained by a diagonalization of this matrix. The eigenvalues  $\lambda_\pm$  that are solutions of the characteristic equation,

$$\lambda^2 - \text{tr}(M)\lambda + \det(M) = 0 \quad [8.139]$$

are written:

$$\lambda_\pm = \frac{\text{tr}(M) \pm \sqrt{\text{tr}^2(M) - 4\det(M)}}{2} \quad [8.140]$$

with:

$$\begin{aligned} \text{tr}(M) &= (R'\widetilde{\rho}_{11} - 2Q'\widetilde{\rho}_{12})s^2 + \frac{\eta\phi^2}{k_0}(P' + R' + 2Q')s \\ \det(M) &= -(P'R' - Q'^2)\widetilde{\rho}_{12}^2 s^4 + \frac{\eta\phi^2}{k_0}(P'R' - Q'^2)(\widetilde{\rho}_{11} + 2\widetilde{\rho}_{12})s^3. \end{aligned}$$

Equations satisfied by the modes  $\Phi^\pm$  are, therefore,

$$\Delta\Phi^\pm = \lambda_\pm\Phi^\pm. \quad [8.141]$$

In the Laplace domain, these eigenvalues are functions of the variable  $s$ . In the time domain, they become operators that act on the functions  $\phi_k$  of the variable  $t$ .

Therefore, when  $\det(M)/\text{tr}^2(M) \ll 1$ , it is possible to develop the expressions [8.140] and thus obtain:

$$\lambda_+ \approx \text{tr}(M) - \frac{\det(M)}{\text{tr}(M)} \quad \text{and} \quad \lambda_- \approx \frac{\det(M)}{\text{tr}(M)}. \quad [8.142]$$

The division of the two polynomials  $\det(M)/\text{tr}(M)$  yields:

$$\frac{\det(M)}{\text{tr}(M)} = -\frac{\widetilde{\rho_{12}}^2}{R\widetilde{\rho_{11}} - 2Q\widetilde{\rho_{12}}}s^2 + \frac{\eta\phi^2}{k_0} \frac{R\widetilde{\rho_{11}}^2 - (Q+R)\widetilde{\rho_{11}}\widetilde{\rho_{12}} + (P+Q-2Q)\widetilde{\rho_{12}}^2}{(R\widetilde{\rho_{11}} - 2Q\widetilde{\rho_{12}})^2}s + \dots$$

where the  $\dots$  terms are of the order  $k \leq 0$  in  $s$ . In this case, the eigenvalues  $\lambda_{\pm}$  become:

$$\begin{aligned}\lambda_+ &= \left( \frac{R\widetilde{\rho_{11}} - 2Q\widetilde{\rho_{12}}}{PR - Q^2} + \frac{\widetilde{\rho_{12}}^2}{R\widetilde{\rho_{11}} - 2Q\widetilde{\rho_{12}}} \right) s^2 \\ &+ \frac{\eta\phi^2}{k_0} \left( \frac{P+R+2Q}{PR-Q^2} - \frac{R\widetilde{\rho_{11}}^2 - (Q+R)\widetilde{\rho_{11}}\widetilde{\rho_{12}} + (P+Q-2Q)\widetilde{\rho_{12}}^2}{(R\widetilde{\rho_{11}} - 2Q\widetilde{\rho_{12}})^2} \right) s + \dots \\ \lambda_- &= -\frac{\widetilde{\rho_{12}}^2}{R\widetilde{\rho_{11}} - 2Q\widetilde{\rho_{12}}}s^2 \\ &+ \frac{\eta\phi^2}{k_0} \frac{R\widetilde{\rho_{11}}^2 - (Q+R)\widetilde{\rho_{11}}\widetilde{\rho_{12}} + (P+Q-2Q)\widetilde{\rho_{12}}^2}{(R\widetilde{\rho_{11}} - 2Q\widetilde{\rho_{12}})^2}s + \dots\end{aligned}$$

The temporal equations are expressed as:

$$\Delta\varphi^+(\vec{r}, t) = A_+ \frac{\partial^2}{\partial t^2} \varphi^+(\vec{r}, t) + B_+ \frac{\partial}{\partial t} \varphi^+(\vec{r}, t) \quad [8.143]$$

$$\Delta\varphi^-(\vec{r}, t) = A_- \frac{\partial^2}{\partial t^2} \varphi^-(\vec{r}, t) + B_- \frac{\partial}{\partial t} \varphi^-(\vec{r}, t), \quad [8.144]$$

where:

$$\begin{aligned}A_+ &= \frac{R\widetilde{\rho_{11}} - 2Q\widetilde{\rho_{12}}}{PR - Q^2} + \frac{\widetilde{\rho_{12}}^2}{R\widetilde{\rho_{11}} - 2Q\widetilde{\rho_{12}}} \\ B_+ &= \frac{\eta\phi^2}{k_0} \left( \frac{P+R+2Q}{PR-Q^2} - \frac{R\widetilde{\rho_{11}}^2 - (Q+R)\widetilde{\rho_{11}}\widetilde{\rho_{12}} + (P+Q-2Q)\widetilde{\rho_{12}}^2}{(R\widetilde{\rho_{11}} - 2Q\widetilde{\rho_{12}})^2} \right) \\ A_- &= -\frac{\widetilde{\rho_{12}}^2}{R\widetilde{\rho_{11}} - 2Q\widetilde{\rho_{12}}} \\ B_- &= \frac{\eta\phi^2}{k_0} \frac{R\widetilde{\rho_{11}}^2 - (Q+R)\widetilde{\rho_{11}}\widetilde{\rho_{12}} + (P+Q-2Q)\widetilde{\rho_{12}}^2}{(R\widetilde{\rho_{11}} - 2Q\widetilde{\rho_{12}})^2}.\end{aligned}$$



When the frequency is such that inertial effects are negligible compared to the viscous effects, the equations of motion are reduced to the following system:

$$\frac{\eta\phi^2}{k_0} \begin{pmatrix} 1 & -1 \\ -1 & 1 \end{pmatrix} \frac{\partial}{\partial t} \begin{pmatrix} \varphi_1 \\ \varphi_2 \end{pmatrix} = \begin{pmatrix} P & Q \\ Q & R \end{pmatrix} \Delta \begin{pmatrix} \varphi_1 \\ \varphi_2 \end{pmatrix}. \quad [8.145]$$

We therefore have, in the Laplace domain,

$$\Delta \begin{pmatrix} \Phi_1 \\ \Phi_2 \end{pmatrix} = \frac{\eta\phi^2}{k_0} \begin{pmatrix} (Q' + R')s & -(Q' + R')s \\ -(P' + Q')s & (P' + Q')s \end{pmatrix} \begin{pmatrix} \Phi_1 \\ \Phi_2 \end{pmatrix}. \quad [8.146]$$

The eigenvalues  $\lambda_{\pm}$ , that are solutions of equation,

$$\lambda^2 - \frac{\eta\phi^2}{k_0} (P' + R' + 2Q')s\lambda = 0 \quad [8.147]$$

read:

$$\lambda_- = 0 \quad \text{and} \quad \lambda_+ = \frac{\eta\phi^2}{k_0} (P' + R' + 2Q')s. \quad [8.148]$$

This result yields the following temporal equations

$$\Delta\varphi^+(\vec{r}, t) = \frac{\eta\phi^2(P + R + 2Q)}{k_0(PR - Q^2)} \frac{\partial}{\partial t} \varphi^+(\vec{r}, t) \quad [8.149]$$

$$\Delta\varphi^-(\vec{r}, t) = 0 \quad [8.150]$$

We therefore obtain a diffusion equation for the mode  $\varphi^+(\vec{r}, t)$  with the diffusion coefficient:

$$D = \frac{k_0(PR - Q^2)}{\eta\phi^2(P + R + 2Q)}. \quad [8.151]$$

Replacing the quantities  $P$ ,  $Q$  and  $R$  with their values, the diffusion coefficient  $D$  becomes:

$$D \approx \frac{k_0 K_f}{\eta\phi} \frac{1}{1 + \frac{K_f}{\phi(K_b + 4N/3)}}. \quad [8.152]$$

For a material with a very rigid structure ( $K_b, N \gg K_f$ ), the previous expression of  $D$  simplifies to [JOH 87]:

$$D \approx \frac{k_0 K_f}{\eta\phi}. \quad [8.153]$$

*Transverse waves*

In the case of transverse waves, the movements of the phases read  $u = \vec{\nabla} \wedge \vec{\psi}_1$  and  $U = \vec{\nabla} \wedge \vec{\psi}_2$ . The equations of motion of the fluid and solid phases are therefore given by:

$$\begin{aligned} \widetilde{\rho}_{11} \frac{\partial^2 \vec{\psi}_1}{\partial t^2} + \widetilde{\rho}_{12} \frac{\partial^2 \vec{\psi}_2}{\partial t^2} + \frac{\eta \phi^2}{k_0} \left( \frac{\partial \vec{\psi}_1}{\partial t} - \frac{\partial \vec{\psi}_2}{\partial t} \right) &= -N \vec{\nabla} \wedge (\vec{\nabla} \wedge \vec{\psi}_1), \\ \widetilde{\rho}_{12} \frac{\partial^2 \vec{\psi}_1}{\partial t^2} + \frac{\eta \phi^2}{k_0} \left( \frac{\partial \vec{\psi}_2}{\partial t} - \frac{\partial \vec{\psi}_1}{\partial t} \right) &= 0. \end{aligned}$$

Taking the Laplace transforms of these two equations with respect to time, we then obtain:

$$\begin{aligned} \left( \widetilde{\rho}_{11} s^2 + \frac{\eta \phi^2}{k_0} s \right) \vec{\Psi}_1(\vec{r}, s) + \left( \widetilde{\rho}_{12} s^2 - \frac{\eta \phi^2}{k_0} s \right) \vec{\Psi}_2(\vec{r}, s) \\ = -N \vec{\nabla} \wedge (\vec{\nabla} \wedge \vec{\Psi}_1(\vec{r}, s)), \\ \left( \widetilde{\rho}_{12} s^2 - \frac{\eta \phi^2}{k_0} s \right) \vec{\Psi}_1(\vec{r}, s) + \frac{\eta \phi^2}{k_0} s \vec{\Psi}_2(\vec{r}, s) = 0. \end{aligned}$$

The second equation of this system shows that the movement of the fluid is directly proportional to the movement of the solid matrix. Due to its viscosity, the fluid is led by the solid in its movement. In this case, a single shear wave exists. Writing the expression of the movement of the fluid as a function of the movement of the solid we obtain:

$$\vec{\Psi}_2(\vec{r}, s) = - \left( \frac{\widetilde{\rho}_{12} k_0 s}{\eta \phi^2} - 1 \right) \vec{\Psi}_1(\vec{r}, s). \quad [8.154]$$

Reporting it in the first equation of the system, and returning to the time domain, we finally obtain the equation for the shear waves:

$$\Delta \vec{\psi}_1 - \frac{\widetilde{\rho}_{11} + 2\widetilde{\rho}_{12}}{N} \frac{\partial^2 \vec{\psi}_1}{\partial t^2} + \frac{\widetilde{\rho}_{12}^2 k_0}{N \eta \phi^2} \frac{\partial^3 \vec{\psi}_1}{\partial t^3} = 0. \quad [8.155]$$

This equation is the same type as the one established by Pierce [PIE 81]: the third-order derivative with respect to time is a correction term to the classical propagation equation, due to the viscous effects. The second term of this equation shows that the density of the material subject to the shear waves is  $\widetilde{\rho}_{11} + 2\widetilde{\rho}_{12} = (1 - \phi)\rho_s + \phi\rho_f$ , thus corresponding to the entire porous material: at very low frequencies, the effects of the viscosity are such that the entire fluid is “stuck” to the solid. Thus the shear wave propagates in the solid structure ( $N$  is the shear modulus of the solid structure only). The fluid contributes passively to this propagation, by increasing the mass of the vibrating structure.

*Low frequencies*

At low frequencies, the dynamic tortuosity  $\alpha(\omega)$  becomes:

$$\alpha(\omega) \simeq \alpha + \frac{\eta\phi}{j\omega\rho_f k_0}. \quad [8.156]$$

The densities therefore read:

$$\begin{aligned} \rho_{11} &= \rho_1 - \phi\rho_f(\alpha - 1) + \frac{\eta\phi^2}{j\omega k_0} = \widetilde{\rho}_{11} + \frac{\eta\phi^2}{j\omega k_0}, \\ \rho_{12} &= -\phi\rho_f(\alpha - 1) - \frac{\eta\phi^2}{j\omega k_0} = \widetilde{\rho}_{12} - \frac{\eta\phi^2}{j\omega k_0}, \\ \rho_{22} &= \phi\rho_f\alpha + \frac{\eta\phi^2}{j\omega k_0}, \end{aligned}$$

where we now have  $\widetilde{\rho}_{11} = \rho_1 + \phi\rho_f(\alpha - 1)$ ,  $\widetilde{\rho}_{12} = -\phi\rho_f(\alpha - 1)$  and  $\widetilde{\rho}_{22} = \phi\rho_f\alpha$ .

*Longitudinal waves*

For the compression waves, the equations of movement are:

$$\begin{aligned} \begin{pmatrix} \widetilde{\rho}_{11} & \widetilde{\rho}_{12} \\ \widetilde{\rho}_{12} & \widetilde{\rho}_{22} \end{pmatrix} \frac{\partial^2}{\partial t^2} \begin{pmatrix} \varphi_1 \\ \varphi_2 \end{pmatrix} + \frac{\eta\phi^2}{k_0} \begin{pmatrix} 1 & -1 \\ -1 & 1 \end{pmatrix} \frac{\partial}{\partial t} \begin{pmatrix} \varphi_1 \\ \varphi_2 \end{pmatrix} \\ = \begin{pmatrix} P & Q \\ Q & R \end{pmatrix} \Delta \begin{pmatrix} \varphi_1 \\ \varphi_2 \end{pmatrix}; \end{aligned} \quad [8.157]$$

in the Laplace domain, this system is associated to the matrix

$$\begin{bmatrix} (R'\widetilde{\rho}_{11} - Q'\widetilde{\rho}_{12})s^2 + \frac{\eta\phi^2}{k_0}(R' + Q')s & (-Q'\widetilde{\rho}_{22} + R'\widetilde{\rho}_{12})s^2 - \frac{\eta\phi^2}{k_0}(R' + Q')s \\ (-Q'\widetilde{\rho}_{11} + P'\widetilde{\rho}_{12})s^2 - \frac{\eta\phi^2}{k_0}(P' + Q')s & (P'\widetilde{\rho}_{22} - Q'\widetilde{\rho}_{12})s^2 + \frac{\eta\phi^2}{k_0}(P' + Q')s \end{bmatrix}.$$

In this case, the trace and the determinant of matrix  $M$  are:

$$\begin{aligned} \text{tr}(M) &= (P'\widetilde{\rho}_{22} + R'\widetilde{\rho}_{11} - 2Q'\widetilde{\rho}_{12})s^2 + \frac{\eta\phi^2}{k_0}(P' + R' + 2Q')s \\ \det(M) &= (P'R' - Q'^2) \left( (\widetilde{\rho}_{11}\widetilde{\rho}_{22} - \widetilde{\rho}_{12}^2)s^4 + \frac{\eta\phi^2}{k_0}(\widetilde{\rho}_{11} + \widetilde{\rho}_{22} + 2\widetilde{\rho}_{12})s^3 \right). \end{aligned}$$

*Transverse waves*

At low frequencies, the equations governing the transverse movements of the porous material are similar to the equations for very low frequencies, up to the term corresponding to the density of the fluid:

$$\begin{aligned}\widetilde{\rho}_{11} \frac{\partial^2 \vec{\psi}_1}{\partial t^2} + \widetilde{\rho}_{12} \frac{\partial^2 \vec{\psi}_2}{\partial t^2} + \frac{\eta \phi^2}{k_0} \left( \frac{\partial \vec{\psi}_1}{\partial t} - \frac{\partial \vec{\psi}_2}{\partial t} \right) &= -N \vec{\nabla} \wedge (\vec{\nabla} \wedge \vec{\psi}_1), \\ \widetilde{\rho}_{12} \frac{\partial^2 \vec{\psi}_1}{\partial t^2} + \widetilde{\rho}_{22} \frac{\partial^2 \vec{\psi}_2}{\partial t^2} + \frac{\eta \phi^2}{k_0} \left( \frac{\partial \vec{\psi}_2}{\partial t} - \frac{\partial \vec{\psi}_1}{\partial t} \right) &= 0.\end{aligned}$$

We therefore have, in the Laplace domain:

$$\begin{aligned}\left( \widetilde{\rho}_{11} s^2 + \frac{\eta \phi^2}{k_0} s \right) \vec{\Psi}_1(\vec{r}, s) + \left( \widetilde{\rho}_{12} s^2 - \frac{\eta \phi^2}{k_0} s \right) \vec{\Psi}_2(\vec{r}, s) \\ = -N \vec{\nabla} \wedge (\vec{\nabla} \wedge \vec{\Psi}_1(\vec{r}, s)), \\ \left( \widetilde{\rho}_{12} s^2 - \frac{\eta \phi^2}{k_0} s \right) \vec{\Psi}_1(\vec{r}, s) + \left( \widetilde{\rho}_{22} s^2 + \frac{\eta \phi^2}{k_0} s \right) \vec{\Psi}_2(\vec{r}, s) = 0.\end{aligned}$$

From the second equation, we obtain the following expression of  $\vec{\Psi}_2(\vec{r}, s)$ :

$$\vec{\Psi}_2(\vec{r}, s) = -\frac{\widetilde{\rho}_{12} s^2 - \frac{\eta \phi^2}{k_0} s}{\widetilde{\rho}_{22} s^2 + \frac{\eta \phi^2}{k_0} s} \vec{\Psi}_1(\vec{r}, s).$$

This expression is reported in the first equation above, and we finally find the propagation equation for shear waves in the Laplace domain:

$$\begin{aligned}\frac{(\widetilde{\rho}_{11} \widetilde{\rho}_{22} - \widetilde{\rho}_{12}^2) s^4 + \frac{\eta \phi^2}{k_0} (\widetilde{\rho}_{11} + \widetilde{\rho}_{22} + 2\widetilde{\rho}_{12}) s^3}{\widetilde{\rho}_{22} s^2 + \frac{\eta \phi^2}{k_0} s} \vec{\Psi}_1(\vec{r}, s) \\ = -N \vec{\nabla} \wedge (\vec{\nabla} \wedge \vec{\Psi}_1(\vec{r}, s)).\end{aligned}$$

Dividing the two  $s$ -variable polynomials, we obtain:

$$\begin{aligned}\frac{\widetilde{\rho}_{11} \widetilde{\rho}_{22} - \widetilde{\rho}_{12}^2}{\widetilde{\rho}_{22}} s^2 + \frac{\eta \phi^2}{k_0} \left( \frac{\widetilde{\rho}_{22} + \widetilde{\rho}_{12}}{\widetilde{\rho}_{22}} \right)^2 s - \left( \frac{\eta \phi^2}{k_0} \right)^2 \left( \frac{\widetilde{\rho}_{22} + \widetilde{\rho}_{12}}{\widetilde{\rho}_{22}} \right)^2 \frac{1}{\widetilde{\rho}_{22}} + \dots \\ = -N \vec{\nabla} \wedge (\vec{\nabla} \wedge \vec{\Psi}_1(\vec{r}, s)),\end{aligned}$$

[8.158]

where  $\dots$  represents the powers of  $s$  of lower orders. Excluding the constant term, it can be noted that these terms vary as  $\phi^n$  with  $n \geq 4$ . Consequently, they quickly become negligible. Restricting to the  $s$  term, the temporal equation for shear waves becomes:

$$\Delta \vec{\psi}_1(\vec{r}, t) - \frac{\widetilde{\rho}_{11}\widetilde{\rho}_{22} - \widetilde{\rho}_{12}^2}{N\widetilde{\rho}_{22}} \frac{\partial^2 \vec{\psi}_1}{\partial t^2} - \frac{\eta\phi^2}{Nk_0} \left( \frac{\widetilde{\rho}_{22} + \widetilde{\rho}_{12}}{\widetilde{\rho}_{22}} \right)^2 \frac{\partial \vec{\psi}_1}{\partial t} = 0. \quad [8.159]$$

In the case of low frequencies, the shear waves propagate in the solid skeleton with the velocity:

$$v_t = \sqrt{\frac{N\widetilde{\rho}_{22}}{\widetilde{\rho}_{11}\widetilde{\rho}_{22} - \widetilde{\rho}_{12}^2}}. \quad [8.160]$$

Writing explicitly the density term of the porous material involved in the vibration and the dissipation term,

$$\rho = \widetilde{\rho}_{11} - \frac{\widetilde{\rho}_{12}^2}{\widetilde{\rho}_{22}} = (1 - \phi)\rho_s + \phi\rho_f(1 - 1/\alpha). \quad [8.161]$$

$$\rho = \widetilde{\rho}_{11} - \frac{\widetilde{\rho}_{12}^2}{\widetilde{\rho}_{22}} = (1 - \phi)\rho_s + \phi\rho_f(1 - 1/\alpha). \quad [8.162]$$

The equation for shear waves can be finally written:

$$\Delta \vec{\psi}_1(\vec{r}, t) - \frac{(1 - \phi)\rho_s + \phi\rho_f(1 - 1/\alpha)}{N} \frac{\partial^2 \vec{\psi}_1}{\partial t^2} - \frac{\eta\phi^2}{\alpha^2 N k_0} \frac{\partial \vec{\psi}_1}{\partial t} = 0. \quad [8.163]$$

Contrary to what occurs at very low frequencies, not all the fluid inside the pores is set in motion by the structure. Only the fraction  $(1 - 1/\alpha)$  of the fluid participates in the transverse movements of the porous material.

### High frequencies

The case of high frequencies is the most interesting as the phenomena caused by time dispersion and attenuation are the more complex. Consequently, we will lay out all the calculations related to the propagation velocities, attenuations and contributions of the slow and fast displacement modes of the solid and the fluid.

In the case of high frequencies, the development of the susceptibility  $\alpha(\omega)$  is:

$$\alpha(\omega) \approx \alpha_\infty \left( 1 + \frac{2}{\Lambda} \sqrt{\frac{\eta}{j\omega\rho_f}} \right). \quad [8.164]$$

The densities are therefore:

$$\begin{aligned}\rho_{11} &= \rho_1 - \phi \rho_f (\alpha_\infty - 1) + \frac{2\rho_f \alpha_\infty}{\Lambda} \sqrt{\frac{\eta}{j\omega \rho_f}} = \widetilde{\rho}_{11} + \frac{2\rho_f \alpha_\infty}{\Lambda} \sqrt{\frac{\eta}{j\omega \rho_f}}, \\ \rho_{12} &= -\phi \rho_f (\alpha_\infty - 1) - \frac{2\rho_f \alpha_\infty}{\Lambda} \sqrt{\frac{\eta}{j\omega \rho_f}} = \widetilde{\rho}_{12} - \frac{2\rho_f \alpha_\infty}{\Lambda} \sqrt{\frac{\eta}{j\omega \rho_f}}, \\ \rho_{22} &= \phi \rho_f \alpha_\infty + \frac{2\rho_f \alpha_\infty}{\Lambda} \sqrt{\frac{\eta}{j\omega \rho_f}} = \widetilde{\rho}_{22} + \frac{2\rho_f \alpha_\infty}{\Lambda} \sqrt{\frac{\eta}{j\omega \rho_f}},\end{aligned}$$

where we now set  $\widetilde{\rho}_{11} = \rho_1 + \phi \rho_f (\alpha_\infty - 1)$ ,  $\widetilde{\rho}_{12} = -\phi \rho_f (\alpha_\infty - 1)$  and  $\widetilde{\rho}_{22} = \phi \rho_f \alpha_\infty$ .

### Longitudinal waves

The propagation equation of longitudinal waves then takes the form:

$$\begin{aligned}\begin{pmatrix} \widetilde{\rho}_{11} & \widetilde{\rho}_{12} \\ \widetilde{\rho}_{12} & \widetilde{\rho}_{22} \end{pmatrix} \frac{\partial^2}{\partial t^2} \begin{pmatrix} \varphi_1 \\ \varphi_2 \end{pmatrix} + \frac{2\rho_f \alpha_\infty}{\Lambda} \sqrt{\frac{\eta}{\rho_f}} \begin{pmatrix} 1 & -1 \\ -1 & 1 \end{pmatrix} \frac{\partial^{3/2}}{\partial t^{3/2}} \begin{pmatrix} \varphi_1 \\ \varphi_2 \end{pmatrix} \\ = \begin{pmatrix} P & Q \\ Q & R \end{pmatrix} \Delta \begin{pmatrix} \varphi_1 \\ \varphi_2 \end{pmatrix}.\end{aligned}\quad [8.165]$$

In the Laplace domain, this system becomes:

$$\Delta \begin{pmatrix} \Phi_1 \\ \Phi_2 \end{pmatrix} = M \begin{pmatrix} \Phi_1 \\ \Phi_2 \end{pmatrix}.\quad [8.166]$$

where the matrix  $M$  is defined by:

$$\begin{aligned}M(1,1) &= (R' \widetilde{\rho}_{11} - Q' \widetilde{\rho}_{12}) s^2 + \frac{2\rho_f \alpha_\infty}{\Lambda} \sqrt{\frac{\eta}{\rho_f}} (Q' + R') s^{3/2}, \\ M(1,2) &= (-Q' \widetilde{\rho}_{22} + R' \widetilde{\rho}_{12}) s^2 - \frac{2\rho_f \alpha_\infty}{\Lambda} \sqrt{\frac{\eta}{\rho_f}} (Q' + R') s^{3/2}, \\ M(2,1) &= (-Q' \widetilde{\rho}_{11} + P' \widetilde{\rho}_{12}) s^2 - \frac{2\rho_f \alpha_\infty}{\Lambda} \sqrt{\frac{\eta}{\rho_f}} (P' + Q') s^{3/2}, \\ M(2,2) &= (P' \widetilde{\rho}_{22} - Q' \widetilde{\rho}_{12}) s^2 + \frac{2\rho_f \alpha_\infty}{\Lambda} \sqrt{\frac{\eta}{\rho_f}} (P' + Q') s^{3/2}.\end{aligned}$$

The trace and determinant of this matrix are given by:

$$\text{tr}(M) = (P' \widetilde{\rho}_{22} + R' \widetilde{\rho}_{11} - 2Q' \widetilde{\rho}_{12}) s^2 + \frac{2\rho_f \alpha_\infty}{\Lambda} \sqrt{\frac{\eta}{\rho_f}} (P' + R' + 2Q') s^{3/2}$$

$$\det(M) = (P'R' - Q'^2) \left( (\widetilde{\rho_{11}}\widetilde{\rho_{22}} - \widetilde{\rho_{12}}^2) s^4 + \frac{2\rho_f\alpha_\infty}{\Lambda} \sqrt{\frac{\eta}{\rho_f}} (\widetilde{\rho_{11}} + \widetilde{\rho_{22}} + 2\widetilde{\rho_{12}}) s^{3/2} \right).$$

*Calculation of the displacements of the solid and of the fluid*

To solve the problem in the time domain, it is necessary to first solve the system [8.166]. For this purpose, we search for the fast and slow modes by decoupling the modes  $\Phi_k$ . The contributions of these modes to the displacements of the phases of the porous material are the eigenvectors of matrix  $M$ , associated with the eigenvalues  $\lambda_\pm$ , whose form is:

$$V_+ = \begin{pmatrix} 1 \\ t(s) \end{pmatrix} \quad \text{and} \quad V_- = \begin{pmatrix} 1 \\ T(s) \end{pmatrix}, \quad [8.167]$$

with:

$$t(z) = \frac{\lambda_- - a_{11}}{a_{12}} \quad [8.168]$$

$$T(z) = \frac{a_{22} - \lambda_-}{a_{12}}. \quad [8.169]$$

Therefore the functions  $\Phi_k$  verify the equations:

$$\frac{\partial^2}{\partial x^2} (\Phi_1 + \Phi_2) = \lambda_- (\Phi_1 + \Phi_2) \quad [8.170]$$

$$\frac{\partial^2}{\partial x^2} (t(z)\Phi_1 + T(z)\Phi_2) = \lambda_+ (t(z)\Phi_1 + T(z)\Phi_2). \quad [8.171]$$

The solutions of this equation corresponding to progressive waves in the direction of positive  $x$  are such that:

$$\Phi_1(x, s) + \Phi_2(x, s) = k_1(s) e^{-x\sqrt{\lambda_-}} \quad [8.172]$$

$$t(s)\Phi_1(x, s) + T(s)\Phi_2(x, s) = k_2(s) e^{-x\sqrt{\lambda_+}}, \quad [8.173]$$

or, after having developed the calculations:

$$\Phi_1(x, s) = k_1(s) \frac{t(s)}{T(s) - t(s)} e^{-x\sqrt{\lambda_-}} - k_2(s) \frac{1}{T(s) - t(s)} e^{-x\sqrt{\lambda_+}}$$

$$\Phi_2(x, s) = k_2(s) \frac{1}{T(s) - t(s)} e^{-x\sqrt{\lambda_+}} - k_1(s) \frac{t(s)}{T(s) - t(s)} e^{-x\sqrt{\lambda_-}}.$$

In these equations, the functions  $k_1(s)$  and  $k_2(s)$  are the integration constants to be determined, for example, from the boundary conditions. To write the solutions in the time domain, we have to specify the various terms of the previous relationships as elementary functions of the variable  $s$ . Thus, we have:

$$\frac{1}{T(s) - t(s)} = \frac{a_{12}}{\lambda_+ - \lambda_-} \quad [8.174]$$

$$\frac{t(s)}{T(s) - t(s)} = \frac{\lambda_- - a_{12}}{\lambda_+ - \lambda_-}, \quad [8.175]$$

with:

$$\begin{aligned} \lambda_+ - \lambda_- &= \frac{P\widetilde{\rho_{22}} - 2R\widetilde{\rho_{11}}}{PR}s^2 \\ &+ \frac{AP\widetilde{\rho_{22}} - 2R\rho_1\widetilde{\rho_{22}} - 2R\phi\rho_0\widetilde{\rho_{22}} + 2R\widetilde{\rho_{11}}\widetilde{\rho_{22}} - 2R\widetilde{\rho_{22}}^2}{PR\widetilde{\rho_{22}}}s^{3/2} \\ \lambda_- - a_{12} &= \frac{Q\widetilde{\rho_{22}}^2 - R\widetilde{\rho_2}^2}{PR\widetilde{\rho_{22}}}s^2 \\ &+ \frac{R((\rho_1 + \phi\rho_0)\widetilde{\rho_{22}} - \widetilde{\rho_{11}}\widetilde{\rho_{22}} + \widetilde{\rho_{12}}^2) + A(R + Q)\widetilde{\rho_{22}}}{PR\widetilde{\rho_{22}}}s^{3/2} \end{aligned}$$

and:

$$A = 2\rho_0\phi\frac{\alpha_\infty}{\Lambda}\sqrt{\frac{\eta\pi}{\rho_f}}.$$

From the identity:

$$\frac{as^2 + bs^{3/2}}{cs^2 + ds^{3/2}} = \frac{a}{c} \left[ 1 + \left( \frac{b}{a} - \frac{d}{c} \right) \frac{1}{\sqrt{s} + d/c} \right], \quad [8.176]$$

we obtain:

$$\frac{t(s)}{T(s) - t(s)} = a_1 \left[ 1 + \frac{b_1 - c_1}{\sqrt{s} + c_1} \right], \quad [8.177]$$

$$\frac{1}{T(s) - t(s)} = a_2 \left[ 1 + \frac{b_2 - c_2}{\sqrt{s} + c_2} \right], \quad [8.178]$$

where we have:

$$a_1 = \frac{Q\widetilde{\rho_{22}}^2 - R\widetilde{\rho_2}^2}{P\widetilde{\rho_{22}}^2 - 2R\widetilde{\rho_{11}}\widetilde{\rho_{22}}}, \quad [8.179]$$

$$b_1 = \frac{(\rho_1 + \phi\rho_0)\widetilde{\rho_{22}} + (\widetilde{\rho_{22}} - \widetilde{\rho_{12}}^2) + A(Q + R)\widetilde{\rho_{22}}}{Q\widetilde{\rho_{22}}^2 - R\widetilde{\rho_{12}}^2}, \quad [8.180]$$



$$c_1 = \frac{AP\tilde{\rho}_{22} - 2R\rho_1\tilde{\rho}_{22} - 2R\phi\rho_0\tilde{\rho}_{22} + 2R\rho_{11}\tilde{\rho}_{22} - 2R\tilde{\rho}_{12}^2}{P\tilde{\rho}_{22}^2 - 2R\rho_{11}\tilde{\rho}_{22}}, \quad [8.181]$$

$$a_2 = \frac{R\widetilde{\rho_{12}} - Q\widetilde{\rho_{22}}}{P\widetilde{\rho_{22}} - 2R\widetilde{\rho_{11}}}, \quad [8.182]$$

$$b_2 = \frac{A(Q + R)}{Q\widetilde{\rho_{22}} - R\widetilde{\rho_{12}}}, \quad [8.183]$$

$$c_2 = c_1 = c. \quad [8.184]$$

The determination of the inverse Laplace transforms of the different expressions leads to the following relationships:

$$\begin{aligned} \mathcal{L}^{-1}\left\{\frac{t(s)}{T(s) - t(s)}\right\} &= a_1 \left[ \delta(t) + \frac{b_1 - c}{\sqrt{\pi t}} + c(b_1 - c)e^{c^2 t} \operatorname{erfc}(c\sqrt{t}) \right] \\ &= \mathfrak{F}(a_1, b_1, c, t), \end{aligned}$$

$$\begin{aligned} \mathcal{L}^{-1}\left\{\frac{1}{T(s) - t(s)}\right\} &= a_2 \left[ \delta(t) + \frac{b_2 - c}{\sqrt{\pi t}} + c(b_2 - c)e^{c^2 t} \operatorname{erfc}(c\sqrt{t}) \right] \\ &= \mathfrak{F}(a_2, b_2, c, t), \end{aligned}$$

where  $\operatorname{erfc}(x)$  is the complementary error function defined by:

$$\operatorname{erfc}(x) = \frac{2}{\sqrt{\pi}} \int_x^\infty e^{-u^2} du = 1 - \operatorname{erf}(x) = 1 - \frac{2}{\sqrt{\pi}} \int_0^x e^{-u^2} du.$$

Since the eigenvalues  $\lambda_\pm$  can be written as:

$$\lambda = \alpha s^2 + \beta s\sqrt{s} = \alpha \left[ \left( s + \frac{\beta}{2\alpha}\sqrt{s} \right)^2 - \left( \frac{\beta}{2\alpha}\sqrt{s} \right)^2 \right],$$

we can easily show that:

$$\begin{aligned} e^{-x\sqrt{\lambda}} &= e^{-x\sqrt{\alpha}\sqrt{(s + \frac{\beta}{2\alpha}\sqrt{s})^2 - (\frac{\beta}{2\alpha}\sqrt{s})^2}}, \\ &= e^{-x\sqrt{\alpha}(s + \frac{\beta}{2\alpha}\sqrt{s})} \\ &\quad + \frac{x\beta}{2\sqrt{\alpha}}\sqrt{s} \int_{x\sqrt{\alpha}}^\infty e^{-\eta(s + \frac{\beta}{2\alpha}\sqrt{s})} \frac{I_1\left(\frac{\beta}{2\alpha}\sqrt{s}\sqrt{\eta^2 - \alpha x^2}\right)}{\sqrt{\eta^2 - \alpha x^2}} d\eta. \end{aligned}$$

To calculate  $\mathcal{L}^{-1}\{e^{-x\sqrt{\lambda}}\}$ , we now have to evaluate the expressions:

$$E_1 = \mathcal{L}^{-1}\left\{e^{-x\sqrt{\alpha}(s+\frac{\beta}{2\alpha}\sqrt{s})}\right\} \text{ and}$$

$$E_2 = \mathcal{L}^{-1}\left\{\sqrt{s} \exp\left(-\eta\left(s+\frac{\beta}{2\alpha}\sqrt{s}\right)\right) I_1\left(\sqrt{s}\frac{\beta}{2\alpha}\sqrt{\eta^2-\alpha x^2}\right)\right\}.$$

#### 8.4.7.1. Calculation of $E_1$

We can easily show that:

$$\mathcal{L}^{-1}\left\{e^{-x\sqrt{\alpha}(s+\frac{\beta}{2\alpha}\sqrt{s})}\right\} = \mathcal{L}^{-1}\left\{e^{-x\sqrt{\alpha}s}\right\} * \mathcal{L}^{-1}\left\{e^{-\frac{x\beta}{2\sqrt{\alpha}}\sqrt{s}}\right\} \quad [8.185]$$

where  $*$  corresponds to the convolution with respect to the dual variable of  $s$ . However, we obtain, by definition of the Dirac function:

$$\mathcal{L}^{-1}\left\{e^{-x\sqrt{\alpha}s}\right\} = \delta(t-x\sqrt{\alpha}) \quad [8.186]$$

and

$$\mathcal{L}^{-1}\left\{e^{-\frac{x\beta}{2\sqrt{\alpha}}\sqrt{s}}\right\} = \frac{1}{4\sqrt{\pi}} \frac{x\beta}{\sqrt{\alpha}} \frac{1}{t^{3/2}} \exp\left(-\frac{x^2\beta^2}{16\alpha t}\right). \quad [8.187]$$

and finally,

$$\mathcal{L}^{-1}\left\{e^{-x\sqrt{\alpha}(s+\frac{\beta}{2\alpha}\sqrt{s})}\right\} = \frac{1}{4\sqrt{\pi}} \frac{x\beta}{\sqrt{\alpha}} \frac{1}{(t-x\sqrt{\alpha})^{3/2}} \exp\left(-\frac{x^2\beta^2}{16\alpha(t-x\sqrt{\alpha})}\right).$$

#### 8.4.7.2. Calculation of $E_2$

From the relationships:

$$E_2 = \delta(t-\eta) * \mathcal{L}^{-1}\left\{\sqrt{s} \exp\left(-\frac{\eta\beta}{2\alpha}\sqrt{s}\right) I_1\left(\sqrt{s}\frac{\beta}{2\alpha}\sqrt{\eta^2-\alpha x^2}\right)\right\} \quad [8.188]$$

and

$$\begin{aligned} & \mathcal{L}^{-1}\left\{\sqrt{s} \exp\left(-\frac{\eta\beta}{2\alpha}\sqrt{s}\right) I_1\left(\sqrt{s}\frac{\beta}{2\alpha}\sqrt{\eta^2-\alpha x^2}\right)\right\} \\ &= -\frac{2}{\pi^{3/2}} \frac{1}{\sqrt{t}} \int_0^1 \exp\left[-\frac{(\mu\frac{\beta}{2\alpha}(\eta+\sqrt{\eta^2-\alpha x^2}))^2}{4t}\right] \frac{\mu d\mu}{\sqrt{1-\mu^2}}, \end{aligned} \quad [8.189]$$

we immediately obtain the following equality:

$$E_2 = -\frac{2}{\pi^{3/2}} \frac{1}{\sqrt{t-\eta}} \int_0^1 \exp \left[ -\frac{(\mu \frac{\beta}{2\alpha} (\eta + \sqrt{\eta^2 - \alpha x^2}))^2}{4(t-\eta)} \right] \frac{\mu d\mu}{\sqrt{1-\mu^2}}. \quad [8.190]$$

To summarize writing  $G(\alpha, \beta, t) = \mathcal{L}^{-1}\{e^{-x\sqrt{\lambda}}\}$ , we have:

$$G(\alpha, \beta, t) = \begin{cases} 0 & \text{if } 0 \leq t \leq x\sqrt{\alpha} \\ \frac{x\beta}{\sqrt{\alpha}} \left[ \mathfrak{R}(t) + \int_0^{t-x\sqrt{\alpha}} H(t, \zeta) d\zeta \right] & \text{otherwise,} \end{cases} \quad [8.191]$$

with:

$$\begin{aligned} \mathfrak{R}(t) &= \frac{1}{4\sqrt{\pi}} \frac{1}{(t-x\sqrt{\alpha})^{3/2}} \exp \left( \frac{x^2\beta^2}{16\alpha(t-x\sqrt{\alpha})} \right), \\ H(t, \zeta) &= -\frac{1}{\pi^{3/2}} \frac{1}{\sqrt{\zeta}} \frac{1}{\sqrt{(t-\zeta)^2 - \alpha x^2}} h(t, \zeta), \\ h(t, \zeta) &= \int_0^1 \exp \left( -\frac{\beta^2 (\mu \sqrt{(t-\zeta)^2 - \alpha x^2} + t - \zeta)}{16\alpha^2 \zeta} \right) \frac{\mu d\mu}{\sqrt{1-\mu^2}}. \end{aligned}$$

The displacement potentials  $\phi_k(x, t)$  are written as follows:

$$\begin{aligned} \phi_1(x, t) &= \Im(a_1, b_1, c, t) * \mathcal{L}^{-1}\{k_1(s)\} * G(\alpha, \beta, t) \\ &\quad - \Im(a_1, b_1, c, t) * \mathcal{L}^{-1}\{k_1(s)\} * G(\alpha, \beta, t) \\ \phi_2(x, t) &= \Re(a_1, b_1, c, t) * \mathcal{L}^{-1}\{k_1(s)\} * G(\alpha, \beta, t) \\ &\quad - \Im(a_1, b_1, c, t) * \mathcal{L}^{-1}\{k_1(s)\} * G(\alpha, \beta, t). \end{aligned}$$

### Transverse waves

At high frequencies, the equations of motion for the transverse displacements are:

$$\begin{aligned} \widetilde{\rho}_{11} \frac{\partial^2 \vec{\psi}_1}{\partial t^2} + \widetilde{\rho}_{12} \frac{\partial^2 \vec{\psi}_2}{\partial t^2} + \frac{2\rho_f \alpha_\infty}{\Lambda} \sqrt{\frac{\eta}{\rho_f}} \left( \frac{\partial^{3/2} \vec{\psi}_1}{\partial t^{3/2}} - \frac{\partial^{3/2} \vec{\psi}_2}{\partial t^{3/2}} \right) &= -N \vec{\nabla} \wedge (\vec{\nabla} \wedge \vec{\psi}_1), \\ \widetilde{\rho}_{12} \frac{\partial^2 \vec{\psi}_1}{\partial t^2} + \widetilde{\rho}_{22} \frac{\partial^2 \vec{\psi}_2}{\partial t^2} + \frac{2\rho_f \alpha_\infty}{\Lambda} \sqrt{\frac{\eta}{\rho_f}} \left( \frac{\partial^{3/2} \vec{\psi}_2}{\partial t^{3/2}} - \frac{\partial^{3/2} \vec{\psi}_1}{\partial t^{3/2}} \right) &= 0. \end{aligned}$$

In the Laplace domain, they become:

$$\begin{aligned}
 & \left( \widetilde{\rho}_{11} s^2 + \frac{2\rho_f \alpha_\infty}{\Lambda} \sqrt{\frac{\eta}{\rho_f}} s^{3/2} \right) \vec{\Psi}_1(\vec{r}, s) + \left( \widetilde{\rho}_{12} s^2 - \frac{2\rho_f \alpha_\infty}{\Lambda} \sqrt{\frac{\eta}{\rho_f}} s^{3/2} \right) \vec{\Psi}_2(\vec{r}, s) \\
 & = -N \vec{\nabla} \wedge (\vec{\nabla} \wedge \vec{\Psi}_1(\vec{r}, s)), \\
 & \left( \widetilde{\rho}_{12} s^2 - \frac{2\rho_f \alpha_\infty}{\Lambda} \sqrt{\frac{\eta}{\rho_f}} s^{3/2} \right) \vec{\Psi}_1(\vec{r}, s) \\
 & + \left( \widetilde{\rho}_{22} s^2 + \frac{2\rho_f \alpha_\infty}{\Lambda} \sqrt{\frac{\eta}{\rho_f}} s^{3/2} \right) \vec{\Psi}_2(\vec{r}, s) = 0.
 \end{aligned}$$

Applying to the first equation the value of  $\vec{\Psi}_1(\vec{r}, s)$  obtained from the second equation, we find:

$$\begin{aligned}
 & \frac{(\widetilde{\rho}_{11} \widetilde{\rho}_{22} - \widetilde{\rho}_{12}^2) s^4 + \frac{2\rho_f \alpha_\infty}{\Lambda} \sqrt{\frac{\eta}{\rho_f}} (\widetilde{\rho}_{11} + \widetilde{\rho}_{22} + 2\widetilde{\rho}_{12}) s^{7/2}}{\widetilde{\rho}_{22} s^2 + \frac{2\rho_f \alpha_\infty}{\Lambda} \sqrt{\frac{\eta}{\rho_f}} s^{3/2}} \vec{\Psi}_1(\vec{r}, s) \\
 & = -N \vec{\nabla} \wedge (\vec{\nabla} \wedge \vec{\Psi}_1(\vec{r}, s)).
 \end{aligned}$$

After a division of the two  $s$  polynomes, and, keeping only the significant terms, we finally obtain:

$$\begin{aligned}
 & \frac{\widetilde{\rho}_{11} \widetilde{\rho}_{22} - \widetilde{\rho}_{12}^2}{\widetilde{\rho}_{22}} s^2 + \frac{2\rho_f \alpha_\infty}{\Lambda} \sqrt{\frac{\eta}{\rho_f}} \left( \frac{\widetilde{\rho}_{22} + \widetilde{\rho}_{12}}{\widetilde{\rho}_{22}} \right)^2 s^{3/2} \\
 & - \left( \frac{2\rho_f \alpha_\infty}{\Lambda} \sqrt{\frac{\eta}{\rho_f}} \right)^2 \left( \frac{\widetilde{\rho}_{22} + \widetilde{\rho}_{12}}{\widetilde{\rho}_{22}} \right)^2 \frac{1}{\widetilde{\rho}_{22}} s \\
 & = -N \vec{\nabla} \wedge (\vec{\nabla} \wedge \vec{\Psi}_1(\vec{r}, s)).
 \end{aligned} \tag{8.192}$$

In the temporal domain, this equation therefore yields:

$$\begin{aligned}
 \Delta \vec{\Psi}_1(\vec{r}, s) & = \frac{\widetilde{\rho}_{11} \widetilde{\rho}_{22} - \widetilde{\rho}_{12}^2}{N \widetilde{\rho}_{22}} \frac{\partial^2 \vec{\Psi}_1}{\partial t^2} \\
 & + \frac{2\rho_f \alpha_\infty}{N \Lambda} \sqrt{\frac{\eta}{\rho_f}} \left( \frac{\widetilde{\rho}_{22} - \widetilde{\rho}_{12}}{\widetilde{\rho}_{22}} \right)^2 \frac{\partial^{3/2} \vec{\Psi}_1}{\partial t^{3/2}} \\
 & + \left( \frac{2\rho_f \alpha_\infty}{\Lambda} \sqrt{\frac{\eta}{\rho_f}} \right)^2 \left( \frac{\widetilde{\rho}_{22} + \widetilde{\rho}_{12}}{\widetilde{\rho}_{22}} \right)^2 \frac{1}{N \widetilde{\rho}_{22}} \frac{\partial \vec{\Psi}_1}{\partial t}.
 \end{aligned} \tag{8.193}$$

Explicitly writing the density terms, this expression can be rewritten as follows:

$$\Delta \vec{\Psi}_1(\vec{r}, s) = \frac{(1 - \phi)\rho_s + \phi\rho_f(1 - 1/\alpha)}{N} \frac{\partial^2 \vec{\Psi}_1}{\partial t^2} + \frac{2\rho_f}{N\Lambda\alpha_\infty} \sqrt{\frac{\eta}{\rho_f}} \frac{\partial^{3/2} \vec{\Psi}_1}{\partial t^{3/2}} + \left( \frac{2}{\Lambda} \sqrt{\frac{\eta}{\rho_f}} \right)^2 \frac{\rho_f}{N\phi\alpha_\infty} \frac{\partial \vec{\Psi}_1}{\partial t}. \quad [8.194]$$

## 8.5. Bibliography

- [ALL 92b] ALLARD J.F. and CHAMPOUX Y., “New empirical equations for sound propagation in rigid frame fibrous materials”, *J. Acoust. Soc. Am.*, vol. 91, no. 6, pp. 3346–3353, 1992.
- [AUR 95] AURIAULT J.L., BORNE L. and CHAMBON R., “Dynamics of porous saturated media, checking of the generalized law of Dracy”, *J. Acoust. Soc. Am.*, vol. 77, no. 5, pp. 1641–1650, 1985.
- [BAG 83] BAGLEY R.L. and TORVIK P.J., “On the fractional calculus model of viscoelastic behavior”, *J. Rheol.*, vol. 30, no. 1, pp. 133–155, 1983.
- [BIO 56a] BIOT M.A., “Theory of propagation of elastic waves in a fluid-saturated porous solid. I. Low-frequency range”, *J. Acoust. Soc. Am.*, vol. 28, no. 2, pp. 168–178, 1956.
- [BIO 56b] BIOT M.A., “Theory of propagation of elastic waves in a fluid-saturated porous solid. II. Higher frequency range”, *J. Acoust. Soc. Am.*, vol. 28, no. 2, pp. 179–191, 1956.
- [BOU 87] BOUTIN C., BONNET G. and BARD P.Y., “Green’s functions and associated sources in infinite and stratified poroelastic media”, *Geophys. J. R. astr. Soc.*, vol. 90, pp. 521–550, 1987.
- [BUR 81] BURRIDGE R. and KELLER J.B., “Poroelasticity equations derived from microstructure”, *J. Acoust. Soc. Am.*, vol. 70, no. 4, pp. 1140–1146, 1981.
- [CAP 66] CAPUTO M., “Linear models of dissipation whose  $Q$  is almost frequency independent”, *Annali di Geofisica*, vol. 19, no. 4, pp. 383–393, 1966.
- [CAP 71] CAPUTO M. and MAINARDI F., “Linear models of dissipation in anelastic solids”, *Riv. Nuovo Cimento*, vol. 1, no. 2, pp. 161–198, 1971.
- [CAR 96] CARCIONE J.M. and QUIROGA-GOODE G., “Full frequency-range transient solution for compressional waves in a fluid-saturated viscoacoustic porous medium”, *Geophys. Prospect.*, vol. 44, no. 1, pp. 99–129, 1996.
- [FEL 00] FELLAH Z.E.A. and DEPOLLIER C., “Transient acoustic wave propagation in rigid porous media: A time domain approach”, *J. Acoust. Soc. Am.*, vol. 107, no. 2, pp. 683–688, 2000.
- [FEL 01] FELLAH Z.E.A., DEPOLLIER C. and FELLAH M., “Direct and inverse scattering problem in porous material having a rigid frame by fractional calculus based method”, *J. Sound and Vibration*, vol. 244, no. 2, pp. 3659–3666, 2001.

- [FEL 02] FELLAH Z.E.A., DEPOLLIER C. and FELLAH M., "Application of fractional calculus to the sound waves propagation in rigid porous materials: Validation via ultrasonic measurements", *Acta Acustica United with Acustica*, vol. 88, no. 1, pp. 34–39, 2002.
- [FEL 03] FELLAH Z.E.A., FELLAH M., LAURIKS W. and DEPOLLIER C., "Direct and inverse scattering of transient acoustic waves by a slab of rigid porous material", *J. Acoust. Soc. Am.*, vol. 113, no. 1, pp. 61–72, 2003.
- [FEL 03a] FELLAH Z.E.A., FELLAH M., LAURIKS W., DEPOLLIER C., ANGEL Y. and CHAPELON J.Y., "Solution in time domain of ultrasonic propagation equation in porous material", *Wave Motion*, vol. 38, no. 2, pp. 151–163, 2003.
- [FEL 03b] FELLAH Z.E.A., BERGER S., LAURIKS W., DEPOLLIER C., ARISTEGUI C. and CHAPELON J. Y., "Measuring the porosity and the tortuosity of porous materials via reflected waves at oblique incidence", *J. Acoust. Soc. Am.*, vol. 113, no. 5, pp. 2424–2433, 2003.
- [FEL 03c] FELLAH Z.E.A., BERGER S., LAURIKS W., DEPOLLIER C. and CHAPELON J.Y., "Inverse problem in air-saturated porous media via reflected waves", *Rev. Sci. Inst.*, vol. 74, no. 5, pp. 2871–2879, 2003.
- [FEL 03d] FELLAH Z.E.A., BERGER S., LAURIKS W., DEPOLLIER C., TROMPETTE P. and CHAPELON J.Y., "Ultrasonic measurement of the porosity and tortuosity of air-saturated random packings of beads", *J. Appl. Phys.*, no. 93, no. 11, pp. 9352–9359, 2003.
- [FEL 03e] FELLAH Z.E.A., MITRI F., DEPOLLIER C., BERGER S., LAURIKS W. and CHAPELON J.Y., "Characterization of porous materials with a rigid frame via reflected waves", *J. Appl. Phys.*, vol. 94, no. 12, pp. 7914–7922, 2003.
- [FEL 03f] FELLAH Z.E.A., DEPOLLIER C., BERGER S., LAURIKS W., TROMPETTE P. and CHAPELON J.Y., "Determination of transport parameters in air saturated porous materials via ultrasonic reflected waves", *J. Acoust. Soc. Am.*, vol. 114, no. 5, pp. 2561–2569, 2003.
- [JOH 86] JOHNSON D.L., "Recent developments in the acoustic properties of porous media", in *Proc. Int. School of Physics "Enrico Fermi"*, North Holland Publishing Co., Amsterdam, pp. 255–290, 1986.
- [JOH 87] JOHNSON D.L., KOPLIK J. and DASHEN R., "Theory of dynamic permeability and tortuosity in fluid-saturated porous media", *J. Fluid. Mech.*, vol. 176, pp. 379–402, 1987.
- [KHI 68] KIRCHHOFF G., "Ueber die Einfluss der Wärmeleitung in einem Gase auf die Schallbewegung", *Annalen der Physik Leipzig*, vol. 134, pp. 177–193, 1868 (English translation (1974) in: LINDSAY, R.B. (ed.), *Physical Acoustics*, Downden, Hutchinson and Ross, Stroudsburg).
- [LAF 93] LAFARGE D., Propagation du son dans les matériaux poreux à structure rigide saturés par un fluide viscothermique, PhD Thesis, The University of Maine, 1993.
- [LAF 96] LAFARGE D., LEMARNIER P., ALLARD J.F. and TARNOW V., "Dynamic compressibility of air in porous structures at audible frequencies", *J. Acoust. Soc. Am.*, vol. 4, no. 102, pp. 1995–2006, 1996.
- [LEI 45] LEIBNITZ G.W., *Math. Schrift*, vol. 2, p. 301, 1845.

- [MAT 94] MATIGNON D., Représentations en variables d'état de modèles de guides d'ondes avec dérivation fractionnaire, PhD Thesis, University of Paris XI Orsay, 1994.
- [MIL 93] MILLER K.S. and ROSS B., *An Introduction to the Fractional Calculus and Fractional Differential Equations*, John Wiley & Sons, New York, 1993.
- [NOR 86] NORRIS A. N., "On the viscodynamic operator in Biot's equations of poroelasticity", *J. Wave Mat. Interact.*, vol. 1, pp. 365–380, 1986.
- [OLD 74] OLDHAM K.B. and SPANIER J., *The Fractional Calculus*, Academic Press, New York, 1974.
- [PIE 81] PIERCE A.D., *Acoustics an Introduction to its Physical Principles and Applications*, McGraw-Hill, New York, 1981.
- [POD 99] PODLUBNY I., *Fractional Differential Equations*, Academic Press, San Diego, 1999.
- [RIE 96] RIEWE F., "Nonconservative Lagrangian and Hamiltonian mechanics", *Phys. Rev. E*, vol. 53, no. 2, pp. 1890–1899, 1996.
- [RIE 97] RIEWE F., "Mechanics with fractional derivatives", *Phys. Rev. E*, vol. 55, no. 3, pp. 3581–3592, 1997.
- [SAM 93] SAMKO S.G., KILBAS A.A. and MARICHEV O.I., *Fractional Integrals and Derivatives Theory and Applications*, Gordon and Breach Publishers, Amsterdam, 1993.
- [ZWI 49] ZWIKKER C. and KOSTEN C.W., *Sound Absorbing Materials*, Elsevier, 1949.

This page intentionally left blank



## Chapter 9

# Scattering in Porous Media

### 9.1. Introduction

In Chapters 6, 7 and 8, wavelengths are assumed to be much greater than the characteristic dimension associated with inhomogeneities present in porous material. We can omit the scattering phenomena and there is a macroscopic description of the propagation in terms of an equivalent effective medium (equivalent fluid, or medium described by the Biot's theory).

When the wavelengths can no longer be considered much greater than inhomogeneities present in the media, we enter into the domain of multiple scattering. For plastic foams and fibrous materials commonly used for their absorption properties, this happens in the range of ultrasonic frequencies.

In this section we give some basic results about the multiple scattering in 2D diluted media, like the one shown in Figure 9.1.

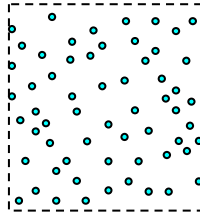


**Figure 9.1.** *fluid medium with diluted solid inclusions  
(disks in 2D, spheres in 3D)*

In general, the detailed calculation of the effects of multiple scattering is not readily feasible. However, materials used for sound absorption often have a porosity close to 1, approximately  $\phi = 0.98$ , and there is essentially a collection of fibers of small radius ( $> 10 \mu m$ ) separated by distances of 10 times this radius in the medium.

With “scatterers” such as cylinders or spheres, in low concentration, a quite simple closed-form calculation of the multiple scattering (not taking into account high orders of scattering) is possible. In this idealized image of the structure of the material, the viscous and thermal losses can be introduced analytically in the form of surface admittances of solid inclusions.

By doing this, it can be shown that the calculation of multiple scattering is coherent with the high frequency limits of the model of the equivalent fluid (section 6.1.2.14), before predicting deviations due to scattering phenomena in higher frequency ranges.

### **9.1.1. Analysis of multiple scattering in the context of the Independent Scattering Approximation (ISA)**

In situations where multiple scattering occurs, but we are interested in the actual properties of the medium, two parts generally have to be considered in the acoustic field propagating in the disordered medium: the coherent and incoherent parts. The coherent one is found by averaging over the possible configurations of the medium, and this is the one we observe on a macroscopic scale.

A quantity of interest which describes the coherent wave propagation in a multiple scattering medium is Green’s function averaged over many configurations [SHE 95]. This function can be written as

$$\langle G \rangle(\omega, \vec{k}) = \frac{1}{k_0^2 - k^2 - \Sigma(\omega, \vec{k})}, \quad [9.1]$$

where  $\langle \dots \rangle$  denotes the average over configurations,  $k_0$  is the wavenumber in the free fluid medium,  $\omega$  is the pulsation,  $\vec{k}$  is the wave vector, and  $\Sigma(\omega, \vec{k})$  is the so-called self energy.

The self energy that arises due to local deviations of the medium wavenumber from the uniform-medium value  $k_0$ , contains information about the multiple scattering. In particular, in a regime where the self energy does not depend on  $\vec{k}$ , it becomes possible to define an effective medium, seen as a homogeneous medium by the coherent component of the wave [SHE 95]. According to equation [9.1], the propagation of the coherent wave is described by an effective wave number  $k_e$  defined by,

$$k_e^2 = k_0^2 - \Sigma(\omega), \quad [9.2]$$

and the problem reduces to the calculation of the self energy  $\Sigma(\omega)$ .

The *Independent Scattering Approximation* assumes that there is no correlation between the scatterers [TSA 00]. In this approximation, the self energy, used to renormalize the effective wave number of the multiple scattering medium, is given by [LAG 96],

$$\Sigma(\omega) = n \langle \vec{k}_0 | t | \vec{k}_0 \rangle, \quad [9.3]$$

where  $n$  is the density of scatterers in the medium, and  $\langle \vec{k}_0 | t | \vec{k}_0 \rangle$  the forward scattering term of the t-matrix for a single scatterer. Discarding correlations between scatterers, approximation [9.3] may be correct only in a diluted limit.

### 9.1.2. Array of cylinders in air

#### 9.1.2.1. Basic scattering problem

We consider a random array of cylinders placed in air (Figure 9.1) and we apply the above theory. In air, propagation of the acoustic pressure  $p$  is governed by the Helmholtz equation,

$$\Delta p + k_0^2 p = 0. \quad [9.4]$$

In order to apply the above theory, we must solve the elementary problem of the scattering of a plane wave  $e^{i\vec{k}_0 \cdot \vec{r}}$  by a solid inclusion of radius  $R$  located at the origin of the coordinate system (Figure 9.2).

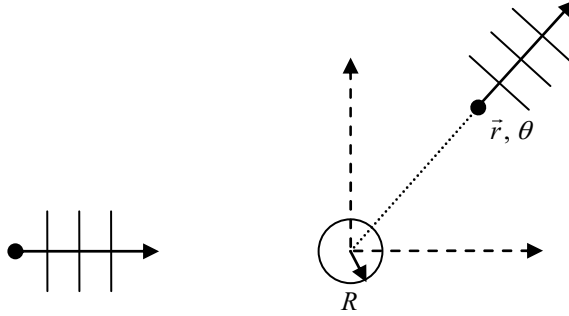


**Figure 9.2.** *Geometry of the elementary scattering problem*

The plane wave  $e^{i\vec{k}_0 \cdot \vec{r}}$  can be written as a sum of the Bessel functions,  $J_m(k_0 r) \cos(m\theta)$ ,

$$e^{i\vec{k}_0 \cdot \vec{r}} = \sum_{m=0}^{\infty} i^m (2 - \delta_{m0}) J_m(k_0 r) \cos(m\theta). \quad [9.5]$$

The scattered field is expanded on the outgoing Hankel functions  $H_m^1(k_0 r) \cos(m\theta)$ . The total acoustic pressure (incident and scattered fields) is written

$$\begin{aligned} p(r, \theta) &= \sum_{m=0}^{\infty} p_m(r, \theta) \\ &= \sum_{m=0}^{\infty} i^m (2 - \delta_{m0}) \{ J_m(k_0 r) + D_m H_m^1(k_0 r) \} \cos(m\theta), \end{aligned} \quad [9.6]$$

where  $D_m$  are the scattering coefficients. Different expressions for the  $D_m$  coefficients can be obtained depending on the properties of the scatterer and the

fluid. They depend on the boundary conditions on the interface  $r = R$  between the fluid and the solid inclusion.

We consider here only the two simple following cases: (i) rigid scatterers and perfect fluid, (ii) rigid motionless scatterers and thermoviscous fluid in a high frequency limit  $\delta \ll R$ , where  $\delta$  is the thickness of the boundary layer. In the first case, the condition that the normal speed is zero at  $r = R$  yields

$$D_m = -\frac{J'_m(k_0 R)}{H'_m(k_0 R)}. \quad [9.7]$$

In the second case we must take into account the thin viscous and thermal boundary layers in contact with the solid surface  $r = R$ . The scattering coefficients  $D_m$  including these effects are obtained as follows.

In the case of a plane wave incident on a motionless flat surface of large heat capacity, taking into account the viscous and thermal boundary layers, leads us to define an equivalent admittance  $\beta$  which relates the pressure  $p$  and its normal derivative by  $-i\beta k_0 p = \partial p / \partial n$ . A simple calculation shows that the admittance  $\beta$  has the following form [MOR 87],

$$\beta = \frac{1-i}{2} k_0 \left[ (\gamma-1)\delta' + \left( 1 - \frac{k_{0\perp}^2}{k_0^2} \right) \delta \right], \quad [9.8]$$

where  $\delta$  and  $\delta'$  are the thicknesses of the thermal and viscous layers (c.f. section 6.1.2.11) and  $k_{0\perp}$  is the normal component of the wave vector. In our case, the scatterer is not flat, but in the limit  $\delta \ll R$  it can be considered as effectively flat at the spatial scale of the boundary layer. An expression for the admittance  $\beta_m$  seen by a component  $m$  of the field can be obtained from [9.8] by identifying the normal component of the wave number  $k_{0\perp}$  with the radial wave number  $k_r$ , defined by  $k_r^2 = k_0^2 - m^2 / r^2$ :

$$\beta_m = \frac{1-i}{2} k_0 \left[ (\gamma-1)\delta' + \frac{m^2}{k_0^2 R^2} \delta \right]. \quad [9.9]$$

This equivalent admittance  $\beta_m$  relates the component  $p_m$  of the acoustic pressure to its normal derivative according to the equation (written at  $r = R$ ),

$$-i\beta_m k_0 p_m = \partial p_m / \partial r . \quad [9.10]$$

The application of equations [9.6], [9.10], yields the following scattering coefficients, which take into account the viscous and thermal losses at the boundaries,

$$D_m = - \frac{J'_m(k_0 R) + i\beta_m J_m(k_0 R)}{H'_m(k_0 R) + i\beta_m H_m(k_0 R)} . \quad [9.11]$$

#### 9.1.2.2. *ISA and ISA $\beta$*

The self energy  $\Sigma(\omega)$  can be expressed directly from the scattering coefficients  $D_m$ . We obtain the expression [LAG 96]

$$\Sigma(\omega) = 4ni \sum_{m=0}^{\infty} (2 - \delta_{m0}) D_m . \quad [9.12]$$

In the following, *ISA* will denote the general pattern obtained by replacing in [9.12] the scattering coefficients by their expression given in [9.7]. *ISA $\beta$*  will denote the model obtained by replacing in [9.12] the scattering coefficients by [9.11], taking into account the viscous and thermal losses.

Using [9.12], [9.2] and [9.7] (*ISA* model) or [9.11] (*ISA $\beta$*  model), the effective wave number  $k_e$  can be explicitly evaluated.

#### 9.1.2.3. *Long wavelength limit*

In the range of long wavelength, the *ISA $\beta$*  results must be coherent with those given by the long wavelength theory of section 6.1.2.

On one hand, when the wavelength becomes very large compared to the scatterer radius  $R$ ,  $k_0 R \rightarrow 0$ , we only have a Rayleigh scattering (monopole and dipole radiation). The self energy summation in expression [9.12] may be limited to  $m = 0, 1$ , and the Bessel and Hankel functions in equation [9.11] may be developed in powers of  $k_0 R$ . The result, restricted to the first order of  $k_0 R$ , is given by

$$k_e^2 = k_0^2 \left\{ 1 + f \left[ 1 + (1+i) \left( \frac{2\delta}{R} + (\gamma-1) \frac{\delta'}{R} \right) \right] \right\} , \quad [9.13]$$

where  $f = n\pi R^2 = 1 - \phi$  is the solid–fluid ratio (specific volume of cylinders = 1–porosity).

On the other hand, assuming that we simultaneously ensure the conditions  $\lambda \gg L_h$  and  $\delta, \delta' \ll R$ , the results of the “frozen” high frequency limit from the equivalent fluid theory (section 6.1.2) should be applicable, so that

$$k_e^2 = k_0^2 \alpha_\infty \left\{ 1 + (1+i) \left( \frac{\delta}{\Lambda} + (\gamma-1) \frac{\delta'}{\Lambda'} \right) \right\}. \quad [9.14]$$

This expression derives from the general formula  $k_e = k_0 \sqrt{\alpha(\omega)\beta(\omega)}$ , (c.f. [6.129]) in which the “frozen” expressions of the quantities  $\alpha(\omega)$  and  $\beta(\omega)$  are used.

We note that the result of the  $ISAB$  [9.13] is thought to be correct only in a diluted limit. The result [9.14] is correct, whatever the concentration of the medium. The effect of the correlations between the positions of the scatterers, not included in the result of the  $ISAB$ , will affect the terms of higher order in  $f$  that consequently cannot be discarded when the concentration increases. Therefore, in order to compare those two results properly, we must restrict [9.14] to the only terms that are proportional to the concentration  $f$ .

For a diluted limit, we show [TOU 04] that the following results are exact, up to the first order in  $f$ ,

$$\alpha_\infty = 1 + f, \quad \frac{1}{\Lambda} = \frac{2f}{R}, \quad \frac{1}{\Lambda'} = \frac{f}{R}. \quad [9.15]$$

Thus, up to the first order in  $f$  and in the long wavelength limit, the multiple scattering computation  $ISAB$  is coherent with the results of the equivalent “frozen” fluid limit.

#### 9.1.2.4. Application to polyurethane foams and other fibrous materials

In the ultrasonic frequency range, if the frequency is high enough, the corresponding wavelength becomes small enough, such that the scattering phenomena appear significantly. Attenuation  $e^{-\text{Im}(k_e)x}$  and phase velocities  $v = \omega / \text{Re}(k_e)$  are no longer described in a pertinent manner by the equivalent “frozen” fluid limit [9.14]. This issue has been studied [TOU 04] on polyurethane foams with open cells having low resistivities. For example, on a foam with a

resistivity  $\sigma = \eta / k_0 \approx 1000 \text{ kg m}^{-3} \text{ s}^{-1}$ , it appears that scattering is not negligible for a frequency larger than about 80 kHz.

Below this frequency, attenuation and phase velocities remain coherent with the equivalent fluid model. Above that frequency, the equivalent fluid model is no longer appropriate. Despite the complicated geometry of the foam, it appears that the measured attenuation and phase velocities are very adequately reproduced by the multiple scattering model  $ISA\beta$  with two parameters. Those two parameters are an equivalent radius  $R$  of the scatterers, and an equivalent concentration  $n$  of the scatterers (or alternatively an equivalent fraction  $f = n\pi R^2$ ). It is generally enough to reproduce the observed behavior.

## 9.2. Bibliography

- [LAG 96] Lagendijk A., van Tiggelen B.A., “Resonant multiple scattering of light”, *Phys. Rep.*, 270, 143, 1996
- [MOR 87] Morse P.M., Ingard K.U., *Theoretical Acoustics*, Princeton University Press, Princeton, 1987
- [SHE 95] Sheng P., *Introduction to Wave Scattering, Localization, and Mesoscopic Phenomena*, Academic Press, New York, 1995
- [TOU 04] Tournat V., Pagneux V., Lafarge D., Jaouen L., “Multiple scattering of acoustic waves and porous absorbing media”, *Phys. Rev.*, E 70, 1, 2004
- [TSA 00] Tsang L., Kong J.A., Ding K.H., *Scattering of Electromagnetic Waves, Vol. 1: Theory and Applications*, Wiley Interscience, New York, 2000



## Chapter 10

# Stratified Porous Media

### 10.1. Introduction

Many studies of the acoustic properties of layered materials have been conducted [EWI 57, BRE 60]. The starting point of this research is to study the propagation of sound in a layer of material. The problem is then generalized to the association of several of these layers. The combined materials are similar: they are fluids or viscoelastic solids, isotropic or non-isotropic.

In this chapter we will focus on laminated media with at least one layer of porous material.

The modelization of sound propagation in a layer of material can be done using matrices under certain conditions that will be explained later. Different matrix representations exist:

- The *transfer matrices* connect the stresses and velocities on one side of the layer (the whole form what we will now call a *state vector*) to stresses and velocities on the other side.
- The *impedance matrices* connect the stresses to velocities on both sides of the layer being studied.

The transfer matrices are used to model multilayers [ALL 87], since they characterize the propagation of a state vector through each layer. Moreover, impedance matrices are interesting to highlight certain properties of the layers, especially the reciprocity [ALL 92, ALL 93b, CAS 45, KER 89, LAM 84].

The numerical prediction of laminate media properties is very simple when the layers are made of the same type of material (fluid, solid or porous medium): we can simply multiply the matrices that describe the propagation in each layer. However, when the layers vary in nature, it is necessary to use a general prediction of the acoustic properties of a multilayered medium. This method is based on the use of transfer matrices defined above, and *interface matrices*, used to connect the state vectors of two successive layers.

In the first two sections, we will present the modelization of the plane wave propagation in a layer of material (fluid, solid or porous material). In the third paragraph, we will then study the association of these layers through a general method, leading to the full acoustic characterization of a multilayered medium.

## 10.2. Matrix representation of the propagation in fluid or solid layers

### 10.2.1. Propagation in fluids

A layer of material with thickness  $L$ , between two semi-infinite layers of air, is represented in Figure 10.1. A plane wave in air hits this layer on the left-hand side, with an incidence angle  $\theta$ . The incidence plane is  $(xOz)$ .

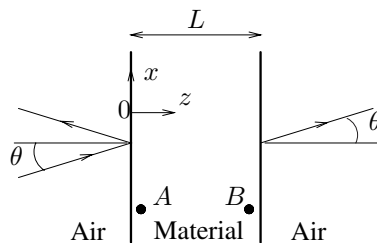


**Figure 10.1.** Layer of material (thickness  $L$ ) in air. An incident plane wave hits the material with an incidence angle  $\theta$ , propagating from the left-hand side

It should be noted that Figure 10.1 describes the Snell-Descartes laws: for the reflected and transmitted waves represented in this figure, the incidence angle is equal to the reflection angle and the emerging angle of the transmitted plane wave in air, after propagation through the layer (on the right-hand side of the material), is also  $\theta$ . The layer must be invariant by translation in all directions included in the parallel planes  $(xOy)$  limiting this layer. The material must therefore be uniform parallel to its surface. If the material is not homogenous along the  $z$ -axis, the propagation can be modeled by subdividing the layer into a sufficient number of homogenous sub-layers. The properties of these sub-layers vary as functions of  $z$ .

The time convention being used is  $e^{j\omega t}$ . Let  $p_i$  be the pressure associated with the incident wave, with a unitary amplitude:

$$p_i = e^{-j(kx+k_z z)}. \quad [10.1]$$

In this expression,  $k$  and  $k_z$  are the two non-zero components of the wave vector on the  $0x$  and  $0z$  directions, respectively. They satisfy the following equation:

$$k^2 + k_z^2 = k_0^2 = \frac{\omega^2}{c_0^2} \quad [10.2]$$

where  $k_0$  and  $c_0$  are respectively the wave number and the sound speed in air. These two quantities are considered real with a good approximation. The incidence angle is given by:

$$\theta = \arctan(k/k_z). \quad [10.3]$$

The  $k$  component is preserved in each layer, regardless of the material (Snell-Descartes law). If the relationship:

$$k > k_0 \quad [10.4]$$

is verified, then the  $k_z$  component is a pure imaginary complex number, and the angle  $\theta$  is also complex. In this case, we are talking about an inhomogenous incident plane wave, i.e. a propagation of a plane wave in the  $0x$  direction, with an amplitude that decreases in the  $0z$  direction.

The incident plane wave yields the generation of a reflected plane wave  $p_r$  at  $x = 0$ , with a complex amplitude  $R$ :

$$p_r = Re^{-j(kx-k_z z)}, \quad [10.5]$$

and a transmitted plane wave  $p_t$  at  $x = L$ , with a complex amplitude  $T$ :

$$p_t = Te^{-j(kx+k_z z)}. \quad [10.6]$$

In the previous two equations,  $R$  and  $T$  are respectively the reflection and transmission coefficients of the layer of thickness  $L$ . In this layer, there is a superposition of waves propagating in the direction  $0z$  and in the opposite direction.

Let us focus now on the problem of a fluid layer of density and sound speed  $\rho_f$  and  $c_f$ , respectively. Viscothermal losses in the fluid can be taken into account by considering an effective complex density and compressibility. Here, we are focusing only on fluids where the dissipation is low enough to be neglected for the acoustic frequencies considered. We define the state vector  $V^f$  of a fluid layer by the relationship:

$$V^f = \begin{pmatrix} p \\ v \end{pmatrix}, \quad [10.7]$$

and we can also note:

$$V_-^f = \begin{pmatrix} p^- \\ v^- \end{pmatrix} \quad \text{and} \quad V_+^f = \begin{pmatrix} p^+ \\ v^+ \end{pmatrix}, \quad [10.8]$$

the state vectors at  $A$  ( $x = 0$  in the fluid) and  $B$  ( $x = L$  in the fluid), respectively. The terms  $v^+$  and  $v^-$  designate the projections of the acoustic speeds on the  $0z$  axis. The sound propagation in the layer of material can be written in the following well-known matrix form [BRU 98]:

$$V_-^f = \begin{pmatrix} \cos(k_z L) & j \frac{\omega \rho_f}{k_z} \sin(k_z L) \\ j \frac{k_z}{\omega \rho_f} \sin(k_z L) & \cos(k_z L) \end{pmatrix} V_+^f = [T_f] V_+^f. \quad [10.9]$$

The matrix  $[T_f]$  is the transfer matrix of a fluid. With the previous notations, we have  $p^- = p_i + p_r$  and  $p^+ = p_t$ . Equation [10.9] can be rewritten as follows:

$$\begin{pmatrix} p^- \\ p^+ \end{pmatrix} = \frac{j\omega\rho_f}{k_z} \begin{pmatrix} -\cot(k_z L) & \frac{1}{\sin(k_z L)} \\ \frac{-1}{\sin(k_z L)} & \cot(k_z L) \end{pmatrix} \begin{pmatrix} v^- \\ v^+ \end{pmatrix} = [Z_f] \begin{pmatrix} v^- \\ v^+ \end{pmatrix}, \quad [10.10]$$

where  $[Z_f]$  is the impedance matrix of a layer of fluid of thickness  $L$ .

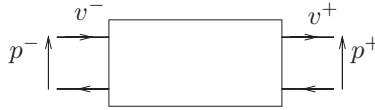


**Figure 10.2.** *Quadrupole equivalent to a layer of fluid*

The layer can be represented by the quadrupole shown in Figure 10.2. This quadrupole is reciprocal because the matrix  $[Z_f]$  satisfies the following property:

$$Z_{12} = -Z_{21} = \frac{j\omega\rho_f}{k_z \sin(k_z L)}. \quad [10.11]$$

The negative sign in equation [10.11] comes from the fact that a positive product of the variables  $p^-$  and  $v^-$  is connected to an energy flow going into the material, while a positive product of the quantities  $p^+$  and  $v^+$  is connected to an energy flow going out of the layer (see Figure 10.2). In section 10.4.3.2, we will see an interesting result of this property. The quadrupole of Figure 10.2 is obviously symmetric because the system is geometrically symmetric. Therefore, we have:

$$Z_{11} = -Z_{22}. \quad [10.12]$$

The negative sign is due to the same sign convention for acoustic speeds on each side of the layer.

### 10.2.2. Propagation in viscoelastic solids – reciprocity and antireciprocity

The propagation of sound in solid media is very well known. Two types of wave propagation can occur:

- compression waves, or longitudinal waves;
- shear waves, or transverse waves.

A layer of solid is characterized by its thickness  $L$ , its density  $\rho_a$  and its two Lamé coefficients  $\lambda$  and  $\mu$ . In the case of a viscoelastic solid, the coefficients  $\lambda$  and  $\mu$  are complex numbers, which are connected to the Young's modulus  $E$  and the Poisson coefficient  $\nu$  of the solid by the following equations:

$$\lambda = \frac{E\nu}{(1+\nu)(1-2\nu)}, \quad [10.13]$$

$$\text{and } \mu = \frac{E}{2(1+\nu)}. \quad [10.14]$$

These two waves propagate at different velocities: the first, called *slow wave*, corresponding to the shear wave, propagates at the complex velocity  $v_t = \sqrt{\mu/\rho_s}$ ; the second, called *rapid wave*, propagates at the velocity  $v_\ell = \sqrt{(\lambda + \mu)/\rho_s}$ .

The transfer matrix of a viscoelastic solid layer was calculated by Fold and Loggins in 1977 [FOL 77]. It consists of a  $(4 \times 4)$  matrix, that links the state vector:

$$(v_z, v_x, \sigma_z, \sigma_x)^t \quad [10.15]$$

on each side of the layer, with some axes and time conventions that differ from those adopted in section 10.2.1. The incidence plane is  $x0z$ . The quantities  $v_x$  and  $v_z$  are the projections of the acoustic velocity on the  $0x$  and  $0z$  axes.  $\sigma_x, \sigma_z$  are the tangential and normal stresses acting on a plane ( $x0y$ ) of the solid. The  $t$  superscript in equation [10.15] means a line-to-column transposition of the line vector. To simplify the subsequent calculations, we choose to follow the conventions chosen in the paragraph on fluids. The calculations of the transfer matrix  $[T_s]$  were conducted again, by choosing the following state vectors:

$$\begin{pmatrix} v_z \\ v_x \\ \sigma_z \\ \sigma_x \end{pmatrix}_A = [T_s] \begin{pmatrix} v_z \\ v_x \\ \sigma_z \\ \sigma_x \end{pmatrix}_B. \quad [10.16]$$

The elements of the matrix  $[T_s]$  are given in Appendix 10.5.1. The solid layer can also be represented by an impedance matrix  $[Z_s]$  whose elements, calculated in Appendix 10.5.2, link the stresses on both sides to the velocities as indicated below:

$$\begin{pmatrix} \sigma_z^A \\ \sigma_x^A \\ \sigma_z^B \\ \sigma_x^B \end{pmatrix} = [Z_s] \begin{pmatrix} v_z^A \\ v_x^A \\ v_z^B \\ v_x^B \end{pmatrix}. \quad [10.17]$$

This matrix has the following structure:

$$[Z_s] = \begin{bmatrix} Z_{11} & Z_{12} & Z_{13} & Z_{14} \\ -Z_{12} & Z_{22} & Z_{23} & Z_{24} \\ -Z_{13} & Z_{23} & Z_{33} & Z_{34} \\ Z_{14} & -Z_{24} & -Z_{34} & Z_{44} \end{bmatrix}. \quad [10.18]$$

The symmetry of the layer yields some other symmetries between the elements of the matrix, but they do not concern us because considering a multilayer structure made of two different solids is enough to lose these symmetries. The relationships  $Z_{31} = -Z_{13}$  and  $Z_{42} = -Z_{24}$  correspond to the reciprocal behavior described in the case of a fluid (note a change of the sign of the power flow on each side of the material). Other relationships that appear in the matrix  $[Z_s]$  are linked to the reciprocity properties of the solid layer.

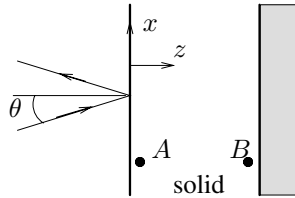


**Figure 10.3.** A layer of viscoelastic solid fixed on a perfectly rigid wall

Let us consider the acoustic system illustrated in Figure 10.3. This is a viscoelastic solid which is pasted onto a perfectly rigid wall. This particular configuration requires the acoustic velocity to cancel at B. The layer can be represented by the quadrupole shown in Figure 10.4, with which an impedance matrix  $[z]$  may be associated, so that:

$$\begin{pmatrix} \sigma_z \\ \sigma_x \end{pmatrix}_A = [z] \begin{pmatrix} v_z \\ v_x \end{pmatrix}_A. \quad [10.19]$$

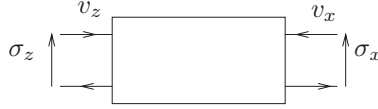


**Figure 10.4.** *Quadrupole equivalent to a solid layer stuck on a rigid wall, linking the constraints to the velocities at point A (see Figure 10.3)*

The elements of the matrix  $[z]$  may be calculated from the elements of the matrix  $[T_s]$ . Replacing the velocity with zero in equation [10.16], we obtain the following system of equations:

$$\begin{aligned} v_z^A &= T_{13}\sigma_z^B + T_{14}\sigma_x^B \\ v_x^A &= T_{23}\sigma_z^B + T_{24}\sigma_x^B \\ \sigma_z^A &= T_{33}\sigma_z^B + T_{34}\sigma_x^B \\ \sigma_x^A &= T_{43}\sigma_z^B + T_{44}\sigma_x^B. \end{aligned} \quad [10.20]$$

By eliminating the constraints in B, we obtain the elements of the matrix  $[z]$ :

$$[z] = \frac{1}{\Delta} \begin{pmatrix} T_{33}T_{24} - T_{34}T_{23} & T_{34}T_{13} - T_{33}T_{14} \\ T_{43}T_{24} - T_{44}T_{23} & T_{44}T_{13} - T_{43}T_{14} \end{pmatrix}, \quad [10.21]$$

with

$$\Delta = T_{13}T_{24} - T_{14}T_{23}. \quad [10.22]$$

Replacing the elements of  $[T_s]$  with their values, it is possible to verify that:

$$z_{12} = -z_{21}, \quad [10.23]$$

and the quadrupole of Figure 10.4 is antireciprocal.

Relationship [10.23] can also be demonstrated without calculation. In a different context, Casimir [CAS 45] showed that the reciprocity of a system depends on its behavior during time reversal: *if a linear physical system is filmed by a camera, and we look at its behavior when the film is shown in reverse order, then the laws of mechanics are always satisfied*. During time reversal, the sound speeds and the incidence angle  $\theta$  become the opposite of their initial values. The tangential stresses  $\sigma_x$  and tangential velocities  $v_x$  are odd functions of  $\theta$ . The elements of matrix  $[Z_s]$  linking the tangential stresses and velocities on the same side of the material are therefore opposed to one another:

$$Z_{21} = -Z_{12}, \quad [10.24]$$

$$\text{and } Z_{43} = -Z_{34}. \quad [10.25]$$

The relationships:

$$Z_{41} = Z_{14} \quad [10.26]$$

$$\text{and } Z_{32} = Z_{23}, \quad [10.27]$$

are combinations of the two previous phenomena (matrix elements linking the terms whose sign changes when inverting time, and characterizing two different faces).

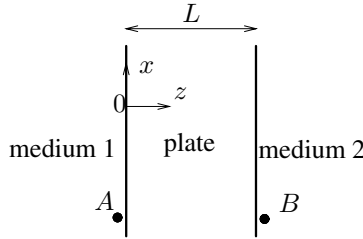


**Figure 10.5.** A viscoelastic plate of thickness  $L$  surrounded by two media of any kind

### 10.2.3. Acoustic behavior of a viscoelastic plate

If its thickness is sufficiently low, a layer of elastic solid can be modeled as a plate subjected to bending vibrations. A plate is represented in Figure 10.5, and is characterized by:

- its thickness  $L$ ;
- its density  $\rho_p$ ;
- and its bending stiffness  $D$ , depending on the Young's modulus  $E$  and the Poisson coefficient  $\nu$  of the solid:

$$D = \frac{EL^3}{12(1 - \nu^2)}. \quad [10.28]$$

The movement equation of the plate is given by:

$$\left( \frac{D}{j\omega} \frac{\partial^4}{\partial x^4} + j\omega\rho_p L \right) v = \frac{L}{2} \left( \frac{\partial \sigma_x^A}{\partial x} + \frac{\partial \sigma_x^B}{\partial x} \right) - \sigma_z^A + \sigma_z^B, \quad [10.29]$$

where  $v$  is the projection of the vibration speed of the plate along the  $0z$  axis,  $\sigma_x^A$  and  $\sigma_x^B$  are the tangential stresses applied on sides A and B respectively, and  $\sigma_z^A$  and  $\sigma_z^B$  are the normal stresses. In addition to equation [10.29], we also have the following relationships linking the velocities on each side of the plate:

$$v_z^A = v_z^B = v, \quad [10.30]$$



$$v_x^A = -v_x^B, \quad [10.31]$$

$$\text{and } v_x^B = \frac{L}{2} \frac{\partial v_z^B}{\partial x}. \quad [10.32]$$

The Snell-Descartes laws impose that (see equation [10.1]):

$$\frac{\partial}{\partial x} = -jk, \quad \forall z. \quad [10.33]$$

So, using the following notations:

$$s1 = \frac{Dk^4}{j\omega} + j\omega\rho_p L \quad [10.34]$$

$$\text{and } s2 = jk \frac{L}{2}, \quad [10.35]$$

equation [10.29] reads:

$$s1v + s2(\sigma_x^A + \sigma_x^B) + \sigma_z^A - \sigma_z^B = 0, \quad [10.36]$$

and the formulae given by [10.32] yield:

$$v_z^A = v_z^B = v, \quad [10.37]$$

$$v_x^A = -v_x^B, \quad [10.38]$$

$$\text{and } v_x^B = -s2v_z^B. \quad [10.39]$$

It is important to note that in the case of a plate, unlike all the previous cases, relations [10.29]–[10.32] connect the state vectors of the media adjacent to the plate (A and B are outside of the plate in Figure 10.5). In particular, equation [10.29] can be simplified in the absence of tangential stresses in materials located on both sides of the plate.

The impedance matrix does not exist for a plate. However, the admittance matrix can be calculated from equations [10.36]–[10.39]. We thus obtain the relationship:

$$\begin{pmatrix} v_z^A \\ v_x^A \\ v_z^B \\ v_x^B \end{pmatrix} = \begin{pmatrix} -\frac{1}{s1} & -\frac{s2}{s1} & \frac{1}{s1} & -\frac{s2}{s1} \\ \frac{s2}{s1} & \frac{s2 \, s2}{s1} & -\frac{s2}{s1} & \frac{s2 \, s2}{s1} \\ -\frac{1}{s1} & -\frac{s2}{s1} & \frac{1}{s1} & -\frac{s2}{s1} \\ -\frac{s2}{s1} & -\frac{s2 \, s2}{s1} & \frac{s2}{s1} & -\frac{s2 \, s2}{s1} \end{pmatrix} \begin{pmatrix} \sigma_z^A \\ \sigma_x^A \\ \sigma_z^B \\ \sigma_x^B \end{pmatrix}. \quad [10.40]$$

This admittance matrix obviously has the same symmetry as the admittance matrix linked to a viscoelastic solid.

### 10.3. Matrix representation of the propagation in porous layers

#### 10.3.1. Propagation in porous media with a rigid structure – equivalent fluid model

The propagation of sound in a porous medium with a rigid structure is entirely determined by knowledge of the effective density and incompressibility of the equivalent fluid that can be evaluated using formulae [6.127] and [6.128]. The parameters characterizing a layer of material with a rigid structure of thickness  $L$  are as follows:

- $\phi$  the porosity;
- $\sigma$  the resistance to the passage of air;
- $\alpha_\infty$  the tortuosity;
- $\Lambda$  the characteristic viscous length; and
- $\Lambda'$  the characteristic thermal length.

The characteristic impedance of the medium is defined by:

$$Z(\omega) = \sqrt{K_{\text{eff}} \rho_{\text{eff}}}, \quad [10.41]$$

and the complex propagation constant  $k_J$  by:

$$k_J = \omega \sqrt{\frac{\rho_{\text{eff}}}{K_{\text{eff}}}}. \quad [10.42]$$

The transfer and impedance matrices of the layer of thickness  $L$  are identical to those obtained for a fluid (see equations [10.9] and [10.10]):

$$[T_J] = [T_f] \quad \text{and} \quad [Z_J] = [Z_f], \quad [10.43]$$

and the same reciprocity properties can be observed. The state vector of a porous material with a rigid structure is

$$V_J = \begin{pmatrix} p \\ v \end{pmatrix}, \quad [10.44]$$

where  $p$  and  $v$  respectively refer to the pressure and to the normal macroscopic speed *in the pores*. Unlike a real fluid, there is a factor  $\phi$  between this speed  $v$  and the sound speed in air outside the material. Indeed, let us consider a porous medium with a rigid structure placed on a rigid floor. The surfacic impedance of the material is given by:

$$Z = \frac{p}{\phi v} = \frac{Z_{\text{fluid}}}{\phi}, \quad [10.45]$$

where  $Z_{\text{fluid}}$  represents the surfacic impedance of a layer of fluid, because the speed in open air in contact with the porous layer is  $\phi v$ .

### 10.3.2. Matrix representation of the propagation in porous media with an elastic structure – Biot's model

The modelization of the propagation in porous materials, when the structure can no longer be regarded as inert (vibration of the structure), was carried out by Biot in seismic studies of rocks soaked with oil or salted water. This is an environment where thermal effects within the pores are negligible. Considering porous materials whose fluid phase is air, a model that takes into account the thermal effects is essential. See Chapter 7 for a detailed description of Biot's theory.

A layer of porous material with a flexible structure of thickness  $L$  is characterized by the previously identified parameters (see the paragraph about materials with a rigid structure). Three additional parameters are needed to take into account the vibrations of the structure:

- the density  $\rho_p$ ;
- the shear modulus  $N$ ;
- and Poisson's coefficient  $\nu$  of the structure.

Let us suppose that a plane incident wave in air generates an acoustic field in a porous layer, possibly placed in a complex laminated material. There will be six waves propagating in the layer, three waves propagating from left to right, and three other waves propagating from right to left. This is an environment with six degrees of freedom. A layer of porous material is modeled using a  $6 \times 6$  transfer matrix:  $[T_B]$ . This matrix was calculated by Depollier [DEP 89]. To keep the conventions used for the fluid in section 10.2.1, the elements of the matrix are given in Appendix 10.5.3. The state vector  $V^B$  for a porous medium with a flexible structure is as follows:

$$V^B = \begin{pmatrix} v_z^f \\ v_z^s \\ v_x^s \\ \sigma_z^f \\ \sigma_z^s \\ \sigma_x^s \end{pmatrix}, \quad [10.46]$$

where the index corresponds to the projection axis ( $0x$  or  $0z$ ) and the superscript to the phase being considered ( $f$  = fluid,  $s$  = solid). For example,  $v_z^f$  is the projection of the macroscopic acoustic speed of the fluid on the  $Oz$  axis.

The elements of the impedance matrix  $Z_B$  were numerically calculated for different materials. It appears that the matrix  $Z_B$  has the following symmetries:

$$[Z_B] = \begin{pmatrix} Z_{11} & Z_{12} & Z_{13} & Z_{14} & Z_{15} & Z_{16} \\ Z_{12} & Z_{22} & Z_{23} & Z_{24} & Z_{25} & Z_{26} \\ -Z_{13} & -Z_{23} & Z_{33} & Z_{34} & Z_{35} & Z_{36} \\ -Z_{14} & -Z_{24} & Z_{34} & Z_{44} & Z_{45} & Z_{46} \\ -Z_{15} & -Z_{25} & Z_{35} & Z_{45} & Z_{55} & Z_{56} \\ Z_{16} & Z_{26} & -Z_{36} & -Z_{46} & -Z_{56} & Z_{66} \end{pmatrix}. \quad [10.47]$$

The reciprocity arguments used for the impedance matrix  $[Z_s]$  of the solid explain in the same way the symmetries highlighted in the matrix  $[Z_B]$ . Biot's theory satisfies the fundamental invariances, and thus provides an impedance matrix which has the same structure as the matrix of a solid medium.

## 10.4. Modelization and properties of multilayered media

### 10.4.1. Generalities

In sections 10.2 and 10.3, we presented the modelization of the propagation in a simple material consisting of a single layer. However, it appears that such a material is rarely used in practice: the number of degrees of freedom is too small for a good fit of acoustic properties to real configurations. In return, the increasing complexity of multilayered media makes it difficult to intuitively predict their acoustic properties. It is therefore useful to have reliable models for such materials [BRO 95].

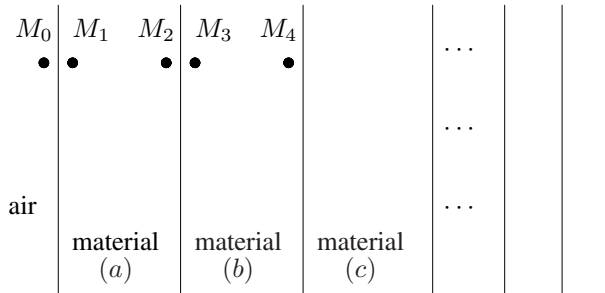


**Figure 10.6.** A multilayered medium in contact with air on its left-hand side

Let us consider a multilayered medium as represented in Figure 10.6. The transfer matrices introduced in sections 10.2 and 10.3 enable us to link the state vectors of points  $M_{2n-1}$  and  $M_{2n}$ , where  $n$  is an integer, using the relationship:

$$V^a(M_{2n-1}) = [T_a] V^a(M_{2n}) \quad \text{with} \quad \forall n \in \mathbb{N}. \quad [10.48]$$

The matrix  $[T_a]$  is an even order (2, 4 or 6) square matrix. The letter  $a$  specifies the type of material.

Writing the continuity relations for the constraints and the flow conservation at the interface between two adjacent layers can link their state vector, in the matrix form, as follows:

$$[I_{ab}]V^a(M_{2n}) + [J_{ab}]V^b(M_{2n+1}) = 0. \quad [10.49]$$

The matrices  $[I_{ab}]$  and  $[J_{ab}]$  are called interface matrices. These matrices are of any dimension. The indices  $a$  and  $b$  designate the two layers in contact. The major problem in this modelization of multilayered media is that the overall matrix that defines the multilayered structure cannot in all cases be obtained from a “simple” matrix calculation (inversion, multiplication or addition). Indeed, the matrix  $[I_{ab}]$  is not always a square matrix.

Generally, the propagation in the material is entirely defined by the following equations:

$$\begin{cases} [I_{ab}]V^a(M_0) + [J_{ab}][T_b]V^b(M_2) = 0 \\ [I_{bc}]V^b(M_2) + [J_{bc}][T_c]V^c(M_4) = 0 \\ \vdots \end{cases} \quad [10.50]$$

This system contains as many equations as there are layers of material, and can be written in a matrix form as follows:

$$[T]V^T = 0, \quad [10.51]$$

where

$$V^T = [V^a(M_0), V^b(M_2), V^c(M_4), \dots]^t, \quad [10.52]$$

and

$$[T] = \begin{pmatrix} [I_{ab}] & [J_{ab}][T_b] & [0] & [0] & \cdots \\ [0] & [I_{bc}] & [J_{bc}][T_c] & [0] & \cdots \\ \vdots & [0] & \vdots & \vdots & \ddots \end{pmatrix}, \quad [10.53]$$

in which  $[0]$  represents the zero matrix (a matrix whose terms are all zero). In these equations, the vector  $V^a(M_0)$  can be noted  $V^a(M_0) = (p^-, v^-)^t$  since the point  $M_0$  is located in air.

It is possible to verify that the matrix  $[T]$  always has fewer lines than columns. Indeed, in order to completely determine the acoustic field, some information is still missing. We first need to specify the boundary conditions imposed on the multilayered structure, i.e. how it is used (bonded to a rigid floor, placed on a layer of air of finite thickness or not ...). However, the amplitude of the incident pressure field should be introduced. The knowledge of these two quantities fully expresses the acoustic field at any point of the multilayered structure. In practice, the second condition will allow us to introduce the problem the physical quantity we are interested in (the surfacic impedance, the reflection and transmission coefficients, etc.). It may be noted that the matrix  $[T]$  enables going from a point  $M_0$  in air (incident field) to a point  $M_{2n}$  (where  $n \in \mathbb{N}$ ) in the last layer of the multilayered material.

In order to clarify the method presented in this introduction, we will apply it to the most elementary and usual cases, then we will evaluate a particular problem.

### 10.4.2. The matrix representation

#### 10.4.2.1. Transfer matrix

The transfer matrices for a layer of material with thickness  $L$  have been calculated in the previous two sections. We can now model a multilayered structure composed of fluid, solid or porous materials. We will see that the case of a plate is treated in a different way, but this treatment can fit perfectly in the general method presented here.

#### 10.4.2.2. Interface matrix between two identical media

The purpose of this section is not to exhaustively present the existing interface matrices related to different combinations of layers, but to show how the common continuity or conservation relations at the interface between two media can be written, as well as some interface matrices samples arising from these equations.

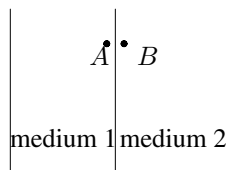


**Figure 10.7.** Interface between medium 1 and medium 2

Let us consider two *identical media* represented in Figure 10.7. The term “identical media” means materials of the same type (fluid, solid or porous).

In the case of a fluid or a solid, the stresses and velocities at  $A$  and  $B$  are equal, therefore the corresponding state vectors are identical:

$$V^{s,f}(A) = V^{s,f}(B). \quad [10.54]$$

The matrix  $[I_{f,f}]$  or  $[I_{s,s}]$  is the identity matrix  $\mathbb{I}$  and:

$$[J_{f,f}] = [J_{s,s}] = -\mathbb{I}. \quad [10.55]$$

The case of a porous material is more complex. If the structure of the porous medium is at rest, the materials are regarded as equivalent fluids (Johnson-Allard-Champoux model) and the conditions at the interface read:

$$p_A = p_B \quad [10.56]$$

$$\phi_A v_A = \phi_B v_B$$

where  $\phi_A$  and  $\phi_B$  are the porosities of the medium at  $A$  and  $B$ , respectively. Equations [10.56] represent the continuity of constraints and the flow conservation, respectively. These equations can be written as:

$$\begin{pmatrix} p_A \\ v_A \end{pmatrix} - \begin{pmatrix} 1 & 0 \\ 0 & \phi_B/\phi_A \end{pmatrix} \begin{pmatrix} p_B \\ v_B \end{pmatrix} = 0. \quad [10.57]$$

The matrix  $[I_{J,J}]$  is, once again, the identity matrix.

Deresiewicz and Skalak [DER 63] determined the following boundary conditions for a porous structure that can vibrate:

$$\begin{aligned} \sigma_z^s(A) + \sigma_z^f(A) &= \sigma_z^s(B) + \sigma_z^f(B), \\ \sigma_z^f(A)/\phi_A &= \sigma_z^f(B)/\phi_B, \\ \sigma_x^s(A) &= \sigma_x^s(B), \\ v_z^s(A) &= v_z^s(B), \\ v_s^x(A) &= v_s^x(B), \\ (v_z^f(A) - v_z^s(A))\phi_A &= (v_z^f(B) - v_z^s(B))\phi_B, \end{aligned} \quad [10.58]$$

which can also be written as:

$$\begin{pmatrix} v_z^f \\ v_x^s \\ v_x^s \\ \sigma_z^f \\ \sigma_z^s \\ \sigma_x^s \end{pmatrix}_A - \begin{pmatrix} \phi_B/\phi_A & 1 - \phi_B/\phi_A & 0 & 0 & 0 & 0 \\ 0 & 1 & 0 & 0 & 0 & 0 \\ 0 & 0 & 1 & 0 & 0 & 0 \\ 0 & 0 & 0 & \phi_A/\phi_B & 0 & 0 \\ 0 & 0 & 0 & 1 - \phi_A/\phi_B & 1 & 0 \\ 0 & 0 & 0 & 0 & 0 & 1 \end{pmatrix} \begin{pmatrix} v_z^f \\ v_x^s \\ v_x^s \\ \sigma_z^f \\ \sigma_z^s \\ \sigma_x^s \end{pmatrix}_B = 0. \quad [10.59]$$

We once more have the equality:

$$[I_{B,B}] = \mathbb{I}. \quad [10.60]$$

The coefficients of the matrix  $[J_{B,B}]$  are very simple since they only depend on the porosity of the two media. Moreover, if  $\phi_A = \phi_B$ , then the matrix  $[J_{B,B}]$  becomes the identity matrix up to the sign.

When the two media in contact are of the same type, we find that the matrix  $[I]$  in equations [10.57]–[10.59] can always be taken as the unitary matrix. As a practical consequence, the direct multiplication of transfer matrices and interface matrices is possible, which reduces the bi-layer to a single layer characterized by a single transfer matrix.

#### 10.4.2.3. Interface matrix between two different media

Let us now study the case of two adjacent layers of different types.

##### *Fluid – solid*

The boundary conditions between a fluid (identified by point  $A$ ) and a solid (point  $B$ ) are:

$$\begin{aligned} -p(A) &= \sigma_z(B), \\ v(A) &= v_z(B), \\ 0 &= \sigma_x(B). \end{aligned} \quad [10.61]$$

The interface relationship is therefore the following:

$$[I_{f,s}]V^f(A) + [J_{f,s}]V^s(B) = 0, \quad [10.62]$$

where

$$[I_{f,s}] = \begin{pmatrix} 0 & -1 \\ 1 & 0 \\ 0 & 0 \end{pmatrix} \text{ and } [J_{f,s}] = \begin{pmatrix} 1 & 0 & 0 & 0 \\ 0 & 0 & 1 & 0 \\ 0 & 0 & 0 & 1 \end{pmatrix}. \quad [10.63]$$



*Fluid – porous medium with a flexible structure*

The boundary conditions are as follows:

$$\begin{aligned}
 v(A) &= \phi_B v_z^f(B) + (1 - \phi_B) v_z^s(B), \\
 -\phi_B p(A) &= \sigma_z^f(B), \\
 -(1 - \phi_B) p(A) &= \sigma_z^s(B), \\
 0 &= \sigma_x^s(B),
 \end{aligned} \tag{10.64}$$

which can be written as

$$[I_{f,B}] V^f(A) + [J_{f,B}] V^B(B) = 0, \tag{10.65}$$

where

$$[I_{f,B}] = \begin{pmatrix} 0 & -1 \\ \phi_B & 0 \\ 1 - \phi_B & 0 \\ 0 & 0 \end{pmatrix}, \tag{10.66}$$

and

$$[J_{f,B}] = \begin{pmatrix} \phi_B & 1 - \phi_B & 0 & 0 & 0 & 0 \\ 0 & 0 & 0 & 1 & 0 & 0 \\ 0 & 0 & 0 & 0 & 1 & 0 \\ 0 & 0 & 0 & 0 & 0 & 1 \end{pmatrix}. \tag{10.67}$$

*Fluid – porous medium with a rigid structure*

The continuity relationships between the two media are:

$$\begin{aligned}
 p(A) &= p(B), \\
 v(A) &= \phi_B v(B).
 \end{aligned} \tag{10.68}$$

Therefore, we have

$$[I_{f,J}] V^f(A) + [J_{f,J}] V^J(B) = 0, \tag{10.69}$$

where

$$[I_{f,J}] = \mathbb{I} \quad \text{and} \quad [J_{f,J}] = \begin{bmatrix} -1 & 0 \\ 0 & -\phi_B \end{bmatrix}. \tag{10.70}$$

*Solid – porous medium with a flexible structure*

The boundary conditions between these two materials read as follows:

$$\begin{aligned}
 v_z(A) &= v_z^s(B) = v_z^f(B), \\
 v_x(A) &= v_x^s(B), \\
 \sigma_x(A) &= \sigma_x^s(B), \\
 \sigma_z(A) &= \sigma_z^f(B) + \sigma_z^s(B).
 \end{aligned}
 \tag{10.71}$$

They can also be written in the general matrix form given by [10.49]:

$$[I_{s,B}]V^s(A) + [J_{s,B}]V^B(B) = 0, \tag{10.72}$$

with

$$[I_{s,B}] = \begin{bmatrix} 0 & 0 & 0 & -1 \\ 0 & -1 & 0 & 0 \\ 0 & 0 & -1 & 0 \\ -1 & 0 & 0 & 0 \\ -1 & 0 & 0 & 0 \end{bmatrix}, \tag{10.73}$$

and

$$[J_{s,B}] = \begin{bmatrix} 0 & 0 & 0 & 0 & 0 & 1 \\ 0 & 0 & 1 & 0 & 0 & 0 \\ 0 & 0 & 0 & 1 & 1 & 0 \\ 1 & 0 & 0 & 0 & 0 & 0 \\ 0 & 1 & 0 & 0 & 0 & 0 \end{bmatrix}. \tag{10.74}$$

The few examples above show that the calculation of interface matrices between two media is very simple. It is not necessary to consider all the possible combinations.

*10.4.2.4. Plates*

We will see in the following, that the plates can be modeled using an interface-like relationship, i.e. through two matrices  $[I]$  and  $[J]$ . The plate serves as an “interface” between the two media.

In section 10.2.3, we noted that equation [10.29] depends on the nature of the environments adjacent to the plate. The matrices  $[I]$  and  $[J]$  therefore have the same dependence. Consequently, we use the following notations:  $[I_{ab}^{\text{pl}}]$  and  $[J_{ab}^{\text{pl}}]$ , where  $a$  and  $b$  correspond to the media on each side of the plate.

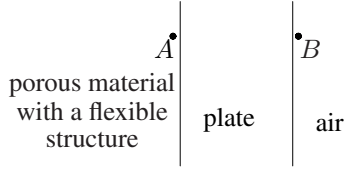


**Figure 10.8.** *Diagram of a plate surrounded by air and a porous material with flexible structure (Biot)*

To illustrate our purpose, we consider a more concrete example illustrated in Figure 10.8. This is a plate surrounded by air and a porous material with a flexible structure: our goal is to find the relationship between the state vectors  $V^B(A)$  and  $V^f(B)$ . There is no tangential strain in air at  $B$ . In this particular case, equations [10.36] and [10.39] become:

$$\begin{aligned} s1v + s2\sigma_x^s(A) + \sigma_z^f(A) + \sigma_z^s(A) + p(B) &= 0, \\ v_z(B) &= v_z^f(A) = v_z^s(A) = v, \\ v_x^s(A) &= -s2v_z(B), \end{aligned} \quad [10.75]$$

which can read:

$$\begin{pmatrix} 0 & 0 & 0 & 1 & 1 & s2 \\ -1 & 0 & 0 & 0 & 0 & 0 \\ 0 & -1 & 0 & 0 & 0 & 0 \\ s2 & 0 & 1 & 0 & 0 & 0 \end{pmatrix} \begin{pmatrix} v_z^f \\ v_z^s \\ v_x^s \\ \sigma_z^f \\ \sigma_z^s \\ \sigma_x^s \end{pmatrix}_A + \begin{pmatrix} 1 & s1 \\ 0 & 1 \\ 0 & 1 \\ 0 & 0 \end{pmatrix} \begin{pmatrix} p \\ v \end{pmatrix}_B = 0. \quad [10.76]$$

This is effectively an interface-like relationship, with:

$$[I_{B,f}^{\text{pl}}] = \begin{pmatrix} 0 & 0 & 0 & 1 & 1 & s2 \\ -1 & 0 & 0 & 0 & 0 & 0 \\ 0 & -1 & 0 & 0 & 0 & 0 \\ s2 & 0 & 1 & 0 & 0 & 0 \end{pmatrix} \quad \text{and} \quad [J_{B,f}^{\text{pl}}] = \begin{pmatrix} 1 & s1 \\ 0 & 1 \\ 0 & 1 \\ 0 & 0 \end{pmatrix}. \quad [10.77]$$

The particular cases of different external media are immediate, therefore we do not address these cases here.

### 10.4.3. Evaluation of the properties of multilayered structures

In the previous chapter, we saw how to specify the interface relationships between different layers. We can now build the matrix  $[T]$  of equation [10.51] from the transfer matrices of the multilayered structure.

The properties of the multilayered medium depend on how it is used. There are two major cases: 1) the material is in contact with a rigid wall, or 2) in contact with two semi-infinite fluids on each side. In the first case, the multilayered medium is characterized by its usual surfacic impedance  $Z_1$ . In the second case, it is also interesting to determine its transmission coefficient  $T$ , as well as the reflection coefficient of the back-side of the medium.

#### 10.4.3.1. Multilayered medium placed on a rigid floor

The process described in this section also applies if the multilayered structure is separated from the perfectly rigid plane by an air space, since it is equivalent to just considering a laminated material consisting of the initial multilayered medium *plus* the air space. We can then apply the general treatment.

The fact that the multilayered structure is glued on the rigid plane imposes that the acoustic velocities are equal to zero on this plane. We just have to add the additional equations, related to the cancelation of velocities, to the general equations of matrix  $[T]$ . The number of equations to add depends on the material type of the last layer. This gives the following equation system:

$$[M] V^T = \begin{bmatrix} [T] \\ \text{additional equations} \end{bmatrix} V^T = 0, \quad [10.78]$$

where the matrix  $[M]$  still has  $n - 1$  lines, where  $n$  is the number of columns.

If we define the usual surfacic impedance of the multilayered structure by:

$$Z_1 = \frac{p^-}{v^-}, \quad [10.79]$$

we can also add the following equation:

$$p^- - Z_1 v^- = 0, \quad [10.80]$$

to the equation system described by matrix  $[M]$ . We then obtain  $n$  following equations with  $n$  unknowns:

$$\begin{bmatrix} 1 & -Z_1 & 0 & \cdots & 0 \\ & & [M] & & \end{bmatrix} V^T = 0. \quad [10.81]$$

If the determinant of this system is equal to zero, we can obtain  $Z_1$  using the formula:

$$M^1 + Z_1 M^2 = 0, \quad [10.82]$$

where  $M^1$  and  $M^2$  represent the determinant of the matrix  $M$  whose column #1, #2 respectively, was removed. The reflection coefficient  $R_1$  of the material is obtained by the following expression:

$$R_1 = \frac{Z_1 - \rho_0 c_0 / \cos \theta}{Z_1 + \rho_0 c_0 / \cos \theta}, \quad [10.83]$$

where  $\rho_0$  and  $c_0$  are respectively the density and speed in air, and  $\theta$  is the incidence angle. We can also calculate the absorption coefficient  $\alpha_1$ :

$$\alpha_1 = 1 - |R_1|^2, \quad [10.84]$$

where  $|R_1|$  is the complex modulus of  $R_1$ . The calculation of the properties of the multilayered structure reduces to a calculation of two determinants.

#### 10.4.3.2. Multilayered structure surrounded by 2 semi-infinite layers of air

If the multilayered structure is surrounded by two semi-infinite layers of air, it is useful to know the properties of both sides of the multilayered medium. For this purpose, we consider two incident plane waves, at an incidence angle  $\theta$ , on both sides of the multilayered medium. This configuration is illustrated in Figure 10.9. A plane wave of amplitude  $G$  (at  $A$ ) is incident from the left-hand side of the material, we can therefore associate a reflected plane wave of amplitude  $GR_1$  (at  $A$ ) and a transmitted

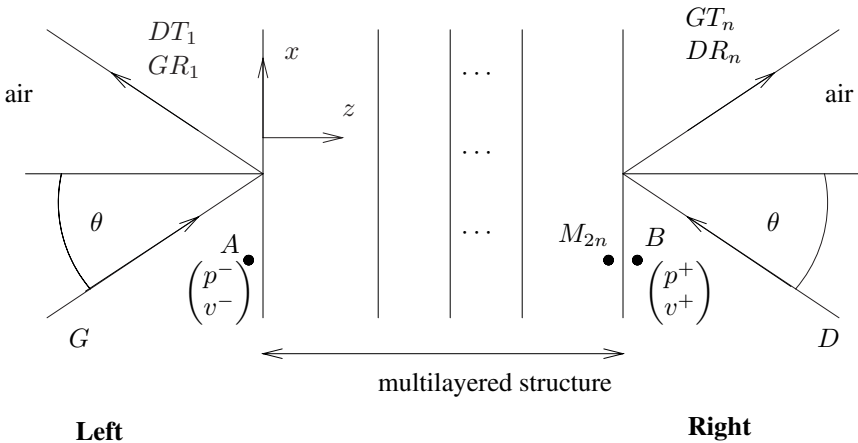


**Figure 10.9.** Multilayered structure surrounded by two semi-infinite layers of air. Two incident plane waves, with the same incidence angle  $\theta$ , propagate on both sides of the structure

plane wave of amplitude  $GT_n$  (at  $B$ ). Similarly, a plane wave of amplitude  $D$  (at  $B$ ) is incident on the right-hand side of the material; a reflected wave  $DR_n$  (at  $B$ ) and transmitted wave  $DT_1$  (at  $A$ ) can be associated with this second incident wave.

Note  $p^-$  and  $v^-$  the pressure and the component of the total velocity on the  $0z$  axis on the left-hand side at  $A$ , and  $p^+$  and  $v^+$  the pressure and the projection of the total velocity on the  $0z$  axis on the right-hand side at  $B$ . Using these conditions we can write:

$$\begin{aligned} p^- &= G(1 + R_1) + DT_1, \\ \rho_0 c_0 / \cos \theta \, v^- &= G(1 - R_1) - DT_1, \\ p^+ &= GT_n + (1 + R_n)D, \\ \rho_0 c_0 / \cos \theta \, v^+ &= GT_n + (-1 + R_n)D. \end{aligned} \quad [10.85]$$

Thus, noting  $\tau = \frac{D}{G}$ , we obtain the impedance  $Z_1$ :

$$Z_1 = \frac{p^-}{v^-} = \frac{\rho_0 c_0}{\cos \theta} \cdot \frac{1 + R_1 + T_1 \tau}{1 - R_1 - T_1 \tau}, \quad [10.86]$$

on the left-hand side of the multilayered structure, and the impedance  $Z_n$ :

$$Z_n = \frac{p^+}{-v^+} = \frac{\rho_0 c_0}{\cos \theta} \cdot \frac{(1 + R_n)\tau + T_n}{(1 - R_n)\tau - T_n}, \quad [10.87]$$

on the right-hand side. To know the usual impedance on each side, it is enough to set  $\tau = 0$  in the first case, and to make  $\tau$  tend to infinity in the second case. The previous calculations are entirely independent of the multilayered structure composition.

If we start from the matrix formulation described by equation [10.51], we have to use the interface relationship between the last layer of the multilayered structure and air to ensure the symmetry of the problem. Then we obtain matrix  $[M]$ :

$$[M] = \begin{bmatrix} [T] \\ [I_{d,f}]V^d(M_{2n}) + [J_{d,f}]V^f(B) \end{bmatrix}, \quad [10.88]$$

where  $d$  and  $f$  respectively represent the last layer and the fluid,  $B$  is a point located in air and  $M_{2n}$  is a point located in the last layer (see Figure 10.9). This matrix satisfies the following relationship:

$$[M] V^T = 0, \quad [10.89]$$

where

$$V^T = [p^-, v^-, V^a, V^b, \dots, p^+, v^+]^t. \quad [10.90]$$

The matrix  $[M]$  always has  $n - 2$  lines, if  $n$  is its number of columns. The two additional equations:

$$\begin{aligned} p^- - Z_1 v^- &= 0, \\ p^+ + Z_n v^+ &= 0, \end{aligned} \quad [10.91]$$

enable us to complete the system of equations. After calculating and determining the determinant of the system (see Appendix 10.5.4), we obtain the expression of the surfacic impedances on each side:

$$Z_1 = -\frac{M^{1,n-1} + M^{1,n} \rho_0 c_0 / \cos \theta}{M^{2,n-1} + M^{2,n} \rho_0 c_0 / \cos \theta}, \quad [10.92]$$

and

$$Z_n = \frac{M^{1,n-1} - M^{2,n-1} \rho_0 c_0 / \cos \theta}{M^{1,n} - M^{2,n} \rho_0 c_0 / \cos \theta}, \quad [10.93]$$

where  $M^{i,j}$  is the determinant of the matrix  $[M]$ , in which the  $i$ th and  $j$ th columns have been removed.

Calculation of the two transmission coefficients can be made using a similar method. This is sufficient to change equations [10.91]. In the case of a transmission from left to right (see Figure 10.9), we have  $\tau = D/G = 0$ , and equations [10.85] read:

$$\begin{aligned} T_n / (1 + R_1) p^- - p^+ &= 0 \\ p^+ - \rho_0 c_0 / \cos \theta v^+ &= 0. \end{aligned} \quad [10.94]$$

Replacing equations [10.91] with [10.94] and by specifying that the determinant of the system is equal to zero, we obtain (see Appendix 10.5.5):

$$T_n = \frac{(1 + R_1) \rho_0 c_0 / \cos \theta M^{n-1,n}}{M^{1,n-1} + \rho_0 c_0 / \cos \theta M^{1,n}}. \quad [10.95]$$

Similarly, making  $\tau$  tend to infinity, the transmission coefficient in the other direction is:

$$T_1 = \frac{(1 + R_n) \rho_0 c_0 / \cos \theta M^{1,2}}{M^{1,n-1} - \rho_0 c_0 / \cos \theta M^{2,n-1}}. \quad [10.96]$$

In the case of a multilayered structure made from a combination of fluids, solids, plates or porous materials, we could show that [ALL 93a, ALL 93b]:

$$T_1 = T_n = T. \quad [10.97]$$

This property is a consequence of the reciprocity conditions for the layers of materials described in sections 10.2 and 10.3. Indeed, a multilayered structure in air can be modeled by a  $(2 \times 2)$  matrix:

$$\begin{pmatrix} p^- \\ v^- \end{pmatrix} = \begin{pmatrix} a & b \\ c & d \end{pmatrix} \begin{pmatrix} p^+ \\ v^+ \end{pmatrix}. \quad [10.98]$$

The calculation of this matrix can be extremely complex, but it can be shown that this matrix is always reciprocal. It has the following property:

$$ad - bc = 1, \quad [10.99]$$

which implies that  $T_1 = T_n$  (see pages 254–256 of reference [ALL 93a]). From equations [10.95] and [10.96], it is possible to obtain the relationship:

$$T_n = \frac{M^{n-1,n}}{M^{1,2}} T_1. \quad [10.100]$$

and yet, it turns out that numerically  $M^{n-1,n} = M^{1,2}$ .

## 10.5. Appendices

### 10.5.1. Appendix A: elements of the transfer matrix $[T_s]$ of a viscoelastic solid

The transfer matrix  $[T_s]$  of equation [10.16] for a solid viscoelastic layer of thickness  $L = z_B - z_A$  is exposed below.

The following notations are used:

$$E = \frac{\alpha}{k}, \quad F = \frac{\beta}{k}, \quad G = 2 \frac{k^2}{k_t^2}, \quad H = \rho_s \frac{\omega}{k}.$$

Quantities  $\alpha$  and  $\beta$  are defined by the following equations:

$$\alpha = \sqrt{k_\ell^2 - k^2}, \quad \beta = \sqrt{k_t^2 - k^2},$$

where  $k_\ell = \omega/v_\ell$  and  $k_t = \omega/v_t$  are the wave numbers associated with the longitudinal and transverse wave respectively. Thus, the 16 coefficients of the matrix  $[T_s]$  are:

$$T_s(1, 1) = (1 - G) \cos \alpha L + G \cos \beta L,$$

$$T_s(1, 2) = -i \frac{EFG \sin \alpha L + (G - 1) \sin \beta L}{F},$$

$$T_s(1, 3) = i \frac{EF \sin \alpha L + \sin \beta L}{FH},$$



$$\begin{aligned}
T_s(1, 4) &= \frac{\cos \beta L - \cos \alpha L}{H}, \\
T_s(2, 1) &= i \frac{(G - 1) \sin \alpha L + EFG \sin \beta L}{E}, \\
T_s(2, 2) &= G \cos \alpha L + (1 - G) \cos \beta L, \\
T_s(2, 3) &= T_s(1, 4), \\
T_s(2, 4) &= i \frac{\sin \alpha L + EF \sin \beta L}{EH}, \\
T_s(3, 1) &= iH \frac{(1 - G^2) \sin \alpha L + EFG^2 \sin \beta L}{E}, \\
T_s(3, 2) &= (1 - G)GH (\cos \beta L - \cos \alpha L), \\
T_s(3, 3) &= T_s(1, 1), \\
T_s(3, 4) &= T_s(2, 1), \\
T_s(4, 1) &= T_s(3, 2), \\
T_s(4, 2) &= iH \frac{EFG^2 \sin \alpha L + (1 - G^2) \sin \beta L}{F}, \\
T_s(4, 3) &= T_s(1, 2), \\
T_s(4, 4) &= T_s(2, 2).
\end{aligned}$$

### 10.5.2. Appendix B: elements of the impedance matrix $[Z_s]$ of a viscoelastic solid

Using the same notations as in Appendix 10.5.1, the impedance matrix  $[Z_s]$  of a viscoelastic solid layer of thickness  $L = z_B - z_A$  is written:

$$[Z_s] = \frac{-H^2}{2(1 - \cos \alpha L \cos \beta L) + (1/EF + EF) \sin \alpha L \sin \beta L} [Z'],$$

where the 16 coefficients of the  $[Z']$  matrix are given by:

$$\begin{aligned}
Z'(1, 1) &= i \frac{\cos \beta L \sin \alpha L + EF \cos \alpha L \sin \beta L}{EH}, \\
Z'(1, 2) &= \frac{1 - 2G}{H} + (2G - 1) \frac{\cos \alpha L \cos \beta L}{H} \\
&\quad + \left( \frac{1 - G}{EF} - EFG \right) \frac{\sin \alpha L \sin \beta L}{H},
\end{aligned}$$

$$\begin{aligned}
Z'(1,3) &= -i \frac{\sin \alpha L + EF \sin \beta L}{EH}, \\
Z'(1,4) &= \frac{\cos \alpha L - \cos \beta L}{H}, \\
Z'(2,1) &= -Z'(1,2), \\
Z'(2,2) &= i \frac{EF \cos \beta L \sin \alpha L + \cos \alpha L \sin \beta L}{FH}, \\
Z'(2,3) &= Z'(1,4), \\
Z'(2,4) &= -i \frac{EF \sin \alpha L + \sin \beta L}{FH}, \\
Z'(3,1) &= -Z'(1,3), \\
Z'(3,2) &= Z'(2,3), \\
Z'(3,3) &= -Z'(1,1), \\
Z'(3,4) &= Z'(1,2), \\
Z'(4,1) &= Z'(1,4), \\
Z'(4,2) &= -Z'(2,4), \\
Z'(4,3) &= -Z'(3,4), \\
Z'(4,4) &= -Z'(2,2).
\end{aligned}$$

### 10.5.3. Appendix C: elements of the transfer matrix $[T_B]$ of a porous material with elastic frame – Biot model

The 36 coefficients of the transfer matrix  $[T_B]$  of a porous medium having an elastic frame of thickness  $L$ , obtained from the Biot model, are given in this appendix. The matrix  $[T_B]$  allows us to link the state vectors of the porous medium defined by equation [10.46].

The terms  $\alpha_i$ , with  $i = 1, 2, 3$ , represent the components of the wave numbers of the three Biot waves along the axis normal to the medium surface. These components are defined by:

$$\alpha_i = \sqrt{k_i^2 - k^2} \quad \text{with } i = 1, 2, 3,$$

where  $k_1^2$  and  $k_2^2$  represent the two compression waves and  $k_3^2$  the shear wave.

Quantities  $\mu_i$ , with  $i = 1, 2, 3$ , are the ratios of the amplitude of air displacement to the amplitude of the porous structure displacement, for each type of wave (compression, shear). Coefficients  $\Delta$ ,  $C_i$  and  $D_i$ , with  $i = 1, 2$ , are defined by the following relationships:

$$\begin{aligned}\Delta &= D_1(C_2 + 2Nk^2) - D_2(C_1 + 2Nk^2), \\ C_i &= (P + Q\mu_i)(k^2 + \alpha_i^2) - 2Nk^2 \quad \text{with } i = 1, 2, \\ D_i &= (R\mu_i + Q)(k^2 + \alpha_i^2) \quad \text{with } i = 1, 2.\end{aligned}$$

Finally, to simplify the writing, we used the following notations:

$$\begin{aligned}\mathbf{p}_i &= \cos \alpha_i L \quad \text{with } i = 1, 2, 3, \\ \mathbf{q}_i &= \sin \alpha_i L \quad \text{with } i = 1, 2, 3.\end{aligned}$$

The coefficients of the transfer matrix are therefore given by:

$$\begin{aligned}T_B(1, 1) &= \frac{\mu_1 \mathbf{p}_1 - \mu_2 \mathbf{p}_2}{\mu_1 - \mu_2}, \\ T_B(1, 2) &= \frac{\mathbf{p}_1 C_1 (C_2 + 2Nk^2) - \mathbf{p}_2 C_2 (C_1 + 2Nk^2) - 2Nk^2 \mathbf{p}_3 (C_1 - C_2)}{\Delta}, \\ T_B(1, 3) &= \frac{jk}{\Delta} \left[ 2N(\alpha_1 \mu_1 \mathbf{q}_1 D_2 - \alpha_2 \mu_2 \mathbf{q}_2 D_1) - \frac{\mu_3 \mathbf{q}_3}{\alpha_3} (C_1 D_2 - C_2 D_1) \right], \\ T_B(1, 4) &= \frac{j\omega}{\Delta} \left[ -\alpha_1 \mu_1^2 \mathbf{q}_1 D_2 + \alpha_2 \mu_2^2 \mathbf{q}_2 D_1 + \frac{k^2 \mu_3^2 \mathbf{q}_3}{\alpha_3} (D_1 - D_2) \right], \\ T_B(1, 5) &= \frac{j\omega}{\Delta} \left[ -\alpha_1 \mu_1 \mathbf{q}_1 D_2 + \alpha_2 \mu_2 \mathbf{q}_2 D_1 + \frac{k^2 \mu_3 \mathbf{q}_3}{\alpha_3} (D_1 - D_2) \right], \\ T_B(1, 6) &= \frac{\omega k}{N(k^2 + \alpha_3^2)} \left( \mathbf{p}_1 \mu_1 \frac{\mu_3 - \mu_2}{\mu_2 - \mu_1} + \mathbf{p}_2 \mu_2 \frac{\mu_1 - \mu_3}{\mu_2 - \mu_1} + \mathbf{p}_3 \mu_3 \right), \\ T_B(2, 1) &= \frac{\mathbf{p}_1 - \mathbf{p}_2}{\mu_1 - \mu_2}, \\ T_B(2, 2) &= \frac{\mathbf{p}_2 C_2 D_1 - \mathbf{p}_1 C_1 D_2 - 2Nk^2 \mathbf{p}_3 (D_2 - D_1)}{\Delta}, \\ T_B(2, 3) &= \frac{jk}{\Delta} \left[ 2N(\alpha_1 \mathbf{q}_1 D_2 - \alpha_2 \mathbf{q}_2 D_1) - \frac{\mathbf{q}_3}{\alpha_3} (C_1 D_2 - C_2 D_1) \right], \\ T_B(2, 4) &= T_B(1, 5),\end{aligned}$$

$$T_B(2, 5) = \frac{j\omega}{\Delta} \left[ -\alpha_1 \mathbf{q}_1 D_2 + \alpha_2 \mathbf{q}_2 D_1 + \frac{k^2 \mathbf{q}_3}{\alpha_3} (D_1 - D_2) \right],$$

$$T_B(2, 6) = \frac{\omega k}{N(k^2 + \alpha_3^2)} \left( \mathbf{p}_1 \frac{\mu_3 - \mu_2}{\mu_2 - \mu_1} + \mathbf{p}_2 \frac{\mu_1 - \mu_3}{\mu_2 - \mu_1} + \mathbf{p}_3 \right),$$

$$T_B(3, 1) = jk \frac{\alpha_1 \mathbf{q}_2 - \alpha_2 \mathbf{q}_1}{\alpha_1 \alpha_2 (\mu_1 - \mu_2)},$$

$$T_B(3, 2) = \frac{jk}{k^2 + \alpha_3^2} \left( \frac{C_1 \mathbf{q}_1}{N \alpha_1} \frac{\mu_3 - \mu_2}{\mu_2 - \mu_1} + \frac{C_2 \mathbf{q}_2}{N \alpha_2} \frac{\mu_1 - \mu_3}{\mu_2 - \mu_1} + 2 \mathbf{q}_3 \alpha_3 \right),$$

$$T_B(3, 3) = \frac{2Nk^2 (\mathbf{p}_2 D_1 - \mathbf{p}_1 D_2) - \mathbf{p}_3 (C_1 D_2 - C_2 D_1)}{\Delta},$$

$$T_B(3, 4) = T_B(1, 6),$$

$$T_B(3, 5) = T_B(2, 6),$$

$$T_B(3, 6) = \frac{j\omega}{N(k^2 + \alpha_3^2)} \left( \frac{k^2 \mathbf{q}_1}{\alpha_1} \frac{\mu_2 - \mu_3}{\mu_2 - \mu_1} + \frac{k^2 \mathbf{q}_2}{\alpha_2} \frac{\mu_3 - \mu_1}{\mu_2 - \mu_1} + \alpha_3 \mathbf{q}_3 \right),$$

$$T_B(4, 1) = \frac{j}{\omega(\mu_1 - \mu_2)} \left( \frac{\mathbf{q}_1 D_1}{\alpha_1} - \frac{\mathbf{q}_2 D_2}{\alpha_2} \right),$$

$$T_B(4, 2) = j \frac{\alpha_2 C_1 \mathbf{q}_1 - \alpha_1 C_2 \mathbf{q}_2}{\omega \alpha_1 \alpha_2 (\mu_1 - \mu_2)},$$

$$T_B(4, 3) = \frac{-2Nk}{\omega(\mu_1 - \mu_2)} (\mathbf{p}_1 - \mathbf{p}_2),$$

$$T_B(4, 4) = T_B(1, 1),$$

$$T_B(4, 5) = T_B(2, 1),$$

$$T_B(4, 6) = T_B(3, 1),$$

$$T_B(5, 1) = T_B(4, 2),$$

$$T_B(5, 2) = \frac{C_1 \mathbf{q}_1 \alpha_2 (\mu_2 (\alpha_3^2 - k^2) + 2k^2 \mu_3) - C_2 \mathbf{q}_2 \alpha_1 (\mu_1 (\alpha_3^2 - k^2) + 2k^2 \mu_3)}{j\omega \alpha_1 \alpha_2 (\alpha_3^2 + k^2) (\mu_1 - \mu_2)} \\ - \frac{4N \alpha_1 \alpha_2 \alpha_3 k^2 (\mu_1 - \mu_2) \mathbf{q}_3}{j\omega \alpha_1 \alpha_2 (\alpha_3^2 + k^2) (\mu_1 - \mu_2)},$$

$$T_B(5, 3) = \frac{2Nk}{\omega \Delta} (C_1 D_2 \mathbf{p}_1 - C_2 D_1 \mathbf{p}_2 - (C_1 D_2 - C_2 D_1) \mathbf{p}_3),$$

$$T_B(5, 4) = T_B(1, 2),$$

$$T_B(5, 5) = T_B(2, 2),$$

$$T_B(5, 6) = T_B(3, 2),$$

$$T_B(6, 1) = T_B(4, 3),$$

$$T_B(6, 2) = T_B(5, 3),$$

$$T_B(6, 3) = \frac{jNk^2}{\omega\Delta} \left[ 4N(\alpha_1 \mathbf{q}_1 D_2 - \alpha_2 \mathbf{q}_2 D_1) - \mathbf{q}_3 \alpha_3^2 - k^2 k^2 \alpha_3 (C_1 D_2 - C_2 D_1) \right],$$

$$T_B(6, 4) = T_B(1, 3),$$

$$T_B(6, 5) = T_B(2, 3),$$

$$T_B(6, 6) = T_B(3, 3).$$

#### 10.5.4. Appendix D: calculation of the surface impedances on both sides of a multi-layered medium surrounded by two semi-infinite layers of air

In order to calculate the surface impedances on both sides of a multi-layered medium surrounded by two semi-infinite air layers, it is necessary to calculate the zero of the determinant of the matrix composed by the matrix  $[M]$  (of size  $n - 2 \times n$ ) from equation [10.89], and by the two additional equations [10.91]. We obtain the following matrix  $[A]$ :

$$[A] = \begin{bmatrix} 1 & -Z_1 & 0 & \cdots & 0 \\ & [ & M & ] & \\ 0 & \cdots & 0 & 1 & Z_n \end{bmatrix}.$$

The calculation of the determinant gives:

$$\text{Det}[A] = \text{Det} \begin{bmatrix} [ & M^1 & ] \\ 0 & \cdots & 0 & 1 & Z_n \end{bmatrix} + Z_1 \text{Det} \begin{bmatrix} [ & M^2 & ] \\ 0 & \cdots & 0 & 1 & Z_n \end{bmatrix},$$

where  $M^i$  designates the matrix  $[M]$ , in which the  $i$ th column has been removed, then:

$$\text{Det}[A] = -M^{1,n-1} + Z_n M^{1,n} - Z_1 M^{2,n-1} + Z_1 Z_n M^{2,n},$$

where  $M^{i,j}$  designates the determinant of  $[M]$ , in which the  $i$ th and  $j$ th columns have been removed. By setting this determinant equal to zero and using equations [10.86]

and [10.87], we obtain:

$$\begin{aligned}
 & -M^{1,n-1} \left[ -T_n(1+R_1) + \tau(T_1T_n + (1-R_1)(1-R_n)) - \tau^2T_1(1-R_n) \right] \\
 & + \frac{\rho_0c_0}{\cos\theta} M^{1,n} \left[ T_n(1-R_1) + \tau((1+R_n)(1-R_1) - T_1T_n) - \tau^2T_1(1+R_n) \right] \\
 & - \frac{\rho_0c_0}{\cos\theta} M^{2,n-1} \left[ -T_n(1+R_1) + \tau((1+R_1)(1-R_n) - T_1T_n) + \tau^2T_1(1-R_n) \right] \\
 & + \left( \frac{\rho_0c_0}{\cos\theta} \right)^2 M^{2,n} \left[ T_n(1+R_1) + \tau((1+R_1)(1+R_n) + T_1T_n) + \tau^2T_1(1+R_n) \right] \\
 & = 0,
 \end{aligned}$$

which gives, for the zero order in  $\tau$ :

$$\begin{aligned}
 & M^{1,n-1} + \frac{\rho_0c_0}{\cos\theta} M^{1,n} + \frac{\rho_0c_0}{\cos\theta} M^{2,n-1} + \left( \frac{\rho_0c_0}{\cos\theta} \right)^2 M^{2,n} \\
 & = R_1 \left[ M^{1,n-1} + \frac{\rho_0c_0}{\cos\theta} M^{1,n} - \frac{\rho_0c_0}{\cos\theta} M^{2,n-1} - \left( \frac{\rho_0c_0}{\cos\theta} \right)^2 M^{2,n} \right],
 \end{aligned}$$

and for the second order:

$$\begin{aligned}
 & M^{1,n-1} - \frac{\rho_0c_0}{\cos\theta} M^{1,n} - \frac{\rho_0c_0}{\cos\theta} M^{2,n-1} + \left( \frac{\rho_0c_0}{\cos\theta} \right)^2 M^{2,n} \\
 & = R_n \left[ M^{1,n-1} + \frac{\rho_0c_0}{\cos\theta} M^{1,n} - \frac{\rho_0c_0}{\cos\theta} M^{2,n-1} - \left( \frac{\rho_0c_0}{\cos\theta} \right)^2 M^{2,n} \right].
 \end{aligned}$$

The reflection coefficients, extracted from these two equations, allow us to calculate the impedances on each side of the layered medium with the formulae:

$$Z_1 = \frac{\rho_0c_0}{\cos\theta} \frac{1+R_1}{1-R_1}, \quad Z_n = \frac{\rho_0c_0}{\cos\theta} \frac{1+R_n}{1-R_n},$$

which gives:

$$Z_1 \frac{\cos\theta}{\rho_0c_0} = - \frac{M^{1,n-1} + M^{1,n} \rho_0c_0 / \cos\theta}{M^{2,n-1} \rho_0c_0 / \cos\theta + M^{2,n} (\rho_0c_0 / \cos\theta)^2},$$

and

$$Z_2 \frac{\cos\theta}{\rho_0c_0} = \frac{M^{1,n-1} - M^{2,n-1} \rho_0c_0 / \cos\theta}{M^{1,n} \rho_0c_0 / \cos\theta - M^{2,n} (\rho_0c_0 / \cos\theta)^2},$$

and therefore the sought formulae [10.92] and [10.93].

### 10.5.5. Appendix E: calculation of the transmission coefficient $T_n$ through a multi-layered medium surrounded by two semi-infinite air layers

The transmission coefficient  $T_n$  through a multi-layered medium surrounded by two semi-infinite air layers can be calculated by finding the root of the determinant of the following matrix:

$$\text{Det} \begin{bmatrix} \frac{T_n}{1+R_1} & 0 & \cdots & -1 & 0 \\ & [M] & & & \\ 0 & \cdots & 0 & 1 & -\frac{\rho_0 c_0}{\cos \theta} \end{bmatrix} = 0,$$

made of the matrix  $[M]$  (of dimension  $n-2 \times n$ ) from equation [10.89] and of the two additional equations [10.94]. We then obtain the following relationship (where  $M^i$  corresponds to the matrix  $[M]$ , in which the  $i$ th column has been removed):

$$\frac{T_n}{1+R_1} \begin{bmatrix} [M^1] \\ 0 \cdots 0 \quad 1 \quad -\frac{\rho_0 c_0}{\cos \theta} \end{bmatrix} - \begin{bmatrix} [M^{n-1}] \\ 0 \cdots 0 \quad 0 \quad -\frac{\rho_0 c_0}{\cos \theta} \end{bmatrix} = 0.$$

This relationship can be rewritten as follows (where  $M^{i,j}$  is the determinant of the matrix  $[M]$ , in which the  $i$ th and  $j$ th columns have been both removed):

$$\frac{T_n}{1+R_1} \left[ -M^{1,n-1} - \frac{\rho_0 c_0}{\cos \theta} M^{1,n} \right] + \frac{\rho_0 c_0}{\cos \theta} M^{n-1,n} = 0.$$

This is exactly the expression given in [10.95].

A similar calculation obtains equation [10.96]: it is sufficient to find the root of the determinant of the following matrix:

$$\text{Det} \begin{bmatrix} 1 & \frac{\rho_0 c_0}{\cos \theta} & 0 & \cdots & 0 \\ & [M] & & & \\ -1 & 0 & \cdots & \frac{T_1}{1+R_n} & 0 \end{bmatrix} = 0.$$

## 10.6. Bibliography

[ALL 87] ALLARD J.F., CHAMPOUX Y. and DEPOLLIER C., “Modelization of layered sound absorbing materials with transfert matrices”, *J. Acoust. Soc. Amer.*, vol. 82, pp. 1792–1796, 1987.

- [ALL 92] ALLARD J.F., BROUARD B., LAFARGE D. and LAURIKS W., "Time reversal and reciprocity in sound propagation through elastic and porous layers", *Appl. Phys. Lett.*, vol. 61, pp. 1166–1167, 1992.
- [ALL 93a] ALLARD J.F., *Propagation of Sound in Porous Media: Modelling Sound Absorbing Materials*, Chapman and Hall, London, 1993.
- [ALL 93b] ALLARD J. F., BROUARD B., LAFARGE D. and LAURIKS W., "Reciprocity and antireciprocity in sound transmission through layered materials including elastic and porous media", *Wave Motion*, vol. 17, pp. 329–335, 1993.
- [BRE 60] BREKHOVSKIKH L.M., *Waves in Layered Media*, Academic Press, New York, 1960.
- [BRO 95] BROUARD B., LAFARGE D. and ALLARD J., "A general method of modelling sound propagation in layered media", *J. Sound Vib.*, vol. 183, no. 1, pp. 129–142, 1995.
- [BRU 98] BRUNEAU M., *Manuel d'acoustique fondamentale*, Hermes, 1998.
- [CAS 45] CASIMIR H.B.G., "On Onsager's principle of microscopic reversibility", *Review of Modern Physics*, vol. 17, pp. 343–350, 1945.
- [DEP 89] DEPOLLIER C., Théorie de Biot et prédiction des propriétés acoustiques des matériaux poreux. Propagation dans les milieux acoustiques désordonnés, PhD Thesis, University of Maine, France, 1989.
- [DER 63] DERESIEWICZ H. and SKALAK R., "On uniqueness in dynamic poroelasticity", *Bull. Seismol. Soc. Am.*, vol. 53, pp. 783–788, 1963.
- [EWI 57] EWING W.M., JARDETZKY W.S. and PRESS F., *Elastic Waves in Layered Media*, McGraw-Hill, New York, 1957.
- [FOL 77] FOLDS D.L. and LOGGINS D.C., "Transmission and reflection of ultrasonic waves in layered media", *J. Acoust. Soc. Amer.*, vol. 62, pp. 1102–1109, 1977.
- [KER 89] KERGOMARD J., "A propos des deux types de réciprocité en électroacoustique", *Journal d'Acoustique*, vol. 2, pp. 421–425, 1989.
- [LAM 84] LAMPTON M. and BURKE J.R., "Time reversal and reciprocity", *Acustica*, vol. 56, pp. 23–28, 1984.



## Chapter 11

# Surface Wave Propagation

### 11.1. Introduction

#### 11.1.1. *Summary*

Surface waves associated with fluid–porous material interfaces have been studied using Biot’s theory [BIO 56] by Feng and Johnson [FEN 83]. The results of their study and some more recent developments are reported in section 11.1.2 on heavy fluid–porous material interfaces. In the case of light saturating fluids (air), the study of Feng and Johnson is supplemented by developments on thin porous layers, and more generally porous materials with high surface impedance. These cases are important in architectural acoustics (carpet and other thin sound-absorbent materials) and in environmental acoustics.

#### 11.1.2. *Porous material–heavy-fluid interfaces*

In order to simplify their study, Feng and Johnson neglected viscous and structural damping. Thus the nature of modes (surface waves, damped pseudo-surface waves) appears more clearly. This simplifying assumption is called by the authors “high-frequency limit” and is not physically feasible, because the interaction due to viscosity decreases with the frequency, but scattering by the structure appears before the viscous forces can be neglected.

At an elastic fluid–solid interface, there is always a surface wave called a Stoneley wave (or Scholte wave) [ACH 73] with a smaller velocity than all the bulk waves in the fluid and the solid. If the velocity of the transverse waves in the solid is greater than that of the bulk waves in the fluid, there is also a pseudo-surface wave, the pseudo Rayleigh wave [BRE 60], propagating faster than the waves in the fluid. This wave is damped because it loses energy, radiated by the bulk wave in the fluid. In the case of a fluid–porous material interface, the characteristics of the different surface waves can be obtained from the boundary conditions which are:

$$\sigma_{zz}^s + \sigma_{zz}^f = -p \quad [11.1]$$

$$\phi u_z^f + (1 - \phi)u_z^s = U_z \quad [11.2]$$

$$\sigma_{xz}^s = 0 \quad [11.3]$$

In these equations,  $\sigma$  designates the stress tensors for the fluid (superscript  $f$ ) and the solid (superscript  $s$ ) in the porous material,  $p$  designate the pressure in the outside fluid, and  $\phi$  is the porosity. Stresses are forces per unit of surface area of material, thus  $\sigma_{zz}^f = -\phi p_i$ , with  $p_i$  the pressure in the porous material. The  $u$  are the components of the particle displacement for both phases in the porous material, with the same conventions as for  $\sigma$ , and  $U_z$  is the  $z$ -component of the outside fluid displacement. There is one last condition that takes two different forms depending on whether the porous material is directly in contact with the outside fluid or has an impervious surface. In the first case, the fourth condition is written

$$p_i = p, \quad [11.4]$$

and in the second case

$$U_z = u_z. \quad [11.5]$$

A surface wave will include a wave in the open air and three Biot waves in the porous material. It will be defined by four coefficients related to the amplitude of each of these waves that will be the unknowns of four equations among the five previous equations the external excitation being removed. More specifically, Feng and Johnson obtained these coefficients from the displacements related to these waves. The surface wave is associated with a  $k_x$  component of the wave number in the plane of the interface that is common to the four waves that constitute it. The components along an axis perpendicular to the surface are given by

$$k_z^i = \pm \sqrt{(k^i)^2 - k_x^2} \quad i = 1, 4, \quad [11.6]$$

where  $k^j$  are the wave numbers associated with the four waves, which are all real in the conditions chosen by Feng and Johnson. To ensure that the system of four equations [11.1] – [11.3], and [11.4] or [11.5], has a non-zero solution, the associated determinant must be zero, which sets at a given frequency the  $k_x$  component. For a surface wave,  $k_x$  is real and the different  $k_z$  associated with the four waves are imaginary, so that the surface wave propagates without damping at the velocity  $\omega/k_x$  and its components decrease exponentially starting from the interface. For a pseudo-surface wave,  $k_x$  and the different  $k_z$  are complex. Research of the zeros of the determinant must be made numerically. There are many solutions, and those associated with a sufficiently low imaginary part of  $k_x$  were selected. Two surface waves similar to the pseudo-Rayleigh wave and the Stoneley wave were discovered. The situation is complicated by the presence of the slow wave, which may be slower than the Stoneley wave, in which case the Stoneley wave becomes a pseudo Stoneley wave, because it radiates into the slow wave. Finally, a new surface wave, slower than the slow wave, was discovered theoretically, mainly in the case of porous materials covered with an impervious membrane. This wave is difficult to detect but has been observed by Adler and Nagy [ADL 94]. The changes created by structural and viscous damping, which can be very important, do not alter the hierarchy defined by Feng and Johnson, even though waves without damping no longer exist in this context [GUB 04], [ALL 04]. The observation of Rayleigh and Stoneley waves or pseudo-waves on heavy fluid–porous material interfaces is a relatively common experiment.

### 11.1.3. *Porous material–light-fluid interfaces*

#### 11.1.3.1. *Partial decoupling and its consequences*

The situation can be described by the same equations as in the case of heavy fluids, but the simple description deriving from the partial decoupling for porous structures with pervious surface is not obvious in this context. The partial decoupling is a property due to the density difference between the air and usual porous structures. An acoustic source in the air will stimulate the porous structure weakly, but the vibrations of the porous structure will be slightly disturbed by the air, which will nevertheless be driven by the displacements of the structure. The structure will have, as a result of a solid stimulation, the same answer as if it was in a vacuum. A Rayleigh wave could therefore be observed, as predicted by Feng and Johnson. In the case of an aerial stimulation, the structure can often, with a good approximation, be considered motionless, and the air in the structure can be replaced by the equivalent free fluid. It should be noted that a porous layer, of porosity  $\phi$ , saturated by an equivalent fluid of effective density  $\rho_l$  and compressibility  $\chi_l$ , may be replaced by a layer of fluid of density  $\rho_l/\phi$  and compressibility  $\chi_l/\phi$ . Thus, the properties associated with semi-infinite porous layers described in section 11.1.3.2 can be obtained by a direct transposition of the results of Brekovskikh and Godin

[BRE 92] on the fluid–fluid interfaces. Two cases are considered in the following sections, the porous layer being either considered as a semi-infinite layer or as a thin layer.

#### 11.1.3.2. *Semi-infinite porous layer*

Broadly speaking, with a  $z$ -axis leaving the porous layer, we made the choice for the space–time dependency of the wave reflected by the porous layer coupled with an incident wave in the  $xz$ -plane, of the following expression

$$p_r = R(\cos \theta) \exp(-i\omega t + izk_a \cos \theta + ixk_a \sin \theta) . \quad [11.7]$$

A surface wave propagating in air is associated with a pole of the reflection coefficient  $R$  of the porous layer, given by

$$R(\cos \theta) = \frac{Z_1 \cos \theta - Z_a \phi \cos \theta_1}{Z_1 \cos \theta + Z_a \phi \cos \theta_1} , \quad [11.8]$$

where  $Z_a$  and  $Z_l$  are the characteristic impedances of the air and the equivalent fluid, respectively,  $\theta$  and  $\theta_l$  are the angles of incidence and refraction, respectively. These angles satisfy the relationship

$$\cos \theta_1 = \left( 1 - \frac{k_a^2}{k_l^2} (1 - \cos^2 \theta) \right)^{1/2} , \quad [11.9]$$

where  $k_a$  and  $k_l$  are the wave numbers in the air and in the equivalent fluid, respectively. The pole associated with an angle of incidence  $\theta_p$  satisfying

$$\sin \theta_p = \left[ \left( \frac{m^2}{\phi^2} - n^2 \right) / \left( \frac{m^2}{\phi^2} - 1 \right) \right]^{1/2} , \quad [11.10]$$

$$\cos \theta_p = - \left[ \left( n^2 - 1 \right) / \left( \frac{m^2}{\phi^2} - 1 \right) \right]^{1/2} , \quad [11.11]$$

where  $n=k_l/k_a$  and  $m=\rho_l/\rho_a$ ,  $\rho_l$  and  $\rho_a$  are the densities of the equivalent fluid and the air, respectively. If damping is suppressed,  $\sin \theta_p$  is real and less than one and  $\cos \theta_p$  is real. The contribution of the pole is not localized near the surface, due to the vertical component of the wave number that is real. With the damping terms,  $\sin \theta_p$  and  $\cos \theta_p$  are complex, but  $\text{Re}(\sin \theta_p)$  remains less than one with the propagation

models previously exposed. This condition implies [BRE 60], [BRE 92] that the pole is not associated, in the case of a point-like or linear sound source, with a surface wave propagating at long distance. The simple physical phenomenon associated with this pole is obvious when  $\theta_p$  is replaced by  $\theta_b$  such that  $\cos\theta_b = -\cos\theta_p$ . Replacing  $\cos\theta$  by  $-\cos\theta$  in equation [11.8] changes a pole into a zero of the reflection coefficient, and  $\theta_b$  is therefore the Brewster's angle of total refraction [HIC 05]. If damping caused by viscosity and heat exchanges is neglected,  $\theta_b$  is real and less than  $\pi/2$ , for which there is no reflected wave. It should be noted that the electric field of a vertical dipole above a conductor, or the acoustic field of a monopole above a semi-infinite porous layer, are governed by very similar equations and properties of poles, and its contribution shown here can be found in electromagnetism (see Brekhovskih [BRE 60], and Bănos [BAN 66] with its very comprehensive historical study).

#### 11.1.3.3. *Thin porous layer*

Assuming that the porous structure is motionless, the surface impedance of a porous layer of thickness  $l$  mounted on a rigid waterproof support is written

$$Z_s(\theta) = \frac{iZ_1}{\phi \cos \theta_1} \cot k_1 l \cos \theta_1. \quad [11.12]$$

We will call “thin layer”, a layer of thickness  $l$  much smaller than the wavelength in the equivalent fluid, so that  $|k_l|l$  is less than 1. This property depends both on the frequency and on the thickness. The reflection coefficient is expressed by

$$R(\cos \theta) = \frac{Z_s(\theta) - Z_a / \cos \theta}{Z_s(\theta) + Z_a / \cos \theta}. \quad [11.13]$$

There is an infinite number of poles given by

$$\cos \theta = -\frac{Z_a}{Z_s(\theta)}. \quad [11.14]$$

For a thin porous layer, a pole at an angle of incidence  $\theta_p$  close to  $\pi/2$  exists [ALL 97]. Developments of the first order in  $\cos\theta$  and  $l$  in equations [11.9] and [11.12] transposed in [11.14] give

$$\cos \theta_p = \frac{i\phi k_a l}{m} (n^2 - 1), \quad [11.15]$$

$$\sin \theta_p = 1 + \frac{\phi^2 k_a^2 l^2}{2m^2} (n^2 - 1)^2. \quad [11.16]$$

There is no other pole near  $\theta_p$  because in equation [11.13]  $Z_s$  is stationary, but  $Z_a/\cos\theta$  varies rapidly with  $\cos\theta$  for  $\theta$  close to  $\pi/2$ . Expressions [11.15], [11.16] of  $\sin\theta_p$  and  $\cos\theta_p$  are only valid if  $|k_l|l \ll 1$ , but iterative methods can be used to obtain  $\theta_p$  when this condition is no longer valid. For a porous layer characterized by a resistivity  $\sigma = 33000 \text{ Nm}^{-4}\text{s}$ , a tortuosity  $\alpha_\infty = 1.1$ , a porosity  $\phi = 0.98$ , and viscous and thermal characteristic lengths  $\Lambda = 50\mu\text{m}$ ,  $\Lambda' = 100\mu\text{m}$ ,  $\sin\theta_p$  predicted for the pole closest to  $\pi/2$  is represented in term of the thickness at 1 kHz in Figure 11.1. The predictions were obtained from the following expressions of  $\rho_1$  and  $\chi_1$  [ALL 93]

$$\rho_1 = \alpha_\infty \rho_a \left( 1 + \frac{i\sigma\phi}{\rho_a \alpha_\infty \omega} \left( 1 - \frac{4i\alpha_\infty^2 \eta \rho_a \omega}{\sigma^2 \Lambda^2 \phi^2} \right)^{1/2} \right), \quad [11.17]$$

$$\chi = \frac{\gamma P_0}{\gamma - (\gamma - 1) \left[ 1 - \frac{\sigma\phi}{i \text{Pr} \omega \rho_a \alpha_\infty} \left( 1 - \frac{4i\alpha_\infty^2 \eta \rho_a \omega \text{Pr}}{\sigma^2 \Lambda^2 \phi^2} \right)^{1/2} \right]^{-1}}, \quad [11.18]$$

where  $\eta$  is the air viscosity and  $\text{Pr}$  the Prandtl number.

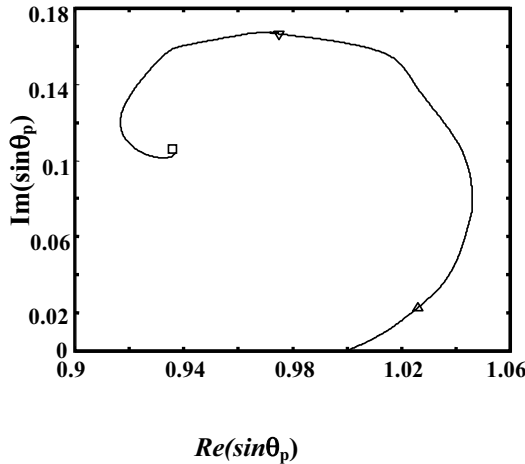


**Figure 11.1.** Path described in the plane  $[Re(\sin\theta), Im(\sin\theta)]$  by  $\sin\theta_p$  in term of the thickness  $l$ ,  $\Delta$   $l=1.25\text{cm}$ ,  $\nabla$   $l=3.75\text{ cm}$ ,  $\square$  semi-infinite layer

If damping is suppressed,  $\cos\theta_p$  is imaginary, so that the wave in the air is localized near the surface, and  $\sin\theta_p$  is real and greater than 1, and the wave propagates without damping on the surface with a velocity slower than the sound velocity. This velocity is greater than that of bulk waves in the porous material, and the refracted wave therefore propagates in the  $z$ -direction. Nevertheless, the surface wave does not radiate energy to the refracted wave. With the total reflection on the underside of the porous material, the field in the porous layer is a trapped mode that moves horizontally without damping, with the same velocity as the surface wave. The surface wave can be regarded as the evanescent wave accompanying, in the air, the mode that is trapped in the material. Damping in the material will result in damping of the propagation parallel to the surface, and in adding a real component to  $\cos\theta_p$ . As in the case of a semi-infinite porous layer, there is an electromagnetic phenomenon very similar to this kind of surface wave. It is the reflection of electromagnetic TM waves by a conductor covered with a dielectric [COL 60].

#### 11.1.3.4. Localizations of the poles

Rayleigh and Stoneley waves and pseudo-waves above a porous layer saturated by a heavy fluid show a great similarity with those existing above an elastic solid, and detection methods for these waves are the same. To detect the Rayleigh wave on plastic foam saturated with air, we must take into account two characteristics of this porous medium, its very low rigidity, which yields a velocity of about 50m/s, and a strong structural damping, with a loss angle of about 1/10 or more. Regarding the waves created on the air-thin porous layer interface by a source in the air, the evaluation of the contribution of the pole does not seem to be easily achievable in the time domain, due to the rapid variation of velocity with frequency. A simple method can be used to measure  $\theta_p$  when  $\theta_p$  is close to  $\pi/2$ , and thus clarify the properties of the possibly associated surface wave.

The starting point of the method is an approximation obtained by Chien and Soroka [CHI 75], of the field  $p_r$  created by a monopole and reflected by a surface of impedance  $Z_s$  independent of the angle of incidence. Such a surface presents a pole at  $\cos\theta_p$  given by

$$\cos\theta_p = -\frac{Z_a}{Z_s}, \quad [11.19]$$

and  $p_r$  is given by

$$p_r = \frac{\exp(ik_a R_1)}{R_1} [R(\cos\theta_0) + (1 - R(\cos\theta_0))F(w)], \quad [11.20]$$

$$F(w) = 1 + i\sqrt{\pi}w \exp(-w^2) \operatorname{erfc}(-iw), \quad [11.21]$$

$$w = \sqrt{\frac{1}{2} k_a R_l} \exp \frac{\pi i}{4} (\cos \theta_0 - \cos \theta_p). \quad [11.22]$$

where  $\theta_0$  is the specular reflection angle and  $R_l$  is the distance between the source image (symmetrically with respect to the reflective surface) and the receiver (see Figure 11.2).

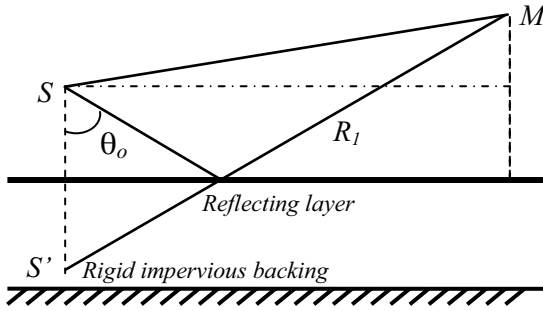


**Figure 11.2.** Source  $S$ , its image  $S'$  and the receiver  $M$ ,  $S'M=R_l$ ,  $\theta_0$  is the specular reflection angle

This expression is only valid when  $\theta_p$  and  $\theta_0$  are close to  $\pi/2$ . For a porous layer with a low resistance to the passage of air and a tortuosity close to 1, the surface impedance can vary considerably with the angle of incidence. It was shown in the case of thin layers [ALL 03], and semi-infinite layers if the pole is sufficiently close to  $\pi/2$  [HIC 05], that the previous expression of  $p_r$  can still be used. Physically, this corresponds to the fact that  $\cos \theta_l$  is relatively stationary to  $\cos \theta$  for small values of  $\cos \theta$ . Contributions to  $p_r$  are associated with the values of the reflection coefficient in a range including  $\theta_p$  and  $\theta_0$  where  $\cos \theta$  remains small if  $\theta_p$  and  $\theta_0$  are close to  $\pi/2$ . The impedance varies slightly in this range and the best approximation for the reflection coefficient is obtained by setting the impedance constant at its value for  $\theta = \theta_p$ . A constant impedance plane can therefore replace the porous surface with a pole at  $\theta_p$ , whose impedance is then given by

$$Z_s(\theta_p) = -\frac{Z_a}{\cos \theta_p}. \quad [11.23]$$



The quantity  $Z_s(\theta_p)/Z_a$ , measured for a layer of thickness 1.25 cm of the material defined in [11.1.3.3], is shown in Figure 11.3. A description of the evaluation process of this quantity is given in [ALL 03].

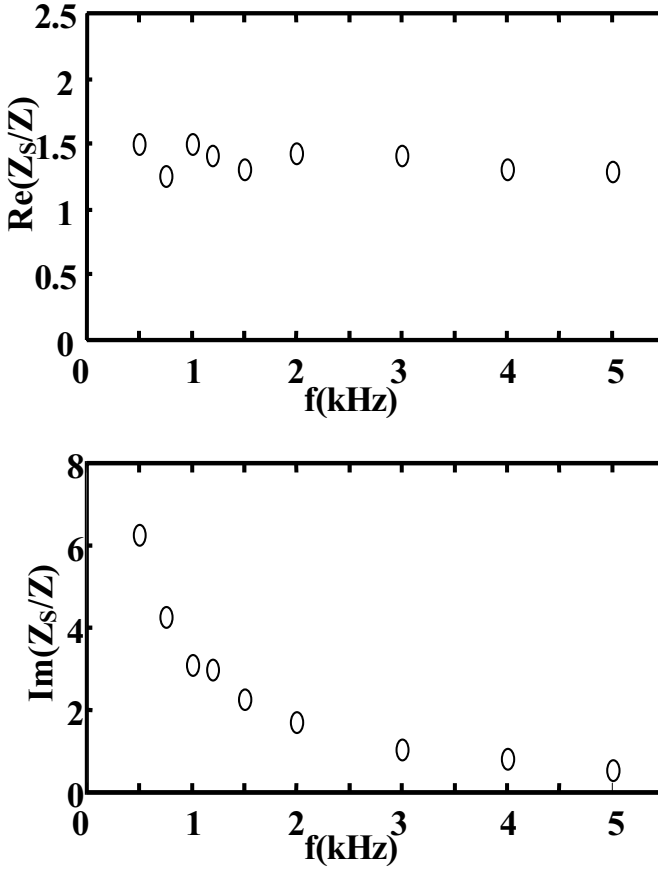


**Figure 11.3.** Reduced impedance  $Z_s(\theta_p)/Z_a$  measured for a layer of thickness  $l = 1.25$  cm of the material defined in [11.1.3.3]

This reduced impedance is close to the reduced impedance at  $\theta = \pi/2$ . The localization of a pole near  $\pi/2$  may allow an evaluation of the impedance close to grazing incidence.

## 11.2. Bibliography

- [ACH 73] Achenbach J. D., *Wave Propagation in Elastic Solids*, North Holland, 1973.
- [ADL 94] Adler L., Nagy P. B., "Measurement of acoustic surface waves on fluid-filled porous rocks", *J. Geophysical Research*, 99, 17863–9, 1994.
- [ALL 93] Allard J. F., *Propagation of Sound in Porous Media. Modelling sound absorbing materials*. Elsevier, 1993.
- [ALL 97] Allard J. F., Lauriks W., "Poles and zeros of the plane wave reflection coefficient for porous surfaces", *Acustica united with Acta Acustica*, 83, 1045–52, 1997.
- [ALL 03] Allard J. F., Henry M., Garetton V., Jansens G., Lauriks W., "Impedance measurements around grazing incidence for nonlocally reacting thin porous layers", *J. Acoust. Soc. Am.*, 113, 1210–15, 2003.
- [ALL 04] Allard J. F. Henry M., Petillon S., Lauriks W., "Laser induced surface modes at water–elastic and poroelastic solid interfaces", *J. Appl. Phys.*, 95, 528–36, 2004.
- [BAN 66] Baños A., *Dipole Radiation in the Presence of a Conducting Half-space*, Pergamon, 1966.
- [BIO 56] Biot M., "The theory of propagation of elastic waves in a fluid-saturated porous fluid. I. Low frequency range. II. Higher frequency range", *J. Acoust. Soc. Am.*, 28, 168–91, 1956.
- [BRE 60] Brekhovskikh L. M., *Waves in Layered Media*, Academic Press, New York, 1960.
- [BRE 92] Brekhovskikh L., Godin O., *Acoustics of Layered Media II, Point source and Bounded Beams*, Springer, 1992.
- [CHI 75] Chien C. F., Soroka W. W., "Sound propagation along an impedance plane", *J. Sound Vib.*, 43, 9–20, 1975.
- [COL 60] Collin R. E., *Field Theory of Guided Waves*, McGraw-Hill, 1960.
- [FEN 83] Feng S., Johnson D. L., "High-frequency acoustic properties of a fluid/porous solid interface. I. New surface mode. II. The 2d reflection Green function", *J. Acoust. Soc. Am.*, 74, 906–14, 1983.
- [GUB 04] Gubaidullin A. A., Kuchugurina O. Y., Smeulders D. J. M. and Wisse C. J., "Frequency-dependent acoustic properties of a fluid/porous solid interface", *J. Acoust. Soc. Am.*, 116, 1474–80, 2004.
- [HIC 05] Hickey C., Leary D., Allard J. F., Henry M., "Impedance and Brewster angle measurement for thick porous layers", *J. Acoust. Soc. Am.*, 118, 1503–9, 2005.

## Chapter 12

# The Finite Element Method for Porous Materials

### 12.1. Introduction

#### 12.1.1. *Position of the problem*

To reduce the noise and vibration perturbations, it is beneficial to use the dissipative properties of poroelastic materials. These materials are generally not used alone, but rather inserted in composite mechanical assemblies made of elastic structures, poroelastic materials and air insertions. If these structures are assemblies of layers of materials, they are called multilayer complexes. If the porous material is modified by an addition of solid or fluid inclusions, the term heterogenous porous material is widely used. To predict the vibratory response of such assemblies, closed form solutions can not generally be obtained and the calculation of the vibroacoustic response must then be calculated using numerical techniques.

#### 12.1.2. *Outline of the finite element method*

The finite element method (FEM) is nowadays the most common numerical method used in static and dynamic structures for the resolution of boundary problems. The boundary problem is continuous and the general principle of these numerical methods is to approach this continuous problem with a finite number of degrees of freedom. This method derives its popularity from its flexibility, considering its

general nature or its implementation. Moreover, it is based on convergence theorems from functional analysis, obtaining the validity criteria of the method. However, these mathematical results may be directly interpreted from the physical point of view either as the solution of a minimizing energy problem (provided, however, that some symmetry properties are verified – which is not always the case) or as an analogy with the classical principle of the virtual powers.

Unlike other methods, such as the finite difference method, the discretization is not directly conducted on the partial differential equations themselves, but on an equivalent integral formulation called the variational formulation. The first step of the method is to obtain this variational formulation. The  $\Omega$  domain occupied by the structure is then divided into a finite number of subdomains called mesh. On each mesh, a number of points called nodes are selected, and a set of functions called interpolation functions are used to calculate the unknown parameters at each element of the mesh according to the values of these parameters at the nodes. The discretized problem is then obtained by writing the relations between the unknown nodal parameters to obtain a linear system of equations. Once this system is solved, it is then possible to determine, represent or use the approached solution. The FEM is described in detail in many books [RAV 98, ZIE 89]. We will focus here on its application to porous materials.

### **12.1.3. History of the finite element method for porous materials**

The FEM began to be used to predict the response of structures involving porous materials in the 1990s. The first formulations proposed involved variables corresponding to the displacements of the solid phase and fluid phase: we can mention the work of Kang and Bolton [KAN 95, KAN 96, KAN 97, KAN 99] or the work of Panneton and Atalla [PAN 96a, PAN 96b, PAN 97]. Other formulations where the displacement of the fluid phase was replaced by a relative displacement between the two phases have since appeared [COY 94, COY 95, JOH 95, VIG 97]. Nevertheless, these formulations based on the movement had the disadvantage of being relatively difficult to implement. It also became apparent that the most intuitive variable to describe a fluid environment was not its displacement, but the pressure. Atalla *et al.* [ATA 98] proposed a mixed formulation displacement-pressure, based on an assumption of harmonic movement, and obtained the first mixed finite element systems for porous materials. Several variations were then derived from the original formulation, each of which is best suited to manage the given boundary or coupling conditions. An exhaustive review was made by Sgard [SGA 02]. The methods based on this formulation are today the most widely used. Nevertheless, although the number of degrees of freedom per node is currently 4 and not 6, the systems obtained by this method are still large, and, of course, frequency-dependent. More recently, works in functional analysis have been conducted to justify the existence of such solutions, but also to deal in an optimal manner, the stages of discretization and thereby to reduce the numerical cost of the method [HÖR 03].

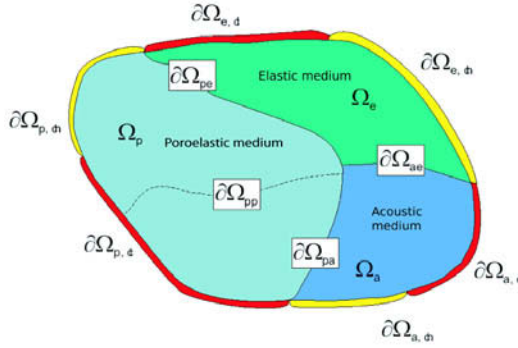


Figure 12.1. Coupled problem

#### 12.1.4. Continuous problems considered

Biot's theory provides us with a set of partial differential equations and boundary conditions governing the homogenized porous material. Figure 12.1 presents a coupled, poro-elasto-acoustic, three-dimensional problem. It is here a composite structure made of structures of various kinds; porous material, elastic solid and acoustic cavities. Each subdomain is described by a set of partial differential equations and boundary conditions at the borders that reflect the continuity relationships.

We will describe them using the formulations  $\{\mathbf{u}, \mathbf{U}\}$  and  $\{\mathbf{u}, P\}$ .

We will consider a poroelastic sub-structure occupying an area ( $\Omega$ ) of the physical space. This sub-structure is limited by its border  $\Gamma$ , which can itself be partitioned as described below.

---

$S_d$	Interface where the displacement is imposed
$S_c$	Interface where the stress is imposed
$\Gamma_{pe}$	Interface with an elastic medium
$\Gamma_{pa}$	Interface with an acoustic medium
$\Gamma_{pp}$	Interface with a poroelastic medium

---

In the case of a single porous medium, we clearly have  $\Gamma_{pe} \cup \Gamma_{pa} \cup \Gamma_{pp} = \emptyset$ .

## 12.2. Boundary problem equations

### 12.2.1. The $\{\mathbf{u}, \mathbf{U}\}$ formulation

We briefly recall here that the relations of the dynamics for the solid phase and the fluid phase of the homogenized porous material are given by Biot's theory:

$$\nabla \cdot \boldsymbol{\sigma}^s = -\omega^2 (\tilde{\rho}_{11} \mathbf{u} + \tilde{\rho}_{12} \mathbf{U}), \quad [12.1a]$$

$$\nabla \cdot \boldsymbol{\sigma}^f = -\omega^2 (\widetilde{\rho}_{12} \mathbf{u} + \widetilde{\rho}_{22} \mathbf{U}). \quad [12.1b]$$

### 12.2.2. The $\{\mathbf{u}, P\}$ formulation

The  $\{\mathbf{u}, P\}$  formulation was proposed by Atalla *et al.* in 1998 [ATA 98]. This formulation is based on a change of variable taking the divergence of equation [12.1b] which becomes:

$$-h\Delta P = -\omega^2 (\widetilde{\rho}_{22} \nabla \cdot \mathbf{U} + \widetilde{\rho}_{12} \nabla \cdot \mathbf{u}). \quad [12.2]$$

To eliminate the term with  $\nabla \cdot \mathbf{U}$  Atalla *et al.* have proposed using the stress strain relation of the fluid phase. We therefore have:<sup>1</sup>

$$\nabla \cdot \mathbf{U} = -\frac{h}{\widetilde{R}} P - \frac{\widetilde{Q}}{\widetilde{R}} \nabla \cdot \mathbf{u}. \quad [12.3]$$

Equation [12.2] is then equivalent to the equation of motion of the fluid phase, using a  $\{\mathbf{u}, P\}$  formulation,

$$\Delta P + \frac{\omega^2}{\widetilde{c}^2} P - \frac{\widetilde{\rho}_{22}\omega^2}{h^2} \widetilde{\gamma} \nabla \cdot \mathbf{u} = 0, \quad [12.4]$$

introducing the terms,

$$\widetilde{\gamma} = h \left( \frac{\widetilde{\rho}_{12}}{\widetilde{\rho}_{22}} - \frac{\widetilde{Q}}{\widetilde{R}} \right) \quad \text{and} \quad \widetilde{c}^2 = \frac{\widetilde{R}}{\widetilde{\rho}_{22}}. \quad [12.5]$$

To eliminate the displacement of the fluid phase in the equation of motion of the solid phase, we have to eliminate the dependence on inertial terms. For this purpose, Atalla *et al.* proposed, in the harmonic system, extracting this variable from the equation of motion of the fluid phase:

$$-h\nabla P = -\omega^2 \widetilde{\rho}_{22} \mathbf{U} - \omega^2 \widetilde{\rho}_{12} \mathbf{u} \implies \mathbf{U} = \frac{h}{\widetilde{\rho}_{22}\omega^2} \nabla P - \frac{\widetilde{\rho}_{12}}{\widetilde{\rho}_{22}} \mathbf{u}. \quad [12.6]$$

The second step is to eliminate the displacement variable of the fluid phase in the stress tensor of the solid phase. To do so, relationship [12.3] is used, again to define the following tensor:

$$\boldsymbol{\sigma}_{\emptyset}^s(\mathbf{u}) = \boldsymbol{\sigma}^s(\mathbf{u}, \mathbf{U}) + h \frac{\widetilde{Q}}{\widetilde{R}} P \mathbb{I}. \quad [12.7]$$

---

1. This relation can be expressed in the following way: the change in volume of the fluid phase is due to a change of pressure in the pore network, but also to the expansion of the solid phase.

We can notice that this tensor only depends on the movement of the solid phase, and is identical to the tensor of solid stresses for  $P = 0$ . It is also called the *in-vacuo* stress tensor. Its use permits the appearance of  $\tilde{\gamma}$  in the equation of the movement of the solid phase, which yields:

$$\nabla \cdot \sigma_{\emptyset}^s(\mathbf{u}) + \tilde{\rho}\omega^2\mathbf{u} + \tilde{\gamma}\nabla P = 0, \quad [12.8]$$

with the introduction of

$$\tilde{\rho} = \widetilde{\rho_{11}} - \frac{\widetilde{\rho_{12}}^2}{\widetilde{\rho_{22}}}. \quad [12.9]$$

We now have the set of two partial differential equations (PDEs) [12.8] and [12.4] using the  $\{\mathbf{u}, P\}$  formulation. We have presented the partial differential equations governing the porous materials in two formulations. We shall now see how to write the boundary conditions.

### 12.2.3. The boundary conditions

When writing the boundary conditions, the five types of interfaces presented above should be considered. The full description of the expressions for each formulation and each interface is not the purpose of this section. We will simply present the different values that remain unchanged and how the relationships can be found.

On the interface  $S_d$  we impose a given displacement  $\mathbf{u}_0$ . Two relations are inferred from this condition. The first reflects the continuity of the displacement at the interface, and the second expresses the continuity of the normal displacement of the porous material and the normal displacement  $\mathbf{u}_0 \cdot \mathbf{n}$ . These relations are, thus, naturally written using the  $\{\mathbf{u}, \mathbf{U}\}$  formulation. Since the second relation involves the movement of the fluid phase, its notation using a mixed formulation will be obtained projecting the expression [12.6] on the normal of the surface. We thus obtain:

$$\mathbf{U}|_{S_d} \cdot \mathbf{n} = \frac{h}{\widetilde{\rho_{22}\omega^2}} \frac{\partial P}{\partial n} - \frac{\widetilde{\rho_{12}}}{\widetilde{\rho_{22}}} \mathbf{u}|_{S_d} \cdot \mathbf{n}. \quad [12.10]$$

On  $S_c$  where we impose the pressure per unit of surface  $P_{imp}$ , we use two relations on the stresses that reflect the continuity of forces on the interface as well as the continuity of the pressure. In the displacement formulation, we then have two Neumann boundary conditions on the stress tensors of the solid and fluid. In the mixed formulation, a relationship is deduced for the *in-vacuo* stress tensor and the condition of imposed pressure is naturally written.

On  $\Gamma_{pe}$  (interface with an elastic domain), we can write four relations. The first two equations reflect the continuity of normal stress between the two phases in contact, the third reflects the continuity of the normal displacement of the fluid phase and the last reflects the continuity of the displacement of the solid phase.

On  $\Gamma_{pa}$ , only three conditions are imposed. Indeed, for the acoustic environment considered consisting of a perfect fluid, which does not contribute to shear waves, there is no continuity condition of the tangential speed. The first two relationships reflect the continuity of normal stresses between the two phases in contact, the latter reflecting the continuity of the displacements, normal to the interface.

On  $\Gamma_{pp}$  (interface between two poroelastic phases), we can write four relations reflecting the continuity of the total stress, of the pressure, of the displacement of the solid phase and of the normal flow at the level of the interface.

These boundary problems are well posed in the cases considered in acoustics, where the porous media are open. As stated above, these equations are never directly discretized. We begin with the variational formulation of the problem.

### 12.3. Poroelastic variational formulations

We discuss here the several different poroelastic variational formulations. The variational formulation of the problem is equivalent to the formulation of the boundary problem based on the theorem of virtual powers. We can easily show that the boundary problem involves the variational formulation. The opposite is true only in the sense of the distributions. The advantage is that this variational formulation will be discretized in a fairly rich manner.

#### 12.3.1. The displacement formulations

The weak integral formulation of a poroelastic domain contained in a volume  $\Omega$  is given by Panneton [PAN 96a, PAN 96b]. The first step consists of multiplying each of the equations of displacement [12.1] by an admissible displacement field, i.e. verifying the corresponding boundary conditions,  $\delta \mathbf{u}$  for the solid phase and  $\delta \mathbf{U}$  for the fluid phase. The equations are then integrated on the volume  $\Omega$ . We then obtain the two equations:

$$\int_{\Omega} \nabla \cdot \boldsymbol{\sigma}^s \delta \mathbf{u} \, d\Omega + \int_{\Omega} \omega^2 (\tilde{\rho}_{11} \mathbf{u} + \tilde{\rho}_{12} \mathbf{U}) \delta \mathbf{u} \, d\Omega = 0, \quad [12.11a]$$

$$\int_{\Omega} \nabla \cdot \boldsymbol{\sigma}^f \delta \mathbf{U} \, d\Omega + \int_{\Omega} \omega^2 (\tilde{\rho}_{12} \mathbf{u} + \tilde{\rho}_{22} \mathbf{U}) \delta \mathbf{U} \, d\Omega = 0. \quad [12.11b]$$

The first integral of each of these equations is then rewritten using Green's formula and yields:

$$\begin{aligned} & \int_{\Omega} (\boldsymbol{\sigma}^s(\mathbf{u}, \mathbf{U}) \boldsymbol{\varepsilon}^s(\delta \mathbf{u}) - \omega^2 (\tilde{\rho}_{11} \mathbf{u} \cdot \delta \mathbf{u} + \tilde{\rho}_{12} \mathbf{U} \cdot \delta \mathbf{u})) \, d\Omega \\ & = \oint_{\partial\Omega} [\boldsymbol{\sigma}^s(\mathbf{u}, \mathbf{U}) \cdot \mathbf{n}] \delta \mathbf{u} \, d\Gamma \quad \forall \delta \mathbf{u} \end{aligned} \quad [12.12a]$$



$$\begin{aligned}
& \int_{\Omega} (\sigma^f(\mathbf{u}, \mathbf{U}) \varepsilon^f(\delta \mathbf{U}) - \omega^2 (\widetilde{\rho}_{22} \mathbf{U} \cdot \delta \mathbf{U} + \widetilde{\rho}_{12} \mathbf{u} \cdot \delta \mathbf{U})) d\Omega \\
& = \oint_{\partial\Omega} [\sigma^f(\mathbf{u}, \mathbf{U}) \cdot \mathbf{n}] \delta \mathbf{U} d\Gamma \quad \forall \delta \mathbf{U}.
\end{aligned} \tag{12.12b}$$

This system of two equations is called the variational formulation of the poroelastic problem in motion. This construction shows clearly that the solution of the boundary problem is a solution of the variational problem.

### 12.3.2. Mixed formulations

In mixed formulations, the methodology to obtain the variational formulation remains the same using displacement and pressure fields. Several mixed formulations were developed and implemented. They all have, however, the same starting point which is the  $\{\mathbf{u}, P\}$  formulation given by Atalla *et al.* [ATA 98]. This reads:

$$\begin{aligned}
& \int_{\Omega} \sigma_{\emptyset}^s(\mathbf{u}) \varepsilon^s(\delta \mathbf{u}) d\Omega - \omega^2 \int_{\Omega} \widetilde{\rho} \mathbf{u} \cdot \delta \mathbf{u} d\Omega - \int_{\Omega} \widetilde{\gamma} \nabla P \cdot \delta \mathbf{u} d\Omega \\
& - \oint_{\partial\Omega} [\sigma_{\emptyset}^s(\mathbf{u}) \cdot \mathbf{n}] \delta \mathbf{u} d\Gamma \quad \forall \delta \mathbf{u},
\end{aligned} \tag{12.13a}$$

$$\begin{aligned}
& \int_{\Omega} \left[ \frac{h^2}{\omega^2 \widetilde{\rho}_{22}} \nabla P \cdot \nabla \delta P - \frac{h^2}{\widetilde{R}} P \delta P \right] d\Omega - \int_{\Omega} \widetilde{\gamma} \mathbf{u} \cdot \nabla \delta P d\Omega \\
& + \oint_{\partial\Omega} \left[ \widetilde{\gamma} \mathbf{u} \cdot \mathbf{n} - \frac{h^2}{\widetilde{\rho}_{22} \omega^2} \frac{\partial P}{\partial n} \right] \delta P d\Gamma \quad \forall \delta P.
\end{aligned} \tag{12.13b}$$

This original formulation was then written under several variants, that differ from each other by rewriting the boundary integrals using the divergence theorem. In 2001, Atalla *et al.* proposed an alternate layout for this formulation:

$$\begin{aligned}
& \int_{\Omega} \left( \sigma_{\emptyset}^s(\mathbf{u}) \varepsilon^s(\delta \mathbf{u}) - \omega^2 \widetilde{\rho} \mathbf{u} \cdot \delta \mathbf{u} - \frac{h}{\widetilde{\alpha}} \nabla P \cdot \delta \mathbf{u} h \left( 1 + \frac{\widetilde{Q}}{\widetilde{R}} \right) P \nabla \cdot \delta \mathbf{u} \right) d\Omega \\
& - \oint_{\partial\Omega} [\sigma^t(\mathbf{u}, P) \cdot \mathbf{n}] \delta \mathbf{u} d\Gamma \quad \forall \delta \mathbf{u},
\end{aligned} \tag{12.14a}$$

$$\begin{aligned}
& \int_{\Omega} \left( \frac{h^2}{\omega^2 \widetilde{\rho}_{22}} \nabla P \cdot \nabla \delta P - \frac{h^2}{\widetilde{R}} P \delta P - \frac{h}{\widetilde{\alpha}} \mathbf{u} \cdot \nabla \delta P h \left( 1 + \frac{\widetilde{Q}}{\widetilde{R}} \right) \nabla \cdot \mathbf{u} \delta P \right) d\Omega \\
& - \oint_{\partial\Omega} h (U_n - u_n) \delta P d\Gamma \quad \forall \delta P.
\end{aligned} \tag{12.14b}$$

Without the help of the porous model, this formulation is naturally coupled with elastic or acoustic structures. It is therefore interesting to model heterogenous porous materials.

#### 12.4. Discretized systems

The next step is to discretize the integrals involved in the variational formulations. One can express them with the nodal values of the fields and using the interpolation functions. Indeed, we have for each of the elements:

$$u^e = [N_u]^e \mathbf{u}_e \quad U^e = [N_U]^e \mathbf{U}_e, \quad [12.15]$$

where  $u^e$  and  $U^e$  are the values of the continuous field,  $\mathbf{u}^e$  and  $\mathbf{U}^e$  the values of the field at the nodes, and  $[N_u]$  and  $[N_U]$  correspond to form-factor functions on element  $e$ . These relationships enable us to obtain the discretization of the elementary integrals. Therefore, we can build for example:

$$\int_{\Omega} \delta \mathbf{u}^t [N_u]^e \mathbf{u} d\Omega = \delta \mathbf{u}^t \left( \int_{\Omega} \delta [N_u]^e [N_u]^e d\Omega \right) \mathbf{u} = \delta \mathbf{u}^t [E_1]^e \mathbf{u}. \quad [12.16]$$

$[E_1]^e$  is called the elementary matrix. It is also possible to discretize the other integrals in the same way. Equation [12.12a] then yields:

$$\delta \mathbf{u}^t \left( [\hat{\mathbf{K}}_{ss}] \mathbf{u} + [\hat{\mathbf{K}}_{sf}] \mathbf{U} - \omega^2 \tilde{\rho}_{11} [\hat{\mathbf{M}}_{ss}] \mathbf{u} - \omega^2 \tilde{\rho}_{12} [\hat{\mathbf{M}}_{sf}] \mathbf{U} - \mathbf{F}^s \right) = 0. \quad [12.17a]$$

The matrices involved in these equations were constructed by assembling elementary matrices.

$$\delta \mathbf{U}^t \left( [\hat{\mathbf{K}}_{sf}]^t \mathbf{u} + [\hat{\mathbf{K}}_{ff}] \mathbf{U} - \omega^2 \tilde{\rho}_{12} [\hat{\mathbf{M}}_{sf}]^t \mathbf{u} - \omega^2 \tilde{\rho}_{22} [\hat{\mathbf{M}}_{ff}] \mathbf{U} - \mathbf{F}^f \right) = 0. \quad [12.17b]$$

The matrix of the linear problem to be solved is therefore written as:

$$\begin{bmatrix} [\hat{\mathbf{K}}_{ss}] & [\hat{\mathbf{K}}_{sf}] \\ [\hat{\mathbf{K}}_{sf}]^t & [\hat{\mathbf{K}}_{ff}] \end{bmatrix} \begin{Bmatrix} \mathbf{u} \\ \mathbf{U} \end{Bmatrix} - \omega^2 \begin{bmatrix} \tilde{\rho}_{11} [\hat{\mathbf{M}}_{ss}] & \tilde{\rho}_{12} [\hat{\mathbf{M}}_{sf}] \\ \tilde{\rho}_{12} [\hat{\mathbf{M}}_{sf}]^t & \tilde{\rho}_{22} [\hat{\mathbf{M}}_{ff}] \end{bmatrix} \begin{Bmatrix} \mathbf{u} \\ \mathbf{U} \end{Bmatrix} = \begin{Bmatrix} \mathbf{F}^s \\ \mathbf{F}^f \end{Bmatrix}. \quad [12.18]$$

The poroelastic problem using the  $\{\mathbf{u}, P\}$  formulation is therefore given by [ATA 98] and uses the matrix:

$$\begin{bmatrix} (1 + j\eta_s) [\mathbf{K}_{\text{int}}] + (j\omega)^2 \tilde{\rho} [\mathbf{M}_{\text{int}}] & -\tilde{\gamma} [\mathbf{C}_{\text{int}}] \\ -\omega^2 \tilde{\gamma} [\mathbf{C}_{\text{int}}]^t & \frac{h^2}{\tilde{\rho}_{22}} [\mathbf{H}_{\text{int}}] - \omega^2 \frac{h^2}{R} [\mathbf{Q}_{\text{int}}] \end{bmatrix} \begin{Bmatrix} \mathbf{u} \\ P \end{Bmatrix} = \begin{Bmatrix} \mathbf{F}^s \\ \mathbf{F}^f \end{Bmatrix}. \quad [12.19]$$

$[\mathbf{K}_{\text{int}}]$ ,  $[\mathbf{M}_{\text{int}}]$  are associated with the stiffness matrix, and with the mass matrix of the solid phase, respectively.  $[\mathbf{H}_{\text{int}}]$  and  $[\mathbf{Q}_{\text{int}}]$  are associated with the matrices of kinetic energy and of compression of the fluid phase, respectively. These matrices come from discretization using the finite element method.

It is possible to make the system symmetrical<sup>2</sup>, writing it as:

$$\begin{bmatrix} (j\omega)^2[\tilde{\mathbf{K}}] + (j\omega)^4[\tilde{\mathbf{M}}] & -(j\omega)^2[\tilde{\mathbf{C}}] \\ -(j\omega)^2[\tilde{\mathbf{C}}]^t & [\tilde{\mathbf{H}}] - (j\omega)^2[\tilde{\mathbf{Q}}] \end{bmatrix} \begin{Bmatrix} \mathbf{u} \\ \mathbf{P} \end{Bmatrix} = \begin{Bmatrix} \mathbf{F}^s \\ \mathbf{F}^f \end{Bmatrix}. \quad [12.20]$$

This formulation requires the construction of five global matrices. However, the obtained systems are generally ill-conditioned, due to the non-homogenous nature of the variables. Therefore, algorithms of resolution should reflect this feature. Note, however, that this does not present a limitation in modern practice because such conditions are usually able to be accepted.

#### 12.4.1. Discussion about discretization

The resolution of a vibroacoustic problem involving an elastic structure, a fluid medium and a poroelastic medium will require discretization of each of these domains. For several reasons, the domain that will determine the size of the system is the poroelastic domain:

- Wavelengths of the Biot's waves are generally smaller than those of acoustic waves. To meet the mesh criterion of six nodes per wavelength, we will require a larger nodal density in the porous domain than in the fluid domain [DAU 01].
- The poroelastic area is meshed by volume elements, requiring a discretization in the 3 spatial directions, unlike the elements of structures – plates or shells – requiring only a mesh in 2 directions.
- The number of degrees of freedom per node of the poroelastic elements is 4 to 6 depending on whether it uses a mixed or displacement formulation, 4 to 6 times higher than a component of the fluid.

Thus, it appears that the presence of the porous material will impose some rules for the determination of an adequate mesh, these rules are quite strong for the discretization. This therefore limits the scope of such methods because it requires relatively important calculation means. Nevertheless, they are now the only way to study this type of problem [PAN 96b, DAU 03].

The comparison between the displacement formulation and the pressure formulation indicates that the number of unknowns per node is more limited for the

---

2. Real symmetry.

mixed formulations for an equivalent mesh. The equivalence between the required meshes to ensure the convergence of each of the formulations is a point that still needs to be studied [DAZ 08]. It is important to note that although the mixed formulation has fewer nodes, it requires the calculation of an additional matrix to take into account the volume coupling between the two phases. The construction time of the systems to be resolved is therefore more important. However, for large scale problems the most expensive step, in terms of computation time, is the resolution of the linear system that is directly linked to the number of degrees of freedom of the system. The mixed formulations therefore seem more interesting in terms of computation time, but they are more difficult to address – especially for a programmer unfamiliar with this domain. In regards to the discretization, the usual linear elements provide satisfactory results for a fluid, but may not correctly converge for a poroelastic material. These elements do not correctly take into account the shear and bending deformations. To correct this defect, the order of the functions of interpolation can be increased using quadratic elements, or hierarchical finite elements. These elements can converge without refining the mesh. However, the elementary matrices require a greater calculation time – depending on the order of these matrices. Another method consists of using modified linear elements so that deformations shearing and bending are properly taken into account. Due to the size of systems to be solved, the use of finite poroelastic elements remained until recently limited to reduce-sized configurations that can give a good representation of real structures. This drives to the development and the use of simplified models [DAU 03, DOU 07, DAZ 09]. Nevertheless, the arrival of powerful means of calculation at affordable prices now permits us to relatively easily address the complex problems stated in the introduction. Note that recently, a new displacement formulation proposed by Dazel [DAZ 07] allows the use of a much more efficient resolution method based on normal modes [DAZ 09].

## 12.5. Conclusion

This section was designed to introduce the numerical modeling of porous materials, using the finite element method. After presenting the historical context, the relevant problems with the boundary conditions have been recalled, then poroelastic variational formulations have been presented. The discretization of these variational formulations was then exposed and discussed. Possible examples of such techniques will be presented in Chapter 28.

## 12.6. Bibliography

- [ATA 98] ATALLA N., PANNETON R. and DEBERGUE P., “A mixed displacement-pressure formulation for poroelastic materials”, *J. Acoust. Soc. Am.*, vol. 104, no. 3, pp. 1444–1452, 1998.
- [DAU 01] DAUCHEZ N., SAHRAOUI S. and ATALLA N., “Convergence of poroelastic finite element based on Biot displacement formulation”, *J. Acoust. Soc. Am.*, vol. 109, no. 1, pp. 33–40, 2001.

- [DAU 03] DAUCHEZ N., SAHRAOUI S. and ATALLA N., “Investigation and modelling of damping in a plate with a bonded porous layer”, *J. Sound Vib.*, vol. 265, no. 2, pp. 437–449, 2003.
- [DAZ 07] DAZEL O., BROUARD B., DEPOLLIÉ C. and GRIFFITHS S., “An alternative biot’s displacement formulation for porous materials”, *Journ. Acoustical Society of America*, vol. 121, pp. 3509–3516, 2007.
- [DAZ 08] DAZEL O., SGARD F., BECOT F.-X. and ATALLA N., “Expressions of dissipated powers and stored energies in poroelastic media modeled by  $\{u, U\}$  and  $\{u, P\}$  formulations”, *J. Acoust. Soc. Am.*, vol. 123, no. 4, pp. 2054–2063, 2008.
- [DAZ 09] DAZEL O., BROUARD B., DAUCHEZ N. and GESLAIN A., “Enhanced Biot’s finite element displacement formulation for porous materials and original resolution methods based on normal modes”, accepted in *Acta Acustica-Acustica*, 2009.
- [DOU 07] DOUTRES O., DAUCHEZ N., GENEVAUX J.-M. and DAZEL O., “Validity of the limp model for porous materials: A criterion based on the Biot theory”, *J. Acoust. Soc. Am.*, vol. 122, no. 4, pp. 1845–2476, 2007.
- [COY 94] COYETTE J. and PELERIN Y., “A generalized procedure for modeling multi-layer insulation systems”, *Proceedings of the 19th International Seminar on Modal Analysis*, pp. 1189–1199, 1994.
- [COY 95] COYETTE J. and WYNENDAELE H., “A finite element model for predicting the acoustic transmission characteristics of layered structures”, *Proceedings of Inter-Noise 95*, pp. 1279–1282, 1995.
- [HÖR 03] HÖRLIN N.-E. and GÖRANSSON P., “Complex fluid displacement behaviour of a layered porous material”, *Tenth International Congress on Sound and Vibration*, Stockholm, Sweden, pp. 2179–2186, 2003.
- [JOH 95] JOHANSEN T., ALLARD J.-F. and BROUARD B., “Finite element method for predicting the acoustical properties of porous samples”, *Acta Acustica*, vol. 3, pp. 487–491, 1995.
- [KAN 95] KANG Y. and BOLTON J., “Finite element modeling of isotropic porous materials coupled with acoustical finite elements”, *J. Acoust. Soc. Am.*, vol. 98, no. 1, pp. 635–643, 1995.
- [KAN 96] KANG Y. and BOLTON J., “A finite element model for sound transmission through foam-lined double-panel structures”, *J. Acoust. Soc. Am.*, vol. 99, no. 5, pp. 2755–2765, 1996.
- [KAN 97] KANG Y. and BOLTON J., “Sound transmission, through elastic porous wedges and foam layers having spatially graded properties”, *J. Acoust. Soc. Am.*, vol. 102, no. 6, pp. 3319–3332, 1997.
- [KAN 99] KANG Y., GARDNER B. and BOLTON J., “An axisymmetric poroelastic finite element formulation”, *J. Acoust. Soc. Am.*, vol. 106, no. 2, pp. 565–574, 1999.
- [PAN 96a] PANNETON R., Modélisation numérique tridimensionnelle par éléments finis des milieux poroélastiques, PhD Thesis, University of Sherbrooke, Canada, 1996.

- [PAN 96b] PANNETON R. and ATALLA N., “Numerical prediction of sound transmission through multilayer systems with isotropic poroelastic materials”, *J. Acoust. Soc. Am.*, vol. 100, no. 1, pp. 346–354, 1996.
- [PAN 97] PANNETON R. and ATALLA N., “An efficient finite element scheme for solving the three-dimensional poroelasticity problem in acoustics”, *J. Acoust. Soc. Am.*, vol. 101, no. 5, pp. 3287–3298, 1997.
- [RAV 98] RAVIART P.-A. and THOMAS J.-M., *Introduction À L’analyse Numérique Des Équations Aux Dérivées Partielles*, Dunod, 1998.
- [SGA 02] SGARD F., *Modélisation Par Éléments-Finis Des Structures Multi-Couches Complexes Dans Le Domaine Des Basses Fréquences*, PhD Thesis, Claude Bernard University Lyon I – INSA Lyon, 2002.
- [VIG 97] VIGRAN T., KELDERS L., LAURIKS W., LECLAIRE P. and JOHANSEN T., “Prediction and measurements of the influence of boundary conditions in a standing wave tube”, *Acta Acustica*, vol. 83, pp. 419–423, 1997.
- [ZIE 89] ZIENKIEWICZ O.-C. and TAYLOR R.-L., *The Finite Element Method: Basic Formulation and Linear Problems*, 4th edition, vol. 1, McGraw-Hill, London, Great Britain, 1989.

Part 3

## Experimental and Numerical Methods

This page intentionally left blank



## Chapter 13

# Transducer for Bulk Waves

### 13.1. Introduction

The experimental study of acoustic wave propagation requires devices called transducers, which are able to generate these waves and detect them efficiently. The means used depend on the practical constraints and technological possibilities. For example, if no mechanical contact with the sample is allowed, a solution is to generate bulk or surface acoustic waves with a laser pulse and to detect it after propagation by optical interferometry [ROY 96a]. At low frequencies ( $f < 1$  MHz) and when the acoustic impedance  $Z$  of the propagation medium is relatively small ( $Z < 10$  MRayl.), the coupling with the transducer can be achieved thanks to the air [SCH 95].

In most cases, the transducer is a damped electromechanical resonator consisting of a piezoelectric solid carrying two electrodes, either in direct contact with the propagation medium, or through a liquid (water). A plate of large lateral dimensions compared to the wavelength  $\lambda$  and of thickness  $d$  of the same order of magnitude as  $\lambda/2$  generates plane bulk waves, preferentially at the frequency  $f_P = V_P/2d$  where  $V_P$  is the speed of the elastic waves (longitudinal or transverse) in the piezoelectric material. The operation of such a transducer can be analyzed according to a one-dimensional model [KIN 87]. Before developing this model, we note the essential properties of the propagation of elastic waves in a piezoelectric medium. Examples of impulse and frequency responses are given in the last section.

### 13.1.1. Piezoelectric materials – structures

The piezoelectric material is the key element of a transducer because it converts electrical energy from an external source into acoustic energy which can be used in the form of a bulk wave propagating in the medium that we consider and vice versa.

Piezoelectricity reflects the linear dependence between the mechanical and electrical properties of some anisotropic materials. The direct piezoelectric effect, discovered by Pierre and Jacques Curie in 1880, expresses the appearance of a polarization, i.e. an electrical induction  $D$ , in a dielectric subjected to a strain  $S$ :

$$D = \varepsilon^S E + eS. \quad [13.1]$$

$\varepsilon^S$  and  $e$  are, respectively, the dielectric constant (at a constant strain) and the piezoelectric constant. The inverse piezoelectric effect, predicted by Lippman one year later, indicates that a piezoelectric solid placed in an electrical field distorts itself. The mechanical stress  $T$  is expressed by the formula:

$$T = c^E S - eE, \quad [13.2]$$

which generalizes Hooke's law (equation [1.43]).  $c^E$  is the stiffness constant when the electrical field is held constant. The fact that the proportionality coefficients for the two effects are opposite to each other [ROY 96b] results from thermodynamic considerations. The first effect is used to detect elastic waves, the second one for generating them.

With tensor notation and using the summation convention on the repeated indices, the behavior laws of a piezoelectric solid are written:

$$T_{ij} = c_{ijkl}^E S_{kl} - e_{kij} E_k \quad \text{and} \quad D_j = \varepsilon_{jk}^S E_k + e_{jkl} S_{kl}. \quad [13.3]$$

Due to the symmetry of the strain tensor ( $S_{kl} = S_{lk}$ ), the piezoelectric tensor, of rank 3, has only 18 components  $e_{j\alpha}$  with  $j = 1$  to 3 and  $\alpha = 1$  to 6. The index  $\alpha$  corresponds to the pair ( $kl$ ) according to the following correspondence:

$$(11) \rightarrow 1, (22) \rightarrow 2, (33) \rightarrow 3, (23) = (32) \rightarrow 4, (13) = (31) \rightarrow 5, (12) = (21) \rightarrow 6.$$

These constants can be set out in a  $3 \times 6$  table and their values are typically between 0.1 and 20 C/m<sup>2</sup>.

$$e_{i\alpha} = \begin{vmatrix} e_{11} & e_{12} & e_{13} & e_{14} & e_{15} & e_{16} \\ e_{21} & e_{22} & e_{23} & e_{24} & e_{25} & e_{26} \\ e_{31} & e_{32} & e_{33} & e_{34} & e_{35} & e_{36} \end{vmatrix} \quad [13.4]$$

The ability of a piezoelectric material to generate elastic waves is measured by its electromechanical coupling coefficient  $K$ . This coefficient expresses the influence of the piezoelectricity on the velocity  $V$  of the elastic waves, by definition:

$$K^2 = \frac{V^2 - V'^2}{V^2} \quad [13.5]$$

where  $V'$  is the velocity calculated without taking account the piezoelectric effect.

The equations of propagation result from the application of Newton's second law and Poisson's equation, which governs quasi-static electrical phenomena:

$$\frac{\partial T_{ij}}{\partial x_j} = \rho \frac{\partial^2 u_i}{\partial t^2} \quad \text{and} \quad \frac{\partial D_j}{\partial x_j} = \rho_e, \quad [13.6 \text{ and } 13.7]$$

where  $\rho$  is the mass density and  $\rho_e$  the density of free charges.

Given the expressions of the strain  $S_{ij}$  and of the electric field  $E_k$  as functions of the mechanical displacement  $u_l$  and the electrical potential  $\phi$ :

$$S_{kl} = \frac{1}{2} \left( \frac{\partial u_l}{\partial x_k} + \frac{\partial u_k}{\partial x_l} \right) \quad \text{and} \quad E_k = -\frac{\partial \phi}{\partial x_k}, \quad [13.8]$$

and substituting in equations [13.3] leads, in the absence of electrical sources ( $\rho_e = 0$ ), to four homogeneous second-order differential equations ( $i = 1, 2, 3$ ):

$$\left\{ \begin{array}{l} \frac{\partial^2}{\partial x_j \partial x_k} (c_{ijkl} u_l + e_{kij} \phi) = \rho \frac{\partial^2 u_i}{\partial t^2} \\ \frac{\partial^2}{\partial x_j \partial x_k} (\epsilon_{jk}^S \phi - e_{jkl} u_l) = 0. \end{array} \right. \quad [13.9]$$

The solution in the form of plane waves, with a polarization  $p_l$ , propagating in the direction of the unit vector  $n_j$  at the phase velocity  $V = \omega/k$ :

$$u_i = p_i \exp i(\omega t - kn_j x_j) \quad \text{and} \quad \phi = \phi_0 \exp i(\omega t - kn_j x_j) \quad [13.10]$$

leads, by writing

$$\Gamma_{il} = c_{ijkl}^E n_j n_k, \quad \gamma_l = e_{jkl} n_j n_k, \quad \varepsilon^S = \varepsilon_{jk}^S n_j n_k, \quad [13.11]$$

to the system of equations ( $i = 1, 2, 3$ )

$$\Gamma_{il} p_l + \gamma_i \phi_0 = \rho V^2 p_i \quad \text{and} \quad \gamma_l p_l - \varepsilon^S \phi_0 = 0, \quad [13.12]$$

which generalizes the Christoffel equations (section 1.2.2) that describe the behavior of a non-piezoelectric material. The elimination of the electric potential  $\phi_0$  leads to

$$\bar{\Gamma}_{il} p_l = \rho V^2 p_i \quad \text{with} \quad \bar{\Gamma}_{il} = \Gamma_{il} + \frac{\gamma_i \gamma_l}{\varepsilon^S}. \quad [13.13]$$

The velocity  $V$  and the polarization  $p_l$  of the plane elastic waves propagating in a piezoelectric solid can be obtained by looking for the eigenvalues and eigenvectors of the Christoffel matrix  $\bar{\Gamma}_{il}$ . Since this matrix is symmetric, the three eigenvalues are real and the eigenvectors are mutually orthogonal. The velocity of the three plane waves propagating in the same direction are solutions of the secular equation:

$$\det[\bar{\Gamma}_{il} - \rho V^2 \delta_{il}] = 0. \quad [13.14]$$

In an anisotropic medium, the propagation of plane elastic waves is illustrated by the slowness surface, obtained from the vector  $\mathbf{m} = \mathbf{n}/V$  drawn from an arbitrary origin O. It is composed of three layers, one for the quasi-longitudinal wave and one for each transverse or quasi-transverse wave (section 1.2.2.3).

Figure 13.1 refers to lithium niobate ( $\text{LiNbO}_3$ ) which belongs to the trigonal class  $3m$ . The dashed curves have been calculated ignoring the piezoelectric effect. The transverse wave (T) polarized along the  $X$ -axis, perpendicular to the propagation plane  $YZ$ , is not piezoelectrically coupled ( $V = V'$ ). For the other two modes ( $QL$  and  $QT$ ), the difference between the solid and dashed curves, illustrates the electromechanical coupling.

By multiplying the Christoffel equation [13.12] by the complex conjugate  $p_i^*$  of the polarization, which is assumed to be normalized ( $p_i p_i^* = 1$ ), it becomes:

$$\rho V^2 = \Gamma_{il} p_l p_i^* + \frac{|\gamma_i p_i|^2}{\epsilon^S} \quad \text{and} \quad \rho V'^2 = \Gamma_{il} p_l' p_i'^* . \quad [13.15]$$

As the polarizations  $p_i$  and  $p_i'$  are similar (they are identical if the mode is purely longitudinal or transverse), the square of the electromechanical coupling coefficient [13.5] can be written as

$$K^2 = \frac{|\gamma_i p_i|^2}{\epsilon^S \Gamma_{il} p_l p_i^* + |\gamma_i p_i|^2} = \frac{e^2}{\epsilon^S c^E + e^2} \quad [13.16]$$

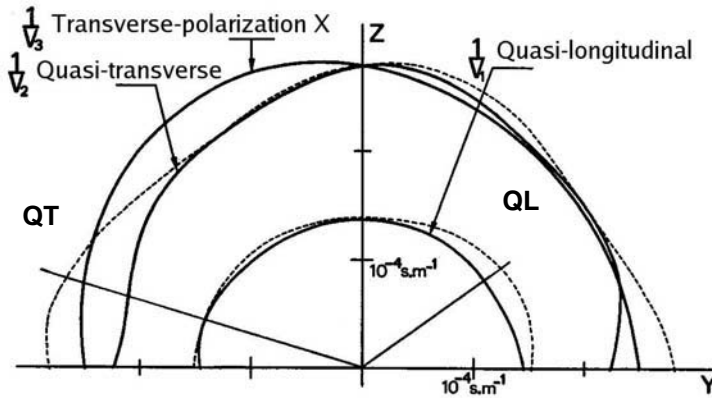


**Figure 13.1.** Section of the slowness surface of lithium niobate in the YZ plane. The dashed curves do not take into account the piezoelectric effect.

where  $e = |\gamma_i p_i|$  has the dimension of a piezoelectric constant and  $c^E = \Gamma_{il} p_l p_i^*$  of a stiffness constant. This coefficient (less than unity) is also expressed as a function of the average densities of the acoustic and electrical potential energies:

$$\begin{cases} e_p^{(ac)} = \frac{1}{2} c_{ijkl} S_{ij} S_{kl}^* = \frac{1}{2} \Gamma_{il} p_i^* p_l k^2 \\ e_p^{(el)} = \frac{1}{2} \epsilon_{jk}^S E_j E_k^* = \frac{1}{2} \epsilon^S |\phi_0|^2 k^2 = \frac{1}{2\epsilon^S} |\gamma_i p_i|^2 k^2. \end{cases}$$

From [13.16]

$$K^2 = \frac{e_p^{(el)}}{e_p^{(ac)} + e_p^{(el)}},$$

the square of the electromechanical coupling coefficient is the ratio of the electric potential energy to the total potential energy. This factor characterizes the ability of the piezoelectric material to generate acoustic waves. Indeed, whatever its polarization, the electric field associated with a plane wave is longitudinal. The inverse piezoelectric effect, plane acoustic waves are generated by applying an electric field perpendicular to the face of the plate. For example, the curves in Figure 13.1 show that a quasi-longitudinal (*QL*) wave is generated selectively by a crystal plate having a cut  $Y + 36^\circ$  ( $K_L = 0.49$ ,  $K_T = 0$ ) and a quasi-transverse (*QT*) wave is generated selectively by a plate of cut  $Y + 163^\circ$  with a coupling coefficient  $K_T = 0.62$  ( $K_L = 0$ ).

The *structure* of the transducer (Figure 13.2) and the choice of the piezoelectric material, whose thickness is a fraction of the wavelength  $\lambda$ , depend on the frequency of the waves to be generated and of the propagation medium (solid or liquid). It is characterized by its acoustic impedance  $Z = \rho V$ , which is expressed in MRayl. ( $10^6$  Rayl.).

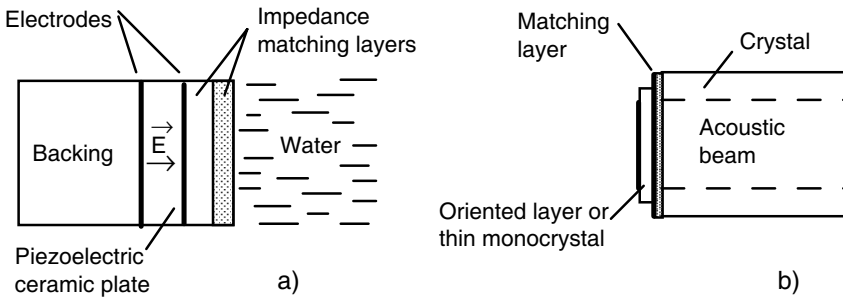


**Figure 13.2.** Structure of a single element plane transducer used to generate bulk waves, a) at low frequencies ( $f < 25$  MHz), b) at intermediate and high frequencies ( $f > 25$  MHz)

*Low frequencies* ( $f < 25$  MHz  $\rightarrow \lambda/2 > 0.1$  mm). The material is very often a piezoelectric ceramic plate whose faces are metal-coated and loaded on the back with an absorbing medium that damps the resonator and consequently widens the bandwidth (Figure 13.2a). However, in non-destructive testing and in medical ultrasound, the acoustic impedance of piezoelectric ceramics ( $Z_P \geq 30$  MRayl. with  $V_P \cong 4,500$  m/s and  $\rho_P \cong 7,500$  kg/m<sup>3</sup>) is too large compared to that of the propagation medium (water or the human body:  $Z \cong 1.5$  MRayl. with  $V \cong 1,500$  m/s

and  $\rho \cong 10^3 \text{ kg/m}^3$ ). The mechanical matching between the transducer and the propagation medium, which is needed to increase the efficiency of the “electrical energy  $\leftrightarrow$  mechanical energy” conversion, requires the use of intermediate layers. One way to reduce the number of matching layers is to use a *piezocomposite material*. The transducer is composed of active ceramic elements, in the form of rods, for example, embedded in a passive resin, with a much smaller acoustic impedance (3 MRayl.). The overall impedance of the transducer is thereby lower (5 to 15 MRayl., for a volume fraction of ceramic between 15 and 50%). Contrary to appearance, the electromechanical coupling coefficient is larger than that of a homogeneous plate. Indeed, for the same supply voltage, a rod surrounded by a relatively soft material vibrates more than a rod embedded in a ceramic block. Nevertheless, the piezocomposite transducer, very commonly used, has the disadvantage of a limited operating frequency ( $f \leq 15 \text{ MHz}$ ); this results from the fact that the period of the rods in the polymer matrix must be small compared to the overall thickness. Another variety of transducers based on polymers and copolymers such as P(VDF-TrFE), a compound of vinylidene fluoride (VDF) and trifluoroethylene (TrFE), able to operate at frequencies larger than 100 MHz, present some advantages: their flexibility allows a wide range of shapes, their low acoustic impedance avoids the use of a matching layer, their low cost and availability leads to applications in medical acoustic and non-destructive testing (acoustic microscopy).

*Intermediate frequencies* ( $25 \text{ MHz} < f < 500 \text{ MHz} \rightarrow 5 \text{ }\mu\text{m} < \lambda/2 < 100 \text{ }\mu\text{m}$ ). One technique is to paste with a resin or to solder, using indium metallic diffusion under pressure, a thick monocrystal ( $>100 \text{ }\mu\text{m}$ ), and then to reduce it to the desired thickness by polishing. Figure 13.2b shows a transducer for acoustic microscopy, acousto-optic interaction or a high frequency delay line. Due to its high electromechanical coupling coefficient, lithium niobate is often used for this kind of application.

*High frequencies* ( $f > 1 \text{ GHz} \rightarrow \lambda/2 < 3 \text{ }\mu\text{m}$ ). The piezoelectric material is deposited in the form of a thin layer onto the substrate already coated with a metallic film constituting the internal electrode. Most often it is a layer of zinc oxide (ZnO) or of aluminum nitride (AlN) deposited by sputtering on an alumina monocrystal (sapphire). This propagation medium undergoes very small losses at high frequencies. As the  $A_6$  axis of ZnO is always perpendicular to the surface, the piezoelectric layer generates only longitudinal waves. In order to create high frequency transverse waves, a plate of lithium niobate of cut  $Y + 163^\circ$  must be soldered by diffusion and reduced to the desired thickness (some  $\mu\text{m}$ ) first by polishing, and then by chemical etching or ion bombardment. In this kind of transducer, the role of the electrodes, at least that of the internal electrode, must be considered.

The main piezoelectric materials and their most relevant characteristics as transducers are given in Table 13.1.

Material	Section	Polar.	V (m/s)	Z(Mrayl.)	K	$\epsilon^s/\epsilon_0$
LiNbO <sub>3</sub>	Y + 36°	Quasi-L	7340	34.5	0.49	38.8
LiNbO <sub>3</sub>	Y + 163°	Quasi-T	4560	21.4	0.62	42.8
PZT4 Ceramic	Z	L	4560	34.2	0.51	633
PZT4 Ceramic	Z	T ⊥ Z	2600	19.5	0.71	735
P(VDF-TrFE)	Z	L	2400	4.5	0.30	6.0
ZnO	Z	L	6400	36.3	0.28	8.8
AlN	Z	L	10400	34	0.17	8.5

**Table 13.1.** Velocity ( $V$ ), acoustic impedance ( $Z$ ), electromechanical coupling coefficient ( $K$ ) and relative permittivity ( $\epsilon^s/\epsilon_0$ ) for the main piezoelectric materials used as transducers

### 13.1.2. One-dimensional model – equivalent circuits

We assume that the thickness  $d$  of the piezoelectric slab, large compared to one of its electrodes, is small compared to its lateral dimensions. The voltage is applied (or gathered if the transducer is working in the receiving mode) between those electrodes. Under these circumstances, a one-dimensional model (without subscript of coordinates) is enough (Figure 13.3). An analysis method consists of associating this structure with an electromechanical circuit obtained by juxtaposing the equivalent circuit to the different parts, force and particle velocity playing similar roles to the voltage and the electrical intensity.

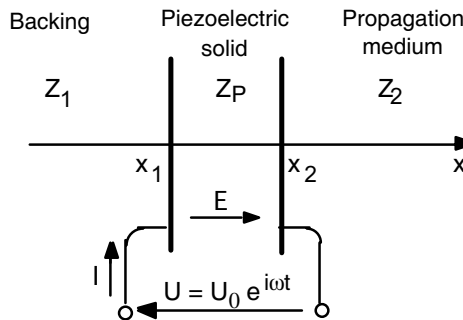


**Figure 13.3.** One-dimensional model of a low frequency transducer. It is divided into three parts: the propagation medium of impedance  $Z_2$ , the piezoelectric material of impedance  $Z_P$  and the backing medium of impedance  $Z_1$



### 13.1.2.1. Impedance matrix

If the conditions for the generation of a pure longitudinal or transverse wave are fulfilled, the state equations of the piezoelectric solid reduce to [13.1] and [13.2], where  $c^E$ ,  $\epsilon^S$  and  $e$  are appropriate constants given the orientation of the crystallographic axis and the type of wave. For example, in the case of a Z-cut piezoelectric ceramic or zinc oxide layer and for a longitudinal wave:  $c^E = c_{33}^E$ ,  $e = e_{33}$  and  $\epsilon^S = \epsilon_{33}^S$ .

From Poisson's equation [13.7], the electrical induction  $D$  is uniform in the insulating piezoelectric solid ( $\rho_e = 0 \rightarrow \partial D / \partial x = 0$ ). The charge conservation equation imposes a uniform current density  $j$ :

$$\frac{\partial D}{\partial t} = j(t) = \frac{I(t)}{A},$$

where  $I$  is the current intensity and  $A$  the area of the electrodes.

Eliminating the electric field  $E$  in equations [13.1] and [13.2] in order to express the stress as a function of the electrical induction  $D$

$$T = c^D \frac{\partial u}{\partial x} - hD, \quad \text{where} \quad h = \frac{e}{\epsilon^S} \quad [13.17]$$

and introducing the stiffness at constant electrical induction  $c^D = c^E + e^2 / \epsilon^S$ . By differentiating with respect to time, we obtain the particle velocity  $v = \partial u / \partial t$ :

$$\frac{\partial T}{\partial t} = c^D \frac{\partial v}{\partial x} - \frac{h}{A} I(t). \quad [13.18]$$

Differentiating equation [13.17] with respect to  $x$  and considering dynamic equation [13.6], leads to:

$$c^D \frac{\partial^2 v}{\partial x^2} = \rho \frac{\partial^2 v}{\partial t^2}. \quad [13.19]$$

The solution of this equation of propagation is the sum of two waves, of amplitudes  $a$  and  $b$ , propagating in opposite directions at velocity  $V = \sqrt{c^D / \rho}$ ; in the harmonic regime and omitting the factor  $e^{i\omega t}$ :

$$v = a e^{-ikx} + b e^{ikx}. \quad [13.20]$$

The mechanical stress is deduced from relation [13.17] by replacing the particle velocity  $v$  by its expression given in [13.20]:

$$T = -\frac{c^D k}{\omega} (a e^{-ikx} - b e^{ikx}) - \frac{h}{i\omega A} I. \quad [13.21]$$

As  $c^D = \rho V^2$ , the acoustic impedance of the medium is  $Z = c^D k / \omega$ .

A piezoelectric slab of thickness  $d = x_2 - x_1$  is submitted to a voltage  $U$  and to forces  $F_1$  and  $F_2$  on the faces of abscissa  $x_1$  and  $x_2$  from the surrounding material. The mechanical stress corresponding to a traction exerted on the piezoelectric solid, the forces  $F = -AT$  applied on a slab of section  $A$ , are proportional to the mechanical impedance  $Z = Z A$ :

$$\begin{cases} F_1 = -AT(x_1) = Z (a e^{-ikx_1} - b e^{ikx_1}) + \frac{h}{i\omega} I \\ F_2 = -AT(x_2) = Z (a e^{-ikx_2} - b e^{ikx_2}) + \frac{h}{i\omega} I \end{cases}$$

To express the forces  $F_1$  and  $F_2$  in terms of the velocities at the two faces:

$$v_1 = v(x_1) = a e^{-ikx_1} + b e^{ikx_1} \quad \text{and} \quad v_2 = -v(x_2), \quad [13.22]$$

it is enough to eliminate the amplitudes  $a$  and  $b$ :

$$\begin{cases} F_1 = -iZ \left( \frac{v_1}{\tan kd} + \frac{v_2}{\sin kd} \right) + \frac{h}{i\omega} I \\ F_2 = -iZ \left( \frac{v_1}{\sin kd} + \frac{v_2}{\tan kd} \right) + \frac{h}{i\omega} I \end{cases} \quad [13.23]$$

The voltage  $U$  applied to the electrodes (Figure 13.3) is calculated from the electric field  $E$ :

$$U = \int_{x_1}^{x_2} E dx \quad \text{with} \quad E = -h \frac{\partial u}{\partial x} + \frac{D}{\epsilon^S}.$$

This expression can be written as a function of the displacement current  $I = i\omega DA$  and the velocities  $v_1 = i\omega u(x_1)$  and  $v_2 = -i\omega u(x_2)$

$$U = \frac{h}{i\omega}(v_1 + v_2) + \frac{I}{i\omega C_0} \quad \text{where} \quad C_0 = \frac{\varepsilon^s A}{d} \quad [13.24]$$

is the static capacity of the rigidly bound transducer. Equations [13.23] and [13.24] can be written in the following form:

$$\begin{bmatrix} F_1 \\ F_2 \\ U \end{bmatrix} = -i \begin{bmatrix} Z / \tan kd & Z / \sin kd & h/\omega \\ Z / \sin kd & Z / \tan kd & h/\omega \\ h/\omega & h/\omega & 1/C_0 \omega \end{bmatrix} \begin{bmatrix} v_1 \\ v_2 \\ I \end{bmatrix} \quad [13.25]$$

which reveals the impedance matrix  $[Z]$  of the three port circuit shown on Figure 13.4. This matrix is symmetric because the acoustic ports 1 and 2 are equivalent.

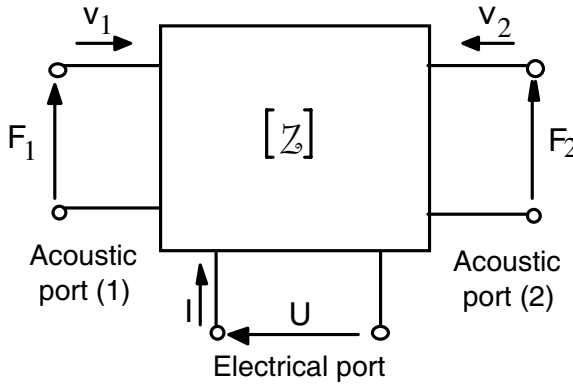


**Figure 13.4.** Hexapole with two acoustic ports and one electric port representing a slab of piezoelectric material

#### 13.1.2.2. Equivalent circuits

An *infinite non-piezoelectric medium*, of cross-section  $A$ , in which a progressive wave propagates (in the direction of increasing  $x$ ) is represented by its mechanical impedance  $Z = \rho VA$ , ratio of the force  $F = -AT$  to the particle velocity  $v$ .

The equivalent circuit of a (non-piezoelectric) slab of *finite thickness*  $d$  and cross-section  $A$ , is deduced from equation [13.23] with  $h = 0$ . Given the equality  $1/\tan kd = (1/\sin kd) - \tan(kd/2)$ , it becomes:

$$\begin{cases} F_1 = -i \frac{Z}{\sin kd} (v_1 + v_2) + iZ \tan\left(\frac{kd}{2}\right) v_1 \\ F_2 = -i \frac{Z}{\sin kd} (v_1 + v_2) + iZ \tan\left(\frac{kd}{2}\right) v_2 \end{cases} \quad [13.26]$$

These relations are obtained by applying Kirchoff's laws to the circuit in Figure 13.5a. The coaxial line element of length  $d$  and characteristic impedance  $Z$  in Figure 13.5b, which follows the same laws, is also an equivalent circuit for the solid slab.

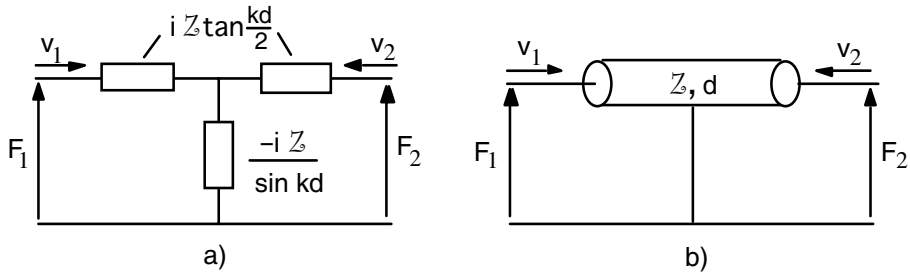


**Figure 13.5.** Equivalent circuit for a non-piezoelectric solid slab of thickness  $d$  and mechanical impedance  $Z$  : a) T-circuit, b) transmission line element

When the *material* is *piezoelectric*, there is an additional force  $f$  in the right-hand side of equations [13.23]:

$$f = \frac{h}{i\omega} I = hC_0 \left[ U - \frac{h}{i\omega} (v_1 + v_2) \right]. \quad [13.27]$$

It must be introduced in the central branch of the circuits in Figure 13.5 which is traversed by the velocity  $v_1 + v_2$ . It is obtained by using an electromechanical transformer with a ratio  $hC_0$  and a negative capacitance  $-C_0$  set in series in the primary circuit (Figure 13.6) so that the potential difference at the ends of the primary winding is equal to the term between square brackets in equation [13.27], i.e. to  $f/hC_0$ .

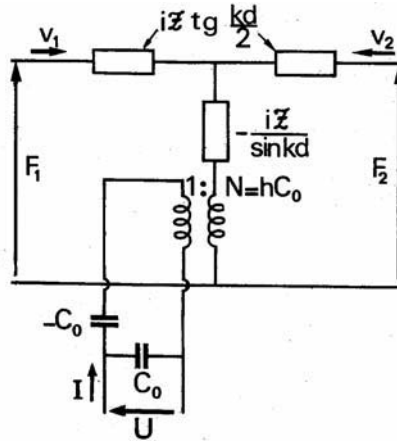


**Figure 13.6.** (Mason's) Electromechanical circuit equivalent to a piezoelectric slab of thickness  $d$ , cross-section  $A$ , mechanical impedance  $Z$

In the circuit proposed by Redwood [RED 61], the T-circuit is replaced by the line element in Figure 13.5b. It can be seen as a coaxial cable with the outer conductor connected to the transformer secondary. Another equivalent circuit is constituted by a transmission line representing the propagation and by an electromechanical transformer modeling the energy conversion. The particle velocity is introduced in the middle of the line. This is the KLM model of Krimholtz, Leedom and Matthaei [KRI 70].

The equivalent circuit of the transducer or loaded resonator, is obtained by combining in cascade the circuits related to each component medium.

### 13.1.3. Frequency and time responses – emitted power

In its simplest version (Figure 13.3), a single element transducer generating bulk waves includes a piezoelectric slab of thickness  $d$ , cross-section  $A$ , mechanical impedance  $Z_P = AZ_P$ , an absorbing backing medium of acoustic impedance  $Z_1$ . It is rigidly bound to the propagation medium of impedance  $Z_2$ . By transferring the forces  $F_1 = -Z_1 v_1$  and  $F_2 = -Z_2 v_2$  in equations [13.25], it becomes:

$$\begin{bmatrix} iZ_1 + Z_P / \tan kd & Z_P / \sin kd & h/\omega \\ Z_P / \sin kd & iZ_2 + Z_P / \tan kd & h/\omega \\ h/\omega & h/\omega & 1/C_0 \omega \end{bmatrix} \begin{bmatrix} v_1 \\ v_2 \\ I \end{bmatrix} = \begin{bmatrix} 0 \\ 0 \\ iU \end{bmatrix} \quad [13.28]$$

The inversion of this system leads, after a few lines of calculation, to the particle velocity  $v = -v_2$  in the propagation medium:

$$v = \frac{h C_0 (i Z_1 - Z_P \tan \theta) U}{(Z_1 + Z_2) Z_P [\cotan 2\theta - K^2 / 2\theta] + i [Z_1 Z_2 + Z_P^2 - Z_P^2 K^2 (\tan \theta) / \theta]} \quad [13.29]$$

with

$$\theta = \frac{kd}{2} = \frac{\pi}{2} \frac{f}{f_P}, \quad \text{with} \quad f_P = \frac{V_P}{2d}. \quad [13.30]$$

As  $h = e/\varepsilon^S$  and  $C_0 = \varepsilon^S A/d$  and by introducing the ratios of the acoustic impedances  $r_1 = Z_1 / Z_P = Z_1 / Z_P$  and  $r_2 = Z_2 / Z_P$ , this velocity can be written as follows

$$v = v_0 H(r_1, r_2, \theta) U \quad \text{with} \quad v_0 = \frac{e}{Z_P d}. \quad [13.31]$$

It depends on the relative frequency  $f/f_P$  through the variable  $\theta$  and the dimensionless function

$$H(r_1, r_2, \theta) = \frac{r_1 + i \tan \theta}{1 + r_1 r_2 - K^2 (\tan \theta) / \theta + i (r_1 + r_2) [(K^2 / 2\theta) - \cotan \theta]} \quad [13.32]$$

which defines the *frequency response*  $H(f)$  of the transducer. Its values are close to unity. For example, when the three impedances are equal ( $r_1 = r_2 = 1$ ) and at the central frequency  $f_P$ , for which  $\theta = \pi/2$ , we find

$$H(1, 1, \frac{\pi}{2}) = \frac{1}{1 + 2iK^2 / \pi} \cong 1 \quad \text{if} \quad K^2 \ll 1.$$

The particle velocity is of the same order of magnitude as the quantity  $v_0 = e/Z_P d$ , which strictly depends on the piezoelectric material. For a ceramic of the PZT-5A kind, those characteristics are:

$$V_P = 4\,350 \text{ m/s}, \quad Z_P = 33.7 \text{ MRayl.}, \quad e = e_{33} = 23 \text{ C/m}^2.$$

At a frequency  $f_P = 3$  MHz ( $d = 0.72$  mm),  $v_0$  is close to  $10^{-3}$  ms<sup>-1</sup>/V and the particle velocity is equal to 10 cm/s for a voltage of amplitude  $U = 100$  V. It would be higher in the case of a piezocomposite material, with a smaller impedance  $Z_P$ .

The *mechanical displacement*  $u = v/i\omega$  is given by the expression

$$u = \frac{e}{c^D} \frac{H(f)}{2i\theta} \quad \text{with} \quad c^D = \rho V_P^2. \quad [13.33]$$

Under the same conditions [ $r_1 = r_2 = 1$  and  $f = f_P \rightarrow H(f_P) \cong 1$ ], the mechanical displacement amplitude  $u_0 \cong e/\pi c^D$ , is equal to 0.05 nm/V, or 5 nm for a harmonic voltage amplitude of 100 V.

In the sinusoidal regime, the *emitted power* at each time:  $P(t) = F_2 v$  with  $F_2 = -AZ_2 v_2 = AZ_2 v$ , has the following average value:

$$\langle P \rangle = \frac{1}{2} AZ_2 |v|^2 = \frac{1}{2} A r_2 \frac{e^2}{Z_P d^2} |H(f)|^2 |U|^2.$$

Given the relations  $C_0 = \epsilon^S A/d$  and  $Z_P = c^D/V_P$ , the square of the electromechanical coupling coefficient (defined by equation [13.16]:  $K^2 = e^2/\epsilon^S c^D$ ) and the resonance frequency  $f_P = V_P/2d$  of the free plate appear. The emitted power is proportional to  $K^2$  as well as to the square of the frequency response modulus:

$$\langle P \rangle = K^2 C_0 f_P r_2 |H(f)|^2 |U|^2. \quad [13.34]$$

It depends on the ratio of the acoustic impedances  $r_1$  and  $r_2$ .

The curves shown in Figure 13.7 have been drawn for a ceramic of type PZT-5A ( $Z_P = 33.7$  MRayl), and a duralumin propagation medium ( $Z_2 = 17.6$  MRayl.  $\rightarrow r_2 = 0.52$ ), as functions of the relative frequency  $f/f_P$ . The shape of these curves according to the impedance  $Z_1$  of the backing medium is understandable. When it is lower than the impedance of the piezoelectric material ( $r_1 = 0.2$  and  $0.5$ ), the latter, both of whose faces are practically free, vibrates at half-wavelength ( $d = \lambda_P/2$ ). The acoustic power emitted is maximum for  $f = f_P$ . Conversely, when  $Z_1$  is greater than  $Z_P$  ( $r_1 = 3$ ), the plate, of which one face is nearly free and the other is almost blocked, vibrates in  $\lambda_P/4$  and  $3\lambda_P/4$ . The radiated acoustic power is maximum in the vicinity of  $f_P/2$  and  $3f_P/2$ . The value  $r_1 = 1$  ( $Z_1 = Z_P$ ) leads to a flat frequency response around the central frequency  $f_P$ . The relative bandwidth exceeds 100%.

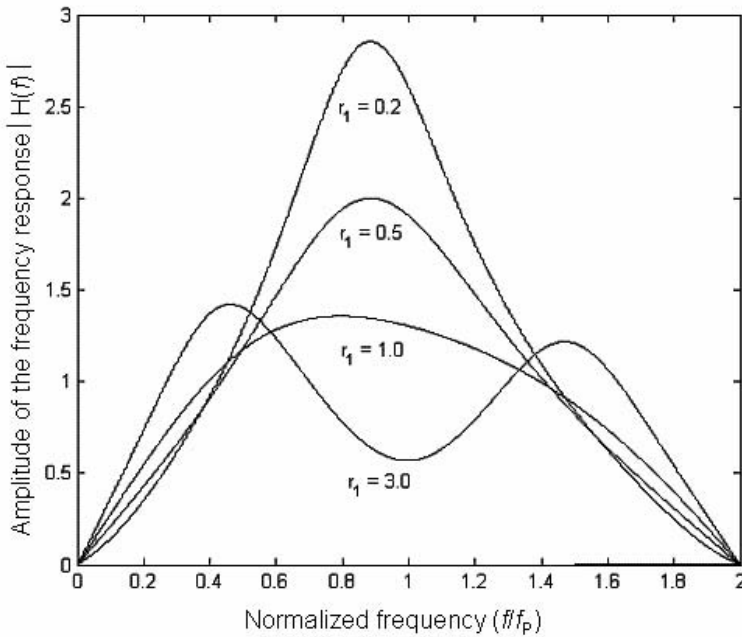


**Figure 13.7.** Amplitude of the frequency response  $H(f)$  for a piezoelectric PZT ceramic transducer, of impedance  $Z_P$ , for a duralumin propagation medium and a backing medium of impedance  $Z_1 = r_1 Z_P$  ( $r_1 = 0.2; 0.5; 1; 3$ )

*Time responses.* In the fields of non-destructive testing of materials and medical ultrasounds, the transducer operates in the impulse regime. The axial resolution is related to the time duration of the emitted acoustic pulse, which depends on the bandwidth of the transducer. The impulse response  $h(t)$  is deduced from the inverse Fourier transform of the frequency response  $H(f)$ . Making the variable change  $\zeta = f/f_P$ , it becomes:

$$h(t) = f_P \int_{-\infty}^{+\infty} H(\zeta) e^{-i2\pi\zeta f_P t} d\zeta = f_P h_N(f_P t) \quad [13.35]$$

where  $h_N(f_P t)$  is the normalized impulse response (no dimension). This is plotted in Figure 13.8 for the four previous values of the acoustic impedance ratio  $r_1 = Z_1/Z_P$ . When  $Z_1 = Z_P$ , the acoustic pulse is very short and almost bipolar (curve *c*). Curves *a* and *b* show that the particle velocity and the oscillations are larger when the transducer, hardly softened, resonates in the vicinity of the central frequency  $f_P$ . The response shown in Figure 13.8d ( $r_1 = 3$ ) highlights the spectral components around  $3f_P/2$ .



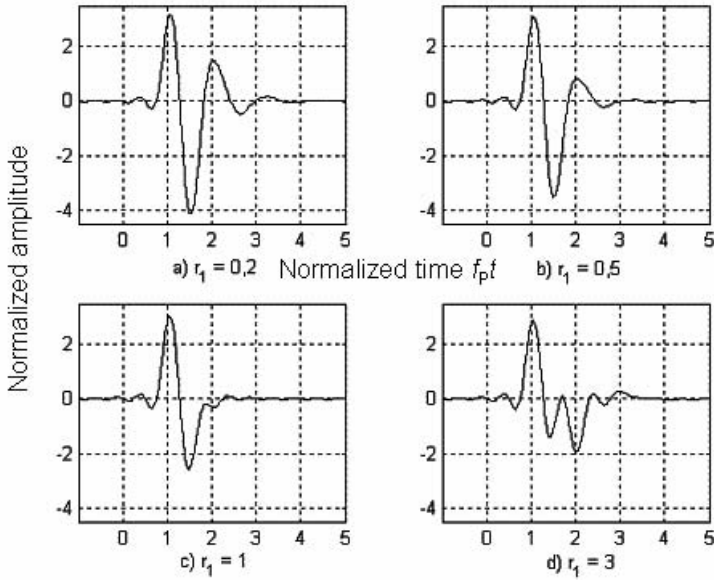


**Figure 13.8.** Normalized impulse responses  $h_N(f_p t)$  calculated for a PZT ceramic transducer, of impedance  $Z_P$ , a duralumin propagation medium and a backing medium of impedance  $r_1 Z_P$  with  $r_1 = 0.2; 0.5; 1; 3$

The particle velocity  $v(t)$  is found from the convolution of the impulse response  $h(t)$  with the voltage  $U(t)$  applied to the transducer. Denoting the Fourier transform of  $U(t)$  by  $\bar{U}(f)$ , and using equation [13.31]:

$$v(t) = v_0 h(t) \otimes U(t). \quad [13.36]$$

The applied voltage is usually a rectangular pulse of height  $U_m$  and duration  $\Theta$  shorter than  $1/f_p$ . The transducer response is similar to the impulse response with a multiplying coefficient  $U_m \Theta$  equal to the area of the pulse. Introducing the normalized impulse response, leads to:

$$v(t) = v_0 U_m \Theta f_p h_N(f_p t) \quad \text{if} \quad \Theta f_p < 0.3.$$

*Order of magnitude:* the amplitude of the particle velocity is proportional to the duration  $\Theta$  of the pulse. Due to the convolution, the length of the acoustic pulse increases if the condition  $\Theta f_p \ll 1$  is no longer satisfied; a good trade-off is  $\Theta f_p \approx 0.3$ . With  $v_0 = 10^{-3} \text{ m s}^{-1}/\text{V}$ , as the maximal value of  $h_N$  is close to 3

(Figure 13.8), the peak velocity  $v_m$  reaches 0.27 m/s for an applied voltage  $U_m = 300$  V.

### 13.2. Bibliography

- [KIN 87] KINO G.S., *Acoustic Waves. Devices, Imaging and Analog Signal Processing*. Prentice-Hall, 1987.
- [KRI 70] KRIMHOLTZ R., LEEDOM D.A., MATTHAEI G.L., “New equivalent circuit for elementary piezoelectric transducers”, *Electron. Lett.*, vol ; 6, p. 398-399, 1970.
- [RED 61] REDWOOD M., “Transient performance of a piezoelectric transducer”. *J. Acoust. Soc. Amer.*, vol. 33, p. 527-536, 1961.
- [ROY 96a] ROYER D., “Génération et détection optiques d’ondes élastiques”, *Techniques de l’Ingénieur*, article E 4415, 1996.
- [ROY 96b] ROYER D., DIEULESAINT E., *Ondes élastiques dans les solides, Propagation libre et guidée*, Masson, 1996.
- [SCH 95] SCHINDEL D.W., HUTCHINS D.A., ZOU L., SAYER M., “The design and characterisation of micromachined air-coupled capacitive transducers”, *IEEE Trans. Ultrason. Ferro. Freq. Cont.*, vol. 42, pp. 42-50, 1995.

## Chapter 14

# Modeling of Ultrasonic Beams

### 14.1. Introduction

The exploration of materials or media using ultrasound requires knowing with sufficient precision how the ultrasonic beams take form. They are usually created using ultrasonic transducers. The modeling of these beams has been studied for a long time, first by analytical methods that had as their main disadvantage the ability to calculate only relatively simple cases and then, thanks to advancements in information technology, by numerical methods that can simulate more complex cases, closer to actual cases encountered in practice. The following sections present some methods for the numerical simulation of the field radiated by ultrasonic transducers. Moreover, the reciprocity principle allows us to calculate the sensitivity of a receiver to a point source. In this way, it is possible to simulate completely an experiment involving both an emitter and a receiver.

### 14.2. Plane wave decomposition

This method is based on a holographic principle of reconstruction using the knowledge of the field on a plane (three-dimensional case) or on a straight line (two-dimensional case). This knowledge can either come from *a priori* assumptions on the transducer (e.g. piston type vibration, possible phase shift to introduce the focus, etc.), or from measurements to take into account a real transducer.

### 14.2.1. Monochromatic regime

#### 14.2.1.1. Homogenous medium

We consider a transducer emitting a monochromatic beam of pulsation  $\omega$  in a homogenous medium. We suppose that we know, in a reference plane, a variable (that we will write with complex notation, see Chapter 1) characterizing the field (this may be a scalar variable such as the velocity potential, a vector variable such as the particle displacement, or any other variable). The reference plane is usually the front face of the transducer. We choose as reference coordinate system  $\mathcal{R} = (\overrightarrow{Ox_1}, \overrightarrow{Ox_2}, \overrightarrow{Ox_3})$ , whose first two axes  $\overrightarrow{Ox_1}$  and  $\overrightarrow{Ox_2}$  are in the reference plane and the third one is perpendicular to it and oriented in the direction the field will be modeled.

We note  $\varphi(x_1, x_2, x_3)$  the variable characterizing the field at the point M and  $\varphi_0(x_1, x_2) = \varphi(x_1, x_2, 0)$ , its value in the reference plane. Using the diffraction theory developed in optics [GOO 72], the calculation of the ultrasonic field is deduced from the double spatial Fourier transform of its expression in the reference plane. Indeed, if we represent this field as an infinite sum of plane waves, of wave number vector  $\vec{k} (k_1, k_2, k_3)$ , as it is written in equation [14.3], its value in the reference plane  $x_3 = 0$  reduces to the integral

$$\varphi(x_1, x_2, 0) = \iint \hat{\varphi}_0(k_1, k_2) \exp\{-i(k_1 x_1 + k_2 x_2)\} dk_1 dk_2, \quad [14.1]$$

hence, by inverse Fourier transform

$$\hat{\varphi}_0(k_1, k_2) = \frac{1}{4\pi^2} \iint \varphi_0(x_1, x_2) \exp\{i(k_1 x_1 + k_2 x_2)\} dx_1 dx_2. \quad [14.2]$$

The function  $\hat{\varphi}_0(k_1, k_2)$  is often called angular spectrum (of plane waves). The variables  $k_1$  and  $k_2$  take all the values from  $-\infty$  to  $+\infty$ .

At every point M of coordinates  $(x_1, x_2, x_3)$ , the field is therefore given by the expression:

$$\varphi(x_1, x_2, x_3) = \iint \hat{\varphi}_0(k_1, k_2) \exp\{-i(k_1 x_1 + k_2 x_2) - ik_3 x_3\} dk_1 dk_2, \quad [14.3]$$

in which  $k_3$  is calculated, if the medium is homogenous and isotropic with the propagation velocity V, with the help of the dispersion relation:

$$k_1^2 + k_2^2 + k_3^2 = \omega^2 / V^2 = k^2. \quad [14.4]$$

Two types of waves are considered in integral [14.3]: the propagative waves for which  $k_3$  is real, and the evanescent waves for which  $k_3$  is imaginary. For each of these cases,  $k_3$  can respectively be written in the form:

$$k_3 = \pm \sqrt{\frac{\omega^2}{V^2} - k_1^2 - k_2^2}, \quad \text{if} \quad k_1^2 + k_2^2 < \frac{\omega^2}{V^2}, \quad [14.5]$$

and

$$k_3 = \pm i \sqrt{k_1^2 + k_2^2 - \frac{\omega^2}{V^2}}, \quad \text{if} \quad k_1^2 + k_2^2 > \frac{\omega^2}{V^2}. \quad [14.6]$$

The condition of radiation to infinity imposes that  $k_3$  must be chosen such that the waves propagate (propagative waves) or decrease (evanescent waves) in the direction of  $\vec{Ox_3}$ . This condition allows the choice of the sign of  $k_3$ . Considering the harmonic dependence in time which is here of the form  $\exp\{i\omega t\}$ , for the positive pulsations which are the only ones considered here, the sign of  $k_3$  will be positive in formula [14.5], and negative in formula [14.6].

We can see in formula [14.3] that if  $x_3$  is equal to a constant  $x_3^0$  (observation in a plane parallel to the reference plane),  $\varphi(x_1, x_2, x_3^0)$  is deduced from  $\varphi_0(x_1, x_2)$  by using a transfer function  $H(k_1, k_2; x_3^0)$  defined in the Fourier plane  $(k_1, k_2)$  by:

$$H(k_1, k_2; x_3^0) = \exp\left\{-i\left(\sqrt{k^2 - k_1^2 - k_2^2} \cdot x_3^0\right)\right\}. \quad [14.7]$$

It is therefore very easy to calculate the acoustic field  $\varphi(x_1, x_2, x_3^0)$  in a plane parallel to the reference plane. The successive operations are:

- calculation of the angular spectrum  $\hat{\varphi}_0(k_1, k_2)$  in the reference plane by a two-dimensional (inverse) Fourier transform;
- multiplication by the transfer function defined by formula [14.7] (taking into account the propagation between the two planes);
- determination of  $\varphi(x_1, x_2, x_3^0)$  by Fourier transform.

In order to find the field in a plane that is not parallel to the reference plane, it is enough to make a change of coordinate system and to express formula [14.3] in this new system.  $\mathcal{R}' = (\overrightarrow{O'x'_1}, \overrightarrow{O'x'_2}, \overrightarrow{O'x'_3})$  We note  $(x'_1, x'_2, x'_3)$  the coordinates of the current point in the new coordinate system and  $(k'_1, k'_2, k'_3)$  the new components of the current wavenumber vector  $\vec{k}$ . Nevertheless, it should be noted that this change of variables in integral [14.3] will be bijective only in the case of a beam with a small opening angle (collimated) with sufficiently low angles of incidence (see Chapter 21). In order to move into the new coordinate system, we will write formula [14.3] successively:

$$\varphi(x_1, x_2, x_3) = \iint \hat{\varphi}_0(k_1, k_2) \exp\left\{-i\vec{k} \cdot \overrightarrow{OM}\right\} dk_1 dk_2$$

$$\varphi(x'_1, x'_2, x'_3) = \iint \hat{\varphi}_0(k'_1, k'_2) \exp\left\{-i\vec{k} \cdot (\overrightarrow{OO'} + \overrightarrow{O'M})\right\} \left| \frac{\partial(k_1, k_2)}{\partial(k'_1, k'_2)} \right| dk'_1 dk'_2$$

where  $\left| \frac{\partial(k_1, k_2)}{\partial(k'_1, k'_2)} \right|$  is the Jacobian determinant corresponding to the change of coordinate system. So as to simplify the writing, we simply note

$$\hat{\varphi}_0(k'_1, k'_2) = \hat{\varphi}_0[k_1(k'_1, k'_2), k_2(k'_1, k'_2)] .$$

The integral above is written explicitly as a function of the coordinates of point M in the new coordinate system:

$$\begin{aligned} \varphi(x'_1, x'_2, x'_3) = \iint \hat{\varphi}_0(k'_1, k'_2) \exp\left\{-i\phi_{\overrightarrow{OO'}}\right\} \\ \exp\left\{-i(k'_1 x'_1 + k'_2 x'_2 + k'_3 x'_3)\right\} \left| \frac{\partial(k_1, k_2)}{\partial(k'_1, k'_2)} \right| dk'_1 dk'_2, \end{aligned} \quad [14.8]$$

with  $\phi_{\overrightarrow{OO'}} = \vec{k} \cdot \overrightarrow{OO'}$ .

The value  $k'_3$  is also determined as a function of  $k'_1$  and  $k'_2$  with the dispersion relation:

$$k_1'^2 + k_2'^2 + k_3'^2 = k^2 = \omega^2 / V^2 \quad [14.9]$$

With  $x'_3 = x_3^0$  constant, expression [14.8] can also be interpreted as a two-dimensional Fourier transform on the new variables  $k'_1$  and  $k'_2$ . The calculation of the acoustic field in an ordinary plane consequently requires the following steps:

- calculation of the angular spectrum in the reference plane by a two-dimensional (inverse) Fourier transform;
- determination of the decomposition into plane waves in the new coordinate system, in the plane  $(\vec{O'x'_1}, \vec{O'x'_2})$ : calculation of  $\hat{\varphi}_0(k'_1, k'_2)$  as a function of the new variables  $k'_1$  and  $k'_2$ , taking into account the change of origin of the coordinate system by the phase difference  $\phi_{\vec{OO'}}$ , calculation of the new integration variables  $dk'_1 dk'_2$ ;
- propagation to the plane  $x'_3 = x_3^0$  (between parallel planes);
- determination of  $\varphi(x'_1, x'_2, x_3^0)$  by Fourier transform.

#### 14.2.1.2. Case of a fluid medium

In the case of a fluid propagation medium, the variable  $\varphi$  characterizing the field can be the velocity potential defined by equation [1.15, Chapter 1] or the acoustic pressure defined by equation [1.16, Chapter 1]. As mentioned above, we conventionally removed the subscript 1 to express the acoustic parameters. If, in the reference plane the normal speed  $v_0(x_1, x_2)$  is known (for example in the case of a transducer vibrating in the piston mode, i.e. if all the points on its front face vibrate in phase with a constant amplitude), the pressure in the fluid is directly expressed as a function of this parameter. In fact, for each plane wave of the decomposition, the amplitude of the normal component in the reference plane can be written:

$$\hat{v}_0(k_1, k_2) = -ik_3 \hat{\varphi}_0(k_1, k_2), \quad [14.10]$$

and the pressure field:

$$p(x_1, x_2, x_3) = -i\omega\rho_0\varphi(x_1, x_2, x_3). \quad [14.11]$$

Expression [14.3] is now written:

$$p(x_1, x_2, x_3) = \omega\rho_0 \iint \frac{\hat{v}_0(k_1, k_2)}{k_3} \exp\{-i(k_1x_1 + k_2x_2) - ik_3x_3\} dk_1 dk_2, \quad [14.12]$$

$k_3$  still being deduced from formulae [14.5] and [14.6], the sign being determined by the comments in the section following these formulae.

#### 14.2.1.3. Media separated by a plane interface

In the case of two media separated by a plane interface, the simplest method is to choose a new coordinate system  $\mathcal{R}'$  linked to the interface (generally  $\overrightarrow{O'x'_1}$  and  $\overrightarrow{O'x'_2}$  will be chosen in the plane of the interface). In this new coordinate system, the first two components  $k'_1$  and  $k'_2$  of the wavenumber vectors are unchanged for the transmitted and reflected waves, the third component being calculated by the respective dispersion relations of the two media (Snell–Descartes' law); the choice of sign for this third component is always deduced from the condition of radiation to infinity. The expression of the field at any point of the second medium is then written:

$$\begin{aligned} \varphi(x'_1, x'_2, x'_3) = & \iint \mathcal{T}(k'_1, k'_2) \hat{\varphi}_0(k'_1, k'_2) \exp\left\{-i\phi_{\overrightarrow{OO'}}\right\} \\ & \cdot \exp\left\{-i(k'_1x'_1 + k'_2x'_2 + k'_3x'_3)\right\} \left| \frac{\partial(k_1, k_2)}{\partial(k'_1, k'_2)} \right| dk'_1 dk'_2, \end{aligned} \quad [14.13]$$

where  $\mathcal{T}(k'_1, k'_2)$  is the transmission coefficient of the wave of wavenumber vector  $(k'_1, k'_2, k'_3)$ ,  $k'_3$  being obtained by the dispersion relation of this medium.

Note that if the second medium is solid, it is necessary to make a separate calculation for each kind of wave and the transverse waves (or the QL and QT waves if the medium is anisotropic) must be described by a vectorial parameter (particle displacement, particle velocity or potential vector).

If the observation plane is parallel to the (plane) interface ( $x'_3 = x'^0_3$ ), formula [14.13] is still expressed as the Fourier transform of a function involving the angular spectrum of the transmitter after a few transformations that are only multiplicative factors of this function. It is always possible to calculate the ultrasonic field in any plane making a new change of coordinate system, as it is possible to iterate the process in order to treat the case of reflection and transmission on any number of interfaces.

The method was explained for the calculation of the ultrasonic field transmitted through the interface. It applies in the same way to the reflected field, by replacing the transmission coefficient by the reflection coefficient.



This method has the advantage of being valid in both near-field and far-field domains and to implicitly take into account all the phenomena involved (evanescent waves, surface waves etc.).

In order to handle cases of excitation profiles (given in the reference plane) that are not integrable analytically, it is interesting to perform successive Fourier transforms numerically. An interesting solution is to use the Fast Fourier Transform algorithm (FFT). This algorithm performs the calculation globally on a large number of points, and has the advantage of allowing a real time-saving, but it imposes some requirements, including having a constant discretization step. Although it is possible, and not excessively restrictive, to choose such a step in the reference plane, the changes of coordinate system and/or the transmission through an interface alters this property of the step to be constant. To use the FFT, it is then necessary to resample the ultrasonic field with a matching discretization step.

Figure 14.1 represents an example of a field calculated by this method in two-dimensional geometry. The transducer is focused (focal length 90 mm), its frequency is 5 MHz, and its size is 20 mm with a speed profile on its front face of Hanning type. It is immersed in water, its center being at the origin of the coordinate system. The beam interacts with an interface between water and aluminum. The distance between the transducer and the impact point of the beam along its axis is 50 mm. The incidence angle of the main beam is  $20^\circ$ , which is larger than the critical angle for the water–aluminum compression waves. We thus observe only shear waves in aluminum. As expected, refraction deflects the beam in aluminum (refraction angle of around  $50^\circ$ ) and moves the focal point closer to the interface. A more detailed analysis based on this type of calculation shows that the prediction obtained by the geometric approximation (acoustic rays is not sufficient in many cases. We may also note interferences in the fluid between the incident beam and the reflected beam on that figure.

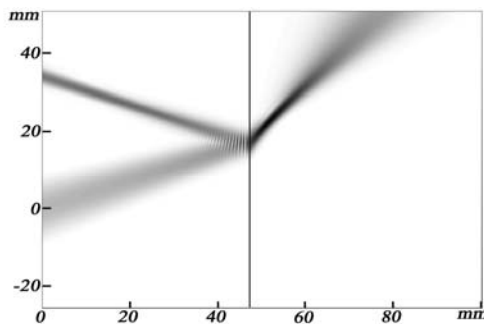


**Figure 14.1.** Field produced by a transducer of frequency 5 MHz, focal distance 90 mm interacting with a water–aluminum interface, the incidence angle of the beam is  $20^\circ$

### 14.2.2. Impulse regime

The formalism described previously can easily be extended to the impulse or broadband regime through the introduction of an additional Fourier transform in the time domain. Knowing  $\varphi_0(x_1, x_2; t)$  in the reference plane, the decomposition of the field into monochromatic waves is written:

$$\varphi_0(x_1, x_2; t) = \frac{1}{2\pi} \iiint \hat{\varphi}_0(k_1, k_2; \omega) \exp\{i(\omega t - k_1 x_1 - k_2 x_2)\} d\omega dk_1 dk_2, \quad [14.14]$$

with:

$$\hat{\varphi}_0(k_1, k_2; \omega) = \frac{1}{4\pi^2} \iiint \varphi_0(x_1, x_2; t) \exp\{-i(\omega t - k_1 x_1 - k_2 x_2)\} dt dx_1 dx_2 \quad [14.15]$$

Note: as the function  $\varphi_0(x_1, x_2; t)$  only takes real values, it leads to the following property for its Fourier transform

$$\hat{\varphi}_0^*(k_1, k_2; \omega) = \hat{\varphi}_0(-k_1, -k_2; -\omega), \quad [14.16]$$

where  $\hat{\varphi}_0^*$  refers to the complex conjugate of  $\hat{\varphi}_0(k_1, k_2; \omega)$ .

The field  $\varphi$  can be deduced at any point by the following expression:

$$\varphi(x_1, x_2, x_3; t) = \frac{1}{2\pi} \iiint \hat{\varphi}_0(k_1, k_2; \omega) \exp\{i(\omega t - k_1 x_1 - k_2 x_2) - ik_3 x_3\} d\omega dk_1 dk_2. \quad [14.17]$$

Equation [14.17] shows that to calculate the field at any point in the medium, it is enough to know the angular spectrum  $\hat{\varphi}_0(k_1, k_2; \omega)$  of the vibrating front face of the transducer (or any other reference plane). The formalism is the same as that previously described by performing an additional Fourier transform in the time domain. The projection of the wavenumber vector on axis  $\overrightarrow{Ox_3}$  is always given by equations [14.5] and [14.6], respectively for propagative and evanescent waves.

In formula [14.17], the integration is done on the pulsations which are both positive and negative. In this case, to meet the requirement of radiation to infinity, the choice of the sign of  $k_3$  depends on the sign of the pulsation, it is positive for the positive pulsations and negative for negative pulsations in formula [14.5] and vice versa in formula [14.6]. Thereby these equations are written:

$$k_3 = \text{sign}(\omega) \sqrt{\frac{\omega^2}{V^2} - k_1^2 - k_2^2}, \quad \text{if} \quad k_1^2 + k_2^2 < \frac{\omega^2}{V^2}, \quad [14.18]$$

and

$$k_3 = -i \cdot \text{sign}(\omega) \sqrt{k_1^2 + k_2^2 - \frac{\omega^2}{V^2}}, \quad \text{if} \quad k_1^2 + k_2^2 > \frac{\omega^2}{V^2}. \quad [14.19]$$

### 14.2.3. Decomposition into impulse plane waves

#### 14.2.3.1. Homogenous medium

Propagation in a homogenous medium can be deduced from the previous formalism through the change of variable transforming the wave number vector  $\vec{k}$  which depends on the pulsation  $\omega$ , into the slowness vector  $\vec{m}$ , itself independent of the pulsation, defined by:

$$\vec{m} = \vec{k} / \omega = \vec{n} / V, \quad [14.20]$$

where  $\vec{n}$  is the unitary vector indicating the propagation direction of each plane wave resulting from the propagation.

Expression [14.14] can now be written:

$$\varphi_0(x_1, x_2; t) = \frac{1}{2\pi} \iiint \hat{\varphi}_0(\omega m_1, \omega m_2; \omega) \exp\{i\omega(t - m_1 x_1 - m_2 x_2)\} \omega^2 d\omega dm_1 dm_2 \quad [14.21]$$

or

$$\varphi_0(x_1, x_2; t) = \iint \Phi_0(m_1, m_2; t - m_1 x_1 - m_2 x_2) dm_1 dm_2, \quad [14.22]$$

where the integration over  $\omega$  was calculated by applying:

$$\Phi_0(m_1, m_2; t) = \frac{1}{2\pi} \int \hat{\varphi}_0(\omega m_1, \omega m_2; \omega) \exp\{i\omega t\} \omega^2 d\omega. \quad [14.23]$$

It should be noted that according to the property [14.16] of the function  $\hat{\phi}_0$ , the function  $\Phi_0(m_1, m_2; t)$  only takes real values.

At point O, origin of the reference system  $\mathcal{R}$ , equation [14.21] becomes:

$$\varphi_0(0, 0; t) = \iint \Phi_0(m_1, m_2; t) dm_1 dm_2 \quad [14.24]$$

Equations [14.23] and [14.24] represent, at point O, the decomposition of the beam into impulse plane waves with a propagation direction parallel to the direction of the slowness vector  $\vec{m}$ . By analogy with the monochromatic angular spectrum, this formulation will be called impulse angular spectrum. As in the previous formalism, the expression of  $\varphi$  at any point in space, is deduced from the following expression:

$$\begin{aligned} \varphi(x_1, x_2, x_3; t) &= \frac{1}{2\pi} \iiint \hat{\phi}_0(\omega m_1, \omega m_2; \omega) \\ &\quad \cdot \exp\{i\omega(t - m_1 x_1 - m_2 x_2 - m_3 x_3)\} \omega^2 d\omega dm_1 dm_2, \quad [14.25] \\ &= \iint \Phi_0(m_1, m_2; t - m_1 x_1 - m_2 x_2 - m_3 x_3) dm_1 dm_2, \end{aligned}$$

with

$$m_3 = \sqrt{\frac{1}{V^2} - m_1^2 - m_2^2}. \quad [14.26]$$

Note that equation [14.25] is the summation of all impulse plane waves delayed by the time they need to propagate from the origin O of the coordinate system to the observation point (see Figure 14.2). These delays can easily be calculated from elementary geometrical considerations. The contribution of evanescent waves is negligible as soon as the observation point is far enough from the reference plane, and the integration in equation [14.25] may be limited to the propagative waves (that is to say over the domain defined by  $m_1^2 + m_2^2 < 1/V^2$ ).

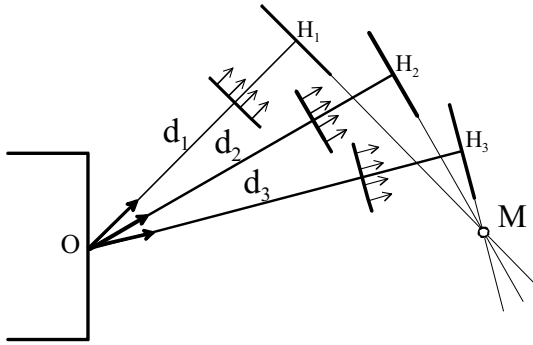


**Figure 14.2.** Representation of the propagation of each plane wave from the origin  $O$  to the observation point  $M$ , for a homogenous medium

In terms of numerical calculations, the advantage of this method is that the longest operation (i.e. the decomposition into impulse plane waves) has to be done only once for a given transducer. This step requires a triple Fourier transform, which is followed, after a change of variable, by an inverse Fourier transform. Then it is enough to make a simple summation of temporal waveforms for each direction, after having delayed them according to the geometrical conditions (incidence angle, position of the observation point, etc.) considered.

We now assume, as in the monochromatic case, that the medium is fluid and that we know the normal velocity  $v_0(x_1, x_2; t)$  of the front face of the transducer. If the scalar quantity used previously  $\varphi(x_1, x_2, x_3; t)$  is a velocity potential (see formula [1.15], Chapter 1), it can be expressed as a function of the normal component of velocity on the front face of the transducer, and the expression of the pressure field can be inferred:

$$\begin{aligned}
 p(x_1, x_2, x_3; t) &= -\rho_0 \frac{\partial \varphi(x_1, x_2, x_3; t)}{\partial t} \\
 &= \rho_0 \iint \left[ \frac{V_0(m_1, m_2; t - m_1 x_1 - m_2 x_2 - m_3 x_3)}{m_3} \right] dm_1 dm_2 \quad [14.27]
 \end{aligned}$$

with

$$V_0(m_1, m_2; t) = \frac{1}{2\pi} \int \hat{v}_0(\omega m_1, \omega m_2; \omega) \exp\{i\omega t\} \omega^2 d\omega \quad [14.28]$$

This expression is valid at any point of the fluid in the half-space such as  $x_3 > 0$ .

#### 14.2.3.2. Fluid–solid media separated by a plane interface

In the case of a plane interface separating two media, the first being fluid and the second solid, we define as in the monochromatic regime, a coordinate system linked to the interface  $\mathcal{R}' = (\overrightarrow{O'x'_1}, \overrightarrow{O'x'_2}, \overrightarrow{O'x'_3})$  with  $\overrightarrow{O'x'_1}$  and  $\overrightarrow{O'x'_2}$  in the interface plane.

Each plane wave that forms the beam, emitted in the direction of the slowness vector  $\vec{m}$  in the fluid, is refracted by the fluid–solid interface into a longitudinal wave and a transverse wave. The characteristics of these waves are given by the Snell–Descartes laws. If the observation point is not very close to the interface, it is possible to take into account, for the summation, only the propagative waves. For the incidence angles between the two critical angles, the only mode to take into account is the transverse mode, the transmission coefficient has in that case a complex value.

Then formula [14.25] becomes:

$$\begin{aligned} \varphi(x'_1, x'_2, x'_3; t) &= \frac{1}{2\pi} \iiint \mathcal{T}(m_1, m_2) \hat{\phi}_0(\omega m_1, \omega m_2; \omega) \\ &\quad \cdot \exp\{i\omega(t - \tau_0)\} \omega^2 d\omega dm_1 dm_2, \\ &= \iint \mathcal{T}(m_1, m_2) \Phi_0(m_1, m_2; t - \tau_0) dm_1 dm_2, \end{aligned} \quad [14.29]$$

where  $x'_1, x'_2, x'_3$  are the coordinates of the observation point  $M$  in the coordinate system  $\mathcal{R}'$ ,  $\mathcal{T}(m_1, m_2)$  is the transmission coefficient and  $\tau_0$  is the time for the wave to propagate from point  $O$  (origin of the reference system  $\mathcal{R}$ ) to the observation point  $M$  (see Figure 14.3). This is equal to:

$$\tau_0 = \frac{\overline{OP}}{V_0} + \frac{\overline{PH}}{V_L} = \frac{\overline{OO'} \cdot \vec{l}}{V_0 (\vec{n} \cdot \vec{l})} + \overline{PM} \cdot \vec{m}'. \quad [14.30]$$

where  $\vec{l}$  is the unitary vector of the axis  $\overrightarrow{Ox'_3}$ ,  $V_L$  and  $\vec{m}'$  are, respectively, the velocity and the slowness vectors of the refracted wave.  $\vec{X}$  represents the algebraic value of  $X$ .

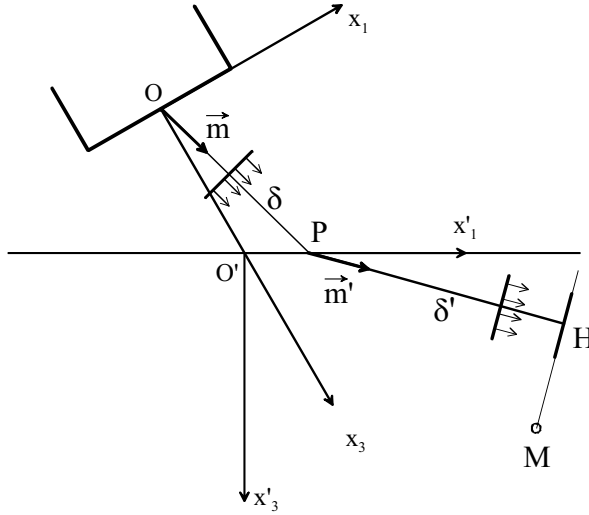


**Figure 14.3.** Representation of the propagation of a plane wave from the origin  $O$  to the observation point  $M$ , in the presence of a plane interface

In the case of compression waves,  $\varphi$  and  $\Phi_0$  can represent a scalar potential. When we take into account only the propagative waves, the transmission coefficient is real. Thus the result given by formula [14.29] is real.

However in the case of the shear waves, the field depends on a vectorial potential. We choose to represent this field by the displacement vector in both the fluid and the solid. Its decomposition into plane waves leads to an expression that is identical to formula [14.22], replacing  $\varphi_0$  by  $\vec{u}_0$  and  $\hat{\varphi}_0$  by  $\hat{\vec{u}}_0$ .  $\hat{\vec{u}}_0$  is factorized into an amplitude  $\hat{a}_0$  which depends on  $m_1$ ,  $m_2$  and  $\omega$ , and a (unitary) polarization vector  $\hat{\vec{P}}_0$  which depends only on  $m_1$  and  $m_2$  (since these waves are longitudinal waves in the fluid,  $\hat{\vec{P}}_0$  is a unitary vector in the direction  $\vec{m}$ ).

Each transverse plane wave transmitted through the fluid–solid interface has a direction that is given by Snell–Descartes’ law (the same  $m_1$ ,  $m_2$  as the incident wave,  $m_3$  given by the dispersion relationship in the solid). Its polarization vector  $\hat{\vec{P}}^{tr}(m_1, m_2)$  is deduced from the propagation direction (this direction is orthogonal to  $\vec{m}$ , and contained in the plane defined by  $\vec{m}$  and the normal to the interface). Its amplitude is equal to the amplitude  $\hat{a}_0$  multiplied by a transmission coefficient  $\mathcal{T}$  (for more details on the transmission of plane waves through a plane fluid–solid

interface; see Chapter 2). Note that beyond the first critical angle, the transmission coefficient is complex and the sign of its imaginary part is changed for the negative frequencies, it can be written:

$$T(m_1, m_2) = T'(m_1, m_2) + i \operatorname{sign}(\omega) T''(m_1, m_2). \quad [14.31]$$

The expression of the displacement field for the shear wave in the solid is now written:

$$\begin{aligned} \vec{u}(x'_1, x'_2, x'_3; t) = & \frac{1}{2\pi} \iiint (T' + i \operatorname{sign}(\omega) T'') \hat{a}_0(\omega m_1, \omega m_2; \omega) \\ & \cdot \hat{P}^{tr}(m_1, m_2) \exp\{i\omega(t - m_1 x_1 - m_2 x_2 - m_3 x_3)\} \omega^2 d\omega dm_1 dm_2 \end{aligned} \quad [14.32]$$

We can proceed as in [14.23]:

$$\vec{U}_0(m_1, m_2; t) = \frac{1}{2\pi} \int \hat{a}_0(\omega m_1, \omega m_2; \omega) \hat{P}^{tr}(m_1, m_2) \exp\{i\omega t\} \omega^2 d\omega. \quad [14.33]$$

Knowing that the Hilbert Transform of  $\vec{U}_0$  can be expressed by:

$$\begin{aligned} \operatorname{TH}[\vec{U}_0(m_1, m_2; t)] = & \frac{1}{2\pi} \int -i \operatorname{sign}(\omega) \hat{a}_0(\omega m_1, \omega m_2; \omega) \\ & \cdot \hat{P}^{tr}(m_1, m_2) \exp\{i\omega t\} \omega^2 d\omega, \end{aligned} \quad [14.34]$$

we obtain the expression of the shear wave field with the help of the following expression:

$$\begin{aligned} \vec{u}(x'_1, x'_2, x'_3; t) = & \frac{1}{2\pi} \iint T'(m_1, m_2) \vec{U}_0(m_1, m_2; t - \tau_0) dm_1 dm_2 \\ & - \frac{1}{2\pi} \iint T''(m_1, m_2) \operatorname{TH}[\vec{U}_0(m_1, m_2; t - \tau_0)] dm_1 dm_2. \end{aligned} \quad [14.35]$$

As stated previously in the monochromatic case, the ultrasonic field reflected by the interface can be calculated by the same principle, using the reflection coefficients instead of the transmission coefficients.



### 14.3. The pencil method

The modeling of ultrasonic beams radiated by transducers in specimens made of materials of various kinds finds its worth in industrial applications of non-destructive testing (see Volume 3). The knowledge of these beams is used to define and optimize the conditions of a test by increasing the number of parametric studies: it may be used, for example, to define the characteristics of a transducer before its manufacture, in order to adapt and optimize it to a given testing configuration. It also offers assistance in interpreting the results of examinations. In addition, a computed ultrasonic field can be used as input data for a model dealing with the interaction of waves with defects [RAI 00].

Such an industrial context imposes certain conditions on the models used, through the range of validity and the performance expected. The model presented here has been developed to meet the needs of efficiency, computation time having to be short in order to simulate a large number of configurations, but also for applicability: we want to be able to compute fields generated by transducers of various kinds (by the shape of their radiating surface or of their lens, being standard monolithic or phased-array, etc.) in specimens as complex as stainless steel welds [CHA 00, GEN 99, LHE00] or multilayered composite materials [GEN 03a, DEY 05]. The model is therefore developed to deal with the case of anisotropic and heterogenous materials, as well as specimens of complex geometries. In order to be realistic, it must also be three-dimensional.

This leads to use a so called semi-analytical approach, that is to say combining analytical methods and numerical integrations. As will be seen, the radiation integral, which describes the diffraction of the ultrasonic source, will be evaluated *numerically* by discretization of the radiating source surface into infinitesimal sources in order to consider a general case. The ultrasonic field generated by each of these sources will be approximated by a *closed-form* formulation involving no integral calculus, in order to increase calculation efficiency. This last point is realized by means of the pencil method.

The model presented here has been developed at the French Atomic Energy Commission (CEA) and integrated into the software platform called CIVA, a simulation software for non-destructive testing [CAL 03]. This has led to numerous validations of the method proposed here in both academic and industrial configurations<sup>1</sup>.

---

1. For a detailed description of the CIVA platform and its ranges of application, visit <http://www-civa.cea.fr>.

### 14.3.1. General principle of modeling an ultrasonic beam using the pencil method

Let us first consider a transducer immersed in a fluid and an observation point M within the same medium. The field generated by the radiating surface at M is described by the Rayleigh–Sommerfeld radiation integral [GOO 68]:

$$\varphi(M) = \iint_{P \in \text{trad}} V_0(P) \frac{e^{jkr}}{2\pi r} e^{-j\omega t} dS. \quad [14.36]$$

The quantity  $\varphi(M)$  is the acoustic potential generated at M,  $V_0(P)$  is the particle velocity normal to the radiating surface of the transducer at P,  $r$  is the distance between P and M,  $k$  is the wavenumber and  $\omega$  the pulsation. The Rayleigh integral can be interpreted as a (continuous) sum of elementary contributions due to point sources of infinitesimal surface  $dS$ . It is used to evaluate the interferences of these elementary contributions, i.e. the diffraction by the whole radiating surface. The integrant represents the elementary field generated in an isotropic homogenous medium by a point-like elementary source (of infinitesimal surface  $dS$ ) vibrating with a particle velocity  $V_0$ . This field decreases as the inverse of the distance of propagation between P and M.

We can extend this formulation to cases where the observation point is no longer located in the medium containing the transducer, but in a second medium of any nature<sup>2</sup> (isotropic, anisotropic solid, etc.), based on the assumption that we are able to generalize the concept of elementary field introduced above to the complex case of heterogenous and anisotropic media. Such an elementary field, noted  $G(P,M)$ , is the Green's function<sup>3</sup> of the problem (response to a point-like source). This is the quantity that is evaluated under approximations in the following, by means of the pencil formalism.

Moreover, as we wish to take into account all possible transducer geometries, the summation over their radiating surface, as represented by the integral given in equation [14.36], is evaluated numerically from all elementary fields generated by all the source points that discretize the radiating surface.

---

2. In the following, it is assumed that the transducer to be modeled is immersed in a fluid medium; it is also a realistic hypothesis in the case of transducers mounted on a wedge (Plexiglas wedge ensuring the coupling between the transducer and the medium to be tested), as soon as one ignores the effect of transverse waves generated in this solid medium [LER 97].

3. Depending on the quantity we wish to calculate at M,  $G$  can be scalar, vectorial or tensorial (scalar potential, polarization, stress, etc.).

Before describing the pencil method, we will mention a well-known approximation: let us consider a point-like source in an isotropic and infinite fluid. This source radiates a diverging spherical wave which has a complex valued expression, in particular because the generated pressure and velocity are not in phase. However, as soon as the observation point is far enough from the source (in practice, when the distance between them is greater than a few wavelengths), pressure and velocity are almost in phase, and then the wave has the behavior of a plane wave with a wave vector that would be directed from the source to the observation point. The only difference from the plane wave lies in the fact that its amplitude evolves with the inverse of the distance, while that of the plane wave in an infinite medium remains constant.

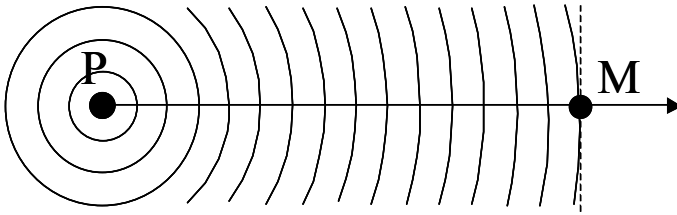


**Figure 14.4.** *Spherical wave in an infinite medium seen as a plane wave far away from the source point*

To summarize and generalize, the wave arising from a point source is seen, at a fixed observation point, as a wave with the behavior of a plane wave, but its amplitude decreases with the propagation distance. The pencil method aims to apply exactly the same approximation, considering complex propagation, possibly in anisotropic and/or heterogeneous media. So we need to characterize this plane wave and determine the changes in its amplitude.

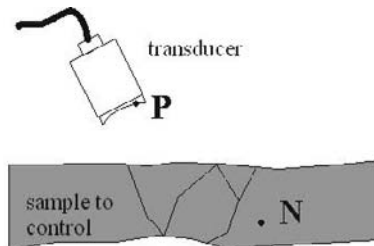


**Figure 14.5.** *Typical simulation configuration: an anisotropic heterogeneous sample is examined by a standard transducer. This problem is handled as a set of subproblems to evaluate the field generated by a point-like source  $P$  at the calculation point  $N$*

The situation to model is the one described in Figure 14.5: we seek to calculate the ultrasonic field radiated at a calculation point N located in a solid medium that can be anisotropic and/or heterogenous, the source is a point P on the active surface of the transducer being located in a fluid medium; this source is separated from the observation point by one or more interfaces of arbitrary geometry. The wave generated was originally spherical, but it is distorted each time it propagates through an interface, depending on its geometry and the materials crossed. To illustrate this behavior, Figure 14.6 shows the successive wavefronts of a longitudinal wave refracted from a fluid medium into an isotropic solid medium.

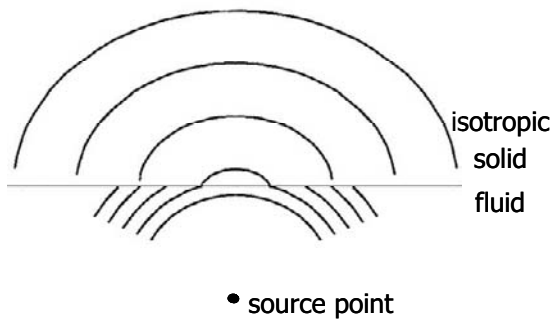


**Figure 14.6.** Successive wavefronts of a wave radiated by a point-like source, first spherical and then deforming itself while refracted in the solid material (wavefronts become elliptical in the case of an isotropic solid). Only the longitudinal wave is shown in the solid. For the illustration, the characteristics of water for the fluid and steel for the solid were used

### 14.3.2. The Fermat path

Before we worry about the amplitude of the wave at the observation point, we need to know what plane wave (defined by a wave vector  $\mathbf{k}$ ) we must use for the approximation. For this purpose, we briefly introduce the principle of the stationary phase. But before we discuss the mathematical formalism, we consider, as an illustration, the case where two semi-infinite media are separated by a plane interface. It is a situation similar to that of a lifeguard in the famous following problem:

A lifeguard on the beach at point A, sees a swimmer who is drowning at point B. The “interface” between the beach and the sea is straight (Figure 14.7). Knowing that the life guard runs on the beach at a speed  $V_1$  and swims in the sea at a slower speed  $V_2$ , which path will be the fastest one to reach the swimmer? Noting M the point where the lifeguard enters the water, the optimal path AMB is the one that satisfies the Snell–Descartes condition  $\sin\theta_1/V_1 = \sin\theta_2/V_2$  (see equation [2.35], section 2.1.2.4, Chapter 2).

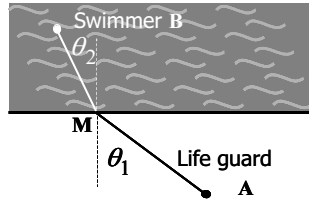


**Figure 14.7.** *The life guard problem*

We now transpose this problem by replacing the lifeguard in the sea by an omnidirectional light source radiating a wave which propagates at a speed  $V_1$  in the first medium (the beach) and at a speed  $V_2$  in the second medium (the sea). Pierre de Fermat (1601–65) outlined that, in this situation, the light follows the fastest path, as did the lifeguard. For an observation point B located in the second medium, the light seems to come from the point M along the direction MB. The same applies for an acoustic wave. It is the Fermat path. In the problem that we are studying, we select a privileged path between the source point and the observation point that allows us to define a plane wave whose wave vector is parallel to this path (at least in the isotropic medium). Moreover, the plane wave behavior is satisfied at each interface since the Snell–Descartes principle applies.

A rigorous mathematical approach can lead to the same conclusions while generalizing the Fermat principle. It is based on the Fourier decomposition (see section 14.1.1) of the spherical wave radiated by the point-like source, which can be represented by an infinite double sum of plane waves. This decomposition is given at a point of coordinates  $(x, y, z)$  located in the medium containing the source from the Weyl formulation [WEY 19]:

$$\frac{e^{jkr}}{r} = \frac{j}{2\pi} \iint \frac{e^{j(k_x x + k_y y + k_z z)}}{k_z} dk_x dk_y, \quad [14.37]$$

where each plane wave is represented by the two components of its wave vector  $k_x$  and  $k_y$  (in a plane parallel to the interface). The third component is deduced from the first two thanks to the slowness surface (see section 1.2.2.3, Chapter 1) of the material in which the wave propagates, for the type of wave considered.

The entire plane wave spectrum represents the wave resulting from the point source in the plane  $z = 0$  containing it. Each component of this spectrum, i.e. each plane wave, propagates all the way to the plane  $z = z_1$  of the interface and then to the plane  $z = z_2$  containing the calculation point, using the propagators  $e^{k_{1z}z_1}$  and  $e^{k_{2z}z_2}$ . To calculate the field  $\Delta U(N)$  obtained at the observation point, a summation

of all plane waves that propagate from the source to the observation point N is then performed by inverse Fourier transformation. We obtain:<sup>4</sup>

$$\Delta U(N) = \frac{jV_0\Delta S}{4\pi^2} \iint \frac{e^{j(k_x x + k_y y + k_{1z} z_1 + k_{2z} z_2)}}{k_{1z}} dk_x dk_y . \quad [14.38]$$

The field at the observation point N results from the evaluation of this integral. This is where the principle of the stationary phase is used. The function to be integrated above presents a rapidly oscillating phase in the integration domain, compared with its modulus. Thus, this integrand is represented in the complex plane by a vector whose norm is almost constant, but which turns quickly around the origin. The sum of the different values of this vector, given by the integral above, will therefore give negligible result. Non-negligible contributions appear only when this vector stops turning on itself, i.e. close to points where the phase is stationary, i.e. the function that defines the phase presents an extremum. When the phase looks like the one in equation [14.38], a point of stationary phase is defined by

$$\begin{cases} x + z_1 \frac{\partial k_{1z}}{\partial k_x} + z_2 \frac{\partial k_{2z}}{\partial k_x} = 0 \\ y + z_1 \frac{\partial k_{1z}}{\partial k_y} + z_2 \frac{\partial k_{2z}}{\partial k_y} = 0 \end{cases} \quad [14.39]$$

Solving the system above is a means of estimating the pair  $(k_x, k_y)$ , which defines the wave vectors of a plane wave propagating in different materials. In a situation similar to the lifeguard problem, or to the problem studied by Fermat, we obtain a pair of values corresponding to the two wave vectors located along each segment of the Fermat path. This development based on the stationary phase theorem gives a mathematical justification to the principle enunciated empirically by Fermat. It also helps to extend the definition of the Fermat path which is no longer simply the fastest one for the wave, but the path in which the phase is an extremum. It is also called the stationary phase path or the geometrical acoustics path.

If the wave that we consider crosses one or more anisotropic media, the Fermat path is obtained by taking into account the fact that the direction of the phase is no longer parallel to the direction of energy. In the case of two semi-infinite media

---

4. At first, we assume that no energy is lost in the transmission from the first medium to the second (the transmission coefficient is taken to be 1). This assumption has no consequence on the Fermat path. In order to accurately predict phenomena at interfaces, coefficients of transmission and of reflection, with or without mode conversion, will be introduced later when computing the field on the basis of the pencil method.

separated by a plane interface, the first medium being fluid and the second being an anisotropic solid, we can introduce in system [14.39], the speed of energy  $V_2^e$  of the wave in the second medium. Indeed, as it is normal to the slowness surface (see equation [1.88], section 1.2.2.3, Chapter 1), it can be written as

$$V_2^e = V_{2z}^e \begin{pmatrix} -\frac{\partial k_{2z}}{\partial k_x} \\ -\frac{\partial k_{2z}}{\partial k_y} \\ 1 \end{pmatrix}. \quad [14.40]$$

In other words, we have  $\partial k_{2z} / \partial k_x = -V_{2x}^e / V_{2z}^e$  and  $\partial k_{2z} / \partial k_y = -V_{2y}^e / V_{2z}^e$ .

The substitution of these quantities into the system [14.39] defining the Fermat path helps us to establish that when the direction of phase and the direction of energy are not parallel, the main path is defined by the directions of energy of a plane wave from the point source, which is bent according to the Snell–Descartes law (conservation of the tangential component of the wave vector), and whose energy vector points in the direction of the calculation point.

Strictly speaking, the stationary phase approximation (see [STA 86, WAL 95]) helps to evaluate a closed-form expression of the integral [14.38], based on the assumption that only the points of the stationary phase defined above (and their neighborhood) generate a significant contribution. An asymptotic development of the phase function is performed around the points of the stationary phase, thus revealing integral forms for which a closed-form solution is known: such a method of calculation is called an asymptotic method. It is possible to obtain very accurate results without performing integral calculus thanks to this method [STA 86, GEN 98].

Note that the function representing the phase can have several extrema, the slowness surface of the resulting wave then having one or more point(s) of inflection (this may sometimes be the case for quasi-transverse waves in anisotropic materials). This means that for a same pair source point/calculation point, several geometric paths are possible. In this case, the elementary field generated by the point source is the sum of the contributions calculated along each of the Fermat paths<sup>5</sup>.

---

5. This statement, however, presents a restriction: to ensure that the summation is possible, i.e. for the validity of the approximation, these paths should be distinct, different enough from

Here, we use the method of stationary phase only to define the generalized concept of the Fermat path. Knowing this path is a mean to set one (sometimes more) ray(s) connecting a source and a calculation point. We also know the wave vector associated with this ray, which enables us to assimilate the behavior of the wave propagating along the ray to that of a plane wave. The evolution of the acoustic amplitude carried by this wave (the factor  $1/r$  in the canonical case of the infinite fluid) is obtained by the pencil method that will be described below.

However it is useful to note that the stationary phase method, when applied with asymptotic developments of order 2, is equivalent to the pencil method described here. Both methods implement approximations that are of the same order, as has been demonstrated in [GEN 99]. Nevertheless, the geometric formalism of pencils is best suited to deal with non-canonical problems such as the calculation of ultrasonic field in a heterogenous and anisotropic medium of complex geometry.

#### 14.3.3. *Definition of a pencil*

A source of pressure in a fluid medium is omnidirectional. If we represent it with rays, it is necessary to send them in all directions in an equivalent manner. At least, it is the technique that we would use if we wanted to model the propagation using a pure ray modeling approach. It would then be convenient to count the density of rays passing near the observation point to quantify the acoustic intensity radiated at this point [NOR 80].

However, it is known that, according to what is described above, the only significant contributions lie around one or more points of stationary phase. The pencil method allows us to consider only this neighborhood, by transposing the formalism of the concept of phase to the concept of rays: the stationary phase point is associated to the geometric Fermat path, while the vicinity of the stationary phase point is associated with all the rays spreading near the Fermat path (notion of *paraxial ray*, the ray associated with the Fermat path being the *axial ray*). The method has been developed following the formalism described in [DES 72] for electromagnetic waves in isotropic media. It is also extended to the case of heterogenous and/or anisotropic, complex materials. The theory of rays used in seismology uses a slightly different formalism, but approximations are similar [CER 01].

---

one another. Otherwise, we are in the presence of a caustic, a region of *natural* focusing of the energy. The pencil method can not be used, as its degree of asymptotic approximation (see below) is not sufficient. A method for dealing with the specific problem of caustics, and still connected to the pencil formalism, has been developed and proposed in [GEN 98] and [GEN 99].



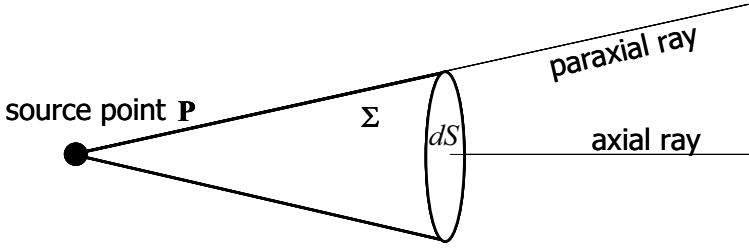


**Figure 14.8.** Definition of a pencil. Axial and paraxial rays

A pencil is a set of rays coming from the point source and located in a cone, whose vertex is the source point (Figure 14.8). Its angle is theoretically infinitesimal. The center of the pencil is the *axial ray*. It follows the Fermat path as defined above. A *paraxial ray* is also considered, belonging to the envelope of the pencil and representing the vicinity of the axial ray. During its propagation, the pencil, initially cone-shaped, will deform itself depending on the medias and interfaces crossed.

We follow a principle of energy conservation inside the pencil. The energy sent by the source in the pencil must emerge from it. This energy is written  $I_\Omega d\Omega$ , where  $I_\Omega$  is the intensity of the source per unit of solid angle, and  $d\Omega$  is the solid angle covered by the pencil. It is assumed that the flow of energy through the side of the pencil, noted  $\Sigma$  in Figure 14.8, is zero. The whole energy will therefore cross the section  $dS$  of the pencil. This energy can be expressed from the intensity  $I(N)$  at the considered calculation point, by  $I(N) dS$ . So we have

$$\frac{I(N)}{I_\Omega} = \frac{1}{R_f^2} = \frac{d\Omega}{dS}. \quad [14.41]$$

This ratio shows that the evolution of the intensity with the propagation of a given wave, is the square of the evolution of its amplitude. Therefore, it is the quantity we need. It is called the *divergence factor*. The magnitude  $R_f$ , which represents it, has the dimension of a distance.

Suppose a simple homogenous fluid medium of propagation. The pencil does not undergo any deformation and remains perfectly cone-shaped. If a distance  $r$  separates the source from the calculation point N, the section  $dS$  will be simply written  $r^2 d\Omega$ , and the intensity ratio above becomes  $1/r^2$ . Therefore we can again find the basic result mentioned in the introduction, that the amplitude of a spherical wave evolves with the inverse of the distance from the source to the observation

point (we recall that the intensity is homogenous to the square of the magnitude of displacement).

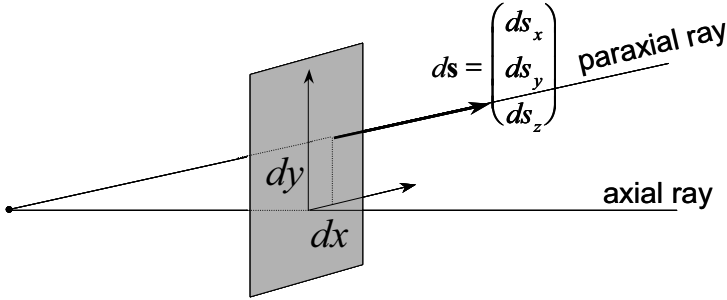


**Figure 14.9.** Definition of the components of the pencil vector

In order to know the evolution of the section of the pencil during its propagation, the pencil is represented by the expression of the paraxial ray relative to the axial ray, as shown in Figure 14.9 (the differentiation is infinitesimal). It takes place in a plane perpendicular to the wave vector associated with the axial ray at a given propagation time. As the wave vector is perpendicular to the wavefront, the plane we defined contains the basic surface  $dS$  that we must evaluate, even in the case of the propagation in an anisotropic medium.

The paraxial ray is represented by a four component vector, made up of two position parameters and two direction parameters. The position of the paraxial ray relative to the axial ray is defined by the two parameters  $dx$  and  $dy$ , estimated in the plane defined above. In order to obtain the other two parameters, the infinitesimal difference between the wave vectors associated with the paraxial and axial rays is estimated. This quantity is represented by the two components  $ds_x$  and  $ds_y$ .

The vector  $\psi$  which consists of those four parameters is known as the *pencil vector*.

We have:

$$\psi = \begin{pmatrix} dx \\ dy \\ ds_x \\ ds_y \end{pmatrix}. \quad [14.42]$$

The same pencil, at different propagation times, will be represented by different pencil vectors. Two of them are of a particular importance: the initial pencil vector at the source point  $\psi_P$  and the final vector at the calculation point  $\psi_N$ . We express them by:

$$\psi_P = \begin{pmatrix} 0 \\ 0 \\ ds_x^0 \\ ds_y^0 \end{pmatrix} \text{ and } \psi_N = \begin{pmatrix} dx' \\ dy' \\ ds'_x \\ ds'_y \end{pmatrix}. \quad [14.43]$$

It should be noted that we can evaluate from these quantities the initial solid angle of the pencil  $d\Omega$  :

$$d\Omega = ds_x^0 ds_y^0 / s^2 \quad [14.44]$$

where  $s$  is the slowness of the wave in the medium containing the source. Similarly, we have

$$dS = dx' dy' \quad [14.45]$$

To find the divergence factor  $R_I$ , introduced in [14.41] and which is the ratio of the two quantities above, we must know how to link the pencil vector at the calculation point to the initial pencil vector. But we will see that these two vectors can be connected linearly through a matrix that does not depend on the four components of the pencil. This matrix, that we denote  $L$  and which is a  $4 \times 4$  matrix, is called *pencil propagation matrix*. This matrix will often be expressed through its four  $2 \times 2$  submatrices, denoted by  $A$ ,  $B$ ,  $C$  and  $D$ :

$$\psi_N = L \cdot \psi_P = \begin{pmatrix} A & B \\ C & D \end{pmatrix} \cdot \psi_P. \quad [14.46]$$

Thus, the evolution of the acoustic intensity will be given, if we ignore – in a first step – the interaction coefficients at interfaces (reflection, transmission with or without mode conversion), by the divergence factor expressed as follows:

$$R_I^2 = s^2 \det B. \quad [14.47]$$

The major advantage of such formalism is that a complex propagation may be represented by a succession of elementary propagation steps. The global pencil

propagation matrix will be obtained by a product of propagation matrices, each representing a particular step of the propagation. In the following, we establish the formulation of various elementary matrices corresponding to different elementary cases we want to handle: propagation in a homogenous isotropic medium, propagation in a homogenous anisotropic medium, interaction with a curved interface, and possibly separating two anisotropic media.

#### 14.3.4. Propagation of a pencil

In this section, we try to link the pencil vectors  $\psi$  and  $\psi'$  representing the same pencil at two different positions in the same isotropic medium,  $\psi$  being the starting position and  $\psi'$  the final one. We will note  $dx$  and  $dx'$  (respectively  $ds$  and  $ds'$ ) the vectors constituted by the first two (respectively last two) components of  $\psi$  and  $\psi'$ .

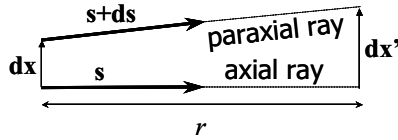


Figure 14.10. Evolution of a pencil in an isotropic medium

First, we describe the propagation of a pencil in an isotropic material. In such a configuration, the link between  $\psi$  and  $\psi'$  is simply a homothetic relationship, where the final position depends only on the initial position  $dx$  and on the initial direction  $ds$  (Figure 14.10). We have:

$$dx' = dx + \frac{r}{s} ds, \quad [14.48-a]$$

$$ds' = ds, \quad [14.48-b]$$

where  $r$  is the propagation distance and  $s$  the slowness of the wave considered in the propagation medium. The pencil propagation matrix in an isotropic material simply writes:

$$\psi' = \begin{pmatrix} 1 & 0 & r/s & 0 \\ 0 & 1 & 0 & r/s \\ 0 & 0 & 1 & 0 \\ 0 & 0 & 0 & 1 \end{pmatrix} \cdot \psi. \quad [14.49]$$

Let us now consider the case where the pencil crosses an interface separating two isotropic media. We first assume that the interface is plane. Here, no propagation is taken into account, since it is treated separately by other matrices. We therefore connect the pencil vector immediately before the interface to the pencil vector immediately after the interface [LEE 82]. Locally, as there is no propagation, it is assumed that the paraxial ray does not have enough time to get away from the axial ray, so both rays are parallel.<sup>6</sup>

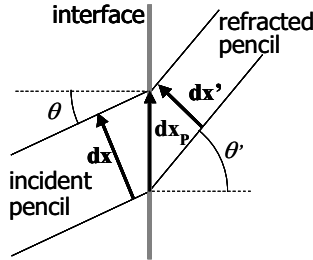


**Figure 14.11.** *Refraction of a pencil at a plane interface between two isotropic media*

By geometrical construction (see Figure 14.11), the projection  $dx_p$  of  $dx$  on the interface plane following the direction of the incident axial ray is the same as the projection  $dx'$  following the outgoing axial ray. Denoted  $\Theta$  and  $\Theta'$  the two corresponding projection matrices, assuming that the  $x$ -axis used to express the pencil is perpendicular to the incidence plane (and therefore parallel to the interface), we have:

$$dx = \begin{pmatrix} 1 & 0 \\ 0 & \cos \theta \end{pmatrix} \cdot dx_p = \Theta \cdot dx_p, \text{ and}$$

$$dx' = \begin{pmatrix} 1 & 0 \\ 0 & \cos \theta' \end{pmatrix} \cdot dx_p = \Theta' \cdot dx_p, \quad [14.50]$$

where  $\theta$  and  $\theta'$  denote the incident and refracted angles. The vectors  $ds$  and  $ds'$  are connected by the Snell–Descartes law (conservation of the tangential component of the wave vector), which can be expressed using the same matrices by:

$$ds' = \Theta'^{-1} \Theta ds. \quad [14.51]$$

6. We deal locally with a tube of rays, that is to say a non-diverging pencil.

Thus, the crossing of a plane interface by a pencil results in the following pencil propagation matrix:

$$\Psi' = \begin{pmatrix} \Theta' \Theta^{-1} & 0 \\ 0 & \Theta'^{-1} \Theta \end{pmatrix} \cdot \Psi \quad [14.52]$$

This expression can be used to describe both a reflection and a refraction. In all cases, the angles must be defined relative to the normal to the interface pointing in the direction of the medium of refraction. Thus, the incident and refracted angles will be smaller than  $\pi/2$  while the angle of reflection will be larger than  $\pi/2$ .

Suppose now that the interface is not plane but has a curvature defined by  $C_{\text{int}}$  (a  $2 \times 2$  matrix of curvature evaluated in a coordinate system whose  $x$ -axis is orthogonal to the incidence plane). Thus, if  $p$  is the normal vector to the interface at the impact location of the axial ray, the paraxial ray will see a normal  $p+dp$ , which will depend on the position of its impact on the interface (that is to say the quantity  $dx_p$  introduced above) and on the curvature of the interface. The definition of the curvature matrix allows us to write:

$$dp = C_{\text{int}} \cdot dx_p \quad [14.53]$$

It is assumed that the effect of the curvature of the interface takes place only at the level of an additional divergence of the pencil, i.e. the component  $dx'$  is unchanged, only  $ds'$  is affected (indeed the evolution of  $dx$  is of less importance). The projection  $ds_p$  of  $ds$  on the interface will depend on the evolution of its normal, represented by  $dp$ . We have:

$$ds_p = \Theta \cdot ds - s \cos \theta dp = \Theta \cdot ds - s \cos \theta C_{\text{int}} \Theta^{-1} dx. \quad [14.54]$$

We see that this projection now depends, quite logically, on the initial difference  $dx$  between the axial and paraxial rays. Applying the same relation with the outgoing pencil yields the following formulation of the pencil propagation matrix through a curved interface:

$$\Psi' = \begin{pmatrix} \Theta' \Theta^{-1} & 0 \\ h \Theta'^{-1} C_{\text{int}} \Theta^{-1} & \Theta'^{-1} \Theta \end{pmatrix} \cdot \Psi, \quad [14.55]$$

with  $h = s' \cos \theta' - s \cos \theta$ .

We now consider the case where the pencil propagates in a homogenous anisotropic material. In such a situation, we must take into account the fact that the

axial and paraxial rays are oriented in the direction of energy, and that it is orthogonal to the slowness surface. The pencil is always expressed in a plane that is orthogonal to the wave vector of the axial ray, which is tangential to the wavefront. Three orthonormal vectors  $x$ ,  $y$  and  $z$  will define a coordinate system associated with the pencil if  $x$  and  $y$  are tangential to the wavefront and if  $z$  is oriented along the wave vector of the axial ray. In this coordinate system, the anisotropic material may be characterized by its slowness surfaces, which derive directly from its elastic constants. We will note  $g$  the function that defines the slowness surface associated with the type of wave considered in the coordinate system defined above. We have  $s_z = g(s_x, s_y)$ .

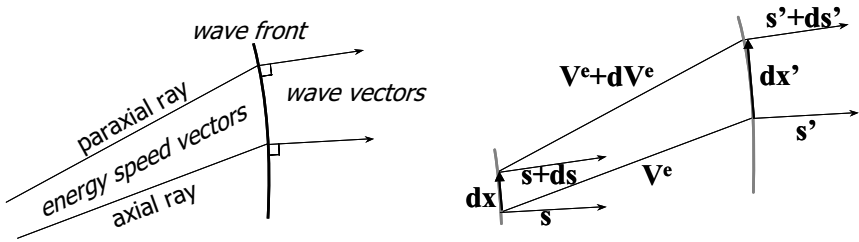


**Figure 14.12.** Definition of a pencil in an isotropic medium

Figure 14.12 shows how the different quantities evolve. Depending on the difference  $ds$  between the wave vectors of the axial and paraxial rays, the directions of the rays, represented by the energy velocities, will differ by a quantity  $dV^e$ , which can be obtained from  $ds$  and the slowness surface  $g$ . The energy velocity is parallel to a vector  $m$ , defined, similarly to equation [14.40], by:

$$m = \begin{pmatrix} -\frac{\partial g}{\partial s_x} \\ -\frac{\partial g}{\partial s_y} \\ 1 \end{pmatrix}.$$

It can therefore be inferred that a ray will evolve from a position  $x$  to a position  $x'$  following the formula:

$$\mathbf{x}' = \mathbf{x} + r_k \begin{pmatrix} -\frac{\partial g}{\partial s_x} \\ -\frac{\partial g}{\partial s_y} \end{pmatrix}. \quad [14.56]$$

The differentiation of this equation allows us to write the infinitesimal difference between the axial and paraxial rays, and thus express the pencil  $\psi'$  as a function of the initial pencil  $\psi$ . Therefore, we have the following pencil propagation matrix:

$$\psi' = \begin{bmatrix} 1 & 0 & -2r_k g_{2,0} & -r_k g_{1,1} \\ 0 & 1 & -r_k g_{1,1} & -2r_k g_{0,2} \\ 0 & 0 & 1 & 0 \\ 0 & 0 & 0 & 1 \end{bmatrix} \cdot \psi, \quad [14.57]$$

where  $g_{nm}$  corresponds to the second derivative of the slowness surface in the considered direction and is given by:

$$g_{nm} = \frac{\partial^{n+m} g}{n! m! \partial s_x^n \partial s_y^m}.$$

The quantity  $r_k$  is the propagation distance, measured in the direction of the wave vector. From this formula, we can see that the divergence of the energy during the propagation in an anisotropic material depends on the Gaussian curvature of the slowness surface (which is expressed by its second derivative), in agreement with the results obtained by Northrop and Wolfe [NOR 80].

We now analyze how a pencil vector is affected by an interface separating two anisotropic media. We seek to establish an expression similar to that given by [14.55] adapted to the anisotropic case. For this purpose, we choose the coordinate system  $x_i, y_i, z_i$ , associated with the interface:  $x_i$  and  $y_i$  are parallel to the interface and  $z_i$  is normal to it. The vector  $x_i$  is chosen perpendicular to the incidence plane defined by  $z_i$  and the axial wave vector. A generic vector expressed in this system will have the coordinates  $x_i, y_i, z_i$ .

As previously, the coordinate system defined by the vectors  $x, y$  and  $z$  is linked to the pencil (here the incident pencil). The vector  $z$  is oriented along the incident wave vector, and  $x$  is supposed to be parallel to the interface (i.e. parallel to  $x_i$ ). A generic vector expressed in this frame will have the coordinates  $x, y, z$ .



The transformation matrix from the first coordinate system to the second is expressed by:

$$\begin{pmatrix} x \\ y \\ z \end{pmatrix} = \begin{pmatrix} 1 & 0 & 0 \\ 0 & \cos \theta & -\sin \theta \\ 0 & \sin \theta & \cos \theta \end{pmatrix} \cdot \begin{pmatrix} x_i \\ y_i \\ z_i \end{pmatrix}. \quad [14.58]$$

where  $\theta$  is the angle between  $z$  and  $z_i$  (incidence angle defined by the wave vectors).

In the coordinate system associated with the interface, we can write the infinitesimal changes  $ds_p$  of the slowness vector (difference between the slowness associated with the axial ray and that associated with the paraxial ray). Using the function  $f$  that represents the slowness surface in the coordinate system of the interface, so that  $s_{pz} = f(s_{px}, s_{py})$ , and its first derivative  $f_{10}$  (with respect to  $s_{px}$ ) and  $f_{01}$  (with respect to  $s_{py}$ ), we have

$$ds = ds_{px}x_i + ds_{py}y_i + (f_{10}ds_{px} + f_{01}ds_{py})z_i. \quad [14.59]$$

Writing this vector in the coordinate system associated with the ray, and using the transformation matrix given by equation [14.58], we obtain the two components of the same vector in the coordinate system associated with the incident ray (which are therefore also the last two components of the incident pencil vector):

$$\begin{pmatrix} ds_x \\ ds_y \end{pmatrix} = \begin{pmatrix} 1 & 0 \\ -\sin \theta f_{10} & \cos \theta - \sin \theta f_{01} \end{pmatrix} \cdot \begin{pmatrix} ds_{px} \\ ds_{py} \end{pmatrix}. \quad [14.60]$$

We also express the vector  $dx_p$ , its projection oriented in the direction of energy of the vector  $dx$  on the interface. To do so, we apply two successive changes of coordinate system to  $dx$ . The first one consists of moving from the coordinate system associated with the ray to that associated with the interface, using the inverse of the matrix given by equation [14.58] (which is also its transposed matrix). The resulting vector is noted  $dv_i$ , and is expressed by:

$$dv_i = \begin{pmatrix} dx \\ \cos \theta dy \\ -\sin \theta dy \end{pmatrix}. \quad [14.61]$$

Then, a new coordinate system is defined from the vectors  $x_i$  and  $y_i$  parallel to the interface and the vector  $m$  parallel to the direction of energy of the incident axial beam, defined in the coordinate system of the interface by:

$$\mathbf{m} = \begin{pmatrix} -f_{10} \\ -f_{01} \\ 1 \end{pmatrix}. \quad [14.62]$$

The transformation matrix  $\mathbf{P}$  to this non-orthonormal coordinate system is expressed by:

$$\mathbf{P} = \begin{pmatrix} 1 & 0 & f_{10} \\ 0 & 1 & f_{01} \\ 0 & 0 & 1 \end{pmatrix}. \quad [14.63]$$

The interest of such a coordinate system is as follows: to obtain the projection of a vector (expressed in this coordinate system) along  $\mathbf{m}$  on the interface, it is enough to force its third component to be null. Thus, expressing the vector  $\mathbf{P} \cdot d\mathbf{v}$  and nullifying its last component, we find the expression of the projection  $dx_p$  of  $d\mathbf{x}$  following the direction of energy  $\mathbf{m}$ . We have:

$$\begin{pmatrix} dx_p \\ dy_p \end{pmatrix} = \begin{pmatrix} 1 & -\sin \theta f_{10} \\ 0 & \cos \theta - \sin \theta f_{01} \end{pmatrix} \cdot \begin{pmatrix} dx \\ dy \end{pmatrix}. \quad [14.64]$$

If we introduce the matrix  $\Theta$  expressed by

$$\Theta = \frac{1}{\cos \theta - \sin \theta f_{01}} \begin{pmatrix} \cos \theta - \sin \theta f_{01} & \sin \theta f_{10} \\ 0 & 1 \end{pmatrix}, \quad [14.65]$$

equations [14.60] and [14.64], connecting the components of the incident pencil vector to the projections  $dx_p$  and  $ds_p$  on the interface, can be re-written in the form<sup>7</sup>

$$ds = \Theta^{-T} \cdot ds_p \text{ and } d\mathbf{x} = \Theta \cdot d\mathbf{x}_p.$$

These same formulae can be written to connect the components of the refracted or reflected pencils to the quantities projected on the interface, introducing the projection matrix  $\Theta'$ . We can thus link the two pencil vectors before and after the interface by

---

7. The superscript “-T” represents the transposition of the inverse matrix, which is equivalent to the inverse of the transposed matrix. In the expressions of pencil propagation matrices for the isotropic cases, transposition does not appear because the matrices involved are symmetric.

$$\psi' = \begin{pmatrix} \Theta' \Theta^{-1} & 0 \\ 0 & \Theta'^{-T} \Theta^T \end{pmatrix} \cdot \psi. \quad [14.66]$$

This equation is a generalization of expression [14.52] to the anisotropic cases. In the same way, if the interface presents a curvature given by the matrix  $C_{\text{int}}$ , the pencil propagation matrix will be expressed in a similar form to that given in the isotropic case (equation [14.55]), the main difference residing in the expression of the projection matrices  $\Theta$ . We have

$$\psi' = \begin{pmatrix} \Theta' \Theta^{-1} & 0 \\ h \Theta'^{-T} C_{\text{int}} \Theta^{-1} & \Theta'^{-T} \Theta^T \end{pmatrix} \cdot \psi \quad [14.67]$$

where the quantity  $h$  was defined in equation [14.55].

Once all these basic steps are established, the propagation of a pencil in a heterogenous complex material is a succession of these elementary propagations. Thus, a simple product of pencil propagation matrices describes the complete evolution of the pencil. However, a precaution is required to ensure that the expressions of pencil propagation matrices given above can be applied: we should, whenever an interface is involved, place the vector  $x$  of the beam coordinate system parallel to the interface. Therefore, we need to turn the ray coordinate system around its axis  $z$ . If  $\alpha$  is the desired angle of rotation, the pencil vector is transformed as:

$$\psi' = \begin{pmatrix} \cos \alpha & \sin \alpha & 0 & 0 \\ -\sin \alpha & \cos \alpha & 0 & 0 \\ 0 & 0 & \cos \alpha & \sin \alpha \\ 0 & 0 & -\sin \alpha & \cos \alpha \end{pmatrix} \cdot \psi \quad [14.68]$$

where  $\psi$  and  $\psi'$  are respectively the pencil vectors before and after the rotation.

All the above developments make it possible to write the evolution of a pencil during its propagation mathematically, in a series of isotropic or anisotropic media separated by interfaces of any geometry, and this from the source point to the calculation point. We can therefore express the elementary ultrasonic field due to the elementary source at this calculation point.

### 14.3.5. *Reconstruction of the ultrasonic field*

Equations [14.41] and [14.47] make it possible, when the pencil propagation matrix describing the entire propagation from the source point to the calculation

point has been written, to obtain the ratio between the intensity at the calculation point and that at the source.

In order to re-introduce such elementary contributions obtained thanks to the pencil theory into the radiation integral (equation [14.36]), it is interesting to express the initial intensity as a function of the particle velocity  $V_0$  normal to the radiating surface (a quantity appearing in the Rayleigh–Sommerfeld integral). We show that an elementary source point associated with an element of surface  $\Delta S$  of the vibrating transducer with a particle velocity  $V_0$  generates an acoustic intensity per unit of solid angle  $I_\Omega$  expressed by

$$I_\Omega = \frac{\rho c (V_0 \Delta S)^2}{8\lambda^2}, \quad [14.69]$$

where  $\rho$ ,  $c$  and  $\lambda$  are respectively the density, velocity and wavelength in the medium in which the transducer is immersed.

In the same way, we can express the intensity at the calculation point  $I(N)$  from the elementary particle displacement noted  $\Delta U(N)$  generated by the source point, by writing that it is equal to half the norm of the Poynting vector [ROY 96b]. We have:

$$I(N) = -\frac{1}{2} \rho' c' \omega^2 (\Delta U(N))^2, \quad [14.70]$$

where  $\rho'$  and  $c'$  are respectively the density and velocity for the considered wave type (longitudinal or transverse) in the medium where the observation point is located, and  $\omega$  is the pulsation.

In addition, the evolution of the acoustic intensity described by the divergence factor from the pencil method does not take into account the effects on the amplitude of transmission or reflection involved at each interface. These effects are represented by the reflection or transmission coefficients of the plane wave associated with the axial ray (see section 1.1.3, Chapter 1). We may take into account this extra loss of energy in a separate way, as a multiplying factor that results from the product of the complex valued transmission or reflection coefficients (associated with a plane wave corresponding to the axial ray of the pencil) at each interface.

Equations [14.69] and [14.70], associated with the pencil method and the calculation of transmission and reflection coefficients at each interface, allow us to express the elementary particle displacements caused by elementary radiating surfaces. Then the sum of these elementary contributions is evaluated, thus expressing the diffraction by the extended source that corresponds to the radiating surface of the transducer. Using this method, we can calculate the ultrasonic field

generated by a transducer of any geometry in any heterogenous and anisotropic medium.

Since broadband ultrasonic transducers (i.e. with an impulsive excitation signal) are widely used, it is interesting to express the ultrasonic field in its transient form (impulse response). To do so, the elementary contribution associated with a pencil will be represented by a Dirac pulse whose amplitude is given by the previous developments, and shifted by the propagation time along the considered acoustic path (time 0 corresponds to the excitation of the transducer). The impulse diffraction integral is then evaluated by a discrete summation of these elementary pulses.

We can also deduce from each elementary particle displacement other elastodynamic quantities such as potentials, stresses, and so on, as long as the hypothesis of a plane wave is made locally for each pencil. We can then synthesize an ultrasonic field for each of these different quantities.

#### 14.3.6. Example

In order to illustrate the pencil method presented above, it is used here to calculate the ultrasonic field radiated by a transducer in a steel sample that contains a weld (see Figure 14.13). The base material considered here is made of isotropic steel (with density 7.8 and velocities  $5.9 \text{ ms}^{-1}$  and  $3.23 \text{ ms}^{-1}$  for longitudinal and transverse waves, respectively). It is located on both sides of the weld.

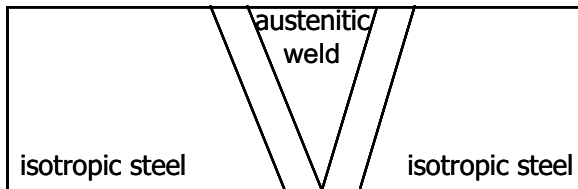


**Figure 14.13.** Outline of the heterogenous anisotropic sample to be tested

The welding process and conditions of solidification (*dendritic* growth due to the existence of thermal gradients) imply that the material inside the weld is both anisotropic and heterogenous. An orthotropic austenitic steel (stainless steel) constitutes the three volumes of the weld in the middle of the sample. The geometry of volumes constituting the weld has been greatly simplified here, compared to realistic cases that have been studied in [CHA 00]. The three volumes of the weld consist of the same anisotropic material, and differ only in their crystallographic

orientations. The nine independent elasticity constants defining this material are provided in Table 14.1; its density is 7.8.

$c_{11}$	$c_{12}$	$c_{13}$	$c_{22}$	$c_{23}$	$c_{33}$	$c_{44}$	$c_{55}$	$c_{66}$
250	112	180	250	138	250	117	91.5	70

**Table 14.1.** Elastic constants of the austenitic steel in GPa

The transducer used in this simulated examination is designed and positioned in order to generate a longitudinal ultrasonic beam refracted at 60° from the vertical in the isotropic steel (Fermat surface transducer). It has a diameter of 40 mm and radiates a broadband signal of center frequency 2.5 MHz. Under the conditions for which it is optimized, it generates the beam shown in Figure 14.14.

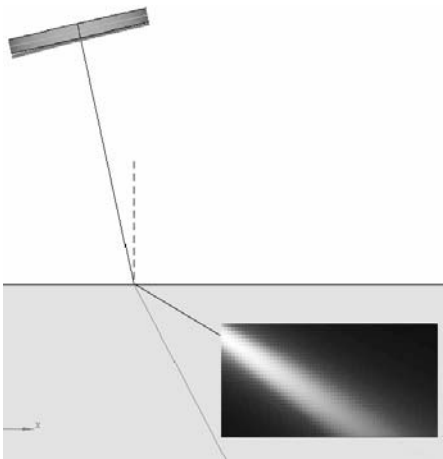


**Figure 14.14.** Beam generated in the isotropic steel by the transducer L60°

When the transducer approaches the weld, its anisotropic and heterogenous nature modifies the ultrasonic field (see Figure 14.15): the beam is deviated and distorted because of the anisotropy and the refraction at the various interfaces crossed. At the center of the weld, the inclination of the beam is about 45°, while it is 60° in the isotropic base material.

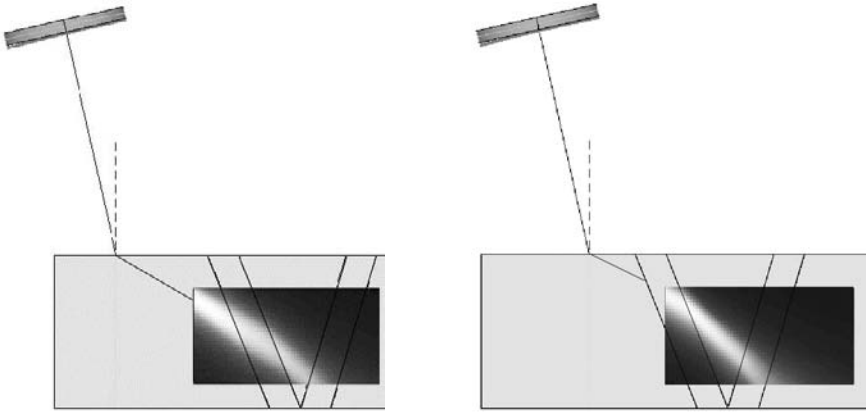


**Figure 14.15.** *Ultrasonic beams radiated through an austenitic weld, for two positions of the transducer. Only longitudinal and quasi-longitudinal waves generated by transmission are taken into account here*

Through this simple example, we can see the strong influence of the anisotropic and heterogeneous nature of a medium on the propagation of ultrasonic beams.<sup>8</sup> The deviations, distortions, divisions, attenuations or amplifications of beam that may arise in these situations, if they are not reliably known, can lead to misinterpretation of examination results (mirage effects, etc.) and lead to errors in characterizing, positioning and measuring potential flaws. A tool able to predict these behaviors, as permitted by the pencil method described here, is therefore essential, both for the definition of testing configurations and for the interpretation of their results.

### 14.3.7. Conclusions

The pencil method presented here can be used to model the ultrasonic field radiated by a point-like source of ultrasound in any material, possibly heterogeneous and anisotropic, i.e. the Green's function. Combined with the radiation integral for an extended radiating surface (the Rayleigh–Sommerfeld integral), we can predict transducer diffraction effects in complex materials.

It has been shown that the energy carried by such a wave is seen at a given observation point as propagating around one (or a finite number of) path(s) equal to the path(s) of geometrical acoustics.

---

8. Other examples of applications illustrating the interest of modeling ultrasonic fields in complex materials for realistic configurations can be found in references [CHA 00, GEN 03a, HA 105].

The pencil method is based on a geometric description of the neighborhood of the (axial) ray located along this path. It describes the evolution of the ultrasonic intensity carried by the elementary wave propagating from a source point along this ray. A matrix formalism is used to describe a complex propagation including the crossing of curved interfaces and the propagation in different isotropic or anisotropic media as the juxtaposition of elementary problems.

Eventually, the ultrasonic field radiated by any transducer in a complex material can be obtained by the summation of elementary contributions associated with different source points sampling the radiating surface. Examples of fields calculated by this method have illustrated this approach.

The same approach has been extended to deal with the propagation of bulk waves in a medium with a propagation speed gradient, in which the axial rays of the pencils no longer follow straight lines [GEN 03b], or even to deal with Rayleigh waves propagating on the surface of a sample immersed in a fluid, resulting from the refraction of a beam of bulk waves in the fluid [LHE 05].

#### 14.4. Bibliography

- [CAL 03] CALMON P., "Recent developments in NDT simulation", *Proceedings of the 5<sup>th</sup> World Congress on Ultrasonics*, pp. 443-446, 2003.
- [CER 01] CERVENY V., *Seismic Ray Theory*, Cambridge University Press, 2001.
- [CHA 00] CHASSIGNOLE B., VILLARD D., N'GUYEN VAN CHI G., GENGEMBRE N. AND LHÉMERY A., "Ultrasonic propagation in austenitic stainless steel welds. Approximate model and numerical methods results and comparison with experiments", *Review of Progress in QNDE 19*, pp. 153-160, 2000.
- [DES 72] DESCHAMPS G. A., "Ray techniques in electromagnetics", *Proc. IEEE 60* (9, pp. 1022-1035), 1972.
- [DEY 05] DEYDIER S., GENGEMBRE N., CALMON P., MENGELING V. AND PÉTILLON O., "Ultrasonic field computation into multilayered composite materials using a homogenization method based on ray theory", *Review of Progress in QNDE*, Vol. 24, pp. 1057-1064, 2005.
- [GEN 98] GENGEMBRE N., LHÉMERY A. AND CALMON P., "Calculation of wideband ultrasonic fields radiated by water-coupled transducers into anisotropic media", *Review of Progress in QNDE* Vol. 17, pp. 899-906, 1998.
- [GEN 99] GENGEMBRE N., Modélisation du champ ultrasonore rayonné dans un solide anisotrope et hétérogène par un traducteur immergé, PhD thesis, University of Paris 7, 1999.



- [GEN 03a] GENGEMBRE N., CALMON P., PÉTILLON O. AND CHATILLON S., “Prediction of ultrasonic fields into composite multi-layered structures : homogenization approach for the direct field and statistical approach for the inner reflections”, *Review of Progress in QNDE* Vol. 22, pp. 957-965, 2003.
- [GEN 03b] GENGEMBRE N., “Pencil method for ultrasonic beam computation”, in *Proceedings of the 5<sup>th</sup> World Congress on Ultrasonics*, pp. 1533-1536, 2003.
- [GOO 68] GOODMAN J. W., *Introduction to Fourier Optics*, McGraw-Hill, New-York, 1968.
- [GOO 72] GOODMAN J.W., *Introduction à l'optique de Fourier et à l'holographie*, Masson 1972.
- [LEE 82] LEE S. W., SHESHADRI M. S., JAMNEJAD V. AND MITTRA R., “Refraction at a curved dielectric interface: geometrical optics solutions”, *IEEE Trans. Microwave Theory Tech.* MTT-30, pp. 12-19, 1982.
- [LHE 00] LHÉMERY A., CALMON P., LECŒUR-TAÏBI I., RAILLON R. AND PARADIS L., “Modeling tools for ultrasonic inspection of welds”, *NDT & E Int.* 33, pp. 499-513, 2000.
- [LHE 05] LHÉMERY A., LEYMARIE N., CALMON P. AND COULETTE R., “Simultaneous calculation of bulk and surface transient waves radiated by water-coupled ultrasonic transducers”, *Review of Progress in QNDE*, Vol. 24, pp. 1002-1009, 2005.
- [NOR 80] NORTHROP G. A., WOLFE J. P., “Ballistic phonon imaging in Germanium”, *Phys. Rev. B*-22, pp. 6196-6212, 1980.
- [RAI 00] RAILLON R. AND LECŒUR-TAÏBI I., “Transient elastodynamic model for beam defect interaction. Application to nondestructive testing”, *Ultrasonics* 38, pp. 527-530, 2000.
- [ROY 96b] ROYER D., DIEULESAINT E., *Ondes élastiques dans les solides, Propagation libre et guidée*, Masson, 1996.
- [STA 86] STAMNES J. J., *Waves in Focal Region*, A. Hilger, 1986.
- [WAL 95] WALTHER A., *The Ray and Wave Theory of Lenses*, Cambridge University Press, 1995.
- [WEY 19] WEYL H., “Ausbreitung electromagnetischer Wellen über einem ebenen Leiter”, *Ann. Phys. Lpz.* 60, pp. 481–500, 1919.

This page intentionally left blank

## Chapter 15

# Time-Reversal of Waves

### 15.1. Overview

Time-reversal is one of those concepts that always interests and fascinates many physicists. It so happens that this fundamental symmetry of physics, invariance by time-reversal, can be used in the field of waves – acoustics and recently in electromagnetism – in order to create a wide variety of experiments and instruments which are relevant to fundamental physics and whose applications range from medicine to telecommunications, underwater acoustics, seismology, non-destructive testing, domotics.

#### 15.1.1. *Introduction*

The evolution of the performance of electronic components, gives the opportunity of realizing real time-reversal mirrors (TRM) that allow a wave to revive all stages of its past life. These devices exploit the fact that, in most cases, the propagation of acoustic waves (audible and ultrasonic) and electromagnetic waves is a reversible process. Whatever the strains suffered in a complex propagation medium by a wave radiated by a source (refraction, multiple scattering, reverberation), there always exists, theoretically, a dual wave able to travel in the opposite direction along the same complex paths, and which exactly converges with the initial source. The main interest of a TRM is to effectively create this dual wave, from an array of reversible (receiving and transmitting) antennas, A/D and D/A

(analog–digital) converters and electronic memories, and thus to be able to focus a wave energy through very complex propagation media. An acoustic time-reversal mirror has a surface made of many piezoelectric transducers, which alternately play the role of microphone and loudspeaker. The acoustic wave radiated from any source is first measured by all the microphones and recorded in electronic memories. Then in a second step (the time-reversal phase), all these memories are read again *in the reverse order*. More precisely, the chronology of the signals received by each microphone (not the succession of syllables) is reversed. The signals which arrived last are read first and vice versa. All microphones then go, in a synchronous way, to the loudspeaker mode and are fed by the “temporally reversed” signals from the electronic memories. This produces new initial radiation conditions, and because of the reversibility, the radiated wave has no other choice but to relive, step by step, all stages of its past life, back to the initial source. Of course, this type of mirror has a very different behavior from that of an ordinary mirror. A time-reversal mirror makes the “real” image of the source on itself, while an ordinary mirror produces a virtual image of the source.

The surprising strength of this technique has been verified in a wide variety of experimental situations, ranging from the ultrasound propagation of small wavelengths (millimeter) in the human body over distances of several decimeters, to the propagation of acoustic metric wave in the sea over dozens of kilometers, and recently to the propagation of electromagnetic centimetric waves over several hundred meters [FIN 97] [FIN 03].

### 15.1.2. Time-reversal of acoustic waves: principle

We consider the propagation of an ultrasonic wave in a non-dissipative and heterogenous medium, with a compressibility  $\kappa(\mathbf{r})$  and a density  $\rho(\mathbf{r})$  which vary with the observation point  $\mathbf{r}$ . By introducing the velocity of sound defined by  $c(\mathbf{r}) = (\rho(\mathbf{r})\kappa(\mathbf{r}))^{-1/2}$ , we obtain the propagation equation for a pressure field  $p(\mathbf{r}, t)$ :

$$\vec{\nabla} \cdot \left( \frac{\vec{\nabla} p}{\rho} \right) - \frac{1}{\rho c^2} \frac{\partial^2 p}{\partial t^2} = 0 \quad [15.1]$$

By observing the previous equation, we can see its specific behavior with respect to the temporal variable  $t$ . Indeed, it contains only one temporal operator that is a second-order derivative. This property is the starting point of the time-reversal concept. Indeed, one immediate consequence of this property is that if  $p(\mathbf{r}, t)$  is a solution of the wave propagation equation, then  $p(\mathbf{r}, -t)$  is also solution of the same

equation. This property reflects the invariance of the propagation equation to a time-reversal operation. However, this property is valid only in a non-dissipative medium. If the propagation in the medium is influenced by absorption phenomena, some temporal derivative of odd order may appear and the invariance by time-reversal is lost. However, it should be noted that if the absorption coefficient of ultrasonic waves is sufficiently low in the frequency range of the waves used during the experiment, the invariance by time-reversal remains valid.

This property of symmetry has been illustrated by Stokes in the classic case of reflection and transmission of a plane wave along a plane interface between two media with different sound speeds. Consider an incident wave of normalized amplitude 1 propagating from a medium 1 to the medium 2. We can observe a reflected wave of amplitude  $R$  and a transmitted wave of amplitude  $T$  (Figure 15.1a). Based on this configuration in which the pressure field  $p(\mathbf{r}, t)$  results from these three plane waves, Stokes tried to check if this experiment could be “temporally returned” or not. He used the fact that a time-reversal operation is equivalent for a plane wave to a reversal of the direction of the wave vector. Thus, the temporally returned solution  $p(\mathbf{r}, -t)$  can be described by a new set of three plane waves: two incident waves of amplitude  $R$  and  $T$ , respectively running from the medium 1 to the medium 2 and from the medium 2 to the medium 1, followed by a transmitted wave of amplitude 1 propagating in medium 1 (see Figure 15.1b). We can easily check that this new wave field is also a solution of the wave equation. Indeed, if we define the reflection and transmission coefficients of an incident wave coming from medium 2, the principle of superposition shows that the two incident plane waves generate four plane waves, two propagating in medium 1 with a resulting amplitude  $R^2 + TT'$  and the other two propagating in medium 2 with a resulting amplitude  $RT + TR'$ . An elementary calculation of the reflection and transmission coefficients  $R$ ,  $T$ ,  $R'$  and  $T'$  allows the checking of the following relationships:

$$R^2 + TT' = 1 \quad [15.2]$$

$$R + R' = 0 \quad [15.3]$$

This example shows that the wave equation can be directly interpreted as the time-reversed of the previous situation.

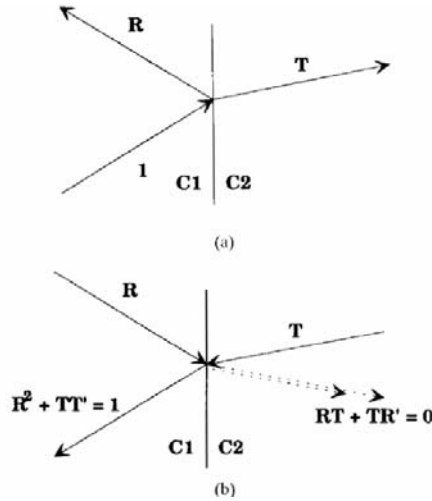


**Figure 15.1.** (a) Reflection and transmission of a plane wave at the plane interface between two media with different sound speeds; (b) time-reversal of situation (a)

As a matter of fact, these simple arguments can be generalized to any type of incident acoustic field and any geometry and/or heterogeneity of the medium. It is important to note that both relations written above are only valid if the reflected and transmitted plane waves have a real wavenumber  $k$  (i.e. purely propagative waves). In a more general situation, the incident field also contains evanescent components. These evanescent waves can be created by specific incidence angles or, for example, when an incident ultrasonic beam is diffracted by a medium with a compressibility  $\kappa(\mathbf{r})$  which contains spatial frequencies smaller than the wavelength. The evanescent waves can not easily be time-reversed since their direction is indefinite. The superposition of propagative and evanescent waves leads to a limitation of the time-reversal process. Because of the limited bandwidth of the incident field, some of the information is lost during the process of time-reversal.

### 15.1.3. Time-reversal cavities and mirrors

We return to the principle of an ideal experiment of wave time-reversal. The easiest thought experiment is to imagine a source of waves surrounded by a completely closed surface covered with piezoelectric transducers. The wave field radiated during the first step is measured and recorded by all transducers. For the second step, we impose this field in time-reversed chronology on the same surface. The surface now behaves as an emitter and then generates a time-reversed field, dual

to the initial field; this dual field converges exactly on the initial source, for both homogenous and heterogenous mediums (Figure 15.2).

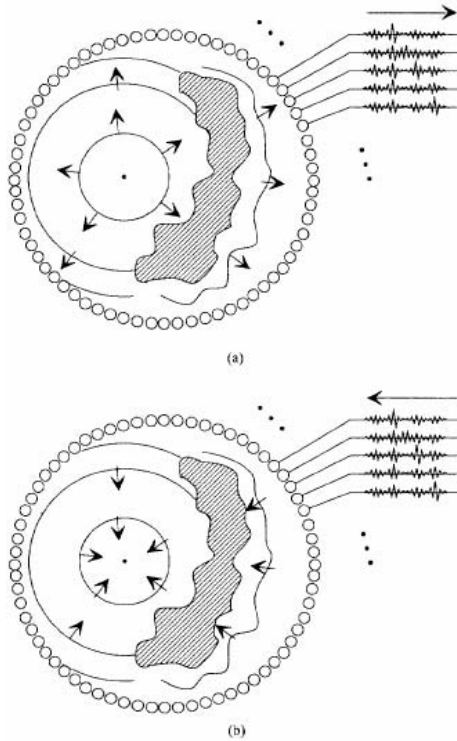


**Figure 15.2.** The concept of a time-reversal cavity. (a) Recording phase: the surface of a closed cavity is covered with piezoelectric transducers operating both in transmission and reception. A point source emits a wavefront propagating and being distorted by the heterogeneities of the medium. The distorted wave field is received by each element of the cavity. (b) Time-reversal phase: The signals are recorded, temporally reversed and re-emitted by the elements of the cavity. The temporally reversed pressure field propagates and refocuses exactly on the position of the initial source

In this way, we physically build what physicists call the “advanced” solution of the radiation problem. It is a dual solution of the “delayed” solution which is usually the only one observed. It is known that whenever we try to predict the radiation of a source, the time-reversal invariance of wave equations represents a serious problem for physicists. There are indeed, mathematically, always two possible solutions: one for which the field radiated by the source propagates as a divergent wave which reaches the observation points after the source has been turned on. This solution suits us perfectly because it verifies the causality principle and it is called the

“delayed” solution. In a medium with a uniform velocity  $c$ , this solution can be written in the form  $s(t - r/c)$  where  $s(t)$  is a function that depends on the temporal modulation of the source and  $r$  is the distance from the observation point to the point source. There is also a second solution that does not satisfy the causality principle: the “advanced” solution where the field radiated by the source reaches the rest of the space before the source is turned on, and which is written  $s(t + r/c)$  !!!! Although this solution seems perfectly absurd, it is important to know that major physicists as Feynman and Wheeler have, with some success, tried to interpret the theory of electromagnetic radiation by taking into account both advanced and delayed solutions.

Of course, in our case, everything is causal, and we build a solution that looks like the advanced solution: it is a wave that converges on the source instead of diverging from it, like the delayed solution. However, we need to make a small note concerning the outcome of the advanced solution. The field re-emitted by the time-reversal mirror looks for some time like a wave converging towards the source, but a wave *does not know how to stop* (it always has a speed) and when the convergent wave reaches the location of the initial source, it “collapses” and reverses in the form of a diverging wave. There is then an interference around the source between the converging and the diverging waves. It is no longer the advanced wave that is created, but *the advanced wave minus the delayed wave* (indeed, the diverging wave leaves with a sign opposite that of the convergent wave). If the wave used in the experiment is sinusoidal and contains a certain number of wavelengths, we can show very simply that a constructive interference is created around the point source between these two waves over a spatial area of half the wavelength. This is the diffraction limit. More precisely, for an initial point-like source emitting a brief radiation with a wide spectral content, the “reversed” field focuses on the source, but in the form of a focal spot whose dimensions are about half the minimum wavelength emitted.

The process of time-reversal focusing acts like an inverse filter of the transfer function of diffraction, which describes the propagation from the source to the points on the closed surface. However, we have observed that this inverse filter is not perfect, since we do not refocus on an infinitely thin spot corresponding to the initial point source. We can re-interpret this diffraction limit using the concept of evanescent waves. Indeed, the evanescent waves emitted by the source are not propagative and they are subject to a very fast spatial exponential decrease. So, they can not be recorded or time-reversed on the surface. These evanescent waves are clearly not reversible, since they would be subject to another spatial exponential decrease after reemission. Thus, the diffraction acts like a low-pass filter for the spatial frequencies, since the spatial frequencies corresponding to evanescent waves ( $>1/\lambda$ ) are lost during the propagation. We reach the classical limit of diffraction



here, which prohibits the focal spot obtained by time-reversal to become smaller than half the wavelength. Note that in order to achieve infinitely thin focal spots, below the limits of diffraction, it should be possible to prevent the divergent wave appearing, or at least propagating, after the converging wave front reaches the focus (the initial source point). That could be achieved by a new source located at the initial source location, and that we shall call an *acoustic sink* [ROS 02]. This source emits the time-reversed part  $s(-t)$  of the signal initially issued<sup>1</sup>. Rather than absorbing the incident radiation, this acoustic pit emits, actively, at the right time, a second diverging wave that yields destructive interferences with the normal diverging wave (phase opposition). These perfectly destructive interferences produced by the anti-noise approach between the two diverging waves lead to focus spots much smaller than the diffraction limit.

For practical purposes, a time-reversal cavity would be difficult to achieve and the time-reversal operation is done on a limited aperture known as the *time-reversal mirror* (TRM). Its limited angular aperture involves another low-pass filter for the angular frequencies that can be issued by the array. Its cut-off frequency is more restrictive than that due to the evanescent waves:

- In a homogenous medium, it depends on the angular aperture of the array and the result is a focal diffraction spot whose width is proportional to the product of the wavelength  $\lambda$  by the angular aperture  $F/D$  of the array (Figure 15.3).

- In a heterogenous medium, decomposition into plane waves is no longer really appropriate, and it is often difficult to predict the behavior of the TRM. It depends heavily on the nature of the heterogeneities of the medium. Thus, under certain configurations, A. Derode *et al.* showed that the focal zone of diffraction obtained by time-reversal can become narrower than in a homogenous medium, when a large number of random scatterers is placed between the TRM and the focus zone [DER 95]. The time-reversal takes advantage of the reverberations to increase the apparent angular aperture of the array.

---

1. Strictly speaking, the reversibility of the experience is shown by the invariance by time-reversal of the wave equation [1.36] in volume 1, which takes into account the term source  $S_{m0}(t)$ . It should therefore be logical to have  $S_{m0}(-t) = S_{m0}(t)$ . Otherwise, during the second phase of the time-reversal experience, we should not only reissue  $p(r, -t)$  on the borders of the cavity but also  $S_{m0}(-t)$  at the focus.

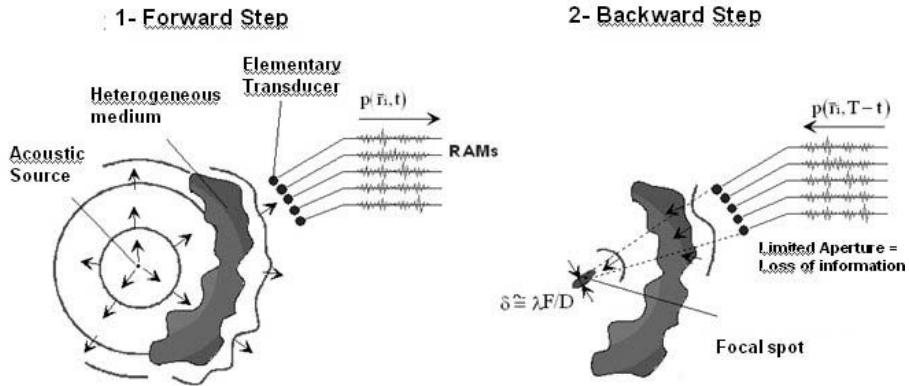


**Figure 15.3.** Principle of focusing by time-reversal using a limited aperture

#### 15.1.4. Time-reversal or temporal and spatial adapted filtering

In a heterogeneous medium, the technique of focusing by time-reversal is extremely robust compared with the traditional techniques of focusing by using time-delay laws. It can be shown mathematically that for any configuration of transducers, time-reversal is the optimal solution in a non-dissipative medium. Indeed, time-reversal focalization produces the temporal and spatial adapted filter of the transfer function between the array elements and the target.

The time-reversal concept is strongly linked to that of the adapted filter in signal processing. This well-known principle describes the fact that the output of a linear system with an impulse response  $h(t)$  is maximized when the input signal is  $h(-t)$ . The output signal of the linear system is then written  $h(t) \otimes h(-t)$ . This is an odd function whose maximum is reached at  $t = 0$  and is given by the total energy of the input signal.

We will show that for a given energy emitted by the transducer array, the solution obtained by time-reversal focusing is that which allows the maximization of the energy received at the target focal point. In order to do this, we will seek the optimal set of impulse signals transmitted by a set of transducers  $E_i$  located at  $r_i$  in order to focus at  $r_0$ .

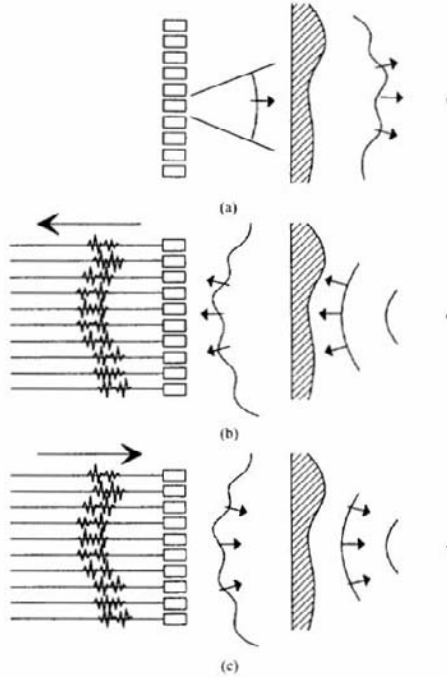


**Figure 15.4.** The three classic steps of the time-reversal process to focus in a heterogenous medium: (a) illumination of the medium by the array, (b) reflection by the target and recording of the signals received on the TRM, (c) time-reversal of these signals and re-emission throughout the array

As we can see in Figure 15.4, the process of time-reversal is made of three steps. During the first step, after having been illuminated by the transducer array, a point-like reflector located at  $r_0$  behaves like an active acoustic source. The electrical signal  $s_i(t)$  observed on element  $E_i$  of the array is given by

$$s_i(t) = h_i^{ae}(t) \otimes h_i(r_0, t) \quad [15.4]$$

where  $h_i^{ae}(t)$  is the acoustoelectric impulse response of the transducer that connects, during the emission, the electrical input signal to the normal displacement on the surface of the piezo-electric element and, during the reception, the acoustic force received by the sensor to the generated electrical signal (assuming here that this acoustoelectric response is the same in emission and in reception).  $h_i(r_0, t)$  is the diffraction impulse response connecting element  $E_i$  of the array at  $r_0$  and therefore characterizing the propagation in the medium. It was assumed here that the theorem of spatial reciprocity can be applied in the propagation medium, meaning that the

impulse response connecting the point  $r_0$  to element  $E_i$  is the same as that connecting element  $E_i$  to the point  $r_0$ .

During the second step of the process, these signals are stored in memory for each element of the array. This step is illustrated in Figure 15.5 for a homogenous medium and in Figure 15.6 for a heterogenous medium. Note that in the latter case, the signals on each element of the array can have completely different temporal forms.

During the third stage of the process, these signals are temporally reversed and we get a new electrical signal issued:

$$h_i^{ae}(T-t) \otimes h_i(r_0, T-t) \quad [15.5]$$

where  $T$  is a temporal constant introduced in order to preserve the causality of the experiment. These signals are then retransmitted through the same elements of the array. In order to calculate the total acoustic field obtained at the focal point  $r_0$  of the TRM, we first consider the individual contribution of each transducer  $E_i$ . This field issues from the convolution product of the applied electrical signal  $h_i^{ae}(T-t) \otimes h_i(r_0, T-t)$  with the acoustoelectric impulse response in transmission of the concerned transducer and the diffraction impulse response characterizing the propagation up to  $r_0$ :

$$h_i^{ae}(T-t) \otimes h_i(r_0, T-t) \otimes h_i(r_0, t) \otimes h_i^{ae}(t) \quad [15.6]$$

As shown in the previous equation, the input electrical signal (the time-reversed signal) is the optimal input signal for the linear system defined by the two consecutive impulse responses  $h_i^{ae}(t)$  and  $h_i(r_0, t)$ . The maximal pressure field is received at  $r_0$  at time  $T$  regardless of the position of the element  $E_i$  (Figures 15.5 and 15.6). The total pressure field created at  $r_0$  by the TRM is obtained by the simultaneous transmission of all time-reversed individual pressure fields. We then obtain at  $r_0$  the summation of each individual contribution:

$$\sum_i h_i^{ae}(T-t) \otimes h_i(r_0, T-t) \otimes h_i(r_0, t) \otimes h_i^{ae}(t) \quad [15.7]$$

All the individual signals reach their maximum at the same time  $T$  and therefore interfere constructively. This process of adapted collective filtering produces a maximum field at  $r_0$  for a fixed energy on input of the array. This process is illustrated in Figures 15.5 and 15.6.

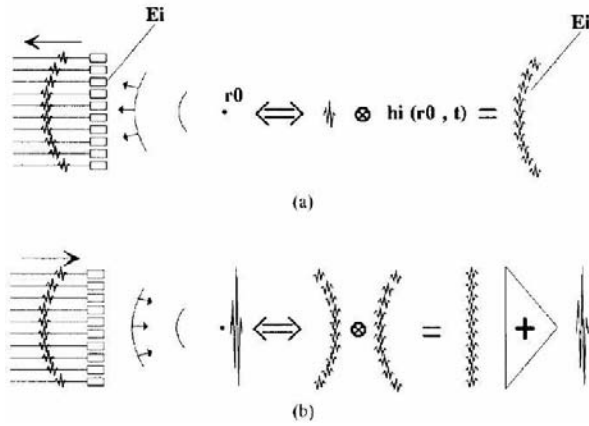


**Figure 15.5.** Concept of adapted filtering directed during time-reversal focusing in homogenous medium. (a) On the left-hand side of the figure, the spherical wave coming from the source is received by the array. On the right-hand side of the figure, the signals received by each individual element correspond to equation [15.4]. (b) The left-hand side represents the propagation of the time-reversed field to the target. The right-hand side represents the mathematical construction of the individual pressure fields created at  $r_0$ . They result from the convolution product of the two wave fronts described in equation [15.6]

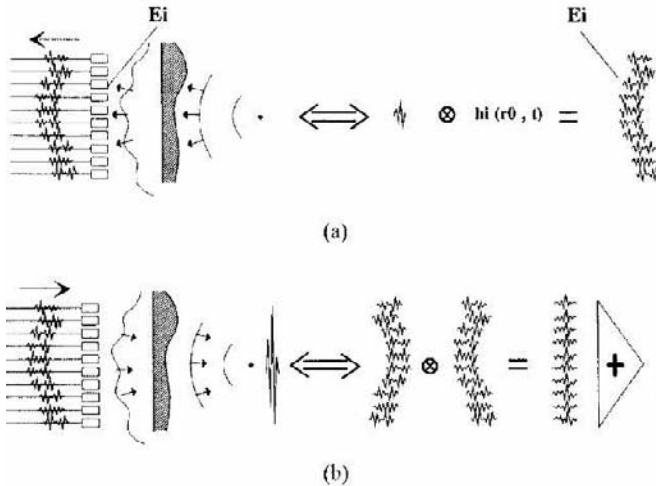


**Figure 15.6.** Concept of adapted filtering directed during time-reversal focusing in a heterogenous medium. (a) and (b) are similar to Figures 15.5 (a) and (b) except for the presence of the heterogenities which totally distort the initial spherical wavefront coming from the source. The signals received on the array are very complicated and the signals received on each element can have completely different temporal forms. (b) In accordance with equation [15.6], the individual waves reach their maximum at the same time at the initial source point

It should be noted here that this result is valid for any geometry of the transducer array. For example, a transducer array may have suffered an undesired geometric distortion during its design. The time-reversal process is a self-adaptive method which can correct these effects. Beyond this type of correction, it should be noted that the analysis that has been done is only based on the theorem of spatial reciprocity. In this sense, it is therefore valid for any heterogenous medium, whatever its complexity. In this case, individual contributions can have completely different individual forms, time-reversal ensures that their maximum will always reach the point  $r_0$  at the same time  $T$ . We have shown that time-reversal achieves an adapted temporal filter of the transfer function between  $r_0$  and the transducer array. A similar demonstration was carried out in the spatial domain by Tanter *et al.* [TAN 00].

#### 15.1.5. *The iterative time-reversal*

One advantage of the technique of time-reversal focusing is that it is very easy to choose the temporal origin and the duration of the signals to be re-emitted. This is done by defining a temporal window that selects in the memories the signals that will have to be time-reversed. When the medium of interest has several reflectors, the time-reversal process does not directly allow focusing on one of the reflectors only. Indeed, if the medium contains, for example, two targets of different reflectivity (Figure 15.7), the time-reversal of the echoes that are coming from these two targets will produce two wavefronts which will refocus simultaneously on the two targets. The mirror produces the real acoustic image of the two targets on themselves. The wavefront with the greatest amplitude illuminates the more reflective target, whereas, meanwhile, the wavefront with the lowest amplitude illuminates the second target. It is assumed here that there is no multiple scattering between the two targets. After the first illumination by time-reversal, the wavefront reflected by the second target is still lower compared with that of the main target. Thus, by iterating the time-reversal process, it will be possible to progressively select the target of greatest reflectivity [PRA 91]. The process converges and eventually produces a wavefront focusing strictly on the main target. Once the beam is focused on this target, iteration does not change the result. We have created a first “invariant” for the time-reversal focusing process. It should be noted that the process will converge only if the two targets are resolved, meaning that the first target is located outside the focal spot of the second target.

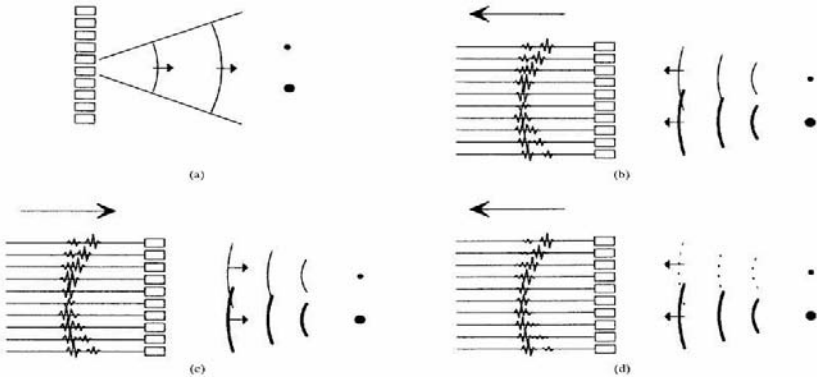


**Figure 15.7.** Principle of iterative time-reversal. (a) a first wave illuminates the two targets, (b) the reflected waves are recorded by the array, (c) then re-issued after being time-reversed, (d) the new reflected waves are recorded before a new time-reversal operation.

After a few iterations, the process converges to the emission of a wavefront focusing strictly on the main target

We can subtract the wavefront corresponding to the first invariant of the set of echoes in order to no longer illuminate this target, and a new iteration will allow us to select the second target (in terms of the reflectivity). There is then a second invariant of the time-reversal operation etc. This approach can be conducted using hardware, and gives a method of detecting all targets in a medium very quickly, and of finding all the optimal wavefronts focusing on each target. The big advantage of this method is to allow the best correction of all aberrations [MON 04]. Another approach has been developed by C. Prada. Rather than physically performing all these iterations in the medium, we exploit the linearity of the described operations in order to perform all these operations using software. We first measure all the inter-element ultrasonic impulse responses collected by the transducer array: if the array has  $N$  transmitter/receiver transducers, we measure  $N^2$  signals. Then, the method consists of simulating the time-reversal operation, and of looking for these invariants by calculating the “eigenvectors” and the eigenvalues of a matrix which is deduced from all the impulse responses. This is the D.O.R.T. method (French acronym for *Décomposition de l'Opérateur de Retournement Temporel* – Decomposition of the time-reversal operator) [PRA 94].

From these various principles, we can develop some methods of detecting targets, and even in some cases methods of destruction. We can also develop methods of classification and imaging. In the first case, the iterative method is faster to implement and has been tested in the domain of lithotripsy (destruction of kidney stones) and non-destructive testing. Some focalization-pursuit and very precise biological kidney stone destruction systems have been developed that reliably focus

an impulse wave of high amplitude (1000 bars) on a stone that moves with the breathing of the patient.

Concerning classification and imaging, the D.O.R.T. method is more appropriate, and it is the subject of multiple researches in underwater acoustics, non-destructive testing and electromagnetism. The study of the spectrum of the temporal operator of a complex target gives very rich information on the target, and this line of research is being developed by several teams interested in the classification of targets in acoustics and electromagnetism.

## 15.2. Bibliography

- [DER 95] A. DERODE, P. ROUX, M. FINK, "Robust Acoustic time reversal with high order multiple scattering", *Physical Review Letters*, Vol 75, 23, p 4206-4209, December 1995.
- [FIN 97] M. FINK, "Time reversed Acoustics", *Physics Today*, 20, p.34-40, March 97.
- [FIN 03] M. FINK, G. MONTALDO AND M. TANTER, "Time reversal acoustics in biomedical engineering", *Annual Review of Biomedical Engineering*, Vol 5, 2003.
- [MON 04] G. MONTALDO, M. TANTER, M. FINK, "Revisiting iterative time reversal: real time detection of multiple targets", *J. Acoust. Soc. Am.* 115 (2), p 776-784, 2004.
- [PRA 94] C. PRADA, M. FINK, "Eigenmodes of the time reversal operator : a solution to selective focusing in multiple target media", *Wave Motion*, Vol 20, p 151- 163, 1994.
- [ROS 02] J. DE ROSNY, M. FINK, "Overcoming the diffraction limit in wave physics using a time-reversal mirror and a novel acoustic sink", *Physical Review Letters* 89 (12), p 124301, 2002.
- [TAN 00] M. TANTER, J.L. THOMAS, M. FINK, "Time reversal and the inverse filter", *J. Acoust. Soc. Am.*, 108 (1), p 223-234, July 2000.



## Chapter 16

# Introduction to Inverse Scattering in Acoustics and Elasticity

This introduction to inverse problems for acoustic or elastic waves does not aim to be an exhaustive presentation of their theoretical and numerical difficulties, nor of their applications in fields of interest – including those of evaluation and non-destructive testing (NDT) of artificial structures, or the characterization of the human body, two topics among those discussed in detail in other chapters of this book. We only wish to highlight general elements that can be found in a relevant way in many of the inverse problems we can meet in practice. Perhaps more importantly, we also wish to give to the interested reader some guidelines for further research, based on a list of publications from the recent international literature, in addition to some examples from different works to which the authors have been contributing in acoustic and elastic topological identification, an investigation which we believe to be useful for our purpose here.

### 16.1. General framework

Referring to the thorough analysis conducted in [SAB 00], the problem addressed can be summarized as follows: let us consider a set of characteristic parameters of a system, artificial or natural,  $\mathcal{P}$  (density, Lamé parameters, compression or shear wave celerities, or any other relevant factor) linked to a set of observables  $\mathcal{O}$  (displacement, pressure, etc.) through “laws of nature”  $\mathcal{L}$ . Let  $\mathcal{M}$  be a mathematical model, more or less sophisticated, which would be the best description of these laws with equations or systems of equations (differential, integrals, partial derivatives and combinations), and

with appropriate boundary and/or initial conditions. Then, the solution of the “direct problem” consists of calculating  $\mathcal{O}$  from the known  $\mathcal{M}$  and  $\mathcal{P}$  sets; while the “inverse problem” consists of finding the parameters  $\mathcal{P}$  from the measurements  $\mathcal{O}$  and from the laws  $\mathcal{M}$

$$\mathcal{O} = \mathcal{L}(\mathcal{P}) \simeq \mathcal{M}(\mathcal{P}). \quad [16.1]$$

As stated, many fields of application exist, for example:

- geophysics, and civil or environmental engineering [FOK 93, HOO 95], where the main issue is the identification of natural or artificial buried structures from elastic (seismic) measurements, acquired on the surface or in a borehole (there is also obvious interest in similar situations in underwater acoustics);
- non-destructive testing and evaluation [LEO 02, Sch 02a, KUN 03], where the objective is to characterize defects (cracks, inclusions or corrosion, delamination, burns, etc.) affecting a part or a set of pieces of metal, or composite, which may modify the nominal behavior or affect the safety during the use of this material;
- biological media imaging [SCH 02b], particularly within the human body to detect various abnormalities (such as inclusions) affecting it, or to detect via maps of elastic parameters an abnormal behavior of the tissues or other significant elements;
- the characterization of materials [KUN 03], which is focused on the evaluation of their mechanical properties from the response provided to a known solicitation.

From this we already see we are facing a huge subject, which is testified by [SAB 00], as well as [BON 99]. Thus we will now only consider the specific issue of identification, characterization and/or imaging of complex passive objects at rest, active sources or vibrating bodies (in terms of acoustics and vibro-acoustics) being henceforth excluded.

## 16.2. Inverse problem of wave scattering

The generic problem of wave scattering, as envisaged in the following, can be presented as follows (Figure 16.1). We consider one or more objects or obstacles (we could also use terms like inhomogeneities, inclusions, defects and so on) of limited spatial extension, and of characteristic parameters  $\mathcal{P}$ , found in a well-known host environment, whose parameters can be estimated beforehand. This host environment can be finite, semi-infinite, or infinite, with a simple or complex configuration. The whole system is excited by one or more sources with known characteristics. The so-called secondary (or scattered) fields or displacements (the observable  $\mathcal{O}$  referring to equation [16.1]), resulting from the interaction between the wave and the host medium, including all obstacles, are then collected by appropriate receivers. We consider here the framework of acoustics or elasticity and assume that the variations are small enough that the perturbations induced by the objects are linear with respect to the excitation.

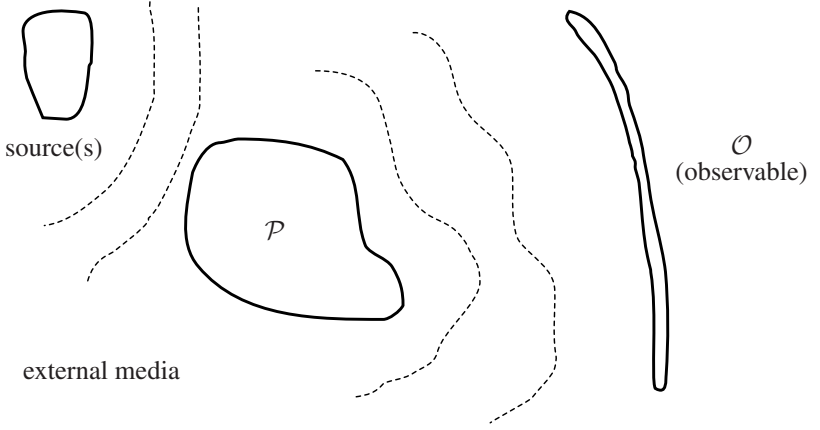


**Figure 16.1.** *The usual wave diffraction problem*

As a matter of fact, the information concerning the investigated properties of these objects (locations, sizes, shapes, parameters of constitutive materials, etc.) appears to be present in coded form in the signal(s) acquired by receivers. Their “decoding”, i.e., the solution of the *inverse problem*, can extract from this (these) signal(s) the parameters of interest, occasionally with the higher objective that consists of their quantitative characterization, or, often in a more realistic way (with a lesser degree of complexity), in order to produce images that properly represent these objects.

In an optimal situation, the knowledge of the “inverse laws of nature”, which we note here  $\mathcal{L}^{-1}$  (and its approached mathematical model  $\mathcal{M}^{-1}$ ), should enable the reconstruction of the parameters of interest  $\mathcal{P}$  by applying a relationship similar to [16.1] and given by

$$\mathcal{P} = \mathcal{L}^{-1}(\mathcal{O}) \simeq \mathcal{M}^{-1}(\mathcal{O}). \quad [16.2]$$

However, in practice, the mere existence of  $\mathcal{M}^{-1}$  is not guaranteed (e.g., the same observable  $\mathcal{O}$  can be obtained for several values of  $\mathcal{P}$ ), and obtaining an explicit formulation of  $\mathcal{M}^{-1}$ , if any, is possible only in very limited cases, which reduces its use.

So, some other schemes have to be implemented to overcome this difficulty. The most frequently chosen path is to solve equation [16.2] via an iterative optimization scheme (Figure 16.2) which consists of finding the “best” possible solution, without ever explicitly calculating  $\mathcal{M}^{-1}$ . This scheme enables the determination of an optimal set of parameters,  $\mathcal{P}_{\text{optimal}}$ , so that the difference between the measurements  $\zeta$  and the solution  $\mathcal{O} = \mathcal{M}(\mathcal{P})$  is minimum:

$$\mathcal{P}_{\text{optimal}} = \underset{\mathcal{P}}{\text{Argmin}} \left( \text{mes} [\zeta - \mathcal{M}(\mathcal{P})] \right), \quad [16.3]$$

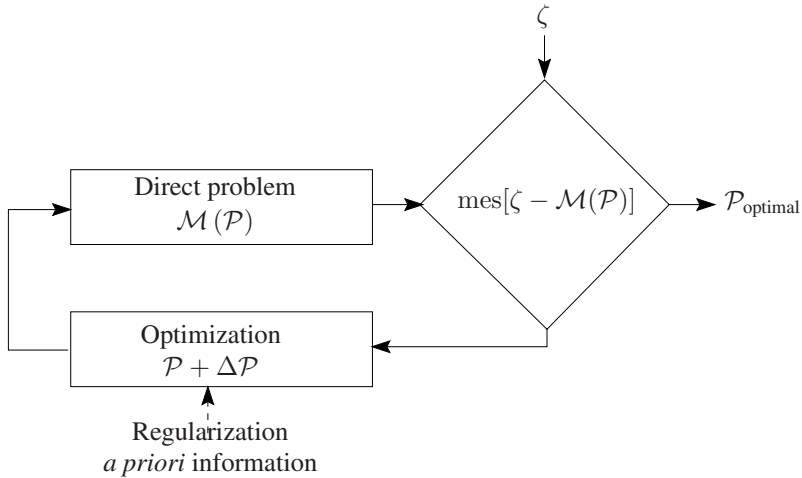


**Figure 16.2.** Solution scheme for the inverse problem, optimizing the fit of the measured data to the theoretical solution

where  $\text{mes}[\cdot]$  is a judiciously chosen measurement of this discrepancy (this term describing the fit of the measured data to the theoretical solution is often called cost function, objective function, goal function, etc.). Of course, the choice of this cost function depends on the solution sought, the application proposed, etc.

The successive steps of the inversion process can be sketched as follows: (i) choice of an initial set of parameters  $\mathcal{P}$ ; (ii) solution of the direct problem; (iii) calculation of the discrepancy between the data  $\zeta$  and the solution of the direct problem, knowing that if it is deemed sufficiently small compared to a chosen criterion, the process stops and the corresponding solution  $\mathcal{P}_{\text{optimal}}$  is obtained; otherwise, the process goes on; (iv) optimization process, in which a correction is carried out on all parameters so the discrepancy should be narrowing. At this stage of the process, constraints on corrections can be incorporated in order to favor certain solutions on the basis of *a priori* information. Then the process returns to stage (ii) and repeats.

These inverse problems are not linear since the observed fields do not linearly depend upon the parameters of the objects. They are also ill-conditioned problems: without discussing the concept in the required detail [TIK 74], existence, uniqueness and continuity of the inverse solution with respect to the data cannot be ensured simultaneously. From a practical point of view, this means in particular that some small variations in the data set can yield large changes in the calculated parameters. In addition to these fundamental obstacles, we also must not forget some more classic difficulties, related to the imperfections of the data itself (random or systematic errors), and of the models.

Thus, the chosen model yields an approximated description of a real situation, and the inversion can for example be carried out by neglecting a significant part of the interaction phenomena occurring between the host medium and the objects, such as multiple scattering. Under such approximations, linear models can be successfully applied. For example, it is often true when the wavelengths are either large or small, compared to a relevant size of the objects. We will get back to this matter later.

Taking into account the above, the key focus is the construction and implementation of resolution methods for these inverse problems that lead to solutions:

- which are precise enough to be useful and stable with respect to the errors from the models or from the data, which is ensured through adjustments (typically operating on the norms of the solutions, their derivatives, or some special functions resulting from the application of particular operators on these solutions), and the incorporation before and/or during the inversion process of some *a priori* information on objects (compactness, positivity, connectivity, limited amplitudes, etc.);
- which can be obtained fairly quickly, especially in the case of complex structures or of important size (which depends, of course, on the computers used, and on the chosen numerical methods). Their construction method must also take into account the form and the limitations of data as precisely as possible, but be simultaneously broad enough to remain useful in the real situations encountered, those not necessarily being nominal.

### 16.3. Direct problem

The resolution of the corresponding direct problems is a necessary first step, required in any study of inverse problems. It allows:

- a validation of the formulation of the acoustic or elastic quantities (fields, displacements, or any associated function, including potentials), chosen by comparison with synthetic results (described in the literature, for example), or experimental measurements. The latter may then have been obtained either under controlled laboratory conditions (a key step in practice), or by on-site measurements (with all the constraints of the real world);
- the acquisition of synthetic data that will provide a wide variety of feasibility tests, robustness or accuracy of the inversions (we often use the term “numerical experiment”);
- a better understanding of the physical interaction phenomena that are involved, including, in ideal situations, the identification of key parameters of the objects (and of their hosts); parameters that can be expected to be those aimed by the inversion process, or those only that can be retrieved effectively.

In addition, such a work requires the development of fast and efficient calculation modules that can be used during the inversion process. Indeed, a significant difficulty

with most solutions of inverse problems lies in the need for repetitive (and usually expensive in terms of computation time) calculations of the quantities modeled for some given environments.

It is important to note that strong formulations are most frequently used, as a common starting point for the direct problem and for the inverse problem, including intermediate cases resulting from approximations, like the Born approximation, or the Neumann series or extensions (sometimes used in the low-frequency range [DAS 00]), or the Kirchhoff formulation (a high-frequency approach) [LAN 02b]. These formulations are based on the use of Green functions, which can either be scalar (acoustic fluid propagation medium) or tensor (solid elastic propagation medium), and which are obtained as solutions to properly set differential systems, including specific boundary conditions (on the boundaries of the objects themselves, of the host medium, and naturally at infinity). These Green functions generally lead to the formulation of the scattering phenomenon via integral equations, e.g., Lippmann-Schwinger integral equations.

Of course, direct calculations can also be based on weak formulations that lead to finite-element methods and their multiple variants and extensions, emphasizing that the classical works of [HOO 95] highlighted the equivalence of these two types of representations, and the similarities with traditional numerical techniques based on them, i.e. moment and finite-element methods.

It is important to emphasize here that nothing forbids the use of alternate techniques such as finite-difference methods and variants and/or extensions, especially in the case of complex environments (in terms of geometry, of distribution of the electromagnetic or elastic parameters) for which either the Green solutions are unknown or too complicated to obtain, or the finite-element method proves to be inappropriate or too costly to implement.

## 16.4. Optimizations

Here we limit ourselves to the description of the main approaches, including advantages and disadvantages. We then provide the reader with some references that we consider pertinent in this domain.

First, recall that the purpose of optimization in an inversion process consists of finding, inside a restricted search space described by the set of possible solutions, the particular solution that optimizes the adequacy of the data with the theoretical solution (thus, the particular solution that minimizes the cost function). Of course, the more complex the problem, the more difficult the search for the optimal solution.

One possible approach is to browse the entire search space, to calculate every possible solution of the corresponding cost function (which requires the solution of

the direct problem every time), and finally to retain the solution leading to the lowest cost function. It is obvious that this method is expensive in terms of calculation time and becomes unrealistic in the case of problems of large dimensions, or in the case of parameter spaces  $\mathcal{P}$  having large dimensions (large number of degrees of freedom).

This is the reason why some optimization methods have been developed that can be divided (at least grossly speaking) into two classes called “global” and “local” optimizations. We give here a short description of these two classes.

- *Local optimization*: these methods are based on the idea that, starting from an initial, well-chosen solution, the direction of the displacement in the space of solutions to estimate a better solution is obtained from the estimation of the gradient of the cost function with respect to the parameters. A fairly rapid convergence process often results. However, these methods have two major limitations: (i) the choice of the cost function, which must be differentiable with respect to the parameters; (ii) the known risk that the process converges onto a local minimum of the cost function. In this case, the algorithm is stuck at this local minimum, it fails and cannot converge to the desired global minimum. Among many books on optimization, let us mention [BON 97].

- *Global optimization*: one of the oldest methods is the Monte Carlo method. It consists of a random walk inside the space of possible solutions, where at each explored solution, the corresponding cost function is evaluated and compared to the best solution already obtained, keeping the new solution if it provides a lower cost. The process is repeated until a stopping criterion is met. Such a method has the disadvantage that each random possible solution is independent on all previously explored solutions. Thus, other methods have been developed in order to take into account the previously obtained information when a new solution is proposed. Among them, we should mention simulated annealing (based on the theory of thermodynamics) and genetic algorithms (using the theory of evolution of a population in a given area). These two well-known methods are open to many variations and adaptations [MIC 97].

As might be expected, approaches combining global optimization and local optimization have been proposed, combining the ability to browse the space of possible solutions and the rapid convergence of these two optimization classes.

In addition to this classification of minimization algorithms into two main families, some new distinction can be proposed depending on the information expected by the user.

- *Cartography*: the search area is divided into 2D pixels or 3D voxels in which the physical parameters are assumed constant; in all the following, we use the term “pixel” for simplification. The gradient algorithms therefore estimate the value of each parameter within each pixel, and then produce a map that describes the variations of the physical properties of the proposed setting. A still relevant illustration of the gradient methods used in acoustic and electromagnetic inversion is proposed

in [VAN 97]. While most of these algorithms solve a non-linear problem using the solution of successive linear problems (the Newton-Kantorovich method, and its equivalents or variants, such as the distorted Born method, and the iterative Born method), some are directly developed to take into account the non-linearity of the problem (the conjugate-gradient method, the modified gradient method, and the contrast-source inversion method, limiting us to the best-known methods in the specialized literature; each of these methods can be of course extended with specific additions; each method is also characterized by specific pros and cons).

– *Contour reconstruction*: Unlike cartography, the contour reconstruction methods (a line in 2-D, a surface in 3-D) aim at determining the boundaries of obstacles, those being considered as homogenous or at least made of a set of homogenous parts. These boundaries evolve in space with the calculations of shape gradients, obtained in most cases from the solution to a wisely chosen problem, called the “adjoint problem”. Nowadays, these methods are rather classical ones. They are based on electromagnetic or elastic contour integral formulations, for which the unknown parameters are coefficients that describe the boundaries of the unknown obstacles. One of the major limitations, however, is that the number of obstacles to be built (or at least an upper limit of that number) must be known in advance. Therefore, new methods have recently been developed to enable, if necessary and in a natural fashion, the appearance or disappearance of obstacles. Such common methods are controlled evolution methods, based on level sets. In practice, these methods combine two approaches. The first is based on the work described, for example, by [SET 99], leading to a representation of the boundary of an obstacle of unknown topology using the zero level of a level-sets. [SAN 96] is a pioneer investigation of this approach in the field of inverse scattering problems. The second method is based on works on velocity methods, widely considered in the design of optimal shapes [DEL 01, SOK 92]. Finally, we can change the contour, using the global evolution of the level set, involving topological derivatives throughout the search domain, optimizing its shape via an adequacy criterion to the training data (e.g. including judicious constraints on the perimeter or surface, and/or the area or volume of the obstacle(s)).

The choice of search parameters is a major difficulty in solving inverse problems. This choice is based on a balance between the expected and/or desired speed of the algorithms, the complexity of the model used, and the desired accuracy of the solution. While most of the work done here aims at complete characterization (with a few approximations, or even better with no approximations), several paths leading to approximate solutions can be followed:

– *Search of an equivalent obstacle*: the obstacle being investigated is replaced by a canonical equivalent obstacle (circular cylinder, ellipsoid, and its degenerated forms – the sphere is frequently the only one considered – or other shapes adapted to the application), canonical obstacle whose position, physical parameters and relevant geometric descriptors are to be determined in a more or less complex way, as illustrated for example by [WIR 02] and cited references.



– *Search of equivalent sources*: the obstacle being investigated is replaced by an equivalent set of discrete sources or by a distribution of equivalent sources whose positions and amplitudes contain, in more or less complex forms, electromagnetic, elastic, or geometric information that characterize the obstacle; an abundant literature refers to this approach, including, among other pioneer contributions, [ANG 97]. The reader may also refer to [LAM 00] for an application in shallow underwater acoustics.

### 16.5. Other approaches

In addition to these techniques focused on the solution of non-linear inverse problems, we can mention some others, including diffraction tomography or filtered backpropagation and variants for which there are many recent references [PEY 96, LAN 02a]. These techniques are based on linearized versions of the equations to be considered. This linearization of the equations is mostly done within the Born approximation framework in the case of scatterers with a low contrast of physical parameters with respect to the environment (weakly diffractive). We also use the Kirchhoff approximation (used in physical optics) in the case of scatterers that can be considered non-penetrable (very high contrast of the parameters with respect to the environment). These formulations lead to fast solution algorithms, mostly involving fast Fourier transforms (measurements along straight lines or in planar surfaces).

Recently in [COL 96], an original method for the reconstruction of the obstacle boundaries was proposed, entitled *linear sampling*. Originally proposed for the reconstruction of the boundaries of impenetrable obstacles from the scattered far field, it is based on a linear relationship between the far field and a gauge function, the norm of which tends towards infinity on the contours of the obstacles. Then, the aim of the method is to find all points for which this norm is infinite. Many extensions have followed this initial work (including factorization methods), particularly in the case of near field inverse problems [FAT 04]. In connection with this, and originally highlighted by [CHE 01], we also note that we can address the problem of the localization of quite small scatterers (small compared to the wavelength used to explore them) with numerous established or developing works, particularly on time reversal (including a recent tutorial [FIN 01]) and/or about approaches involving the MUSIC (*multiple signal classification*) algorithm, as illustrated by [KIR 02, AMM 05].

Finally, the case of limited environments, for which complete data on the boundaries (Dirichlet-Neumann boundary conditions) are available, can be treated using the method based on *reciprocity violation*. It is based on the fact that two acoustic states are linked together by a reciprocity relationship involving integrals on all boundary contours of the environment considered. In the absence of an obstacle, that identity holds true for external measurements and for any state (known as *adjoint*) satisfying the wave equations. A violation of this reciprocity principle thus indicates the existence of an object (simple or multiple) to be identified. A judicious

choice of the adjoint state enables us in some cases to extract some information on the obstacle by explicit calculations. For example, a recent development [BUI 04] has shown that the convex hull of the obstacle can be calculated from assessments of the instantaneous reciprocity violation, for adjoint fields, such as properly chosen planar propagative waves.

## 16.6. General configuration

It is worth mentioning that many inversion studies are limited to a generic configuration, which is often chosen as significant local idealization of the structure to be tested. The generic configuration is also often used to set some assumptions or concepts, the application coming later.

Indeed, the host environment is frequently assumed to be uniform in parts, such as homogenous layers separated by planar parallel interfaces; circular cylindrical tubes, or even spherical cavities or spherical blocks, can also be relevant. The sources that create the sound illumination (remember that we consider an active situation) can be, as already indicated, either plane and generated at infinity, or localized. Line sources, point-like sources and dipoles considerably simplify the analysis, but more sophisticated radiating devices, such as linear or surface arrays, must also be considered. They are located either on the first interface, or at some finite distance from it (including the possibility of being in direct contact with it), or inside the host medium (inside a particular layer medium for example). The receivers (limited number of receivers) provide access to the scattered field, which is therefore linked to the objects buried in the host medium. They are also located either on the surface or within the host environment.

The data obtained are described in the literature as being *aspect-limited*: in summary, it is not possible to turn around the whole obstacle. To partially compensate the loss of information resulting from this limitation, measurements are performed (as far as possible) for several harmonic frequencies (within a given bandwidth in the impulse system), and for sources and receivers having several geometries, leading to mono-, bi- or multi-static experimental setups, with a more or less specific coverage in space and frequency.

As a consequence of this limited aspect, let us consider theorems for the uniqueness of inversions. Usually, these theorems, applied to acoustics, are focused on uniqueness from scattering patterns associated to the obstacles [COL 98], with some subtle (and largely discussed) extensions to elasticity, also including the two fundamental cases of (i) the crack and (ii) the inclusion of planar section or finite volume. They appear to be only known in the unrestricted configurations of scattering objects in a (free) homogenous propagation medium. This increases the complexity of interpretation of the inversion results. Meanwhile, the case of a stratified medium instead of a mainly homogenous half-space increases the complexity of the

mathematical formulation, and of the numerical computation of the Green functions or Green tensors, on which strong formulations, mostly used as previously indicated, are based.

## 16.7. Illustrations

### 16.7.1. *Controlled evolution of level sets*

The following description is based on [RAM 02b]. For a more sophisticated analysis, the reader could refer to fundamental publications such as [RAM 02a] and abundant references therein.

We consider a homogenous cylindrical object  $\Omega$ , with a planar section of arbitrary (not necessarily connected) yet sufficiently smooth boundary contour. This object is assumed to be fully buried inside a domain  $\mathcal{D}$  of space (free, half-space, slice of material) and illuminated by sources operating in the harmonic system. The field is collected by suitable receivers, providing a certain set  $\mathcal{S}$  of field values  $\zeta$ . The analysis is applicable in the case of TM or TE polarization in electromagnetics, and also in fluid acoustics. In this latter situation, the variations of the velocity of compressional waves (or the variation of the compressibility) can be described through the introduction of a contrast function  $\chi$  of the appropriate quantity (this contrast function can be a complex number) that is zero outside the object. The boundary conditions in this case are written as transmission conditions (an impenetrable object will be modeled through the introduction of heavy losses inside it). Consequently, some domain integral equations (rigorous and based on the application of the Green theorems) yield expressions of the scattered fields, denoted as  $U_d$ , in the measurement domain  $\mathcal{S}$ , those being functions of the fields  $U$  existing in the domain  $\mathcal{D}$  (observation equation), the latter themselves solutions of state equations, such as those of Lippmann-Schwinger.

The solution method itself is implicit, and is based on a fixed Cartesian grid space (allowing the pre-calculation of Green discrete functions, the numerical calculations then being carried out by applying a method of moments to the integral wave equations) and time (with some possible adaptive choices of this parameter). It calculates the temporal evolution at time  $t$  of a function of level sets  $\phi$ , the level 0 now defines the boundary contour  $\Gamma_t$ . The negative values of this function are associated with points located inside the domain  $\Omega_t$ , whereas positive values correspond to points located outside  $\Omega_t$ . This applies at any time  $t$ .

The existence of a velocity field  $V$  for the deformation of  $\Omega_t$ , normal to that contour  $\Gamma_t$  (the object or the parts of the object are closed, only normal velocities are then taken into account), therefore means that  $\phi$  satisfies an Hamilton-Jacobi evolution equation [SET 99], in space  $\mathbf{x}$  and in time  $t$ :

$$\frac{\partial}{\partial t} \phi(t, \mathbf{x}) + V(t, \mathbf{r}) |\nabla \phi(t, \mathbf{x})| = 0, \quad \mathbf{r} \in \mathcal{D}. \quad [16.4]$$

It remains to build velocity  $V$  that transforms an initial domain  $\Omega_0$  into a more satisfying  $\Omega_t$ . In other words, the cost function  $J(\Omega_t)$ , defined as the norm  $\|U_d - \zeta\|_S^2$  of the difference between the measured and calculated data on  $S$ , has a decreasing amplitude, or is such that  $dJ/dt$  is negative, up to numerical uncertainties and discretization errors. Some penalty terms for the area and/or perimeter can be incorporated into the cost function, and this induces suitable changes of the velocity  $V$ . This construction yields the derivative of  $J$  at time  $t$ , through the construction of a minimum-maximum of a Lagrangian  $\mathcal{L}$ , avoiding a heavy derivation of the field with respect to the deformation of the domain. Indeed, the control theory, e.g. [SOK 92, DEL 01], shows that the derivative for which we search is equal to the partial derivative of the Lagrangian evaluated at its saddle point (proved unique in our particular case), this derivative calling for a shape gradient  $g$ , originally defined on the contour and then extended to the whole search domain. This extension was originally completed in a heuristic manner, but later validated through the concept of *topological derivation*. This concept is still up to date in electromagnetics as well as in elasticity, as is illustrated by the example presented in the next section.

Thus, in the case of a contrast of velocity of compressional waves between the fluid environment and the object (transmission conditions),  $g$  simply boils down on the contour to the product  $\chi \Re(Up)$ , where  $\Re$  designates the real part,  $U$  the direct state (i.e. the solution of the direct scattering problem to be solved), and  $p$  the adjoint state that satisfies the same propagation and transmission equations as the direct state, but whose source is made of the complex conjugate distribution of the difference between data and the fields associated with the object effectively built at the considered time,  $U_d - \zeta$ , on  $S$ .

It could be shown that the quantity  $(J(\Omega + \Omega_\varepsilon) - J(\Omega))/\text{mes}(\Omega_\varepsilon)$  also has the value  $\chi \Re(Up)$  for every point  $\mathbf{x}$  of  $\mathcal{D}$ . For this purpose, we must define  $\Omega_\varepsilon$  as being a domain of contrast  $\chi$  of  $\mathcal{D}$ , simply connected and with fairly regular contour, for which the measure  $\text{mes}(\Omega_\varepsilon)$  tends towards zero with the real parameter  $\varepsilon$  (in this case, the domain  $\Omega_\varepsilon$  collapses and converges to  $\mathbf{x}$ ). We also note  $J(\Omega + \Omega_\varepsilon)$  and  $J(\Omega)$  the values of the function  $J$  with and without this perturbation  $\Omega_\varepsilon$ , respectively.

We do not address here the difficulty related to the nature of the shape gradients  $g$  during the appearance or disappearance of domains. In a few words, any change of the topology (for example by fusion or fission of domains, the normals being in particular undefined at the junction or break points) represents a problem for the definition of function spaces and for an appropriate formulation of the evolution equation. Nowadays, such problem cannot be considered solved. Yet, the numerical approach is valid, as illustrated by many practical examples.

The application of the above is illustrated by the reconstruction of two fluid obstacles of different size (one is about  $\lambda \times \lambda$ , the other  $\lambda/3 \times \lambda$ ) buried into an homogenous fluid environment. The wavelength in this environment  $\lambda$  is given by

$c/f$ , where  $c$  is the velocity of compression waves (1470 m/s) and  $f$  the operation frequency of the sources (1 MHz). Both obstacles have the same characteristic velocity (1800 m/s). The whole system is illuminated by 4 line sources, regularly distributed over a circle of radius  $2\lambda$ . The scattered field is measured by 32 receivers, also regularly distributed over the same circle. The synthetic data are obtained by numerical solutions of the direct problem. Consequently, they are not affected by noise measurement. Note that the domain where the obstacles are sought is located in the center of the system and has a size of  $5\lambda/3 \times 5\lambda/3$ .

Figure 16.3 displays the two best reconstructions (in the sense of solutions that minimize the cost function) obtained with two different variants of the method of level sets. Both methods have been initialized by a single square obstacle (Figure 16.3a). In the first approach (Figure 16.3b), the contrast is known and

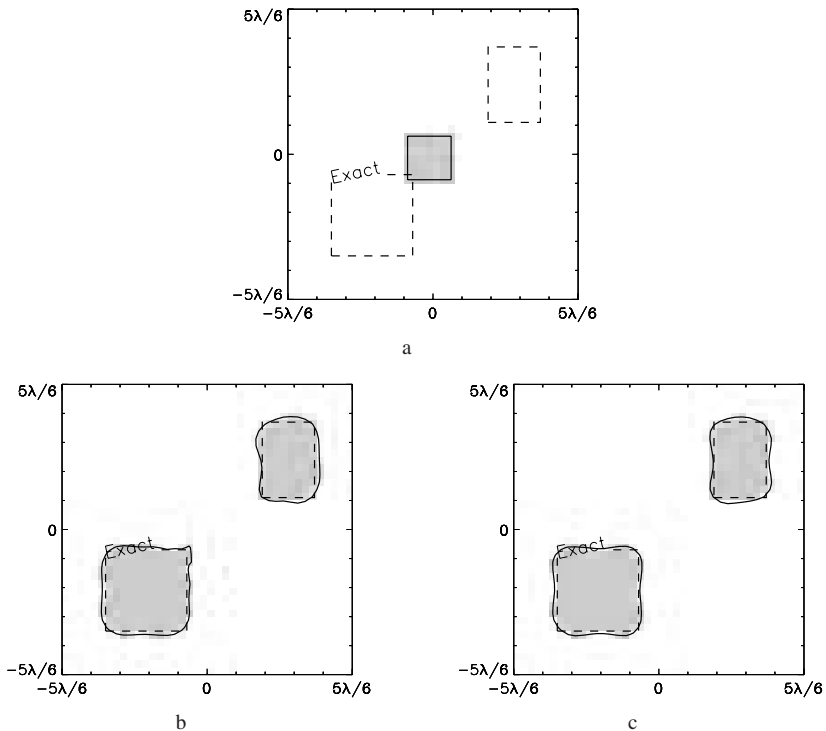


**Figure 16.3.** Reconstruction of an object consisting of two separate parts with the same contrast. Initialization process (a) best solution obtained (b) using the method of evolution of level sets, (c) same as (b), combined with a method of contrast reconstruction. The dashed and solid lines correspond with the exact and reconstructed boundaries (the level zero of all levels), respectively. The shaded area corresponds with the interior of the object

fixed, the boundary, in this case, being the only unknown. In the second variant (Figure 16.3c), boundary and contrast of the obstacle are both unknown. This latter situation is handled by alternating the use of (i) the evolution process, and (ii) an evaluation of the contrast, the domain being fixed (the initial velocity for the obstacle has been chosen here as 2,000 m/s). This evaluation of the contrast is performed by a non-linear Levenberg-Marquardt algorithm involving a Lagrangian formalism in order to rigorously express the derivative with respect to the contrast [RAM 03].

### 16.7.2. Topological derivative

In this section, we consider the identification of a rigid obstacle (or a set of such obstacles) in a three-dimensional acoustic environment (limited or not), excited by unitary point-like sources, successively applied at the positions  $\mathbf{x}_i^S$  ( $1 \leq i \leq N$ ). The field  $u$  scattered by the objects is assumed to be measured by receivers located at  $\mathbf{x}_j^m$  ( $1 \leq j \leq M$ ). The problem is equivalent to the reconstruction of the contour  $\Gamma$  of an obstacle delimited by  $\Omega$ , this obstacle being single or multiple. It is natural to introduce the following cost function:

$$\mathcal{J}(\Omega) = \frac{1}{2} \sum_{i=1}^N \left\{ \sum_{j=1}^M \|u_{\Omega}^{(i)}(\mathbf{x}_j^m) - \xi^{(i)}(\mathbf{x}_j^m)\|^2 \right\}$$

where:

- $u_{\Omega}^{(i)}$  represents the acoustic field scattered for the source  $\mathbf{x}_i^S$  and a given configuration  $\Omega$  of the obstacle;
- $\xi^{(i)}$  represents the corresponding measured scattered field (the domain  $\Omega$ , or in equivalent manner, the surface  $\Gamma$ , thus behaves as the parameter  $\mathcal{P}$  in [16.3]).

Minimizing  $\mathcal{J}(\Omega)$  using traditional methods requires a choice of initial configuration  $\Omega^{(0)}$ . It is desirable to make this choice in a pertinent manner. If  $\mathcal{D}$  represents the environment without obstacle, it is interesting to try to assess the impact on the cost function of the presence of a small obstacle  $\Omega_{\varepsilon}(\mathbf{x}^o)$  of well-known shape (for example a spherical obstacle), with a characteristic size  $\varepsilon$  and volume  $\varepsilon^3 V$ , centered at a point  $\mathbf{x}^o$  in  $\mathcal{D}$ . In this particular situation, we establish that the cost function can be developed in the following form

$$\mathcal{J}(\Omega_{\varepsilon}(\mathbf{x}^o)) - \mathcal{J}(\emptyset) = \varepsilon^3 V T(\mathbf{x}^o) + o(\varepsilon^3)$$

where  $T(\mathbf{x}^o)$ , the *topological derivative* of  $\mathcal{J}$  at  $\mathbf{x}^o$ , is a function of:

- 1) the incident fields  $u^{(i)}$  associated with each source;
- 2) the adjoint fields  $v^{(i)}$  generated by the superposition of the sources, whose intensities are complex conjugates of the differences  $u_{\Omega}^{(i)}(\mathbf{x}_j^m) - \xi^{(i)}(\mathbf{x}_j^m)$  applied to receivers.

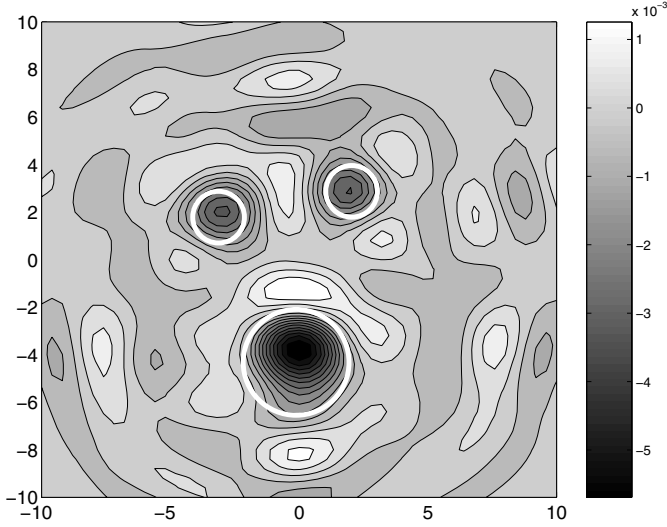


**Figure 16.4.** Identification of a set of three rigid spherical objects (centered at  $(-3, 2, -3)$ ,  $(2, 3, -3)$  and  $(0, -4, -4)$ , radii 1, 1 and 2, represented by white circles) in an acoustic half space  $x_3 \leq 0$ : distribution of  $\mathcal{T}$  in the plane  $x_3 = -3$

This function can be written as follows:

$$\mathcal{T}(\mathbf{x}^o) = \sum_{i=1}^N \left[ \nabla u^{(i)} \cdot \mathbf{A} \cdot \nabla v^{(i)} - \frac{4\pi^2}{\lambda^2} u^{(i)} v^{(i)} \right] (\mathbf{x}^o) \quad [16.5]$$

where the second-order tensor  $\mathbf{A}$  depends only upon the chosen form for  $\Gamma_\varepsilon(\mathbf{x}^o)$  (for a spherical shape, we show that  $A_{ab} = (3/2)\delta_{ab}$ ). In order to minimize  $\mathcal{J}(\Omega)$ , the “interesting” regions of space are those for which the topological derivative  $\mathcal{T}(\mathbf{x}^o)$  is negative. For example, we can heuristically consider the latter as a first approximation of the obstacle sought. This approach is currently being explored to overcome the similar inverse problem in elastodynamics [BON 04].

As an example, let us consider the problem of identifying a set of three rigid spherical objects (centered at  $(-3, 2, -3)$ ,  $(2, 3, -3)$  and  $(0, -4, -4)$ , radii 1, 1 and 2, in arbitrary units) in an acoustic half space  $x_3 \leq 0$ , such that the wavelength  $\lambda = (2\pi/1, 1)$ . We consider  $N = 4$  point-like sources located at  $\mathbf{x}^S = (\pm 5, \pm 5, 0)$  from the surface  $\{x_3 = 0\}$ , on which a condition of zero velocity is also assumed. We consider  $M = 9$  receivers  $\mathbf{x}^m = ((0, \pm 5), (0, \pm 5), 0)$ . Figure 16.4 shows the topological derivative field  $\mathcal{T}(\mathbf{x}^o)$  calculated on a mesh of points  $\mathbf{x}^o$  in the plane  $x_3 = -3$ . The lowest negative values of  $\mathcal{T}(\mathbf{x}^o)$  correspond to the horizontal location of the objects, and the absolute minimum of  $\mathcal{T}(\mathbf{x}^o)$  indicates the largest object.

It is important to note that the numerical calculation of the topological derivative field  $\mathcal{T}(\mathbf{x}^o)$  is easy and cheap, compared to the cost of a numerical optimization algorithm for the same inverse problem. But the field  $u$  is necessary to assess the initial value of the cost function. The adjoint fields are evaluated either by explicit formulations (integral representations), or by the solution of an adjoint boundary problem, for which the operator has already been built and factorized for the calculation of  $u$ . Equation [16.5], or its variants in other contexts, can be quickly evaluated. Many extensions of the concept of topological derivative, originally introduced for topological optimization of structures [ESC 94], whose application to inverse problems is just beginning, are under consideration.

## 16.8. Bibliography

- [AMM 05] AMMARI H., IAKOVLEVA E. and LESSELIER D., “A MUSIC algorithm for locating small inclusions buried in a half space from the scattering amplitude at a fixed frequency”, *Multiscale Modeling & Simulation*, vol. 3, pp. 597–628, 2005.
- [ANG 97] ANGELL T.S., JIANG J. and KLEINMAN R.E., “A distributed source method for inverse acoustic scattering”, *Inverse Problems*, vol. 13, pp. 531–346, 1997.
- [BON 97] BONNANS F., GILBERT J.C., LEMARÉCHAL C. and SAGASTIZABAL C., *Optimisation Numérique – Aspects Théoriques et Pratiques*, Springer Verlag, Berlin, 1997.
- [BON 99] BONNET M. (Ed.), *Problèmes Inverses : de l’Expérimentation à la Modélisation*, vol. 22 of *Arago*, Observatoire Français des Techniques Avancées (OFTA), Tec & Doc edition, 1999.
- [BON 04] BONNET M. and GUZINA B.B., “Sounding of finite solid bodies by way of topological derivative”, *Int. J. Num. Meth. Engng*, vol. 61, pp. 2344–2373, 2004.
- [BUI 04] BUI H.D., CONSTANTINESCU A. and MAIGRE H., “Numerical identification of linear cracks in 2D elastodynamics using the instantaneous reciprocity gap”, *Inverse Problems*, vol. 20, pp. 993–1001, 2004.
- [CHE 01] CHENEY M., “The linear sampling method and the MUSIC algorithm”, *Inverse Problems*, vol. 17, pp. 591–595, 2001.
- [COL 96] COLTON D. and KIRSCH A., “A simple method for solving inverse scattering problems in the resonance region”, *Inverse Problems*, vol. 12, pp. 383–393, 1996.
- [COL 98] COLTON D. and KRESS R., *Inverse Acoustic and Electromagnetic Scattering*, 2nd. ed., Springer Verlag, Berlin, 1998.
- [DAS 00] DASSIOS G. and KLEINMAN R.E., *Low Frequency Scattering*, Oxford University Press, Oxford, 2000.
- [DEL 01] DELFOUR M.C. and ZOLÉSIO J.-P., *Shapes and Geometries: Analysis, Differential Calculus and Optimization*, SIAM, Philadelphia, 2001.
- [ESC 94] ESCHENAUER H.A., KOBELEV V.V. and SCHUMACHER A., “Bubble method for topology and shape optimization of structures”, *Structural Optimization*, vol. 8, pp. 42–51, 1994.



- [FAT 04] FATA S.N. and GUZINA B.B., "A linear sampling method for near-field inverse problems in elastodynamics", *Inverse Problems*, vol. 20, pp. 713–736, 2004.
- [FIN 01] FINK M. and PRADA C., "Acoustical time-reversal mirrors", *Inverse Problems*, vol. 17, pp. R1–R38, 2001.
- [FOK 93] FOKKEMA J. and VAN DEN BERG P.M., *Seismic Applications of Acoustic Reciprocity*, Elsevier, Amsterdam, 1993.
- [HOO 95] DE HOOP A.T., *Handbook of Radiation and Scattering of Waves: Acoustic Waves in Fluids, Elastic Waves in Solids, Electromagnetic Waves*, Academic Press, San Diego, 1995.
- [KIR 02] KIRSCH A., "The MUSIC algorithm and the factorisation method in inverse scattering theory for inhomogeneous media", *Inverse Problems*, vol. 18, pp. 1025–1040, 2002.
- [KUN 03] KUNDU T., "Preface to the special I2M issue on ultrasonic methods for material characterization", *Instrumentation, Mesure, Métrologie*, vol. 3, pp. 1775–1794, 2003.
- [LAM 00] LAMBERT M. and LESSELIER D., "Distributed source method for retrieval of the cross-sectional contour of an impenetrable cylindrical obstacle immersed in a shallow water waveguide", *ACUSTICA – Acustica united with Acta Acustica*, vol. 86, pp. 15–24, 2000.
- [LAN 02a] LANGENBERG K.J., "Linear scalar inverse scattering", in PIKE R. and SABATIER P. (Eds.), *Scattering – Scattering and Inverse Scattering in Pure and Applied Science*, pp. 121–141, Academic Press, London, 2002.
- [LAN 02b] LANGENBERG K.J., MARKLEIN R. and MAYER K., "Applications to nondestructive testing with ultrasound", in PIKE R. and SABATIER P. (Eds.), *Scattering – Scattering and Inverse Scattering in Pure and Applied Science*, pp. 594–617, Academic Press, London, 2002.
- [LEO 02] LEONARD K.R., MALYARENKO E.V. and HINDERS M.K., "Ultrasonic Lamb waves tomography", *Inverse Problems*, vol. 18, pp. 1795–1808, 2002.
- [MIC 97] MICHALEWICZ Z., *Genetic Algorithms + Data Structures = Evolution Programs*, Springer Verlag, Berlin, 1997.
- [PEY 96] PEYRIN F., GARNERO L. and MAGNIN I., "Introduction à l'imagerie tomographique 2D et 3D reposant sur une propagation en ligne droite. Cas de la tomographie par rayon X, par émission et par ultrasons", *Traitement du Signal*, vol. 13, no. 4, pp. 381–440, 1996.
- [RAM 02a] RAMANANJAONA C., LAMBERT M., LESSELIER D. and ZOLÉSIO J.-P., "On novel developments of controlled evolution of level sets in the field of inverse shape problems", *Radio Sci.*, vol. 37, 2002.
- [RAM 02b] RAMANANJAONA C., ZOLÉSIO J.-P., LAMBERT M. and LESSELIER D., "Nonlinearized inversion of buried scatterers: fast marching, topology-free solution methods", *Proc. Journées Internationales de Nice sur les Antennes, Mini-Symposium on Inverse Scattering*, vol. 2, pp. 13–18, 2002.
- [RAM 03] RAMANANJAONA C., LAMBERT M., LESSELIER D. and ZOLÉSIO J.-P., "Linear scalar inverse scattering", in WIRGIN A. (Ed.), *Acoustics, Mechanics, and the Related Topics of Mathematical Analysis*, pp. 243–250, World Scientific, London, 2003.

- [SAB 00] SABATIER P.C., “Past and future of inverse problems”, *J. Math. Phys.*, vol. 41, no. 6, pp. 4082–4124, June 2000.
- [SAN 96] SANTOSA F., “A level-set approach for inverse problems involving obstacles”, *ESAIM: Control, Optimisation and Calculus of Variations*, vol. 1, pp. 17–33, 1996.
- [Sch 02a] SCHMERR JR. L.W., SONG S.-J. and SEDOV A., “Ultrasonic flaw sizing inverse problems”, *Inverse Problems*, vol. 18, pp. 1775–1794, 2002.
- [SCH 02b] SCHMITZ G., “Ultrasound in medical diagnosis”, in PIKE R. and SABATIER P. (Eds.), *Scattering – Scattering and Inverse Scattering in Pure and Applied Science*, pp. 162–174, Academic Press, London, 2002.
- [SET 99] SETHIAN J.A., *Level Set Methods and Fast Marching Methods*, 2nd edition, Cambridge University Press, Cambridge, 1999.
- [SOK 92] SOKOLOWSKI J. and ZOLÉSIO J.-P., *Introduction to Shape Optimization. Shape Sensitivity Analysis*, Springer, Berlin, 1992.
- [TIK 74] TIKHONOV A. and ARSÉNINE V., *Méthodes de Résolution de Problèmes Mal Posés*, MIR, Moscow, 1974.
- [VAN 97] VAN DEN BERG P.M. and KLEINMAN R.E., “Gradient methods in inverse acoustic and electromagnetic scattering”, in CHAVENT G. and SABATIER P.C. (Eds.), *Large-Scale Optimization with Applications*, pp. 143–158, Springer, Berlin, 1997.
- [WIR 02] WIRGIN A., “Acoustical imaging: classical and emerging methods for applications in macrophysics”, in PIKE R. and SABATIER P. (Eds.), *Scattering – Scattering and Inverse Scattering in Pure and Applied Science*, pp. 95–120, Academic Press, London, 2002.

Part 4

## Nonlinear Acoustics

This page intentionally left blank

## Chapter 17

# Nonlinear Acoustic Phenomena in Micro-inhomogenous Media

### 17.1. Introduction

Nonlinear acoustics in solids uses acoustic means to study the deviation of the material's behavior with respect to i) the linear Hooke's law, which connects the stress tensor  $T_{ij}$  and the deformation tensor  $s_{ij}$  and to ii) the linear relationship between  $s_{ij}$  and the gradient of the particle displacement tensor  $\partial u_i / \partial x_j$  [ZAR 71, BRE 84, NAZ 88, ZHE 99, OST 01]. This domain is called nonlinear acoustics because deviations from the linear relationship are by definition nonlinear in terms of the deformation. By definition, the gradient of the acoustic displacement is very small ( $|\partial u_i / \partial x_j| \ll 1$ ), which implies that the deviations relative to the linear Hookes's law (the nonlinearity of the equation of state of a material) and relative to the linear relationship between  $S_{ij}$  and  $\partial u_i / \partial x_j$  (the kinematic or geometric nonlinearity) are small. However, in acoustics, powerful methods are developed for the measurements of acoustic velocity and attenuation with very high precision. So the variation in acoustic velocity and attenuation with increasing wave amplitude are observed experimentally in many materials and can be related to the acoustic nonlinearity of the materials. However, it is much more important that nonlinear acoustics proposes for the evaluation of materials, additionally qualitatively different methods which are possible only due to the existence of material nonlinearity. These methods are based on the interactions of acoustic waves that change the frequency spectrum of the signal. Such processes are only possible in the presence of nonlinearity within the material. In particular, the interaction of different acoustic waves can

generate in the material new frequencies that were not present in the initial excitation [ZAR 71, ZHE 99]. The intersection of two acoustic beams in an homogenous but nonlinear material will initiate scattered waves radiated from the intersection region not just at new frequencies but also in different directions from those of the primary waves [JON 63, CHI 64, SAT 85]. The acoustic signals at these new frequencies and in these new propagation directions, if detected, are the fingerprints of the nonlinearity existence. They are background free in the sense that, if there were no acoustic nonlinearity, they would be absent. This provides an increased sensitivity for methods based on the detection of new frequency components, both for assessing the actual nonlinear parameter of the material, but also for the tomography of the nonlinear parameter.

Research activity in nonlinear acoustics can be separated into two complementary and mutually penetrating parts. On the one hand, when a phenomenon that depends on the wave amplitude is observed experimentally, it is necessary to understand what kind of wave interaction can explain such phenomenon. This requires the study of nonlinear processes for different phenomenological models of acoustic nonlinearity, i.e. for different phenomenological models of the nonlinear stress/strain relationship. Obviously, the choice of the model is not arbitrary, but is defined by the knowledge of material mechanics. On the other hand, even when a phenomenological model for a particular observation is established, it is necessary to find the relationship of the phenomenological parameters of the model to the microscopic structure of the material. It is a necessary step for the quantitative application of methods of nonlinear acoustics in the evaluation of materials. The theoretical explanation of the stress/strain relationships experimentally observed at the macroscopic scale, starting from the physical phenomena taking place at micro- or even nano-scopic level is a classic mechanical problem. Thus, future progress in this second part of nonlinear acoustics is closely linked to advances in theoretical mechanics of micro-structures such as dislocations, cracks, contacts, etc. [MOR 00, KRA 88, KNO 73].

## 17.2. Models of acoustic nonlinearities in micro-inhomogenous media

The nonlinear equation of motion, simplified by taking into account the fact that the acoustic disturbances are weak, but still keeping the first nonlinear terms, is a fundamental equation of nonlinear acoustics of solids. Considering that the material is isotropic at a macroscopic level and neglecting in the discussion that follows the interactions between the longitudinal and transverse waves, the equation of motion for a plane wave propagating along the  $x$  axis can be written as [ZAR 71, LAN 59]:

$$\rho \frac{\partial^2 u}{\partial t^2} = \frac{\partial T}{\partial x}, \quad [17.1]$$

where  $\rho$  is the material density at equilibrium,  $u$  is the mechanical displacement associated with the acoustic wave,  $T$  is the stress and  $t$  is time. This equation is

nonlinear because of i) the dependence of the stress  $T$  on the strain  $s$  ( $T = T(s)$ ), which is actually always nonlinear (physical nonlinearity); and ii) the nonlinearity of the relationship between strain and the displacement gradient for longitudinal waves (called kinematic or geometric nonlinearity):

$$s = \frac{\partial u}{\partial x} + \frac{1}{2} \left( \frac{\partial u}{\partial x} \right)^2. \quad [17.2]$$

For shear plane waves, the kinematic nonlinearity is absent, the second term of the right-hand side of equation [17.2] does not appear.

### 17.2.1. Elastic nonlinearity of an ideal solid

Qualitatively, a material can be considered an ideal elastic solid in terms of acoustics, if the acoustic load is not able, even temporarily, to change the internal structure of the material. In other words, the material is elastic if the acoustic wave does not cause any relative displacement between atoms or molecules that are larger than the inter-atomic or intermolecular distance. At first glance, it seems that the acoustic forces acting on the atoms are so small compared with the inter-atomic forces that they are not able to change the structure of the solid, and all materials should behave elastically. However, this is not the case for materials having, in the absence of solicitation, structural inhomogenities that can concentrate the acoustic stress when a wave propagates. The materials containing such inhomogenities (cracks, grains, delaminations, etc.) with characteristic sizes larger than the intermolecular distances in solids, but smaller than the acoustic wavelength, are called micro-inhomogenous materials [NAZ 88]. The concentration of the stress on these inhomogenities during propagation of acoustic waves can produce the fracture of inter-atomic or intermolecular links, as well as large relative displacements of atoms. Therefore, it can be concluded that an ideal elastic solid does not include such structural defects. In the absence of stress concentration, the atoms move near their equilibrium position determined by the inter-atomic potential. The nonlinearity of the stress/strain relationship comes from the deviation of the inter-atomic potential near its minimum (where an atom is located in the absence of mechanical stress) from an exact parabolic profile. This produces a reaction force on the atom, when it is displaced from its equilibrium position, which is not proportional to the relative displacement of atoms. In Figure 17.1a, the continuous curve shows qualitatively the dependence of the inter-atomic force on the distance  $\delta$  between two atoms. The broken line represents the linear approximation in the vicinity of the equilibrium position  $\delta = b_0$ .

The departure from linearity in force versus particle separation relationship at the atomic level, results in the nonlinearity of the macroscopic stress/strain relationship. It is important that, during the quasi-static loading of an ideal solid, the position

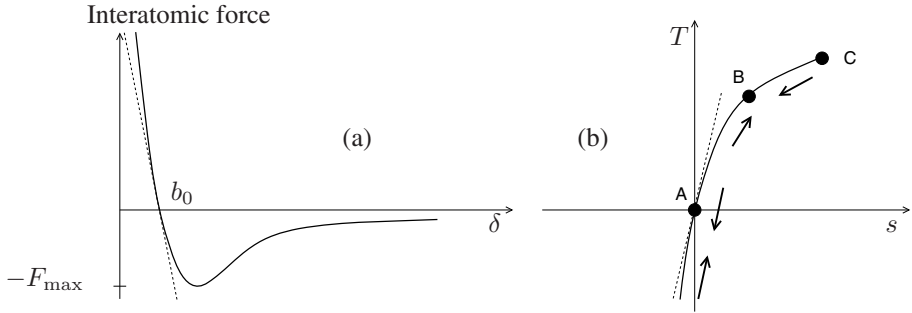


**Figure 17.1.** (a) Qualitative dependence of the interatomic force on the separation distance  $\delta$  between two atoms; (b) a typical stress/strain relationship for ideal elastic solids. The material transforms through the same sequence of states  $(T, s)$  during loading and unloading. Arrows indicate the direction of changes in stress and strain

of atoms is controlled solely by the applied stress, or in an equivalent way, by the strain (deformation). The stress/strain relationship of an ideal elastic solid is a “holomorphic” function (a single value of the stress corresponds to a particular value of the strain and vice versa) as shown in Figure 17.1b.

The stress and strain are measured here relative to static initial values, which are assumed to remain unchanged during the acoustic experiment. For a low acoustic solicitation, the stress/strain relationship of Figure 17.1b can be approximated by its Taylor expansion:

$$T(s) \simeq T(0) + T'(0)s + \frac{1}{2!}T''(0)s^2 + \frac{1}{3!}T'''(0)s^3 + \dots \quad [17.3]$$

The prime signs denote the derivatives of the stress with respect to the strain  $s$ . Usually, the materials become softer in tension and stiffer in compression. This corresponds to  $T''(0) < 0$ . The combination of equations [17.1], [17.2] and [17.3] gives the following nonlinear wave equation:

$$\begin{aligned} \rho \frac{\partial^2 u}{\partial t^2} - T'(0) \left\{ 1 + \frac{T''(0)}{T'(0)} \left[ 1 + \frac{T'(0)}{T''(0)} \right] \frac{\partial u}{\partial x} \right. \\ \left. + \frac{T'''(0)}{2T'(0)} \left[ 1 + \frac{3T''(0)}{T'''(0)} \right] \left( \frac{\partial u}{\partial x} \right)^2 \right\} \frac{\partial^2 u}{\partial x^2} = 0, \end{aligned} \quad [17.4]$$

where we keep the terms of the third power in the gradient of the displacement  $\partial u / \partial x$ . This equation can be rewritten as:

$$\frac{\partial^2 u}{\partial t^2} - c_0^2 \left\{ 1 - \epsilon \frac{\partial u}{\partial x} + \beta \left( \frac{\partial u}{\partial x} \right)^2 \right\} \frac{\partial^2 u}{\partial x^2} = 0, \quad [17.5]$$



where  $c_0$  can be identified with the propagation velocity of the linear acoustic wave (a wave with an amplitude supposed to be infinitely small),  $\epsilon$  and  $\beta$  are dimensionless parameters of quadratic and cubic elastic nonlinearity, respectively. The relationship between these parameters and the derivatives of the stress/strain law is obtained by comparing equations [17.4] and [17.5].

If  $s_{NL}$  is the strain scale that characterizes the beginning of the deviation of the stress/strain relationship relative to Hooke's law, the nonlinearity parameters can be estimated as  $\epsilon \propto s_{NL}^{-1} - 1$  and  $\beta \propto s_{NL}^{-1}(s_{NL}^{-1} - 3)/2$ . It should be noted that the second terms in the latter expressions are associated with the kinematic nonlinearity (see equation [17.2]). They disappear for plane shear waves and even in the case of longitudinal waves their contribution remains very low in most cases. In fact, it is possible to obtain an estimation of  $s_{NL}$  using the known theoretical estimations of the forces that are necessary to break the ideal crystals [KNO 73], based themselves on estimations of the maximal attractive force  $F_{\max}$  between atoms (see Figure 17.1a). The latter theoretical estimation links the fracture stress  $T_f$ , necessary for the destruction of a material, to the Young modulus  $E$  ( $T_f \simeq E/10$ ). From this relationship, and associating  $s_{NL}$  to the rupture strain, it is deduced  $s_{NL} \simeq 0,1$ . Consequently, the kinematic nonlinearity does not have a dominant role in the solids, the values of the quadratic elastic nonlinearity parameter are typically  $\epsilon \simeq 1 - 10$ . It is important to mention here that the rupture of micro-inhomogenous solids takes place at strain levels of about two orders of magnitude lower than those just above, indicating the presence of structural defects. In this media, the kinematic nonlinearity is completely negligible.

It should also be noted that the ratio of the quadratic and cubic nonlinear terms in equation [17.5] can be estimated as  $(\beta/\epsilon)(\partial u/\partial x) \propto |\partial u/\partial x|/s_{NL} \ll 1$ . This inequality can be considered the definition of nonlinear acoustics. By definition, nonlinear acoustics aims to probe the nonlinearity of materials by using dynamical values of  $|\partial u/\partial x|$  which are significantly smaller than  $s_{NL}$ . Although the cubic term of the nonlinear equation [17.5] is estimated as much lower than the quadratic term, it is retained in the equations for the following reasons.

First, the quadratic term is absent for shear waves in ideal isotropic elastic solids, for symmetry reasons [ZAR 71]. In fact, shear waves are characterized by  $T''(0) = 0$ , because the stress should change its sign when the shear strain  $s = \partial u/\partial x$  does (note that the displacement  $u$  of the shear wave is normal to the  $x$  axis). This means that the Taylor development [17.3] should not include even terms of strain. Therefore, the cubic nonlinearity can be the dominant elastic nonlinearity for shear waves.

Secondly, the cubic term of equation [17.5] is kept for methodological purposes, in order to compare the nonlinear processes associated with the quadratic nonlinearity (of even symmetry) and associated with cubic nonlinearity (of odd symmetry), to those associated with hysteretic quadratic nonlinearity (which has to be introduced into

equation [17.5] in the case of micro-inhomogenous media). The hysteretic quadratic nonlinearity, as will be demonstrated, is quadratic in acoustic wave amplitude (as the quadratic elastic nonlinearity), but has an odd symmetry (as the cubic elastic nonlinearity).

### 17.2.2. Hysteretic nonlinearity of micro-inhomogenous media

The indication that for micro-inhomogenous materials it might be necessary to modify the description of the acoustic nonlinearity presented above for ideal elastic solids is given first of all by the observation that their stress/strain relationship deviates from the form presented in Figure 17.1b. For the nonlinear acoustics, the most important observations, accumulated on the mechanics of micro-inhomogenous materials, are the following:

1) If a micro-inhomogenous medium is loaded ( $\partial T/\partial t > 0$ ) from an initial state  $T(0)$  along a curve  $A \rightarrow B \rightarrow C$  (see Figure 17.2a) to reach a maximum stress  $T_{\max}$ , and then this stress starts to diminish ( $\partial T/\partial t < 0$ , unloading), then the stress/strain dependence during the unloading phase is different from the dependence observed during the loading phase. The material evolves along a curve  $C \rightarrow D \rightarrow E \rightarrow F$ , as illustrated in Figure 17.2a. The difference in material strain (volume) for the same magnitude of stress during initial loading and subsequent unloading (compare points B and D, and also A and E in Figure 17.2a) indicates that the material structure is modified. It is plausible that the changes in the material structure result from the stress concentration in the vicinity of micro-inhomogeneities. It is common to say that, in addition to the elastic deformation, the micro-inhomogenous medium also exhibits plastic deformation.

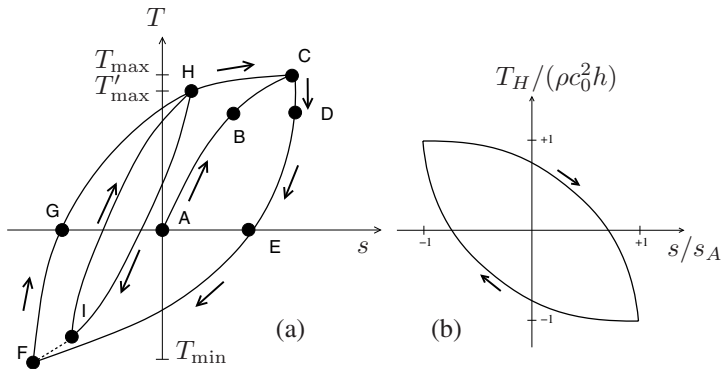


**Figure 17.2.** (a) A typical stress/strain relationship for micro-inhomogenous elastic solids. Different curves are followed by the material state  $(T, s)$  during loading and unloading phases. The arrows indicate the direction in which each particular path is followed. (b) Modeling in nonlinear acoustics of the hysteretic contribution to the nonlinear stress/strain relationship by parabolic curves on the plane  $(T, s)$

2) If the unloading stops at a stress level  $T_{\min}$  corresponding to the point F in Figure 17.2a, and then a new loading phase starts, the path  $F \rightarrow G \rightarrow H$  (see Figure 17.2a) is followed, varying from the previous paths. However, if the reloading continues up to  $T \geq T_{\max}$ , the reloading curve will pass exactly through the point C of the first stress reversal. The material has memorized this reversal point C. In fact, the material is continuously memorizing the reversal points (both of stress maximum and stress minimum) during the protocol of stress application, and is erasing this memory only by completing stress/strain loops to which the reverse points contribute [HUE 79, MRO 75, HOL 81, DOW 93]. For example, if the loading phase does not stop at point C but at point H with  $T'_{\max} < T_{\max}$ , followed by the unloading phase, point H will be stored until the unloading (dotted curve in Figure 17.2a) passes through point F and the loop  $F \rightarrow H \rightarrow F$  is completed, or the internal loop  $H \rightarrow I \rightarrow H$  is completed.

More details and rigorous mathematical definition of this so-called discrete end-point memory can be found elsewhere [MAY 91, KRA 89, BER 98]. For the current stage of discussion it is important that if the first reversal point C is not passed but again serves as a stress reversal point then the subsequent unloading will follow exactly the same path as the first unloading and will arrive point F. If the point F serves again as a stress reversal point then the second reloading will exactly reproduce the first reloading path. In other words, if the stress continues to oscillate between  $T_{\max}$  and  $T_{\min}$ , the unique and stable stress/strain loop CEFGC will correspond to this periodic loading protocol (Figure 17.2a).

So from experimental observations it follows that even the quasi-static stress/strain relationship in micro-inhomogenous material is hysteretic. The strain  $s$  in the material depends not only on the stress  $T$ , but also on the sign of  $\partial T / \partial t$ . Surely, it can be equivalently stated that the stress depends not only on the strain but also on the sign of the strain rate  $\partial s / \partial t$ . The structure of the material at fixed stress (strain) depends on the loading history and is different in loading and unloading. In the particular case of a periodic process with two reversal points over a period, the stress/strain dependence is described by a single hysteresis loop. However, it is important that in each period the material returns to the same points of the stress/strain plane (located on the loop). It means that all the plastic deformations (i.e. all structural changes of the material) are perfectly reversible during a period and there are no accumulating structural changes.

Surely, in reality nothing is perfect and effects such as cyclic creep or cyclic hardening and softening slowly modify the stress/strain loop [HUE 79, HOL 81, DOW 93], because there are always some irreversible change in material structure because of material heating. These slow effects, taking place at time scales significantly exceeding the acoustic wave period, are not considered here.

From a nonlinear acoustics point of view, the most important of the previously described effects is that they are inherently nonlinear. The quasi-static stress/strain

loop presented in Figure 17.2a is composed of two nonlinear parts. It is impossible to build a closed loop of a non-zero surface area by combining two purely linear parts. Therefore, additional terms, responsible for differences between the curves in Figures 17.1b and 17.2a, should be taken into account in the nonlinear acoustic theory of micro-inhomogeneous media. It should be noted that hysteresis is always associated with dissipation. The mechanical energy dissipated by the acoustic field varying along a closed loop on the  $(T, s)$  plane, is positive (equal to the surface area of the loop). Nonlinear hysteresis inevitably introduces in the material nonlinear dissipation, which does not occur in ideal nonlinear solids.

In order to avoid possible misunderstanding, it is important to emphasize that the observed hysteresis is essentially quasi-static, i.e. in the ideal case, it corresponds to an infinitely slow speed of stress (or strain) variation. From the point of view of general physics, hysteresis should necessarily decrease when the material is loaded slower and slower [BER 98, GUS 05c]. This is due to thermal fluctuations that continuously push the system to a single equilibrium state (corresponding to an absolute minimum of the free energy [BER 98]). Hysteresis, which is represented in Figure 17.2 as two possible states of the material for the same loading, can take place at frequencies of the acoustic action such that thermal fluctuations do not have enough time, during an acoustic period, to place the system at its absolute minimum of free energy. The system can be found with a finite probability at a local minimum of free energy (in a metastable state). The theory that takes into account thermal fluctuations in micro-inhomogeneous media [GUS 05c], also predicts that the higher the amplitude of mechanical loading, the more difficult it is for thermal fluctuations to retain the system in a single equilibrium state. This is why, even at a very low frequency but high strain amplitude ( $\sim 10^{-4} - 10^{-3}$ ), the stress/strain-rate independent loops (as in Figure 17.2a) are usually observed in mechanical experiments [HOL 81, ZOB 75].

The acoustic experiments are generally conducted at higher frequencies ( $\geq 1\text{kHz}$ ) and at much lower strain levels ( $\leq 10^{-5}$ ) than mechanical experiments. Therefore, the role of thermal fluctuations in the material behavior and the deviations from the quasi-static curves (Figure 17.2a) may be more significant. However, it is important to note that many acoustic experiments [NAZ 88, ZHE 99, OST 01, GUY 99] can be interpreted by applying quasi-static (frequency-independent) models of hysteretic nonlinearity. There are only a few experiments showing a diminishing of hysteretic nonlinearity at strain levels  $\sim 10^{-6} - 10^{-7}$  and frequencies  $\sim 1 - 10\text{kHz}$  in metals with dislocations [NOW 50], in polycrystalline metals [NAZ 02] and geomaterials [TEN 04]. That is why the frequency-independent model of hysteretic nonlinearity which is analyzed in more detail in section 17.2.3.

The assumption of the rate-independent hysteresis is important because nonlinear acoustic experiments do not evaluate the stress/strain relationship explicitly, but they provide indirect data that can be used for identification of some of the properties of this relationship. Nonlinear acoustic experiments provide data on nonlinear parameters of

the stress/strain relationship only if there is a model to describe it. A particular model of hysteretic acoustic nonlinearity should be chosen following the insights provided by known quasi-static measurements [HOL 81, ZOB 75, MCK 74], and in agreement with theoretical ideas [GUS 05c, GUS 98a, CAP 02] (see section 17.2.5) predicting the material behavior at low excitation amplitudes and high excitation frequencies, possible in acoustics.

When the description of the hysteretic behavior, as presented in Figure 17.2a, is introduced in nonlinear acoustics, it is very useful to take into account the fact that the acoustic loading is weak (small deformations). Therefore, in the first approximation, hysteresis loops  $T = T(s)$  may be approximated by parabolic functions (nonlinear polynomials of the lowest order – order 2 – in strain). This greatly simplifies the mathematical descriptions of nonlinear hysteresis. But the difficulty of describing the memory of micro-inhomogenous media is still present and the stress/strain relationship should generally depend on the whole history of the material loading. This complication can be avoided (as shown in Figure 17.2a) if a periodic loading is assumed, and the process is then analyzed between reversal points of the periodic movement. In particular, for a process with a single minimum  $s_{\min}$  and a single maximum  $s_{\max}$  in a period, the hysteretic part of the stress/strain relationship can be described in terms of the deviation of the strain  $s$  compared with the average value  $(s_{\max} - s_{\min})/2$  as

$$T_H = \rho c_0^2 h \left[ \frac{1}{2} (s_A^2 - s^2) \operatorname{sign} \left( \frac{\partial s}{\partial t} \right) - s_A s \right]. \quad [17.6]$$

In this equation, the dimensionless phenomenological parameter  $h > 0$  characterizes the importance of the hysteretic nonlinearity, and the acoustic stress  $T_H$ , as well as the acoustic strain  $s$ , can be either shear or longitudinal. The notation  $s_A$  is used for the strain amplitude of the periodic acoustic wave. The subscript “ $H$ ” is introduced to describe the hysteretic nature of the considered nonlinearity, which is illustrated in Figure 17.2b.

Note that the different orientation of the hysteresis loop shown in Figure 17.2b, compared with the orientation in Figure 17.2a, is due to the fact that the elastic part of the stress/strain relationship is included in the loop in Figure 17.2a, while only the hysteretic part is shown in Figure 17.2b. Since  $|hs_A| \ll 1$ , the relation [17.6] describes a small correction to the linear Hooke’s law  $T = T'(0)s$ , in addition to the existing nonlinear terms of equation [17.3]. It is easy to imagine that the addition of a linear dominant contribution (with  $T'(0) > 0$ ) to equation [17.6] will immediately reorientate the loop in Figure 17.2b from the second and fourth quadrants of the plane  $(T, s)$  to the first and third quadrants, in agreement with experimental quasi-static observations.

The hysteretic nonlinearity described by relation [17.6] is called hysteretic quadratic nonlinearity, because it is quadratic in strain amplitude. In addition to the

transformation of the acoustic wave spectrum, this nonlinearity is also responsible for the nonlinear dissipation of sound, with an absorption coefficient of a sinusoidal wave proportional to the wave amplitude [GRA 66, NOW 72, GUY 99, GUS 97]. The parameter  $h$  that characterizes the hysteretic nonlinearity is supposed to increase if additional micro-mechanical elements (e.g. cracks or dislocations) are created in the material, without affecting the parameters of the mechanical elements existing previously. In polycrystalline metals, ceramics, rocks, this parameter is around  $10^2 - 10^4$  [NAZ 88, OST 01, GUY 99], exceeds the parameter of elastic quadratic nonlinearity. The hysteretic quadratic nonlinearity can be dominant in consolidated micro-inhomogenous materials.

#### 17.2.2.1. *Micromechanical elements with hysteretic behavior*

The hysteretic nonlinearity has been described above phenomenologically. However, on the one hand, there is a microscopic mechanical motion (“stick/slip” motion of contacts under shear loading [MIN 53, JOH 87]), which is described precisely in small acoustic loading systems by the model of equation [17.6]. On the other hand, there is a large number of known micromechanical elements (contacts with adhesion subject to a longitudinal loading [JOH 71, BUR 93, BUR 97, BUR 99], Griffith’s cracks [HOL 80] and dislocations [GRA 66, NOW 72], for example) that are able to generate the hysteretic behavior described by equation [17.6], if these elements are so numerous in the material, that it is necessary to take into account the statistics of the distribution of their individual parameters. It even appears that, when the hysteretic loops of individual micro-mechanical elements deviate significantly from the form presented in Figure 17.2b, their total contribution to the macroscopic stress/strain relationship can be described in a first approximation by the model of hysteretic quadratic nonlinearity in equation [17.6].

The common characteristic of all hysteretic elements is that their mechanics allow several possible metastable states, several configurations. In addition to the stable configuration of the absolute minimum of free energy, there are additional metastable configurations (local minima of the free energy, which could also be created by an external loading), which are separated from the stable configuration by energy barriers. An acoustic loading can initiate transitions between the different states of the elements. The transition between two states, accompanied by an energy dissipation, may take place in both directions, but at different levels of mechanical loading, resulting in a hysteresis effect in the behavior of the element.

In the following, an instructive example of a possible hysteretic micro-mechanical element is presented qualitatively, in order to illustrate the basic principles of hysteretic behavior.

#### 17.2.2.2. *Mechanical hysteresis of elements with two potential energy wells*

There exist simple models for the micro-mechanical elements, where the potential wells for the element motion can be theoretically predicted. An instructive example

is provided by the analysis of the plane interface between two elastic bodies in contact, subjected to the action of an acoustic field [GUS 03c, MOU 02, GUS 04] (see Figure 17.3).

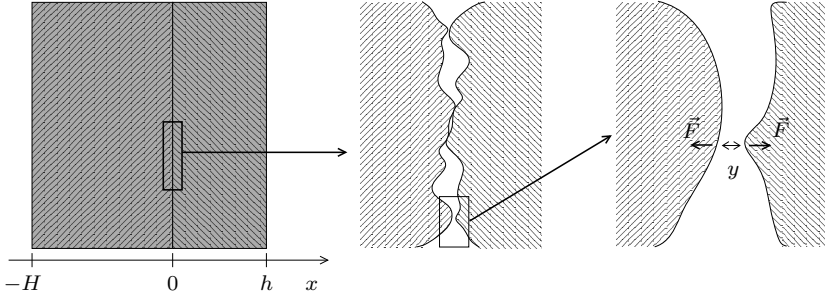


**Figure 17.3.** Schematic representation of the nonlinear interface located in the plane  $x = 0$ .  $\vec{F}$  is the interaction force (per unit surface area) between the surfaces  $x = 0 - 0$  and  $x = 0 + 0$  corresponding to the interface;  $y = u(x = 0 + 0) - u(x = 0 - 0)$  is the width of the interface;  $u(x)$  is the mechanical displacement

For the description of an unbonded interface [RIC 79, RUD 94, ZAI 95] in the existing nonlinear acoustics model, it is assumed that a single possible equilibrium width of the interface is controlled by an effective force  $F_{\text{eff}}$ , that is, by the superposition of the external forces applied to the sample (i.e. the static pressure  $p = -T_0$  applied at  $x = -H$  and  $x = h$  in Figure 17.3, for example) [RIC 79, BUC 78, SOL 93] and the repulsion force  $F$  due to intermediate contacts or due to complete dynamic contact between the surfaces  $x = 0 \pm 0$ . In this case, the effective force is a monotonous decreasing function of the interface width  $y$  of the type presented in Figure 17.4a.

In Figure 17.4a,  $y_0$  denotes the equilibrium separation distance between the surfaces. The vertical line at  $y = 0$  takes into account that the mutual penetration of the surfaces  $x = 0 - 0$  and  $x = 0 + 0$  (that is the region  $y < 0$ ) is forbidden. In the case when the intermediate contacts between the surfaces are approximated by Hertzian contacts of height  $d$  (which is significantly smaller than their curvature radius  $R$ ), the force  $F$  in the region  $0 \leq y \leq d$  can be modeled by  $F = F_H \propto (d - y)^{3/2}$ . It is common to model the real distribution of the effective force by a piece-wise linear distribution (Figure 17.4b) or by an impact type distribution (Figure 17.4c,d). In contrast to the models in Figure 17.4a–d adopted for the unbonded interfaces, both the theories for the bonded interfaces [JOH 71, PAN 95, JOH 76] and the theories of an individual contact between a tip and a surface [BUR 99, ISR 99] take into account the existence of the attractive forces between the surfaces, (or between the tip and the surface) responsible for the



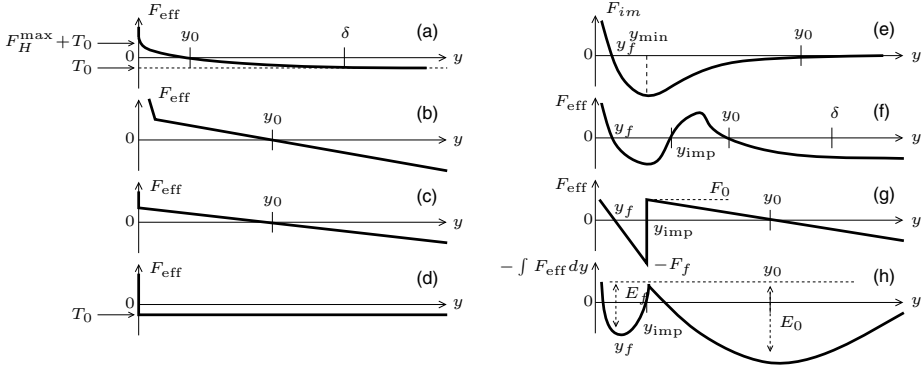


**Figure 17.4.** (left) Qualitative models of a long distance effective interaction force  $F_{\text{eff}}(y)$  for the interface without adhesion: an interaction  $F_{\text{eff}}(y) \propto F_H + T_0$  through Hertz contacts at distance  $y \leq d$  (a); a piecewise linear approximation (b); a piecewise linear approximation with instantaneous impact (c); Richardson model [RIC 79] (d). The pre-stress is noted  $T_0 < 0$ . (right) Qualitative models for the effective force  $F_{\text{eff}}(y)$  between adhesive surfaces composing the interface: a short distance intermolecular force  $F_{\text{im}}(y)$  (schematic representation) (e); an effective force  $F_{\text{eff}}(y) \propto F_{\text{im}} + F_H + T_0$  (f); a piecewise linear approximation for the effective force (g); distribution of the interaction potential in the case of a bistable interface (h)

adhesion phenomenon. In the case where there is no external preloading ( $T_0 = 0$ ) and no surface roughness, a dependence of the intermolecular forces  $F_{\text{im}}$  acting between the plane surfaces is presented schematically in Figure 17.4e (compare with Figure 17.4a). The equilibrium width  $y_f$  in Figure 17.4e is of the order of the inter-atomic distance. However, the attraction force can be effective at much larger separation distances between the surfaces [BUR 93, BUR 99, ISR 99], though usually significantly shorter than the scale of the surface roughness  $d$  ( $y_f < y_{\text{min}} \ll d$ ). It should be mentioned that intermolecular force is far from being a single positive attractive force between the two surfaces [BUR 93, BUR 99, BHU 95]. For example, capillary forces due to the presence of liquids at the interface, can contribute among others the others [BUR 99, ISR 99, BHU 95]. In this situation, the application of a soft enough external loading in the case of sufficiently soft intermediate contacts  $0 < F_H^{\text{max}} + T_0 < -F_{\text{min}} \equiv -F(y_{\text{min}})$  leads to the distribution of the effective force  $F_{\text{eff}} = F + T_0$  with two possible positions of stable equilibrium ( $y = y_o$  and  $y = y_f$  in Figure 17.4f). It should be noted that the impact position  $y = y_{\text{imp}}$  in Figure 17.4f,g is an unstable equilibrium position. The qualitative piecewise linear approximation for the effective force providing two possible equilibrium widths of the interface is presented in Figure 17.4g. The higher slope of the force in the region  $0 < y < y_{\text{imp}}$  accounts for the shorter scales and the higher amplitudes of the attractive forces in the considered system in comparison with the long scale distribution of  $F_{\text{eff}}$ . The piecewise linear modeling of the effective force corresponds



to an effective potential composed of two parabolic wells in Figure 17.4h. In agreement with the terminology existing in other branches of mechanics and physics, the micro-mechanical element considered here is a two levels system.

The physical existence of the dependence of the effective forces on the separation distance, as presented in Figure 17.4f,g, is confirmed by multiple experiments in atomic force microscopy (see for example [BUR 99, ISR 99, BHU 95] and references therein). With the help of the force curve in Figure 17.4g, the behavior of the tip of an atomic force microscope (AFM) when its quasi-static loading varies, can be described as follows (see Figure 17.5). Let the initial equilibrium position be  $y = y_o$  (Figure 17.5a). We start to diminish  $T_0 < 0$  by introducing a variation  $\Delta T_0 < 0$ . This provides the shift of the total curve  $F_{\text{eff}} = F + T_0$  downward, and it moves the equilibrium position to the left. When  $\Delta T_0 = -F_o$ , the separation width  $y = y_o$  becomes equal to  $y_{\text{imp}}$  (see the notations in Figures 17.4g and 17.5a), the equilibrium becomes unstable and the separation distance diminishes by a jump to the value  $y = y_f$  (Figure 17.5b). Note that the position  $y_f$  is also shifted to the left when  $\Delta T_0 < 0$  is applied. This jump corresponds to the jump of the tip to the contact, observed in AFM [BUR 99, ISR 99, BHU 95]. If we now want to separate surfaces, it is not enough to remove the static stress  $\Delta T_0 < 0$  (see Figure 17.5c for  $\Delta T_0 = 0$ ,  $\partial \Delta T_0 / \partial t > 0$ ), but it is necessary to apply  $\Delta T_0 = F_f > 0$ . Only when  $\Delta T_0 = F_f > 0$ , the equilibrium position  $y = y_f$  coincides with  $y_{\text{imp}}$  and the separation distance will increase with a jump (Figure 17.5d). Thus, the effective

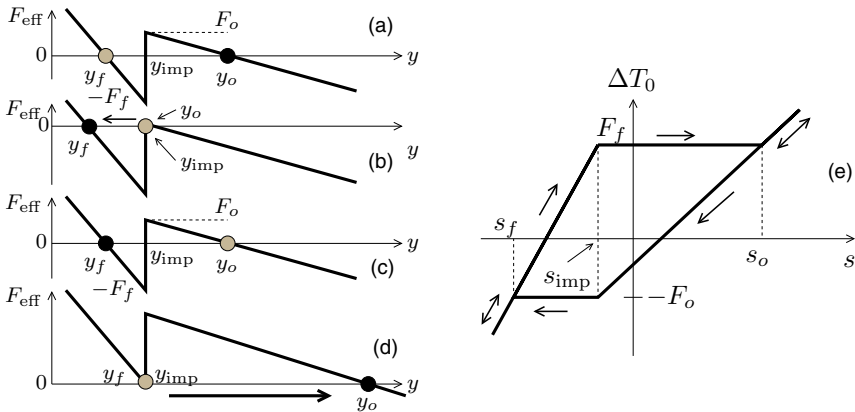


**Figure 17.5.** Illustration of the variation of the effective force with the increase of the pressure on the interface. The filled disks represent an occupied state, and the blank discs an unoccupied state. The system spontaneously changes its state through jumps when the coordinate of the occupied state coincides with the position of the unstable equilibrium (b, d). The occupied state in the intermediate position (a, c) among the two possible states depends on the history of the loading process. (e) Description of the stress/strain relationship  $\Delta T_0 - s$  for mechanical hysteresis of the interface

force curve in Figure 17.4g properly takes into account the basic features of the mechanical hysteresis observed in the quasi-static behavior of the AFM. However, it must be stated here that the so-called adhesion hysteresis [BUR 99], due to possible dependence of some type of attractive forces on the sign of the separation gap variation, is not taken into account by the single valued dependence of  $F + T_0$  on  $y$  (Figure 17.4f,g). The qualitative conditions  $0 < F_H^{\max} + T_0 < -F_{\min}$  proposed above for the bistable interface correspond to the following well-known fact in AFM: the weaker the cantilever is, the greater the mechanical hysteresis effects.

The basic idea can be formulated as follows. Since complicated effective forces were observed during the interaction of a surface with one contact only (the tip of the AFM), there is no reason to reject the possibility that a complex system of this kind can be achieved in the interaction of a group of contacts with a surface (i.e. during the interaction of rough surfaces). Similar situations are likely to appear also in the interaction between the surfaces of a crack, despite the fact that the initial equilibrium width of the crack  $y_o$  ("open" state) is due to a relatively complicated distribution of the stress around the crack. Neither an external loading nor a surface roughness is necessary to keep the crack in this position of equilibrium. Clearly, the effective force keeping the crack in the open position can be modeled by a distribution of the type presented in Figure 17.4b,c. In addition, the dependence of the effective force on the separation  $y$  between the lips of the crack can be estimated by  $F_{\text{eff}} \simeq E(y_o/2L)[(y_o - y)/y_o]$ . Here,  $E$  is the Young modulus of the material and  $2L$  is the characteristic length of the crack (or its diameter). The estimation takes into account the fact that a circular crack is  $(L/y_o) \gg 1$  times softer than the surrounding material. Therefore, when the attraction forces are included in the modeling (and in the case of a sufficiently flexible crack  $(L/y_o) \gg 1$ ), the total effective force can be modeled by curves f and g in Figure 17.4. It is interesting to note that the hysteresis phenomenon was observed when a closure of a nominal plane crack was experimentally approximated by the motion of two nominally flat surfaces in contact [SCH 83]. The stress/strain dependence corresponding to a loading-unloading procedure described in Figure 17.5a–d is presented in Figure 17.5e. The strain  $s_{\text{imp}}$  in Figure 17.5e corresponds to a separation of the surfaces equal to the impact distance  $y_{\text{imp}}$ .

It is clear that the separation between surfaces in Figure 17.3, and the form of the asperities which can be opened or closed by the external loading, are different for different local positions along the interface. Therefore, in order to get a stress/strain relationship for the complex interface (or for the crack), the individual stress/strain relationship, of the kind presented in Figure 17.5e, should be averaged over the possible values of their parameters, which can be different for different elements. These parameters are, for example, the critical stresses  $F_o$  and  $F_f$ , or the jump amplitudes  $s_o - s_{\text{imp}}$  and  $s_{\text{imp}} - s_f$ . Note that the linear rigidity of the element close to the local equilibrium point in Figure 17.4g,h can also be different for each

element. If the contacts between the lips of the crack are taken into account, the average should be calculated over all possible contacts of all the cracks. This average leads to an effective stress/strain relationship which is hysteretic. Moreover, it can be shown [MAY 91, KRA 89, BER 98] that the hysteresis of the individual response of the micro-mechanical elements is responsible for the memory effects discussed in section 17.2.2. For the following analysis, it is important that the averaged stress/strain relationship contains, for most of the known models of micro-mechanical elements (such as Griffith's cracks, contacts with sticking and dislocations) an important part which can be identified as a quadratic hysteretic nonlinearity. In other words, the hysteretic loop composed of parabolic paths can model the total hysteretic behavior, even if hysteretic contributions of higher order are possible. It should also be noted that the strain jumps (opening/closing of contacts) are accompanied by rigidity jumps (changes in elastic modulus) of the micro-mechanical elements (see Figure 17.5e). The element has a different rigidity for  $s > s_o$  and  $s < s_f$ , demonstrating a bi-modulus elasticity [NAZ 88, ZHE 99]. This part of the individual element behavior contributes to the elastic nonlinearity of the micro-inhomogenous material, and to the cubic hysteretic nonlinearity.

The presentation in Figure 17.5 can be used to discuss the limitations of the hysteresis model that does not depend on the loading frequency (rate independent hysteresis), a model which will be widely used and accepted in the following (section 17.2.3). These limitations in mechanics are the same as those existing in magnetism [BER 98].

The first limitation concerns the maximum strain rates (i.e. the values of maximum strain and the maximum frequency). In fact, the jumps have been represented in Figure 17.5e by horizontal lines, by assuming that they are instantaneous. In reality, each jump is accompanied by a sudden decrease of the elastic energy of the medium. Therefore, energy is irreversibly dissipated in the form of heat (thermal energy). The configuration change of the element by a jump and thermalization of the released energy takes time. There is therefore a characteristic time in the system. In the rate independent approximation, it is assumed that an external action on the system remains unchanged during the time necessary to make a jump. In this approximation, the external field just creates the conditions for a system instability and spontaneously (or thermally induced) jumps from a local minimum of energy to another one. However, when significant changes of external action occur during jumps, rate independent model is not valid. The system does not evolve through a sequence of spontaneous jumps anymore, but rather approaches a system of forced dynamics, controlled by the external loading [BER 98, CAP 02]. At a high frequency and high acoustic wave amplitude, the characteristic time for thermally stimulated transitions can significantly exceed the acoustic period, and the individual elements do not have enough time to change their state, even when the loading makes it favorable from the energy point of view (see also section 17.2.5).

The second limitation concerns the minimum strain rates (i.e. the magnitude of the minimum strain and the minimum frequency). In fact, the model presented above in Figure 17.5 does not take into account the fact that any system exhibits a spontaneous inevitable relaxation to the thermodynamical equilibrium under the action of thermal agitation. Even if the forces tend to keep the system in an initially occupied energy well, the thermal agitation gradually makes the other minima available, on long time scales. The system visits the states neighboring the initial state  $y = y_o$  in Figure 17.5a and 17.4g,h, for example, due to the random thermal fluctuations (the necessary energy for the transition is borrowed from the thermal reservoir). When the system occasionally reaches a local maximum of energy separating, in Figure 17.4h, the initial state  $y_o$  from the neighboring energy well, it spontaneously jumps to the state  $y_f$ , which becomes accessible through this mechanism. For sufficiently long times, the system reaches the thermodynamic equilibrium, which is characterized by the probability distribution of finding the system in the state  $y_o$  or  $y_f$ . The probability for the system to occupy any given state is controlled by Boltzmann statistics. The rapidity of approach of the equilibrium is determined by the height of the energy barrier separating the neighboring minima of energy, compared with the energy of thermal agitation, proportional to the absolute temperature. If the strain rate is low enough to allow the system to relax to the thermodynamic equilibrium, the hysteresis disappears [BER 98, GUS 05c]. Instead of finding the system, characterized by the same energy potential relief, in one of the two different states depending on the sign of the strain rate (i.e. depending on the loading or unloading), the system is found in the same single state thermodynamic equilibrium. Thus, the thermally activated processes destroy hysteresis and bistability. It can be argued that the thermal processes destroy the persistent memory in the system [BER 98, BER 96]. Only in the absence of thermal agitation, the considered system remains in a state (for example in the state  $y = y_o$  described in Figure 17.5a) for an infinitely long time, if the external loading is not changed, and this produces a persistent memory effect. It can be concluded that the hysteresis phenomenon is observable if the strain rate is sufficiently high (in particular, the acoustic frequency must be high enough) to prevent the system relaxation to the thermal equilibrium states.

Despite the fact that rate-independent hysteresis theoretically exists only when the strain rate takes appropriate values, this approximation is very useful in nonlinear acoustics. Most experiments in nonlinear acoustics of micro-inhomogenous media can be explained within the frame of the hysteresis independent of the strain rate. The theoretical estimations [GUS 05c] confirm that the domain for validity of this model is very large.

### ***17.2.3. Nonlinear acoustic waves in micro-inhomogenous materials with hysteresis independent of the strain rate***

Before presenting, in sections 17.2.4–17.2.6 the other theoretical models for acoustic nonlinearity of micro-inhomogenous media, the analysis of the simplest

nonlinear acoustic processes in media with hysteresis independent of the strain rate is accomplished in this section. This simple analysis is useful because of its potential to describe the experimental results in nonlinear acoustics of micro-inhomogenous materials. The models and mathematics involved help us to understand the fundamental differences that exist in the role of elastic and hysteretic nonlinearities in the acoustic processes, and aid in explaining the fundamental nonlinear effects (such as the shift of the resonance frequency of a bar made of a micro-inhomogenous medium, proportional to the wave amplitude [NAZ 88, OST 01, GRA 66, LEB 99]). Usually, some more general models are applied for the acoustic nonlinearity of micro-inhomogenous materials (see sections 17.2.5 and [GUS 05c]), however, only if the experimental data cannot be fitted by the model of rate-independent hysteresis.

In this section, the simplest case of a periodic acoustic loading, characterized by equal amplitudes of the maximum and minimum strain ( $|s_{\min}| = s_{\max} = s_A$ ), is analyzed. The contribution [17.6] of the hysteretic elements (the hystérons [KRA 89, TOR 99]) to the macroscopic stress/strain relationship of micro-inhomogenous materials formally consists of two parts. The part depending on the strain rate sign (the term proportional to  $\text{sign}(\partial s / \partial t)$ ) describes a loop in the plane  $(T_H, s)$  and is fully responsible for the corresponding hysteretic nonlinear dissipation. The part independent of the strain rate sign (the term proportional to  $s_A s$ ) orients the hysteresis loop in the plane  $(T_H, s)$  and contributes to the total elastic nonlinearity in the stress  $T$ /strain  $s$  relationship. The fact that the nonlinear contribution to the  $T - s$  relationship contains a part depending on the strain rate sign is the first and the most important in principle difference between this nonlinearity and the quadratic or cubic elastic nonlinearity described by equation [17.3]. Because of losses, introduced by this nonlinearity (and which are physically due to inelastic jumps of the hystérons from one state to another initiated by the acoustic loading), it can be qualified as inelastic nonlinearity. It is tempting to attribute only the notation of the inelastic nonlinearity to the first term of relationship [17.6], because the second term of this equation does not contribute to losses. However, when the term of inelastic nonlinearity is attributed to the total  $T_H = T_H(s)$ , this better reflects the physical reality that “elastic” and “inelastic” parts of the hysteretic nonlinearity only exist together. The other differences of the (inelastic) hysteretic nonlinear contribution to the stress  $T$ , compared with the quadratic and cubic elastic contributions, are more formal. The (inelastic) hysteretic contribution to  $T$ , described by  $T_H = T_H(s)$ , is quadratic in acoustic strain amplitude  $s_A$ , similar to the quadratic elastic contribution  $T_{el}^{(2)}$  in equation [17.3] ( $|T_H| \propto |T_{el}^{(2)}| \propto s_A^2$ ), but differs from the latter in its symmetry ( $T_H(-s, -\partial s / \partial t) = -T_H(s, \partial s / \partial t)$  while  $T_{el}^{(2)}(-s) = T_{el}^{(2)}(s)$ ). Due to the quadratic dependence on  $s_A$ , the nonlinearity associated with  $T_H = T_H(s)$  is called quadratic hysteretic nonlinearity [NAZ 88, OST 01, GUS 05c, GUS 98a, GUS 97]. It is a nonlinearity of odd symmetry. The symmetry of the hysteretic quadratic nonlinearity thus coincides with the symmetry of the cubic elastic nonlinearity in equation [17.3] ( $T_{el}^{(3)}(-s) \propto -T_{el}^{(3)}(s)$ ). However, the contributions of  $T_H = T_H(s)$

and  $T_{el}^{(3)}$  to  $T$  differ in their strain amplitude dependence ( $|T_H| \propto s_A^2$ ,  $|T_{el}^{(3)}| \propto s_A^3$ ). Therefore, the hysteretic quadratic nonlinearity contains some features of the quadratic and cubic elastic nonlinearities, but is quite different.

The purpose of the following analysis is to demonstrate to the reader how these principle or formal differences manifest themselves in nonlinear acoustic phenomena which take place in micro-inhomogenous materials. The derivation of a nonlinear wave equation, necessary for this analysis, requires the expression for the contribution of  $T_H$  to the material modulus

$$E_H \equiv \partial T_H / \partial s = \rho c_0^2 h [-\text{sign}(\partial s / \partial t) s - s_A]. \quad [17.7]$$

The “bow tie” dependence [17.7] of the contribution  $E_H$  of the hysterons to the modulus, is presented in Figure 17.6. It should be mentioned that the extraction of the “bow tie” behavior of  $E_H \equiv \partial T_H / \partial s$  from the analysis of quasi-static experimental data in mechanics is so widespread that the image of the bow tie in the plane  $(E_H, s)$  (as in Figure 17.6) is tightly associated with the hysteretic nonlinearity, just like the image of a hysteretic loop  $T(s)$  in the plane  $(T, s)$  (as in Figure 17.2).

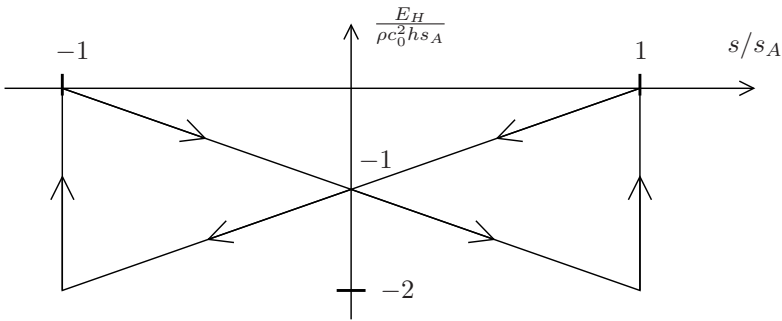


**Figure 17.6.** “Bow tie” dependence on the strain of the contribution  $E_H$  of micro-mechanical hysteretic elements to the elastic modulus. Arrows indicate the direction of change of the strain and the modulus in the case of a periodic acoustic loading, with a single maximum  $s_A$  and a single minimum  $-s_A$  of strain over one period

Two important conclusions can be made from the analysis of equation [17.7]. Firstly, the part depending on the strain rate sign in  $T_H$  induces a part depending on the strain rate sign in  $E_H$  (the first term of equation [17.7]). Secondly, the contribution  $E_H$  of the hysteron to the total modulus  $E \equiv \partial T / \partial s$  is always negative ( $E_H \leq 0$  for  $h > 0$ ). Therefore, the existence of hysteretic micro-mechanical elements leads to a softening of the material. This provides a possible explanation for many experimental observations of softening of micro-inhomogenous material subjected to cyclic acoustic loading [NAZ 88, OST 01, GUY 99].

However, modification of the elastic modulus, by adding the contribution  $E_H/\rho$  of equation [17.7] to the coefficient of the second term of equation [17.5], is not sufficient for taking into account all the contributions of the quadratic hysteretic nonlinearity presented in equation [17.6] to nonlinear acoustic processes. In fact, when the contribution  $T_H$  of [17.6] is added to the local stress  $T$  in the right-hand side term of equation [17.1], the contribution of the hysteresis independent of the strain rate,

$$\begin{aligned}\partial T_H / \partial x &= (\partial T_H / \partial s) \partial s / \partial x + (\partial T_H / \partial s_A) \partial s_A / \partial x \\ &\equiv E_H \partial s / \partial x + (\partial T_H / \partial s_A) \partial s_A / \partial x,\end{aligned}\quad [17.8]$$

contains, in addition to the term  $E_H(\partial s / \partial x)$  associated with the hysteresis of the modulus, the term  $(\partial T_H / \partial s_A) \partial s_A / \partial x$  associated with the explicit dependence of the hysteretic stress [17.6] on the amplitude of the acoustic wave, because of the explicit memory existing in the material of the reversal point of the periodic acoustic loading (see section 17.2.2).

The nonlinear wave equation including the quadratic and cubic elastic nonlinearities and the quadratic hysteretic nonlinearity independent of the strain rate has the form:

$$\begin{aligned}\frac{\partial^2 u}{\partial t^2} - c_0^2 \left\{ 1 - \varepsilon \frac{\partial u}{\partial x} + \beta \left( \frac{\partial u}{\partial x} \right)^2 \right. \\ \left. - h \left[ \left( \frac{\partial u}{\partial x} \right)^A + \left( \frac{\partial u}{\partial x} \right) \operatorname{sign} \left( \frac{\partial^2 u}{\partial x \partial t} \right) \right] \right\} \frac{\partial^2 u}{\partial x^2} \\ = c_0^2 h \left\{ \left[ \left( \frac{\partial u}{\partial x} \right)^A \operatorname{sign} \left( \frac{\partial^2 u}{\partial x \partial t} \right) - \frac{\partial u}{\partial x} \right] \frac{\partial}{\partial x} \left[ \left( \frac{\partial u}{\partial x} \right)^A \right] \right. \\ \left. + \frac{1}{2} \left[ \left( \left( \frac{\partial u}{\partial x} \right)^A \right)^2 - \left( \frac{\partial u}{\partial x} \right)^2 \right] \frac{\partial}{\partial x} \left[ \operatorname{sign} \left( \frac{\partial^2 u}{\partial x \partial t} \right) \right] \right\}.\end{aligned}\quad [17.9]$$

However, it is easy to understand that the spatial derivative in the last term of equation [17.9] causes Dirac  $\delta$ -peaks at the exact positions of strain extrema, where the factor  $((\partial u / \partial x)^A)^2 - (\partial u / \partial x)^2$  is equal to zero. Therefore, only the term proportional to  $\partial s_A / \partial x \equiv \partial(\partial u / \partial x)^A / \partial x$  contributes to the right-hand side term of equation [17.9]. Note that the kinematic nonlinearity of equation [17.2] has been neglected to obtain the hysteretic nonlinear contribution in equation [17.9]. Consequently, only the quadratic part in displacement gradient  $\partial u / \partial x$  of the hysteretic nonlinearity is taken into account.

In a first approximation, the nonlinear terms are neglected and the solution of equation [17.9] is sought in the form of a sine wave propagating to the right

( $u = u_1 = A \sin(\omega t - kx + \phi)$ ), it reveals the linear relationship between the wave number  $k$  and the cyclic frequency  $\omega$  of the acoustic wave ( $k = \omega/c_0 \equiv k_0$ ). The last relationship demonstrates the non-dispersive character of the acoustic wave in the considered model. The linear acoustic waves propagate at the same velocity  $c_0$  at all frequencies. The solution of the first approximation can be rewritten in the form

$$u = u_1 = A \sin [\omega(t - x/c_0) + \phi] \equiv A \sin(\omega\tau + \phi), \quad [17.10]$$

where the amplitude  $A$  and the phase  $\phi$  are constant. In the following, it is assumed that the frequency  $\omega$  is positive.

In the second approximation, the weak acoustic nonlinearity is taken into account, i.e. the solution of equation [17.10], is substituted in the nonlinear terms of equation [17.9]. The quadratic elastic nonlinearity produces the acoustic sources of the second harmonic:

$$-c_0^2 \varepsilon \left( \frac{\partial u}{\partial x} \right) \frac{\partial^2 u}{\partial x^2} = -\frac{\varepsilon \omega^3 A^2}{2c_0} \sin [2(\omega\tau + \phi)]. \quad [17.11]$$

The cubic elastic nonlinearity produces the source of third harmonic and influences the wave at the fundamental frequency

$$c_0^2 \beta \left( \frac{\partial u}{\partial x} \right)^2 \frac{\partial^2 u}{\partial x^2} = -\frac{\beta \omega^4 A^3}{4c_0^2} \left\{ \sin [3(\omega\tau + \phi)] + \sin[\omega\tau + \phi] \right\}. \quad [17.12]$$

The quadratic hysteretic nonlinearity produces sources at all odd harmonics and influences the wave at the fundamental frequency

$$\begin{aligned} & -c_0^2 h \left[ \left( \frac{\partial u}{\partial x} \right)^A + \text{sign} \left( \frac{\partial^2 u}{\partial x \partial t} \right) \left( \frac{\partial u}{\partial x} \right) \right] \frac{\partial^2 u}{\partial x^2} \\ &= \frac{h \omega^3 A^2}{2c_0} \left\{ 2 \sin(\omega\tau + \phi) - \frac{8}{\pi} \left[ \frac{1}{3} \cos(\omega\tau + \phi) - \sum_{m=1}^{+\infty} \frac{\cos [(2m+1)(\omega\tau + \phi)]}{(2m-1)(2m+3)} \right] \right\}. \end{aligned} \quad [17.13]$$

Clearly, only the part depending of the strain rate sign in the hysteretic quadratic nonlinearity is able to excite all the odd harmonics in a single interaction of the waves (after a first stage of successive approximations).

It is worth noting here that the right-hand term of equation [17.9] does not contribute to the nonlinear sources in this approximation, because  $\partial A / \partial x = 0$ . It can be shown [GUS 05b] that the contribution of the right-hand term of [17.9] to the nonlinear processes is negligible compared with the contribution of the hysteresis



of the modulus (as presented in equation [17.7]), even in the general case of weak interaction of co-propagating waves. However, the right-hand term of equation [17.9] is important in the interactions of counter-propagating acoustic waves [GUS 05b], especially in acoustic resonators [GUS 05a, OST 05].

From equations [17.11] – [17.13], it can be concluded that the nonlinearity of the material leads to the modification of the wave spectrum, and also of the parameters of the wave at the fundamental frequency. Due to the weak nonlinearity, these modifications accumulate slowly with time (compared with the changes that take place during an acoustic period), resulting in a slow evolution of the acoustic field. This physical reality can be formalized by the following mathematical expression of the acoustic field:

$$u = u_2 = A(\mu t) \sin [\omega \tau + \phi(\mu t)] + u'(\mu t, \omega \tau). \quad [17.14]$$

In this equation,  $u'$  describes the new spectral components of the acoustic field. The small dimensionless parameter  $\mu \ll 1$ , placed in the arguments of the functions before the time  $t$ , indicates that the function varies slowly with time. Therefore, as the two processes depending on time have different time scales, they are explicitly described in proposed solution [17.14] by different arguments ( $\tau = t - x/c_0$  and  $t$ ). The first argument  $\tau$ , describing the wave profile variations on a one-period scale, is called the “fast” time. The second argument  $t$  is introduced to describe the accumulation of distortions of the wave profile, taking place on a scale significantly exceeding the wave period. It is called the “slow” time [RUD 77]. The introduction of the coefficient  $\mu$  in front of the slow variable is more of a tradition than a necessity [RUD 77]. In fact,  $\mu$  only appears in this argument to remind us that the derivative with respect to this variable is much smaller than the derivative with respect to  $\tau$ . The other way to mathematically express the idea of a slow variation of the wave profile consists of writing the temporal derivative in the form

$$\partial/\partial t = \mu \partial/\partial t + \partial/\partial \tau. \quad [17.15]$$

When a solution like [17.14] is substituted into the left-hand side of equation [17.9], and relationships [17.15] and  $\partial/\partial x = -(1/c_0)\partial/\partial \tau$  are used, it appears that the terms of zero order in  $\mu$  ( $\mu^0 \sim 1$ ) are mutually canceled. By neglecting the terms of order  $\mu^2$ , and retaining only the terms of order  $\mu$ , the linear part of the left-hand side can be written in the form  $2\mu[\omega A_t \cos(\omega \tau + \phi) - \omega A \phi_t \sin(\omega \tau + \phi) + u'_{t\tau}]$ . By keeping the linear terms in the left-hand side, and moving the nonlinear terms to the right-hand side, the equations describing the amplitude and phase variations of the fundamental wave are obtained:

$$A_t = - \left( \frac{2}{3\pi} \frac{h\omega^2}{c_0} A \right) A \equiv - \frac{A}{t_H(A)}, \quad [17.16]$$

$$\phi_t = -\frac{h\omega^2 A}{2c_0} + \frac{\beta\omega^3 A^2}{8c_0^2}. \quad [17.17]$$

The equation that describes the generation of higher harmonics in a single act of nonlinear acoustic interaction is also obtained:

$$\begin{aligned} u'_{t\tau} &= -\frac{\varepsilon\omega^3 A^2}{4c_0} \sin [2(\omega\tau + \phi)] - \frac{\beta\omega^4 A^3}{8c_0^2} \sin [3(\omega\tau + \phi)] \\ &+ \frac{2h\omega^3 A^2}{\pi c_0} \sum_{m=1}^{+\infty} \frac{\cos [(2m+1)(\omega\tau + \phi)]}{(2m-1)(2m+3)} \\ &\equiv u'_{\tau}/t_{NL}(A). \end{aligned} \quad [17.18]$$

The solutions presented by formulae [17.16]–[17.18] give the possibility of comparing the roles of the different acoustic nonlinearities. From equation [17.16], it follows that only the hysteretic nonlinearity influences the amplitude of the fundamental wave, in a first approximation (in the first step of the nonlinear interaction phenomenon), introducing fundamental wave absorption (because  $h > 0$ ). This absorption is nonlinear as it depends on the wave amplitude. According to equation [17.16], the absorption coefficient is proportional to the wave amplitude:

$$\alpha_H = \frac{1}{c_0 t_H(A)} = \frac{2}{3\pi} h \left( \frac{\omega}{c_0} \right)^2 A \sim A^1. \quad [17.19]$$

It should be mentioned here that the separation of the fast and slow time scales applied in the analysis reduces the validity of the obtained formula [17.16] to the domain controlled by inequality  $t_H \gg \omega^{-1}$ , corresponding to  $\alpha_H \ll k$ . Each of these inequalities can be rewritten in terms of a condition on the acoustic displacement amplitude  $A \ll (3\pi)/(2h)(1/k) \sim \lambda/h$ , or on the acoustic Mach number  $M \equiv s_A$ ,

$$s_A \ll \frac{3\pi}{2h}. \quad [17.20]$$

Solution [17.17] demonstrates that the hysteretic nonlinearity and the cubic nonlinearity modify the velocity of the fundamental wave. In order to evaluate this modification, it is sufficient to take into account that from the point of view of propagative waves [17.10], the slow variation in time is equivalent to a slow variation with the distance  $x = c_0 t$ . Therefore,  $\phi_t \simeq c_0 \phi_x$ , equation [17.17] can be integrated and the phase can be presented in the form,

$$\phi = \phi_0 + \frac{1}{c_0} \left( \frac{\partial \phi}{\partial t} \right) x, \quad [17.21]$$

where  $\phi_0$  is the phase obtained when the nonlinear interactions are neglected. Assuming that the modifications  $\Delta c_{NL}$  of the wave velocity, resulting from the nonlinearity of the material, are small ( $\Delta c_{NL} \ll c_0$ ), the solution contained in [17.14], [17.17] and [17.21], can be combined in the form  $u_2 - u' = A \sin[\omega(t - \frac{x}{c_0 + \Delta c_{NL}}) + \phi_0]$ , where

$$\Delta c_{NL} = \frac{1}{k} \frac{\partial \phi}{\partial t} = \left( -\frac{h\omega A}{2} + \frac{\beta\omega^2 A^2}{8c_0} \right). \quad [17.22]$$

According to [17.22], the velocity of the fundamental wave is modified by the nonlinearities of odd symmetry. The quadratic elastic nonlinearity, which has an even symmetry, does not affect the sound velocity within the frame of the first approximation. Because  $h > 0$ , the hysteretic nonlinearity slows down the acoustic wave  $\Delta c_H \equiv -(h\omega/2)A = -(h/2)c_0 s_A < 0$  (this is equivalent to a softening of the material). The sign of the speed change  $\Delta c_\beta$  induced by the elastic cubic nonlinearity depends on the sign of  $\beta$ . It is important to note that  $|\Delta c_H|$  increases proportionally with the wave amplitude, while  $|\Delta c_\beta|$  is quadratic in amplitude. It is an important difference, which helps to identify the dominant nonlinearity from the analysis of experimental data (see section 18.2.3, Chapter 18). The condition  $|\Delta c_{NL}| \ll c_0$ , required for the validity of the obtained formula, leads in the case of hysteretic nonlinearity to conditions on the wave amplitude, which are similar to those of equation [17.20]. In the case of a cubic nonlinearity, the restrictions on the amplitude of the strain wave have the form:

$$s_A \ll 2\sqrt{2}/\sqrt{\beta}. \quad [17.23]$$

In agreement with solution [17.18], the second harmonic is excited only by the quadratic elastic nonlinearity (because of the even symmetry of this nonlinearity). The nonlinearities with odd symmetry excite the higher odd harmonics. The important characteristics of the quadratic hysteretic nonlinearity is its ability to excite all odd harmonics in a single act of nonlinear interaction, while the elastic nonlinearities only do so in several acts, sequentially, beginning with the first higher harmonics. The elastic nonlinearities can only excite waves at frequencies exceeding  $2\omega$  and  $3\omega$ , by cascade process (contained in the higher orders of successive approximations) [ZAR 71, RUD 77]. The reason for this particularity of quadratic hysteretic nonlinearity is in its infinite order.

From the evaluation of the nonlinear processes described by equations [17.11]–[17.13], it is clear that in the case of the quadratic elastic nonlinearity, the generation of the frequency  $2\omega$  is due to the fact that the wave amplitude dependent contribution to the modulus, oscillates at frequency  $\omega$ . This causes the following process of frequency mixing  $\omega + \omega = 2\omega$  and  $\omega - \omega = 0$ . In the case of cubic elastic nonlinearity, the part of the modulus depending on the wave amplitude ( $\sim \beta(\frac{\partial u}{\partial x})^2$ )

contains the second harmonic  $2\omega$  and the zero frequency (induced averaged value). This results in the generation of the third harmonic  $2\omega + \omega \rightarrow 3\omega$  and in the action on the fundamental wave  $2\omega - \omega \rightarrow \omega$ ,  $0 + \omega \rightarrow \omega$ . The finite order of elastic nonlinearities corresponds to a limited number of acoustic frequencies interacting in a single nonlinear scattering process. However, the fact that the variation in time of the hysteretic contribution to the nonlinear modulus ( $\sim h[(\frac{\partial u}{\partial x})^A + \text{sign}(\frac{\partial^2 u}{\partial x \partial t}) \frac{\partial u}{\partial x}]$ ) contains mathematical singularities in the reversal points of the strain (see Figure 17.2b), demonstrates the presence of an infinite number of frequencies. This reveals the infinite order of the hysteretic quadratic nonlinearity. In practical purposes, in the case of hysteretic quadratic nonlinearity, the part of the modulus depending on the wave amplitude contains all even frequencies  $2n\omega$  ( $n = 1, 2, 3 \dots$ ), and the zero frequency  $\omega = 0$  ( $n = 0$ ). This leads to the parametric generation of all odd harmonics in a single process ( $2n\omega + \omega \rightarrow (2n+1)\omega$ ,  $n \neq 0$ ;  $2n\omega - \omega \rightarrow (2n-1)\omega$ ,  $n \neq 0, 1$ ) and the action on the fundamental ( $0 + \omega \rightarrow \omega$ ,  $2\omega - \omega \rightarrow \omega$ ). To conclude with the comparison of the consequences of a single process of nonlinear interaction associated with different kinds of nonlinearities, the validity condition of equation [17.18] is given by the following inequality:  $t_{NL}(A) \gg \omega^{-1}$ . In the case of cubic and hysteretic nonlinearities, these conditions are similar to [17.20] and [17.23]. In the case of quadratic elastic nonlinearity, the restrictions on the amplitude have the form

$$s_A \ll 8/\varepsilon, \quad [17.24]$$

which is always fulfilled in nonlinear acoustics.

It should be clearly understood that conditions [17.20], [17.23] and [17.24] do not guarantee that the solutions obtained by integration of equations [17.16]–[17.18] correspond to the physical reality in the situations where several consecutive processes of nonlinear interaction could take place. For example, it is well known that the quadratic elastic nonlinearity can, due to the process of cascade harmonic generation, cause the formation of what is commonly called a weak shock in an initially sinusoidal profile of a strain wave [RUD 77]. In this case, the contribution to equation [17.14] of the fundamental frequency is not dominant compared with the contribution  $u'(\mu t, \omega \tau)$  coming from the other spectral components (the wave profile differs significantly from a monochromatic profile), and this contribution  $u'(\mu t, \omega \tau)$  must be included in the nonlinear terms of equations [17.16]–[17.18]. The theoretical analysis of the solutions of equation [17.9] beyond the method of successive approximations, made in [GUS 97, GUS 98a, GUS 02c, ALE 04a], demonstrates that in micro-inhomogeneous mediums the quadratic hysteretic nonlinearity can also cause an important deviation from the monochromatic wave profile. In particular, discontinuities in the temporal derivatives of the strain (corresponding to shocks in the temporal profiles of the strain rate) can appear close to the maximum and the minimum of the loading history, either in a monochromatic mode [GUS 98a, GUS 97, GUS 02c], or in a pulsed mode, with a broadband spectrum [GUS 00, GUS 03a]. The characteristic distance at which an

important change of the wave profile takes place caused by a quadratic hysteretic nonlinearity can be estimated as:

$$x_H \sim 1/(khs_A) \quad [17.25]$$

which differs from the estimation of the distance of shock formation associated with the quadratic elastic nonlinearity [RUD 77] only by replacing the parameter  $\varepsilon$  with the parameter  $h$ . This is an expected result because of the quadratic nature of the considered nonlinearities. The generation of the profile of strain waves with peaks of low curvature radius has also been predicted for ring resonators made of materials with hysteretic quadratic nonlinearity [GUS 03b]. It should be highlighted that the effects predicting a strong nonlinear modification of the wave profile can be experimentally observed only if the characteristic length [17.25] is shorter than the other characteristic lengths associated with the linear attenuation process, including diffraction, absorption or scattering, or with the nonlinear processes of shock formation caused by quadratic elastic nonlinearity.

Although the model of hysteresis independent of the strain rate is adequate in many cases, there are an increasing number of experiments indicating that the dependence of the hysteretic nonlinearity on the amplitude of the strain rate (and not only on its sign) must be taken into account by the general theory, and that other nonlinearity mechanisms, not presented here, can appear in micro-inhomogenous materials. The possibilities for developing hysteresis models depending on the strain rate, including nonlinear absorption of the non-hysteretic nature, and elastic nonlinearity of a power 3/2 (Hertz contacts), are presented in the following sections.

#### **17.2.4. Nonlinear and non-hysteretic absorption in micro-inhomogenous materials**

Many experiments (see [ZAI 00, NAZ 93, NAZ 95, ZAI 02a, ZAI 02b, ZAI 03] and their references) indicate that for micro-inhomogenous materials, there are other possibilities of nonlinear acoustic dissipation mechanisms, in addition to the one related to the hysteretic nonlinearity, see equation [17.19]. It is well documented that the acoustic wave can induce an additional absorption, or alternatively a transparency for another wave, depending on the nature of the material and the conditions of the experiment [ZAI 02a, ZAI 03]. The effects of self-induced absorption and self-induced transparency (i.e. the influence of the acoustic wave on its own absorption) have also been observed [NAZ 93, NAZ 95, FIL 08].

There is currently no general and widely accepted theory describing these phenomena. However, from a physical point of view, it seems reasonable to assume, as a first approximation, that the presence of a wave in the material could change the existing mechanisms for the absorption of another wave, instead of creating new mechanisms of energy dissipation (although, in principle, the second possibility cannot be excluded *a priori*).

The most general phenomenological description of the linear absorption of sound in the material may be formulated by assuming that it can be attributed to some relaxation processes in the material. It is generally accepted that the physical parameters of a system cannot instantaneously follow the external excitation, instead they reach their equilibrium values required by the external action with some delay. This leads to memory or rheology phenomena in the system: the current value of a parameter depends not only on the current value of the external loading, but generally also on the complete history of the external action. In many cases, the approach of a parameter to a new equilibrium value can be approximated as being exponential in time. In nonlinear acoustics [RUD 77], this phenomenological approach is attributed to Mandelshtam and Leontovich, and can be formalized mathematically as indicated below. It is assumed that the acoustic stress  $T$  (i.e. the deviation of the stress from its value without acoustic loading) depends not only on the strain  $s$ , but also on some additional parameters related to some additional internal degrees of freedom of the material. Assuming the existence of a single additional internal parameter, the deviation of its current value from its value without acoustic loading is denoted by  $p$ . In other words,  $p$  can be called the acoustic value of the parameter. Thus, the stress is described by the function  $T = T(s, p)$ . Considering all the acoustic variables are small (with appropriate normalization if necessary), this relationship can be approximated by the first two terms of its expansion in Taylor series

$$T = T(s, p) \cong \frac{\partial T}{\partial s}(0, 0)s + \frac{\partial T}{\partial p}(0, 0)p. \quad [17.26]$$

It is the parameter  $p$ , that approaches its equilibrium (quasi-static) value  $p_0(s(t))$ , corresponding to the current value of the strain  $s(t)$ , not instantly but with a delay.

The dynamics of this delay phenomenon is approximated by the equation

$$\frac{\partial p}{\partial t} = -\frac{1}{\tau_R} [p - p_0(s)], \quad [17.27]$$

where  $\tau_R$  is the relaxation time. The solution of equation [17.27] leads to:

$$p = \frac{1}{\tau_R} \int_{-\infty}^t p_0(s) e^{-\frac{(t-t')}{\tau_R}} dt'. \quad [17.28]$$

As expected, and in agreement with equation [17.28], the value  $p$  of the internal parameter does not coincide with the value  $p_0$  of this parameter at equilibrium, but has a memory of strain loading history. However, this memory effect weakens exponentially over time.

In linear acoustics, it is also assumed that the equilibrium (static) value of the unspecified parameter is itself proportional to the acoustic strain. In other words, it is

assumed that the dependence  $p_0 = p_0(s)$  is analytical and can be approximated by the first term of its expansion in Taylor series  $p_0(s) \cong \partial p_0 / \partial s(0)s$ . Using equation [17.28], the stress/strain relationship [17.26] takes the final form:

$$T \equiv Es - \Delta \bar{E} \int_{-\infty}^t \frac{\partial s}{\partial t'} e^{-\frac{(t-t')}{\tau_R}} dt', \quad [17.29]$$

where  $E = \partial T / \partial s(0, 0) + \partial T / \partial p(0, 0) \partial p_0 / \partial s(0)$  is the static (in equilibrium) Young modulus of the material, and  $\Delta \bar{E} = \partial T / \partial p(0, 0) \partial p_0 / \partial s(0)$  is the contribution of the internal parameter to this modulus (i.e. the contribution of an additional degree of freedom of the system). In acoustics, the second term of equation [17.29] usually describes just a small deviation from the static Hooke's law.

When rheological model [17.29] is substituted in [17.1], and a plane acoustic wave of number  $k$  and frequency  $\omega$  ( $u \propto \exp[i(kx - \omega t)]$ ,  $s = \partial u / \partial x$ ) is assumed, the dispersion relationship  $k = k(\omega)$  for acoustic waves in the material is obtained. The real part of the wave number describes the phase velocity of sound:

$$c \equiv \frac{\omega}{\Re(k)} \cong \left( \frac{E}{\rho} \right)^{1/2} \left[ 1 + \left( \frac{-\Delta \bar{E}}{2E} \right) \frac{\omega^2}{\omega^2 + \tau_R^{-2}} \right], \quad [17.30]$$

and the imaginary part of the wave number provides the sound absorption coefficient

$$\alpha \equiv \Im(k) \cong \left( \frac{E}{\rho} \right)^{-1/2} \left( \frac{-\Delta \bar{E}}{2E} \right) \frac{\omega^2 \tau_R^{-1}}{\omega^2 + \tau_R^{-2}}. \quad [17.31]$$

Note that according to prediction [17.31], the absorption of acoustic energy requires that  $\Delta \bar{E} < 0$ , i.e. the “softening” of the material. In the derivation of [17.30] and [17.31] the assumption  $|\Delta \bar{E}|/E \ll 1$ , essential for weak deviation of the materials rheology from Hooke's law, has been used. In agreement with [17.30] the speed of sound at high frequencies  $c(\omega \gg \tau_R^{-1}) \cong (E/\rho)^{1/2} [1 + |\Delta \bar{E}|/2E] \equiv c_\infty$  exceeds the speed of sound in quasi-equilibrium at low frequencies  $c(\omega \ll \tau_R^{-1}) \cong (E/\rho)^{1/2} \equiv c_0$ . Therefore, the importance of the contribution due to the relaxation in the stress/strain relationship can be characterized by the parameter  $|\Delta \bar{E}|/2E \cong (c_\infty/c_0) - 1$ .

[17.31] describes, for frequencies significantly lower than the inverse of the relaxation time ( $\omega \ll \tau_R^{-1}$ ), a viscous-type absorption with a coefficient  $\alpha \propto \omega^2$ . The growth of the absorption coefficient with the increase of the acoustic frequency, described by [17.31], reaches saturation at high frequencies ( $\omega \gg \tau_R^{-1}$ ). It is important to note that the decrement of the acoustic wave in a medium with a single relaxation process exhibits a of resonance type behavior:

$$D \equiv 2\pi \frac{\Im m(k)}{\Re e(k)} \cong \pi \left( \frac{|\Delta \bar{E}|}{E} \right) \frac{\omega \tau_R^{-1}}{\omega^2 + \tau_R^{-2}}. \quad [17.32]$$

As predicted by [17.32], the maximum of the decrement occurs when  $\omega = \tau_R^{-1}$ . The decrement increases at low frequencies and decreases at high frequencies:

$$D \cong \pi \left( \frac{|\Delta \bar{E}|}{E} \right) \begin{cases} \omega \tau_R & \text{if } \omega \ll \tau_R^{-1} \\ (\omega \tau_R)^{-1} & \text{if } \omega \gg \tau_R^{-1} \end{cases}. \quad [17.33]$$

The importance of the described relaxation model is related to the possibility of modeling practically any kind of dependence of the decrement on frequency, by assuming a continuous spectrum of the relaxation times in the system, and by choosing an appropriate continuous dependence of the “density” distribution of the relaxation strength  $\Delta E(\tau_R)$  on the relaxation time:

$$D \cong \frac{\pi}{E} \int_0^\infty |\Delta E(\tau_R)| \frac{\omega \tau_R^{-1}}{\omega^2 + \tau_R^{-2}} d\tau_R. \quad [17.34]$$

In other words, any dependence  $D = D(\omega)$  can be modeled as a superposition of dependencies of the [17.32] type.

From a nonlinear acoustics point of view, the nonlinear phenomena in the framework of phenomenological models [17.32] and [17.34] are possible if the propagation of an acoustic wave in the material changes the relaxation times and/or the relaxation strength  $\Delta E$  (or its density distribution  $\Delta E(\tau_R)$ ). For example, if in the presence of a sufficiently strong acoustic wave the relaxation time  $\tau_R$  in model [17.32] increases, this then causes the shift of resonance curve [17.32] of the decrement in the direction of low frequencies (see Figure 17.7, where  $\tau_{R2} > \tau_{R1}$ ). The material begins to absorb more at low frequencies  $\omega < 1/\sqrt{\tau_{R1}\tau_{R2}}$ , demonstrating self-induced absorption. It absorbs less at high frequencies  $\omega > 1/\sqrt{\tau_{R1}\tau_{R2}}$ , demonstrating the self-induced transparency. The increase or decrease of the modulus  $\Delta \bar{E}$  with the increase of the acoustic wave amplitude causes an induced absorption or an induced transparency, respectively, at all frequencies. This qualitative description [FIL 06] provides an insight into how nonlinear absorption and nonlinear transparency may be understood on a phenomenological basis. To understand the physics of the nonlinear dissipative phenomena, it is necessary to study various macroscopic and microscopic models for the possible relaxation processes. One of these models is connected to the irreversible process of heat conduction close to contacts between the lips of a crack in damaged materials, or between the grains in granular materials, and will be analyzed in detail in Chapter 18 [ZAI 02a, ZAI 02b, ZAI 03, FIL 08, FIL 06]. In the latter case, the relaxation time  $\tau_R$  depends on the contact surface area, which can vary in the presence of an acoustic wave, while the modulus  $\Delta \bar{E}$  depends on the number of contacts dissipating the acoustic energy (this number may increase or decrease in the acoustic wave field).



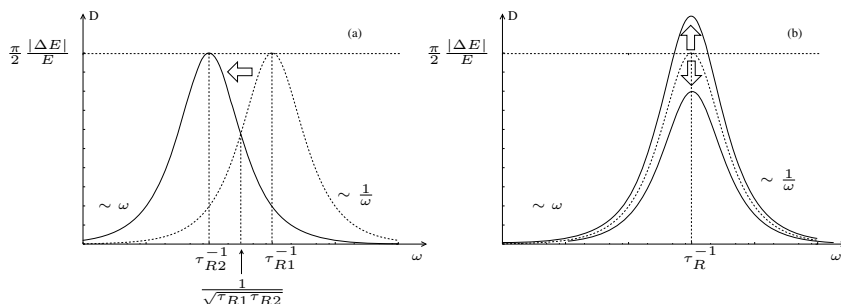


**Figure 17.7.** (a) Modification of the dependence of acoustic decrement  $D$  on the frequency  $\omega$ , due to the acoustically induced increase of the characteristic relaxation time ( $\tau_{R2} > \tau_{R1}$ ). The additional absorption and transparency are induced at frequencies  $\omega < 1/\sqrt{\tau_{R1}\tau_{R2}}$  and  $\omega > 1/\sqrt{\tau_{R1}\tau_{R2}}$ , respectively. (b) Modification of acoustic decrement due to the change of the number of dissipative contacts. If the number of absorbers increases/decreases, the self-induced absorption/transparency can be observed

### 17.2.5. Hysteretic nonlinearity of relaxation processes or relaxation of the hysteretic nonlinearity

In the case of micro-inhomogenous materials, at least a part of the delay in the response of the material to an external loading can be due to micro-mechanical elements (dislocations, cracks, contacts, etc.). This is clear from previous discussions in section 17.2.2.1 on particular micro-mechanical elements which have hysteretic properties. In fact, the jumps of an element from a state that becomes unstable because of acoustic loading, to the closest metastable state, are not instantaneous and take some time. For example, it obviously takes some time for a crack to change its configuration (to open or to close). The jump in strain at critical levels of stress in the model of hysteron (Figure 17.5) is not instantaneous. As mentioned earlier, this consideration limits the validity of the rate-independent (quasi-static) model of the hysteretic nonlinearity presented in section 17.2.3 to acoustic frequencies that are not too high (the frequency must be lower than the inverse of the jump duration) and not too low (the frequency must be higher than the inverse of the time necessary to reach complete equilibrium in the system).

The simplest phenomenological extension of the earlier model of rate-independent hysteresis to higher frequencies can be obtained by combining the theory presented in section 17.2.2 with the theory of relaxation processes presented in section 17.2.4. This theoretical generalization [GUS 98a] may be understood as the theory of nonlinear hysterons with relaxation, or as the theory of relaxation with additional degrees of freedom, which are hysteretic in their responses to the acoustic loading.

In fact, the theory of relaxation presented in section 17.2.4 offers a way to predict the transient behavior (dynamics) of any parameter  $p$  if its behavior at equilibrium  $p_0$ ,

in response to the strain, is known and if we assume the existence of a single relaxation time  $\tau_R$  for this degree of freedom (see equation [17.28]). Using [17.28], the dynamic contribution of a hysteron, for which only one relaxation time  $\tau_R(s_o, s_f)$  is taken into account, may be presented in the form:

$$T_h'^{dyn} = \frac{1}{\tau_R} \int_{-\infty}^t T_h'(s, s_{t'}) e^{-\frac{(t-t')}{\tau_R(s_o, s_f)}} dt',$$

where the stress at the hysteretic elements is identified to parameter  $p$ , and where  $T_h'$  under the integral is the quasi-static stress/strain relationship (for example Figure 17.5e). Clearly, a possible dependence of the relaxation time of the individual hysteretic elements on the parameters  $s_o$  and  $s_f$  of the hysterons can provide additional complications in the statistical summation of contributions due to hysterons. However, assuming in a first approximation that the relaxation times do not vary significantly among different hysterons that are activated by the acoustic loading, the order of the integrations over time and over the distribution of elements can be switched. With this approximation of a single relaxation time [GUS 98a], the dynamic contribution of all the hysteretic elements  $T_H^{dyn}$  is related to the quasi-static total contribution  $T_H$  (predicted by any theory of rate-independent hysteresis, including the one previously presented) by:

$$T_H^{dyn} = \frac{1}{\tau_R} \int_{-\infty}^t T_H(s, s_{t'}) e^{-\frac{(t-t')}{\tau_R}} dt'. \quad [17.35]$$

Assuming a periodic loading characterized by the cyclic frequency  $\omega$  it is useful to introduce into [17.35] the normalized time variable  $\theta = \omega t$ , and to rewrite [17.35] in three different forms:

$$\begin{aligned} T_H^{dyn} &= \frac{1}{\omega \tau_R} \int_{-\infty}^{\theta} T_H(s, s_{\theta'}) e^{-\frac{(\theta-\theta')}{\omega \tau_R}} d\theta' \\ &= \sum_{n=0}^{\infty} (-1)^n (\omega \tau_R)^n \frac{\partial^n T_H}{\partial \theta^n}(\theta) \\ &= \sum_{n=1}^{\infty} (-1)^{n-1} \frac{1}{(\omega \tau_R)^n} \int_{-\infty}^{\theta} \int_{-\infty}^{\theta_1} \cdots \int_{-\infty}^{\theta_{n-1}} T_H(\theta_n) d\theta_1 d\theta_2 \cdots d\theta_n. \end{aligned} \quad [17.36]$$

Both infinite sums in [17.36] are obtained through formal integration by parts of the relaxation integral [17.35]. The first infinite sum is useful for describing the acoustic response at low frequencies  $\omega \ll \tau_R^{-1}$ , where only a few first leading terms of the expansion in series can be retained:

$$T_H^{dyn}(\omega \ll \tau_R^{-1}) \simeq T_H - (\omega \tau_R) \frac{\partial T_H}{\partial \theta}(\theta) + \cdots \quad [17.37]$$

The second series in [17.36] provides the principal term of the asymptotic behavior at high frequencies  $\omega \gg \tau_R^{-1}$

$$T_H^{dyn}(\omega \gg \tau_R^{-1}) \simeq \frac{1}{\omega \tau_R} \int_{-\infty}^{\theta} T_H(s, s_{\theta_1}) d\theta_1. \quad [17.38]$$

Asymptotic model [17.37] confirms that, at frequencies  $\omega \ll \tau_R^{-1}$ , the dynamic response can be accurately predicted by the rate-independent model of nonlinear hysteresis, and that small corrections can be obtained if necessary. The asymptotic model of [17.38] predicts that, at frequencies exceeding the inverse of the relaxation time of micro-mechanical elements ( $\omega \gg \tau_R^{-1}$ ), the contribution of the hysteretic nonlinearity to the total stress/strain relationship of the material diminishes inverse proportionally to the frequency. Model [17.38] also predicts that, when the frequency increases, the hysteresis loop shrinks along the stress axis without changing its functional form. Both theoretical predictions for the asymptotic behavior at high frequencies of the hysteretic nonlinearity, i.e. for the shape of the hysteresis loop and for  $T_H \propto \omega^{-1}$ , are linked to the hypothesis of a single relaxation time in the system. However, even if the relaxation time of individual elements depend heavily on strain in the strain interval accessible for the acoustic loading, it is expected that the predicted behavior will occur at frequencies that are much higher than the inverse of the smallest relaxation time of the elements. It is quite possible that the relaxation mechanism described above, which predicts a decrease of the role of hysteretic nonlinearity with frequency, could be at least partially responsible for some experimental observations of a diminishing of the effective parameter of hysteretic quadratic nonlinearity with increasing acoustic frequency in ceramics and poly-crystalline metals [NA 94, NAZ 00].

### 17.2.6. Hertzian nonlinearity in unconsolidated granular materials

In unconsolidated granular materials, the major contribution of the acoustic nonlinearity comes from the Hertz contacts [BEL 94, TOU 04, BEL 97, TOU 05]. The nonlinearity of an individual contact between two spherical surfaces is due to the fact that the rigidity of the contact varies when the loading is changed (because the surface of the contact changes). The stress/strain relationship in a granular medium, where all the contacts of an individual spherical bead are equally loaded and the macroscopic strain in the medium is  $\bar{s}$ , can be presented in the form [BEL 97]

$$\bar{T} = -\bar{n} \frac{(1-\alpha)E}{3\pi(1-\nu^2)} (-\bar{s})^{3/2} H(-\bar{s}) \equiv -\bar{n} T_G (-\bar{s})^{3/2} H(-\bar{s}), \quad [17.39]$$

where  $\alpha$  is the porosity,  $\nu$  is the Poisson coefficient,  $E$  is the Young modulus and  $\bar{n}$  is the average number of contacts of an individual bead with its neighbors. Stress/strain relationship [17.39] is the direct consequence of a Hertz-type relation [JOH 87]

for a single contact, when the adhesion hysteresis is neglected. The Heaviside function  $H(-\bar{s})$  takes into account the fact that the unconsolidated material must be compressed when it is loaded ( $\bar{s} < 0$ ). It should be noted that the local stress and the local strain (microscopic) in the vicinity of a contact differ from those in equation [17.39]. Noting that the total macroscopic strain  $\bar{s}$  consists of a static part  $s_0$  (pre-loading) and a dynamic acoustic part  $s$  ( $\bar{s} = s_0 + s$ ), the stress  $\bar{T}$  can be expressed by the relationship:

$$\bar{T} = -\bar{n}T_G(-s_0 - s)^{3/2}H(-s_0 - s). \quad [17.40]$$

If the strain amplitude of the acoustic wave  $s_A$  is much lower than that of the pre-loading  $s_A \ll -s_0$ , then the expansion in Taylor series of equation [17.40] provides:

$$\bar{T} \simeq -\bar{n}T_G \left[ (-s_0)^{3/2} + \frac{3}{2}(-s_0)^{1/2}s - \frac{3}{8}(-s_0)^{-1/2}s^2 + \dots \right]. \quad [17.41]$$

Therefore, when  $s_A \ll |s_0|$ , the Hertz contacts contribute, in a first approximation, to the elastic quadratic nonlinearity of the material and the corresponding nonlinear parameter  $\bar{\varepsilon}$  (in agreement with the definition introduced by equations [17.4] and [17.5]) is given by:

$$\bar{\varepsilon} \equiv -\frac{T''(s=0)}{T'(s=0)} - 1 = \frac{1}{2(-s_0)} - 1 \simeq \frac{1}{2(-s_0)}.$$

It is clear that, when  $(-s_0) \leq 10^{-2}$ , the nonlinearity of Hertz contacts dominates over the nonlinearity resulting from the nonlinear elasticity of the material composing the grains ( $|\varepsilon| \simeq 1 - 10$ , see section 17.2.1).

In the opposite limiting case  $s_A \gg |s_0|$ , the compression during half a period of the acoustic wave ( $-s > 0$ ) provides the dominant contribution to the stress field:

$$\bar{T} = -\bar{n}T_G(-s)^{3/2}H(-s) \quad [17.42]$$

This relationship describes the acoustic nonlinearity of a power  $3/2$ , characteristic of the weak quasi-static loading Hertz contacts (compare equations [17.42] and [17.39]). The asymptotics formulated in equations [17.41] and [17.42] indicate that, in granular materials, there may be a transition from the quadratic nonlinearity to the nonlinearity of Hertz (of a power  $3/2$ ) when the amplitude of the acoustic strain increases from  $s_A \ll |s_0|$  to  $s_A \gg |s_0|$ .

In reality, physics is much more complex because the contacts in a granular material are not equally loaded [JAE 96, TOU 04]: some contacts are weakly loaded,

while other contacts are strongly loaded, and there are even contacts that are not loaded at all (i.e. these contacts can be created by acoustic loading or by increase of pre-loading). The natural generalization of the result [17.40] to the case of a distribution  $n(s_0)$  of pre-loaded contacts is:

$$\bar{T} = -\bar{n}T_G \int_{-\infty}^{-s} n(s_0) (-s_0 - s)^{3/2} ds_0 \quad [17.43]$$

The upper bound of this integral takes into account the absence of contribution to the stress of not loaded contacts (open contacts), and the distribution function  $n(s_0)$  is normalized:

$$\int_{-\infty}^{+\infty} n(s_0) ds_0 = 1.$$

The formal expansion in Taylor series of equation [17.43] for a weak acoustic wave provides:

$$\begin{aligned} \frac{\bar{T}}{\bar{n}T_G} &\simeq - \int_{-\infty}^0 n(s_0) (-s_0)^{3/2} ds_0 + \frac{3}{2} \left[ \int_{-\infty}^0 n(s_0) (-s_0)^{1/2} ds_0 \right] s \\ &\quad - \frac{3}{8} \left[ \int_{-\infty}^0 n(s_0) (-s_0)^{-1/2} ds_0 \right] s^2 + \dots \end{aligned}$$

The coefficient  $(-s_0)^{1/2}$  in the second integral ensures that only the strongly loaded contacts in the granular material could control the linear acoustic properties (in particular, the speed of sound). However, the coefficient  $(-s_0)^{-1/2}$  in the third integral indicates that the weakly loaded contacts in the distribution  $n(s_0)$  could provide the main contribution to nonlinearity. The nonlinear parameter depends on the distribution of the contact preloading:

$$\bar{\varepsilon} \simeq \frac{\int_{-\infty}^0 n(s_0) (-s_0)^{-1/2} ds_0}{2 \int_{-\infty}^0 n(s_0) (-s_0)^{1/2} ds_0}.$$

Recent experiments [TOU 04, TOU 05] described in Chapter 18 confirm these basic ideas about the nonlinear acoustic behavior of unconsolidated granular materials, in particular, the possible dependence of nonlinear acoustic effects of a power  $3/2$  on the excitation amplitude.

### 17.3. Conclusions

Theoretical models for the acoustic nonlinearity of micro-inhomogenous media presented here generally help to link the nonlinear acoustic responses of a

material with characteristic parameters of the micromechanical elements of this material. These models can be used both to understand the fundamental physical processes underlying the nonlinear acoustic effects observed experimentally, and to develop qualitative or quantitative methods for non-destructive evaluation of micro-inhomogenous materials.

Even using the simplest method of successive approximations (section 17.2.3), it was possible to predict particular features of some nonlinear acoustic processes in micro-inhomogenous media of nonlinear process of non-collinear interaction in media with a hysteretic quadratic nonlinearity independent of the loading rate [GUS 02b, GUS 02a], self-modulation instability of acoustic waves [GUS 01], self-demodulation of acoustic signals (parametric emission process) [GUS 98b], and absorption of sound by sound [GUS 05b, GUS 03d]. For example, it has been predicted theoretically [GUS 03d] that a high-frequency acoustic signal with low amplitude can cause either an induced absorption or an induced transparency for an intense harmonic wave, depending on their relative phase shift. The possibility of induced transparency has also been confirmed for the case of hysteretic nonlinearity by avoiding the method of successive approximations and taking into account the fact that the acoustic field, in the process of frequency mixing, cannot be described as a field with a single minimum and a single maximum over a period. Therefore, memory of turning points in loading history (discrete memory section 17.2.1) must be taken into account more precisely [ALE 04a, ALE 04b, ZAI 05].

Although these theoretical models are still in development and in an improving phase, they can already be used in this form to explain the phenomena of nonlinear acoustics in micro-inhomogenous materials and materials with cracks. Some references of such applications of the presented theories have been given previously in this chapter, without discussing the details of each experiment. In the following (Chapter 18), more details are given on classic and modern experimental methods, involving nonlinear acoustic phenomena in micro-inhomogenous media (including damaged material and granular materials). The usefulness of theories presented in section 17.2 for the analysis of experimental results presented in Chapter 18 will be demonstrated.

#### 17.4. Bibliography

- [ALE 04a] ALESHIN V., GUSEV V.E. and ZAITSEV V.YU., “Propagation of acoustic waves of non simplex form in a material with hysteretic quadratic nonlinearity and numerical simulations”, *J. Computational Acoustics*, vol. 12, pp. 319–354, 2004.
- [ALE 04b] ALESHIN V., GUSEV V.E. and ZAITSEV V.YU., “Propagation of the initially bi-harmonic sound waves in 1-D semi-infinite media with hysteretic nonlinearity”, *Ultrasonics*, vol. 42, pp. 1053–1059, 2004.

- [BEL 94] BELYAEVA I.Y., ZAITSEV V.YU. and TIMANIN E.M., "Experimental study of nonlinear elastic properties of granular media with nonideal packing", *Acoust. Phys.*, vol. 40, pp. 789–793, 1994.
- [BEL 97] BELYAEVA I.Y., OSTROVSKY L.A. and ZAITSEV V.YU., "Microstructure induced nonlinearity of unconsolidated rocks as related to seismic diagnostics problems", *Nonlinear Processes in Geophysics*, vol. 4, pp. 4–10, 1997.
- [BER 96] BERTOTTI G., "Energetic and thermodynamic aspects of hysteresis", *Phys. Rev. Lett.*, vol. 76, pp. 1739–1742, 1996.
- [BER 98] BERTOTTI G., *Hysteresis in Magnetism*, Academic, Boston, 1998.
- [BHU 95] BHUSHAN B., ISRAELACHVILI J.N. and LANDMANN U., "Nanotribology: friction, wear and lubrication at the atomic scale", *Nature*, vol. 374, pp. 607–616, 1995.
- [BRE 84] BREAZEALE M.A. and PHILIP J., "Determination of third-order elastic constants from ultrasonic harmonic generation measurements", in MASON W.P. and THURSTON R.N. (Eds.), *Physical Acoustics, Principles and Methods*, vol. XVIII, Academic Press, Orlando, 1984.
- [BUC 78] BUCK O., MORRIS W.L. and RICHARDSON J.M., "Acoustic harmonic generation at unbonded interfaces and fatigue cracks", *Appl. Phys. Lett.*, vol. 33, pp. 371–373, 1978.
- [BUR 93] BURNHAM N.A., COLTON R.J. and POLLOCK K.M., "Interpretation of force curves in force microscopy", *Nanotechnology*, vol. 4, pp. 64–80, 1993.
- [BUR 97] BURNHAM N.A., BEHREND O.P., OULEVEY F., GREMAUD G., GALLO P.-J., GOURDON D., DUPAS E., KULIK A.J., POLLACK H.M. and BRIGGS G.A.D., "How does a tip tap?", *Nanotechnology*, vol. 8, pp. 67–75, 1997.
- [BUR 99] BURNHAM N.A. and KULIK A.J., "Surface forces and adhesion", in BUSHNAN B. (Ed.), *Handbook of Micro/Nano Tribology*, CRC Press, Boca Racon, 1999.
- [CAP 02] CAPOGROSSO-SANSONE B. and GUYER R.A., "Dynamic model of hysteretic elastic systems", *Phys. Rev. B*, vol. 66, p. 224101, 2002.
- [CHI 64] CHILDRESS J.D. and HAMBRICK C.G., "Interaction between elastic waves in an isotropic solid", *Phys. Rev.*, vol. 136, pp. A411–A418, 1964.
- [DOW 93] DOWLING N.E., *Mechanical Behavior of Materials. Engineering Methods for Deformation, Fracture, and Fatigue*, Prentice-Hall, Inc., Englewood Cliffs, 1993.
- [FIL 06] FILLINGER L., ZAITSEV V.YU., GUSEV V.E. and CASTAGNÈDE B., "Nonlinear relaxational absorption/transparency for acoustic waves due to thermoelastic effect", *Acustica-Acta-Acustica*, vol. 92, pp. 24–34, 2006.
- [FIL 08] FILLINGER L., CASTAGNÈDE B. and GUSEV V.E., "Self-modulation of acoustic waves in resonant bars", *J. Sound and Vib.*, vol. 318, pp. 527–548, 2008.
- [GRA 66] GRANATO A.V. and LUCKE K., "The vibrating string model of dislocation damping", in MASON W.P. (Ed.), *Physical Acoustics, Principles and Methods*, vol. IV, Part A, Academic Press, New York, 1966.

- [GUS 97] GUSEV V.E., LAURIKS W. and THOEN J., “Nonlinear bulk and surface shear waves in materials with hysteresis and end-point memory”, *Phys. Lett. A*, vol. 232, pp. 77–86, 1997.
- [GUS 98a] GUSEV V., LAURIKS W. and THOEN J., “Dispersion of nonlinearity, nonlinear dispersion, and absorption of sound in micro-inhomogeneous materials”, *J. Acoust. Soc. Am.*, vol. 103, pp. 3216–3226, 1998.
- [GUS 98b] GUSEV V.E., “Parametric source in a medium with hysteretic quadratic nonlinearity”, *Acoust. Lett.*, vol. 22, pp. 30–34, 1998.
- [GUS 00] GUSEV V.E., “Propagation of the acoustic pulses in the materials with hysteretic nonlinearity”, *J. Acoust. Soc. Am.*, vol. 107, pp. 3047–3058, 2000.
- [GUS 01] GUSEV V.E., “Self-modulation instability in materials with hysteretic nonlinearity”, *Wave Motion*, vol. 33, pp. 145–153, 2001.
- [GUS 02a] GUSEV V.E., “Multiple focused-waves production by parametric mixing in a layer with hysteretic quadratic nonlinearity”, *Ultrasonics*, vol. 40, pp. 697–702, 2002.
- [GUS 02b] GUSEV V.E., “Theory of non-collinear interactions of the acoustic waves in the materials with hysteretic quadratic nonlinearity”, *J. Acoust. Soc. Am.*, vol. 111, pp. 80–94, 2002.
- [GUS 02c] GUSEV V.E. and ALESHIN V., “Strain wave evolution equation for nonlinear propagation in materials with mesoscopic mechanical elements”, *J. Acoust. Soc. Am.*, vol. 112, pp. 2666–2679, 2002.
- [GUS 03a] GUSEV V.E., “Propagation of acoustic pulses in a medium with hysteretic nonlinearity prepared by preloading”, *Acustica-Acta-Acustica*, vol. 89, pp. 445–450, 2003.
- [GUS 03b] GUSEV V.E., “Quasi-synchronous excitation of acoustic waves in materials with hysteretic quadratic nonlinearity”, *Wave Motion*, vol. 38, pp. 241–250, 2003.
- [GUS 03c] GUSEV V.E., CASTAGNÈDE B. and MOUSSATOV A., “Hysteresis in response of nonlinear bistable interface to continuously varying acoustic loading”, *Ultrasonics*, vol. 41, pp. 643–654, 2003.
- [GUS 03d] GUSEV V.E. and ZAITSEV V.YU., “Acoustic dither injection in a medium with hysteretic quadratic nonlinearity”, *Phys. Lett. A*, vol. 314, pp. 117–125, 2003.
- [GUS 04] GUSEV V.E., “Frequency dependence of dynamic hysteresis in the interaction of acoustic waves with interface”, *J. Acoust. Soc. Am.*, vol. 115, pp. 1044–1048, 2004.
- [GUS 05a] GUSEV V., “On the interaction of the counter-propagating acoustic waves in resonant rods composed of material with hysteretic quadratic nonlinearity”, *J. Acoust. Soc. Am.*, vol. 117, pp. 1850–1857, 2005.
- [GUS 05b] GUSEV V., “Revised theory for the interaction of the counter-propagating acoustic waves in materials with hysteresis of nonlinearity”, *Wave Motion*, vol. 42, pp. 97–108, 2005.
- [GUS 05c] GUSEV V.E. and TOURNAT V., “Amplitude- and frequency-dependent nonlinearities in the presence of thermally-induced transitions in the Preisach model of acoustic hysteresis”, *Phys. Rev. B*, vol. 72, p. 054104, 2005.



- [GUY 99] GUYER R.A. and JOHNSON P.A., "Nonlinear mesoscopic elasticity : evidence of a new class of materials", *Phys. Today*, vol. 52, pp. 30–35, 1999.
- [HOL 80] HOLCOMB D.J. and STEVENS J.L., "The reversible Griffith crack: a variable model for dilatancy", *J. Geophys. Res.*, vol. 85, pp. 7101–7107, 1980.
- [HOL 81] HOLCOMB D.J., "Relaxation, and microfracturing of dilatant rock", *Geophys. Res.*, vol. 86, pp. 6235–6248, 1981.
- [HUE 79] HUECKEL T. and NOVA R., "Some hysteresis effects of the behaviour of geological media", *Int. J. Solids Structures*, vol. 15, pp. 625–642, 1979.
- [ISR 99] ISRAELACHVILI J.N. and BERMAN A.D., "Surface forces and microrheology of molecularly thin liquid films", in BUSHNAN B. (Ed.), *Handbook of Micro/Nanotribology*, Chapter 9, pp. 371–425, CRC Press, Boca Raton, 1999.
- [JAE 96] JAEGER H.M., NAGEL S.R. and BERHINGER R.P., "The physics of granular materials", *Physics Today*, vol. 4, pp. 32–38, 1996.
- [JOH 71] JOHNSON K.L., KENDALL K. and ROBERTS A.D., "Surface energy and the contact of elastic bodies", *Proc. R. Soc. Lond. A*, vol. 324, pp. 301–313, 1971.
- [JOH 76] JOHNSON K.L., "Adhesion at contact of solids", in KOITER W.T. (Ed.), *Theoretical and Applied Mechanics*, North-Holland, New York, 1976.
- [JOH 87] JOHNSON K.L., *Contact Mechanics*, Cambridge University Press, Cambridge, 1987.
- [JON 63] JONES G.L. and KOBETT D.R., "Interaction of elastic waves in an isotropic solid", *J. Acoust. Soc. Am*, vol. 35, pp. 5–10, 1963.
- [KNO 73] KNOTT J.F., *Fundamentals of Fracture Mechanics*, John Wiley & Sons, New York, 1973.
- [KRA 88] KRAUSZ A.S. and KRAUSZ K., *Fracture Kinetics of Crack Growth*, Kluwer Academic Publishers, Dordrecht, 1988.
- [KRA 89] KRASNOSELSKII M.A. and POKROVSKII A.V., *Systems with Hysteresis*, Springer-Verlag, Berlin, 1989.
- [LAN 59] LANDAU L.D. and LIFSHITZ E.M., *Theory of Elasticity*, Pergamon, New York, 1959.
- [LEB 99] LEBEDEV A.B., "Amplitude-dependent elastic-modulus defect in main dislocation-hysteresis models", *Phys. Solid State*, vol. 41, pp. 1105–1111, 1999.
- [MAY 91] MAYERGOYZ I.D., *Mathematical Models of Hysteresis*, Springer, New York, 1991.
- [MCK 74] MCKAVANAGH B. and STACEY F.D., "Mechanical hysteresis in rocks at low strain amplitudes and seismic frequencies", *Phys. Earth Planetary Interiors*, vol. 8, pp. 246–250, 1974.
- [MIN 53] MINDLIN R.D. and DERESIEWICZ H., "Elastic spheres in contact under varying oblique forces", *J. Appl. Mech.*, pp. 327–344, 1953.
- [MOR 00] MOROZOV N. and PETROV Y., *Dynamics of Fracture*, Springer-Verlag, Berlin, 2000.

- [MOU 02] MOUSSATOV A., CASTAGNÈDE B. and GUSEV V.E., “Frequency up-conversion and frequency down-conversion of acoustic waves in damaged materials”, *Phys. Lett. A*, vol. 301, pp. 281–290, 2002.
- [MRO 75] MROZ Z. and LIND N.L., “Simplified theories of cyclic plasticity”, *Acta Mechanica*, vol. 22, pp. 131–152, 1975.
- [NA 94] NA J.K. and BREAZEALE M.A., “Ultrasonic nonlinear properties of lead zirconate-titanate ceramics”, *J. Acoust. Soc. Am.*, vol. 95, pp. 3213–3221, 1994.
- [NAZ 88] NAZAROV V.E., OSTROVSKY L.A., SOUSTOVA I.A. and SUTIN A.M., “Nonlinear acoustics of micro-inhomogeneous media”, *Phys. Earth Planet. Inter.*, vol. 50, pp. 65–73, 1988.
- [NAZ 93] NAZAROV V.E. and ZIMENKOV S.V., “Self-action of acoustic waves in rocks”, *Acoustics Lett.*, vol. 16, pp. 218–221, 1993.
- [NAZ 95] NAZAROV V.E., “Self-action of acoustic waves in media with nonlinear dissipation”, *Acoust. Phys.*, vol. 41, pp. 305–307, 1995.
- [NAZ 00] NAZAROV V.E., “Amplitude dependence of internal friction in zinc”, *Acoust. Phys.*, vol. 46, pp. 186–190, 2000.
- [NAZ 02] NAZAROV V.E., RADOSTIN A.V. and SOUSTOVA I.A., “Effect of an intense sound wave on the acoustic properties of a sandstone bar resonator. Experiment”, *Acoust. Phys.*, vol. 48, pp. 76–80, 2002.
- [NOW 50] NOWICK A.S., “Variation of amplitude-dependent internal friction in single crystal copper with frequency and temperature”, *Phys. Rev.*, vol. 80, pp. 249–257, 1950.
- [NOW 72] NOWICK A.S. and BERRY B.S., *Anelastic Relaxation in Crystalline Solids*, Academic Press, New York, 1972.
- [OST 01] OSTROVSKY L.A. and JOHNSON P.A., “Dynamic nonlinear elasticity of geomaterials”, *Rivista del Nuovo Cimento*, vol. 24, pp. 1–46, 2001.
- [OST 05] OSTROVSKY L.A., “Wave interaction in acoustic resonators with and without hysteresis”, *J. Acoust. Soc. Am.*, vol. 116, pp. 3348–3353, 2005.
- [PAN 95] PANGRAZ S. and ARNOLD W., *Review of Progress in QNDE*, vol. 13, THOMSON D.O. and CHIMENTI D.E. (Eds.), Plenum Press, New York, 1995.
- [RIC 79] RICHARDSON J.M., “Harmonic generation at an unbonded interface. I. Planar interface between semi-infinite elastic media”, *Int. J. Engng. Sci.*, vol. 17, pp. 73–85, 1979.
- [RUD 77] RUDENKO O.V. and SOLUYAN S.I., *Theoretical Foundations of Nonlinear Acoustics*, Consultants Bureau, New York, 1977.
- [RUD 94] RUDENKO O.V. and CHIN A.W., “Nonlinear acoustic properties of a rough surface contact and acousto-diagnostics of a roughness height distribution”, *Acoust. Phys.*, vol. 40, pp. 593–596, 1994.
- [SAT 85] SATO T., FUKUSIMA A. and ISHIDA N., “Nonlinear parameter tomography system using counterpropagating probe and pump waves”, *Ultrasonic Imaging*, vol. 7, pp. 49–59, 1985.

- [SCH 83] SCHOLZ C.H. and HICKMAN S.H., "Hysteresis in the closure of a nominally flat crack", *J. Geophys. Res.*, vol. 88, pp. 6501–6504, 1983.
- [SOL 93] SOLODOV I.Y. and CHIN A.W., "Popping nonlinearity and chaos in vibrations of contact interface between solids", *Acoust. Phys.*, vol. 39, pp. 476–479, 1993.
- [TEN 04] TENCATE J.A., PASQUALINI D., HABIL S., HEITMANN R., HIGDON D. and JOHNSON P.A., "Nonlinear and non-equilibrium dynamics in geomaterials", *Phys. Rev. Lett.*, vol. 93, no. 6, p. 065501, 2004.
- [TOR 99] TORRE E.D., *Magnetic Hysteresis*, IEEE Press, New York, 1999.
- [TOU 04] TOURNAT V., ZAITSEV V.YU., GUSEV V.E., NAZAROV V., BÉQUIN P. and CASTAGNÈDE B., "Probing weak forces in granular media through nonlinear dilatancy: clapping contacts and polarization anisotropy", *Phys. Rev. Lett.*, vol. 92, p. 085502, 2004.
- [TOU 05] TOURNAT V., GUSEV V.E., ZAITSEV V.YU., NAZAROV V.E. and CASTAGNÈDE B., "Probing granular media via nonlinear acoustic effects", *Review Progress in QNDE*, vol. 24, pp. 369–376, 2005.
- [ZAI 95] ZAITSEV V.YU., SUTIN A.M., BELYAEVA I.Y. and NAZAROV V.E., "Nonlinear interaction of acoustic waves due to cracks and its possible usage for crack detection", *J. Vibration and Control*, vol. 1, pp. 335–344, 1995.
- [ZAI 00] ZAITSEV V.YU. and SAS P., "Dissipation in micro-inhomogeneous solids: inherent amplitude dependent losses of a non-hysteretical and non-frictional type", *Acustica-Acta-Acustica*, vol. 86, pp. 429–445, 2000.
- [ZAI 02a] ZAITSEV V.YU., GUSEV V.E. and CASTAGNÈDE B., "Luxembourg-Gorky effect retooled for elastic waves: a mechanism and experimental evidence", *Phys. Rev. Lett.*, vol. 89, p. 105502, 2002.
- [ZAI 02b] ZAITSEV V.YU., GUSEV V.E. and CASTAGNÈDE B., "Observation of Luxembourg-Gorky effect for elastic waves", *Ultrasonics*, vol. 40, pp. 627–631, 2002.
- [ZAI 03] ZAITSEV V.YU., GUSEV V.E. and CASTAGNÈDE B., "Thermoelastic mechanism of logarithmic slow dynamics and memory in elastic wave interaction with individual cracks", *Phys. Rev. Lett.*, vol. 90, p. 075501, 2003.
- [ZAI 05] ZAITSEV V.YU., GUSEV V.E. and ZAITSEV V.YU., "Mutually induced variation in dissipation and elasticity for oscillations in hysteretic materials: non-simplex interaction regimes", *Ultrasonics*, vol. 43, pp. 699–709, 2005.
- [ZAR 71] ZAREMBO L.K. and KRASILNIKOV V.A., "Nonlinear phenomena in the propagation of elastic waves in solids", *Sov. Phys. Uspekhi*, vol. 13, pp. 778–797, 1971.
- [ZHE 99] ZHENG Y., MAEV R.G. and SOLODOV I.Y., "Nonlinear acoustic applications for materials characterization", *Can. J. Phys.*, vol. 77, pp. 927–967, 1999.
- [ZOB 75] ZOBAEK M.D. and BYERLEE J.D., "The effect of cyclic differential stress on dilatancy in Westerly granite under uniaxial and triaxial conditions", *J. Geophys. Res.*, vol. 80, pp. 1526–1530, 1975.

This page intentionally left blank

## Chapter 18

# Non-destructive Evaluation of Micro-inhomogenous Solids by Nonlinear Acoustic Methods

### 18.1. Introduction

The purpose of this section is not to produce an exhaustive list of experimental methods for nonlinear acoustics used in micro-inhomogenous materials (including damaged materials) until today, but rather to present some emerging experimental methods of the late 20th century. These experimental results are able to be interpreted thanks to recent adapted theoretical developments. Some of these developments are presented in Chapter 17. Comprehensive information on earlier nonlinear acoustic methods are available in journal papers [ZAR 71, BRE 84, OST 01, NAZ 88b, ZHE 99].

In order to differentiate the methods having recently emerged in nonlinear acoustics of micro-inhomogenous media, it is useful, from a methodological point of view, to divide the experimental approaches into two groups: the “classic” approaches and the “modern” or “non-classic” approaches. From our point of view, the so-called “classic” methods are those based on the study of i) acousto-elasticity [ZAR 71, ZHE 99], ii) the generation of higher harmonics (and more generally the frequency-mixing) by cascading nonlinear elastic processes [ZAR 71, BRE 84, OST 01, NAZ 88b, ZHE 99], and iii) the resonance frequency shift and modification of the quality factor of vibrating bars, when the acoustic amplitude increases [OST 01,

NAZ 88b, ZHE 99]. The term “classic” is linked to the long history of their use in nonlinear acoustics. So-called “modern” methods have been introduced more recently. They are based on the study of the threshold nonlinear acoustic effects in materials containing individual cracks (e.g. the subharmonic generation) [SOL 02, MOU 03], or on the modulation transfer effects from one acoustic wave to another through the dissipative nonlinear processes [ZAI 02a, ZAI 02b]. These methods are qualified as “modern”, not only because they are recent, but also because they involve such physical conceptions, that are significantly different from the “classic” methods. It should be noted that the advances in nonlinear acoustics of micro-inhomogenous materials are linked to both the development of “modern” methods and to the improvement of “classic” methods with their subsequent application to modern problems of nonlinear acoustics, including in particular the study of “non-classic” nonlinearities (non-elastic, i.e. characterized by hysteresis and/or dissipation, see Chapter 17) in acoustics.

Often, in literature [OST 01, GUY 99], all nonlinearities, except the elastic nonlinearity of a homogenous ideal material, are qualified as “non-classic” nonlinearities, despite the fact that the hysteretic nonlinearity has been studied for more than 60 years [REA 40, NOW 50, GRA 66, NOW 72, LEB 99]. Searching into literature, it is therefore important to distinguish between “classic” and “modern” methods, and the mechanisms of “classic” and “non-classic” nonlinearities.

## 18.2. Classic methods

### 18.2.1. Acousto-elasticity

The acousto-elastic method, in its “classic” form, allows us to assess the nonlinear acoustic parameters of various materials by measuring the influence of the static stress (or static strain) on the speed of sound, that is through the observation of the interaction of acoustic waves with stationary elastic fields.

The dominant terms in the Taylor series of the speed of sound  $c$  as a function of the external strain  $s_{\text{ext}}$  can be written as  $c(s_{\text{ext}}) = c_0 + c_1 s_{\text{ext}} + c_2 s_{\text{ext}}^2 + \dots$ . In this expression,  $c_0 = c(s_{\text{ext}} = 0)$  corresponds to the speed of sound without additional strain applied to the material, and  $c_n (n = 1, 2, \dots)$  is the acousto-elastic coefficient of order  $n$  characterizing the nonlinearity of the material. It should be noted that in a linear material, the speed of sound should not be dependent on strain ( $c(s_{\text{ext}}) = c_0 = \text{const}$ ). A modern version of the “classic” acousto-elastic method is the assessment of the second order acousto-elastic coefficient  $c_2$ , by measuring the variation of the speed of sound during a period of a low-frequency (dynamic) harmonic excitation  $s_{\text{ext}} = s_{\text{ext}}(t)$  [NAG 98], Figure 18.1. Due to the symmetries, the first order acousto-elastic coefficient is eliminated and the second order coefficient is determined by finding the best fit between a quadratic polynomial and the experimental data obtained during each loading cycle.

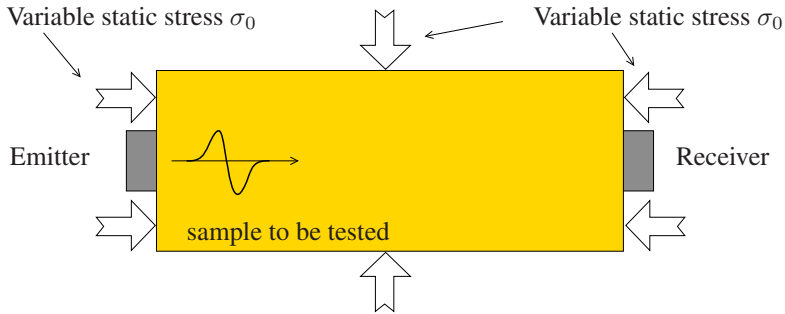


**Figure 18.1.** Schematic representation of the classic nonlinear acousto-elastic method. An ultrasonic burst is generated by an emitting transducer and detected after propagation by a receiving transducer. The ultrasound propagation speed is determined through the measurements of the acoustic propagation time between emitter and receiver separated by a known distance. In this method, the variation of this speed is discussed in terms of the static (“classic” method) or quasi-static (“modern” method) stress applied to the material

The method has been applied to the characterization of fatigue damage in the cyclic loading process of various materials (including plastics, metals, composites and adhesives). The experimental results [NAG 98] confirm that the nonlinear acoustic parameter  $c_2$  is an earlier and more sensitive indicator of fatigue damage than its linear counterpart  $c_0$  (linked to the linear elastic modulus).

The non-consolidated granular media are grain assemblies with non-cohesive elastic contacts. Dry sand is a good representative of such materials. In the example below, the grains are well-calibrated glass beads, with a diameter of 2 mm. A static force, in addition to the gravity force, is applied along the (vertical) revolution axis of the cylindrical tank (see Figure 18.2) that contains the grains (the gravity force becomes negligible compared to the static force applied to the grains). One conventional application of the acousto-elasticity method is the study of the dependence on static pressure, of the speed of elastic waves propagating in the solid skeleton (porous solid) of a granular assembly. Knowing the propagation distance, it is possible, using the time-of-flight method, to measure an effective velocity of longitudinal waves and transverse waves [TOU 04c, JIA 99, MAC 04]. The measured longitudinal and shear velocities as functions of the stress applied along the acoustic wave propagation direction are presented in Figure 18.3 [TOU 04c]. The logarithmic scale shows that the propagation speed  $v$  behaves as a power function of the pressure  $v \propto P_0^\alpha$ , where  $P_0$  is the applied static stress and  $\alpha$  is a coefficient between 1/4 and 1/6. The different evolution for the longitudinal wave and the shear wave indicates a static load anisotropy [TOU 04c].

Starting from these observations, and using the Hertz contact model [TOU 04c, MAC 04] (see section 17.2.6, Chapter 17), it is possible to obtain some information

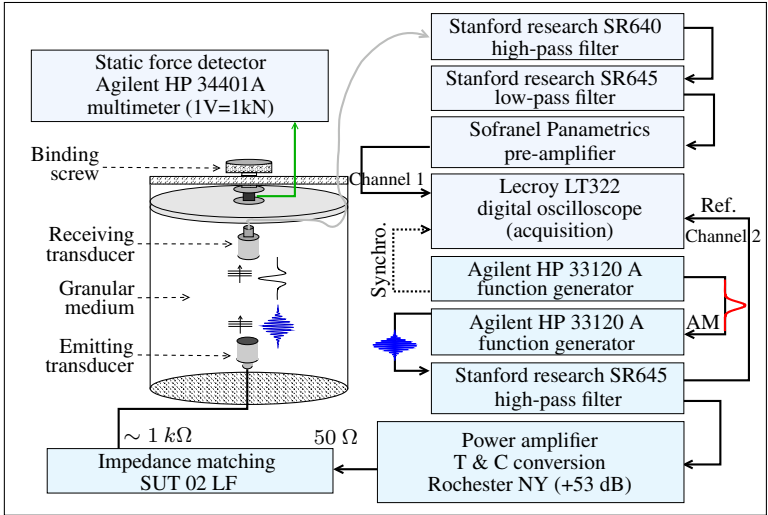


**Figure 18.2.** Diagram of an experimental setup used for the study of the parametric antenna in non-consolidated granular media

on the average number of contacts per bead (also called coordination number), and in particular on the evolution of this number with  $P_0$ .

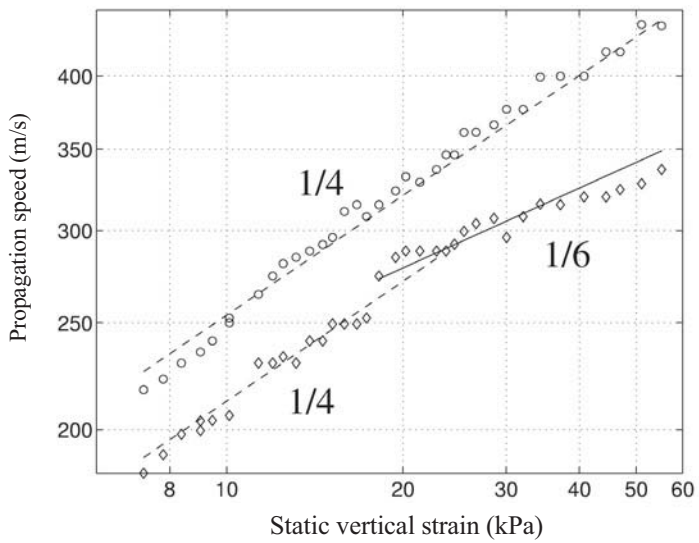


**Figure 18.3.** Evolution of the propagation speed of longitudinal waves (circles) and shear waves (diamonds), as functions of the uni-axial static pressure, based on the estimation of the time-of-flight of an ultrasonic pulse



### 18.2.2. Frequency-mixing

The harmonic generation method (or “finite amplitude method” [ZHE 99]) in its “classic” form allows us to assess the nonlinear acoustic parameters of various materials by measuring the amplitudes of higher harmonics (usually the second harmonic  $2\omega$  or third harmonic  $3\omega$ ). These harmonics are generated during the propagation of an initially monochromatic pumping wave with frequency  $\omega$ , that is through the self action of an initially pure tone [ZAR 71, BRE 84, OST 01, NAZ 88b, ZHE 99, YOS 01] (see Figure 18.4).

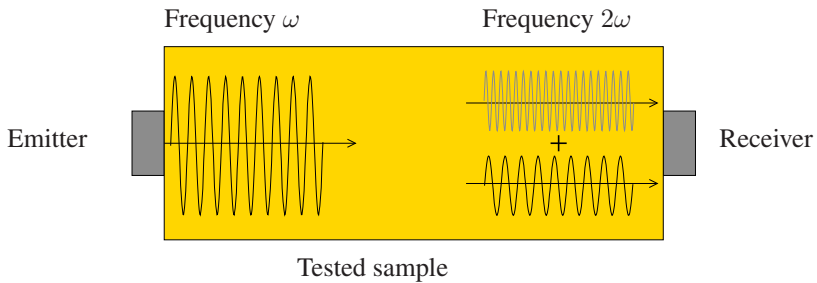


**Figure 18.4.** Schematic representation of the classic nonlinear frequency-mixing method in the case of the second harmonic generation ( $\omega + \omega \rightarrow 2\omega$ )

The ability to estimate the nonlinear acoustic parameters from the amplitude measurements of the various spectral components (emitted by the transducer, and generated due to the nonlinearity of the material) comes from the basic formulations of nonlinear acoustics [ZAR 71, BRE 84, OST 01, NAZ 88b, ZHE 99, YOS 01], see Chapter 17. During recent years, there has been a growing interest in applying the method of harmonic generation for the characterization of material processing and degradation (caused by fatigue, for instance) [YOS 01, JHA 02, BEL 94]. The correlation between the nonlinear parameter  $\varepsilon$  and the fatigue of the material has been well established [YOS 01, JHA 02].

Recently, these methods have been applied to granular media [BEL 94, TOU 04a]. The power dependencies of the amplitude of higher harmonics as functions of the amplitude of the fundamental wave (pumping wave) are typical of the Hertz nonlinearity. As this nonlinearity is high compared with that of consolidated materials, the harmonic generation process with mode conversion had been observed and then studied [TOU 04a]. In particular, the process of interaction between two transverse phonons at the frequency  $\omega_{TA}$ , giving a longitudinal phonon at the frequency  $2\omega_{LA}$  ( $\omega_{TA} + \omega_{TA} \rightarrow 2\omega_{LA}$ , process theoretically authorized in homogenous materials) has been observed. In Figure 18.5, the amplitude dynamics of the signal received by a longitudinal transducer at the frequency  $2\omega$  is represented as a function of the amplitude of the fundamental shear wave at the frequency  $\omega$ ,

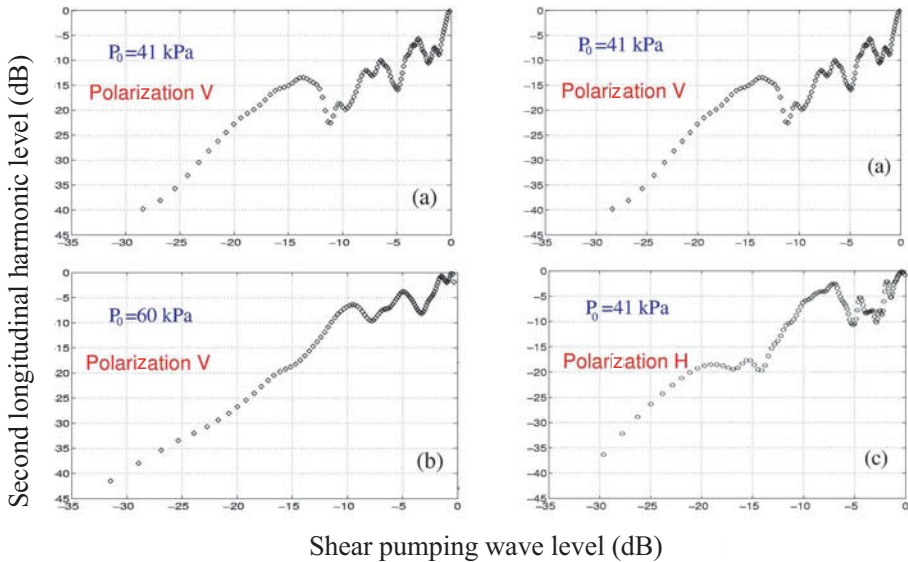


**Figure 18.5.** Amplitude of the longitudinal second harmonic, as a function of the fundamental shear wave level, for two applied static pressures  $P_0$  and different polarizations: the vertical polarization (V) is along the direction of the static uni-axial loading, and the horizontal polarization (H) is orthogonal to this axis. The 0 dB reference corresponds to an amplitude of acoustic strain  $\varepsilon_A \simeq 10^{-5}$

for different polarizations of the wave and for various values of the applied static pressure  $P_0$ . This experiment was conducted with a setup similar to the one shown in Figure 18.2 (except that the wave propagation was along an horizontal axis). The uni-axial static stress creates an anisotropy of the mechanic loading in the material, the vertical contacts being more heavily pre-stressed (strong contacts) than the horizontal contacts (weaker contacts). For an acoustic propagation along an horizontal axis, two shear transducers were used, one oriented vertically (V polarization) along the “strong” contacts, the other horizontally (H polarization) along the “weaker” contacts. An “unconventional” feature of these evolution curves of amplitudes is their non-monotonous behavior, with a series of minima and maxima. As presented in section 17.2.3, Chapter 17, the dependence classically observed for the amplitude of the second harmonic as a function of the amplitude of the fundamental wave in a medium with an elastic quadratic nonlinearity, is quadratic, and therefore monotonous. In the case of granular media, two features enable us to explain this non-monotonous behavior of the second harmonic amplitude as a function of the fundamental wave amplitude, which could be usually observed only as a function of distance and only in dispersive media. First, this phenomenon may be due to the mode conversion that results in an asynchronism between the pumping shear waves (fundamental wave, effective nonlinear source for the second

harmonic) and the second longitudinal harmonic. The second phenomenon that may explain this behavior is “clapping” (opening and closing) of contacts under the action of the acoustic wave that can occur when the acoustic amplitude is sufficiently high. As the clapping phenomenon, controlled by the pumping wave amplitude, influences the effective length of the volumetric nonlinear acoustic sources, this actual length depends on the amplitude of the excitation [TOU 04a]. Because of the asynchronism between the sources and the signal they generate, a variation of the length of the nonlinear interaction (effective length of sources) implies a variable phase relationship on the border of the interaction region. Thus, for a given amplitude of the excitation, the sources ( $\omega_{TA}$ ) and the resulting signal ( $2\omega_{LA}$ ) are in phase at the border of the region of nonlinear sources (which corresponds to a maximum efficiency). For another value of this amplitude, they will be in antiphase (which corresponds to a minimum efficiency). Therefore, the position of the first minimum gives some information on the initial of clapping of an important part of the weakest contacts. In Figure 18.5, the first minimum of curve (a) appears for an amplitude of the acoustic strain  $\varepsilon_A \sim -12$  dB, while the first minimum of curve (b), corresponding to a higher applied static pressure, is at  $\varepsilon_A \sim -8$  dB (the contacts are more heavily pre-stressed on average). The anisotropy in the medium can also be probed by this method, by identifying for example the first minimum for different polarizations of the pumping shear wave. On Figure 18.5, the curves (a) and (d) are obtained under the same applied static pressure for two orthogonal wave polarizations, and clearly show an anisotropy of nonlinearity characterized by the difference of 3 – 5 dB in pumping wave amplitudes, visible when identifying the amplitude of excitation for which the first minimum is found.

A “modern” trend is also to apply the measurement of harmonics under the conditions of resonance vibration of the samples. These samples are not only micro-inhomogeneous materials with a “non-classic” hysteretic nonlinearity [OST 01, GUY 99], but also damaged (cracked) micro-inhomogeneous materials [Van 00b, Van 01], ceramics, rocks.

Experiments confirm the general trend of an increase of the “non-classic” hysteretic nonlinearity [ZHE 99, OST 01], Chapter 17, in the damaged micro-inhomogeneous materials.

The process of harmonic generation is a special case of the various frequency-mixing acoustic processes that are possible in nonlinear materials, and matches the following frequency summation rules:  $\omega + \omega = 2\omega$ ,  $\omega + 2\omega = 3\omega$ , ... (in the case of a quadratic elastic nonlinearity), and  $\omega + \omega + \omega = 3\omega$  (in the case of a cubic elastic nonlinearity) for example (see section 17.2.3, Chapter 17). We recall here that these rules are the direct consequences of the fundamental law of energy conservation. Another method derived from the “classic” frequency-mixing method uses the interaction of a high frequency acoustic wave  $\omega$  (probing wave) with a much lower frequency acoustic wave  $\Omega$ ,  $\Omega \ll \omega$  (pumping wave). The

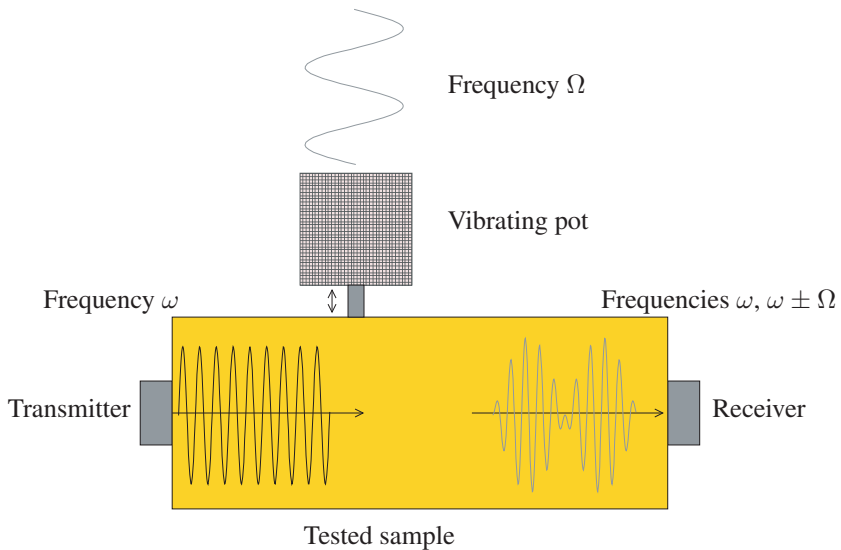


**Figure 18.6.** Schematic representation of the classic nonlinear frequency-mixing method using the modulation phenomenon ( $\omega$  and  $\Omega \rightarrow \omega \pm \Omega$ )

low-frequency wave is sometimes called the “vibration” and this derived method is then called “nonlinear vibro-acoustic method” [SUT 98, DON 01] (see Figure 18.6). In the frequency domain, the result of this interaction appears as peaks around the frequency  $\omega$  of the probing wave. In the case of an elastic quadratic nonlinearity, the mixing frequencies are  $\omega + \Omega$  and  $\omega - \Omega$ . In the time domain, the effect of the mixing of  $\omega$  and  $\Omega$  manifests itself as a low frequency modulation of the amplitude of the high frequency acoustic wave (as illustrated qualitatively in Figure 18.6). The application of this modulation effect to detect cracks was patented in 1975 [SES 75], which confirms the “classic” label of this method. The modulation of sound by a vibration was experimentally observed on different materials (metals, composites, concrete, granular rocks, glasses) with different types of defects: cracks, delamination, microstructural damage. Recent experiments [Van 00b] in micro-inhomogenous cracked materials, revealed the possibility of an efficient frequency-mixing phenomenon of the type  $\omega \pm 2\Omega$ , which is associated with the “non-classic” hysteretic nonlinearity (section 17.2.3, Chapter 17). Some other experimental observations [ZAI 00] indicate that the generation of lateral peaks  $\omega \pm \Omega$  is associated not with a quadratic elastic nonlinearity, but with a dissipative “non-classic” type nonlinearity (which is not related to the hysteretic nonlinearity, but to a phenomenon of nonlinear absorption associated with a relaxation process; see section 17.2.4, Chapter 17, [ZAI 02a, ZAI 02b, FIL 06b, FIL 08]).

One more sub-method of the “classic” method of frequency-mixing is the evaluation of the demodulation (or frequency-down conversion) process in the case of an amplitude-modulated sine wave. For example, in the case of the sinusoidal modulation (at the low frequency  $\Omega$ ) of a pumping wave of high frequency  $\omega$  ( $\Omega \ll \omega$ ), the initial wave spectrum contains the frequencies  $\omega, \omega \pm \Omega$ . The excitation by frequency-mixing of the lower frequencies  $\omega - (\omega - \Omega) = \Omega$ ,  $(\omega + \Omega) - \omega = \Omega$  and  $(\omega + \Omega) - (\omega - \Omega) = 2\Omega$  is allowed for these waves in materials with a quadratic elastic nonlinearity. These processes therefore lead to the generation of low-frequency signals with frequencies  $\Omega$  and  $2\Omega$ . This is the operating principle of the parametric emission antenna (see [NOV 80] and references therein), working in a continuous mode, which can generate highly directive low frequency waves using relatively small transducers. In the case of an impulse modulation of high frequency waves (wave packet), the spectrum of the low frequency signal obtained after demodulation in a material with quadratic elastic nonlinearity is linked to the spectrum of the intensity envelope of the initially signal sent (see Figure 18.2). Because of this process, the parametric emission is often called the “parametric demodulation process” (or self-demodulation). The “classic” application for this nonlinear acoustic method is mainly in underwater acoustics, where directive and weakly absorbed (with long propagation distances) low frequency signals are generated. The self-demodulation of seismic waves was also observed some time ago [BER 88].

This “classic” method of nonlinearly demodulated acoustic wave evaluation recently found modern applications in the diagnosis of the nonlinearity of granular and cracked media [ZAI 99, MOU 01, TOU 03, MOU 02, TOU 04c]. In particular, the sensitivity of the demodulation process to the character (ballistic or diffusive) of the high-frequency wave propagation in granular media was demonstrated [TOU 02, TOU 03], as well as the demodulation accompanied by an acoustic mode conversion (of pumping shear waves converted into demodulated longitudinal waves) [TOU 04c]. The parametric emission antenna allows the characterization of the anisotropy of the orientation of force chains in granular assemblies [TOU 04c]. In Figure 18.7, the behavior of the amplitude of the demodulated signal (low frequency signal) is drawn as a function of the excitation level of the pumping wave (high frequency), for two different initial polarizations of the pumping shear wave. The configuration corresponds to a wave propagation direction that is orthogonal to the static uni-axial stress (see the insert in the right-hand side of the figure). The experimental setup, similar to that of Figure 18.2, was implemented for this study. The application of a static uni-axial stress leads to the formation of a series of force chains (paths connecting the grains with contacts that support a constraint that is higher than the average), typical of granular media, preferentially oriented along the direction of this static stress, and thus creating an anisotropy of the loading of contacts in the medium. This anisotropy is both of linear (it concerns the elastic modulus of order 1), and of nonlinear elasticity because the elastic modulus of order 2 also depends on the static stress, in the approximation of the Hertz contacts (see section 17.2.6, Chapter 17).

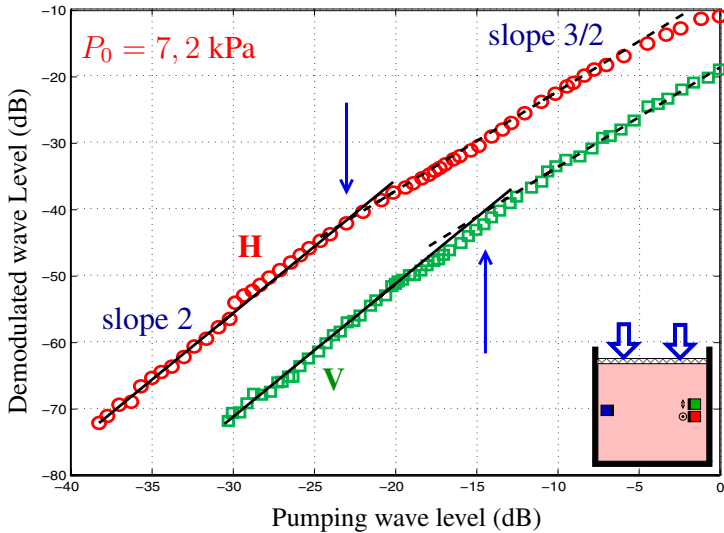


**Figure 18.7.** Demodulated longitudinal wave level as a function of the pumping shear wave level, for two polarizations: the vertical polarization (V) is along the direction of the uni-axial static loading, and the horizontal polarization (H) is orthogonal to this direction. The 0 dB reference on the x-axis corresponds to an acoustic strain amplitude of  $\varepsilon_A \simeq 2 \cdot 10^{-4}$

The anisotropy of the nonlinearity can be quantified by the observed difference in efficiency of the demodulation of shear waves polarized along the direction of the applied stress (V) and orthogonal to it (H). The behavior of the amplitude of the demodulated wave as a function of the excitation level is first quadratic, which is the classic dependence observed in air or water for example. Then, a transition to a law with a power 3/2 takes place, for higher amplitudes of the excitation. This latter dependence is attributed to the previously mentioned phenomenon “clapping”, due to the opening and closing of the contacts under the action of the acoustic wave. In Figure 18.7, the transition between a quadratic dependence and the dependence of a power 3/2 takes place for different amplitudes of the excitation, which provides an additional opportunity to characterize the anisotropy of the nonlinearity of the medium [TOU 04c]. The inverse problem, which consists of determining the distribution of static contact forces in the medium from these curves, is promising because of the high sensitivity of the nonlinear acoustic methods to the weakest contacts in the medium (see Chapter 17).

An additional modern application of this very specific frequency-mixing nonlinear process is the application of parametric antenna in air for the diagnosis of porous materials [CAS 03, SAE 04, CAS 06]. Recently, the improvement of the technology for ultrasonic emitters in terms of their coupling with air and their efficiency, has not only permitted us to observe this phenomenon of frequency-mixing in air, but also to

market the first antennas for applications in the field of audible acoustics. The greatest interest of this method is the very high directivity of the low frequency radiation, because of the accumulation of nonlinear effects over the propagation distance of pumping waves. This high directivity of a “low frequency” wave in the audible domain, emitted by an antenna made of virtual ultrasonic sources in air, themselves initially generated by a small transducer (a few centimeters in diameter), was recently used for the study of soundproofing porous materials [CAS 03, SAE 04, CAS 06]. These materials are made of a solid skeleton (polyurethane, metal) saturated with air, and can be modeled, under certain conditions, as an equivalent fluid medium, with parameters depending on frequency. The acoustic characterization methods used nowadays for these materials are the Kundt tube method, working at frequencies of a few hundred Hertz; and the ultrasonic methods usually for frequencies between 40 kHz and 300 kHz. It remains therefore a poorly covered frequency band, and also has significant frequency variation of the phase velocity and acoustic attenuation, between a few hundred Hz and a few dozen kHz. From the technology of current commercial parametric antennas and the physical properties of air, the useful frequency band is within the range of around 500 Hz and 20 kHz, which is precisely in the frequency range that is inaccessible using existing methods. In addition, the very high directivity of the radiated beam avoids any reflections that could be caused by the walls of the room where the experiment is conducted, and the local plane wave enables us to make accurate measurements of the phase velocity in the porous medium.

In Figure 18.8, the principle of the parametric effect antenna for the characterization of porous materials is schematically represented. Two main configurations are possible to obtain the parameters, on which usual models for the acoustic propagation in such media are based: a configuration using the “transmission” mode, illustrated in Figure 18.8; and a configuration using the “reflection” mode, when the the microphone is located with respect to the material on the same side as the transducer. In the “transmission” mode, the signal transmitted through the material is compared with a reference signal measured in the absence of the material. The comparison of the phase and amplitude spectra provides access to determination of the attenuation and phase velocity of acoustic waves in the material.

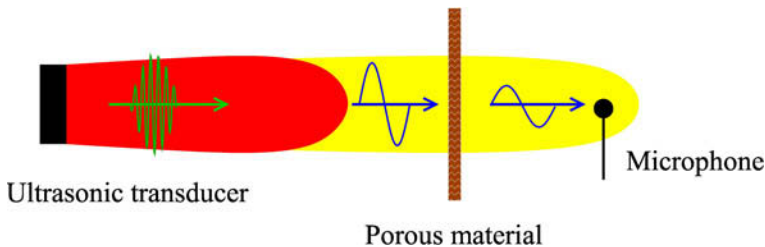


**Figure 18.8.** Schematic representation of the parametric antenna used in air for the acoustic characterization of a slab of porous material



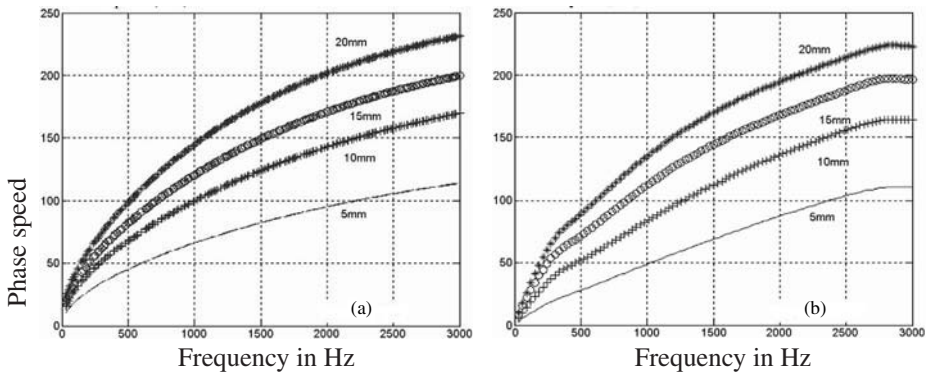


**Figure 18.9.** Phase velocity as a function of frequency in four similar porous materials with different compressions (the thinner, 5 mm, is the most compressed). (a) Results from the equivalent fluid model, (b) Experimental results obtained with the parametric antenna

In Figure 18.9, the phase velocity in felt-type soundproofing materials for cars is modeled and measured using a parametric antenna. The experimental results are in very good agreement with predictions from the classic equivalent fluid model. The short term goal is the on-site use of this method, particularly in room acoustics or for the online control of materials.

### 18.2.3. Nonlinear resonance

The nonlinear acoustic method based on the evaluation of the vibrations of solid resonators or of columns of compressed granular materials, through the analysis of the resonance frequency shift and of the quality factor variation with the increase of the excitation amplitude, is another “classic” method in nonlinear acoustics. It has been applied to studies of the inelastic relaxation (internal friction) in crystalline solids for over 60 years [REA 40, NOW 50, GRA 66, NOW 72, LEB 99]. It is important to note that initially, it was discovered in multiple situations that the shift of the resonance frequency and the decrease of the quality factor are proportional to the amplitude of the wave in the resonator. This contradicts theories considering an elastic nonlinearity only. These observations were attributed to the hysteretic nonlinearity [REA 40, NOW 50, GRA 66, NOW 72], in particular the hysteresis of the dislocations movement [NOW 50, GRA 66, ASA 70]. It has been shown, in section 17.2.3, Chapter 17, that the hysteretic quadratic nonlinearity yields a decrease of the sound velocity (and hence of the resonance frequency) proportional to the amplitude of the wave. Thus, the “non-classic” hysteretic nonlinearity was revealed through a “classic” resonance method, many years ago.

The new interest in hysteretic “non-classic” nonlinearity at the end of the 20th century was mainly due to the transition from studies of crystals [NOW 50, GRA 66]



and micro-crystalline metals [NAZ 88a, NAZ 88b] to extensive studies of rocks, in which the hysteretic “non-classic” nonlinearity is also present [OST 01, GUY 99, GUY 95, JOH 96]. Modern applications of the “classic” resonance method are numerous. They provide more and more comprehensive information for understanding the “non-classic” nonlinear properties of materials.

First, there is an increasing number of observations showing that the hysteretic nonlinearity increases when a micro-inhomogeneous material, initially intact, is damaged [Van 00a, Van 00b, Van 01]. This opens the way for non-destructive evaluation of damage in rocks, micro-crystalline metals, ceramics, composites, etc.

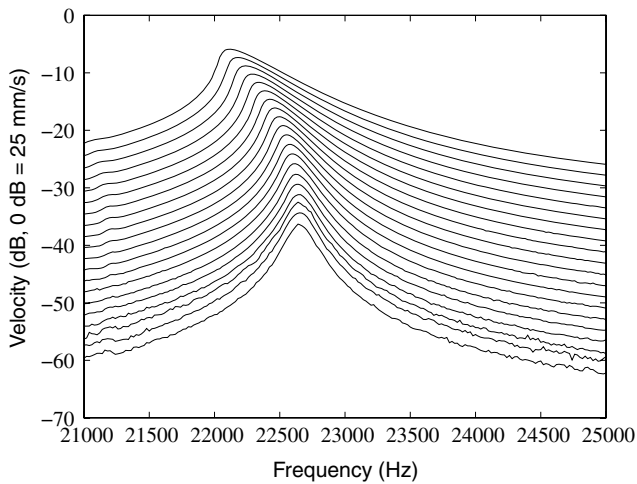


**Figure 18.10.** Representation of the evolution of a  $3\lambda/4$  resonance as a function of the excitation amplitude in a damaged graphite bar. Each curve corresponds to a given amplitude of the excitation. In this case, there is a strong shift in the resonance frequency

Second, the resonance experiments provide more and more evidence that there are transitions between the different types of acoustic nonlinearity with an increase in the wave amplitude [NOW 50, NAZ 00, TEN 04]. For example, the negligible role of the “non-classic” hysteretic nonlinearity at very low amplitudes of the acoustic loading [NOW 50] is confirmed by recent experiments [TEN 04]. One possible explanation for the absence of the quadratic hysteretic nonlinearity for low amplitudes of acoustic excitations may be due to thermal fluctuations, which are pushing the micro-mechanical elements to the unique equilibrium state, thus destroying their bi-stable behavior and hysteresis [GUS 05].

Third, the resonance bar experiments show that in micro-inhomogeneous media, some other mechanisms of nonlinear dissipation (in addition to the mechanism

of nonlinear hysteretic dissipation [NOW 50, GRA 66, ASA 70] described in section 17.2.3, Chapter 17) can be important. At least in part, nonlinear dissipation of the non-hysteretic nature can be attributed to the nonlinear relaxation absorption mechanism described in section 2.4, Chapter 17 [FIL 06a]. The non-hysteretic nonlinear dissipation may be the underlying mechanism of the self-modulation effects [FIL 06b, FIL 08] and of the Luxembourg-Gorky effect [ZAI 02a, ZAI 02b]. These two effects will be presented later.

Fourth, the resonance bar experiments provide more and more confirmation of the existence of a dispersion of the nonlinearity (dependence of the nonlinear parameters of the material on the frequency of the acoustic loading) [NAZ 00]. The nonlinear parameters extracted from the analysis of the various resonances of a bar are different. Usually, the hysteretic nonlinearity decreases when the frequency increases [NAZ 00]. A qualitative explanation of this type of behavior is proposed in section 17.2.5, Chapter 17 [GUS 05, GUS 98]. With increasing frequency, the transition to a “quasi-frozen” behavior of the micro-mechanical elements takes place. The hysteretic elements have less and less time to accomplish their nonlinear motion (transition from one equilibrium state to another).

This short description of the modern applications of “classic” nonlinear acoustic methods (acousto-elasticity, frequency-mixing and nonlinear resonance) highlights the extreme utility of “classic” methods. Additional advantages might be provided by application in non-destructive testing also of some newly emerged methods described below.

### 18.3. Modern experiments

#### 18.3.1. *The Luxembourg-Gorky effect (modulation transfer)*

The effect of modulation transfer, observed in acoustics recently [ZAI 02a, ZAI 02b], is similar to a nonlinear wave phenomenon in intense electro-magnetic waves, which had been discovered experimentally much earlier. The nonlinear acoustic phenomenon observed is as follows. A high frequency carrier wave (at frequency  $\omega_1$ ) is electronically modulated with the low frequency  $\Omega \ll \omega_1$ , generating a powerful pumping acoustic wave (composed of the frequency components  $\omega_1 + \Omega$ ,  $\omega_1$  and  $\omega_1 - \Omega$ ) which is sent into the material or structure being tested. This material is then examined (probed) by a harmonic acoustic wave at a different frequency  $\omega_2$  and with a low amplitude. In the presence of a crack (Figure 18.11), new frequency components emerge in the nonlinear acoustic response, like the sidelobes at frequencies  $\omega_2 \pm \Omega$ ,  $\omega_2 \pm 2\Omega$ . Therefore, a modulation transfer takes place, from a pumping carrier wave at frequency  $\omega_1$  to a probing wave at frequency  $\omega_2$  (see Figure 18.12). The name of this phenomenon, Luxembourg-Gorky (LG), comes from the same modulation transfer effect observed more than 70 years ago for radio waves that propagate in the ionosphere. In the first independent

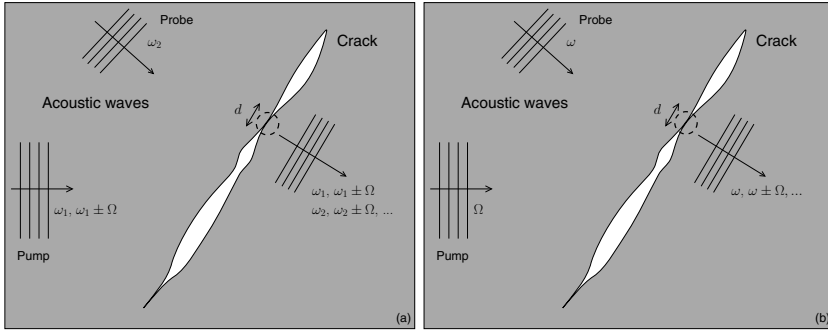


**Figure 18.11.** Nonlinear acoustic phenomena associated with absorption of acoustic waves by cracks. (a) The Luxembourg-Gorky effect consists in a transfer of modulation at low frequency  $\Omega$  from a powerful carrier wave at high frequency  $\omega_1$  (pump) to a weak probe wave at high frequency  $\omega_2$ . (b) The nonlinear vibro-acoustic effect consists in the modulation of a weak probe wave at high frequency  $\omega$  by a strong pump wave at low frequency  $\Omega$

observations of this modulation transfer in radiowaves, the Luxembourg and Gorky radio-stations were involved. Note that the physics of the LG effect is fundamentally different from that associated with the classic nonlinear acoustic effects: for the latter, the frequency-mixing process is usually attributed to the elastic part of the nonlinear stress/strain relationship (real part of the elastic moduli), while the LG effect of the modulation transfer is associated with the inelastic (imaginary) part of these moduli. In particular, the modulation transfer (LG effect) can be attributed in some experiments to a nonlinear acoustic absorption due to thermoelasticity [ZAI 02a, ZAI 02b, FIL 06a] (and not to the nonlinear acoustic elasticity like in the so-called “classic” methods), which is enhanced in the material or structure by the presence of defects, cracks, etc. The first observations of the LG effect have been made in glass bars containing cracks.

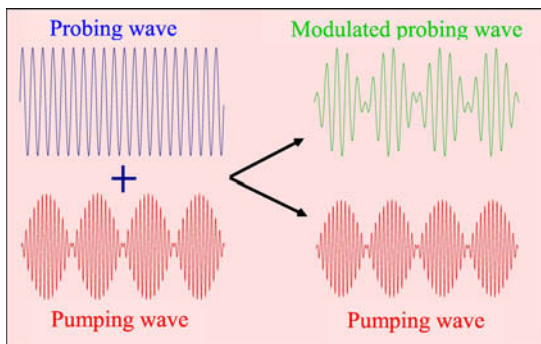


**Figure 18.12.** Schematic representation of the “Luxembourg-Gorky” interaction

The simplest theoretical model explaining the nonlinear acoustic absorption is based on i) the analysis of individual mechanical contacts under the action of acoustic “loading” due to the pumping wave and ii) the nonlinear response that follows. Imagine, as a simplified illustration, a single contact between the two lips of a crack (micro-Hertzian contact, see Figure 18.11). The interaction of an incident acoustic wave at the frequency  $\Omega$  with the crack causes a stress in the contact area that is concentrated in a spherical volume of diameter  $d$ , of the order of the diameter of the Hertz contact area, which is then heavily deformed. Inhomogeneous deformations due to the acoustic wave around the contact are much larger than those in regions located far from this contact.

The inhomogeneous deformation induces an inhomogeneous temperature distribution in the material, in the vicinity of the contact, and thus an irreversible process of heat conduction takes place, leading to the absorption of acoustic energy [LAN 59]. The thermal diffusion is a possible relaxation process in materials, and its influence on acoustic propagation can be taken into account in the frame of the acoustic waves for materials theory where relaxation is possible, section 17.2.4, Chapter 17. In particular, the characteristic frequency of the sound absorption peak due to the presence of a contact can be estimated as  $\omega_R = \tau_R^{-1} \sim \chi/d^2$ , where  $\chi$  is the thermal diffusivity of the material. Therefore, when the diameter of the contact varies due to the action of the pumping acoustic field, the position of the resonance peak varies, modifying the absorption of the sound at the probing frequency [FIL 06a]. It was demonstrated that this amplitude-dependent absorption mechanism may be responsible for frequency-mixing processes like  $\omega \pm n\Omega$  in nonlinear vibro-acoustics [ZAI 00]: the variation of the diameter of the contact follows the vibration of the sample at the frequency  $\Omega$  and the pumping spectral component at  $\Omega$  mixes with the probing frequency  $\omega$ . The physics of the LG effect is essentially different. The modulation transfer in the LG effect is not determined by the instantaneous response of the material under the action of the pumping wave, but by the response of the material that is temporally averaged over the period of the pumping wave carrier. The change in the average absorption of the signals is related to the average shift of the relaxation frequency  $\omega_R$  in the acoustic oscillating field of the pumping wave. This shift occurs even in the hypothetical case of linear contacts when the acoustic loading does not change their average size, because the relaxational absorption is a nonlinear function of the diameter of the contact [FIL 06a]. However, due to the strong elastic nonlinearity of the Hertz contacts, a significant shift of  $\omega_R$  also comes from the change of the average diameter of the contact in the acoustic field. The averaging process may be described as the generation of the new frequency ( $\omega_{\text{pump}} - \omega_{\text{pump}} = 0$ ). Actually, in the LG effect, a slow modulation of the pumping wave at the frequency  $\Omega$  is used to visualize the average static influence of the pumping wave on the material, by ensuring that the response of the material is quasi-static. The pumping wave containing the frequencies  $\omega_{\text{pump}}$  and  $\omega_{\text{pump}} \pm \Omega$  is demodulated ( $\omega_{\text{pump}} - (\omega_{\text{pump}} \pm \Omega) = \mp\Omega$ ), and the probing wave is used to detect

the quasi-static variations of the properties of the material at frequency  $\Omega$ . Variation of the absorption with the frequency  $\Omega$  will modulate the probe, resulting in a modulation transfer of the frequency  $\Omega$  of the pumping wave to the probing wave.

Theoretically, a similar modulation transfer may be associated with purely elastic modulation processes of the probing wave in reflection from (or transmission by) contacts of slowly variable cross-section. However, there are currently more and more experimental observations [ZAI 02a, ZAI 02b, FIL 08] demonstrating that the excitation of cracked bars by strong pumping waves mainly modifies the absorption, and not the velocity or the spatial structure of the probing wave (the pumping wave significantly alters the quality factor  $Q$  of the resonator, but not the resonance frequency). The LG method shares with the nonlinear vibro-acoustic method an advantage in comparison with the method of harmonic generation in the material launching of the new spectral components of interest ( $\omega_{probe} \pm \Omega$ ) by the signal generators and amplifiers and their generation in the layers coupling the attenuators to the tested samples can be importantly reduced, using independent actuators for pumping and probing acoustic waves. An advantage of the LG method, compared with the sound modulation by vibration method, is the ability to use the equipment suitable for the same particular frequency range (ultrasonic for instance) both for pump and probe waves, while the equipments for the high frequency probing wave and low frequency pumping wave in vibro-acoustics are often quite different.

Our current understanding of the LG effect (as presented above) immediately demonstrates the potential benefits of this method in terms of applications for non destructive characterization. The most important point is the direct relationship between the thermoelastic resonant absorption and the dimensions of the heated region, which are controlled by the dimensions of the contacts and cracks. Accordingly, the evaluation of the thermo-elastic nonlinear absorption through the LG effect should be able to provide quantitative information on the dimensions of cracks and contacts. In the first experiments, the dimensions of contacts between the lips of an individual crack were estimated [ZAI 02a]. This is one of the advantages of the nonlinear acoustic method of modulation transfer compared with conventional methods.

Ultimately, the most fundamental idea in the discussion above is not the LG effect itself, but rather in demonstrating that the cracks and contacts can be probed by recording the changes in the acoustical absorption of materials and structures induced by the thermo-elastic effect. In fact, two effects occur:

- 1) an almost instantaneous change the amplitude of the probing wave at the beginning of the pumping wave action (fast dynamics, possible mechanism discussed above);

- 2) a slow variation of the amplitude of the probing wave linked to the slow evolution of the thermo-elastic state of the contact itself. This state is associated with

i) the average heating of the region by the absorbed acoustic energy following the start of the excitation of pumping acoustic waves, or ii) the cooling of this region when the excitation of the pumping wave stops (slow dynamics [ZAI 03]).

Slow dynamics is observed in experiments as a slow change in the acoustic response of the material under an acoustic loading. In very general terms, slow dynamics can be understood as a relaxation of the system to a new equilibrium state (which in the presence of acoustic loading may be different from the initial state). The process of heat conduction is just one of the possible relaxation processes contributing to slow dynamics in micro-inhomogeneous materials. For most physical systems, the transition of a system to a stable state from a metastable state is strongly related to thermal fluctuations. In mechanics, thermal phonons (a high frequency acoustic noise associated with thermal fluctuations) participate in the relaxation process and can contribute to the slow dynamic processes. In many cases, this type of relaxation can be viewed as temperature/thermal phonons-assisted transitions of the system over the energy barriers [CAT 00, GUS 05]. Note that the dynamics induced by a slow heating of contacts and cracks, in an acoustic field, generally depends on the size of the heated area. Thus, monitoring of the slow dynamics provides information on the dimensions of the zone of stress/strain concentration and the size of the contacts.

The LG effect was also observed in non-consolidated granular media [ZAI 05], where a large part of the nonlinear absorption may be due to the hysteretic nonlinearity (caused by hysteresis in stick-slip motion of the contacts and adhesion hysteresis of the contacts), which contributes to the absorption of waves and variations of their propagation velocity (see section 17.2.3, Chapter 17). With increasing oscillation amplitude, the acoustic resonances in the granular columns not only broaden (their quality factor decreases) but also shift [STO 89, INS 08]. Therefore, both the elastic part of the hysteretic nonlinearity and the nonlinear absorption can contribute to the LG effect in granular materials.

In Figure 18.13, the amplitudes of the probing wave at its fundamental frequency and the amplitude of the first lateral modulation lobe of the probe (resulting from the modulation transfer from the original pumping wave to the probing wave) are plotted as functions of time. In an initial approximation, and very schematically, the fundamental component of the probing wave provides information on the linear wave propagation and linear properties of the medium, while the modulation sidelobe characterizes the nonlinear properties of the medium. In this experiment [ZAI 05] vibration taps at times 10, 50, 75 and 100 seconds (Figure 18.13) were launched to slightly modify the medium. These taps are produced by a low-frequency shaker located at the bottom of the container. It is clearly visible in Figure 18.13 that the amplitude of the sidelobe is very sensitive to small perturbations of the medium state, while the amplitude of the fundamental component remains practically unchanged. The nonlinear acoustic properties vary greatly, while the linear acoustic properties

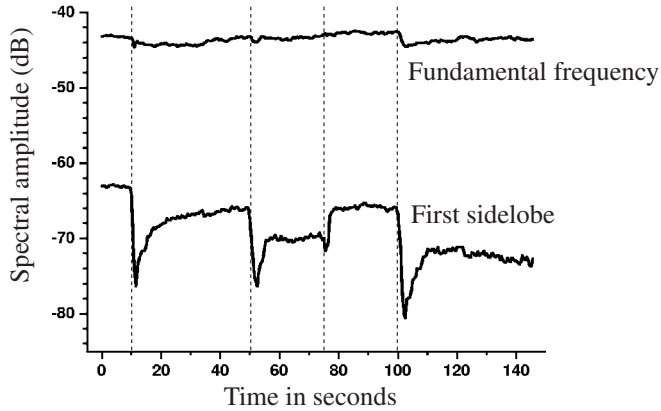


**Figure 18.13.** Comparison of the sensitivity of linear (fundamental frequency) and nonlinear (modulation sidelobe generated by the Luxembourg-Gorky effect) acoustic signals with “seismic event” in granular materials

remain virtually unchanged. The observed high sensitivity of the signal generated by nonlinear process to “seismic events” is due to the fact that the dominant contribution to acoustic nonlinearity of the granular medium is provided by the weakest contacts (section 17.2.6, Chapter 17) and they are the first ones to be influenced by a small perturbation of the medium.

### 18.3.2. Self-modulation instability and bistability

The bistability and self-modulation instability of acoustic waves [FIL 06b] are other physical effects that can be attributed, in some cases, to a manifestation of the nonlinear absorption, and that have been recently used as indicators of defects in materials. Qualitatively, these effects can be interpreted as follows: the energy dissipation rate of the acoustic wave is proportional to  $\alpha(A)A^2$ , where  $A$  is the wave amplitude and  $\alpha(A)$  is the absorption coefficient, dependent on the amplitude.

If the sample has a nonlinear transparency ( $\partial\alpha(A)/\partial A < 0$ ) as represented in Figure 18.14a, and if  $\alpha(A)$  decreases faster than  $1/A^2$  within an amplitude range  $A_1 < A < A_2$ , then, in this interval, the energy dissipation decreases when the wave amplitude increases (Figure 18.14b). The existence of a negative differential energy dissipation ( $\partial(\alpha(A)A^2)/\partial A < 0$ ) is the indication of the instability of the linear harmonic waves, whose amplitudes are in the considered interval  $A_1 < A < A_2$ . Imagine that in an acoustic resonator, the continuous increase of the excitation power (emitted by the transmitter)  $P$  from  $P = 0$  to  $P = P_1$  leads to a continuously increasing amplitude of the acoustic wave from  $A = 0$  to  $A = A_1$ . Then, the additional increase of excitation power will, through the increase of the acoustic wave amplitude, be followed by a decrease of the dissipation, therefore resulting

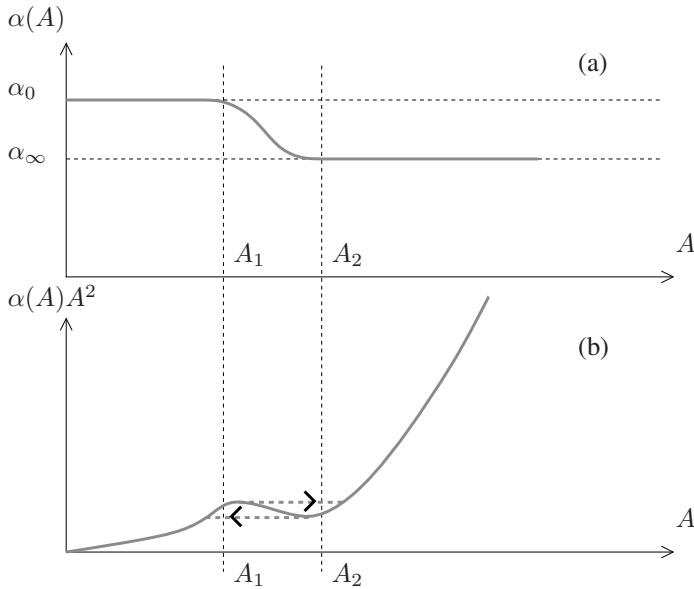


**Figure 18.14.** Qualitative presentation of the acoustic absorption coefficient (a) and of the density of acoustic energy dissipated (b), as functions of the amplitude of the wave. The material must include a region where the absorption decreases rapidly enough with the amplitude (induced transparency). The arrows indicate acoustic amplitude jumps, when the power introduced in the resonator varies continuously

in an additional increase of the wave amplitude, and so on. As a consequence, the amplitude of the wave increases abruptly.

At the end of this process (this jump), the amplitude of the acoustic wave will be within the interval  $A > A_2$ , corresponding to the second part of the growing dissipation curve shown in Figure 18.14a. If later, the excitation power begins to decrease, then a jump in the opposite direction takes place when the power  $P$  falls below  $P_2$  (corresponding to an acoustic amplitude  $A_2$ ). Note that  $P_2 < P_1$ . Therefore, the system exhibits a bistability: the amplitude of the acoustic waves excited in the interval  $P_2 \leq P \leq P_1$  will be different if the excitation is increasing or decreasing. A necessary condition for bistability is that the waves of amplitudes  $0 < A < A_1$  and  $A_2 < A < +\infty$  correspond to real and stable movements of the system. The detailed theoretical analysis of the stability of the system indicates that this is the case for a slight detuning between the excitation frequency of the transducer and the resonance frequency of the bar with one rigid end and another free end [FIL 06a]. The amplitude jump phenomenon in the vicinity of the resonance has been experimentally observed [FIL 06b, FIL 08], as illustrated by Figure 18.15a. However, for a large enough difference between the excitation and resonance frequencies, it may become possible that when the excitation increases within a finite domain of power from a



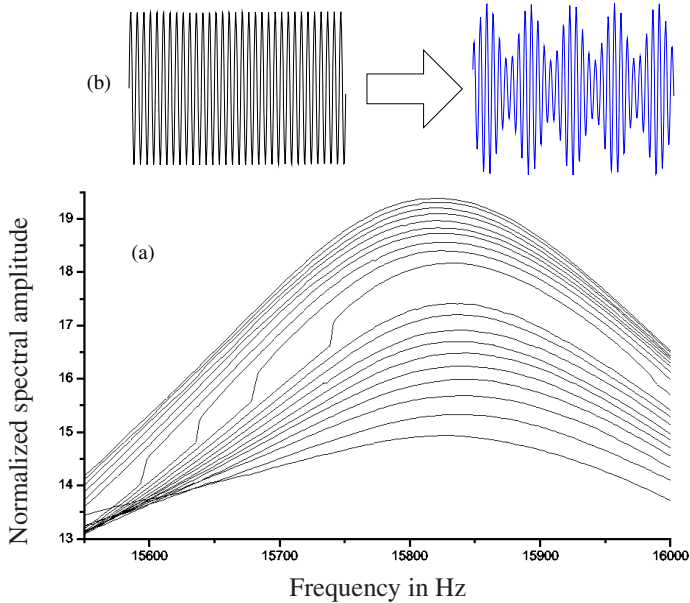


**Figure 18.15.** (a) nonlinear resonance curves with characteristic amplitude jumps for the bar exhibiting a self-induced acoustic transparency. The highest curves correspond to the highest excitation amplitudes. Within a limited interval of excitation amplitudes and in the case of a detuning between the excitation and resonance frequencies, the self-modulation instability phenomenon may take place (b)

given threshold value, the only authorized stationary (although unstable) state for the oscillator corresponds theoretically to the case of a wave of amplitude in the interval  $A_1 < A < A_2$  (corresponding to a negative differential dissipation of energy). In this case, instability leads to a self-modulation of the acoustic wave, as illustrated in Figure 18.15b by a periodic variation of the amplitude of the harmonic wave, with a period exceeding the wave period (slow modulation). This self-modulation was observed experimentally [FIL 06b, FIL 08]. The self-modulation and bistability phenomena are both indicators of a strong nonlinearity of the material and can be applied to its testing.

### 18.3.3. Nonlinear acoustic effects with a threshold

Nonlinear acoustic effects exhibiting a threshold in amplitude were observed for the first time in solids in 2002 [SOL 02]. Above a given level of the acoustic wave emitted in the cracked material, the excitation of the sub-harmonic wave (which is the acoustic wave at the frequency  $\omega/2$ ) was observed. The subsequent increase in the amplitude of the pumping wave was accompanied by a significant increase of efficiency in the generation of higher harmonics  $2\omega$ ,  $3\omega$ , and the emergence of

frequencies  $3\omega/2$ ,  $5\omega/2$ , etc. Moreover, when the amplitude of the pumping wave is then reduced, the sub-harmonic wave disappears also with a threshold effect, but at a threshold amplitude lower than that necessary for its appearance. In other words, a hysteresis in the response of the crack for a periodic loading of variable amplitude appears (self-induced dynamic hysteresis). This observation does not require resonance phenomena to increase the amplitude of acoustic waves above the threshold level. These experiments have been conducted in the propagative system: they have been conducted with surface acoustic waves, which can concentrate the acoustic energy near the surface. The application of surface acoustic waves is obviously limited to the diagnosis of cracks located near the surface of the sample.

The threshold nonlinear acoustics phenomena during the interaction of acoustic propagative bulk waves were observed a little bit later [MOU 03]. The results are qualitatively different from those obtained for the surface waves:

- the threshold excitation level for the sharp increase of the generation of higher harmonics  $2\omega$ ,  $3\omega$  is lower than the excitation threshold of the subharmonic  $\omega/2$  (Figure 18.16);
- the sudden increase in the higher harmonics is accompanied by a fall in the transmitted signal at frequency  $\omega$  of the pumping wave (Figure 18.16);
- the dynamic hysteresis phenomenon is observed for all spectral components (i.e. for  $\omega$ ,  $2\omega$ ,  $3\omega$ , ...,  $\omega/2$ , etc.).

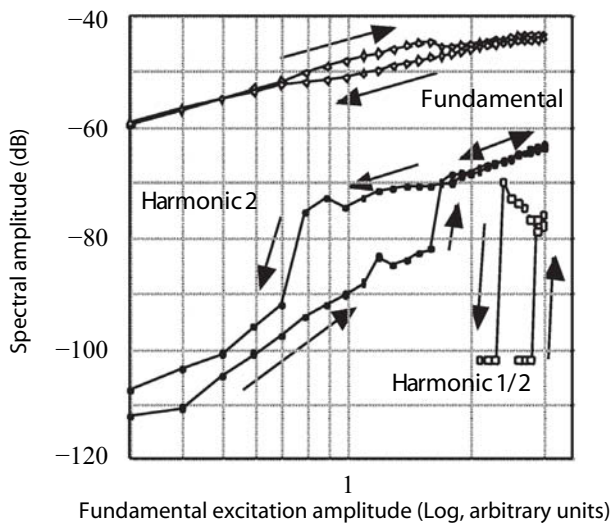


**Figure 18.16.** Variations of the amplitude of the signals detected at frequencies  $\omega$ ,  $2\omega$  and  $\omega/2$ , as a function of the excitation amplitude at the fundamental frequency  $\omega$ . A dynamic hysteresis phenomenon is observed in response to the acoustic loading when the excitation amplitude is initially increased, and then decreased

However, the most important point is not the difference of the threshold phenomena and their sequences with increasing amplitude of the pumping wave, but rather the very existence of these threshold phenomena. In fact, if the observed thresholds could be linked to some parameters of cracks, then the experimental determination of the amplitude threshold of the pumping wave could provide a quantitative information on the parameters of such cracks.

Nowadays, the observed phenomenon is being attributed to the hysteresis of the appearance and disappearance of the intermittent contacts clapping between the lips of a crack [MOU 03, GUS 03, GUS 04]. The distance between the opposite asperities of a crack's lips can be much smaller than the average width of the crack and consequently, the acoustic wave can induce their clapping or tapping. It is well documented that the nonlinearity of the clapping contacts is significantly higher than the elastic nonlinearity of homogenous materials, and is even higher than the nonlinearity of non-clapping contacts. This is due to abrupt changes in the movements of the clapping contacts during impact.

The system of interaction between the acoustic field and the crack depends on the ratio of the acoustic wavelength  $\lambda$  to the characteristic length of the crack  $L$ . If  $(\lambda/L) \ll 1$ , the action of the acoustic field can be modeled by local sinusoidal forces  $f_{ac}$  applied to the interacting asperities. The model is mathematically equivalent to that of a forced impact oscillator [SHA 83, PET 92]. The motion of the lips of the crack in the vicinity of its narrowest part can be qualitatively described as the motion of two interacting masses, excited by a controlled external acoustic stress  $\sigma_{ac}$ . Fortunately, the theory of impact oscillations is sufficiently developed to be useful for interpreting the experiments presented here. Whether we use the simplest model with an instantaneous impact law [FOA 94a] (of the type presented in Figure 17.4c, Chapter 17), or a more realistic model for the impact [FOA 94b], with the Hertz contact law (like the situation presented in Figure 17.4a, Chapter 17) the theory predicts that a sinusoidal non-impacting oscillation becomes unstable with an increase of the amplitude, when the oscillating masses come into contact for the first time. The numerical solution [FOA 94b] demonstrates that a further increase of the force can lead to a new stabilization of the oscillator at an impact motion, with the same period but not sinusoidal (nonlinear). Then, if the amplitude of the acoustic pumping wave decreases, the system shows a hysteresis phenomenon when coming back to a non-impacting oscillation. The scenario described here provides a possible explanation for the appearance in experiments [MOU 03] of clapping, which starts at acoustic amplitudes that are higher than those necessary to stop the clapping. As clapping provides the additional mechanism of strong acoustic nonlinearity [BUC 78, SOL 93, BEL 94, PUT 94], this scenario explains both the observed increase in the threshold for higher harmonics and the hysteresis phenomenon in their amplitude behavior. The hysteresis at the fundamental frequency (self-induced hysteresis) may be due to the hysteresis of the vibration amplitude of the contacts at the fundamental frequency, and/or to the hysteresis of energy loss of the fundamental

acoustic wave to the generation of harmonics and to the heating of intermittent contacts.

If the amplitude of the acoustic pumping wave keeps increasing (after the clapping threshold), then at some level of excitation, the transition takes place first towards a doubling of the period, and then towards a multiplying by four of the period, as predicted numerically [FOA 94b]. This is the beginning of a period doubling cascade. It is important to note that, from a theoretical point of view, in returning from an oscillation with doubled period back to an oscillation with the initial period hysteresis may exist [PET 92]. Recently, a hysteresis in the excitation of sub-harmonics was observed for a nanoscopic contact [BUR 95]. The description above gives a possible physical explanation for the behavior of the amplitude of the sub-harmonic ( $\omega/2$ ) observed in experiments [MOU 03].

In the opposite extreme, for the acoustically small crack ( $\lambda/L \gg 1$ ), the scenario of forced motion of the crack also explains the observed hysteresis phenomenon. In this system, the oscillations of the lips of the crack precisely follow the displacement  $u_{ac}$  in the acoustic field. The nonlinear interaction between the lips of the crack causes a variation in the average local width of the crack that depends on the amplitude of the acoustic wave. In other words, the amplitude of the sinusoidal oscillation of the lips of the crack, which takes place in an effective field (see Figure 17.4f,g, Chapter 17) is controlled by the acoustic field, but the average distance between the lips of the crack is controlled by the effective force  $F_{\text{eff}}$ . The clapping acts as a mechanical diode, demodulating the vibration of the lips of the crack ( $\omega - \omega = 0$ ). In the presence of the acoustic wave, the distance between opposite asperities  $2y_{ac}$  differs from  $2y_0$  and can be found through the equilibrium condition  $\langle F_{\text{eff}}(y_{ac} + u_{ac}) \rangle = 0$ , where  $\langle \dots \rangle$  is used to describe the averaging over a wave period  $T$ , and only a part of the acoustic displacement that modifies the distance between the lips of the crack must be taken into account [MOU 03, GUS 03, GUS 04]. The analysis [MOU 03] shows that, if the attraction force in the impact plane is higher than the repulsive force ( $F_f > F_o$  in Figure 4.4g), then the non-impacting original system  $y_{ac} = y_0$  becomes unstable when for  $u_{ac} = y_0 - y_{\text{imp}}$  the lips start to make contact, and the width of the crack begins to decrease. If simultaneously, the crack has a lower energy in the opened state than in closed state, then the return to an opened position happens at lower amplitudes of the acoustic wave. Note that even the sinusoidal motion of the lips of the crack is a source of harmonics, due to the nonlinearity of the interaction force in the system of clapping contacts. Thus, the theoretically predicted behavior qualitatively reproduces the hysteresis phenomenon observed in experiments [MOU 03].

It is important to mention that the model considered for the contact between the lips of a crack immersed into a material matrix (Figure 18.11) is a model with two minima of the potential, corresponding to the opened and closed positions of the contact. This model is a generalized model for an individual two-level mechanical element, which is presented Chapter 17. We recall that the averaging over the

statistical distribution of individual hysteretic elements formally predicts a hysteretic nonlinearity with no threshold, because of the wide distribution of possible values for the parameters of individual elements (such as  $y_0$ ,  $y_{imp}$  and  $y_c$ , for example, see section 17.2.2, Chapter 17). It can be concluded that, the pronounced threshold effects experimentally observed in [MOU 03] are due to the fact that the acoustic field interacts with a single or a few hysteretic elements. Therefore, experiments of this kind could provide information about the individual micro-mechanical hysteretic elements.

In unconsolidated granular media, threshold effects may also occur due to intermittent opening of the initially closed weakest contacts by the acoustic wave (clapping phenomenon); or due to intermittent closing of the narrowest initially opened gaps between the beads (tapping phenomenon) [TOU 04b]. By analogy with the impact oscillator widely studied in mechanics [DEW 00, MOO 87, PET 92, FOA 94a, FOA 94b], instability may occur as soon as “impacting” starts (“clapping” or “tapping”). This causes the period to double (generation of the subharmonic  $1/2$ ), and opens a path to acoustic chaos, due to a period-doubling cascade [FEI 78, LAU 96]. Of course, in an unconsolidated granular medium, a distribution of individual thresholds exists because of a wide statistical distribution of contact pre-loadings, the lowest thresholds (in amplitude) being those related to the weakest contacts (or narrowest gaps). In Figure 18.17, the amplitude spectra of the signals detected in an unconsolidated layer of granular glass beads are presented. The initial excitation is monochromatic, at a frequency of 12 kHz. The static pressure applied to the granular medium is around 300 kPa. For acoustic strains with a low amplitude ( $s_A \simeq 4 \cdot 10^{-9}$ ), the spectrum above the measurement noise level in Figure 18.17a is monochromatic.

If the excitation amplitude is increased ( $s_A \simeq 4 \cdot 10^{-7}$  for curve b), other spectral peaks appear, at the double frequency  $2\omega$ , triple frequency  $3\omega$ , but also at sub-harmonic frequencies  $\omega/2$  and  $3\omega/4$ . For an even higher amplitude ( $s_A \simeq 10^{-6}$  for curve c), the noise level increases rapidly and harmonics  $3\omega/2$ ,  $5\omega/2$  start to emerge from noise. Finally, for  $s_A \simeq 10^{-5}$  for curve d, the noise spectrum widens and only the harmonics  $n\omega$  and  $n\omega/2$  ( $n = 1, 2, 3, \dots$ ) emerge from the noise. It is important to note that the strain excitation amplitude for which the harmonic  $\omega/2$  emerges from noise is lower than  $s_A \simeq 4 \cdot 10^{-7}$ , which is more than 1,000 times lower than the average static strain of the contacts in the medium. Therefore, only the weakest contacts in the medium are participating in the period-doubling nonlinear process. Their contribution to the observed signal is visible because of their important role in the nonlinear properties of the medium (section 17.2.6, Chapter 17). This method of nonlinear acoustics, through detection of an amplitude threshold for the generation of harmonic  $\omega/2$ , or through the measurement of the relative amplitudes of the fundamental, harmonics and sub-harmonics, is likely to provide in perspective quantitative information on the ratio of weak and strong contacts in the medium, or even on the statistical distribution of the contact forces in granular medium.

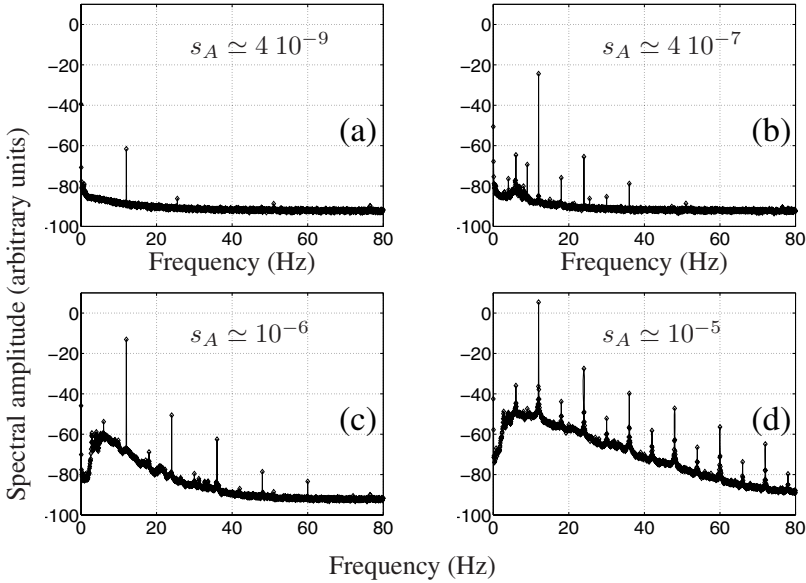


**Figure 18.17.** Amplitude spectra of the detected signals from a layer of a non-consolidated granular medium subjected to a static uni-axial stress of 300 kPa. The four spectra are obtained for four amplitudes of the strain excitation level  $s_A$

### 18.3.4. Conclusions

The experimental results described in this section demonstrate the high sensitivity of nonlinear acoustic methods to the micro-inhomogeneities of materials, especially to the presence in the material of weak contacts, related to cracks, grain or rough interfaces, for example. In addition to classic methods of acousto-elasticity, frequency-mixing and resonant vibrations, modern methods of modulation transfer, dynamic hysteresis, excitation of sub-harmonics and self-modulation have been tested and implemented these last years. These new methods allow for non-destructive testing of the properties of individual micro-mechanical elements composing the material. For example, hysteresis in the response of an individual micro-mechanical element to acoustic loading, related to bistability (or multistability) of an individual micro-mechanical element, can be monitored and applied for material characterization.

The ability to test individual cracks, interfaces and contacts, significantly broadens the perspectives for applications of nonlinear acoustic methods in the domain of monitoring and evaluation of materials and structures. Classic and modern nonlinear acoustic methods can be applied to emerging scientific issues, such as non-destructive testing of micro-systems or nano-structured materials.

## 18.4. Bibliography

- [ASA 70] ASANO S., “Theory of nonlinear damping due to dislocation hysteresis”, *J. Phys. Soc. Japan*, vol. 29, pp. 952–963, 1970.
- [BEL 94] BELYAEVA I.Y., ZAITSEV V.Y. and TIMANIN E.M., “Experimental study of nonlinear elastic properties of granular media with nonideal packing”, *Acoustical Physics*, vol. 40, pp. 789–793, 1994.
- [BER 88] BERESNEV I.A. and NOVIKOV A.V., “Experimental investigation of nonlinear seismic effects”, *Phys. Earth Planetary Interiors*, vol. 50, pp. 83–87, 1988.
- [BRE 84] BREAZEALE M.A. and PHILIP J., *Physical Acoustics, Principle and Methods: Determination of Third-order Elastic Constants from Ultrasonic Harmonic Generation Measurements*, vol. XVIII, Academic Press, Orlando, 1984.
- [BUC 78] BUCK O., MORRIS W.L. and RICHARDSON J.M., “Acoustic harmonic generation at unbonded interfaces and fatigue cracks”, *Appl. Phys. Lett.*, vol. 33, pp. 371–373, 1978.
- [BUR 95] BURNHAM N.A., KULIK A.J., GREMAUD G. and BRIGGS G.A.D., “Nanosubharmonics: The dynamics of small nonlinear contacts”, *Phys. Rev. Lett.*, vol. 74, pp. 5092–5095, 1995.
- [CAS 03] CASTAGNÈDE B., TOURNAT V., MOUSSATOV A. and GUSEV V., “Procédé de caractérisation physique des matériaux poro-élastiques”, *French Patent*, vol. 0303913, 2003.
- [CAS 06] CASTAGNÈDE B., SAEID M., MOUSSATOV A., GUSEV V. and TOURNAT V., “Reflection and transmission at normal incidence onto air-saturated porous materials and direct measurements based on parametric demodulated ultrasonic waves”, *Ultrasonics*, vol. 44, pp. 221–229, 2006.
- [CAT 00] CATE J.A.T., SMITH E. and GUYER R.A., “Universal slow dynamics of granular solids”, *Phys. Rev. Lett.*, vol. 85, pp. 1020–1023, 2000.
- [DEW 00] DE WEGER J., VAN DE WATER W. and MOLLHAAR J., “Grazing impact oscillations”, *Phys. Rev. E*, vol. 62, pp. 2030–2041, 2000.
- [DON 01] DONSKOY D.M. and SUTIN A.M., “Nonlinear acoustic interaction on contact interfaces and its use for nondestructive testing”, *NDT&E International*, vol. 34, pp. 231–238, 2001.
- [FEI 78] FEIGENBAUM M., “Quantitative universality for a class of nonlinear transformations”, *J. Stat. Phys.*, vol. 19, pp. 25–52, 1978.
- [FIL 06a] FILLINGER L., ZAITSEV V., GUSEV V. and CASTAGNÈDE B., “Nonlinear relaxational absorption/transparency for acoustic waves due to thermoelastic effect”, *Acustica Acta-Acustica*, vol. 92, pp. 24–34, 2006.
- [FIL 06b] FILLINGER L., ZAITSEV V., GUSEV V. and CASTAGNÈDE B., “Wave self-modulation in an acoustic resonator due to self-induced transparency”, *Europhysics Lett.*, vol. 76, pp. 229–235, 2006.
- [FIL 08] FILLINGER L., ZAITSEV V., GUSEV V. and CASTAGNÈDE B., “Self-modulation of acoustic waves in resonant bars”, *Journal of Sound and Vibrations*, vol. 318, pp. 527–548, 2008.



- [FOA 94a] FOALE S., “Analytical determination of bifurcations in an impact oscillator”, *Proc. R. Soc. London, Ser. A*, vol. 347, pp. 353–364, 1994.
- [FOA 94b] FOALE S. and BISHOP S.R., “Bifurcations in impact oscillations”, *Nonlinear Dyn.*, vol. 6, pp. 285–299, 1994.
- [GRA 66] GRANATO A.V. and LUCKE K., “The vibrating string model of dislocation damping”, in MASON W.P. and THURSTON R.N. (Eds.), *Physical Acoustics, Principles and Methods*, vol. IV, part A, Academic Press, New York, 1966.
- [GUS 98] GUSEV V., LAURIKS W. and THOEN J., “Dispersion of nonlinearity, nonlinear dispersion, and absorption of sound in micro-inhomogeneous materials”, *J. Acoust. Soc. Am.*, vol. 103, pp. 3216–3226, 1998.
- [GUS 03] GUSEV V., CASTAGNÈDE B. and MOUSSATOV A., “Hysteresis in response of nonlinear bistable interface to continuously varying acoustic loading”, *Ultrasonics*, vol. 41, pp. 643–654, 2003.
- [GUS 04] GUSEV V., “Frequency dependence of dynamic hysteresis in the interaction of acoustic wave with interface”, *J. Acoust. Soc. Am.*, vol. 115, pp. 1044–1048, 2004.
- [GUS 05] GUSEV V. and TOURNAT V., “Amplitude- and frequency-dependent nonlinearities in the presence of thermally-induced transitions in the Preisach model of acoustic hysteresis”, *Phys. Rev. B*, vol. 72, p. 054104, 2005.
- [GUY 95] GUYER R.A., MCCALL K.R. and BOITNOTT G.N., “Hysteresis, discrete memory, and nonlinear wave propagation in rock: a new paradigm”, *Phys. Rev. Lett.*, vol. 74, pp. 3491–3494, 1995.
- [GUY 99] GUYER R.A. and JOHNSON P.A., “Nonlinear mesoscopic elasticity : evidence of a new class of materials”, *Phys. Today*, vol. 52, pp. 30–35, 1999.
- [INS 08] INSERRA C., TOURNAT V. and GUSEV V., “Characterization of granular compaction by nonlinear acoustic resonance method”, *Appl. Phys. Lett.*, vol. 92, 191916, 2008.
- [JHA 02] JHANG K.-Y., “Applications of nonlinear ultrasonics to the NDE of material degradation”, *IEEE Trans. UFFC*, vol. 47, pp. 540–548, 2002.
- [JIA 99] JIA X., CAROLI C. and VELICKY B., “Ultrasound propagation in externally stressed granular media”, *Phys. Rev. Lett.*, vol. 82, pp. 1863–1866, 1999.
- [JOH 96] JOHNSON P.A., ZINSZNER B. and RASOLOFOSAON P.N.J., “Resonance and elastic nonlinear phenomena in rock”, *J. Geophys. Res.*, vol. 101, pp. 11553–11564, 1996.
- [LAN 59] LANDAU L.D. and LIFSHITZ E.M., *Theory of Elasticity*, Pergamon, New-York, 1959.
- [LAU 96] LAUTERBORN W., “Nonlinear dynamics in acoustics”, *Acustica Acta-Acustica*, vol. 82, pp. 546–555, 1996.
- [LEB 99] LEBEDEV A.B., “Amplitude-dependent elastic-modulus defect in main dislocation-hysteresis models”, *Phys. Solid State*, vol. 41, pp. 1105–1111, 1999.
- [MAC 04] MACKSE H.A., GLAND N., JOHNSON D.L. and SCHWARTZ L., “Granular packings: nonlinear elasticity, sound propagation and collective relaxation dynamics”, *Phys. Rev. E*, vol. 70, p. 061302, 2004.



- [MOO 87] MOON F.C., *Chaotic Vibrations. An Introduction for Applied Scientists and Engineers*, John Wiley & Sons, New-York, 1987.
- [MOU 01] MOUSSATOV A., CASTAGNÈDE B. and GUSEV V., "Observation of nonlinear interaction of acoustic waves in granular materials: demodulation process", *Phys. Lett. A*, vol. 283, pp. 216–223, 2001.
- [MOU 02] MOUSSATOV A., CASTAGNÈDE B. and GUSEV V., "Frequency up-conversion and frequency down-conversion of acoustic waves in damaged materials", *Phys. Lett. A*, vol. 301, pp. 281–290, 2002.
- [MOU 03] MOUSSATOV A., GUSEV V. and CASTAGNÈDE B., "Self-induced hysteresis for nonlinear acoustic waves in cracked materials", *Phys. Rev. Lett.*, vol. 90, p. 124301, 2003.
- [NAG 98] NAGY P.B., "Fatigue damage assesment by nonlinear ultrasonic material characterization", *Ultrasonics*, vol. 36, pp. 375–381, 1998.
- [NAZ 88a] NAZAROV V.E., OSTROVSKY L.A., SOUSTOVA I.A. and SUTIN A.M., "Anomalous acoustic nonlinearity in metals", *Sov. Phys. Acoust.*, vol. 34, pp. 284–289, 1988.
- [NAZ 88b] NAZAROV V.E., OSTROVSKY L.A., SOUSTOVA I.A. and SUTIN A.M., "Nonlinear acoustics of micro-inhomogeneous media", *Phys. Earth Planet. Inter.*, vol. 50, pp. 65–73, 1988.
- [NAZ 00] NAZAROV V.E., "Amplitude dependence of internal friction in zinc", *Acoustical Physics*, vol. 46, pp. 186–190, 2000.
- [NOV 80] NOVIKOV B., RUDENKO O. and TIMOSHENKO V., *Nonlinear Underwater Acoustics*, AIP, NY, 1980.
- [NOW 50] NOWICK A.S., "Variation of amplitude-dependent internal friction in single crystal copper with frequency and temperature", *Phys. Rev.*, vol. 80, pp. 249–257, 1950.
- [NOW 72] NOWICK A.S. and BERRY B.S., *Anelastic Relaxation in Crystalline Solids*, Academic Press, New York, 1972.
- [OST 01] OSTROVSKY L.A. and JOHNSON P.A., "Dynamic nonlinear elasticity of geomaterials", *Rivista del Nuovo Cimento*, vol. 24, pp. 1–46, 2001.
- [PET 92] PETERKA F. and VACIK J., "Transition to chaotic motion in mechanical systems with impacts", *J. Sound Vib.*, vol. 154, pp. 95–115, 1992.
- [PUT 94] PUTMAN C.A.J., DER VERF K.O.V., GROOTH B.G.D., HULST N.F.V. and GREVE J., "Tapping mode atomic force microscopy in liquid", *Appl. Phys. Lett.*, vol. 64, pp. 2454–2456, 1994.
- [REA 40] READ T.A., "The internal friction of single metal crystals", *Phys. Rev.*, vol. 58, pp. 371–380, 1940.
- [SAE 04] SAEID M., CASTAGNÈDE B., MOUSSATOV A., TOURNAT V. and GUSEV V., "Application of nonlinearly demodulated acoustic signals for the measurements of the acoustic coefficient of reflexion for air saturated porous materials", *CR Mécanique*, vol. 332, pp. 849–858, 2004.

- [SES 75] SESSLER J.G. and WEISS V., "Crack detection apparatus and method", *US Patent*, vol. 3867836, 1975.
- [SHA 83] SHAW S.W. and HOLMES P.J., "A periodically forced piecewise linear oscillator", *J. Sound Vib.*, vol. 90, pp. 129–155, 1983.
- [SOL 93] SOLODOV I.Y. and CHIN A.W., "Popping nonlinearity and chaos in vibrations of contact interface between solids", *Acoust. Phys.*, vol. 39, p. 476, 1993.
- [SOL 02] SOLODOV I.Y. and KORSHAK B.A., "Instability, Chaos, and Memory in Acoustic Wave Crack Interaction", *Phys. Rev. Lett.*, vol. 88, p. 014303, 2002.
- [STO 89] STOLL R.D., *Sediment Acoustics*, vol. 26, Lecture Notes in Earth Sciences, Springer-Verlag, 1989.
- [SUT 98] SUTIN A.M. and DONSKOY D.M., "Vibro-acoustic modulation nondestructive evaluation technique", *Proc. SPIE*, vol. 3397, pp. 226–237, 1998.
- [TEN 04] TENCATE J.A., PASQUALINI D., HABIL S., HEITMANN R., HIGDON D. and JOHNSON P.A., "Nonlinear and non-equilibrium dynamics in geomaterials", *Phys. Rev. Lett.*, vol. 93, no. 6, p. 065501, 2004.
- [TOU 02] TOURNAT V., GUSEV V. and CASTAGNÈDE B., "Influence of ballistic to diffusion transition in primary waves propagation on parametric antenna operation in granular medium", *Phys. Rev. E*, vol. 66, p. 041303, 2002.
- [TOU 03] TOURNAT V., CASTAGNÈDE B., GUSEV V. and BÉQUIN P., "Self-demodulation acoustic signatures for nonlinear propagation in glass beads", *CR Mécanique*, vol. 331, pp. 119–125, 2003.
- [TOU 04a] TOURNAT V., GUSEV V.E., ZAITSEV V.Y. and CASTAGNÈDE B., "Acoustic second harmonic generation with shear to longitudinal mode conversion in granular media", *Europhysics Lett.*, vol. 66, pp. 798–804, 2004.
- [TOU 04b] TOURNAT V., GUSEV V. and CASTAGNÈDE B., "Subharmonics and noise excitation in transmission of acoustic wave through unconsolidated granular medium", *Phys. Lett. A*, vol. 326, no. 5-6, pp. 340–348, 2004.
- [TOU 04c] TOURNAT V., ZAITSEV V.Y., GUSEV V.E., NAZAROV V.E., BÉQUIN P. and CASTAGNÈDE B., "Probing weak forces in granular media through nonlinear dilatancy: clapping contacts and polarization anisotropy", *Phys. Rev. Lett.*, vol. 92, p. 085502, 2004.
- [Van 00a] VAN-DEN-ABEELE K. and VISSCHER J.D., "Damage assessment in reinforced concrete using spectral and temporal nonlinear vibration techniques", *Cement and Concrete Res.*, vol. 30, pp. 1453–1464, 2000.
- [Van 00b] VAN-DEN-ABEELE K.E.-A., JOHNSON P.A. and SUTIN A., "Nonlinear elastic wave spectroscopy (NEWS) techniques to discern material damage, Part I: nonlinear wave modulation spectroscopy (NWMS)", *Res. Nondestr. Eval.*, vol. 12, pp. 17–30, 2000.
- [Van 01] VAN-DEN-ABEELE K.E.-A., JOHNSON P.A. and SUTIN A., "Micro-damage diagnostics using nonlinear elastic wave spectroscopy (NEWS)", *NDT&E International*, vol. 34, pp. 239–248, 2001.

- [YOS 01] YOST W.T., CANTRELL J.H. and NA J.K., “Nonlinear ultrasonic pulsed measurements and applications to metal processing and fatigue”, in *Review of QNDE*, vol. 20, AIP, 2001.
- [ZAI 99] ZAITSEV V.Y., KOLPAKOV A.B. and NAZAROV V.E., “Detection of acoustic pulses in river sand: experiments”, *Acoust. Phys.*, vol. 45, pp. 202–208, 1999.
- [ZAI 00] ZAITSEV V.Y. and SAS P., “Dissipation in micro-inhomogeneous solids: inherent amplitude dependent losses of a non-hysteretical and non-frictional type”, *Acustica Acta-Acustica*, vol. 86, pp. 429–445, 2000.
- [ZAI 02a] ZAITSEV V., GUSEV V. and CASTAGNÈDE B., “Luxembourg-Gorky effect retooled for elastic waves: a mechanism and experimental evidence”, *Phys. Rev. Lett.*, vol. 89, p. 105502, 2002.
- [ZAI 02b] ZAITSEV V., GUSEV V. and CASTAGNÈDE B., “Observation of Luxembourg-Gorky effect for elastic waves”, *Ultrasonics*, vol. 40, pp. 627–631, 2002.
- [ZAI 03] ZAITSEV V., GUSEV V. and CASTAGNÈDE B., “Thermoelastic mechanism of logarithmic slow dynamics and memory in elastic wave interaction with individual cracks”, *Phys. Rev. Lett.*, vol. 90, p. 075501, 2003.
- [ZAI 05] ZAITSEV V.Y., NAZAROV V.E., TOURNAT V., GUSEV V.E. and CASTAGNÈDE B., “Luxemburg-Gorky effect in a granular medium: probing perturbations of the material state via cross-modulation of elastic waves”, *Europhysics Lett.*, vol. 70, pp. 1–7, 2005.
- [ZAR 71] ZAREMBO L.K. and KRASILNIKOV V.A., “Nonlinear phenomena in the propagation of elastic waves in solids”, *Sov. Phys. Uspekhi*, vol. 13, pp. 778–797, 1971.
- [ZHE 99] ZHENG Y., MAEV R.G. and SOLODOV I.Y., “Nonlinear acoustic applications for materials characterization”, *Can. J. Phys.*, vol. 77, pp. 927–967, 1999.

This page intentionally left blank

Part 5

## The Green Function in Anisotropic Media

This page intentionally left blank

## Chapter 19

# The Cagniard–de Hoop Method

### 19.1. Introduction

This section gathers some elements of calculation and graphical interpretations on the Cagniard–de Hoop method applied to the evaluation of the elastodynamic Green functions ([CAG 39], [HOO 60], [JOH 74], [PAY 83]). We should note that because the scope of this technique is very broad ([KEN 83], [NAY 95], [GRI 04]) and that the mathematical developments require great strictness, these pages are absolutely not exhaustive. We hope they may provoke the reader's interest into using such an approach with certain problems of wave propagation.

The issue is as follows: what is the dynamic response of a purely elastic solid to a localized and transient source? It is through the calculation of the elastodynamic Green function that we can reach it. To obtain such a transient solution, many approaches exist. They each have advantages and drawbacks. Users aware of the performance and shortcomings of each method will make their choice accordingly. Here, an accurate analytical technique is suggested to address this problem: the Cagniard–de Hoop method associated with the notion of the generalized-ray. As an analytical extension of Fourier acoustics in the complex plane of the slowness, the Cagniard–de Hoop method provides temporal content to the concept of the generalized-ray [VDH 87].

In a first step, a brief mathematical overview of the principle of the method is introduced, and the notion of the inhomogeneous plane wave is addressed. Then, we use the joint Laplace–Fourier transform in order to solve the differential equations of elastodynamics, for which source terms are considered. Solutions to the problem of propagation in anisotropic media are given in the dual Laplace–Fourier space and will be used as a starting point for applications to different practical cases. Five applications are proposed, mainly by considering the problems of two-dimensional propagation (line-sources) in order to simplify the derivations and therefore facilitate the understanding of the method. The first two points concern the calculation of the impulse response for infinite media (isotropic and anisotropic cases). The next two deal with the dynamic response of the isotropic and anisotropic half-spaces to a source located on the surface. The last point considers the impulse response on the surface of an anisotropic half-space subjected to a point force [BES 98]. It is especially for the elastodynamic response of the half-space (Lamb problem) that the Cagniard–de Hoop method is of most interest ([MOU 95] and [MOU 96]).

The objective of this part is to provide a methodological guide rather than exhaustive details that would require many pages. The main appeal of the technique in question lies in the change of variables “time-slowness” and the distortion of the paths of the integrals in the complex plane. That is why, for educational purposes, we propose the case of two-dimensional, instead of three-dimensional propagation, for which an additional integration (often performed numerically) remains.

## 19.2. Preliminaries

### 19.2.1. Principle of the Cagniard–de Hoop method

We first introduce  $G(x_1, x_3, t)$  the Green function or impulse response, of a two-dimensional problem (this problem can be scalar, vectorial or more generally tensorial) to an acoustic source whose spatio-temporal dependence is  $\delta(x_1)\delta(x_3)\delta(t)$ . The medium is supposed to be infinite and homogeneous. We use the Laplace transform over time ( $t \rightarrow p$ ) and Fourier transform on the first spatial variable ( $x_1 \rightarrow -ips_1$ ), where  $k_1 = -ips_1$  is the Fourier parameter, and  $s_1$  the slowness in the  $x_1$  direction. The Green function  $\tilde{G}(x_3, s_1, p)$  in the dual domain, that is, the solution of the partial differential equations of elastodynamics, can be written formally as a linear combination of terms such as:  $\varphi(s_1, p)\exp[-ps_3(s_1)x_3]$ , where  $s_1$  and  $s_3$  are connected by the characteristic equations of propagation in the medium. This expression shows an exponential function (the phase term for the Laplace transform) due to the propagation phenomenon. Once the problem is solved in the dual domain, we find the original solution in the real (physical) domain  $(x_1, x_3, t)$  thanks to two inverse transforms. But before going further, let us consider as a first step the solution in the  $p$  domain.



It is assumed that  $\varphi(s_1, p)$  does not depend on  $p$ , or that  $\varphi$  is proportional to a power of  $p$ :  $\varphi = p^\alpha \Phi(s_1)$ ,  $\alpha \in \mathbb{N}$ . This solution is obtained by performing an inverse Fourier transform (so-called ‘spatial’ inverse Fourier transform), namely:

$$\hat{G}(x_1, x_3, p) = p^\alpha \int_{-\infty}^{+\infty} \Phi(s_1) e^{-p(s_1 x_1 + s_3 x_3)} ds_1. \quad [19.1]$$

Suppose now that we can find a change of variables  $s_1 \rightarrow \tau = f(s_1)$ , like  $\tau = s_1 x_1 + s_3 x_3$  with  $\tau$  a real positive number homogenous to a time, then the integral [19.1] can be rewritten as follows:

$$\hat{G}(x_1, x_3, p) = p^\alpha \int_T^{+\infty} F(x_1, x_3, \tau) e^{-p\tau} d\tau, \quad [19.2]$$

where the function  $F$  just results from a rewriting of  $\Phi$  taking into account the change of variables (including the Jacobian), and  $T$  is a real positive lower limit for the integration. The initial objective was to determine the original solution in space and time, i.e.  $G(x_1, x_3, t)$ . By observing the structure of integral [19.2], we recognize the expression of a direct Laplace transform in time. By direct identification, and with the help of the properties of the Laplace transform such as the uniqueness, we can directly access the solution of the problem in the physical domain:

$$G(x_1, x_3, t) = \begin{cases} 0 & \text{for } -\infty < t < T \\ \frac{\partial^\alpha}{\partial t^\alpha} F(x_1, x_3, t) & \text{for } t > T \end{cases} \quad [19.3]$$

Thus, without explicit calculations of both transforms, we obtain the solution in an analytical form in the time and space domain of the causal Green function corresponding to a line-like source of impulse type  $\delta(x_1)\delta(x_3)\delta(t)$ . Here the quantity  $T$  would be an arrival time and  $F$  the “wave form” function of the impulse response which depends explicitly on the positions  $(x_1, x_3)$  and the time  $t$ .

### 19.2.2. Inhomogenous plane waves

The “spatial” Fourier transform with a real transformation parameter involves the concept of angular spectrum (see Figure 19.1).

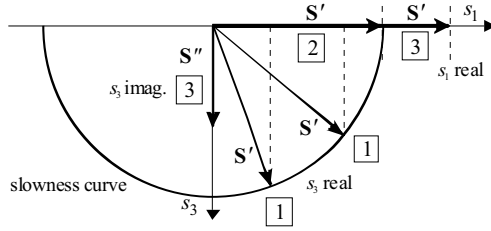


**Figure 19.1.** The real and complex slowness vectors  $\mathbf{S}'$  and  $\mathbf{S}' + i\mathbf{S}''$  of the plane waves of the angular spectrum of the Fourier transform for real values of  $s_1$ . Three cases are displayed: 1) when  $s_3$  is real (case 1); 2) when  $s_3 = 0$  (case 2); 3) when  $s_3$  is imaginary (case 3)

A part of the values of  $s_1$  correspond to homogenous bulk waves, i.e. to plane waves whose slowness vector is real (slowness [1] in Figure 19.1). Beyond a certain value for  $s_1$  ([2]), the quantity  $s_3$  becomes purely imaginary (or more generally complex in the case of anisotropic media) and the plane waves therefore have a component of attenuation along  $x_3$  (evanescent plane waves [3]). The change of variables  $s_1 \rightarrow \tau$  used to obtain formulation [19.2] from expression [19.1] with  $\tau \in \Re^+$ , requires the persistent use of plane waves with complex slowness-vector. These waves are so-called “inhomogenous” plane waves. The field of particle displacement  $\mathbf{u}$  of such waves is given by:

$$\mathbf{u}(\mathbf{M}, t) = A\mathbf{P}e^{i\omega(t-\mathbf{S}\cdot\mathbf{M})} = A\mathbf{P}e^{i\omega(t-\mathbf{S}'\cdot\mathbf{M})}e^{-\omega\mathbf{S}''\cdot\mathbf{M}}, \quad [19.4]$$

where  $\mathbf{S} = \mathbf{S}' - i\mathbf{S}''$  is the complex slowness vector and  $\mathbf{M}$  the position vector. The vector  $\mathbf{S}'$  is associated with the phase variation and the vector  $\mathbf{S}''$  related to the amplitude variation. Here,  $A$  and  $\mathbf{P}$  are respectively the complex amplitude and the complex polarization vector which reflect an elliptical displacement of the particles. With a compact formulation, the change of variables mentioned above becomes:  $\mathbf{S} \cdot \mathbf{M} = \tau$  with  $\tau \in \Re^+$ . So we have, by separating real and imaginary parts:

$$\begin{cases} \mathbf{S}' \cdot \mathbf{M} = \tau \\ \mathbf{S}'' \cdot \mathbf{M} = 0 \end{cases} \quad [19.5]$$

From the second equation of the system given in equation [19.5], we can deduce that  $\mathbf{S}''$  is orthogonal to  $\mathbf{M}$  for all the values of  $\tau \in \Re^+$  for which  $\mathbf{S}'' \neq \mathbf{0}$ . But there is a general property for the inhomogenous plane waves propagating in purely elastic media, which is the orthogonality of the damping vector with the energy propagation direction [HAY 84]:  $\mathbf{S}'' \cdot \mathbf{F} = 0$ ; where  $\mathbf{F}$  is the mean flow of energy of these waves (see section 1.2.2.2, Chapter 1). Therefore the change of variables

simply means the search, while the time  $\tau$  increases, for all the inhomogeneous plane waves whose energy propagates in the direction of observation  $\mathbf{M}$ , and whose time of flight from the source (located at  $\mathbf{O}$ ) to the observation point (located at  $\mathbf{M}$ ) is  $\tau = \mathbf{S}' \cdot \mathbf{M}$ . For example, Figure 19.2 shows three inhomogeneous plane waves for which the energy propagates in the same direction  $\mathbf{M}$  ( $\mathbf{S}'' \cdot \mathbf{M} = 0$ ), but with different time of flight from  $\mathbf{O}$  to  $\mathbf{M}$ .

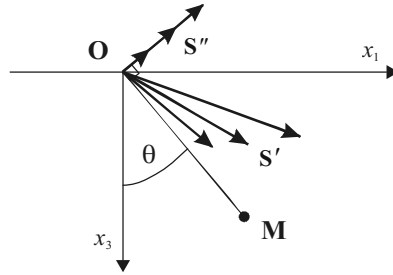


**Figure 19.2.** *Three different inhomogeneous plane waves for which the energy propagates in the observation direction  $\mathbf{M}$  (general scheme for a non-isotropic medium)*

The inhomogeneous plane wave is a key concept of the “physical” understanding of the Cagniard–de Hoop method. Indeed, good expertise in transform algebra, in the analysis of complex functions and in the calculation of integrals with change of variables, is more than sufficient to achieve some theoretical Green functions in elastodynamics with this technique, and for many problems of propagation. However, it would be of little help for a physicist to be confined to strict mathematical results, without being able to observe elements of physical analysis that go well beyond the rigor of the calculation. That is why we will try, as often as possible, to illustrate the principles and the peculiarities of the Cagniard–de Hoop method, by using inhomogeneous plane waves and their characteristics.

### 19.3. Propagation in anisotropic media

This section re-introduces, for the specific needs of this chapter, the equations required for the calculation of impulse responses in purely elastic media. The solutions to the equations of elasticity, including the boundary conditions of our problem, are sought in the dual Laplace–Fourier space. These developments, based on those of Van der Hijden [VDH 87], are general and refer to three-dimensional solutions for anisotropic media.

### 19.3.1. Equations of elastodynamics

The system of partial differential equations for linear elastodynamics in elastic media is composed of 1) the equation of momentum conservation and 2) the constitutive equation of the medium (here, Hooke's law). The latter is written in the form of a linearized equation for the strain rate

$$\begin{cases} \rho \partial_t v_i = \partial_j \sigma_{ij} + f_i \\ \frac{1}{2} (\partial_i v_j + \partial_j v_i) = S_{ijkl} \partial_l \sigma_{kl} + h_{ij} \end{cases} \quad [19.6]$$

where  $\rho$  is the mass density of the medium,  $v_i$  the particle velocity vector,  $\sigma_{ij}$  the symmetric stress tensor,  $f_i$  the density vector of bulk force,  $S_{ijkl}$  the compliance tensor and  $h_{ij}$  the bulk density tensor of sources of strain rate (including dilatation and shear sources). By introducing the stiffness tensor  $c_{ijkl}$  and using its symmetries, we obtain

$$\begin{cases} \partial_j \sigma_{ij} = \rho \partial_t v_i - f_i \\ c_{ijkl} \partial_l v_k = \partial_t \sigma_{ij} + c_{ijkl} h_{kl} \end{cases} \quad [19.7]$$

The Laplace transform applied on the time variable is defined as

$$\hat{v}_i(x_1, x_2, x_3, p) = \int_0^{+\infty} v_i(x_1, x_2, x_3, t) e^{-pt} dt, \quad [19.8]$$

where  $p$  is the real and positive Laplace parameter. To be more concise in the expression of the multiple dimension Fourier transform, we use a Greek character subscript ( $\alpha$  for example) to identify the Fourier parameters. These subscripts take the values 1 and 2. The Fourier transform over the spatial variables is

$$\tilde{v}_i(s_1, s_2, x_3, p) = \int_{-\infty}^{+\infty} \int_{-\infty}^{+\infty} \hat{v}_i(x_1, x_2, x_3, p) e^{ps_\alpha x_\alpha} dx_1 dx_2, \quad [19.9]$$

after having set  $k_\alpha = -ips_\alpha$ , where  $k_\alpha$  are the real parameters of the Fourier transform. The quantities  $s_\alpha$  (which have the physical dimension of a slowness) are purely imaginary. As a consequence, the inverse Fourier transform can be written as follows

$$\hat{v}_i(x_1, x_2, x_3, p) = (p/2i\pi)^2 \int_{-\infty}^{+\infty} \int_{-\infty}^{+\infty} \tilde{v}_i(s_1, s_2, x_3, p) e^{-ps_\alpha x_\alpha} ds_1 ds_2. \quad [19.10]$$

The differential operators in the physical domain become  $\partial_t \rightarrow p$  and  $\partial_\alpha \rightarrow -ps_\alpha$  in the dual domain. Applying the Fourier and Laplace transforms, and using the correspondence of the differential operators, system [19.7] becomes

$$\begin{cases} \partial_3 \tilde{\sigma}_{i3} = p\rho\tilde{v}_i + ps_\alpha \tilde{\sigma}_{i\alpha} - \tilde{f}_i \\ c_{ijk3} \partial_3 \tilde{v}_k = pc_{ijk\beta s} \beta \tilde{v}_k + p\tilde{\sigma}_{ij} + c_{ijkl} \tilde{h}_{kl} \end{cases} \quad [19.11]$$

where we have isolated on the left-hand side all terms on which  $\partial_3$  operates, and on the right-hand side all others terms that are not affected by this operator. To determine the solutions of this system, two ways are possible: we can either eliminate the components of the stress tensor from the different equations of the system, in which case we obtain the second order wave equation written for the particle velocities; or we write system [19.11] as a first order differential form over the 6-dimension vector  $(\tilde{v}_i, \tilde{\sigma}_{i3})^T$ . The latter approach directly provides the jump conditions on the acoustic field at the source. In the following developments, we consider the second option. The second equation of system [19.11] is divided into two parts,  $j = 3$  for the first and  $j = \alpha$  (1 or 2) for the second:

$$\begin{cases} c_{i3k3} \partial_3 \tilde{v}_k = pc_{i3k\beta s} \beta \tilde{v}_k + p\tilde{\sigma}_{i3} + c_{i3kl} \tilde{h}_{kl} \\ c_{i\alpha k3} \partial_3 \tilde{v}_k = pc_{i\alpha k\beta s} \beta \tilde{v}_k + p\tilde{\sigma}_{i\alpha} + c_{i\alpha kl} \tilde{h}_{kl} \end{cases} \quad [19.12]$$

We extract  $\partial_3 \tilde{v}_k$  from the first equation by introducing the tensor  $K_{ni}$  such as  $K_{ni} c_{i3k3} = \delta_{nk}$ ,  $\delta_{nk}$  being the Kronecker delta. We obtain

$$\partial_3 \tilde{v}_n = K_{ni} \left( pc_{i3k\beta s} \beta \tilde{v}_k + p\tilde{\sigma}_{i3} + c_{i3kl} \tilde{h}_{kl} \right). \quad [19.13]$$

We introduce this last value of  $\partial_3 \tilde{v}_n$  in the second equation of [19.12], therefore resulting in the expression of  $\tilde{\sigma}_{i\alpha}$ :

$$\tilde{\sigma}_{i\alpha} = -D_{i\alpha k\beta s} \beta \tilde{v}_k - p^{-1} D_{i\alpha kl} \tilde{h}_{kl} + c_{i\alpha k3} K_{kr} \tilde{\sigma}_{r3}, \quad [19.14]$$

after setting:

$$D_{i\alpha kl} = c_{i\alpha kl} - c_{i\alpha p3} K_{pr} c_{r3kl}. \quad [19.15]$$

Knowing now the expression  $\tilde{\sigma}_{i\alpha}$ , we replace it in the equation of motion (first equation of system [19.11]) to reach the following system

$$\begin{cases} \partial_3 \tilde{v}_i = p K_{ir} c_{r3k} \beta s_\beta \tilde{v}_k + p K_{ir} \tilde{\sigma}_{r3} + K_{ir} c_{r3kl} \tilde{h}_{kl} \\ \partial_3 \tilde{\sigma}_{i3} = p (\rho \delta_{ik} - D_{i\alpha k} \beta s_\alpha s_\beta) \tilde{v}_k + p s_\alpha c_{i\alpha k3} K_{kr} \tilde{\sigma}_{r3} - s_\alpha D_{i\alpha kl} \tilde{h}_{kl} - \tilde{f}_i \end{cases} \quad [19.16]$$

This system can be symbolically written in the form

$$\partial_3 \tilde{W}_I = -p \Theta_{IJ} \tilde{W}_J + \tilde{F}_I, \quad [19.17]$$

where  $\tilde{W}_I$ , the unknown vector ( $I = 1..6$ ), contains the three components of the particle velocities and the three components of the stress acting on a surface orthogonal to the  $x_3$  axis:

$$\tilde{W}_I(x_3) = (\tilde{v}_i(x_3), -\tilde{\sigma}_{i3}(x_3))^T, \quad [19.18]$$

The interesting point here is the vector  $\tilde{F}_I$  which directly gives the jump conditions depending on the nature of the source:

$$\tilde{F}_I = \begin{pmatrix} K_{ir} c_{r3kl} \tilde{h}_{kl} \\ \tilde{f}_i + s_\alpha D_{i\alpha kl} \tilde{h}_{kl} \end{pmatrix}. \quad [19.19]$$

For example, in the case of an isotropic medium where the elasticity tensor is:  $c_{ijkl} = \lambda \delta_{ij} \delta_{kl} + \mu (\delta_{ik} \delta_{jl} + \delta_{il} \delta_{jk})$ , where  $\lambda$  and  $\mu$  are the two Lamé coefficients, the tensor  $K_{ij}$  is written:

$$K_{ij} = -\frac{\lambda + \mu}{\mu(\lambda + 2\mu)} \delta_{i3} \delta_{j3} + \frac{1}{\mu} \delta_{ij}, \quad [19.20]$$

and the complete expression of  $\tilde{F}_I$  then becomes:

$$\tilde{F}_I = \begin{pmatrix} \tilde{h}_{31} + \tilde{h}_{13} \\ \tilde{h}_{32} + \tilde{h}_{23} \\ \frac{\lambda}{\lambda + 2\mu}(\tilde{h}_{11} + \tilde{h}_{22}) + \tilde{h}_{33} \\ \tilde{f}_1 + \frac{2\lambda\mu}{\lambda + 2\mu}(\tilde{h}_{11} + \tilde{h}_{22})s_1 + \mu(\tilde{h}_{\alpha 1} + \tilde{h}_{1\alpha})s_\alpha \\ \tilde{f}_2 + \frac{2\lambda\mu}{\lambda + 2\mu}(\tilde{h}_{11} + \tilde{h}_{22})s_2 + \mu(\tilde{h}_{\alpha 2} + \tilde{h}_{2\alpha})s_\alpha \\ \tilde{f}_3 \end{pmatrix}. \quad [19.21]$$

### 19.3.2. Solutions of the homogenous and non-homogenous wave-equation

The wave equation is obtained from the following system made of the equation of motion and the constitutive relation:

$$\begin{cases} \rho \partial_t v_i - \partial_j \sigma_{ij} = f_i \\ \partial_t \sigma_{ij} = c_{ijkl} \partial_k v_l - c_{ijkl} h_{kl} \end{cases} \quad [19.22]$$

By differentiating the first equation with respect to time ( $\partial_t$ ) and contracting the second with the operator  $\partial_j$ , we can combine these two resulting equations to obtain the wave equation; defined in terms of the particle velocities field, we obtain:

$$\rho \partial_t^2 v_i - c_{ijkl} \partial_j \partial_k v_l = \partial_t f_i - c_{ijkl} \partial_j h_{kl}, \quad [19.23]$$

or in terms of the displacements field:

$$\rho \partial_t^2 u_i - c_{ijkl} \partial_j \partial_k u_l = f_i - c_{ijkl} \partial_j \varepsilon_{kl}, \quad [19.24]$$

$\varepsilon_{kl}$  denoting the source of strain. After the application of the transforms on the homogenous equation (without the sources, the right-hand side is set to zero), we get a system of differential equations with respect to the variable  $x_3$ . The solutions of the homogenous equations are of the form  $\tilde{u}_i(x_3, s_1, s_2, p) = A P_i e^{-p s_3 x_3}$ , where the slowness components satisfy the characteristic Christoffel equation:

$$|\Gamma_{il} - \rho \delta_{il}| = 0, \quad [19.25]$$

where  $\Gamma_{il} = c_{ijkl}s_js_k$ . For each value of the pair  $(s_1, s_2)$ , we obtain six possible solutions for  $s_3$  satisfying the Christoffel equation; these solutions will be noted  $s_3^{(\pm n)}$  with  $n = 1..3$  (the superscript corresponding to the wave type) and the sign  $+$  or  $-$  indicates the direction of propagation of the wave ( $+$  for the waves propagating in direction of increasing values of  $x_3$  and  $-$  for waves propagating in the opposite direction). For each “vertical slowness”  $s_3^{(\pm n)}(s_1, s_2)$ , we associate the corresponding eigenvector  $P_i^{(\pm n)}$  that provides the wave polarization. The amplitudes  $A^{(\pm n)}$  will be determined by the jump conditions at the source position. Assuming that the source is located at  $x_3 = 0$ , then in the half-space  $x_3 > 0$  the wave-field should be bounded when  $x_3 \rightarrow +\infty$ . Since the Laplace parameter  $p$  is real and positive, only solutions such that  $\text{Re}(s_3) > 0$  are acceptable (i.e.  $s_3^{(+n)}$ ). For the half-space  $x_3 < 0$ , only the other three solutions such that  $\text{Re}(s_3) < 0$  are acceptable ( $s_3^{(-n)}$ ). We remember that in the initial settings of transforms,  $s_1$  and  $s_2$  are purely imaginary and that the criterion  $\text{Re}(s_3x_3) > 0$  always separates the six solutions into two groups of three partial waves, propagating (or being attenuated) in opposite directions, whether the medium is isotropic or anisotropic [VDH 87]. The full solution is therefore written for a source located at  $x_3 = 0$ :

$$\tilde{u}_i(x_3, s_1, s_2, p) = \begin{cases} \tilde{u}_i^-(x_3, s_1, s_2, p) = \sum_{n=1}^3 A^{(-n)} P_i^{(-n)} e^{-ps_3^{(-n)}x_3}, & -\infty < x_3 < 0 \\ \tilde{u}_i^+(x_3, s_1, s_2, p) = \sum_{n=1}^3 A^{(+n)} P_i^{(+n)} e^{-ps_3^{(+n)}x_3}, & 0 < x_3 < +\infty \end{cases} \quad [19.26]$$

The solution of the non-homogenous wave equation (with sources) is obtained by writing the jump conditions at the sources. We are interested here in the Green function of the problem; consequently, the space and time dependence of the source terms  $f_i$  and  $h_{kl}$  is  $\Phi(x_1, x_2, x_3, t) = \delta(x_1)\delta(x_2)\delta(x_3)\delta(t)$ . In the dual domain, the image of the function  $\Phi$  is  $\Phi(x_3, s_1, s_2, p) = \delta(x_3)$ . Looking at system [19.17], we note that the function  $\partial_3 \tilde{W}_I$  contains a delta function at the source location ( $x_3 = 0$ ). We can deduce that the function  $\tilde{W}_I$  (and therefore  $\tilde{v}_i$  and  $\tilde{\sigma}_{i3}$ ) undergoes a jump at  $x_3 = 0$ :

$$\lim_{x_3 \rightarrow 0^+} \tilde{W}_I - \lim_{x_3 \rightarrow 0^-} \tilde{W}_I = S_I, \quad [19.27]$$

where  $S_I$  is the amplitude vector of the jump defined by:  $\tilde{F}_I(x_3, s_1, s_2, p) = S_I(s_1, s_2, p)\delta(x_3)$ . Since the total field  $\tilde{W}_I$  is a linear combination of the elementary solutions under the form of plane waves appearing in [19.26], equation



[19.27] leads to a linear system of dimension six from which the amplitudes  $A^{(\pm n)}$  are obtained:

$$L_{IJ}A_J = S_I. \quad [19.28]$$

Each column of the matrix  $L_{IJ}$  is made of the vector  $\tilde{W}_I$ , expressed at  $x_3 = 0$ , corresponding only to the field produced by the plane wave  $J$ . The resolution of this system gives the value of the vector  $A_J$ , that is to say  $A^{(\pm n)}$ . The solution  $\tilde{u}_i(x_3, s_1, s_2, p)$  in the dual domain is then entirely determined. The corresponding solution in the real (physical) domain is written as the multiple inverse Fourier–Laplace transform over the parameters  $p$ ,  $s_1$  and  $s_2$ , of the function  $\tilde{u}_i(x_3, s_1, s_2, p)$ :

$$u_i(x_1, x_2, x_3, t) = \frac{1}{(2i\pi)^3} \int_{c-i\infty}^{c+i\infty} p^2 e^{pt} dp \int_{-i\infty}^{+i\infty} \int_{-i\infty}^{+i\infty} \tilde{u}_i(x_3, s_1, s_2, p) e^{-ps_a x_a} ds_1 ds_2. \quad [19.29]$$

At this stage, many approaches exist to find the function  $u_i(x_1, x_2, x_3, t)$  from such an integral form. They can be purely numerical, based on a direct calculation using the Fast Fourier Transform algorithm, or they can approximate the integrals as in methods such as “stationary phase”. The accuracy and the rapidity of obtaining  $u_i(x_1, x_2, x_3, t)$  are variable according to the methods, and the preference of a user for this or that technique will depend strongly on the requirements, the computing means available and the analysis of results hoped for.

In the following, we propose to use the Cagniard–de Hoop method to get an expression of the solution  $u_i(x_1, x_2, x_3, t)$ . The main advantage of this technique is to provide an accurate evaluation of the elastodynamic Green function that is difficult to reach by other means. In first place, the didactic two-dimensional case, resulting from the problem of a line-source, will be presented. The derivations for isotropic and anisotropic media will be separated. Finally, the calculations for obtaining the surface response to a point-like source (3D case) acting on an anisotropic half-space, will be exposed.

#### 19.4. Two-dimensional Green function in an infinite isotropic medium

We calculate in this section the two-dimensional elastodynamic Green function of an infinite isotropic solid. We consider that the problem does not depend on the  $x_2$  coordinate, which corresponds to the problem of calculating the Green function for a transient infinite line-source parallel to the  $x_2$ -axis. Only the two waves polarized in the plane  $(x_1, x_3)$  are kept, and therefore all quantities subscripted 2 no longer appear (see Figure 19.3).

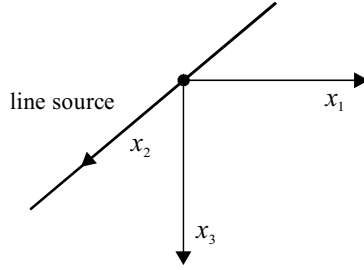


**Figure 19.3.** *Setting of the two-dimensional problem*

The partial solutions in the dual domain are given by:

$$\tilde{u}_i^{\pm}(x_3, s_1, p) = \sum_{n=1}^2 A^{(\pm n)} P_i^{(\pm n)} e^{-p s_3^{(\pm n)} x_3}, \quad [19.30]$$

where  $A^{(\pm n)}$ ,  $P_i^{(\pm n)}$  and  $s_3^{(\pm n)}$  are functions of  $s_1$ . For an isotropic material, these functions identify the longitudinal ( $L$  or  $n = 1$ ) and transverse ( $T$  or  $n = 2$ ) waves polarized in the plane  $(x_1, x_3)$ . For longitudinal waves, we have:  $s_3^{(+1)} = (s_L^2 - s_1^2)^{\frac{1}{2}}$  with  $\text{Re}(s_3^{(+1)}) > 0$  and  $s_3^{(-1)} = -s_3^{(+1)}$ ; and for transverse waves:  $s_3^{(+2)} = (s_T^2 - s_1^2)^{\frac{1}{2}}$  with  $\text{Re}(s_3^{(+2)}) > 0$  and  $s_3^{(-2)} = -s_3^{(+2)}$ . The quantities  $s_L$  and  $s_T$  are defined as the slowness of the longitudinal and transverse homogenous plane waves:  $s_L = \sqrt{\rho/(\lambda + 2\mu)} = c_L^{-1}$  and  $s_T = \sqrt{\rho/\mu} = c_T^{-1}$ .

Let us write the solution in the Laplace domain. It is obtained by writing the inverse Fourier transform over the slowness  $s_1$ :

$$\hat{u}_i^{\pm}(x_1, x_3, p) = \frac{p}{2i\pi} \sum_{n=1}^2 \int_{-i\infty}^{+i\infty} A^{(\pm n)} P_i^{(\pm n)} e^{-p(s_1 x_1 + s_3^{(\pm n)} x_3)} ds_1. \quad [19.31]$$

The field  $\hat{u}_i^{\pm}(x_1, x_3, p)$  is expressed as the sum of two integrals: one for the longitudinal waves and one for the transverse waves. Both integrals are handled independently. The Cagniard-de Hoop transformation aims, using a change of variables of type  $s_1 \rightarrow \tau = f(s_1)$ , to exhibit the kernel of the Laplace transform  $e^{-p\tau}$  in expression [19.31]. Without loss of generality, we can assume that  $x_3 \geq 0$ , in which case only  $\hat{u}_i^{+}(x_1, x_3, p)$  is going to be calculated, and the superscript  $+$  is now omitted. Thus, changes of variables for both integrals [19.31] are written in the following manner for longitudinal ( $L$ ) and transverse ( $T$ ) waves:

$$\tau = s_1 x_1 + s_3^{L,T} (s_1) x_3, \quad [19.32]$$

with  $\tau \in [0, +\infty[$ . This parametric equation defines a path in the complex plane of  $s_1$ . What follows shows how to determine those paths in the complex plane.

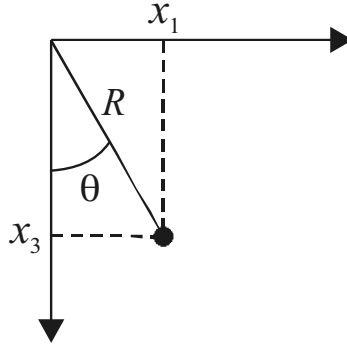


**Figure 19.4.** Polar coordinates

Setting  $x_1 = R \sin \theta$  and  $x_3 = R \cos \theta$  (polar coordinates representation, see Figure 19.4), and using the expression of the functions  $s_3^{L,T}$  with respect to  $s_1$  (previously given), we get the following polynomial equations of degree 2:

$$s_1^2 - \frac{2\tau \sin \theta}{R} s_1 + \frac{\tau^2}{R^2} - s_{L,T}^2 \cos^2 \theta = 0. \quad [19.33]$$

The two solutions provide two paths of integration for each type of wave. After setting  $T_{L,T} = R s_{L,T}$ , the parametric equations of the contours  $s_1^{L,T}(\tau)$  are given by:

$$s_1^{L,T}(\tau) = \frac{\tau \sin \theta}{R} \pm \frac{\cos \theta}{R} \sqrt{T_{L,T}^2 - \tau^2}. \quad [19.34]$$

We can immediately see that these trajectories have two distinct parts: one being along the real axis and the other one located in the complex plane of  $s_1$ :

$$s_1^{L,T}(\tau) = \begin{cases} \frac{\tau \sin \theta}{R} \pm \frac{\cos \theta}{R} \sqrt{T_{L,T}^2 - \tau^2} & \text{for } 0 < \tau < T_{L,T} \\ \frac{\tau \sin \theta}{R} \pm i \frac{\cos \theta}{R} \sqrt{\tau^2 - T_{L,T}^2} & \text{for } T_{L,T} < \tau < +\infty \end{cases} \quad [19.35]$$

Moreover, we note that for a given type of wave ( $L$  or  $T$ ), the two trajectories, defined by the signs  $\pm$  in front of the radical, differ when they are real, and are symmetric with respect to the real axis when they are complex (Figure 19.5). It can also be shown that the two contour integrals in [19.31] are totally uncorrelated, due to the fact that the functions  $A^L$  and  $P_i^L$  (respectively  $A^T$  and  $P_i^T$ ) are independent of  $s_3^T$  (respectively  $s_3^L$ ). Thus, there is a complex plane for each problem, and the derivations made for one type of wave completely apply to the other type.

The functions  $s_3^{L,T}$  are multivalued functions of the variable  $s_1$ . It is therefore necessary to define cuts in the complex plane of  $s_1$  to ensure that the integrands of [19.31] are single-valued and holomorphic in the region where the contours lie, and then being able to apply the Cauchy integral theorem. The branch points related to the cancellation of the radical  $(s_{L,T}^2 - s_1^2)^{\frac{1}{2}}$  are  $s_1 = s_{L,T}$  and  $s_1 = -s_{L,T}$ . We choose cuts that start from these points and extend to infinity along the real axis of  $s_1$ . The functions  $A^{L,T}$  and  $P_i^{L,T}$  having no singularity (poles) within the closed contour (Figure 19.5), the Cauchy integral theorem states that (see Figure 19.5):

$$I - C^{+\infty} - \Gamma^+ - c^+ + c^\pm + c^- + \Gamma^- + C^{-\infty} = 0, \quad [19.36]$$

where  $I$  is the integral considered on the path along the imaginary axis;  $c^+$  and  $c^-$  are the real part of the Cagniard contour;  $\Gamma^+$  and  $\Gamma^-$  the complex part of the Cagniard integration contour;  $C^{+\infty}$  and  $C^{-\infty}$  the paths linking at infinity the Cagniard contour to the original contour  $I$ ; and  $c^\pm$  the path on the real axis joining the path  $c^+$  and  $c^-$ . The contributions to the integral on the paths  $-c^+$ ,  $c^-$  and  $c^\pm$  cancel each other because they constitute a closed integration contour on the real axis where the cuts do not lie. Moreover, for isotropic media  $\text{Re}(s_1 x_1) > 0$  and  $\text{Re}(s_3 x_3) > 0$ , and since the Laplace parameter  $p$  is real and positive, it is not difficult to demonstrate that the contour integrals over  $C^{+\infty}$  and  $C^{-\infty}$  are zero. Finally, we see that

$$I = \Gamma^+ - \Gamma^-, \quad [19.37]$$

where  $\Gamma^+ - \Gamma^-$  is the path in the complex plane of  $s_1$  called the Cagniard-de Hoop contour. Using formulation [19.35], it is observed that the intersection point of the Cagniard-de Hoop contour with the real axis is always located between two branch points. Thus, the cuts are never crossed by the parameterized contour [19.34].

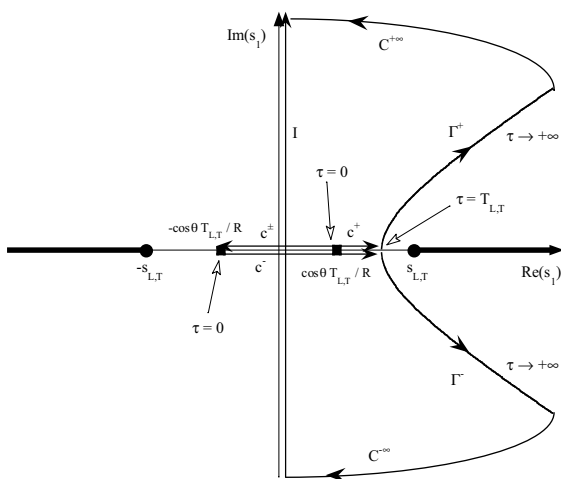


**Figure 19.5.**  $\Gamma$  is the original path of the contour integral [19.31],  $C^+$  and  $\Gamma^+$  define the Cagniard integration contour in the half-plane  $\text{Im}(s_1) > 0$ ;  $C^-$  and  $\Gamma^-$  the Cagniard integration contour in the half-plane  $\text{Im}(s_1) < 0$ ;  $C^{\pm}$ ,  $C^{+\infty}$  and  $C^{-\infty}$  are paths which close the overall integration contour. The points  $s_1 = s_{1,T}$  and  $s_1 = -s_{1,T}$  are the branch points of the functions  $s_2^{\pm(n)}(s_1)$ , from which leave the cuts that extend to infinity on the real axis

Another important point is the symmetry of the integrand in formulation [19.31]. The functions  $s_3^{L,T}$  satisfy the relationship

$$s_3(\overline{s}_1) = \overline{s}_3(s_1), \quad [19.38]$$

where  $\bar{s}_1$  is the complex conjugate of  $s_1$ . Since the functions  $A^{L,T}(s_1, p)$  and  $P_i^{L,T}(s_1, p)$  come from the resolution of linear systems in which only  $s_1$  and real quantities appear, they also have the same symmetry:

$$\begin{aligned} A^{L,T}(\bar{s}_1, p) &= \bar{A}^{L,T}(s_1, p), \\ P_i^{L,T}(\bar{s}_1, p) &= \bar{P}_i^{L,T}(s_1, p). \end{aligned} \quad [19.39]$$

Because the contours  $\Gamma^+$  and  $\Gamma^-$  are symmetric with respect to the real axis, we symbolically have  $\Gamma^- = \bar{\Gamma}^+$ ; therefore:  $\Gamma^+ - \Gamma^- = \Gamma^+ - \bar{\Gamma}^+$ . The original integral I can finally be written as:

$$I = 2i \operatorname{Im} \left[ \Gamma^+ \right]. \quad [19.40]$$

The contour  $\Gamma^+$  is parameterized by  $\tau \in [T_{L,T}, +\infty[$  where  $T_{L,T} = Rs_{L,T}$ . The polarizations  $P_i^{L,T}$  are functions that do not depend on frequency, therefore on the parameter  $p$  (see section 1.2.2, Chapter 1). The amplitudes  $A^{L,T}$  are inversely proportional to  $p$  for a source whose time dependence is  $\delta(t)$ . By setting  $A^{L,T}(s_1, p) = p^{-1}B^{L,T}(s_1)$ , the displacement field in the Laplace domain, given by the equation [19.31] and for  $x_3 \geq 0$  becomes, for the longitudinal and transverse waves

$$\hat{u}_i^{L,T}(x_1, x_3, p) = \frac{1}{\pi} \int_{\Gamma^+} \text{Im} \left[ B^{L,T}(s_1) P_i^{L,T}(s_1) e^{-p(s_1 x_1 + s_3^{L,T} x_3)} \right] ds_1. \quad [19.41]$$

Making the change of variable  $s_1 \rightarrow \tau$ , [19.41] becomes

$$\hat{u}_i^{L,T}(x_1, x_3, p) = \frac{1}{\pi} \int_{T_{L,T}}^{+\infty} \text{Im} \left[ B^{L,T}(s_1) P_i^{L,T}(s_1) \frac{\partial s_1}{\partial \tau} \right] e^{-p\tau} d\tau, \quad [19.42]$$

where, as a reminder,  $s_1(\tau)$  is a complex function of the real variable  $\tau$ .

At this stage we still have an expression of the Green function in the Laplace domain. We now have to calculate the solution in the time domain  $t$ . Given the independence of the functions  $B^{L,T}$  and  $P_i^{L,T}$  with respect to  $p$ , and the uniqueness theorem of the Laplace transform with real and positive values of the transform parameter (Lerch theorem), we can identify directly the solution in the time domain, which happens to be the integrand in formula [19.42]:

$$u_i^{L,T}(x_1, x_3, t) = \begin{cases} 0 & \text{for } t < T_{L,T} \\ \frac{1}{\pi} \text{Im} \left[ B^{L,T}(s_1) P_i^{L,T}(s_1) \frac{\partial s_1}{\partial t} \right] & \text{for } T_{L,T} < t < +\infty \end{cases} \quad [19.43]$$

where  $s_1 = s_1^L(t)$  for the longitudinal waves, and  $s_1 = s_1^T(t)$  for the transverse waves. Thus, we immediately get the Green function in an analytical form, knowing that  $B^{L,T}$  and  $P_i^{L,T}$  are functions of  $s_1$  and that  $s_1$  takes its successive values in accordance with the equations of the Cagniard-de Hoop integration contour ( $s_1^L$  and  $s_1^T$ ) set by the time. Let us remember that the complex path of  $s_1$  also depends on the position of the observation point  $(x_1, x_3)$ . The full solution for the displacement field from the impulse source is achieved by simple summation of both contributions  $L$  and  $T$ :

$$u_i(x_1, x_3, t) = u_i^L(x_1, x_3, t) + u_i^T(x_1, x_3, t). \quad [19.44]$$

### 19.4.1. Analysis of the result

Each contribution has its own start time,  $T_L$  for the  $L$  waves, and  $T_T$  for the  $T$ -waves. Thus, the causality principle is satisfied as shown by the result [19.43] that does not predict any perturbation before the arrival of waves  $L$ . It may be noted that three types of terms appear in the formulation [19.43]. The first consists of the functions  $B^{L,T}(s_1)$  that represent the amplitude of the waves and are calculated from the jump conditions induced by the source. These are the only terms depending on the source. For a single observation point and another source type, the functions  $P_i^{L,T}(s_1)$  and  $\partial_t s_1$  do not need to be recalculated. The functions  $P_i^{L,T}(s_1)$  represent the polarization of the waves (depending on their type  $L$  or  $T$ ) that evolves with time. Finally, the term  $\partial_t s_1$  depends on the time variation of the structure of the inhomogeneous plane waves (complex slownesses) that contribute to the response. Along the complex contours, its expression is:

$$\frac{\partial s_1}{\partial t} = \frac{\sin \theta}{R} \pm i \frac{t \cos \theta}{R \sqrt{t^2 - T_{L,T}^2}}. \quad [19.45]$$

At the arrival time of the perturbation  $t = T_{L,T}$ , the function  $\partial_t s_1$  is singular:

$$\left. \frac{\partial s_1}{\partial t} \right|_{t=T_{L,T}^+} = \pm i\infty. \quad [19.46]$$

At those times, the contours leave the real axis orthogonally, and singularities appear in the Green function.

### 19.4.2. Why “generalized-rays”?

This designation refers to the structure of the plane waves involved in the kernel  $e^{-P(s_1 x_1 + s_3 x_3)}$  modified into  $e^{-Pt}$  by the Cagniard–de Hoop transformation. For each value of time, the contributions to the Green function for the  $L$ - and  $T$ -waves come from a specific plane wave for which the slowness vector is complex, except at the arrival time for which the plane wave is homogeneous (real slowness vector). This latter leads to a singularity in the impulse response. The equation of the Cagniard integration contour  $t = \mathbf{S} \cdot \mathbf{M}$ , where  $\mathbf{M}$  is the position of the observation point (or the observation direction when the source is located at the origin of the frame), can be partially decomposed between real and imaginary parts, knowing that  $\mathbf{S}$  is a complex vector and  $t$  a real scalar:

$$\begin{cases} \mathbf{S}' \cdot \mathbf{M} = t \\ \mathbf{S}'' \cdot \mathbf{M} = 0 \end{cases} \quad [19.47]$$

As a consequence, the plane waves involved are those whose plane of constant phase takes a time  $t$  to propagate from the source to the point  $\mathbf{M}$ , and whose direction of decreasing amplitude is orthogonal to the direction of observation. However, an important property of the inhomogenous plane waves in purely elastic media is that their acoustic energy flux is perpendicular to their damping direction  $\mathbf{S}''$  [HAY 84]. Indeed, in a medium where there is no mechanical loss, the energy carried by the waves must propagate without loss of amplitude. The system given in [19.47] can then be literally understood as the search, as time increases, of the inhomogenous plane waves for which the energy propagates in the observation direction and the time of flight is equal to  $t$ . If we simply look at the dispersion equation of plane waves in an isotropic medium, we have  $\mathbf{S} \cdot \mathbf{S} = s_{L,T}^2$  or, by separating real and imaginary parts:

$$\begin{cases} \mathbf{S}' \cdot \mathbf{S}' - \mathbf{S}'' \cdot \mathbf{S}'' = s_{L,T}^2 \\ \mathbf{S}' \cdot \mathbf{S}'' = 0 \end{cases} \quad [19.48]$$

we see that the norms of  $\mathbf{S}'$  and  $\mathbf{S}''$  both increase simultaneously. The increasing values of the norm of  $\mathbf{S}'$  indicate decreasing phase velocities, and thus longer time of propagation for a fixed propagation distance. That is what is expressed by the path of the Cagniard–de Hoop contour. The concept of ray occurs naturally in the fact that the energy flux of all the plane waves described by the Cagniard contour are oriented in the observation direction, like the classical concept of rays in geometrical acoustics. In our context, rays are “generalized” because they are no longer objects whose expression results from an asymptotic approximation, but they are objects with ‘energetic’ characteristics to which are associated 1) a temporal content whose spectrum contains all frequencies (response to  $\delta(t)$ ); and 2) a structure in terms of plane waves with complex slowness.

#### 19.4.3. Graphical interpretation of the Cagniard–de Hoop method

A graphical illustration of the Cagniard–de Hoop method has been given by Kraut [KRA 63]. It is simply a graphical resolution of the equation governing the change of variables used in this method. First, the quantities  $s_1$  and  $s_3$  are linked together by the dispersion equation:  $s_1^2 + s_3^2 = s_{L,T}^2$ . In the slowness plane  $(s_1, s_3)$ , the set of real solutions is a circle of radius  $s_{L,T}$ .



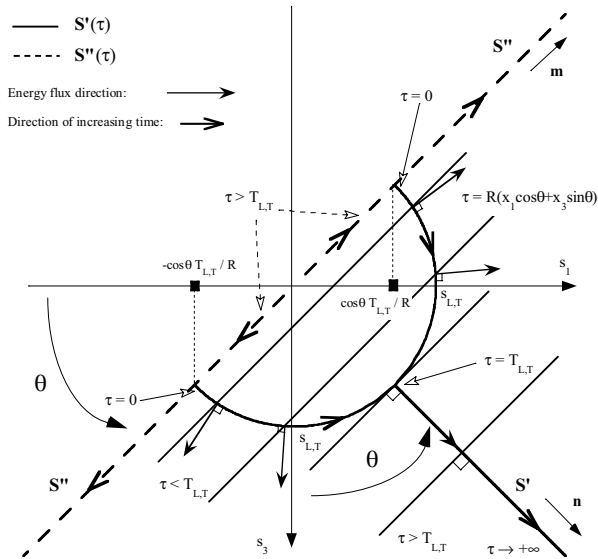


**Figure 19.6.** Graphical interpretation of the Cagniard–de Hoop transformation

Then, still in the plane  $(s_1, s_3)$ , the equation of the integration contours  $\tau = s_1 x_1 + s_3 x_3$ , which can be rewritten as  $\tau/R = s_1 \sin \theta + s_3 \cos \theta$ , corresponds to straight lines orthogonal to the direction  $\mathbf{n} = (\sin \theta, \cos \theta)^T$ , and at a distance of  $\tau/R$  from the origin. The simultaneous resolution of the two equations is given by the intersection points between these straight lines, whose location is set by  $\tau$ , and the slowness curve. For  $\tau/R < s_{L,T}$ , there are, as shown in Figure 19.6, two intersections that map points of the Cagniard contour, located on the real axis of the complex plane of  $s_1$ . We can graphically realize that these two real solutions cannot contribute to the Green function, insofar as (from the point of view of acoustic rays) the group velocities (which are normal to the slowness surfaces, see section 1.2.2.3, Chapter 1) associated with these plane waves are not oriented along the observation direction  $\mathbf{n}$ . When  $\tau/R$  reaches the value  $s_{L,T}$ , the parameterized straight line becomes tangential to the circle, and there is a double solution to the problem (it corresponds to the intersection point of the complex part of the Cagniard contour and the real axis of the complex plane of  $s_1$ ). In this configuration, that is, at the point of tangency, the normal to the slowness curve is oriented along the direction  $\mathbf{n}$ , and the Fermat principle is satisfied (in the sense of a minimization of a time of flight):

$$\frac{\partial \tau}{\partial s_1} = 0 \quad \text{or} \quad \left| \frac{\partial s_1}{\partial \tau} \right| = +\infty. \quad [19.49]$$

We can interpret this as an arrival time of the wave, in the geometrical acoustics point of view. Then, for  $\tau/R > s_{L,T}$ , the parameterized straight line and the real slowness curve no longer intersect. We must in this case imagine a complex extension of the slowness curve from the former tangency point, for which the real part describes a straight line of direction  $\mathbf{n}$  in the plane  $(\text{Re}(s_1), \text{Re}(s_3))$ , and the imaginary part of this curve is formed by another straight line in the plane  $(\text{Im}(s_1), \text{Im}(s_3))$  along the direction  $\mathbf{m}$  (with  $\mathbf{n} \cdot \mathbf{m} = 0$ ) and passing through the origin. This latter straight line follows the locations of the end point of vectors  $\mathbf{S}''$  when plane waves are inhomogenous. Figure 19.7 shows the different inhomogenous plane waves over time in the frame  $(\mathbf{n}, \mathbf{m})$ . The “structural” dispersion of these plane waves is such that the phase slowness (or the time of flight) increases with the increasing values of the inhomogeneity parameter (i.e. the norm of  $\mathbf{S}''$ ).

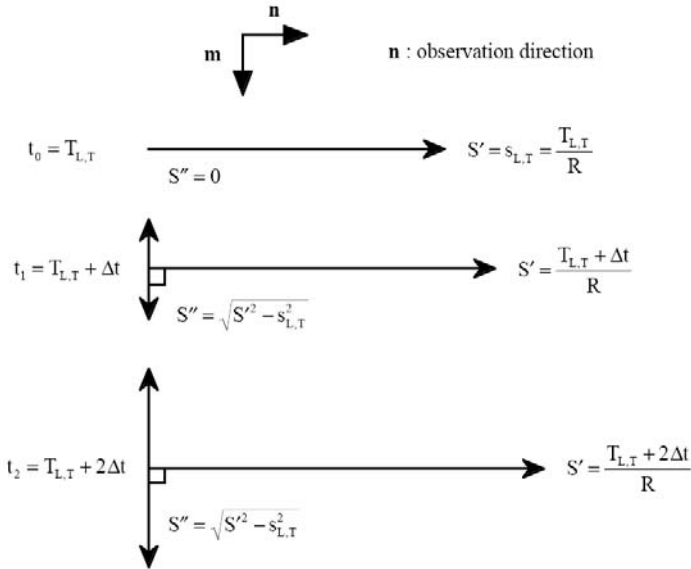


**Figure 19.7.** Structure of inhomogenous plane waves as a function of time (for an isotropic medium)

Note that for each value of  $t$ , there are two inhomogenous plane waves with the required properties [19.47] (with  $\mathbf{S}''$  orthogonal to  $\mathbf{n}$  and oriented on both sides of  $\mathbf{n}$ ).

#### 19.4.4. Some examples of waveforms

The following results are examples of impulse responses to an isotropic source of expansion, i.e. a line-source of type  $h_{ii} = \delta(x_1)\delta(x_3)\delta(t)$  or  $\varepsilon_{ii} = \delta(x_1)\delta(x_3)H(t)$ , and for a line-source of vertical force, i.e.  $f_3\delta(x_1)\delta(x_3)\delta(t)$ . The considered propagation medium is aluminum, for which the acoustic characteristics are:  $\rho = 2.7 \text{ g cm}^{-3}$ ,  $c_L = 6.4 \text{ mm}\mu\text{s}^{-1}$ ,  $c_T = 3.2 \text{ mm}\mu\text{s}^{-1}$ . The components of the particle displacement in polar coordinates are  $u_r$  and  $u_\theta$  (shown in Figure 19.8); they are calculated for a propagation distance  $R = 1 \text{ mm}$  and for different observation angles (Figure 19.9). The waveforms are characterized by singularities at the (geometric) arrival time of the different modes. It should be noted that some singularities may disappear if their amplitude of displacement ( $B^{L,T}(s_1(t))P_i^{L,T}(s_1(t))$ ) is zero at the arrival time. It is the case for the  $T$ -wave on the signal 19.9b and for the  $L$ -wave on the signal 19.9d. These two signals then have a discontinuity of their first derivative. Finally, the source also may not generate all modes, as is the case for a source of axi-symmetric bulk expansion in an isotropic medium (see Figure 19.9a). The transverse mode is then not excited.

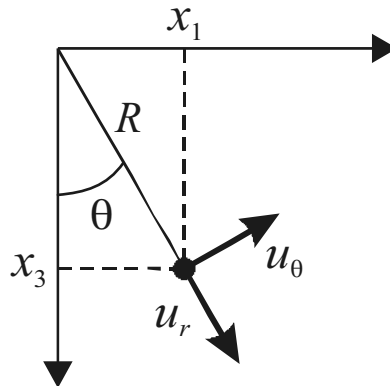


**Figure 19.8.** Polar coordinates for the displacement field

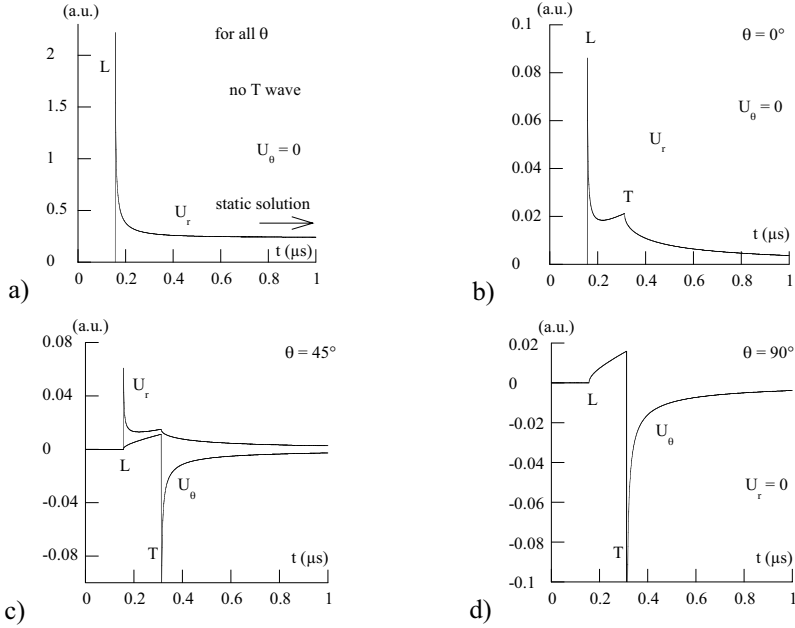


**Figure 19.9.** Particle displacement field  $u_r$  and  $u_\theta$  of the impulse response for a line-source. a): isotropic expansion source  $h_{ii} = \delta(x_1)\delta(x_3)\delta(t)$   
b), c) and d): vertical force source  $f_3\delta(x_1)\delta(x_3)\delta(t)$

### 19.5. Two-dimensional Green function in an infinite anisotropic medium

It is proposed in this section to study the impulse response for anisotropic media with orthotropic symmetry. We still consider, for the same concerns of understanding, a two-dimensional case for the propagation, i.e. a source of line type extended along the  $x_2$  axis, and that coincides with a symmetry axis of the medium. For what follows, only the sources that generate waves polarized in the symmetry plane are considered. SH waves are then not present in this problem. The propagation equations and the expression of the source (jump conditions) in the dual domain are those provided in section 19.3, in which the quantities subscripted 2 are removed. By setting  $\hat{c}_{ijkl} = \rho^{-1}c_{ijkl}$  and using the contracted notation of the elasticity tensor components, the Christoffel equation is written in two dimensions and only for the waves polarized in the plane  $(x_1, x_3)$  :

$$\begin{vmatrix} \widehat{c}_{11}s_1^2 + \widehat{c}_{55}s_3^2 - 1 & (\widehat{c}_{13} + \widehat{c}_{55})s_1s_3 \\ (\widehat{c}_{13} + \widehat{c}_{55})s_1s_3 & \widehat{c}_{55}s_1^2 + \widehat{c}_{33}s_3^2 - 1 \end{vmatrix} = 0. \quad [19.50]$$

Once developed, this determinant is written in a polynomial form of the variable  $s_3$ :

$$as_3^4 + bs_3^2 + c = 0, \quad [19.51]$$

which coefficients are functions of  $s_1$ :

$$\begin{cases} a = \widehat{c}_{33}\widehat{c}_{55} \\ b = (\widehat{c}_{11}\widehat{c}_{33} - \widehat{c}_{13}(\widehat{c}_{13} + 2\widehat{c}_{55}))s_1^2 - (\widehat{c}_{33} + \widehat{c}_{55}) \\ c = \widehat{c}_{11}\widehat{c}_{55}s_1^4 - (\widehat{c}_{11} + \widehat{c}_{55})s_1^2 + 1 \end{cases} \quad [19.52]$$

The functions  $s_3(s_1)$  are inferred from the resolution of equation [19.51]. The four solutions for  $s_3$  are:

$$s_3(s_1) = \pm\sqrt{B(s_1) \pm \sqrt{C(s_1)}}, \quad [19.53]$$

where  $B = -b/2a$ ,  $C = \Delta/4a^2$  and  $\Delta = b^2 - 4ac$ . We set  $D^\pm = B \pm \sqrt{C}$ . The sign of the internal square root indicates the type of the wave:  $+\sqrt{C}$  for quasi-transverse waves (which we still note  $T$ ), and  $-\sqrt{C}$  for quasi-longitudinal waves ( $L$ ). Concerning the sign of the main square root, it is linked to the direction of the wave propagation along the  $x_3$  axis.

With the same goals as the previous section, the original contour (located on the imaginary axis of  $s_1$ ) of the solution expressed in the Laplace domain is going to be distorted, in agreement with the Cagniard change of variables:  $\tau = s_1x_1 + s_3x_3$  with  $\tau \in \mathbb{R}^+$ . Compared to the case of the isotropic medium, only the Cagniard–de Hoop contours are drastically modified in equation [19.31]. This is because the slowness surfaces in anisotropic media are no longer circles (2D) or spheres (3D), but much more complicated surfaces.

### 19.5.1. Equations of the contours (Cagniard–de Hoop polynomial)

The aim of this section is to establish the equations that will provide the Cagniard contours for anisotropic media. In order to do this, we can write  $s_3$  as a function of  $s_1$  from the change of variables [19.32] in polar coordinates:

$$s_3 = \frac{\tau}{R \cos \theta} - s_1 \tan \theta, \quad [19.54]$$

then plugging this expression into Christoffel equation [19.51]. Thus, we obtain a new expression of the Christoffel equation as a multivariate polynomial  $H(s_1, \tau)$  of the variable  $s_1$  and  $\tau$ . Collecting powers of  $s_1$  in  $H$ , we obtain the following expression:

$$H(s_1, \tau) = \sum_{n=0}^4 a_n(\tau) s_1^n, \quad [19.55]$$

$$\left\{ \begin{array}{l} a_4 = [\hat{c}_{33}\hat{c}_{55} \tan^2 \theta + \hat{c}_{11}\hat{c}_{33} - \hat{c}_{13}(\hat{c}_{13} + 2\hat{c}_{55})] \tan^2 \theta + \hat{c}_{11}\hat{c}_{55} \\ a_3 = -2 \frac{\tan \theta}{\cos \theta} [2\hat{c}_{33}\hat{c}_{55} \tan^2 \theta + \hat{c}_{11}\hat{c}_{33} - \hat{c}_{13}(\hat{c}_{13} + 2\hat{c}_{55})] \frac{\tau}{R} \\ a_2 = \frac{1}{\cos^2 \theta} [6\hat{c}_{33}\hat{c}_{55} \tan^2 \theta + \hat{c}_{11}\hat{c}_{33} - \hat{c}_{13}(\hat{c}_{13} + 2\hat{c}_{55})] \left(\frac{\tau}{R}\right)^2 \\ \quad - \tan^2 \theta (\hat{c}_{33} + \hat{c}_{55}) - (\hat{c}_{11} + \hat{c}_{55}) \\ a_1 = -4\hat{c}_{33}\hat{c}_{55} \frac{\tan \theta}{\cos^3 \theta} \left(\frac{\tau}{R}\right)^3 + 2 \frac{\tan \theta}{\cos \theta} (\hat{c}_{33} + \hat{c}_{55}) \frac{\tau}{R} \\ a_0 = \frac{1}{\cos^2 \theta} \left[ \frac{\hat{c}_{33}\hat{c}_{55}}{\cos^2 \theta} \left(\frac{\tau}{R}\right)^4 - (\hat{c}_{33} + \hat{c}_{55}) \left(\frac{\tau}{R}\right)^2 \right] + 1 \end{array} \right. \quad [19.56]$$

Note that when  $\theta = \pi/2$ , the coefficients  $a_n(\tau)$  are singular, but from equation [19.54], we can directly determine the expression of  $s_1$  with no use of the Christoffel equation in this case:

$$s_1(\tau) \Big|_{\theta=\frac{\pi}{2}} = \frac{\tau}{R}. \quad [19.57]$$

The parameterized contour  $s_1(\tau)$  is then located on the real axis of the complex plane of  $s_1$ . For each value of  $\tau$ , we can therefore solve the polynomial  $H(s_1, \tau)$ , which will provide the four values of  $s_1$ . Note that as  $\tau$  is real, the coefficients  $a_n(\tau)$  are real too. Hence, the solutions  $s_1$  can be purely real or complex conjugated, two by two. Before implementing the change of variables  $s_1 \rightarrow \tau$ , we must check that the functions to integrate are holomorphic in the domain where the Cauchy integral theorem is applied. We can show that the functions  $A(s_1, p)$  and  $P_i(s_1)$  do not have any pole, and their only existing singularities are those of functions  $s_3(s_1)$  that appear in all terms of integral [19.31]. Looking at equation [19.53], we find that these singularities result from the branch points of the functions  $\sqrt{C}$  and  $\sqrt{D^\pm}$  for which:

$$\left| \frac{\partial s_3}{\partial s_1} \right| = \infty. \quad [19.58]$$

These branch points are calculated from the cancelation of the functions under the corresponding square root:

$$\begin{cases} C(s_1) = 0 \\ D^\pm(s_1) = 0 \end{cases} \quad [19.59]$$

The functions  $C(s_1)$  and  $D^\pm(s_1)$  are polynomials of  $s_1$ . There are four zeros of  $D^\pm$  that are always located on the real axis of  $s_1$ . In the plane  $(s_1, s_3)$ , they correspond to the intersection points of the slowness curves with the  $s_1$  axis. There are also four zeros for  $C$  that correspond to the double solutions that ensure the equality of  $s_3^L (= \sqrt{B - \sqrt{C}})$  and  $s_3^T (= \sqrt{B + \sqrt{C}})$ . Those zeros can be purely real, purely imaginary or complex depending on the concavity of the slowness curves compared to the  $s_1$  axis. We choose for the cuts the loci of  $s_1$  for which  $\sqrt{D^\pm}$  and  $\sqrt{C}$  are purely imaginary (i.e. the loci of  $s_1$  such that  $D^\pm(s_1) \in \mathfrak{R}^-$  and  $C(s_1) \in \mathfrak{R}^-$ ).

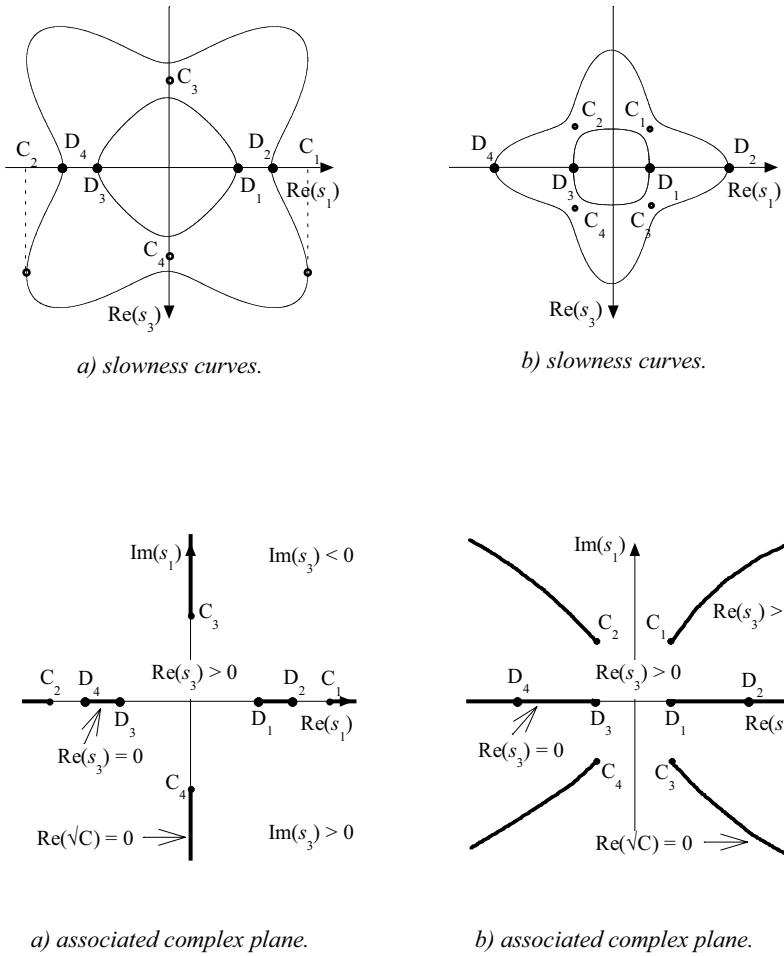


**Figure 19.10.** Two types of complex planes for anisotropic media in the presence of inflection points on the slowness curves: a) slowness concavity along axis 1; b) slowness concavity out of axis 1. Bold lines represent branch cuts, and the dots refer to the branch points

Figures 19.10a and b show two typical configurations for which the branch points have different positions. This example concerns a material with cubic symmetry, for which the slowness curves have concave parts (silicon or copper crystal, for example). Since the complex plane has been supplied with the adequate



cuts to ensure the functions  $s_3(s_1)$  to be single-valued and holomorphic (except maybe at singularities and along branch cuts – meromorphic functions), the Cagniard–de Hoop contour integration is ready to be carried out.

### 19.5.2. Practical aspects when using the Cagniard–de Hoop contours

In order to perform contour integration with the help of the Cagniard contours, the integrands must be holomorphic functions. It necessarily entails holomorphy of all functions  $s_3(s_1)$  (i.e.  $s_3^L$  and  $s_3^T$ ) for a given contour  $s_1(t)$ . Theoretically, the Cauchy–Riemann equations have to be satisfied at all points in the region where the contours lie. But in practice, when computing the Cagniard contours  $s_1(t)$  numerically, holomorphy of  $s_3(s_1)$  is not ensured as easily as that. Some clear and effective practical criteria are required to select from [19.53] the correct values of  $s_3$  corresponding to the appropriate Riemann sheets, along the continuous contours parameterized by the time.

#### 19.5.2.1. Holomorphy of the functions $s_3(s_1)$

Still within the context of calculating the Green function for positive values of  $x_3$ , the condition  $\text{Re}(s_3) > 0$  is not always sufficient (in particular for wave propagation in anisotropic media) to carry out analytical continuation of  $s_3$  and then to avoid crossings of branch cuts by the calculated contours. Typically in case a) of Figure 19.10, it is necessary to take into account the Cauchy–Riemann equations:

$$\frac{\partial \text{Re}(s_3)}{\partial \text{Re}(s_1)} = \frac{\partial \text{Im}(s_3)}{\partial \text{Im}(s_1)} \quad \text{and} \quad \frac{\partial \text{Re}(s_3)}{\partial \text{Im}(s_1)} = -\frac{\partial \text{Im}(s_3)}{\partial \text{Re}(s_1)}, \quad [19.60]$$

to follow the correct trajectory for the contours. As a result, in case a), the interconnection of the  $L$ - and  $T$ -modes imply that  $s_3^L$  can have either positive or negative values for its real part. At the same time, the Cauchy–Riemann equations are not really practicable. That is why another set of equations, based on the change of variables of Cagniard–de Hoop, and aiming to solve the problem, is preferred.

#### 19.5.2.2. The branch selection and the issue of continuity of the functions $s_3(s_1)$

Let us recall the main steps of evaluating the Green function for anisotropic media. From the expression of the solution in Laplace domain [19.31], the

displacement field is given by the contributions of two inverse-transform integrals, one for each type of wave. The initial paths for integration are deformed in the complex plane of  $s_1$ , in accordance with the Cagniard change of variables: it then leads to two different contours,  $s_1^L(t)$  and  $s_1^T(t)$ , associated with the corresponding integral (i.e. corresponding wave). Now, for a given integral (or a given wave,  $L$  or  $T$ ), the amplitude  $A$  that has to be determined from jump conditions at the source, involves one value of the horizontal slowness  $s_1$ : that coming from the corresponding Cagniard contour; and two values of the vertical slowness  $s_3$ : those of the two partial waves getting involved in the calculation of  $A$  and both having  $s_1$  as horizontal slowness (Snell's law). Therefore, the calculation of  $A^L$  requires the knowledge of:  $s_1^L(t)$  for the contour; and,  $s_3^L(s_1^L)$  and  $s_3^T(s_1^L)$  for the two partial waves. It is essential to note that in this case the amplitude of the partial  $T$ -wave is not needed and not even calculated. Concerning the calculation of  $A^T$  in the second path integral, the quantities to determine are:  $s_1^T(t)$ ,  $s_3^L(s_1^T)$  and  $s_3^T(s_1^T)$ .

In order to carry out the contour integrations over the Cagniard paths, the functions  $A^L(s_1^L)$  et  $A^T(s_1^T)$  must be holomorphic. And it strongly depends, of course, on the properties of the aforementioned set of slownesses. Extracting the two contours  $s_1^L(t)$  and  $s_1^T(t)$  from the four solutions of [19.55] is done according to the two following options:

- either  $s_1$  is complex, and then it or its complex conjugate that is also a solution of [19.55] can be selected (here, by convention, the solution with a positive imaginary part is retained, see [19.40]);

- either  $s_1$  is real, and the criterion to be satisfied is:  $s_1 ds_1 / dt > 0$ , in order to take into account the path integral along the branch cut and away from the branch point. This path physically refers to the head-wave contribution (see below section 19.6.1.1).

Having determined the two contours  $s_1^L(t)$  and  $s_1^T(t)$ , the vertical slownesses of the corresponding waves,  $s_3^L(s_1^L)$  and  $s_3^T(s_1^T)$  are directly given by the definition of the Cagniard contour [19.54], and satisfy the Cauchy–Riemann equations. The determination of  $s_3^T(s_1^L)$  and  $s_3^L(s_1^T)$  now remains. As we have already seen in section 19.4.2, the Cagniard–de Hoop change of variables represents

a set of equations specifying the bulk inhomogenous plane waves whose energy propagates in a given direction and that have a certain time of flight. Therefore, we intend to use those equations as a criterion for detecting the appropriate plane waves propagating in the half-space containing the point of observation. Then it enables us to simply select the relevant branches for the functions  $s_3$ .

From a physical point of view, it actually represents an energy criterion for inhomogenous plane waves, for which the energy flux must be directed towards the half-space that contains the observation point in relation to the source (direction  $\theta$ ). This criterion is simple to use and also very general. Considering equation [19.32] for positive times, we have the following system:

$$\begin{cases} \operatorname{Re}(s_1 \sin \theta + s_3 \cos \theta) > 0 \\ \operatorname{Im}(s_1 \sin \theta + s_3 \cos \theta) = 0 \end{cases} \quad [19.61]$$

Developing the real and imaginary parts yields:

$$\begin{cases} \operatorname{Re}(s_1) \sin \theta + \operatorname{Re}(s_3) \cos \theta > 0 \\ \operatorname{Im}(s_1) \sin \theta + \operatorname{Im}(s_3) \cos \theta = 0 \end{cases} \quad [19.62]$$

If  $\theta \in ]-\frac{\pi}{2}, \frac{\pi}{2}[$ , we obtain

$$\begin{cases} \operatorname{Re}(s_1) \tan \theta + \operatorname{Re}(s_3) > 0 \\ \tan \theta = -\frac{\operatorname{Im}(s_3)}{\operatorname{Im}(s_1)} \end{cases} \quad [19.63]$$

Using the value of  $\tan \theta$ , we obtain

$$-\frac{\operatorname{Re}(s_1) \operatorname{Im}(s_3)}{\operatorname{Im}(s_1)} + \operatorname{Re}(s_3) > 0. \quad [19.64]$$

Thus we obtain the conditions

$$\begin{cases} \operatorname{Re}(s_3) \operatorname{Im}(s_1) - \operatorname{Re}(s_1) \operatorname{Im}(s_3) > 0 & \text{if } \operatorname{Im}(s_1) > 0 \\ \operatorname{Re}(s_3) \operatorname{Im}(s_1) - \operatorname{Re}(s_1) \operatorname{Im}(s_3) < 0 & \text{if } \operatorname{Im}(s_1) < 0 \end{cases} \quad [19.65]$$

This set of equations can be written in a condensed form:  $\text{Im}(s_1 \bar{s}_3) \text{Im}(s_1) > 0$  when  $\theta \in ]-\frac{\pi}{2}, \frac{\pi}{2}[$ . This test may be applied to find out the correct sign for functions  $s_3$  involved in the integrals of [19.31]. Except at wave-arrivals, the impulse response is required to be continuous. However, along the calculated contours, the function  $s_3$  may not be continuous, and special attention must be paid.

#### 19.5.2.3. Issue of the crossing of cuts associated with the branch points of type $C$ by Cagniard contours (continuity of functions $s_3$ )

There are configurations for which the Cagniard contours, as defined by equation [19.55], cross branch cuts of type  $C$ . These difficulties can easily be avoided. Indeed, by definition, after the passage of such a cut, the square root  $\sqrt{C}$  undergoes a phase jump of  $\pi$ , and therefore the function  $s_3^L$  (respectively  $s_3^T$ ) becomes  $s_3^T$  (respectively  $s_3^L$ ). On a practical point of view, two reasons are sufficient to ignore this problem and to ensure the final result [19.43] is continuous:

- 1) it can be shown that when these cuts are crossed, they are crossed twice: once for each Cagniard contour  $s_1^L(t)$  and  $s_1^T(t)$ ;
- 2) The final solution for the Green function is written as the sum of the contributions of type  $L$  (contour  $s_1^L(t)$ ) and of type  $T$  (contour  $s_1^T(t)$ ).

From these two statements, we deduce that the two paths swap across the cut of  $\sqrt{C}$  (even though at different times):  $s_3^L(s_1) \rightarrow s_3^T(s_1)$  and  $s_3^T(s_1) \rightarrow s_3^L(s_1)$ . There is an interconnection of the modes. Hence, a contour initially of type  $L$  for the early values of the time  $t$ , can be changed to the type  $T$  afterwards, and vice versa. In order to use the Cauchy integral theorem, it is then necessary to add the path integrals all around the cut of type  $C$  to avoid crossings, and thus keep the same branch for  $s_3$ . In detail, it is easy to show that these additional path integrals cancel each other. Finally, we can pay no attention to those latter contours and let the Cagniard contours cross the branch cuts of type  $C$ . When calculating the functions  $s_3$  along the contour, only their continuity is important, and there is no need to bother about the change of type of wave.

#### 19.5.3. Examples of waveforms

The following two examples concern the Green functions for a copper crystal [100] whose mechanical properties are: the mass density  $\rho = 8.93 \text{ g cm}^{-3}$ , and three independent elasticity constants of the cubic symmetry material

$C_{11} = C_{33} = 170 \text{ GPa}$ ,  $C_{13} = 123 \text{ GPa}$ ,  $C_{55} = 75.5 \text{ GPa}$ . Two observation directions are considered: the first one ( $\theta = 10^\circ$ ) has four intersections with the group velocity curves (one intersection with the quasi-longitudinal wave sheet, and three with the quasi-transverse wave sheet); the second direction ( $\theta = 28^\circ$ ) has only two intersections with the group velocity curves (one intersection with each sheet), but is very close (in terms of angle) to the cuspidal tip of the wave fronts. The phase slowness and group velocities of the copper crystal are shown in Figure 19.11.

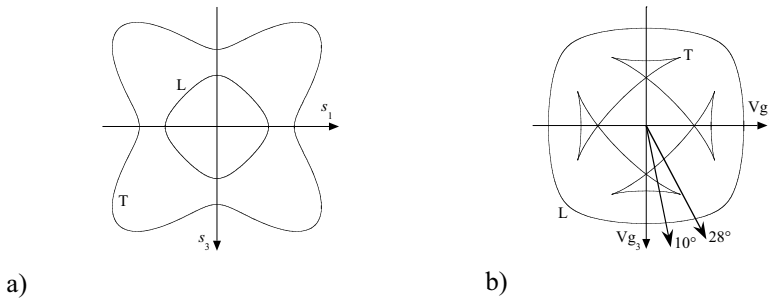


**Figure 19.11.** *Acoustic propagation properties of the copper crystal [100]: a) phase slowness; b) group velocities and observation directions*

In both cases, the Cagniard–de Hoop contours in the complex plane of  $s_1$  and the real part of the associated phase slowness ( $\text{Re}(s_1), \text{Re}(s_3)$ ) are presented; we also show the waveforms (radial displacement  $u_r$  and azimuthal displacement  $u_\theta$ ). The considered source is a line of vertical force ( $f_3 \delta(x_1) \delta(x_3)$ ) and the propagation distance is  $R = 1 \text{ mm}$ .

For an observation direction of  $10^\circ$ , the four intersections of this direction with the group velocity curves yield four wave-arrivals; therefore four singularities in the impulse–response occur. One is associated with the  $L$ -polarized wave ( $L$ ) and the three other ones to the  $T$ -polarized waves ( $T_1, T_2, T_3$ ). Moreover, from an analytical point of view, the arrival times  $L$ ,  $T_1$  and  $T_2$  come from the Cagniard contour  $s_1^L(t)$  while the contour  $s_1^T(t)$  provides only one arrival ( $T_3$ ), as shown in Figure 19.12. In the Cagniard–de Hoop method, the two slowness curves of the quasi-longitudinal and quasi-transverse modes are connected by a path in the complex plane (see section 19.5.2.3).

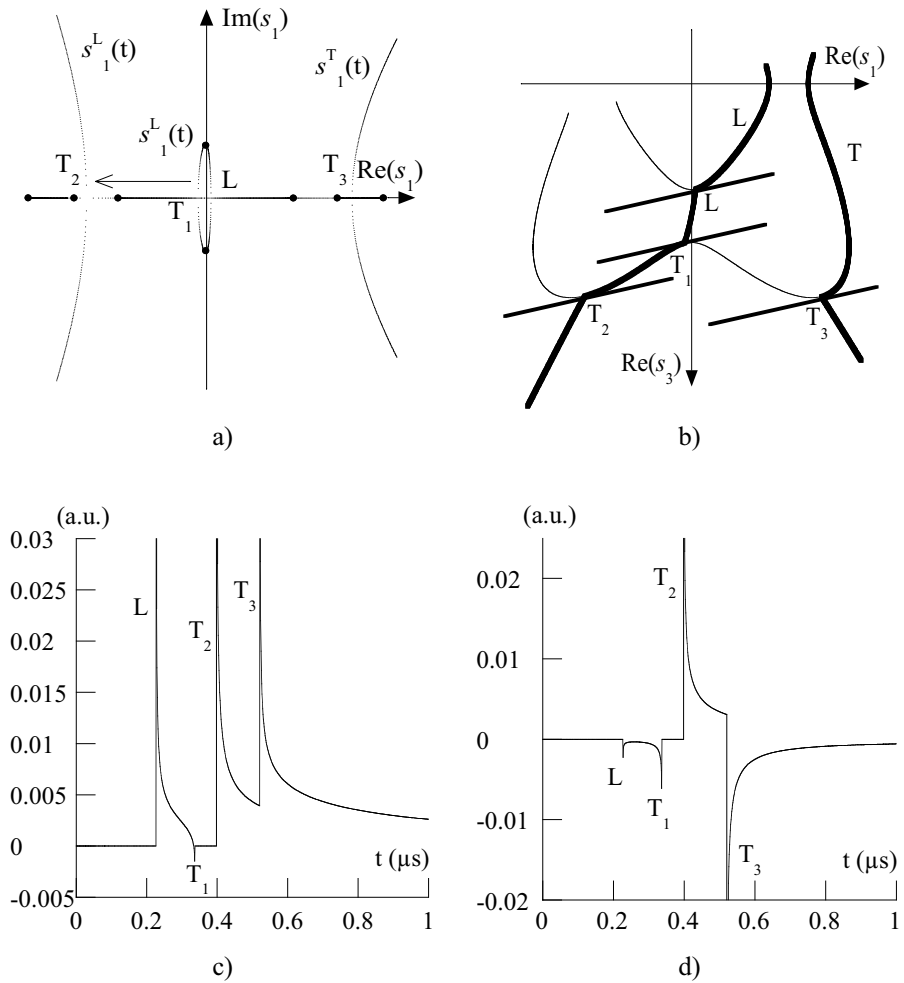


**Figure 19.12.** Illustration of the impulse-response calculation for a copper crystal subjected to a line of vertical force and for an observation direction of  $10^\circ$ : a) Cagniard-de Hoop contours; b) real slowness (thin curves), and real part of the phase slowness associated with the complex Cagniard-de Hoop contours (bold curves); c) radial displacement; d) azimuthal displacement

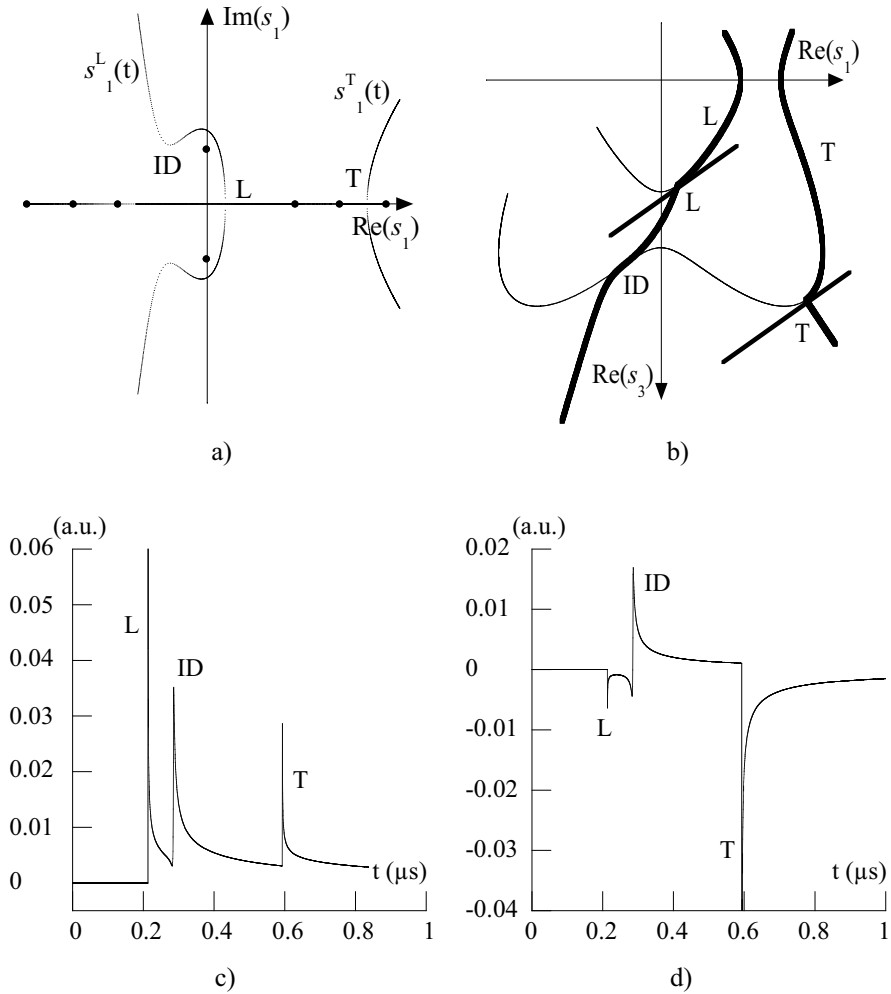


**Figure 19.13.** Illustration of the impulse–response calculation for a copper crystal subjected to a line of vertical force and an observation direction of  $28^\circ$ : a) Cagniard–de Hoop contours; b) real slowness (thin curves), and real part of the phase slowness associated with the complex Cagniard–de Hoop contours (bold curves); c) radial displacement; d) azimuthal displacement

For the observation direction at  $28^\circ$ , there are only two intersections with group velocity curves, and therefore only two singularities in the impulse response (one for the quasi-longitudinal wave noted  $L$ , and one for the quasi-transverse wave noted  $T$ ).

However, given the angular proximity with the cusp tip of the group velocity curves, the contour  $s_1^L(t)$  undergoes a rapid time variation in the area noted ID (see Figures 19.13a and 19.13b, for which there are no more wave-arrivals in the strict sense, i.e.  $ds_1/dt \neq \infty$ , but where  $ds_1/dt$  keeps prominent values. As a consequence, the impulse–response shows contributions that are not singular but very marked as shown by Figures 19.13c and 19.13d. These contributions are usually interpreted as ‘internal diffraction’ effects (noted ID in the Figures), and are specific to the anisotropic characteristic of elasticity in acoustic propagation in homogenous media.

### 19.6. Two-dimensional Lamb problem

We now seek the Green function of a homogenous elastic half-space ( $x_3 \geq 0$ ) for a line-source located at the surface and extended along the  $x_2$  axis. The problem is therefore invariant by translation along this axis.

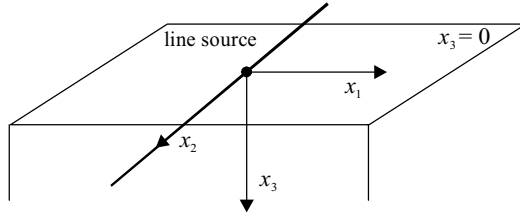


**Figure 19.14.** Configuration of the Lamb problem

The source  $S_i$  under consideration is defined in the following manner:

$$S_i(x_1, x_3, t) = F_i \delta(t) \delta(x_1) \delta(x_3). \quad [19.66]$$

Globally, it may be noted that the calculation of the Green function of this problem is treated the same way as for the infinite medium (same solutions to the propagation equations, same handling of the jump conditions at the source), with some important changes regarding the path integration along the Cagniard contour.

The application of the source  $S_i$  corresponds in the Fourier–Laplace domain to imposing at  $x_3 = 0$  the traction vector  $F_i$  :

$$\left[ \tilde{\sigma}_{i3}(x_3, s_1, p) \right]_{x_3=0} = F_i. \quad [19.67]$$



We write the  $2 \times 2$  system of boundary conditions on the surface in the following form:

$$\begin{pmatrix} \tilde{\sigma}_{13}^L & \tilde{\sigma}_{13}^T \\ \tilde{\sigma}_{33}^L & \tilde{\sigma}_{33}^T \end{pmatrix} \begin{pmatrix} A_L \\ A_T \end{pmatrix} = \begin{pmatrix} F_1 \\ F_3 \end{pmatrix}. \quad [19.68]$$

The resolution of this system provides the functions  $A_L(s_1, p)$  and  $A_T(s_1, p)$  in which, the functions  $s_3^L(s_1)$  and  $s_3^T(s_1)$  corresponding to the longitudinal and transverse waves appear simultaneously, contrary to the case of the infinite medium. The  $L$  and  $T$  waves are coupled at the surface. This implies that we are obliged to deal simultaneously with the Cagniard–de Hoop contours for the generalized  $L$  and  $T$  rays, in the same complex plane. That is to say, that we must take into account all branch points and cuts of both functions  $s_3^L(s_1)$  and  $s_3^T(s_1)$  at once. In addition, the functions  $A_{L,T}$  now have a new singularity in the form of a pole  $s_1 = \pm s_R$  located on the real axis of the complex plane of  $s_1$ , beyond the real branch points. This pole corresponds to the Rayleigh surface wave. For isotropic media, the complex plane of  $s_1$  is then equipped with branch points associated with  $L$  and  $T$  waves and their respective cuts, as well as the Rayleigh wave pole.

### 19.6.1. Isotropic medium

#### 19.6.1.1. The head-wave

When the two Cagniard contours  $L$  and  $T$  do not intersect the cuts (Figure 19.15 a), the Cauchy integral theorem can be used directly and the contour integration is similar to the case of the infinite medium. However, there is a critical observation angle  $\theta_{\text{lim}}$  beyond which the contour of the transverse wave can cross the cut on the real axis (while the contour of the longitudinal wave never crosses it). Thus, applying the Cauchy integral theorem for the  $T$ -wave requires a path integration going round the branch point at  $s_1 = s_L$  (Figure 19.15 b). Fortunately, this path running alongside the real axis is included in the parameterized contour  $s_1^T(t)$ . It suffices then to start the calculation of the  $T$ -wave contribution at the time  $T_{HW}$  defined below in [19.69] instead of at  $T_T$ . This path integral along the cut represents the contribution of the head-wave to the response function, in the interval of time  $[T_{HW}, T_T]$ . The head-wave results from the diffraction of the  $L$ -wave front at the free surface, giving rise to a plane front of  $T$ -wave in the bulk. A commonly

used picture for explaining head-wave existence in terms of acoustic rays is provided in Figure 19.16.

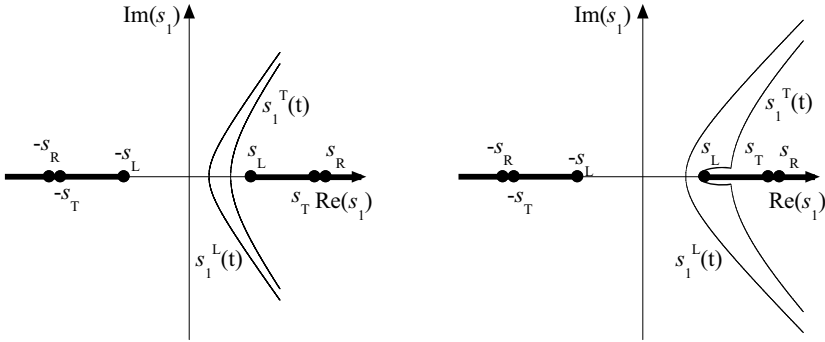


**Figure 19.15.** Cagniard contours for an isotropic half-space. a) no branch-cut integral: no head-wave; b) branch-cut integral: head-wave contribution

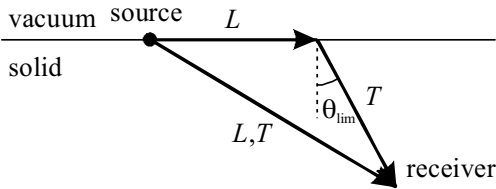


**Figure 19.16.** Conversion of the grazing acoustic ray of type  $L$ , in a ray of type  $T$  propagating in the volume and constituting the head-wave

Note that there are three possible configurations for rays to propagate from a source placed on the surface to a point located in the bulk:

- a direct path source–receiver for a ray of type  $L$ ;
- a direct path source–receiver for a ray of type  $T$ ;
- a path made up of an  $L$ -ray grazing the surface and converted into a  $T$ -ray.

The third case accounts for the structure (in terms of rays) of the head-wave that is observable for an observation angle source–receiver  $\theta$ , larger than or equal to the transverse-to-longitudinal critical angle  $\theta_{\text{lim}} = \arcsin(c_T/c_L)$ . The head-wave front is the plane front, which connects the  $L$  and  $T$  fronts. It stretches out as a straight

line from the position of the  $L$ -front on the surface to the point of contact with the  $T$ -front (Figure 19.17b).

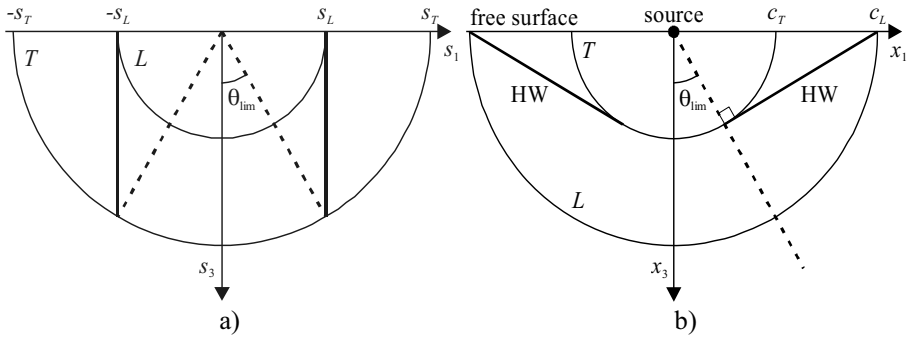


**Figure 19.17.** Head-waves: a) diagram of the phase slowness curves showing the critical angle; b) head-waves and bulk-waves fronts at  $t = 1$

The arrival time of the head-wave at the observation point is given by the value of the parameter  $\tau$  in [19.32] for the contour  $s_3^T(s_1)$ , at the branch point  $s_1 = s_L$ . At this point,  $\tau$  has a minimum value  $T_{HW}$  on the contour that is given by the expression:

$$\frac{T_{HW}}{R} = s_L \sin \theta + s_3^T(s_L) \cos \theta. \quad [19.69]$$

#### 19.6.1.2. The Rayleigh wave

From the equation of contours [19.35], we can see that, apart from the case  $\theta = \frac{\pi}{2}$  (observation point at the surface), the contour integration does not involve the Rayleigh-wave pole. Consequently, there is no residue calculation to be performed. Regarding the impulse–response calculation at the surface, the Cagniard–de Hoop contours follow the real axis of  $s_1$  and therefore involve the Rayleigh-wave pole (Figure 19.18). The path-integral contribution on the infinitesimal arc  $C_R$  bypassing the pole can be calculated from the residue of the integrands at that pole, and provides an additional contribution to equation [19.43] already obtained.

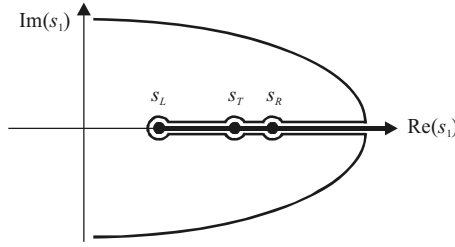


**Figure 19.18.** Cagniard–de Hoop contour for an observation point at the surface

In section 19.4, it was shown that the integral performed along the initial contour (imaginary axis) is equal to that considered along the Cagniard–de Hoop contour. By adding the contribution due to the path integral over  $C_R$ , we get for  $x_3 = 0$  (as  $\exp(-ps_3^{L,T} x_3)$  disappears):

$$\begin{aligned} \frac{1}{2i\pi} \int_{-i\infty}^{+i\infty} B^{L,T} P_i^{L,T} e^{-ps_1 x_1} ds_1 &= \frac{1}{\pi} \text{Im} \left[ \int_{\Gamma^+} B^{L,T} P_i^{L,T} e^{-ps_1 x_1} ds_1 \right] \\ &+ \frac{1}{\pi} \text{Im} \left[ -i\pi \text{Res} \left( B^{L,T} P_i^{L,T} e^{-ps_1 x_1} \right) \Big|_{s_1=s_R} \right] \end{aligned} \quad [19.70]$$

The second term in the right-hand side of equation [19.70] (that we can denote  $^R \hat{u}_i^{L,T}(x_1, x_3 = 0, p)$ ), can be expressed in the time domain as:

$$^R u_i^{L,T}(x_1, x_3 = 0, t) = -\text{Re} \left[ \text{Res} \left( B^{L,T} P_i^{L,T} \right) \Big|_{s_1=s_R} \right] \delta(t - s_R x_1), \quad [19.71]$$

knowing that the functions  $B^{L,T}$  and  $P_i^{L,T}$  did not depend on  $p$ . Thus the impulse response at the surface contains a delta function over time, delayed by a time  $t_R = s_R x_1$ . This contribution can sometimes disappear for some components of  $u_i^{L,T}$ , when the residue in equation [19.71] is purely imaginary. Generally in this case, the aforementioned components of the wave-field are singular at time  $t = t_R$ , revealing a discontinuity in the response.

#### 19.6.1.3. Waveforms for a transient vertical force

We consider the case of an aluminum half-space subjected to a line-source of normal traction  $F_3 \delta(t) \delta(x_1) \delta(x_3)$ . Two directions of observation are chosen:

$\theta = 90^\circ$ , to obtain the surface response; and  $\theta = 60^\circ$ , in order to observe the head-wave contribution (see Figure 19.19). In the first case, there is a singularity on the vertical displacement  $u_3$  at the arrival time of the Rayleigh wave, and a delta function  $\delta(t - s_R x_1)$  on the horizontal displacement  $u_1$ .

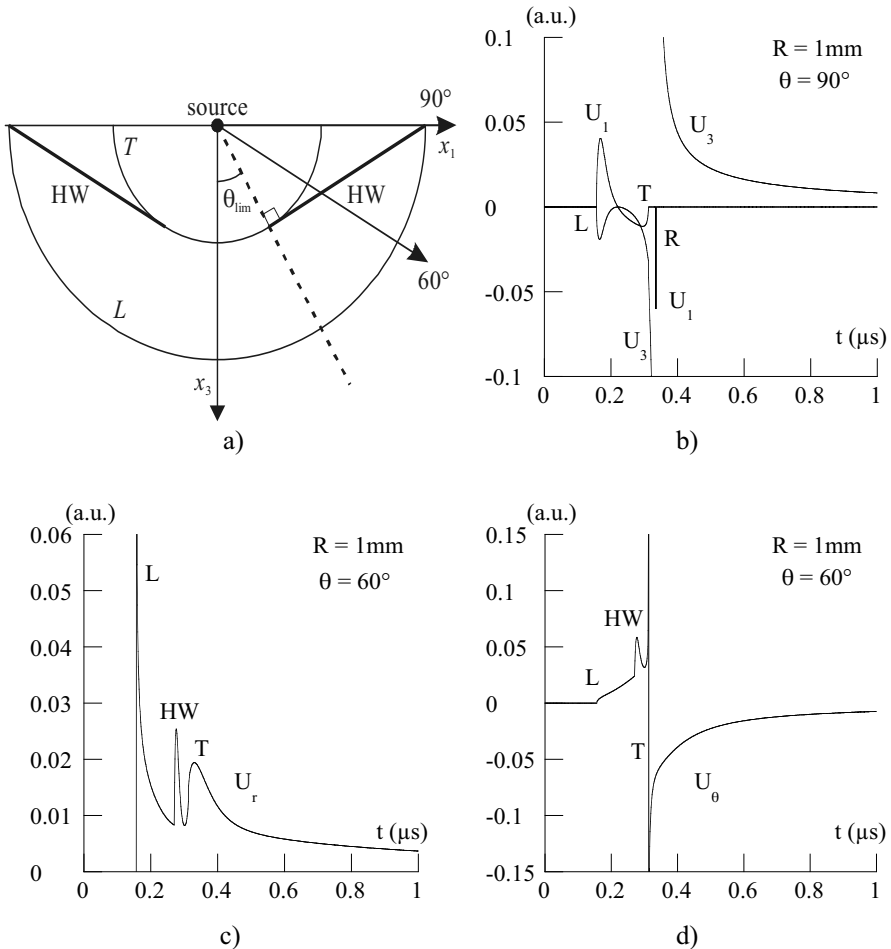


**Figure 19.19.** Impulse response for an aluminum isotropic half-space. The source is a line of vertical force at the surface. a) scheme exhibiting wave fronts; b) response at the surface (displacements  $u_1$  and  $u_3$ ); c) radial displacement for the observation direction  $60^\circ$ ; d) azimuthal displacement for the observation direction  $60^\circ$ . The distance source–observation point is  $R = 1\text{ mm}$  in all cases

### 19.6.2. Anisotropic medium

On the whole, the main steps of the calculation of the Green function for an anisotropic half-space are roughly the same as for the isotropic case. Note that some peculiarities of the wave propagation in anisotropic media, such as concavity of the slowness curves, may affect the contour integration. It mainly concerns head-waves.

#### 19.6.2.1. The issue of head-waves for the contour integration

When the branch points of type  $C$  are not located on the real axis, the process of handling path integrals along the branch cut is strictly identical to that of the isotropic case. However, if the group-velocity curves are folded along axis 1 (as in the example illustrated by Figure 19.21 a), the problem varies slightly in the result, but does not differ fundamentally from the point of view of the integration in the complex plane. Because of the anisotropy, the number of branch points is greater, and we must ensure that the integrands remain analytic within the domain where the contour integration is performed. Two typical examples are shown in Figures 19.20, in the presence of a wave-surface folding located on the  $x_1$  axis (Figure 19.10.a). Case a) concerns a contour integration of type  $L$  ( $s_1^L$ ) along the cut between the branch points  $D_1$  and  $D_2$ . The situation is actually the same as in the isotropic case. The part of the path integration along the cut and bypassing the point  $D_1$  provides the contribution of a head-wave. Case b) exemplifies the situation for the  $T$ -wave, for which the Cagniard contour is composed of an infinite path crossing the real axis in between cuts, and a path surrounding the finite-length cut  $D_1 D_2$ . This contribution appears in the form of a head-wave beginning at time  $T_{HW_1}$  (corresponding to the point  $D_1$ ) and finishing at time  $T_{HW_2}$  (corresponding to the point  $D_2$ ). Between the time  $T_{HW_2}$  and the arrival time of the  $T$ -wavefront (time at which the contour crosses the real axis vertically), there is a lacuna in the response of the  $T$ -wave. An illustration of the head-wave fronts for a copper crystal is shown in Figure 19.21.

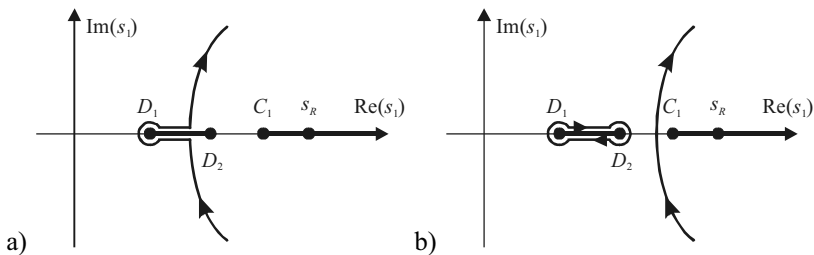


**Figure 19.20.** Two types of contours in the complex plane when using the Cauchy integral theorem: a) partial branch-cut integral along the segment  $D_1 D_2$ ; b) complete branch-cut integral along the segment  $D_1 D_2$

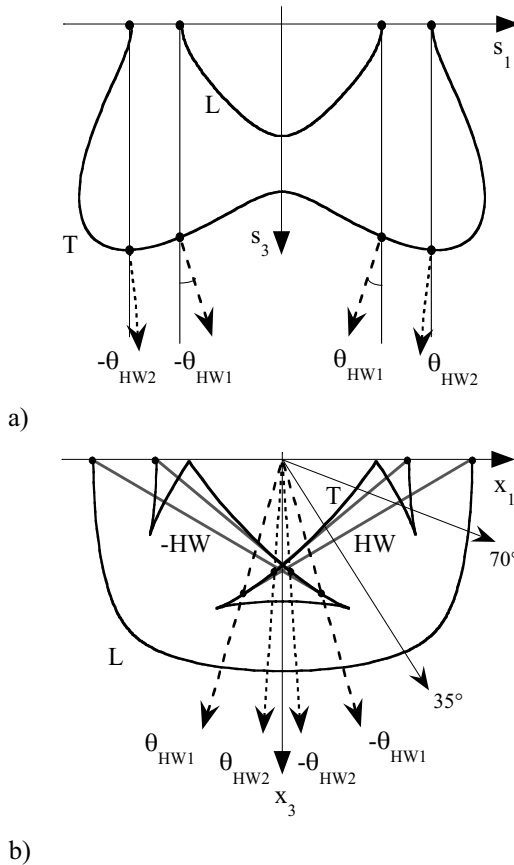


**Figure 19.21.** Head-waves for a copper crystal [100]: a) critical angles of the head-waves on the phase slowness curves; b) head-wave and bulk-wave fronts

#### 19.6.2.2. Waveforms for a transient line-source of vertical force

Compared with the impulse responses obtained for isotropic media, the impulse responses of the Lamb problem in anisotropic media are much more complicated to analyze. All analytical aspects of the Cagniard–de Hoop method can therefore be very helpful to understand the waveforms. Figure 19.22 shows the Green functions in the directions  $35^\circ$  and  $70^\circ$  of the copper crystal half-space, subjected to a line of vertical force. Many features are present on these waveforms, such as: multiple arrivals of quasi-transverse wave fronts; internal diffraction in the proximity of the cuspidal tip of the bulk-wave fronts; presence of two head-wave fronts. For the observation direction  $35^\circ$  which is relatively close to the tip of the cusp, the

contribution (ID) of the internal diffraction is visible on the impulse-response. Regarding the observation direction at  $70^\circ$ , it crosses the wave surfaces of the quasi-transverse mode three times, which involves three arrival times for this mode ( $T_1$ ,  $T_2$  and  $T_3$ ). Note also that for this observation direction the waveform exhibits a lacuna (null field) between the arrival times  $T_1$  and  $T_2$ , which corresponds to the inner area of the folded part of the group velocities, crossed by the observation direction.

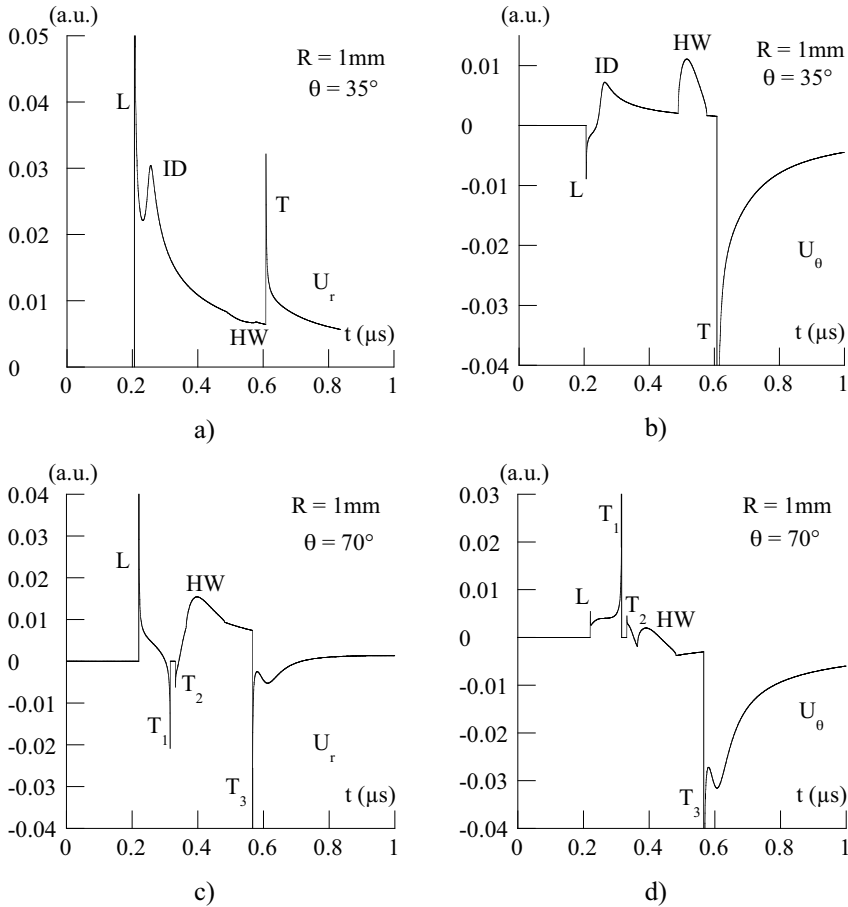


**Figure 19.22.** Impulse-response for a copper crystal half-space subjected to a line-source of vertical force. a) radial displacement for the direction  $35^\circ$ ; b) azimuthal displacement for the observation direction  $35^\circ$ ; c) radial displacement for the direction  $70^\circ$ ; d) azimuthal displacement for the observation direction  $70^\circ$ . The source-observation point distance is  $R = 1\text{ mm}$  in all cases



### 19.7. Three-dimensional Green function on the surface of an anisotropic medium

The purpose of this section is to show that the Cagniard–de Hoop method allows an immediate interpretation of the radiation of Rayleigh waves at the surface of an anisotropic half-space. For this, we use a transient and point-like excitation of Dirac delta function type. The source is therefore represented by a force field, whose components are of the form:  $A\delta(x_1)\delta(x_2)\delta(t)$ . It is located on a plane surface  $(x_1, x_2)$  of a half-space (see Figure 19.14 by considering a point-like force). In order to avoid unnecessarily complex developments, the calculation of the 3D response will only be made for an observation point located on the surface. The components of the displacement field in the direction  $x_\alpha$  ( $\alpha = 1 \dots 3$ ), at any point on the surface and at any time  $t$ , are then given, in accordance with section 19.2, by the following triple integral:

$$u_\alpha(x_1, x_2, t) = \frac{1}{(2i\pi)^3} \int_{-i\infty}^{+i\infty} \int_{-i\infty}^{+i\infty} \int_{-i\infty}^{+i\infty} \tilde{g}_\alpha(s_1, s_2, p) e^{p(t-s_1x_1-s_2x_2)} ds_1 ds_2 dp \quad [19.72]$$

where the function is given by:

$$\tilde{g}_\alpha(s_1, s_2, p) = p^2 \sum_{n=L, T_1, T_2} A^n(s_1, s_2, p) P_\alpha^n(s_1, s_2). \quad [19.73]$$

This expression has been obtained from the decomposition of the source in terms of the three partial modes (one quasi-longitudinal ( $n = L$ ) and two quasi-transverse ( $n = T_1, n = T_2$ )). The components of the normalized polarization vector along the  $x_\alpha$  axis are noted  $P_\alpha^n(s_1, s_2)$  and the amplitudes  $A^n(s_1, s_2, p)$  are given by solving the homogenous problem for a free surface, presented in 2D in section 19.6, and generalized here to a 3D case, through the linear system:

$$M \begin{pmatrix} A^L \\ A^{T_1} \\ A^{T_2} \end{pmatrix} = \begin{pmatrix} F_1 \\ F_2 \\ F_3 \end{pmatrix}, \text{ with } M = \begin{pmatrix} \tilde{\sigma}_{13}^L & \tilde{\sigma}_{13}^{T_1} & \tilde{\sigma}_{13}^{T_2} \\ \tilde{\sigma}_{23}^L & \tilde{\sigma}_{23}^{T_1} & \tilde{\sigma}_{23}^{T_2} \\ \tilde{\sigma}_{33}^L & \tilde{\sigma}_{33}^{T_1} & \tilde{\sigma}_{33}^{T_2} \end{pmatrix}. \quad [19.74]$$

To ensure that the Cagniard–de Hoop method is useable, it is important to note that the strain components, expressed at  $x_3 = 0$ ,  $\tilde{\sigma}_{ij}^n$  are proportional to the frequency  $p$ . As a consequence, since the quantities  $F_i$  are constant, the amplitudes are inversely proportional to  $p$ . As a result, they take the form:  $A^n(s_1, s_2, p) = B^n(s_1, s_2) / p$ . The spectrum introduced in [19.73] is therefore a linear function of frequency and is expressed by:

$$\tilde{g}_\alpha(s_1, s_2, p) = p \tilde{h}_\alpha(s_1, s_2), \quad [19.75]$$

$$\text{where: } \tilde{h}_\alpha(s_1, s_2) = \sum_{n=L, T1, T2} B^n(s_1, s_2) P_\alpha^n(s_1, s_2).$$

The theorem of Laplace transform derivation shows that the velocity field is the temporal derivative of the function  $U_\alpha(x_1, x_2, t)$ , such as:

$$u_\alpha(x_1, x_2, t) = \frac{d}{dt} U_\alpha(x_1, x_2, t), \quad [19.76]$$

with:

$$U_\alpha(x_1, x_2, t) = \frac{1}{(2i\pi)^3} \int_{-i\infty}^{+i\infty} \int_{-i\infty}^{+i\infty} \int_{-i\infty}^{+i\infty} \tilde{h}_\alpha(s_1, s_2) e^{p(t-s_1x_1-s_2x_2)} ds_1 ds_2 dp. \quad [19.77]$$

The Cagniard–de Hoop method is now partially applicable in equation [19.77] if we make the following change of variables:

$$x_1 = r \cos \varphi, \quad x_2 = r \sin \varphi, \quad s_1 = s \cos \theta, \quad s_2 = s \sin \theta. \quad [19.78]$$

Indeed, the function  $U_\alpha(t, r, \varphi)$  is now expressed by:

$$U_\alpha(t, r, \varphi) = \frac{1}{2i\pi} \int_{-\pi/2}^{+\pi/2} \tilde{F}_\alpha(t, r, \varphi, \theta) d\theta, \quad [19.79]$$

where:

$$\tilde{F}_\alpha(t, r, \varphi, \theta) = \frac{1}{(2i\pi)^2} \int_{-i\infty}^{+i\infty} \left( \int_0^{+i\infty} ds + \int_0^{-i\infty} ds \right) \tilde{H}_\alpha(\theta, s) e^{p(t-sr \cos(\theta-\varphi))} dp, \quad [19.80]$$

where, after the change of variables:  $\tilde{h}_\alpha(s_1, s_2) \rightarrow \tilde{H}_\alpha(\theta, s)$ . Integral [19.80] is of the same type as those presented in [19.31]. It can therefore be treated similarly. To do so, we introduce the integration contour change given by:

$$s(\theta) = \frac{t}{r \cos(\theta - \varphi)}. \quad [19.81]$$

After some calculation steps that we do not present in detail, the total field takes the form [BES 98]:

$$U_{\alpha}(t, r, \varphi) = U_{vp}(t, r, \varphi) + U_s(r, \varphi) + U_R(t, r, \varphi). \quad [19.82]$$

The function

$$U_{vp}(t, r, \varphi) = -\frac{1}{2\pi^2} VP \int_{-\pi/2}^{+\pi/2} \operatorname{Re} \left( s \tilde{H}_i(\theta, s) \frac{ds}{dt} \right)_{s=\frac{t}{r \cos(\theta-\varphi)}} d\theta \quad [19.83]$$

corresponds to the principal value in the sense of Cauchy. Its calculation requires the use of numerical methods. In this case, i.e. obtaining the field on the surface, it mainly contains information on the skimming waves. The contribution

$$U_s(r, \varphi) = -\frac{1}{2\pi} \operatorname{Im} \left( \operatorname{Res} \left( s \tilde{H}_i(\theta, s) \frac{ds}{dt} \right)_{\theta=\pm\pi/2+\varphi} \right) \quad [19.84]$$

comes from the discontinuity introduced by the change of variables [19.81]. In this equation,  $\operatorname{Res}(\cdot)_{x=x_0}$  points to the calculation of the residue at  $x = x_0$ . This is the static component of the total field. Finally, the function

$$U_R(t, r, \varphi) = -\frac{1}{2\pi} \operatorname{Im} \int_{-\pi/2}^{+\pi/2} \int_{-i\infty}^{+i\infty} R_R(\theta) e^{p(t-\tau(\theta, s_R(\theta)))} dp d\theta \quad [19.85]$$

gives the contribution of the Rayleigh poles, where:

$$R_R(\theta) = \operatorname{Res} \left( s \tilde{H}_i(\theta, s) \right)_{s=s_R(\theta)} \quad [19.86]$$

and

$$\tau(\theta, s) = sr \cos(\theta - \varphi). \quad [19.87]$$

For a fixed value of the angle  $\theta$ , the slowness  $s_R(\theta)$  satisfies the Rayleigh equation, which is given by the determinant cancellation of the matrix  $M$  introduced in [19.74], i.e.  $\det(M) = D(\theta, s_R(\theta)) = 0$  for  $s = s_R(\theta)$ . The calculation of the integral over  $p$  expressed in [19.85] leads to:

$$U_R(t, r, \varphi) = -\frac{1}{2\pi} \operatorname{Im} \int_{-\pi/2}^{+\pi/2} R_R(\theta) \delta(t - \tau(\theta, s_R(\theta))) d\theta. \quad [19.88]$$

For a fixed time, this latter integral is not zero for the angles  $\theta_i$  such as:

$$\begin{cases} t - \tau(\theta, s_R(\theta)) = 0 \\ D(\theta, s_R(\theta)) = 0 \end{cases} \quad \text{for } \theta = \theta_i. \quad [19.89]$$

If the Cagniard-de Hoop method described above is applicable, it requires special attention considering the possible sign change of the slowness  $s$  depending on the value of the angle  $\theta - \varphi$  (see [19.81]). Thus, since the time  $t$  is positive, we have the conditions:

$$s > 0, \text{ if } \cos(\theta - \varphi) > 0, \text{ and } s < 0, \text{ if } \cos(\theta - \varphi) < 0. \quad [19.90]$$

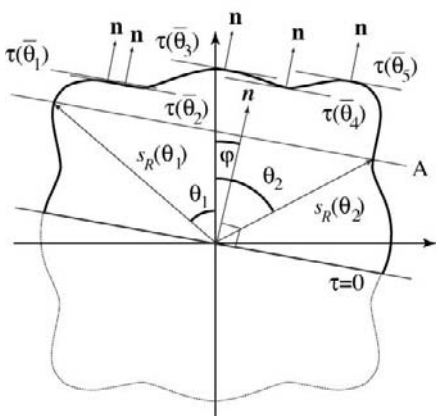


**Figure 19.23.** Phase slowness of Rayleigh waves in polar coordinates  $s_R(\theta)$ . Contributions taken into account for the calculation of the integral [19.88] for  $\varphi = 10^\circ$  (thick line)

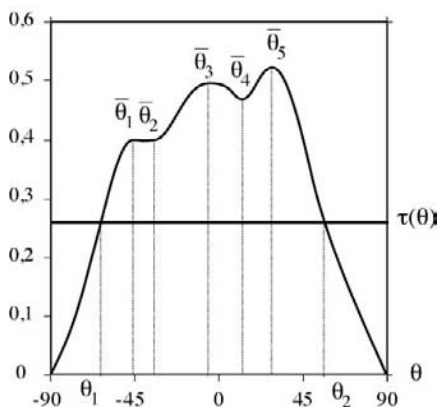


**Figure 19.24.** Arrival times of the Rayleigh waves as functions of the integration angle  $\theta$  for  $\varphi = 10^\circ$

Conditions [19.90] are also applied to the choices of the Rayleigh poles. Thus, varying the angle  $\theta$  from  $-\pi/2$  to  $+\pi/2$ , we actually describe the slowness surface of the Rayleigh waves, solution of [19.89], from  $\varphi - \pi/2$  to  $\varphi + \pi/2$ . To reiterate, let us consider Figure 19.23, which represents the slowness curve of the Rayleigh waves for a half-space constituted by a copper crystal. For an observation direction  $\mathbf{n}$  of angle  $\varphi = 10^\circ$ , the solutions taken into account in the evaluation of

integral [19.88] are identified by a thick line. The plotting of the associated function  $\tau(\theta, s_R(\theta))$  for different values of  $\theta$  is shown in Figure 19.24 for a distance  $r=5$  mm. It is clear that this function is not single-valued. Indeed, for the chosen material, there exists between two and four possible angles for which a Rayleigh wave is excited.

For example, at time  $t = \tau(\theta)$ , i. e. for the horizontal line drawn in Figure 19.24 and for the line orthogonal to the direction  $\mathbf{n}$  noted A in Figure 19.23, two waves propagate in phase direction  $\theta_1$  and  $\theta_2$ . Note that the angle  $\theta$  is not necessarily the phase angle, but it can be equal to  $\theta - \pi$  considering the conditions [19.90]. To calculate the integral [19.88] using the properties of Dirac delta function distributions, it is necessary to make the variables change  $\tau = r s_R(\theta) \cos(\theta - \varphi)$  and to split this integral as follows:

$$U_R(t, r, \varphi) = \sum_{j=0}^m U_{Rj}(t, r, \varphi), \quad [19.91]$$

where:

$$U_{Rj}(t, r, \varphi) = -\frac{1}{2\pi} \text{Im} \left( \int_{\tau_i}^{\tau_{i+1}} Q_j(\tau) \delta(t - \tau) \left( \frac{\partial \tau}{\partial \theta} \Big|_{\theta=\theta_j} \right)^{-1} d\tau \right), \quad [19.92]$$

with  $Q_j(\tau) = s_R(\theta_j) R_R(\theta_j)$ . The integration bounds are such that  $\tau_j = \tau(\bar{\theta}_j)$ , for  $0 < j < m$ , where the angles  $\bar{\theta}_j$  correspond to the specific points for which the function  $\tau(\theta)$  admits extrema, whose number is  $m$ . The extreme values, in agreement with [19.90], are given by  $\tau_0 = 0$  and  $\tau_{m+1} = 0$ . The angle  $\theta_j$  indicates the unique value of the phase angle associated with time  $\tau(\theta)$ , for  $\tau_i < \tau(\theta) < \tau_{i+1}$ . For each value of  $j$ , integral [19.92] is equal to zero if the time is outside this range. Therefore, the resolution of [19.90] is Moreno longer a problem and, taking into account the variation of the function  $\tau(\theta)$ , we obtain:

$$U_R(t, r, \varphi) = -\frac{1}{2\pi} \sum_{i=0}^n \text{Im} \left( Q_i(\tau) \left( \frac{\partial \tau}{\partial \theta} \Big|_{\theta=\theta_i} \right)^{-1} \right)_{\tau=t}, \quad [19.93]$$

where  $n$  is, for a fixed time, the number of excited Rayleigh waves ( $n=2$  in Figure 19.24).

We now consider this contribution in detail. If, for a given observation point, a Rayleigh wave, associated with the angle  $\theta_i$ , contributes to the displacement, it does

not necessarily lead to a discontinuity. Indeed, a discontinuity is visible in the waveform only when  $\partial\tau/\partial\theta=0$ , which coincides with the angles  $\theta_i=\bar{\theta}_j$ . These singular angles, as the rays described for the bulk waves (section 19.4.3), correspond to the fact that the observation direction defined by the vector  $\mathbf{n}$  is normal to the Rayleigh slowness surface (see Figures 19.23 and 19.24). For the direction chosen as an example, five rays propagate and reach the observation point at time  $rs_R(\bar{\theta}_j)$ . When the observation direction  $\varphi$  varies, the energy velocities  $c_e(\varphi)=1/s_R(\bar{\theta}_j)$  associated with the possible rays, are plotted in polar coordinates on Figure 19.26.

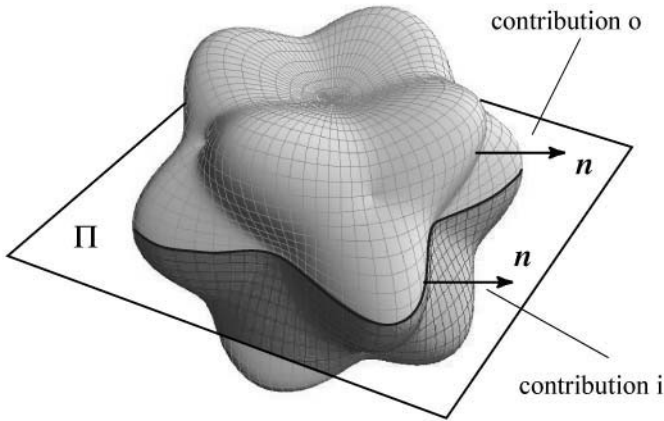


**Figure 19.25.** 3D view of the slowness surface of the mode  $T_1$  in a copper crystal.  
*Differentiation of the contributions: i – in the plane interface (noted  $\Pi$ ); o – out of the plane interface*

Before analyzing the waveforms in detail, it is important to give some indications on the skimming waves. These surface waves correspond to the particular bulk waves for which the energy velocity is oriented in the observation direction. This direction  $\mathbf{n}$  is contained in the interface plane, identified by  $\Pi$  in Figure 19.25. As the considered problem is 3D, all the possible rays must be taken into account. Two cases are then to be considered in connection with orientation of the slowness vectors. Either these vectors are in the interface plane (these rays will be noted i, for “in-plane”), or they are outside the interface plane (these rays will be noted o, for “out-plane”). For these two different contributions, the energy velocities of these waves are reported on Figure 19.27 as a function of the observation angle, for the three modes  $L$ ,  $T_1$ ,  $T_2$ .

From a normal force, i.e.  $(F_1, F_2, F_3)^T = (0, 0, 1)^T$ , and for the calculation of the normal displacement  $u_3(t, r, \varphi)$ , we analyze the relative contributions that appear in

expression [19.82]. The three functions that constitute this expression are plotted on Figure 19.28 for  $\varphi = 0^\circ$ . Note first that these three functions are not causal and that, from this point of view, only their sum (see Figure 19.29) ensures that the total response has a physical sense. Indeed, the field becomes equal to zero before the arrival of the fastest skimming wave front (i.e. the  $L$  wave, noted  $i1$  in the figures below).

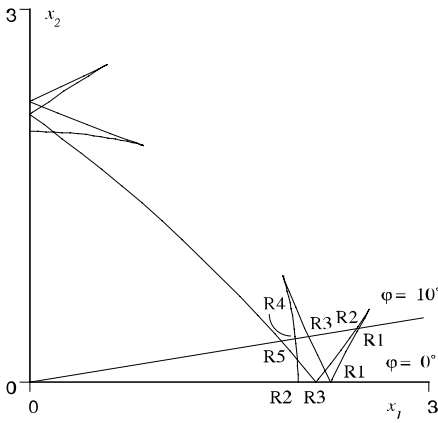


**Figure 19.26.** Energy velocities of the Rayleigh waves in polar coordinates

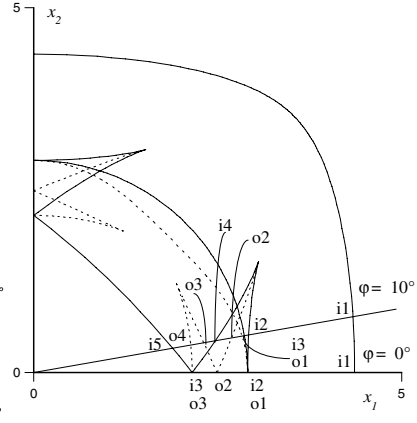


**Figure 19.27.** Energy velocities of the skimming waves in polar coordinates  $c_e(\varphi)$

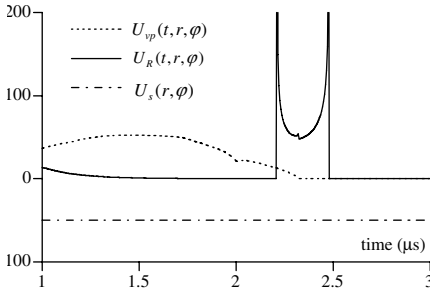


**Figure 19.28.** Values of the three contributions to the waveform  $u_3(t, r, \varphi)$  as functions of  $t$ , for  $r = 5 \text{ mm}$  and  $\varphi = 0^\circ$

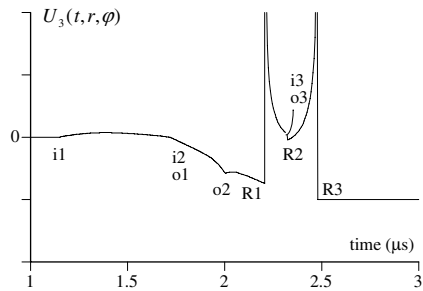


**Figure 19.29.** Total field  $U_3(t, r, \varphi)$  associated to Figure 19.28

The Cauchy principal value  $U_{vp}(t, r, \varphi)$  has discontinuities on its derivative at the arrival time of the skimming waves. They are noted  $i1$ ,  $i2$ ,  $i3$ ,  $o1$ ,  $o2$  and  $o3$  in

Figure 19.29. Note moreover that for this component of the Green tensor, the Cauchy principal value becomes equal to zero after the arrival of the slowest skimming waves (i3 and o3). The contribution of the Rayleigh wavefront to the normal displacement of the interface appears, of course, only in the evaluation of the function  $U_R(t, r, \varphi)$ . Three Rayleigh waves are observed. They are noted R1, R2 and R3 on Figure 19.29. Referring to Figure 19.26 for an observation angle  $\varphi = 0^\circ$ , we see that three rays effectively exist. In fact, among the five solutions, four degenerate into two double roots. Finally, we note that the static component  $U_s(r, \varphi)$  ensures that the solution is effectively causal.

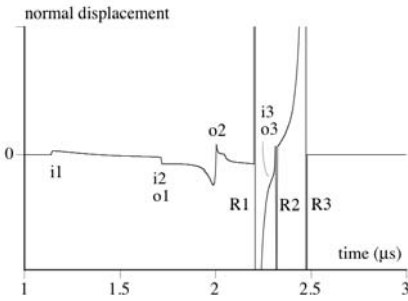


**Figure 19.30.** Normal displacement  $u_3(t, r, \varphi)$  for  $r = 5 \text{ mm}$  and  $\varphi = 0^\circ$

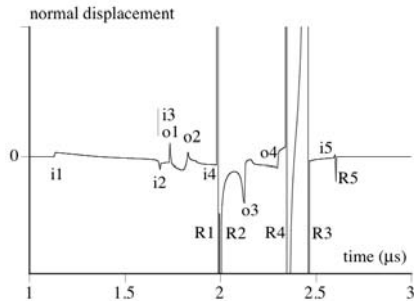


**Figure 19.31.** Normal displacement  $u_3(t, r, \varphi)$  for  $r = 5 \text{ mm}$  and  $\varphi = 10^\circ$

These results are related to the calculation of the function  $U_3(t, r, \varphi)$ . This function must be derived with respect to time to obtain the normal displacement field  $u_3(t, r, \varphi)$ . This is shown on Figure 19.30. Finally, to conclude this section, choosing the observation angle  $\varphi = 10^\circ$ , it can be noted that the five predictable wave arrivals mentioned in Figure 19.24 are observed in Figure 19.31.

A comparison between the arrival times of the different waves and the normal displacement field  $u_3(t, r, \varphi)$  is shown in Figure 19.32, where the calculated waveforms are plotted in polar coordinates for a complete rotation of  $360^\circ$ . In this picture, the time has been converted into velocity by the equation  $v = t / r$  and the amplitude is in grayscale to allow a comparison with ray curves presented in Figures 19.26 and 19.27. There is a perfect match between the arrival times of the wavefronts and the abrupt changes in the normal displacement of the surface. This accordance is very good, except on the areas extending the cusps, whether those of the Rayleigh waves (noted R) or those of the skimming waves (noted r). These phenomena, mentioned quickly in section 19.6.2.2 as internal diffraction, are not written under equations in this book. To make a complementary description, it is necessary to use generalized complex rays (see [DES 04] for bulk waves and [DES 09] for surface waves).



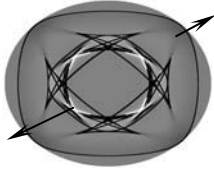


**Figure 19.32.** *Calculated normal displacement  $u_3(r/t, \varphi)$  for  $r = 5$  mm.*

— : fronts of the rays of the skimming and Rayleigh waves resulting from Figures 19.26 and 19.27



**Figure 19.33.** *Measured normal displacement  $u_3(r/t, \varphi)$  on the surface of a copper crystal for  $r = 5$  mm*

Finally, to conclude this chapter, based on generation and detection experiments of ultrasonic waves by LASER methods, presented in reference [HUE 05], the results of measurements of the Green function are shown in Figure 19.33. In this type of experiment, the detection and the source are both point-like, as it is a laser impact. It is then understandable that this optical system offers a local and direct measurement of the Green function. This explains the perfect agreement between theory and experiment.

## 19.8. Bibliography

- [BES 98] Bescond B., Deschamps M., “Dynamical surface response of a semi-infinite anisotropic elastic media to an impulsive force”, *J. Acoust. Soc. Am.*, Vol. 103(1), 114–24, 1998
- [BUR 71] Burridge R., “Lamb’s problem for an anisotropic half-space”, *Q. J. Mech. Appl. Math.*, 24, 81–98, 1970
- [CAG 39] Cagniard L., *Réflexion et Réfraction des Ondes Sismiques Progressives*, Gauthier-Villars, Paris, 1939
- [DES 04] Deschamps M., Poncelet O., “Complex Rays and Internal Diffraction at the Cusp Edge”, in V. G. Goldstein and G. A. Maugin, (Eds.), *Surface waves and laminated bodies and defect detection*, Kluwer Academic Publishers, 2004
- [DES 09] Deschamps M., Huet G., “Complex surface rays associated with inhomogeneous skimming and Rayleigh waves”, *Int. Journal of Non-Linear Mechanics*, in press, 2009
- [GRI 04] Grimal Q., Naïli S., Watzky A., “A method for calculating the axisymmetric response of a two-layered half-space under dynamic concentrated loading”, *Journal of Sound and Vibration*, Volume 276, 755–80, 2004

- [HAY 84] Hayes M., “Inhomogenous plane waves”, *Arch. Rational Mech. Anal.*, Vol. 85, 41–79, 1984
- [HOO 60] De Hoop A. T., “A modification of Cagniard’s method for solving seismic pulse problems”, *Applied Scientific Research* 8, 349–56, 1960
- [HUE 05] Huet G., Rossignol C., Deschamps M., Qian M., Every A. G., “Green function of an anisotropic half space. Comparison between measurements and complex (and real) rays theory”, *World Congress on Ultrasonics*, Beijing, 2005
- [JOH 74] Johnson L. R., “Green’s function for Lamb’s problem”, *Geophysical Journal of the Royal Astronomical Society*, 37: 99–131, 1974
- [KEN 83] Kennett B. L. N., “Seismic Wave Propagation in Stratified Media”, Cambridge Monographs on Mechanics and Applied Mathematics”, Cambridge University Press, Cambridge, 1983
- [KRA 63] Kraut E. A., “Advances in the theory of anisotropic elastic wave propagation”, *Reviews of Geophysics*, Vol. 1, No. 3, 401–48, 1963
- [MOU 95] Mourad A., Deschamps M., “Lamb’s problem for an anisotropic half-space studied by the Cagniard–de Hoop method”, *J. Acoust. Soc. Am.*, Vol. 97(5), 3194, 1995
- [MOU 96] Mourad A., Deschamps M., Castagnède B., “Acoustic waves generated by an line impact in an anisotropic medium”, *Acustica-Acta Acustica*, 82, 839–51, 1996
- [NAY 95] Nayfeh A. H. *Wave Propagation in Layered Anisotropic Media with Application to Composites*, North Holland Publishing, 1995
- [PAY 83] Payton R. G., “Elastic wave propagation in transversely isotropic media”, *Series in Mechanics of elastic and Inelastic Solids*, Martinus Nijhoff publishers, The Hague, vol. 4, 1983
- [PON 01] Poncelet O., “Réponse transitoire à une source impulsionnelle en milieu anisotrope. Calcul de fonctions de Green par la méthode de Cagniard–de Hoop”, *Cours de l’École des ondes “Ondes élastiques dans les solides”*, INRIA-Rocquencourt, 12–16 November 2001
- [SHU 00] Shuvalov A. L., “On the theory of wave propagation in anisotropic plates”, *Proc. R. Soc. Lond. A* 456, 2197–222, 2000
- [VDH 87] Van Der Hijden J. H. M. T., “Propagation of transient elastic waves in stratified anisotropic media”, *North-Holland series in Applied Mathematics and Mechanics*, Elsevier Science Publishers, Amsterdam, vol. 32, 1980.

Part 6

# Linear Methods of Ultrasonic Non-Destructive Testing and Evaluation

This page intentionally left blank

## Chapter 20

# Measurement of Viscoelastic Modules

The determination of the mechanical properties of materials is a necessary and delicate objective in order to study the behavior of the structure in its environment. From structural analysis to material resistance or elastodynamic, stiffness moduli constitute the input data of the models used.

### 20.1. Introduction

This section aims to present some procedures and results for the ultrasonic characterization of mechanical properties of materials. First, a general approach to this issue and some basic principles will be described. Then, the mathematical aspect of the inversion scheme, which depends on a model and some measured quantities, will be presented. Finally, two measurement techniques will be presented and illustrated, using results from the non-destructive evaluation of viscoelastic properties of materials constituting a homogenous plate or a layer within a stratified plate. The first technique requires the immersion in water of the measuring system and the samples to be tested; the other one occurs in air thanks to the relatively recent technology of ultrasonic transducers.

#### 20.1.1. *General principle*

The measurement of the mechanical properties of materials by ultrasonic means consists of the resolution of an inverse problem which is made of two steps: (1) measuring an ultrasonic quantity (propagation velocity or wave amplitude, transfer

function of the material, etc.) and (2) using a model to simulate this quantity by varying the inputs (searched mechanical properties) until the simulation result is the most adequate with the measurements. The optimization procedure of the searched parameters is made with classical numerical routines, Newton–Raphson or Simplex methods, for example. For a maximum efficiency of the characterization techniques, several criteria must be satisfied:

- The ultrasonic measurements must be of good quality, that is to say with little noise, and repeatable with errors as small as possible.
- The model must represent accurately the physical phenomenon. Every simplifying assumption must be justified by the measurement conditions.
- The measured and calculated ultrasonic quantity must be sensible to the searched mechanical characteristics, that is to say it must be a significant conveyor of information concerning these properties.
- The problem must have a unique solution, at least in a range of values which have a physical meaning.
- The numerical procedure used to optimize the mechanical characteristic values must be robust and fast.
- The final result must be estimated with a certain error. This error will be influenced by the quality of the measurements and by their sensitivity to the searched mechanical parameters.

Depending on the type of quantity being characterized, the numerical models, the measuring techniques or the optimization procedures can differ significantly. In this section, the objective is to measure some moduli, noted  $C_{ij} = C'_{ij} + i C''_{ij}$ , representative of elasticity (real part  $C'_{ij}$ ) and viscoelasticity (imaginary part  $C''_{ij}$ ) of isotropic or anisotropic materials. The propagation of ultrasonic waves in a plane perpendicular to a plate-like sample constituting the material being characterized is considered. As illustrated in Figure 20.1, this plate is located in a Cartesian system with axes  $x_1$ ,  $x_2$  and  $x_3$ . As orthotropic symmetry corresponds to most of the materials met in industrial sectors, nine elasticity or viscoelasticity moduli at most have to be measured. Generally, we choose to align the axis of the system with the material axis of symmetry, which simplifies the stiffness tensor form as well as the equations needed to model the ultrasonic quantities measured. We often note  $P_{12}$  and  $P_{13}$  the principal planes of the material, defined by the axis couples  $(x_1, x_2)$  and  $(x_1, x_3)$ , respectively.

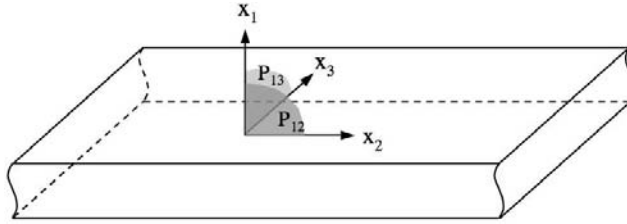


**Figure 20.1.** Geometry of the tested samples and orientation in the Cartesian system

Furthermore, as illustrated in Figure 20.2., the common characterization techniques use transducers immersed in a fluid (water or air) surrounding the sample to generate and detect ultrasonic waves in materials [ROK 02], [LOB 00], [LEY 02], [CAS 00a], [ZHA 99], [CAS 00b]. Consequently, if the propagation plane, made of the incident wave direction and the normal to the plate, coincides with a principal plane of the material, then the strains produced by the waves propagating in the material are different to zero only in this plane (plane strains condition). In this case, the plate can be seen as infinite in the direction perpendicular to the plane, thus making the calculation model easier. The characterization then consists of measuring four (real or complex) moduli representative of elasticity or viscoelasticity of the symmetry plane. For example, we identify moduli  $C_{11}$ ,  $C_{22}$ ,  $C_{12}$  and  $C_{66}$  of plane  $P_{12}$  or moduli  $C_{11}$ ,  $C_{33}$ ,  $C_{13}$  and  $C_{55}$  of plane  $P_{13}$ .

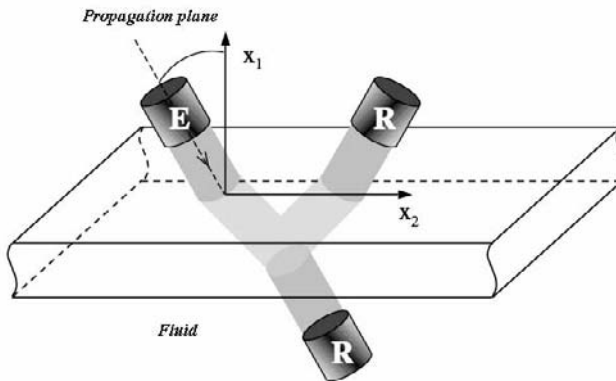


**Figure 20.2.** Generation and detection of ultrasonic waves by immersed transducers (water, air, etc.). The propagation plane, made of the incident wave and the normal to the sample, coincides with plane  $P_{12}$  defined in Figure 20.1

Conversely, if the propagation plane does not coincide with a principal plane, then the waves propagating in the material may produce non-zero strains in the three directions of the coordinate system. The plane strains assumption is no longer allowed. Under these conditions, to obtain the nine elasticity or viscoelasticity moduli of an orthotropic material, we first measure the seven moduli  $C_{11}$ ,  $C_{22}$ ,  $C_{12}$ ,  $C_{66}$ ,  $C_{33}$ ,  $C_{13}$  and  $C_{55}$  of the two symmetry planes, then we search the values of  $C_{23}$  and  $C_{44}$ , with the help of additional ultrasonic measurements made on at least one non-principal plane. Sometimes, when the moduli  $C_{23}$  and  $C_{44}$  appear as a linear combination form in the propagation equations, it is necessary to make several measurements in more than one non-principal plane, to avoid an infinity of possible solutions for  $C_{23}$  and  $C_{44}$ . If not sufficient, a contact measurement of one of the two moduli enables the complete solution of the problem [HOS 01a].

### 20.1.2. General scheme of an inverse problem

The resolution of an inverse problem consists of finding a vector  $\mathbf{P}$  made of  $p_r$  ( $r \in [1..R]$ ) unknowns, from measured data and with a model which links these quantities. These unknowns are, for example, the elasticity (or viscoelasticity) moduli, and the experimental data are the ultrasonic wave velocities or amplitudes (longitudinal or transverse bulk waves, Lamb waves, etc.) or transfer functions of the tested material (ratio between the spectra of scattered and incident acoustic fields). Depending on the type of the measured quantity, the model to be used will be one of those described in Chapter 3. Let us note  $\tilde{V}_{s=1\dots q}$ , where  $q \geq R$ , the set of  $q$  experimental values relative to the measured quantity. Thanks to the Newton–Raphson or Simplex methods [PRE 97], the inverse problem consists of finding the best estimation  $\tilde{\mathbf{P}}$  of the vector  $\mathbf{P}$  which minimizes the following functional:

$$F(\tilde{\mathbf{P}}) = \sum_{s=1}^q \left( \tilde{V}_s - V(\tilde{\mathbf{P}})|_s \right)^2 \quad [20.1]$$

where  $\tilde{\mathbf{P}} = \mathbf{P} + \delta\mathbf{P} = [p_r + \delta p_r]$  is the “optimal solution” vector  $\mathbf{P}$  plus an “error” vector  $\delta\mathbf{P}$ .  $V$  is a function of the unknown components  $p_r$ , given by the model.

When  $F(\tilde{\mathbf{P}})$  is minimal, then the vector  $\mathbf{grad}_{\mathbf{P}}(F) = \left[ \frac{\partial F}{\partial p_r} \right]$  is zero. Consequently,

the gradient of  $F(\tilde{\mathbf{P}})$ , given by the relation  $\mathbf{grad}_{\tilde{\mathbf{P}}}(F) = \mathbf{grad}_{\mathbf{P}}(F) + \mathbf{grad}_{\delta\mathbf{P}}(F)$ , is reduced to the expression  $\mathbf{grad}_{\tilde{\mathbf{P}}}(F) = 0 + \mathbf{grad}_{\delta\mathbf{P}}(F) = H \delta\mathbf{P}$ , where the operator  $H$



is defined by the matrix  $[\mathbf{H}] = \left[ \frac{\partial^2 F}{\partial p_{r_1} \partial p_{r_2}} \right]$ . Consequently, the increment used for the Newton–Raphson routine is  $\delta p_{r_1} = \left( \frac{\partial^2 F}{\partial p_{r_1} \partial p_{r_2}} \right)^{-1} \frac{\partial F}{\partial p_{r_1}}$ . The minimizing algorithm gives the best estimation of vector  $\tilde{\mathbf{P}} = [p_r + \delta p_r]$  with an error  $\delta p_r$  on each component  $p_r$ , so

$$V(\tilde{\mathbf{P}})|_s = V(\mathbf{P})|_s + \sum_r \frac{\partial V(\mathbf{P})}{\partial p_r} \Big|_s \delta p_r \quad [20.2]$$

It is generally impossible to establish a closed form of the term  $\mathbf{grad}_{\tilde{\mathbf{P}}} F(\tilde{\mathbf{P}})$  or of the operator  $H$ . All the minimizing steps of the function  $F(\tilde{\mathbf{P}})$  are then performed numerically. For each experimental data  $\tilde{V}_s$ , the nearest solution  $V(\tilde{\mathbf{P}})|_s$  is obtained by the Newton–Raphson or Simplex algorithm. The vector  $\tilde{\mathbf{P}} = \{\tilde{C}_{11}, \tilde{C}_{jj}, \tilde{C}_{lj}, \tilde{C}_{kk}\}$  (with  $(j, k) = (2, 6)$  or  $(3, 5)$  for the principal planes  $P_{12}$  or  $P_{13}$ , respectively,) or  $\tilde{\mathbf{P}} = \{\tilde{C}_{23}, \tilde{C}_{44}\}$  (if the propagation occurs in a non principal plane and if the moduli in planes  $P_{12}$  and  $P_{13}$  are known), used to calculate the function  $V(\tilde{\mathbf{P}})|_s$  at the first iteration, is established using the start value estimated by the user. This estimation can be based on experimental data  $\tilde{V}_s$  which gives an indication of the approximate characteristics of the material. Thus, the term  $F(\tilde{\mathbf{P}})$ , its gradient and the operator  $H$  are calculated numerically. If the initial values of the searched parameters are far enough from the real values, the Newton–Raphson routine is quite slow, particularly when the convergence interval is chosen to be very small in order to obtain very accurate results for the  $C_{ij}$  coefficients. On the contrary, the Simplex algorithm enables us to approach the searched solutions very quickly. It is therefore often used for approaching the solution, the Newton–Raphson algorithm being then used to refine the result. The error calculation of the optimized parameters is based on the estimation of the insensitivity matrix. This quite complex procedure will not be described here, but the reader will find its detailed presentation in references [CAS 00a], [HOS 01a].

### 20.1.3. Material characterization by measurement of the transmitted ultrasonic field

This technique consists of i) measuring the transmitted ultrasonic field (TUF) by a plate immersed in a fluid and illuminated by a plane wave with a variable incident

angle  $\theta$  (Figure 20.3), and ii) simulating this field with the help of a model whose inputs (problem unknowns) will be optimized so that the difference between measured and predicted fields is minimal. The experimental process consists first of measuring the temporal signal delivered by an ultrasonic receiver (R) without sample (reference signal  $r(t)$ ); we then measure all signals  $\{s(t, \theta)\}$  transmitted by the sample for several incidences  $\theta$ . Then, the frequency spectra  $R(f)$  and  $\{S(f, \theta)\}$  of  $r(t)$  and  $\{s(t, \theta)\}$ , respectively, are calculated. The modulus of the spectra ratio,  $\left| \frac{S(f, \theta)}{R(f)} \right|$ , corresponds to the plate transfer function, also called the transmission coefficient, which can be predicted by one of the models presented in Chapter 3. The plate can be made of one or several layers of material. The transmission coefficient depends on the frequency  $f$  and on the incident angle  $\theta$ , and also on the characteristics of the immersion medium (density  $\rho_f$  and adiabatic compressibility coefficient  $\chi_f$  of the fluid), and on the properties of the plate layers (thickness  $h_n$ , density  $\rho_n$  and elasticity or viscoelasticity moduli  $C_{ij}^n$ , where  $n$  identifies each layer). In this problem, all these parameters are known (or measured independently of the ultrasonic technique) apart from the thickness and the moduli of one of the layers, which will be named, for example,  $m$ . We also assume that the density  $\rho_m$  of the material constituting the layer  $m$  is known. The calculated transmission coefficient can thus be represented by the function  $T_{\text{calculated}}(f, \theta, \rho_f, \chi_f, h_n, \rho_n, C_{ij}^n, \rho_m, h_m, C_{ij}^m)$ . This stratified plate has  $N$  layers, one of them has to be characterized, layer  $m$ , all the others have known properties and are represented by  $n$  which is any of the  $N-1$  remaining layers.

The resolution of the inverse problem could consist of varying the unknowns ( $h_m$  and  $C_{ij}^m$ ) until we obtain the best possible agreement (in the meaning of least squares) between the calculated and measured transmission coefficients. In reality, a subtlety consists of not dividing the spectra  $\{S(f, \theta)\}$  by the reference spectrum  $R(f)$  because the latter, depending on the temporal form of the excitation, may have values very close to zero, which could cause some numerical problems during the evaluation of the division. An alternative consists of multiplying  $R(f)$  by the theoretical transmission coefficient. This is equivalent to simulating the spectra of the transmitted signals  $\{S(f, \theta)\}$  considering, in the model, that the excitation is strictly identical to that used during the experiments. The inverse problem is thus the confrontation of all the calculated and measured spectra  $\{S(f, \theta)\}$ , resulting in the optimization of the unknowns  $h_m$  and  $C_{ij}^m$ .

The procedure consists of minimizing the functional given by equation [20.1],

$$\text{where } \tilde{V}_s = \left| R_{\text{measured}}(f) \times T_{\text{calculated}}(f, \theta, \rho_f, \chi_f, h_n, \rho_n, C_{ij}^n, \rho_m, \underbrace{h_m, C_{ij}^m}_{\text{optimized}}) \right| \quad \text{and}$$

$$V(\mathbf{P}) \Big|_s = |S_{\text{measured}}(f, \theta)|.$$

To improve the transmission efficiency during the experiments, the coupling medium between transducers and sample is generally water [ROK 02], [LOB 00], [LEY 02], [CAS 00a], but recent progress in air-coupled transducers [HOS 01b], [TRE 98] enables us to make measurements in air [ZHA 99], [CAS 00b]. Figure 20.3 presents some photographs of both types of measurement benches. To optimize the system efficiency, the emitter (E) is excited by a temporal signal whose frequency spectrum coincides with its bandwidth, and the signals delivered by the receiver (R) are amplified and filtered. The transducers are chosen for their frequency bandwidth, following a compromise that influences the efficiency of the technique: it must be sufficiently low to allow the consideration of each layer of the plate as a homogenous medium at the wavelength scale, but sufficiently high so that the sensitivity of the transmitted ultrasonic field (TUF) to the searched properties is significant. The angle  $\theta$  between the incident wave and the normal to the sample varies step by step between  $0^\circ$  (normal incidence) and the value of the transverse critical angle; this limit is easy to spot as the TUF is zero beyond it (the transverse and longitudinal waves are then evanescent and propagate along the insonified surface). About ten angular values are often sufficient to obtain the necessary information concerning the material characterization. The data thus obtained constitute the set  $\{s(t, \theta)\}$  which is then turned into a diagram  $\{S(f, \theta)\}$ . This diagram is then the support of information required to solve the inverse problem. Moreover, as for most of the propagation theories, the model used to simulate the transmitted ultrasonic field is based on the plane wave assumption, which considerably simplifies the calculations, because it eliminates the necessity of summing over several plane waves in different directions to reconstruct the bounded beams. The counterpart is that the experimental technique must fulfill, at best, this assumption, so that the measurements are comparable to the numerical predictions. For this, it is necessary to use transducers whose dimensions are big compared to the wavelength in the coupling medium; such transducers are thus of high directivity. In water, two pairs of rectangular IMASONIC [IMA 09] sensors are used: a pair of type 3258A of bandwidth  $[0.2 - 1]$  MHz down to  $-15$  dB, and of dimensions 40 mm by 100 mm, and a pair of type 4367A of bandwidth  $[75 - 240]$  kHz down to  $-15$  dB, and of dimensions 40 mm by 150 mm. In air, circular FOGALE NANOTECH [FOG 09] electrostatic sensors of bandwidth  $[100 - 400]$  kHz down to  $-15$  dB, and of diameter 50 mm, are used. This equipment enables us to cover a large frequency spectrum with a ratio “size-to-wavelength” comprising between 15 and 60, enabling us to consider the plane wave assumption as fully satisfied.

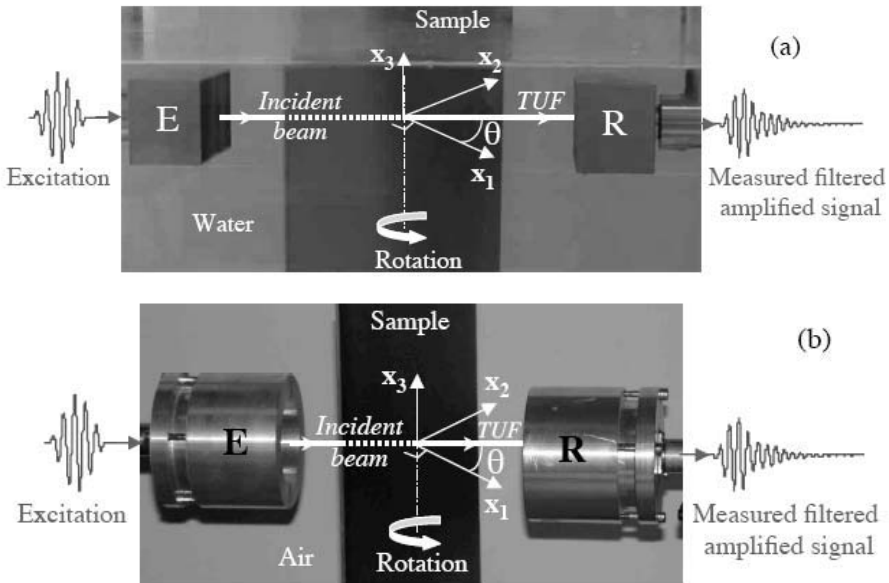


**Figure 20.3.** Photographs of characterization benches using transmitted ultrasonic fields; (a) water immersion technique and (b) air-coupled technique

#### 20.1.3.1. Characterization of simple plates by water immersion

This section presents a characterization example of a composite plate, immersed in water, made of unidirectional glass fibers embedded in an epoxy matrix, of

thickness 3.2 mm and density  $1940 \text{ kgm}^{-3}$ . Figure 20.4a shows the TUF when the

propagation plane coincides with the plane containing the fibers (symmetry plane  $P_{13}$ ) and for an incident angle of  $5^\circ$ . Figure 20.4b corresponds to the propagation in a non-principal plane making an angle of  $75^\circ$  with the direction of the fibers, and for an angle of incidence of  $40^\circ$ . The frequency range extends from 0.2 to 0.8 MHz. At these frequencies, the wavelengths of the waves propagating in the material are larger than a few millimeters. The homogenous medium assumption is thus fulfilled for this material, since its fibres are about several micrometers in diameter, and its plies are about  $100 \mu\text{m}$  thick.. The TUF spectra, calculated with some initial values of the complex viscoelasticity moduli, are presented by dotted lines (---). The values of the real parts  $C'_{ij}$  are chosen as a function of the assumed material stiffness, and

the imaginary parts  $C''_{ij}$  are fixed around 2 or 3 % of  $C'_{ij}$ . An approximate initial value is also assigned to the plate thickness. These parameters, provided in Table 20.1, serve as initial data to the numerical process of the inverse problem. The thickness and moduli optimization being done, the spectra are calculated again (—). Of course, the spectra calculated with the initial values correspond rarely to the measurements ( $\blacklozenge\blacklozenge\blacklozenge$ ), contrary to the spectra calculated with the optimized values.

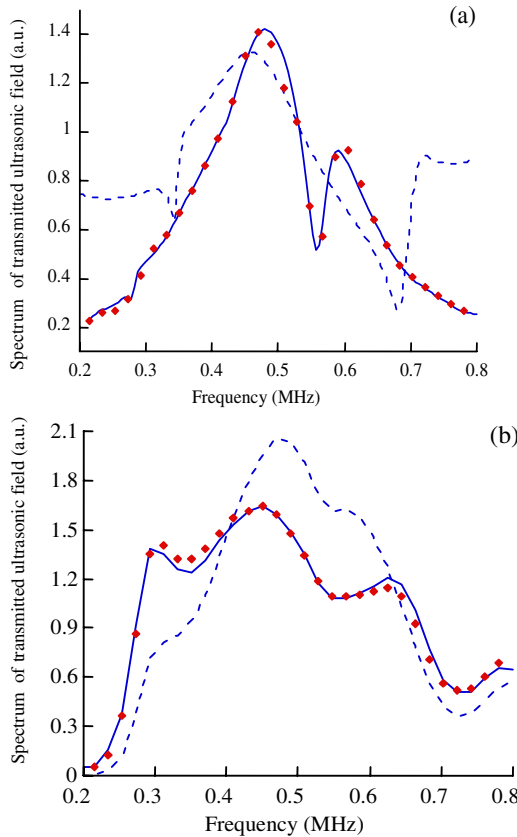


**Figure 20.4.** Spectra of transmitted ultrasonic fields for a unidirectional glass/epoxy plate immersed in water; (a) incident angle 5° and propagation in the plane  $P_{13}$  containing the fibers, (b) incident angle 40° and propagation in a plane making an angle of 75° with the fibers; Calculations with initial (---) and optimized (—) values of the complex moduli, ( $\blacklozenge\blacklozenge\blacklozenge$ ) measurements

The characterization measurements for this composite sample are given in Table 20.1. They enable us to check the hexagonal symmetry of this material, the

plane  $P_{12}$  perpendicular to the fibers being an isotropic transverse plane. In the same way, it is possible to characterize orthotropic materials ( $[0_3/90]$  stacking for example) or isotropic materials (metals, glasses, polymers, etc.).

	h	$C_{11}$	$C_{22}$	$C_{12}$	$C_{66}$	$C_{33}$	$C_{13}$	$C_{55}$	$C_{23}$	$C_{44}$
Initial values	3	15 + I 0.3	15 + I 0.3	10 + I 0.2	7 + I 0.1	35 + I 0.7	10 + I 0.2	8 + I 0.1	7 + I 0.1	7 + I 0.1
Optimized values	3.2 ± 0.1	19 ± 0.5 + I 0.9 ± 0.1	21 ± 0.9 + I 0.9 ± 0.2	9.1 ± 0.4 + I 0.3 ± 0.1	5.2 ± 0.1 + I 0.2 ± 0.1	54 ± 4 + I 2 ± 1	8.3 ± 0.9 + I 0.3 ± 0.2	6 ± 0.2 + I 0.3 ± 0.1	9.3 ± 0.4 + I 0.5 ± 0.1	5.7 ± 0.3 + I 0.3 ± 0.1

**Table 20.1.** Thickness (mm) and viscoelasticity moduli (GPa) measured for a unidirectional glass/epoxy plate coupled by water, transmitted ultrasonic fields technique

20.1.3.2. Characterization of simple plates placed in air

This section presents some characterization results obtained without contact, with the help of air-coupled ultrasonic transducers [CAS 00b]. The first sample is a Plexiglas plate of thickness 3.9 mm and density  $1200 \text{ kgm}^{-3}$ . The second sample is precisely the unidirectional glass/epoxy composite plate, which has been previously characterized in water. Figure 20.5 shows the TUF spectra for these two samples, for the same incident angle of  $12^\circ$ . In the case of the composite sample (Figure 20.5b), propagation occurs in the plane  $P_{12}$  perpendicular to the fibers.

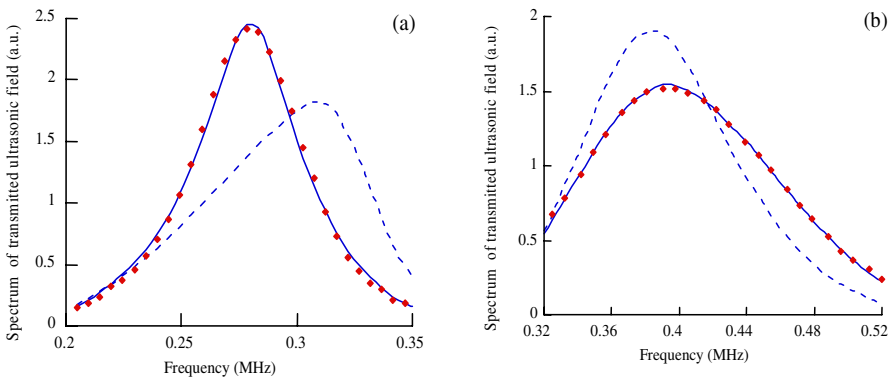


**Figure 20.5.** Spectra of the transmitted ultrasonic fields for a plate placed in air and for an incident angle of  $12^\circ$ ; (a) Plexiglas, (b) propagation in the plane  $P_{12}$  perpendicular to the fibers of the glass/epoxy composite; calculations with initial (---) and optimized (—) values of the moduli, (◆◆◆) measurements

The characterization results for these materials (only the principal planes  $P_{12}$  and  $P_{13}$  for the composite) are given in Tables 20.2 and 20.3, respectively. The isotropy laws,  $C_{11} = C_{22}$  and  $C_{12} = C_{11} - 2 C_{66}$ , are verified by the optimized values of the Plexiglas moduli. Moreover, these values remain unchanged, within the measurements errors, whatever the sample orientation in the coordinate system, thus confirming the material isotropy.

	h	$C_{11}$	$C_{22}$	$C_{12}$	$C_{66}$
Initial values	4	$10 \pm 1.0.2$	$10 \pm 1.0.2$	$5 \pm 1.0.1$	$3 \pm 1.0.06$
Optimized values	$3.9 \pm 0.1$	$8.5 \pm 0.1 +$ $1.0.36 \pm 0.02$	$8.3 \pm 0.2 +$ $1.0.6 \pm 0.2$	$3.9 \pm 0.1 +$ $1.0.12 \pm 0.08$	$2.5 \pm 0.2 +$ $1.0.1 \pm 0.1$

**Table 20.2.** Thickness (mm) and viscoelasticity moduli (GPa) measured for the Plexiglas plate by air-coupled transmitted ultrasonic fields technique

The optimized values of thickness and moduli of the composite agree perfectly with the results obtained using the water immersion technique, which validates the characterization process in air, which depends on recent transducer technology.

	h	$C_{11}$	$C_{22}$	$C_{12}$	$C_{66}$	$C_{33}$	$C_{13}$	$C_{55}$
Initial values	3	$15 \pm 1.0.3$	$15 \pm 1.0.3$	$10 \pm 1.0.2$	$7 \pm 1.0.1$	$35 \pm 1.0.7$	$10 \pm 1.0.2$	$8 \pm 1.0.1$
Optimized values	$3.2 \pm 0.1$	$19.1 \pm 0.2 +$ $1.0.9 \pm 0.1$	$19.5 \pm 0.3 +$ $1.0.9 \pm 0.3$	$8.8 \pm 0.1 +$ $1.0.3 \pm 0.1$	$5 \pm 0.1 +$ $1.0.3 \pm 0.2$	$50 \pm 1 +$ $1.1.8 \pm 0.9$	$8.4 \pm 0.2 +$ $1.0.2 \pm 0.1$	$5.8 \pm 0.2 +$ $1.0.3 \pm 0.2$

**Table 20.3.** Thickness (mm) and viscoelasticity moduli (GPa) measured for the composite glass/epoxy plate by air-coupled transmitted ultrasonic fields technique.

### 20.1.3.3. Characterization of a layer in a stratified plate

The goal is now to measure the thickness and the viscoelastic properties of a material (core) likely to be altered under the influence of aggressive environments (extreme temperatures, humidity, etc.), and embedded between two plates (skins) whose characteristics are known and supposed quasi-invariable. The measurement of the ultrasonic field transmitted by the trilayer, for several incidences, enables us to estimate the thickness and the complex viscoelastic moduli of the core, during the product life.

The first trilayer is an aeronautic industry radome. It is made of two glass/epoxy skins, with thicknesses equal to 1.3 and 4 mm and mass density equal to  $1560 \text{ kgm}^{-3}$ , separated by a core (rigid foam with closed pores) of estimated thickness 7.4 mm and mass density  $140 \text{ kgm}^{-3}$ . Water immersion of this structure

being banned, measurements are made with the help of air-coupled transducers. The frequency range is sufficiently low to ensure wavelengths that are significantly larger than the dimensions of the internal structure of the three linked elements (pores diameter, thickness of the material plies). Each element can thus be considered as a homogenous medium, so fulfilling the assumption of the models presented in Chapter 3, and likely to be used in the inversion process. Figure 20.6a presents spectra of measured (◆◆◆) and calculated TUF with initial (---) and optimized (—) values of thickness and complex modulus  $C_{11}$  of the foam core, for a normal incidence ( $\theta = 0^\circ$ ).

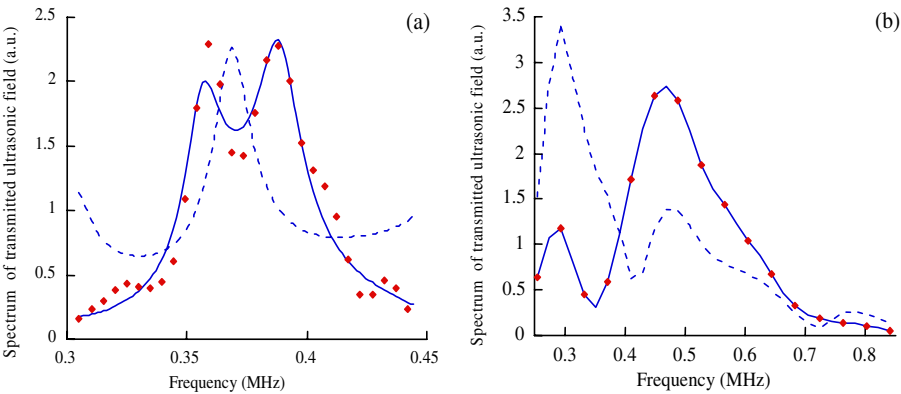


**Figure 20.6.** Spectra of ultrasonic fields transmitted by trilayered plates; (a) composite skin – foam core – composite skin (radome) placed in air and for  $0^\circ$  incident angle, (b) glass–glue–glass placed in water and for an incident angle of  $40^\circ$ ; calculations with initial (---) and optimized (—) values of the core moduli, (◆◆◆) mMeasurements

The characterization results for this foam core are given in Table 20.4. They enable us to check, within measurement errors, the isotropy of the material, as indicated by its manufacturer. Moreover, these results have been confirmed by measurements made on a separated foam plate (not presented here).

	h	$C_{11}$	$C_{22}$	$C_{12}$	$C_{66}$
Initial values	7	$1 \pm 1.02$	$1 \pm 1.02$	$0.5 \pm 1.01$	$0.2 \pm 1.01$
Optimized values	$7.3 \pm 0.1$	$0.48 \pm 0.03 +$ $1.03 \pm 0.01$	$0.55 \pm 0.05 +$ $1.04 \pm 0.01$	$0.22 \pm 0.03 +$ $1.01 \pm 0.005$	$0.14 \pm 0.02 +$ $1.006 \pm 0.003$

**Table 20.4.** Thickness (mm) and viscoelastic moduli (GPa) measured for the rigid foam core placed between two composite skins by air-coupled transmitted ultrasonic fields technique



The second trilayer consists of two glass plates, both of thickness 2 mm, linked by quite a thick layer of epoxy-based glue ( $> 1$  mm), with mass density equal to  $1000 \text{ kgm}^{-3}$ . Bonding is more and more widespread for assembling elements in many industrial sectors. It is thus crucial to be able to non-destructively control the quality of bonds. This implies characterizing the cohesive properties of the bond line (glue), and also the adhesive properties of interfaces. In this example, we assume the interface adhesion is satisfactory, due to the quasi-perfect state of the surfaces of the assembled glass plates, and the absence of air bubbles at the glue–glass interfaces (visually monitored through the glass). The goal is then to estimate the glue cohesion, measuring its complex viscoelastic moduli. The acoustic impedance of glass being quite large, it is better to use water-immersion than air-coupled TUF measurements. Figure 20.6.b presents the spectra of measured TUF (◆◆◆) and calculated TUF with initial (---) and optimized (—) values of the thickness and the complex moduli of the glue, for an angle of incidence of  $40^\circ$ . The characterization results are given in Table 20.5. They enable us to check, within measurement errors, the isotropic symmetry of the glue, and also that its cohesive properties are correct since the measured moduli are quite similar to those of epoxy. A significant decrease in these values would point out weakening of the glue. The thickness estimation is also consistent and has been controlled using a micrometer.

	H	$C_{11}$	$C_{22}$	$C_{12}$	$C_{66}$
Initial values	1	$5 + 10.3$	$5 + 10.3$	$3 + 10.15$	$1.5 + 10.075$
Optimized values	$1.3 \pm 0.05$	$5.9 \pm 0.3 + 10.7 \pm 0.2$	$5.6 \pm 0.3 + 10.4 \pm 0.2$	$3.4 \pm 0.2 + 10.3 \pm 0.1$	$1.1 \pm 0.2 + 10.1 \pm 0.05$

**Table 20.5.** Thickness (mm) and viscoelastic modules (GPa) measured for glue placed between two glass sheets by air-coupled transmitted ultrasonic fields technique

### 20.1.4. Conclusion

The presented characterization technique is based on measurement of the ultrasonic field transmitted (TUF) by a plate immersed in a fluid. It allows the thickness and mechanical properties of elastic or viscoelastic materials to be quantified. The tested material can constitute the whole sample or only a specific layer in it. This sample has to be of plane geometry and accessible from both sides to set the ultrasonic transducers. The coupling fluid between the transducers and the sample ensures the energy transfer necessary to insonify the plate and to detect the transmitted ultrasonic field. In the case of materials having high acoustic impedance (metals, glass, etc.), immersion in water is necessary, which leads to a dismantling,

drying and reassembling of the tested components. Conversely, for materials having a low or medium acoustic impedance (foams, woods, polymers, composites with organic-based matrices, etc.), air-coupling is possible thanks to significant technical progress accomplished recently in the domain of air-coupled ultrasonic transducers. This makes the measurement process easier and can enable, in some cases, the dismantling of parts to characterize to be skipped. Finally, the Simplex numerical method is very robust and often ensures a good convergence towards the exact solution of all the moduli of the propagation plane, even with poorly evaluated initial data. Consequently, its use is quite simple, even for non-technical people.

Other ultrasonic methods of characterization exist such as, for example, the well-known time-of-flight and attenuation measurements technique for longitudinal and transverse waves in plates [HOS 01a]. However, the transmitted ultrasonic field (TUF) method has a great advantage compared with this technique. Indeed the latter requires separating in time the various echoes between different surfaces, thus imposing a minimal limit to the thickness of the tested samples (generally 3 mm for frequencies around one MHz). Moreover, it requires the whole sample (and not only the internal layers) to be comparable to a homogenous medium at the wavelength scale. Consequently, in the case of stratified plates, the choice of the characterization frequency results from a compromise between the homogenous medium condition and the need of the various echoes to be separated in time. This choice is not always possible due to the sample geometry. On the contrary, the TUF technique does not require this temporal separation of echoes, and thus does not impose a minimal thickness for samples. However, the sensitivity of the measured field to the searched viscoelastic moduli will depend on the frequency–thickness product. Consequently, the user will prefer transducers with quite a high frequency (2 to 3 MHz) for the characterization of a plate or of a very thin internal layer ( $h < 1$  mm). This frequency could be as high as needed, as long as the element to characterize (plate or internal layers) remains homogenous at the wavelength scale.

Among the other characterization techniques, we can mention those based on the propagation of guided waves, like Lamb modes for example, which present some advantages [CHI 97]. First, these waves can be generated and detected placing the transducers at the same side of the sample, thus making the characterization of single-sided access components possible. Moreover, if the sample is not plane but has a small curvature characterized by a ratio  $R/h > 8$ , where  $R$  is the curvature radius and  $h$  the thickness, then the Lamb waves behave as if the medium were plane, and a Cartesian bidimensional model suits in the inverse problem resolution. On the contrary, if  $R/h < 8$ , then the curvature has a significant effect on the waves, making circumferential, helicoidal, axisymmetric, etc. modes appear. It is thus necessary to use an adapted model written in cylindrical coordinates [PAV 99]. On a practical level, considering the immersion of a sample in water, the adaptation of its impedance to that of piezoelectric transducers is often very restrictive as, during

their propagation, the guided waves may radiate a huge part of their energy into water. They are then quickly attenuated, making measurements difficult, especially because this process requires moving the receiver along the propagation path of the waves to measure their characteristics, necessary to identify the material properties. An alternative consists of using air-coupled ultrasonic transducers for generating and detecting guided waves, the technique thus becoming without contact. However, this process is only possible for materials with low or medium acoustic impedance. In other cases, a solution could be to use a piezoelectric transmitter in contact with the sample, and an air-coupled ultrasonic receiver, which can easily be moved to measure the characteristics of waves. This process is proposed in reference [CAS 02], but has allowed, so far, for the characterization of real parts (stiffnesses) of the complex viscoelastic moduli, only. This guided-waves-based method makes it possible to obtain the properties of a homogenous plate or of a homogenous layer located within a stratified medium. The estimation of the imaginary parts begins to be possible thanks to recent developments [CIN 04], but some progress is still needed in this domain.

In spite of the performance of the ultrasonic techniques mentioned in this section, it is important to keep in mind that the measured moduli are representative of the materials' dynamic behavior, as they are obtained from excitations of hundreds of kilohertz or several megahertz. Depending on whether the materials are elastic or viscoelastic, the moduli values measured in a dynamic regime will either be very small or large, respectively, different from values which would be measured in static or quasi-static regimes using mechanical tests (traction, torsion, etc.). Before any data are used, it is thus important to indicate their range of validity. For example, ultrasonic measurement results could be used to predict the behavior of a material in a static or quasi-static regime only if this material is elastic. Conversely, the values of moduli measured by ultrasounds for an elastic or viscoelastic material could always be used as input data to simulate wave propagation or diffraction by a flaw in a structure, in the purpose of setting an ultrasonic non-destructive testing process.

## 20.2. Bibliography

- [CAS 00a] Castaings M., Hosten B., Kundu T., "Inversion of ultrasonic, plane-wave transmission data in composite plates to infer viscoelastic material properties", *NDT & E Intern.*, vol. 33(6), 377–92, 2000.
- [CAS 00b] Castaings M., Hosten B., "Air-coupled measurement of plane-wave, ultrasonic plate transmission for characterizing anisotropic, viscoelastic materials", *Journal Ultrasonics*, vol. 38, 781–6, 2000.

- [CAS 02] Castaings M., “Contrôle et évaluation non destructifs de matériaux par ondes ultrasonores guidées”, *Habilitation à Diriger des Recherches de l’Université Bordeaux 1*, n° d’ordre 230, 2002, available at: [www.lmp.u-bordeaux.fr/~um/Castaings/](http://www.lmp.u-bordeaux.fr/~um/Castaings/).
- [CHI 97] Chimenti D.E., “Guided waves in plates and their use in materials characterization”, *Appl. Mech. Rev.*, 50, 247–84, 1997.
- [CIN 04] Cinquin M., Suivi par ondes guidées de l’état de santé de réservoirs composites. Thesis, University of Bordeaux 1, n° d’ordre 2934, 2004, available at: <http://www.lmp.u-bordeaux1.fr/>.
- [FOG 09] Fogale Nanotech, Available at: [www.fogale.fr](http://www.fogale.fr), 4 May 2009.
- [HOS 01a] Hosten B., “Ultrasonic Through-Transmission Method for Measuring the Complex Stiffness Moduli of Composite Materials”, Chapter 3 of *Volume I: Dynamic Methods for Measuring the Elastic Properties of Solids*, Every A. and Sachse W. (Eds.), Handbook of Elastic Properties of Solids, Liquids, and Gases, Academic Press, 2001.
- [HOS 01b] Hosten B., Biateau C., Castaings M., Rozière D., “Etude et caractérisation de transducteurs à couplage par air pour l’évaluation et le contrôle non destructifs des matériaux”, *Instrumentation Mesure Métrologie*, vol. 1 (1–2), 169–89, 2001.
- [IMA] Imasonic, Available at: [www.imasonic.com/](http://www.imasonic.com/), 4 May 2009.
- [LEY 02] Leymarie N. *et al.*, “Identification of complex stiffness tensor from waveform reconstruction”, *J. Acoust. Soc. Am.*, 111 (3), 1232–1244, 2002.
- [LOB 00] Lobkis O.I., Chimenti D.E., Zhang H., “In-plane elastic property characterization in composite plates”, *J. Acoust. Soc. Am.*, 107 (4), 1852–8, 2000.
- [PAV 99] Pavlakovic B., Lowe M., “A general purpose approach to calculating the longitudinal and flexural modes of multi-layered embedded transversely isotropic cylinders”, *Review of Progress in Quantitative NDE*, D.O. Thompson and D.E. Chimenti (Eds.), vol. 18, Plenum Press, New York, 239–46, 1999.
- [PRE 97] Press W.H., Teukolsky S.A., Vetterling W.T., Flannery B.P., *Numerical Recipes in C – The Art of Scientific Computing*, Cambridge Univ. Press 2<sup>nd</sup> ed., 1997.
- [ROK 02] Rokhlin S.I., Wang L., “Ultrasonic waves in layered anisotropic media: characterization of multidirectional composites”, *Int. Journal of Solids and Structures*, 39, 5529–45, 2002.
- [TRE 98] Trétout H., “Review of advanced ultrasonic techniques for aerospace structures”, *ECDNT Proceedings (NDT.net)*, vol. 3 (9), 1998.
- [ZHA 99] Zhang H., Chimenti D. E., “Air-Coupled Ultrasonic Beam Transmission Applied to Material Characterization”, *Review of Progress in Quantitative NDE*, D. O. Thompson and D. E. Chimenti, (eds), vol 18, , Plenum Press, New York, 1273–80, 1999.

## Chapter 21

# Interaction of an Ultrasonic Field with a Composite Plate

### 21.1. Introduction

As indicated in Chapter 14, the numerical simulation of experimentation for the ultrasonic testing of composite plates can gather useful information for the determination and optimization of testing parameters. The calculation requires taking into account, with sufficient precision, the formation of ultrasonic beams, generally created by transducers, as well as the interaction of these beams with the multilayered structures which model the composite materials.

In the case where the transducer can be simulated by a transmitter plane, and where the composite structure is composed of parallel plane layers, the plane waves decomposition method, introduced in Chapter 14, can be advantageously used.

This section describes the procedure for the implementation of this method. The plane multilayered structure is made of  $Q$  layers composed of (generally anisotropic) elastic solids. It separates a fluid  $F^{(0)}$ , in which is located the transmitter and eventually the reflection receiver, from a fluid  $F^{(Q+1)}$ , generally identical to the fluid  $F^{(0)}$ , in which a transmission receiver could be located.

The geometry describing the problem, as well as the choice of the various coordinate systems necessary to the calculation, are described in the following section 21.1.1. The general form of spatial Fourier representations for the reflected and transmitted ultrasonic fields is also established. Section 21.1.2. shows how a particular choice of receiving planes in reflection and transmission allows the calculation of these Fourier integrals by the FFT algorithm without the introduction of the Jacobean resulting from a variable change, which is generally necessary (see section 14.1.1, Chapter 14, equation [14.8] for example).

### 21.1.1. Geometry of the problem and writing of the fields by spatial Fourier representations

The geometry of the problem is illustrated on Figure 21.1. In particular, three space coordinate systems, necessary to the calculation, are indicated:

- the coordinate system  $\mathcal{R}^E = (O^E, X_1^E, X_2^E, X_3^E)$  linked to the transmitter plane;
- the coordinate system  $\mathcal{R} = (O, x_1, x_2, x_3)$  linked to the first interface of the multilayered structure;
- the coordinate system  $\mathcal{R}' = (O', x_1, x_2, x'_3)$ , of the same basis as the former but with different origin, linked to the last interface of the structure.

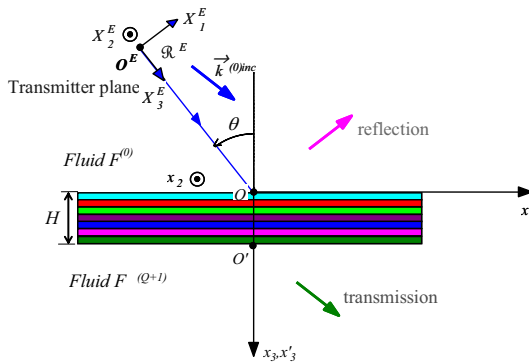


**Figure 21.1.** Geometry of the problem

The emitting conditions, on the transmitter plane  $X_3^E = 0$ , concern the normal component  $u_3^E$  of the particle displacement in the fluid  $F^{(0)}$ . This emission will be

assumed monochromatic. The given amplitude distribution  $u_{30}^E(X_1^E, X_2^E)$  is generally symmetric with respect to the origin  $O^E$  of the plane. The  $O^E X_3^E$  - axis is then called acoustic axis of the transmitted beam in the fluid  $F^{(0)}$ . The angle  $\theta$ , made by this acoustic axis with the normal  $Ox_3$  to the structure planes, is referred to as the incident beam angle.

The amplitude distribution  $u_{30}^E(X_1^E, X_2^E)$  will generally be complex valued. An adapted choice of the phase factor of this distribution allows the simulation of a focalized beam.

With the aim of writing the boundary conditions along the plane interfaces separating the diverse fluid and solid media, representing the acoustic fields with the particular displacement  $\vec{u}$  is a good choice.

Thus the incident field will be described by the Fourier integral representation of its displacement field:

$$\vec{u}^{inc}(X_1^E, X_2^E, X_3^E) = \int_{-\infty}^{+\infty} \int_{-\infty}^{+\infty} \vec{U}_E^{inc}(K_1^E, K_2^E) e^{-i\vec{k}^{(0)inc} \cdot \vec{O^E M}} dK_1^E dK_2^E, \quad [21.1]$$

where the temporal dependence  $e^{i\omega t}$  is implicit. The coordinate system  $\mathcal{R}^E$  is used here for this representation. The subscript  $E$  of the angular spectrum vector  $\vec{U}_E^{inc}$  means that the displacement amplitudes are referenced in the plane  $(O^E, X_1^E, X_2^E)$ . More explicitly,

$$\vec{u}^{inc}(X_1^E, X_2^E, X_3^E) = \int_{-\infty}^{+\infty} \int_{-\infty}^{+\infty} \vec{U}_E^{inc}(K_1^E, K_2^E) e^{-i(K_1^E X_1^E + K_2^E X_2^E + K_3^{(0)E} X_3^E)} dK_1^E dK_2^E, \quad [21.2]$$

where the components  $K_1^E, K_2^E, K_3^{(0)E}$  of the wavevector  $\vec{k}^{(0)inc}(K_1^E, K_2^E)$  in the basis  $\mathcal{B}^E$  associated with the coordinate system  $\mathcal{R}^E$  are related to each other by the dispersion relation in the fluid  $F^{(0)}$ :

$$\left\| \vec{k}^{(0)inc} \right\|^2 = \left( K_1^E \right)^2 + \left( K_2^E \right)^2 + \left( K_3^{(0)E} \right)^2 = \left( k^{(0)} \right)^2 = \left( \frac{\omega}{V^{(0)}} \right)^2. \quad [21.3]$$

Equation [21.3] enables us to express  $K_3^{(0)E}$  as a function of the integration variables  $K_1^E, K_2^E$ . The root choice for  $K_3^{(0)E}$  is imposed by the fact that the plane  $X_3^E = 0$  emits the acoustic beam in the half-space  $X_3^E > 0$ . This situation is expressed by a propagation or attenuation direction towards increasing  $X_3^E$  for each plane wave involved in representation [21.2]:

$$\vec{u}_{K_1^E, K_2^E}^{inc} = \vec{U}_E^{inc} \left( K_1^E, K_2^E \right) e^{-i \left( K_1^E X_1^E + K_2^E X_2^E + K_3^{(0)E} X_3^E \right)}. \quad [21.4]$$

The current plane wave [21.4] propagates in the fluid  $F^{(0)}$ . This current wave is thus longitudinal, and the corresponding displacement vector  $\vec{U}_E^{inc} \left( K_1^E, K_2^E \right)$  is collinear to the wavevector  $\vec{k}^{(0)inc} \left( K_1^E, K_2^E \right)$ . We can write:

$$\vec{U}_E^{inc} \left( K_1^E, K_2^E \right) = A_E^{inc} \left( K_1^E, K_2^E \right) \frac{\vec{k}^{(0)inc} \left( K_1^E, K_2^E \right)}{k^{(0)}}, \quad [21.5]$$

where we have highlighted the unitary vector in the wave propagation direction, and where  $A_E^{inc}$  is the displacement amplitude referenced in the transmitter plane  $\left( O^E, X_1^E, X_2^E \right)$ .

Consequently, the displacement field in the fluid is in fact a scalar field depending on the amplitude function  $A_E^{inc} \left( K_1^E, K_2^E \right)$ . This last one will be determined by inverse Fourier transformation from the data  $u_{30}^E \left( X_1^E, X_2^E \right)$  on the emitting plane as it has been seen in section 14.2.1, Chapter 14, equation [14.2]. In the present case, the emitting condition is written



$$u_{30}^E(X_1^E, X_2^E) = \int_{-\infty-\infty}^{+\infty+\infty} A_E^{inc}(K_1^E, K_2^E) \frac{K_3^{(0)E}}{k^{(0)}} e^{-i(K_1^E X_1^E + K_2^E X_2^E)} dK_1^E dK_2^E, \quad [21.6]$$

and it leads, by Fourier inversion, to the following integral expression for the amplitude  $A_E^{inc}(K_1^E, K_2^E)$ :

$$A_E^{inc}(K_1^E, K_2^E) = \frac{k^{(0)}}{K_3^{(0)E}} \frac{1}{(2\pi)^2} \int_{-\infty-\infty}^{+\infty+\infty} u_{30}^E(X_1^E, X_2^E) e^{i(K_1^E X_1^E + K_2^E X_2^E)} dX_1^E dX_2^E. \quad [21.7]$$

The Incident field [21.1] is thus perfectly determined by the knowledge of the plane waves that are present in its integral representation.

The following calculation consists of studying the interaction of each plane wave with the multilayered structure modeling the composite plate. For that purpose, we will apply one of the methods presented in Chapter 3, section 3.1.2 in order to determine the plane waves reflected in fluid  $F^{(0)}$  and transmitted in fluid  $F^{(Q+1)}$ .

The implementation of these standard methods, which involve identities with respect to the interfaces variables  $x_1, x_2$  (Figure 21.1) to express the physical continuity conditions, requires making a change of coordinate system to express the incident plane wave. The new coordinate system has to be linked to the multilayered structure geometry. We will choose the coordinate system  $\mathcal{R} = (O, x_1, x_2, x_3)$  where the origin  $O$  is taken at the impact point of the acoustic axis of the incident beam with the first interface of the structure.

The coordinate system change thus consists of a translation of the origin  $O^E$  towards the new origin  $O$ , followed by a rotation of angle  $\theta$  (beam incident angle). The translation corresponds to a phase change for the amplitude of the plane wave (see section 14.1.1, Chapter 14, equation [14.8]). The rotation corresponds to a change of projection basis to express the components of the wavevector  $\vec{k}^{(0)inc}$  and of the position vector  $\vec{OM}$ . According to the scalar product invariance, expression [21.4] of the incident plane wave, in the coordinate system  $\mathcal{R}$ , is finally written

$$\vec{u}_{K_1^E, K_2^E}^{inc}(x_1, x_2, x_3) = \vec{U}^{inc}(k_1, k_2) e^{-i(k_1 x_1 + k_2 x_2 + k_3^{(0)} x_3)}, \quad [21.8]$$

where  $k_1, k_2, k_3^{(0)}$  are the components of the wavevector  $\vec{k}^{(0)inc}(K_1^E, K_2^E)$  in the basis  $\mathbf{B}$  associated with the coordinate system  $\mathcal{R}$ , and where we have set:

$$\vec{U}^{inc}(k_1, k_2) = \vec{U}_E^{inc} \left[ K_1^E(k_1, k_2), K_2^E(k_1, k_2) \right] e^{-i\vec{k}^{(0)inc} \cdot \overrightarrow{O^E O}}, \quad [21.9]$$

the notation  $\vec{U}^{inc}$  without index  $E$  meaning that the displacement amplitudes are now referenced in the plane  $(O, x_1, x_2)$ .

The classical basis change formulae for the rotation of angle  $\theta$  allow us to easily express the old components  $K_1^E, K_2^E$  (and  $K_3^{(0)E}$ ) as a function of the new ones  $k_1, k_2$  (and  $k_3^{(0)}$ ) and vice versa.

The methods presented in section 3.1.2 of Chapter 3, thus apply directly to an incident plane wave written in the form [21.8]. The reflected plane wave, expressed in the same coordinate system  $\mathcal{R}$ , is searched according to the following form:

$$\vec{u}_{K_1^E, K_2^E}^{ref}(x_1, x_2, x_3) = \vec{U}^{ref}(k_1, k_2) e^{-i(k_1 x_1 + k_2 x_2 - k_3^{(0)} x_3)}. \quad [21.10]$$

In accordance with the comments which have been made on the optimal choice of phase origin for the amplitudes of the diverse plane waves involved in this problem, and in order to avoid the excessively high numerical values that may appear in the case of evanescent waves, it is logical to represent the transmitted wave in the coordinate system  $\mathcal{R}' = (O', x_1, x_2, x'_3)$  whose origin  $O'$  is located on the last interface of the structure, as indicated on Figure 21.1. The transmitted wave is then searched on the form:

$$\vec{u}_{K_1^E, K_2^E}^{tr}(x_1, x_2, x'_3) = \vec{U}^{tr}(k_1, k_2) e^{-i(k_1 x_1 + k_2 x_2 + k_3^{(Q+1)} x'_3)}. \quad [21.11]$$

The application of the methods described in section 3.1.2, Chapter 3 then leads to the determination of the amplitudes  $\vec{U}^{ref}(k_1, k_2)$  and  $\vec{U}^{tr}(k_1, k_2)$  through a reflection coefficient  $\mathcal{R}(k_1, k_2)$  and a transmission coefficient  $\mathcal{T}(k_1, k_2)$ . For example, because of the longitudinal property of these reflected or transmitted plane waves, the angular spectrum vector of the reflected wave can always be written:

$$\vec{U}^{ref}(k_1, k_2) = A^{ref}(k_1, k_2) \frac{k_1 \vec{e}_{x_1} + k_2 \vec{e}_{x_2} - k_3^{(0)} \vec{e}_{x_3}}{k^{(0)}}, \quad [21.12-a]$$

where the basis  $\mathbf{B} = (\vec{e}_{x_1}, \vec{e}_{x_2}, \vec{e}_{x_3})$  refers to the orthonormate basis of the coordinate system  $\mathcal{R}$ .

This amplitude  $A^{ref}(k_1, k_2)$  of the reflected field can be expressed as a function of the incident angle in the form:

$$A^{ref}(k_1, k_2) = \mathcal{R}(k_1, k_2) A^{inc}(k_1, k_2), \quad [21.12-b]$$

where we have set out

$$A^{inc}(k_1, k_2) = A_E^{inc} \left[ K_1^E(k_1, k_2), K_2^E(k_1, k_2) \right] e^{-i\vec{k}^{(0)inc} \cdot \overrightarrow{O^E O}}, \quad [21.13]$$

the amplitudes  $A^{inc}$  and  $A_E^{inc}$  being referenced in the planes  $(O, x_1, x_2)$  and  $(O^E, X_1^E, X_2^E)$ , respectively.

In addition, the angular spectrum vector of the transmitted wave is written

$$\vec{U}^{tr}(k_1, k_2) = A^{tr}(k_1, k_2) \frac{k_1 \vec{e}_{x_1} + k_2 \vec{e}_{x_2} + k_3^{(Q+1)} \vec{e}_{x_3}}{k^{(Q+1)}}, \quad [21.14-a]$$

where the amplitude  $A^{tr}(k_1, k_2)$  of the transmitted field can be expressed as a function of the incident field in the form

$$A^{tr}(k_1, k_2) = \mathcal{T}(k_1, k_2) A^{inc}(k_1, k_2). \quad [21.14-b]$$

*Comment:* For a non-null incident angle  $\theta$ , the Fourier integral representation of the incident field [21.1] contains some plane waves which have a wavevector  $\vec{k}^{(0)inc}(K_1^E, K_2^E)$  directed (in projection) towards the negative  $x_3$ . This arrangement, unusual for a plane wave described as “incident”, must, however, be taken into account for the calculation of the reflection and transmission coefficients  $\mathcal{R}(k_1, k_2)$  and  $\mathcal{T}(k_1, k_2)$ . The propagation direction of the reflected and

transmitted plane waves associated with such an incident wave has to be changed, in projection on the  $Ox_3$ -axis, in comparison with the usual writing.

However, if the incident beam is not opened much angularly (we will say that the beam is collimated) and if the incident angle  $\theta$  is not too large, the useful integration range in the plane  $(K_1^E, K_2^E)$  will be limited to a domain in the neighborhood of the origin that is sufficiently small, in order to be able to ignore this difficulty.

The last step of the calculation consists of applying the superposition principle (linearity of the propagation equations and boundary conditions) to the integral representation [21.1]. The global incident field, described by this Fourier integral, yields a reflected and a transmitted field which could be expressed as the integral of the reflected and transmitted plane waves, respectively, inferred from the current incident plane wave, as they have just been calculated (equations [21.10] to [21.14b]).

First, these current incident, reflected and transmitted plane waves remain indexed to the pair  $(K_1^E, K_2^E)$  of initial integration variables on the basis associated with the transmitter. Returning to these initial variables, according to which the amplitude of the incident field  $A_E^{inc}(K_1^E, K_2^E)$  has been calculated (equation [21.7]), we can write the integral representations for the reflected and transmitted fields in the following form:

$$\vec{u}^{ref}(x_1, x_2, x_3) = \int_{-\infty}^{+\infty} \int_{-\infty}^{+\infty} \vec{U}^{ref}(K_1^E, K_2^E) e^{-i(k_1 x_1 + k_2 x_2 - k_3^{(0)} x_3)} dK_1^E dK_2^E, \quad [21.15]$$

$$\vec{u}^{tr}(x_1, x_2, x_3) = \int_{-\infty}^{+\infty} \int_{-\infty}^{+\infty} \vec{U}^{tr}(K_1^E, K_2^E) e^{-i(k_1 x_1 + k_2 x_2 + k_3^{(Q+1)} x_3)} dK_1^E dK_2^E, \quad [21.16]$$

where the components  $k_1, k_2$  of the wavevector, as well as the third associated components  $k_3^{(0)}$  and  $k_3^{(Q+1)}$  in the fluids  $F^{(0)}$  and  $F^{(Q+1)}$ , are some known functions of the integration variables  $K_1^E, K_2^E$ . We choose here the simplified notation:

$$\vec{U}^{ref}(K_1^E, K_2^E) = \vec{U}^{ref} \left[ k_1(K_1^E, K_2^E), k_2(K_1^E, K_2^E) \right], \quad [21.17]$$

and

$$\vec{U}^{tr}(K_1^E, K_2^E) = \vec{U}^{tr} \left[ k_1(K_1^E, K_2^E), k_2(K_1^E, K_2^E) \right]. \quad [21.18]$$

It should be noted that representations [21.15] and [21.16] are not, strictly speaking, Fourier integrals, as the integration variables  $K_1^E, K_2^E$  differ from the conjugate variables  $k_1, k_2$ , dual of  $x_1, x_2$ .

However, their numerical estimation, using classical methods, is possible and relatively fast using matrix programming methods. It enables us to calculate the physical field at points of coordinates  $(x_1, x_2, x_3)$  linked to the geometry of the structure, while keeping the transmitter plane as an integration plane. This avoids several singularities.

On the contrary, if we wish to use, for the numerical calculation of the reflected and transmitted fields, the classical (double) FFT algorithm, we must transform representations [21.15] and [21.16] in order to obtain authentic Fourier integrals. This can be made, for example, for a not very opened (collimated) beam with a low incident angle, taking  $k_1, k_2$  as new integration variables. It is then necessary to introduce the Jacobian of this variable change as has been explained in Chapter 14.1.1, equation [14.8]. The FFT method then provides the physical field values in planes parallel to the interfaces of the structure.

If we wish to calculate, using the FFT method, the reflected or transmitted fields in other families of planes, for example in a receiving plane, in reflection in fluid  $F^{(0)}$  or in transmission in fluid  $F^{(Q+1)}$ , it will be necessary to introduce other integration variables. The following section shows how, with a judicious choice of these receiving planes, the calculation of the integral representations by FFT can remain simple, in particular avoiding the introduction of the Jacobian determinant and the singularities that this Jacobian risks to produce for the integral calculation, taking account some multivalued functions.

### 21.1.2. Implementation of a field-calculation method by FFT algorithm

The Integral representations [21.15] and [21.16] obtained in the previous section for the reflected and transmitted fields can be also written:

$$\vec{u}^{ref}(x_1, x_2, x_3) = \int_{-\infty-\infty}^{+\infty+\infty} \vec{U}^{ref}(K_1^E, K_2^E) e^{-i\vec{k}^{(0)ref} \cdot \overrightarrow{OM}} dK_1^E dK_2^E, \quad [21.19]$$

and

$$\vec{u}^{tr}(x_1, x_2, x'_3) = \int_{-\infty-\infty}^{+\infty+\infty} \vec{U}^{tr}(K_1^E, K_2^E) e^{-i\vec{k}^{(Q+1)tr} \cdot \overrightarrow{O'M}} dK_1^E dK_2^E, \quad [21.20]$$

where the wavevectors  $\vec{k}^{(0)ref}$  and  $\vec{k}^{(Q+1)tr}$  appear explicitly, in the fluid  $F^{(0)}$  and  $F^{(Q+1)}$ , respectively, associated with the current reflected and transmitted plane waves.

As already pointed out, representations [21.19] and [21.20] are not Fourier integrals. For that purpose, it is necessary that the integration variables are chosen among the components of the wavevectors written in the exponentials.

To calculate the double Fourier integrals by the FFT algorithm, it is also advisable to choose in the physical space, for each integral, the plane of the equidistributed points occurring in the construction of the associated discrete Fourier transformation (DFT). For this purpose, for the numerical estimation of the reflected and transmitted fields, we introduce two new coordinate systems  $\mathcal{R}^R = (O^R, X_1^R, X_2^R, X_3^R)$  and  $\mathcal{R}^T = (O^T, X_1^T, X_2^T, X_3^T)$ , linked to the receiving planes in reflection and in transmission, respectively (Figure 21.2). These coordinate systems are chosen such that the receiving plane in reflection, in which the discrete points will be located, corresponds to the plane  $X_3^R = 0$ , and the receiving plane in transmission to the plane  $X_3^T = 0$ .

Using the coordinate system  $\mathcal{R}^R$ , integral representation [21.19] can be written

$$\vec{u}^{ref}(X_1^R, X_2^R, X_3^R) = \int_{-\infty-\infty}^{+\infty+\infty} \vec{U}_R^{ref}(K_1^R, K_2^R) e^{-i\vec{k}^{(0)ref} \cdot \overline{O^R M}} \frac{\partial(K_1^E, K_2^E)}{\partial(K_1^R, K_2^R)} dK_1^R dK_2^R, \quad [21.21]$$

where  $K_1^R, K_2^R$  (and  $K_3^{(0)R}$ ) now refer to the components of the wavevector  $\vec{k}^{(0)ref}$  in basis  $\mathcal{B}^R$  of coordinate system  $\mathcal{R}^R$  and where we have set out:

$$\vec{U}_R^{ref}(K_1^R, K_2^R) = \vec{U}^{ref}[K_1^E(K_1^R, K_2^R), K_2^E(K_1^R, K_2^R)] e^{-i\vec{k}^{(0)ref} \cdot \overline{O O^R}}. \quad [21.22]$$

For any choice of the coordinate system  $\mathcal{R}^R$ , integral [1.21] contains the Jacobian that describes the change of the old integration variables  $K_1^E, K_2^E$  to the new ones  $K_1^R, K_2^R$ . This integral will generally be applied on generally multivalued functions.

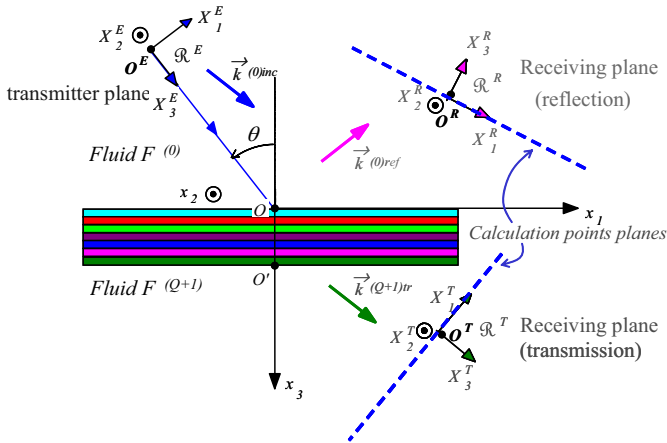


**Figure 21.2.** Choice of receiving planes in reflection and in transmission and associated coordinate systems – general situation

It must be noted that the calculation of functions  $K_1^E(K_1^R, K_2^R), K_2^E(K_1^R, K_2^R)$  is made by the following correspondence, where the intermediate coordinate system  $\mathcal{R}$ , and thus the incident angle  $\theta$ , are necessarily involved:

$$\vec{k}^{(0)inc} \xrightarrow{(\mathcal{B}^E)} \{K_1^E, K_2^E\} \xrightarrow{(\mathcal{B})} \{k_1, k_2, (k_3^{(0)})\} \Rightarrow \vec{k}^{(0)ref} \xrightarrow{(\mathcal{B}^R)} \{K_1^R, K_2^R\}, \quad [21.23]$$

where the symmetry law of  $\vec{k}^{(0)inc}$  and  $\vec{k}^{(0)ref}$  with respect to the interface  $x_3 = 0$  must be used.

For any choice of the coordinate system  $\mathcal{R}^R$ , this correspondence will generally not be unique and the Jacobian in the integral may take infinite values. Here also, the use of incident collimated beams will often allow this difficulty to be ignored.

A similar process can be applied to transform integral representation [21.20] of the transmitted field using the coordinate system  $\mathcal{R}^T$ . We will write:

$$\vec{u}^{tr}(X_1^T, X_2^T, X_3^T) = \int_{-\infty-\infty}^{+\infty+\infty} \vec{U}_T^{tr}(K_1^T, K_2^T) e^{-i\vec{k}^{(Q+1)tr} \cdot \overline{O^T M}} \frac{\partial(K_1^E, K_2^E)}{\partial(K_1^T, K_2^T)} dK_1^T dK_2^T, \quad [21.24]$$

where  $K_1^T, K_2^T$  (and  $K_3^{(Q+1)T}$ ) refer to the components of the wavevector  $\vec{k}^{(Q+1)tr}$  in the basis  $\mathcal{B}^T$  of coordinate system  $\mathcal{R}^T$  and where we have set out:

$$\vec{U}_T^{tr}(K_1^T, K_2^T) = \vec{U}^{tr} \left[ K_1^E(K_1^T, K_2^T), K_2^E(K_1^T, K_2^T) \right] e^{-i\vec{k}^{(Q+1)tr} \cdot \overline{O^T O^T}}. \quad [21.25]$$

The correspondence between the old variables  $K_1^E, K_2^E$  and the new ones  $K_1^T, K_2^T$  is written:

$$\vec{k}^{(0)inc} \xrightarrow{(\mathcal{B}^E)} \{K_1^E, K_2^E\} \xrightarrow{(\mathcal{B})} \{k_1, k_2, (k_3^{(0)})\} \Rightarrow \vec{k}^{(Q+1)tr} \xrightarrow{(\mathcal{B}^T)} \{K_1^T, K_2^T\}, \quad [21.26]$$

where the refraction law must be used to deduce the transmitted wavevector  $\vec{k}^{(Q+1)tr}$  from the incident one  $\vec{k}^{(0)inc}$ . Again, for any choice of the coordinate system  $\mathcal{R}^T$ , the Jacobian appearing in integral [21.24] can take infinite values and the integral can involve multivalued functions.



We will now choose favored locations for the coordinate systems  $\mathcal{R}^R$  and  $\mathcal{R}^T$ . We assume here that the two extreme fluids  $F^{(0)}$  and  $F^{(Q+1)}$  are identical, so that the incident and transmitted wavevector are equal:

$$\vec{k}^{(0)inc} = \vec{k}^{(0)tr}. \quad [21.27]$$

Under these conditions, if the coordinate system  $\mathcal{R}^T$  is chosen to have the same basis as the coordinate system  $\mathcal{R}^E$ , which amounts to choosing a receiving plane in transmission parallel to the transmitter plane (Figure 21.3), correspondence [21.26] is simply written:

$$K_1^T = K_1^E, \quad K_2^T = K_2^E, \quad (K_3^{(0)T} = K_3^{(0)E}), \quad [21.28]$$

then the Jacobian of integral [21.24] is equal to 1. This integral is thus written:

$$\vec{u}^{tr}(X_1^T, X_2^T, X_3^T) = \int_{-\infty-\infty}^{+\infty+\infty} \vec{U}_T^{tr}(K_1^E, K_2^E) e^{-i\vec{k}^{(0)inc} \cdot \vec{O}^T M} dK_1^E dK_2^E, \quad [21.29]$$

or more explicitly

$$\vec{u}^{tr}(X_1^T, X_2^T, X_3^T) = \int_{-\infty-\infty}^{+\infty+\infty} \vec{U}_T^{tr}(K_1^E, K_2^E) e^{-i(K_1^E X_1^T + K_2^E X_2^T + K_3^{(0)E} X_3^T)} dK_1^E dK_2^E. \quad [21.30]$$

An analogous approach can be followed for the reflected field calculation. Now the wavevectors  $\vec{k}^{(0)inc}$  and  $\vec{k}^{(0)ref}$  are not equal but are symmetric with respect to the interface  $x_3 = 0$ . Thus, if we choose for  $\mathcal{R}^R$  a coordinate system whose associated basis  $\mathcal{B}^R$  is the symmetric of basis  $\mathcal{B}^E$  of the coordinate system  $\mathcal{R}^E$  with respect to the plane  $x_3 = 0$  (Figure 21.3), the components of the wavevector  $\vec{k}^{(0)ref}$  in basis  $\mathcal{B}^R$  will be equal to those of vector  $\vec{k}^{(0)inc}$  in basis  $\mathcal{B}^E$ . Correspondence [1.23] is reduced to the equalities:

$$K_1^R = K_1^E, \quad K_2^R = K_2^E, \quad (K_3^{(0)R} = K_3^{(0)E}), \quad [21.31]$$

and the Jacobian of the variables change is equal to 1.

In this particular case, integral [21.24] is simplified on the form

$$\vec{u}^{ref}(X_1^R, X_2^R, X_3^R) = \int_{-\infty}^{+\infty} \int_{-\infty}^{+\infty} \vec{U}_R^{ref}(K_1^E, K_2^E) e^{-i\vec{k}^{(0)ref} \cdot \vec{O}^R M} dK_1^E dK_2^E, \quad [21.32]$$

that can be written explicitly

$$\vec{u}^{ref}(X_1^R, X_2^R, X_3^R) = \int_{-\infty}^{+\infty} \int_{-\infty}^{+\infty} \vec{U}_R^{ref}(K_1^E, K_2^E) e^{-i(K_1^E X_1^R + K_2^E X_2^R + K_3^{(0)E} X_3^R)} dK_1^E dK_2^E. \quad [21.33]$$

It should be noted that the basis  $\mathbf{B}^R$ , deduced from basis  $\mathbf{B}^E$  by symmetry with respect to the interface planes, is an indirect basis.

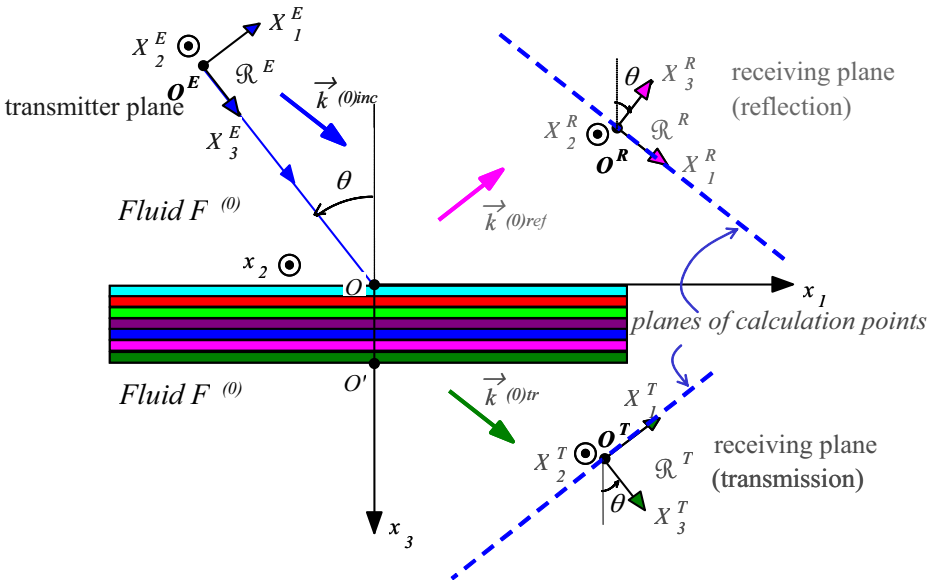


**Figure 21.3.** Choice of the receiving planes in reflection and in transmission and associated coordinate systems – particular configuration

In the chosen receiving planes in reflection and in transmission, the displacement fields will be written:

$$\vec{u}^{ref}(X_1^R, X_2^R, 0) = \iint_{-\infty-\infty}^{+\infty+\infty} \vec{U}_R^{ref}(K_1^E, K_2^E) e^{-i(K_1^E X_1^R + K_2^E X_2^R)} dK_1^E dK_2^E, \quad [21.34]$$

$$\vec{u}^{tr}(X_1^T, X_2^T, 0) = \iint_{-\infty-\infty}^{+\infty+\infty} \vec{U}_T^{tr}(K_1^E, K_2^E) e^{-i(K_1^E X_1^T + K_2^E X_2^T)} dK_1^E dK_2^E. \quad [21.35]$$

Representations [21.34] and [21.35] are double Fourier transformations which can be numerically estimated by a FFT algorithm.

It can be interesting to calculate the reflected and transmitted acoustic fields in terms of the acoustic pressure, in particular in receiving planes. Let us remember that for any plane monochromatic wave, propagating in fluid  $F^{(0)}$ , the pressure and displacement amplitudes, referenced in the same plane, are related by

$$P(K_1, K_2, \omega) = \frac{i\rho^{(0)}\omega^2}{K_3(K_1, K_2, \omega)} \vec{U}(K_1, K_2, \omega) \vec{e}_{X_3}, \quad [21.36]$$

where  $K_3(K_1, K_2, \omega)$  represents the wavevector component on the axis of the unitary vector  $\vec{e}_{X_3}$ .

The reflected pressure field can thus be expressed, in the coordinate system  $\mathcal{R}^R$ , by the integral representation

$$p^{ref}(X_1^R, X_2^R, X_3^R) = i\rho^{(0)}\omega^2 \iint_{-\infty-\infty}^{+\infty+\infty} \frac{\vec{U}_R^{ref}(K_1^E, K_2^E) \vec{e}_{X_3^R}}{K_3^{(0)E}} e^{-i(K_1^E X_1^R + K_2^E X_2^R + K_3^{(0)E} X_3^R)} dK_1^E dK_2^E. \quad [21.37]$$

Taking into account equations [21.9] and [1.22] translating the changes of reference planes for amplitude phases, and equation [21.12 b] introducing the

reflection coefficient, equation [21.37] can be written as a function of the data on the transmitter using the following final form:

$$p^{ref}(X_1^R, X_2^R, X_3^R) = i\rho^{(0)}\omega^2 \int_{-\infty-\infty}^{+\infty+\infty} \mathbf{R} \frac{U_{30}^E}{K_3^{(0)E}} e^{-i\phi_{ER}^{ref}} e^{-i(K_1^E X_1^R + K_2^E X_2^R + K_3^{(0)E} X_3^R)} dK_1^E dK_2^E, \quad [21.38]$$

where we have introduced the phase shift term

$$\phi_{ER}^{ref}(K_1^E, K_2^E) = \vec{k}^{(0)inc} \cdot \overrightarrow{O^E O} + \vec{k}^{(0)ref} \cdot \overrightarrow{OO^R}, \quad [21.39]$$

and where the amplitude  $U_{30}^E$  is associated with the data on the transmitter by the inverse Fourier transformation, deduced from [21.7],

$$U_{30}^E(K_1^E, K_2^E) = \frac{1}{(2\pi)^2} \int_{-\infty-\infty}^{+\infty+\infty} u_{30}^E(X_1^E, X_2^E) e^{i(K_1^E X_1^E + K_2^E X_2^E)} dX_1^E dX_2^E. \quad [21.40]$$

In addition, the transmitted pressure field will be expressed, in the coordinate system  $\mathcal{R}^T$ , by the integral representation

$$p^{tr}(X_1^T, X_2^T, X_3^T) = i\rho^{(0)}\omega^2 \int_{-\infty-\infty}^{+\infty+\infty} \int_{-\infty-\infty}^{+\infty+\infty} \frac{\vec{U}_T^{tr}(K_1^E, K_2^E) \cdot \vec{e}_{X_3^T}}{K_3^{(0)E}} e^{-i(K_1^E X_1^T + K_2^E X_2^T + K_3^{(0)E} X_3^T)} dK_1^E dK_2^E. \quad [21.41]$$

Similarly, taking into account equations [21.9] and [21.25] translating the changes of reference planes for amplitude phases, and equation [21.14 b] introducing the transmission coefficient, equation [21.41] can be written as a function of the data on the transmitter using the following final form:

$$p^{tr}(X_1^T, X_2^T, X_3^T) = i\rho^{(0)}\omega^2 \int_{-\infty-\infty}^{+\infty+\infty} \int_{-\infty-\infty}^{+\infty+\infty} \mathbf{T} \frac{U_{30}^E}{K_3^{(0)E}} e^{-i\phi_{ET}^{tr}} e^{-i(K_1^E X_1^T + K_2^E X_2^T + K_3^{(0)E} X_3^T)} dK_1^E dK_2^E, \quad [21.42]$$

where we have introduced the phase shift term

$$\phi_{ET}^{tr}(K_1^E, K_2^E) = \vec{k}^{(0)inc} \cdot \overrightarrow{O^E O} + \vec{k}^{(0)tr} \cdot \overrightarrow{O' O^T}, \quad [21.43]$$

the transmission coefficient  $T$  being referenced with respect to the plane  $(O' x_1 x_2)$ .

It should be noted that, because of equations [21.28] and [21.31], the sampling is the same in the transmitter plane and in the receiving planes (in reflection and in transmission).

In summary, the calculation principle is the following:

1) The motion of the transducer front side is simulated by the normal displacement on the corresponding plane through an analytic expression. Experimental measurements taking into account a real transducer can also be used, which allows us to simulate a whole experiment.

2) This field is decomposed into plane waves which propagate in the emission fluid. For each plane wave, we know how to process analytically (or numerically) the problem of its propagation in the medium, and its interaction with a plane interface.

3) The reflection and transmission coefficients are calculated (for each plane oblique monochromatic wave) using one of the methods described in section 3.1.2 or 3.1.3 of Chapter 3 (global matrix method, transfer matrix method, stiffness or surfacic impedance matrices method).

4) A Fourier transform, calculated numerically either by classical integration methods, or by a FFT algorithm, enables then to return to the spatial domain. We can thus reconstruct the displacement field in a receiving plane corresponding to the reflected or to the transmitted field.

Figure 21.4 shows a calculation example of field reflected in water, in a plane parallel to a unidirectional carbon/epoxy plate whose characteristics are given in Table 21.1, and shows the specular reflection area and the non specular one, when a Lamb mode is excited in the plate.

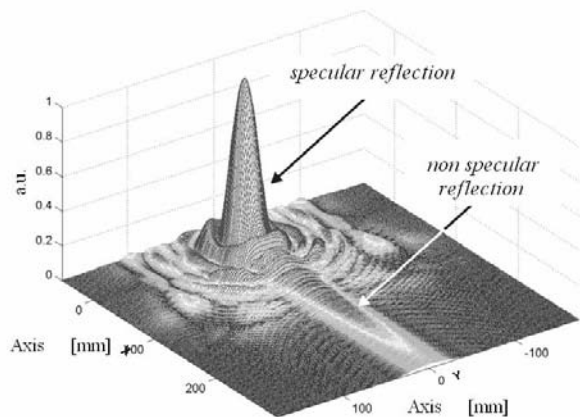


**Figure 21.4.** Reflected pressure field, in a plane parallel to a unidirectional carbon/epoxy plate of thickness  $H = 0.59\text{ mm}$ ,  $f = 1.35\text{ MHz}$ , mode  $S_0$ , the 6th-order axis being parallel to the axis  $x_1$ . Figure extracted from [POT 05]

$C_{11}$	$C_{12}$	$C_{22}$	$C_{23}$	$C_{44}$	$C_{55}$	$\rho\text{ (kg/m}^3\text{)}$
126	6.7	13.7	7.1	3.3	5.8	1580

**Table 21.1.** Elastic constants in GPa of carbon/epoxy when the symmetry axis  $A_6$  (hexagonal symmetry) is parallel to  $x_1$ -axis, with  $c_{55} = (c_{22} - c_{23})/2$ .

Extracted from [CAS 93]

21.2. Bibliography

[CAS 93] Castaings M., Propagation ultrasonore dans les milieux stratifiés plans constitués de matériaux absorbants et orthotropes, PhD, University of Bordeaux I, 1993

[POT 05] Potel C., Baly S., de Belleval J.F., Lowe M., Gagniol Ph., “Deviation of a monochromatic Lamb wave beam in anisotropic multilayered media: asymptotic analysis, numerical and experimental results”, *IEEE Trans. Ultrasonics Ferroel. Freq. Contr.*, 52 (6), 987–1001, 2005

## Chapter 22

# Flaw Detection by Lamb Waves

### 22.1. Introduction

A great number of elements used in the aeronautical industry are thick structures with large surface areas. Composites being increasingly used in this type of structure, we need to control these elements to a greater extent. This is often done using ultrasound with normal incidence, but this requires the control to be of a very long duration. The use of Lamb waves (see Chapter 5) would enable us to control a whole band of the structure with a single scanning direction, and consequently to significantly reduce the duration of the control. In fact, Lamb waves have some advantages in comparison with the other types of elastic waves such as bulk or surface waves:

- Lamb waves are naturally guided by a plate and thus have a relatively low attenuation during their propagation;
- we can choose modes for which there is no dead zone in the plate thickness;
- the presence of a flaw modifies the propagation of these plate waves, and thus a displacement along a line enables us to control the whole surface (Figure 22.1).

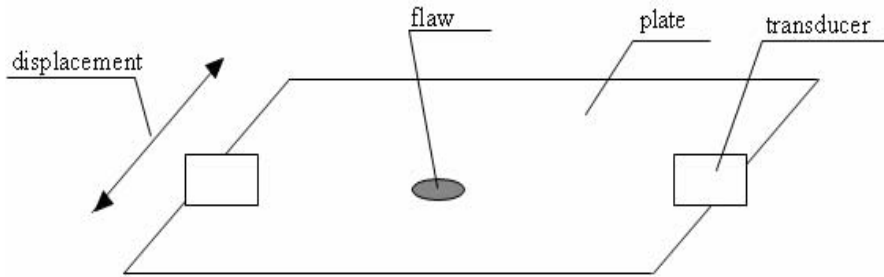


**Figure 22.1.** *Displacement of a transducer along a line, in order to control the whole surface*

One of the easiest ways to generate these waves consists of using a transducer with oblique incidence in a fluid, classically water (total or partial immersion).

Sections 22.1.1 and 22.1.2 give the results of experiments made on four carbon/epoxy plates with a Teflon flaw, using a transmission set-up (section 22.1.1) and a pitch-catch set-up (section 22.1.2). The calculation of the stress distribution as a function of the thickness can also give some pieces of information (section 22.1.3). Finally, a deviation phenomenon of the modal wave beam (Lamb waves) in a unidirectional composite plate is described in section 22.1.4, which helps, during a control with Lamb waves, to take into account the anisotropy.

### 22.1.1. *Transmission control*

Some experiments have been made on four carbon/epoxy plates provided by EADS, each having a mirror symmetry and eight plies of thickness 0.15 mm [POT 97]:

- two flawless plates, of sequences  $0^\circ/90^\circ$  and  $0^\circ/45^\circ/90^\circ/135^\circ$ ;
- two plates having a Teflon flaw of dimensions  $8 \times 25 \text{ mm}^2$ , located between the third and fourth plies, of sequences  $0^\circ/90^\circ$  and  $0^\circ/45^\circ/90^\circ/135^\circ$ .

A classical method for the experimental generation of generalized Lamb waves consists of placing two transducers of the same nominal frequency on the same side of the plate [NAY 88], and inclining them with the angle corresponding to the Lamb wave propagation at the transducer frequency. An equivalent method, chosen here for its simplicity of assembly, consists of placing the two transducers on both sides of the plate [FAR 94]. As shown in Figure 22.2, this enables the inclination of the plate to be adjusted, once the adjusting of the two transducers is completed.



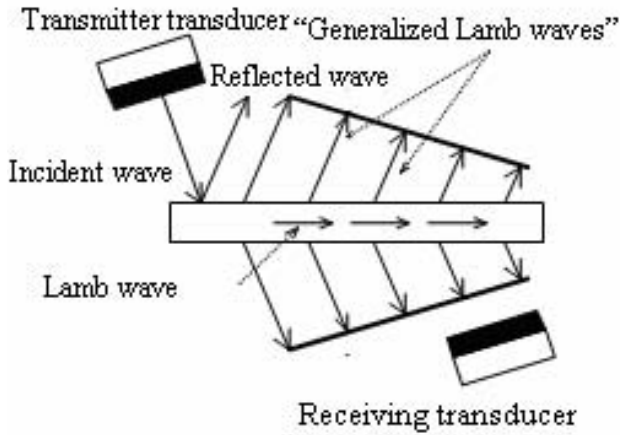


**Figure 22.2.** *Transmission set-up enabling the generation of Lamb waves*

The problem is as follows: knowing that the presence of the flaw modifies the Lamb wave propagation, but which mode will enable this flaw to be detected?

A Lamb mode which propagates in the unflawed part of the plate will be disturbed by the presence of a flaw, and this will provoke a mode conversion. A second mode conversion will occur after the flaw, and a strong attenuation of the incident mode will then be observed. The approach followed here consists of analyzing the dispersion curves of Lamb waves, obtained by the method described in section 5.1.4.1, Chapter 5, for the healthy plate (Figure 22.3) and the plates (three plies, see Figure 22.4) above and below the flaw, and to choose the adequate Lamb wave. In fact, if mode ② or mode ③ are near mode ①, mode ④, after the flaw, will be also near it, and the flaw will not be detected. On the contrary, if mode ② or mode ③ is different from mode ①, mode ④ will also be different, and the flaw will be detectable (Figure 22.5).

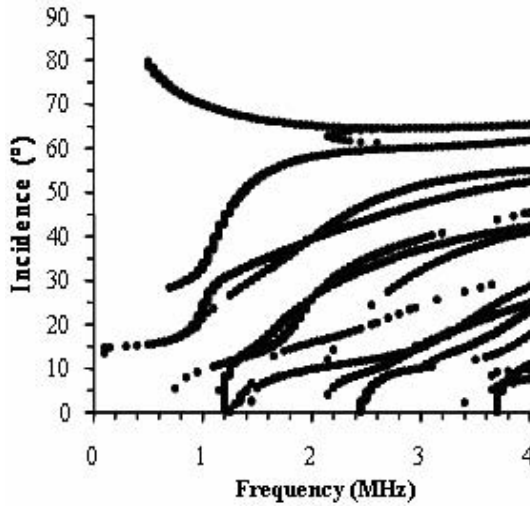


**Figure 22.3.** Dispersion curves of Lamb modes for a carbon/epoxy composite plate  $\{0^\circ/45^\circ/90^\circ/135^\circ\}_0$  with 8 plies in mirror symmetry. Calculation realized with the elastic constants of Table 21.1, Chapter 21

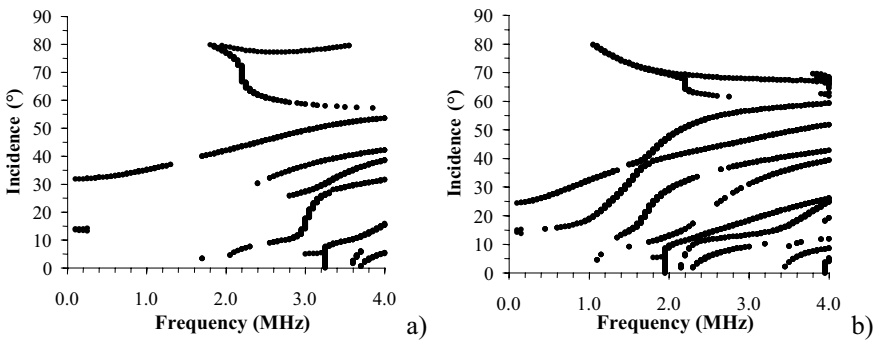


**Figure 22.4.** Dispersion curves of Lamb modes for a) 3 carbon/epoxy plies  $0^\circ/45^\circ/90^\circ$ , b) 5 carbon/epoxy plies  $135^\circ/135^\circ/90^\circ/45^\circ/0^\circ$

Thus, we observe in Figure.22.6 two signals corresponding to a plate  $\{0^\circ/45^\circ/90^\circ/135^\circ\}_0$  with and without a flaw. A decrease of the signal amplitude corresponds to the presence of the flaw.

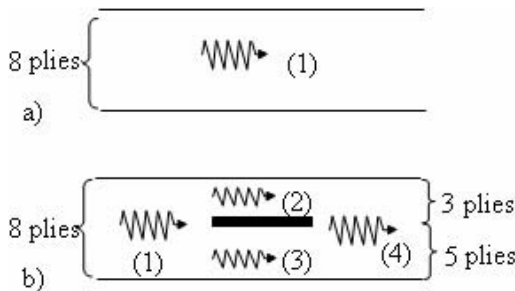


**Figure 22.5.** Lamb modes conversion in a healthy plate a) and in a plate with a flaw between the 3rd and the 4th plies b)

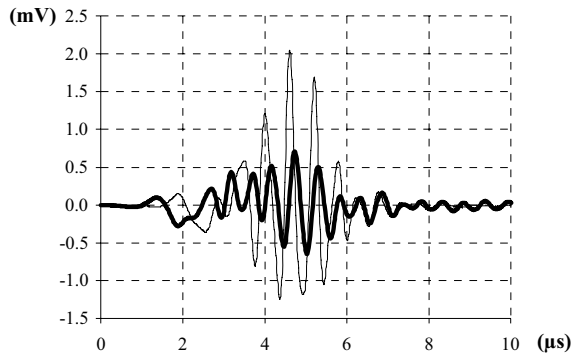


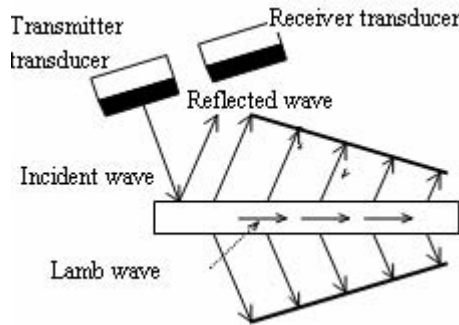
**Figure 22.6.** Flaw detection with a transmission set-up for a carbon/epoxy plate  $\{0^\circ/45^\circ/90^\circ/135^\circ\}_0$ , with 8 plies in mirror symmetry.  $10.3^\circ$  incidence, frequency of 2 MHz. Thick line: healthy plate; large line: plate with flaw

### 22.1.2. Scan control

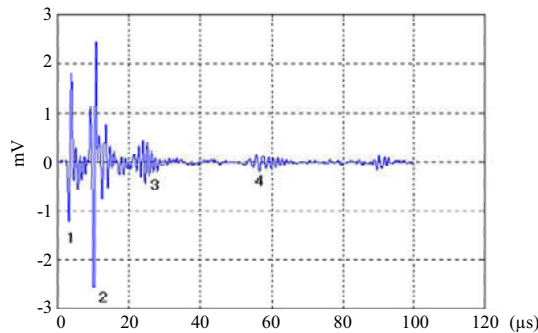
Another experimental system consists of placing the transmitter and the receiver on the same plane [FAR 94], as shown in Figure 22.7. When the two transducers are tilted with an angle corresponding to a Lamb mode, only one signal, corresponding to a flaw, will be received by the receiver.

Figure 22.8 represents a characteristic signal obtained in such a configuration for a plate  $\{0^\circ/45^\circ/90^\circ/135^\circ\}_0$  with a flaw, at a frequency of 1 MHz and an incidence of  $4^\circ$ .

- Echo ① corresponds to the specular reflection on the surface of the plate, related to the fact that the transducer has a beam with a certain angular aperture.
- Echo ② corresponds to a Lamb wave radiation towards left.
- Echo ③ corresponds to the echo from the flaw. The signal envelope is maximal when the two transducers point directly at the flaw.
- As the plate extremity can be compared to a geometrical flaw, echo ④ corresponds to it. Depending on the mode used, this echo is not always observed in the same time as echo ③ from the flaw.



**Figure 22.7.** *Pitch–catch set-up*



**Figure 22.8.** *Flaw detection by a pitch–catch set-up for a carbon/epoxy plate  $\{0^\circ/45^\circ/90^\circ/135^\circ\}_0^\circ$  having 8 plies in mirror symmetry. Characteristic signal obtained at a frequency of 1 MHz and for an incident angle equal to  $4^\circ$*

In the same way as for a control with normal incidence, it is possible, by single direction scanning, to obtain a cartography of the plate using a Lamb wave, as shown in Figure 22.9. The first vertical line corresponds to echoes ① and ②, always present, whether a flaw is present or not; its amplitude is superior to that of the echo from the flaw. The clearest part corresponds to the flaw.

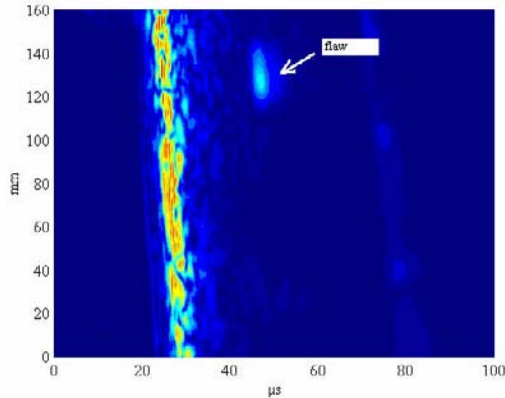


**Figure 22.9.** Cartography, using Lamb waves, of a carbon/epoxy plate  $\{0^\circ/90^\circ\}_{0^\circ}$  with 8 plies in mirror symmetry

### 22.1.3. Control using the stress distribution

Some cartographies using Lamb waves can also allow the visualization of diverse flaw types. Consequently, some experiments have been carried on a composite with five layers of thickness 0.197 mm each, (fibers SCS-6 in a Ti-6Al-4V matrix), with a stacking  $0^\circ/90^\circ$  and a mirror symmetry [KUN 96, MAS 97]. The first layer had no flaw, the second one a debonding, the third one some broken fibers, the fourth one missing fibers and the fifth one no flaw. Two controls, made around the incidence and the frequency at which a Lamb mode is obtained, enabled, depending on the case, the detection of a particular flaw, as shown on Figures 22.10 extracted from [KUN 96]. The calculation of stresses with plane waves has enabled the understanding that when a flaw is visible in a layer, the stress distribution in this layer is more important than in the other layers. In fact, the material being symmetrical, the stress distribution during the propagation of a Lamb mode is also symmetric. However, the experiments have been carried at frequencies either inferior, or superior to those for which a Lamb mode is generated, and that causes a stress dissymmetry. Thus, when the missing fibers are clearly observed in the fourth layer (Figure 22.10 a), experiments have been carried for frequencies greater than the one for which we obtain a Lamb mode: the normal stress in the fourth layer was

greater than that in the second layer (Figure 22.11a). Conversely, in the case of Figure 22.10b, these missing fibers are a lot less clearly observed, as the frequency was smaller than that for which a Lamb mode is obtained: the normal stresses in the fourth layer were also weaker than those in the second layer (Figure 22.11b).

The key for knowing if a flaw will be detected better in one layer or another is thus the stress distribution as a function of the thickness [KUN 01].

$C_{11}$	$C_{12}$	$C_{13}$	$C_{33}$	$C_{44}$	$\rho \text{ (kgm}^{-3}\text{)}$
150	96	50	900	70	4100

**Table 22.1.** Elastic constants in GPa (fibers SCS-6 in a Ti-6Al-4V matrix)  
when the symmetry axis  $A_6$  is parallel to the  $x_3$ -axis

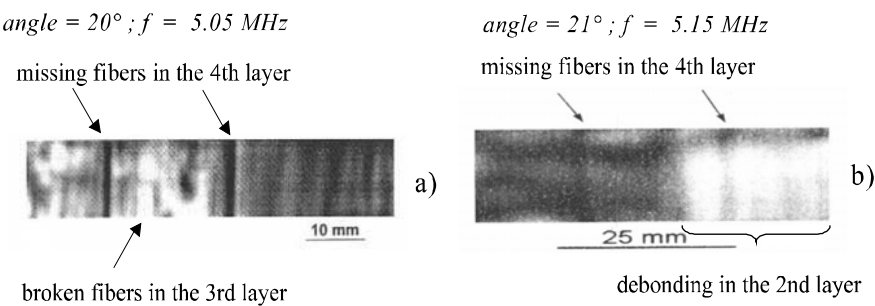


**Figure 22.10.** Lamb wave cartographies. Figures extracted from [KUN 96]

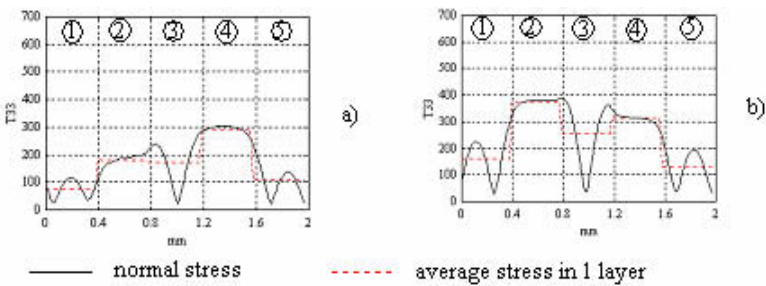


**Figure 22.11.** Normal stress distribution in a 0°/90° mirror with 5 layers, in Siliceous Carbonate, as a function of thickness. Calculation made with the constants of Table 1.7. a):  $\theta = 20^\circ$  and  $f = 5.05 \text{ MHz}$  ; b):  $\theta = 21^\circ$  and  $f = 5.15 \text{ MHz}$

#### 22.1.4. Deviation of the Lamb wave beam

The reflected pressure field of Figure 21.4 of Chapter 21. (reproduced on Figure 22.12b), has been obtained when a Lamb mode is excited in a unidirectional carbon/epoxy composite plate, fibers being contained in the sagittal plane (Figure 22.12a). The Lamb wave beam (non specular reflection area) propagates in the direction of the fibers, and thus parallel to the sagittal plane.

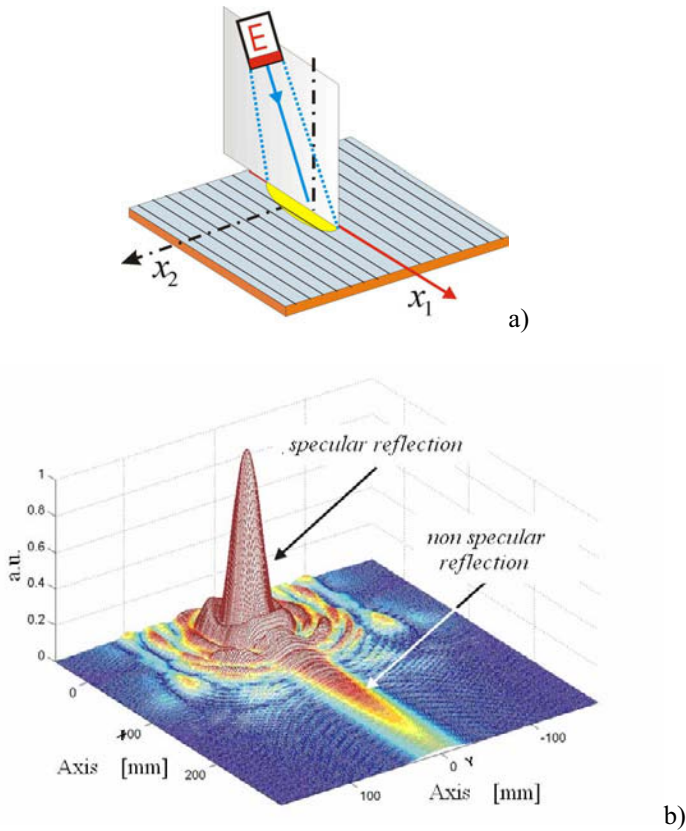


**Figure 22.12.** Reflected pressure field, in a plane parallel to a unidirectional carbon/epoxy plate of thickness  $H = 0.59$  mm,  $f = 1.35$  MHz, mode  $S_0$ , 6-order axis being parallel to the  $x_1$ -axis. Figure extracted from [POT 05]

When the fibers are no longer in the sagittal plane, depending on the chosen Lamb mode, the Lamb wave beam cannot propagate parallel to the sagittal plane. This is the case in Figure 22.13, when fibers make an angle of  $45^\circ$  with the sagittal plane.

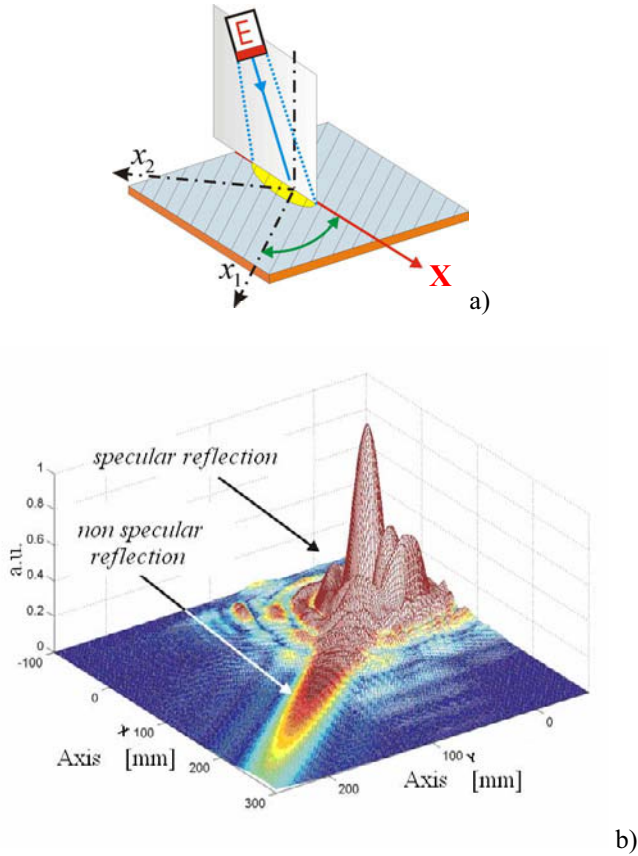


**Figure 22.13.** Reflected pressure field, in a plane parallel to a unidirectional carbon/epoxy plate of thickness  $H = 0.59$  mm,  $f = 1.35$  MHz, mode  $S_0$ , 6-order axis making an angle of  $45^\circ$  with the  $x_1$ -axis. Figure extracted from [POT 05]

In fact, when some modal waves, such as Lamb or Rayleigh waves, are excited locally in a structure, the incident beam, because of its bounded property, will yield a modal wave beam on the structure. This beam then radiates in the surrounding medium. Because of the material anisotropy, the modal wave beam direction undergoes a deviation with respect to the sagittal plane of the incident bounded beam (Figure 22.14), then re-radiates in an oblique plane [POT 01, POT 05].



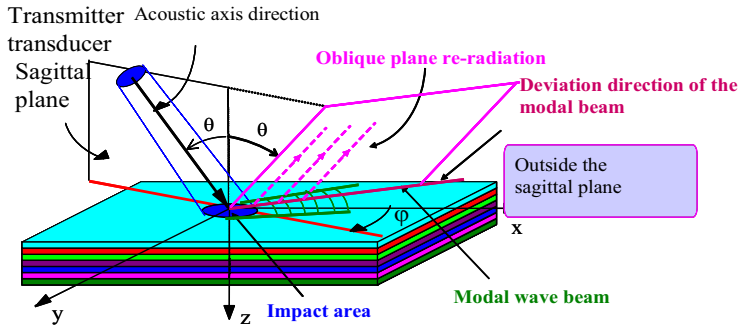


**Figure 22.14.** Deflection and re-radiation of the modal beam

The deviation direction of the modal beam can be predicted by plotting the Lamb slowness curves, at a fixed frequency, as a function of the sagittal plane orientation, given by the angle  $\varphi$  (Figure 22.15). Because of the anisotropy, these curves are not circular. By an asymptotic analysis in the far field domain, and using the stationary phase method [POT 01, POT 05], it is possible to predict the deviation direction of the modal beam in the structure. In fact, it is sufficient to go to the point corresponding, on the slowness curve, to the projection of the main wavevector of the transducer acoustic axis in the plane of the plate. The incident beam also yields waves in the neighborhood of this point on the curve, and these waves take part in the quasi-resonance phenomenon. A bounded beam of modal waves is then yielded in the structure, centered on the main group line, that is to say that the most energetic part of this modal beam is located along the group direction corresponding to the main wavenumber vector of the acoustic axis. This group direction is given by the direction of the normal to the slowness curve at this point (Figure 22.16) [POT 01, NEA 01, POT 05].

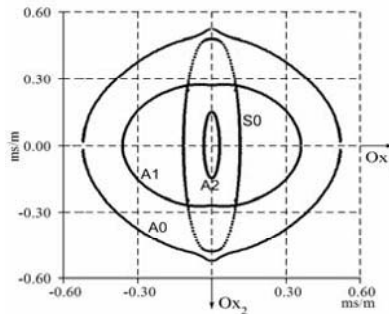


**Figure 22.15.** Lamb waves slowness curves for a unidirectional carbon/epoxy layer (fibers direction parallel to  $Ox_1$ ).  $f.h. = 1 \text{ MHz.mm}$ . Figure extracted from [POT 05]

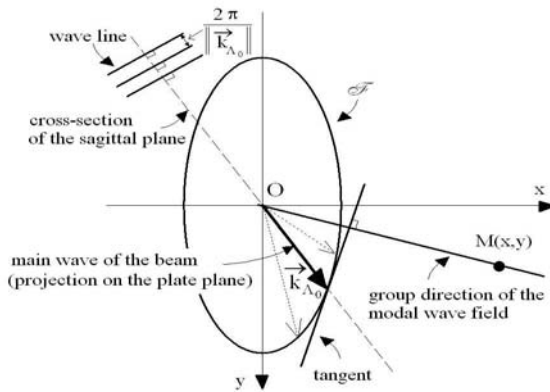


**Figure 22.16.** Achievement of the principal group direction of the modal wave field for a particular branch  $\mathcal{F}$  of the modal curve

The modal wave beam re-radiates in the fluid following an oblique plane containing the principal group direction and the acoustic axis of the reflected specular beam. The intersection of this oblique plane with the interface plane is the group direction of the modal beam. The non-specular effects [NEU 73, BER 73, ROU 85] will thus be observed in this oblique plane and no longer in the sagittal plane.

## 22.2. Bibliography

- [BER 73] Bertoni H.L., Tamir T., “Unified theory of Rayleigh-angle phenomena for acoustic beams at liquid–solid interfaces”, *Appl. Phys.*, 5, 157–72, 1973
- [FAR 94] Farlow R., Hayward G., “Real-time ultrasonic techniques suitable for implementing non-contact NDT systems employing piezoceramic composite transducers”, *Insight*, 36, 12, 926–35, 1994
- [KUN 96] Kundu T., Maslov K., Karpur P., Matikas T.E., Nicolaou P.D., “A Lamb wave scanning approach for the mapping of defects in [0/90] titanium matrix composites”, *Ultrasonics*, 34, 43–49, 1996
- [KUN 01] Kundu T., Potel C., de Belleval J.F., “Importance of the Near Lamb Mode Imaging of Multilayered Composite Plates”, *Ultrasonics*, 39, 283–90, 2001
- [MAS 97] Maslov K., Kundu T., “Selection of Lamb modes for detecting internal defects in composite laminates”, *Ultrasonics*, 35, 141–150, 1997
- [NAY 88] Nayfeh A.H., Chimenti D.E., “Propagation of guided waves in fluid-coupled plates of fiber-reinforced composite”, *J. Acoust. Soc. Am.*, 83, (5), 1736–43, 1988

- [NEA 01] Neau G., Deschamps M., Lowe M. J. S., “Group velocity of Lamb waves in anisotropic plates: comparison between theory and experiment”, in D.O. Thompson and D.E. Chimenti (Eds.), *Review of Progress in Quantitative NDE*, American Institute of Physics, New York, 20, pp. 81–8, 2001
- [NEU 73] Neubauer W.G., “Ultrasonic reflection of a bounded beam at Rayleigh and critical angles for a plane liquid/solid interface”, *J. Appl. Phys.*, 44, 48–53, 1973
- [POT 97] Potel C., Baly S., de Belleval J.F., Pétillon O., Arnaud J.L., “Utilisation des ondes de Lamb pour détecter des défauts dans les matériaux composites”, *Cofrend Nantes '97*, 1, 363–7, 1997
- [POT 01] Potel C., Gatignol Ph., de Belleval J.F., “Deviation of the modal waves excited by an ultrasonic monochromatic beam in an anisotropic layer”, *C. R. Acad. Sci. Paris. Mec. Phys. Astr.*, 329, 11, 815–22, 2001
- [POT 05] Potel C., Baly S., de Belleval J.F., Lowe M., Gatignol Ph., “Deviation of a monochromatic Lamb wave beam in anisotropic multilayered media: asymptotic analysis, numerical and experimental results”, *IEEE Trans. Ultrasonics Ferroel. Freq. Contr.*, 52 (6), 987–1001, 2005
- [ROU 85] Rousseau M., Gatignol Ph., “Asymptotic analysis of nonspecular effects for the reflection and transmission of Gaussian beam incident on a solid plate”, *J. Acoust. Soc. Am.*, 80, 325–32, 1985

This page intentionally left blank

## Chapter 23

# Non-Destructive Testing of Concrete by Ultrasonic Methods

### 23.1. Non-destructive testing of concrete by ultrasonic methods

Concrete was widely used during the period of reconstruction after the destruction of the Second World War and in the following 30 years of economic prosperity. Other concrete structures are even older and were built during the first half of the 20<sup>th</sup> century. All these works have ageing and some “natural” deteriorations appear with time, not to mention the cases of premature failures and some defects. The economic stakes of renovation and prolongation of these works are huge, the monitoring and the renovation of these works corresponding to the French national market, for example about 50 billion euros [TOU 98].

Non-Destructive Testing and Evaluation plays a part at several levels in the monitoring process of a structure. The part played by the tests is important, and establishing norms and recommendations enables us to ensure *a priori* rigorous information. Most of the time, ‘in situ’ measurements are compared to results obtained with reference samples. Some models can also be used to quantify a surety indicator and to compare it to required levels in order to determine the remaining life potential of the structure. It should be noted that, during the measurement, the huge variability of some non-controlled parameters of the material, or of environmental conditions, imposes the need for caution when considering the absolute threshold. It is one difficulty of NDT and NDE applied to concrete, *a fortiori* in situ.

Heterogeneity and the variety of flaws or characteristics to estimate generate a widely open set of prospecting techniques. Techniques based on generation and propagation of mechanical waves, so-called “acoustic”, constitute an important part of the NDT applied to concrete.

In this section, we will focus more specifically on ultrasonic NDT. First, we will present the material and its ageing or flaws; then we will talk about the materials and industrial tests currently used to control them. Finally, we will deal with the significant advances in research, which aim to make measurement and waves propagation control in concrete more reliable in order to consider the inversion of measurements obtained in situ.

### **23.1.1. *The material***

#### **23.1.1.1. *Constitution***

Concrete is a highly heterogenous material. There are many works which consider its composition, its implementation and its characteristics [BAR 92], [DRE 95]. Depending on its use, concrete is made of aggregates of variable dimensions from 0.08 to 100 mm, of binders such as lime or Portland, pozzolanic aluminous, or quick-set cements, made with water, rods or reinforcement fibers.

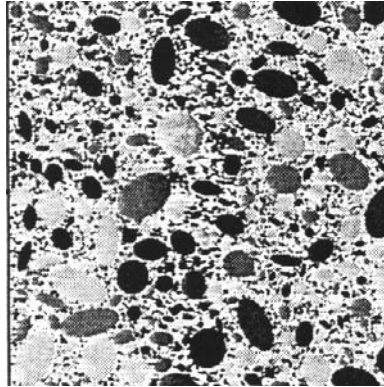


**Figure 23.1.** *Concrete section*

The water/cement ratio (W/C) generally takes values between 0.04 and 0.5. The water brought during fabrication includes the volume necessary to hydrate the cement, but also the volume easing the implementation. This last amount has to be removed after the fabrication of concrete by desiccation. Curing comes with a heat emission (up to 80°C), with hydraulic thermal shrinkage (final volume <  $\Sigma$  initial

volume), with a desiccation shrinkage (water surplus evaporation). These changes of dimensions (around 0.03%) yield stresses which create microcracks. It is one of the initial types of concrete damage. Moreover, there is some porosity due to concrete curing whose rate varies from 25% to 3%, or only 1% in the best cases. The dimension of the pores is large (from angstrom to micrometer).

The porous volume and the network of microcracks strongly influence the mechanical resistance, as well as the propagation of acoustic waves, depending on the nature of the interstitial constituent, and it also governs the potential penetration of exterior substances, which may be aggressive towards the structure (water, chlorine, carbon, etc.). It should be noted that the first centimeters of the material, called “cover concrete”, have a crucial importance on concrete durability as they constitute a protective layer.

#### 23.1.1.2. *Mechanical characterization*

The most used mechanical characteristics are  $R_c$  (compressive strength at 28 days, norm NF P 18–406: from 20 to 120 MPa),  $E$  (elasticity modulus, from 20,000 to 70,000 MPa),  $\nu$  (Poisson’s ratio (from 0.18 to 0.25)),  $\rho$  (density, from 2,200 to 2,500 kg/m<sup>3</sup>).

The compression resistance varies as a function of the binder class, of the concrete age, of the ratio  $W/C$ , of the dimension of the largest granulates and of the concrete density. The flexural or tensile strength (around 5 MPa) and the concrete toughness (2 to 3 MPa  $\sqrt{m}$ ) are low because of the porosity or cracks rate. The concrete must work in compression. The traction resistance of a structure is ensured by the metallic reinforcements, and/or by cables which establish the pre-stresses, enabling to keep the concrete compressed. The concrete is thus the matrix. The state of links of adherence between reinforcements and matrix, and the state of health of these reinforcements, are thus important questions asked by manufacturers and end users of concrete structures.

#### 23.1.1.3. *Ageing*

Ageing can be of chemical (attack by chlorides, sulfates, carbon or alkalines), mechanical or thermal (frost defrost cycle, heating, fire) origin. In most cases, the major consequence is the increase in density of microcracks, and sometimes porosity increases, resulting in some alteration of the mechanical characteristics that can be significant. These damage must be estimated as precisely as possible in amplitude and in distribution inside the structure. The identification of damaged parts of a structure is called zoning. In some cases, chemical attacks tend to depassivate the metallic reinforcements and to bring corrosion into the reinforcements when there is some water. It is a frequent cause of irreversible deterioration because of the reinforcement importance in the mechanical resistance of structures.

Ruptures are generally caused by the propagation of cracks. The cracks are generated by the coalescence of microcracks due to damage or by tiredness by mechanical loading cycles. In pre- or post-stressed concretes, we also observe the quality of the ducts filled by a “grout” which ensures cable protection. Finally the evolution of the stress yielded by these reinforcements is an important element in the life of the structure.

All this ageing has to be mastered and/or to be controlled with non-destructive techniques, among which acoustic wave propagation has an important part.

### **23.1.2. Implementation of ultrasonic measurements**

#### *23.1.2.1. Techniques*

On-site non-destructive testing by analysis of the propagation of mechanical waves in concrete, also called acoustic waves, can be categorized into three main groups:

- Ultrasonic techniques have been developed over many years. Their numerous applications require a good mastery of the measurement chain. The techniques of wave propagation by transmission enable us to know the thickness of the structure or the velocity of acoustic waves in the material. Techniques involving surface waves enable us to test the cover concrete or to detect cracks. Industrial applications allow identifying segregations, layers, damage, flaws, vacuums, porosity rates or delaminations.

- Acoustic emission [PRO 02] is a global method based on the spontaneous generation of elastic waves by the structure. The equipment is limited to reception, and is often made of several ultrasonic low-frequency sensors. The goals are to detect and localize, in real time, the emission, that is to say the flaws. The technique is particularly well-adapted to the inspection and observation of large volumes during operation, to follow the evolution of the flaw or the damage.

- The impact–echo method [CAR 94] consists of analyzing the frequency response of a structure, such as tiles with parallel sides, set in vibration. It enables us to obtain measurements of thickness or to detect a vacuum or pre-stressed tendons, or to position some interfaces, such as delaminations between materials of different mechanical impedances. The measuring device is very easy to use and is made of a generator (hammer or ball) and the receptor sensor of piezoelectric or accelerometer type.



The application, the implementation and the current limitations of these techniques are detailed in the case of the industrial evaluation of constructions made of concrete [BRE 05].

In the frame of this section, we will limit the study to ultrasonic techniques.

#### 23.1.2.2. *Equipment, methodology*

In the case of ultrasonic testing, measurements are made by reflection or by transmission. Transmission can be generated in the volume or in the surface.

The equipment used consists of a traditional ultrasonic chain. However, because of the huge attenuation of the wave in concrete, it is essential to work with low-frequency waves. Basic industrial applications require sensors from 24 to 50 kHz. The excitation voltages of these transducers can reach 1,000 V. In some cases, the tests are made with accelerometers.

Some research works explore the complementary range from 100 to 1,000 kHz.

The usual measuring element is the velocity, which is sensitive to the evolutions of the microstructure and to the type of material. The attenuation, as well as the evolution of the frequency spectrum of the waves, are some of the parameters used in the laboratory but not yet industrially.

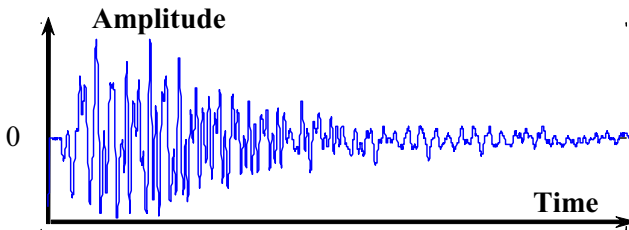


**Figure 23.2.** *Ultrasonic signal in transmission amplitude – time  
(transducer 24 kHz – duration 3 milliseconds)*

The low-frequency signals (Figure 23.2) are very energetic and propagate over long distances, but their damping is very weak and only the exploitation in term of time of flight can be made.

Signals with higher frequencies propagate over smaller distances, but their attenuation is stronger. They allow more relevant estimation of the attenuation of the signal.

The more frequently use method consists of simple measurements of the propagation velocity of the wave in the material. The norm [EN 12504-4] defines the determination method of the velocity of ultrasonic waves. It can be linked to the mechanical characteristics of the material and to the geometrical characteristics of the test parts. The correlations are often delicate.

One difficulty is due to the large divergence of the ultrasonic beam caused by the use of low frequencies, with the spatial scattering of waves because of the interactions waves – scatterers (granulates – cracks). For an example, [MIL 55] gives the distribution of compression, shear and Rayleigh waves in a semi-infinite medium (Figure 23.3) in the case of an impulsional point-like source. The presence at the surface, as well as inside the material, of several wave types enables us to make transmission measurements in the volume or on the surface only. Conversely, successive waves approaching the sensor and the waves reflected on the edges of the structure often allow only a processing of the waves limited to the arrival time of the first component.

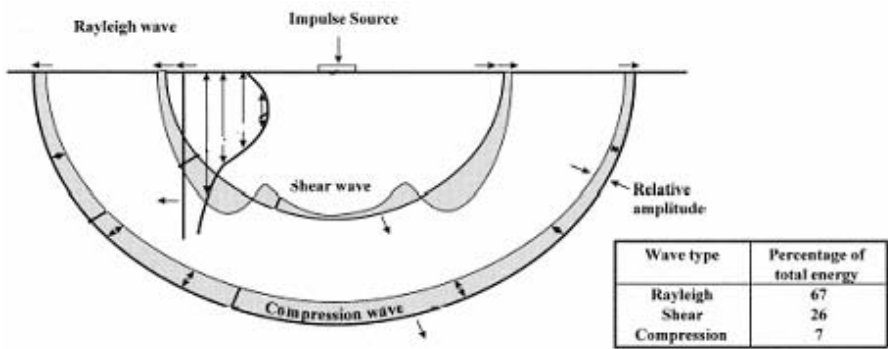


**Figure 23.3.** *Waves propagating in a semi-infinite medium from an impulsional point-like source [MIL 55]*

Measurement of the attenuation also allows the characterization of the concrete, but the industrial applications are not yet operational. However, the first results tend to prove that this parameter has a high sensitivity to the evolutions of the concrete. Some research works aim to improve this method.

A last area of development consists of analyzing the variations of the frequency spectrum in amplitude or in phase, and in trying to link the evolution of the concrete dispersivity to modifications of the concrete microstructure, to the nature, distribution and dimensions of the components, porosities and cracks as well as water contained in the concrete. These evolutions are mainly sensitive when the

concrete is young or when it is being damaged. Some devices based on these measurements are being developed and marketed. However, their industrial applications are still limited.

It is interesting to quote ultrasonic tomography. This technique is based on the measurement of a great number of times of flight between several emitters and receivers distributed on the structure perimeter in a plane. It is then possible to establish a 3D cartography of flaws and anomalies found in the structure.

This technique is used on works of large dimensions (dams, locks) or in piles. An industrial example consists of controlling some piles by placing some transducers which we move simultaneously along the pile in several cylindrical reservations. It is thus possible to display the data on an image such as the one in Figure 23.4.

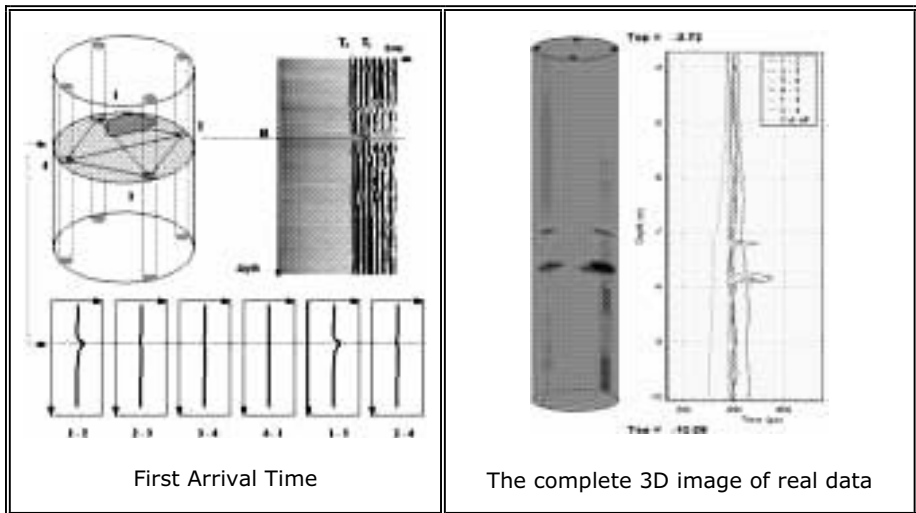


**Figure 23.4.** Principle and results of the testing of a pile by ultrasonic tomography [VOL 03]

#### 23.1.2.3. Limits and problems encountered

The concrete and structures to control combine most of the difficulties we can find in acoustic testings. There are three types of problems:

a) Implementation of the measurements, namely with the need for a contact between the transducer and the surface (this last one can be sometimes dirty or rough), the difficulty to access both sides and the large dimensions of structures.

b) Interpretation and exploitation of information is sometimes difficult. They are linked to the interaction material – the wave. The concrete is heterogeneous, anisotropic, inelastic or/and non-linear elastic. The expected consequences are:

- a strong attenuation, some structure noise (multi-scattering or multiple reflections) and a large divergence of the beam;
- some beam deflections (reinforcement bars);
- a partial loss of wave coherence;
- some velocity variations as a function of frequency, stress, dimensions to test, geometry, water rate, carbonation, composition, temperature, concrete maturity and chemical or mechanical damage.

c) Calibration in order to go back to the relevant parameters of concrete. These calibrations are defined for the concrete of the scanned structure. They can be achieved directly on the structure from the velocity measurements in reference areas known to be undamaged. It is also possible to refer to some measurements obtained on corings removed from the structure, or else made during the work fabrication. We can remember that many measurements of absolute values of mechanical properties have been tried on the basis of correlations with acoustic measurements, but industrial implementation causes some precision problems. The correlations depend on many experimental parameters. It is possible to make only relative measurements, and that is the zoning principle.

A judicious choice of the frequency of sensors and measuring equipment can solve some of these problems. In all cases, it is important to put into place more and more competitive techniques. Current, or developing, improvements concern the equipment, and also information processing. But the problems of linking observables to some evolutions of the equipment have justified the need to understand the ultrasonic beam propagating in the concrete better, namely analyzing the beam – material interactions. The final goal is to master the direct problem in order to solve the inversion.

### ***23.1.3. Examples of applications and developments***

The development of new methods or procedures is justified by the difficulty of the specific application of general methods used in the testing on composites or metallic materials. The heterogeneity of the material and the geometry of structures are the main reasons for it.

Many parameters have an influence on the values of ultrasonic velocity and attenuation. In addition to concrete composition parameters, to its ageing and to the testing conditions, in the case of on-site testing, the length covered by the wave in concrete can be unattainable, and the influence of the structure's geometry on the wave path is sometimes hard to control. If we add the practical problem of sometimes limited access to both sides, it can become impossible to calculate the velocity and attenuation precisely.

An example of industrial work and three examples of laboratory work show the particular uses of ultrasonic waves.

#### 23.1.3.1. Zoning example

Zoning is a common use of ultrasonic techniques in the industry. The goal is to identify and to determine the structure areas with low potential of mechanical resistance. Definition of the measurement points is a major element of the efficiency of the testing method.

The calibration is made from corings removed from areas well-known for their health (general case of old works), or on samples representative of concrete and of its ageing if they are conserved in controlled conditions. The link between the velocity evolution of the ultrasonic wave and the resistance to compression can be established. The minimum uncertainty is often greater than  $\pm 20\%$ .

The presented testing concerns two penthouses of a stadium built in 1937 [CAN 73]. Each penthouse is made of four roof trusses on which a slab lies (Figure 23.5).

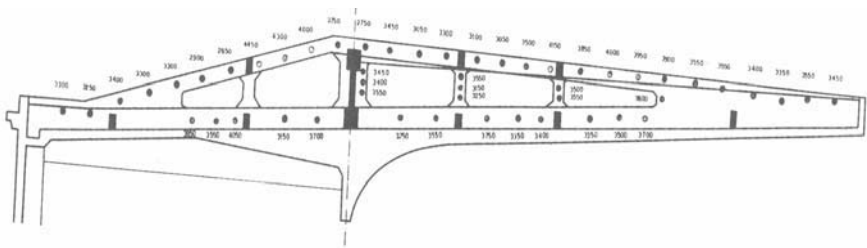


**Figure 23.5.** *Layout of a penthouse roof truss [CAN 73]*

The structure is made of reinforced concrete and shows some detachments of the superficial coating, some cracks, calcite deposits, framework corrosion and consequent blasting of concrete.

The goal of the measurements is to estimate the concrete quality and to find the damaged areas by estimating the compressive strength in each measurement point. All areas have to be tested if they are accessible. A preliminary definition of measurement lines must allow optimizing the testing, namely by taking into account the frameworks localized by electromagnetic low-frequency waves.

The exercise has involved roof trusses and slabs. Tests have been made following the classical surface and transmission scanning methods with work site equipment. Measurement lines are 2 meters long and have been plotted at 45° from the reinforcement bars. Each measurement line has ten measurement points. Each slab has been scanned by surface measurements. They are made by holding a fixed transmitter transducer and by moving the receptor transducer from point to point along the line. For each position, the distance is known and the time of flight is measured. The velocity is deduced.

Each roof truss has been scanned with 700 points.

The correlation between compression strength  $R_c$  and ultrasonic longitudinal wave velocity  $V_L$  has been verified with six corings because no concrete samples were taken when the work was carried out. The deduced relationship is:

$$\log R_c = 418 * 10^{-6} + 4,125 * V_L \quad [23.1]$$

$R_c$  is in bars and  $V_L$  in m/s. The correlation coefficient is about 0.98.

It should be noted that this relationship is only usable in the frame of this particular application. According to the extent of the structure and to the variations of environmental parameters undergone by the structure, as well as the variable experimental conditions during the measurements, it is likely that some of the evolutions of the velocity measurements can be attributed to causes other than variations of mechanical resistance. The north–south exposition of the structure's side as well as the heterogeneity of the concrete' are some causes of major error.

Results have been exploited in two forms:

a) The velocity values from the measurements at each point have been transcribed in planes with a quality scale previously established: (damaged concrete)  $3,400 \text{ m/s} < V_L < 3,900 \text{ m/s}$  (healthy concrete).

b) The average and the standard deviation obtained from measurements on each roof truss have allowed the qualitative assessment of the roof truss and the slab concrete.

The velocities obtained on the whole work vary from 2,850 to 4,450 m/s with an average value of 3,650 m/s. The correlations with the compressive strength are made from the calibration curve or formula. Only some measurement points on the work present some resistance to local compression deduced from velocity measurements below 260 bars. One of the spans is globally the worst and the concrete is *a priori* quite heterogenous.

Scanning has allowed underlining the existence of a strong cracking process, not visible by the eye, in the slabs of both galleries.

In addition to the difficulties of calibration and the necessity of first seeking the reinforcement bars, we have to specify the problems of difficult accessibilities for transmission measurements and the huge number of measurements required.

The proposed repairs consist of removing the waterproofing and the damaged concrete and of stripping the corroded reinforcement bars before protecting the frameworks by an epoxy-paint film, injecting the more significant cracks and redoing the watertightness.

#### 23.1.3.2. *Examples of crack detection*

##### 23.1.3.2.1. Surface cracks

One of the most delicate concrete elements is the covering concrete or surface layer, which has a fundamental role in the evolution of the resistance during time. In fact, this superficial layer is the most important protection against exterior attacks, namely against risks of water and/or chloride ions penetration which may damage the reinforcement bars. The estimation of quality and state of health is a crucial stake in the frame of prolongation of the structure's lifetime. This has led to innovative research actions.

[HEV 98] has developed a method allowing the estimation of the depth of a crack emerging in the surface.

Let us remind ourselves the method (Figure 23.6) proposed by the British Standard [BS 86] which consists of inserting a sensor in the area to scan and in moving a second one along a given direction. Sometimes, it is a set of sensors placed in line.

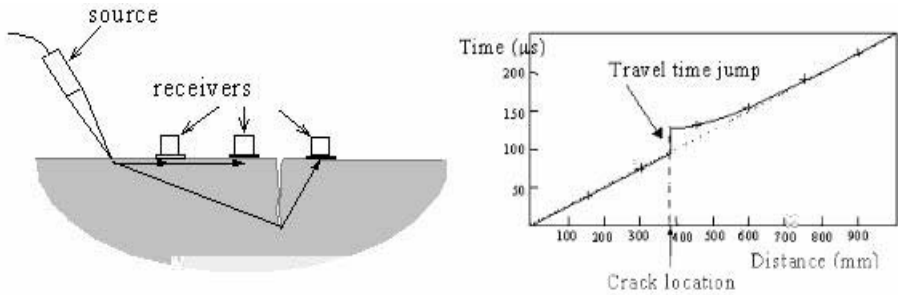


**Figure 23.6.** Detection of a surface crack [BS 86]

The compression P waves propagate temporally proportionally to the path length, and when they find a crack on the way, the proportionality is broken and the wave is diffracted by the crack extremity. Based on the amplitude of this “jump”, it is often possible to determine the position and depth of the crack by a relationship such as:

$$t = \frac{1}{V_p} (x_1^2 + h^2)^{1/2} + (x_2^2 + h^2)^{1/2} \quad [23.2]$$

with  $t$  the time of flight,  $x_1$  the distance from the emitter to the crack,  $x_2$  the distance from the receiver to the crack,  $h$  the crack depth.

The velocity  $V_p$  is determined from the measurement of the time of flight of the P wave between the transmitter and the receiver located on the path upstream of the crack. It is sometimes very difficult to estimate the crack size with precision.

Based on the propagation principle of surface waves, a technique of depth measurement has been developed.

This wave type, made of a compression part and a shear part, propagates in the surface, yielding an elliptic path of particles. The penetration depth is around the wavelength.



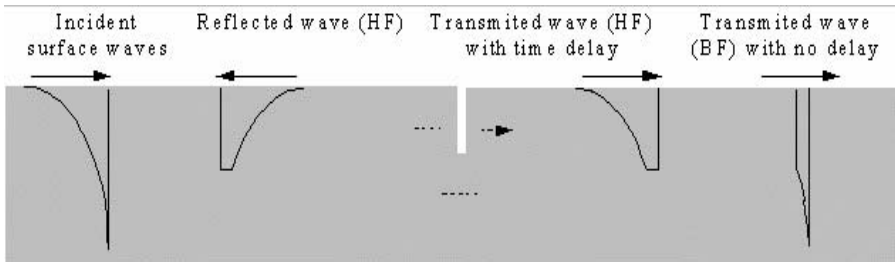


**Figure 23.7.** *Interaction surface wave – emerging crack [HEV 98]*

When they cross a crack (Figure 23.7), the smallest wavelengths are reflected, whereas the biggest are transmitted, without those which have been reflected. A cut-off frequency then appears in the frequency analysis of the signal transmitted between a transmitter and a receiver.

The interaction wave–crack has been studied by the Indirect Boundary Element Method (IBEM) [PED 94].

An image of the horizontal and vertical components of the surface waves (central frequency = 20 kHz) propagating in a concrete beam is given by Figure 23.8. The crack is 16 cm long. The energy decrease of the transmitted wave is obvious. The amplitude ratio  $U_t/U_i$  is the comparison element. The numerical work in this study contributes to the confirmation of the experimental results, and specially to the study of the influence of several parameters (crack aperture, contact points of inner edges, presence of water) on the underlined phenomenon.

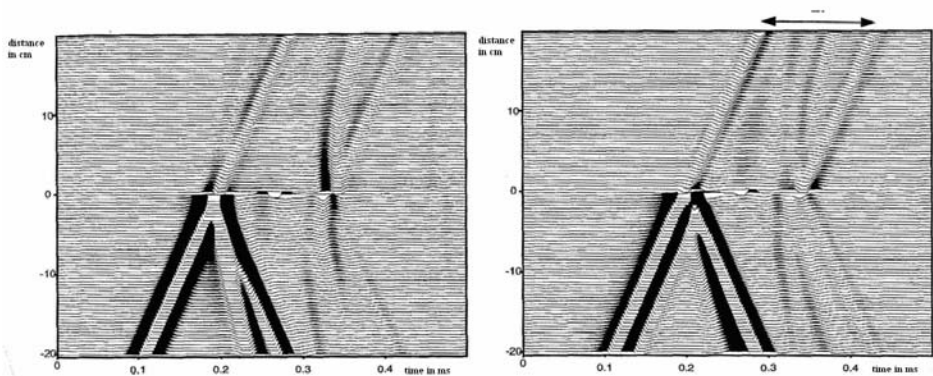


**Figure 23.8.** *Amplitude of horizontal and vertical components as functions of time (abscissa) of the surface wave crossing a crack of 16 cm [HEV 98]*

Figure 23.9 allows the translation of the evolution of amplitude spectra ratio (calculated from numerical data) as a function of frequency. The cut-off frequency is defined from observations. It corresponds to the lowest frequency such as the curve slope is equal to 0.075. The numbers referring to the curves correspond to the length of tested cracks.

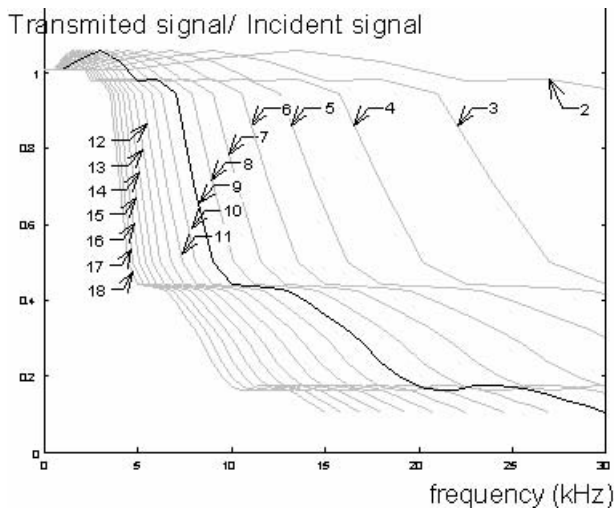


**Figure 23.9.** *Ratio of amplitude spectra (transmitted / incident) as a function of frequency [HEV 98]*

These results are valid only in the range where the Rayleigh wave propagates in a semi-infinite isotropic homogenous medium with wavelengths sufficiently big with respect to the size of the scatterers, so that we can neglect multiple scattering.

The absence of perturbation on the depth estimation (due to the partial or total filling of the crack by water) has been studied by numerical simulation. The study of potential contact between inner edges of the crack has shown that, in the case of compression waves, the gathered information is the depth of the first contact. Conversely, in the case of surface waves, some additional problems on the determination of the crack size can appear.

#### 23.1.3.2.2. In-depth cracks

In the case of in-depth crack detection, some recent developments of transducers have been made. The association of several pieces of information from several transducers based on the SAFT technique, or information on delay management (phased array) seems promising.

In order to improve the signal-to-noise ratio, first, the multi-sensors technique is based on six inline transducers (Figure 23.10). One of the sensors is the emitter and the others are the receivers. The acquiring assembly is moved.

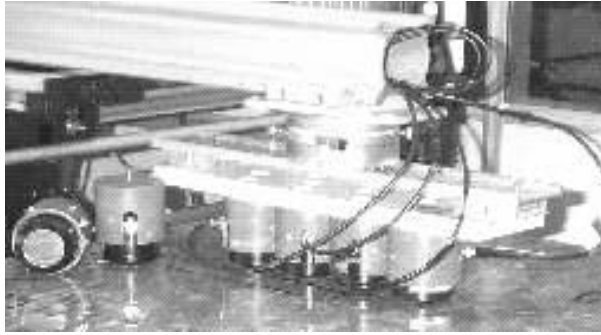


**Figure 23.10.** *Multi-sensor device [PAR 05]*

The SAFT technique allows rebuilding information from the different prospecting points in time and in space. The information is rebuilt on the form of a BScan whose axis corresponds to the alignment of the sensors.

The second technique consists of putting several sensors in spidergram following the “phased arrays” technique and in focusing on the expected position of flaws managing the emission temporal delays of the different sensors. The focalization allows concentrating the energy of the ultrasonic waves and increasing the signal-to-noise ratio of the information returned by the flaw [PAR 05].

Because of the strong attenuation of waves in concrete, the tests have been made with sensors of 250 kHz on a block  $800 \times 800 \times 600 \text{ mm}^3$  (medium cement with granulates from 0 to 20 mm). Some artificial cracks have been made. Each facet has a surface of  $40 \times 70 \text{ mm}^2$  and the squared holes have an edge of 50 mm. The cracks of aperture  $100 \text{ }\mu\text{m}$  are supposed to be perfect reflectors.

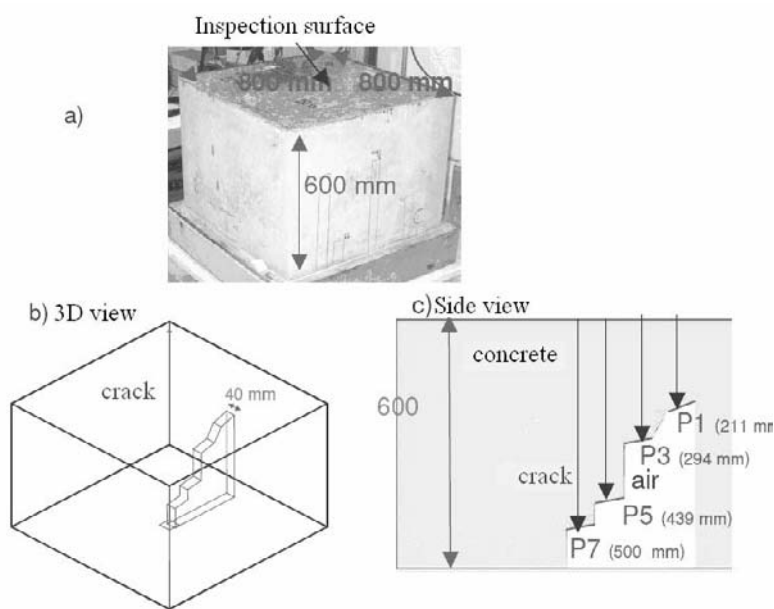


Figure 23.11. Concrete sample with artificial multifaceted cracks [PAR 05]

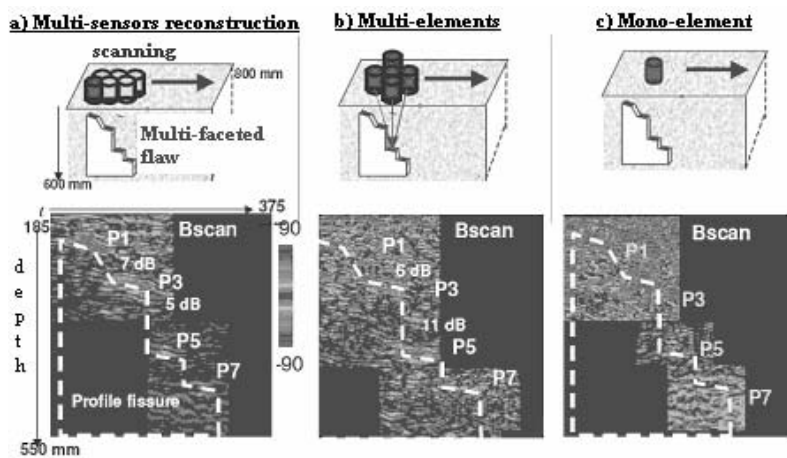
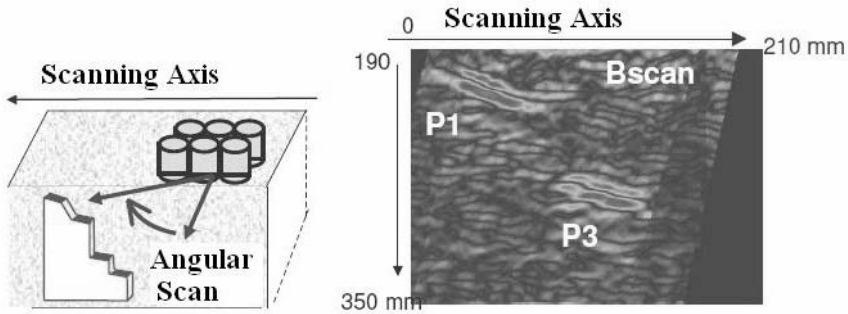


Figure 23.12. Crack profiles and BScan obtained by a) multi-sensors reconstruction; b) multi-element focalization at  $L0^\circ$ ; c) mono-sensor measurement [PAR 05]

The results (Figure 23.12) clearly show the improvement brought about by these techniques applied to concrete. Thus, it becomes possible to detect some flaws at about 500 mm in depth thanks to the focalization, and to isolate information concerning the cracks near to the surface.

A first approach of TomoSFT has been developed, generating delays on multi-elements, allowing prospecting and focalization with an incident angle variable with respect to the facets. The exploitation is made by the BScan reconstruction using the SAFT technique. The results (Figure 23.13) allow improvement of the flaw definition.



**Figure 23.13.** BScan by TomoSFT for three inspection angles ( $10^{\circ}$ – $13^{\circ}$ – $15^{\circ}$ ) [PAR 05]

This type of technique will be developed incorporating, among other things, a morphology mastery of the ultrasonic beam propagating in concrete, even in reinforced concrete.

#### 23.1.3.3. Analysis of concrete slabs

To answer the problem of damage in the area near the surface of concrete in massive structures (dams and locks) as well as the delamination of bridges and pavements, the *Spectral Analysis of Surface Waves* method has been improved, analyzing the propagation modes of dispersive waves (Rayleigh and Lamb waves). The *Multichannel Analysis Surface Waves* method has been applied to the theoretical case of concrete structures as well as the experimental aspect [WAR 05].

The principle consists of establishing a seismogram (signal–distance image) based on multiple acquisitions, multiplexed or not (Figure 23.14). Several positions of the source allow increasing the number of signals.

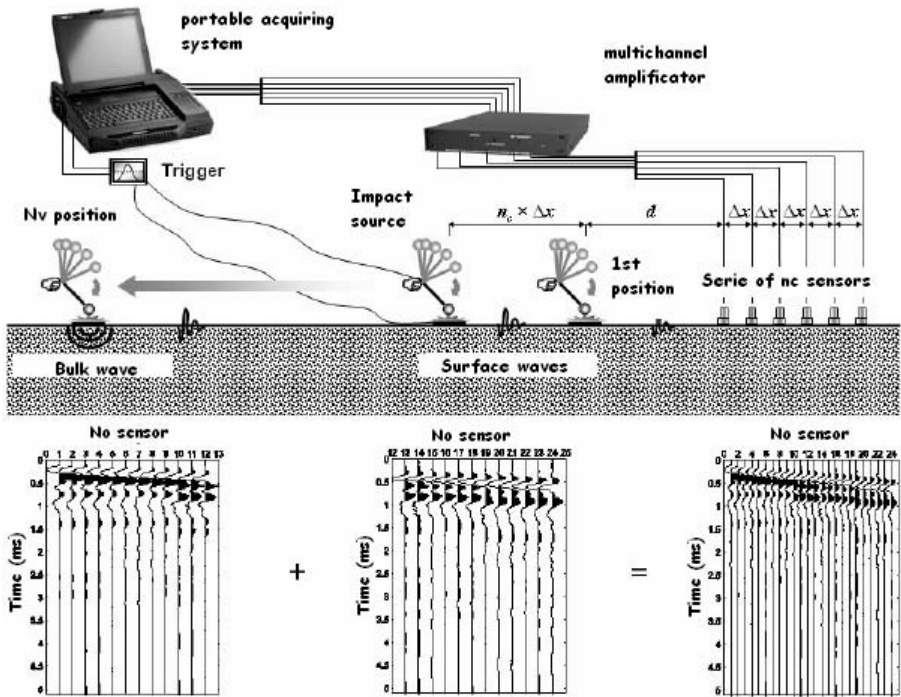


**Figure 23.14.** Principle of acquisition of dispersive waves in a concrete slab [WAR 05]

The frequency–wavenumber analysis consists of doing two successive Fourier transforms following the time  $t$  and space  $x$  axes. The result is the energy distribution of signals which can be represented in the wavenumber–frequency space, or in the wavelength–phase velocity space, or else in the phase velocity–frequency space. The last one is used most.

The experimental measurements are correlated with the theoretical solutions of propagation of Lamb and Rayleigh waves calculated for the case of stratified structures laying on an infinite half-space [RYD 04]. In Figure 23.15, the theoretical solutions are in white.

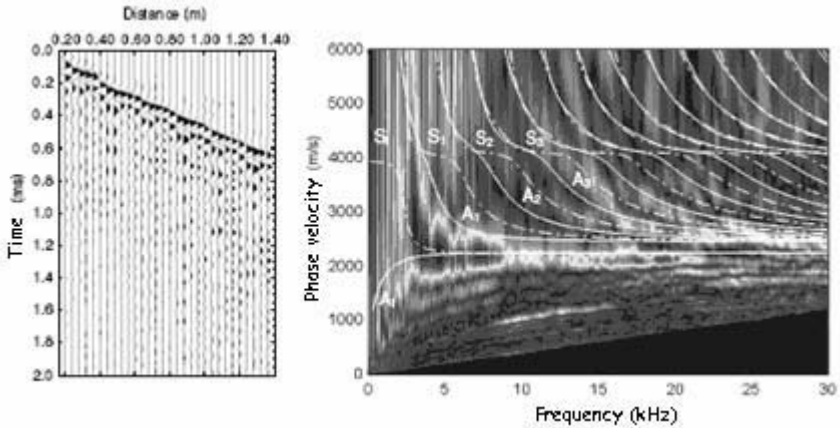


**Figure 23.15.** Seismogram and corresponding dispersion image on a slab with two layers of different concretes. The theoretical propagation modes are in white [WAR 05].

First, the Lamb solution is optimized for propagation modes of superior orders which are more linked to the slab properties than the fundamental modes  $A_0$  and  $S_0$ . The velocities of these modes tend towards the value of shear wave velocity in the material. The inversion is made on the basis of the knowledge of this velocity (2450 m/s) and of the slab thickness (0.8 m), iterating on the value of Poisson's ratio (final value = 0.22).

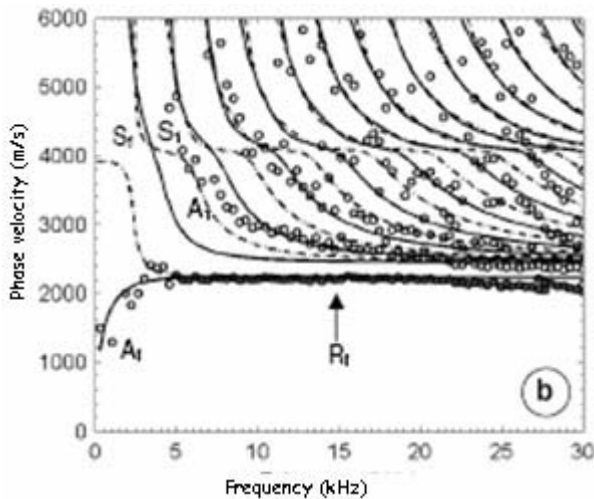


**Figure 23.16.** Plotting of energy maxima and theoretical propagation modes of waves in a concrete slab with two layers [WAR 05]

In a second step, the local energy maxima are isolated on the picture (Figure 23.16) and the fundamental mode of Rayleigh waves is deduced. The complete formation of Rayleigh waves is observable for frequencies above 5 kHz when the two fundamental modes superimpose on one another in velocity for wavelengths below half the tested slab thickness. This curve of phase velocity of the fundamental mode is inverted to obtain the velocity evolution of shear waves in each layer, as well as the layers' thickness, from assumptions or knowledge such as layer discretization.

Knowing the shear velocities, Poisson's ratio and the density ( $2400 \text{ kg/m}^3$ ), it is thus easy to deduce the elasticity modulus (Figure 23.17).

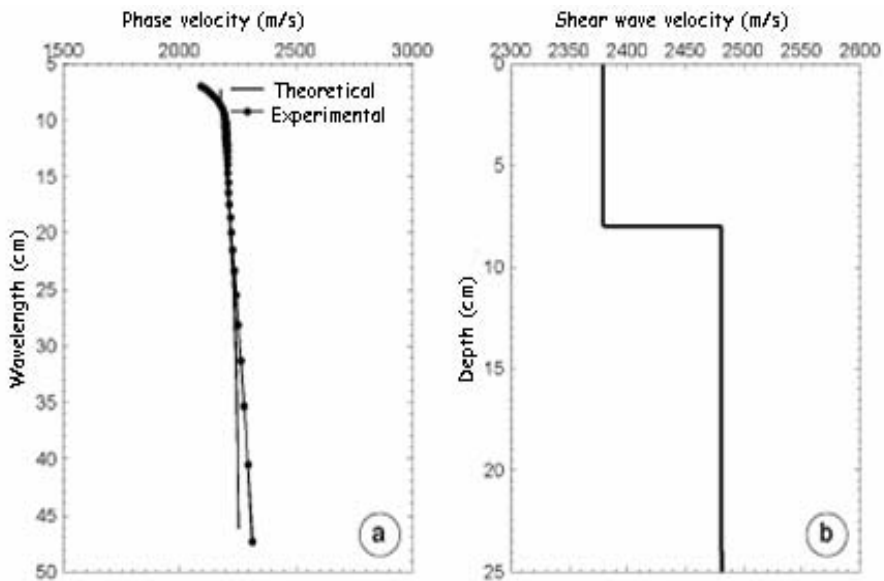


**Figure 23.17.** Evolution of the phase velocity of the fundamental mode of the Rayleigh wave and of the elasticity modulus in the surface of a bi-layered concrete slab [WAR 05]

This approach has allowed localizing some delaminations by using Lamb waves. The reinforcement bars have shown little influence on dispersion curves.



It should also be mentioned that some rules exist which limit or enable the optimization of the measurements, and that it is possible to reduce the number of useful signals to six in favorable cases. This technique should answer a real need for *on-site* testing.

#### 23.1.3.4. Determination of the concrete setting time

In the frame of a dam realization in Roller-Compacted Concrete (RCC), the mastery of the workability time allows ensuring the link by chemical bridgings between the grains of two layers deposited successively.

The measurement of this cure time in the case of matrix with fast kinetic can not be done by a simple follow-up of the ultrasonic wave velocity. The concrete being a scalable frequency filter, we study ([GAR 95], [COR 95]) the case of a concrete setting following the evolution of the material microstructure from the follow-up of the energy and of the wave frequency spectrum. This allows us to underline a new ultrasonic indicator characterizing the cure time.

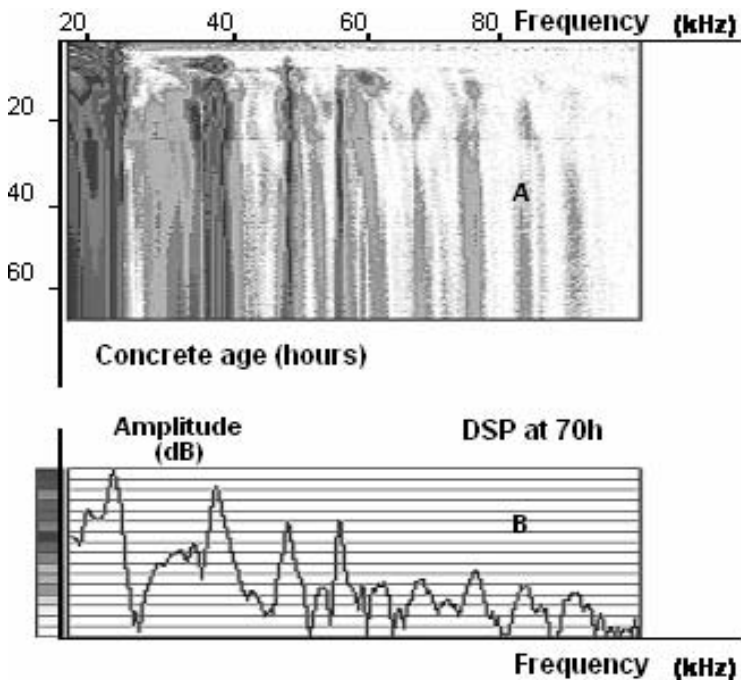


**Figure 23.18.** A) Density Spectral Power – age of concrete. B) Amplitude spectrum of the transmitted wave for an age of 70 hours [GAR 95]

The distribution of the amplitude spectrum of the wave is given on Figure 23.18b as an example, for the signal obtained at 70 hours. An image of the evolution of the power spectral density is given as a function of the concrete age on Figure 23.18a.

It shows in the first setting times that the wave energy hardly passes in the high frequencies whereas, when time increases, the grains are connected and the transmitted energy consequently increases. High frequencies are no longer filtered.

A simulation of the acoustical behavior of concrete during setting allows underlining the importance of inter-granular bridgings in solidification and wave propagation phenomena. It underlines the contributions to ultrasonic wave transmission of i) the present constituents and ii) the bridgings created during time between grains and grain clusters.

It is defined:

a) the aggregate volume which contains the whole of the present solid constituents (granulates, fillers, ettringite, CSH, monosulfo-aluminate) as well as porosities. We propose that ultrasonic waves go through the aggregate volume only in a time  $T_1$ . The chemical transformations of constituents existing in the column “aggregate” during the solidification follow first-order kinetics, which correspond to volume transformations. The materials characteristic and distribution are thus calculated at all times. The velocity in the homogenized aggregate ( $V_{\text{aggregate}}$ ) is then calculated by a model of self-consistent type;

b) the bridging volume which ensures the transfer of ultrasonic waves from grain to grain. We propose that the ultrasonic waves go through it in a time  $T_2$ . The transformations in the “bridging” column characterize the formation of physical links between the grains and follow second-order kinetics corresponding to surfacic transformations. The bridging ratio  $p$  varies from 0 to 1.

The ultrasonic waves go through the whole sample in a time  $T = T_1 + T_2$ . The velocity of ultrasonic waves ( $V_{\text{simulated}}$ ) is deduced from the length  $L$  of the sample.

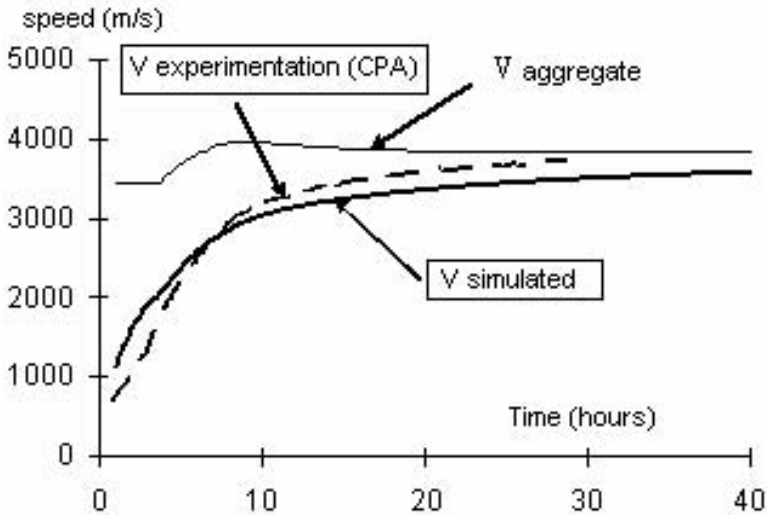


**Figure 23.19.** Evolution as a function of time of the experimental velocity (CPA matrix) and of the calculated velocity of ultrasonic waves in the aggregate column and in the simulated assembly [GAR 95]

The comparison of experimentation ( $V_{\text{experimentation}}$ ) on cement of Portland type (CPA) and of the model is shown on Figure 23.19. The experimental assembly is made of an emitter transducer and a receiver associated with a generator, an amplifier and an oscilloscope recording the signals. The central frequency of the transducers is 24 kHz. Taking into account the aggregate alone is not sufficient. It is mandatory to introduce the bridging notion to underline a correspondence between simulation and experimentation.

Some analyses of microstructures (Scanning Electron Microscope) and mechanical tests have led us to follow the evolution of the material during its youth. The cure time is defined from a systematic particularity during time of the evolution of the maximum amplitude of the 22 kHz ultrasonic wave, as shown on Figure 23.20. The setting time corresponds temporally to the start of massive formation of hydrates of CSH type which form, in the case of two tested concretes, the principal component of the finished concrete.

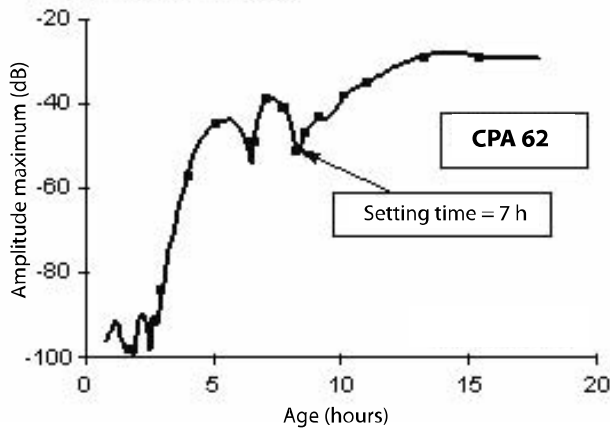


**Figure 23.20.** Evolution as a function of the concrete age of the amplitude maximum for the frequency 22 kHz [GAR 95]

The transmitted ultrasonic wave increases with time as well as the bridging ratio. Tests have shown the repeatability and sensitivity of this analysis on CPA and LRCC cements.

This process, which uses the frequency spectrum of the ultrasonic signal, must enable the avoidance of the velocity measurement. The precise knowledge of the distance in the case of limited accessibility does not become a priority. It is possible to imagine this principle being used on a wave reflected on the bottom surface, without knowing precisely the distance. Such use can also be considered by working on the spectrum of surface waves.

#### 23.1.3.5. Back-scattered waves in concrete

The exploitation of back-scattered waves in concrete is a perfectly adapted technique in the case of on-site testing. The grains, cracks or porosities of the concrete lead to much back-scattered information. The implementation is *a priori* simple. The back-scattered noise has been often analyzed in order to identify its signature and suppress it. In concrete, the goal is the reverse. It is to link its amplitude and attenuation with some disorders, depending on the material and its state of health.

This study is applied to concrete submitted to a temperature gradient which can reach 200°C. This stress type yields damage in the form of a crack more or less

huge, depending on the temperature reached. The back-scattered waves result from the interaction between the incident wave and the obstacles crossed, which are then granulates, porosities and cracks.

#### 23.1.3.5.1. Model of back-scattered signal

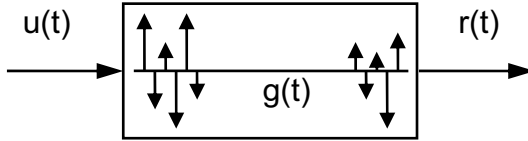


**Figure 23.21.** Principle of the discrete simulation of the back-scattered signal

The back-scattered signal (Figure 23.21) is the convolution of the impulse response of the transducer ( $u(t)$ ) by that of the scanned medium ( $g(t)$ ):

$$r(t) = u(t) * g(t) \quad [23.3]$$

The simulation of the ultrasonic signal is made by a large-band pulse with a Gaussian envelope:

$$u(t) = e^{-\gamma t^2} \cdot e^{i\omega t} \quad [23.4]$$

where  $\omega$  is the central pulsation of the pulse and  $\gamma$  the inverse of the square of the temporal width of the pulse.

The medium is considered as elastic, linear, isotropic and heterogenous; the dissipation effects related to the absorption are not taken into account. The scatterers are the grains and/or the cracks.

The impulse response of the medium is

$$g(t) = \sum_{k=1}^M \sigma_{sk} \cdot e^{-\alpha_d \cdot C_p \cdot \tau_k} \cdot \delta(t - \tau_k) \quad [23.5]$$

with:

$M$  the (finite) number of obstacles also called scatterers;

$\sigma_{sk}$  is the scattering cross-section of a scatterer;

$\tau_k$  is the temporal position of the scatterer on the axis of the ultrasonic beam;

$\alpha_d$  is the attenuation coefficient by scattering (only related to the scattering on heterogenities).

The multiple interactions between scatterers are not integrated in the model. Simple scattering only, is thus taken into account. The back-scattered signal is written:

$$r(t) = \sum_{k=1}^M \sigma_{sk} \cdot e^{-\alpha_d C_p \cdot \tau_k} \cdot e^{i \cdot \omega \cdot (t - \tau_k)} \cdot e^{-\gamma \cdot (t - \tau_k)^2} \quad [23.6]$$

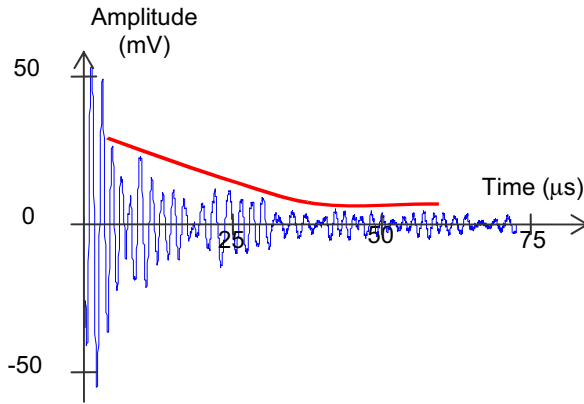


**Figure 23.22.** *Simulated back-scattered signal and its envelope [CHA 03a]*

Following the process proposed by [SAN 88], it is possible to extract the coefficient  $\alpha_d C_p$  from the signal envelope (Figure 23.22). The velocity knowledge then allows the deduction of the value of an attenuation coefficient of back-scattered waves  $\alpha_d$ .

#### 23.1.3.5.2. Extension of the model to the concrete scanning

Concrete is a heterogenous material made of a cement matrix and rock inclusions. Its damage generally begins with the appearance and evolution of microcracks. We are thus confronted with two different types of scatterers which we introduce in the model in the form of two terms in the following equation [CHA 03a]:

$$g(t) = \sum_{j=1}^{Mg} \sigma_{sj} \cdot e^{-\alpha_d \cdot C_p \cdot \tau_j} \cdot \delta(t - \tau_j) + \sum_{k=1}^{Mm} \sigma_{sk} \cdot e^{-\alpha_d \cdot C_p \cdot \tau_k} \cdot \delta(t - \tau_k) \quad [23.7]$$

where the first sum refers to the scattering related to the composition ( $\sigma_{sj}$  is the scattering cross-section of a granulate) and the second to scattering related to the damage ( $\sigma_{sk}$  is the scattering cross-section of a crack).

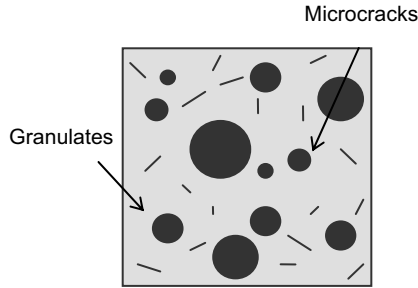


**Figure 23.23.** *Simulated concrete*

The granulates in our concrete being not very elongated, we model them by spheres (Figure 23.23). The damage which appears on the form of microcracks is taken into account in the model by some disks. In this study, we work only on relative values in amplitude, so an approach to calculation of scattered sections  $\sigma_{sj}$  for the spheres and  $\sigma_{sk}$  for the disks has been chosen.

Different classical compositions of concrete (mortar, micro-concrete, concrete) have been simulated. Some damage states by microcracks are then introduced.

From an inversion process on simulated data (inverse crime), the range of depths or frequencies useable is 140 mm for a frequency of 500 kHz and 40 mm for 2.5 MHz.

The experimental study carried out on samples damaged thermally by a thermal containment in a range varying from 20°C (non-damaged) to 200°C (highly damaged), has shown a high sensitivity of the attenuation coefficient (deduced from the back-scattered waves) to the frequency and the damage. The attenuation is more important when the frequency increases. Figure 23.24 shows the attenuation evolution with damage for the measurements made at a central frequency of the sensor of 500 kHz.

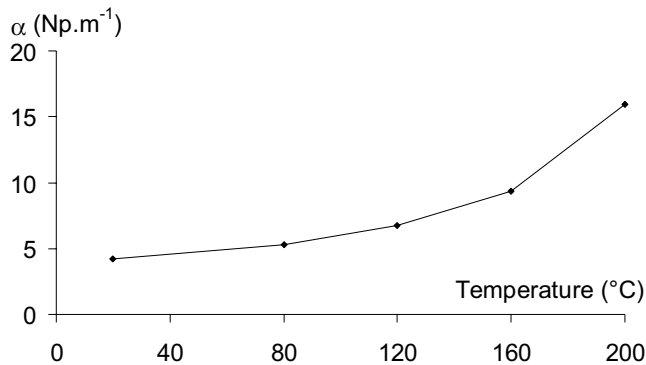


**Figure 23.24.** Evolution of the attenuation coefficient as a function of temperature (damage) and frequency [CHA 03a]

It has also been shown that the exploitation of back-scattered waves can be considered, for concretes near the surface, from 40 mm (2.5 MHz) to 140 mm (500 kHz) with relatively easy on-site implementation. The concrete ageing was due to a thermal stress, but the principle is applicable to all types of damage which yields modifications of the microstructure. This approach can be completed by introducing the equations of multiple scatterings.

#### 23.1.4. Homogenization applied to concrete

The several analyses presented formerly are based on an approach and an argument coming from the knowledge and mastery of material evolutions, of information processing as well as waves propagation. This pragmatic approach of NDT in civil engineering must be based on a theoretical description of the physical phenomena. A precise description of the direct problem becomes important in order to then have strong models for the inverse problem. The propagation of ultrasonic waves in concrete must namely bring into play the phenomena of multiple scatterings, which are characteristic of wave propagation in concrete [CHA 03a].

##### 23.1.4.1. Waves – scatterers interactions

The equations of bulk waves in the case of a homogenous, linear, elastic and isotropic medium of density  $\rho$ , are used to estimate the mechanical characteristics of the material. In the case of concrete, which is a very heterogenous material, each granulate can be seen as a scatterer. When the wavelength is around the aggregate length, this aggregate can scatter the wave in the matrix and thus disturb its



propagation in concrete. This perturbation can modify the velocity and attenuation, and depends on frequency. At the scale of the material, the scattering becomes multiple and the wave can scatter towards the front, keeping or losing its coherence, as well as towards the back. The waves scattered towards the back give back-scattered waves and the incoherent waves scattered towards the front yield the Coda (end of the ultrasonic signal for heterogenous media). We will deal with the coherent part scattered towards the front.

The scattering can be simple or multiple (Figure 23.25).

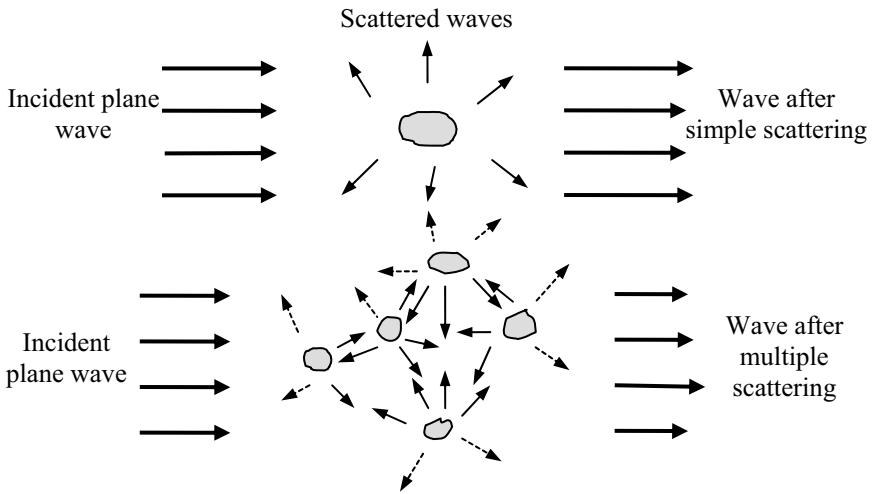


**Figure 23.25.** *Principle of multiple scattering*

The substitution in equation [WAT 61] enables us to define a field scattered by the obstacle  $\varphi_{\text{diff}}$  which depends on the field generated by the incident plane wave  $\varphi_{\text{inc}}$ . Let us introduce a linear operator  $T(\vec{r}')$ , depending on media, on incident waves and on the shapes of scatterers. It allows modeling the field scattered by an obstacle centered in  $\vec{r}'$ :

$$\varphi_{\text{diff}}(\vec{r} / \vec{r}') = T(\vec{r}').\varphi_{\text{inc}}(\vec{r}) \quad [23.8]$$

The total field in  $\vec{r}$  is then

$$\varphi(\vec{r}) = \varphi_{\text{inc}}(\vec{r}) + T(\vec{r}').\varphi_{\text{inc}}(\vec{r}) \quad [23.9]$$

For  $N$  scatterers located at points  $(\vec{r}_1, \dots, \vec{r}_j, \dots, \vec{r}_N)$ , it becomes

$$\varphi(\vec{r}) = \varphi_{inc}(\vec{r}) + \sum_{j=1}^N T(\vec{r}_j) \varphi_E(\vec{r} / \vec{r}_j; \vec{r}_1, \dots, \vec{r}_N) \quad [23.10]$$

The excitation field  $\varphi_E(\vec{r} / \vec{r}_j; \vec{r}_1, \dots, \vec{r}_N)$  of the scatterer in  $\vec{r}_j$  comes from the composition of the incident field and the fields scattered by all other scatterers. It is obtained by

$$\varphi_E(\vec{r} / \vec{r}_j; \vec{r}_1, \dots, \vec{r}_N) = \varphi_{inc}(\vec{r}) + \sum_{\substack{k=1 \\ k \neq j}}^N T(\vec{r}_k) \varphi_E(\vec{r} / \vec{r}_k; \vec{r}_1, \dots, \vec{r}_N) \quad [23.11]$$

Generalizing, we obtain:

$$\begin{aligned} \varphi(\vec{r}) = & \varphi_{inc}(\vec{r}) + \sum_{j=1}^N T_j [\varphi_{inc}(\vec{r})] + \sum_{j=1}^N \sum_{\substack{k=1 \\ k \neq j}}^N T(\vec{r}_k) T(\vec{r}_j) \varphi_{inc}(\vec{r}) \\ & + \sum_{j=1}^N \sum_{\substack{k=1 \\ k \neq j}}^N \sum_{\substack{l=1 \\ l \neq k}}^N T(\vec{r}_l) T(\vec{r}_k) T(\vec{r}_j) \varphi_{inc}(\vec{r}) + \dots \end{aligned} \quad [23.12]$$

Simple scattering consists of limiting the problem to the two first terms. This corresponds to the well-known Born approximation.

#### 23.1.4.2. Homogenization

For highly heterogenous materials (more than 5% of scatterers), simple scattering is no longer valid, and the notion of equivalent material enables us to homogenize the medium considering average configurations.

If we define the probability of obtaining the scatterer  $j$  at the position  $\vec{r}_j$  by

$$p(\vec{r}_j) = \int_V \dots \int_V p(\vec{r}_1, \dots, \vec{r}_N) dv_1 \dots dv_{j-1} dv_{j+1} \dots dv_N \quad [23.13]$$

where  $dv_i$  is a small volume element centered in  $\vec{r}_i$  and  $V$  is the total volume accessible to scatterers.

The probability of obtaining the scatterer  $j$  at the position  $\vec{r}_j$  and the scatterer  $k$  in  $\vec{r}_k$  is:

$$p(\vec{r}_j, \vec{r}_k) = \int_V p(\vec{r}_1, \dots, \vec{r}_N) dv_1 \dots dv_{j-1} \cdot dv_{j+1} \dots dv_{k-1} \cdot dv_{k+1} \dots dv_N \quad [23.14]$$

The densities of scatterers are obtained by:

$$\begin{cases} n(\vec{r}_j) = N \cdot p(\vec{r}_j) \\ \text{and } n(\vec{r}_j; \vec{r}_k) = (N-1) p(\vec{r}_j; \vec{r}_k) \end{cases} \quad [23.15].$$

The statistical means on the set of possible configurations are applied on the total field integrating the multiple scattering, defined by the former equations. We obtain a set of  $N$  equations from which we extract the first three average values:

$$\begin{cases} \langle \varphi(\vec{r}) \rangle = \varphi_{\text{inc}}(\vec{r}) + \int_V n(\vec{r}') T(\vec{r}') \langle \varphi_E(\vec{r} / \vec{r}'; \vec{r}') \rangle \cdot dv' \\ \langle \varphi_E(\vec{r} / \vec{r}_j; \vec{r}_j) \rangle = \varphi_{\text{inc}}(\vec{r}) + \int_V n(\vec{r}'; \vec{r}_j) T(\vec{r}') \langle \varphi_E(\vec{r} / \vec{r}'; \vec{r}', \vec{r}_j) \rangle \cdot dv' \\ \langle \varphi_E(\vec{r} / \vec{r}_j; \vec{r}_j, \vec{r}_k) \rangle = \varphi_{\text{inc}}(\vec{r}) + \int_V n(\vec{r}'; \vec{r}_j, \vec{r}_k) T(\vec{r}') \langle \varphi_E(\vec{r} / \vec{r}'; \vec{r}', \vec{r}_j, \vec{r}_k) \rangle \cdot dv' \end{cases} \quad [23.16]$$

The different dynamic models suggest breaking these relationships at different levels to define an effective field which describes the propagation of coherent wave in the medium, that is to say an average field which satisfies Helmholtz's equation.

$$\langle \varphi(\vec{r}) \rangle = \varphi_0 \cdot e^{i(k^* \cdot \vec{r})} \quad [23.17]$$

with

$$k^* = \frac{2\pi f}{c} + i\alpha^* \quad [23.18]$$

The propagation characteristics of this (longitudinal or transverse) wave are defined by the complex wavenumber in the equivalent medium,  $k^*$  (the asterisk refers to the equivalent medium), whose real part is linked to the phase velocity  $c^*$  and the imaginary part is the attenuation  $\alpha^*$ .

To simplify the problem, a quasi-crystalline approximation (thus a sequencing one) is implemented to limit the problem to the first two equations and to the knowledge of the first scatterer.

In the case of spherical scatterers, the different fields are broken up on the basis of Legendre polynomials.

The propagation direction is considered following a direction  $\vec{Z}$  and the origin is taken in  $\vec{r}_1$  :

$$\left\{ \begin{array}{l} \langle \varphi(\vec{r}) \rangle = e^{i.k_1.z_1} \cdot \sum_{n=0}^{\infty} a_{n0} \cdot j_n(k_1|\vec{r} - \vec{r}_1|) \cdot P_n^0(\cos(\theta_{\vec{r}\vec{r}_1})) \\ \langle \varphi_E(\vec{r}/\vec{r}_1; \vec{r}_1) \rangle = \sum_{n=0}^{\infty} E_{n0}(z_1) \cdot j_n(k_1|\vec{r} - \vec{r}_1|) \cdot P_n^0(\cos(\theta_{\vec{r}\vec{r}_1})) \\ T(\vec{r}_1) \cdot \langle \varphi_E(\vec{r}/\vec{r}_1; \vec{r}_1) \rangle = \sum_{n=0}^{\infty} E_{n0}(z_1) \cdot T_{n0n0}(\vec{r}_1) \cdot h_n(k_1|\vec{r} - \vec{r}_1|) \cdot P_n^0(\cos(\theta_{\vec{r}\vec{r}_1})) \end{array} \right. \quad [23.19]$$

where  $a_{n0}$  are the known expansion coefficients of the incident non-scattered field,  $E_{n0}(z_1)$  are the unknown coefficients of the excitation field in  $z_1$ ,  $T_{n0n0}(\vec{r}_1)$  is the coefficient of the T-Matrix for the obstacle located in  $\vec{r}_1$  and  $k_1$  is the longitudinal wavenumber in the matrix.

From this system, we can extract the coefficients  $E_{n0}$

$$E_{n0}(z_1) = e^{i.k_1.z_1} + \sum_{j=0}^{\infty} i^{-j} \cdot T_{j0j0} \cdot \sum_s (-i)^s \cdot \mathcal{A}(0, j|0, n|s) \cdot \int_V E_{j0}(z') \cdot n(\vec{r}'; \vec{r}_1) \cdot h_s(k_1|\vec{r}' - \vec{r}_1|) \cdot P_s^0(\cos(\theta_{\vec{r}'\vec{r}_1})) \cdot dV \quad [23.20]$$

Waterman and Truell [WAT 76] make the assumption that the scatterer density is constant in the medium and that interpenetration is impossible. The scatterers are supposed spherical, of radius  $a$ .

They deduce, applying the (optical) extinction theorem, a simple formalism by the estimation of  $E_{n0}$ . The result is of the form:

$$\left(\frac{k^*}{k_1}\right)^2 = \left[1 + \frac{2\pi n_0 \cdot f(0)}{k_1^2}\right]^2 - \left[\frac{2\pi n_0 \cdot f(\pi)}{k_1^2}\right]^2 \quad [23.21]$$

where  $f(0)$  and  $f(\pi)$  correspond to the amplitudes scattered toward the front and the back on an obstacle alone.

These functions are determined by putting into the equation the scattering in the far field assumption (stable spherical wave).

In the case of a spherical obstacle for longitudinal plane waves:

$$f_{\ell 1}(\theta) = \frac{1}{i \cdot k_{\ell 1}} \cdot \sum_{n=0}^{\infty} (2n+1) (T^{11})_{n0n0}^{\ell 1} \cdot P_n^0(\cos(\theta)) \quad [23.22]$$

The linear operator of the T matrix [VAR 76] is defined from the knowledge of the incident and scattered displacement fields which are written in the matrix 1:

$$\overrightarrow{u}_{inc}^1(\vec{r}) = \sum_{\sigma=1}^2 \sum_{p=0}^{\infty} \sum_{q=0}^p \left[ a_{pq}^{\sigma} \cdot Reg \left[ \overrightarrow{\phi}_{pq}^{1\sigma}(\vec{r}) \right] + b_{pq}^{\sigma} \cdot Reg \left[ \overrightarrow{\psi}_{pq}^{1\sigma}(\vec{r}) \right] + c_{pq}^{\sigma} \cdot Reg \left[ \overrightarrow{\chi}_{pq}^{1\sigma}(\vec{r}) \right] \right] \quad [23.23]$$

$\vec{r}$  being outside the obstacle;

$$\overrightarrow{u}_{diff}^1(\vec{r}) = \sum_{\sigma=1}^2 \sum_{n=0}^{\infty} \sum_{m=0}^n \left[ \alpha_{nm}^{\sigma} \overrightarrow{\phi}_{nm}^{1\sigma}(\vec{r}) + \beta_{nm}^{\sigma} \overrightarrow{\psi}_{nm}^{1\sigma}(\vec{r}) + \gamma_{nm}^{\sigma} \overrightarrow{\chi}_{nm}^{1\sigma}(\vec{r}) \right], \quad [23.24]$$

$\vec{r}$  being inside the obstacle;

where  $\alpha_{nm}^{\sigma}$ ,  $\beta_{nm}^{\sigma}$  and  $\gamma_{nm}^{\sigma}$  are the unknown expansion coefficients of the scattered field, and  $a_{pq}^{\sigma}$ ,  $b_{pq}^{\sigma}$  and  $c_{pq}^{\sigma}$  the known expansion coefficients of the incident field.

The definition of regular vectorial potentials at the origin (noted  $\text{Reg}[\dots]$ ) brings into play the Legendre associated polynomials  $P_n^m$  of degree  $(n-m)$  and Hankel's function  $H_n$  of first kind and of order  $n$ .

These coefficients enable  $\overrightarrow{u}_{\text{inc}}^1$  to verify the vectorial wave propagation equation.

The matrix operator  $T$  allows linking the known and unknown expansion coefficients.

$$\begin{bmatrix} \alpha_{nm}^\sigma \\ \beta_{nm}^\sigma \\ \gamma_{nm}^\sigma \end{bmatrix} = \begin{bmatrix} (T^{11})_{nmpq}^\sigma & (T^{12})_{nmpq}^\sigma & (T^{13})_{nmpq}^\sigma \\ (T^{21})_{nmpq}^\sigma & (T^{22})_{nmpq}^\sigma & (T^{23})_{nmpq}^\sigma \\ (T^{31})_{nmpq}^\sigma & (T^{32})_{nmpq}^\sigma & (T^{33})_{nmpq}^\sigma \end{bmatrix} \begin{bmatrix} a_{pq}^v \\ b_{pq}^v \\ c_{pq}^v \end{bmatrix} \quad [23.25]$$

There is a sum on the repeated subscripts and superscripts  $(v, p, q)$ , but the consideration of geometrical problems allows us to break the sum into several unities, or eventually several tens, or so. We can also cancel some elements of this matrix of matrices.

The matrix coefficients refer to the different possible mode conversions, so:

- $T^{11}$  describes the transformation of the incident longitudinal wave into scattered longitudinal waves;
- $T^{21}$  describes the transformation of the incident longitudinal wave into scattered transverse waves (1<sup>st</sup> polarization);
- $T^{31}$  describes the transformation of the incident longitudinal wave into scattered transverse waves (2<sup>nd</sup> polarization).

The interest of using the matrix,  $T$  is to have all conversion modes in the equations. The calculation of the coefficients of this matrix is made through a decomposition matrix  $Q$  [VAR 79].

### 23.1.4.3. Application to concrete

In the case of concrete, we make three assumptions:

- the part which becomes incoherent because of the multiple wave interactions with the different scatterers, has a weak amplitude and will not be taken into account;
- the attenuation part linked to the absorption (internal friction and warming up) is neglected with respect to the scattering in heterogenous solids;
- the scatterers are assimilated to spheres or spheroids for granulates.

In some limits, the heterogenous concrete medium is homogenized (Figure 23.26) transforming it in an equivalent material for which it is possible to determine the velocity and the attenuation [CHA 03b].

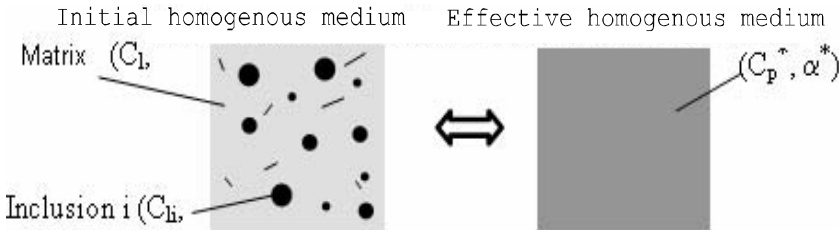


**Figure 23.26.** Principle of concrete homogenization

In the case of scatterers of several sizes or natures and of different types, it is possible to average the parameters such as the size  $a$  or the type  $\alpha$  of scatterers.

$$\left(\frac{k^*}{k_1}\right)^2 = \left[1 + \frac{2\pi n_0 \langle f(0) \rangle}{k_1^2}\right]^2 - \left[\frac{2\pi n_0 \langle f(\pi) \rangle}{k_1^2}\right]^2 \quad [23.26]$$

$$\text{with } \langle f(\theta) \rangle = \int_{\alpha} p(a) f(\theta, a) da \quad [23.27]$$

where  $p(a)$  is the distribution function of the sizes of scatterers;

$$\text{or } \langle f(\theta) \rangle = \int_{\alpha} p(\alpha) f(\theta, \alpha) d\alpha \quad [23.28]$$

where  $p(\alpha)$  is the distribution function of the types of scatterers.

#### 23.1.4.4. Follow-up of concrete damage

In order to take into account the damage, the morphology of the porosities is the sphere and that of cracks is a disk or a spheroid. By hypothesis, an assembly of flattened cracks randomly distributed in position or in orientation with respect to the initial path of the ultrasonic beam will have an average effect on the beam, similar to that of an assembly of spheres of the same determined dimension.

The size importance, as well as that of volume ratio of air spheres, is shown by Figure 23.27.

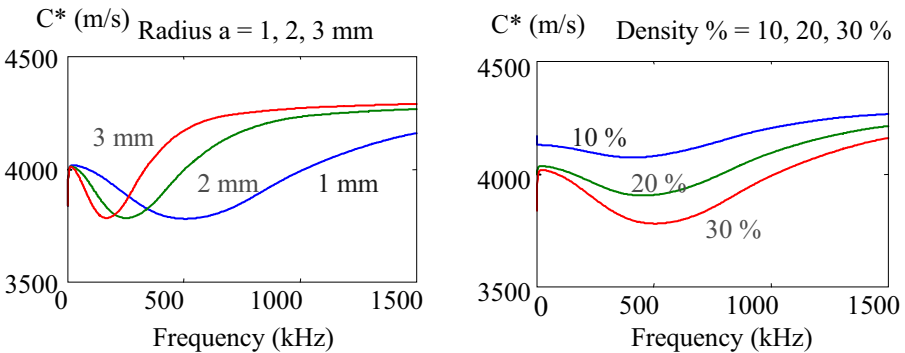


**Figure 23.27.** Calculation of the velocity and the attenuation as a function of the frequency of an ultrasonic transmitted wave through a medium consisting of a homogeneous matrix and polystyrene balls of variable diameter and density [CHA 03b]

The results show a systematic decrease of the velocity for a frequency evolving with the size of air spheres (from 1 to 3 mm) and for an amplitude depending on the bulk ratio of scatterer (from 10 to 30%). This decrease can be the determinant element of characteristics measuring the average scatterers and their distribution.

#### 23.1.4.5. Experimental validation

It is necessary to validate these variations experimentally, in order to consider this observation as an indicator of the evolution of the microstructure and the damage.

Some specific test specimens have enabled us to make some samples similar to the description used in the model developed from the works of Waterman and Truell. The samples are of size  $\phi$  250 mm and thickness 45 mm.



Velocity and attenuation measurements have been made on an experimental assembly validated by a calculation of uncertainties (Figure 23.28).

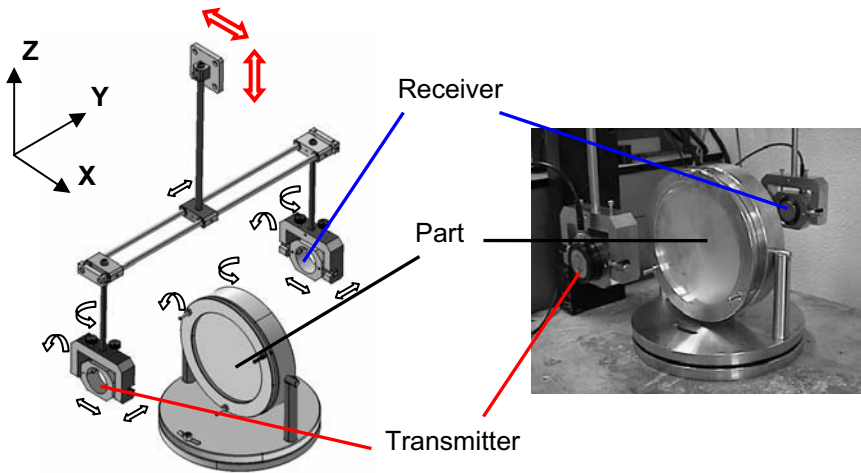


**Figure 23.28.** *Experimental assembly for velocity and attenuation measurements in immersion [CHA 03b]*

The experimental set-up in immersion enables us to validate the far field hypothesis and to master the paths and distances travelled by ultrasonic waves. The scatterers are some polystyrene balls in a mortar or concrete matrix (Table 23.1).

Material	Density ( $\text{kg.m}^{-3}$ )	LW Velocity ( $\text{m.s}^{-1}$ )	TW Velocity ( $\text{m.s}^{-1}$ )
Rock	2,650	5,700	3,200
Expanded Polystyrene	17	330	-
Matrix	2,145	4,320	

**Table 23.1.** *Characteristics of test sample materials [CHA 03b]*

Three transducer pairs are used to work on the largest possible bandwidth.

The measurement is obtained by comparison with the path in water and the path in water and in the test specimen.

From the transfer functions of the media met by the waves, the velocity and attenuation parameters are determined as functions of the frequency.

Incorporating the correction of the beam divergence, due to the far field assumption, the uncertainties in concrete on the velocity measurement is of  $\pm 50$  m/s and that of the attenuation measurement is  $\pm 2$  Np  $\text{m}^{-1}$ .

The tests carried out on a cement matrix including 30% polystyrene balls of  $\phi=3$  mm show an interesting agreement between tests and calculated values (Figure 23.29). The experimental results made from three different transducer pairs (Exp fc=central frequency 250, 500, and 1,000 kHz show a divergence only for the low frequencies).

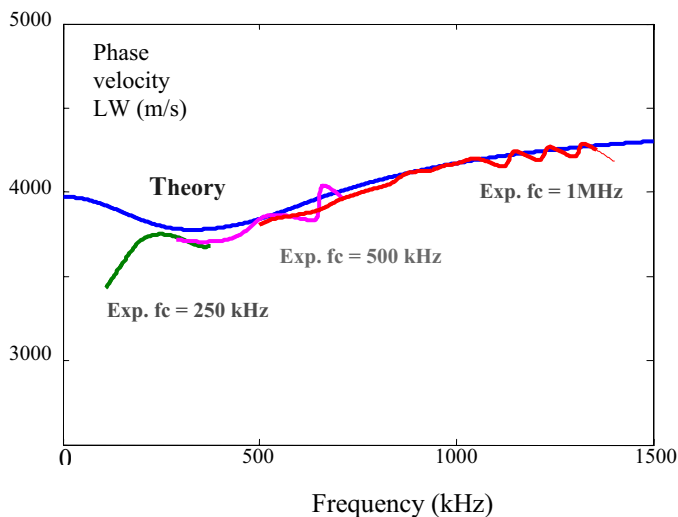


**Figure 23.29.** Comparison of values of calculated and measured phase velocities for a test sample including 30% polystyrene balls [CHA 3b]

We find again in this case a minimum of the velocity, experimentally checked in term of amplitude and frequency distribution.

#### 23.1.4.6. Application to a specific concrete

This same development is presented (Figure 23.30) with a material similar to concrete, made of 40% cement, 30% sand and 30% aggregates (black curve). To simulate a supposed homogeneous isotropic damage, we add 10% of polystyrene balls instead of the 10% cement (red curve). The blue curves show the evolution of phase velocity and attenuation as a function of the frequency.

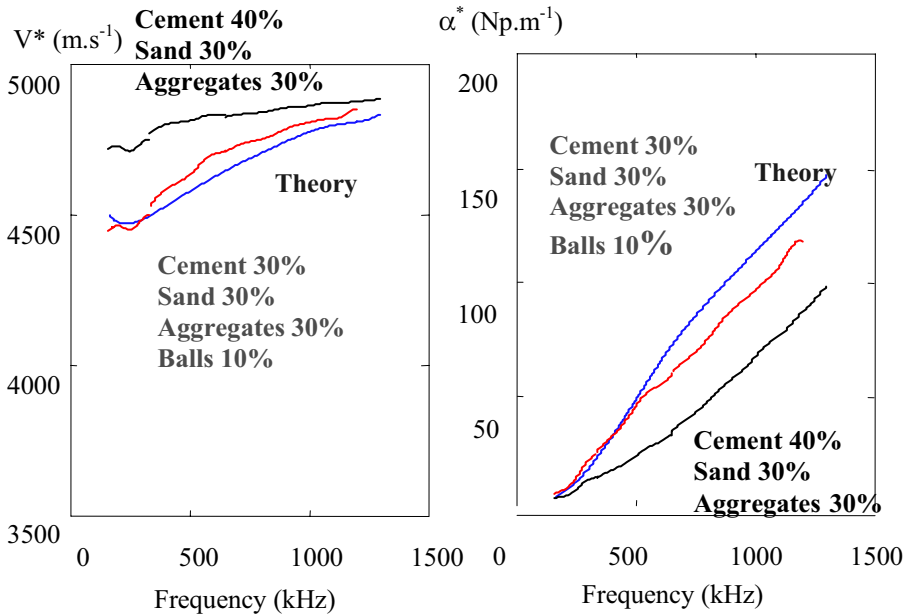


**Figure 23.30.** Comparison of calculated and measured values of phase velocities and attenuation as functions of frequency for a test sample including 10% polystyrene balls, 30% sand, 30%, aggregates and 30 % cement [CHA 03b]

We again find the minimum of the phase velocity as predicted by the calculation. The calculations which give the attenuation show a very important evolution of the attenuation coefficients.

#### 23.1.4.7. Conclusion

Taking into account multi-scattering in concrete has enabled us to develop a simulation, as a function of the frequency, of the evolutions of the velocity and attenuation of the ultrasonic waves propagating into the concrete test specimen. Such an approach is an example of the simulation process, which tends towards a more realistic representation of experimental and environmental conditions in the frame of Non-Destructive Evaluation of concrete.

#### 23.1.5. Conclusions

Non-destructive testing and evaluation of concrete structures, by analysis of acoustic waves has been done for a long time, but robust empirical approaches have only enabled questions to be partially answered. Today, some development and

research approaches are being made to take into account the major role of influential parameters, and thus improve the whole aspect of testing.

Some progress has been made in the domain of the generation and reception of waves, as well as in the procedures of data evaluation and processing. In particular, taking into account multi-scattering of coherent waves has to be the object of further developments. It will be necessary, among other things, to follow the content and distribution of water and gels trapped in the porosities and/or cracks. It will also be important to show the wave interaction with obstacles nearer and nearer to the reality, in term of morphology. This will be an important step of the simulation of the direct problem.

The research topics concerning back-scattering and incoherent waves are also the object of important developments. They allow the use of all possible and pertinent data sources to construct, spatially and energetically, acoustic wave propagation, revealing many mechanical characteristics of the concrete.

### 23.2. Bibliography

- [BAR 92] Baron J., Ollivier J. P., *La durabilité des bétons*, ATHIL, 455, 1992
- [BRE 05] Breyse D., Abraham O., *Méthodologie d'évaluation non destructive de l'état d'altération des ouvrages en béton*, Edition Presses Ponts et Chaussées, 560, 2005
- [BS 86] British Standard, "Recommendation for the measurement of velocity of ultrasonic pulses in concrete, Testing concrete", *BS 1881*: Part 203, 1986
- [CAN 73] Cannard G., Carracilli J., Prost J., Venec Y., "Auscultation dynamique des superstructures par les méthodes classiques", *Rapport de recherche LCPC*, n°34, 1973
- [CAR 94] Carino N.J., "Nondestructive testing of concrete: history and challenges, Concrete Technology – Past, Present and Future", *V.M. Malhotra Symposium*, Ed Mehta, 623–678, 1994
- [CHA 03a] Chaix J.F., Garnier V., Corneloup G., "Concrete damage evolution analysis by backscattered ultrasonic waves", *NDT&E International*, Vol. 36, 461–9, 2003
- [CHA 03b] Chaix J. F., Caractérisation non destructif de l'endommagement de bétons: Apport de la multidiffusion ultrasonore, PhD thesis, University of the Mediterranean, 2003
- [COR 95] Corneloup G., Garnier V., "Analyse ultrasonore du temps de prise de béton compacté roulé", *Materials and Structures*, Vol. 29, n°189, 295–304, 1996
- [DRE 95] Dreux G., Festa J., *Nouveau guide du béton*, 7th edition, 317, Ed. Eyrolles, 1995
- [EN 12504-4] "Testing concrete in structures – Part 4: Determination of ultrasonic pulse velocity", *European Norm EN 12504-4*

- [HEV 98] Hévin G., Abraham O., Pedersen H.A., Campillo M., "Characterisation of surface cracks with Rayleigh waves: a numerical model", *International Journal of Nondestructive Testing and Evaluation*, 31(4), 289–97, 1998
- [GAR 95] Garnier V., Corneloup G., Sprauel J. M., Perfumo J. C., "Setting time of roller compacted concrete by spectral analysis of transmitted ultrasonic signals", *NDT International*, Vol. 28, n°1, 15–22, 1995
- [MIL 55] Miller G. F., Pursey H., *On the Partition of Energy between Elastic Waves in a Semi-Infinite Solid*, Royal Society, London, Series A Vol. 233, n°1192, 55–69, 1955
- [PAR 05] Paris O., Poidevin C., Rambach J.M., Nahas G., "Imagerie ultrasonore dans les bétons", *Proceedings of the CONFRED Congress of Beaune*, June 2005
- [PED 94] Pederson H. A., Sanchez-Sesma F. J., Campillo M., "Three dimensional scattering by two dimensional topographies", *Bull. Seism. Soc. Am.*, Vol. 84, 1169–83, 1994
- [PRO 02] Proust A., Lenain J.C., "Acoustic emission monitoring of civil infrastructures (Application of damage detection in full scale concrete structure)", *Proceedings of EWGAE 2002 25th European Conference on Acoustic Testing*, Praha, 2002
- [RYD 04] Ryden N., Park C. B., Ulriksen P., Miller R.D., "Multimodal approach to seismic pavement testing", *Journal of Geotechnical and Geoenvironmental Engineering*, 130(6), 636–45, 2004
- [SAN 88] Saniie J., Wang T., Bilgutay N.M., "Statistical evaluation of backscattered ultrasonic grain signals", *Journal of Acoustical Society of America*, Vol. 84, No. 1, 400–8, 1988
- [TOU 98] Touret J. P., *Surveillance et réhabilitation des ouvrages, Actes du colloque Recherche & Innovation en Génie Civil*, French Research Ministry, Paris, p. 25, 2 April 1998
- [VAR 76] Varatharajulu V., Pao Y.H., "Scattering matrix for elastic waves – I Theory", *Journal of Acoustical Society of America*, Vol. 60, 556–66, 1976
- [VAR 79] Varadan V.V., Varadan V.K., "Scattering matrix for elastic waves - III. Application to spheroids", *Journal of Acoustical Society of America*, Vol. 65, 896–905, 1979
- [VOL 03] Volkovoy Y., Stain R., "Ultrasonic Cross Hole Testing of Deep Foundations - 3D imaging", *Proceeding of Non-Destructive Testing in Civil Engineering*, Berlin, 16-19 September 2003
- [WAR 05] Wardany R. A., Caractérisation non destructive des structures en béton au moyen des ondes dispersives de Rayleigh et de Lamb, Thèse de doctorat ès sciences appliquées, University of Sherbrooke Quebec, Canada, 2005
- [WAT 61] Waterman P.C., Truell R., "Multiple scattering of waves", *Journal of Mathematical Physics*, Vol. 2, No. 4, 512–37, 1961
- [WAT 71] Waterman P.C., "Matrix theory of elastic wave scattering", *Journal of the Acoustical Society of America*, Vol. 60, No. 3, 567–580, 1976

This page intentionally left blank

## Chapter 24

# Non-Destructive Evaluation and Testing and Structural Health Monitoring of Composite Materials by Ultrasound and Acoustic Emission

### 24.1. Introduction

Ultrasonic Non-Destructive Evaluation (NDE) and Non-Destructive Testing (NDT) of materials are set apart by their respective objectives. NDE aims to measure or characterize certain properties of materials, namely mechanical and/or structural ones. NDT aims to search for and characterize the flaws likely to diminish the mechanical quality, and even to lead to the failure of the material or structure. However, these two fields are deeply linked, as each measurement of property can be used for testing.

In NDT, a material or a structure will be considered “healthy” if, during a scanning, the (signal) parameters chosen as indicators do not show significant variation with respect to a reference threshold fixed beforehand. In spite of its qualitative nature, this definition of a healthy material is by far the most used by the community of engineers and researchers in NDT. In some cases, this approach is not

quite satisfactory, namely in mechanics and in material engineering where more quantitative quantities are searched and studied because their developments might give judicious information about the micro-structural state and for the healthy state of the material, namely in presence of a diffuse damage. In the frame of health monitoring, NDE can offer more adapted solutions, namely for complex materials such as the composite materials for which the search of reliable testing and evaluation methods are the purpose of intensive researches.

Generally, NDE methods are based on the interaction of a physical field with the material, its micro-structure and the potential flaws it contains. Depending on cases, we use electromagnetic radiation (Foucault current, microwaves, X-Rays, etc.), or mechanical waves (ultrasound, sound). Ultrasonic methods are preferred when the testing concerns some parts of large dimensions or of large thicknesses. Moreover, these waves are intimately related to the elastic properties of the media supporting the propagation. These properties can be identified and followed as a function of the different stresses (mechanical, hygrothermal, etc). Among these characteristics, the elasticity constants are important data for several mechanical as well as metallurgical reasons. The determination of these quantities by ultrasound has been largely presented in this work and we will not return to this subject (see Chapter 20). We will try to show that ultrasonic evaluation, by means of the characteristics it allows us to identify, can become a competitive tool of health testing and monitoring of the structure material, namely having been in service for many years. In parallel, recent progress in acoustic emission shows that this method allows us to follow, in real time while a part is being stressed, the damage, and to quantitatively characterize these mechanisms in some cases. This tool can be advantageously coupled with a method of non-destructive bulk observation such as ultrasonic evaluation, likely to bring some complementary information. Some recent work has shown the relevance of this global approach for the health monitoring of composite materials based on polymer matrices [NEC 05a].

Our contribution to this work covers these two aspects and tries to show the relevance of this global approach for the health monitoring of materials. First, we present a study of ultrasonic non-destructive evaluation of composites based on polymer matrices in hygrothermal ageing. Then, we present some results illustrating the potentialities of acoustic emission as a quantitative characteristic mean of damaging mechanisms. We finish our topic by showing the interest of a global approach to ultrasonic evaluation coupled with acoustic emission in a prospect of global health monitoring of materials and structures.



### 24.1.1. Health monitoring of polymer matrix based composites in hygrothermal ageing

#### 24.1.1.1. The materials

The composite materials studied in this section are composed of epoxy matrices reinforced by glass fibers oriented in the same direction. They come from an industrial process of filament winding and by unidirectional pre-preg molding by stress, respectively. The matrix is obtained by crosslinking of a resin DGEBA with an anhydride hardener [DUC 01]. For the ultrasonic measurements, we have parallelepipedic test samples are taken of composite sheets. Figure 24.1 presents the symmetry axes and the reference planes considered in the following. Axis 1 refers to the fiber axis, whereas the orthogonal axes 2 and 3 form the plane P23 perpendicular to the fiber axis. The orthogonal axes 1 and 3 define the plane P13 parallel to the fiber axis. The plane P45 is thus located at  $45^\circ$  with respect to the planes P23 and P13. The plane P12 refers to the parallel faces of largest dimension parallel to the fiber axis.

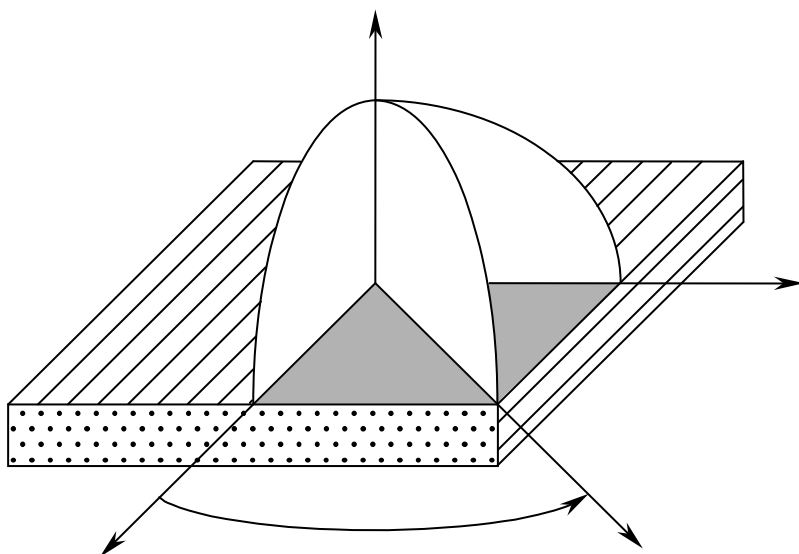


**Figure 24.1.** Symmetry axes of the unidirectional glass/epoxy composite and ultrasonic propagation plane

These composites, made in the form of multilayered composites with cross-folds, are used as structural material for water piping in nuclear power plants. The goal of this work is to detect the damage of these materials resulting from high temperature water (fibers–matrix decohesion and matrix cracking), the fibers' failure appearing only during well-advanced global failure of the material.

#### 24.1.1.2. *Hygrothermal ageing: ultrasonic speed and stiffness loss*

The followed approach to estimate this damage consists of characterizing the effect of hygrothermal ageing on mechanical behavior. Thus, we have first studied elastic anisotropy in terms of ultrasonic velocity, and identified the elasticity constants of the material in its virgin, initial state [DUC 01]. The material damage has then been estimated in terms of ultrasonic velocity and stiffness loss during 25 days in accelerated ageing conditions at 70°C in distilled water. The method of determination of elastic constants has already been presented in this book and will not be explained here [DUC 01]. The technique used for measuring the propagation velocities in variable incidence is an impulse technique in immersion. The transducers used in this case have a central frequency of 2.25 MHz. The test sample, a leaf with parallel faces of regular surfaces and thickness (Figure 24.1), is put in a coupling liquid (in this case, water) between a transmitter and a receiver. This configuration allows the incidence angle of the plane wave generated by the transmitter to be varied with respect to the normal to the sample face. In the most general case, three bulk waves can be generated in the material by mode conversion at the water/material interface: a quasi-longitudinal wave and two quasi-transverse waves.

The velocity measurement begins by the acquisition of a so-called reference signal which corresponds to the path of an ultrasonic pulse between the transmitter and the receiver in water. Once the sample is inserted between the transmitter and the receiver, the so-called measurement signal is acquired. The propagation velocity, corresponding to the path in the sample, is then deduced, by varying the incident angle, from the gap between propagation times of the measurement signals and the reference signal. In this case, the gap is obtained by cross-correlation of these signals. Some geometrical considerations lead to a simple expression of the propagation velocity of the ultrasonic wave in the material in variable incidence [ELG 01]. The material has been damaged in water during the 25 days in accelerated ageing conditions at 70°C. These velocities have been measured in the initial state and after 10, 20 and 25 days, respectively. Figures 24.2 and 24.3 present the quasi-longitudinal and quasi-transverse velocities, respectively, measured in plane P23. Figures 24.4 and 24.5 present the quasi-longitudinal and quasi-transverse velocities, respectively, measured in plane P13. The measured velocities, represented by points associated with an uncertainty bar, are drawn as functions of the propagation angle in the sample for different ageing periods.

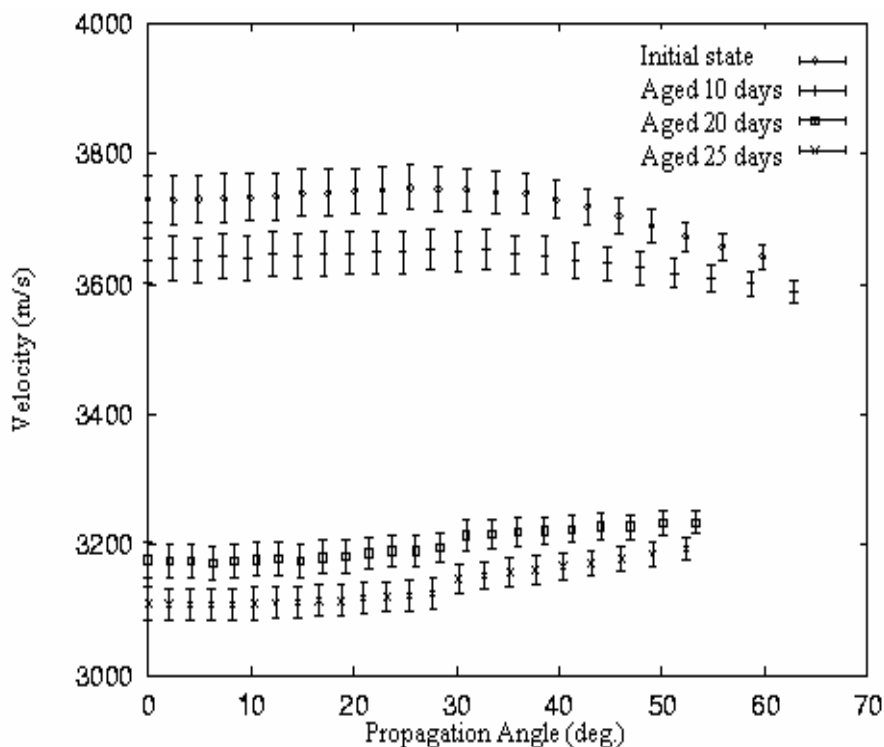


**Figure 24.2.** Unidirectional composite, quasi-longitudinal velocities measured in plane P23 (perpendicular to the fibers) for different ageing periods

The velocities measured in planes P23 and P13 decrease with ageing time. However, this decrease depends on the propagation direction. For example, the quasi-longitudinal velocities measured at normal incidence present a bigger decrease than the quasi-longitudinal velocities measured in oblique incidence. This observation is qualitatively related to the anisotropy of the development of elastic properties during ageing. Apart from the quasi-transverse velocities in the plane P23, the velocity decrease is not linear, but happens mostly during 10 and 20 days of ageing.

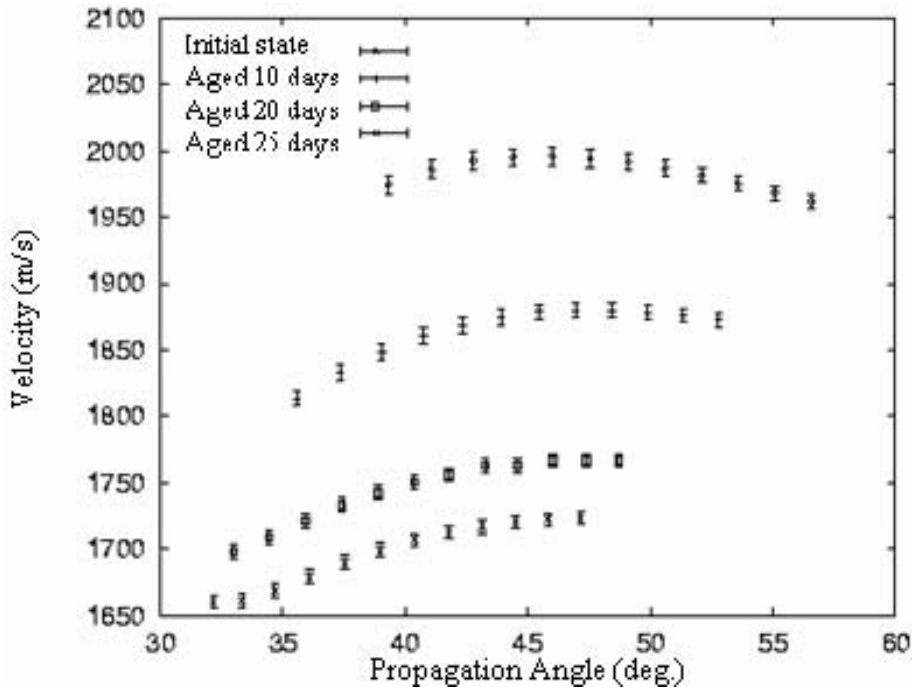


**Figure 24.3.** Unidirectional composite, quasi-transverse velocities measured in plane P23 for different ageing periods

Figures 24.2 and 24.3 show that, in the initial state, the velocities measured in plane P23 show small variations with respect to the propagation angle, compared to the variations observed in the plane P13. Thus, in the initial state, plane P23 can be considered as close to the isotropic case for ultrasonic propagation. Consequently, the elastic behavior of the composite can be treated with the assumption of transverse anisotropy with five independent elastic constants [ROY 96].

The velocity development in plane P23 reveals the appearance of some anisotropy during the ageing in this plane, initially close to the isotropy. Thus, the ultrasonic follow-up of the hygrothermal ageing in terms of the development of propagation velocities highlights the possible development of the elastic behavior of the unidirectional composite from a transverse isotropy toward an orthotropic behavior with nine independent elastic constants.

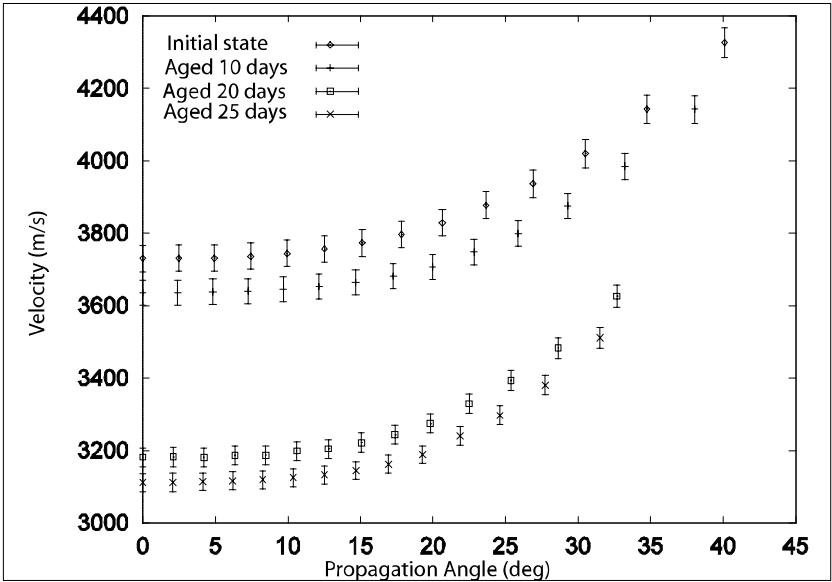


**Figure 24.4.** Unidirectional composite, quasi-longitudinal velocities measured in plane P13 for different ageing periods

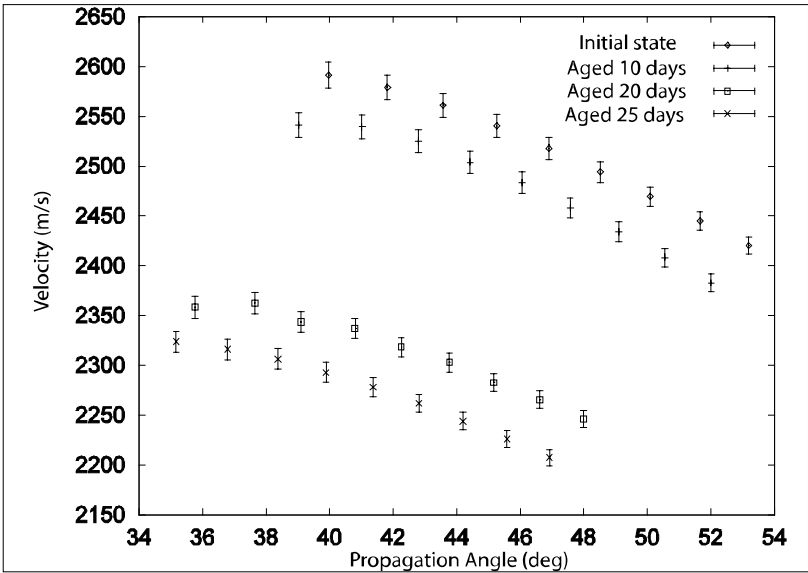


**Figure 24.5.** Unidirectional composite, quasi-transverse velocities measured in plane P13 for different ageing periods

The assumption of orthotropic elastic behavior determines the elastic constants of this composite in the initial state and during ageing. However, the small thickness of the sample does not enable the measurement of quasi-transverse velocities in plane P45. The absence of these velocities allows only a partial determination of elasticity constants in the orthotropic assumption (seven only among the nine elasticity constants that describe this kind of anisotropy) [ELG 01]. In these conditions, Table 24.1 brings together the elasticity constants and the associated uncertainties, determined by optimization from the measured velocities in planes P23 and P13 [DUC 01].

t	$C_{11}$	$C_{22}$	$C_{33}$	$C_{23}$	$C_{13}$	$C_{44}$	$C_{55}$
0	71,5±1,4	30,2±0,4	30,7±0,3	13,2±0,2	15,4±0,2	7,7±0,2	8,3±0,3
10	68,9±1,4	29,1±0,4	29,2±0,3	14,0±0,1	14,3±0,2	6,7±0,2	7,6±0,3
20	63,1±1,5	26,5±0,5	22,3±0,2	10,8±0,2	10,4±0,2	4,8±0,2	6,7±0,2
25	62,6±1,5	26,4±0,4	21,3±0,2	10,9±0,1	10,2±0,2	4,3±0,2	6,0±0,2

**Table 24.1.** Elasticity constants  $C_{ij}$  (GPa) as function of time  $t$  (days)

The hygrothermal ageing of the composite causes a global and important decrease of the elasticity constants. However, this decrease appears different depending on the constants, as indicated in Table 24.1. The anisotropic development of the elastic behavior of the composite, which has just been dealt with qualitatively in terms of the development of the ultrasonic propagation velocities, can now be studied quantitatively through the macroscopic variables of damage. This is the subject of the next sub-section, where we will also suggest an interpretation of this damage, from a micro-structural observation of the 25 days old composite.

#### 24.1.1.3. Hygrothermal ageing: variables of damage

The results above show that at this ageing stage, the density of flaws, distributed homogeneously in the scanned area, appears sufficient to lead to a significant development of elastic properties (Table 24.1). We use, in the following, the variable of damage  $D_{ij}$  describing this damaging phenomenon macroscopically. The diagonal components  $D_{ii}$  of this tensor are expressed simply as a function of i) the elastic constants  $C_{ij}$  during the damaging and ii) the elastic constants of the material in its non-damaged initial state  $C_{ij}^0$  [BAS 92].

$$D_{ii} = 1 - \frac{C_{ii}}{C_{ii}^0} \quad i = 1, \dots, 6 \quad [24.1]$$

The non-diagonal components of the tensor  $D_{ij}$  ( $i \neq j$ ), whose expressions as functions of the  $C_{ij}$  are more complicated, have not led to significant variation and thus will not be considered. Variables  $D_{11}$ ,  $D_{22}$  and  $D_{33}$  quantify the damage along the principal axes 1, 2 and 3, respectively, whereas  $D_{44}$  and  $D_{55}$  characterize the damage in the principal shear planes P23 and P13, respectively (Figure 24.1). These variables of damage  $D_{ii}$  can vary between 0 and 1; the value 0 refers to the initial state (supposed healthy) and the value 1 to failure. Figure 24.6 shows the developments of variables  $D_{11}$ ,  $D_{22}$  and  $D_{33}$  obtained for the composite as a function of the ageing time.

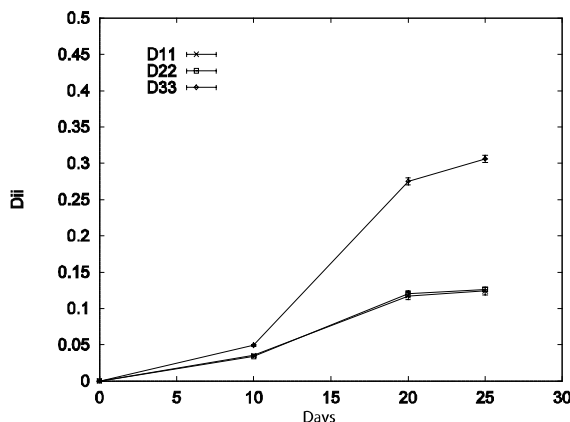


Figure 24.6. Parameters of damage in principal directions

Figure 24.7 shows the development of variables  $D_{44}$  and  $D_{55}$  in the same conditions.

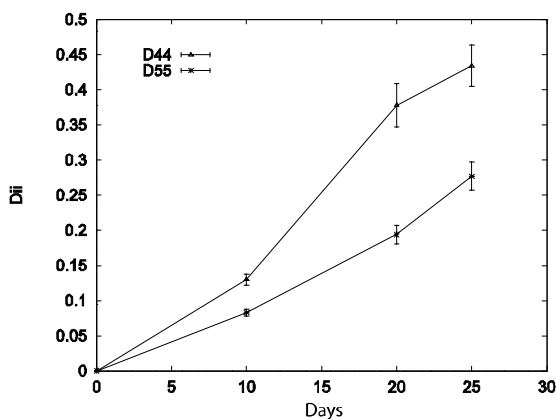
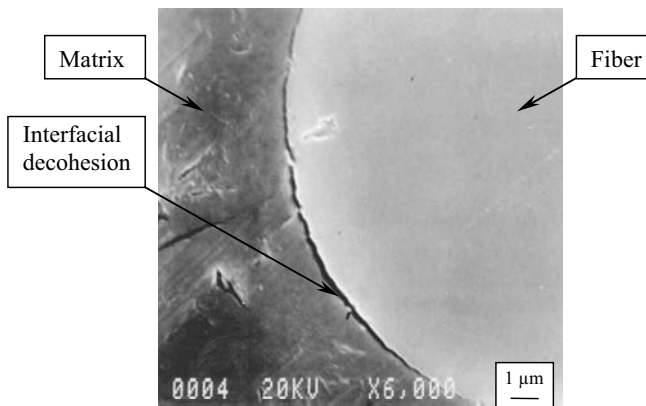


Figure 24.7. Parameters of damage in principal planes

The development of the variables of damage  $D_{ii}$  illustrates the strongly anisotropic nature of this damaging phenomenon. Indeed, these developments show a much bigger stiffness loss along direction 3, normal to the sample, than along directions 1 and 2. In addition, the variable of damage  $D_{44}$  presents a significantly greater development, reaching a value of about 0.45 (Figure 24.7). This increase of variable  $D_{44}$  shows a large decrease of the shear stiffness in plane P23. The shear of plane P23, perpendicular to the fibers' axis, stresses the fiber/matrix bond strongly, which leads us to suppose that the increase of variable  $D_{44}$  is directly related to an alteration of this bond during the ageing. However, the former observations would suggest an irregular damage distribution at the fiber/matrix interface. The increase of  $D_{33}$  compared to  $D_{22}$  suggests that the bond deterioration, and thus the deterioration of the fiber/matrix interface, is much more significant in areas where the fiber is oriented along direction 3. An assumption made to explain this orientation consists of considering that ultrasonic waves used in normal incidence stress the fiber pole directed along axis 3 much more, where the fiber/matrix bond is more exposed to the absorption front of hot water. To confirm these hypotheses, we have performed a study with a scanning electronic microscope on the 25-days aged composite. Figure 24.8 presents a negative picture of this observation performed on a transverse section of the composite.



**Figure 24.8.** Observation with a scanning electronic microscope: transverse section

This figure clearly shows the presence of an area of interfacial decohesion between the fiber and the matrix, which does not occur on the entire contour of the fiber. This decohesion is directed preferentially towards direction 3, which corresponds to the direction of diffusion in water along the sample thickness [ELG 01].



### 24.1.2. *On-site health monitoring of polymer based composites stressed in creep: global ultrasonic and acoustic emission approach*

#### 24.1.2.1. *Materials*

Two major families of composite materials based on a polymer matrix have been studied in this sub-section: some unidirectional composites and some with cross-folds  $[\pm 62^\circ]_{12}$  and  $[90/35^\circ]_{12}$ . For the cross-folded sheets noted  $[\pm 62^\circ]_{12}$ , 12 folds of unidirectional composites (UD) are dispersed in a polyester matrix at  $\pm 62^\circ$  with respect to the stress axis. The composites  $[90/35^\circ]_{12}$  are made of 12 folds of UD dispersed in a polyester matrix at  $90^\circ$  and  $35^\circ$  with respect to the stress axis, respectively.

#### 24.1.2.2. *The acoustic emission*

Composite materials with a polymer matrix, the objects of this study, are today extensively used in many sectors (nuclear, aeronautical, automotive and naval transport, civil engineering, etc.). The health monitoring of these materials in use is a necessity. The goal of this health monitoring is to detect and quantify on-site the damage of the material. The methods of health monitoring must also, eventually, lead to the determination of whether the damaged structure must be replaced or can still be used. In the former case, it is necessary to determine its remaining lifetime. To reach these objectives, the acoustical emission (AE), which corresponds to the elastic energy radiated by the stressed material, has many advantages, in particular that of being a passive testing mean applicable on structures in use. Figure 24.9 illustrates its principle. However, this very competitive tool for the health monitoring of materials is, most of the time, only used in a qualitative way as a global damaging indicator.

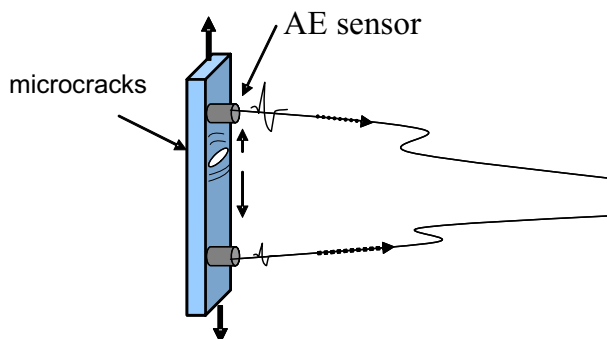


**Figure 24.9.** *Principle of the acoustical emission, stressed material generating an acoustical wave*

Then, the current research works on AE are mostly dedicated to the identification and discrimination of damaging mechanisms, and to the estimation of the remaining lifetime of materials and structures, from the relevant parameters extracted from AE signals. Our contribution to this book is within this framework.

Most of the analyses of data from acoustical emission are based on a conventional analysis of the temporal parameters such as signal amplitude, energy, count number etc. Figure 24.10 represents a typical AE signal obtained from composites based on polymer matrices. The signals of acoustical emissions generated by composite materials based on polymer matrices are generally discrete signals. On these signals, several parameters can be defined as indicated on Figure 24.10.

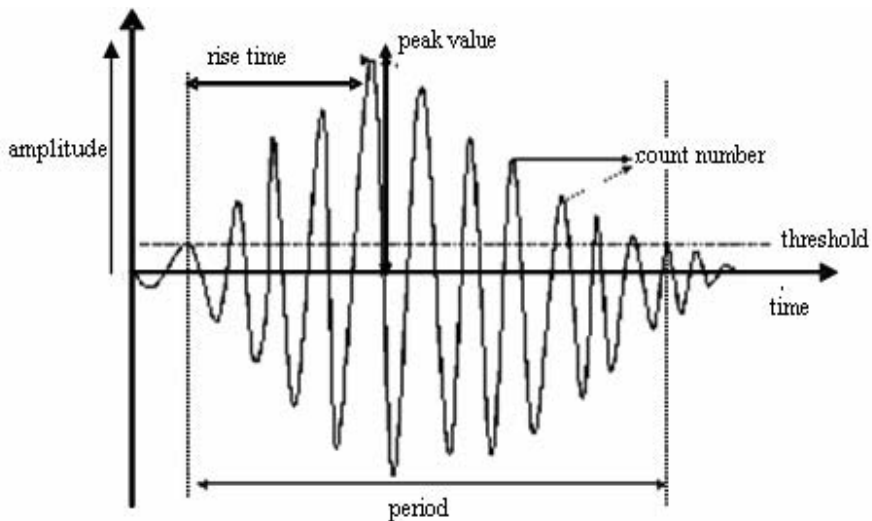


**Figure 24.10.** *Principal parameters of a discrete burst of acoustical emission*

In the following, we will show that a conventional analysis of these parameters enables us, in some simple cases (reference materials under simple stresses), to link AE signals to the well-identified damage. However, for industrial materials (cross-folded composites, SMC, etc.), the identification of damaging mechanisms requires a multivariable statistical analysis of relevant parameters, due to the complexity of the phenomena involved.

In this article, we first briefly present the results of the conventional analysis of the acoustical emission on reference materials (matrix alone and unidirectional composites). The multivariable statistical analysis, enabling the discrimination of the damaging modes as a function of the AE signals, is then applied to the data coming from tensile and creep testings on composites based on more complex polymers, namely cross-folded.

#### 24.1.2.3. Identification of acoustical signatures of damaging mechanisms: conventional analysis

The identification of acoustical signatures of damaging mechanisms of composite materials based on polymer matrices is generally carried in a progressive way [HUG 02, NEC 05a]. Some tests on pure resin enable, for example, identification of the AE signals characteristic of the matricial microcrack. Figure 24.11 represents a typical signal of this damaging mechanism; this type of signal representative of the matricial microcrack is generally called signal of type A [HUG 02].

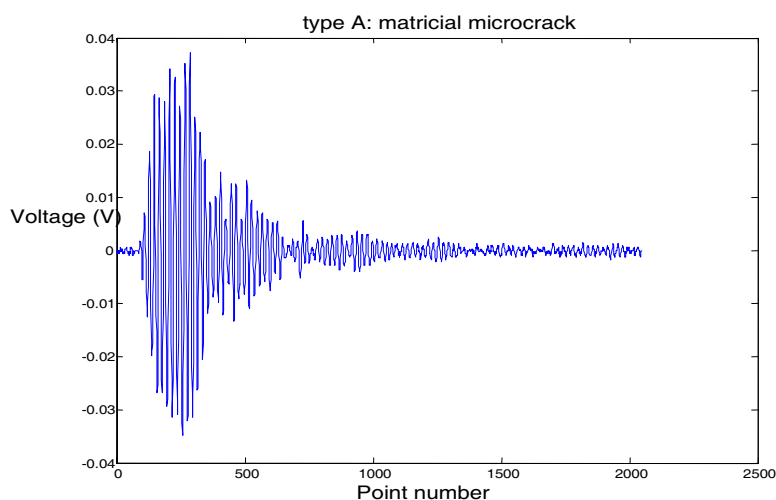


**Figure 24.11.** *Acoustical signature of matricial microcrack*

Some tests of deviated tension carried on samples of unidirectional composite yield matricial microcrack and interfacial decohesions. The AE signals of the matricial microcrack being already identified, this type of test reveals the acoustical signatures of the interfacial decohesion. A typical example of this type of signal, denominated signals of type B, is represented in Figure 24.12.

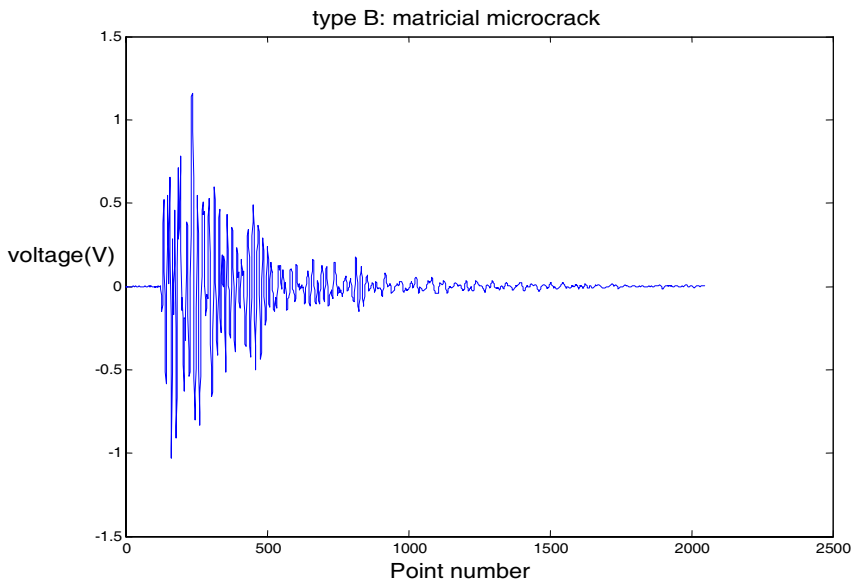


**Figure 24.12.** *Acoustical signature of the fiber/matrix decohesion*

These signals differ by their respective energies and amplitudes, the signals of type B being much more energetic than those of type A. They also differ by their temporal lengths, those of type B being shorter. Some authors have done some tests on single-fiber composites (resin, polyester and glass fiber), identifying signals of so-called type C representative of the fiber rupture [HUG 02]. Some authors have shown that these elementary damaging mechanisms stimulated in uniaxial tension on other unidirectional composites (epoxy matrix, carbon fibers) gave similar acoustical signatures, leading them to think that these former were little influenced by the nature of components of unidirectional composites based on polymer matrices [BAR 94]. We have tried to see if these acoustical signatures depend on the test type. In order to do this, some unidirectional composites have been stressed in creep and their acoustical emission has been studied. The creep test consists of applying a constant stress to the material and in following its distortion with time. Figure 24.13 represents such a test on a unidirectional composite stressed at  $45^\circ$  with respect to the fibers' axis. On this figure, the acoustical activity recorded during the test is also represented in terms of the cumulated count number.

The conventional analysis based on the amplitude and the length of these creep tests on unidirectional composites has shown that the damaging mechanisms involved here (that is to say, the matricial microcrack and the fiber/matrix

decohesion) have acoustical signatures similar to those identified during the tension tests with forced velocity.

This result leads us to think that the acoustical signatures do not depend on the stress type either.

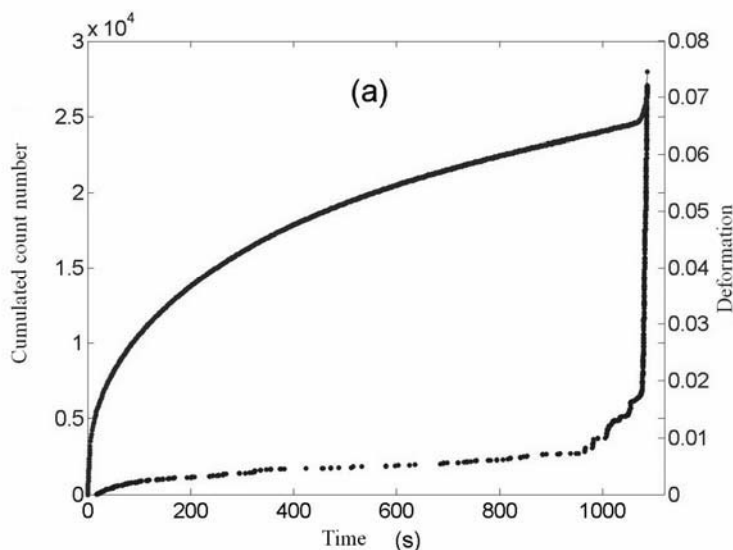


**Figure 24.13.** Creep test on a unidirectional composite stressed at  $45^\circ$  with respect to the fibers' axis, deformation as a function of time and acoustical activity in terms of the cumulated count number

If this qualitative classification is sufficiently efficient to describe the damaging mechanisms of these reference materials, it is insufficient to estimate the relative importance of the identified damaging modes and their kinetic of development during the stress. To reach these objectives, a multivariable statistical analysis must be implemented. It is the topic of the next section where such an analysis is made on unidirectional composites and cross-folded composites.

#### 24.1.2.4. Multi-parameters statistical analysis of acoustical emission signals: cross-folded composites based on unidirectional polymer stressed in creep

The methods of multivariable statistical analysis enable us to define the resemblances or the differences between the data, taking into account  $d$  characteristics. These data, represented by form vectors with  $d$  components, thus  $d$  parameters, are grouped in classes according to the principle of shape recognition [DUB 90], each class defining a damaging type. To do this, the method of fuzzy

C-means clustering is used [BEZ 81]. This coalescence algorithm has the advantage of providing a fuzzy partition of the space of data representation, that is to say each form vector is localized in the space of data representation with the help of membership values comprised in the interval  $[0,1]$ , enabling its location with respect to the set of classes present. A membership value of 0 to a class means that the pattern vector is far from the class since a membership value of 1 means that the pattern vector strongly belongs to the class. The input of the algorithm is the number of classes  $M$ . The descriptors constituting the form vectors are the parameters issued from the temporal study (length, amplitude, energy, count number, etc.). After data separation by the algorithm into  $M$  classes, it is necessary to identify *a posteriori* the highlighted classes. This classification is made by comparing the distributions of amplitude and energy within each class with the distributions reported in the literature. Before testing this approach on cross-folded composites, we have applied it on unidirectional composites stressed in creep at  $45^\circ$  with respect to the fibers' axis. As two damaging mechanisms have been identified on these materials, the number of chosen classes is two. The descriptors used for the classification are the energy and the amplitude. The result obtained is presented in Figure 24.14.

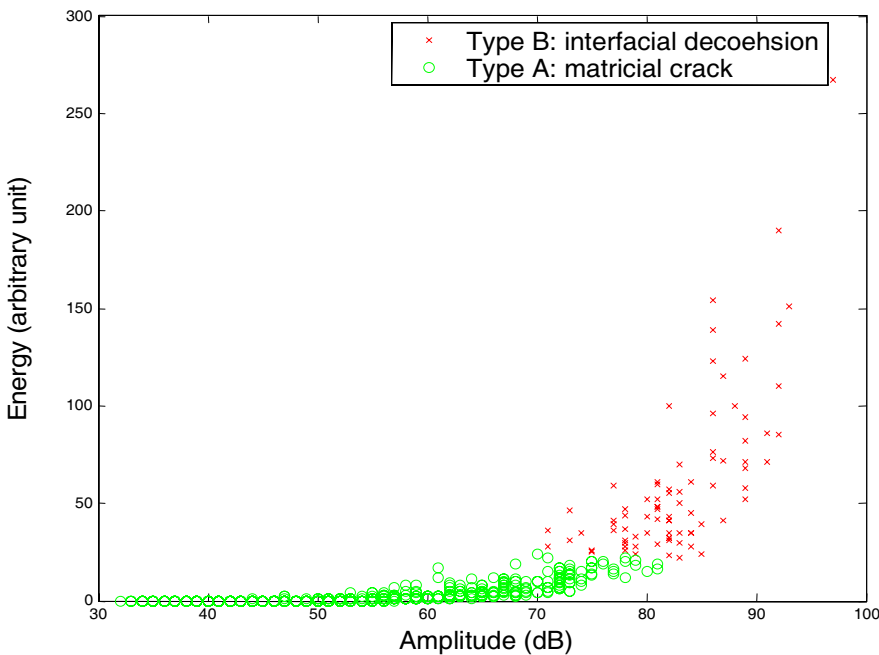


**Figure 24.14.** Unidirectional composite, separation of AE data in two classes

The two classes are clearly identified. We find again the matricial crack centered around 55 dB and the interfacial decohesion around 80 dB. The use of the rise time and count number as descriptors gives some similar results in terms of the classification. Figure 24.15 represents the apparition chronology of the two types of signals during the test.

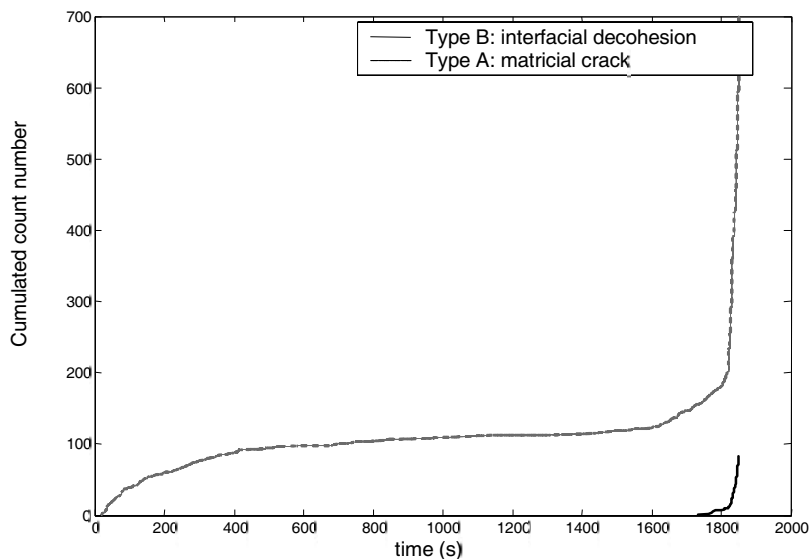


**Figure 24.15.** *Unidirectional composite, chronology of apparition of the two classes of signals during the creep test*

This representation enables us to see the progress of the different damaging mechanisms. Then, during primary creep (up to 400 seconds), the detected signals are of small amplitude and correspond to signals of type A, characteristic of the matricial crack. During the secondary creep (from 400 to 1,600 seconds), some signals of type B are added, corresponding to the apparition of the fibers/matrix decohesion. The rate of signals of type B increases significantly during the tertiary creep (beyond 1,700 seconds). The classification method used is not supervised, as the structuring of the space of representation of the data in classes is made without information of the damaging type corresponding to each piece of data. However, it is quite simple to implement and gives some quite satisfactory results, even for the more complicated materials such as cross-folded composites  $[\pm 62^\circ]_{12}$ , as we will see

in the following. Let us note the development by some authors of some non-supervised approaches such as auto-organizer maps of Kohonen [HUG 02].

The cross-folded composite materials  $[\pm 62^\circ]_{12}$ , are made of 12 unidirectional folds disposed in a polyester matrix of  $\pm 62^\circ$  with respect to the stress axis. In addition to the matricial microcrack and the fiber/matrix decohesion, some delaminations are likely to develop in this multilayered material [NEC 05a]. The fuzzy C-means clustering method is thus tested with three classes. The descriptors used for this classification are the energy and the temporal length. The result obtained is presented in Figure 24.16.

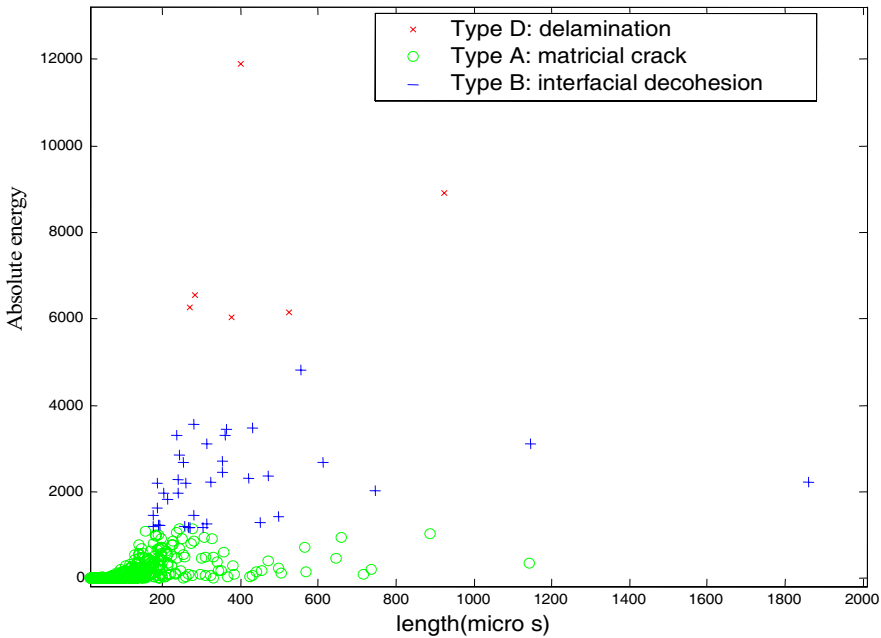


**Figure 24.16.** Cross-folded composite  $[\pm 62^\circ]_{12}$ , separation of AE data in 3 classes

The three damaging classes that we expected are clearly identified. We again find the matricial crack and the interfacial decohesion. We add, to these two damaging mechanisms, a third mechanism, probably linked to the delamination. Figure 24.17 represents the chronology of apparition of these three signal types during the test.



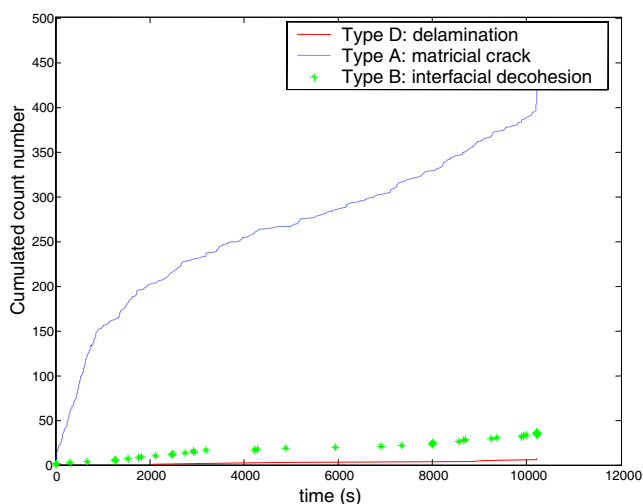


**Figure 24.17.** *Cross-folded composite  $[\pm 62^\circ]_{12}$ , chronology of apparition of the three signals classes during the creep test*

This representation again enables us to see the progress of the different damaging mechanisms, showing the predominance of the matricial microcrack but also the apparition of the fiber/matrix decohesion; delamination appears immediately after the test starts.

#### 24.1.2.5. *Health evaluation and monitoring: global ultrasonic and acoustical emission approach*

In the following, and to conclude this contribution, we show the feasibility of the global non-destructive approach of the health evaluation and monitoring of materials, which matches the acoustical approach and the ultrasonic evaluation. This innovative approach consists of on-site measurement of the elastic properties of the stressed material by ultrasound and the simultaneous acquisition of the AE produced. Then, we can link the stiffness loss, at the macroscopic scale measured by ultrasound, to the microscopic damaging mechanism through the signals of the acoustical emission under stress conditions. This approach has required the development of a particular assembly, enabling the measurement of the ultrasonic velocity in the direction of the test sample thickness and the simultaneous

acquisition of acoustical emission through two transducers fixed to the sample extremities [NEC 05a]. The operating scheme of such an assembly is illustrated in Figure 24.18. Then, from the measurement of the ultrasonic velocity, it is possible to simply go back to the elastic properties in the thickness direction [NEC 05a].

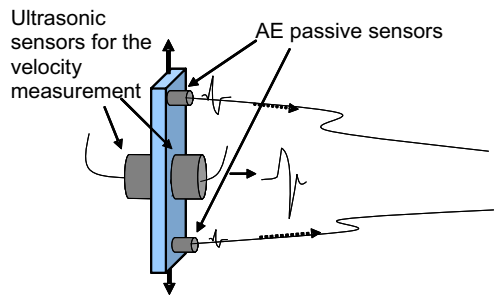


**Figure 24.18.** Operating scheme of the global approach; some ultrasonic sensors in the thickness direction (transmitter and receiver) enable measurement of the propagation velocity in the thickness direction; some acoustic emission sensors put in the extremities of the sample acquire the acoustical emission generated by the material

Figure 24.19 shows an example of result obtained on a cross-folded composite [90/35]<sub>12</sub>.

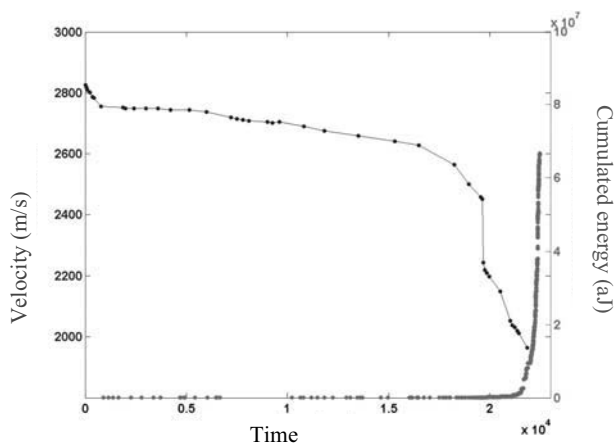


**Figure 24.19.** Ultrasonic velocity measured in the thickness direction in transmission and acoustical emission in terms of the cumulative energy for composite [90/35]<sub>12</sub>

From the measurement of the velocity, the elastic constant in the thickness direction has been determined, as well as the corresponding variable of damage (this variable is noted  $D_{US}$ ). In parallel, from the acoustical emission data, a variable of damage noted  $D_{EA}$  is defined:

$$D_{EA} = \frac{N}{N_t} \quad [24.2]$$

where  $N$  is the current count number, and  $N_t$  the total count number at the end of the test. Thus,  $D_{EA}$  is comprised between 0 and 1: the value 0 corresponds to the virgin state at the beginning of the test, and the value 1 to the failure at the end of the test. The variables  $D_{US}$  and  $D_{EA}$  can then be advantageously compared.

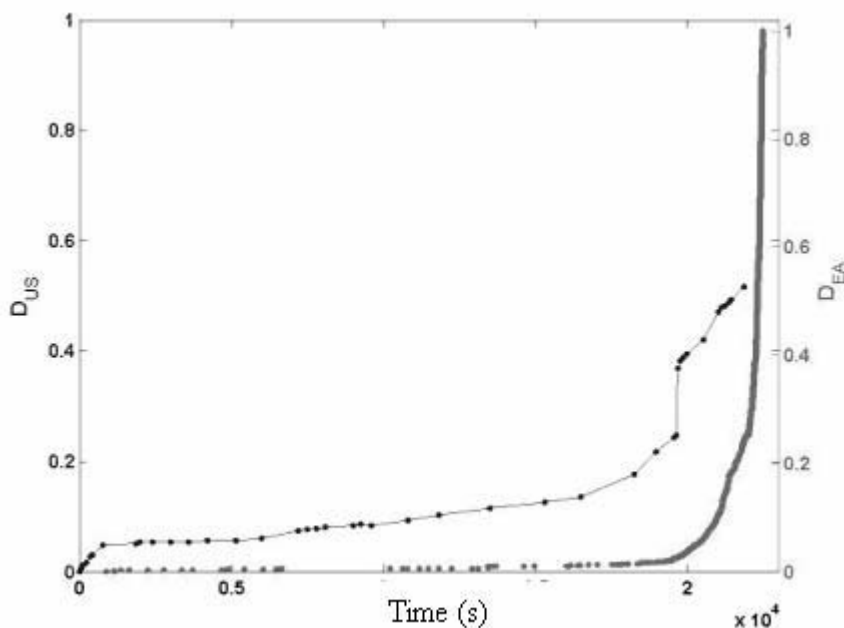


**Figure 24.20.** Ultrasonic and acoustical emission variable of damage for the composite  $[90/35]_{12}$  stressed in creep

We note a quite good correlation between the ultrasonic variables of damage and those of acoustical emission during the three creep phases (this correlation is also clearly visible in Figure 24.19 where the decrease of the velocity, observed along the test is qualitatively well-correlated to the acoustical emission). The ultrasonic

variable seems more sensitive at the beginning of the test and during the secondary creep. This may be due to the fact that during this period, some AE signals are too weak to be detected, their amplitude being below the threshold fixed by the AE acquiring system (in order to eliminate some noise sources). Conversely, in the tertiary creep area and namely in the failure neighborhood, the variable of damage related to the AE varies very quickly, showing the AE sensitivity in this area. The two approaches appear to be very complementary for this material. This result illustrates well the relevance of this global approach.

### 24.1.3. Conclusions

In the state-of-the-art industrial sectors (terrestrial transport, aerospace, nuclear, civil engineering, etc.), the damage of structural materials is a key point for the mastery of durability and reliability of components in use. If ultrasonic methods are very competitive for the characterization of damage, namely anisotropic as we have shown, acoustical emission can turn out to be a very efficient quantitative method, working in real time, of enabling the identification of damaging mechanisms using their acoustical signatures. Beyond these characterization problems, for which some great steps have been made, the problem which appears now concerns the estimation of the remaining lifetime of materials and structures in use. In fact, in order to reach this objective, it is necessary not only to quantify the damage, but also to identify the different precursor mechanisms which are responsible for it and which we can follow on-site. To respond to this problem, acoustical methods are interesting, namely the acoustical emission because of its capacity to follow the damage in real time, and also to detect and characterize these precursor events. Some recent results have shown that, for these heterogeneous materials, namely composites stressed in creep, the radiated acoustical energy varies with time according to a power law near the failure [NEC 05b]. Then, a statistical analysis of AE, beyond the identification of damaging mechanisms involved, could enable us, using models from statistical physics, to reach this goal of the estimation of the remaining lifetime.

## 24.2. Bibliography

- [BAR 94] Barre, S. and M.-L. Benzeggagh, "On the use of acoustic emission to investigate damage mechanisms in glass-fibre-reinforced polypropylene", *Composites Science and Technology*, 52, 369–76, 1994
- [BAS 92] Baste, S., El Guerjouma, R. and Audoin, B., "Effect of microcracking on the macroscopic behaviour of ceramic matrix composites: ultrasonic evaluation of anisotropic damage", *Mechanics of Materials*, 14, 1, 15–31, 1992
- [BEZ 81] Bezdek J. C., *Pattern Recognition with Fuzzy Objective Function Algorithms*, Plenum Press, 1981

- [DUB 90] Dubuisson B., *Diagnostic et reconnaissance des formes*, Paris: Hermes Science Publications, 1990
- [DUC 01] Ducret D., El Guerjouma R., Jayet Y., Baboux J.C., “Anisotropic damage evaluation in polymer fiber composites under hygrothermal aging by means of ultrasonic techniques”, *Review of Progress in Quantitative Non Destructive Evaluation*, 20 B, 1199–206, 2000
- [ELG 01] El Guerjouma R., Baboux J.C., Ducret D., Godin N., Guy P., Huguet S., Jayet Y. Monnier T., “Non-destructive evaluation of damage and failure of fiber reinforced polymer composites using ultrasonic waves and acoustic emission”, *Advanced Engineering Materials*, 3, 8, 601–8, 2001
- [HUG 02] Huguet S., Godin N., Gaertner R., Salmon L., Villard D., “Use of acoustic emission to identify damage modes in glass fibre reinforced polyester”, *Comp. Sci. Tech.*, 62, 10-11, 1433–1444, 2002
- [NEC 05a] Nechad H., Helmstetter A., El Guerjouma R., Sornette D., “Andrade and Critical Time-to-Failure Laws in Fiber–Matrix Composites: Experiments and Model”, *Journal of the Mechanics and Physics of Solids*, 53, 5, 1099–127 May 2005
- [NEC 05b] Nechad H., Helmstetter A., El Guerjouma R., Sornette D., “Creep Ruptures in Heterogeneous Materials”, *Phys. Rev. Lett.* 94, 045501, 2005
- [ROY 96] Royer, D., Dieulesaint, E., *Ondes élastiques dans les solides – Tome 1: Propagation libre et guidée*. Paris: Masson, 1996

This page intentionally left blank

Part 7

## Characterization of Poroelastic Materials

This page intentionally left blank



## Chapter 25

# Metrology of Physical Parameters of Absorbing Materials

### 25.1. Introduction

#### 25.1.1. *Acoustical parameters*

##### 25.1.1.1. *Porosity*

The porosity  $\phi$  of a porous material is defined as the ratio of the fluid volume saturating a material to the total volume of the material. It is a dimensionless quantity which can vary from 0 (solid, non porous material) to 1 (free fluid medium). This parameter, which characterizes the internal geometry of the porous material (in which the acoustical wave can propagate) is not always simple to obtain precisely. Used for a long time in geology, it can be measured by comparing the volume of a rock to the volume of water it can absorb. This method cannot be used without damage, in the case of acoustical materials.

In the case where the material density and the porous structure are known, a simple ratio enables us to obtain the porosity. This can be used for glass wool, but the precision is not always perfect as it requires both measurement of the volume and measurement of the mass of a glass wool sample, with all the uncertainties entailed.

---

Chapter written by Michel HENRY, Christophe AYRAULT, Bernard CASTAGNÈDE, Zine EL ABIDINE FELLAH, Claude DEPOLIER, Mohamed FELLAH, Walter LAURIKS and Sohbi SAHRAOUI.

The method proposed here is a non-destructive method. It consists of measuring the volume of air included in a sample of porous material, using the properties of a perfect gas. A device working on this principle has been described by Beranek [BER 42].

#### 25.1.1.1.1. Principle of the measurement

To make this measurement, we put the sample in a closed cavity whose volume can be changed, moving a small piston (Figure 25.1).

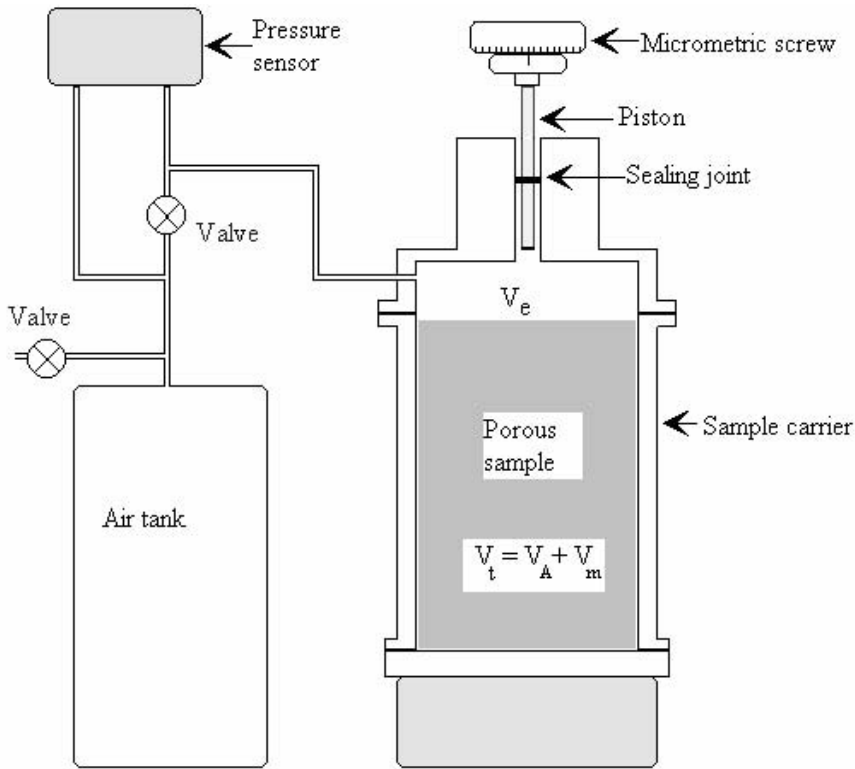


**Figure 25.1.** Schematic device for the measurement of a material's porosity

We can write:

$$V_t = V_A + V_m \quad [25.1]$$

using the following notations:

- $V_t$  = total volume of the sample;
- $V_A$  = volume of interconnected pores or volume of the air in the sample;
- $V_m$  = volume occupied by the solid structure of the sample;
- $V_e$  = exterior volume occupied by the air in the closed cavity;
- $P$  = pressure in the cavity.

The total volume  $V$  occupied by the air will be:

$$V = V_e + V_A \quad [25.2]$$

Initially, the pressure  $P$  and the volume  $V$  of the cavity are equal to the atmospheric pressure  $P_o$  and the volume  $V_o$ , respectively. We modify the volume  $V$  of the cavity with the piston. In normal conditions of temperature and pressure, the air behaves like a perfect gas. If the transformation is isotherm, the law of Boyle–Mariotte,  $PV = P_o V_o = \text{constant}$ , is verified during the transformation. If  $\Delta V$  is the volume variation and  $\Delta P$  the corresponding pressure variation, we have:

$$P_o V_o = (P_o + \Delta P)(V_o + \Delta V). \quad [25.3]$$

We then deduce the initial total volume of air:

$$V_o = -\frac{P_o + \Delta P}{\Delta P} \Delta V. \quad [25.4]$$

The sign – reminds us simply that  $\Delta V$  and  $\Delta P$  are of opposite signs. The material porosity is thus given by:

$$\phi = \frac{V_A}{V_t} = \frac{V_o - V_e}{V_t}. \quad [25.5]$$

#### 25.1.1.1.2. Experimental assembly

The sketch of Figure 25.2 describes the outcome with all the elements referred to by a number.

1: A sample carrier in brass.

2: Cell of the porosimeter. It consists of two parts. In the lower part, made of brass, we find the steel piston of diameter 5 mm and of length 60 mm. Airtightness is obtained with the help of a toric gasket. The sample carrier is fixed on that part,

which has a pressure tap. The upper part is aluminum and ensures the joint between the piston and the micrometer (element no. 3), which is fixed above.

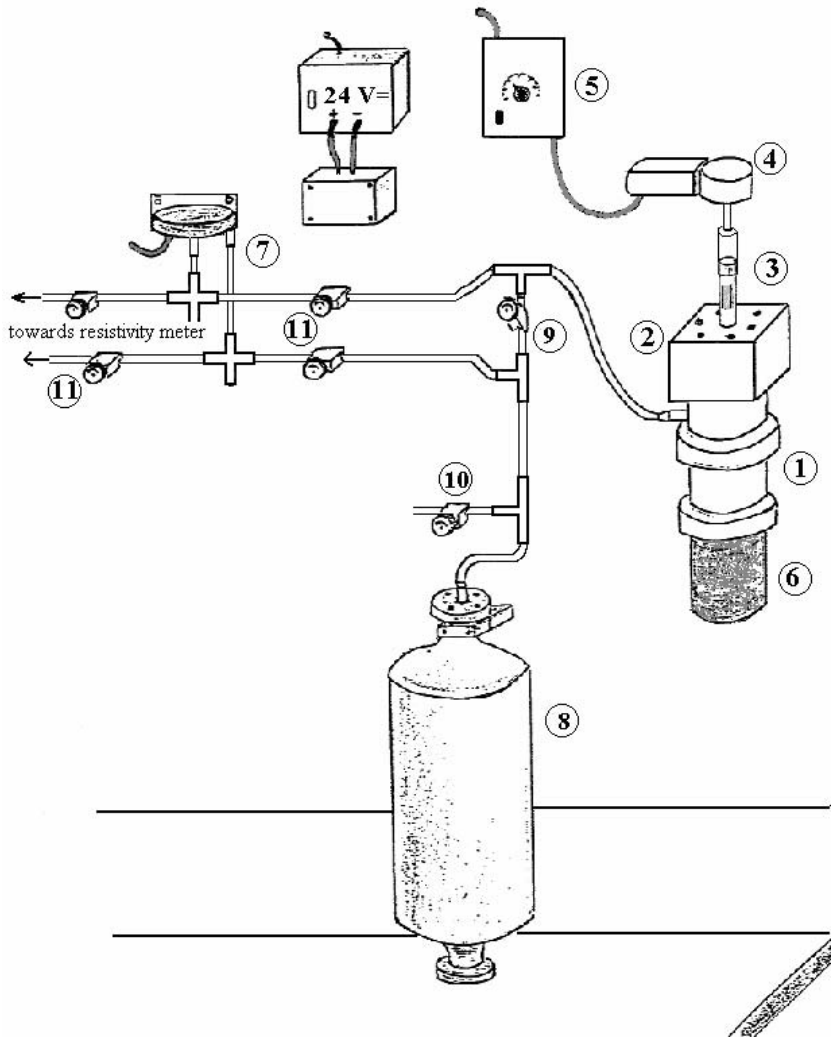


**Figure 25.2.** *Schema of the device for the measurement of porosity*

3: Precision micrometer. Its display is numeric and it enables us to know the displacement of the piston. The precision of the measurement is  $\pm 0.001$  mm.

4: Direct-current motor. It enables the piston to be moved uniformly through the micrometer. The joint is ensured by adherence, so that the two elements break away in case of locking of the piston, avoiding damage to the micrometer. The velocity can vary from 0 to 3,000 rev.

5: Electronic regulator. It serves to supply the motor (no. 4) and to vary the motor velocity. A luminous on-off switch enables the interlock or the release of the motor at every given velocity. That is chosen so that the transformation duration, corresponding to a maximum variation of pressure of the order of 1 millibar, is comprised between 5 and 10 seconds.

6: Bronze mass of 5kg. It is fixed at the basis of the sample carrier with the help of a ring. It closes the cavity of the porosimeter behind the sample hermetically. Moreover, its important thermal capacity ensures the thermal stability of the system, the transformation having to be isotherm.

7: Assembly of a differential pressure measuring transducer and a power supply, used also for the resistivity meter. The transducer measures the differential pressure between the starting pressure, which is the atmospheric pressure  $P_o$ , and the final pressure in the cavity of the porosimeter.

8: Air tank of great capacity with respect to the volume  $V$  of air in the porosimeter and of around 12 liters. It is used in order to isolate the system from the variations of atmospheric pressure, and consequently to keep a stable initial reference pressure.

9: Valve. It enables the isolation of the cell of the porosimeter from the air tank. It is thus closed at the start of the procedure.

10: Valve. It ensures that the air tank and the whole system are all at atmospheric pressure. It is the first valve to close before beginning the measurement.

11: Valves. Opened or closed, they enable the transducer (no. 7) to be used for the resistivity meter as well as for the porosimeter. Of course, before all measurements, the valves communicating with the resistivity meter must be closed, and those linking the transducer to the porosimeter must be opened. All the pipes, the air tank, the bronze mass, the cell of the porosimeter and the sample carrier are coated by insulating thermal materials in order to avoid any heat transfer towards the outside. It is also necessary to know the absolute reference pressure  $P_o$ . This measurement is made at the beginning of the procedure and is obtained thanks to a FORTIN barometer (of the same type as those used by the national meteorology service for the calibration of their devices). This quicksilver barometer comes with a data sheet enabling us to make some corrections to the pressure read in mmHg, up to

a precision of 0.05 mmHg. Indeed, to ensure a good precision of the readings, it is necessary to make a correction in temperature (in order to take into account the dilatation of the different components of the barometer), a relative correction to the variation of the gravity field (function of latitude and altitude) and a correction of the capillarity. That being done, the pressure  $P_o$  is known with a relative uncertainty less than 0.013%.

#### 25.1.1.1.3. Operating procedure

The pressure transducer is switched on first. The voltage output of the transducer is linked to a voltmeter with digital display; this enables us to follow the pressure evolution in the porosimeter and to scope every anomaly. It is also linked to an acquiring device driven by a computer. A computer program, in which some visual and sonorous messages (to guide the operations: valves and motor handling, measurement of  $P_o$ , etc.) are included, ensures the data treatment.

Once the sample is put into the cavity made by the sample carrier fixed on the cell of the porosimeter, with the bronze mass closing the other extremity, we wait a moment to let the system reach its thermodynamic equilibrium. We then isolate the device from the exterior (valve no. 10), we increase the temperature and the atmospheric pressure. We then slowly close valve no. 9 to isolate the air tank (at the initial reference pressure) of the cavity of the porosimeter. The first recordings are performed with valve no. 1 closed. To take into account a small drift, mainly due to a small heat contribution of the heating device of the transducer (which can appear before as well as after the bulk variation), the pressure difference is noted down every second during 90 seconds. The motor is activated 25 seconds after starting the measurement. During this time the pressure variation is around 1 millibar. This operation lasts around a dozen seconds. The motor being stopped, we note down the value of the displacement of the piston indicated by the micrometer, waiting for the end of the recording. Once that is ended, we can move the piston into its initial position and open valves no. 9 and 10. The porosimeter is then ready for another measurement.

#### 25.1.1.1.4. Precision

The obtained precision for the value of the porosity is obviously related to the quality of the measurement devices (differential transducer, micrometric screw, barometers) and to the attention given during the operation. It also depends strongly on the sample volume (a volume as large as possible is preferable), on the ratio sample volume/sample carrier volume (the best precision is obtained for a ratio of 1). Taking into account the former conditions, we generally obtain the porosity with a precision of 1%.

### 25.1.1.2. Air flow resistivity

When a porous material, placed in a tube with airtight walls, is crossed by a continuous air flow, we notice that a difference of pressure appears between its two extremities (Figure 25.3).

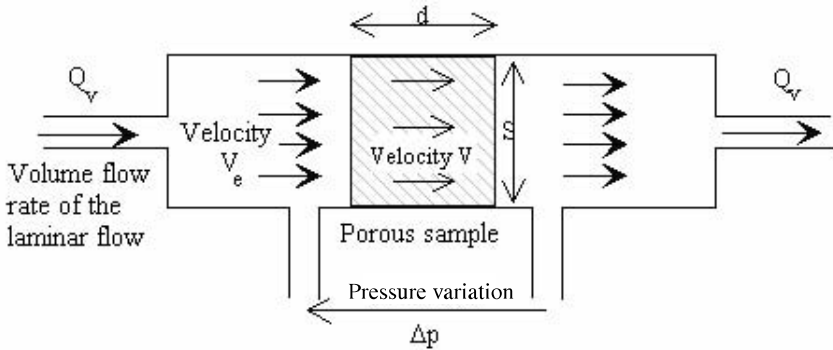


**Figure 25.3.** The resistance to the air passing corresponds to the ratio of pressure variation on the volume flow rate  $R = \Delta p / Q_v$

If the flow is laminar and for quite weak rates, there is a proportionality relationship between the rate ( $Q_v$ ) and the pressure variation ( $\Delta p$ ) given by Darcy's law [LAN 71]:

$$\Delta p = R \cdot Q_v . \quad [25.6]$$

The coefficient  $R$  corresponds to the resistance to the fluid passing (here the air) and can thus be defined by the ratio  $\Delta p / Q_v$ .

For a homogenous porous material, this resistance is proportional to the length  $d$  and inversely proportional to a cross-section  $S$ . Consequently, we can define a characteristic quantity of the material and the fluid, the air flow resistivity, as being the resistance of the material of the section and of unitary length. Denoted  $\sigma$ , this air flow resistivity can be written:

$$\sigma = \frac{S}{d} R . \quad [25.7]$$

Using the units of the international system,  $\Delta p$  is expressed in Pascal (1 Pa corresponding to  $1 \text{ kg} \cdot \text{m}^{-1} \cdot \text{s}^{-2}$ ) and  $Q_v$  in  $\text{m}^3 \cdot \text{s}^{-1}$ . Thus, the resistance  $R$  is expressed in  $\text{kg} \cdot \text{m}^{-4} \cdot \text{s}^{-1}$  and  $\sigma$  in  $\text{kg} \cdot \text{m}^{-3} \cdot \text{s}^{-1}$ . This parameter depends on the internal geometry

of the material, but also on the geometry of the fluid. It is related to the Darcy permeability  $k_o$  by the relationship:

$$\sigma = \frac{\eta}{k_o}, \quad [25.8]$$

where  $\eta$  is the dynamic viscosity of the fluid. For the air, we have  $\eta = 1.84 \cdot 10^{-5}$  poiseuille ( $\text{kg} \cdot \text{m} \cdot \text{s}^{-1}$ ).

The quantity  $k_o$  is homogenous to a surface and corresponds to an available area for the fluid flow. It is expressed in  $\text{m}^2$  but we can also find it in darcy (1 darcy

corresponds to  $9.87 \times 10^{-13} \text{ m}^2$ ). This parameter does not depend on the nature of

the fluid but only on the internal geometry of the porous material. In air acoustics, we often use the resistivity  $\sigma$  to characterize a material being immersed in water, while in fluid physics,  $k_o$  is usually preferred, as the intrinsic parameter of the porous material. It plays an important part for very low frequencies, and that is why it is interesting to measure it.

#### 25.1.1.2.1. Principle of the measurement

Resistance to air flow can be calculated from the measurement of the pressure loss between both extremities of the sample, crossed by a known air flow. The use of a differential pressure measuring transducer, which is sufficiently sensitive, enables us to have a measurement of a pressure difference with a good precision. The flow measurement is, on the contrary, more delicate and the best way to do it consists of passing an air flow across a calibrated resistance. Then the flow rate is obtained by the measurement of the pressure loss at the bounds of the resistance. To avoid this rate measurement, the method we chose is the one developed by Stinson [STI 88]. The principle is equivalent to a voltage divider bridge (Figure 25.4). We use a continuous rate flow of air passing across two resistances connected in series. One is a known calibrated resistance: it is the reference. The other one is unknown: it is the sample to test.



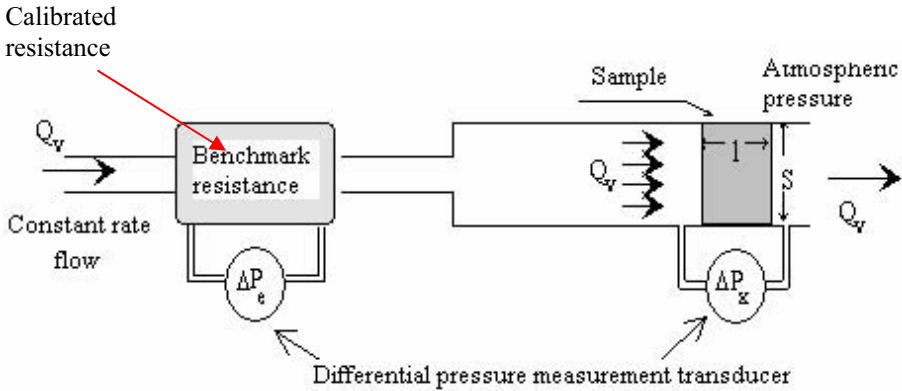


**Figure 25.4.** Schematic device for the measurement of a resistance to air flow

For a same rate  $Q_v$  crossing the two resistances, we measure the pressure losses  $\Delta P_e$  at the bounds of the calibrated resistance  $R_e$  and  $\Delta P_x$  at the bounds of the unknown resistance  $R_x$ . We obtain the relationship:

$$R_x = \frac{\Delta P_x}{\Delta P_e} R_e. \quad [25.9]$$

The expression of  $\sigma$  as a function of the measured quantities is then:

$$\sigma = \frac{\Delta P_x}{\Delta P_e} \frac{S}{d} R_e. \quad [25.10]$$

Consequently, the measurement of a resistivity is equivalent to the comparison between two differential pressures by the same type of sensor. The knowledge of the flow rate is not necessary, it is enough to ensure that it is the same for the two resistances, and that it is not too high, so that the behavior of the material remains linear.

#### 25.1.1.2.2. Breadboard

A detailed description of the breadboard can be found in the collection “Techniques de l'Ingénieur” [BRO 03].

#### 25.1.1.2.3. Precision

The putting into place of the sample in the sample carrier plays a crucial part. For a great resistance, the slightest leak will lead to a decrease of the measured value. This aspect is difficult to take into account for precision of results. However,

handling with care and taking into account the precision of the differential pressure measuring transducers, the recorder and the calibrated resistance, the measurement of a resistance to the air passing can be made with less than 1% uncertainty. The uncertainty on the resistivity will automatically increase by the inevitable uncertainty on the sample sizes. For the section, it is around 0.2%. For the length, the uncertainty will be all the more weak since the length is huge. If the samples are thick (around 10 mm), it is possible to increase the precision measuring the resistance of several of these samples, put one after another. Moreover, if the material is a little inhomogenous, this method enables us to obtain a good estimation of the average resistivity of the porous material.

### 25.1.1.3. Tortuosity, characteristic lengths

#### 25.1.1.3.1. Static method

The tortuosity  $\alpha_\infty$  plays an important part for high frequencies. This parameter corresponds to the limit of the dynamic tortuosity when the frequency tends towards infinity. This parameter translates the fact that the fluid, which behaves as a perfect incompressible fluid, must sinuously sidestep the solid parts of the structure which occur in its way. It characterizes the inertial effects.

For a porous medium saturated by a perfect fluid, Brown [BRO 80] has demonstrated the equivalence between (1) the field of microscopic velocities of the fluid subjected to a pressure gradient and (2) the field of microscopic velocities of ions (or microscopic velocities of currents) of the fluid, if its conductivity is uniform and if it is subjected to a gradient of electrical potential (we suppose that the structure is not conducting). We can link very simply the tortuosity to the electrical resistivities  $r_f$  and  $r$  of the fluid and of the material saturated by the same fluid, respectively, by the relationship: 
$$\frac{r}{r_f} = \frac{\alpha_\infty}{\phi}.$$

This equivalence has been verified experimentally on glass balls by Johnson *et al.* [JOH 82-1] and [JOH 82-2]. This analogy has been developed by Lafarge [LAF 93]. The tortuosity of a material of porosity  $\phi$ , whose structure is not a conductor, can be obtained by a non-acoustical method, measuring its electrical resistivity when it is saturated by a conductor fluid.

#### – Principle of the measurement

We put two current electrodes at the extremities of a sample carrier of section  $S$  and length  $L$ , and fill this carrier sample with an electrolyte of resistivity  $r_f$  (Figure 25.5).

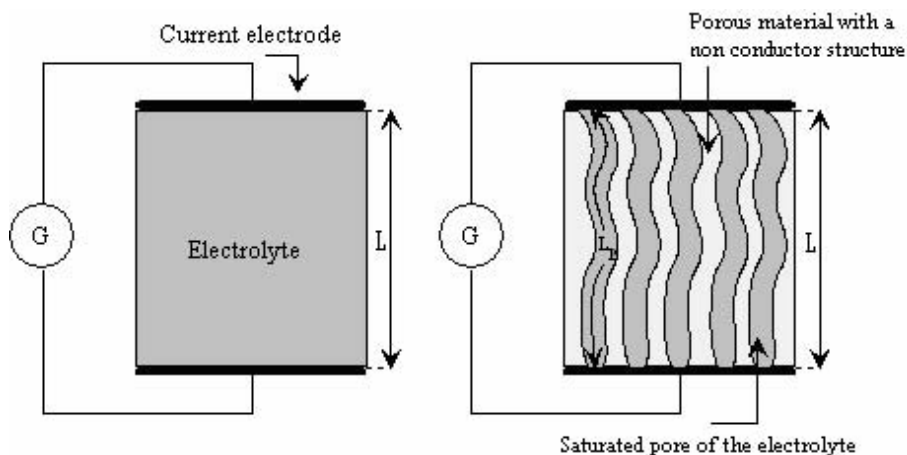


**Figure 25.5.** Basic principle for an electrical measurement of tortuosity

The electrical resistance opposed by the fluid to the current passing and measured at the extremities of the two electrodes is  $R_f = r_f L/S$ . The measured resistance when the same sample carrier is filled with a porous material saturated by the same electrolyte is  $R = r L/S$ , where  $r$  is the resistivity of the saturated material. Thus, the tortuosity  $\alpha_\infty$  also corresponds to  $\alpha_\infty = \phi R/R_f$ . In both cases, if we manage to have the same intensity circulating between the electrodes, the voltage ratio between the two extremities of the sample carrier is equal to the resistance ratio. In this situation, it is useless to know the electrolyte resistivity. The principle is identical to that used for the measurement of the resistivity to air flow (comparative method).

To avoid successive manipulations (they always yield errors), the assembly has been modified to separate the measurement electrodes from the current ones. The diagram of the new measurement principle is represented in Figure 25.6. The measurement electrodes are platinum wires parallel to the two current electrodes in silver. Their only role is to ensure the measurement of voltages through a voltmeter of great internal impedance. A simple comparison of voltages  $V_1$  and  $V_2$  (see Figure 25.6) enables us to obtain the resistance ratio between the sample and the electrolyte.

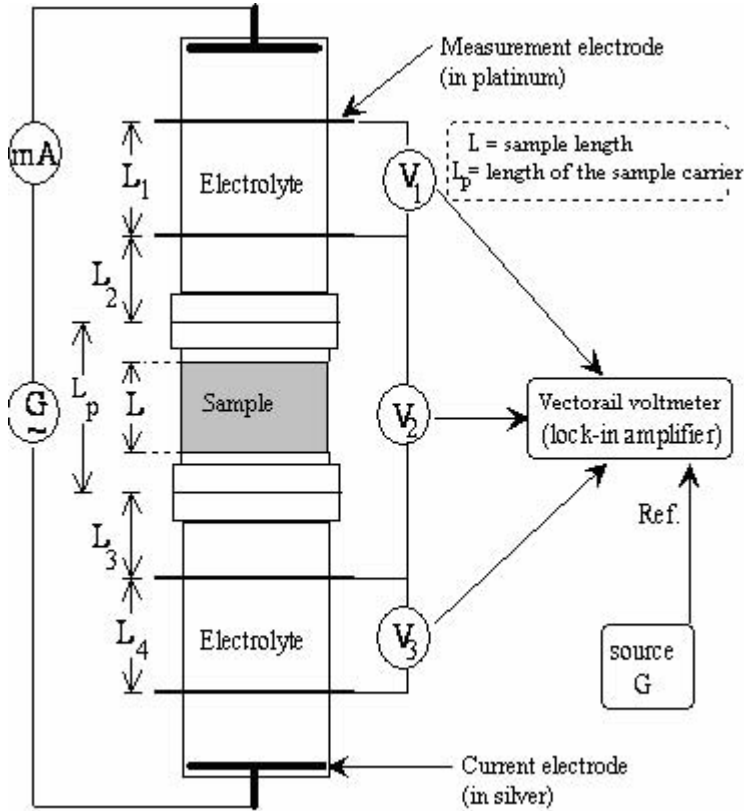


**Figure 25.6.** Schematic device for tortuosity measurement

Using this comparative method, the conductivity or resistivity of the solution does not affect the measurement. The nature of the electrolyte as well as its concentration no longer matters. For the conductor solution, we choose a solution of sodium chloride (NaCl), which is a neutral solution easy to obtain. In principle, the nature of the current does not intervene. Using a sine wave voltage generator, we avoid a polarization of the electrodes. The current electrodes are disks of diameter slightly less than that of the electrolytic cell. All the electrodes are located in parallel planes. The platinum wires are thus on equipotential surfaces. With the notations used in Figure 25.6, a simple calculation gives the expression of the tortuosity:

$$\alpha_{\infty} = \phi \left[ 1 + \frac{1}{L} \left( \frac{V_2}{V_1} L_1 - L_2 - L_3 - L_p \right) \right]. \quad [25.11]$$

The lengths  $L_1$ ,  $L_2$ ,  $L_3$  and the length  $L_p$  of the sample carrier are set by construction. The precision on the tortuosity measurement depends on the precision with which these lengths are known, as well as the precision of the measurements of the length  $L$ , of the porosity  $\phi$  of the material, and of the voltages  $V_1$  and  $V_2$ . Obviously, this measurement has a meaning only if the sample is perfectly saturated. If some air pockets are confined in the structure of the material, this will lead to an increase in its resistivity, and consequently to an increase of the tortuosity value. To ensure a good saturation of the sample, a hydropneumatic circuit has been added; it allows us to create a partial vacuum in the cell before filling it with the electrolyte. Finally, a fourth measurement electrode has been added. It enables us to check the good working of the assembly, the ratio  $V_1/V_3$  having to correspond to the ratio  $L_1/L_4$ .

#### *– Precision and validation*

A simple program allows us to displaying the tortuosity value with a precision depending on that existing for porosity and on the different lengths involved in the calculation. Provided that the sample is perfectly saturated, it is possible to obtain tortuosity values with a precision from 1.5 to 2%.

There is also another technique enabling, by ultrasonic measurements, us to obtain the tortuosity of a porous material. Some measurements made on different samples by the two methods have allowed validating the two systems. In the acoustical laboratory of the Maine University (Le Mans, France), we have currently the ability to measure the tortuosity of a material by two very different methods. In most cases, we prefer to use the ultrasonic method. Actually, it does not require the knowledge of the material porosity, contrary to the electrical method for which the precision on the tortuosity is strongly related to the one we have on the measurement of the porosity. Moreover, it is not destructive and faster to implement. These two methods are in fact complementary. Actually, for some materials having a strong absorption, the ultrasonic measurement is no longer possible. In this case, we can use the tortuosimeter.

#### 25.1.1.3.2. Frequency methods

##### *Interest of frequency methods*

The methods of characterization by ultrasound enable us to easily return to the high-frequency characteristics of the porous material (tortuosity  $\alpha_\infty$  and characteristic visco-thermal lengths  $\Lambda$  and  $\Lambda'$ ), and porosity  $\phi$  in some cases (see sub-section 25.1.1.3.3 on temporal methods).

The interests of these methods are multiple. First, the propagation models are simpler for high frequencies (from several kHz or from several dozens of kHz

depending on the materials). Actually, in the asymptotic high-frequency range, and under the equivalent fluid assumption (which is generally the case in high frequency domain), the dynamic tortuosity  $\alpha(\omega)$  and the dynamic compressibility  $\beta(\omega)$  are written [JOH 87] [CHA 91]:

$$\alpha(\omega) = \alpha_{\infty} \left( 1 + (1 - j) \frac{\delta}{\Lambda} \right), \quad [25.12]$$

where  $\delta$  is the viscous skin thickness,  $\beta(\omega)$  is defined by

$$\beta(\omega) = 1 + (\gamma - 1)(1 - j) \frac{\delta'}{\Lambda'}, \quad [25.13]$$

$\delta'$  is the thermal skin thickness and  $\gamma$  the adiabatic constant. Thus, the complex velocity

$$c'(\omega) = \sqrt{\frac{K_a}{\rho_0 \alpha(\omega) \beta(\omega)}}, \quad [25.14]$$

where  $K_a$  is the modulus of adiabatic incompressibility and  $\rho_0$  the fluid density, involves only three characteristic parameters for high frequencies ( $\alpha_{\infty}$ ,  $\Lambda$  and  $\Lambda'$ ), the porosity  $\phi$  intervening also in the expressions of transmission and reflection coefficients.

Furthermore, experimentations of ultrasonic characterization are simple to implement. The significant directivity of ultrasonic beams enables us to carry out some measurements on samples of small size. The use of specific ultrasonic transducers, sometimes a little focalized and strongly damped, enables us to work in broadband (impulsional state) or tight band (*burst*), particularly for low frequencies (below 50 kHz) for which the transducers are not sufficiently damped. These signals with very small temporal support thus enable us to characterize thick materials (several centimeters).

In this sub-section, the measured quantities are the velocity and the transmission and reflection coefficients. These are expressed as functions of the frequency, and the searched characteristic parameters are deduced from the asymptotic high-frequency expressions of these quantities. These frequency methods were the first methods developed in the frame of ultrasonic characterization of porous materials in the beginning of the 1990s and are widely used today. A complementary method based on the static pressure variations of the saturating fluid has been developed more recently. In this latter case, the measured quantities are expressed as functions

of the static pressure. This method enables us to examine more absorbing materials and to separate the losses by viscothermicity and scattering, when the characterization is confronted with this problem. This section finally presents the application of these methods for the determination of the anisotropy and the heterogeneity of porous materials.

### *Classic experimental protocol*

The measurements are found in transmission or in reflection with one or two transducers (Figure 25.7).

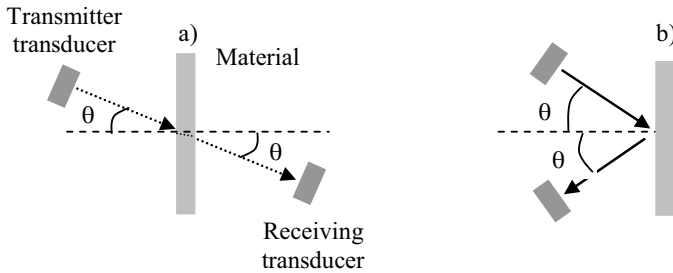


**Figure 25.7.** *Figures of the measurements in transmission (a) and in reflection (b) for variable incidence*

In transmission, most of the measurements are made in normal incidence ( $\theta=0^\circ$ ). Two measurements are made, one without the sample (the so-called reference measurement) and the other one with the sample. Two signals are then obtained – the second one being attenuated or delayed (Figure 25.8). From this delay or attenuation, we can deduce the velocity and the transmission coefficient. The excitation signals are pulses (broadband measurement) or bursts (tight band measurement to work at a fixed frequency). The velocity is calculated by the relationship:

$$c(\omega) = \frac{c_0}{1 + \frac{c_0 \Delta t}{L}}, \quad [25.15]$$

where  $c_0$  is the sound velocity in the fluid and  $L$  the thickness of the material. The delay  $\Delta t$  between the signals is calculated by cross-correlation in the case of bursts, or is equal to  $(\phi_{ref} - \phi_{ech})/\omega$  in the case of a pulse,  $\phi_{ref}$  and  $\phi_{ech}$  being the unwrapped phases of the reference and sample signals [SAC 78]. The transmission is estimated

by the energy ratio of each signal in the first case, by the broadband spectrums ratio in the latter case.

In reflection, a first reference measurement is made, putting a supposed perfectly reflecting material (metal plate) on the medium surface or putting the two transducers face to face in normal incidence. The second measurement is made according to Figure 25.8 b in the presence of the sample. If the reflection angle is zero, only one transducer is used as a transmitter and a receiver at the same time.

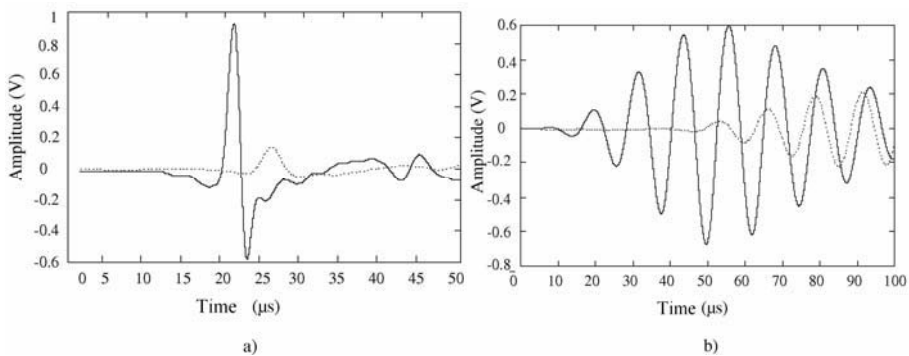


**Figure 25.8.** Examples of signals measured in transmission with pulses (a) or bursts (b): signal without sample (reference signal, continuous line), signal passed through a porous material (dotted line). In reflection, the signals are similar, with an absence of time-lag between the two signals

### Measurement of the velocity

In the asymptotic high-frequency range, the phase velocity  $c(\omega)$ , real part of the complex velocity  $c'(\omega)$ , takes the following simplified form:

$$c(\omega) = \frac{c_0}{\sqrt{\alpha_\infty}} \left( 1 - \frac{\delta}{2} \left( \frac{1}{\Lambda} + \frac{\gamma - 1}{\sqrt{Pr} \Lambda'} \right) \right), \quad [25.16]$$

where  $Pr$  is the Prandtl number of the saturating fluid. The minimization can thus be realized on this quantity to estimate the parameters. However, it is easier to take interest in the square of the real part of the refraction index [BRO 96]:

$$n_r^2(\omega) = \left( \frac{c_0}{c(\omega)} \right)^2 = \alpha_\infty \left( 1 + \frac{1}{\sqrt{\omega}} \sqrt{\frac{2\eta}{\rho_0}} \left( \frac{1}{\Lambda} + \frac{\gamma - 1}{\sqrt{Pr} \Lambda'} \right) \right) \quad [25.17]$$



where  $\eta$  is the fluid viscosity. It immediately appears that  $n_r^2$  is a linear function of the variable  $1/\sqrt{\omega}$  (Figure 25.9a beyond 50 kHz). The intercept point gives the value of the tortuosity  $\alpha_\infty$  directly, whereas the slope gives an equivalent viscothermal length  $l_{vt}$ , combination of the two characteristic lengths  $\Lambda$  and  $\Lambda'$ :

$$l_{vt} = \left( \frac{l}{\Lambda} + \frac{\gamma - l}{\sqrt{Pr} \Lambda'} \right)^{-1}. \quad [25.18]$$

The viscous characteristic length  $\Lambda$  is obtained using the knowledge of the thermal characteristic length  $\Lambda'$  or by fixing the ratio  $\Lambda'/\Lambda$ . This ratio is generally not precisely known. However, experimentation shows that it is often between 2 and 3. It is rigorously worth 2 for infinite cylindrical pores, and is very near two for fibrous materials.

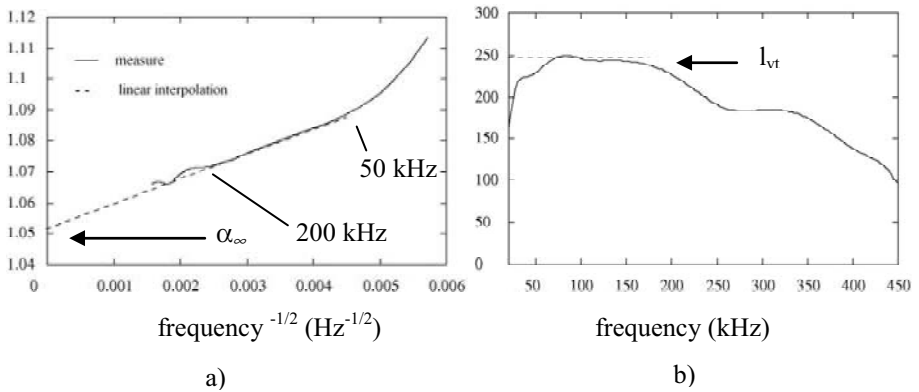


**Figure 25.9.** Propagation index  $n_r^2$ , as a function of the inverse square root of frequency (a), and factor  $Q\delta$  function (see equation 25.21) of frequency (b). For high-frequencies,  $n_r^2(\omega^{-1/2})$  follows a linear behavior from 50 kHz before being disturbed by scattering from 200 kHz. The factor  $Q\delta(\omega)$  tends towards  $l_{vt}$ , then decreases because of scattering

The use of several gases (the system of Figure 25.7a is put in a watertight vessel) enables us to obtain the two characteristic lengths independently, prompted by the fact that the thermodynamic parameters  $\gamma$  and  $Pr$  are functions of the gas considered in equation [25.18] (Figure 25.10) [LEC 96].

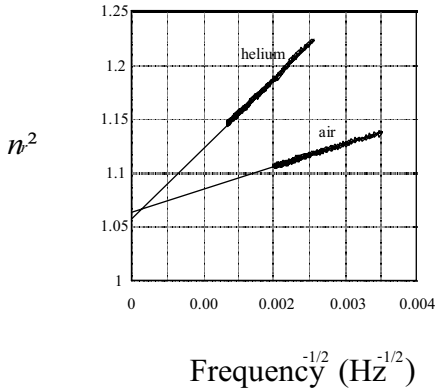


**Figure 25.10.** Propagation index, as a function of the inverse square root of frequency, for a material saturated with air or helium

#### Measurement of the transmission coefficient

For a porous isotropic transverse material described by the equivalent fluid model, the transmission coefficient  $T(\theta, \omega)$ , as a function of the incident angle  $\theta$ , takes the following form [MEL 96]:

$$T(\theta, \omega) = \left( \frac{4 \cos \theta}{Z_0} \frac{\phi k_z}{k_n Z_m} \right) \exp(-ik_z L) \left/ \left( \frac{\cos \theta}{Z_0} + \frac{\phi k_z}{k_n Z_m} \right)^2 \right. . \quad [25.19]$$

where  $Z_0 = \rho_0 c_0$  is the acoustical impedance of the saturating fluid,  $Z_m = \sqrt{\rho_0 K_a \alpha(\omega) \beta(\omega)}$  the acoustical impedance of the porous material,  $k_z = k_n \sqrt{1 - (k_y^2 / k_p^2)}$ ,  $k_y = k \sin \theta$ ,  $(k_z^2 / k_n^2) + (k_y^2 / k_p^2) = 1$ . Here,  $k$  is the wavevector,  $k_n$  its component along the direction normal to the material surface, and  $k_p$  its planar component.

In general, the measurements are found in normal incidence. In the high-frequency range and in normal incidence, the transmission coefficient  $T$  becomes:

$$|T(\omega)| = \frac{1}{\varepsilon} \exp \left( - \frac{\omega \sqrt{\alpha_\infty} \delta L}{2 c_0 l_{vt}} \right). \quad [25.20]$$

with  $\varepsilon = \frac{(\sqrt{\alpha_\infty} + \phi)^2}{4\phi\sqrt{\alpha_\infty}}$ . In most cases, the porosity and the tortuosity are near 1, and

the term  $\varepsilon$  also. It is thus possible to simplify this expression, keeping only the exponential term. The transmission coefficient then becomes directly proportional to the tortuosity and to the characteristic lengths.

With this hypothesis, the equivalent viscothermal length  $l_{vt}$  can be directly estimated by calculating the quantity  $Q\delta(\omega)$ , where  $Q(\omega)$  is the quality factor:

$$Q\delta(\omega) = \frac{\omega L \delta(\omega)}{2|\ln|T(\omega)||c(\omega)} \xrightarrow{\omega \rightarrow \infty} l_{vt}. \quad [25.21]$$

This quantity reaches a constant in high-frequency (before scattering appears), whose value is that of the equivalent characteristic viscothermal length (Figure 25.9b).

This method and the velocity measurement by pulse remain efficient as long as the transmission through the porous material is sufficient, which is the case of not very resistive materials. In the case of more resistive materials, the signal-to-noise ratio decreases. The phase unwrapping is thus very delicate, and the extraction of the required parameters is difficult. In this case, the measurement is made at a fixed frequency with bursts. The viscous characteristic length is obtained from the calculation of the quantity  $Q\delta(\omega)$  measured for a sufficiently high frequency. This value is supposed to be equal to  $l_{vt}$ . The tortuosity is deduced from equation [25.17], with the knowledge of  $l_{vt}$ . In this case, it must be verified that the viscous characteristic length is largely superior to the viscous skin thickness.

### *Measurement of the reflection coefficient*

For an isotropic transverse porous material described by the equivalent fluid model, the reflection coefficient  $R(\theta, \omega)$ , as a function of the incident angle  $\theta$ , is provided by the following expression [MEL 96]:

$$R(\theta, \omega) = \left( \frac{\cos \theta}{Z_0} - \frac{\phi k_z}{k_n Z_m} \right) / \left( \frac{\cos \theta}{Z_0} + \frac{\phi k_z}{k_n Z_m} \right). \quad [25.22]$$

Figure 25.11.a presents some characteristic examples of the reflection coefficient as a function of the incident angle for materials having supported different compression rates. The aspect of these curves  $R(\theta, \omega)$  is relatively universal [CAS 98, CAS 01]. Namely, the reflection coefficient cancels for the value of the Brewster angle  $\theta_B$  provided by the following equation:

$$\sin(\theta_B) = \sqrt{\frac{\alpha_{\infty n} - \phi^2}{\alpha_{\infty n} - \frac{\phi^2}{\alpha_{\infty p}}}}. \quad [25.23]$$

Consequently, with the knowledge of the porosity, the measurement of this angle gives the normal  $\alpha_{\infty n}$  and planar  $\alpha_{\infty p}$  components of the tortuosity for an anisotropic material. The measurements of the reflection coefficient are made in a specular configuration (generally from 15 to 75°), for which the reflection angle is equal to the incident one (Figure 25.7b). In the example presented, the angular excursion is limited between 50 and 75° with an angular step of 0.5°. The angular recording of the transmission coefficient is generally made between -60 and +60°. During a transmission scanning, the angular variations of velocities and the transmission coefficients are both recorded at the same time. The precise values of velocities give access to the polar diagram of tortuosity. A characteristic example, for the same plates tested in reflection, is presented in Figure 25.11b.

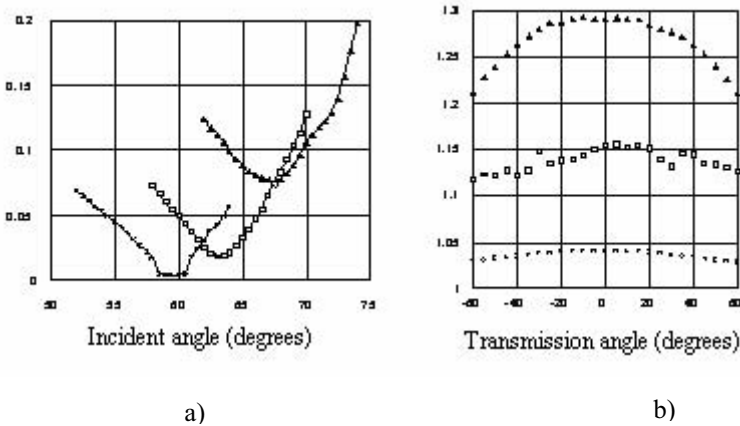


**Figure 25.11.** Reflection coefficient (a) as a function of the incident angle and tortuosity (b) as a function of the transmission angle, for three materials of type automobile felt with different compression rates (S: thickness 5 mm; q: thickness 10 mm; l: thickness 20 mm).

### Measurement with variable static pressure

When the materials are highly resistive, these methods by transmission fail and the methods by reflection provide only the tortuosity and the porosity. On the other hand, asymptotic high-frequency models do not take into account scattering. In some cases, and particularly in those of resistive materials, the validity of asymptotic expressions is reached for frequencies that are sufficiently high (several dozens of

kHz) to ensure the existence of the scattering phenomenon. A complementary method has thus been developed to overcome these problems [AYR 98].

Measurements are made in transmission with normal incidence, varying the static pressure  $P_0$  of the saturating fluid. The assembly of Figure 25.7a is put in a watertight vessel. Increasing the density of the fluid, this measuring principle enables us to go through the materials more easily because of a better transducer–fluid coupling and an increased transmission in the material itself (this increased transmission is due to a decrease of the viscous and thermal skin thicknesses  $\delta = \sqrt{2\eta/\rho_0\omega}$  and  $\delta' = \delta/\sqrt{Pr}$ ).

The measured quantities are the velocity and the transmission coefficient. The quantities  $n_r^2$  and  $T$  in equations [25.17] and [25.20] can be rewritten as functions of the variable  $P_0$  instead of  $\omega$ .

$$n_r^2(\omega, P_0) = \alpha_\infty \left( 1 + \frac{1}{\sqrt{\omega P_0}} \sqrt{\frac{2\eta R_0 T_0}{M_0}} l_{vt}^{-1} \right) \quad [25.24]$$

and

$$\ln|T(\omega, P_0)| = \ln(\varepsilon) + \sqrt{\frac{\omega}{P_0}} \sqrt{\frac{2\eta R_0 T_0}{M_0}} \frac{L}{2c_0} \sqrt{\alpha_\infty} l_{vt}^{-1} \quad [25.25]$$

where  $\varepsilon = \frac{(\sqrt{\alpha_\infty} + \phi)^2}{4\phi\sqrt{\alpha_\infty}}$ . The terms  $R_0$ ,  $T_0$  and  $M_0$  are respectively the Gas Constant, the temperature and the molar mass of the saturating fluid. Here, it also appears clearly that  $n_r^2$  and  $T$  are linear functions of the variable  $1/\sqrt{P_0}$ . The intercept point of  $n_r^2$  provides the tortuosity, whereas the slope of the linear curves provides the length  $l_{vt}$ . Figure 25.12 shows an example of measurements made at variable pressure.

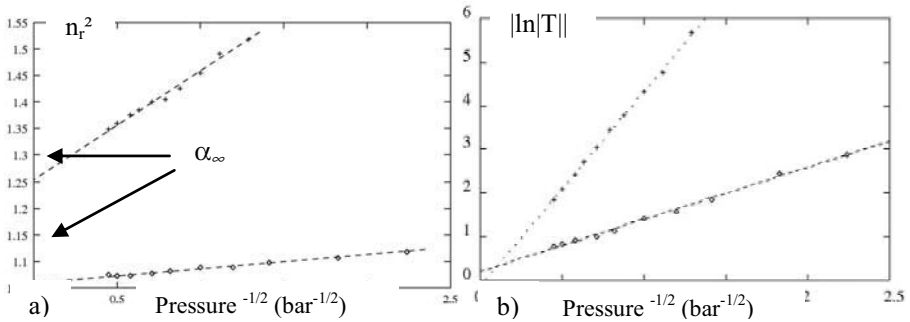


**Figure 25.12.** Propagation (a) and transmission (b) index as functions of the inverse square root of the static pressure for two polyurethane foams at 100 kHz

When the characterization is made at high frequency (beyond 100 kHz), scattering appears as shown on Figure 25.13b for transmission. Indeed, the term  $\ln(\epsilon)$  is near 0 for many materials (porosity and tortuosity near 1). The energy dissipation, due to scattering when the frequency increases, leads to a decrease of the transmission coefficient  $T$ , and thus to an increase of the quantity  $|\ln|T||$ .

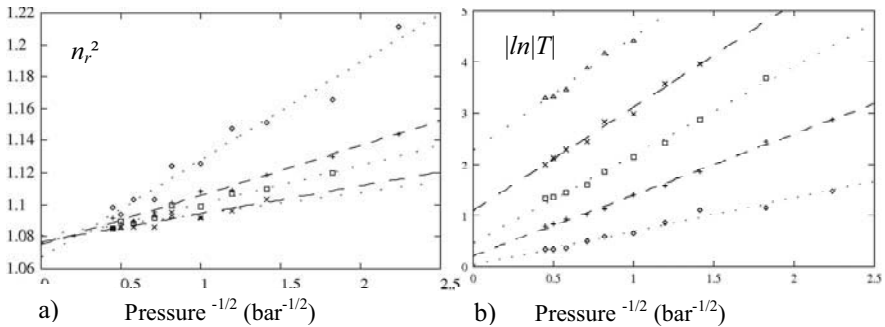


**Figure 25.13.** Propagation (a) and transmission (b) index as functions of the inverse square root of the static pressure for a polyurethane foam: 30 kHz ( $\phi$ ), 100 kHz (+), 200 kHz ( $\square$ ), 300 kHz ( $\times$ ) and 400 kHz ( $\Delta$ ). Scattering appears here from 100 kHz as the quantity  $|\ln|T||$  no longer tends towards zero

We can then show that, in presence of weak scattering (Rayleigh state), the term  $|\ln|T_d||$  is written as a function of  $|\ln|T||$  without scattering (equation [25.25]) [AYR 05]:

$$\| \ln |T_d| \| = \| \ln |T| \| + \frac{L}{2l_d}, \quad [25.26]$$

where  $l_d$ , called scattering length, is given by:

$$l_d = \left( a(1-\phi) \frac{1}{R} \left( \frac{R}{\lambda} \right)^n \right)^{-1}, \quad [25.27]$$

with  $n = 3$  or  $4$  for a 2D or 3D propagation [CON 88, SOR 89]. The parameter  $a$  is a dimensionless constant,  $R$  the average diameter of the solid scattering structures (granularity, fibers, etc) and  $\lambda$  the wavelength. In a first approximation, the additional term  $L/l_d$  in equation [25.26] can be considered as constant. Thus, the term  $\| \ln |T| \|$  is simply translated by a constant and its gradient does not change. Then, it is possible to estimate its length  $l_{vr}$ .

The propagation index  $n_{rd}^2$  with scattering is expressed as a function of the propagation index  $n_r^2$  without scattering, through the relationship:

$$n_{rd}^2 = n_r^2 \left( 1 + \frac{\lambda}{l_d} \right)^2. \quad [25.28]$$

In a first approximation, the term  $\lambda/l_d$  can be considered small and the propagation index is not very much modified, thus enabling the extraction of parameters. The weak scattering model, coupled to the equivalent fluid assumption, described by equations [25.26] and [25.28], enables a very good fit on the measurements from the curves shown in Figure 25.13, pointing out the good validity of this weak scattering model for the description of the scattering phenomenon involved in little-diffusing polyurethane foams [GRI 05]. The characteristic parameters obtained in the presence of weak scattering correspond to the reference measurements (classical frequency method with ambient pressure described before) as we obtain, from an average of the different measured frequencies,  $\alpha_\infty = 1.07 \pm 0.01$  for a reference of 1.05, and  $\Lambda = 269 \pm 27 \mu\text{m}$  (from  $n_r^2$ ) and  $\Lambda = 315 \pm 12 \mu\text{m}$  (from  $\| \ln |T| \|$ ) for a reference of  $300 \mu\text{m}$ .

This assumption of loss separation by viscothermicity and scattering [NAG 95] remains valid in the case of quite strong scattering (agglomerates of glass balls for example), concerning transmission [AYR 05].

The measurements presented above have been found up to 6 bars. In preparation for the characterization of more resistive materials, studies are currently undertaken up to 18 bars and show a non-negligible interaction between the structure and the densified air [GRI 05]. The equivalent fluid model no longer fits. One of the proposed hypotheses is that the densified air is sufficiently heavy to produce a global motion of the material, but not enough to distort the structure. This behavior could be described by the Biot model, in which the terms of strain energy would be negligible compared to the terms of kinetic energy. These works are the topic of current researches.

### *Application to the characterization of anisotropy and heterogeneity*

#### Anisotropy

From the values of porosity and tortuosity, it is possible to estimate the Brewster angle for different materials. This angle is generally comprised between 40 and 70°. The example of Figure 25.11 corresponds to three felt-like materials. Some anisotropy seems to exist as shown by other results obtained on plastic foams [CAS 98]. It was particularly demonstrated that the Brewster angle for a foam with parameters  $\alpha_{\infty} = 1.2$  and  $\varphi = 0.98$  is  $\theta = 50.7^\circ$ , whereas, for the same material considered as anisotropic with  $\alpha_{\infty 1} = 1.2$  and  $\alpha_{\infty 3} = 1.4$ , the Brewster angle calculated from equation [25.23] becomes  $\theta = 43.0^\circ$ , a value that conforms to that of the experimentation (Figure 25.14a).

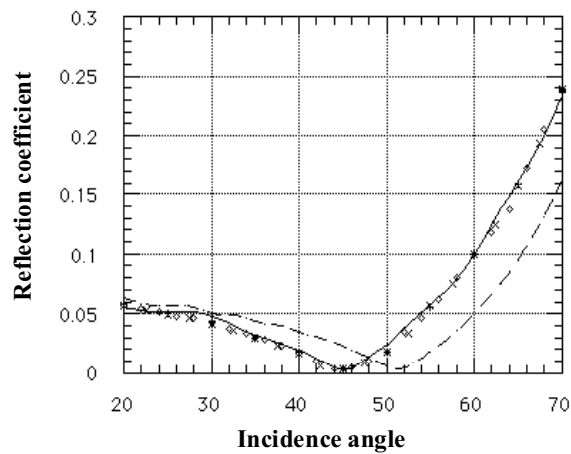
Other works related to the anisotropy of acoustical properties of porous materials have been accomplished in the frame of the Biot theory [MEL 98, AKN 97] or with the equivalent fluid model [CAS 01, MEL 95-a]. In this second case, it has been shown that the influence of anisotropy on the transmission coefficient is weaker than on the reflection coefficient. On the contrary, the experimental reading of the transmission coefficient as a function of the angle gives information on the symmetry around the normal and then enables us to know, in the case of an anisotropic material, the angular position of the principal anisotropy axes (see Figure 25.14). Furthermore, the angular behavior of the tortuosity is very interesting. In the case of an anisotropic porous material, the tortuosity takes an elliptical form [MEL 95-a]:

$$\alpha_{\infty}(\theta) = \alpha_{\infty 3} \cos^2 \theta + \alpha_{\infty 1} \sin^2 \theta. \quad [25.29]$$

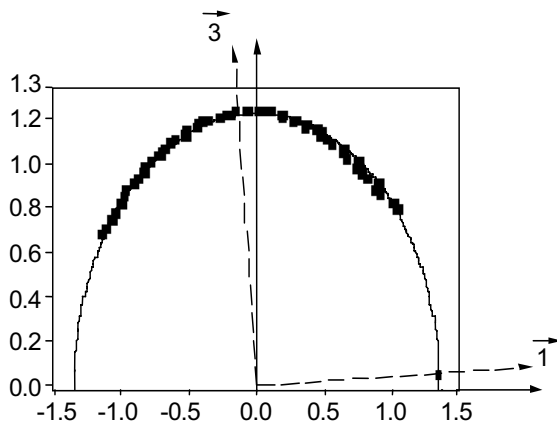
where  $\alpha_{\infty 3}$  and  $\alpha_{\infty 1}$  represent the principal tortuosities defined along the 1- and 3-axes, and where  $\theta$  is the angle between the wavevector and the direction along the normal to the sample (that is to say the 3-axis). An example is presented on Figure 25.14b for a plastic foam [MEL 95-a]. The use of an inversion algorithm enables us to obtain the principal tortuosities  $\alpha_{\infty 3} = 1.22 \pm 0.01$  and  $\alpha_{\infty 1} = 1.34 \pm$



0.01. These values are calculated up to 1% from the measurements made with a normal incidence for samples specially cut for that.



(a)



(b)

**Figure 25.14.** Reflection coefficient as a function of the incidence angle (a): comparison of experimental (symbols) and theoretical values in the case of an isotropic (dotted line) and anisotropic (continuous line) material; Polar diagram of the tortuosity as a function of the transmission angle for a reticulated foam (b): comparison between the theoretical prediction (continuous line) and the experimental measurements (  $\square$  )

### *Heterogeneity*

Porous absorbing materials are heterogenous, and in many cases, this heterogeneity is significant, around several dozens of percents, sometimes even more. This trend is inherent to the biphasic nature of these materials, in the complexity of their micro-geometry, but also in the imperfections related to their fabrication (material cluster in some areas, presences of plops, etc.). Ultrasonic techniques are well-adapted to make bidimensional cartographies of the acoustical parameters (measurements of propagation velocities providing the tortuosity, and attenuation reading providing the characteristic lengths). The main strengths of these techniques come from the fact that they are contactless, that the frequency can be easily modified (changing transducers, or modifying the adjustments of the emission electronics), and that a 2D scanning is made possible with a spatial step, which is of the same order of magnitude as the piezoelectric sensors used.

There is a correlation which is not fortuitous between the 2D cartography of the transmission coefficient and that of the velocity measurement (and following on the apparent tortuosity). In that case, the light areas of one of the two pictures correspond to the dark areas of the other diagram (and inversely) [MEL 95-b].

This comes from the fact that when a material is more “tortuous”, the penetration of ultrasounds in the material is more difficult, and in consequence, the transmission coefficient is weaker. Besides, this result is directly explainable from equation [25.20], indicating that when the tortuosity increases, the transmission decreases because of the dependency with the exponential term. The differences obtained can be important, around 5 to 10% on the tortuosity, but around 40% on the characteristic length. The implication of these results indicates that this heterogeneity of absorption properties must be taken into account in the design of absorbing materials. Other measurements have been made for other configurations. For example, some property gradients have been highlighted for some plastic foams. This result is well known by industries manufacturing plastic foams; it is due to a gravity effect during the process, the foam at the bottom of the tank being denser than that at the top of the tank.

### *Perspectives and conclusions*

Ultrasonic frequency methods appear as being complementary to the classic acoustical techniques working in the audio range, to characterize the absorption and soundproofing properties of porous materials. They allow us to measure with precision, speed and reliability, some relevant physical parameters of the propagation models (the tortuosity, the characteristic lengths, and in some cases the porosity (see section 25.1.1.3.3)), even in the presence of weak scattering. They enable us to finally characterize the anisotropy of materials finely, as well as their heterogeneity, which can be high in some cases.

### 25.1.1.3.3. Temporal methods (*ZF, CD*)

The porosity and the tortuosity can be measured from the reflected wave in a porous material in the inertial state at high frequencies [FEL 01, FEL 03a, FEL 03c, FEL 03d, FEL 03e]. Indeed, the study of the sensitivity of the porosity and tortuosity on the reflected wave shows that these quantities have a great sensitivity on the wave reflected at the first interface.

In the inertial state (high frequencies), the expression of the reflection operator for an oblique incidence  $\theta$  is given [FEL 03b] by:

$$\tilde{R}(t) = r(t) + R(t) \quad [25.30]$$

where

$$r(t) = \left( \frac{1-E}{1+E} \right) \delta(t) \quad , \quad R(t) = - \frac{4E(1-E)}{(1+E)^3} F\left(t, \frac{2L}{c}\right), \quad E = \frac{\varphi \sqrt{1 - \frac{\sin^2 \theta}{\alpha_\infty}}}{\sqrt{\alpha_\infty} \cos \theta}$$

The first term of this expression is equivalent to the reflection by the first interface of the porous material ( $x = 0$ ). The part of the wave corresponding to this term is instantaneously reflected by the material. This wave is not dispersive but simply attenuated by the factor  $(\sqrt{\alpha_\infty} - \varphi) / (\sqrt{\alpha_\infty} + \varphi)$ . The second term corresponds to the wave reflected by the second interface ( $x = L$ ), having travelled twice the thickness of the porous material. The porosity and the tortuosity can be measured by solving the inverse problem by the least squares method (for example), minimizing the difference between the experimental reflected waves (at different incidence angles) and the simulated reflected waves from the reflection operator [FEL 03b, FEL 03d]. For some porous materials saturated with air, which are weakly resistive, the wave reflected by the second interface can be detected experimentally [FEL 03d]. In that case, it is possible to measure the characteristic viscous length.

The transmitted wave is often used to measure the tortuosity and the characteristic viscous length [FEL 01, FEL 02] (the ratio between the characteristic thermal length and the viscous one is generally fixed at 3). The porosity cannot be obtained from the transmitted wave; indeed its sensitivity is very weak in transmission. The use of reflected and transmitted waves is necessary for the determination of the porosity, tortuosity and characteristic viscous length.

### 25.1.2. Mechanical parameters

Materials having a large porosity (polymer foams, rock wools etc.) are widely used in building and transportation to fight noise pollution. The Biot model, initially developed for the mechanics of rocks saturated with oil, enables us to understand the acoustical behavior of porous material saturated with air.

Historically, naturally porous materials such as corks or sponges have generated the interest of scientists: as an example, we can refer to the microscopic observations of R. Hooke presented in his monograph published in 1664 (Gibson [GIB 88]). Since then, engineering sciences, inspired by these mechanically optimized structures (the stiffnesses to density ratio increases significantly), have enabled the terrestrial architectural developments we can benefit from today, and mainly the fast development of aeronautics with composite materials (honeycomb structures for example) [GOR 94]. Other fields such as soil mechanics are also concerned with the various mechanical behaviors of porous materials. The characterizations of the subsoils, and namely hydrocarbon prospecting, have motivated researches on propagations in porous media in mechanics and acoustics. In this field, the contributions of Biot [BIO 41] have allowed the rapid development of the mechanics of porous materials [COU 91]. Finally, the recent arrival of plastic materials have enabled the production of artificial porous materials such as plastic foams (or fibrous materials), which are often used in industrial applications like acoustical absorbers [ALL 93].

#### 25.1.2.1. Laws of mechanical behavior of foams

In a compression test, three areas can be distinguished: a linear elastic area, a plateau which corresponds to the cell buckling, followed by a state of densification as shown by Figure 25.15. In acoustics, it is the first area which matters to understand the mechanisms of propagations in the solid phase.

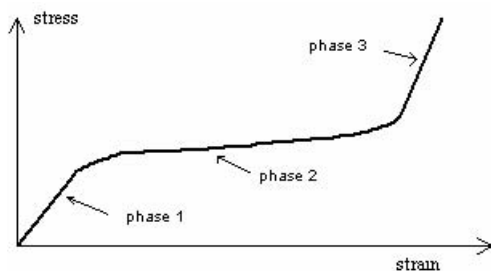


**Figure 25.15.** Stress–strain curve in compression

In general, the waves propagate simultaneously in both phases. For an isotropic material, the displacements  $U$  and  $u$  of the fluid and the solid, respectively, are governed by the following equations [BIO 56, 57]:

$$\begin{aligned}\rho_{11} \frac{\partial^2 u}{\partial t^2} + \rho_{12} \frac{\partial^2 U}{\partial t^2} &= P \nabla(\nabla \cdot u) + Q \nabla(\nabla \cdot U) - N \nabla \times \nabla \times u, \\ \rho_{22} \frac{\partial^2 U}{\partial t^2} + \rho_{12} \frac{\partial^2 u}{\partial t^2} &= R \nabla(\nabla \cdot U) + Q \nabla(\nabla \cdot u)\end{aligned}\quad [25.31]$$

The  $\rho_{ij}$  coefficients correspond to the variations of the apparent mass of the solid and of the fluid, and the parameters  $P$ ,  $N$ ,  $R$  and  $Q$  take into account the two elastic coefficients of the solid, the bulk modulus of the fluid and the porosity of the porous medium [ALL 93].

For an isotropic medium, the stress–strain relationships are written:

$$\begin{aligned}\sigma^s_{ij} &= [(P - 2N)\varepsilon^s + Q\varepsilon^f]\delta_{ij} + 2N\varepsilon^s_{ij} \\ \sigma^f_{ij} &= (Q\varepsilon^s + R\varepsilon^f)\delta_{ij}\end{aligned}\quad [25.32]$$

where  $\varepsilon^s$  and  $\varepsilon^f$  represent the trace of the strain tensor in the solid and fluid phases, respectively.

#### 25.1.2.1.1. Viscoelastic behavior

The organic matrix (polyurethane for example) constituting the foam has a viscoelastic behavior. For an isotropic material, the Young modulus  $E^*$  and the Poisson coefficient  $\nu^*$  are complex and depend on the excitation frequency  $\omega$  [FER 80]:

$$E^*(\omega) = E_1(\omega) + jE_2(\omega) \quad [25.33]$$

$$\nu^*(\omega) = \nu_1(\omega) + j\nu_2(\omega) \quad [25.34]$$

where indices 1 and 2 correspond to the real and complex parts, respectively. Moreover, the viscoelastic behavior is non-linear as  $E^*$  and  $\nu^*$  can also depend on the amplitude of the excitation.

#### 25.1.2.1.2. The structural models

The first of these models appeared in the 1960s, a period of important industrial development of plastic foams, with the works of Gent [GEN 59, 63, 66] and Ko

[KO 65]. Allowing a static description for highly porous materials, these models have significantly improved the understanding of the different strain mechanisms; the monograph of Gibson and Ashby [GIB 88] put together a large part of these results.

The structural models give a correspondence between the law of mechanical behavior of the skeleton (at the macroscopic scale) and that of the solid phase of which it is made (at the microscopic scale). The skeleton can be assimilated into an assembly of embedded beams (making nodes) forming a 3D structure. These beams form cells whose topology is largely dealt with in the literature [GIB 88], [WAR 97]. A fine simulation of the mechanical behavior requires taking into account the variability in size and shape of the cells constituting the foam. However, it is possible to consider the skeleton as perfectly periodical and to suppose that this regularity is affected by geometrical imperfections of small amplitudes.

#### 25.1.2.2. *Techniques of measurements of the viscoelastic constants*

In the domain of metrology, the flexible foams with open porosity pose some problems which can be summarized as follows:

- the sample can only have simple geometrical shapes (parallelepiped, cylinder), which limits the loading configurations;
- its biphasic nature requires us to take into account the saturating fluid, whose coupling effects can be paramount;
- the mode of fabrication of these foams often introduces an anisotropy, as we will see further.

We will present a measurement method at low frequency, a range where we can neglect the inertial effects and the influence of the saturating fluid. For the foams with an organic matrix, we could extend the measurement range thanks to the principle of time–temperature equivalence.

##### 25.1.2.2.1. Mechanical strength tester at low frequency

For isotropic materials, we determine  $E^*(\omega)$  from tensile or compression testings in a quasi-static state (inertial effects neglected in low frequency for samples of small dimensions) [MAR 97, DAU 02] or by a resonance method (mass–spring system) [PRI 82]. The shear modulus  $G^*(\omega)$  is obtained with similar methods in an appropriate configuration.

Figure 25.16 presents the experimental bench used to apply an axial compression on cubic samples made of flexible foams. The different elements are identified on the figure, their role being discussed in the next sections.

The sample (5) is located at the center of the assembly, slightly pre-tensioned between two horizontal plates covered by a very thick glass-paper; one of the plates is fixed to the frame (2), the other one (3) is fixed on the table of a vibrator (1) which base is fixed to the frame. Consequently, the sample closes a kinematic chain in which it receives all the axial vibrations of the vibrator.

The role of the glass-paper is to avoid any sliding in the horizontal plane of the lower and upper faces of the sample. Then, when the sample is slightly pre-tensioned, we obtain an efficient embedding without using an adhesive. The sample can easily be dismantled without being damaged: it can be used for a measurement along another direction.

During the excitation with a linear chirp, we measure:

- the applied force  $f$  is measured thanks to a piezoelectric sensor (6);
- the vertical displacement  $d_1$  of the lower face of the sample is measured thanks to an induction sensor (4);
- the horizontal displacements  $d_2$  of the center of the lateral faces are measured thanks to a laser vibration meter.

This method has the advantage of simultaneously obtaining  $E^*$  and  $\nu^*$  when the isotropy is verified after a measurement in the three directions.

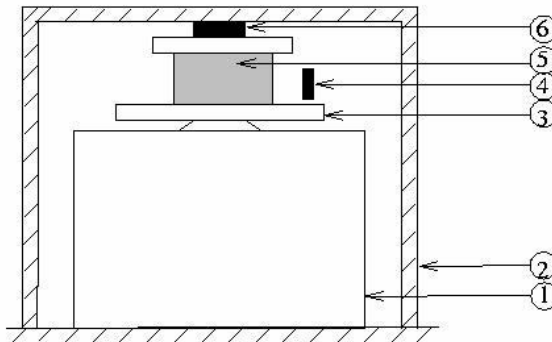


**Figure 25.16.** Test bench of compression

For a given frequency of the excitation, the test bench described above enables us to obtain the sample stiffness:

$$K^*(\omega) = \frac{f(\omega)}{d_1(\omega)} \quad [25.35]$$

and the transfer function:

$$T^*(\omega) = \frac{d_2(\omega)}{d_1(\omega)} \quad [25.36]$$

For isotropic foams,  $K^*$  and  $T^*$  depend on  $E^*$  and  $\nu^*$  through the relationships:

$$K^*(\omega) = K[E^*(\omega), \nu^*(\omega)] \quad [25.37]$$

$$T^*(\omega) = T[E^*(\omega), \nu^*(\omega)] \quad [25.38]$$

The extraction of the parameters  $E^*$  and  $\nu^*$  is obtained by numerical simulation (finite elements), limiting ourselves to a quasi-static description which is verified in the frequency range 1Hz–100Hz for the foams studied. This simulation shows that, for a cube of side  $L$ , the stiffness is of the following form:

$$K = \frac{EL(1-\nu)}{h(\nu)} \quad [25.39]$$

where the function  $h$  is represented in Figure 25.17 and decreases from 1 to 0.4. Furthermore, the transfer function  $T$  only depends on  $\nu$ :

$$T = g(\nu) \quad [25.40]$$

where the function  $g$  is represented in Figure 25.17.



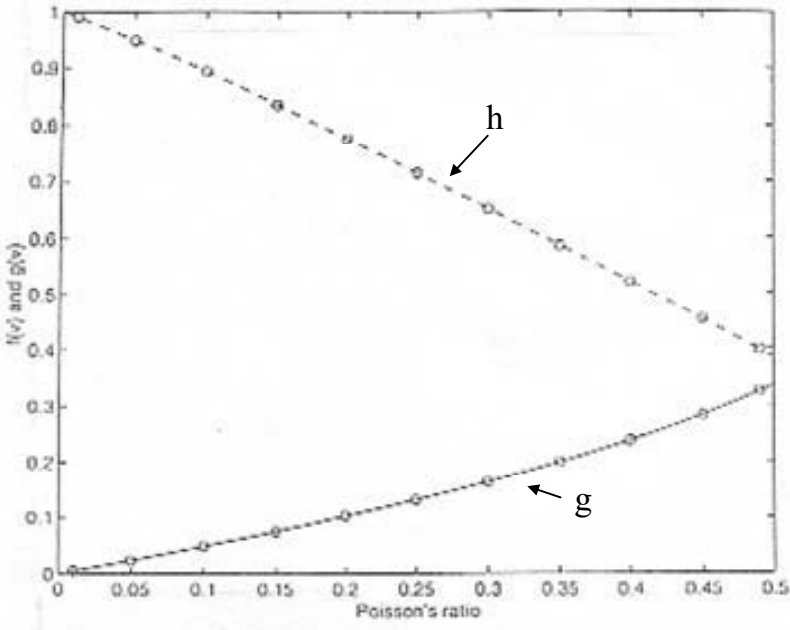


**Figure 25.17.** Representation of functions  $h$  and  $g$

Industrial foams with open porosity (Recticel) have been tested at ambient temperature (20°C) in the frequency range 1Hz–100Hz. We observe that the function  $T$  for these materials is real and does not depend on frequency. Thus, in this frequency range,  $\nu$  is real and constant. From these observations and the numerical results described below, relationships [25.35] and [25.36] take the following forms:

$$K^*(\omega) = \frac{E^*(\omega)L(1-\nu)}{h(\nu)} \quad [25.41]$$

$$T^*(\omega) = g(\nu) \quad [25.42]$$

These relationships allow us to obtain  $\nu$ , then  $E^*(\omega)$ , at the chosen frequency in the measurement range. For the studied foams, the results are presented in Figure 25.17. It should be noted that this measurement method, limited to low frequencies, is valid for foams having a small resistance to air flow.

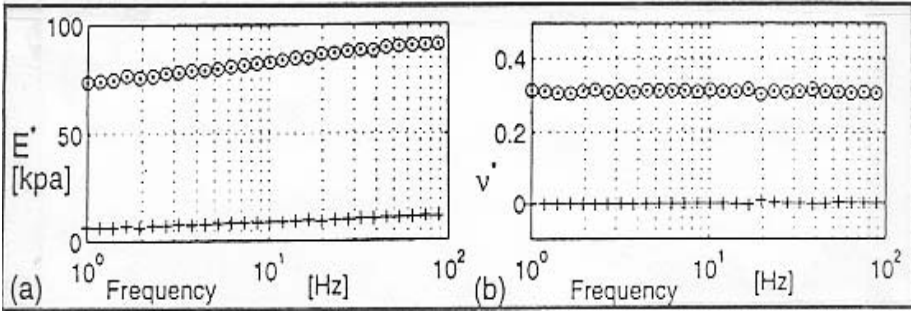


**Figure 25.18.** Real and imaginary parts of the Young's modulus and Poisson coefficient as functions of frequency

#### 25.1.2.2.2. Principle of time–temperature equivalence

The solution to measuring the viscoelastic constants of organic materials in a large frequency range is to use the properties of time–temperature equivalence. This principle of equivalence is based on the method of reduced variables expressed as follows [FER 80]:

$$\begin{aligned} G'(\omega, T_0) &= b_T G'(a_T \omega, T_1) \\ G''(\omega, T_0) &= b_T G''(a_T \omega, T_1) \end{aligned} \quad [25.43]$$

where  $G'$  and  $G''$  are an elasticity modulus and the corresponding loss modulus, respectively;  $\omega$  refers to the pulsation;  $a_T$  and  $b_T$  are two translation coefficients depending on the temperature  $T$ . Thus, measuring the complex elasticity modulus on a reduced frequency range at different temperatures, we can draw an index contour covering a large frequency range at a fixed temperature  $T_0$ , by shifting the curves at the temperature  $T_1$ , as shown by relationships [25.43].

Figure 25.19 shows the values of  $G'$  and  $G''$  measured at five temperatures (0°, 5°, 10°, 15° and 20°C) in the frequency range 0–16 Hz. Figure 25.20 shows the predicted values, with the help of the equivalence principle, of  $G'$  and  $G''$  at 20°C in the frequency range 0–3000Hz.

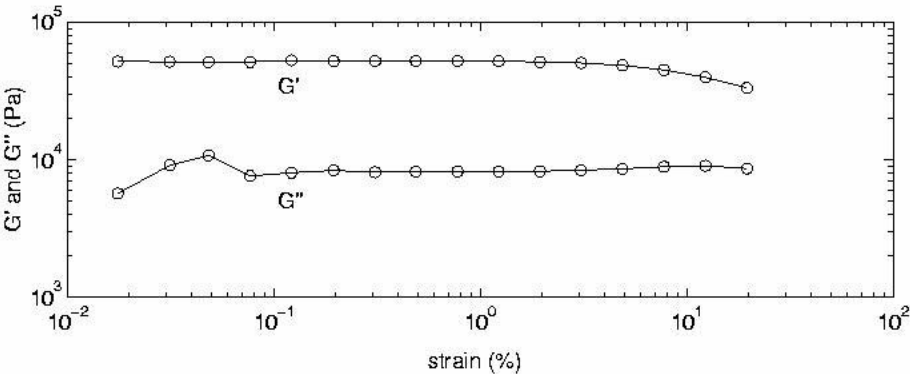


Figure 25.19. Real and imaginary parts of the stiffness modulus measured at low frequency

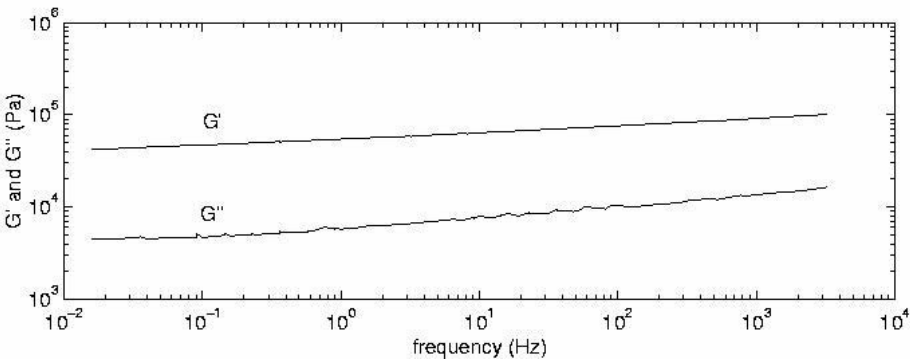
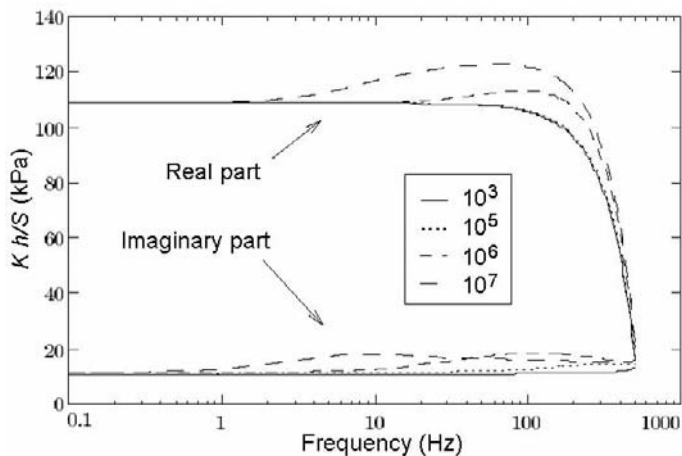


Figure 25.20. Real and imaginary parts of the stiffness modulus predicted on five decades

25.1.2.2.3. Influence of the saturating fluid

As indicated above, the method used is limited in frequency, and concerns only low-resistive materials [ETC 99, DAU 02]. These limits have been estimated with the help of a finite element simulation as shown on Figure 25.21.



**Figure 25.21.** *Stiffness as a function of frequency for several resistivities to the air flow; real and imaginary parts*

#### 25.1.2.2.4. Problems relative to anisotropy

Polymer foams often present a transverse anisotropy which can be explained by their mode of fabrication. The longitudinal direction corresponds to the (vertical) inflation direction during the foaming, which occurs after the polymer extrusion. Thus, the cells show an elongated form in this direction, which increases the stiffness compared to the other two directions [MEL 98]. It is obvious that other phenomena can be involved during this process (thermal effects, border effects, gravity, etc.) and cause some observed shifts with respect to the transverse isotropy: heterogeneity and gradient of geometrical, mechanical or acoustical properties (porosity), orthotropy or absence of correspondence between the principal axes and the supposed symmetry axes of the foams.

Generally, the studied foams have a transverse isotropy in the horizontal plane. We will denote  $L$ ,  $T$  and  $T'$  the longitudinal and transverse directions.

For the test bench described above, we do some measurements on a cubic sample following the three dimension of the cube, to determine the three stiffnesses:

$$\begin{aligned}
 K_{LL}^* &= \frac{f_L}{d_L} \\
 K_{TT}^* &= \frac{f_T}{d_T} \\
 K_{T'T'}^* &= \frac{f_{T'}}{d_{T'}}
 \end{aligned}
 \tag{25.44}$$

where  $f$  and  $d$  represent the forces and displacements measured along the direction  $L$ ,  $T$  or  $T'$  indicated by the subscript.

We also measure six transfer functions (two for each direction); for example, in the configuration illustrated by Figure 25.22, we obtain:

$$\begin{aligned}
 T_{LT}^* &= \frac{d_L}{d_T} \\
 T_{LT'}^* &= \frac{d_L}{d_{T'}}
 \end{aligned}
 \tag{25.45}$$

The other four transfer functions are:  $T_{TL}^*$ ,  $T_{TT'}^*$ ,  $T_{T'L}^*$  and  $T_{T'T}^*$ .

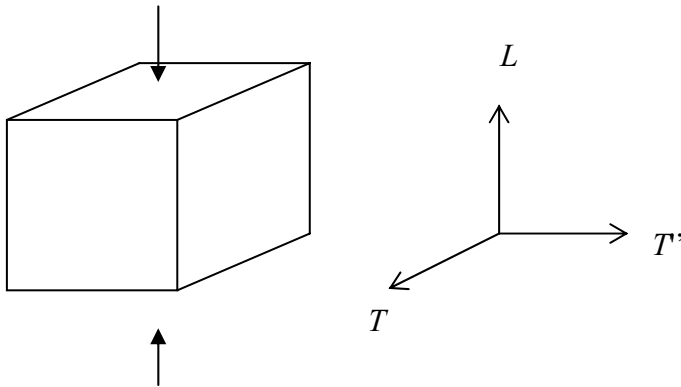


**Figure 25.22.** Sample loading in the longitudinal direction

For isotropic transverse foams, directions  $T$  and  $T'$  are equivalent; the nine measurements are reduced to five independent parameters, which are used in the numerical inversion to determine the Young moduli  $E_L$  and  $E_T$ , the shear modulus  $G_{LT}$  and the Poisson coefficients  $\nu_{TT}$  and  $\nu_{LT}$ .

With:

$$E_L^* = E_L(1 + j\eta_s) \quad [25.46]$$

where  $\eta_s$  represents the structural damping which has the same value for the other moduli; in addition, the Poisson coefficients  $\nu_{TT}$  and  $\nu_{LT}$  are real. On a Recticel foam of density 30 and porosity 0.97, we obtain the following results:

$$E_L = 172 \text{ kPa}$$

$$E_T = 104 \text{ kPa}$$

$$G_{LT} = 80 \text{ kPa}$$

$$\nu_{LT} = 1.5$$

$$\nu_{TT} = 0.2$$

$$\eta_s = 0.1$$

#### 25.1.2.2.5. Stiffness measurement of porous plates

Porous materials used as absorbing materials are generally more or less thick plates, from which it is not always possible to cut a cubical sample of reasonable dimensions to use the test bench described above. We have implemented a method for measuring deflection stiffness of a plate, determining its eigen pulsations and its vibration modes.

The device is represented on Figure 25.23. The sample is a plate of porous material (foam or fibrous) in the embedded–free–embedded–free configuration. The fixing system is simple and modular, so that plates of different thicknesses can be tested. The excitation is mechanical and is made through a vibrator. The excitation signal is a MLS (maximum length sequence) of degree 14, sampled at 3,000 Hz and made of 10 periods. The signal generation and its processing are controlled by a computer. The velocities are measured with a laser vibrometer at several points of the plate by the scanning of a robot.

The results obtained by monophasic inversion are consistent and give good information on the plate stiffness and on the material isotropy [ETC 01].

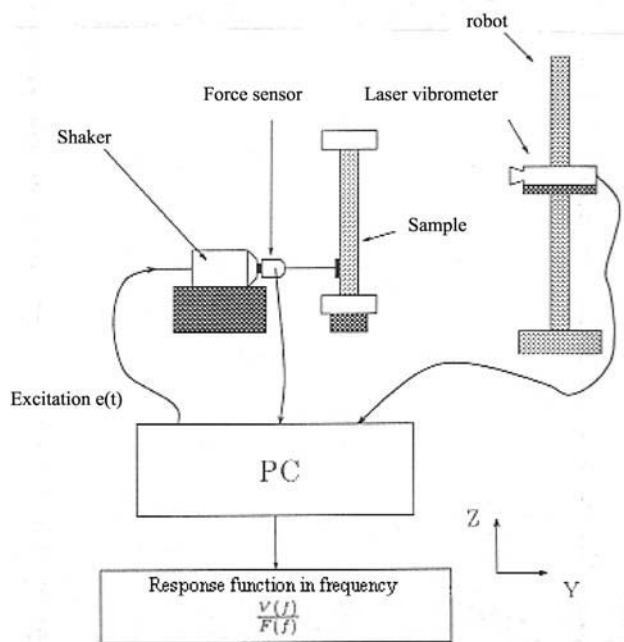


**Figure 25.23.** Device for the measurement of deflection stiffnesses of a porous plate

## 25.2. Bibliography

- [AKN 97] A. Aknine, B. Castagnède, C. Depollier, “Réflexion/réfraction d’ondes acoustiques à l’interface fluide – matériaux poreux”, *C. R. Acad. Sci. Paris*, vol. II, n°324, 501–11, 1997
- [ALL 93] J.-F. Allard, *Propagation of Sound in Porous Media: Modeling Sound Absorbing Materials*, Chapman & Hall, London, 1993
- [AYR 98] C. Ayrault, A. Moussatov, B. Castagnède, D. Lafarge, “Ultrasonic characterization of plastic foams via measurements with static pressure variations”, *Appl. Phys. Lett.*, 74 (21), 3224–6, 1999
- [AYR 05] C. Ayrault, S. Griffiths, “Caractérisation ultrasonore de matériaux poreux très absorbants à pression statique variable”, *Actes du XVII<sup>ème</sup> Congrès Français de Mécanique*, n°329, Troyes, 29 August – 2 September 2005
- [BER 42] L.L. Beranek, “Acoustic impedance of porous materials”, *J. Acoust. Soc. Am.*, n°13, 248–60, 1942
- [BIO 41] M.A. Biot, “General theory of three dimensional consolidation”, *J. Appl. Phys.*, 12, 155–64, 1941

- [BIO 56] M.A. Biot, "The theory of propagation of elastic waves in a fluid-saturated porous solid. I. Low frequency range II. Higher frequency range", *J. Acoust. Soc. Am.*, 28, 168–91, 1956
- [BIO 57] M.A. Biot and D.G. Willis, "The elastic coefficients of the theory of consolidation", *J. Appl. Mechanics*, (24), 594–601, 1957
- [BRO 96] N. Brown, M. Melon, V. Montembault, B. Castagnède, W. Lauriks, P. Leclaire, "Evaluation of the viscous characteristic length of air-saturated porous materials from the ultrasonic dispersion curve", *C. R. Acad. Sci. Paris 322 série II*, p. 121–7, 1996
- [BRO 03] B. Brouard, B. Castagnède, M. Henry, D. Lafarge, S. Sahraoui, "Mesure des propriétés acoustiques des matériaux poreux", *Collection Techniques de l'ingénieur*, R 6 120 – 7 - 10, 2003
- [BRO 80] R. J. S. Brown, "Connection between formation factor for electrical resistivity and fluid–solid coupling factor in Biot's equations for acoustic waves in fluid-filled media", *Geophys*, n°45, 1269–75, 1980
- [CAS 98] B. Castagnède, A. Aknine, C. Depollier, M. Melon, "Ultrasonic characterization of the anisotropic behaviour of air-saturated porous materials", *Ultrasonics*, 36, 323–41, 1998
- [CAS 01] B. Castagnède, A. Moussatov, V. Tarnow, "Parametric study of the influence of compression of the acoustical anisotropy of automotive felts", *C. R. Acad. Sci., Paris*, 2 (329), 295–301, 2001
- [CHA 91] Y. Champoux, J. F. Allard, "Dynamic tortuosity and Bulk modulus in air-saturated porous media", *J. Appl. Phys.*, 70(4), 1975–9, 1991
- [CON 88] C.A. Condat, "Acoustic localization and resonant scattering", *J. Acoust. Soc. Am.*, 83(2), 441–52, 1988
- [COU 91] O. Coussy: "*Mécanique des milieux poreux*", Technip, Paris, 1991
- [DAU 02] N. Dauchez, M. Etchessahar, S. Sahraoui, "On measurement of mechanical properties of sound absorbing materials", *Second Biot Conference on Poromechanics*, Grenoble, 2002
- [ETC 99] M. Etchessahar, N. Dauchez, S. Sahraoui, "Comportement des mousses acoustiques aux basses frequencies", *14ème Congrès Français de Mécanique, Toulouse*, 6 pages (CD ROM), 30/08-03/09/1999
- [ETC 01] M. Etchessahar, S. Sahraoui, B. Brouard, "Bending vibrations of a rectangular thin porous plate", *C. R. Acad. Sci. Paris*, t. 329, Series II b, 615–20, 2001
- [ETC 05] M. Etchessahar, S. Sahraoui, L. Benyahia, J-F. Tassin, "Frequency dependance of mechanical properties of acoustic foams", *J. Acous. Soc. of Am.*, 117 (3), 1114–21, 2005
- [FEL 01] Z.E.A. Fellah, C. Depollier, M. Fellah, "Direct and inverse scattering problem in porous material having a rigid frame by fractional calculus based method", *J. Sound and Vibration*, 244 (2), 3659, 2001



- [FEL 02] Z.E.A. Fellah, C. Depollier, M. Fellah, "Application of fractional calculus to the propagation in rigid porous materials: Validation via ultrasonic measurements", *Acta Acustica united with Acustica*, 87, 34, 2002
- [FEL 03-a] Z.E.A. Fellah., S. Berger, W. Lauriks, C. Depollier, J.Y. Chapelon, "Inverse problem in air-saturated porous media via reflected waves", *Rev. Sci. Inst.*, 74 (5), 2871, 2003
- [FEL 03-b] Z.E.A. Fellah, S. Berger, W. Lauriks, C. Depollier, C. Aristegui, J.Y. Chapelon, "Measuring the porosity and the tortuosity of porous materials via reflected waves at oblique incidence", *J. Acoust. Soc. Am.*, 113 (5), 2424, 2003
- [FEL 03-c] Z.E.A. Fellah, S. Berger, W. Lauriks, C. Depollier, P. Trompette, J.Y. Chapelon, "Ultrasonic measuring of the porosity and tortuosity of air-saturated random packings of beads", *J. Appl. Phys.*, (93), 9352, 2003
- [FEL 03-d] Z.E.A. Fellah, F. Mitri, C. Depollier, S. Berger, W. Lauriks, J.Y. Chapelon, "Characterization of porous materials having a rigid frame via reflected waves", *J. Appl. Phys.*, 94 (12), 7914, 2003
- [FEL 03-e] Z.E.A. Fellah, C. Depollier, S. Berger, W. Lauriks, P. Trompette, J.Y. Chapelon, "Detemination of transport parameters in air saturated porous materials via ultrasonic reflected waves", *J. Acoust. Soc. Am.*, 113, 2561 (5), 2003
- [FER 80] J.D. Ferry, *Viscoelastic Properties of Polymers*, John Wiley & Sons, 1980
- [GEN 59] A.N. Gent and A.G. Thomas, "Deformation of foamed elastic materials", *J. Appl. Polymer Sci.*, 1, 107–13, 1959
- [GEN 63] A.N. Gent and A.G. Thomas, "Mechanics of foamed elastic materials", *Rubber Chem. Tech.*, 36, 597–610, 1963
- [GEN 66] A.N. Gent and K.C. Rusch, "Viscoelastic behavior of open cell foams", *Rubber Chem. Tech.*, 39, 389–96, 1966
- [GIB 88] L.J. Gibson and M.F. Ashby, *Cellular Solids: Structure and Properties*, Pergamon Press, Oxford, 1988
- [GOR 94] J.E. Gordon: *Structures et matériaux*, Pour la Science, Diffusion Belin, 1994
- [GRI 05] S. Griffiths, C. Ayrault, "Ultrasonic characterization of porous materials with high air flow resistivity", *Proceedings of the Symposium on the Acoustics of Poro-Elastic Materials*, ENTPE, Lyon, France December 7–8–9, 2005
- [JOH 82-1] D. L. Johnson, T. J. Plona, "Acoustic slow wave and the consolidation transition", *J. Acoust. Soc. Am.*, n°72, 556–65, 1982
- [JOH 82-2] D. L. Johnson, T. J. Plona, C. Scala, F. Pasieb and H. Kojima, "Tortuosity and acoustic slow waves", *Phys. Rev. Lett.*, n°49, 1840–4, 1982
- [JOH 87] D. L. Johnson, J. Koplik, R. Dashen, "Theory of dynamic permeability and tortuosity in fluid-saturated porous media", *J. Fluid Mech.*, 176, 379–402, 1987
- [KO 65] W.L. KO, "Deformation of foamed elastomers", *J. Cellular Plastics*, 1, 45–50, 1965.

- [LAF 93] D. Lafarge, Propagation du son dans les matériaux poreux à structure rigide saturés par un fluide viscothermique, Thesis, University of Maine, France, 1993
- [LAN 71] L.L. Landau, E. Lifchitz, *Mécanique des fluides.*, Editions Mir, Moscow, 1971
- [LEC 96] P. Leclaire, L. Kelders, W. Lauriks, M. Melon, N. Brown, B. Castagnède, "Ultrasonic wave propagation in reticulated foams saturated by different gases – High frequency limit of classical model", *Appl. Phys. Lett.*, 69(18), 2641–3, 1996
- [MAR 97] E. Mariez, S. Sahraoui, J.F. Allard, "Elastic constants of polyurethane foam's skeleton for Biot model", *Proceed. Internoise 97* (Budapest, august 25–27), 951–4, 1997
- [MEL 95-a] M. Melon, D. Lafarge, B. Castagnède, "Measurement of tortuosity of anisotropic acoustic materials", *J. Appl. Phys.*, 78(8), p. 4929–33, 1995
- [MEL 95-b] M. Melon, B. Castagnède, "Measurement of anisotropic transmission and reflection coefficients and tortuosity of porous media at low ultrasonic frequencies, tortuosity of anisotropic acoustic materials", *J. Acoust. Soc. Am.*, 98(2), 1228–30, 1995
- [MEL 96] M. Melon, Caractérisation de matériaux poreux par ultrasons basse-fréquence (20–500 kHz), Thèse, Université du Maine, 1996
- [MEL 98] M. Melon, E. Mariez, C. Ayrault, S. Sahraoui, "Acoustical and mechanical characterization of anisotropic open cell foams", *J. Acoust. Soc. Am.*, 104, 2622–7, 1998
- [NAG 95] P. B. Nagy, D. L. Johnson, "Improved materials characterization by pressure-dependent ultrasonic attenuation in air-filled permeable solids", *Appl. Phys. Lett.*, 68(26), 3707–9, 1996
- [PRI 82] T. Pritz: "Transfer function method for investigating the complex modulus of acoustic materials: rod-like specimen", *J. Sound Vib.*, 81(3), 359–76, 1982
- [SAC 78] W. Sasche, Y. Pao, "On the determination of phase and group velocity of dispersive waves in solids", *J. Appl. Phys.*, 49(8), 4320–7, 1978
- [SOR 89] D. Sornette, "Acoustic waves in random media, I. Weak disorder regime", *Acustica*, 67, 199–215, 1989
- [STI 88] M. R. Stinson, G. A Daigle, "Electronic system for the measurement of flow resistance", *J. Acoust. Soc. Am.*, n°83, 2422–8, 1988
- [WAR 97] W.E. Warren and A.M. Kraynick, "The linear elastic behavior of low-density Kelvin foam with open-cells", *J. Appl. Mech.*, 64, 787–94, 1997

## Chapter 26

# Metrology of Acoustical Properties of Absorbing Materials: Surface Impedance

### 26.1. Introduction

#### 26.1.1. *Method of the Kundt tube*

Let us suppose that the material has a plane contact surface with air and that a sounding harmonic wave in homogenous air strikes the material with a normal incidence. The material's reaction is characterized by its surfacic impedance  $Z_s$ . This acoustical quantity, found by measurement, depends in particular on the complex wavenumber  $q(\omega)$  and on the characteristic impedance  $Z_c(\omega)$  of the porous medium, these functions being related to the dynamic tortuosity  $\alpha(\omega)$  and to the normalized compressibility  $\beta(\omega)$ , respectively, by the relationships:

$$q(\omega) = q_o \sqrt{\alpha \cdot \beta} \quad [26.1]$$

$$Z_c = Z_o \sqrt{\frac{\alpha}{\beta}} \quad [26.2]$$

with  $q_o = \frac{\omega}{c_o} = \omega \sqrt{\frac{\rho_o}{K_a}}$  and  $Z_o = \sqrt{\rho_o K_a}$  corresponding to the same quantities for the free fluid characterized by its density  $\rho_o$  and its adiabatic bulk modulus  $K_a$ , respectively.

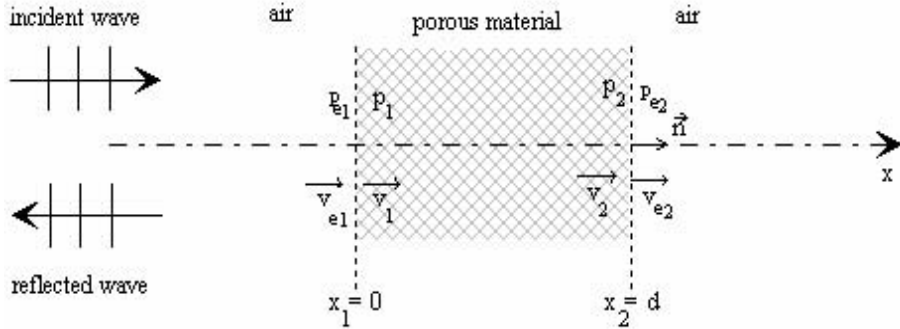


**Figure 26.1.** Surface impedance in normal incidence

The acoustical characterization of a material is thus made through the measurement of the surface impedance of this material. Let us consider a layer of porous material of thickness  $d$  located between two air layers. Figure 26.1 represents a plane wave propagating in a direction  $Ox$  perpendicular to the surface of a material immersed in air. A part of this wave is reflected and yields a combination of two waves, back and forth, in the exterior air. If  $p_{e1}$  is the acoustic pressure and  $\vec{v}_{e1}$  the particular velocity normal to the material surface, in the air, at  $x_1 = 0$ , the surface impedance  $Z_{s1}$  is defined by:

$$Z_{s1} = \frac{p_{e1}}{v_{e1}}. \quad [26.3]$$

Using the conditions of pressure continuity and flow conservation, we can link this impedance to the acoustical quantities on the surface, immediately within the material, by:

$$Z_{s1} = \frac{p_1}{\phi v_1} = \frac{1}{\phi} Z_s(1) \quad [26.4]$$

where  $\phi$  is the material porosity and  $Z_s(1)$  the surface impedance at  $x_1 = 0$ , defined from the acoustic pressure  $p_1$  and the particular velocity  $v_1$  in air inside the material. The same relationship exists at the second surface at  $x_2 = d$  and is written in the following form:

$$Z_{s2} = \frac{p_{e2}}{v_{e2}} = \frac{p_2}{\phi v_2} = \frac{1}{\phi} Z_s(2). \quad [26.5]$$

If the impedance  $Z_{s2}$  is known, as well as the wavenumber  $q(\omega)$  and the characteristic impedance  $Z_c(\omega)$ , it is possible to obtain the expression of  $Z_{s1}$  as a function of these quantities. This calculation is classic in acoustics and we can refer for example to the work of J. F. Allard [ALL 93]. We obtain the following relationship between  $Z_s(1)$  and  $Z_s(2)$ :

$$Z_s(1) = Z_c \frac{Z_c + i Z_s(2) \cot(qd)}{Z_s(2) + i Z_c \cot(qd)}. \quad [26.6]$$

The surface impedance  $Z_{s1}$  is then written:

$$Z_{s1} = \frac{Z_c}{\phi} \frac{Z_c + i \phi Z_{s2} \cot(qd)}{\phi Z_{s2} + i Z_c \cot(qd)}. \quad [26.7]$$

It is convenient to introduce a dimensionless surface impedance (or reduced surface impedance), which will be used in the following and is defined generally by:

$$Z = \frac{Z_s}{Z_o}, \quad [26.8]$$

where  $Z_o = \rho_o c_o$  is the characteristic impedance of the unlimited fluid. Let us assume that, if the second air layer is semi-infinite,  $Z_{s2} = Z_o$  (reduced impedance  $Z_2 = 1$ ). We can give the expression of the reduced impedance  $Z_1$  as a function of the reduced impedance  $Z_2$ , replacing  $q(\omega)$  and  $Z_c(\omega)$  by their expression as functions of the dynamic tortuosity  $\alpha(\omega)$  and of the compressibility  $\beta(\omega)$ . We finally obtain:

$$Z_1 = \frac{1}{\phi} \sqrt{\frac{\alpha}{\beta}} \frac{\sqrt{\frac{\alpha}{\beta}} + i\phi Z_2 \cot(q_o d \sqrt{\alpha\beta})}{\phi Z_2 + i\sqrt{\frac{\alpha}{\beta}} \cot(q_o d \sqrt{\alpha\beta})}. \quad [26.9]$$

The surface impedance contains information on the pair  $\alpha(\omega)$  and  $\beta(\omega)$ . Measuring the impedances with the same material placed in two different configurations, it is possible to obtain the dynamic tortuosity  $\alpha$  and the normalized compressibility  $\beta$ .

Finally, we can quote an interesting specific case, when the material is set on a rigid backing. The surface impedance  $Z_2$  is then infinite and the reduced impedance for the material becomes:

$$Z_1 = \frac{i}{\phi} \sqrt{\frac{\alpha}{\beta}} \cot\left(\frac{\omega}{c_o} d \sqrt{\alpha\beta}\right). \quad [26.10]$$

To have a situation which is really different from the former, the sample can be located in front of a cavity whose length  $l$  corresponds, for a given frequency, to  $\lambda/4$  (up to a multiple of  $\lambda/2$ ). The surface impedance of such a cavity being zero, the reduced surface impedance  $Z_1'$  of the material is obtained with  $Z_2 = 0$ , which gives:

$$Z_1' = \frac{-i}{\phi} \sqrt{\frac{\alpha}{\beta}} \tan(q_o d \sqrt{\alpha\beta}). \quad [26.11]$$

The surface impedance appears as the acoustical quantity characterizing the acoustical behavior of the material, from which it is possible, if the measurements are sufficiently precise, to find the functions  $\alpha$  and  $\beta$ .

If  $R$  represents the complex reflection coefficient, i.e. the ratio of the complex amplitudes of the reflected wave and incident wave at the surface of the sample, its reduced impedance can be written:

$$Z = \frac{1 + R}{1 - R}. \quad [26.12]$$

The absorption coefficient in energy  $\Sigma$ , defined as the flux of absorbed energy divided by the flux of incident energy, is thus given by:

$$\Sigma = 1 - |R|^2. \quad [26.13]$$

Practically, this coefficient is of great interest for industry. But because it depends only on the modulus of  $R$ , it brings less information than the surfacic impedance.

### 26.1.2. *T.M.T.C. method of the Kundt tube*

The measurement of a surface impedance can be made in free field or using a pipe of stationary waves, also known as Kundt tube. The study of sound propagation in a tube can be found in most works in acoustics (see M. Bruneau [BRU 83]). A sound source placed at an extremity of a tube yields a plane incident wave which is partially reflected by the studied material which closes the other extremity of the tube. The incident and reflected waves interfere, and yield a system of stationary waves. For sufficiently low frequencies, the wave that propagates along the tube's axis has the characteristics of a plane wave. The use of a tube is thus interesting only for low frequencies. In our case, the tube diameter is 44.36 mm and the cutting frequency is thus around 4,500 Hz, which enables us to cover a frequency range from 50 to 4,000 Hz. The low-frequency limitation is only of technical order as we will see in the following.

There are different methods of performing the measurement of the surface impedance of a material using one, two or several microphones. Each has its own advantages and disadvantages. To obtain some precise measurements, we have developed in our laboratory (Maine University, Le Mans, France) a method using two microphones fixed on the tube. It is the T.M.T.C. method (Two-Microphone-Three-Calibration).

Initially, this method was proposed by V. Gibiat and F. Laloë [GIB 90] for the measurement of the input impedance of musical wind instruments. To calibrate the two fixed microphones, we use three closed empty cavities, and this is the origin of the name chosen for this method: two microphones and three calibrations (T.M.T.C.). We use a closed tube in which we generate a plane harmonic wave, of fixed frequency  $f$ , with the help of a loudspeaker located at one of the extremities, the other extremity being occupied by the sample, for which we want to measure the surface impedance. Two microphones ( $n^{\circ}1$  and  $n^{\circ}2$ ) are fixed on the wall of the tube and are separated by a distance  $e$  (microphonic spacing). Microphone  $n^{\circ}1$  is at a distance  $s$  from the plane  $x = 0$  that corresponds to the sample's face near the loudspeaker; this plane is called the measurement plane. The experimental setup is illustrated in Figure 26.3.

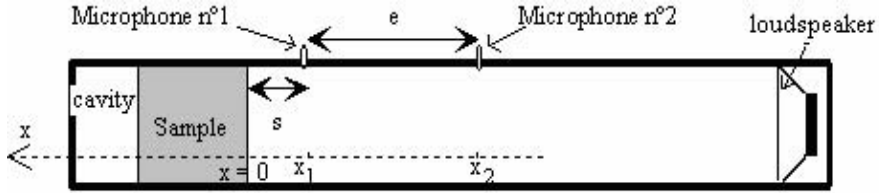


**Figure 26.2.** Surface impedance in normal incidence

If  $p_o$  and  $v_o$  are the acoustic pressure and velocities in the measurement plane ( $x = 0$ ), the surface impedance is given by  $Z_s = p_o/v_o$ . The pressure signals  $S_1$  and  $S_2$  delivered by the two microphones n°1 and n°2, respectively, are proportional to the corresponding acoustic pressures  $p_1$  and  $p_2$ . The acoustic pressures and velocities  $p_1, v_1$  and  $p_2, v_2$  can be expressed as functions of  $p_o$  and  $v_o$ . The signals  $S_1$  and  $S_2$  are then a linear combination of  $p_o$  and  $v_o$ :

$$\begin{aligned} S_1 &= a_{11}p_o + a_{12}v_o \\ S_2 &= a_{21}p_o + a_{22}v_o \end{aligned} \quad [26.14]$$

where the coefficients  $a_{ii}$  are dependent on the geometry of the system ( $s, e$ , etc.), on the acoustical properties of air in the pipe (wavenumber  $q'$ , characteristic impedance  $Z_o$ , etc.), on the gain and finally on the two microphones. The signal ratio  $y = S_2/S_1$  can be written:

$$y = \frac{S_2}{S_1} = \frac{a_{21}Z_s + a_{22}}{a_{11}Z_s + a_{12}}. \quad [26.15]$$

Inverting this relationship, we obtain the surface impedance  $Z_s$ :

$$Z_s = \frac{a_{22} - a_{12} \cdot y}{a_{11} \cdot y - a_{21}}. \quad [26.16]$$

Dividing this relationship by the characteristic impedance of air  $Z_o = \rho_o c_o$ , the reduced impedance of the measurement surface  $x = 0$  is given by the relationship:



$$Z = \frac{A \cdot y + B}{y - y_o}, \quad [26.17]$$

$$\text{with } A = -\frac{a_{12}}{Z_o a_{11}} ; B = \frac{a_{22}}{Z_o a_{11}} ; y_o = \frac{a_{21}}{a_{11}}.$$

The calibration will consist of determining these three coefficients  $A$ ,  $B$  and  $y_o$ , coefficients depending on the geometrical configuration and on the microphones, in order to then have the reduced impedance of the studied surface by the measurement of the signal ratio  $S_2/S_1$ . Measuring this ratio “ $y$ ” for three surfaces whose impedances are known, we obtain a system of equations with three unknowns, which has to be solved. A fourth measurement with the studied material enables us to determine its reduced impedance, based on the condition that the system did not endorse any modification between these different measurements (same temperature, frequency, lengths  $s$  and  $e$ , etc.). The best-known surfacic impedances are the input impedances of cylindrical cavities with a rigid bottom. If  $d_j$  is the length of the cavity, the reduced input impedance can be written:

$$Z_j = i \cdot \cot(q' d_j), \quad [26.18]$$

where  $q'$  is the wavenumber of a plane harmonic wave propagating in the tube. This wavenumber is a complex value that takes into account the viscous and thermal effects in the tube and, consequently, differs from the wavenumber  $q_o$  of the unlimited fluid. Sound tubes have been the subject of many studies and we can refer to the works of J. Kergomard ([KER 91] and [CAU 84]) or M. Bruneau ([BRU 82] and [BRU 83]). We can start with a first cavity of length zero, i.e. put a rigid wall in the measurement plane (see Figure 26.3). Called cap (or cavity n°0) in the following, the surface impedance of this cavity can be considered as infinite and the measurement of the signal ratio corresponds to the coefficient  $y_o$ . Denoting  $y_j$  the signal ratio  $S_{2j}/S_{1j}$  obtained for the cavity n° $j$  (with  $j = 0, 1, 2$ ) of reduced input impedance  $Z_j$ , we can write:

$$\begin{cases} Z_1 = \frac{A y_1 + B}{y_1 - y_o} \\ Z_2 = \frac{A y_2 + B}{y_2 - y_o} \end{cases} \quad [26.19]$$

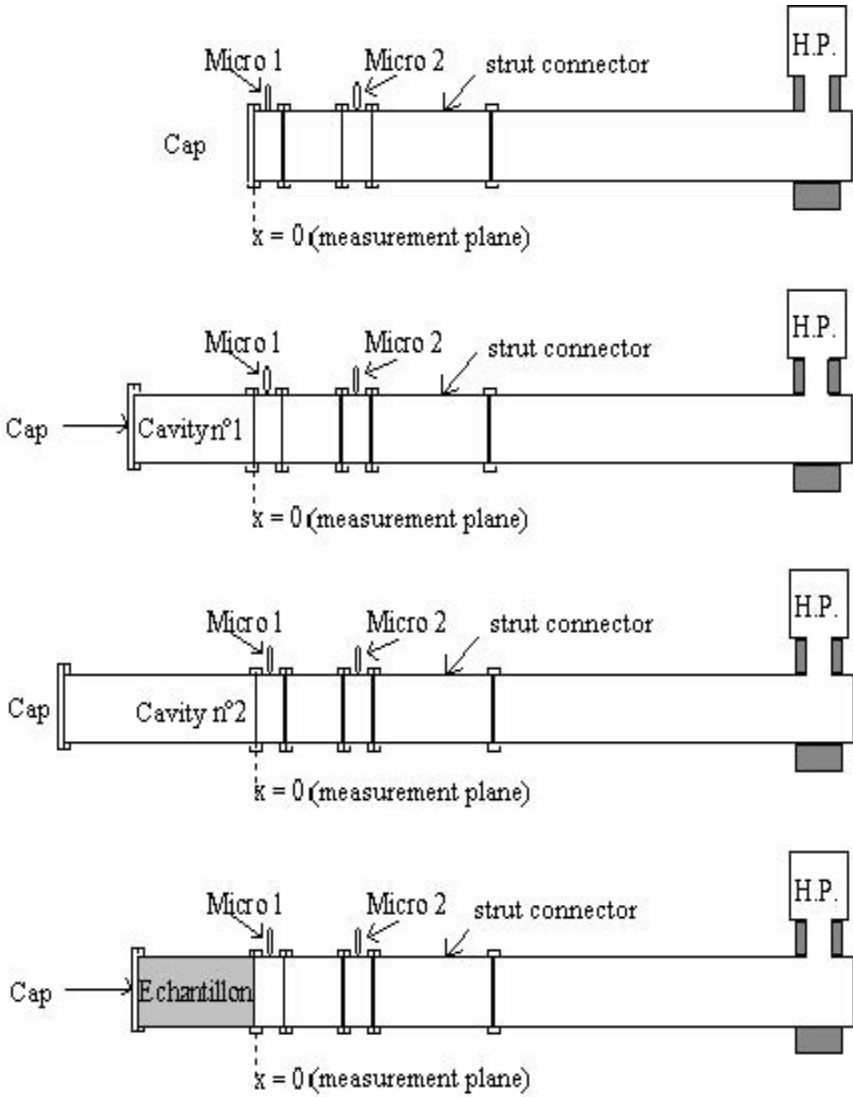


**Figure 26.3.** *Measurement principle for the T.M.T.C. method*

From this linear system, we can find the expression of the coefficients  $A$  and  $B$  as functions of the measurements  $y_0$ ,  $y_1$ ,  $y_2$  and of the reduced impedances of two cavities  $Z_1$  and  $Z_2$ . A fourth measurement “ $y$ ”, made this time by putting the surface

of a material at the level of the measurement plane, gives us the following reduced surface impedance  $Z$ :

$$Z = \frac{Z_1(y_1 - y_o)(y - y_2) + Z_2(y_2 - y_o)(y_1 - y)}{(y - y_o)(y_1 - y_2)}. \quad [26.20]$$

A detailed study has enabled us to obtain very precise measurements if some conditions are fulfilled. It is necessary to make the measurements at some frequencies for which the space between the two microphones corresponds to an odd number of quarter-waves. Likewise, for the calibration, cavities 2 and 3 must correspond to cavities in  $\lambda/8$  and  $3\lambda/8$ , respectively. We thus work with a frequency comb, the fundamental frequency being imposed by the spacing between the two microphones. Finally, it is important to specify that the calibration being made with the three cavities, it can be used for more than two years as long as nothing is modified on the test bench.

### – Applications

From the two impedances  $Z_1$  (rigid bottom) and  $Z_1'$  (quarter-wave cavity) whose expressions have been given formerly, we can extract the two functions  $\alpha(\omega)$  and  $\beta(\omega)$  without any approximation. Consequently, we obtain:

$$\beta(\omega) = \frac{1}{\phi q_o d} \left( \frac{\text{Arc tan}^2 \left( \pm \sqrt{-\frac{Z_1'}{Z_1}} \right)}{Z_1 Z_1'} \right)^{\frac{1}{2}} \quad [26.21]$$

$$\alpha(\omega) = \beta(\omega) \cdot \phi^2 Z_1 Z_1' = \phi \frac{Z_1 Z_1'}{q_o d} \text{Arc tan} \left( \pm \sqrt{-\frac{Z_1'}{Z_1}} \right), \quad [26.22]$$

where the sign  $\pm$  is chosen so that the real part of the impedance  $Z_1'$  is positive. The determination of the arctangent function is made by unwrapping the phase.

The relevant parameters  $\phi$ ,  $\sigma$ ,  $\alpha_\infty$  being measurable by various methods detailed above, it is thus possible to have a good estimation of the parameters  $\Lambda$  and  $\Lambda'$ , the viscous and thermal characteristic lengths which are involved in the functions  $\alpha(\omega)$

and  $\beta(\omega)$ , respectively. A comparison between these measured functions and the models enables the determination of these parameters.

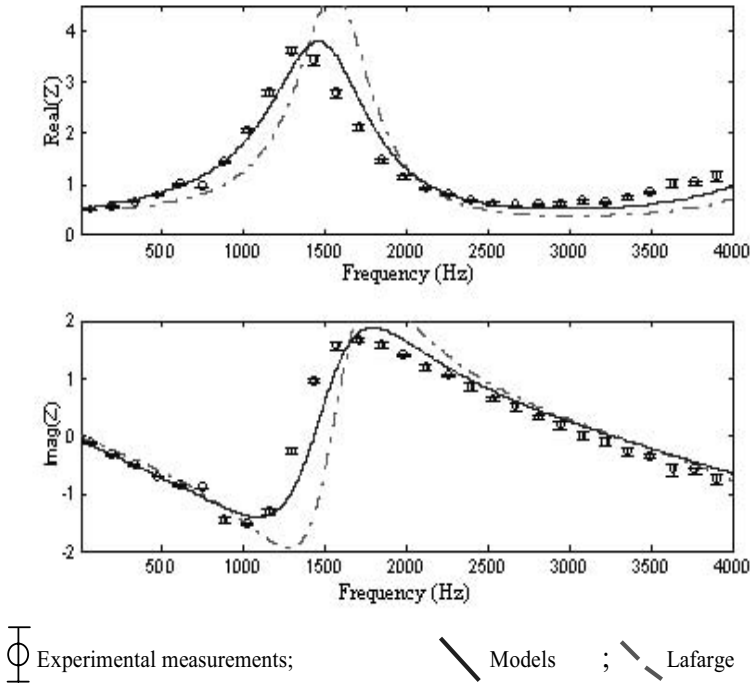


**Figure 26.4.** Reduced surfacic impedance  $Z_l'$  for foam n°1

The graphs presented in Figures 26.4 and 26.5 show what we can obtain on two polyurethane foams. For foam n°1 ( $\phi = 0.98$ ,  $\sigma = 4,750$  s.i. and  $\alpha_\infty = 1.2$ ), the value of  $\Lambda$ , for which the surface impedance curve  $Z_l'$  (a quarter-wave cavity being put behind the sample) best coincides with the models proposed in chapter 2, is  $2 \times 10^{-4}$  m. Likewise, the value of  $\Lambda'$  for foam n°2 ( $\phi = 0.97$ ,  $\sigma = 10,000$  s.i. and  $\alpha_\infty = 1.04$ ) given by the best coincidence with the measurements of surface impedance  $Z_l$  (the sample being put against a rigid wall) is  $3 \times 10^{-4}$  m. These results have been confirmed by ultrasonic measurements.

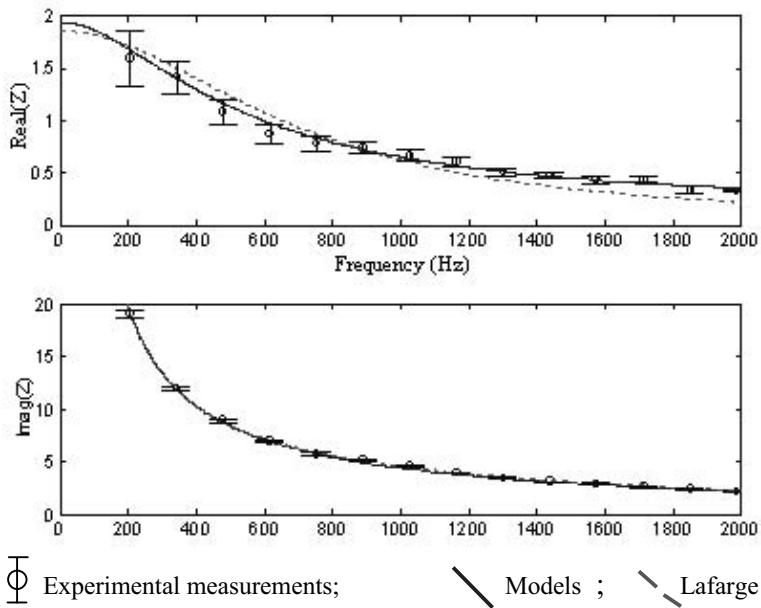


**Figure 26.5.** Reduced surface impedance  $Z_1$  for foam n°2  
(set on a rigid impervious backing)

### 26.1.3. Other methods: Chung and Blaser

Some ultrasonic methods for the measurement of parameters such as  $\alpha_\infty$ ,  $A$  and  $A'$  have enabled us to validate these different techniques.

There are also other principles for the measurement of surface impedance. The most classical technique used to determine the surface impedance of a material is the search for a stationary wave by moving a microphone probe inside the tube, in order to reconstitute the wave pattern. We can determine the modulus and the phase of the reflection coefficient  $R$  by measuring the maximum and minimum amplitudes in the tube, as well as the position  $x_l$  of the nearest minimum of pressure, the distance being measured from the sample [ALL 93]. We can then deduce the surface impedance. This method, simple in appearance, presents several disadvantages. A good determination of maximum and minimum pressures requires a great number of measurements made by moving the microphone probe, and this for a given frequency. To determine the impedance as a function of frequency, it is necessary to repeat these measurements for each different frequency. The time spent making each

measurement can become very important. Moreover, the signal-to-noise ratio becomes very weak near the minimal pressures, which causes a decrease of measurement precision. Another technical problem appears for low frequencies. At 100 Hz for example, we must be able to move the probe along a distance of around 3.5 m. Such a long probe, apart from the load, will attenuate the measured signal, and thus the signal-to-noise ratio.

To avoid the necessity of the probe displacement in the tube, methods using two microphones have been developed [AST 86]. One of them is the method of Chung and Blaser [CHU 80]. In this case, we use a doublet of microphones fixed on the inner surface of the tube. By measuring the transfer function between the two pressure signals delivered by the microphones, it is possible to obtain the reflection coefficient. The obtained result depends on the distance between the two microphones and on that between the first microphone and the surface of the studied material. The responses in amplitude and phase of the two microphones are never perfectly identical, so it is necessary to perform a calibration of the system. We thus make two consecutive measurements with any absorbing material, inverting the two microphones. Using this method, the measurement time is reduced, but the precision of the results obtained is closely related to that of the position of the microphones. In particular, inverting them inevitably introduces some errors.

Finally, we can mention the microphone doublet technique [ALL 92], a measurement technique in free field developed in our laboratory (Le Mans, France). This method, performed in an anechoic room, consists of measuring the acoustic pressure at two positions above the material, and then returning to the surface impedance. This method gives good results for high frequencies, but is not usable below 500 Hz for thicknesses of several centimeters of common materials. More recently, a new method, based on the works of Tamura [TAM 90] and usable for lower frequencies, has been developed by B. Brouard [BRO 94]: the holographic method. However, for precise measurements of surface impedances at low frequencies, the technique in free field is not ideal.

## 26.2. Bibliography

- [ALL 92] J. F. Allard, D. Lafarge, "Free field measurement at high frequencies of the impedance of porous layer", *Second International Congress on Recent Developments in Air-and Structure-Borne Sound and Vibration*, p. 4–6, Auburn University, U.S.A., March, 1992
- [ALL 93] J.-F. Allard, *Propagation of Sound in Porous Media: Modeling Sound Absorbing Materials*, Chapman & Hall, London, 1993

- [AST 86] ASTM, Standard Test Method for Impedance and Absorption of Acoustical Materials Using a Tube, Two Microphones and a Digital Frequency Analysis System, ASTM standard E 1050–86, 1986
- [BRO 94] B. Brouard, D. Lafarge J. F. Allard, “Measurement and prediction of the surface impedance of a resonant sound absorbing structure”, *Acta Acustica*, n°2, 301–6, 1994
- [BRU 82] M. Bruneau, J. Kergomard,– “Constante de propagation dans un tuyau cylindrique”, *Fortschritte der Akustik, FASE/DAGA '82*, 719–22, Göttingen, 1982
- [BRU 83] M. Bruneau, *Introduction aux Théories de l'Acoustique*, Publications de l'Université du Maine, Le Mans, 1983
- [CHU 80] J. Y. Chung, D. A. Blaser, “Transfer function method of measuring induct acoustic properties: I-Theory, II-Experiment”, *J. Acoust. Soc. Am.*, n°68, 907–21, 1980
- [CAU 84] R. Caussé, J. Kergomard, X. Lurton, “Input impedance of brass musical instruments–comparison between experiment and numerical models”, *J. Acoust. Am.*, Janvier, n°75 (1), 241–54, 1984
- [GIB 90] V. Gibiat, F. Laloe, “Acoustical impedance measurements by the Two-Microphone-Three-Calibration (T.M.T.C.) method”, *J. Acoust. Soc. Am.*, n°88, 2533–545, 1990
- [KER 91] J. Kergomard, J. D. Polack, J. Gilbert, “Vitesse de propagation d'une onde plane impulsionnelle dans un tuyau sonore”, *J. Acoustique*, n°4, 467–83, 1991
- [KO 65] W.L. Ko, “Deformation of foamed elastomers”, *J. Cellular Plastics*, 1, 45–50, 1965
- [TAM 90] M. Tamura, “Spatial Fourier transform method of measuring reflection coefficients at oblique incidence. I: Theory and numerical examples”, *J. Acoust. Soc. Amer.*, vol. 88, 2259–64, 1990

This page intentionally left blank



## Chapter 27

# The Nearfield Acoustical Holography Method

The near-field holography method uses the principles of holography: the knowledge of a pressure field on an infinite plane enables us, under certain conditions – that will be described later – to rebuild or understand the backpropagation of the pressure field on another parallel plane [MAY 85]. In our case, measuring the pressure field on two infinite planes and parallel to the surface of the material allows us to deduce the reflection coefficient of the material since the backpropagation of one plane on another depends on this coefficient [TAM 90].

Using a 2D Fourier transform, this method allows us to measure the reflection coefficient of a plane wave, for all angles, and for inhomogenous incidental plane waves. The position of the source, close to the material, allows measurements in open fields for frequencies up to 200 Hz. The high frequency limitation is mainly due to the source [ALL 95].

### 27.1. Principles of the acoustical holography

The acoustic holography consists of replicating the pressure field  $\psi(\vec{r}_D)$  verifying the equation of propagation:

$$\Delta\psi(\vec{r}_D) - \frac{1}{c_0^2} \frac{\partial^2 \psi(\vec{r}_D)}{\partial t^2} = 0, \quad \forall \vec{r}_D \in D, \forall t, \quad [27.1]$$

in a domain  $D$  from the experimental knowledge of the pressure field  $\psi(\vec{r}_S, t)$  on a surface  $S$  circling  $D$  [MAY 85]. The surface  $S$  is theoretically chosen so that the field  $\psi(\vec{r}_S, t)$  is zero or negligible on a part of this surface to avoid boundary effects.

We obtain from the homogenous Helmholtz equation:

$$(\Delta + k_0^2)\psi_\omega(\vec{r}_D) = 0, \quad \text{for } \vec{r}_D \in D, \quad [27.2]$$

where  $k_0 = 2\pi f/c_0$  is the wave number in the air. The domain  $D$  cannot contain any acoustic source. In order to resolve the system, we use the Helmholtz-Huygens radiation integral [BRU 98]. The solution  $\psi_\omega(\vec{r}_D)$  reads:

$$\psi_\omega(\vec{r}_D) = \iint_S \left[ G(\vec{r}_D, \vec{r}_S) \frac{\partial \psi_\omega(\vec{r}_S)}{\partial n_S} - \psi_\omega(\vec{r}_S) \frac{\partial G(\vec{r}_D, \vec{r}_S)}{\partial n_S} \right] dS. \quad [27.3]$$

In this equation,  $\partial/\partial n_S$  indicates that the normal derivative along the outgoing normal to the surface  $S$  and  $G(\vec{r}_D, \vec{r}_S)$  is a Green's function verifying:

$$(\Delta + k^2)G(\vec{r}_D, \vec{r}_o) = -\delta(\vec{r}_D, \vec{r}_o) \quad \text{in } D. \quad [27.4]$$

Choosing a Green's function verifying:

$$G(\vec{r}_D, \vec{r}_o) = 0 \quad \text{for } \vec{r}_o \in S, \quad [27.5]$$

equation [27.3] therefore yields:

$$\psi_\omega(\vec{r}_D) = - \iint_S \psi_\omega(\vec{r}_S) \frac{\partial G(\vec{r}_D, \vec{r}_S)}{\partial n_S} dS. \quad [27.6]$$

This equation provides a way to calculate the pressure at point  $\vec{r}_D \in D$  from the knowledge of the pressure on the surface  $S$ .

## 27.2. Application to plane geometries

A judicious choice of the surface  $S$  permits us to simplify the following equations. The surface  $S$  is represented in Figure 27.1: it is composed of an infinite plane  $P$ , where  $z = z_P$  and a half-sphere  $\mathfrak{R}$ . The radius of the half-sphere tends towards infinity.

For a limited source, it is possible to place the source so that the pressure field on  $\mathfrak{R}$  is zero:

$$\psi(\vec{r}) = 0 \quad \text{for } \vec{r} \in \mathfrak{R}. \quad [27.7]$$

Equation [27.6] therefore becomes:

$$\psi_\omega(\vec{r}_D) = - \iint_P \psi_\omega(\vec{r}_P) \frac{\partial G(\vec{r}_D, \vec{r}_P)}{\partial n_S} dS. \quad [27.8]$$

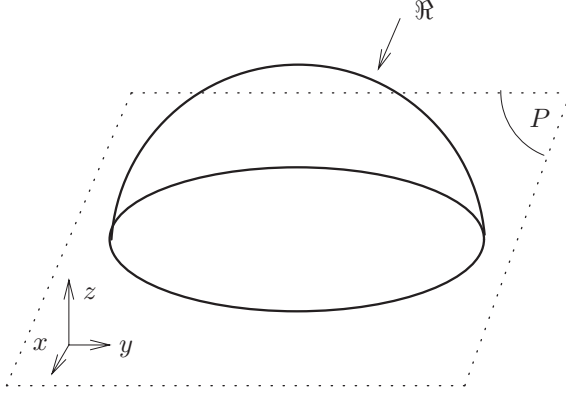


**Figure 27.1.** Surface  $S$  made of an infinite plane  $P$  and a half-sphere  $\mathfrak{R}$ .  
The radius of the half-sphere tends to infinity

The method of images permits the construction of a Green's function, verifying the equation:

$$G(\vec{r}_D, \vec{r}_o) = 0, \quad \text{for } \vec{r}_o \in P. \quad [27.9]$$

Indeed, it is enough to choose:

$$G(\vec{r}_D, \vec{r}_o) = \frac{e^{-jk|\vec{R}|}}{4\pi|\vec{R}|} - \frac{e^{-jk|\vec{R}'|}}{4\pi|\vec{R}'|}, \quad [27.10]$$

with

$$R = |\vec{R}| = \sqrt{(x_D - x_o)^2 + (y_D - y_o)^2 + (z_D - z_o)^2}, \quad [27.11]$$

and

$$R' = |\vec{R}'| = \sqrt{(x_D - x_o)^2 + (y_D - y_o)^2 + (z_D + z_o - 2z_P)^2}. \quad [27.12]$$

Function  $G$  verifies equation [27.4] and vanishes for  $R = R'$ , which is the case for  $z_o = z_P$ . (The Green's function is also zero on the half-sphere  $\mathfrak{R}$  represented in Figure 27.1.) The normal derivative of function  $G$  is:

$$\begin{aligned} \frac{\partial G}{\partial n} \Big|_{z_o=z_P} &= \frac{\partial G}{\partial z_o} \Big|_{z_o=z_P} \\ &= \frac{1}{4\pi} \left[ \frac{\partial R}{\partial z_o} \cdot \frac{\partial}{\partial R} \left( \frac{e^{-jkR}}{R} \right) - \frac{\partial R'}{\partial z_o} \cdot \frac{\partial}{\partial R'} \left( \frac{e^{-jkR'}}{R'} \right) \right] \Big|_{z_o=z_P}. \end{aligned} \quad [27.13]$$

Using the following relationships:

$$\left. \frac{\partial R}{\partial z_o} \right|_{z_o=z_P} = - \left. \frac{(z_D - z_o)}{R} \right|_{z_o=z_P} = - \frac{(z_D - z_P)}{R_P}, \quad [27.14]$$

and

$$\left. \frac{\partial R'}{\partial z_o} \right|_{z_o=z_P} = \frac{(z_D - z_P)}{R_P}, \quad [27.15]$$

with

$$R_P = \sqrt{(x_D - x_o)^2 + (y_D - y_o)^2 + (z_D - z_P)^2}, \quad [27.16]$$

in addition to the following equations:

$$\begin{aligned} \left. \frac{\partial}{\partial R} \left( \frac{e^{-jkR}}{R} \right) \right|_{z_o=z_P} &= \frac{(-jkR - 1)}{R} \cdot \left. \frac{e^{-jkR}}{R} \right|_{z_o=z_P} \\ &= - \frac{(1 + jkR_P)}{R_P^2} e^{-jkR_P}. \end{aligned} \quad [27.17]$$

equation [27.13] becomes:

$$\left. \frac{\partial G}{\partial z_o} \right|_{z_o=z_P} = \frac{2(z_D - z_P)(1 + jkR_P)}{4\pi R_P^3} e^{-jkR_P}. \quad [27.18]$$

We can rewrite this equation in the following form:

$$\left. \frac{\partial G}{\partial z_o} \right|_{z_o=z_P} = -2 \frac{\partial}{\partial \alpha} \left\{ \frac{e^{-jk\sqrt{(x-x_o)^2 + (y-y_o)^2 + \alpha^2}}}{4\pi\sqrt{(x-x_o)^2 + (y-y_o)^2 + \alpha^2}} \right\} \Big|_{\alpha=z_D-z_P}. \quad [27.19]$$

### 27.3. Backpropagation

To simplify the notations, we will write:

$$\left. \frac{\partial G}{\partial z_o} \right|_{z_o=z_P} = G'(x - x_o, y - y_o, z - z_P). \quad [27.20]$$

Equation [27.8] is written as a convolution:

$$\begin{aligned} \psi_\omega(x_D, y_D, z_D) \\ = \iint_{-\infty}^{+\infty} \psi_\omega(x_o, y_o, z_P) G'(x_D - x_o, y_D - y_o, z_D - z_P) dx_o dy_o. \end{aligned} \quad [27.21]$$

Using the convolution theorem and the notation:

$$\widetilde{\psi}_\omega(k_x, k_y, z) = \iint_{-\infty}^{+\infty} \psi_\omega(x, y, z) e^{-j(k_x x + k_y y)} dx dy \quad [27.22]$$

for the 2D Fourier transform, equation [27.8] becomes a simple product of two functions:

$$\widetilde{\psi}_\omega(k_x, k_y, z_D) = \widetilde{\psi}_\omega(k_x, k_y, z_P) \widetilde{G}'(k_x, k_y, z_D - z_P). \quad [27.23]$$

The function  $\widetilde{G}'$  can be explicitly calculated from equation [27.19]:

$$\widetilde{G}'(k_x, k_y, z_D - z_P) = \begin{cases} e^{j\sqrt{k_0^2 - k_x^2 - k_y^2}(z_D - z_P)} & \text{if } k_x^2 + k_y^2 \leq k_0^2, \\ e^{-\sqrt{k_x^2 + k_y^2 - k_0^2}(z_D - z_P)} & \text{otherwise.} \end{cases} \quad [27.24]$$

#### 27.4. Physical interpretation

Equation [27.23] allows us to build a relation between the pressure field on plane  $z = z_P$  and the field of pressure on plane  $z = z_D$  in the Fourier domain, using function  $\widetilde{G}'$ , called the *propagator*. The 2D Fourier transform consists of decomposing the pressure field at an altitude  $z$  into a continuous sum of plane waves:

$$e^{+j(k_x x + k_y y)},$$

with the amplitudes  $\widetilde{\psi}_\omega(k_x, k_y, z)$  respectively, propagating along the  $z$  axis, with the wave vector  $(k_x, k_y, \sqrt{k_0^2 - k_x^2 - k_y^2})$ . Two separate cases arise:

- if  $k_x^2 + k_y^2 \leq k_0^2$ , the backpropagation of the plane wave is only a phase shift,
- if  $k_x^2 + k_y^2 > k_0^2$ , the amplitude of the plane wave decreases (or increases) exponentially, in the direction  $0z$ .

We have propagative waves in the first case and evanescent waves in the second case.

Experimentally, holography consists of measuring the pressure on a plane  $P$ , then calculating the spatial 2D Fourier transform, backpropagating it to a plane  $P'$  generally closer to the source and then evaluating the inverse Fourier transform. The main problem is usually met with the evanescent backpropagated waves; because when the acoustic level measured for the evanescent waves is very low (far from the source), backpropagation exponentially increases the noise.

#### 27.5. Principle of the experience developed by Tamura

The open field measurement of the reflection coefficient for an oblique incidence can be carried out in various ways [ALL 85, ALL 89, HU 90, HU 94, ING 51].

In 1980, Frisk *et al.* [FRI 80], who were interested in measuring the reflection of plane waves at the bottom of the oceans proposed a method using the 2D Fourier transform. The source-receiver configuration allowed them to temporally separate the incident wave from the wave reflected on the bottom of the ocean, so that the reflection coefficient is directly accessible, knowing all the parameters of the source and the pressure measured on a plane parallel to the surface.

In 1990, Tamura presented a new method of measurement [TAM 90] where knowledge of the properties of the source is not necessary. This method consists of measuring the pressure field on two planes, parallel and close to the surface of the material, then, using the Fourier transform, isolating the incident plane wave from the reflected plane wave, and therefore calculating the reflection coefficient of the material.

## 27.6. Hypothesis

A scheme of the experiment is represented in Figure 27.2. The material located in  $z = 0$  is supposed to be infinite and plane. A point-like source is placed at  $z = z_s$  on the  $0z$  axis. The acoustic field radiated by this source is supposed to have a cylindrical symmetry along the  $0z$  axis. If the material being studied is homogenous and has the

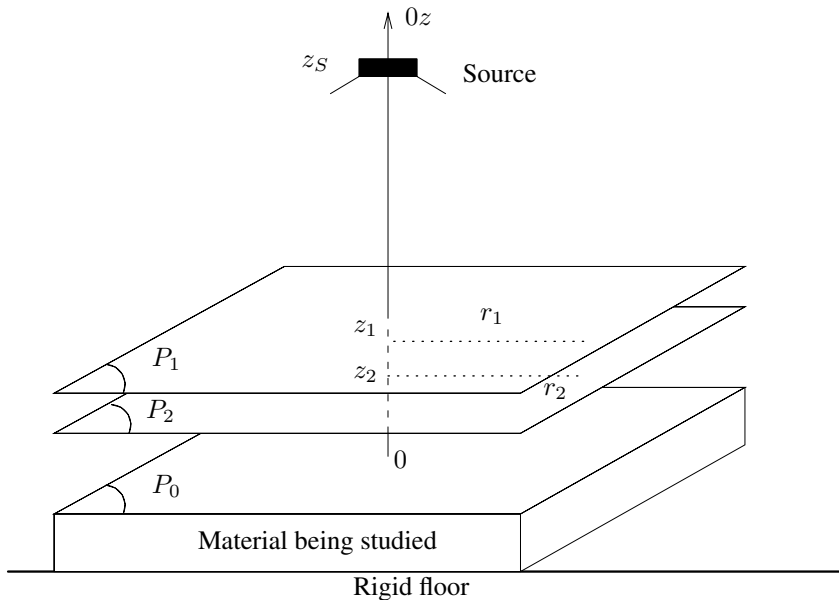


**Figure 27.2.** Description of the Tamura experiment. The two parallel planes  $P_1(z = z_1)$  and  $P_2(z = z_2)$  located above the material are represented. The acoustic source is positioned at  $z = z_s$  on the  $0z$  axis

same properties in all directions parallel to the plane  $z = 0$  (i.e. planar isotropy), the reflected field therefore also has a cylindrical symmetry along the  $z$ -axis. To determine the pressure on the planes  $P_1$  and  $P_2$ , one has only to measure the pressure on two radii  $r_1$  and  $r_2$ . Using the cylindrical coordinates  $(r, z)$ , it is easy to show (see Appendix 27.9) that the 2D Fourier transform can be written:

$$p(k, z) = \int_0^\infty p(r, z) J_0(kr) r dr, \quad [27.25]$$

where  $J_0$  is the Bessel function of the first kind of order 0. Equation [27.25] is also called the Fourier-Bessel transform or Hankel transform. The inverse transform reads:

$$p(r, z) = \int_0^\infty p(k, z) J_0(kr) k dk. \quad [27.26]$$

### 27.7. Theory

Suppose that a monopole source is located in  $z = z_s$ , the incident field emitted by the source with the pulsation  $\omega$  can be written, using the Sommerfeld integral [SOM 49],

$$p^i(r, z) = \frac{e^{-jk_0 R}}{R} = \int_0^\infty \frac{k}{jk_z} e^{-jk_z |z - z_s|} J_0(kr) dk, \quad [27.27]$$

where  $R$  is given by:

$$R = \sqrt{r^2 + (z - z_s)^2}. \quad [27.28]$$

The wavenumbers  $k$ ,  $k_z$  and  $k_0$  are related to each other via the dispersion relation:

$$\frac{\omega^2}{c_0^2} = k_0^2 = k_z^2 + k^2. \quad [27.29]$$

Equation [27.27] represents the decomposition of the incident field into a continuous sum of plane waves. From this equation, it is easy to determine the field reflected on the material and also the total field measured. For the dispersion relation, there are two cases:

$$k_z = \sqrt{k_0^2 - k^2} \quad \text{for } 0 \leq k \leq k_0, \quad [27.30]$$

$$k_z = -j\sqrt{k^2 - k_0^2} \quad \text{for } k > k_0. \quad [27.31]$$

In the first case, described by equation [27.30], the term  $e^{jk_z |z - z_s|}$  can be associated to an homogenous, incident plane wave, for the angle of incidence  $\theta$  given by:

$$\theta = \arctan\left(\frac{k}{k_z}\right). \quad [27.32]$$

This angle is real and its values are between  $0^\circ$  and  $90^\circ$ . A reflected plane wave corresponds to this incident plane wave. This wave is reflected with the same angle  $\theta$  and a reflection coefficient written  $R(\theta) = R(k)$ , depending only on the material being studied.

In equation [27.31], the number  $k_z$  is a pure imaginary number. The incident waves are now inhomogenous, they propagate along the direction  $r$  and are attenuated along the  $0z$  axis. The sign of equation [27.31] can be used to ensure correct radiation conditions of the source towards infinity. The angle of incidence given by equation [27.32] is now a complex number, it can be written as  $\theta = \pi/2 + j\alpha$  where  $\alpha$  is a real number. With these inhomogenous incident plane waves are associated with inhomogenous reflected plane waves with the same angle  $\theta$  and with the reflection coefficient  $R(\theta) = R(k)$ .

The reflected pressure field can therefore be written as:

$$p^r(r, z) = \int_0^\infty \frac{k}{jk_z} e^{+jk_z|z+z_s|} R(k) J_0(kr) dk, \quad [27.33]$$

and the total field measured at  $z_1 < z_s$  is:

$$\begin{aligned} p(r, z_1) &= p^i(r, z_1) + p^r(r, z_1) \\ &= \int_0^\infty \frac{e^{+jk_z z_s}}{jk_z} [e^{-jk_z z_1} + R(k)e^{+jk_z z_1}] J_0(kr) k dk. \end{aligned} \quad [27.34]$$

Using an inverse Hankel transform, equation [27.34] becomes:

$$\frac{e^{+jk_z z_s}}{jk_z} [e^{-jk_z z_1} + R(k)e^{+jk_z z_1}] = \int_0^\infty p(r, z_1) J_0(kr) r dr. \quad [27.35]$$

The following notation:

$$I_{z_1} = \int_0^\infty p(r, z_1) J_0(kr) r dr = p(k, z_1), \quad [27.36]$$

corresponds to the Hankel transform of the total pressure, measured the altitude  $z_1$ . Measuring the pressure for two different altitudes  $z_1$  and  $z_2$ , the reflection coefficient can be calculated using the formula:

$$\frac{e^{-jk_z z_1} + R(k)e^{+jk_z z_1}}{e^{-jk_z z_2} + R(k)e^{+jk_z z_2}} = \frac{I_{z_1}}{I_{z_2}}, \quad [27.37]$$

or

$$R(k) = \frac{e^{-jk_z z_1} I_{z_2} - e^{-jk_z z_2} I_{z_1}}{e^{+jk_z z_2} I_{z_1} - e^{+jk_z z_1} I_{z_2}}. \quad [27.38]$$



The function defined by equation [27.37] represents the propagator, it connects the pressure at  $z = z_1$  to the pressure at  $z = z_2$  and depends on the reflection coefficient of the material. The terms  $e^{\pm jk_z z}$  correspond either to a phase shift if  $k_z$  is real, or an exponential decrease if  $k_z$  is purely imaginary (see section 27.4).

## 27.8. Some remarks

The previous calculation can be generalized to all sources having a cylindrical symmetry around the  $z$ -axis. Indeed, in the case of an arbitrary source having an axial symmetry, the incident field can be written as:

$$p^i(r, z) = \int_0^\infty A(k) \frac{k}{jk_z} e^{-jk_z |z - z_s|} J_0(kr) dk, \quad [27.39]$$

where  $A(k)$  is a function that depends on the nature of the source and balances each plane wave. In the case of a monopole source,

$$A(k) = 1 \quad \forall k \in [0, +\infty[, \quad [27.40]$$

and, in the case of a dipole source along the  $z$ -axis ,

$$A(k) = jk_z. \quad [27.41]$$

The reflection coefficient is always given by equation [27.38] because the function  $A(k)$  disappears in the equations.

In the case of a source that does not have a cylindrical symmetry around the  $z$ -axis, calculations presented by Hu [HU 92] can be made using cylindrical coordinates  $(r, \phi, z)$  in the same way. The reflection coefficient therefore depends on the considered incident plane, but the measurement procedure remains unchanged: the acoustic pressure is measured for two altitudes  $z_1$  and  $z_2$ , a 2D spatial Fourier transform ensures the decomposition of the field into plane waves, finally the reflection coefficient is given by equation [27.38].

Experimentally, several problems concerning the assessment of the Hankel transforms may arise: first the pressure field is measured only for some discrete values of the variable  $r$ ; and second, it is not possible to assess the pressure field beyond a certain radial distance which will be noted  $R_{\max}$ . The integral  $I_{z_1}$  therefore becomes a finite and discrete sum.

In order to limit the error made when evaluating the reflection coefficient  $R$ , the field radiated by the source should decrease as soon as possible when the distance between the source and the sensor increases, or  $R_{\max}$  must be as large as possible [ALL 95].

### 27.9. Appendix A: 2D Fourier transform in cylindrical coordinates

The 2D transform of a function  $f(r)$  can be written (see equation [27.22]):

$$\tilde{f}(k_x, k_y) = \iint_{-\infty}^{+\infty} f(r) e^{-j(k_x x + k_y y)} dx dy.$$

Writing:

$$\begin{aligned} x &= r \cos \theta & y &= r \sin \theta \\ \text{and} \quad k_x &= \kappa \cos \chi & k_y &= \kappa \sin \chi, \end{aligned}$$

we obtain:

$$\tilde{f}(k_x, k_y) = \int_0^\infty \int_0^{2\pi} f(r) e^{-j\kappa r \cos(\theta - \chi)} r dr d\theta,$$

then, writing  $\theta - \chi = \frac{\pi}{2} + \varphi$ , the equation above becomes:

$$\tilde{f}(k_x, k_y) = \int_0^\infty \int_0^{2\pi} f(r) e^{j\kappa r \sin \varphi} r dr d\varphi,$$

which, according to the definition of the Bessel function of the first kind of order 0, is equal to:

$$\tilde{f}(\kappa) = \int_0^\infty f(r) J_0(\kappa r) r dr.$$

### 27.10. Bibliography

- [ALL 85] ALLARD J. and SIEBEN B., “Measurements of acoustic impedance in a free field with two microphones and a spectrum analyser”, *J. Acoust. Soc. Amer.*, vol. 77, pp. 1617–18, 1985.
- [ALL 89] ALLARD J. and CHAMPOUX Y., “In situ free field measurements of the surface acoustic impedance of materials”, *Noise Control Eng. J.*, vol. 32, pp. 15–23, 1989.
- [ALL 95] ALLARD J., LAFARGE D. and TAMURA M., “Spatial Fourier transform method of measuring reflection coefficients at oblique incidence: Part I. Experimental results”, *J. Acoust. Soc. Amer.*, vol. 97, pp. 2255–62, 1995.
- [BRU 98] BRUNEAU M., *Manuel d’acoustique fondamentale*, Hermes, 1998.
- [FRI 80] FRISK G.V., OPPENHEIM A.V. and MARTINEZ D.R., “A technique of measuring the plane wave reflection coefficient of the ocean bottom”, *J. Acoust. Soc. Amer.*, vol. 68, pp. 602–12, 1980.
- [HU 90] HU Z. and BOLTON J.S., “The measurement of plane-wave reflection coefficients by using two-dimensional spatial transforms”, *J. Acoust. Soc. Amer.*, vol. 88, p. S173, 1990.

- [HU 92] HU Z., Measurement and prediction of sound propagation over an absorbing plane, PhD Thesis, Purdue University, 1992.
- [HU 94] HU Z. and BOLTON J.S., "Sound propagation from an arbitrarily oriented multi-pole placed near a plane, finite impedance surface", *J. Sound Vib.*, vol. 170, pp. 637–69, 1994.
- [ING 51] INGARD K.U. and BOLT R.H., "A free-field method of measuring the absorption coefficient of acoustic materials", *J. Acoust. Soc. Amer.*, vol. 23, pp. 509–16, 1951.
- [MAY 85] MAYNARD J.D., WILLIAMS E.G. and LEE Y., "Nearfield acoustical holography: Part I. Theory of generalized holography and the development of NAH", *J. Acoust. Soc. Amer.*, vol. 78, pp. 1395–413, 1985.
- [SOM 49] SOMMERFELD A., *Partial Differential Equations in Physics*, Academic Press, New York, 1949.
- [TAM 90] TAMURA M., "Spatial Fourier transform method of measuring reflection coefficients at oblique incidence. I: Theory and numerical examples", *J. Acoust. Soc. Amer.*, vol. 88, pp. 2259–64, 1990.

This page intentionally left blank

## Chapter 28

# Prediction of Acoustic Properties of Multilayer Structures – Some Examples of Applications

### 28.1. Introduction

The absorption properties of porous media can be used in various ways, including increasing the insulating power of a system. Several configurations will be described in this text. The illustrative curves are simulations obtained with the transfer–matrix method (Chapter 10).

#### 28.1.1. *Absorption*

The aim is to reduce the level of the acoustic wave reflected on a reflective wall. Applications are for example: road walls to attenuate traffic, noise correction of the reverberation time of a room, sound level decreasing in a cavity (a vehicle, a workshop, a tunnel).

##### 28.1.1.1. *Concept of rigid wall*

The absorbing material is usually set against a wall said to be “rigid”, which is an impervious surface (non-porous), stays non-deformable and at rest (the displacement of any point of the wall is zero). If we consider that a 200 mm wall of concrete is a rigid wall, can we consider that this may be also the case for a 7–10 mm steel plate or 13 mm plasterboard? This will not be verified for low

frequencies because of the low inertia of these walls, and probably not around the resonance frequencies of the absorbing material.

Figure 28.1 illustrates the differences between a rigid wall and a steel wall 7–10 mm thick in the case of a three-layer material (porous medium + septum + porous medium, as a mass–spring system (pronounced resonance) covered with a porous layer (high frequency absorption). At low frequencies, the absorption coefficient is higher than in the case of the steel wall. This wall is not quite reflective (inertia too low) so that a part of the incident energy is transmitted through the wall. The resonance frequency is also affected. At high frequencies, there is no difference.

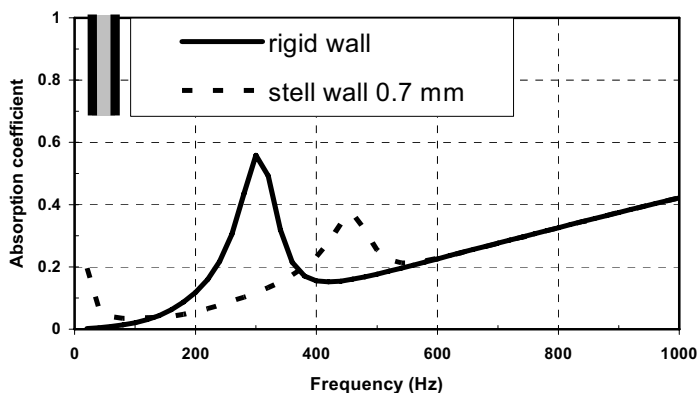


**Figure 28.1.** Influence of the support wall on the absorption coefficient of a multilayer (porous material 1: thickness = 20 mm, resistivity =  $50 \text{ kNsm}^{-4}$ ; septum: surface mass =  $6 \text{ kg/m}$ ; porous material 2: thickness = 12.5 mm, resistivity =  $33 \text{ kNsm}^{-4}$ , Young's modulus = 200 kPa)

#### 28.1.1.2. Porous materials fixed on a rigid skeleton

The absorption coefficient depends mainly on the thickness, frequency and air flow resistivity (Figures 28.2 and 28.3). The absorption becomes significant with a thickness from  $1/10$  to  $1/20$  of the wavelength in air. The optimum thickness corresponds to  $1/4$  for the wavelength in the porous medium. The maximum speed of sound is obtained at this distance from the wall: viscous dissipation is then at a maximum. The latter is primarily a function of the air flow resistivity. Porosity, usually between 0.9 and 0.99, has a small influence (Figure 28.4). Efficiency is improved at low frequencies by reducing the characteristic length or by increasing the tortuosity (Figures 28.5 and 28.6).

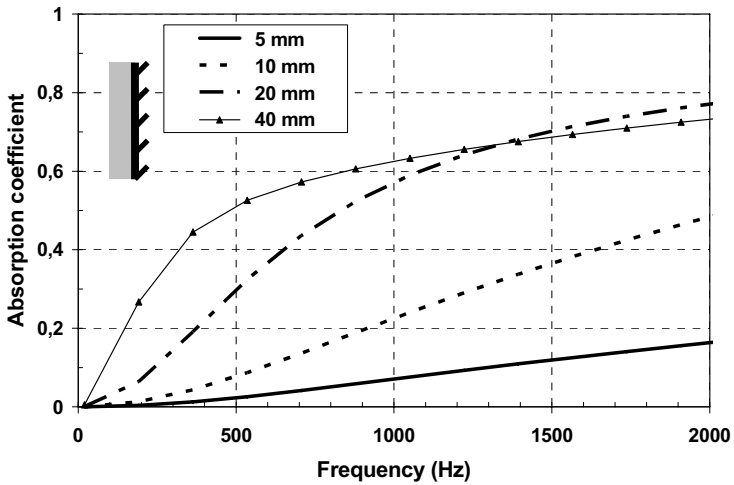


Figure 28.2. Absorption of a porous material fixed on a solid skeleton for different thicknesses (resistivity =  $50 \text{ kNsm}^{-4}$ )

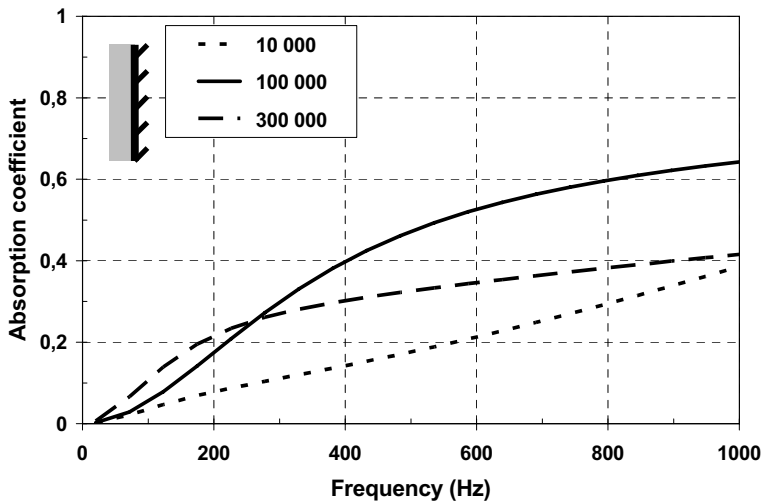
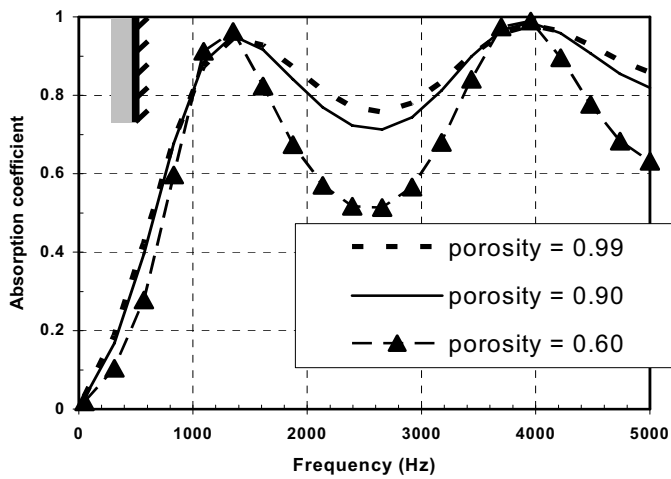
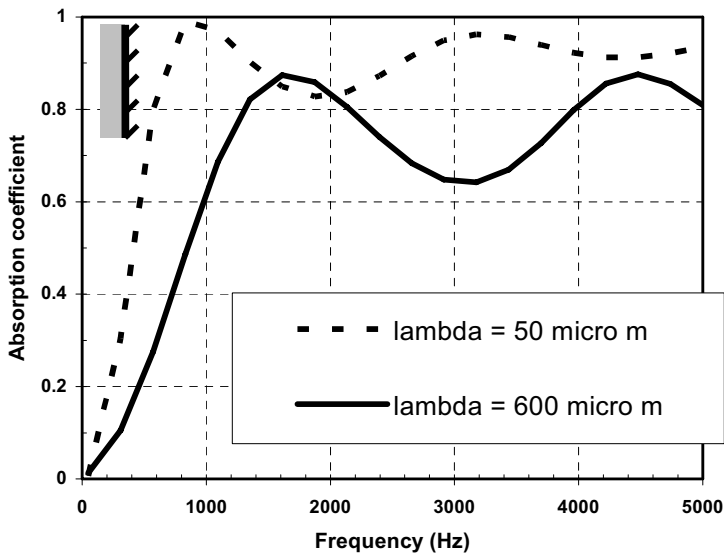


Figure 28.3. Absorption of a porous material fixed on a solid skeleton for different values of the resistivity in  $\text{Nsm}^{-4}$  ( $\text{Th.} = 30 \text{ mm}$ ) ([DEB 00])



**Figure 28.4.** Absorption of a porous material fixed on a solid skeleton for different porosities (thickness of the porous material = 50 mm, resistivity = 7 000 Nsm<sup>-4</sup>)



**Figure 28.5.** Absorption of a porous material fixed on a solid skeleton for different characteristic lengths (thickness of the porous material = 50 mm, resistivity = 7 000 Nsm<sup>-4</sup>,  $\Lambda' = 3 \Lambda$ )



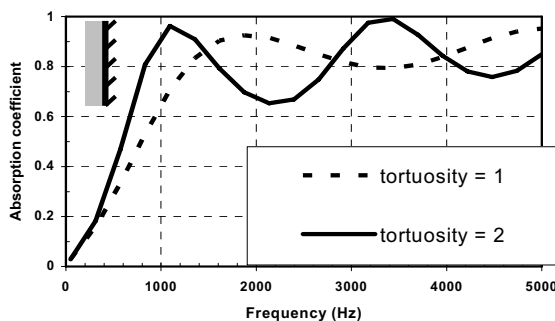


**Figure 28.6.** Absorption of a porous material fixed on a solid skeleton for different tortuosities (thickness of the porous material = 50 mm, resistivity =  $7\,000\text{ Nsm}^{-4}$ )

#### 28.1.1.3. Porous material fixed on a solid skeleton with an air space

An air layer is placed between the porous material and the solid skeleton. It allows the material to be put farther away from the wall, on which the acoustic velocity is zero. It promotes absorption at low frequencies, and degrades only slightly in the medium frequency range (Figure 28.7).

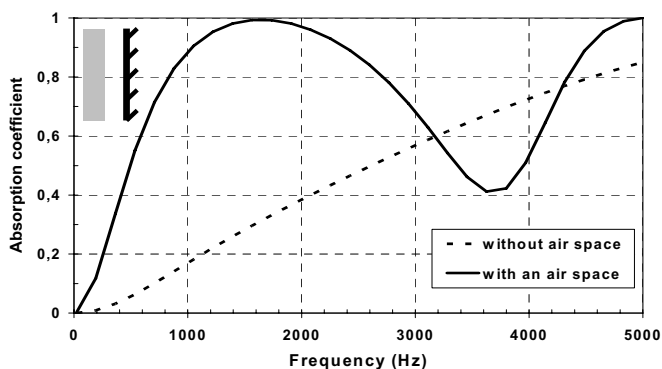


**Figure 28.7.** Absorption of a porous material fixed on a solid skeleton: influence of an air layer (resistivity =  $50\,000\text{ Nsm}^{-4}$ , porous medium thickness = 10 mm; air layer thickness = 40 mm)

#### 28.1.1.4. Inhomogenous absorbing materials

An inhomogenous absorbing material is a juxtaposition of porous elements with a finite dimension, separated by air zones [MEC 89] and [SGA 00]. This setup has several interests in the configurations that have been achieved (Figure 28.8):

– Increased absorption in oblique incidence: the effective surface of the material appears to be greater than the incident wave.

– Impedance adaptation, while increasing the density of the material (case b): this avoids the reflection of acoustic waves on the surface of the material. This is the case for wedges in anechoic rooms, or materials with a relief pattern.

– Creation of cavities to obtain a Helmholtz resonator, or back air space (case c): it can increase the absorption in the low frequency range, by resonance effect.

– Creating an inhomogeneous environment, randomly dividing the two kinds of media (case d): the three phenomena described before can be statistically associated.

The trends are given for a 5.75 cm thick rockwool (Figure 28.9).

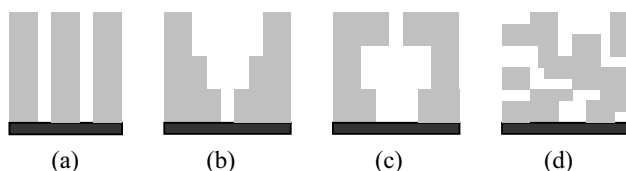


**Figure 28.8.** Porous material with a pattern: (a) spaced paving; (b) progressive augmentation of the material density; (c) cavity formation (Helmholtz resonator effect); (d) statistic repartition

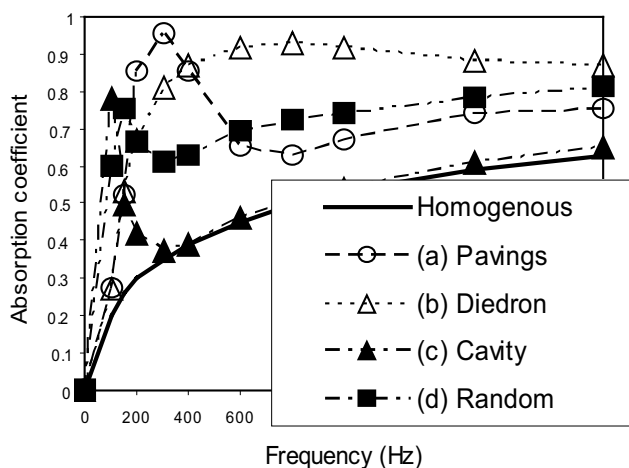


**Figure 28.9.** Absorption coefficient with a porous patterned structure in a diffuse field (Sgard et al., 2000)

#### 28.1.1.5. *Porous material fixed on a solid skeleton, with a surface coating*

Coating is used to cover or to protect the porous layer. This can improve absorption at low frequencies, often with a deterioration at high frequencies:

- Resistive film: this is a porous, low thickness structure with high resistivity (fabric, glass veil), but still porous. Placed on the surface of the structure, where the sound speed is a maximum, the resistive film improves the absorption, especially at low frequencies (Figure 28.10). At high frequencies, if the film is too resistive, a slight deterioration is observed. If the film is less resistive than the layer of porous material, it has no effect.

- Perforated plate: this is a solution used to protect the porous material from impacts (in workshop, sports room). Above a perforation rate of 30%, this coating has little effect. For low perforation rates, the structure can benefit from an improved absorption at low frequencies, often with deterioration at high frequencies, as for a too resistive film (Figure 28.10).

- Impermeable film: this is a thin, impervious layer (from 0.01 mm for a film to a few mm for a septum), often used to protect the porous material from dust and liquid, or to improve performance at low frequencies. The impermeability is defined in comparison with the resistivity of the film, which should tend to infinity. This is the case if the film is not porous. It is modeled by a layer of solid material. The film has two effects (Figure 28.11): an inertial effect, which increases with the frequency, resulting in a degradation of the high frequency absorption, and where the film is fixed on the porous material (there is no air space), and a piston effect, which stimulates the whole material in compression, promoting viscoelastic losses in the skeleton. There is thus an improvement in low-frequency absorption, with deterioration at high frequencies (impedance discontinuity related to the inertia of the film).

- Septum: this is an impermeable layer of large surfacic mass in order to obtain a “spring-mass” system: the resonance frequency depends on the film surfacic mass and on the stiffness of the skeleton. Absorption is a maximum at the resonance of the system, and then it decreases quickly due to the inertia of the septum. To limit the degradation at high frequencies, it is possible to add a low thickness porous layer (Figure 28.12).

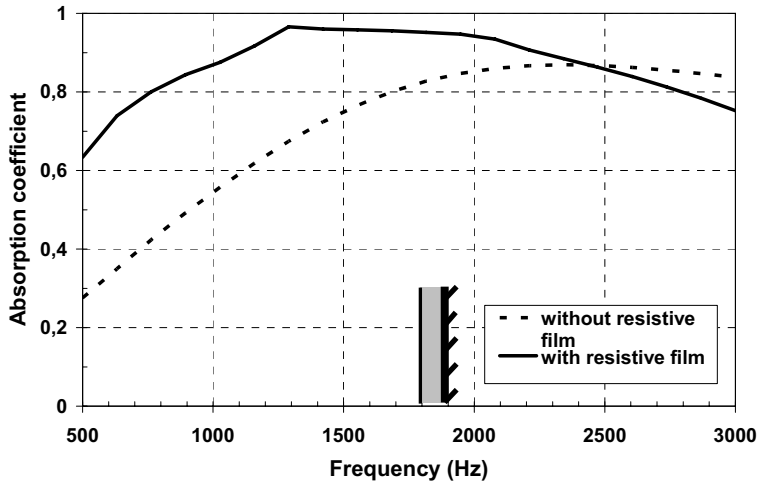


**Figure 28.10.** Porous material with or without resistive film ([ALL 93])  
 (porous material: thickness= 3.8 cm, resistivity =  $5000 \text{ Nsm}^{-4}$ ;  
 resistive film: thickness= 0.45 mm, resistivity=  $1.1 \text{ MNsm}^{-4}$ )

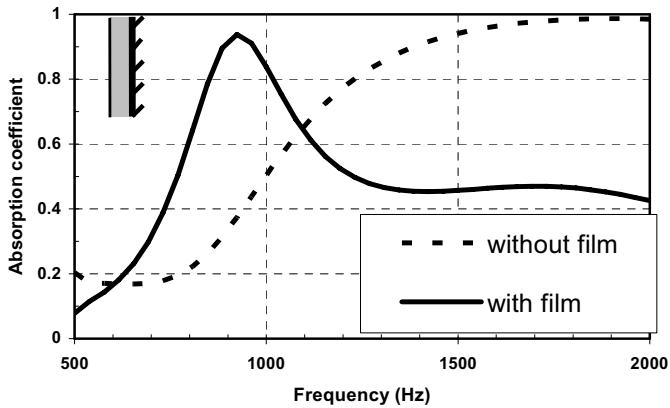


**Figure 28.11.** Porous material with or without non-permeable (porous material: thickness = 21 mm, resistivity=  $70 \text{ kNsm}^{-4}$ , Young's modulus= 50 kPa; film: surfacic mass=  $0.1 \text{ kg/m}^2$ )

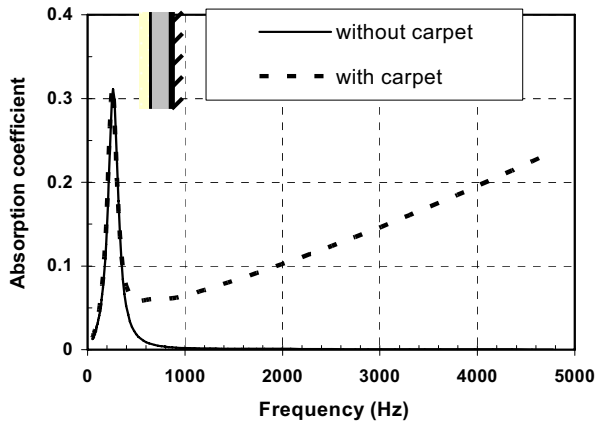


**Figure 28.12.** Porous material with septum and carpet ([BRO 94-b]) (porous material: thickness = 12.5 mm, resistivity =  $33\,000\text{ Nsm}^{-4}$ , Young's modulus = 25 kPa; septum: surfacic mass =  $6\text{ kg/m}^2$ ; carpet: thickness = 7 mm, resistivity =  $20\text{ kNsm}^{-4}$ )

### 28.1.2. Insulation

The purpose of the insulation is to reduce the level of the acoustic wave transmitted through a wall. The porous material is used in combination with one or more reflective layers because it is inefficient if used alone. Figure 28.13 describes a decreasing index that is no more than 14 dB at 10 kHz for 20 mm of quite resistive porous material.

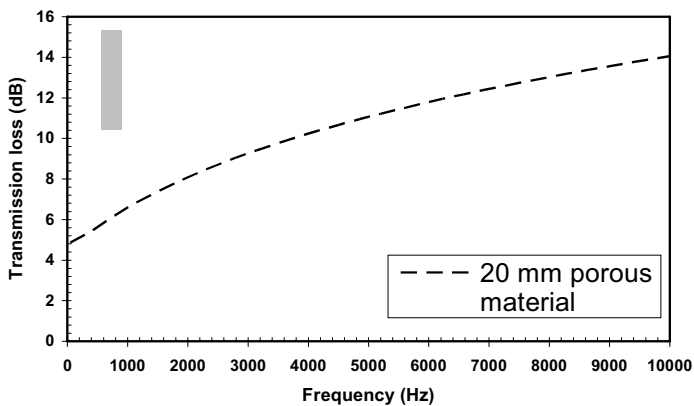


**Figure 28.13.** Transmission loss of a porous layer, 20 mm thick (resistivity =  $50\,000\text{ Nsm}^{-4}$ )

### 28.1.2.1. Double wall separated by a porous material

The system consisting of two walls separated by an air space allows a decoupling above the resonance frequency given by

$$f = \frac{1}{2\pi} \sqrt{\frac{\gamma P_0}{d} \frac{m_1 + m_2}{m_1 m_2}},$$

where  $d$  is the thickness of the air layer,  $\gamma P_0$  the adiabatic compression modulus of air, and  $m_1$  and  $m_2$  the surfacic masses of the two walls.

One of the limitations of this system is the acoustic resonance of the air layer.

The frequency of acoustic modes, indexed  $n$ , is given by  $f_n = nc/2l$ , where  $c$  is the speed of sound and  $l$  the air layer thickness. If the air space is partially filled with a porous material, these resonances are damped, and this increases the overall insulation (Figure 28.14). The air layer should not be completely filled with the porous material, because the transmission via the skeleton might be facilitated, since its Young's modulus is not negligible, compared with the compression modulus of air (addition of spring-constants in parallel) [DOU 07], [DOU 09]. Note that the porous layer may also add significant damping to the wall in contact with it as a viscoelastic layer [DAU 03].

### 28.1.2.2. Spring mass system

The porous material is used as a low rate spring in combination with an impermeable, dense and damped layer (very high critical frequency) (Figure 28.15). This system is efficient above the resonant frequency of the mass–spring system.

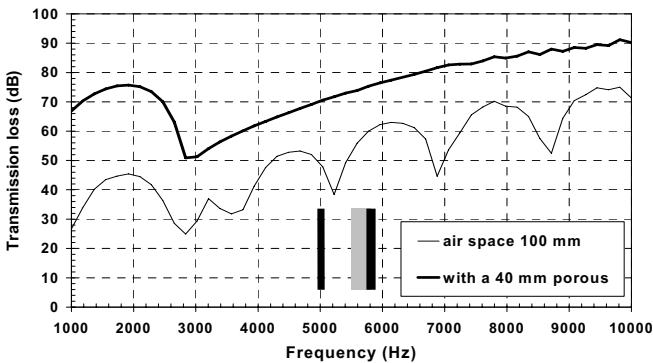


**Figure 28.14.** Double wall: effect of an absorbing material (two 13 mm plasterboards separated by 100 mm)

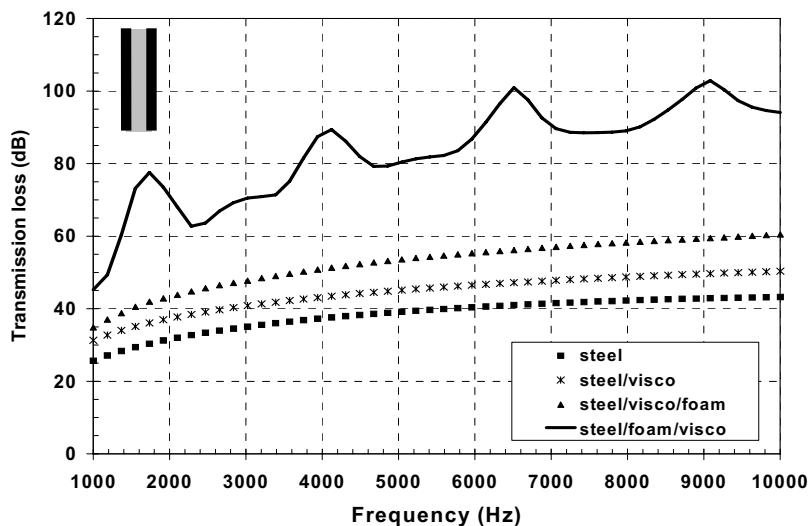


**Figure 28.15.** *Insulation using a spring mass system (continuous line:  
0.7 mm steel wall + 20 mm foam  $E = 40\text{kPa}$  + 2 mm of asphalt)*

## 28.2. Bibliography

- [ALL 93] J.-F. Allard, *Propagation of Sound in Porous Media: Modeling Sound Absorbing Materials*, Chapman & Hall, London, 1993
- [BRO 94] B. Brouard, D. Lafarge, J. F. Allard, "Measurement and prediction of the surface impedance of a resonant sound absorbing structure", *Acta Acustica*, n°2, 301–6, 1994
- [BRO 94-b] B. Brouard, Validation par holographie acoustique de nouveaux modèles pour la propagation des ondes dans les matériaux poreux stratifiés, Thesis, University Maine, 1994
- [DEB 00] A. Debray, Contribution to the study of dissipative silencers: effect of structural vibrations – effect of flow, Thesis, University of Maine, 2000
- [DAU03] N. Dauchez, S. Sahraoui, N. Atalla, "Investigation and modelling of damping in a plate with a bonded porous layer", *J. Sound Vib.*, 265(2), 437–449, 2003
- [DOU07] O. Doutres, N. Dauchez, J.-M. Génevaux, O. Dazel, "Validity of the limp model for porous materials: A criterion based on the Biot theory", *J. Acoust. Soc. Am.*, 122(4), 1845–2476, 2007
- [DOU09] O. Doutres, N. Dauchez, J.-M. Génevaux, O. Dazel, "A frequency independent criterion for describing sound absorbing materials by a limp frame model", *Acta Acustica-Acustica*, 95, 178–181, 2009

[MEC 89] F.P. Mechel, “Iterative solutions for finite-size absorbers”, *Journal of Sound and Vibration*, Vol. 134(3), 489–506, 1989

[SGA 00] F. Sgard, N. Atalla, X. Olny, R. Panneton, “Acoustic absorption of heterogeneous porous materials”, *Internoise 2000*, Nice, 2000



Part 8

## Biomedical Field

This page intentionally left blank

## Chapter 29

# Ultrasonic Characterization of the Bone

### 29.1. Introduction

#### 29.1.1. *In-vitro determination of acoustical and elastic properties*

##### 29.1.1.1. *Introduction*

Knowledge of the mechanical behavior of the bone and the laws that govern this behavior are necessary to characterize the risks of bone fracture, the interface bone–implant, and to establish databases of materials for numerical simulations by the finite element method. The mechanical properties of osseous tissue have been studied for several decades but many questions are still unanswered. It shows the complexity of this biological solid material in its characterization and understanding, and the necessity to continue the researches, as public health remains at stake.

*In vitro*, measurements are intended for the characterization of elastic properties of the bone and can be seen as an alternative to conventional mechanical tests. Unmistakably, the choice of acoustical techniques presents some advantages such as the non-destructive property (avoiding damaging of the material during the test), the possibility of determining elastic properties in the different crystallographic axes of the sample, and the possibility of making a characterization at different scales as a function of the chosen frequency. Some ultrasonic techniques can also be implemented *in vivo* with patients. In this case, measurements reflect the osseous fragility and are useful in determining the risk of fracture for patients suffering from osteoporosis.

The bone is a biological, therefore living, material. First, a short description, from the biological point of view, will be made of the structure and the function of the bone. Then, depending on the type of structure (spongy or cortical bone), some assumptions on the medium will be made in order to use appropriate theory and experiments. The principles of measurements of the acoustical and elastic properties will be illustrated.

The human skeleton has the function of maintaining the human body. It also has another function: the protection of our organs. It is organized according to structural and functional levels whose hierarchy can be described in the following way:

- chemical level;
- cellular level;
- tissue level;
- organ level: bone;
- level of the organ system: skeletal system.

At the chemical level, one third of the osseous material is water, the rest being composed of organic and inorganic (mineral) components. The organic component is called collagen matrix and represents 90 to 95% of the total composition. It is in the form of long, very orientated fibers. These collagen fibers contain a bundle of fibrils and act as a matrix for the deposit of osseous crystals. The inorganic or mineral component is made of apatite crystals whose shortened and molecular formulae are OHAp (hydroxyapatite) and  $\text{Ca}_{10}(\text{PO}_4)_6(\text{OH})_2$ , respectively.

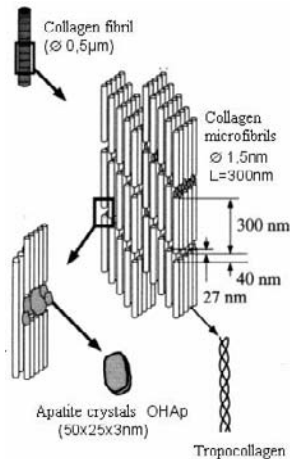


**Figure 29.1.** Organic and inorganic components of the bone

At the cellular level, the cellular elements are represented by three cells: the osteocyte, the osteoblast and the osteoclast. The osteocyte is an ellipsoidal cell, which, through many intra-canalliculi extensions, ensures the passing of the interstitial liquids of the Haver capillaries towards the osseous substance. They generate an activity of osseous resorption and an activity of apposition of new bone at the periosteum. The osteoblast is a mononuclear cell (20  $\mu\text{m}$  to 30  $\mu\text{m}$  of diameter). Its main function is to develop the protein weft (collagen fibers) in the process of ossification. The osteoclast is a polynuclear cell of variable shape (20  $\mu\text{m}$  to 100  $\mu\text{m}$  of diameter); it is an active agent of osseous resorption, especially of the calcified bone, but also of the osteoid tissue (not yet calcified). It takes part in renewal of the bone.

At the tissue level, the bone is a porous, anisotropic and heterogenous medium. It is made of an elastic solid weft (the osseous tissue) saturated by a viscoelastic fluid medium (marrow, blood) and it can take two very different shapes: cortical bone (compact) and spongy bone (trabecular).

Cortical bone is located at the periphery of all the bones and constitutes most of the diaphysis (central part) of the long bones. At the millimeter-scale, human cortical bone is in the form of a dense solid medium. An observation at the scale of the hundreds of microns reveals an architecture organized around a structuring basic element, the osteon. The osteon is a long tight cylinder, whose length is about 10 mm and diameter between around 100 and 300  $\mu\text{m}$ . At the center of each osteon, a so-called “Havers” canal can be found, where vessels and nerves circulate. The diameter of these Havers canals is around 50  $\mu\text{m}$ . The diaphysis of long bones results from a compact assembly of osteons directed along the bone axis. Between the osteons, we can find the interstitial tissue. An observation at the micro scale reveals the structure of the osteons, made of a set of concentric lamellas of osseous matrix of thickness around 5  $\mu\text{m}$  and centered on the Havers canal. Between the concentric lamellas, some cavities can be found, where the osteocytes (osteocytes lacunae) of diameter around 10 to 20  $\mu\text{m}$  are located, interconnected by thick canaliculi. At a submicron-scale, the osseous lamellas are made of an assembly of mineral crystals of hydroxyapatite on an organic matrix. The porosity of the cortical bone remains low (less than 15%, typically around several %).

The very porous spongy or trabecular bone (porosity >70%) is made of a network of thin osseous filaments (osseous spans, trabeculae) and of cavities filled by marrow (porous aspect). The spans, of thickness around 100–150  $\mu\text{m}$ , have the shape of plates or small columns which cross each other and are connected with each other. The average distance between two adjacent spans (distance compared to the dimension of the “pores”) is around 500  $\mu\text{m}$  to 2 mm. Spongy bone fills all the plane bones and the extremities of long bones (epiphysis) (Figure 29.2).

### 29.1.1.2. Theoretical considerations

Biomechanics of the biological tissues is based on the classical mechanics of solid and fluid media. To apply the laws of physical mechanics, we made the assumption of continuous medium to describe the macroscopic behavior of these tissues. This is equivalent to defining an elementary bulk, presenting physical properties similar to those observed macroscopically on a sample of finite dimensions. This elementary bulk must be large with respect to the elements of the microstructure, and small with respect to the studied homogenous bulk. However, these conditions are not always easy to fulfill for biological tissues, because of the multiplicity of hierarchical microstructures, more or less organized. However, it is very useful to use this assumption of continuous medium to describe the macroscopic mechanical behavior of these tissues. Thus, as far as possible, it will be important to verify this basic assumption in order to validate experimental measurements. From a practical point of view, some morphologic analyses are generally used.

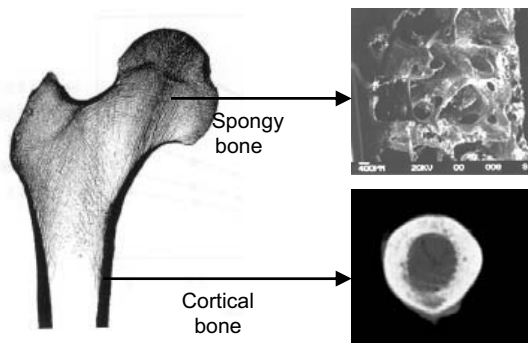


**Figure 29.2.** *Different osseous cortical and spongy tissues constituting the bone*

The first ultrasonic tests were achieved by Yoon and Katz in 1976 [YOO 76] and Ashman in 1984 [ASH 84]. These authors have made the assumption of an elastic anisotropic behavior of the cortical bone. Only the ultrasonic technique allows the determination of the elastic coefficients, and consequently the elastic moduli of an anisotropic material. In fact, the measurements of all the stiffness coefficients can be made on a single specimen contrary to the mechanical tests which do not allow a complete characterization of the elastic properties. The different steps will consist of the preparation of the sample (conservation, cutting) (most important step), followed by the measurement of the densities and propagation velocities in the biological material.

Two assumptions have been made. Depending on the ratio between the wavelength and the transverse dimension of the sample, we consider the medium as limited or unlimited. In the case of a limited medium (the wavelength is greater than the transverse dimension of the sample), the velocities are directly correlated to the mechanical properties (elastic moduli). In the case of an unlimited medium (the wavelength is smaller than the transverse dimension of the sample), the velocities are related to the elastic coefficients; by inversion of the matrix, the elastic moduli are then deduced.

From the fundamental equation of dynamics [29.1], we deduce the propagation equation of a wave in a limited [29.2] and an unlimited [29.7] medium.

$$\frac{\partial \sigma_{ij}}{\partial x_j} = \rho \frac{\partial^2 u_i}{\partial t^2} \Leftrightarrow \text{div} \sigma_{ij} = \rho a_i \quad (i, j = 1, 2, 3) \quad [29.1]$$

$\sigma_{ij}$ : stress tensor;

$u_i(x, t)$ : particle displacement in the  $x_i$  direction;

$a_i$ : acceleration;

$\rho$ : density.

In a limited medium and in the case of a uniaxial stress, Young's modulus  $E$  can be compared to an extension. The lateral effects of inertia induced in the other directions remain negligible; thus, considering Hooke's law,

$$\sigma_{ii} = E_i \varepsilon_{ii} \quad [29.2]$$

$\varepsilon_{ij}$ : strain tensor

we can admit, as a first approximation, the following propagation equation:

$$E_i \frac{\partial^2 u_i}{\partial x_i^2} = \rho \frac{\partial^2 u_i}{\partial t^2} . \quad [29.3]$$

The resolution of equation [29.3] for monochromatic waves gives the relationships between the velocities and the elastic moduli. For longitudinal (compression) and transverse (shear) waves, we obtain, respectively:

$$V_{ii} = \sqrt{\frac{E_i}{\rho}} \quad [29.4]$$

$$V_{ij} = \sqrt{\frac{G_{ij}}{\rho}} \quad [29.5]$$

$V_{ii}$ : velocity of a longitudinal wave propagating in the  $x_i$  direction, with the particle motion in the  $x_i$  direction;

$V_{ij}$ : velocity of a transverse wave propagating in the  $x_i$  direction, with the particle motion in the  $x_j$  direction;

$E_i$ : Young's modulus in the  $x_i$  direction;

$G_{ij}$ : Coulomb (or shear) modulus in the  $i$ - $j$  plane.

In an unlimited medium, the generalized Hooke law is used,

$$\sigma_{ij} = C_{ijkl} \varepsilon_{kl} . \quad [29.6]$$

Thus, the propagation equation to solve is in the form

$$C_{ijkl} \frac{\partial^2 u_l}{\partial x_j \partial x_k} = \rho \frac{\partial^2 u_i}{\partial t^2} . \quad [29.7]$$

$C_{ijkl}$ : elasticity tensor

The assumption of an orthotropic behavior of the bone requires the determination of nine independent elastic coefficients of the elasticity tensor  $[C_{ij}]$ :

$$[C_{ij}] = \begin{bmatrix} C_{11} & C_{12} & C_{13} & 0 & 0 & 0 \\ C_{21} & C_{22} & C_{23} & 0 & 0 & 0 \\ C_{31} & C_{32} & C_{33} & 0 & 0 & 0 \\ 0 & 0 & 0 & C_{44} & 0 & 0 \\ 0 & 0 & 0 & 0 & C_{55} & 0 \\ 0 & 0 & 0 & 0 & 0 & C_{66} \end{bmatrix} \quad [29.8]$$



$$[S_{ij}] = [C_{ij}]^{-1} = \begin{bmatrix} \frac{1}{E_1} & -\frac{\nu_{21}}{E_2} & -\frac{\nu_{31}}{E_3} & 0 & 0 & 0 \\ -\frac{\nu_{12}}{E_1} & \frac{1}{E_2} & -\frac{\nu_{32}}{E_3} & 0 & 0 & 0 \\ -\frac{\nu_{13}}{E_1} & -\frac{\nu_{23}}{E_2} & \frac{1}{E_3} & 0 & 0 & 0 \\ 0 & 0 & 0 & \frac{1}{G_{23}} & 0 & 0 \\ 0 & 0 & 0 & 0 & \frac{1}{G_{31}} & 0 \\ 0 & 0 & 0 & 0 & 0 & \frac{1}{G_{12}} \end{bmatrix} \quad [29.9]$$

$E_i$ : elastic modulus in the direction  $i$ ;

$\nu_{ij}$ : Poisson coefficient for a strain in the direction  $j$  and for a stress applied in the direction  $i$ ;

$G_{ij}$ : shear modulus in the plane  $i-j$ .

The relationships between the velocities and elastic coefficients of an orthotropic material, solutions of equation [29.7], are:

$$\begin{aligned} C_{11} &= \rho V_{11}^2 \\ C_{22} &= \rho V_{22}^2 \\ C_{33} &= \rho V_{33}^2 \\ C_{44} &= \rho V_{23}^2 = \rho V_{32}^2 \\ C_{55} &= \rho V_{13}^2 = \rho V_{31}^2 \\ C_{66} &= \rho V_{12}^2 = \rho V_{21}^2 \\ C_{12} &= \sqrt{(C_{11} + C_{66} - 2\rho V_{12/12}^2)(C_{22} + C_{66} - 2\rho V_{12/12}^2)} - C_{66} \\ C_{13} &= \sqrt{(C_{11} + C_{55} - 2\rho V_{13/13}^2)(C_{33} + C_{55} - 2\rho V_{13/13}^2)} - C_{55} \\ C_{23} &= \sqrt{(C_{22} + C_{44} - 2\rho V_{23/23}^2)(C_{33} + C_{44} - 2\rho V_{23/23}^2)} - C_{44} \end{aligned} \quad [29.10]$$

$V_{ii}$ : velocity of a longitudinal wave propagating in the  $x_i$  direction;

$V_{ij}$ : velocity of the transverse wave propagating in the  $x_i$  direction with the motion of particles in the  $x_j$  direction;

$V_{ij/ij}$ : quasi-longitudinal or quasi-transverse velocity, velocity of the longitudinal or transverse wave propagating in the direction  $(x_i + x_j)/\sqrt{2}$ , with the motion of the particles in the plane  $i-j$ ;

$V_{ij/k}$ : velocity of the quasi-transverse wave propagating in the direction  $(x_i + x_j)/\sqrt{2}$ , with the motion of particles in the direction  $x_k$ .

The following relationships between the elastic properties must be verified, due to thermodynamic restrictions:

$$\begin{aligned} \frac{\nu_{ij}}{E_i} &= \frac{\nu_{ji}}{E_j} \quad i, j = 1, 2, 3 \\ E_i, G_{ij} &> 0, \quad (1 - \nu_{ij}) > 0 \\ 1 - \nu_{12}\nu_{21} - \nu_{23}\nu_{32} - \nu_{31}\nu_{13} - 2\nu_{21}\nu_{32}\nu_{13} &> 0 \\ |\nu_{ij}| &< \sqrt{\frac{E_i}{E_j}} \\ \nu_{21}\nu_{32}\nu_{13} &< \frac{1 - \nu_{21}^2\left(\frac{E_1}{E_2}\right) - \nu_{32}^2\left(\frac{E_1}{E_2}\right) - \nu_{13}^2\left(\frac{E_3}{E_1}\right)}{2} < \frac{1}{2} \end{aligned} \quad [29.11]$$

### 29.1.1.3. Principles of measurement at low frequency

The principle of measurement by ultrasonic transmission as well as the characteristic dimensions of the human osseous samples [HOB 91, 98] are illustrated in Figures 29.3 and 29.4.

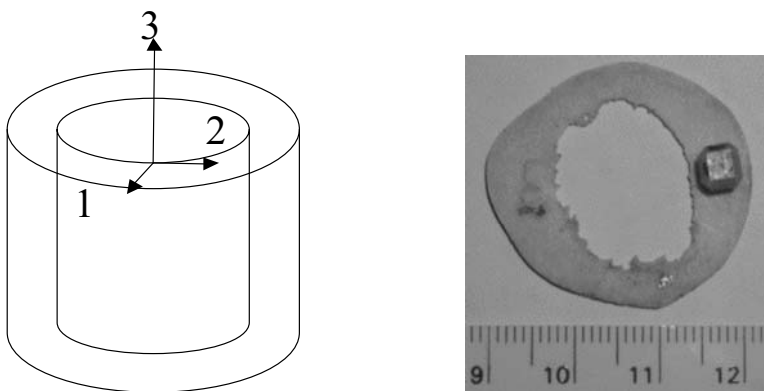


**Figure 29.3.** Cutting along the symmetry axes of the bone, (3) longitudinal, (2) tangential, (1) radial axes

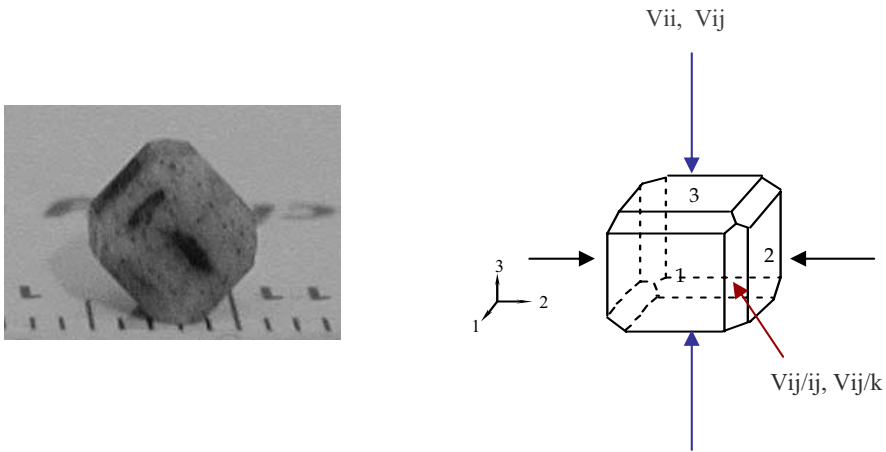


**Figure 29.4.** *Characteristic dimension of an osseous cortical sample; direction of measurement of longitudinal and transverse, quasi-longitudinal and quasi-transverse velocities*

Two systems have been used for the measurement of elastic constants of the human cortical osseous tissue: UTC (Ultrasound Transmission in Contact) and UTI (Ultrasound Transmission in Immersion) [BEN 04a,b].

The first technique (UTC) uses plane sensors with frequencies of 2.25 MHz, and the second one enables a map of the elastic constants, with the help of focalized sensors (5 MHz, 10 MHz), to be obtained. The wavelength is around 1.5 mm at 2.25 MHz and 0.35 mm at 10 MHz (we assume an average propagation velocity for the longitudinal wave of about 3,500 m/s), which remains large with respect to the characteristic dimensions of the pores. Thus, the elastic constants measured at this scale are related both to the intrinsic elastic properties of the osseous tissue and the intracortical porosity at the same time.

The determination of the mechanical properties of the spongy tissues uses the UTC technique with low-frequency sensors, 75 KHz, in order to use equations [29.4] and [29.5]. At the scale of the measurements (wavelength of the longitudinal waves from 1 to 3 cm), we obtain Young's modulus of the structure.

Some much higher frequencies are required to extract the intrinsic elastic properties of the osseous tissue. It is the field of acoustic microscopy, which will be dealt with below.

The principle of the UTC technique consists of generating pulses, through a pulse generator, on a sensor (transmitter), then collecting the transmitted signal on the other sensor (receiver). In the following, the propagation time of the wave through the sample is measured with a numerical oscilloscope (Figure 29.5). This technique allows the determination of the longitudinal, purely transverse, quasi-longitudinal and quasi-transverse velocities on the six faces of the sample.

The UTI technique uses the scanning mode with a pulse generator, an immersed sensor and an oscilloscope. The sensor is moved step-by-step automatically, this allows a map of the velocities to be obtained. The displacement step is 0.5 mm. The osseous sample is immersed in demineralized water kept at a temperature of 20°C. For each acquisition point, two echoes are recorded: the first comes from the reflection at the interface between water and the material (echo 1) and the second from the reflection at the interface between the material and water (echo 2) (Figure 29.6). The calculation of the difference of propagation time between the two echoes enables the velocity to be deduced, knowing the thickness of the sample. This technique measures the propagation velocity in only one direction of the sample. However, it allows the characterization of the spatial distribution of the acoustic properties.

For these two techniques, the necessity of defining a homogenous elementary bulk is one of the biggest difficulties. The sizes of the samples are a cube of around 5 mm for the UTC technique, and a thickness of around 2 mm for the UTI technique.

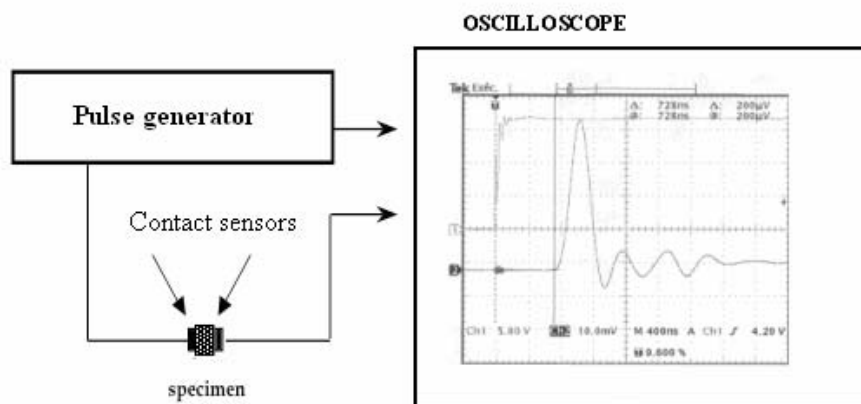


**Figure 29.5.** *System of measurements by transmission with contact sensors (UTC)*

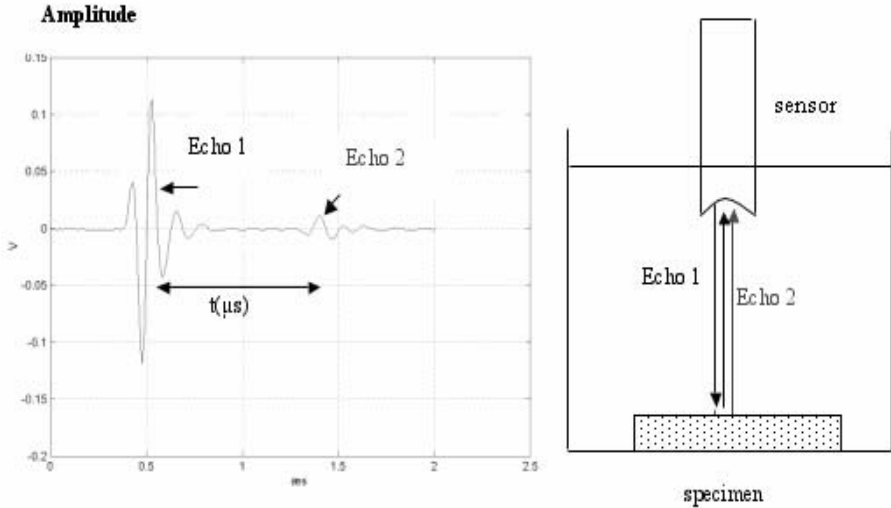


**Figure 29.6.** *System of measurements by transmission with focalized sensors (UTI)*

A calibration step is always necessary before the measurements. Some samples of known acoustical and mechanical properties, with velocities in the same range as the osseous tissue, are used with several dimensions characteristic of human osseous tissue. The following materials are used:

- copper,
- stainless steel,
- Plexiglas,
- PVC.

The range of velocities is from 2,680 to 5,010 m/s.

With the ultrasound transmission in contact (UTC) technique, a map of the mechanical properties of the osseous (cortical and spongy) tissue has been made from samples cut from cadaveric specimens (femur, tibia, humerus, patella, lumbar vertebrae L1 to L5, mandibles, glene) [HOB 91, 98]. This study has highlighted the variability of the mechanical properties depending on the patient, the type of bone, the anatomic location, showing the strong heterogeneity of the bone at the scale of tissues.

Tables 29.1 and 29.2 present some values of acoustic and elastic properties characteristic of a cortical osseous sample (Figure 29.4).

Propagation direction		Type of wave	Velocity (m/s)
(1,0,0)	radial	Longitudinal (L)	$V_{11} = 3,404$
(1,0,0)	radial	Transverse (T)	$V_{12} = 1,702$
(1,0,0)	radial	Transverse (T)	$V_{13} = 1,837$
(0,1,0)	tangential	L	$V_{22} = 3,500$
(0,1,0)	tangential	T	$V_{21} = 1,728$
(0,1,0)	tangential	T	$V_{23} = 1,920$
(0,0,1)	axial	L	$V_{33} = 3,940$
(0,0,1)	axial	T	$V_{31} = 1,871$
(0,0,1)	axial	T	$V_{32} = 1,929$
(1/√2, 1/√2, 0)		L	$V_{12/12} = 3,445$
(1/√2, 1/√2, 0)		T	$V_{12/12} = 1,693$
(1/√2, 1/√2, 0)		T	$V_{12/3} = 1,850$
(1/√2, 0, 1/√2)		L	$V_{13/13} = 3,656$
(1/√2, 0, 1/√2)		T	$V_{13/13} = 1,857$
(1/√2, 0, 1/√2)		T	$V_{13/2} = 1,766$
(0, 1/√2, 1/√2)		L	$V_{23/23} = 3,508$
(0, 1/√2, 1/√2)		T	$V_{23/23} = 1,838$
(0, 1/√2, 1/√2)		T	$V_{23/1} = 1,747$

**Table 29.1.** Example of velocity measurement, the standard deviation varies from 20 to 80m/s

Elastic coefficients (GPa)		Elastic properties	
$C_{11}$	21.9	$E_1$ (GPa)	14.6
$C_{22}$	23.2	$E_2$ (GPa)	15.9
$C_{33}$	29.3	$E_3$ (GPa)	19.3
$C_{44}$	7.04	$G_{23}$ (GPa)	7.04
$C_{55}$	6.62	$G_{31}$ (GPa)	6.62
$C_{66}$	5.50	$G_{12}$ (GPa)	5.50
$C_{12}$	10.8	$\nu_{12}$	0.29
$C_{13}$	13.1	$\nu_{13}$	0.32
$C_{23}$	12.8	$\nu_{23}$	0.29
		$\nu_{21}$	0.32
		$\nu_{31}$	0.42
		$\nu_{32}$	0.36

**Table 29.2.** Example of data of the elastic coefficients and properties of the human osseous tissue (femur). The standard deviation corresponding to the measurement error is 1.5 GPa for the elastic coefficients  $C_{ii}$  (Young moduli), 0.35 GPa for the coefficients  $C_{ij}$  and Coulomb moduli, and 0.02 for the Poisson coefficients

An example of a map of ultrasonic velocities obtained from two sections located at the diaphysis of a human femur is illustrated in Figure 29.7. The sections are localized at 45 and 56% of the total length of the femur, respectively. The values of the velocities vary depending on the periphery, radially and depending on the position of the section. The lower values are on the posterior side (bottom of the section) and in the inside (endosteal area). These variations are strongly correlated to the microporosity. In fact, a relationship linking this microporosity and the acoustic velocity measured in the axial direction has been established [BEN 04].

$$V = 4497P^{-0.0584} \quad (P \neq 0) \quad R^2 = 0.90 \quad [29.12]$$

Concerning spongy human bone, it has been demonstrated that the mechanical properties vary depending on the anatomic location [HOB 91, 98]. In the literature, many studies have demonstrated the correlation between its morphologic and structural properties (as porosity, the connectivity of the osseous spans, the size and the shape of the osseous spans).

From a macrostructural point of view, spongy tissue is strongly heterogenous, and this is the reason for the necessity of defining a minimal homogenous bulk. Moreover, its strongly anisotropic nature requires the determination of the symmetry

axes of the sample before the measurement, when it is possible. On the contrary, we must verify *a posteriori*. In fact, Figure 29.8 illustrates some measurements made on the symmetry axes of the sample, ensuring an appropriate measurement and a correlation with the structural properties [DES 98]. The acoustic and elastic properties measured in the three directions for the two samples from the same femoral head are summarized in Table 29.3.

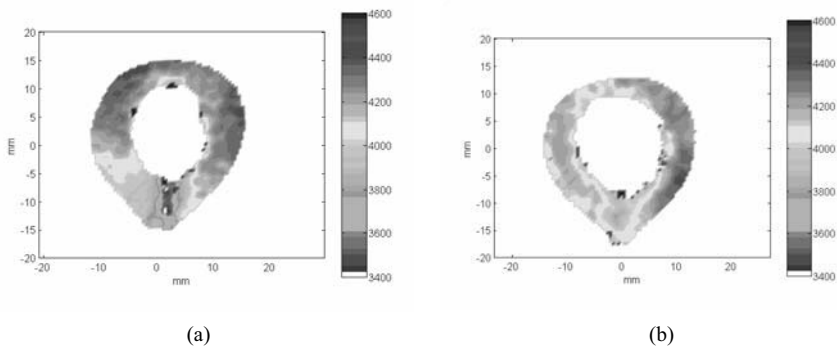


**Figure 29.7.** Map of the acoustic velocities of two sections of a human cortical bone at 45% (a) and 56% (b) of the total length of the femur

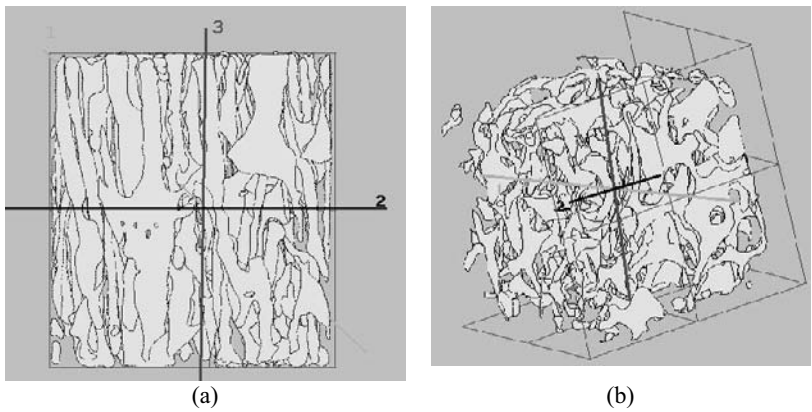


**Figure 29.8.** Samples of spongy bone ( $4 \times 4 \times 4 \text{ mm}^3$ ) from the same human femoral head presenting two different types of structures: sticks (a) and plates (b)



	Sample (a)	Sample (b)
$E_1$ (MPa)	$663 \pm 60$	$1051 \pm 174$
$E_2$ (MPa)	$497 \pm 101$	$883 \pm 154$
$E_3$ (MPa)	$2377 \pm 505$	$1048 \pm 169$

**Table 29.3.** *Acoustic and mechanical properties of samples of spongy tissue of the human femoral head*

#### 29.1.1.4. Principles of the measurements in acoustic microscopy

The acoustic microscope is used in a large range of frequencies, from several dozens of MHz to several GHz. There are two types of configuration of acoustic microscopes. The SAM (Scanning Acoustic Microscopy) works widely in reflection and enables the formation of an image of the amplitude of an ultrasonic signal reflected by the surface of the sample in several seconds. This image provides a detailed map of the spatial distribution of the local mechanical properties (density, elasticity, anisotropy, etc.), which define the reflection coefficient of an object, at the submillimetric or microscopic scale. Other microscopes work in the transmission mode, and enable characteristic ultrasonic parameters, such as the velocity and the attenuation to be obtained. The use of very high frequencies leads to a fast increase of the attenuation, which limits the analysis to the surface of the sample for microscopes working by reflection, and to very thin samples for measurements by transmission [BRI 95].

The schematic diagram of the acoustic microscope by reflection is illustrated in Figure 29.9. The transducer is made of a thick layer of zinc oxide (of several  $\mu\text{m}$ ) lying on the plane face of a bar of synthetic sapphire, of which one of the extremities has the shape of a spherical concave dioptré. The sapphire bar works as a delay line and as an acoustic focusing lens. Water is used as a coupling medium. To ensure a good transmission of the ultrasonic energy between the acoustic lens and water, the spherical part of the sapphire is covered by an antireflection coating of thickness  $\lambda/4$  used to adapt the impedance between the two media. The transducer, connected to a motorized assembly, moves in a plane parallel to the surface of the sample. This surface is scanned by the ultrasonic beam and, the amplitude of the reflected signal is measured point by point. It depends on acoustic characteristics of the specimen studied in an area whose surface is equal to that of the focalization point. The preparation of a sample for acoustic microscopy consists of ensuring the strict parallelism of the faces perpendicular to the beam axis. The scanned surface must be polished so that the size of potential surface flaws (roughness) remains less than the

wavelength. When these conditions are gathered, the variations of the amplitude of the reflected signal (thus of the contrast on the image) are due only to intrinsic material properties of the medium, and not to unevennesses or roughness flaws of the surface. For these measurements, the osseous samples can be fresh or included in polymethylacrylate (PMMA).

The processing of the ultrasonic signals reflected by the sample surface enables the determination of the acoustic impedance ( $Z$ ), an elastic coefficient ( $C_{ii}$ ) or a Young's modulus  $E_i$  following the direction perpendicular to the cutting made. For practical purpose, the estimation of the acoustic impedance (or of the elastic characteristics) of the sample surface is made through the use of a calibration method based on homogenous and isotropic reference materials whose acoustic impedance (or elastic modulus) is known. The curve, linking the reflection coefficient  $R$  to the voltage measured by the receptor when the sample is in the focal area, is established from reference materials. Then, the unknown reflection coefficient of the bone is determined by transferring onto the calibration curve (Figure 29.9d) the amplitude of the signal measured by microscopy, and by reading the corresponding value of the reflection coefficient  $R$ . When the sample is put in the focal area and when the incidence is normal, the generation of shear waves in the solid is negligible. The reflection coefficient  $R$  is then given by the following relationship:

$$R = \frac{Z - Z_0}{Z + Z_0} \quad [29.13]$$

where  $Z_0$  is the acoustic impedance of the coupling medium (water) and  $Z$  the characteristic impedance of the studied sample [HIR 95]. The former relationship can be applied in the case of an isotropic studied object. To determine the elastic properties of the bone considered as orthotropic, we make the assumption of homogeneity and of a transverse local isotropy at the scale of the focal spot, and we estimate the local acoustic impedance from the reflection coefficient determined with the help of relationship [29.13].

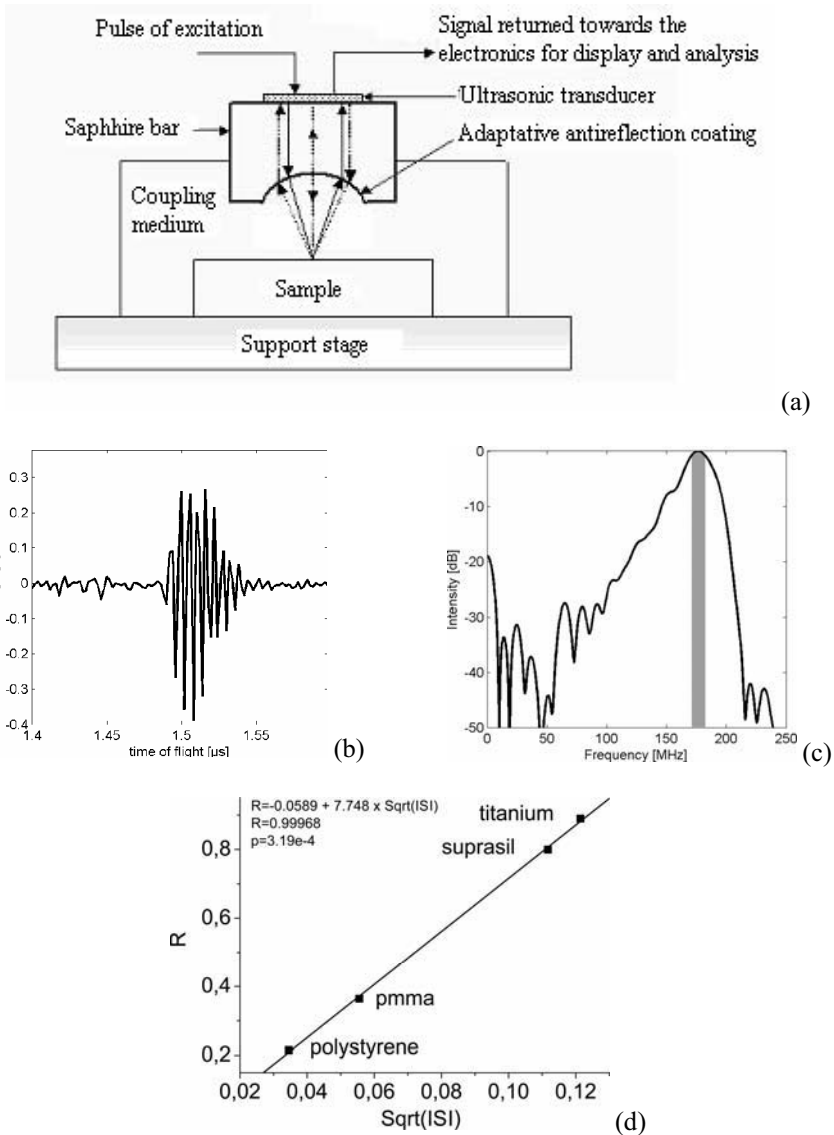


**Figure 29.9.** Schematic diagram of the measurement by scanning acoustic microscopy in reflection. The ultrasonic beam is focused on the sample surface (a). The spectrum (c) of the reflected signal (b) is calculated by Fourier transform. The Integrated Spectral Intensity (ISI) is calculated in a tight frequency band centered on the central frequency. The calibration curve is obtained by transferring the reflection coefficient  $R$  as a function of the integrated spectral intensity ( $\sqrt{ISI}$ ) for a set of known materials (polystyrene, PMMA, Suprasil and titanium) ([RAU 05])

Once the acoustic impedance is obtained, it is easy to deduce the values of the elastic coefficient and Young's modulus, supposing a symmetry of orthotropic type from the following relationships:

$$Z_i = \rho V_{ii} \quad \text{and} \quad c_{ii} = \rho V_{ii}^2 \quad [29.14]$$

$$c_{ii} = \frac{Z_i^2}{\rho} . \quad [29.15]$$

$$E_i = c_{ii} \frac{(1 + \nu)(1 - 2\nu)}{(1 - \nu)} \quad [29.16]$$

where  $i$  is the symmetry direction,  $V_{ii}$  the velocity of the longitudinal wave propagating in the direction  $i$ ,  $\rho$  the bulk density and  $\nu$  the Poisson coefficient [RAU 05]. The calculation of the elastic characteristics assumes that the density and the Poisson modulus are known at the location of the measurement. The Poisson coefficient is generally supposed constant equal to 0.3 in bone. If we make the assumption of a spatially invariable density, the former has to be determined by weighing. It can also be estimated locally at the location of the acoustic measurement by X-ray microtomography or cyclotron radiation [RAU 05].

We illustrate these measurements made by acoustic microscopy from data obtained from human or mouse bones. The spatial resolution of the images is a function of the frequency. Some images of human bones (radius) obtained at 50 MHz (spatial resolution  $\sim 25 \mu\text{m}$ ), 200 MHz (spatial resolution  $\sim 8 \mu\text{m}$ ) and 400 MHz (spatial resolution  $\sim 4 \mu\text{m}$ ) illustrate the fact that, contrary to images obtained at low frequency (cf. Figure 29.7), acoustic microscopy enables information on the microstructure (porosity, osseous spans) of the bone to be obtained (Figure 29.10). In particular, the image of a cortical bone obtained at 200 MHz brings to light the organization of the tissue in osteons (structures more or less circular centered on a canal) separated by interstitial tissue. Then, selecting measurement points in some areas of the osseous tissue, it is possible to estimate the intrinsic elastic properties of the tissue and their spatial variation.

An example of impedance and density maps (femur of mouse) is represented in Figure 29.11. The superposition of the images illustrates the spatial concordance between the two images. The local value of the elastic coefficient (or of the elastic modulus) is obtained by combining the local values of impedance and density according to equation [29.15] (respectively [29.16]). The relationship between the elastic coefficient  $c_{11}$  and the acoustic impedance is illustrated in Figure 29.12.

Table 29.4 presents some values of acoustic and elastic properties (impedance) characteristic of the cortical bone (human radius) (Figure 29.10). Let us note that the values of the elastic coefficient  $c_{33}$  and of the modulus  $E_3$  are higher than the corresponding values given in Table 29.2 (obtained at low frequency). This is explained by the fact that the intrinsic values measured at high frequency are not affected by the bone porosity.

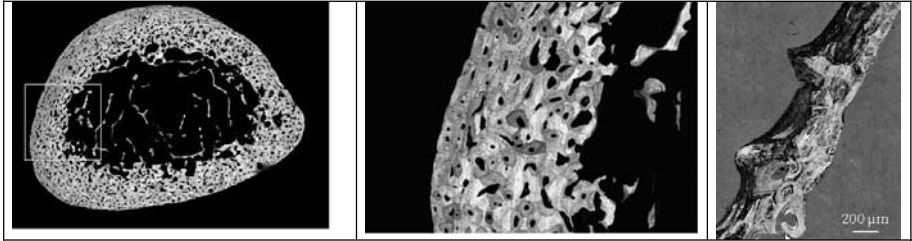


**Figure 29.10.** Image of a section of the human radius obtained in acoustic microscopy by reflection at 50 MHz (left). The amplitude of the reflected signal is represented in grey scale. This type of image enables us to obtain information on the microstructure of the bone as shown in the central image (obtained at 200 MHz, enlargement of the small squared area indicated on the left image) and on the image of an osseous span (obtained at 400 MHz, right image)

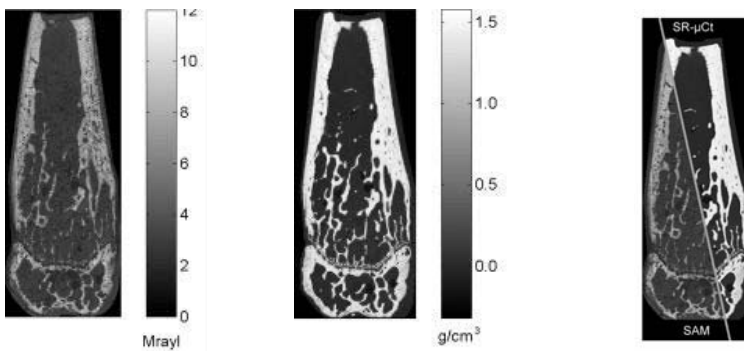


**Figure 29.11.** Images of impedance (left) and of density (center) of a mouse femur. The superposition of two images acquired with the same spatial resolution illustrates the good anatomic concordance (right) and leads to a local estimation, for each pixel of the image, of the elasticity coefficient  $c_{11}$  or of the elasticity modulus  $E_1$

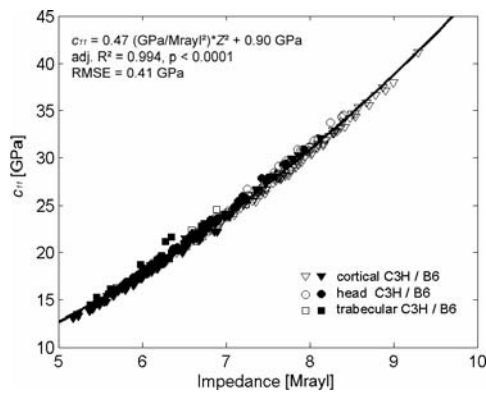


**Figure 29.12.** Correlation between acoustic impedance and  $c_{11}$  for two strains of mice (C3H and B6). Measurements made on the cortical bone, on the spongy bone and on the head of the femur

	Interstitial tissue	Osteons
$Z$ [Mrayl]	$9.2 \pm 1.0$	$7.2 \pm 1.1$
$V_{33}$ [m/s]	$4777 \pm 548$	$3891 \pm 573$
$c_{33}$ [GPa]	$44 \pm 10$	$28.7 \pm 9.0$
$E_3$ [GPa]	$32.5 \pm 4.0$	$21.3 \pm 3.6$

**Table 29.4.** Intrinsic acoustical and elastic properties of the human cortical bone (radius).  
The value of  $E_3$  is obtained from equation [29.16]  
with a Poisson coefficient of 0.3

29.1.1.5. Conclusions

The *in vitro* determination of the elastic properties of the bone from ultrasonic measurements is quite easy. These measurements enable us to characterize the bone response to various physiopathological processes (osseous reaction to the insertion of an implant, osseous fragility, effect of a treatment, osseous phenotype of small animals, etc.) or to respond to the need for simulation by finite elements or finite differences.

The variation of acoustic and mechanical properties depending on the subject, on the type of bone and on the anatomic position as well as on the ultrasonic frequency of measurement is well known. The measurement of intrinsic elastic characteristics is based on acoustic microscopy, whereas measurements at low frequency can replace the mechanical tests, usually done at the macroscopic scale. On the same

organ, the variations of these properties are not negligible and complicate their *in vivo* measurement.

Osseous tissue is an anisotropic material because it fits to the external mechanical stresses. The variations of the mechanical properties of the adult osseous tissue, observed at the tissue scale, are strongly correlated to their morphologic and structural properties.

Bone is a living biological material which does not stop evolving from its birth to its senescence. In this case, the variations of mechanical and acoustic properties are not only linked to the structural variations, but also to physico-chemical ones (ratio of mineral versus organic components, maturity of the apatite crystals, etc.).

### **29.1.2. *In vivo* determination of acoustic properties (ultrasonic bone mineral density test)**

#### **29.1.2.1. *Introduction***

Osseous fragility due to osteoporosis affects an important part of the female population from the menopause onwards. The *in vivo* measurements of the acoustical properties of the bone were proposed in the mid 1980s to detect people with risks of fracture, with the aim of preventing osteoporosis. The ultrasonic tests are based on the transmission of low-frequency ultrasounds (from 250 kHz to 1.25 MHz) through the bone. The different methods can be gathered in two main categories: transverse transmission and the axial one.

#### **29.1.2.2. *Transverse transmission***

Testing arrangements based on the principle of transverse transmission use two broadband sensors (a transmitter and a receiver) placed face to face on both sides of the measured skeletal site (Figure 29.13). It is thus a measurement in transmission, which differentiates the ultrasonic bone mineral density test from other ultrasonic diagnostic applications working in reflection, based on the scanning principle. The measurements are made on peripheral skeletal sites that are easily accessible like the calcaneum (bone of the knuckle) or the phalanx of the hand. The central frequency is 500 kHz for the measurements on the knuckle and 1.25 MHz for the measurements on the phalanx.

The attenuation as a function of frequency and propagation velocity are obtained by a method of substitution which works in two steps and consists of comparing the spectrum  $S(f)$  of the signal transmitted through the bone to the spectrum  $S_{ref}(f)$  of a reference signal acquired through a reference medium whose attenuation is known. The reference medium is generally water, whose attenuation for useful

frequencies ( $< 1$  MHz) can be considered as negligible. This method of substitution enables us to free ourselves from the transfer function of the measuring chain. Let us consider the reference signal  $s_{ref}(t)$ . In the frame of the plane waves approximation, its frequency spectrum can be written in the form:

$$S_{ref}(f) = S_0(f) e^{-ik_0 L} \quad [29.17]$$

where  $S_0(f)$  represents the transfer function of the device (that is to say the spectrum of the transmitted signal between the two sensors when they are in contact),  $k_0 = 2\pi f / V_0$  is the wavevector of the reference medium,  $f$  its frequency,  $V_0$  the propagation velocity of ultrasound in the reference medium and  $L$  the distance between the two sensors.  $s(t)$  is the signal transmitted through the bone. Its spectrum is given by:

$$S(f) = T^2 S_0(f) e^{-i[k_0(L-l)+kl]} e^{-\alpha(f)l} \quad [29.18]$$

where  $T^2$  represents the losses by transmission through the interfaces,  $k = 2\pi f / V_{bone}(f)$  is the wavevector of the bone,  $V_{bone}(f)$  and  $\alpha(f)$  are the propagation velocity and the attenuation coefficient of ultrasound in the bone and  $l$  the crossed thickness of the bone. The ratio of the two spectra can be written in the following form:

$$\frac{S(f)}{S_{ref}(f)} = A(f) e^{-i\Phi(f)} \quad [29.19]$$

$$\text{with } A(f) = T^2 e^{-\alpha(f)l} \text{ and } \Phi(f) = l(k - k_0) \quad [29.20]$$

The attenuation as a function of frequency is simply expressed from the amplitude spectrum:

$$\alpha(f)l = \ln A(f) + \ln T^2 = \ln \left| \frac{S_{ref}(f)}{S(f)} \right| + \ln T^2 \quad [29.21]$$

The variation of the attenuation as a function of frequency is quasi linear (Figure 29.13). Thus, we measure the slope of the attenuation as a function of frequency from the regression line obtained by the least squares method. In clinical practice, this parameter, is generally referred to by the acronym BUA (Broadband Ultrasound Attenuation) and is expressed in dB/MHz. With most of the commercial devices, the crossed thickness  $l$  of bone is not known, and this is the global



attenuation  $\alpha(f)l$ , instead of the attenuation coefficient  $\alpha(f)$ , that is effectively measured. We neglect the soft tissues which surround the bone because their attenuation is much weaker than that of the bone.

An estimation of the propagation velocity (speed of sound, SOS,  $\text{m.s}^{-1}$ ) can be simply obtained from the difference of times of flight  $\Delta t$  between the reference and transmitted signals:

$$V_{os} = \frac{l}{\frac{l}{V_0} + \frac{\Delta t}{l}} \quad [29.22]$$

The time of flight of the signal is determined by the definition of a particular temporal criterion such as a passing by zero, a passing by a pre-determined threshold, a maximum or a minimum of the amplitude. However, because of the dispersion of velocities with frequency, the obtained values of the velocity can vary significantly, depending on the temporal criterion used to detect the arrival of the signal. Another approach consists of estimating the phase velocity  $V_{bone}(f)$  as a function of frequency from the phase  $\Phi(f)$ :

$$V_{os}(f) = \frac{l}{\frac{l}{c_0} + \frac{\Phi(f)}{2\pi f}} \quad [29.23]$$

and in using the average value of the velocity in the useful bandwidth. In all cases, the calculation of the propagation velocity supposes that the crossed thickness of bone is known and neglects the influence of soft tissues.

The sensors are immersed in water or in direct contact with the skin (in this case, an ultrasonic coupling gel is needed). Some devices use fixed sensors. The measurement is thus done at a single point. Other devices enable the obtaining of an image, which allows the automatic selection of an area of measurement and its identical reproduction during repeated examinations of the same person.

The interest of the image is for the improved standardization of the observed site. The image is achieved by measuring the parameters at each point of the observed area, using either mechanical scanning of the sensors (mono-element sensor) or an electronic scanning (matricial sensors) of the ultrasonic beam (Figure 29.14.) [GOM 02].

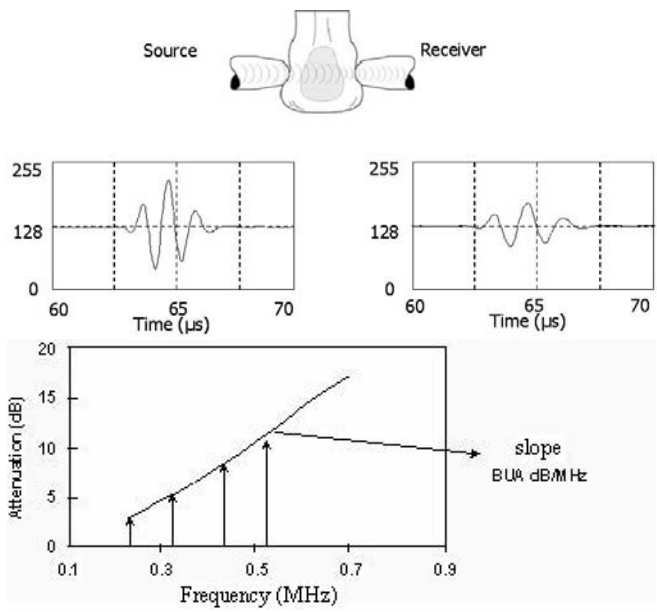


**Figure 29.13.** Transverse transmission. Reference signal (left) and signal transmitted through the knuckle (right) Attenuation as a function of frequency (bottom)

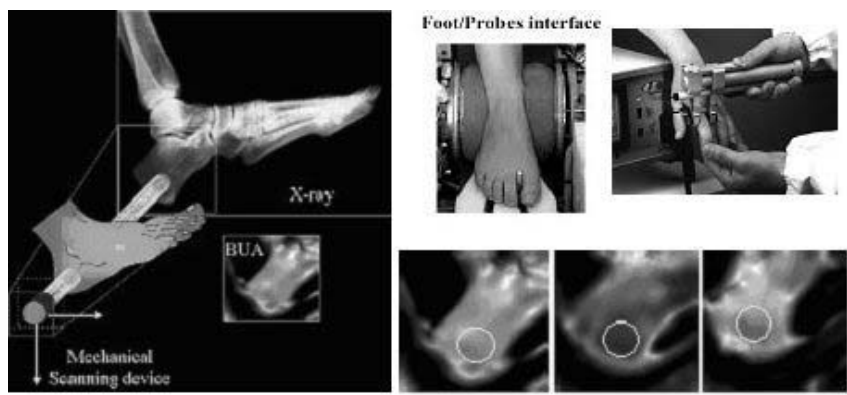


**Figure 29.14.** Measurement on the knuckle and the phalanx (top, right). Image of the attenuation of the knuckle by mechanical (left) or electronic scanning (matricial sensors) of the ultrasonic focalized beam (top, center). In the bottom, at right, illustration of the images obtained for three different people. A circular area of measurement is spotted automatically

Many studies have shown very good correlation between the ultrasonic parameters of the knuckle and the osseous mineral density (bulk density) estimated by X-ray densitometry. The current clinical use of the ultrasonic bone mineral density test for the estimation of the risk of fracture is based on these results. For the phalanx, the measurement in transmission involves the propagation of circumferential waves guided by the cortical envelope (Figure 29.15). The characteristics of propagation of these waves have the particularity of reflecting the bulk density, the cortical porosity and the area of the transverse section; all these bone parameters are important in the determination of the resistivity to fracture.

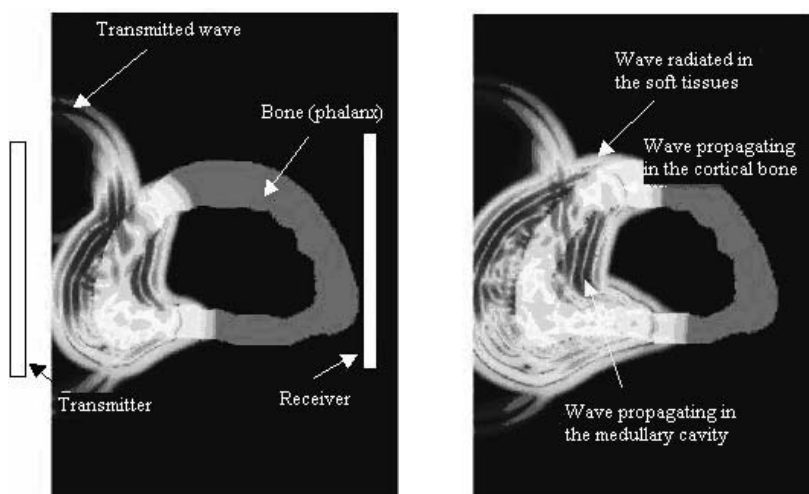


**Figure 29.15.** Simulation by finite differences of the transmission of a plane wavefront through a transverse section of the phalanx ( $t=20\ \mu\text{s}$  at left, and  $t=30\ \mu\text{s}$  at right). The calculation of the field clearly shows the different paths of the incident wave

### 29.1.2.3. Axial transmission

The principle of axial transmission is illustrated in Figure 29.16. The measurement by axial transmission is based on the estimation of the propagation velocity of an ultrasonic wave ( $\sim 1\ \text{MHz}$ ) which propagates along the osseous (cortical) surface between two (or more) sensors aligned at the skin surface. This technique uses the phenomenon of refraction at the critical angle, which is produced when an incident wave passes from a medium with a propagation velocity  $V_1$  to a medium with a propagation velocity  $V_2$ , with  $V_2 > V_1$ . It is the case when a compressional wave ( $V_1 \sim 1,500\ \text{m/s}$ ) is transmitted through the skin towards the cortical bone ( $V_2 \sim 3,500\ \text{to } 4,000\ \text{m/s}$ ). A set of receivers put on the skin surface acquires the passing of a wave radiated by the waves that propagate inside the

cortical bone along the osseous interface. The excitation of these last waves from a source located at the skin surface supposes an appropriate incident angle given by the relationship:

$$\sin \theta_c = \frac{V_1}{V_2} \quad [29.24]$$

where  $V_1$  and  $V_2$  represent the propagation velocities of compressional waves in soft tissues and along the bone axis, respectively. Once excited, these waves radiate only if they propagate faster than the waves in the fluid medium. The angle of radiation is identical to the critical angle of excitation. The corresponding propagation path is represented on Figure 29.16. The technique is based on the estimation of the velocity of the head wave, which is the source of the first signal detected by the receivers. The first signal which reaches the receivers is detected (threshold, passing through zero, etc.) and its time of flight is calculated. In the case of two receivers, the velocity is given by:

$$V_2 = \frac{\Delta r}{\Delta t} \quad [29.25]$$

where  $\Delta r$  is the distance between the two receivers and  $\Delta t$  the difference of arrival time on the two receivers. In the case of  $N$  receivers, the velocity is defined as the inverse of the slope of the regression line calculated from the time of flight as a function of the distance transmitter–receiver.

The variation of the velocity of the head wave as a function of the cortical thickness is represented on Figure 29.16. In the case where the bone thickness ( $e$ ) is larger than the wavelength ( $\lambda$ ) of the compressional waves in the bone, the radiated head wave corresponds to a lateral wave, also called compressional wave of type P in geophysics in the case of an interface between a slow semi-infinite medium (soft tissues) containing the source and a fast semi-infinite medium (cortical bone). Its velocity along the interface is that of the compressional wave refracted in the bone. In the case where the cortical thickness is smaller than the wavelength, the wave propagated in the bone is guided not only by the cortical surface, but also by all the thickness of the cortical area and tends towards a Lamb mode S0 for ratios  $\lambda/e \ll 1$ . The propagation velocity of the head wave is then smaller than that of the lateral wave, but always reflects the osseous material properties. In the case where the bone thickness is close to the wavelength, the nature of the head wave can not be defined without error, because the refracted wave in the bone for angles less than the critical angle yields a reflected wave in the cortical layer, this reflected wave being able to interfere with the lateral wave. The velocity of the head wave changes from the velocity of the lateral wave to that of the guided mode S0 for decreasing values of

the ratio  $\lambda/e$  [BOS 04a]. The propagation velocity of the head wave enables us to characterize the osseous state. It translates a propagation that depends on geometrical and material properties of the osseous medium. Namely, the value of the velocity decreases when the bone porosity increases, when the mineral density decreases or when the cortical thickness decreases [BOS 04b].

Other axial transmission devices based on a quite similar measurement principle take advantage of the propagation of guided waves at lower frequencies ( $\sim 250$  kHz) and allow the identification of the guided mode A0 [LEF 02; NIC 02].

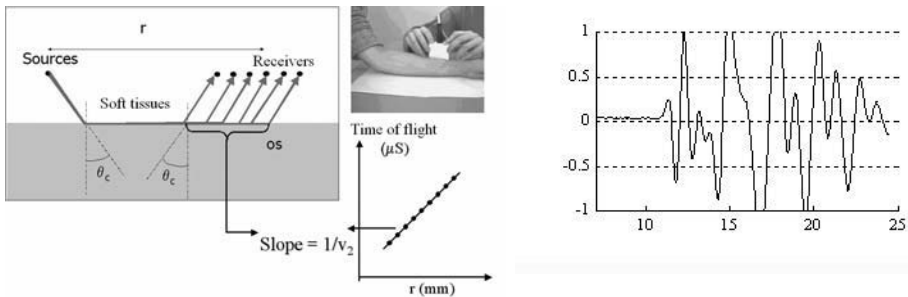


**Figure 29.16.** Schematic diagram of the measurement of the lateral wave for the characterization of the cortical wave and outcome of the test on the radius (left). Radiofrequency signal (right). The velocity is obtained by detection of the first signal (head signal)

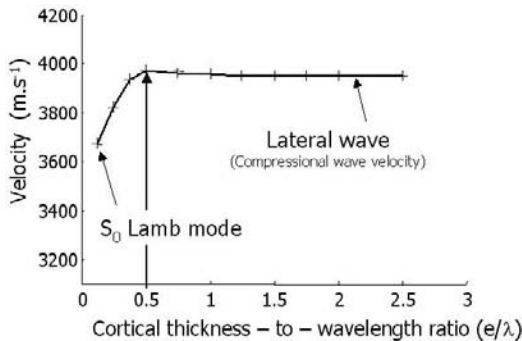


**Figure 29.17.** Variation of the velocity of the head wave as a function of the ratio between cortical thickness and wavelength [from BOS 04a]

#### 29.1.2.4. *Other measurements*

Other measurement methods based on the reflection or the scattering of an incident wave by the osseous structure are currently being studied. Using the phenomenon of total reflection on the cortical bone, reflectometry at the critical angle allows measuring the critical angle for compressional or shearing waves, thanks to a goniometric assembly. The propagation velocity of the wave in the bone is determined from:

$$V_2 = \frac{V_I}{\sin \theta_c} \quad [29.26]$$

These measurements, made at 5 MHz, allow an estimation of the local elastic properties of the cortical bone and its anisotropy. [ANT 97].

The structure of the spongy bone (see section 29.1.1.1) behaves as a strongly heterogenous medium. The interaction of the incident wave with the network of spans is governed by two effects: absorption and scattering. It is difficult to separate these two contributions from the measurements in transmission. On the contrary, the analysis of the “echo” signal reflected by the trabecular structure enables us to separate the contribution of the backscattering, whose characteristics depend on the properties of the scatterers (elastic characteristics, number, size and distance between the spans) [ROU 01].

#### 29.1.2.5. *Clinical data*

There is currently considerable clinical data. These data are mostly similar to those obtained by the X-ray densitometry considered as the reference examination. The influence of age has been observed, showing a faster decrease of the ultrasonic parameters in the years that follow the menopause. Most of the clinical studies have shown that ultrasounds have the same capacity as densitometry to detect the osteoporotic patients from the healthy ones: the values of the ultrasonic parameters are weaker for osteoporotic patients. Some large epidemiological studies [KAH 04] have shown that the prediction of the risk of fracture made using ultrasonic measurements is identical to the prediction made from measurements by X-rays. These studies conclude that ultrasonic measurements constitute a useful clinical test to determine the risk of fracture for menopausal women.

### 29.1.3. Simulation and inverse problems

#### 29.1.3.1. Introduction

Simulation of ultrasonic propagation in the bone is essential to solve the inverse problem and return from the measurements to the osseous properties. The theoretical aspects of the interaction between ultrasounds and the bone remain poorly known. However, the nature of the problem is very different for the cortical and the trabecular bones; it also depends on the fact that we use *in vivo* measurements or *in vitro* tests.

The propagation of an ultrasonic wave is determined by the micro-structural, geometrical and material characteristics of the propagation medium. In the case of *in vitro* tests, we have shown that it is possible, using a linear model of the propagation, to invert the data and return to the elastic characteristics of the bone (see section 29.1.1). This supposes that the bone is considered as a continuous and homogenous medium at the scale of the wavelength, a condition that is generally verified by an adequate choice of the frequency. In the case of the cortical bone, for example, the wavelength for low frequencies ( $f < 1$  MHz,  $\lambda > 4$  mm) really remains larger than the characteristic dimensions of the porosity. It is thus relatively easy to define a volume of homogenization, characterized by an effective density and elastic constants. These effective constants depend at the same time on intrinsic characteristics of the material and its microstructure. In acoustic microscopy (low frequency,  $f > 100$  MHz,  $\lambda < 15$   $\mu\text{m}$ ), the spatial resolution is such that it is possible to measure the intrinsic characteristics of the osseous tissue. The inversion of the data in the case of the spongy bone is less easy for the frequency range used *in vivo*. The spongy bone, with high porosity, is a more complex material than the cortical bone. The characteristic dimension of the heterogeneities (average size of the pores around 500  $\mu\text{m}$  to 2 mm) is close to the wavelength ( $\lambda \sim 3$  mm at 500 kHz) and the propagation medium can be considered as homogenous at the frequencies used. Under these conditions, the coupling phenomena between the solid matrix and the fluid filling the pores can not be neglected. Moreover, the scattering by the osseous spans becomes an important component of the interaction between the wave and the osseous structure.

For a long time *in vitro* ultrasonic tests have been proposed as an alternative to mechanical tests for the measurement of the elastic characteristics of the bone. Conversely, *in vivo* tests are achieved with a different goal: exploring the fragility of the bone (or its resistivity to the fracture). However, the fragility of a material can not be reduced to its elastic characteristics. Other mechanical characteristics are involved. Thus, ultrasonic *in vivo* tests are based on the assumption that the measured parameters reflect some of the osseous properties which play a decisive role in the fragility (elasticity, density, micro-architecture, micro-damaging, etc.).

The inversion of the *in vivo* acquired data thus concentrates on the estimation of these different osseous characteristics.

### 29.1.3.2. *Scattering*

The study of the scattering media is an interesting step towards the resolution of the inverse problem, that is to say towards the estimation of the characteristics of the scatterers. Two approaches have been proposed to describe the scattering by spongy bone. These two approaches generally lie on the simplifying assumption of simple scattering. The osseous spans, whose characteristic dimensions are smaller than the wavelength ( $\lambda \sim 1.5$  mm at 500 kHz), are considered as the principal source of ultrasonic scattering.

The first approach consists of describing the scattered pressure by searching a solution to the wave propagation equation inside and outside the scatterer at the same time (the osseous span), and by applying the boundary conditions appropriate to the interfaces. The scatterer is an elastic isotropic solid immersed in a non-viscous fluid and interacting with an incident plane wave. A closed-form solution can be obtained in the case of scatterers of canonical shape (spherical, cylindrical, etc.). Wear [WEA 99] has proposed to model the trabecular bone as a set of identical cylinders placed randomly in the medium. Under these assumptions, it is possible to obtain from the theory of Faran [FAR 51] an expression of the frequency dependence of the backscattering coefficient for the set of cylinders. The so-obtained frequency dependence is in good agreement with the experimental data, which give a frequency dependence close to  $f^3$  in a low frequency range (Rayleigh scattering when the wavelength is larger than the average size of the scatterers).

The second approach is based on a simulation of the trabecular bone as a random “fluid” medium in which the scatterers (spans) are processed as a random distribution of fluctuations of density and compressibility. This is a more flexible approach to describe the great complexity of the geometry of the medium. The scatterers are considered as sources which disturb the homogenous wave propagation equation in the ambient fluid medium [MOR 86]. This equation is solved by using the formalism of the Green functions, and integrating the contributions of the sources on the volume containing the scatterers. The fluctuations of acoustic properties of the medium (density and compressibility)  $\gamma(\vec{r})$  are given by:

$$\gamma(\vec{r}) = \frac{[\kappa_b(\vec{r}) - \kappa_f]}{\kappa_f} - \frac{[\rho_b(\vec{r}) - \rho_f]}{\rho_b(\vec{r})} \quad [29.27]$$



where the bone and the ambient fluid are characterized by their respective densities  $\rho_b(\vec{r})$  and  $\rho_f$ , and their respective compressibilities  $\kappa_b(\vec{r})$  and  $\kappa_f$ . These fluctuations can also be characterized by their statistical properties of second order, such as their autocorrelation function  $b_\gamma(\Delta\vec{r})$ . This model takes into account only the compressional waves and neglects the possibilities of mode conversion at the fluid–solid interfaces. Under these conditions, the backscattering coefficient is given by the following expression [MOR 86]:

$$\sigma(f) \propto \frac{1}{V} \left| \frac{k_f^2}{4\pi} \iiint_V \gamma(\vec{r}_0) \times e^{-j2\vec{K} \cdot \vec{r}_0} d\vec{r}_0 \right|^2 \quad [29.28]$$

where  $k_f$  is the wavevector in the fluid and  $\vec{K} = -2k_f \vec{z}$ ,  $\vec{z}$  being the unitary vector in the direction of propagation of the incident wave,  $V$  is the scattering volume. Introducing the autocorrelation function of the medium:

$$b_\gamma(\Delta\vec{r}) = \langle \gamma(\vec{r}_1) - \langle \gamma \rangle \rangle \langle \gamma(\vec{r}_2) - \langle \gamma \rangle \rangle \quad [29.29]$$

where  $\Delta\vec{r} = \vec{r}_2 - \vec{r}_1$  represents the vector connecting two points  $\vec{r}_1$  and  $\vec{r}_2$  in the medium, the backscattering coefficient can also be written [MOR 86]:

$$\sigma(f) = \frac{k^4}{16\pi^2 V} \iint_V \langle \gamma^2 \rangle b_\gamma(\Delta\vec{r}) e^{-i\vec{K} \cdot \Delta\vec{r}} dV_1 dV_2 \quad [29.30]$$

where the term  $\langle \gamma^2 \rangle$  describing the root-mean-square fluctuations of the properties of the medium is frequently referred to as acoustic concentration. This parameter describes the “force” with which the medium will scatter the incident wave. Note that, from equation [29.28], the backscattering coefficient is expressed as the spatial Fourier transform of the function  $\gamma(\vec{r})$ . This property is used for the calculation of the backscattering coefficient when the spatial distribution of the fluctuations of acoustic properties is known [PAD 03]. These can be extracted from numerical 3D models of the micro-architecture of the trabecular bone, assuming that the compressibility and the density of the bone are spatially invariant. The 3D image of the micro-architecture is obtained by micro-tomography by synchrotron radiation with a spatial resolution of 10  $\mu\text{m}$  (Figure 29.17). In Figure 29.17 the backscattering coefficient as a function of frequency, predicted from 3D micro-tomographic data (from equation [29.28]), is compared to the experimental data. The good agreement between the predictions and the experiment allows the model of random medium and its assumptions to be validated. In the case of *in vivo* measurements, the micro-architecture and the exact form of the function  $\gamma(\vec{r})$  are not known. The process

then consists of searching an equivalent model of the medium from known closed-form expressions of autocorrelation functions. For example, with a Gaussian autocorrelation function and from equation [29.30], the backscattering coefficient is written [INS 93]:

$$\sigma_b \propto \frac{k^4 \langle \gamma^2 \rangle d^3 (2\pi)^{3/2}}{16\pi^2} e^{-2k^2 d^2} \quad [29.31]$$

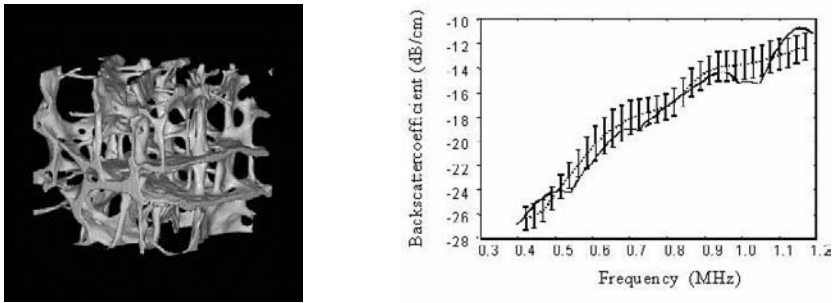


**Figure 29.18.** *Left: 3D reconstruction of micro-architecture (human calcaneum) by micro synchrotron tomography. The backscattering coefficient, obtained by spatial Fourier transform of the image, is in good agreement with the experimental data (average results on 19 samples)*

The interest of expression 29.31 is that, by adjusting the correlation length  $d$ , it is possible to adjust the theoretical and experimental curves of the backscattering coefficient as functions of frequency for each sample. This procedure enables us to estimate the correlation length of the medium, usually considered as an estimator of the size of the scatterers [JEN 04]. The comparison between the correlation lengths and the real sizes of the spans obtained from microtomographic images in Table 29.5 for a set of 19 calcaneum and 37 human femurs shows excellent agreement.

The simulation of the scattering phenomenon is useful to develop a data inversion pattern, aiming at estimating a parameter of osseous micro-architecture.

	Correlation length (data inversion)	Thicknesses of spans (micro-tomography)
Calcaneum (N=19)	$140 \pm 10 \text{ }\mu\text{m}$	$130 \pm 6,5 \text{ }\mu\text{m}$
Femur (N=37)	$134 \pm 15 \text{ }\mu\text{m}$	$132 \pm 12 \text{ }\mu\text{m}$

**Table 29.5.** *Comparison between the correlation lengths and the real sizes of the osseous spans. From [JEN 04]*

### 29.1.3.3. *Poro-elastic theories*

Poro-elastic theories enable us to simulate the behavior of the osseous tissue and are dealt with in Chapter 34.

## 29.2. Bibliography

- [ANT 97] P. Antich, S. Mehta, "Ultrasound critical-angle reflectometry (UCR): a new modality for functional elastometric imaging", *Phys Med Biol.*, 42, 1763–77, 1997
- [ASH 84] R.B. Ahsman, S.C. Cowin, W.C. van Buskirk., J.C. Rice, "A continuous wave technique for the measurement of the elastic properties of cortical bone", *J Biomechanics*, 17, 349–61, 1984
- [BEN 04a] S. Bensamoun, M-C. HoBaTho, S. Luu, J-M, Gherbezza J-F. de Belleval, "Spatial distribution of acoustic and elastic properties of human cortical bone", *J. Biomechanics*, 37(4), 503–10, 2004
- [BEN 04b] S. Bensamoun, J-M. Gherbezza, J-F. de Belleval, M-C. HoBaTho, "Transmission scanning acoustic imaging of human cortical bone and relation with the microstructure", *Clin. Biomechanics*, 19(6), 639–47, 2004
- [BOS 04a] E. Bossy, M. Talmant, P. Laugier, "3-D simulations of ultrasonic axial transmission velocity measurement on cortical bone models", *J Acoust Soc Am*, 115, 2314–2324, 2004
- [BOS 04b] E. Bossy, M. Talmant, F. Peyrin, L. Akrou, P. Cloetens, P. Laugier, "Ultrasound (1 MHz) axial transmission velocity measurements at the radius are sensitive to both mineralization and intracortical porosity: an in vitro study", *J Bone Miner Res.*, 19, 1548–5, 2004.
- [BRI 95] A. Briggs, *Advances in Acoustic Microscopy*, Plenum Press New York, 1995
- [DES 98] B. Destresse, Etude des propriétés mécaniques et morphologiques de l'os spongieux humain, Thesis, Paul Sabatier University, Toulouse III, 1998.
- [FAR 51] J. Faran, "Sound scattering by solid cylinders and spheres", *J Acoust Soc. Am*, 23, 405–18, 1951
- [GOM 02] M.A. Gomez, M. Defontaine, B. Giraudeau, E. Camus, L. Colin, P. Laugier, F. Patat, "In vivo performance of a matrix-based quantitative ultrasound imaging device dedicated to calcaneus investigation", *Ultrasound Med Biol*, 28, 1285–93, 2002
- [HIR 95] S. Hirsekorn, S. Pangraz, G. Weides, W. Arnold, "Measurement of elastic impedance with high spatial resolution using acoustic microscopy", *Applied Physics Letters*, 67, 745–7, 1995
- [HOB 91] M-C. HoBaTho, J.Y. Rho, R.B. Ashman, "Atlas of mechanical properties of human cortical and cancellous bone" in G. Van der Perre, G. Lower, A. Borgwardt (eds.), "In vivo assessment of bone quality by vibration and wave propagation techniques Part II", *Proceedings of the COMAC BME II.26 Meeting*, 45–56, ACCO Publishing, Leuven, 1991

- [HOB 98] M-C. HoBaTho, J.Y. Rho, R.B. Ashman, "Anatomical variation of mechanical properties of cancellous bone in vitro", in G Lowet, P R  gsegger, H Weinans, A Meunier (eds.), *Bone Research in Biomechanics*, IOS Press, 157–73, 1998
- [INS 93] M.F. Insana, D.G. Brown, "Acoustic scattering theory applied to soft biological tissues", in K. K. Shung and G. A. Thieme (eds.), *Ultrasonic Scattering in Biological Tissues*, CRC Press, Boca Raton, Florida, 75–124, 1993
- [JEN 04] F. Jenson, Mod  lisation de la propagation ultrasonore en milieu osseux: application au diagnostic des ost  opathies fragilisantes (ost  oporose), PhD Thesis, University of Paris 7, 2004
- [KAH 04] K.T. Khaw, J. Reeve, R. Luben, S. Bingham, A. Welch, N. Wareham, et al., "Prediction of total and hip fracture risk in men and women by quantitative ultrasound of the calcaneus: EPIC-Norfolk prospective population study", *Lancet*, 363, 197–202, 2004
- [LEF 02] F. Lefebvre, Y. Deblock, P. Campistron, D. Ahite, J.J. Fabre, "Development of a new ultrasonic technique for bone and biomaterials in vitro characterization", *J Biomed Mater Res.*, 63, 441–6, 2002
- [MOR 86] P.M. Morse, K.U. Ingard, *Theoretical Acoustics*, Princeton University Press, Princeton, 1986
- [NIC 02] P.H. Nicholson, P. Moilanen, T. Karkkainen, J. Timonen, S. Cheng, "Guided ultrasonic waves in long bones: modelling, experiment and in vivo application", *Physiol Meas.*, 23(4), 755–68, 2002
- [PAD 03] F Padilla, F Peyrin, P Laugier, "Prediction of backscatter coefficient in trabecular bones using a numerical model of three-dimensional microstructure". *J Acoust Soc Am.*, 113, 1122, 2003
- [RAU 05] K. Raum, I. Legu  rney, F. Chandelier , M. Talmant, A. Sa  ed, F. Peyrin, P. Laugier, "Spatially resolved elastic stiffness mapping in bone – Part I: Assessment of structural and tissue properties with SAM and SR-  CT", submitted to *J Biomechanics*, March 2005
- [ROU 01] C. Roux, V. Roberjot, R. Porcher, S. Kolta, M. Dougados, P. Laugier, "Ultrasonic backscatter and transmission parameters at the os calcis in postmenopausal osteoporosis", *J Bone Miner Res.*, 16, 1353–62, 2001
- [WEA 99] K.A. Wear, "Frequency dependence of ultrasonic backscatter from human trabecular bone: theory and experiment", *J Acoust Soc Am.*, 106, 3659–64., 1999
- [YOO 76] H.S. Yoon, J.L. Katz, "Ultrasonic wave propagation in human cortical bone. Theoretical considerations for hexagonal symmetry", *J Biomechanics*, 9, 407–12, 1976

## Chapter 30

# Medical Ultrasonography

### 30.1. Introduction

#### **30.1.1. *Principles, technology, acquisitions and parameters of influence [CLA 02], [WHI 99], [RIZ 99], [FOS 00], [BER 99], [OND 05]***

Ultrasound imaging is now widely used because of its non-invasive nature, its low cost, and its accessibility in most imaging centers and for almost all human organs. Recent progress has further strengthened its diagnostic nature and it is now open to therapeutic applications. It is therefore essential to understand the basics and principles of operating before seeing the current applications.

##### 30.1.1.1. *Ultrasonic frequency*

The ultrasonic frequency is defined as the vibration frequency of the piezoelectric ceramic emitting and receiving ultrasound. This frequency is characteristic of the probe used. This ceramic has the property of expanding and contracting under the influence of an electrical signal applied on both sides of the ceramic (emission) or under the influence of an incident ultrasonic wave (reception).

At the emission, this series of compressions and expansions generates a longitudinal pressure wave that is transmitted to the surrounding medium and propagates (ultrasonic wave). At the reception, the incident ultrasonic wave distorts

the ceramics; these distortions yield a voltage recorded by the electronic circuit of the assembly.

In medical ultrasound, people use successive transmitted pulses. Under the influence of each electrical pulse, the probe “resonates” at its own frequency (resonance frequency).

#### 30.1.1.2. *The resolution*

Equipment resolution is defined as the smallest distance between two targets ( $\delta$ ) for which the corresponding echoes can still be distinguished. This smallest distance is of the order of magnitude of the ultrasonic wavelength  $\lambda$ . But  $\lambda$  is inversely proportional to the frequency  $f$  ( $c$ : ultrasound velocity in the human body, i.e. 1540 m / s).

$$\delta \cong \lambda = (c/f)$$

So, to achieve a better resolution (smaller  $\delta$ ), we must reduce  $\lambda$ , which is obtained using a higher frequency. A probe of higher frequency can theoretically yield a better resolution. In ultrasound, we actually define three resolutions: the axial, lateral and azimuthal resolutions.

The axial resolution is the shortest distance between two targets, located in the direction of the beam that can be separated on the image. This resolution is linked to the ultrasound pulse duration: a very short pulse helps to separate two targets easily, while a longer pulse gives long temporal echoes that overlap (in this case, the two pulses reflected by the two targets can not be separated in time). It is also dependent on the ultrasound bandwidth used: a narrow bandwidth leads to a deterioration of the resolution, while a large bandwidth improves it. In practice, the ultrasonic axial resolution is very good and we easily get resolutions of the order of the millimeter, for a frequency of 3.5 MHz.

The lateral resolution characterizes the splitting power in the direction perpendicular to the beam propagation, i.e. between two targets located at the same distance from the probe, but on both sides of the shooting axis in the probe plane. This resolution is linked to the aperture of the ultrasound beam and to the dispersion of this beam. A greater aperture promotes this lateral resolution. In an ultrasound system, the lateral resolution is usually worse than the axial resolution.

To focus the beam, we can either use a ceramic shaped as a ball cup, or place in front of the ceramic an “acoustic lens”, or use purely electronic processes. When the focus is well suited, the width of the beam  $\delta$  is given by:

$$\delta \equiv \lambda(F/D)$$

where  $D$  is the disc diameter and  $F$  the focal distance.

Finally, the azimuthal resolution corresponds to the resolution in the transverse plane. It depends on the height of the ceramics used and the ability to focus in the transverse plane. The use of adapted lenses allows this resolution to be improved, but with limits in depth. The use of annular arrays, of arrays of type 1.5D, or lenses called “Hanafy lenses”, will improve this resolution significantly.

### 30.1.1.3. *The exploration depth*

For the user, this corresponds to the depth to which we probe to obtain echoes inside the body. This exploration depth is related to the depth attenuation of the ultrasound beam (resulting from ultrasound–tissue interactions, see Figure 30.1), that mainly follows an exponential law with therefore no theoretical limits. In fact, beyond a certain depth, the ultrasound beam simply becomes too weak, such that echoes can no longer be detected.

The decreasing coefficient of the exponential law is proportional to the frequency following the formula below:

$$I = I_0 \exp[-(\beta f)x]$$

The attenuation increases rapidly with the frequency  $f$ , the value of  $\beta$  being around 1 dB / cm/ MHz. As the attenuation increases with the frequency, in medical ultrasound we have to deal with a compromise between a high frequency (for a good resolution) and a low frequency (to get a good “penetration”).

This is the reason why we use waves located in a fairly limited frequency range, from 2 to 15 MHz, for medical applications. Depending on the depth of the organ to be examined, we can use the maximum frequency that is allowed by attenuation in tissues. Recent years have seen a trend of increasing ultrasonic frequencies used for medical uses, because of constant improvements of signal processing methods.

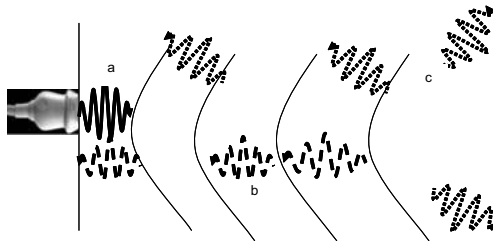


**Figure 30.1.** *Ultrasound – tissues interactions with propagation, (a) reflection, (b) on the interfaces, and (c) waves diffusion*

#### 30.1.1.4. *Gain control*

Because of ultrasound beam attenuation inside the body, the same reflecting structure will give an echo whose magnitude depends on the depth at which it is located. If this structure is several centimeters deep, the echo is much lower. But for a good understanding of images, it is necessary to present echoes from the same structures in the same way, whatever their position in depth. This is done by a variable amplification of echoes, which takes into account the depth (gain control). The purpose of this amplification is to compensate for the attenuation, the gain control setting is available to the operator because the attenuation is variable depending on the subjects and even on the organs examined.

A good adjustment of the gain is essential to show the examined structures on the screen properly. This results in the definition of different settings:

- the general gain: it acts the same way on all echoes, whatever the depth. It is generally used to “adapt” the amplitudes of the echoes, such that 1) we do not obtain a black screen (echoes are too low) and 2) the signals are not completely saturated (echoes are too strong). It is expressed in dB;
- the TGC (time gain control) helps to compensate for the attenuation in depth by using a larger gain for echoes coming from a greater depth (these echoes are more attenuated). This compensation actually achieves a curve whose parameters will fit the patient.

New systems of electronic compensation have recently been proposed, allowing an automatic adjustment for the gain in both directions of ultrasonic wave propagation. These systems allow the gains to be equalized, depending on the depth and taking into account the echogenicity breakdown of the imaged tissue.

#### 30.1.1.5. *Logarithmic compression of the signal*

The gray scale used to represent ultrasound interfaces must allow the strong echoes from reflecting interfaces (bones, gas, etc.) and also the very low echoes from some solid tissues, to be seen simultaneously without presenting false information corresponding to the acoustic or electronic “noise”. However, between the highest and the lowest levels which are useful for diagnosis, there is an amplitude ratio of at least 100 (40 dB), even after the correction of the depth attenuation. This objective is made possible by using a logarithmic “compression” that respects the large echoes amplitudes, to provide the best image quality, where the low and strong echoes are presented simultaneously and in a balanced way. The gap between the lowest and highest gray levels is called the dynamic of the image, and it allows an identification of the different reflective structures.



### 30.1.1.6. *The side functions*

These are additional opportunities to facilitate the use of the devices that current electronics allows us to achieve easily (Figure 30.2).

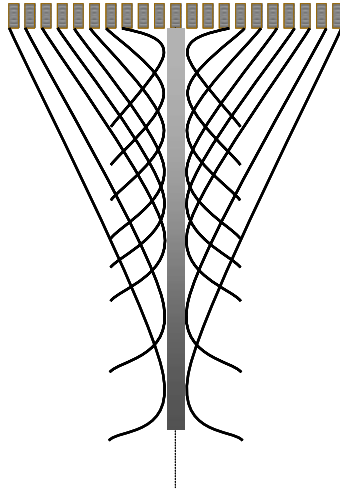


**Figure 30.2.** *Pursuit focus in reception, resulting in some homogeneity of the image in depth*

The zoom: this term is used to designate the various expansions of the area explored on the screen. In general, the choice of the expansion is done before the image is placed in memory (zoom during writing), but on more sophisticated devices it can be done after setting memory (zoom during reading). Some approaches are based on a different management of the ultrasound beam and are not only based on image processing.

The post processing: this term designates the changes that can be applied to the image once it is stored in memory; they essentially consist of a change of the values of gray levels to either enhance or reduce the weakest echoes.

Similarly, an electronic measurement system can be drawn on the image. It shows the distance between two points on the image, directly in millimeters, taking into account the propagation speed of sound, and of course also the current expansion coefficient.

In conclusion, a number of parameters are essential to the creation of an ultrasound image of good quality; these parameters have to be as constant as possible during the repetition of examinations. The current devices include the ability to save all settings (presets), allowing (during practitioner change or after a

power failure) to immediately find the settings considered as optimal by these practitioners.

### **30.1.2. Ultrasound modes**

#### **30.1.2.1. “Real-time” ultrasound B-mode**

The displacement of the ultrasound beam in electronic scanning is done automatically and quickly, which produces each image in a fraction of a second, authorizing the dynamic monitoring of movements of the structures studied.

In all cases, on the display screen, the presentation of echoes is made in “B-mode” (bright mode), meaning that the echoes are represented at a location corresponding to their depth, but their amplitude is used to modulate the brightness of the point, depending on the interaction between the ultrasound beam and the interface encountered.

The various scanning processes in real time are as follows.

##### **30.1.2.1.1. Mechanical scanning**

The probe displacement is provided by a motor. In this case, the probe turns or oscillates around an axis and the ultrasonic lines scan an angular area whose center is the rotation axis of the probe: it is mechanical sector scanning. This mode is used less than previously, due to electronic progress which has allowed better management of ultrasonic lines.

Another method of mechanical sector scanning is to use a fixed transducer, which facilitates the problem of electrical connections, and an acoustic oscillating mirror which deviates the beam, allowing a similar scan of the angular sector. This mode is often used for high-frequency intravascular probes.

In all these devices, a part of the system (the transducer or the mirror) is moving very fast and can not be in direct contact with the skin: the “head” of the probe involving the transducer(s) is a hermetic enclosure filled with a liquid ensuring the transmission of ultrasound to the front of the probe, which is motionless in contact with the skin.

##### **30.1.2.1.2. Linear or convex electronic scanning**

Instead of using a single transducer that is moved by a mechanical process, there may be a series of immobile juxtaposed transducers, which are excited one after the other by adequate electronics to provide the successive lines of the image (linear electronic scanning Figure 30.3). Such linear transducer “sweeps” provide images

formed by parallel or nearly parallel lines depending on the shape of the probe, rectangular or convex.

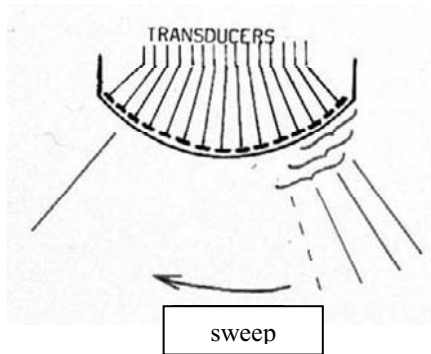


**Figure 30.3.** *Principle of electronic scanning with simultaneous activation of several ceramics in transmission and reception, and then activation of the following group*

#### 30.1.2.1.3. Electronic sector scanning

The term “*phased array*” refers to a process of electronic sector scanning from a small sweep of transducers. Unlike linear scanning where, for each shot, we use only a small group of transducers which is shifted step-by-step during the scan, in the case of the “*phased array*”, every transducer is used to build each line of the image. An electronic system can guide the ultrasound beam in an oblique direction in relation to the axis.

The electronic modification of the delay law from one shot to another allows the shooting angle to change, and so to scan an angular sector, the probe being stationary.

#### 30.1.2.2. The *TM mode* (time motion)

This mode is used to record the movement of structures located on an exploration line. It is practiced either with a probe with a single shooting line, or with a probe with multiple lines, by choosing one of the lines of the image. By convention, as in imaging, the echoes of the explored line are represented vertically, the surface being at the top of the screen, the depth at the bottom. The echoes are viewed in B mode (brightness).

To record the movements of structures located on this line, we transversally scroll the plotting on the screen or on paper, the probe remaining motionless in principle. This gives curves that are characteristic of the movements of structures

located on this shooting line. The vertical scale represents the depth (often marked by a point positioned every 0.5 s). One of the advantages of this method is its ability to store fast kinetic motion with great precision.

### 30.1.2.3. *3D or 4D exploration*

The development of probes specific for the exploration of volumes has opened the way for three-dimensional exploration, also taking into account the temporal variable for 4D imaging. Two approaches are emerging: an approach based on a monodimensional probe associated with a system of motorized travel, and an approach based on sensors of matrix type. The first has been developed significantly in recent years in obstetric imaging. A system of mechanical mobilization ensures a scanning of the volume at a rate less than 10 volumes per second. This imaging is particularly suited for a surface imaging, i.e. with the surface of the volume scrutinized. The possibility of cuts in the volume is also possible, but with limits in terms of resolution. The matrix probes are less advanced, especially in radiology applications. Their scope concerns cardiac ultrasound with a marked contribution in the field of the study of ventricular volumes and exploration of valvular disease.

### 30.1.3. *Vascular study by ultrasonic Doppler*

#### 30.1.3.1. *Principles of the Doppler effect*

When an ultrasound beam (US), emitted by a source, goes through biological tissues, it meets a number of targets, or fixed interfaces. The frequency reflected ( $F_r$ ) by these fixed targets is identical to the emitted frequency ( $F_o$ ). On the other hand, if the target moves, as it is the case for red cells of the circulating blood, there is a change in the frequency of the reflected beam:

$$F_r = F_o \pm \Delta F$$

The frequency difference  $\Delta F$ , called *Doppler frequency*, is positive if the target is moving closer to the source, and negative if it is moving away. In vascular exploration, as a result of the ultrasonic frequencies used, the value of  $\Delta F$  is between 50 Hz and 20 kHz, which corresponds to a range of frequencies perceptible to the human ear.

$$\Delta F = 2V \cdot F_o / c$$

where  $V$  is the moving velocity of the target and  $c$  the US velocity in biological tissues (constant = 1540 m / s). If the target is moving along a different axis,

$$v = V \cdot \cos\theta$$

where  $\theta$  is the angle between the beam axis and the displacement direction of the target, also called Doppler angle. Then, the value of the Doppler frequency becomes:

$$\Delta F = 2V \cdot F_o \cdot \cos \theta / c.$$

We understand here that  $\Delta F$  decreases when the Doppler angle increases (the value of  $\cos \theta$  approaching zero), and is zero when the angle reaches  $90^\circ$  ( $\cos 90^\circ = 0$ ). The calculation of the circulatory velocity therefore requires the knowledge of the Doppler angle:

$$V = \Delta F \cdot c / 2F_o \cdot \cos \theta.$$

In the absence of knowledge of the incidence angle, the target move is determined in terms of frequency shift ( $\Delta F$ , measured in kHz). This frequency shift depends on  $V \cdot \cos \theta$ , it varies, for an equal moving velocity, according to the value of  $\theta$ . The measurement of the actual circulatory velocity (in cm/s) requires the knowledge of the Doppler angle.

#### 30.1.3.2. *Utilization mode of the Doppler*

The Doppler effect can be used in clinical practice in two modes: the continuous mode and the pulsed mode. The two-dimensional Doppler or color Doppler is based on the principle of the pulsed Doppler, but the signal processing techniques are different.

##### 30.1.3.2.1. The continuous Doppler

In a continuous Doppler, there are two crystals within the same sensor: one emits an ultrasonic beam on a continuous basis, and the other one receives the reflected signal, also on a continuous basis (Figure 30.4). The device makes the comparison of the two frequencies  $F_o$  and  $F_r$  thanks to a demodulator that extracts, on a continuous basis, the Doppler frequency. These are lightweight and compact devices, widely used in the study of superficial vessels.

The benefits of continuous Doppler are as follows: its high sensitivity of detecting slow flows, its low acoustic power, the absence of limit for determining the fast velocities and its low cost. However, it also has some limits: the absence of spatial resolution because the received signal is independent of the depth, the measured Doppler frequency is the resultant of the Doppler frequencies extracted from the total signal, that results from an average of the different signals coming from all the vessels crossed.

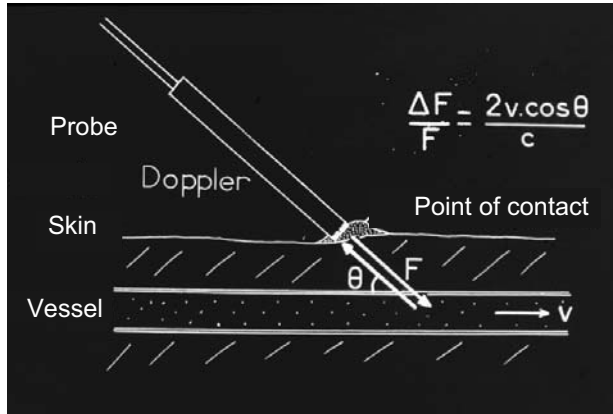


**Figure 30.4.** Principle of the continuous Doppler effect with implementation of a pencil probe with two crystals (emitting and receiving)

#### 30.1.3.2.2. The pulsed Doppler

The pulsed Doppler system is characterized by a single crystal probe which alternately emits an ultrasonic beam and receives the reflected beam. The time between two pulses determines the repetition frequency, also called PRF (Pulse Repetition Frequency). Between these two pulses, the reflected signal is analyzed for a very short time, the Doppler sampling gate. The period between the end of the pulse and the beginning of the Doppler sampling gate determines the selected depth of analysis of the Doppler signal (that is the depth of the sampling volume). The time of analysis of the reflected signal, i.e. the width of the Doppler sampling gate, determines the size of the sampling volume.

The limits of the pulsed Doppler are as follows: its lower sensitivity to detect very slow flows, the increased acoustic power that is necessary and the possible ambiguities in frequency (or aliasing) and in depth. Indeed, according to Shannon's theorem, the time between two impulses will limit the exploration depth ( $d_{\max} = c / 2Fr$ ), and also the maximum frequency detectable without folding artefact ( $F_{\max} = Fr / 2$ ).

#### 30.1.3.2.3. Duplex systems

Duplex systems allow the alternate acquisition of an ultrasound image and the Doppler signal with the same probe, often combining emitting frequencies: we often use a frequency lower than the frequency required for the acquisition of the image in Doppler techniques.

#### 30.1.3.2.4. Bidimensional Doppler or color Doppler

The color Doppler allows the analysis of the Doppler signal in a plane, and this almost simultaneously at all points of this plane. It could be compared to a pulsed multi-depth and multi-line Doppler system. In fact, through a signal processing technique of *autocorrelation* type, it is possible to obtain the Doppler information on the entire length of a line, after two pulses, analyzing changes in the phase between the two reflected signals. However, the low signal-to-noise ratio imposes the repetition of these impulses for each sampled lines, decreasing the frame rate. This process allows the analysis, at a set of sampling volumes located along a shooting line, the three parameters of the ultrasonic signal, namely: the *amplitude*, which allows the reconstruction of the grayscale image, the *phase*, that determines the movement direction of circulating structures, and the *Doppler frequency*, which reflects the circulatory velocity.

The resolution of the color image depends on the size of the sampling volume on each color line and on the density of the color lines sampled among all ultrasound lines of the black and white image. The signal to noise ratio (which determines the quality of the Doppler information) depends on the number of shootings per line.

#### 30.1.3.3. *Signal analysis*

The signal may be analyzed in four forms: an audible signal, an analog plot, a frequency spectrum or a color mapping. The simplest signal processing is actually by audible sound, which allows us to recognize the type of vessel scrutinized instantly, and also to recognize the type of flow, authorizing the identification of vascular stenosis, for example.

##### 30.1.3.3.1. The analog plot

This is the simplest of these processes: using a zero-detection technique, it helps to restore a curve of Doppler frequency extracted by the real time device. However, this curve corresponds to the average of the sampled Doppler frequencies. This process therefore gives no information on the profile of the flow, and in particular on the dispersion of circulatory velocities inside the vessel. This plotting, allowing the detection of anomalies, but not their characterization, is no longer used because of the limitations in hemodynamic information presented.

##### 30.1.3.3.2. The frequency spectrum

The advantage of the frequency spectrum is the ability to restore, in real time, the range of frequencies contained in the Doppler signal, which reflects the range of velocities and the content of each frequency band (group of red blood cells circulating at the same speed) in the vessel. Current calculation performances permit the achievement of *Fast Fourier Transforms (FFT)* adapted to real time.

### 30.1.3.3. Color coding

This latter mode of ultrasound signal processing (in Color Velocity Imaging as a color Doppler or Dynamic Flow) allows us to directly view, on the image, the presence of a flow, its direction and its relative average velocity. The direction of flow compared to the probe is determined by an arbitrary color (by convention, red for the flows which are directed towards the probe and blue for those which go away). Each of these colors will be more saturated towards white if the Doppler frequency increases. Some alternatives have been proposed with the presentation of the power of the Doppler signal: thus the Doppler power presents the information using a single-color mode, with the advantage that it does not depend on the incidence angle, but also does not provide any information on the associated velocity. A combination of power and velocity information is used in the convergence mode.

### 30.1.4. *Nonlinear ultrasound imaging*

Recently, nonlinear effects have been taken into account in ultrasound imaging and this totally changes the ultrasound exploration of tissue itself and microcirculation with the introduction of ultrasound contrast agents [BUR 96], [FRE 98], [TRA 99], [LAW 85], [STA 86], [FIL 99], [WAR 97], [COR 01], [HAR 01], [DAW 99], [MEU 03]. This concept is based on an old observation made by Rayleigh, who was the first to describe the nonlinear response of gaseous bubbles in an acoustic field. This observation led to the observation of the presence of high harmonics of the incident fundamental frequency in the backscattered signal after interaction with a bubble. Taking into account the frequencies of harmonics in ultrasound signal processing has opened the way for a new ultrasound imaging: new nonlinear imaging techniques, with major implications in current and future practice.

#### 30.1.4.1. *Physical basis*

Tissues and mainly water, outside the presence of contrast products, are nonlinear media, with well established nonlinear properties, as demonstrated by P. Burns in 1996 [BUR 96].

When an ultrasonic wave, with a given fundamental frequency  $\omega$  (harmonic 0), goes through a tissue, the reflected signal obviously contains a component of significant amplitude at the same frequency  $\omega$ , but also other components with an amplitude different to zero at frequency multiples of  $\omega$ :  $2\omega$ ,  $3\omega$ , etc. and even also at frequencies lower than  $\omega$ , called subharmonics, such as  $\omega/2$ ,  $\omega/4$ .



The signals reflected at the fundamental frequency result from interfaces and tissue inhomogeneities (conventional ultrasound imaging), while the harmonic signals are the consequence of wave propagation in the tissue.

In a tissue with nonlinear properties, the propagation speed of the sound wave is not constant as in a linear medium (Figure 30.5). This speed is a function of the moving velocity of the medium elements that transmit the disturbance, which can be written as  $c = c_0 + \beta\mu$  where  $\mu$  is the speed of the element and  $\beta$  the nonlinearity coefficient of the medium [BUR 96]. At every moment, the positive peaks of the wave, due to the compression of the tissue at this level, propagates faster than the negative peaks, where there is a tissue relaxation.

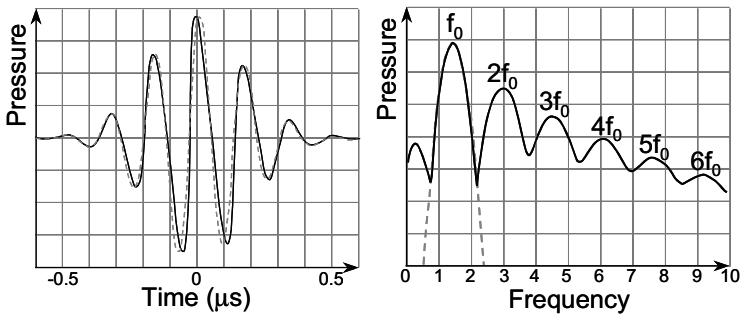


**Figure 30.5.** Principle of the generation of harmonics in tissue. With a progressive distortion (continuous curve) of the initial pulse (dotted curve) depending on the propagation of the pulse in depth, emergence of multiple harmonics of the fundamental frequency  $f_0$

The microbubbles submitted to an ultrasound field behave more like scatterers, whose effect will be maximized if the bubbles are in a liquid and if the ultrasound wavelength is larger than the diameter of the bubble. Responses of ultrasound contrast products to the ultrasound field are heavily dependent on the inner wall and the gas filling the microbubble, whose resonant frequency is in the range of ultrasonic frequencies used in the medical field. However, the average size of the microbubbles and the distribution around this average have a significant influence on the resonance frequency, which is heavily influenced by the greatest size of bubbles in the sample, tending to decrease rapidly with the increase of size. The initial calibration of bubbles is therefore a crucial element, even if changes occur within the vascular compartment. If we consider a stable bubble without ultrasound field, it is in balance under the difference of pressure on both sides of the surface, but also subject to changes in vascular pressure during the cardiac cycle. In the presence of an ultrasound field, the microbubble will tend to increase in size. When the incident ultrasound frequency is close to the resonance frequency of the microbubble, bubbles oscillate around their equilibrium position and therefore

increase their back-scattered energy. The use of moderate acoustic power (about 100 mW/cm<sup>2</sup>) corresponding, according to the machines, to a mechanical index of approximately 0.7, makes these oscillations asymmetric. The temporal and spatial differences between the compression and expansion phases will be at the origin of harmonic frequencies. The presence of an envelope modifies the response of the bubble to the ultrasound field depending on its rigidity (taking into account Young's modulus). The radius change of an ideal non-encapsulated gas bubble is expressed by the Rayleigh–Plesset equation:

$$\rho R R'' + \frac{3}{2} \rho R'^2 = p_{go} \frac{(R_0)^{3\Gamma}}{(R)} + p_v - p_{lo} - \frac{2\sigma}{R} - \delta_t \omega \rho R R' - p_{ac}(t)$$

$$p_{go} = \frac{2\sigma}{R_0} + p_{lo} - p_v$$

$$\delta_t = \delta_{rad} + \delta_{vis} + \delta_{th} + \delta_f$$

$$\delta_f = \frac{Sf}{m\omega}$$

with:

$R$  = instantaneous radius of the microbubble;  $R_0$  = initial radius of the microbubble;

$R'$  and  $R''$  = first and second temporal derivatives of the instantaneous radius of the microbubble;

$\rho$  = density of the surrounding medium;

$p_{go}$  = initial pressure of the gas in the microbubble;

$\Gamma$  = polytropic exponent of the gas;

$p_v$  = vaporization pressure;

$\sigma$  = surface tension coefficient;

$\delta_t$  = total absorption constant;

$\omega$  = angular frequency of the incident acoustic field;

$p_{ac}(t)$  = acoustic pressure as a function of time;

$\delta_{rad}$  = coefficient of energy loss due to radiation;

$\delta_{th}$  = coefficient of energy loss due to heat conduction;

$\delta_{vis}$  = coefficient of energy loss due to the viscosity of the liquid medium;

$\delta_f$  = coefficient of energy loss due to the inner friction forces (inside the inner wall);

$S_f$  = friction parameter of the inner wall;

$m$  = effective mass of the bubble–liquid system.

This equation accounts for the asymmetric variations of the microbubble radius, which is at the origin of the harmonic frequencies detected.

#### 30.1.4.2. *Impact on the ultrasound image [FRE 98], [TRA 99]*

As a result of the generation of harmonics during the propagation of ultrasound waves, the amplitude of the signal increases gradually with the distance from the sensor, until a maximum distance where too strong an absorption of the fundamental frequency leads to a decrease of the response of the tissue. However, the amplitude of harmonics signals is still lower than that of the fundamental frequency. If we ignore the attenuation of the induced wave, the amplitude  $P_2$  of the second harmonic at a distance  $d$  on the propagation axis can be provided by the following equation:

$$P_2 = \left(1 + \frac{B}{2A}\right) \frac{P_o^2 \Pi F}{C_0^3 \rho} d$$

with  $B/A$ : nonlinear constant of the tissue;

$F$  : fundamental frequency;

$\rho$  : tissue density;

$C_0$  : velocity of the negative peak of the wave;

$D$  : distance considered;

$P_o$  : acoustic pressure of the fundamental wave.

The fact that there is almost no nonlinear response from the superficial tissue contributes to the low deterioration of the image, while in linear imaging, the presence of fat, the superficial skin layers, by inhomogenities, and the phase aberrations are among the main causes of distortion of the ultrasonic wave. The disturbance due to the side lobes is significantly reduced in comparison with the fundamental imaging, because of the weakness of the generated harmonic signals. This is due to the low participation of superficial tissues that have an unfocusing effect. The fundamental frequencies on the axis (maximum of energy) generate more harmonics, while the scattered waves, the side lobes and elevation produce harmonics waves of low intensity, which can be considered as non-detectable.

The preponderance of harmonics in the center of the ultrasound beam, where the acoustic pressure is maximal, reflects some autofocalization improving the

resolution on the beam axis. These properties lead to an improvement of the lateral resolution. The higher frequency of the harmonic signals compared to the fundamental helps to improve the axial resolution by reducing the wavelength. The use of low-emitting frequencies leads to a slight deterioration of the axial resolution, which can be regarded as offset by the improvement of the contrast resolution.

The amplitude of acoustic waves, after posterior reinforcements (higher signals behind fluid structures by non-attenuation of the ultrasound beam) or comet tails (reinforcement of the beam behind small size air-content structures) is doubled in harmonic imaging compared to fundamental imaging, enhancing the diagnosis quality.

The acoustic power is not different in harmonic imaging from fundamental imaging, as the generation of harmonic signals depends on the propagation of the fundamental signal in tissues.

In the specific case of microbubbles [COR 01], [HAR 01], [DAW 99], [MEU 03], taking into account the attenuation in depth of the emitted acoustic power explains the differences in the harmonic response in depth because of interactions in the superficial area, resulting in a change of the acoustic power received at one point, and depending on the position of microbubbles with respect to the focal point of the probe.

#### 30.1.4.3. *Image build-up*

Taking into account the harmonic and subharmonic signals in building the image requires the use of broadband sensors, with a frequency range including the fundamental and harmonic frequencies we want to use. For example, for a fundamental frequency of 2 MHz, taking into account the subharmonic 1 MHz and the harmonic 4 MHz imposes a frequency band of 1 to 4 MHz. This is entirely feasible only with currently available sensors that have a wide frequency range, as a result of new materials used.

The difficulty in forming the image signals from the harmonic signals lies in the absence of reciprocal disturbance between the fundamental frequency and harmonic or subharmonic frequencies. We need a perfect control of these frequency ranges during transmission and reception.

Two major principles are used: frequency filtering and phase reversal imaging.

Frequency filtering (Figure 30.5) is based on a completely controlled emission in the fundamental frequency range, and also a perfectly controlled reception in the considered harmonic frequency range. This is achieved by controlling the form of the ultrasonic pulse during the emission using a low-pass filter which does not allow

the emission of excessively high frequencies; similarly, the reception chain contains a high-pass filter which cuts the fundamental frequency range. The difficulty with this method is in the form of the pulse and the cut-off frequencies of the filter, which must avoid losing too much signal and also avoid joint disturbances of the frequency ranges. The advantage is a no loss frame rate.

Pulse inversion imaging (Figure 30.6) is based on the difference of responses from tissues at high and low acoustic pressure. The emission on the same line of 2 almost simultaneous pulses, but with an opposed phase, leads to the reception of different signals, depending on the linear or nonlinear response from the tissues or the bubbles. The linear response leads to two reflected signals with the same shape but with a phase shift of  $180^\circ$ ; the sum of these two reflected signals is equal to zero. By contrast, the nonlinear response of tissues to these two impulses is made of two non-symmetrical signals, whose sum is not zero and proportional to the nonlinear properties of the considered tissue. The limits of this sequence are the sensitivity to the movements of the tissues between the two impulses and the loss of frame rate.

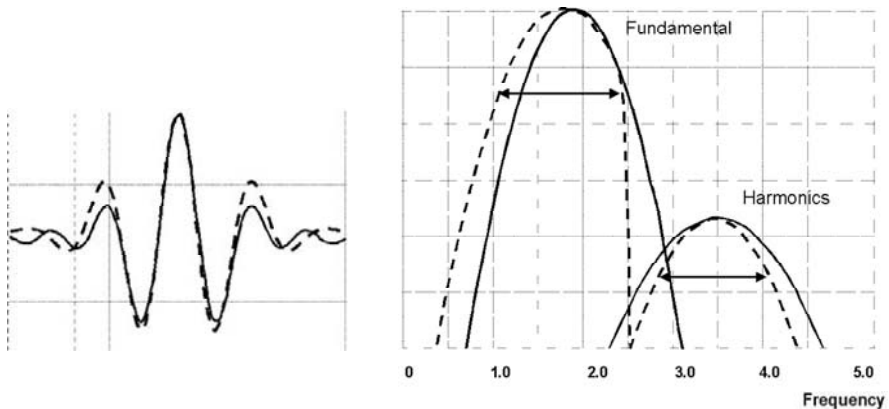


**Figure 30.6.** Principle of the Precise Pulse Shaping (Acuson-Siemens). The pulse normally transmitted (solid line) is slightly modified (dotted line), to separate the fundamental frequency band from the harmonic frequencies band better

Many variations of pulse inversion imaging technique have been proposed such as the emission of phase-shifted pulses on two adjacent lines (authorizing to maintain a high frame rate), the introduction of an amplitude modulation, the use of more than two pulses; the common objective of these methods is to improve the nonlinear information and to eliminate the linear information.

### 30.1.4.4. Clinical applications

#### 30.1.4.4.1. Non-destructive nonlinear imaging

In the absence of contrast products, the nonlinear properties of tissues are used to obtain images with an increased contrast for a better diagnostic quality. In the case of tissues, the use of high MI (Mechanical Index) is essential because it is only for those values that the nonlinear information is important. All organs are concerned: the brain in trans-skull imaging, heart, the abdomen (liver, kidney, pancreas), the pelvis, the fetus (Figure 30.7). At this time, surface imaging applications have been less developed. These applications, that everyone has seen in daily use, have been the object of various articles confirming the contribution of information for better patient care. The clarity of images obtained at great depths of exploration permits in a significant number of cases the avoidance of using invasive body imaging (transoesophageal or transvaginal) to detect anomalies.

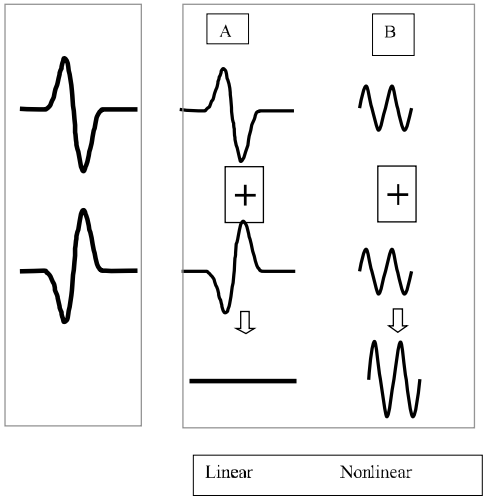


**Figure 30.7.** *Pulse Inversion Mode (ATL-Philips, Siemens, Toshiba). A: By the sum of two consecutive echoes with a reversed phase, the signal resulting from fundamental echoes is zero. B: In contrast, consecutive echoes from nonlinear resonance targets are summed, giving a signal strengthened in harmonics*

In the presence of contrast products, the use of low ( $MI \approx 0.7$ ) or very low ( $MI < 0.2$ ) mechanical index does best from nonlinear properties by limiting the destruction of microbubbles. The duration of the examination depends almost exclusively on the natural lifetime of the microbubbles in the blood compartment. The nonlinear response depends on the characteristics of the gas used, on the inner

wall of the bubble and on the interaction of the ultrasonic pulse with the bubble. Thus, for different products, the nonlinear response will not be identical for the same values of MI. This helps to achieve real-time dynamic ultrasound angiography with a high contrast [LEE 03], [QUA 02], [ALB 03], [ALB 04].

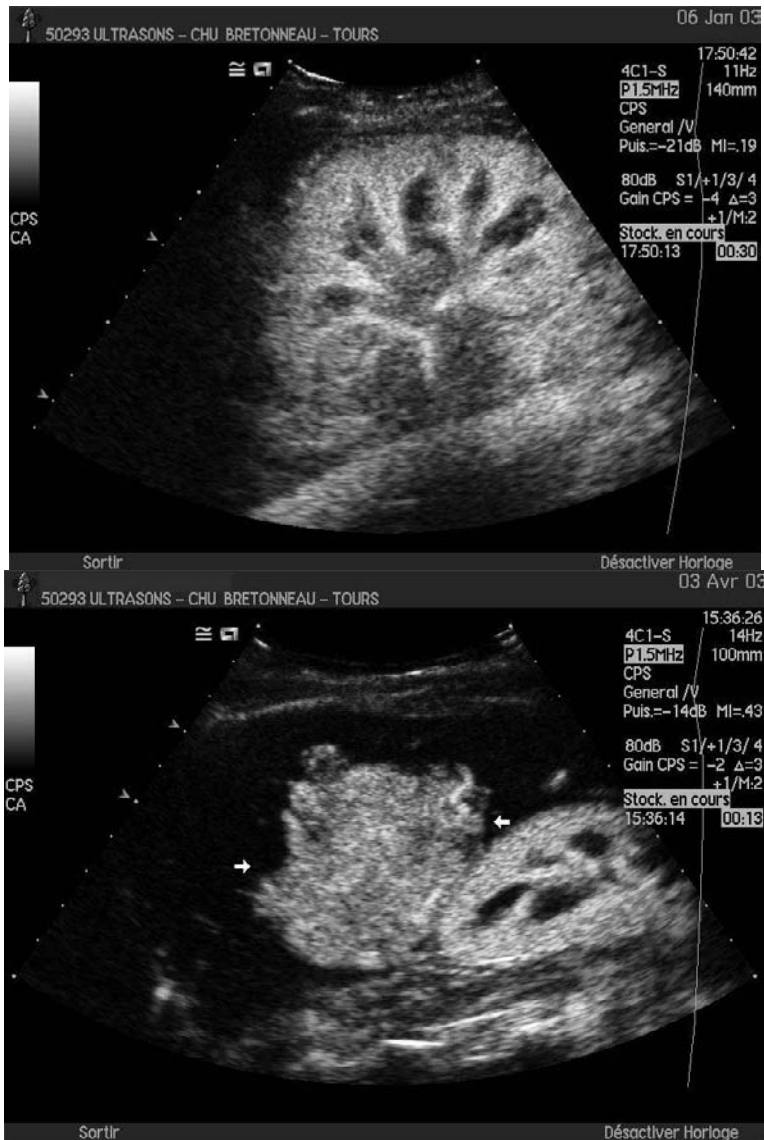


**Figure 30.8.** *Ultrasound images after injection of contrast ultrasound products for the study of renal perfusion (top) and a focal nodular hyperplasia (bottom)*

#### 30.1.4.4.2. Destructive nonlinear imaging

The use of high acoustic powers ( $MI \geq 1$ ) leads to the rupture of the microbubbles' inner wall, producing a signal with strong nonlinear characteristics. This signal will be easily detected, with the disadvantage of its fleeting characteristic as the microbubbles have been destroyed. This has been specially developed for the detection of intra-hepatic lesions in B imaging with a sensitivity that is quite comparable to the one of the spiral scanner. The destruction of bubbles by an ultrasonic pulse has opened the way for research in the determination of blood flow through the detection of vascular filling time after a pulse.

### 30.1.5. *Medical applications of ultrasound*

As noted at the beginning of this chapter, medical applications affect all organs. We will not give details on all the offered opportunities, especially pulmonary, lymphatic, pancreatic or cutaneous. The summary presented aims to attract the reader to the diversity of opportunities.

#### 30.1.5.1. *Cardiac imaging (Figure 30.9)*

Cardiac exploration is usually carried out externally, but may also sometimes require using the oesophageal tract for greater definition of cardiac structures. This may even be supplemented by an invasive exploration of the coronary arteries by Doppler ultrasound. The ultrasound exploration affects the heart morphology (inner walls, ventricles and valves) as much as the cardiac function, with the study of the kinetics of cardiac inner walls or valves (sometimes requiring the use of advanced signal processing softwares), and of the heart performance (ejection volume). The introduction of contrast agents, and now three-dimensional imaging, changes the study of cardiac parameters, improving the quality of information provided, whether or not under a pharmacological test of stimulation (stress echo).



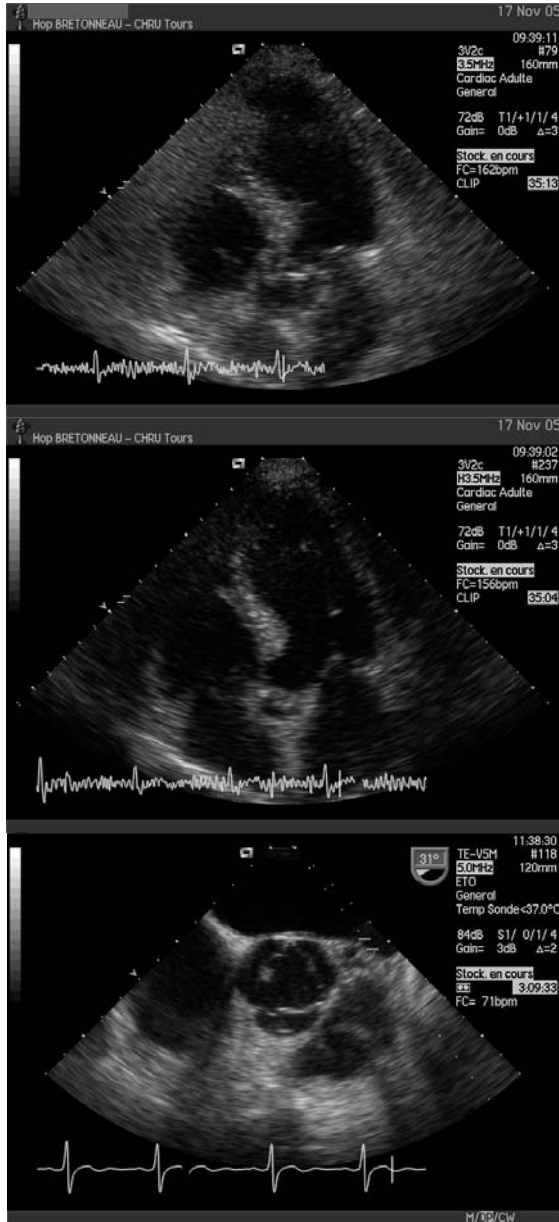


**Figure 30.9.** External ultrasound image of the heart, called “transthoracic”, by fundamental imaging (a), nonlinear imaging (b) and transoesophageal (c). Note the increase in contrast in nonlinear imaging and the improvement of details by the transesophageal method

30.1.5.2. *Hepatic imaging (Figure 30.10)*

Ultrasound exploration of the liver is currently the primary non-cardiac indication of ultrasound imaging. Indeed, the easy access to the liver and the ability of viewing differences in acoustic impedance in an easy way represents an essential tool to the discovery of intra-parenchymal lesions, for which the search for specific diagnostic criteria will lead to clarify the affection involved. The possibility of repeating ultrasound examinations is also a great advantage. More recently, the consideration of ultrasound contrast agents has helped to make this exploration more reliable, both in terms of detection and characterization of injuries.

Thus, ultrasound is at the forefront of exploration for finding secondary liver lesions, the identification of suspicious nodules in a cirrhotic liver, the looking for bile (and vesicular) anomalies or for infectious source. Its performance is better in detection than in characterization of neoplastic diseases, but the introduction of contrast ultrasound has totally changed this situation with, as a consequence, a performance equal or superior to that of a CT-scan or MRI. On the other hand, ultrasound is absolutely successful in exploring bile pathologies. In addition to the traditional approaches through external ultrasound, it is possible to use endo-oesophageal, laparoscopy or operative explorations for detecting small lesions, or to respond to a particular search.





**Figure 30.10.** Liver ultrasound images of hepatocellular carcinoma nodules (previous page) and of a nodule of focal nodular hyperplasia (bottom)

### 30.1.5.3. Renal imaging (Figure 30.11)

As for the liver exploration, ultrasound techniques have a remarkable performance in the exploration of acute or chronic renal dysfunction, seeking for urethral obstructions and/or expansion of renal cavities. The easy identification of kidney stones is a great help for the clinician. The same is true with chronic alterations with “destruction” of functional parenchyma to identify and survey these kidneys compared to biological abnormalities. It is also applicable to the exploration of renal transplants, which are more accessible because of their superficial position.

Regarding tumoral pathology, it is essential to differentiate between cystic lesions (where ultrasound has undeniable diagnostic qualities reinforced by nonlinear imaging) and tissular lesions (where the contribution is more limited in terms of characterization). Thus, if we suspect a neoplastic disease, we will not be able to fully clarify it and to make the report of local extension. This could evolve in the future by contrast imaging.

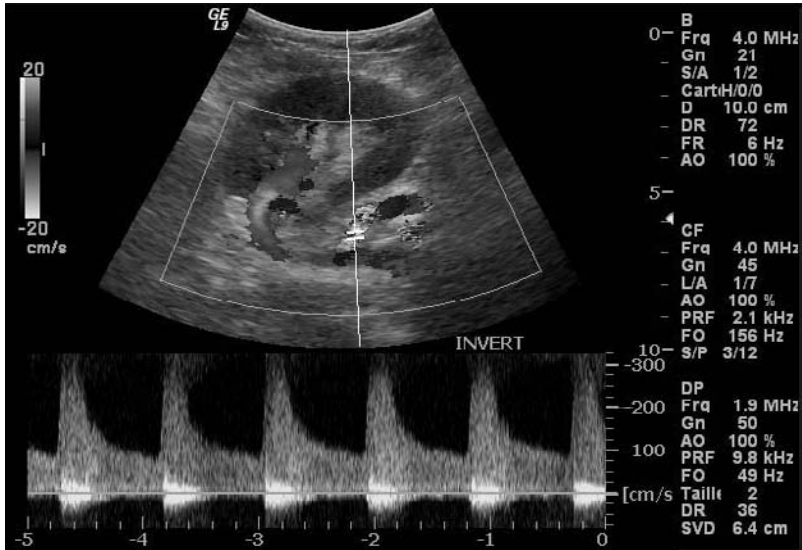


**Figure 30.11.** Color Doppler imaging of an emulgent artery stenosis of transplant, showing the color aliasing at the location of the stenosis, and registration of velocities by pulsed Doppler greater than 3 m / s at this level

#### 30.1.5.4. Obstetric imaging (Figures 30.12 and 30.13)

Ultrasound techniques play a leading role in embryological and fetal imaging. Their non-invasive and non-radiating nature allows the completion of several examinations without inconvenience for the fetus and his mother. It is thus possible to see embryonic echoes from 3 weeks gestational age, to confirm the viability of pregnancy from 4 weeks gestational age, and make early morphological examinations from 10 weeks gestational age. This early review is now the reference examination of screening of chromosomal abnormalities, leading to the outcome of perfectly guided punctures for diagnosis. It is also possible to detect early morphological anomalies, which will either be confirmed in subsequent examinations or lead to appropriate care. Subsequent explorations recommended at 20 and 30 weeks gestational age, will seek to check fetal growth and to detect later diagnosis anomalies. In addition, ultrasonic methods participate in the assessment of fetal well-being, and allow appropriate decisions in terms of delivery to be taken. Thanks to the introduction of three-dimensional imaging, recent progress is quite spectacular and is expected to increase further with matrix probes. If there was limited evidence of profound changes in terms of diagnosis, it is clear that communication with parents has been greatly facilitated [NEL 98], [BEG 00].



**Figure 30.12.** *Ultrasound images of fetal profile (top) and intracerebral fetal structures (bottom) with identification of specific structures that are the callous corpus and the cerebellum*

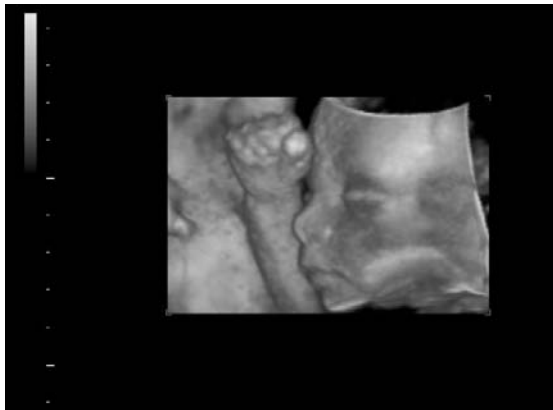


**Figure 30.13.** *Ultrasound three-dimensional surface image of a fetal face and hand*

30.1.5.5. *Pelvic imaging (Figure 30.14)*

This application is certainly one area of choice for ultrasound with the use of endocavitary explorations, which allow a fine exploration of the different organs. This is true for the uterus for research into endometrial (polyp, hyperplasia, etc.), endocavitary (effusion, etc.) and myometrial (fibroma, adenomyosis, etc.) abnormalities. In these indications, ultrasound represents a part of the initial diagnostic review and of local extension. It will also be possible to apprehend the changes caused by a lesion as a result of mini-invasive fitted treatments. In the field of annexal pathology, Doppler ultrasound is also at the forefront for the identification and classification of injuries by seeking relevant diagnostic criteria, guiding the clinician to benign or malignant lesions. Diagnostic elements gathered by Doppler ultrasound at present form the most important guidance for the clinician, again reinforced by contrast agents.

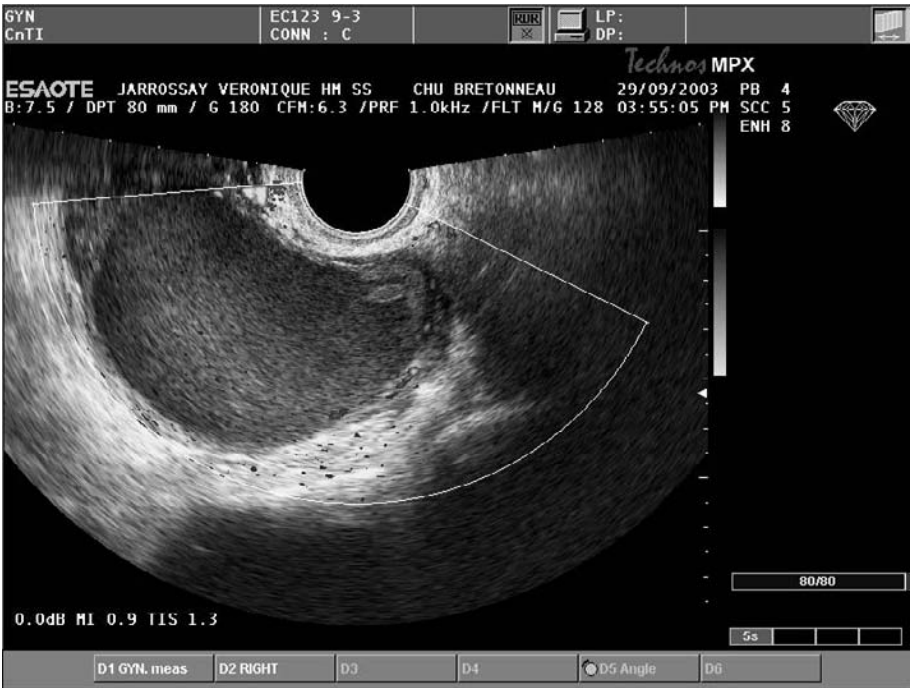


**Figure 30.14.** *Pelvic ultrasound image by transvaginal ultrasound for the exploration of an endometriosis cyst with a few vascular spots visible in power Doppler (note the thin echoes within the cyst)*

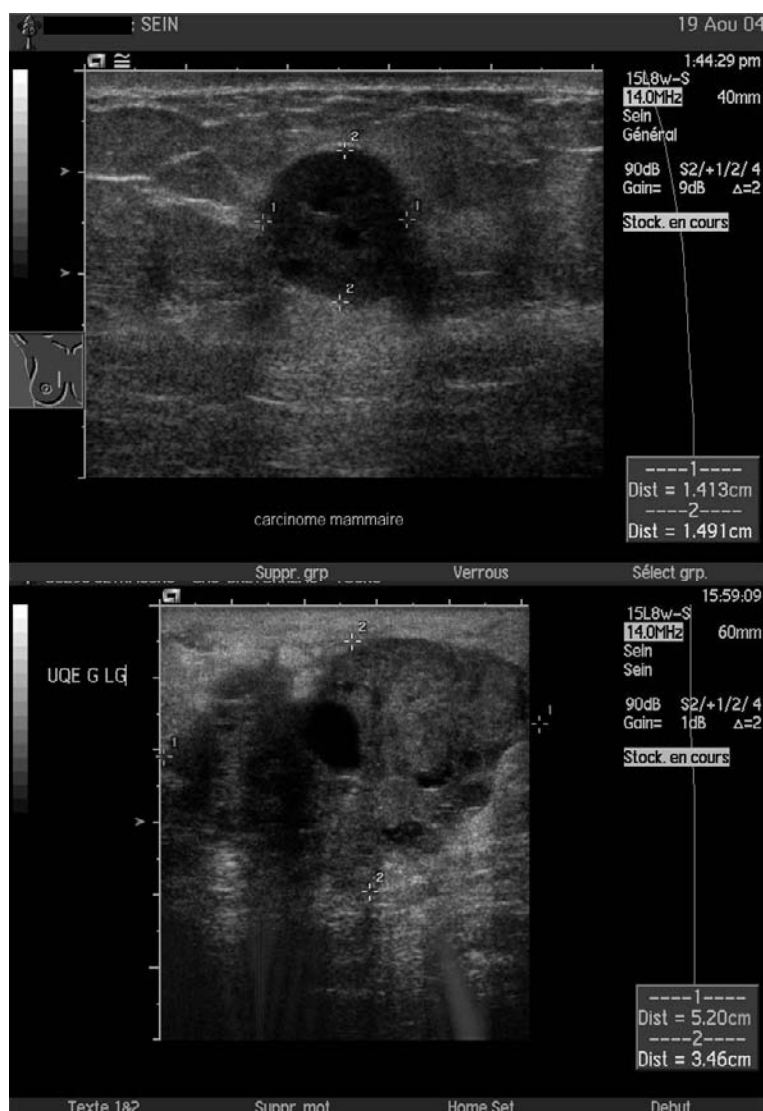


**Figure 30.15.** Ultrasound images of small (top) and large (bottom) neoplastic breast nodules

For men, exploration of the prostate and genital system is widely distributed with an undisputed role in prostate exploration, as in the search for anomalies in the genital route. The ease of use and the possibility of biopsy guidance are a crucial advantage in detecting prostate neoplasia.

30.1.5.6. *Thyroid imaging (Figure 30.16)*

Ultrasonography has altered the approach to thyroid diseases over the last two decades. Its accessibility has made it possible to quickly use high frequencies allowing the identification of nodules unsuspected clinically, as well as the identification of images characteristic of functional anomalies. Moreover, the ultrasound guidance of a fine needle aspiration (FNA) of thyroid nodules is currently the standard method for diagnosing the malignancy of thyroid nodules, thus helping to limit unnecessary surgery.

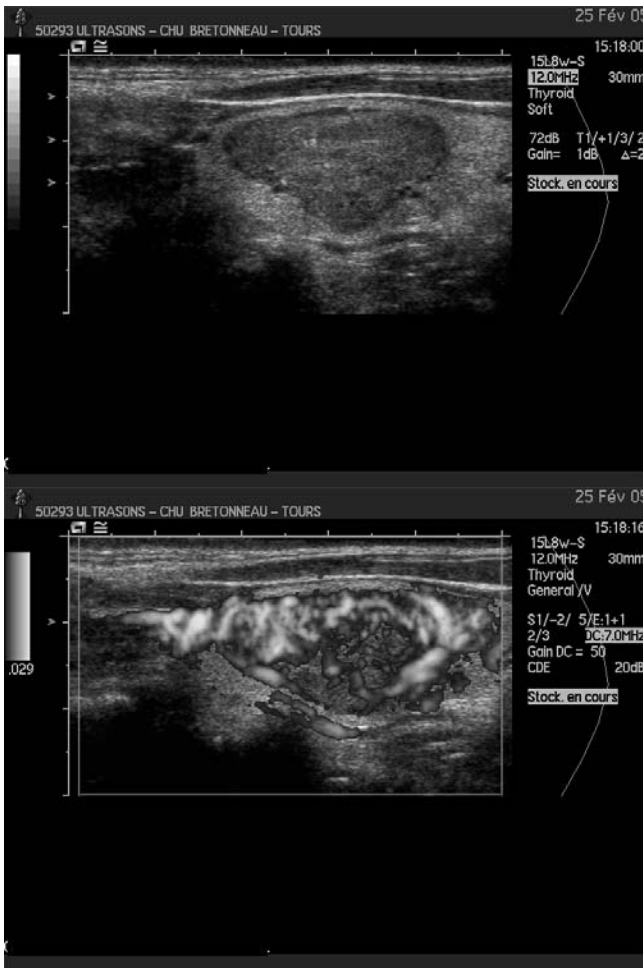


**Figure 30.16.** *Ultrasound image (top) and power Doppler of a neoplastic nodule of the thyroid*



### 30.1.5.7. Ophthalmic imaging (Figure 30.17)

Ophthalmic applications have been one of the first applications of ultrasound, with the identification of a number of corneal diseases, for example, and the precise measurement of the eye for the choice of implants. This is still very important, but progresses in ultrasound has brought new elements to the vascular and tumorous disease. Moreover, high and very high frequency ultrasound is a technique that is essential for the identification of anomalies in the anterior chamber, such as those that may be encountered in glaucoma and tumors of ciliary bodies.

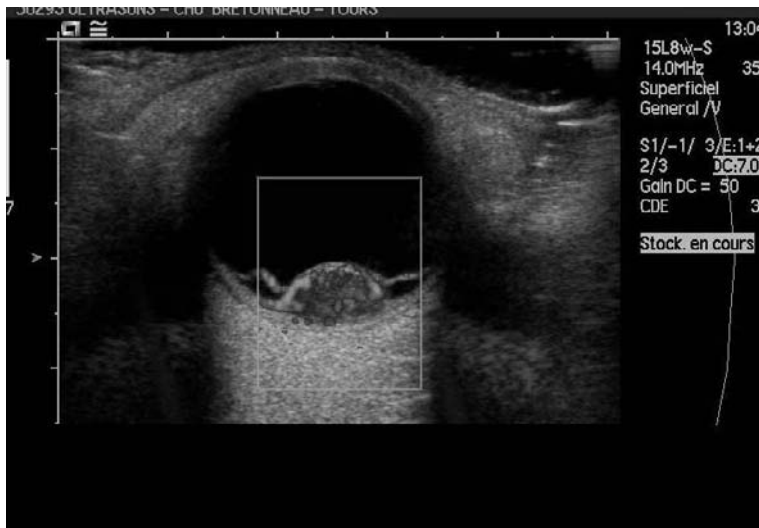


**Figure 30.17.** Doppler ultrasound image of a choroid melanoma within the eye with highlight of the prominent lesion and its marked vasculature

### 30.1.5.8. Vascular imaging (Figure 30.18)

Today, vascular Doppler ultrasound remains the exploration method of choice for superficial and deep vessels, in the search for stenosis or arterial thrombosis, or venous thrombosis. The combination of ultrasound with Doppler techniques thus helps to obtain a display of the content, with reliable determination of hemodynamic parameters, but also of the vessel wall with the detection of parietal anomalies, like plaques responsible for distal complications. Recent progresses of the machines in terms of Doppler are very important, and nowadays allow the detection of small vessels (150  $\mu\text{m}$ ) and a detailed analysis of the Doppler signal. It is in the field of the detection of small vessels that the supply of contrast agents has been the greatest.

Despite its undeniable contributions, endovascular imaging has remained undeveloped, the cost of single-use probes representing a brake to its dissemination.

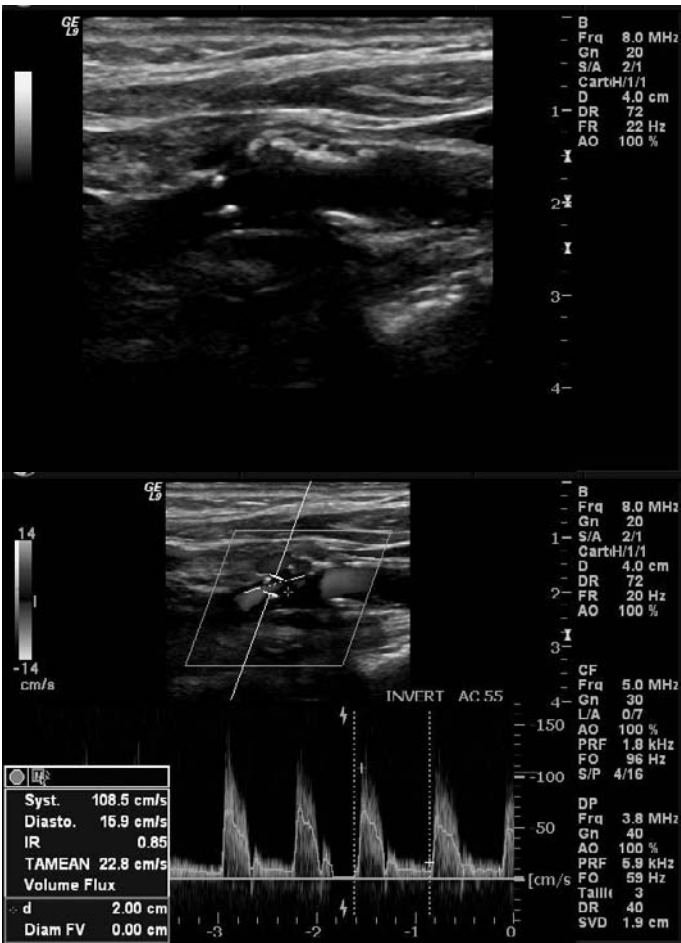


**Figure 30.18.** Presence of calcification in the carotid bifurcation with stenosis effect highlighted in color and pulsed Doppler

30.1.5.9. Musculotendinous exploration

Recently, this domain has become a very rich domain in terms of ultrasonic explorations. Indeed, the improvement of sensors' performances and the need to use dynamic tests for the identification of specific lesions contribute to position ultrasonography at the forefront of exploration techniques of joints, muscles and peripheral ligaments. These musculotendinous lesions can be traumatic or acute and

chronically inflammatory. For the future, there are some reasons to expect significant developments in the investigation of therapeutic effects domains, probably with the help of ultrasound contrast agents. The exploration of nerves also benefits from recent advances, allowing searches of nerve lesions or of the immediate environment.

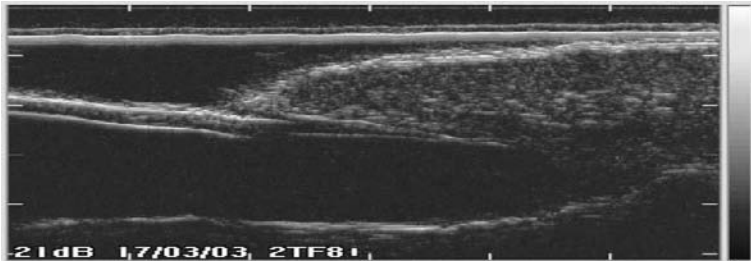


**Figure 30.19.** *High frequency (30 MHz) image of the basis of a fingernail and its matrix*

#### 30.1.5.10. *Brain imaging*

This domain has been neglected for a long time, after having been investigated from the beginning of ultrasound for the detection of expansive intra-cranial lesions. Thereafter, the bone barrier had limited the opportunities of imaging the brain structures. The developments in terms of Doppler imaging first resulted in the hemodynamic study of large intracranial vessels in most cases, but the interposition of the bone was still a limit that could have been eliminated through the use of contrast agents. Ultrasound imaging itself remains limited to a few experiment centers. However, recent reports mention significant progress in the study of cerebral perfusion with the aim of the possibility of detecting ischemic areas in a reliable and easy way.

#### 30.1.5.11. *Future applications (Figure 30.19)*

Today, ultrasound systems and contrast agents are complementary, and this opens the door to more sensitive applications. It is not unrealistic to think that real ultrasound imaging sequences, containing pulses at different frequencies and receiving the fundamental and harmonic frequencies, can still improve the image quality and specificity of the tissue response for a better characterization.

The therapeutic applications coming from microbubbles should benefit from these imaging methods, helping to obtain a tracking of the target area by non-destructive contrast imaging, followed by a targeted mass destruction with the use of high acoustic power. This requires the use of targeted contrast agents whose

development is underway, but not yet fully reached, and the possibility of transporting drugs or genes by these microbubbles.

In terms of technological development, it is important to note the rise of ultrasound elastography [BAM 02], [SAN 03], nowadays mainly in breast, liver and prostate imaging, but we can expect a wider use in the near future, when the problems of algorithms for calculating the appropriate parameters will be solved.

### 30.2. Bibliography

- [ALB 03] Albrecht T., Blomley M.J.K., Burns P.N., Wilson S., Harvey C.J., Leen E. et al., "Improved detection of hepatic metastases with pulse inversion ultrasonography during the liver specific phase of SHU 508 A (Levovist)- multi centre study", *Radiology*, 227, 361–370, 2003
- [ALB 04] Albrecht T., Blomley M., Bolondi L., Claudon M., Correas J.M., Cosgrove D.O., Greiner L., Jager K., Jong N.D., Leen E., Lencioni R., Lindsell D., Martegani A., Solbiati L., Thorelius L., Tranquart F., Weskott H.P., Whittingham T., "Guidelines for the use of contrast agents in ultrasound", *Ultraschall Med.*, 25, 249–256, 2004
- [BAM 02] Bamber J.C., Barbone P.E., Bush N.L., Cosgrove D.O., Doyelt M.M., Fueschsel F.G., Meaney P.M., Miller N.R., Shiina T., Tranquart F., "Progress in freehand elastography of the breast", *IEICE Trans Fundamentals Commun. Electron. Inf. Syst.*, 85, 5–15, 2002
- [BEG 00] Bega G., Lev-Toaff A., "Even experts can benefit from 3-D perspectives", *Diagn. Imaging*, 13–17, 2000
- [BER 99] Berson M., Gregoire J.M., Gens F. et al., "High frequency (20 MHz) ultrasonic devices: advantages and applications", *Eur J. Ultrasound*, 10, 53–63, 1999
- [BUR 96] Burns P., "Harmonic imaging with ultrasound contrast agents", *Clin. Radiol.*, 51, 50–55, 1996
- [CLA 02] Claudon M., Tranquart F., Evans D.H., Lefevre F., Correas J.M., "Advances in ultrasound", *Eur Radiol*, 12, 7–18, 2002
- [COR 01] Correas J.M., Bridal L., Lesavre A., Mejean A., Claudon M., Helenon O., "Ultrasound contrast agents: properties, principles of action, tolerance and artifacts", *Eur. Radiol.*, 11, 1316–1328, 2001
- [DAW 99] Dawson P., Cosgrove D., Grainger R., *Textbook of Contrast Media*, Informa Health Care, 1999
- [FIL 99] Filipczynski L., Kujawska T., Tymkiewiż R., Wojcik J., "Nonlinear and linear propagation of diagnostic ultrasound pulses", *Ultrasound Med. Biol.*, 25, 285–299, 1999
- [FOS 00] Foster F.S., Pavlin C.J., Harasiewicz K.A., Christopher D.A., Turnbull D.H., "Advances in ultrasound biomicroscopy", *Ultrasound Med Biol*, 26, 1–27, 2000

- [FRE 98] Freiherr G., “Harmonic imaging: what it is, how it works”, *Diagn. Imaging Europe*, HU6–HU7, 1998
- [HAR 01] Harvey C.J., Blomley M.J., Eckersley R.J., Cosgrove D.O., “Developments in ultrasound contrast media”, *Eur. Radiol.*, 11, 675–689, 2001
- [LAW 85] Law W., Frizzell L., Dunn F., “Determination of the non-linearity parameter B/A of biological media”, *Ultrasound Med. Biol.*, 11, 307–18, 1985
- [LEE 03] Leen E., Horgan P., “Ultrasound contrast agents for hepatic imaging with nonlinear modes”, *Curr. Probl. Diagn. Radiol.*, 32, 66–87, 2003
- [MEU 03] Meuwly J.Y., Correas J.M., Bleuzen A., Tranquart F., “Mode de détection des produits de contraste échographiques”, *J. de Radiologie*, 85, 2013–2024, 2003
- [NEL 98] Nelson T.R., Pretorius D.H., “Three-dimensional ultrasound imaging”, *Ultrasound Med. Biol.*, 24, 1243–1270, 1998
- [OND 05] Onders R.P., Hallowell P.T., “The era of ultrasonography during laparoscopic cholecystectomy”, *Am. J. Surg.*, 189, 348–51, 2005
- [OUA 02] Quiaia E., Stacul F., Bertolotto M., Locatelli M., Mucelli R.P., “Characterization of focal liver lesions with pulse inversion harmonic imaging (PIHI) using a second generation US contrast agent”, *Acad Radiol.*, 9, Suppl 2, S376–379, August 2002
- [RIZ 99] Rizzatto G., “Evolution of ultrasound transducers: 1.5 and 2D arrays”, *Eur Radiol*, 9, S304–306, 1999
- [SAN 03] Sandrin L., Fourquet B., Hasquenoph J.M., Yon S., Fournier C., Mal F., Christidis C., Ziol M., Poulet B., Kazemi F., Beaugrand M., Palau R., “Transient elastography : a new noninvasive method for assessment of hepatic fibrosis”, *Ultrasound Med. Biol.*, 29, 1705–1713, 2003
- [STA 86] Starritt H., Duck F., Hawkins A., Humphrey V., “The development of harmonic distortion in pulsed finite-amplitude ultrasound passing through liver”, *Phys. Med. Biol.*, 31, 1401–1409, 1986
- [TRA 99] Tranquart F., Eder V., Grenier N., Pourcelot L., “Clinical use of harmonic imaging”, *Ultrasound Med. Biol.*, 25, 889–94, 1999
- [WAR 97] Ward B., Baker A., Humphrey V., “Nonlinear propagation applied to the improvement of resolution in diagnostic medical ultrasound”, *J. Acoust. Soc. Am.*, 101, 143–154, 1997
- [WHI 99] Whittingham T.A., “Broadband transducers”, *Eur Radiol*, 9, S298–303, 1999

This page intentionally left blank

## Chapter 31

# Use of Time-reversal

### 31.1. Use of time-reversal

Because of its ability to learn to focus in an adaptive way in a very short time in complex heterogenous media, time-reversal can be applied successfully in the domain of imaging and ultrasound therapy [FIN 03]. It can be used to correct the distortions induced by the skull on the therapy beam in a treatment of brain tumors by focused high intensity ultrasound. It is also able to learn to follow in real-time the movements of a kidney stone during a lithotripsy treatment, and also to detect, with a better accuracy than conventional ultrasound imaging, the micro-calcifications present in the breast. Applying the principle of time-reversal, focusing on resonant cavities allows, thanks to the great impact of temporal compression of ultrasonic signals, a large increase in the amplitude of the overpressure created by conventional transducers for the destruction of kidney stones.

#### 31.1.1. *Monitoring and destruction of kidney stones by time-reversal*

Extracorporeal ultrasound lithotripsy (destruction of kidney stones or renal lithiasis or gallbladder) appeared in 1980 and can now handle the bulk of renal lithiasis. Nevertheless, although lithiasis can be located precisely with X-ray imaging, existing systems are unable to track in real-time the movements of tissue caused by the breathing of the patient. It is estimated that more than 66% of the shots miss their target and cause damage to surrounding tissues such as local hemorrhage.

### 31.1.1.1. *Correction of respiratory movements by time-reversal*

The principle of adaptive focusing by time-reversal is particularly well suited to this problem. Indeed, the destruction of kidney stones is classically done with an ultrasound beam created by a single spherical piezoelectric dome focused permanently on the same position. However, during treatment, it appears that the patient's respiratory movements move the desired target, which very often moves out of the focus zone of the stone. It is known that less than 20% of the ultrasonic shots actually reach the kidney stone, resulting in an important loss of efficiency and in quite long treatment periods. The Laboratoire Ondes et Acoustique at ESPCI (Paris, France) has developed a time-reversal mirror to track the movements of the stone, and thereby ensure that all the ultrasonic beams effectively reach the desired target. The kidney stone is used as a passive acoustic source, on which the time-reversal mirror learns to “autofocus” (see sections 15.1.2 and 15.1.5).

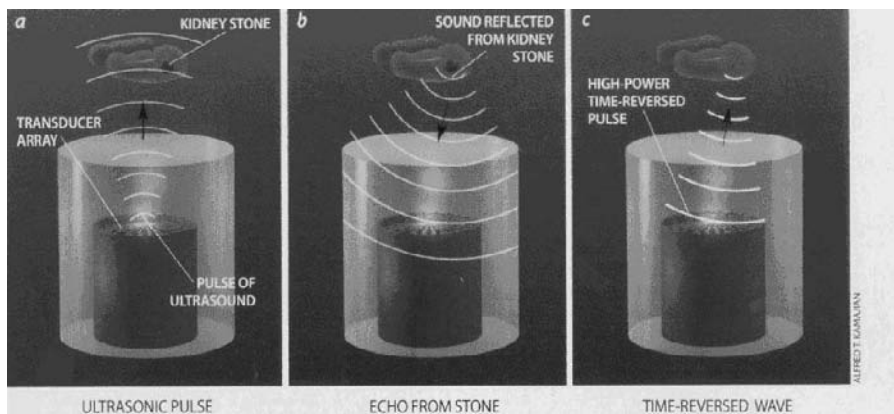


**Figure 31.1.** *Tracking of the movements of a kidney stone through the technique of adaptive focusing by time-reversal*

It is indeed possible, using the method presented in Figure 31.1, to force the system to focus in real time on the desired target. A first wave is emitted, by the array of piezoelectric transducers, of high-electric power (a). Then the backscattered waves mainly come from the kidney stone, because of its great reflectivity compared to the surrounding tissue (b). The backscattered signals are time-reversed and reissued by the transducer array. The ultrasound beam refocuses then naturally on the kidney stone (c). Because of the rapid propagation of ultrasound ( $1500 \text{ m.s}^{-1}$ ), this operation can be repeated over 100 times per second. As the movements caused by the breathing of the patient are much slower, it ensures that the ultrasound beam remains focused on its target.



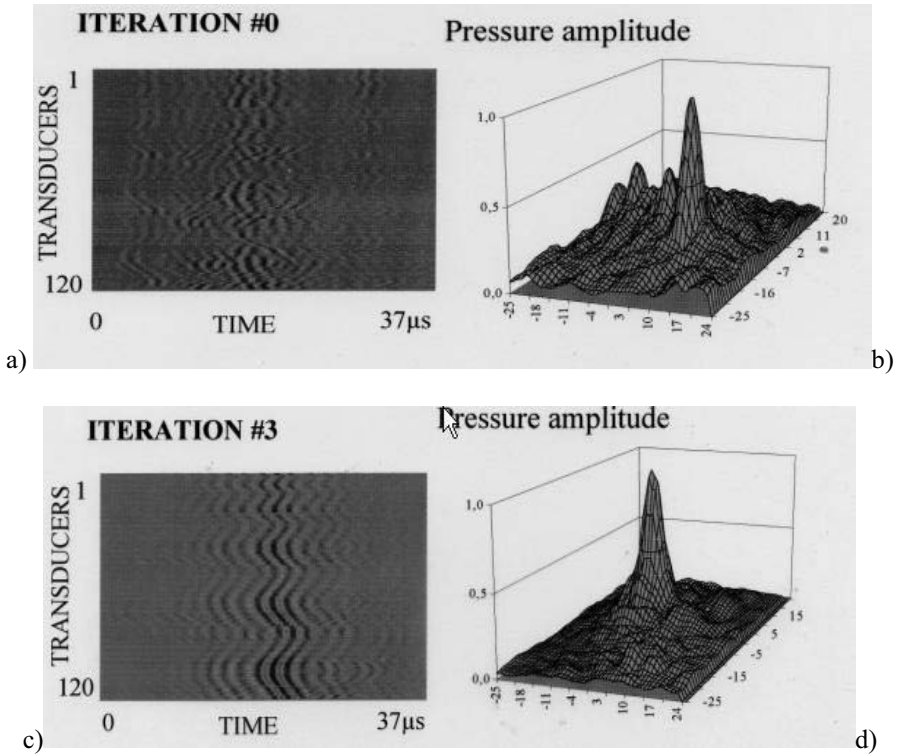


**Figure 31.2.** Ultrasonic echoes received on the transducer array after one (a) and three (c) iterations of the time-reversal process. Spatial distributions of the ultrasound beam in the focalization plane at the first (b) and third (d) iteration

As shown in Figure 31.2, after a few iterations of the time-reversal focalization process, the echoes from the target are perfectly selected compared to echoes from the surrounding tissue, and the quality of the focus beam slims down on the kidney stone. These iterations of the process take place in a very short time (a few tens of  $\mu$ s) and ensure that the ultrasound beam remains permanently focused on the target.

A first prototype including an electronic device of 64 channels operating in parallel has been made in recent years, in collaboration with the company Technomed. The numerous *in vitro* experiments on kidney stones and gallstones have proved its efficiency. The time-reversal mirror helps to locate the lithiasis in less than 40 ms, thus providing real-time monitoring.

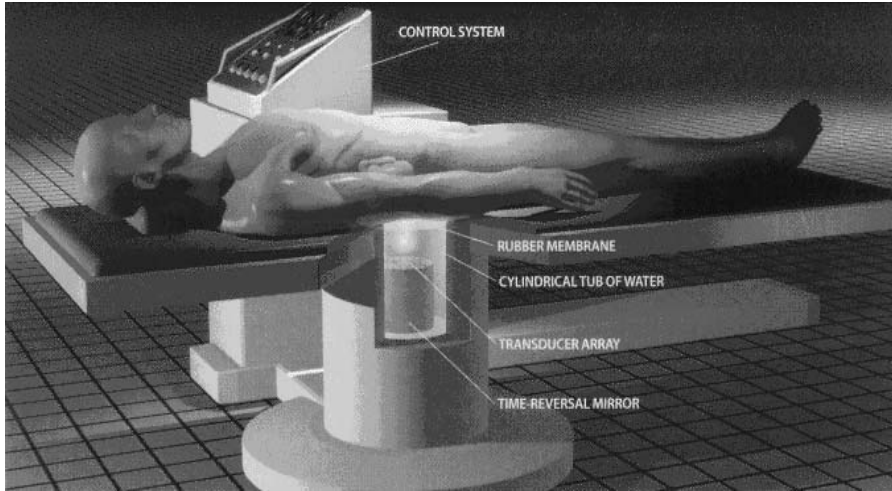


**Figure 31.3.** *Futuristic vision of a time-reversal mirror for the destruction of kidney stones*

Clinical trials at the Cochin hospital in Paris (for nephritic lithiasis) and the Edouard Herriot hospital in Lyon (for cholelithiasis) have also given very encouraging results. We can thus follow the movements of lithiasis in real time. Such a system in its final version could look like the illustration shown in Figure 31.3 [FIN 99].

Due to the large number of piezoelectric transducers necessary to ensure both i) an extremely important overpressure at the acoustic focus, and ii) a capacity of electronic movement of the focal point by several centimeters around the initial focal position, the price of such a system remains prohibitive so far.

#### 31.1.1.2. *Time-reversal and ultrasonic pulse compression*

To remedy this shortcoming, time-reversal focusing may also be used to reduce very substantially the number of necessary transducers to develop such a system. This significant improvement is based on the exploitation by time-reversal processing of the many reverberations of an ultrasonic wave in a solid waveguide [MON 02]. The new system consists of a small number of piezoelectric transducers glued to one end of a solid Duralumin waveguide (see Figure 31.4). The other end of the solid tube is against the skin of the patient.

The acoustic signal coming from a source located at the desired focal point (i.e. from the kidney stone) suffers a big temporal dispersion during its propagation through the solid tube. The signal received by the transducers can have a temporal length 1,000 times larger than the initial impulse (see Figure 31.5b).

After time-reversal and re-emission by the transducers, the resulting wave focuses on the focus point, just as if we were replaying the film of wave propagation in reverse order. Thus, all the energy contained in a signal of several milliseconds is recompressed at the focus to form a signal of a few microseconds.

The result is a huge amplification of the signal, which then ensures the destruction of the stone by mechanical effect. This amplification of the focused signal by time-reversal in a reverberant medium is the acoustic analog of the amplification of light in femtosecond lasers.

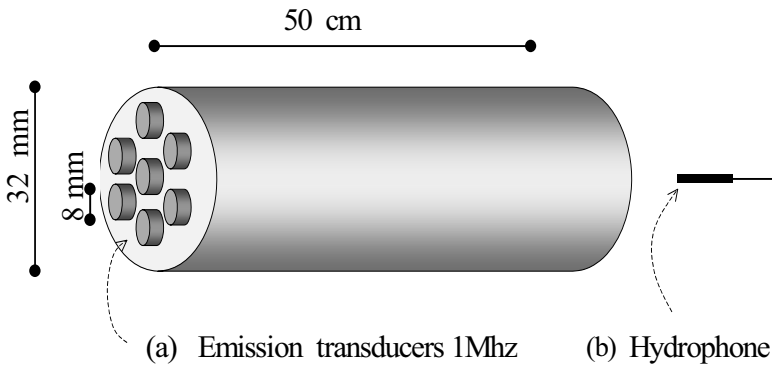


**Figure 31.4.** *Principle of amplification of ultrasonic signal by pulse compression*

Two prototypes have been developed and a maximum gain of 15 (in terms of the acoustic overpressure at the focus) has been experimentally measured. Through the use of reverberations in the solid tube, it should be possible in the future to reduce the number of necessary transducers for real-time tracking of kidney stones by a factor greater than 20!

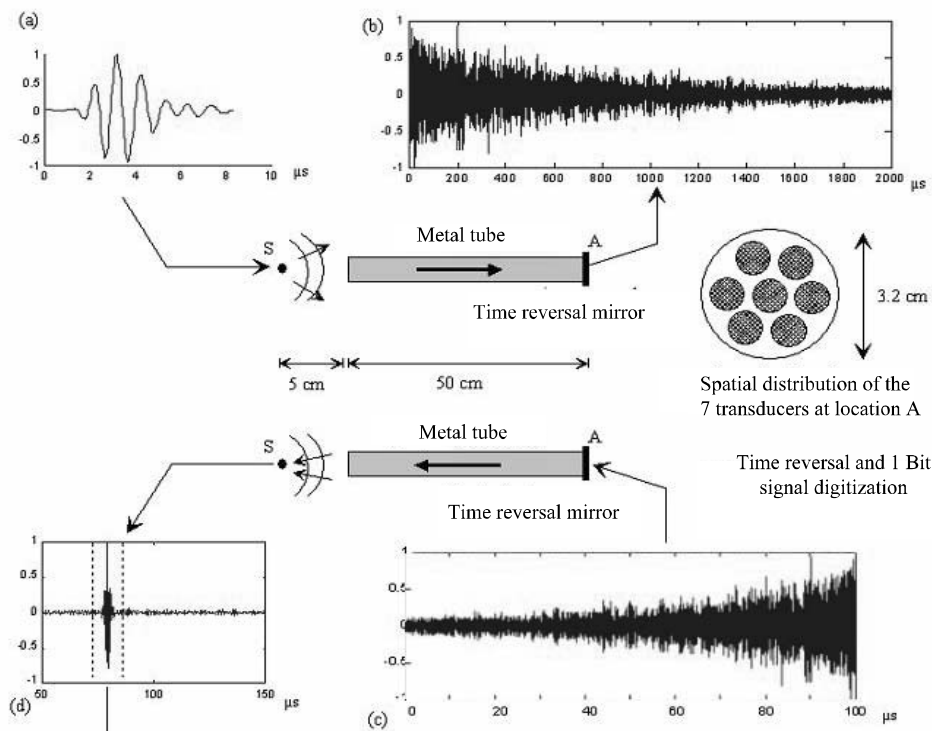


**Figure 31.5.** Principle of ultrasound amplification by temporal recompression.

(a) During the calibration phase, seven transducers of the array record the temporal signal coming from an ultrasound source. (b) the signal is stored in memory. During the experiment, we emit a temporally-reversed signal. This refocuses all the energy of the emission signal at the focal point in a very short time. There is a great temporal compression, which greatly increases the amplitude of the signal at the focus

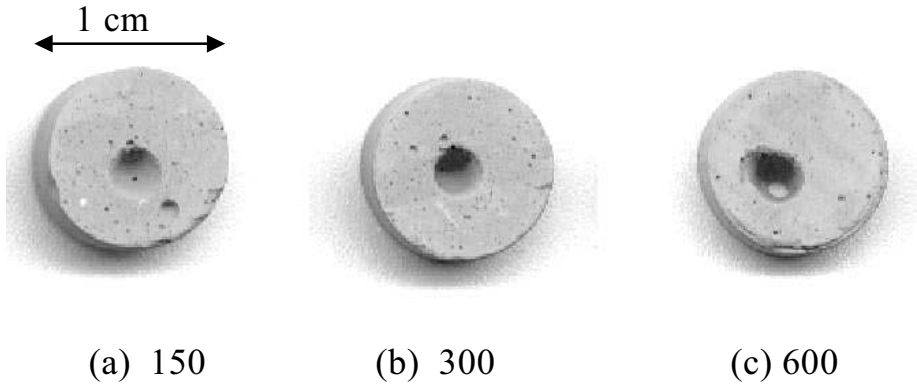


**Figure 31.6.** *Impacts of the ultrasound beam on a piece of chalk for 150, 300 and 600 successive insonifications*

### 31.1.2. *Ultrasound focalization in the brain by time-reversal*

Non-invasive brain surgery using ultrasonic beams is certainly the application for which the contribution of the principle of time-reversal focusing is the most invaluable.

Devices for extracorporeal “surgery” of cancerous brain tumors, for which conventional surgery is too delicate, are currently under development. Their mechanism is based on the use of a focused ultrasound wave to create, at the acoustic focus, a temperature rise sufficient to destroy cells. This focused ultrasound wave is generated by an array made of a large number of piezoelectric transducers spread over an area surrounding the skull [TER 01].

However, the realization of such a focused ultrasound beam is difficult, due to the heterogeneities of biological tissues crossed. In this application, the difficulties are intensified by the large discrepancy between ultrasound speeds in bone and in soft tissues, and also by the significant loss of energy when crossing the bone. This leads to a significant deterioration, or even a deviation of the beam. This constraint involves a focus that fits the medium, and therefore requires the use of an array of piezoelectric transducers operating with an electronic focus. The technique of time-reversal focusing helps to achieve excellent results in terms of correction of the emission beam in these extreme conditions [TAN 98].

Note however that the principle of time-reversal takes advantage of the time-reversal invariance of the wave equation in non-dissipative media. But apart from its heterogeneities in speed of sound and density, the skull is also a medium with absorption heterogeneities. Ultrasound absorption degrades the quality of the focusing by time-reversal. The time-reversal process can be modified to take into account this absorption phenomena in the bone of the skull; this approach may also be extended by a new technique of adaptive focusing called spatio-temporal reverse filtering, which helps to totally correct the damage caused by the bone of the skull on the focused ultrasound beams. This technique generalizes the time-reversal focusing to absorbent media.

#### 31.1.2.1. *Adaptive focusing: time-reversal and biopsy*

The use of time-reversal mirrors is particularly suited for brain therapy. Time-reversal, however, requires the presence at the focal point of an acoustic source, a sensor or a reflector, on which the system initially learns to make an “autofocus”. This reference can be provided during the biopsy, which is a minimally intrusive surgical intervention, made before most major surgery. A tiny acoustic source would be placed at the end of the surgical instrument intended to take a sample of tissue. The treatment then consists of putting the system in adjustment on such a reference throughout the heterogenous medium by issuing a pulse signal from this small acoustic source. The signals received on the transducer array, located against the cranial wall, are stored in memory, and the tiny acoustic source, connected to the surgical instrument, is removed. These received signals are then used to calculate the temporal codes to issue to each element of the array. These emission codes are stored in memory pending the outcome of the biopsy. The system can again focus on the reference point, but the focal point can also be moved electronically around this position to explore the entire tumor. The focalizations obtained have an identical quality to those obtained in a homogeneous medium, and have been obtained up to side-lobe levels of  $-20$  dB. This contrast is quite sufficient for therapy, where the temperature rise is proportional to the energy provided, and is therefore obtained with a contrast larger than 100. On the other hand, the focal point has been moved more than 15 mm on both sides of the reference location, keeping a very good contrast.

#### 31.1.2.2. *Simulated time-reversal: ultrasound focalization guided by X-ray imaging*

To be completely free from the biopsy stage and work in a totally non-invasive way, we can also be guided by Scanner X-ray imaging. It is indeed possible to completely achieve the first stage of time-reversal focusing by simulation. For that, we can use codes from numerical simulation by finite differences, helping to model the propagation of ultrasonic waves in various types of complex heterogenous and absorbent media.

X-ray imaging of the skull of the patient may indeed bring us the input parameters necessary for this calculation code (speed of sound, density of bones, and ultrasonic absorption) to completely model the propagation of ultrasonic waves through the skull. Thus, conducting an examination by X-rays helps to totally model the propagation of the ultrasound beam through the skull.

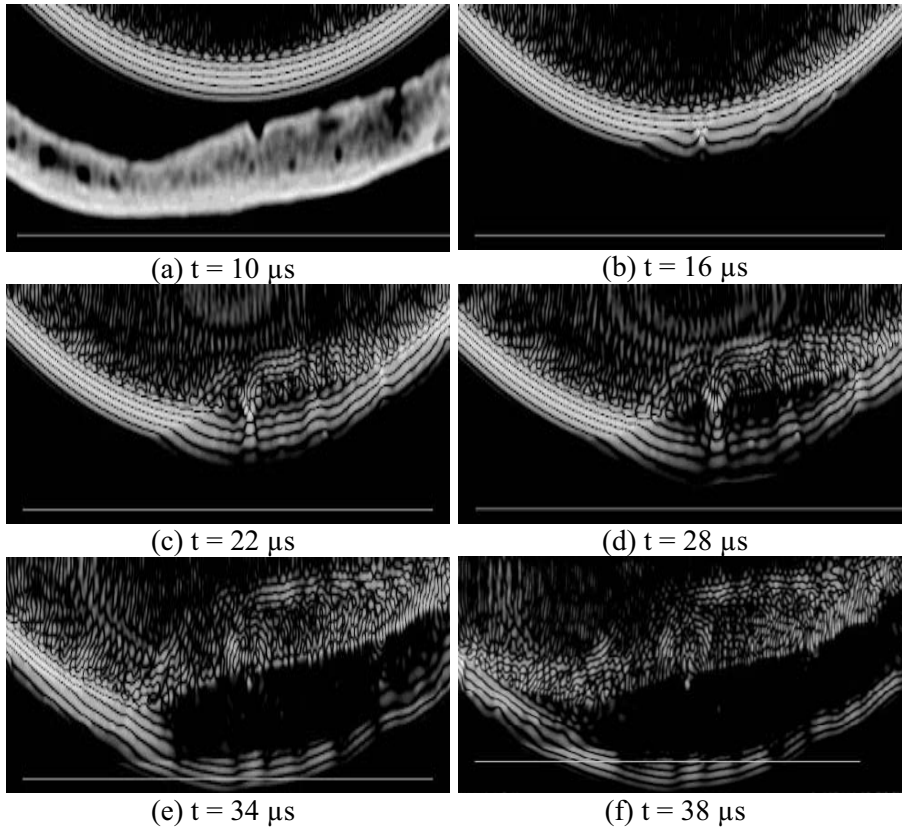


**Figure 31.7.** Numerical simulation of the propagation of a focused ultrasound wave through the bone structure of the skull: two-dimensional image of the ultrasound field at different moments. The acoustic parameters are deducted from the X-ray image of the skull

As shown in Figure 31.8, the correlation between numerical simulations and experiments is extremely good. It will therefore be possible in the near future to be free from the biopsy stage and to make a totally extracorporeal treatment of brain tumors.

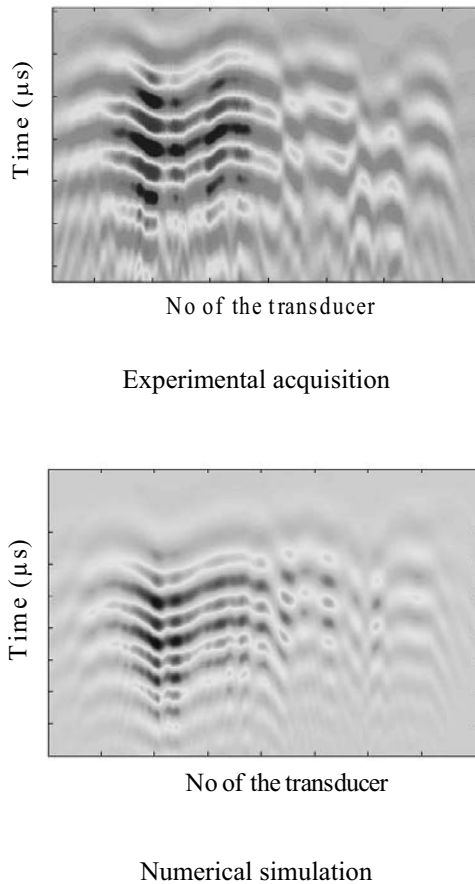


**Figure 31.8.** *Spatio-temporal representation of a plane wave after propagation through the skull: Experimental acquisition and numerical simulation in the same conditions*

**31.1.3. Time-reversal mirror for brain therapy by ultrasound**

A full system of therapy consisting of a multi-element probe of 300 piezoelectric transducers, driven by a multiline electronics of 300 independent and high power emission–transmission cards, was developed in France (see Figure 31.9). This system is currently being tested *in vivo* on animals and performance is extremely encouraging.



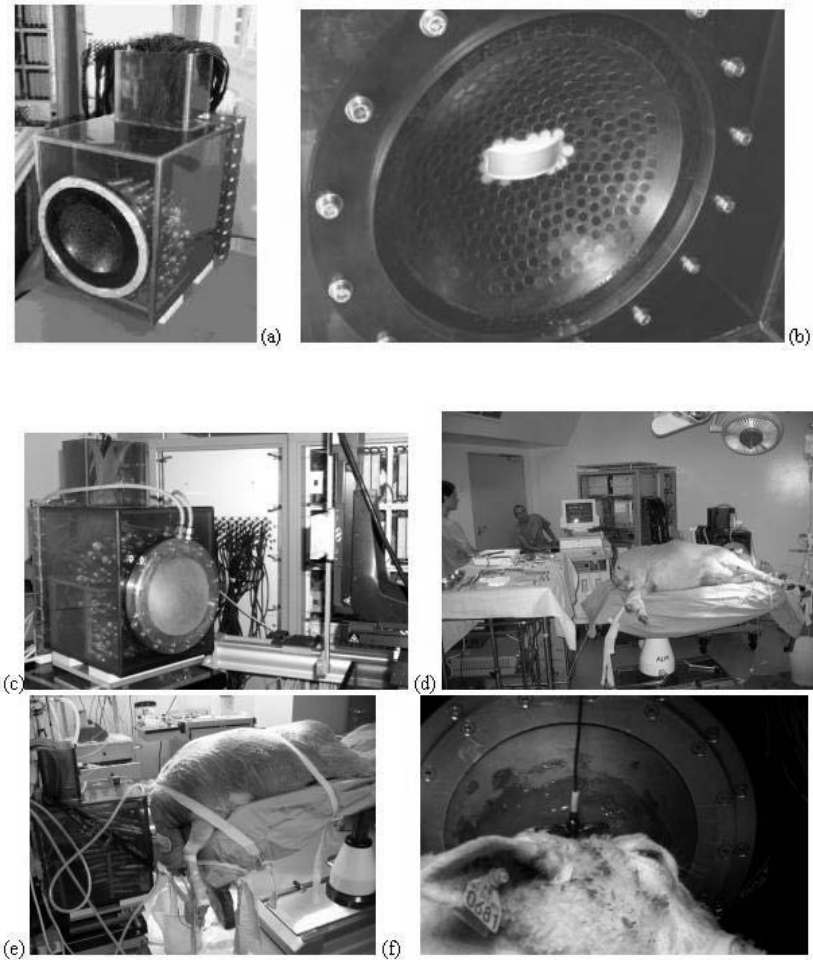


**Figure 31.9.** The time-reversal mirror for ultrasound therapy of brain consists of 300 individual elements that are semi-randomly distributed over a spherical cup of radius 14 cm. (a) Complete system in which we distinguish impedance adaptations boxes inside the Plexiglas cube. (b) Details of the front face of the array, on which we distinguish the semi-random distribution of piezoelectric transducers, and the ultrasound imaging strip located in the system to allow imaging in a 2D plane along the heat beam. (c) Final System: a latex balloon filled with degassed water and thermostatically controlled at  $10^{\circ}\text{C}$  provides the coupling with the skull. Behind these 300 therapy elements + 128 imaging elements, we can notice the electronic transmit-receive board for driving and controlling the therapy and imaging probes. (d) The sheep is placed against the coupling system made of latex. A biopsy is performed to introduce a hydrophone in the vicinity of the treatment area

The technique for correcting aberrations introduced by the cranial wall was experimentally validated using this system, and its performance is more than sufficient to consider clinical application. Following many years of research, this system of very high precision therapy has been validated *in vivo*. Initial tests *in vivo* of this prototype, unique in the world, were carried out on about 20 sheep at the Institut Mutualiste Montsouris (IMM) in February 2004 and 2006.

Figure 31.10 shows the quality of the focalization correction technique through the skull. The focal zone is much thinner with correction of the distortions induced by the skull. Thanks to the time-reversal focusing technique, the acoustic intensity of the beam is much more important at the focus. The necroses carried out (at a focal length 14 cm) by the mirror have a millimetric resolution (Figure 31.11). Once an area has been necrosed, it is possible to reduce the beam electronically in order to treat a full volume point by point.

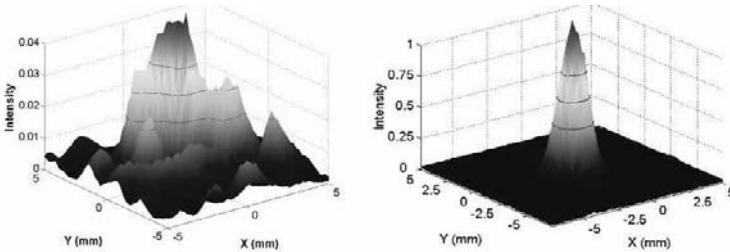


**Figure 31.10.** Spatial distribution of the acoustic intensity of the ultrasound beam obtained through the skull in the focal plane (focal length 12 cm): a) without correction of the beam, b) with correction of the effects due to the skull. The energy at the focus is 25 times higher when the adaptive focalization technique is used. The latter is therefore essential to consider the ultrasound therapy of brain tumors

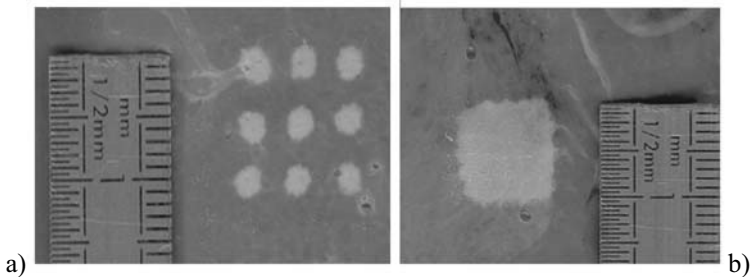


**Figure 31.11.** Necroses conducted in vitro through the cranial wall in degassed samples of liver. a) We can notice that the necrosis conducted is extremely accurate (about 1mm diameter). b) The ultrasound beam can be moved electronically to treat a complete area point by point

### 31.2. Bibliography

- [FIN 99] M. Fink, “Time-reversed acoustics”, *Scientific American*, 281, November, 91–7, 1999
- [FIN 03] M. Fink, G. Montaldo and M. Tanter, “Time-reversal acoustics in biomedical engineering”, *Annu Rev Biomed Eng.*, 5, 465–97, 2003
- [MON 02] G. Montaldo, P. Roux, A. Derode, C. Negreira and M. Fink, “Ultrasound shock wave generator with one-bit time reversal in a dispersive medium, application to lithotripsy”, *Appl Phys Lett.*, 80(5), 897–9, 4 Feb, 2002
- [TAN 98] M. Tanter, J.L. Thomas and M. Fink, “Focusing and steering through absorbing and aberrating layers: Application to ultrasonic propagation through the skull”, *Journal of Acoustical Society of America*, 103 (5), 2403–10, May 1998
- [TER 01] G. Ter Haar, “Acoustic Surgery”, *Physics Today*, Vol 54, N°12, December 2001
- [THO 96] J.-L. Thomas, F. Wu, M. Fink, “Time reversal focusing applied to lithotripsy”, *Ultrasonic Imaging*, 18, 106–21, 1996

This page intentionally left blank

## Chapter 32

# Elastography

### 32.1. Introduction

Since antiquity, doctors have resorted to palpation for the diagnosis of many diseases such as cancer or cirrhosis. Indeed, these diseases are frequently associated with a change in mechanical properties of the organ involved – in most cases, the organic tissue becomes stiffer. For example, the existence of a Young’s modulus contrast between cancer and healthy tissues has been shown in a quantitative manner by Krouskop *et al.* [KRO 98] for breast and prostate. The same study also highlighted the nonlinearity (rigidification under the influence of a stress) and the viscosity (stress–distortion relationship depending on the frequency of solicitation) in these tissues.

The usual imaging techniques (ultrasound, X-rays, MRI) are insensitive to these structural changes and fail to identify a significant number of such injuries. In order to remedy this situation, in the late 1980s a few pioneers suggested the measurement and then the imaging of the mechanical properties of tissues.

In the last 20 years, many studies have been conducted to characterize the mechanical properties of biological tissues [FUK 69, GAL 69, YAM 70, CHE 96, KRO 98]. These mechanical attributes include the shear modulus or the elastic modulus (Young’s modulus), Poisson’s coefficient, or any components of deformation or shear obtained in response to the application of a mechanical load on tissues. Biological tissues are generally viscoelastic. They can be isotropic, like the liver for example, or anisotropic like muscle fibers. The nonlinearity is more or less

dependent on the type of tissue analyzed, ranging from fat which behaves relatively linearly to certain malignant tumors which strongly rigidify under stress. Biological tissues, like many composite materials, are often organized according to a hierarchical structure, implying that the notion of measurement scale must be taken into account when trying to characterize their mechanical properties.

One of the significant characteristics of soft tissues is the important contrast between their shear modulus (order of magnitude 1 kPa) and their compression modulus (order of magnitude 1 GPa). This is due to the high percentage of water in them, this makes these tissues behave like quasi-incompressible materials. The compression modulus is relatively constant in most soft tissues, whether these tissues are healthy or pathological. Besides, due to this relative homogeneity, the speed of compression waves shows small variations between various soft tissues ( $c \approx 1540$  m/s), such that ultrasound can convert travel time to distance. The information that is accessed by palpation does not lie in the compression modulus but in the *shear modulus* of tissues, which presents significant contrasts. That is why medical imaging of elasticity is interested in the shear modulus of tissues, or in their Young's modulus. Indeed, and because of the quasi-incompressible behavior of soft tissues, their Young's modulus  $E$  is approximately proportional to their shear modulus  $\mu$  ( $E \approx 3\mu$ ).

All elasticity imaging techniques are based on the measurement of the *response* of biological tissues to a mechanical *stimulus*. These techniques can be divided into two categories, depending on whether the type of stimulus is static or dynamic. The first category includes ultrasound elastography [OPH 91, OPH 99] and imaging ARFI (acoustic radiation force imaging) [NIG 01]; these techniques provide images of the displacement or the deformation resulting from the application of a static or quasi-static force. The second family includes sonoelasticity [LER 88], magnetic resonance elastography [MUT 95], vibro-acoustography [FAT 98] and transient elastography [CAT 99], which are based on a dynamic excitation that can be vibratory or pulsed. Quasi-static elastography and transient elastography are detailed below.

### 32.1.1. *Quasi-static elastography*

Ultrasound elastography is primarily an imaging technique of the *strain* undergone by an organ under a static or quasi-static force. The application of a stress is used to convert a stiffness contrast, which is not directly measurable, into a deformation contrast, which can be measured. In a first approximation, and assuming that the stress is homogeneously distributed inside the organ, the local deformation is inversely proportional to the local Young's modulus. The strain image, called an elastogram, therefore provides information on the elastic properties

of the tissues observed. Depending on certain assumptions, it is also possible to use reconstruction techniques to establish an image of the Young's or shear modulus.

#### 32.1.1.1. Ultrasound measurement of the axial component of the deformation tensor

Ultrasound elastography is based on ultrasound (see Chapter 30). A brief reminder is necessary here. When an ultrasound scanner emits a short ultrasonic pulse in a given direction (called acoustic axis, or  $z$  axis), it receives the echoes from particles (the "scatterers") existing in the ultrasound beam. The propagation speed of the ultrasonic wave is assumed constant and known, such that the time interval between the transmission and reception ("travel time") gives a measure of the distance between the transmitter (the transducer) and the particle that generated the echo. As a result, the time axis can be directly converted into a distance along the acoustic axis. In biological media, these scatterers are innumerable (cells, etc.) and the ultrasonic signal received by the ultrasonograph (also called RF line, by analogy to radio-frequency) is the sum of all echoes.

Elastography is based on a local measurement of the motion of scatterers, comparing two ultrasonic signals, the first one acquired before and the second one after the application of a quasi-static deformation. This deformation is generated either by pressing with the transducer, or with an independent compressor, or by any other means. If the displacement of the medium is uniaxial and *in the direction of the ultrasound beam* ( $z$  axis), then scatterer displacement results in a change of the travel time of the echo (Figure 32.1.)

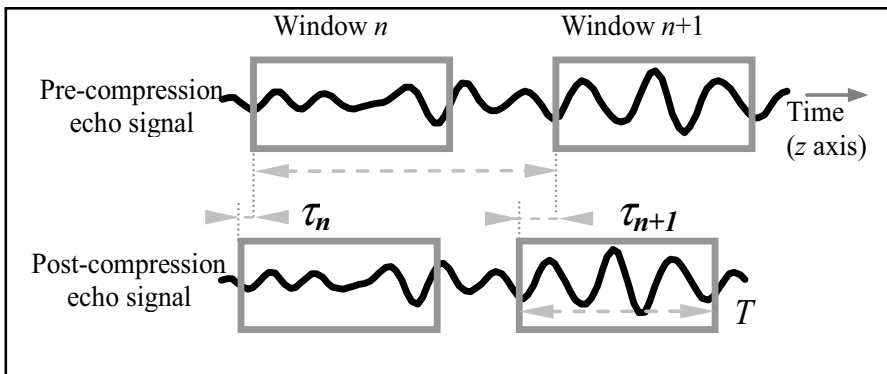


**Figure 32.1.** Principle of elastography:  $\tau_n$  represents the shift for the temporal window  $n$ ,  $\Delta T$  measures the interval between the windows, and  $T$  is the size of the windows

As the speed of ultrasound waves  $c$  is assumed constant and known, the measurement of the time shift  $\tau$  between an echo received before the compression and the same echo received after compression, is used to estimate the axial component  $d_z$  (i.e. in the direction of the ultrasound beam) of the displacement. In practice, the scatterers are too close to each other, so that their individual echoes can not be separated in time. Instead, the echo signal is segmented in windows, each corresponding to a group of scatterers. Such windows are shown in Figure 32.1. The measured displacement corresponds to the average displacement of the corresponding group of scatterers.

$$d_z = \frac{c\tau}{2} \quad [32.1]$$

The factor 2 comes from the round trip of the ultrasonic wave between the transducer and the scatterer. For typical frequencies used in sonography ( $\sim 5$  MHz), the accuracy of the displacement measurement is about  $\pm 1 \mu\text{m}$  for a resolution of about 1 to 2 mm. The basic measurement (the time delay  $\tau$ ) is typically performed by seeking the maximum of the cross-correlation between the pre- and post-compression windows. By moving the window along the  $z$  axis progressively and repeating this process, an estimate of the local displacement component  $dz$  is obtained for each window. The normal component of the strain tensor  $\varepsilon_{zz}$  is then obtained from the gradient of the displacement, the latter being measured in two temporal windows separated by a time interval  $\Delta T$ :

$$\varepsilon_{zz} \approx \frac{\tau_{n+1} - \tau_n}{\Delta T} \quad [32.2]$$

This measurement corresponds to the average strain undergone by the scatterers located between window  $n$  and window  $n + 1$  (it can also be noted that  $n + 1$  could be replaced by  $n + k$ , with  $k$  any constant integer larger than 1, thus providing better precision at the cost of resolution). By repeating this operation for each window pair, strain is estimated along the acoustic axis. The image of the component  $\varepsilon_{zz}$  of the deformations, i.e. the elastogram, is formed by scanning several adjacent axes consecutively. For this operation, we use the “B mode” scanning of the ultrasound scanner.

The deformation applied during the examination remains low: there is a range of deformations, around 1%, for which the precision of the deformation measurement is optimal. For large deformations (typically beyond 5% of deformation), the similarity of the pre- and post-compression signals usually becomes too low to obtain an accurate estimation of the displacement.



### 32.1.1.2. *Measurement of the other components of the displacement vector*

Using signals from a typical ultrasound image, the axial ( $d_z$ ) and lateral ( $d_y$ ) components of the displacement can be measured simultaneously by expanding the search area to the adjacent lines. However, due to the width of the ultrasound beam, the precision of the lateral component measurement (typically  $\pm 10$  to  $\pm 100$   $\mu\text{m}$ ) is not as good as that in the axial direction. The normal  $\varepsilon_{yy}$  and shear  $\varepsilon_{yz}$  components of the deformation tensor are determined from the components  $d_y$  and  $d_z$  of the displacement.

In the future, it will be possible to obtain the third component of the displacement  $d_x$  in the same manner and with similar precision, when 3D transducers become available. This will allow the determination of all components of the strain tensor.

### 32.1.1.3. *Reconstruction of the Young's modulus by inverse problem*

So far, we have considered strain measurements and images. Strain represents the behavior of a material under a given stress. Strain images have been shown to provide valuable clinical information [OPH 99], but strain is not an intrinsic property of the material. That is why a possible additional step is to reconstruct the underlying distribution (or image) of the elasticity modulus. This is an inverse problem that requires some assumption to be made about the mechanical model that appropriately describes the tissues being imaged. Typical models can range from a simple linear elastic material to viscoelastic and/or poroelastic materials. The model includes stiffness parameters that are initially unknown. Estimating these parameters typically requires that an initial guess is made, that the corresponding strain distribution is calculated, and compared to the experimental strain image. The process is repeated to minimize the gap between the simulated displacements and the experimental measurements.

Although promising in theory, in practice the inverse problem approach suffers from several limitations. Firstly, all three components  $d_x$ ,  $d_y$  and  $d_z$  of the displacement are required. Second, conditions on the edges of the image are unknown. Third, the chosen model may or may not be appropriate. Because of the limitations, it is necessary to make certain assumptions (such as zero displacement or zero strain in some direction, rigid or free edges, slip or non-slip conditions, etc.). During a medical examination, the possible violation of these assumptions may lead to the formation of unpredictable and undesirable artefacts in the modulus image. It is therefore not surprising that modulus imaging was not implemented in the first commercially available real-time strain imaging scanners. As will be discussed in section 32.1.2, the more recent techniques of dynamic and transient elastography circumvent most of these limitations, and can provide reliable modulus images, even *in vivo*.

#### 32.1.1.4. Medical applications

In clinical practice, organs move continuously, albeit at different speeds, as a result of breathing, cardiac cycle, and movements of the patient. These unwanted movements result in some scatterers moving outside the ultrasound beam; this effect may completely prevent any measurement of the displacement. To minimize these unwanted movements, a “real time” acquisition is needed, typically with less than 100 ms between the acquisitions of pre- and post-compression images. Small deformations in the order of 1% are sufficient to create an elastogram. Larger deformations can be measured by accumulating several consecutive elastograms.

The first clinical study reported in the literature and including a significant number of patients concerns the diagnosis of breast cancer [GAR 97]. The main problem for this disease is to determine whether the tumor is benign (without serious danger) or malignant (cancer requiring treatment). The study of Garra *et al.* shows that breast cancers appear larger in elastography than in ultrasound, while fibroadenomas (benign) have the same size. This observation could avoid a biopsy (puncture) for many patients.

Many applications may benefit from elasticity imaging, such as the diagnosis of prostate cancer, liver fibrosis, atherosclerosis, or the follow-up care of a patient after a kidney transplant or treatment for cancer by focused ultrasound.

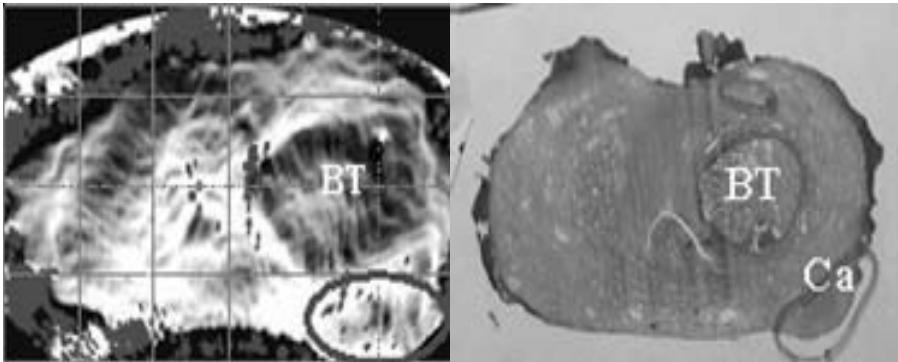


**Figure 32.2.** (a) Elastogram and (b) histological section of a prostate. The distortions range from 0% (black) to 5% (white), red corresponding to areas in which deformation can not be measured. A cancer (surrounded) and a benign tumor (“BT”) are visible on both images [SOU 03]

As we have seen, implementing elastography (strain imaging) on a conventional ultrasound scanner only requires a software modification. In 2005, three manufacturers of medical imaging equipment already proposed ultrasound systems incorporating real-time elastography. In the near future, it is likely that this technique will position itself as a complementary approach to sonography, because of its simplicity of implementation and its low cost.

### ***32.1.2. Dynamic and transient elastography***

Strain imaging does not reveal the elasticity of biological tissues but is rather a qualitative indicator. Indeed, according to Hooke's law, the knowledge of the strain and stress fields is necessary to calculate an elasticity map. But only one component of the strain field can be experimentally considered. The information conveyed by strain maps is thus a combination of the elasticity and stress field. Another domain of research has grown along with the technique of static elastography: dynamic elastography. Both techniques are extremely similar as they use the same correlation algorithms to estimate the displacement field within soft tissues. However, the nature of these displacements is totally different. The static or quasi-static stress field, assumed more or less uniform in static elastography, is replaced by a dynamic stress field in dynamic elastography, which gives rise to the propagation of shear waves. Quantitative elasticity mapping is extracted from the estimate of the propagation characteristics of these waves.

We can trace the history of dynamic elastography until 1981, when R.J. Dickinson proposes a method of quantitative estimation of the natural vibrations of the human body (heartbeats) by correlation of A-scan [DIC 82]. In 1983, A. Eisencher proposed a method called echosismography, in which the natural vibrations are replaced by artificial vibrations with the help of a mechanical vibrating device applied on the surface of biological tissues [EIS 83]. He analyzed the effect of these vibrations, by just looking at the A-scan. T.A. Krouskop in 1987 combined outer vibrations and quantitative detection of vibrations through a Doppler probe [KRO 87]. In subsequent months, this technique was used by Y. Yamakoshi (1990) [YAM 87], R.M. Lerner and K.J. Parker (1988) [LER 88, PAR 90]; this was the beginning of dynamic elastography. The monochromatic outer vibrations were necessary for the establishment of a heterodyne detection system; the trigger of the ultrasound being enslaved to the phase of vibrations.

The disadvantage of monochromatic vibrations lies in the impossibility of separating the compression waves from the shear waves, and the measurements of elasticity can be affected. At the Laboratoire Ondes et Acoustique, an impulse method has been developed, called transient elastography [CAT 99b]. In this approach, the monochromatic vibrations are replaced by pulses or wavetrains. The estimate of the transient displacement field is carried out by an ultrafast ultrasound system (5000 frames per second) capable of real-time tracking of the propagation of low frequency pulse waves. It is then easy to separate shear waves from compression waves and to make reliable measurements of elasticity.

#### 32.1.2.1. *Transient elastography and ultrafast ultrasound*

In the typical experimental device of transient elastography, the medical transducer array (1D bar), mounted on a mechanical vibrator (Bruel & Kaer vibrator of type 4810), transmits, in a piston movement of a few hundreds of microns, a low frequency pulse in biological tissues. At the same time, hundreds of ultrasound images are stored in electronic memories. The front face of the medical array is therefore a source of both ultrasonic waves (5 MHz) and sound waves (typically 100 Hz). If an acquisition rate of a few kHz in emission–reception mode does not represent a major technical difficulty for a single ultrasonic transducer, it is a performance beyond a commercial medical ultrasound device involving a hundred transducers. At this time, the fastest systems reach a refresh frame rate of 50 Hz, perfectly suited to the “real time” visual comfort of practitioners. Ultrasound used in cardiography is faster (70–200 Hz), to monitor the movement of valves. In the acquisition sequence of standard ultrasound devices, the focalization during the emission is carried out sequentially and the final image is built line by line. Each line requires an incompressible time imposed by the travel time of ultrasound until the desired depth of examination. In a sequence of ultrafast ultrasound, the focused emission is replaced by a plane wave generated by all the transducers of the medical array. The focusing at reception is then carried out by software, using classical beam-forming algorithms. The time required to obtain a complete ultrasound image is the travel time of the ultrasound to propagate over the sample. For a typical depth of 10 cm, this travel time is 0.13 ms, which allows a rate of about 8000 frames per second. Finally, from these ultrasound images, correlation algorithms can rebuild the displacement field generated by the low frequency waves in the medium studied [SAN 99a]. Figure 32.3 shows a wavefront (represented in color scale) that corresponds to the propagation of a shear wave in an agar–gelatin gel, whose mechanical properties are similar to those of biological tissues.

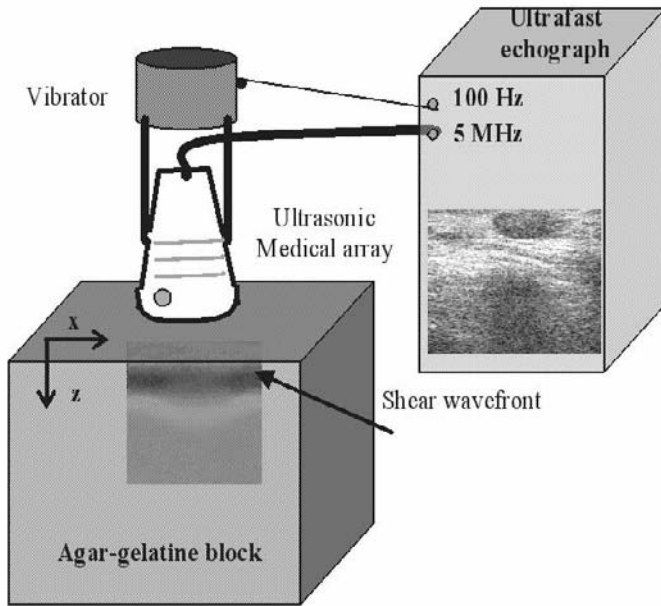


**Figure 32.3.** *Experimental setup of transient elastography. An ultrasonic medical array linked to an ultrafast scanner probes the agar gelatin gel with a rate of 3000 frames per second. A typical ultrasound image is represented on the right of the figure. At the same time, the array mounted on a vibrator generates a pulse of central frequency 100 Hz in the gel. Through a correlation algorithm applied to the 250 ultrasound images stored in memory, the displacement field resulting from low frequency waves (mainly shear waves) is obtained. A typical instantaneous displacement field is represented in color scale. There is a shear wavefront which propagates from top to bottom*

The images shown on Figure 32.4 are extracted from a film obtained in an agar-gelatin gel with a rigid inclusion. We can clearly see the distortion of the wavefront: indeed, a local increase of the elasticity in the inclusion at the center of the image causes a local acceleration of the wave, which explains the lump on the wavefront. If this film helps to detect the presence of a rigid inclusion, it is impossible to give the corresponding shape, position and elasticity exactly. Resolution algorithms for the inverse problem provide this kind of information.

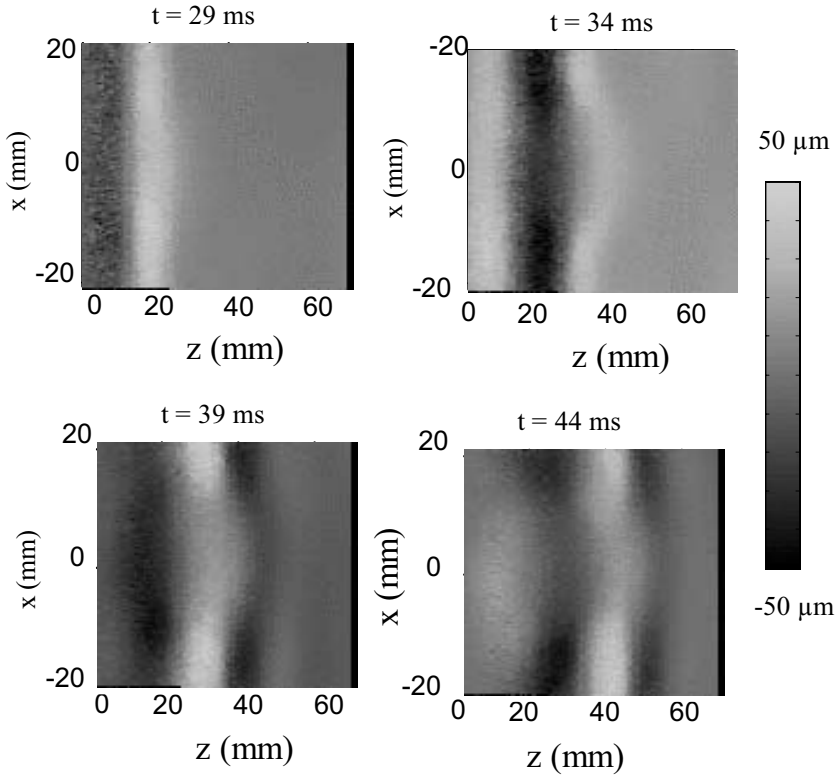


**Figure 32.4.** Four snapshots of the displacement field generated by the propagation (from left to right) of a shear wave in an agar–gelatin gel with the experimental setup described in Figure 32.3. The crossing of a rigid inclusion of 1 cm in diameter at the center of the image clearly distorts the wavefront. The film of displacements contains information on the local mechanical properties of the propagation medium

### 32.1.2.2. The shear waves in the human body

In addition to the big speed difference between the compression and shear waves (up to three orders of magnitude), the propagation of a shear wave in biological tissues is atypical in many other aspects. In Figure 32.5, the maximum of the displacements (longitudinal component) of a shear wave generated by a point-like piston is represented in grayscale and in contour lines. These representations, that characterize the directivity diagram of the shear wave source, show that a maximum of energy is radiated at  $35^\circ$  from the axis of the source. This result is identical to the directivity diagrams obtained in metals with ultrasonic laser sources in ablation mode (silver:  $38^\circ$ , aluminum:  $34^\circ$ ) [SCR 90]. We can see the low influence of the compression wave/shear wave speed ratio on the directivity of the source; typical

values of this ratio are in the range 100–1,000 in biological tissues and 2–3 in metals. But the most important point is that, unlike ultrasonic experiments in which it is almost invisible, the longitudinal component of the shear wave on the axis of the source is extremely important. The reason is that, the wavelength of shear waves being 3 cm, the displacement is observed in the near-field of the source. An integral mathematical solution, given by H. Lamb, D.C. Gakenheimer and J. Miklowitz, shows a good agreement with the experimental results, as illustrated on Figure 32.5 [CAT 99]. By using the infinite space approximation rather than semi infinite, it is possible to obtain the closed-form expression of the near-field shear wave [AKI 80, SAN 04]. The existence of a longitudinal component for the shear wave led to the rise of one-dimension transient elastography. Indeed, it is possible through a single ultrasonic transducer to generate and detect the propagation of a shear wave. The speed measurement helps to estimate the overall elasticity modulus. That is the principle of the Fibroscan®, commercial device designed to measure liver elasticity and to diagnose the state of fibrosis.

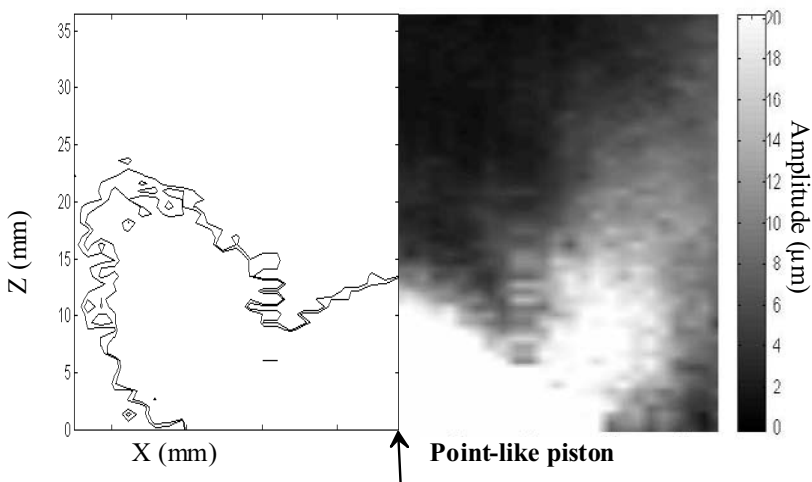


**Figure 32.5.** Right: Image of the maximum displacement field ( $z$  component) of the shear wave generated by a point-like piston. Left: contour lines. The energy of shear waves is radiated from the piston in a direction of  $35^\circ$  from its axis. The existence of a non-zero component of the shear wave on the axis is characteristic of near-field displacements

### 32.1.2.3. Quantitative measurements of mechanical properties of soft solids

The measurements of speeds are made, for example, by measuring the phase of the shear wave at every depth. The shear elasticity modulus  $\mu$  is then calculated by assuming an elastic medium, according to the formula:  $\mu = \rho v^2$ . To avoid bias due to

the near-field, the phase measurement must be made beyond a distance of half a wavelength from the source. The experimental measurements in different materials are collected in Table 32.1.

Soft solids	Conditioning (17°)	Speed	Elasticity
Agar gelatin gel	1%–5%, F=130 Hz	1.75±0.02 m/s	3.36 kPa
	3%–6%, F=100 Hz	5.22±0.02 m/s	29.97 kPa
Liver ( <i>ex vivo</i> )	F=120 Hz	7.3±0.1 m/s	58.6 kPa
Dairy products	Liquid, F=15 Hz	0.51±0.01 m/s	2.60 kPa
	Brewed, F=15 Hz	2.10±0.05 m/s	4.85 kPa
Muscles ( <i>ex vivo</i> )	<i>biceps femoris semitendinosus</i> F=100 Hz	9.94±0.23 m/s	108.6 kPa
	<i>Semi-membranosus</i> F=130 Hz	5.29±0.14 m/s	30.7 kPa
Muscles ( <i>in vivo</i> )	Human biceps F=130 Hz	3.0±0.1 m/s	9.90 kPa
Skin ( <i>in vivo</i> )	Dermis F=130 Hz	85±11 m/s	7.94 MPa
	Hypoderme F=130 Hz	14.8±0.4 m/s	240.9 kPa

**Table 32.1.** *Speeds – examples in some soft solids*

The use of the elastic model is reasonable in the low frequency domain. This domain, which is difficult to define universally, depends heavily on the soft solid considered. In the example of Figure 32.6a, the phase speed of a transverse plane wave into an agar–gelatin gel is constant in the frequency range 50–500 Hz. The elastic model, not represented on the figure, would fully explain the experimental dispersion (red circles). However, a more complex rheological model is necessary to explain the experimental variations of the wave attenuation with frequency. The simplest rheological models are the Voigt (noted V) and Maxwell (noted M) models. These models are both composed of two parts, a dashpot and a spring, mounted in parallel for the first one and in series for the second one. The theoretical predictions, compared with speeds (phase measurements) and attenuations (amplitude measurements) of the experimental plane waves, clearly show that the Voigt model is more efficient. It may seem obvious that a viscous solid model (V) is more appropriate than a viscous fluid model (M) for soft solids, but these experiments illustrate a rather confused situation met in elastography, where both models are used. The reason is twofold. First, rheometers able to test these models from



experimental measurements are confronted with wave propagation problems and do not operate at the frequencies used in elastography. On the other hand, it appears clearly in Figure 32.6a that the measurements of dispersion (the only ones made so far) can hardly decide on the choice of the correct rheological model. However, attenuation measurements of plane waves depending on frequency leave no doubt: the Voigt model better reflects experiments than the Maxwell model. A viscosity of 0.21 Pa.s is estimated from this experiment.

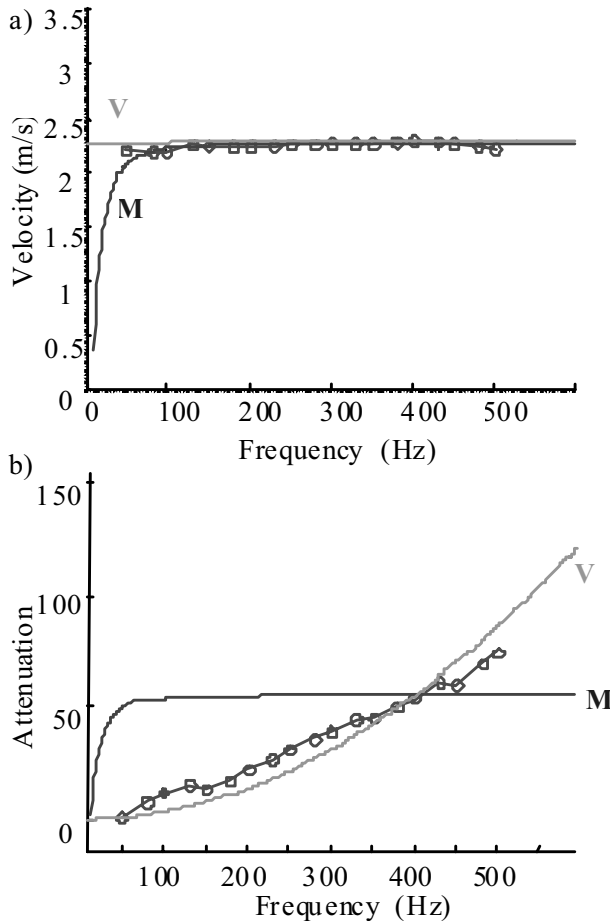


**Figure 32.6.** Speed and attenuation measurements for transverse plane waves at different frequencies. (a) The plane distribution of speeds (circles) is accurately predicted by both the Voigt (V) and Maxwell models (M). (b) However, the prediction of the Maxwell model on the attenuation distribution is clearly not in accordance with the experimental results (circles). The Voigt model is the best of the simple rheological models with two elements

As anisotropy is a rule rather than an exception in biological tissues, it is one of the fundamental mechanical parameters for the characterization, or for medical diagnosis. Experiments of transient elastography have been conducted on the biceps muscle, extensively described in literature, and whose simple structure lends itself well to preliminary studies. The muscle fibers of biceps are all oriented in the same direction and represent a typical case for transverse anisotropy. For this type of anisotropy (hexagonal system), three compression waves and two shear waves can propagate at different speeds. On Figure 32.7, the measurement of speeds of transverse waves along a varying direction  $\theta$  compared to the muscle fibers helps to estimate the elastic constants  $C_{44}$  and  $C_{66}$ . The surprising result is not the bell shape of the speed-angle curve (in agreement with theory), but rather the speed difference between the two perpendicular directions, demonstrating a very important anisotropy. By comparison, a typical anisotropy rate (speeds ratio) of 20% allows seismologists to designate a rock as “strongly anisotropic”. The anisotropy rate of approximately 300% for this *in vitro* muscle can reach 800% in the *in vivo* biceps [GEN 03].

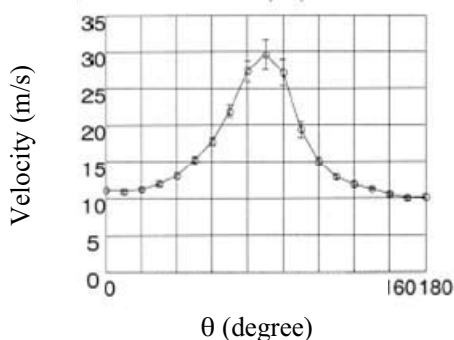


**Figure 32.7.** Experimental speed of a transverse wave whose wavefront has an angle  $\theta$  with the direction of the muscle fibers, and whose polarization is perpendicular. As predicted by the anisotropy theory, the speed of the shear wave is maximum when the wavefront is perpendicular to the fibers ( $\theta = 90^\circ$ )

The harmonic generation of a transverse wave of high amplitude in biological tissues is interesting for two reasons: first because it provides a quantitative estimate of the nonlinearity of these media, and second because a transverse shock wave has never been observed experimentally. The main reason is that the speed of transverse waves in hard solids (metals, crystals, rocks), of the order of a few kilometers per second, makes the achievement of large Mach numbers inaccessible to experiments. In soft solids, the particle velocity of the source, close to the speed of shear waves, can reach large Mach numbers close to unity. The nonlinear effects of the shear

wave, an order of magnitude smaller than those of the compression wave (cubic and quadratic nonlinearity respectively), can be seen in Figure 32.8. Unlike the compression wave, the shear shock wave does not present the famous saw-tooth shape for reasons of symmetry. Moreover, its spectrum is characterized by the existence of odd harmonics only. A very good agreement is reached with a numerical simulation of the modified Burgers equation, which describes the shape of the shear wave during nonlinear propagation. A linear elastic coefficient of 2.5 KPa, and a nonlinear elastic coefficient of 5.1 KPa are estimated in this agar–gelatin gel [CAT 03].

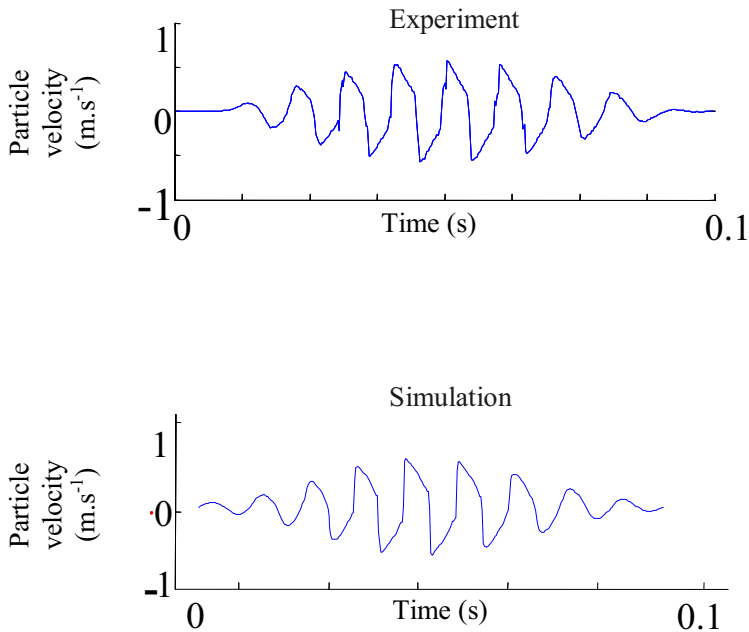


**Figure 32.8.** Comparison between the experimental and theoretical particle velocity of a transverse wavetrain of central frequency 100 Hz. The measurement is made at 15 mm from the source. The nonlinear effects result in tightening of the wave form, including a symmetry with respect to the time axis. On the spectrum of such a signal, only the odd harmonics are present

#### 32.1.2.4. The inverse problem

The inverse problem consists of building an elasticity map from the movie of the displacements  $\bar{u}$  generated by the shear waves. Under certain conditions [CAT 04],

the longitudinal component  $u_z$  of a harmonic shear wave obeys the Helmholtz equation:

$$\Delta TF_t(u_z(x, z)) + k^2 TF_t(u_z(x, z)) = 0 \quad [32.3]$$

We can deduce the local wave vector  $k$  from the temporal Fourier transforms  $TF_t$  of the experimental displacements at each point of the images:

$$k = \sqrt{-\frac{\Delta TF_t(u_z(x, z))}{TF_t(u_z(x, z))}} \quad [32.4]$$

$$\begin{cases} C = \frac{\omega}{\text{Re}(k)} \\ \alpha = \text{Im}(k) \end{cases} \quad [32.5]$$

From the local speed  $C$ , we can deduce the local elasticity  $\mu$  at the angular frequency  $\omega$ , based on the assumption of a constant density ( $1,100\text{kg/m}^3$ ) and using, in a first approximation, a simple model of a perfectly elastic medium. The combination of speed and local attenuation, associated with a rheological model (Voigt solid), helps to build both elasticity and viscosity maps [BER 04c]. However, the measurement of the viscosity, whose effects are often an order of magnitude lower than those of elasticity, is more difficult to implement. An average of the frequencies (30 to 70 Hz) contained in the displacements spectrum refines the final image. In the example illustrated in Figure 32.9, an elasticity map of the *in vivo* breast of a volunteer from the Curie Institute (research group of Professor Martine Meunier) is compared with a standard ultrasound image. A carcinoma of about 1 cm in diameter is visible on both images. It appears that the resolution of the elasticity maps is not limited by the wavelength of shear waves ( $\approx 5$  cm), but by the wavelength of ultrasonic waves. Although these first clinical trials are very encouraging, it appears that the handling of the vibrator-array system by practitioners was not easy and, moreover, that the quality of the displacements field of low frequency waves (in terms of the signal-to-noise ratio) was dependent on the operator. These two facts have pushed J  r  my Bercoff, Mickael Tanter and Mathias Fink to an elastography technique based solely on ultrasound: supersonic shear imaging.

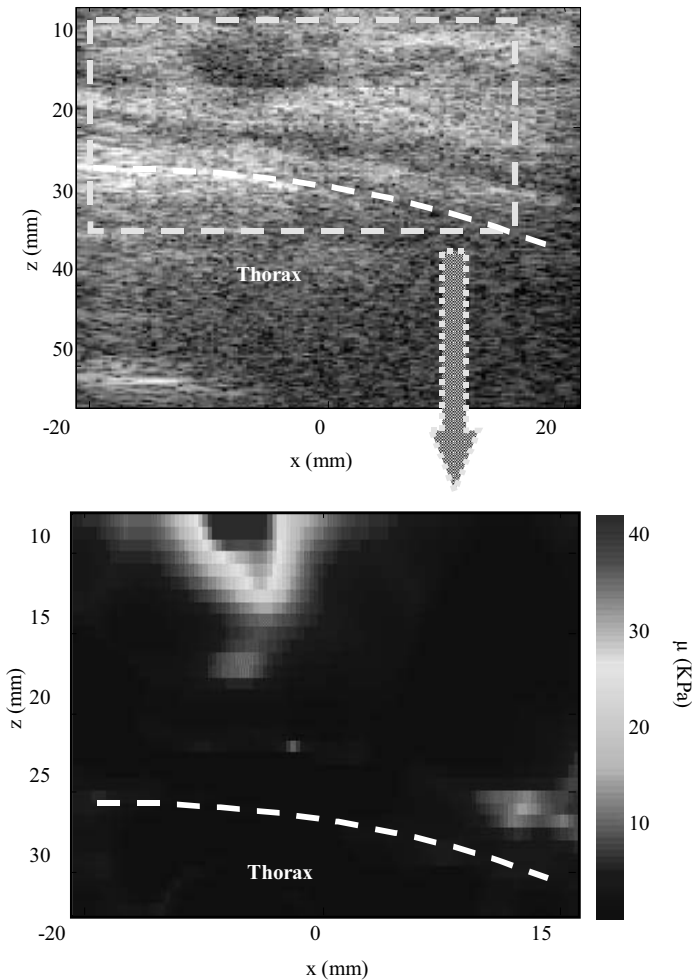


**Figure 32.9.** *In vivo* experiments of transient elastography. The breadboard of Figure 32.3 has been tested on volunteers from the Curie Institute. a) Ultrasound image of the breast obtained from a volunteer, showing a carcinoma of about 1 cm diameter visible by ultrasound. b) The reconstruction by inverse problem gives the quantitative image of the shear modulus in the area defined by the yellow dots. The scale ranges from 0 to 80 kPa

The imaging technique called “supersonic imaging” is based on both the use of the acoustic radiation force and the transient elastography technique. More specifically, in a first step, a high intensity ultrasonic wavetrain of a few hundred

sinusoid arches is focused in tissues. At the focus, a radiation force moves tissues. The system instantly goes to ultrafast ultrasound mode. The disappearance of the radiation force and the return to equilibrium is accompanied by the propagation of a shear wave. Therefore, this technology has the enormous advantage of exempting the practitioner from handling a heavy mechanical vibrator. Globally, the different steps of the process (pressure radiation and propagation of the shear wave) take only 40 ms, and mapping the elasticity of tissues does not greatly alter the actions of the radiologist. In addition, the quasi-simultaneous generation of shear waves at different locations is made by electronic focalizations. This process has not only enabled the study of elastic Mach cones in soft solids [BER 04a], but it also improves, from a practical point of view, the quality of elasticity maps, which are obtained by the inverse problem on the displacement field of shear waves [BER 04b].

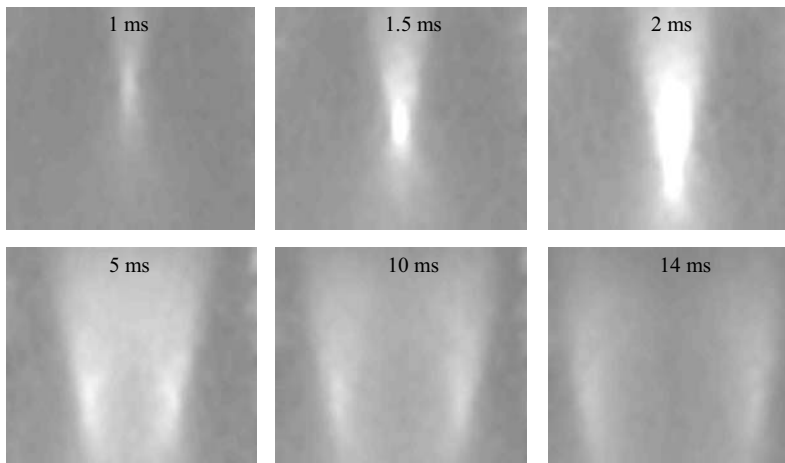


**Figure 32.10.** *Experimental results: generation by pressure radiation of a supersonic shear wave and detection of the displacement field by ultrafast ultrasound in an agar–gelatin gel. The vertical component of the displacement, from 0 to 10  $\mu\text{m}$ , is represented in grayscale at 6 successive times in a 40 x 40 mm area*

Since 1995 (the date of publication in *Science* of the fundamental article from Muthupillari [MUT 95]), MRI elastography has given rise to many publications. One reason for this dynamism is the three-dimensional nature of the information collected by magnetic resonance elastography (MRE). Indeed, although ultrasound techniques are much cheaper, much easier to implement and mostly work in “real time”, they also have the inconvenience of providing only two-dimensional information, in terms of image. The MRE remains leader of 3D elastography

systems, until some ultrafast three-dimensional ultrasound systems are available in the future. Knowing the three-dimensional displacement field of shear waves helps us to obtain, through extremely rigorous algorithms for the inverse problem, information on elasticity, viscosity and even anisotropy, as illustrated by the maps shown in Figure 32.11 [SIN 05]. These *in vivo* experiments on the breast of a volunteer with a fibroadenoma are carried out by Ralph Sinkus. The elasticity, viscosity and anisotropy maps clearly identify the mechanical properties of the tumor.

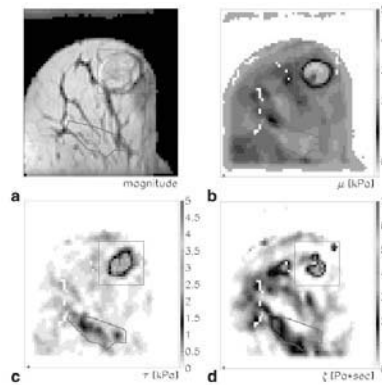


**Figure 32.11.** *In vivo* experimental result of magnetic resonance elastography (MRE) on a volunteer with a fibroadenoma in the breast. (a) The lesion is visible in the red rectangle of the MRI image. The elasticity (b), anisotropy (c) and viscosity (d) maps confirm the presence of a tumor and reveal its mechanical properties

## 32.2. Bibliography

- [AKI 80] K. Aki *et al.*, *Quantitative Seismology, Theory and Methods*, vol. 1, W. H. Freeman and Company, San Francisco: ch. 4, 1980
- [BER 04a] J. Bercoff *et al.*, “Sonic boom in soft materials: The elastic Cerenkov effect”, *Appl. Phys. Lett.*, 84, 2202, 2004
- [BER 04b] J. Bercoff *et al.*, “Supersonic Shear Imaging: a new technique for soft tissues elasticity mapping”, *IEEE Trans. Ultrason., Ferroelec., Freq. Contr.*, 51, 374, 2004
- [BER 04c] J. Bercoff, M. Tanter, M. Muller, M. Fink, “The role of viscosity in the impulse diffraction field of elastic waves induced by the acoustic radiation force”, *IEEE Trans Ultrason Ferroelectr Freq Control* 51(11), 1523–36, 2004
- [CAT 99] S. Catheline *et al.*, “Diffraction field of a low-frequency vibrator in soft tissues using transient elastography”, *IEEE Trans Ultrason Ferroelect Freq Contr.*, 46(4), 1013–20, 1999

- [CAT 99b] S. Catheline *et al.*, “A solution to diffraction biases in sonoelasticity: The acoustic impulse technique”, *J. Acoust. Soc. Am.*, 105, 2941–50, 1999
- [CAT 03] S. Catheline *et al.*, “Observation of Shock Transverse Waves in Elastic Media”, *Physical Review Letters*, 91 (16), 43011–14, 2003
- [CAT 04] S. Catheline *et al.*, “Measurement of viscoelastic properties of soft solid using transient elastography”, *J. Acoust. Soc. Am.*, 116 (6), 3734–41, 2004
- [CHE 96] E.J. Chen *et al.*, “Young’s Modulus measurements of soft tissues with application to elasticity imaging”, *IEEE Trans. Ultras. Ferroel. Freq. Cont.*, 43, 191–4, 1996
- [DIC 82] R.J. Dickinson *et al.*, “Measurement of soft tissue motion using correlation between A-Scans”, *Ultr. Med. & Bio.*, 8, No. 3, 263–71, 1982
- [EIS 83] A. Eizenscher *et al.*, “La palpation échographique rythmée: Echosismographie. Une nouvelle technique de différenciation des tumeurs bénignes et malignes par l’étude ultrasonore de l’élasticité tissulaire”, *J. Radiol.*, 64, No. 4, 255–61, 1983
- [EIS 91] F. Eisenberger *et al.* *Stone Therapy in Urology*, Georg Thieme Verlag, Stuttgart, Germany, 1991
- [FAT 98] M. Fatemi *et al.*, “Ultrasound-stimulated vibro-acoustic spectrography”, *Science*, 280, 82–5, 1998
- FUK 69] H. Fukaya *et al.*, “Stress–strain relations of tissue sheets undergoing uniform two dimensional stretch”, *J. Appl. Physiol.*, 27, 758–62, 1969
- [GAL 69] F.R. Galey, “Elastic properties of fixed and fresh muscle”, *J. Ultrastruct. Res.*, 26, 424–41, 1969
- [GAR 97] B.S. Garra *et al.*, “Elastography of breast lesions: initial clinical results”, *Radiology*, 202, 79–86, 1997
- [GEN 03] J.L. Gennisson *et al.*, “Transient elastography in anisotropic medium: Application to the measurement of slow and fast shear waves velocities in muscles”, *J. Acoust. Soc. Am.*, 114, 536–41, 2003
- [KRO 87] T.A. Krouskop *et al.*, “A pulsed Doppler ultrasonic system for making noninvasive measurements of the mechanical properties of soft tissue”, *J. Rehabil. Res. Dev.*, vol. 24, 1–8, 1987
- [KRO 98] T.A. Krouskop *et al.*, “Elastic moduli of breast and prostate tissues under compression”, *Ultrasonic Imaging*, 20, 260–74, 1998
- [LER 88] R.M. Lerner *et al.*, “Sono-elasticity: Medical elasticity images derived from ultrasound signals in mechanically vibrated targets”, *Acoustic Imaging*, 16, 317–27, 1988
- [MUT 95] R. Muthupillai *et al.*, “Magnetic resonance elastography by direct visualization of propagating acoustic strain waves”, *Science*, 269 (5232), 1854–7, 1995
- [NIG 01] K.R. Nightingale *et al.*, “On the feasibility of remote palpation using acoustic radiation force”, *J Acoust Soc Am.*, 110(1), 625–34, 2001
- [OPH 91] J. Ophir *et al.*, “Elastography: a quantitative method for imaging the elasticity of biological tissues”, *Ultrasonic Imaging*, 13, 111–34, 1991



- [OPH 99] J. Ophir *et al.*, “Elastography: ultrasonic estimation and imaging of the elastic properties of tissues”, *Journal of Engineering in Medicine*, 213(3), 203–33, 1999
- [PAR 90] K.J. Parker *et al.*, “Tissue response to mechanical vibrations for ‘sonoelasticity imaging’”, *Ultrasound Med. Biol.*, vol. 16, no. 3, 241–6, 1990
- [SAN 99-a] L. Sandrin *et al.*, “Time-resolved pulsed elastography with ultra fast imaging”, *Ultrasonic Imaging*, Vol. 21, 259–72, December, 1999
- [SAN 04] L. Sandrin *et al.*, “The role of the coupling term in transient elastography”, *J. Acoust. Soc. Am.*, 115, 76–83, 2004
- [SCR 90] C. B. Scruby *et al.*, *Laser Ultrasonics*, Adam Hilger, New York, 223–324, 1990
- [SIN 05] R. Sinkus *et al.*, “Imaging Anisotropic and Viscous Properties of Breast Tissue by MR-Elastography”, *Magnetic Resonance in Medicine*, 53, 372–87, 2005
- [SOU 03] R. Souchon *et al.*, “Prostate elastography: in vitro study”, *Proc. IEEE Ultrasonics Symp.*, vol. 2, 1251–3, 2003
- [YAM 70] H. Yamada, *Strength of Biological materials*, The Williams & Wilkins Co., Baltimore, MD, 1970
- [YAM 87] Y. Yamakoshi *et al.*, “Imaging the elastic properties using low frequency vibration and probing ultrasonic wave”, *Japanese Meeting of Applied Physics*, Tokyo, 1987

This page intentionally left blank

## Chapter 33

# Ultrasound and Therapy

### 33.1. Introduction

Following Langevin's tests on sonar during the First World War, in which the possibility of tissue destruction by ultrasound was demonstrated, treatment ultrasound was nearly non-existent, and clinical use of ultrasound was primarily for diagnosis. With the development of new transducer technologies as well as advances in guiding and monitoring, therapeutic applications of ultrasound have gained renewed interest in the past two decades. In particular, two clinical applications are used regularly today.

The first, called extracorporeal lithotripsy, aims at applying shock waves to break up kidney stones. The second application seeks to destroy tumors with the heat generated by high intensity focused ultrasound (HIFU = High Intensity Focused Ultrasound).

Both applications, which are discussed within this chapter encompass the different effects that can be induced in tissues by ultrasound. These biological effects can be divided into two categories: thermal effects and non-thermal effects (Figure 33.1). Cavitation induces mechanical stress in tissues and may induce chemical effects. It should be noted that biological effects are mostly the result of a combination of different effects.

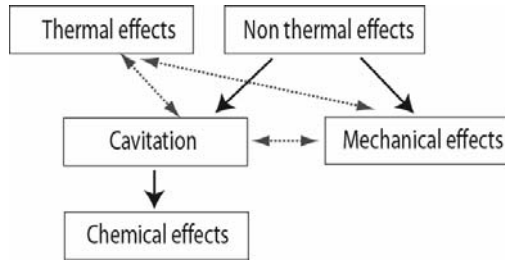


**Figure 33.1.** *The various biological effects of ultrasound usually occur simultaneously during therapeutic applications*

### 33.1.1. *Shock waves and extracorporeal lithotripsy*

#### 33.1.1.1. *History*

The pathophysiology of nephritic lithiasis disease was the subject of intensive research for many years. During this period, the knowledge of the etiology of the disease was considerably improved. However to date, a cure has not been found. The revolution in the treatment of gallstones is mainly due to the emergence of treatment with shock waves, also called lithotripsy treatment (ESWL: *extracorporeal shock wave lithotripsy*). Since the first successful treatment was achieved by Chaussy in 1980 [CHA 80], ESWL has become the indicated treatment of urolithiasis. 85% of urolithiasis are treated with ESWL [SAU 91]. Currently, more than 800 centers of extracorporeal lithotripsy exist in the world, and several million patients have benefited from the success of this technique. The treatment involves the focus of very high amplitude shock waves, generated outside the body of the patient, on the stone to destroy it. Typically, this technique requires no anesthesia or, strictly speaking, a simple analgesia. Many details at the clinical level, about this technique can be found in general journals on this topic [CHA 86, EIS 91]. Treatment with extracorporeal lithotripsy requires:

- a shock wave generator;
- a system of localization of the stone;
- real-time synchronization of the stone's location and the focal point of the shock wave generator.

#### 33.1.1.2. *The various sources of shock waves*

A shock wave (Figure 33.2) is defined as a sudden increase in pressure, with a very short rising time (around 100 ns), followed by a return to normal state (zero pressure) according to an exponential decrease. The total duration of the pulse is about one microsecond and the pressure generated is about 100 MPa (1 MPa = 10 Bars).

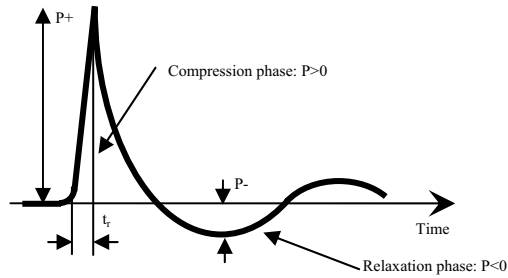


**Figure 33.2.** The shock wave is characterized by a compression phase with a brief rising time (about 10 ns) followed by a relaxation phase that can last several microseconds

#### 33.1.1.2.1. The electro-hydraulic and electroconductive generator

This type of generator uses a point source. Two electrodes are placed in water (Figure 33.3), and a violent electric shock creates a steam bubble. The high-speed expansion of the bubble creates a spherical shock wave. The space between the electrodes being placed at the first focus of a reflecting semi-ellipsoid, the generated shock wave is partially reflected and concentrates its energy on the second focus of the reflector. The electric power is provided by a capacitor with a capacity generally close to 0.1  $\mu\text{F}$ , regularly recharged by a high voltage power supply between 12 and 20 kV. Electrical switching is performed by an air-spark-gap switch.

The transmission of the shock wave from the generator to the patient is done through a coupling medium consisting of degassed water, to avoid the formation of bubbles that absorb and diffuse an important part of the wave. The pressure obtained at the focal point has an amplitude of the order of several tens of MPa. Degassed water is also suitable for use with other types of generators.

In degassed water, plasma forming is a non-reproducible phenomenon involving very significant variations of the pressure pulse. There is a random latency period between the closure of the switch and the emergence of the electric arc. Moreover, the passage of the current between the two electrodes does not cover the complete surface, but occurs only between two points, whose position is unpredictable. A substantial improvement in these generators was proposed by Broyer *et al.* [BRO 96]. It consisted of replacing the electric arc, with an electrical discharge in a conducting liquid medium (Figure 33.4). This generator, also known as an electroconductive generator, allows reproducibility of the pressure wave of the order of the percent. In addition, as the discharge is performed by an infinite number of current lines spread over the whole section of the electrodes, the lifetime of the

electrodes is widely increased. Finally, the constant conductivity in the electrolyte allows the use of a transmission line and to deport the shock wave generator from the electrical discharge setup.

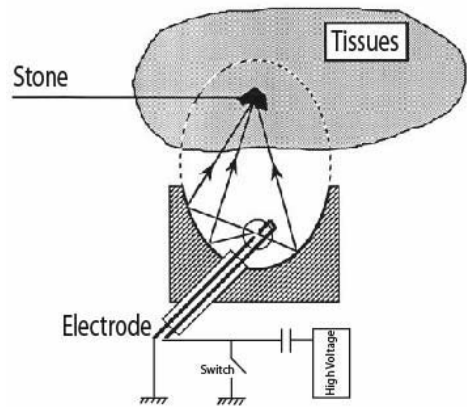


**Figure 33.3.** Principle of electrohydraulic generator. The electric discharge between two electrodes creates a shock wave that, after reflection on the wall of the semi ellipsoid, is focused on the second focal point, where the stone to be destroyed is located

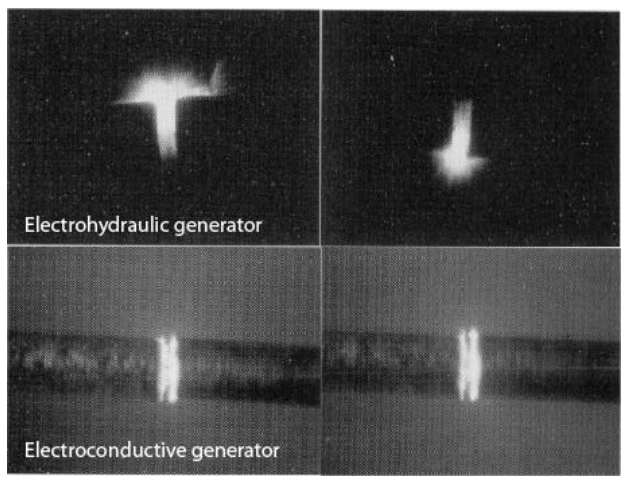


**Figure 33.4.** The location of the arc formation varies from one shock to another in the case of the electrohydraulic generator (top figures), while it is fixed in the case of the electroconductive generator (bottom figures)

### 33.1.1.2.2. The electromagnetic generator

This generator uses an extended source that consists of a metal membrane. It works according to the same principle as the loudspeaker (Figure 33.5). A capacity, charged between 16 and 22 kV, is suddenly discharged through an electromagnetic coil in less than 5  $\mu$ s. The current inside the coil induces an intense magnetic field that pushes the opposite metal membrane. The displacement of the membrane creates a pressure wave that propagates inside a cylinder, and then turns into a shock wave. The focus is then obtained by using an acoustical lens. There is also a variant in which the membrane is cylindrical. The pressure wave is generated radially and focused by reflection on the surface of a semi-paraboloid.

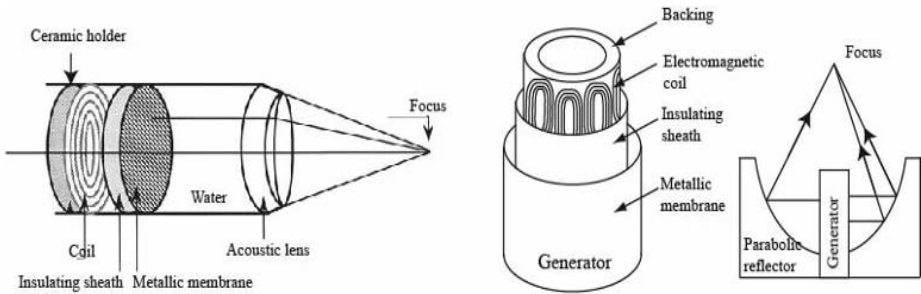


**Figure 33.5.** *The principle of the electromagnetic generator is similar to that of the loudspeaker. The plane or cylindrical membrane is quickly attracted, creating the ultrasonic wave. The focus is ensured by a lens or a parabolic reflector*

### 33.1.1.2.3. The piezoelectric generator

The piezoelectric source consists of a two-dimensional matrix, made of a multitude of elementary piezoelectric transducers, which create a mechanical deformation under the action of an electric field. These transducers are arranged on the inner face of a spherical shell (Figure 33.6). When exposed to an electric shock, they expand and then immediately return to their original state following a specified number of oscillations. The resulting acoustic wave naturally focuses at the center of the sphere. Because of the low pressure on the surface of the spherical shell, it is essential to provide a large emitting surface, resulting in the use of very bulky generators. Today, the efficiency of these generators is still weaker than its competitors and two treatment sessions are required for some stones.

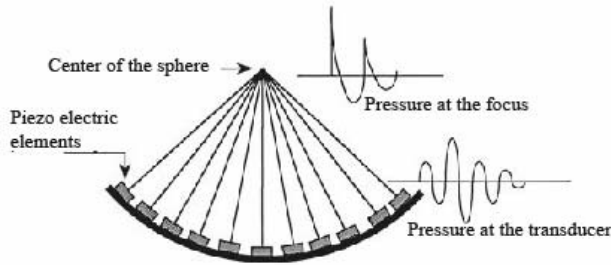


**Figure 33.6.** *Piezoelectric generators are made of a two-dimensional matrix of elementary transducers. The wave focuses naturally at the focal point of the shell*

#### 33.1.1.2.4. The generator–patient coupling

Optimal coupling ensures that the power loss between the generator and the stones to be destroyed is as low as possible. Any interface between two different media attenuates the ultrasonic waves, and thus should be avoided. Two solutions were considered:

- immersion of the body of the patient. This solution was adopted by the Dornier Company; developers of the first lithotripter. This solution is complex because it involves moving the patient in three directions, in order to ensure that the position of the stone coincides with the focal point of shock waves;
- coupling through a membrane.

In immersing the body of the patient, the energy loss of the shock wave is minimal. However, this solution is uncomfortable for the patient, cumbersome, and does not allow for treatment of the stones by a different approach. The use of a membrane is much more flexible and ergonomic. A membrane with an acoustic impedance similar to that of water produces a low level of energy loss. Solutions have been found to change the electrodes easily (in the case of electro-hydraulic and electro-conductive generators) and to avoid the deposit of microbubbles on the membrane. Currently, the energy loss is less than 5% and all manufacturers have chosen this technique.

#### 33.1.1.2.5. Characterization of the shock waves generated by the various generators

Comparison of the acoustic wave generated by each generator can be made through the temporal form of the resulting shock wave at the focus, and the spatial distributions at the focus and at the skin level [COL 89, BUI 95]. After the crossing of the coupling medium and the focalization, the shape of the shock wave is similar to that shown on Figure 33.2. The criteria generally accepted to characterize this type of shock wave include:



- the value of the positive maximal pressure, called compression wave P+;
- the value of the negative maximal pressure, called relaxation wave P-;
- the temporal width at half height  $t_w$ ;
- the rising time  $t_r$ ;
- the pulse duration  $t_p$ .

The exact value of these parameters is quite difficult to determine. There are significant variations reported by different authors, due to the fact that the hydrophones used have a limited bandwidth and the active receiving area is too large (of the order of a square millimeter), resulting in a significant distortion of the wave measured. The maximum value of the pressure is around 100 MPa. The value of the amplitude of the negative pressure (–10 MPa) does not significantly change from one machine to another. This is due to the fact that beyond a certain value of the pressure, the negative pressure waves (relaxation waves) are no longer sent; there is an inhomogeneity of the water. The rising times are a few tens of nanoseconds for piezoelectric and electro-hydraulic machines, and a few hundred nanoseconds for electromagnetic machines. The higher value of the rising time is due to the fact that, as the frequency of the wave generated is lower, the wave has no time to reach the full shock state in its path. The temporal width at half height, of the order of 350 ns, is the same for all generators. The pressure generated by a lithotripter may vary from one shock to another. Reproducibility is good for piezoelectric, electromagnetic and electroconductive generators. For electro-hydraulic machines, standard deviations on the measurement of the pressure are about 25 to 30%, depending on the machine and the wear of the electrode. The energy is not punctually distributed at the geometric focus, rather it is distributed in an ellipsoidal volume, with the major axis given by the propagation direction of ultrasound. The volume depends greatly on the quality of the focalization and the intensity of the shock wave. Poor focalization and a great energy increase the focal volume. The focal stain is wider in the case of electro-hydraulic generators (major axis 6 to 8 cm, short axis approximately 2 to 3 cm), and lower in the case of piezoelectric generators (major axis 3 to 4 cm, short axis approximately 0.5 to 1 cm). Given the spatial distribution of pressure, it is possible to calculate the energy density (energy per unit area) and/or the energy crossing the focal area. The energy density and energy are about four times lower in the case of piezoelectric generators. This is extremely important because the destruction of stones is primarily linked to the wave energy, when the destruction threshold in energy is reached. The aperture is characterized by the angle at the top of the wave heading towards the focal point. This parameter depends on the geometry of the generator. The greater the angle, the more energy is diluted before the focalization. This results in lower pressure and a decrease in pain for the patient. The pressure is 2 to 3 MPa for piezoelectric generators and 2 to 3 times greater for other types.

### 33.1.1.3. *Imaging of the stone*

Identification of the stone is currently done in two different and complementary ways: X-rays and ultrasound. In the case of X-rays, the doctor produces two images of the area of interest from two different angles, in order to obtain the position of the stone in space. This procedure is justified by the fact that X-ray imaging provides only the shadow of the object. This method is expensive and ionizing. It applies to kidney stones (with the exception of radio transparent stones). Ultrasonic tracking consists of making an ultrasound image of the area of interest, thanks to an ultrasonic probe located either on the generator itself, or at the end of an articulated arm whose each joint is equipped with a position coder. This technique is completely non-invasive but requires more experience. Positioning of the stone in front of the focal point of the shock waves is done by a relative movement of the patient with respect to the generator.

### 33.1.1.4. *The mechanisms of fragmentation*

The study of fragmentation was primarily conducted on artificial stones. We can distinguish the direct effects arising from the interaction of the shock wave with the material, and indirect effects, which are due to the medium immediately surrounding the stone [COL 93].

#### 33.1.1.4.1. The direct effects

Given the low difference of the acoustical impedance between tissue and water, the shock wave propagates inside the body and is subject to low refraction and reflection effects only. In contrast, the acoustical impedance of a urinary stone is five to ten times higher than that of tissue. When the shock wave strikes the surface of the stone, a portion of the energy is reflected, creating a compressive force on the surface, on the front face of the stone. A compression wave then propagates through the stone, creating strains along the path. Arriving at the rear of the stone, the compression wave is reflected, creating a relaxation wave, which propagates in the opposite direction inside the stone (Hopkinson effect). Due to the nature of the stone (generally heterogeneous), these multiple strains induce a fragmentation from the periphery to the center, which results in the disintegration of the stone (Figure 33.7). These effects are usually called “spalling” [EIS 91]. A second effect, called “squeezing”, has been highlighted. This effect is due to the fact that the wave velocity inside the stone is higher than in the surrounding medium. Some quasi-static circumferential pressures appear which are responsible for the fracture along meridians or parallels.

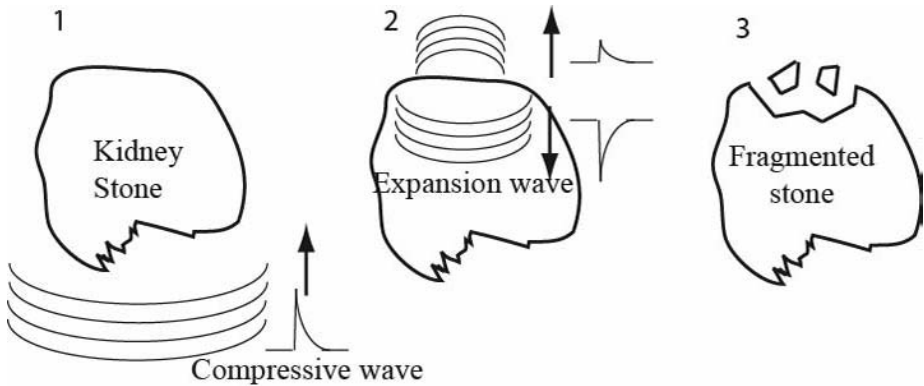


**Figure 33.7.** *The compression wave reaches the stone (1). Due to the tissue–stone impedance ratio, the reflected part of the wave turns into a relaxation wave (2) responsible for the erosion of the stone (3)*

#### 33.1.1.4.2. The indirect effects

In addition to the direct effects of shock waves, the fragmentation of stones is also due to a secondary phenomena associated with the unstable cavitation that is created around the stone. The cavitation occurs because of the negative wave immediately following the shock wave (Figure 33.2). These relaxation waves are also produced by the reflection of shock waves at the interfaces, where the compression waves are transformed into relaxation waves. If the value of the relaxation wave is sufficient, as in lithotripsy, it causes an unstable cavitation in the liquid surrounding the stone (water, blood, urine, bile) and the collapse of microbubbles. Such collapses generate secondary shock waves and microjets, resulting in a gradual erosion of the surface of the stone. A clear demonstration of the importance of this indirect effect was given by Sass [SAS 91], who achieved high speed pictures of the progressive destruction of gallstones.

#### 33.1.2. *High intensity focused ultrasounds for ultrasound surgery*

The current trend is the development of minimally invasive surgical techniques that are more comfortable for the patient, reduce morbidity, and are more economical. High-intensity focused ultrasound has demonstrated its therapeutic potential [LYN 42]. Recent advances in imaging and electronics allow a precise and controlled treatment making HIFU a relevant treatment approach. According to theoretical and experimental studies, the dominant mechanism for the induction of tissue damage is thermic. The cavitation and boiling resulting from pressure regimes and high temperature are also involved in the development of lesions. By focusing

ultrasound waves from outside the body of the patient, coagulation necrosis can be obtained at a depth of 10 cm without damaging the intermediate layers. Endocavitary or interstitial applicators can be inserted near the target if it is inaccessible from outside the body. Since the early 1990s, HIFU has found its place in clinical applications for the treatment of benign and malignant tumors in several medical specialties.

#### 33.1.2.1. *HIFU generators*

The use of high frequency (1–5MHz) and highly focused transducers limits the amount of damage to the focal spot of the transducer (1–5 mm in diameter by 1–2 cm long). The ultrasound intensity used allows for a temperature above 50°C to be obtained within a few seconds, therefore limiting the effects of heat diffusion. This technique is very well-suited to treat either benign or malignant localized tumors. Concave transducers are generally used for focalization, but plane transducers may also be associated with an acoustical lens (Figure 33.8). The treatment of a tumor is done by moving the beam focal spot sequentially point by point over the tumor volume by mechanical means. More sophisticated applicators have been developed for electronic scanning of tumors. The transducer is divided into components driven in an independent manner. The phase differences between the elements help to move the focal point. Dynamic 1D focalization describes when the focal point can be moved only along the acoustical axis of the transducer array. For a 1.5D matrix, the focal point can move only in a sagittal plane of the matrix, as the columns that are symmetrical with respect to the central column are connected together. Finally, with an array made of  $N \times N$  independently supplied elements, it is possible to achieve a 2D focalization.

The most satisfactory treatments involve extracorporeal focused transducers that allow a completely non-invasive remote treatment of the tumor. However, methods using endocavitary or interstitial applicators have been proposed to reach tumors located at a depth inaccessible to extracorporeal HIFU. When the ultrasonic wave encounters bones or gas pockets, it is naturally attenuated and distorted. The attenuation and phase aberrations induce a decrease of the gain in pressure. The pressure can be increased on the surface of the transducer, with the hope of providing enough energy at the focal point. This compensation will alter intermediary tissues, whose temperature also increases. The objective of interstitial or endocavitary mini-invasive probes is to bring the ultrasound source as close as possible to the target, using natural methods, to minimize these attenuation and phase aberrations. It becomes possible to work at higher frequencies in order to increase the efficiency of heating. Compared to extracorporeal applicators, constraints on the size and the ergonomics of the probes are added.

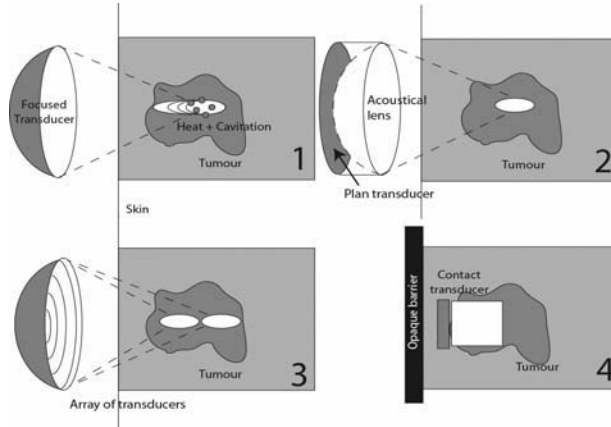


**Figure 33.8.** The various HIFU generators: focused single element extracorporeal applicator (1), plane transducer with acoustical lens (2), dome with annular elements array for dynamic 1D focalization (3) and plane interstitial transducer directly in contact with the tumor (4)

### 33.1.2.2. Mechanisms of tissue destruction involved when applying HIFU

Thermal ablation with HIFU or ultrasonic surgery should not be confused with ultrasonic hyperthermia. Hyperthermia, used in cancer treatment aims to heat the tissue to a temperature of  $43^{\circ}\text{C}$  over one hour. Heating is applied simultaneously with radiotherapy. The aim is to sensitize tumor cells to radiation. Due to the relatively long heating time, perfusion and thermal conductivity make it difficult to obtain uniform heating. Thanks to HIFU, the application, of higher temperatures (above  $50^{\circ}\text{C}$ ) for a few seconds helps to limit the heat sink due to thermal diffusion [BIL 90]. The primary mechanism for obtaining lesions is thermal. The pressures generated at the focal point of the transducers to achieve such temperatures can induce cavitation, which can influence the development mode of coagulation necrosis.

#### 33.1.2.2.1. The temperature

An ultrasonic wave that propagates through biological tissues is partially absorbed. The mechanism of absorption induces a temperature rise, depending both on the thermal conductivity of the medium and the perfusion rate.

If the intensity of a plane wave is  $I_0$  at the source  $x = 0$ , the intensity at  $x$  is given by the exponential decrease

$$I(x) = I_0 e^{-\alpha x}, \quad [33.1]$$

where  $\alpha$  is the attenuation coefficient of the tissues. Considering that the attenuation coefficient is equal to the absorption coefficient ( $\mu$ ), the local heat contribution per volume unit ( $q$ ) is obtained by taking the gradient of the intensity over  $x$ :

$$q(x) = \mu I(x) \quad [33.2]$$

The absorption coefficient increases with frequency, hence the importance of using high frequencies in the heating process. There is still a compromise between the treatment depth and the induced temperature rise. Similarly, for high pressures, the propagation in non-linear regime is accompanied by the generation of higher harmonics that will strengthen the heating of tissues.

The energy absorption of a wave occurs in a visco-elastic medium such as tissue, when fluctuations in the medium density during the passage of the wave are no longer in phase with the pressure fluctuations. The relaxation phenomena reflect the presence of mechanisms of energy transfer occurring during a finite time. The ultrasonic wave transmits energy in a mechanical form to a volume of tissues it crosses. The ultrasonic wave then deviates from its energy equilibrium. Since the return to equilibrium is not in phase with the pressure variations on input of the volume, the ultrasonic wave is attenuated. Consequently, there is a peak on the absorption coefficient, corresponding to a frequency known as the relaxation frequency. Typically, several phenomena coexist, linked to various relaxation times (or relaxation frequencies). The sum of these contributions gives the frequency variation of the total absorption coefficient due to the relaxation phenomena. The absorption phenomenon is described in detail by Hill *et al.* [HIL 04].

The temperature rise, resulting from the absorption of ultrasonic waves, can be obtained by solving the Bio-Heat Transfer Equation, or BHTE [PEN 48]. In a perfused medium, the BHTE takes the following form:

$$\rho_t c_t \frac{\partial T}{\partial t} = k_t \nabla^2 T + m_b c_b (T_a - T) + q \quad [33.3]$$

where  $T$  is the temperature,  $\rho_t$ ,  $c_t$  and  $k_t$  the density, specific heat and thermal conductivity of the tissue, respectively,  $m_b$  the local perfusion ratio and  $c_b$  the specific heat of blood. The left-hand side term is the internal energy variation per volume unit. In the right-hand side term, the Laplacian represents the exchanges by conduction heat and the second term introduces the perfusion phenomenon. These two terms can be neglected in the case of a very short time for the application of the power.

#### 33.1.2.2.2. Cavitation

Acoustic cavitation can be defined as the formation and activity of cavities filled with gas or vapor (bubbles) in a medium insonified by ultrasound. Two types of

cavitation are commonly described in the literature: inertial (or transient) cavitation and non-inertial (or stable) cavitation. Under the inertial cavitation regime, a cavity filled with gas will increase in size during the relaxation phase of an acoustic cycle, before being reduced to a fraction of its original size. The inertia of the bubble governs the deformation during the sudden compression phase. High temperatures and light (sonoluminescence) can be generated locally. The collapse of the bubble is accompanied by the emission of a shock wave, or the formation of free radicals. In the non-inertial cavitation regime, bubbles exposed to the ultrasonic field have rather an oscillatory behavior. By rectified diffusion, they tend to their resonance size. The oscillation of the bubbles may include distortion of their surface or microstreaming phenomena.

Both types of cavitation are involved in HIFU treatments. The bubbles generated (by cavitation or by boiling in the case of excessive heating) at the focal point contribute significantly to the displacement of coagulation necrosis in the direction of the transducer, as demonstrated theoretically by Chavrier [CHA 00]. Compared to the purely linear model that matches the development of thermal injury on the ellipsoidal focal spot of the transducer, experiments show cone shaped lesions, with a base directed towards the transducer [MEA 00]. The phenomena of thermal lens and the increase of the attenuation coefficient related to the temperature rise in front of the focal point also contribute to the migration of the damage to the transducer, but are second order effects.

### 33.1.2.3. *HIFU applications*

Many experimental applications of ultrasonic surgery have been proposed in recent years. HIFU is used either to treat tumors, or to control bleeding [VAE 01]. However, only a few applications, for which devices are commercially available, are used in routine clinical use. They can be separated into two main categories: extracorporeal approaches in gynecology and in liver surgery, and endocavitary applications in urology.

#### 33.1.2.3.1. HIFU extracorporeal applications

Extracorporeal transducers generally operate at lower frequency than endocavitary transducers, in order to limit tissue heating in front of the focal point. They require a focal length that is long enough to reach their target. Less limited in terms of ergonomics, the transducers are larger than endocavitary transducers, in order to increase the pressure gain on the transducer surface at the focus.

ExAblate® 2000 is manufactured by the InSightec company (Tirat Carmel, Israel). This device is approved in many countries for the non-invasive treatment of uterine fibroids. It is a new surgical device that combines HIFU with magnetic

resonance imaging (MRI). The use of MRI helps to monitor the temperature and the dose of the treatment.

Since 1997, the Tumour Therapy System (JC model, Chongqing Haifu™ Technology Co., China) has successfully treated more than 8,000 patients suffering from various cancers in more than 20 centers in China. Approved by conclusive clinical trials conducted at the Churchill Hospital in Oxford (United Kingdom), and created by Ultrasound Therapeutics Ltd., a British company, this equipment was recently awarded the CE certificate. HIFU is generated by a plane transducer equipped with a lens. The focal point is positioned on the target by the operator using ultrasound imaging techniques. To ensure the perfect immobility of the patient throughout the procedure, the operation is conducted under general anesthesia. The Churchill Hospital trials aimed at the treatment of liver tumors. The trials revealed that in 93% of the liver tumors treated, the ablation of the targeted focal point was successful [ILL 05]. In more recent trials, kidney tumors were also treated successfully. Literature reports of the benefits of this procedure for patients with pancreatic cancer, breast cancer and also certain types of bone cancers [WU 04].

#### 33.1.2.3.2. Endocavitary applications of HIFU in urology

Devices are now commercially available for treatment of prostate tumors. Although the extracorporeal approach is feasible [HAC 05], the two commercial devices use an endocavitary approach and HIFU is applied through the rectum. In both cases, treatment is conducted under ultrasound imaging with a rectal probe.

The first clinical application of HIFU was developed by the EDAP Technomed company (Vaulx-en-Velin, France). The Ablatherm device is used for the treatment of prostate cancer, which is the most common cancer for men and second in terms of mortality (after lung cancer). The first treatment of prostate cancer by the Ablatherm device was in 1993. HIFU treatment is minimally invasive; the morbidity is very low. It is performed under spinal anesthesia and the duration of hospitalization is very short. Patients who have suffered a failure in radiotherapy can receive a HIFU treatment [GEL 04]. At the same time, the HIFU treatment is not a therapeutic dead end: the treatment can be repeated, or adjuvant treatments can also be applied. Very positive results have been achieved. A multi-centric European study, concerning 402 patients with an average follow up of 13 months, shows that biopsies carried out are negative for 87.2% of patients, and the level of PSA (Prostate Specific Antigen) is normal for 81.4%.

After being limited to the treatment of benign prostatic hyperplasia [SAN 99b], Sonablate devices (Focus Surgery, Indianapolis, IN, USA) are used to treat prostate cancer [UCH 02]. Regarding the work on prostate adenoma, the results in terms of urine flow, life quality and IPSS (International Prostate Symptom Score) are very positive. HIFU treatment is safe and sustainable over time.



### 33.1.3. Conclusion

Ultrasound is now widely used in clinical therapy. For instance, extracorporeal lithotripsy by shock waves is the first choice for treating kidney stones. HIFU ultrasonic surgery is making its way from research laboratories to clinical treatments of various benign and malignant tumors. Revolutionary new methods of treatment involving ultrasound appear in current literature [TAC 04]. For example, ultrasound, through cavitation, can increase the efficiency of thrombolytic agents in the case of acute myocardial infarct. Among other things, we can mention progress in the following areas:

- the development of new ultrasonic catheters;
- sonodynamic therapy: the chemical activation of medicines by ultrasounds;
- gene therapy: a transfection can be obtained by combining a gene, a microbubble and ultrasounds;
- local delivery of medicines encapsulated in targeted carrying agents which release their contents under the action of ultrasounds.

The emergence of these new applications of ultrasound suggests a more widespread application of ultrasounds in therapy.

### 33.2. Bibliography

- [BIL 90] B.E. Billard *et al.*, “Effects of physical parameters on high temperature ultrasound hyperthermia”, *Ultrasound Med Biol.*, Vol. 16(4), 409–20, 1990
- [BRO 96] P. Broyer *et al.*, “High-efficiency shock-wave generator for extracorporeal lithotripsy”, *Med Biol Eng Comput.*, Vol. 34, 321–8, 1996
- [BUI 95] A. Buizza *et al.*, “The performance of different pressure pulse generators for extracorporeal lithotripsy: a comparison based on commercial lithotripters for kidney stones”, *Ultrasound in Med. & Biol.*, Vol. 21(2), 259–72, 1995
- [CHA 80] C. Chaussy *et al.*, “Extracorporeally induced destruction of kidney stones by shock waves”, *Lancet*, Vol. 20, 1265–8, 1980
- [CHA 86] C. Chaussy (ed.), *Extracorporeal Shock Wave Lithotripsy – Technical Concept, Experimental Research, and Clinical Application*, 2nd, revised and enlarged edition, Karger, Basel, Switzerland, 1986
- [CHA 00] F. Chavrier *et al.*, “Modelling of high-intensity focused ultrasound-induced lesions in the presence of cavitation bubbles”, *J Acoust Soc Am.*, Vol. 108(1), 432–40, 2000
- [COL 89] A.J. Coleman *et al.*, “A survey of the acoustic output of commercial extracorporeal shock wave lithotripters”, *Ultrasound Med. Biol.*, Vol. 3, 213–27, 1989

- [COL 93] A.J. Coleman *et al.*, "A review of the physical properties and biological effects of the high amplitude acoustic fields used in extracorporeal lithotripsy", *Ultrasonics*, Vol. 31, 75–89, 1993
- [EIS 91] F. Eisenberger *et al.*, *Stone Therapy in Urology*, Georg Thieme Verlag, Stuttgart, Germany, 1991
- [GEL 04] A. Gelet *et al.*, "Local recurrence of prostate cancer after external beam radiotherapy: early experience of salvage therapy using high-intensity focused ultrasonography", *Urology*, Vol. 63(4), 625–9, 2004
- [HAC 05] A. Hacker *et al.*, "Extracorporeal application of high-intensity focused ultrasound for prostatic tissue ablation", *BJU Int.*, Vol. 96(1), 71–6, 2005
- [HIL 04] C.R. Hill *et al.*, *Physical Principles of Medical Ultrasonics*, 2<sup>nd</sup> edition, John Wiley & Sons, Ltd, Chichester, West Sussex, England, 2004
- [ILL 05] R.O. Illing *et al.*, "The safety and feasibility of extracorporeal high-intensity focused ultrasound (HIFU) for the treatment of liver and kidney tumours in a Western population", *Br J Cancer*, Vol. 93(8), 890–5, 2005
- [LYN 42] J.G. Lynn *et al.*, "A new method for the generation and use of focused ultrasound in experimental biology", *J. Gen. Physiol.*, Vol. 26, 179–93, 1942
- [MEA 00] P.M. Meaney *et al.*, "The intensity dependence of lesion position shift during focused ultrasound surgery", *Ultrasound Med Biol.*, Vol. 26(3), 441–50, 2000
- [PEN 48] H.H. Pennes, "Analysis of tissue and arterial blood temperatures in the resting human forearm", *J. Appl. Physiol.*, Vol. 1, 93–122, 1948
- [SAN 99b] N.T. Sanghvi *et al.*, "Noninvasive surgery of prostate tissue by high intensity focused ultrasound: an updated report", *Eur J Ultrasound*, Vol. 9(1), 19–29, 1999
- [SAS 91] W. Sass *et al.*, "The mechanisms of stone disintegration by shock waves", *Ultrasound Med. Biol.*, Vol. 17, 239–43, 1991
- [SAU 91] T. Sauerbruch *et al.*, "Gallbladder stones management", *Lancet*, Vol. 338, 1121–4, 1991
- [TAC 04] K. Tachibana, "Emerging technologies in therapeutic ultrasound: thermal ablation to gene delivery", *Hum. Cell*, Vol. 17(1), 7–15, 2004
- [UCH 02] T. Uchida *et al.*, "Transrectal high-intensity focused ultrasound for treatment of patients with stage T1b–2n0m0 localized prostate cancer: a preliminary report", *Urology*, Vol. 59(3), 394–8, 2002
- [VAE 01] S. Vaezy *et al.*, "High intensity focused ultrasound: a method of hemostasis", *Echocardiography*, Vol. 18(4), 309–15, 2001
- [WU 04] F. Wu *et al.*, "Extracorporeal high intensity focused ultrasound ablation in the treatment of 1038 patients with solid carcinomas in China: an overview", *Ultrason Sonochem.*, Vol. 11(3–4), 149–54, 2004.

## Chapter 34

# Ultrasound Characterization of Bone Tissues by Poroelastic Theories

### 34.1. Introduction

Osteoporosis is a disease characterized by a low osseous mass, micro-architectural deterioration of bone tissues, an osseous brittleness and consequently, an increase in risk of fracture. It is, also called the silent disease, it is a common bone disease in which bones become thinner and more porous. Osteoporosis is thus a degenerative pathology of bone tissues narrowly dependent on the cycle of life of the skeleton. It results from imbalance between resumption and osseous formation. It particularly affects the bone trabecular localized mainly in vertebrae, the wrist and the ends of the long bones, and appears especially in menopausal women; where the reduction in estrogen reduces the formation of the bone and increases its resorption. The medical follow-up of this pathology is currently the object of intense research. Several methods were developed: measure mineral density by x-rays or ultrasound. Xrays give images with good resolution but cannot be used frequently given their ionizing nature. Ultrasound provides images with a lower resolution but is without danger to the patient. In this chapter, we are interested in the propagation of the acoustics waves in the trabecular bone, regarded as a porous environment saturated by a fluid. Biot's [BIO 56] theory, developed within the framework of oil research, is well adapted to describe the behavior of the wave acoustics in such a medium. Applied to the trabecular bone, it gives some significant results [WIL 92, LAU 94, HOS 97, FEL 04]. The slow and fast waves predicted by Biot's theory were identified in bovine

cancellous bones in the 1990s by Hosokawa and Otani [HOS 97]. This chapter is organized as follows: after revising Biot's model and the principal results obtained, a temporal modeling of the diffusion (transmission and reflection) of acoustic waves through a porous medium of finite thickness is presented. After this, elements of the inverse problem are given, and the results of the models are finally compared with experimental results.

### 34.2. Model

Biot's theory is the most general model of the propagation of acoustic waves in a saturated porous medium leading to linear equations. It is based on the assumption that the porous medium consists of two continuous media: a solid phase (the solid structure) and fluid phase. This assumption is verified when the wavelength of the acoustic perturbation is large compared to the size of the inhomogeneities of the porous medium (radius of the pores). In Biot's theory, the displacements of the solid phase ( $\vec{u}$ ) and of the fluid phase ( $\vec{U}$ ) obey the equations:

$$\begin{aligned}\tilde{\rho}_{11} \frac{\partial^2 \vec{u}}{\partial t^2} + \tilde{\rho}_{12} \frac{\partial^2 \vec{U}}{\partial t^2} &= P \nabla (\nabla \cdot \vec{u}) + Q \nabla (\nabla \cdot \vec{U}) - N \nabla \wedge (\nabla \wedge \vec{u}), \\ \tilde{\rho}_{12} \frac{\partial^2 \vec{u}}{\partial t^2} + \tilde{\rho}_{22} \frac{\partial^2 \vec{U}}{\partial t^2} &= Q \nabla (\nabla \cdot \vec{u}) + R \nabla (\nabla \cdot \vec{U}).\end{aligned}\quad [34.1]$$

Coefficients  $P$ ,  $Q$  and  $R$  are the elastic coefficients of Biot's theory and  $N$  is the shear modulus of the solid structure.  $P$ ,  $Q$  and  $R$  are functions of the incompressibility modulus of the fluid and solid phases, and the porosity  $\phi$  of the porous material:

$$\begin{aligned}P &= \frac{(1 - \phi)(1 - \phi - \frac{K_b}{K_s})K_s + \phi \frac{K_s}{K_f} K_b}{1 - \phi - \frac{K_b}{K_s} + \phi \frac{K_s}{K_f}} + \frac{4}{3} N, \\ Q &= \frac{1 - \phi - \frac{K_b}{K_s} \phi K_s}{1 - \phi - \frac{K_b}{K_s} + \phi \frac{K_s}{K_f}}, \quad R = \frac{\phi^2 K_s}{1 - \phi - \frac{K_b}{K_s} + \phi \frac{K_s}{K_f}}.\end{aligned}\quad [34.2]$$

$K_f$ ,  $K_s$  and  $K_b$  are, respectively, the incompressibility modulus of the fluid phase in the porous medium, and the solid phase of the structure in vacuum. They depend on the usual mechanical parameters: Young's modulus of the solid  $E_s$ ,  $\nu_s$  and Young's modulus of the skeleton,  $E_b$ ,  $\nu_b$  so that:  $K_s = \frac{E_s}{3(1-2\nu_s)}$ ,  $K_b = \frac{E_b}{3(1-2\nu_b)}$ ,  $N = \frac{E_b}{2(1+\nu_b)}$ .

The densities  $\tilde{\rho}_{kl}$  are defined by:  $\tilde{\rho}_{kl} = \rho_{kl} + (-1)^{k+l} j g(\omega)$ , with  $j^2 = -1$ , and where  $g(\omega)$  models the viscous losses. To define the densities  $\rho_{kl}$ , we have introduced two essential parameters of the porous medium: the dynamic tortuosity  $\alpha(\omega)$  and the characteristic viscous length  $\Lambda$ . At high frequencies (the thickness of the viscous skin depth thickness  $\delta = (\frac{2\eta}{\omega \rho_f})^{\frac{1}{2}}$  is very thin near the radius of the pore),  $\alpha(\omega)$  becomes [JOH 87]:

$$\alpha(\omega) = \alpha_\infty \left( 1 + \frac{2}{\Lambda} \sqrt{\frac{\eta}{j\omega \rho_f}} \right), \quad \omega \rightarrow \infty \quad [34.3]$$

where  $\alpha_\infty$  is the tortuosity of the material. Thus, the densities  $\rho_{kl}$  are given by:  $\rho_{11} + \rho_{12} = (1 - \phi)\rho_s$ ,  $\rho_{12} + \rho_{22} = \phi\rho_f$  and  $\rho_{12} = -\phi\rho_f(\alpha(\omega) - 1)$ .

### 34.3. Longitudinal wave

When considering an acoustic wave arriving at normal incidence on a fluid-porous medium interface, only the longitudinal waves are excited. In this case we can write  $\vec{u} = \nabla \tilde{\phi}_s$  and  $\vec{U} = \nabla \tilde{\phi}_f$ . Reporting these relationships in equations [34.1] we obtain:

$$\Delta \begin{pmatrix} \phi_s \\ \phi_f \end{pmatrix} = M \begin{pmatrix} \phi_s \\ \phi_f \end{pmatrix}, \quad [34.4]$$

where  $M$  is a matrix,  $\Delta$  the Laplace operator and  $\phi_s$  and  $\phi_f$  are the Fourier transforms of  $\tilde{\phi}_s$  and  $\tilde{\phi}_f$  respectively. The solutions of this equation are the superpositions of a fast wave  $\Phi_1$  and slow wave  $\Phi_2$ . The corresponding velocities  $V_{1,2}$  are given by:

$\lambda_{1,2} = \frac{\omega^2}{V_{1,2}^2} = \frac{\text{tr}(M) \pm \sqrt{\text{tr}^2(M) - 4\det(M)}}{2}$ . Therefore:

$$\begin{pmatrix} \Phi_s \\ \Phi_f \end{pmatrix} = \begin{pmatrix} 1 & 1 \\ \chi_1 & \chi_2 \end{pmatrix} \begin{pmatrix} \Phi_1 \\ \Phi_2 \end{pmatrix}, \quad [34.5]$$

where the vectors  $(1, \chi_1)$  and  $(1, \chi_2)$  are the eigenvectors of the matrix  $M$  associated with the eigenvalues  $\lambda_{1,2}$ . The functions  $\Phi_1$  and  $\Phi_2$  are given by:

$$\Phi_1(x, \omega) = \bar{\Phi}_1(\omega)e^{-x\sqrt{\lambda_1(\omega)}} + \bar{\Phi}'_1(\omega)e^{x\sqrt{\lambda_1(\omega)}}, \quad [34.6]$$

$$\Phi_2(x, \omega) = \bar{\Phi}_2(\omega)e^{-x\sqrt{\lambda_2(\omega)}} + \bar{\Phi}'_2(\omega)e^{x\sqrt{\lambda_2(\omega)}}, \quad [34.7]$$

and the values  $\bar{\Phi}_i$  and  $\bar{\Phi}'_i$  are determined from the boundary conditions.

### 34.4. Transmission and reflection operators

In this framework of the temporal model acoustic wave diffusion by a slice of porous material with a finite thickness, the reflection and transmission coefficients are replaced by operators. Their determination takes into account continuity conditions of constraints and deformations.

For the situation represented in Figure 34.1, we can define a reflection operator  $R(t)$  from the pressure,

$$\begin{aligned} p_1(x, t) &= p^i \left( t - \frac{x}{c_0} \right) + p^r \left( t + \frac{x}{c_0} \right) \\ &= \left( \delta \left( t - \frac{x}{c_0} \right) + \tilde{R}(t) * \delta \left( t + \frac{x}{c_0} \right) \right) * p^i(t), \quad x < 0, \end{aligned} \quad [34.8]$$

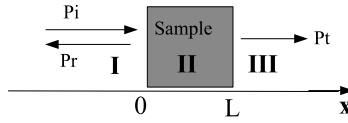


Figure 34.1. Geometric representation

and from Euler's equation in medium I,

$$\rho_f \frac{\partial v_1(x, t)}{\partial t} = -\frac{\partial p_1(x, t)}{\partial x}. \quad [34.9]$$

In medium III ( $x > L$ ), we can define a transmission operator  $T(t)$  by the relation:

$$p_3(x, t) = \tilde{T}(t) * p^i(t) * \delta\left(t - \frac{(x - L)}{c_0}\right). \quad [34.10]$$

The resolution of the operational equations is made into the Laplace domain. The equations of conservation at  $x = 0$  and  $x = L$  of the stress:

$$\mathcal{L}(\sigma^f)(0^+, \omega) = -\phi \mathcal{L}(P_1)(0^-, \omega), \quad \mathcal{L}(\sigma^s)(0^+, \omega) = (1 - \phi) \mathcal{L}(P_1)(0^-, \omega),$$

$$\mathcal{L}(\sigma^f)(L^-, \omega) = -\phi \mathcal{L}(P_3)(0^+, \omega), \quad \mathcal{L}(\sigma^s)(L^-, \omega) = (1 - \phi) \mathcal{L}(P_3)(L^+, \omega).$$

(where  $\mathcal{L}$  is the Laplace operator) and the conservation of the flows,

$$\mathcal{L}(V_1)(0^-, \omega) = (1 - \phi) \mathcal{L}(V_s)(0^+, \omega) + \phi \mathcal{L}(V_f)(0^+, \omega), \quad [34.11]$$

$$\mathcal{L}(V_3)(L^-, \omega) = (1 - \phi) \mathcal{L}(V_s)(L^+, \omega) + \phi \mathcal{L}(V_f)(L^+, \omega),$$

lead to the following expressions:

$$\mathcal{L}(R)(\omega) = \frac{(j\omega \rho_f c_0 F_4(\omega))^2 + 1 - (j\omega F_3(\omega))^2}{(j\omega F_3(\omega) - 1)^2 - (j\omega \rho_f c_0 F_4(\omega))^2}, \quad [34.12]$$

$$\mathcal{L}(T)(\omega) = \frac{2j\omega \rho_f c_0 F_4(\omega)}{(j\omega \rho_f c_0 F_4(\omega))^2 - (j\omega F_3(\omega) - 1)^2}, \quad [34.13]$$

with

$$F_3 = F_1(\omega) \cosh(L\sqrt{\lambda_1(\omega)}) \rho_f c_0 + F_2(\omega) \cosh(L\sqrt{\lambda_2(\omega)}),$$

$$F_4 = F_1 + F_2 \quad \text{and} \quad F_1 = \frac{2(1 + \phi(\chi_1(\omega) - 1))\sqrt{\lambda_1(\omega)}\Psi_1}{\Psi \sinh(L\sqrt{\lambda_1(\omega)})},$$

$$F_2 = \frac{2(1 + \phi(\chi_2(\omega) - 1))\sqrt{\lambda_2(\omega)}\Psi_2}{\Psi \sinh(L\sqrt{\lambda_2(\omega)})}.$$

The coefficients  $\Psi_1(\omega)$ ,  $\Psi_2(\omega)$ ,  $\Psi(\omega)$  are given by:

$$\begin{aligned}\Psi_1(\omega) &= \phi Z_2(\omega) - (1 - \phi) Z_4(\omega), \\ \Psi_2(\omega) &= (1 - \phi) Z_3(\omega) - \phi Z_1(\omega), \\ \Psi(\omega) &= 2(Z_1(\omega) Z_4(\omega) - Z_2(\omega) Z_3(\omega)),\end{aligned}$$

where

$$\begin{aligned}Z_1 &= (P + Q\chi_1(\omega))\lambda_1(\omega), & Z_2 &= (P + Q\chi_2(\omega))\lambda_2(\omega), \\ Z_3 &= (Q + R\chi_1(\omega))\lambda_1(\omega), & Z_4 &= (Q + R\chi_2(\omega))\lambda_2(\omega).\end{aligned}$$

The inverse Laplace transforms of coefficients  $R(\omega)$  and  $T(\omega)$  give the expressions of the reflection and transmission operators  $R(t)$  and  $T(t)$  in the time domain [FEL 04].

### 34.5. Inverse problem

The purpose of the inverse problem is to find values of the parameters of the porous medium, using experimental data from the acoustic wave transmitted through a thickness of the material. In the framework of this study, we have to consider:

- i) the parameters related to the geometry of the pores of the material: porosity, tortuosity, viscous characteristic length.
- ii) the elasticity modulus of the solid structure: Young's modulus  $E_b$  and Poisson's ratio  $\nu_b$ , with all other parameters being fixed. To evaluate these parameters, we use the least squares method:

$$F = \sum_{t_i} [s_{\text{theo}}(t_i) - s_{\text{exp}}(t_i)]^2, \quad [34.14]$$

where  $s_{\text{exp}}(t)$  is the experimental signal and  $s_{\text{theo}}(t)$  is the synthetic signal obtained from the convolution of the incident signal  $e(t)$  with the transmission operator:  $s_{\text{theo}}(t) = T(t) * e(t)$ .

### 34.6. Experimental set-up and results

Experiments are performed in water using two broadband Panametrics A303S plane piezoelectric transducers with a central frequency  $1\text{MHz}$ , used as transmitter and receiver. The ultrasonic signal is produced by a pulse generator ( $HV$ : 5052PR). The acquisition is achieved by a digital oscilloscope Lecroy 9310. The incident wave is only measured between the two transducers, i.e. without sample. Figure 34.2 shows the experimental incident signal (continuous line) and the transmitted signal (dashed

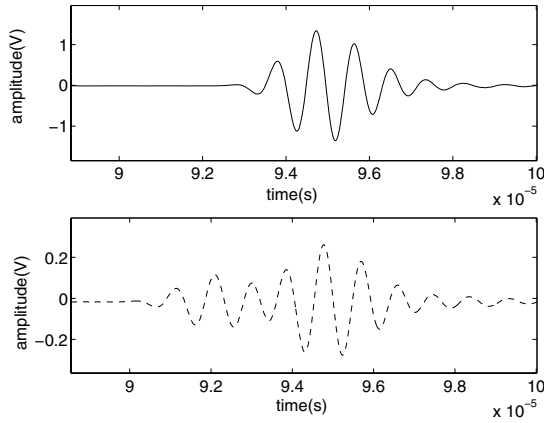


**Figure 34.2.** Incident and transmitted experimental signals

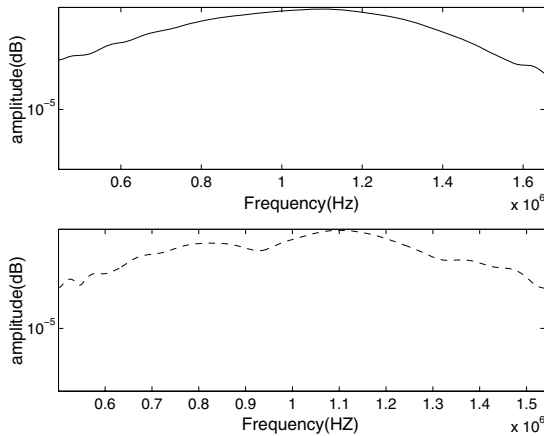


**Figure 34.3.** Spectra of the incident and transmitted signals

line). This last is composed of the slow and fast waves. Figure 34.3 represents the spectrum of these two waves. The results concerning the three bone samples (O1,O2,O3), and a sample of hydroxyapatit (Hy), are summarized in Table 34.1, the values of the fixed parameters are:  $K_f = 2.4$  GPa,  $\rho_f = 930$  k.g.m<sup>-3</sup>, fluid viscosity  $\eta = 10^{-3}$  kg.m.s<sup>-1</sup>,  $\rho_s = 1990$  kg.m<sup>-3</sup>,  $E_s = 10$  GPa,  $\nu_s = 0.3$ . The minimization function is represented as a function of all the important parameters in transmission, we choose a pair of parameters, for example  $\alpha_\infty$  and  $E_b$ . Figure 34.4 represents the sensitivity of function  $F$  to the pair  $(\alpha_\infty, E_b)$ . The transmitted signals, experimental  $s_{\text{exp}}(t)$  (continuous line) and synthetic  $s_{\text{theo}}(t)$  (dashed line) are represented in Figure 34.5.



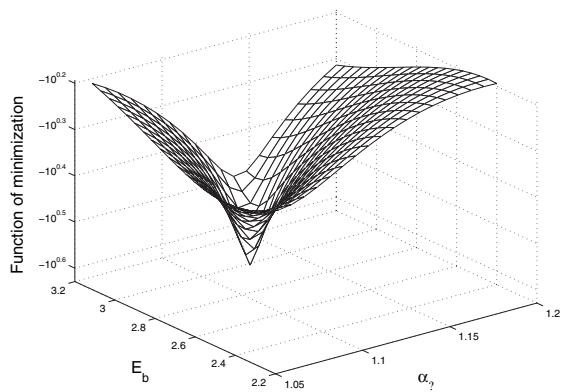


**Figure 34.4.** Variation of the minimization function with tortuosity and the young modulus of the skeleton

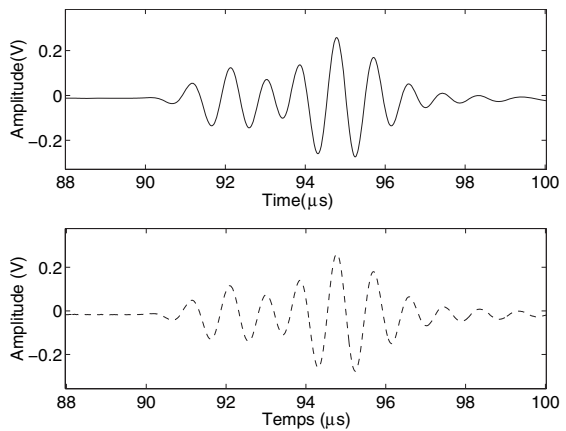


**Figure 34.5.** Experimental transmitted signal (continuous line) and theoretical transmitted signal (dashed line)

	$L$ (mm)	$\phi$	$\alpha_\infty$	$\Lambda$ ( $\mu m$ )	$\nu_b$	$E_b$ (GPa)
O1	10.2	0.72	1.1	14.97	0.22	3.1
O2	12	0.79	1.052	10.12	0.26	2.47
O3	11.2	0.64	1.017	10.44	0.3	3.73
Hy	12.5	0.90	1.13	8.07	0.31	2.16

**Table 34.1.** Result of the minimization

### 34.7. Conclusion

In this chapter, we showed that Biot's theory is well adapted to model the acoustic wave propagation in bone tissues. This theory enables us to consider the physical parameters of the porous medium (that is the cancellous bone) and led to values that were in agreement with other theoretical measurements.

### 34.8. Bibliography

- [BIO 56] BIOT M.A., "The theory of propagation of elastic waves in fluid-saturated porous solid. II. Higher frequency range", *J. Acoust. Soc. Am.*, vol. 28, pp. 179–191, 1956.
- [FEL 04] FELLAH Z.E.A., CHAPELON J.Y., BERGER S., LAURIKS W. and C. DEPOLIER, "Ultrasonic wave propagation in human cancellous bone: Application of Biot theory", *J. Acoust. Soc. Am.*, vol. 116, pp. 61–73, 2004.
- [HOS 97] HOSOKAWA A. and OTANI T., "Ultrasonic wave propagation in bovine cancellous bone", *J. Acoust. Soc. Am.*, vol. 101, pp. 558–562, 1997.
- [JOH 87] JOHNSON D. L., KOPLIK J. and DASHEN R., "Theory of dynamic permeability and tortuosity in fluid-saturated porous media", *J. Fluid. Mech.*, vol. 176, pp. 379–402, 1987.
- [LAU 94] LAURIKS W., THOEN J., VAN ASBROECK I., LOWET G. and VANDERPERRE G., "Propagation of ultrasonic pulses through trabecular bone", *J. Phys. Coll. (Paris)*, vol. 4, pp. 1255–1258, 1994.
- [WIL 92] WILSON J.L., "Ultrasonic wave propagation in cancellous bone and cortical bone: Prediction of some experimental results by Biot theory", *J. Acoust. Soc. Am.*, vol. 91, pp. 1106–1112, 1992.

## Chapter 35

# Acoustic Tomography, Ultrasonic Tomography

### 35.1. Introduction

#### 35.1.1. *Tomography and inverse propagation/scattering*

The word tomography comes from the Greek *tomos*, meaning section. The objective of tomography is therefore to make cross-sectional images of objects. X-ray computed tomography (or tomodensitometry), the reference technique in the domain, obtains this result using X-rays. Acoustic tomography tries to do the same using acoustic waves: ultrasonic waves in the biomedical and non-destructive testing domains, sonic or infrasonic waves (depending on the scales of interest) in geophysics. We send probe signals (usually pulses, i.e. short broadband wave trains) towards the object to be analyzed, using transmitters arranged in a number of points outside the object. Then the field, transmitted or scattered by the object, is captured by receivers situated outside the object. Finally the data are inverted, using ad hoc algorithms.

If we work in two dimensions (using transducers focused in the section plane, or assuming that the signals coming out of the section plane do not re-enter it), the typical geometry of the acquisition device is, if we work in transmission or forward scattering, a circle surrounding the object, or two parallel lines on either side of the object and then move them around. If we work in reflection or backscattering, the typical geometry is a half-circle (minimal geometry; a full circle is also acceptable) or a single line and then move it around the object.

If we work in three dimensions and seek to build a 3D image displayed as various sections (like magnetic resonance imaging in the medical domain), the typical geometry will be a sphere surrounding the object or two parallel planes on both sides of the object and then move them around, if we work in transmission or forward scattering; and a half-sphere or a plane that we then move around the object, if we work in reflection or backscattering. In that case, we use the term “3D tomography”, although it is not completely appropriate.

We will limit the presentation to a generic case in two dimensions. But even in this case, do not classical ultrasonography (or echography) in the medical domain and seismic-reflection in the geophysical domain can already achieve sectional images of the media? What difference is there between these techniques, both acoustic, and acoustic tomography? The difference is minimal if we make the comparison with reflection tomography or, more precisely, with back-scattering in linear geometry. The main difference lies in the formulation of the problem, stated in terms of an inverse problem in tomography, and in terms of waves focusing in ultrasonography (physical focusing) and seismic-reflection (synthetic focusing). As for the means to be used, they are mathematical and numerical for inverse problems, and synthetic focusing (a technique also implemented successfully in geophysics to non-destructive testing by ultrasound), physical (lenses) and/or electronic (antennas treatment) in classical ultrasound. Finally, the difference between synthetic focusing and tomography is tenuous: the first is actually an approximate (but often sufficient) version of the second.

We have seen that two cases have already been identified, depending on whether we are interested in wave transmission or wave scattering measurements (the scattered field being defined as the difference between the total field and the incident field). These measurements are generally made in back-scattering, directly and easily accessible, because naturally separated, in the time domain, from the incident field, with a good signal-to-noise ratio. This is not the case for forward scattering, which can only be achieved by subtracting signals; this operation is difficult to carry out in practice, as digitization of ultrasonic signals is always done on a small number of bits (8 or 10, 12 in the best case).

Both those scenarios, based on very different measurements, define two different acoustic tomography methods: transmission tomography (transmitter and receiver are on opposite sides of the object), reflection and back-scattering tomography (transmitter and receiver are on the same side of the object). Both are based, at least for their basic formalism (there are avatars), on the assumption of *weak heterogeneity* of the object, of *low contrast* compared to the host medium, so that we can use an approximation of straight rays for the transmission modeling and a Born approximation for the scattering. Such an approximation makes sense in the

biomedical domain for soft tissues, which are known to consist primarily of water, resulting in a lot of work for a long time, on biomedical ultrasound tomography.

In what follows, we consider this perspective, and use the term ultrasonic tomography, in preference to the less appropriate term of acoustic tomography.

### 35.1.2. Ultrasonic transmission tomography

#### 35.1.2.1. Geometry of the acquisition setup

Consider two parallel lines, in a host medium of velocity  $C_0$ , on either side of the object  $D$  of velocity  $C(\vec{x})$  of which we want to obtain an image, each carrying one (or several) directive transducers, face to face. Activating a transmitter  $E$  (by sending a pulse), we are only interested in the signal from the receiver  $R$ , which faces it (Figure 35.1), considering that it comes essentially from straight line propagation between the two transducers. It is assumed, therefore, that we may use a theory of straight rays, which means that we use high-frequency signals to implement a ray theory; and that the index or velocity contrast is low enough to ignore the refraction phenomenon that bends the rays.

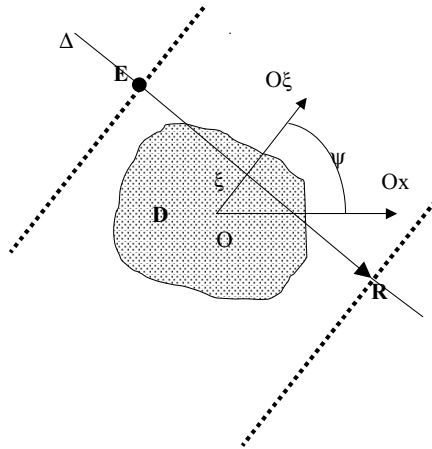


**Figure 35.1.** *Geometry of the acquisition setup*

The travel time of the signal between transmitter  $E$  and receiver  $R$ , easily measurable if we use short signals, is in these conditions:

$$t = \int_{ER} \frac{1}{C(\vec{x})} ds \quad [35.1]$$

and the travel time difference induced by the interposition of the object, measurable for example by performing, firstly, a reference measurement without the object and then carrying out the subtraction:

$$\tau = \int_{ER} \left( \frac{1}{C(\vec{x})} - \frac{1}{C_o} \right) ds \quad [35.2]$$

Or:

$$\tau = \int_{ER} O(\vec{x}) ds \quad [35.3]$$

with, defining as the object, the quantity:

$$O(\vec{x}) = \left( \frac{1}{C(\vec{x})} - \frac{1}{C_o} \right) = \frac{1}{C_o} (n(\vec{x}) - 1) = \frac{1}{C_o} \delta_n(\vec{x}) \quad [35.4]$$

Here,  $n(\vec{x}) = \frac{k(\vec{x})}{k_0} = \frac{C_0}{C(x)}$  is the refractive index of the object compared to the

host medium and  $\delta_n(\vec{x}) = (n(\vec{x}) - 1)$  the index contrast.

With this definition of the object that is now proportional to the index contrast, it is clear that the object is zero outside D. We can therefore extend the integral on the segment ER to an integral on the straight line  $\Delta$  supporting the segment:

$$\tau = \int_{\Delta} O(\vec{x}) ds \quad [35.5]$$

Equation [35.5] shows that  $\tau$  is a projection of O parallel to  $\Delta$ .

If we identify the integration line  $\Delta$  by its distance  $\xi$  to the point O (chosen as the coordinate origin) and the angle  $\psi$  made by its normal with the  $Ox$  axis, equation [35.5] can be written as a function of the object described in Cartesian coordinates  $O(\vec{x}) = O(x, y)$ :

$$\tau(\psi, \xi) = \int_{-\infty}^{+\infty} O(\xi \cos \psi - \eta \sin \psi, \xi \cos \psi + \eta \sin \psi) d\xi \quad [35.6]$$

In addition to the translation scanning along the parallel lines, we can also apply a rotational scanning of the device of amplitude  $\pi$ . This allows a scanning of amplitude  $\pi$  in  $\psi$ , in addition to the scanning in  $\xi$  to be obtained.

The set of projections  $\alpha(\psi, \xi)$  defines the Radon transform of the object  $O$  ([DEA 83], [GRA 02]).

So, the acquisition of the travel-time differences, according to the previously defined protocol, leads us to acquire, up to a multiplying factor, the Radon transform of the index contrast of the object.

### 35.1.2.2. Data inversion

The index contrast (and therefore the index and consequently the velocity) of the object is then obtained from the measurements of travel-time differences by inverting the Radon transform.

The most classic inversion algorithm, the one that is commonly used in standard X-ray tomography, is the summation of the filtered back-projections. This algorithm is written ([DEA 83], [GRA 02]):

$$O(\vec{x}) = O(x, y) = \frac{1}{(2\pi)^2} \int_0^\pi d\psi \int_{-\infty}^{\infty} |K| \hat{P}_\psi(K) e^{iK(x \cos \psi + y \sin \psi)} dK \quad [35.7]$$

where  $\hat{P}_\psi(K) = \int_{-\infty}^{+\infty} P_\psi(\xi) e^{-iK\xi} d\xi$  is the Fourier transform of the projection  $P_\psi(\xi) = \alpha(\psi, \xi)$ .

The algorithm can be broken down as follows:

$$O(\vec{x}) = O(x, y) = \frac{1}{2\pi} \int_0^\pi P_\psi^F(x \cos \psi + y \sin \psi) d\psi ,$$

summation of the back-projections (or spreading) summation of the filtered projections:

$$P_\psi^F(\xi) = \frac{1}{2\pi} \int_{-\infty}^{+\infty} |K| \hat{P}_\psi(K) e^{iK\xi} dK ,$$

i.e. projections  $P_\psi(\xi) = \alpha(\psi, \xi)$  filtered by the filter of transfer function  $|K|$ .

This algorithm is based on the fact that (slice-projection theorem) the 1D Fourier transform of a projection is a slice of the 2D Fourier transform of the object:

$$\hat{P}_\psi(K) = \hat{O}(K, \psi) .$$

From the rebuilt object with a well-defined nature (namely the index contrast, and hence the index and the velocity), we get what we call a *parametric imaging* (reconstruction of the “index” parameter) or a *quantitative imaging*. This can be opposed to classical ultrasound imaging, i.e. echography, that is described as a qualitative method because the pixels of the image are purely morphological and do not have any physical significance (they can not be calibrated according to a specific physical parameter).

### 35.1.2.3. Fan geometry

The previous geometry, in which projections are acquired by a series of translations of transducers along parallel lines and rotations of the device bearing the lines, is the one that was used in the first generation of X-ray tomographs.

The next generations of X-ray tomographs use a circular geometry, in which the generator and the detectors, mounted in battery for rapid acquisitions, are arranged in a circle around the object (Figure 35.2). This kind of geometry is called “fan beam” geometry. It leads to the acquisitions of projections that are no longer parallel, but diverging, in a fan. The easiest way to invert these data is to rearrange them in order to recreate a collection of parallel projections, and then use the standard summation of the filtered back-projection algorithm. Another solution is to transpose the standard algorithm to the fan geometry [GRA 02].

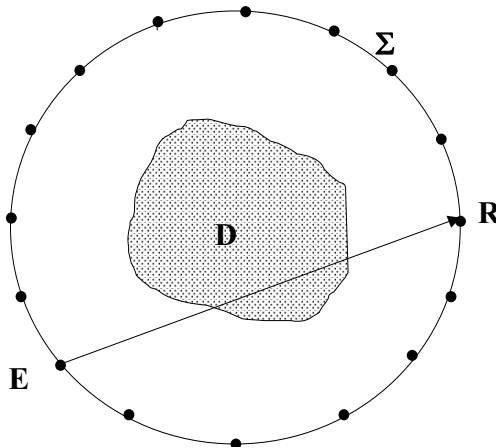


Figure 35.2. Fan geometry



In the ultrasound domain, we can imagine a configuration inspired by this geometry, in which a collection of transducers is spread over a circle  $\Sigma$  around the object D (Figure 35.2). Each transducer (with a wide aperture in the section plane) alternatively behaves as transmitter E and receiver R (this possibility is offered by piezoelectric transduction phenomenon, which is reversible). For a faster acquisition, the signals from all the receivers are acquired simultaneously. To simplify the electronics, we can also specialize the transducers (some are transmitters, others are receivers). In this case, transmitters and receivers are positioned alternately on the support circle.

The problem is that even in soft tissues, with a low contrast, the propagation of ultrasound is not a straight line. Refraction can not be neglected and results, in this type of imaging, in image aberrations. In order to correct these aberrations, we must use at least a curved-ray theory, requiring the use of iterative methods of reconstruction by optimization (quite complex methods, based on a minimization of the discrepancy between the measurements and the estimations when at least using a curved-ray model).

This explains why this kind of tomography has not advanced from research laboratories in the biomedical field. The situation is quite different in geophysics, where experiments are rare and costly, so we do not hesitate to use high level optimization methods coupled with sophisticated numerical modeling algorithms. That is how we can carry out *seismic tomography* in the sonic domain (or acoustic well log), between boreholes, with elastic waves produced by shocks (hammer, explosive, air gun, etc.), in order to analyze the near substratum (in archaeology for example). That is also how we can carry out *seismic tomography* in the infrasonic domain, on the global scale, using natural earthquakes as sources, in order to investigate the terrestrial mantle with waves that have crossed it.

#### 35.1.2.4. *Attenuation tomography*

The same techniques of tomographic reconstruction can be applied to attenuation measurements, instead of travel-time, leading to an attenuation tomography. Then we obtain an image of the attenuation factor in the same way as above for the refractive index or the velocity [GRE 81].

#### 35.1.2.5. *Conclusion on ultrasonic transmission tomography*

The main interest of ultrasonic transmission tomography is to provide a quantitative imaging of the media, at least when we may implement advanced methods based on optimization and sophisticated modeling of the direct problem, taking in account refraction phenomena.

If we want to get an image resolution compatible with the needs of medical imaging using this method, the disadvantage is its complexity, as well as the basic necessity of using double fine spatial scanning that is so expensive in terms of acquisition time or in terms of antenna technology.

As previously mentioned, this explains why the method has not advanced beyond research laboratories in the medical field. But this eventuality can not be rejected, given future technological advances.

### 35.1.3. Ultrasonic diffraction tomography

#### 35.1.3.1. Geometry of the acquisition setup

We now consider that we measure the scattered field, instead of the total field. As in the previous section, we choose to simplify the 2D geometry and assume we are dealing with a collection of transmitters and receivers (or one transmitter and one receiver that we move), with a wide aperture in the section plane and a narrow one in the orthogonal plane (to select a section), and located in a homogenous host medium of density and volume compressibility  $(\rho_0, \chi_0)$  on a circle  $\Sigma$  of center O and radius R surrounding the object D whose characteristics  $(\rho, \chi)$  are variable in space [Figure 35.3].

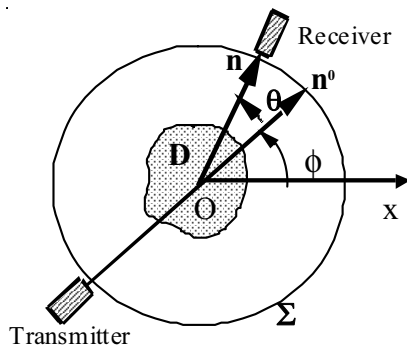


**Figure 35.3.** *Geometry of the acquisition setup*

To simplify the calculations, it is assumed that the circle  $\Sigma$  has a large radius compared to the size of the object D, so that we can perform far-field calculations, both for the incident wave (which is therefore assumed to be a plane wave – good approximation of the far-field of an ideally wide aperture transducer), and for the scattered field, which will be calculated in the asymptotic regime. A near-field calculation is also feasible but complex, and leads to a comparable result.

### 35.1.3.2. Direct problem

Although we usually use large bandwidth pulses (for their temporal resolution properties), calculations are conducted in the harmonic regime after a Fourier transform of the temporal quantities. The calculation can also be done in the time domain, but then missing instructive information about image filtering by the measures.

Considering the field emitted by a transmitter E located on the circle  $\Sigma$ , we model it in the far-field by a harmonic plane wave of pulsation  $\omega$  and incidence direction  $\vec{n}_0$ :  $P_i(\vec{x}, \omega) = P_i^0(\omega)e^{ik_0 \cdot \vec{n}_0 \cdot \vec{x}}$

In the whole space, the field is described by the propagation equation in non-homogenous media [LEF 94]:

$$(\Delta + k_0^2)P = -k_0^2 \mu_\chi P + \text{div}(\gamma_\rho \text{grad} P) \quad [35.8]$$

where  $\mu_\chi = \frac{\chi - \chi_0}{\chi_0}$  and  $\gamma_\rho = \frac{\rho - \rho_0}{\rho}$  are the relative contrasts of compressibility and density of the medium ( $\mu_\chi$  and  $\gamma_\rho$  are equal to zero outside of D).

The propagation equation can be written in the following integral form (Lippmann–Schwinger equation):

$$P(\vec{x}, \omega) = P_i(\vec{x}, \omega) + \int_D G_0(\vec{x}, \vec{x}', \omega) \left[ -k_0^2 \mu_\chi P + \text{div}(\gamma_\rho \text{grad} P) \right] d^2 x' \quad [35.9]$$

where  $G_0$  is the 2D Green's function of the homogenous medium:

$$G_0(\vec{x}, \vec{x}', \omega) = -\frac{i}{4} H_0^{(1)}(k_0 |\vec{x} - \vec{x}'|)$$

In particular, at measurement point  $\vec{y}$  on the circle  $\Sigma$ :

$$P(\vec{y}, \omega) = P_i(\vec{y}, \omega) + \int_D G_0(\vec{y}, \vec{x}', \omega) \left[ -k_0^2 \mu_\chi P + \text{div}(\gamma_\rho \text{grad} P) \right] d^2 x' \quad [35.10]$$

Equations [35.9] and [35.10] are, respectively, the state equation and the measurement equation for the problem considered.

### 35.1.3.3. Inverse problem

The inverse problem that we have to solve is the determination of  $\mu_\chi$  and/or  $\gamma_\rho$  from a number of measurement points  $\vec{y}_i$  on the measuring circle, for emissions under various incidences  $\vec{n}_j$  and frequencies  $\omega_k$  (in fact a frequency continuum if we work with a wide-band pulse).

At this level, we see the wide variety of possible experiments (triplet  $\vec{y}_i, \vec{n}_j, \omega_k$ ), even for a simple circular configuration (we can refer profitably to [LAN 87] for a detailed study).

We notice (see Chapter 16) that the inverse problem to be solved is nonlinear with respect to the parameters to be calculated  $\mu_\chi$  and / or  $\gamma_\rho$ . We linearize it using the Born approximation, which consists of replacing, within the domain integral, the total field by the field that would exist in the absence of the object. Thus, this approximation consists of neglecting the scattered field inside the object (difference between the total field and the incident field:  $P_d(\vec{x}, \omega) = P(\vec{x}, \omega) - P_i(\vec{x}, \omega)$ ) compared with the incident field. Such an approximation (weak scattering) supposes that the parameters sought  $\mu_\chi$  and/or  $\gamma_\rho$  are small, i.e. that the contrast of the object is low compared to the surrounding medium. It also assumes that the object is not too large.

Under these conditions, the state and measurement equations become respectively:

$$P_d(\vec{x}, \omega) = + \int_D G_0(\vec{x}, \vec{x}', \omega) \left[ -k_0^2 \mu_\chi P_i + \text{div}(\gamma_\rho \text{grad} P_i) \right] d^2 x' \quad [35.11]$$

$$P_d(\vec{y}, \omega) = \int_D G_0(\vec{y}, \vec{x}', \omega) \left[ -k_0^2 \mu_\chi P_i + \text{div}(\gamma_\rho \text{grad} P_i) \right] d^2 x' \quad [35.12]$$

An approach consists of sampling the integral using the momentum method and writing the measurement equation for each measurement point  $\vec{y}_i$ , each available incidence  $\vec{n}_j$  and each frequency  $\omega_k$  (obtained from a FFT of the measured temporal signals). That leads to a large linear system that we have “simply” to solve. This is called the class of the algebraic reconstruction methods. We here prefer to continue further in terms of closed-form calculations, falling into the category of closed-form reconstruction methods.

To further simplify the presentation, it is assumed that the measurements are made in far-field, which ultimately leads to the following asymptotic formulation of the measurement equation:

$$P_d^\infty(\vec{y}, \omega) = P_i^0(\omega) \left( \frac{i}{4} \sqrt{\frac{2}{\pi |\vec{y}|}} e^{i(k_0 |\vec{y}| - \frac{\pi}{4})} \right) h(\vec{n}_0, \vec{n}, \omega) \quad [35.13]$$

where  $h(\vec{n}_0, \vec{n}, \omega)$  is the transfer function of the object for the incident direction  $\vec{n}_0$  and the observation direction  $\vec{n} = \frac{\vec{y}}{|\vec{y}|}$  and is equal to:

$$h(\vec{n}_0, \vec{n}, \omega) = \left| k_0 \right|^{3/2} \left[ \hat{\mu}_\chi(\vec{K}) + \vec{n}_0 \cdot \vec{n} \hat{\gamma}_\rho(\vec{K}) \right]_{\vec{K}=k_0(\vec{n}-\vec{n}_0)} \quad [35.14]$$

In this equation,  $\hat{\mu}_\chi(\vec{K})$  and  $\hat{\gamma}_\rho(\vec{K})$  are the spatial Fourier transforms of  $\mu_\chi(\vec{x})$  and  $\gamma_\rho(\vec{x})$  defined by:

$$\hat{\mu}_\chi(\vec{K}) = \int_D \mu_\chi(\vec{x}) e^{-i\vec{K} \cdot \vec{x}} d^2x, \quad \hat{\gamma}_\rho(\vec{K}) = \int_D \gamma_\rho(\vec{x}) e^{-i\vec{K} \cdot \vec{x}} d^2x$$

Each measurement of  $h$  for a triplet  $(\vec{n}_0, \vec{n}, \omega)$  gives access to a point  $\vec{K} = k_0(\vec{n} - \vec{n}_0)$  in the Fourier spectrum plane of a composite object  $O_{(\vec{n}_0, \vec{n})}(\vec{x})$  depending on the scattering angle  $(\vec{n}_0, \vec{n})$  :  $O_{(\vec{n}_0, \vec{n})}(\vec{x}) = \mu_\chi(\vec{x}) + \vec{n}_0 \cdot \vec{n} \gamma_\rho(\vec{x})$  .

As regards the incidence  $\phi = (\vec{i}, \vec{n}_0)$  and scattering  $\theta = (\vec{n}_0, \vec{n})$  angles, these relations are written:

$$h(\phi, \theta, \omega) = \left| \frac{K}{2 \sin(\theta/2)} \right|^{3/2} \hat{O}_\theta(\vec{K}) \Big|_{\vec{K}=K\vec{\xi}}, \quad [35.15]$$

where  $\vec{\xi}$  is the unitary vector of direction  $(\vec{i}, \vec{\xi}) = \psi = (\phi + \theta/2 + \pi/2)$  [35.16]

$K$  is defined by  $K = 2k_0 \sin(\theta/2) = 2 \frac{\omega}{c_0} \sin(\theta/2)$  [35.17]

$$\text{and } O_\theta(\vec{x}) = \mu_\chi(\vec{x}) + \cos \theta \gamma_\rho(\vec{x}) \quad [35.18]$$

In polar coordinates  $(K, \psi)$ , these equations become:

$$h(\phi, \theta, \omega) = \left| \frac{K}{2 \sin(\theta/2)} \right|^{3/2} \hat{O}_\theta(K, \psi) \quad [35.19]$$

$$K = 2k_0 \sin(\theta/2) = 2 \frac{\omega}{c_0} \sin(\theta/2) \quad [35.20]$$

$$\psi = \phi + \theta/2 + \pi/2 \quad [35.21]$$

#### 35.1.3.4. Nature of the object

Equation [35.18] shows that the nature of the object is usually complex. However, for some particular scattering angles, it can be simplified:

– pure forward scattering ( $\theta = 0$ ): in this case, we find the object

$$O_0(\vec{x}) = \mu_\chi(\vec{x}) + \gamma_\rho(\vec{x}) \approx -2\delta_C(\vec{x}), \quad \text{where } \delta_C(\vec{x}) = \frac{C(\vec{x}) - C_0}{C_0} \quad \text{is the relative}$$

contrast of velocity (defined by  $C = \sqrt{\frac{1}{\rho\chi}}$ ), this contrast is small by definition. But

the forward scattering, pure or not, is in fact inaccessible to direct measurement, the diffracted field being drowned in the incident field that is much more intense. This configuration is therefore unusable in practice with regard to diffraction tomography. Therefore, we usually prefer to use transmission tomography protocol in this configuration, working on the total field;

– right angle scattering ( $\theta = \pi/2$ ): in this case, the object reduces to the relative contrast of compressibility  $O_{\pi/2}(\vec{x}) = \mu_\chi(\vec{x})$ . We can consider that this equation is still valid in the neighborhood of  $\theta = \pi/2$ ;

– pure backscattering ( $\theta = \pi$ ): in this situation we find the object

$$O_\pi(\vec{x}) = \mu_\chi(\vec{x}) - \gamma_\rho(\vec{x}) \approx -2\varsigma_Z(\vec{x}), \quad \text{where } \varsigma_Z(\vec{x}) = \frac{Z(\vec{x}) - Z_0}{Z_0} \quad \text{is the relative contrast}$$

of acoustic impedance (defined by  $Z = \sqrt{\frac{1}{\rho C}} = \sqrt{\frac{\rho}{\chi}}$ ); this contrast is small by

definition. We can consider that this equation is still valid in the neighborhood of the backscattering direction.

This is this last configuration, the most easily accessible experimentally (the scattered signal is well discriminated in time), which is generally preferred. It leads, in terms of quantitative or parametric imagery, to acoustic impedance tomography [LEF 85]; and in terms of qualitative imagery, to reflectivity tomography or reflection tomography [LEF 88].

Most works ignore these aspects related to the nature of the object, for example by neglecting the density fluctuations of the medium, regarded as negligible, although they represent the real base of X-ray calculated tomography. The object is then considered in this case to be simply described by a function  $O(\vec{x}) = \mu_{\chi}(\vec{x})$ , the compressibility contrast, whatever the scattering angle.

In what follows, we no longer focus on the physical nature of the object (which arises only for quantitative or parametric imaging), but on its morphology, as in classical ultrasound imaging. This is called the qualitative imaging. The problem thus consists of reconstructing an object  $O(\vec{x})$ , whose nature is not of interest, from measurements of its Fourier spectrum  $\hat{O}(\vec{K})$ .

#### 35.1.3.5. *Reconstruction*

There are two possibilities:

- fill, in an empirical way without particular strategy, the Fourier spectrum of the object through measurements  $h$ , and then proceed, after interpolations on the dyadic grid in the frequency plane, to an inverse 2D-FFT, or use a discretization of the Fourier integral and an algebraic inversion of the system made of the equations on the various measurement points (algebraic method);

- fill the Fourier spectrum by a radial-angular scanning  $(K, \psi)$ , and then proceed, in this new frame, to an inverse Fourier transform. It is this strategy of analytic reconstruction of images that we choose to use here.

This adapted scan is an angular scan of amplitude  $\pi$  depending on the incidence angle  $\phi$ , by turning around the object, which induces a scan of the same amplitude in  $\psi$  of the object spectrum (equation [35.21], keeping a fixed scattering angle in order to have a fixed object [35.18]), and a frequency scan in  $\omega$ , obtained simply by Fourier transform of the used pulse, that is as broadband as possible. This induces a scan in  $K$  of the object spectrum (equation [35.20]).

The object spectrum is obtained from the measurements  $h(\vec{n}_0, \vec{n}, \omega)$  by inverting equations [35.19], [35.20] and [35.21], which gives:

$$\hat{O}_\theta(K, \psi) = \left| \frac{K}{2 \sin(\theta/2)} \right|^{-3/2} h(\phi, \theta, \omega) \quad [35.22]$$

$$\text{with } \omega = \frac{c_0}{2 \sin(\theta/2)} K \quad [35.23]$$

$$\text{and } \phi = \psi - \theta/2 - \pi/2 \quad [35.24]$$

The object itself is obtained by inverse 2D-Fourier transform:

$$O(\vec{x}) = \frac{1}{(2\pi)^2} \int_D \hat{O}(\vec{K}) e^{i\vec{K} \cdot \vec{x}} d^2 K$$

This equation can be written in polar coordinates  $(K, \psi)$  :

$$O(\vec{x}) = O(x, y) = \frac{1}{(2\pi)^2} \int_0^{2\pi} d\psi \int_0^\infty K \hat{O}(K, \psi) e^{iK(x \cos \psi + y \sin \psi)} dK \quad [35.25]$$

or, by applying the analytical extension of  $\hat{O}(K, \psi)$  on  $K \in \mathbb{R}$  :

$$O(\vec{x}) = O(x, y) = \frac{1}{(2\pi)^2} \int_0^\pi d\psi \int_{-\infty}^\infty |K| \hat{O}(K, \psi) e^{iK(x \cos \psi + y \sin \psi)} dK \quad [35.26]$$

Equation [35.26] is no more than the classical expression of the reconstruction by summation of the filtered back-projections used in X-ray tomography, obtained thanks to the slice-projection theorem [DEA 83] [GRA 02], previously used for ultrasonic transmission tomography.

It can be read as follows:

$$O(\vec{x}) = O(x, y) = \frac{1}{2\pi} \int_0^\pi P_\psi^F(x \cos \psi + y \sin \psi) d\psi,$$

summation of back-projections of filtered projections:



$$P_{\psi}^F(\xi) = \frac{1}{2\pi} \int_{-\infty}^{+\infty} K |\hat{O}(K, \psi) e^{iK\xi} dK,$$

with filter of transfer function  $|K|$  of:

$$P_{\psi}(\xi) = \frac{1}{2\pi} \int_{-\infty}^{+\infty} \hat{O}(K, \psi) e^{iK\xi} dK,$$

inverse Fourier transform of  $\hat{P}_{\psi}(K) = \hat{O}(K, \psi)$ , slice along  $\psi$  of the 2D Fourier transform of the object.

$P_{\psi}(\xi)$ , whose 1D Fourier transform is a slice of the 2D Fourier transform of the object, and is, according to the slice-projection theorem, a projection of the object  $O(\vec{x})$  along the direction orthogonal to the direction  $\vec{\xi}$  defined by  $(\vec{i}, \vec{\xi}) = \psi$ . This projection is written, depending on the measurements  $h$ :

$$P_{\psi}(\xi) = 2c_0 \sin(\theta/2) \frac{1}{2\pi} \int_{-\infty}^{+\infty} |\omega|^{-3/2} h(\psi - \theta/2 - \pi/2, \theta, \omega) e^{i \frac{2}{c_0} \sin(\theta/2) \xi \omega} d\omega,$$

$H(\phi, \theta, t)$  is the inverse Fourier transform of  $h(\phi, \theta, \omega)$ , i.e. the scattering impulse response of the object; it results from a filtering of the quantity  $P'_{\psi}(\xi) = 2c_0 \sin(\theta/2) H(\psi - \theta/2 - \pi/2, \theta, \xi)$  by a filter whose transfer function is  $|\omega|^{-3/2}$ .

The temporal measurements of the scattering therefore provide a direct access, through a filter, to the projections of the object. Calculations made in the time domain lead to this result [LEF 88].

However, the spectral band of the signals used (and therefore the incursion in  $K$  they provide) is limited as, sometimes, is the feasible angular incursion. This yields a spatial filtering of the object which we want to rebuild.

#### 35.1.3.6. *Spatial filtering made by the acquisitions*

From an angular point of view, according to equation [35.21], the magnitude of the scan is the same in  $\psi$  and in  $\phi$ , incidence angle.

From the frequency point of view, according to equation [35.20], if the incursion in the frequency domain of the signals used is  $[\omega_{\min}, \omega_{\max}]$ , the incursion in  $K$  they provide is:

$$\left[ K_{\min}, K_{\max} \right] = \left[ 2 \frac{\omega_{\min}}{c_0} \sin(\theta/2), 2 \frac{\omega_{\max}}{c_0} \sin(\theta/2) \right] \quad [35.27]$$

Figure 35.4 shows the spectral coverage provided by an angular scanning of amplitude  $2\pi$  and a spectral scanning of amplitude  $[K_{\min}, K_{\max}]$ .

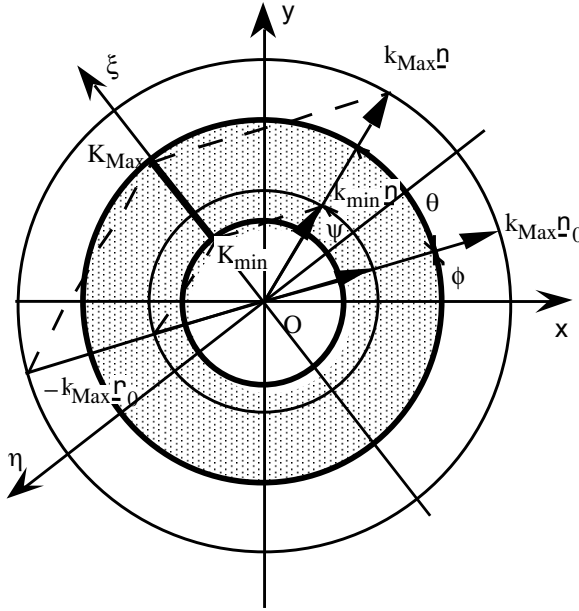


**Figure 35.4.** Typical spectral coverage

The spatial filter applied by the measurements is a crown of center O and width  $\left[ K_{\min}, K_{\max} \right] = \left[ 2 \frac{\omega_{\min}}{c_0} \sin(\theta/2), 2 \frac{\omega_{\max}}{c_0} \sin(\theta/2) \right]$ .

The temporal high frequency filtering of the signals will result in a spatial high frequency filtering of the object, i.e. in a limitation of the image resolution. Equation [35.27] shows that the best resolution for a signal of given spectral band, is obtained by backscattering ( $\theta = \pi$ ) measures. Then we have:

$$\left[ K_{\min}, K_{\max} \right] = \left[ 2 \frac{\omega_{\min}}{c_0}, 2 \frac{\omega_{\max}}{c_0} \right]$$

And the resolution will be even greater if the frequency of the signals used increases.

The temporal low frequency filtering of the signals will result in a spatial low frequency filtering of the object, i.e. a filtering of its slow spatial variations.

Equation [35.27] also shows that, for a signal of given spectral band, the spatial low frequencies are returned better for small values of  $\theta$ , i.e. in forward scattering. But the zero spatial frequency can never be achieved, i) because of the signals used and ii) because of the inability of performing forward scattering measurements. Consequently, we do not have access to the average value of the object, i.e. to the quantitative aspect. This is the great limitation of this kind of tomography, which can provide access to media morphology only, such as classical ultrasound imaging. It is essentially a qualitative imaging technique.

Under these conditions, it is better to sacrifice the spatial low frequencies and carry out measurements in backscattering only, or to avoid moving away from the object too much, in order to reach the best resolution.

#### 35.1.3.7. Fixed scattering angle tomography

We can see that the measurements obtained with a single scattering angle and signals sufficiently broadband are enough to rebuild the object filtered on the crown defined by the spectral band of the signals.

Figure 35.5 shows the result obtained by backscattering ( $\pi = \theta$ ) on a phantom of a biological object in alginate made of 10% of polyethylene micro beads ( $C = 1529 \text{ m}^{-1}$ ,  $\rho = 964 \text{ kg.m}^{-3}$ ,  $\chi = 4,437 \times 10^{-10} \text{ m}^2 \text{N}^{-1}$ , at  $22^\circ$ ), of diameter 4.9 cm, drilled with 8 holes whose diameters range from 1 to 4.5 mm (0.5 mm step), submerged in water which also fills the holes ( $C_0 = 1489 \text{ m.s}^{-1}$ ,  $\rho_0 = 995 \text{ kg.m}^{-3}$ ,  $\chi_0 = 4,533 \times 10^{-10} \text{ m}^2 \text{N}^{-1}$ , at  $22^\circ$ ). In this experiment, we used a broadband ultrasound transducer of central frequency 2.25 MHz, bandwidth [1.4 MHz – 3 MHz] at  $-6\text{dB}$  (and [1.25 MHz – 3.75 MHz] at  $-15 \text{ dB}$ ), excited in the impulse mode. We carried out 180 acquisitions of the backscattered field, every  $2^\circ$ , using a mechanical scanning system. The contrast of the alginate object with respect to the ambient medium and to the holes filled with water was  $\mu_\chi = 2.11 \times 10^{-2}$ ,  $\gamma_\rho = 3.21 \times 10^{-2}$  (signal sampling frequency 20 MHz, quantification on 8 bits, reconstructions on  $512 \times 512$  pixels).

The artefacts inherent in the reconstruction technique by summation of the filtered back-projections are due to the limited number (180) of projections.

This result shows what would be obtained using a circular crown-antenna of 180 elements spaced every  $2^\circ$ , operating in backscattering, i.e. by running each transducer as a transmitter–receiver and using the 180 available backscattered signals.

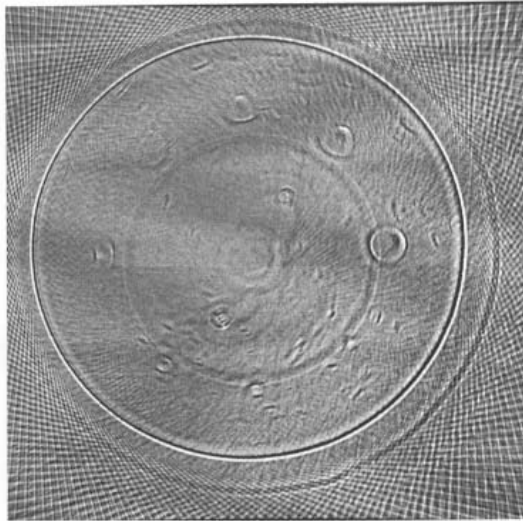


**Figure 35.5.** *Example of result of backscattering tomography*

The same type of image, but with lower quality (lower frequency image filtering, therefore worse resolution), is obtained with a lower scattering angle. For example, this can be achieved by turning the whole transmitter–receiver system (which is kept rigid to keep a fixed scattering angle) around the object.

#### 35.1.3.8. *Multiple scattering angles tomography*

If we have measurements according to several scattering angles, for example by conducting a scanning depending on the scattering angle in addition to the one on the incidence angle, or by using all available measurements on a circular crown-antenna around the object, we can add the reconstructed images from the various scattering angles (and therefore affected by a different spatial filtering), but covering each other for a large part. This results in an important improvement of the signal-to-noise ratio, by exploiting redundant information lying in the data.

Figure 35.6 shows the result obtained with the same phantom as previously used, under the same measurement conditions as above (same transducers, etc.). The images obtained for each scattering angle are now added (however, we avoid

performing too many frontal measurements, the transducer then being dazzled by the incident field). This result therefore simulates the one that would give a circular crown-antenna of 180 elements spaced every  $2^\circ$ , fully exploited, using all available scattering angles, or roughly  $180 \times 120$  scattering measurements. The improvement of the image quality is obvious.

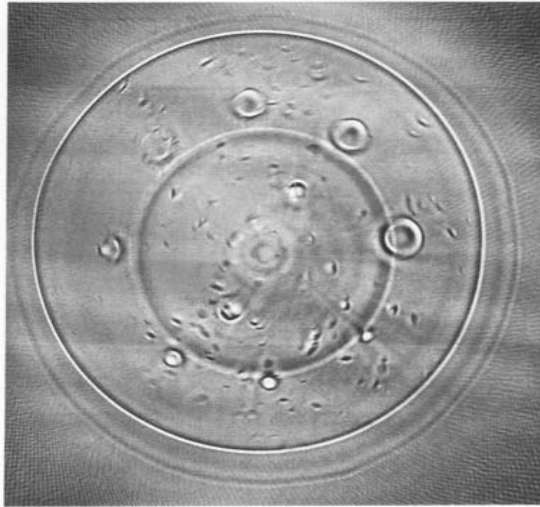


**Figure 35.6.** *Example of result of multiple scattering angles tomography*

#### 35.1.3.9. *Conclusion on ultrasonic diffraction tomography*

Although it leads in its current form, as classical ultrasound echography, to an imaging that is mainly qualitative (more advanced versions can be implemented, possibly leading to quantitative measurements, but at a price that is still too high to consider an application with the current technology), ultrasonic diffraction tomography provides a much better image quality than transmission tomography. The price of these improvements is a reasonable complication, consistent with the evolution of medical ultrasound equipment that now incorporates powerful computers. This gives hope that it will soon leave the “den” of laboratories.

#### 35.1.4. *Conclusion*

For didactic reasons, only basic ultrasonic tomography has been presented (very low contrast media, signals of infinite bandwidth, far-field calculations, etc.), leading to quite academic illustrations. But tomography takes its full extent only

when we leave these limited frameworks, without practical concerns. Thus, quoting only the work of the present authors, that technology can be extended to high-contrast objects like bones in the flesh (problem of detecting osteoporosis [LAS 01], [OUE 02]), to near-field scattering measures [MEN 02], to coupling of transmission and scattering techniques, and build ad hoc systems for a precise application such as breast imaging (for cancer detection [LAS 02], [FER 04]). Works along these lines currently abound in many laboratories. The technique is still in its infancy.

### 35.2. Bibliography

- [DEA 83] S.R. Deans, (ed.), *The Radon Transform and Some of its Applications*, John Wiley & Sons, 1983
- [GRE 81] B.J.F. Greenleaf, "Computerized transmission tomography", in P.D. Edmonds (ed.), *Methods of Experimental Physics: Ultrasonics*, Academic Press, 1981
- [FER 03] R. Ferriere, S. Mensah and J.P. Lefebvre, "Weakly inhomogeneous media tomography", *Ultrasonic Imaging*, 25(2), 122–133, 2003
- [GRA 02] P. Grangeat (ed.), *La Tomographie*, Hermes-Lavoisier, Paris, 2002
- [LAN 87] K.J. Langenberg, "Applied Inverse Problems for Acoustic, Electromagnetic and Elastic Wave Scattering", in P.C. Sabatier (ed.), *Basic methods of tomography and inverse problems*, Adam Hilger, 1987
- [LAS 01] P. E. Lasaygues, J.-P. Lefebvre, "Cancellous and cortical bone imaging by reflected tomography", *Ultrasonic Imaging*, 23(1), 55–70, 2001
- [LAS 02] P. Lasaygues, D. Tanne, S. Mensah and J.P. Lefebvre, "Circular antenna for breast ultrasonic diffraction tomography", *Ultrasonic Imaging*, 24(3), 177–89, 2002
- [LEF 85] J.P. Lefebvre, "La tomographie d'impédance acoustique", *Traitement du Signal*, vol.2, n°2, 103–10, 1985
- [LEF 88] J.P. Lefebvre, "La tomographie ultrasonore en réflexion", *Journ. Acoustique*, Vol.1, n°1–2, 123–8, 1988
- [LEF 94] J.P. Lefebvre, "Bases Physiques de l'acoustique", in P.J.T. Filippi (coord.) *Acoustique Générale*, Editions de Physique, 1994
- [MEA 00] P.M. Meaney, *et al.*, "The intensity dependence of lesion position shift during focused ultrasound surgery", *Ultrasound Med Biol.*, Vol. 26(3), 441–50, 2000
- [MEN 02] S. Mensah and R. Ferriere, "Near-field diffraction tomography", *Ultrasonic Imaging*, 24(1), 13–24, 2002
- [OUE 02] E. Ouedraogo, P. Lasaygues, J.-P. Lefebvre *et al.*, "Contrast and velocity ultrasonic tomography of long bones", *Ultrasonic Imaging*, 24, 135–146, 2002

## List of Authors

Jean-François ALLARD  
LAUM  
University of Maine  
Le Mans  
France

Christophe AYRAULT  
LAUM  
University of Maine  
Le Mans  
France

Cécile BARON  
Institut Jean le Rond d'Alembert  
Paris VI University  
France

Jean-François de BELLEVAL  
Laboratoire Roberval  
UTC  
Compiègne  
France

Aurore BLEUZEN  
Hôpital Bretonneau  
Tours  
France

Marc BONNET  
LMS  
CNRS-ECOLE POLYTECHNIQUE  
Palaiseau  
France

Bruno BROUARD  
LAUM  
University of Maine  
Le Mans  
France

Michel BRUNEAU  
LAUM  
University of Maine  
Le Mans  
France

Pierre CALMON  
LSUT  
CEA-Saclay  
Gif-sur-Yvette  
France

Bernard CASTAGNÈDE  
LAUM  
University of Maine  
Le Mans  
France

Michel CASTAINGS  
LMP  
University of Bordeaux  
Talence  
France

Stefan CATHELIN  
LOA – ESPCI  
Paris  
France

Dominique CATHIGNOL  
INSERM  
Lyon  
France

Jean-François CHAIX  
LCND – IUT  
University of the Mediterranean  
Aix en Provence  
France

Jean-Yves CHAPELON  
INSERM  
Lyon  
France

Gilles CORNELOUP  
LCND – IUT  
University of the Mediterranean  
Aix en Provence  
France

Nicolas DAUCHEZ  
LAUM  
University of Maine  
Le Mans  
France

Olivier DAZEL  
LAUM  
University of Maine  
Le Mans  
France

Claude DEPOLIER  
LAUM  
University of Maine  
Le Mans  
France

Marc DESCHAMPS  
LMP  
University of Bordeaux  
Talence  
France

Zine EL ABIDINE FELLAH  
LMA  
Marseille  
France

Rachid EL GUERJOURA  
LAUM  
University of Maine  
Le Mans  
France



Mohamed FELLAH  
Laboratoire de physique théorique  
USTHB  
Algiers  
Algeria

Mathias FINK  
LOA – ESPCI  
Paris  
France

Vincent GARNIER  
LCND – IUT  
University of the Mediterranean  
Aix en Provence  
France

Philippe GATIGNOL  
Laboratoire Roberval  
UTC  
Compiègne  
France

Nicolas GENGEMBRE  
IRISA-INRIA  
Rennes  
France

Vitaly GUSEV  
LPEC  
University of Maine  
Le Mans  
France

Michel HENRY  
LAUM  
University of Maine  
Le Mans  
France

Marie-Christine HO BA THO  
UTC  
Compiègne  
France

Cyril LAFON  
INSERM  
Lyon  
France

Denis LAFARGE  
LAUM  
University of Maine  
Le Mans  
France

Marc LAMBERT  
L2S-DRE  
CNRS-SUPELEC-Univ. Paris-Sud 11  
Gif-sur-Yvette  
France

Philippe LASAYGUES  
LMA  
Marseille  
France

Pascal LAUGIER  
LIP  
University of Paris VI  
France

Walter LAURIKS  
Université Catholique de Louvain  
Belgium

Jean-Pierre LEFEBVRE  
LMA  
Marseille  
France

Dominique LESSELIER  
L2S-DRE  
CNRS-SUPELEC-Univ. Paris-Sud 11  
Gif-sur-Yvette  
France

Alain LHÉMERY  
LSUT  
CEA-Saclay  
Gif-sur-Yvette  
France

Anne MAREC  
LAUM  
University of Maine  
Le Mans  
France

Serge MENSAH  
LMA  
Marseille  
France

Hanane NECHAD  
LEMA  
Faculté des Sciences et Techniques  
de Tours  
France

Olivier PONCELET  
LMP  
University of Bordeaux  
Talence  
France

Catherine POTEL  
LAUM  
University of Maine  
Le Mans  
France

Léandre POURCELOT  
Hôpital Bretonneau  
Tours  
France

Bruno RICHARD  
Laboratoire de Biophysique  
Faculté de Médecine  
Cochin Port-Royal  
Paris  
France

Daniel ROYER  
LOA - ESPCI  
Paris  
France

Sohbi SAHRAOUI  
LAUM  
University of Maine  
Le Mans  
France

Naima SEBAA  
Université Catholique de Louvain  
Belgium

Alexander SHUVALOV  
LMP  
University of Bordeaux  
Talence  
France

Rémi SOUCHON  
INSERM  
Lyon  
France

Mickaël TANTER  
LOA  
ESPCI  
Paris  
France

Jean-Hugh THOMAS  
LAUM  
University of Maine  
Le Mans  
France

Vincent TOURNAT  
LAUM  
University of Maine  
Le Mans  
France

François TRANQUART  
Bracco Research  
Plan Les Ouates  
Switzerland

This page intentionally left blank

# Index

## A, B

absorption coefficient, 722  
acoustic  
  axis, 579, 581  
  emission, 651, 652, 661, 670, 672, 673  
  tomography, 887  
  velocity, 771  
acquisition setup, 889, 894  
ageing, 652, 653, 654, 655, 656, 657, 658, 659, 660  
air flow resistivity, 683, 717  
air-spark-gap switch, 865  
angular  
  dispersion, 130  
  spectrum, 579, 582, 583  
anisotropic solid, 20, 55  
anisotropy, 654, 655, 656  
antisymmetric mode, 125  
autocorrelation, 803  
axial resolution, 794, 808  
azimuthal resolution, 794, 795

## B

backscattering, 786, 788-790, 887-898, 902-904  
basic scattering problem, 279

basis change, 70, 90, 91  
Bessel functions, 280  
Bio-Heat Transfer Equation (BHTE), 874  
biological tissues, 762, 792  
Biot  
  theory, 205, 206, 211, 277, 317  
  waves, 318  
Born approximation, 888, 896  
boundary conditions, 30, 31, 33, 34, 36, 45, 57, 66, 70, 75, 79, 82, 85, 92, 318  
Boyle–Mariotte law, 679  
brain  
  imaging, 823  
  surgery, 833  
breadboard, 685  
Brewster angle, 321, 695, 700  
bright mode (B-mode), 798  
Broadband Ultrasound Attenuation (BUA), 780  
bulk waves, 341, 396, 564

## C

Cagniard–de Hoop method, 507, 508, 511, 517, 524, 537, 547, 549, 550, 552, 558  
cardiac imaging, 812

cardiography, 848  
 cartography, 409  
 Cauchy integral, 520, 531, 536, 541  
 cavitation, 863, 874  
 ceramic, 793, 794  
 change, 71, 73, 78, 82, 89, 91  
 characteristic, 652  
 Christoffel  
     equation, 20, 64, 344, 515, 516,  
         528, 530  
     matrix, 344  
     tensor, 20, 21, 22, 63, 64  
 collimated, 584, 585, 588  
 color  
     coding, 804  
     Doppler, 803, 804  
 composite plate, 577, 581  
 composites, 61, 93, 94  
 compression wave, 12, 13, 206, 219,  
     220, 869, 870, 871  
 compression–dilatation stresses, 205  
 condition of the radiation *ad*  
     *infinitum*, 114  
 conservation law, 7  
 continuous Doppler, 801, 802  
 contour reconstruction, 410  
 cortical bone, 760, 761, 762, 772,  
     776, 777, 778, 783, 784, 786, 787,  
     791, 792  
 creep, 661, 663, 664, 665, 666, 667,  
     669, 671, 672  
 critical angle, 49, 50, 58, 92  
 cross-correlation, 691  
 cyclotron radiation, 776

## D

D.O.R.T. method, 411, 412  
 darcy, 684  
 decomposition in plane waves, 577  
 densities, 3–8, 23, 24  
 derivation, 410, 414  
 derivative, 416–418

Dirac  
     delta, 549, 553  
     pulse, 393  
 direction of propagation, 18, 19, 20,  
     22, 24, 25  
 dispersion  
     curves, 125, 135  
     equation, 136  
 displacement–stress vector, 67, 68,  
     72, 73, 74, 90  
 domotics, 399  
 Doppler  
     effect, 800, 801, 802  
     frequency, 800, 801, 803, 804

## E

echography, 888, 892, 905  
 echosismography, 847  
 eigenmodes, 113  
 Einstein convention, 10  
 elastic modulus, 765, 774, 776  
 elastic  
     solid, 8  
     wave, 341, 342, 343, 344  
     wave equation, 11, 16  
 elastography, 841, 843, 860, 861  
 electroconductive generator, 865, 866  
 electrolyte resistivity, 687  
 electromagnetic generator, 867  
 electromechanical coupling  
     coefficient, 343, 345, 346, 347,  
     348, 355  
 endocavitary, 872, 876  
 energy conservation, 7, 23  
     law, 7  
 energy velocity, 23, 24, 25, 27, 28  
 equivalent circuits, 351  
 Euler equations, 208, 209, 211  
 evanescent waves, 49

**F**

fan geometry, 892  
 Fast Fourier Transform (FFT), 365, 578, 585, 586, 591, 593  
 Fermat  
   path, 376, 377, 378, 379, 380, 381  
   principle, 525  
   surface transducer, 394  
 fibrous material, 277  
 Fibroscan®, 851  
 field theory, 208  
 fixed embedded wall, 36  
 flexibility tensor, 14  
 Floquet waves, 75, 83, 85, 87, 88, 90, 91, 92, 93  
 fluid  
   medium, 3, 18, 19, 363, 374, 376, 380, 381  
   propagation medium, 363  
 fluid–solid media, 370  
 foam, 571, 572  
 formulation, 408, 421  
 Fourier  
   integrals, 578, 585, 586  
   spectrum plane, 897  
   spectrum, 897, 899  
   transform, 356, 357, 360–366, 369, 508–512, 518, 775, 789, 790, 891, 892, 895, 899–901  
   transformations, 18  
 fragmentation, 870, 871  
 free  
   modes, 113, 114  
   surfaces, 33  
 frequency dispersion, 128  
 fundamental dynamic equation, 4, 9, 10

**G, H**

gain control, 796  
 generalized modal waves, 133  
 global matrix method, 70–73, 78

Green function, 507–509, 516, 517, 522–525, 528, 533, 536, 540, 546, 549, 557, 558, 788, 895  
 group  
   direction, 131, 133  
   velocity, 129, 130  
 guided waves, 123  
 Hanafy lenses, 795  
 Hankel functions, 280, 282  
 Haver capillaries, 761  
 Havers canal, 761  
 Helmholtz  
   equation, 19  
   resonator, 750  
 hepatic imaging, 814  
 HIFU, 863, 871, 872, 873, 875, 876, 877, 878  
   generator, 872  
 Hilbert transform, 372  
 homogenous medium, 360  
 Hooke law, 66, 77, 342, 512, 764  
 human skeleton, 760

**I, J**

identification, 403  
 immersed elastic layer, 126  
 impedance matrix of layer, 76, 77, 349  
 impedant walls, 35  
 impulse regime, 366  
*in vitro*, 759, 829, 838  
*in vivo*, 759, 779, 787, 789, 792, 845, 852, 854, 856, 859  
 incidence plan, 42  
 incident wave, 722, 723  
 independent scattering  
   approximation, 278, 279  
 inhomogenous wave, 58, 68  
 interface  
   of perfect adherence, 38  
   separating a fluid and a solid, 37  
   separating two fluid media, 37  
   separating two elastic solids, 38

inverse Fourier transformation, 580, 592

inverse propagation, 887

isotropic

material, 16, 384

medium, 541

solid, 10, 16, 18, 19, 22, 42, 43

transverse material, 15

“jacketed” material, 215

Jacobian, 585, 587, 588, 589, 590

determinant, 362

## K, L

kidney stone, 827, 828, 829, 831, 863, 870, 877

Kirchoff's law, 352

KLM model, 353

Kronecker delta, 513

Kundt tube, 719, 723

Lagrangian density, 208, 209

Lamb

problem, 508, 540, 547

wave, 124, 125, 126, 133, 564, 574

Lamé constants, 10

Langevin, 863

Laplace transform, 508, 509, 512, 517, 518, 522, 550

Laplace–Fourier transform, 508

lateral resolution, 794, 808

leaky wave, 134, 135

least squares method, 780

level set, 410, 413, 415

linear

acoustics, 5

elasticity, 13

sampling, 411

linearization at the boundaries, 31

Lippmann–Schwinger equation, 408, 895

longitudinal waves, 19, 22, 25, 26, 27

## M

mass conservation law, 4, 6

mass–spring system, 746, 754

matrix of surfacic impedance, 79

mechanical scanning, 798

medical ultrasound, 794, 795, 825

medium

fluid medium, 3, 18, 19, 363, 374, 376, 380, 381

fluid propagation medium, 363

fluid–solid media, 370

homogenous medium, 360

isotropic medium, 541

multilayered, 61, 70, 73, 77, 78, 93, 94

periodic multilayered medium, 82

semi-infinite medium, 784

microbubbles, 805, 808, 810, 812, 823

modal

pattern, 113, 114

pseudo-waves, 133, 135

sub-space, 114, 115

waves, 113, 126, 127, 136

waves in multilayered structures, 127

mode conversion, 44

monochromatic

regime, 360

waves, 17, 18, 19

MRI elastography, 858

multilayered

media, 61, 70, 73, 77, 78, 93, 94

structure, 577, 578, 581

musculotendinous exploration, 822

## N

Newton–Raphson, 562, 565

method, 564

algorithm, 565

non-destructive

nonlinear imaging, 810

testing, 399, 411, 412



nonlinear ultrasound imaging, 804  
 numerical  
   problem, 69, 70, 75, 91  
   stability, 76

## O, P

obstetric imaging, 816  
 ophthalmic imaging, 821  
 optimization, 405, 406, 408, 409, 418  
 orthotropic material, 15  
 osseous tissue, 759, 761, 767, 769,  
   771, 776, 779, 784, 787, 791  
 partial decoupling, 319  
 particle  
   displacement, 51, 65, 66, 67, 318  
   speed, 3, 6  
 pelvic imaging, 818  
 pencil  
   method, 373-375, 378, 380, 392-  
     396  
   propagation matrix, 383, 384, 386,  
     388, 391  
 perfectly reflective wall, 34  
 periodic multilayered medium, 82  
 phase  
   directions, 132  
   velocity, 18, 21, 24, 25, 118, 122,  
     123, 128, 129, 130, 133, 135,  
     781  
 phased array, 799  
 piezocomposite material, 347, 355  
 piezoelectric  
   generator, 867  
   medium, 341, 351  
   solid, 341, 342, 344, 349, 350, 352  
 plane  
   waves, 17, 19, 20, 21  
   interface, 42  
 plastic foams, 277  
 Poisson  
   coefficient, 226, 705, 710, 713,  
     714, 765, 776, 778

  ratio, 10  
 polarization vector, 18  
 polymethylacrylate (PMMA), 774,  
   775  
 polyurethane foams, 698, 699  
 poroelastic material, 845  
 porosimeter, 679, 681, 682  
 porosity, 677-682, 686, 689, 690,  
   695, 696, 698, 700-706, 709, 712,  
   714, 717  
 porous material, 210, 211, 215, 221-  
   228, 277, 317, 319, 677, 678, 683-  
   686, 687, 689, 692, 694, 695, 700,  
   703, 704, 714, 716, 749-753  
 potential  
   energy, 7, 23, 24  
   vector, 12  
 Poynting vector, 23, 392  
 Prandtl number, 692  
 precision micrometer, 680  
 pressure, 3, 4, 5, 8, 9  
 propagation velocity, 767, 768, 779,  
   780, 781, 783, 784, 786  
 pulse inversion imaging, 809

## Q, R

quasi-longitudinal, 22, 25, 26, 27, 55  
 quasi-static elastography, 842  
 Radon transform, 891  
 Rayleigh  
   equation, 551  
   wave, 116, 117, 119, 120, 121,  
     123, 126, 131, 133, 134, 140,  
     318, 319, 323, 541, 543, 545,  
     553, 556  
 Rayleigh-Plesset equation, 806  
 Rayleigh-Sommerfeld integral, 392,  
   395  
   radiation integral, 374  
 reciprocity violation, 411, 412  
 reflected wave, 722

reflection and transmission  
 coefficients, 53, 70, 73, 78, 92, 93  
 reflection coefficient, 582, 592, 695,  
 696, 700, 773, 774, 775  
 relaxation wave, 869, 870, 871  
 renal imaging, 815  
 Riemann sheets, 533  
 rigid wall, 745, 746

## S

sagittal plane, 42, 43  
 SAM, 773, 792  
 scalar potential, 6, 12, 19  
 scanning acoustic microscopy, 773  
 Scholte wave, 318  
 Scholte–Stoneley wave, 121, 123,  
 126, 127  
 seismic tomography, 893  
 seismic-reflection, 888  
 seismology, 399  
 semi-infinite medium, 784  
 septum, 751  
 shear  
 modulus, 209, 215, 225, 226, 765,  
 841, 842, 843, 857  
 wave, 12, 848, 850, 851, 854, 855,  
 856, 858  
 shock wave, 864, 865, 866, 867, 868,  
 869, 870, 871, 875, 877  
 signal-to-noise ratio, 856  
 Simplex  
 algorithm, 565  
 method, 564  
 simulated time-reversal, 834  
 slowness, 63, 64, 65, 66, 72  
 surface, 25, 26, 27, 48, 56, 377,  
 379, 387, 388, 389  
 vector, 25  
 Snell's law, 534  
 Snell–Descartes  
 law, 364, 370, 379, 385  
 reflection and refraction laws, 48

solid/solid interface of the type  
 collage, 39  
 sonoelasticity, 842, 860, 861  
 spongy bone, 761, 772, 778, 786,  
 787, 788  
 state  
 equation, 4  
 vector, 67, 86, 89  
 stiffness  
 matrices of layers, 76  
 tensor, 13, 21, 25  
 Stoneley wave, 116, 121, 123, 318,  
 319  
 strain tensor, 8, 11, 13, 14, 342  
 stress  
 tensor, 8, 9, 11, 13, 16, 17  
 vector, 9, 66  
 stress–strain relationship, 10  
 sub-space of evolution, 114  
 supersonic shear imaging, 856  
 Suprasil, 775  
 surface and interface waves, 116  
 surface impedance, 719, 720, 721,  
 722, 723, 724, 725, 727, 728, 729,  
 730, 731  
 symmetric mode, 125

## T

tangential stress, 224  
 temporal convention, 52  
 therapeutic applications, 863, 864  
 thermal expansion coefficient, 206,  
 225  
 Thomson–Haskell method, 73  
 TH waves, 43  
 thyroid imaging, 820  
 time gain control (TGC), 796  
 time motion (TM) mode, 799  
 time-reversal, 399, 406, 827, 828,  
 829, 830, 831, 833, 834, 839  
 mirror, 399, 828

titanium, 775  
 tomodensitometry, 887  
 tomography, 887, 888, 889, 891, 893,  
 898, 899, 900, 903, 904, 905, 906  
 topological, 403, 418  
 tortuosity, 686, 687, 688, 689, 690,  
 693, 695, 696, 697, 698, 700, 701,  
 702, 703, 716, 717, 718, 746  
 transfer matrix, 70, 73, 74, 75, 76, 78,  
 79, 80, 82, 84, 85, 88, 89, 90, 94  
 method, 73, 745  
 transient elastography, 842, 845, 847,  
 848, 849, 851, 854, 857, 859, 860,  
 861  
 transmission coefficient, 582, 592,  
 593  
 transverse wave, 20, 22, 25, 27, 764,  
 765, 766  
 Tumour Therapy System, 876  
 TV waves, 43  
 Two-Microphone-Three-Calibration  
 (T.M.T.C.), 723, 726, 731

## U

ultrasonic  
 beams, 359, 373, 395, 577  
 characterization, 759  
 echo, 829  
 frequency, 793  
 hyperthermia, 873  
 propagation, 787  
 pulse compression, 830  
 tests, 762, 779, 787  
 tomography, 887  
 wave, 562, 563, 793, 796, 804,  
 807, 867, 872, 873, 874  
 ultrasonography, 793, 820, 888

ultrasound  
 elastography, 842, 843  
 focalization, 833  
 imaging, 793, 823  
 transmission in contact (UTC),  
 767, 768, 769  
 transmission in immersion (UTI),  
 767, 768, 769  
 underwater acoustics, 399, 412  
 “unjacketed” material, 217

## V, W,

variable static pressure, 696  
 vascular imaging, 821  
 vectorial potential, 19  
 velocity of sound, 5  
 velocity potential, 6  
 vibro-acoustography, 842  
 viscoelastic  
 behavior, 705, 717  
 module, 561  
 viscous losses, 206, 207, 227  
 wall  
 impedance, 35  
 reactance, 36  
 resistance, 35  
 wave  
 equation, 6  
 number vector, 18, 19  
 planes, 17, 18  
 surface, 27  
 wavelength, 18

## X, Y

X-ray  
 computed tomography, 887  
 densitometry, 783, 786  
 microtomography, 776  
 Young’s modulus, 10, 226, 713, 754,  
 763, 764, 767, 774, 776